Nasser Ashgriz *Editor*

Handbook of Atomization and Sprays

Theory and Applications

Aroma360 - Exhibit 1028

Springer

Handbook of Atomization and Sprays

N. Ashgriz
Editor

Handbook of Atomization and Sprays

Theory and Applications

Springer

Editor
N. Ashgriz
University of Toronto
Dept. Mechanical & Industrial Engineering
King's College Road 5
M5S 3G8 Toronto Ontario
Canada
ashgriz@mie.utoronto.ca

ISBN 978-1-4419-7263-7 e-ISBN 978-1-4419-7264-4
DOI 10.1007/978-1-4419-7264-4
Springer New York Dordrecht Heidelberg London

Library of Congress Control Number: 2011922132

© Springer Science+Business Media, LLC 2011
All rights reserved. This work may not be translated or copied in whole or in part without the written permission of the publisher (Springer Science+Business Media, LLC, 233 Spring Street, New York, NY 10013, USA), except for brief excerpts in connection with reviews or scholarly analysis. Use in connection with any form of information storage and retrieval, electronic adaptation, computer software, or by similar or dissimilar methodology now known or hereafter developed is forbidden.
The use in this publication of trade names, trademarks, service marks, and similar terms, even if they are not identified as such, is not to be taken as an expression of opinion as to whether or not they are subject to proprietary rights.

Printed on acid-free paper

Springer is part of Springer Science+Business Media (www.springer.com)

Preface

This book is intended to provide an overview of the processes that occur in atomization and spray systems. It covers both the classical, theoretical concepts of atomization and more recent developments. The book is organized into four parts. Part I deals with the basic elements of a liquid that form a spray. These are liquid jets, sheets, and drops. Part II deals with theories of atomization and sprays. Part III discusses spray nozzles and their behavior. Part IV concludes with spray applications.

The atomization process is very complex, involving highly turbulent and convoluted interfaces as well as breakup and coalescence of liquid masses. However, the models currently used to describe the atomization process are based on simple laminar instability theories. In many spray nozzles, a liquid is forced through an orifice. These types of nozzles form a liquid jet at low injection pressures. Therefore, the instability theory of liquid jets is used as a first estimate of the droplets that may be formed by these nozzles. In many other spray nozzles, a liquid sheet is formed prior to atomization. Therefore, the instability theory of a liquid sheet is used for these prefilming nozzles. Part I introduces the instability theories for these two configurations. Linear and nonlinear instabilities of a free liquid jet moving in air and subject to small perturbations are discussed in Chap. 1. These theories intend to provide the growth rate of a disturbance wave. The growth rate of the fastest growing disturbance is later used in the atomization theories to obtain a droplet size due to the breakup of a jet. Therefore, the linear theories provide an estimate of the main droplet size emerging from capillary breakup. Formation of satellite droplets and other effects such as thermocapillarity or swirl are also discussed in this chapter. Chapter 2 is devoted to jet bending and Chap. 3 discusses the linear and nonlinear instability theories for a liquid sheet. Instability of a liquid sheet results in the formation of cylindrical liquid ligaments, which have the same fate as liquid jets. Therefore, liquid sheets and liquid jets in combination are used to describe the atomization process in nozzles that form a film or sheet prior to atomization (prefilming atomizers). The spray itself is made of millions of droplets that flow inside a gas. The interaction of a liquid drop with a coflowing gas, including oscillation, deformation, and breakup, is discussed in Chaps. 4–6. Drops may also collide with each other (Chap. 7) or with the walls of the system (Chap. 8).

Part II utilizes the basic instability theories discussed in Part I to develop models for the atomization and spray systems. Chapters 9–11provide the current atomization theories used in spray systems to predict a droplet size. The most commonly used atomization models, namely, the Taylor analogy breakup (TAB) model, the enhanced-TAB (E-TAB) model, and the WAVE model, and variations and improvements of these models are discussed in Chap. 9; the concept of flash atomization and supercritical injection are introduced in Chaps. 10 and 11, respectively. Chapters 12–16 introduce spray theories dealing with spray evaporation, combustion, and freezing. Spray evaporation is modeled based on evaporation of individual droplets, which is discussed in Chap. 12, by means of the conservation equations for mass, species, and energy of the liquid and gas phases. The results of single droplet evaporation are simplified and used for heat and mass transfer for forced and non-forced convection through Nusselt and Sherwood numbers. Reacting sprays are discussed in Chap. 13, introducing chemical kinetics, ignition processes, and mixing-controlled, flamelet, and PDF combustion models. A brief discussion on the pollutant and particulate models is provided in this chapter as well. Some other important spray issues such as spray group combustion and sprays in non-continuum regimes are also discussed in Part II. Flame propagation modes between neighboring droplets and macroscopic flame propagation modes in spray elements, and the excitation mechanism of group combustion (diffusion flame enclosing droplets) is described in Chap. 14. The evaporation process is altered significantly at low pressures. This is discussed in Chap. 15 for flows in which the mean free path of the evaporated molecules is large compared with the droplet radius. This chapter discusses the kinetic theory of gases as applied to molecules having the Maxwell–Boltzmann distribution of molecular velocities. The concept of the Knudsen regime is introduced to develop a transport equation for the molecules at the droplet interface. Droplet freezing and solidification is considered in Chap. 16 with emphasis on a four-stage model for solidification. Because of the recent enhancement in computational capabilities, direct numerical modeling of the atomization process has become more feasible. The models used for tracking deforming and breaking interfaces to simulate the atomization process are discussed in Chaps. 17 and 18. The spray models that track droplets are introduced in Chaps. 19 and 20. The turbulence models used in spray modeling, including Reynolds-averaged Navier–Stokes (RANS) and large eddy simulation (LES) modeling, are introduced in Chap. 19; the non-continuum-based computational techniques, for example, the lattice Boltzmann method (LBM), are introduced in Chap. 20. Chapters 21 and 22 introduce special topics of spray wall impact and spray-spray impingements and interaction. Chapter 22, in particular, addresses questions like, "is the use of multiple sprays more effective than the use of a single spray, or is it possibly detrimental? And, if the latter is true, can the situation be ameliorated by manipulation of the physics through geometric and other factors that relate to the sprays?"

The main objective of atomization and spray systems is to generate a spray with a desired droplet size and velocity distribution. Part III deals directly with spray nozzles. This part starts with Chap. 23, which discusses the concept of droplet size

distribution. Chapter 24 provides an overview of various spray nozzles and their droplet size distributions. A series of size correlations are included at the end of Chap. 24 for ease of use. Various correlations are compiled from different sources. Chapters 25–33 provide more detailed discussions on different types of nozzles. In particular, plain orifice atomizers, pintle injectors, jet-in-crossflow atomizers, impinging jet atomizers, splash plate nozzles, electrosprays, and several other atomizers are discussed in Part III.

Part IV is devoted to spray applications. This part is by no means exhaustive of all applications and is kept limited to applications in various engines, melt atomization, and several other specific applications. In engine applications, port fuel injection (PFI), throttle-body injection (TBI), direct injection (DI), and diesel injection are discussed in Chap. 34. For gas turbine engines, the modeling methodologies, including LES, of reacting flows in realistic combustor configurations are discussed in Chap. 35. Another spray application extensively discussed in this book is melt atomization and powder generation. Melt atomization, which is the dominant method used commercially to produce metal and alloy powders, is considered in Chap. 36. Mechanisms of melt breakup and atomization, powder morphology, droplet dynamics, and so on are considered. In addition, fundamentals of spray drying, spray pyrolysis, spray freeze drying, low pressure spray pyrolysis, flame spray pyrolysis, and emulsion combustion method are described in Chaps. 37–40. Sprays have an important application in drug delivery to the lungs. Chapter 41 discusses the pharmaceutical aerosol sprays. The book is closed with fire sprinklers discussed in Chap. 42.

N. Ashgriz

Contents

Part I Dynamics of Liquid Jets, Sheets and Drops

1 Capillary Instability of Free Liquid Jets 3
N. Ashgriz and A.L. Yarin

2 Bending and Buckling Instabilities of Free Liquid Jets: Experiments and General Quasi-One-Dimensional Model 55
A.L. Yarin

3 Instability of Liquid Sheets 75
N. Ashgriz, X. Li, and A. Sarchami

4 Dynamics of Liquid Droplets 97
A. Mashayek and N. Ashgriz

5 Oscillation of Droplets and Bubbles 125
N. Ashgriz and M. Movassat

6 Droplet Deformation and Breakup 145
D.R. Guildenbecher, C. López-Rivera, and P.E. Sojka

7 Droplet Collision 157
G. Brenn

8 Droplet Impact on a Solid Surface 183
A.L.N. Moreira, A.S. Moita, and S. Chandra

Part II Atomization and Spray Models

9 Atomization Models 215
C.A. Chryssakis, D.N. Assanis, and F.X. Tanner

10 Flashing Sprays 233
R. Karami and N. Ashgriz

11 Supercritical and Transcritical Injection 255
P. Seebald and P.E. Sojka

12 Evaporating Sprays 263
F.X. Tanner

13 Reacting Sprays 279
F.X. Tanner

14 Spray Group Combustion 299
A. Umemura

15 Droplet Evaporation in the Non-continuum Regime 315
E.J. Davis

16 Droplet Freezing and Solidification 327
F.X. Tanner

17 Numerical Techniques for Simulating the Atomization Process 339
N. Ashgriz

18 Modeling Atomization Using Boundary Element Methods (BEM) ... 359
S.S. Yoon and S.D. Heister

19 Continuum-Based Methods for Sprays 383
F.X. Tanner

20 Lattice Boltzmann Method for Sprays 425
K.N. Premnath and J. Abraham

21 Spray-Wall Impact 441
A.L.N. Moreira and M.R. Oliveira Panão

22 Interacting Sprays 457
J.B. Greenberg

Part III Atomizers and Spray Generators

23 Drop Size Distributions 479
A. Déchelette, E. Babinsky, and P.E. Sojka

24 Spray Nozzles 497
K. Omer and N. Ashgriz

25 Drop-on-Demand Drop Generators 581
M. Eslamian and N. Ashgriz

26 Droplet Stream Generator 603
G. Brenn

27 Plain Orifice Spray Nozzles 625
S.D. Heister

28 Pintle Injectors 647
S.D. Heister

29 Atomization of a Liquid Jet in a Crossflow 657
A. Mashayek and N. Ashgriz

30 Impinging Jet Atomization 685
N. Ashgriz

31 Splash Plate Atomizers 709
A. Sarchami and N. Ashgriz

32 Electrosprays 727
F. Sultan, N. Ashgriz, D.R. Guildenbecher, and P.E. Sojka

33 Swirl, T-Jet and Vibrating-Mesh Atomizers 755
M. Eslamian and N. Ashgriz

Part IV Spray Applications

34 Spray Applications in Internal Combustion Engines 777
K. Lee and J. Abraham

35 Spray Modeling and Predictive Simulations in Realistic Gas-Turbine Engines 811
S.V. Apte and P. Moin

36 Melt Atomization 837
B. Zheng and E.J. Lavernia

37 Spray Drying, Spray Pyrolysis and Spray Freeze Drying 849
M. Eslamian and N. Ashgriz

38 Low-pressure Spray Pyrolysis 861
W.-N. Wang, A. Purwanto, and K. Okuyama

39 Flame Spray Pyrolysis 869
A. Purwanto, W.-N. Wang, and K. Okuyama

40 Particle Production via Emulsion Combustion Spray Method 881
M. Eslamian, M. Ahmed, and N. Ashgriz

41 Pharmaceutical Aerosol Sprays for Drug Delivery to the Lungs ... 899
W.H. Finlay

42 Fire Suppression 909
C. Presser and J.C. Yang

Index 927

Contributors

J. Abraham School of Mechanical Engineering, Purdue University, West Lafayette USA, jabraham@purdue.edu

M. Ahmed Mechanical Engineering Department, Assiut University, Assiut, Egypt

S.V. Apte School of Mechanical, Industrial and Manufacturing Engineering, Oregon State University, Corvallis, OR 97331, USA, sva@engr.orst.edu

N. Ashgriz Department of Mechanical and Industrial Engineering, University of Toronto, Toronto, Ontario, Canada, ashgriz@mie.utoronto.ca

D.N. Assanis Department of Mechanical Engineering, University of Michigan, Ann Arbor, MI, USA, assanis@umich.edu

E. Babinsky Maurice J. Zucrow Laboratories, School of Mechanical Engineering, Purdue University, West Lafayette, IN, USA

G. Brenn Graz University of Technology, Institute of Fluid Mechanics and Heat Transfer, Graz, Austria, brenn@fluidmech.tu-graz.ac.at

S. Chandra Department of Mechanical and Industrial Engineering, University of Toronto, Toronto, Ontario, Canada, Chandra@mie.utoronto.ca

C.A. Chryssakis National Technical University of Athens, School of Naval Architecture & Marine Engineering, Division of Marine Engineering, Heroon Polytechniou 9, GR-15773, Zografou, Athens, Greece, cchryssa@naval.ntua.gr

E.J. Davis Department of Chemical Engineering, Box 351750, University of Washington, Seattle, WA 98195-1750, USA, davis@cheme.washington.edu

A. Déchelette Maurice J. Zucrow Laboratories, School of Mechanical Engineering, Purdue University, West Lafayette, IN, USA

M. Eslamian Department of Mechanical and Industrial Engineering, University of Toronto, Toronto, Ontario, Canada, m.eslamian@utoronto.ca

W.H. Finlay Department of Mechanical Engineering, University of Alberta, Canada, Warren.Finlay@ualberta.ca

J.B. Greenberg Faculty of Aerospace Engineering, Technion, Israel Institute of Technology, Haifa, Israel, aer9801@aerodyne.technion.ac.il

D.R. Guildenbecher Maurice J. Zucrow Laboratories, School of Mechanical Engineering, Purdue University, West Lafayette, IN 47907-2014, USA

S.D. Heister School of Aeronautics and Astronautics, Purdue University, West Lafayette, Indiana, USA, heister@purdue.edu

R. Karami Department of Mechanical and Industrial Engineering, University of Toronto, Toronto, Ontario, Canada

E.J. Lavernia Department of Chemical Engineering and Materials Science, University of California, Davis, CA, USA, lavernia@ucdavis.edu

K. Lee Department of Mechanical Engineering, Hanyang University, South Korea, hylee@hanyang.ac.kr

X. Li Department of Mechanical and Mechatronics Engineering, University of Waterloo, Waterloo, Ontario, Canada

C. López-Rivera School of Mechanical Engineering, Purdue University, West Lafayette, IN, USA

A. Mashayek Department of Physics, University of Toronto, Toronto, Canada

P. Moin Center for Turbulence Research, Stanford University, Palo Alto, CA, USA, moin@stanford.edu

A.S. Moita Department of Mechanical Engineering, Technical University of Lisbon – Instituto Superior Técnico, Lisbon, Portugal, anamoita@dem.ist.utl.pt

A.L.N. Moreira Department of Mechanical Engineering, Technical University of Lisbon – Instituto Superior Técnico, Lisbon, Portugal, moreira@dem.ist.utl.pt

K. Okuyama Department of Chemical Engineering, Hiroshima University, Higashi Hiroshima, Japan, okuyama@hiroshima-.ac.jp

K. Omer Department of Mechanical and Industrial Engineering, University of Toronto, Toronto, Ontario, Canada, kaab.omer@utoronto.ca

M.R. Oliveira Panão Instituto Superior Técnico, IN+ Centro de Estudos em Inovação Tecnologia e Políticas de Desenvolvimento, Lisboa, Portugal, mpanao@dem.ist.utl.pt

K.N. Premnath Mechanical Engineering, University of Wyoming, USA, knandhap@uwyo.edu

C. Presser National Institute of Standards and Technology, 100 Bureau Dr., Stop 8320, Gaithersburg, MD 20899-8320, USA, cpresser@nist.gov

A. Purwanto Department of Chemical Engineering, Hiroshima University, Higashi Hiroshima, Japan; Department of Chemical Engineering, Sebelas Maret University, Surakarta, Indonesia, aguspur@uns.ac.id

A. Sarchami Department of Mechanical and Industrial Engineering, University of Toronto, Toronto, Canada

P. Seebald Maurice J. Zucrow Laboratories, School of Mechanical Engineering, Purdue University, West Lafayette IN, USA

P.E. Sojka Maurice J. Zucrow Laboratories, School of Mechanical Engineering, Purdue University, IN, USA, sojka@purdue.edu

F. Sultan Department of Mechanical and Industrial Engineering, University of Toronto, Toronto, Ontario, Canada, Sultan.farhan@gmail.com

F.X. Tanner Department of Mathematical Sciences, Michigan Technological University, Houghton, MI, USA, tanner@mtu.edu

A. Umemura Department of Aerospace Engineering, Nagoya University, Nagoya, Japan, akira@prop.nuae.nagoya-u.ac.jp

W.-N. Wang Department of Chemical Engineering, Hiroshima University, Higashi Hiroshima, Japan; Department of Energy, Environmental and Chemical Engineering, Washington University in St. Louis, St. Louis, USA, wnwang.yz@gmail.com

J.C. Yang National Institute of Standards and Technology, Gaithersburg, MD, USA, cary@nist.gov

A.L. Yarin Department of Mechanical and Industrial Engineering, University of Illinois at Chicago, Chicago, IL, USA, ayarin@uic.edu

S.S. Yoon School of Mechanical Engineering, Korea University, South Korea, skyoon@korea.ac.kr

B. Zheng Department of Chemical Engineering and Materials Science, University of California, Davis, USA, bzheng@ucdavis.edu

Part I
Dynamics of Liquid Jets, Sheets and Drops

Chapter 1
Capillary Instability of Free Liquid Jets

N. Ashgriz and A.L. Yarin

Abstract This chapter deals with capillary instability of straight free liquid jets moving in air. It begins with linear stability theory for small perturbations of Newtonian liquid jets and discusses the unstable modes, characteristic growth rates, temporal and spatial instabilities and their underlying physical mechanisms. The linear theory also provides an estimate of the main droplet size emerging from capillary breakup. Formation of satellite modes is treated in the framework of either asymptotic methods or direct numerical simulations. Then, such additional effects like thermocapillarity, or swirl are taken into account. In addition, quasi-one-dimensional approach for description of capillary breakup is introduced and illustrated in detail for Newtonian and rheologically complex liquid jets (pseudoplastic, dilatant, and viscoelastic polymeric liquids).

Keywords Capillary instability of liquid jets · Curvature · Elongational rheology · Free liquid jets · Linear stability theory · Nonlinear theory · Quasi-one-dimensional equations · Reynolds number · Rheologically complex liquids (pseudoplastic, dilatant, and viscoelastic polymeric liquids) · Satellite drops · Small perturbations · Spatial instability · Surface tension · Swirl · Temporal instability · Thermocapillarity · Viscosity

Introduction

A liquid jet emanating from a nozzle into an ambient gas may breakup into small drops when it is subjected to even minute disturbances. These disturbances may be in the form of surface displacement, pressure or velocity fluctuations in the supply system or on the jet surface, as well as fluctuations in liquid properties such as temperature, viscosity, or surface tension coefficient. The instability and breakup of

N. Ashgriz (✉)
Department of Mechanical and Industrial Engineering, University of Toronto, Toronto, Canada, L3T 7N
e-mail: ashgriz@mie.utoronto.ca

N. Ashgriz (ed.), *Handbook of Atomization and Sprays*,
DOI 10.1007/978-1-4419-7264-4_1, © Springer Science+Business Media, LLC 2011

liquid jets into drops has been a subject of interest since the early nineteenth century and has continued to this date [1–20].

In order to characterize the instability of a capillary jet, a harmonic disturbance is imposed on the jet and its growth rate and other jet characteristics, such as jet breakup length and satellite formation, are investigated. Different types of disturbances, such as pressure, surface, inlet velocity and temperature disturbances have been used. Pressure disturbances can be due to application of a sound wave on the jet. Surface disturbances can be in the form of using a piezoelectric transducer at the nozzle which contracts and expands periodically by applying a periodic voltage on it. Velocity disturbances can be applied by using an oscillating flow. Temperature disturbances can be introduced by applying a periodic heating on a jet. Temperature changes the liquid surface tension, which affects the capillary action on the jet. Disturbances introduced by adding surfactants to the liquid jet affect it similarly to temperature.

Studies of capillary instability have revealed that a liquid jet is unstable for axial disturbances with wave numbers less than a cut-off wave number k_c, but stable otherwise. For each wavelength of an unstable disturbance one main drop and one or more usually smaller drop(s), referred to as the satellite or spherous drop(s), are formed. Figure 1.1 shows images of a liquid jet becoming unstable when it is subject to small perturbation. It is possible to disturb the jet such that the satellite drops are not formed. Figure 1.2 shows one such breakup.

The classical study of the capillary instability of liquid jets was published in the seminal works of Lord Rayleigh [4, 5]. With the assumption of an inviscid liquid, he obtained an equation for the growth rate of a given axisymmetric surface disturbance by equating the potential and kinetic energies computed for the flow. Further, with the hypothesis that the disturbance with the maximum growth rate would lead to the breakup of the jet, he obtained an expression for the resulting droplet size assuming that it would be of the order of the wavelength of this disturbance. Later Weber [10]

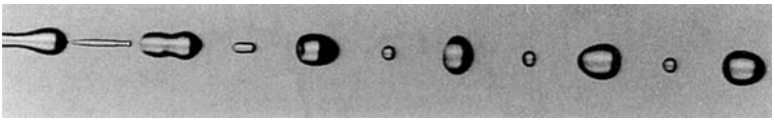


Fig. 1.1 Instability of a water jet with diameter of 0.27 mm and velocity of 3.3 m/s subject to a long wavelength periodic disturbance with wavelength to diameter ratio of 11.3 showing formation of satellite droplets [21, Fig. 16] (Courtesy of the Royal Society)

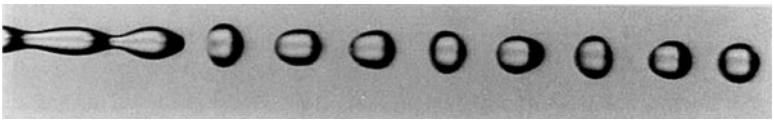


Fig. 1.2 Uniform breakup of a water jet with diameter of 0.27 mm and velocity of 2.9 m/s subject to disturbance wavelength to diameter ratio of 4.6 [21, Fig. 5] (Courtesy of the Royal Society)

included the effect of viscosity in his analysis of the jet breakup based on the three-dimensional partial differential equations of hydrodynamics of Newtonian viscous liquids. He found that the effect of the liquid viscosity is to shift the fastest growing waves to longer wavelengths and to slow down their growth rate, without, however, altering the value of the cut-off wave number.

Theoretical investigations of capillary instability of free liquid jets have been mainly through either perturbation-type analysis or quasi-one-dimensional models. These studies can be divided into two major categories, namely temporal and spatial analysis. In the temporal analysis, an infinite jet, stationary relative to a moving observer is considered and the growth rates of the disturbance amplitudes at all jet cross-sections are determined (standing perturbation waves). In the temporal analysis the imposed perturbations can be oscillatory or exponential in time. In the spatial analysis a semi-infinite jet (e.g., a jet issuing from a nozzle) is considered and the imposed perturbations propagating along the jet may be periodic in time and oscillatory or exponential in space. In the spatial analysis, the growth rate of the disturbance amplitude along a semi-infinite jet is considered with the nozzle conditions fixed. Linear and nonlinear perturbation analysis or numerical methods are also used in each category. Reviews of the theoretical analysis of jet instability are provided by Bogy [14] and more recently by Sirignano and Mehring [20]. This chapter provides an overview of mainly temporal capillary instability of straight liquid jets.

Basic Equations

Consider a fluid domain consisting of a liquid/gas interface. The Navier–Stokes equations (1.1) and the continuing equations (1.2) for an incompressible Newtonian flow describing such a system can be written as:

$$\nabla \cdot \mathbf{u}_i = 0 \tag{1.1}$$

$$\frac{D\mathbf{u}_i}{Dt} = \frac{\partial \mathbf{u}_i}{\partial t} + \mathbf{u}_i \cdot \nabla \mathbf{u}_i = -\frac{\nabla P_i}{\rho_i} + v_i \nabla^2 \mathbf{u}_i + \mathbf{g} + \frac{\mathbf{F}}{\rho} \tag{1.2}$$

where $\mathbf{u}_i$ is the velocity vector, P_i is the pressure, $v_i = \mu_i/\rho_i$ is the kinematic viscosity, μ_i is the coefficient of dynamics viscosity, ρ_i is the density, $\mathbf{g}$ is the gravitational acceleration vector, and $\mathbf{F}$ is the body force. The subscript i may stand for the liquid (l) and its surrounding gas (g).

In the problems with free surfaces and interfaces, two different boundary conditions are implemented at the interface. One is the stress balance and the other is the kinematic condition. The stress balance at the interface between the liquid and its surrounding fluid is one of the main factors in the evolution of the liquid surface shape. This stress is governed by both the surface tension forces and the viscous forces.

$$(p_l - p_g + \sigma\kappa)\mathbf{n} = (\boldsymbol{\tau}_l - \boldsymbol{\tau}_g) \cdot \mathbf{n} \tag{1.3}$$

where $\boldsymbol{\tau}_i$ is the stress tensor, $\mathbf{n}$ is the normal unit vector at the interface, σ is the surface tension coefficient, and κ is the mean interface curvature:

$$\kappa = \nabla \cdot \mathbf{n} = \frac{1}{R_1} + \frac{1}{R_2} \tag{1.4}$$

where R_1 and R_2 are the principal radii of curvature of the interface. For instance, for an axisymmetric jet with instantaneous radius R, the curvature along its axis, x, is written as:

$$\kappa = \frac{1}{R_1} + \frac{1}{R_2} = \left(\frac{1}{R\left(1 + R_x^2\right)^{1/2}} - \frac{R_{xx}}{\left(1 + R_x^2\right)^{3/2}} \right) \tag{1.5}$$

where the subscript x indicates the derivative with respect to x. The kinematic boundary condition implies that fluid does not cross the free-surface, and therefore, the velocity component normal to the interface is continuous across the interface:

$$\mathbf{u}_l \cdot \mathbf{n} = \mathbf{u}_g \cdot \mathbf{n} \tag{1.6}$$

Other boundary conditions depend on the particular problem. For instance, for the instability of an axisymmetric jet, the axisymmetric condition on the axis of the jet is applied.

Once the above equations are nondimensionalized using a length scale (e.g., nozzle or unperturbed jet radius, a), and a velocity scale (e.g., mean jet velocity, U), the following nondimensional numbers appear:

$$Re_i = \frac{\rho_i U_i a}{\mu_i} \tag{1.7}$$

$$We_i = \frac{\rho_i {U_i}^2 a}{\sigma} \tag{1.8}$$

which are the Reynolds and the Weber numbers of the flow, respectively. Reynolds and Weber numbers can be described for the liquid phase, using liquid properties and liquid velocity, or for the gas phase, using the gas properties and gas velocity. The Reynolds number represents the ratio of the inertia to viscous forces, whereas the Weber number represents the ratio of the inertia to surface tension forces. Combining these two numbers to eliminate the velocity, results in Ohnesorge number:

$$Oh = \frac{\sqrt{We}}{Re} = \frac{\mu}{\sqrt{\rho \sigma a}} = \sqrt{Z} \tag{1.9}$$

Ohnesorge number represents fluid properties. Low Oh ($\sqrt{Z}$) numbers represent either a low viscous or a high surface tension fluid. When the gravitational effects are important, the ratio of the gravitational forces to surface tension forces is represented by the Bond number defined as:

$$Bo = \frac{\rho g a^2}{\sigma} \tag{1.10}$$

Other important parameters are the density and viscosity ratio of the two fluids:

$$\varepsilon = \frac{\rho_g}{\rho_l} \tag{1.11}$$

$$\mu_r = \frac{\mu_g}{\mu_l} \tag{1.12}$$

Interface Wave Characteristics

Prior to the analysis of instability of a liquid interface, a discussion on the characteristics of surface waves is provided. When a liquid/gas interface is deformed, as shown in Fig. 1.3, the surface tension forces may tend to bring it back to its equilibrium shape. The equilibrium shape of the interface is defined based on all the forces that may act on it, including the gravitational and pressure forces. On a flat interface, as the disturbed interface tends to move to its equilibrium shape, a wave like propagation appears. If the forces that are acting on the disturbed interface are the surface tension or the capillary forces, the waves are referred to as the capillary waves. The waves on the surfaces of large liquid masses may be under the influence of the gravity forces. Therefore, they are referred to as the gravity waves.

Consider a wave with wavelength λ, frequency $\bar{\omega}$, and a wave amplitude of ζ. Also, let us consider a characteristic velocity of U for the liquid. The characteristic fluid velocity due to the motion of the interface can be estimated based on the amplitude of the disturbance and its characteristic time or $\mathbf{u} \approx \zeta\bar{\omega}$. Therefore, the second derivative of velocity with respect to space, or the Laplacian of the velocity is estimated according to $\nabla^2\mathbf{u} \sim U/\lambda^2$, and, the time derivative of the velocity according to $\partial\mathbf{u}/\partial t \sim U\bar{\omega}$. The order of the magnitude of the convective term can

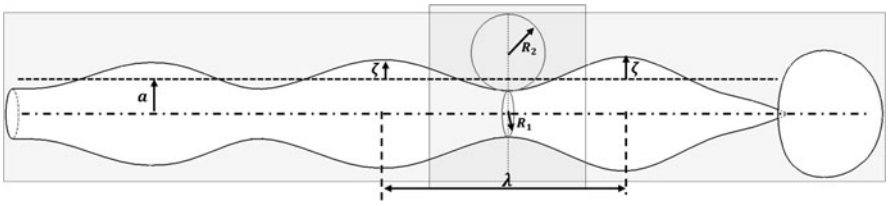


Fig. 1.3 Schematic of an unstable jet

also be written as $(\mathbf{u}\nabla)\mathbf{u} \sim U^2/\lambda \sim \zeta^2\bar{\omega}^2/\lambda$. The above terms can be used to determine the conditions under which the viscous terms can be neglected. One condition is that the first term in (1.2) is larger than the viscous terms: $\partial\mathbf{u}/\partial t >> \nu\nabla^2\mathbf{u}$. Therefore, in order to be able to neglect the viscous terms we should have $\bar{\omega}\lambda^2/\nu >> 1$. This indicates that viscosity may be ignored for long waves. Based on the order of magnitude of the terms provided, the Reynolds number for the flow based on the wavelength can be written as $Re = U\lambda/\nu \approx \zeta\lambda\bar{\omega}/\nu$. For low Reynolds numbers: $\zeta\lambda^2\bar{\omega}/\lambda\nu << 1$. For the last two conditions be simultaneously true, it requires $\zeta/\lambda << 1$, i.e., the wave amplitude must be much smaller than the wavelength. The convective terms are small in comparison with the transient term, $\partial\mathbf{u}/\partial t$, if $U\bar{\omega} >> \zeta^2\bar{\omega}^2/\lambda$ or $\zeta/\lambda << 1$. Therefore, if the wave amplitude is small with respect to wavelength, the nonlinear terms may be neglected.

Temporal Linear Capillary Instability of Inviscid Liquid Jets

In the analysis of a liquid jet, equations (1.1) and (1.2) are written in the cylindrical coordinates with $\mathbf{u_i} = (u_i, v_i, w_i)$, being the velocities in the axial, x, radial, r, and azimuthal, θ, directions, respectively. The continuity equations is:

$$\frac{\partial u_i}{\partial x} + \frac{\partial v_i}{\partial r} + \frac{v_i}{r} + \frac{1}{r}\frac{\partial w_i}{\partial \theta} = 0 \tag{1.13}$$

and the Navier–Stokes equations are given by

$$\rho_i\left(\frac{\partial u_i}{\partial t} + v_i\frac{\partial u_i}{\partial r} + \frac{w_i}{r}\frac{\partial u_i}{\partial \theta} + u_i\frac{\partial u_i}{\partial x}\right) = -\frac{\partial P}{\partial x} + \mu_i\left(\frac{\partial^2 u_i}{\partial r^2} + \frac{1}{r}\frac{\partial u_i}{\partial r} + \frac{1}{r^2}\frac{\partial^2 u_i}{\partial \theta^2} + \frac{\partial^2 u_i}{\partial x^2}\right) + F_x \tag{1.14}$$

$$\rho_i\left(\frac{\partial v_i}{\partial t} + v_i\frac{\partial v_i}{\partial r} + \frac{w_i}{r}\frac{\partial v_i}{\partial \theta} + u_i\frac{\partial v_i}{\partial z} - \frac{{w_i}^2}{r}\right) = -\frac{\partial P_i}{\partial r} + \mu_i\left(\frac{\partial^2 v_i}{\partial r^2} + \frac{1}{r}\frac{\partial v_i}{\partial r} - \frac{v_i}{r^2} + \frac{1}{r^2}\frac{\partial^2 v_i}{\partial \theta^2} + \frac{\partial^2 v_i}{\partial x^2} - \frac{2}{r^2}\frac{\partial w_i}{\partial \theta}\right) + F_r \tag{1.15}$$

$$\rho\left(\frac{\partial w_i}{\partial t} + v_i\frac{\partial w_i}{\partial r} + \frac{v_i w_i}{r} + \frac{w_i}{r}\frac{\partial w_i}{\partial \theta} + u_i\frac{\partial w_i}{\partial x}\right) = -\frac{1}{r}\frac{\partial P_i}{\partial \theta} + \mu_i\left(\frac{\partial^2 w_i}{\partial r^2} + \frac{1}{r}\frac{\partial w_i}{\partial r} - \frac{w_i}{r^2} + \frac{1}{r^2}\frac{\partial^2 w_i}{\partial \theta^2} + \frac{\partial^2 w_i}{\partial x^2} + \frac{2}{r^2}\frac{\partial v_i}{\partial \theta}\right) + F_\theta \tag{1.16}$$

Assuming an inactive surrounding gas, the gas effects can be neglected. The governing equations are then linearized using small perturbation in the velocity, pressure and radius of the jet: $u = \bar{u} + u'$, $v = \bar{v} + v'$, $p = \bar{p} + p'$, and $R = a + \zeta$, where a is the unperturbed radius and ζ is the small surface perturbation. Also, the axial velocity of the jet can be eliminated by a Galilean transformation, therefore, the system can be considered to be a stationary liquid column in inactive environment.

A simple solution for the jet instability is that of an inviscid stationary jet ($\bar{u} = \bar{v} = 0$) subject to an axisymmetric disturbance (no perturbation in θ direction). For this problem, the linearized equations are:

$$\frac{\partial u'}{\partial t} = -\frac{1}{\rho}\frac{\partial p'}{\partial x} \tag{1.17}$$

$$\frac{\partial v'}{\partial t} = -\frac{1}{\rho}\frac{\partial p'}{\partial r} \tag{1.18}$$

$$\frac{1}{r}\frac{\partial r v'}{\partial r} + \frac{\partial u'}{\partial x} = 0 \tag{1.19}$$

and after defining a potential function and integrating the momentum equation, the following relation is found:

$$p' = -\rho\frac{\partial \phi}{\partial t} + \sigma\kappa \tag{1.20}$$

where ϕ is the potential function defined as $v' = \partial\phi/\partial r$, $u' = \partial\phi/\partial x$, $\sigma\kappa$ is the constant of integration, derived from the stationary jet. Furthermore, from the continuity equation, ϕ must be a solution to the Laplacian of potential function, $\nabla^2\phi = 0$, where the Laplacian operator is in the cylindrical coordinates.

Assuming a periodic disturbance to the radius along the x-axis, we seek a solution of the form:

$$\phi = \Phi(r)\exp(ikx + \omega t) \tag{1.21}$$

where $k = 2\pi/\lambda$ is a real positive wave number, with λ being the wavelength, and ω is the growth rate of the disturbance. Axisymmetric disturbances result in a so-called dilatational or varicose waviness of the jet. After substitution in the continuity equation we get:

$$\frac{1}{r}\frac{d}{dr}\left(r\frac{d\Phi}{dr}\right) - k^2\Phi = 0 \tag{1.22}$$

This is a Bessel equation, and its solution consists of the modified Bessel functions I_0 and K_0 of the first kind: $I_n(kr) = (-i)^n J_n(ikr)$. Since K_0 is unbounded

at $r = 0$, it is eliminated, and the solution of (1.22) becomes: $\Phi = AI_0(kr)$. The pressure and the velocity components are then found as:

$$p' = -A\rho\omega I_0(kr)\exp(ikx + \omega t) + \sigma\kappa \tag{1.23}$$

$$v' = AkI_1(kr)\exp(ikx + \omega t) \tag{1.24}$$

$$u' = AikI_0(kr)\exp(ikx + \omega t) \tag{1.25}$$

Rayleigh [5] used a periodic perturbation in both axial and angular direction of the following form: $R = a + \zeta_m \cos kx \cos m\theta$; here, $m = 1$ is termed kink mode and $m \geq 2$ are termed flute modes. However, he showed that the linear instability analysis provides that the jet is stable for all angular disturbances, and it is only the axial disturbances that may be unstable. This is related to the fact that only the axisymmetric perturbations can reduce the surface energy. Therefore, we only consider the axial disturbances.

The amplitude of perturbation, ζ, is related to the radial velocity of the surface by $v' = \partial\zeta/\partial t$ at $r = a$. Therefore, ζ can be determined from (1.24):

$$\zeta = A\frac{k}{a}I_1(ka)\exp(ikx + \omega t) \tag{1.26}$$

The axisymmetric flow conditions (along the axis of the jet) provide:

$$v = 0 \quad \text{and} \quad \frac{\partial v'}{\partial r} = 0 \quad \text{at} \quad r = 0. \tag{1.27}$$

The pressure boundary condition is the Young–Laplace equation (1.3) and (1.4), which for an axisymmetric jet can be written as:

$$\frac{1}{R_1} = \frac{1}{a + \zeta} \tag{1.28}$$

$$\frac{1}{R_2} = \frac{-\zeta_{xx}}{(1 + \zeta_x^2)^{3/2}} \tag{1.29}$$

where subscript x represents the derivative with respect to x ($\zeta_{xx} = \partial^2\zeta/\partial x^2$). Note that normal to the axis, the cross-section is circular with the instantaneous radius of $a + \zeta$. The above equations can be simplified in the linear approximation for small perturbations and using Taylor series expansion, to:

$$\frac{1}{R_1} = \frac{1}{a + \zeta} = \frac{1}{a(1 + \zeta/a)} \approx \frac{1 - \zeta/a}{a} \tag{1.30}$$

and

$$\frac{1}{R_2} = -\zeta_{xx} \tag{1.31}$$

Therefore, the pressure at the jet surface can be determined from:

$$p = \frac{\sigma}{a} - \frac{\sigma}{a^2}\left(\zeta + a^2\zeta_{xx}\right) \tag{1.32}$$

This equation is only valid for small-amplitude disturbances, when the approximation $\zeta/a << 1$ holds. When this expression for p is equated to (1.23) at $r = a$ and simplified in the linear approximation, the amplitude, A, disappears, and we are left with a characteristic relationship between the growth rate and the wave number determining the perturbation spectrum. Solving for the growth rate, we have:

$$\omega^2 = \frac{\sigma k}{\rho a^2}\left(1 - k^2a^2\right)\frac{I_1(ka)}{I_0(ka)} \tag{1.33}$$

where $\omega = \omega_r + i\omega_i$, with ω_r being the growth rate, $i = \sqrt{-1}$, and ω_i being the oscillation frequency.

If the real part of the growth rate is positive, the disturbances grow exponentially in time. The ratio of the modified Bessel functions is positive for all conditions ($I_1/I_0 > 0$). This means that ω is real positive as long as $ka < 1$. This leads to the conclusion that any periodic disturbance to the jet which has a wave number that satisfies $0 < ka < 1$ will make the jet unstable. The growth rate of such an instability will be at the rate described in (1.33). Since the wave number is $k = 2\pi/\lambda$, a jet is unstable for $\lambda > 2\pi a$. In other words, any disturbance with a wavelength larger than the diameter of the jet, makes the jet unstable. Note also that perturbations with $ka > 1$ may result in stable surface oscillations. Since the whole perturbation spectrum is always present in the jet, the fastest growing perturbations always dominate the jet evolution. A plot of the nondimensional growth rate versus the wave number is shown in Fig. 1.4 [18] which compares the growth rates with experimental data, showing good agreement. The maximum growth rate occurs at $ka = 0.697$.

The mechanism of capillary instability can be understood from the expression of (1.33). The first term in the second parentheses, 1, comes from the jet cross-sectional curvature R_1 (radius). The second term $-k^2a^2$ comes from the jet axial curvature R_2. They are of opposite sign. The former represents the capillary pinching in the radial direction; the latter is due to the curvature associated with the other principle direction and represents the capillary force that opposes the capillary pinching. For long waves with $ka < 1$, the capillary pinching dominates over the restoring capillary force. For shorter waves with $ka \geq 1$, the restoring force becomes sufficiently large to overcome the capillary pinching. Perturbations grow only for those (long) wavelengths which decrease the surface energy.

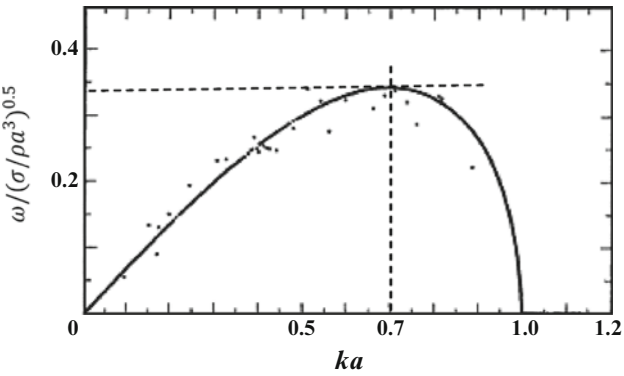


Fig. 1.4 Nondimensional growth rate of capillary axisymmetric perturbations for an inviscid jet in terms of the wave number [18, Fig. 7]. The symbols represent the experimentally measured growth rates for low viscosity jets (Courtesy of Cambridge University Press)

For $ka \ll 1$, $I_1(ka)/I_0(ka) \approx ka/2$. Then, (1.33) reduces to $\omega^2 \approx (\sigma/2\rho a^3(ka)^2 [1-(ka)^2]$, which provides a maximum value for the growth rate as:

$$\omega_{\max} = 0.34\sqrt{\frac{\sigma}{\rho a^3}} = 0.97\sqrt{\frac{\sigma}{\rho D^3}} \tag{1.34}$$

at $ka = 1/\sqrt{2} = 0.707$. This is very close to the fastest growing mode predicted by the exact equation (1.33), which is $ka = 0.697$. Rayleigh argued that for a naturally breaking jet, the most unstable wave causes the jet breakup. Therefore, the size of the droplet can be estimated based on the wavelength of the most unstable wave of $\lambda_{\max} = 9.016a$. If the linear approximation is assumed to be valid until the very breakup, jets break when the amplitude of the disturbance reaches the jet radius, and a droplet is formed by each wavelength of the disturbance. Therefore, the main droplet diameter, d, can be estimated by the volume of the liquid within a wavelength: $d^3 = 6\lambda_{\max}a^2 \approx 54a^3$ or $d \approx 3.78a = 1.89D$, where D is the jet cross-sectional diameter (which is usually assumed to be equal to the orifice diameter).

Jet breakup time and length can be estimated based on the maximum growth rate. Hence, according to (1.33) we expect to see uniformly spaced drops defined by: $L/2\pi a = 1/0.69$ or $L = 9.016a = 4.55D$, where L is the drop spacing. Based on the assumption that disturbance corresponds to $\omega_{\max}$, the radius perturbation is expected to grow as: $\zeta = \zeta_0 \exp(\omega_{\max} t)$, where ζ_0 is the initial perturbation amplitude. Therefore, the time taken to break up a jet, t_b, corresponds to $\zeta = a$ and is equal to:

$$\mathrm{t}_b = \frac{1}{\omega_{\max}} \ln\left(\frac{\mathrm{a}}{\zeta_0}\right) = \left(\frac{\mathrm{C}}{\omega_{\max}}\right) \tag{1.35}$$

where $C = \ln(a/\zeta_0)$. The breakup length of the jet, L_b, can be calculated based on a constant jet velocity, $UL_b = t_b$, and therefore, the breakup length can be written as:

$$\frac{L_b}{D} = 1.04C\sqrt{We} \tag{1.36}$$

Grant and Middleman [22] reported that (1.36) correlated experimental data for capillary breakup of low viscosity liquid jets when a value of $C = 13$ was selected. It is instructive to use this value of C to evaluate the initial perturbation amplitude ζ_0. Taking for the estimate the unperturbed cross-sectional radius $a = 1$ mm, one can find $\zeta_0 = 10^{-3}\exp(-13) = 2.26 \times 10^{-9}$ m $= 2.26$ nm. How plausible such estimates are for liquid jets whose profile is visibly perturbed at the nozzle exit, remains an open question.

Linear Capillary Instability of Viscous Jets

Weber [10] and Chandrasekhar [23] extended Rayleigh's inviscid theory to that of a jet with a kinematic viscosity, $\nu=\mu/\rho$. The axisymmetric solutions for the velocity components of the jet is written as the sum of the inviscid and viscous solutions as $u = u^0 + u^\nu$ and $v = v^0 + v^\nu$, where superscripts 0 represent the inviscid solution and superscripts ν represent the viscous contribution. Substituting these into the components of the momentum balance equations, a pair of partial differential equations for the two velocity components are obtained. A stream function ψ is then introduced and pressure is eliminated from both equations. Again a solution of the following form, $\psi = \psi(r)\exp(ikx + \omega t)$ inevitably exists for an infinite jet (a liquid column). The stream function amplitude is given by the Bessel function $\psi(r) = A_2 r I_1(lr)$, where

$$l^2 \equiv k^2 + \frac{\omega}{\nu} \tag{1.37}$$

The constants are determined from the boundary conditions. The kinematic boundary condition is similar to the inviscid case, ($v = \partial\zeta/\partial t$ at $r = a$), whereas the dynamic boundary conditions change. Namely, the linearized shear stress at the jet surface is set equal to zero, $\tau_{rx} = \mu(\partial u/\partial r + \partial v/\partial x) = 0$ at $r = a$, whereas the linearized condition for the normal stress reads $(\tau_{rr} + p) = \sigma(1/R_1 + 1/R_2)$ at $r = a$. Again, $1/R_1 \approx (1 - \zeta/a)/a$ for a perturbed circular cross-section, and $1/R_2 \approx -\zeta_{xx}$. As a result, the following characteristic equation for the perturbation spectrum is obtained:

$$\omega^2 + \frac{2\nu k^2}{I_0(ka)}\left(I'_1(ka) - \frac{2kl}{k^2 + l^2}\frac{I_1(ka)}{I_1(la)}I'_1(la)\right)\omega = \frac{\sigma k}{\rho a^2}(1 - k^2a^2)\frac{I_1(ka)}{I_0(ka)}\frac{l^2 - k^2}{l^2 + k^2} \tag{1.38}$$

For $ka \ll 1$ (long waves) the above equation is approximated by:

$$\omega^2 + \frac{3\mu(k^2)}{\rho}\omega - \frac{\sigma}{2\rho a^3}(1 - k^2a^2)k^2a^2 = 0 \tag{1.39}$$

which shows that the jet is unstable for disturbances with $ka < 1$. The maximum value of ω is found to be [10, 19]:

$$\omega_{\max} = \left[\left(\frac{8\rho a^3}{\sigma}\right)^{1/2} + \frac{6\mu a}{\sigma}\right]^{-1} \tag{1.40}$$

corresponding to the most dominant wavelength of

$$\lambda^2_{\max} = 8\pi^2a^2\left(1 + \frac{3\mu}{\sqrt{2\rho a\sigma}}\right) = \left(\frac{4\pi^2}{k^2{}_{\max}}\right) \tag{1.41}$$

Figure 1.5 shows the growth rate of the capillary instability for different liquid viscosities. Viscosity dampens the instability with a damping coefficient of $3\mu k^2/\rho$ and shifts the fastest growing perturbations toward longer waves. For $\mu = 0$, Rayleigh solution is obtained, whereas for very viscous jets with $(3\mu k^2/2\rho)^2 \gg \sigma/2\rho a^3$, $\omega = (\sigma/6\mu a)(1 - k^2a^2)$. The breakup length for a viscous jet is found as:

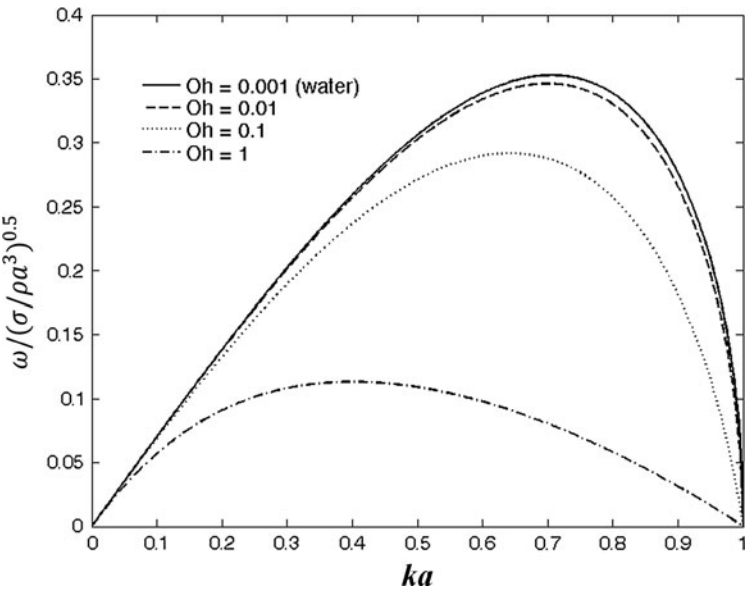


Fig. 1.5 Growth rate of small capillary perturbations of viscous jets instability in terms of the wave number

$$\frac{L_b}{D} = C\left(We^{1/2} + \frac{3We}{Re}\right) = CWe^{1/2}(1 + 3Oh) \tag{1.42}$$

Linear Capillary Instability of a Jet Affected by Aerodynamic Effects

Uniform Jet Velocity Profile

Rayleigh's instability analysis ignores the effect of surrounding gases. The surrounding gas effects become important at high jet-gas relative velocities and cannot be ignored. Weber [10] considered the capillary instability of a liquid jet with a coaxial inviscid gas stream. Later, Sterling and Sleicher [24] modified Weber's analysis and included an empirical coefficient to match the experimental data. Their dispersion equation that takes into account the aerodynamic effects is:

$$\begin{aligned}\left(\frac{\bar{k}I_0(\bar{k})}{2I_1(\bar{k})} + \varepsilon\frac{\bar{k}K_0(\bar{k})}{2K_1(\bar{k})}\right)\omega^2 + \left(2i\varepsilon\frac{U\bar{k}^2K_0(\bar{k})}{2aK_1(\bar{k})} + \frac{\mu\bar{k}^2}{\rho_l a^2}\left[2\bar{k}\frac{I_0(\bar{k})}{I_1(\bar{k})}\right.\right.\\ \left.\left. -1 + \frac{2\bar{k}^2}{\bar{k}_1^2 - \bar{k}^2}\left(\bar{k}\frac{I_0(\bar{k})}{I_1(\bar{k})} - \bar{k}_1\frac{I_0(\bar{k}_1)}{I_1(\bar{k}_1)}\right)\right]\right)\omega\\ = \frac{\sigma}{2\rho_l a^3}\left(1 - \bar{k}^2\right)\bar{k}^2 + \varepsilon\frac{U^2\bar{k}^3}{2a^2}\frac{K_0(\bar{k})}{K_1(\bar{k})}\end{aligned} \tag{1.43}$$

where $\bar{k} = ka$, $\bar{k}_1^2 = \bar{k}^2 + \omega a^2\rho_l/\mu$, and $\varepsilon = \rho_g/\rho_l$, with ρ_l and ρ_g being the liquid and gas density, respectively, and U is a constant and uniform jet-gas relative velocity. In the absence of a gas phase and viscosity (i.e., $\varepsilon = \mu = 0$), (1.43) reduces to Rayleigh's result. For an inviscid liquid in a gaseous surrounding, (1.43) can be written as follows:

$$\begin{aligned}\left(\frac{\bar{k}I_0(\bar{k})}{2I_1(\bar{k})} + \varepsilon\frac{\bar{k}K_0(\bar{k})}{2K_1(\bar{k})}\right)\omega^2 + \left(i\varepsilon\frac{U\bar{k}^2K_0(\bar{k})}{aK_1(\bar{k})}\right)\omega\\ = \frac{\sigma}{2\rho_l a^3}(1 - \bar{k}^2)\bar{k}^2 + \varepsilon\frac{U^2\bar{k}^2}{2a^2}\frac{K_0(\bar{k})}{K_1(\bar{k})}\end{aligned} \tag{1.44}$$

When $\bar{k} = ka \ll 1$(for longwave perturbations), (1.43) can be reduced to:

$$\omega^2 + \frac{3\mu\bar{k}^2}{\rho_l a^2}\omega = \frac{\sigma}{2\rho_l a^3}\left(1-\bar{k}^2\right)\bar{k}^2 + \varepsilon\frac{U^2\bar{k}^3}{2a^2}\frac{K_0(\bar{k})}{K_1(\bar{k})} \tag{1.45}$$

Effect of Velocity Profile on Capillary Breakup

The previously noted analyses did not consider the effect of the velocity profile on capillary breakup. Reitz-Bracco [25] relaxed this assumption, and considered a liquid jet in a gas with a velocity profile in the radial direction. They obtained the following general characteristic equation:

$$\begin{aligned}\omega^2 + 2\nu k^2\omega\left(\frac{I_1'(\bar{k})}{I_0(\bar{k})} - \frac{2kl}{k^2+l^2}\frac{I_1(\bar{k})}{I_0(\bar{k})}\frac{I_1'(\bar{k})}{I_1(\bar{k})}\right)\\ = \frac{\sigma k}{\rho_l a^2}\left(1-\bar{k}^2\right)\left(\frac{l^2-k^2}{l^2+k^2}\right)\frac{I_1(\bar{k})}{I_0(\bar{k})} + \varepsilon\left(U-\frac{i\omega}{k}\right)^2 k^2\left(\frac{l^2-k^2}{l^2+k^2}\right)\frac{I_1(\bar{k})}{I_0(\bar{k})}\frac{K_0(\bar{k})}{K_1(\bar{k})}\end{aligned} \tag{1.46}$$

where $\lim_{\nu\to 0}((l^2-k^2)/(l^2+k^2)) = 1$.

In the absence of viscosity and the gas phase (i.e., $\nu = 0,\ \varepsilon = 0$), (1.46) becomes the same as the Rayleigh's result. And for an inviscid case including surrounding gas effects, (1.46) reduces to [26]:

$$\left(\frac{\bar{k}}{2}\frac{I_0(\bar{k})}{I_1(\bar{k})} + \varepsilon\frac{\bar{k}K_0(\bar{k})}{2K_1(\bar{k})}\right)\omega^2 + \left(i\varepsilon\frac{U\bar{k}^2K_o(\bar{k})}{aK_1(\bar{k})}\right)\omega = \frac{\sigma}{2\rho_l a^3}\left(1-\bar{k}^2\right)\bar{k}^2 + \frac{U^2\bar{k}^2}{2a^2}\frac{K_0(\bar{k})}{K_1(\bar{k})} \tag{1.47}$$

In the limit of short wavelength perturbations, $\bar{k}\to\infty$, and for $\rho_l \gg \rho_g$, the following relation, which is similar to the Kelvin–Helmholtz instability condition [27, 28] is obtained:

$$\omega^2 = \varepsilon U^2k^2 - \frac{\sigma k^3}{\rho_l} \tag{1.48}$$

Quasi-One-Dimensional Approximation to the Jet Equations in the Case of Capillary Breakup

The linear stability theory is exceptional in the sense that it can be fully based on the three-dimensional equations of fluid dynamics. All the additional effects lead to either direct numerical simulations or the asymptotic approximations. One of the most natural ways of the asymptotic description of the dynamics of jets is the quasi-one-dimensional approach. In the quasi-one-dimensional approximation,

a jet is considered as a "directed" continuum, i.e., a long linear object with no lateral dimension, which is characterized by a number of such integral parameters as the cross-sectional radius, flow rate, etc. distributed along the jet axis. This approach is kindred to the hydraulic theory of flows in long pipes (especially, in pipes with flexible elastic walls), and its natural range of validity is linked to flows slowly varying along the jet axis. The relations between three-dimensional fluid mechanics and its quasi-one-dimensional approximation are also similar to those between the theory of elasticity and the theory of bar bending, or between realism and surrealism in art. It is always beneficial to sacrifice the excessive details, and to build on a simplified vision of a peculiar object (in the present case, an elongated thin jet with no significant tractions at the free surface). That is the way to achieve the simplest, physically relevant understanding and description of such an object.

The quasi-one-dimensional approximation was initially introduced in the theory of capillary jet breakup. The mass and longitudinal momentum balance under the assumption of plug velocity and stress profiles in jet cross-sections reads according to Yarin [29]

$$\frac{\partial f}{\partial t} + \frac{\partial Uf}{\partial x} = 0, \quad f = \pi R^2 \tag{1.49}$$

$$\rho f \left(\frac{\partial U}{\partial t} + U \frac{\partial U}{\partial x} \right) = \frac{\partial \tau_{xx} f}{\partial x} + \frac{\partial}{\partial x} \left[\frac{2\pi R \sigma}{(1 + R_x^2)^{1/2}} \right] \tag{1.50}$$

In (1.49) and (1.50), t is time, x is the longitudinal coordinate reckoned along the jet axis, f is the cross-sectional area (R is the cross-sectional radius), U and τ_{xx} are the longitudinal velocity and normal stress in the jet cross-section, respectively, and σ is the surface tension coefficient. For viscous Newtonian liquids, the stress is given by the following expression:

$$\tau_{xx} = 3\mu \frac{\partial U}{\partial x} - \sigma \left\{ \frac{1}{R(1 + R_x^2)^{1/2}} - \frac{R_{xx}}{(1 + R_x^2)^{3/2}} \right\} \tag{1.51}$$

This expression accounts for the fact that the jet surface is subjected to negligible tractions and the deformation of the jet element corresponds in the first approximation to the uniaxial elongation/compression. The viscous term on the right hand side in (1.51) thus naturally involves the Trouton elongational viscosity 3μ, with μ being liquid viscosity; the second term corresponds to the capillary pressure proportional to the local double mean curvature of the jet surface.

Equations 1.49–1.51 represent themselves a slightly modified version of the equations used in [30–32]. The modification introduced in [29] and references therein involves the exact (not the asymptotic) expressions for the capillary force at the jet surface and capillary pressure in the jet cross-section, which allows description of the capillary breakup until formation of drops. A detailed derivation of such equations based on the above-mentioned physical assumptions and the integral mass and momentum balances can be found in the monograph [29]

(see also the later reviews [33, 34]). Note, that there is a number of works where similar equations are constructed as a regular asymptotic expansion of the solutions of the three-dimensional differential equations of fluid mechanics (which were, in their turn, derived from the integral mass and momentum balances) [35]. The latter method is much more involved and yields the same equations.

The slower the cross-sectional radius and longitudinal velocity vary along the jet, the more accurate becomes the quasi-one-dimensional description. Therefore, there is nothing astonishing in the fact that the linear theory of the temporal stability of a slightly perturbed infinite cylindrical thread based on (1.49)–(1.51) yields the long-wave limit of the expression for the perturbation growth rate found in the classical Rayleigh–Weber theory [5, 10] from the three-dimensional equations of fluid mechanics:

$$\frac{\omega\mu a}{\sigma} = -\frac{3}{2}Z\bar{k}^2 + \sqrt{\frac{9}{4}Z^2\bar{k}^4 + \frac{Z\bar{k}^2}{2}(1-\bar{k}^2)} \tag{1.52}$$

where again ω is the perturbation growth rate, $Z = Oh^2$ and the dimensionless perturbation wave number $\bar{k} = ka = 2\pi a/\lambda$. The fastest growth rate corresponds to:

$$\bar{k}_{\max} = \left[2\left(1 + 3\sqrt{\frac{Z}{2}}\right)\right]^{-1/2}$$

It is emphasized that (1.52) is equivalent to the solution of (1.39), and, in the inviscid case, to the long-wave limit of the Rayleigh result.

Similarly, the characteristic equation of the linear spatial stability theory for semi-infinite inviscid jets found in [36] based on (1.49)–(1.51) coincides with the long-wave limit of the exact result found in [13] based on the three-dimensional equations of fluid mechanics (cf. section "Spatiotemporal Instability of a Jet").

A more involved version of the quasi-one-dimensional equations of the dynamics of thin liquid jets was proposed in [37, 38] where radial inertia in the jet cross-section was accounted for. The final version of these equations for a Newtonian viscous jet with a straight axis derived in [37–39] has the form

$$\frac{\partial f}{\partial t} + \frac{\partial Uf}{\partial x} = 0, \quad f = \pi R^2, \tag{1.53}$$

$$\rho f\left(\frac{\partial U}{\partial t} + U\frac{\partial U}{\partial \mathrm{x}}\right) = -\frac{\partial q}{\partial x} + \frac{\partial}{\partial x}\left[\frac{2\pi R\sigma}{(1+R_x^2)^{1/2}}\right] + 2\mu\frac{\partial}{\partial x}\left(f\frac{\partial U}{\partial x}\right) \tag{1.54}$$

$$-\frac{1}{8}\rho\frac{f^2}{\pi}\left[\frac{\partial^2 U}{\partial \mathrm{x}\partial \mathrm{t}} + U\frac{\partial^2 U}{\partial x^2} - \frac{1}{2}\left(\frac{\partial U}{\partial x}\right)^2\right] = q - \left\{\frac{\sigma\pi R}{(1+R_x^2)^{1/2}} - \frac{\sigma f R_{xx}}{(1+R_x^2)^{3/2}}\right\}$$

$$-\frac{1}{8}\mu\frac{\partial}{\partial x}\left(f\frac{\partial^2 U}{\partial \mathrm{x}^2}\right) + \mu f\frac{\partial U}{\partial \mathrm{x}}, \tag{1.55}$$

with q being related to the longitudinal force in the jet cross-section.

After the small, higher order terms in (1.53)–(1.55) are neglected, these equations reduce to (1.49) – (1.51). In [40, 41] (1.53)–(1.55) were used to calculate the growth rate of small axisymmetric perturbations of an infinite jet (thread) of viscous Newtonian liquid and of a semi-infinite inviscid jet. For the infinite viscous jet (thread) the following result was obtained

$$\frac{\omega\mu a}{\sigma} = -\frac{Z\left(24\bar{k}^2 + \bar{k}^4\right)}{2\left(8 + \bar{k}^2\right)} + \sqrt{Z^2\left[\frac{24\bar{k}^2 + \bar{k}^4}{2(8 + \bar{k}^2)}\right]^2 + Z\frac{4\bar{k}^2\left(1 - \bar{k}^2\right)}{8 + \bar{k}^2}} \tag{1.56}$$

In the long-wave range of validity of the quasi-one-dimensional approximation, one has $\bar{k}^2 \ll 1$, and (1.56) naturally reduces to (1.52).

Summarizing, in the linear stability theory of capillary breakup of thin free liquid jets, the quasi-one-dimensional approach allows for a simple and straightforward derivation of the results almost exactly coinciding with those obtained in the framework of a rather tedious analysis of the three-dimensional equations of fluid mechanics. This serves as an important argument for further applications of the quasi-one-dimensional equations to more complex problems, which do not allow or almost do not allow exact solutions, in particular, to the nonlinear stages of the capillary breakup of straight thin liquid jets in air (considered below in this chapter).

The quasi-one-dimensional equations are also popular in studies of electrospraying of straight low-viscous jets, where the additional distributed electric forces enter on the right hand side in (1.50) [42–44]. These equations play an important role in the theory of melt spinning process where surface tension effects are negligible, whereas viscous forces and jet cooling and solidification are significant [29]. The quasi-one-dimensional equations represent the most important tool in the studies of capillary breakup of non-Newtonian, rheologically complex jets considered in detail later in this chapter.

Spatiotemporal Instability of a Jet

In the previous discussions, the liquid jet is considered to be infinitely long and k is assumed to be real. Thus, the disturbances must grow or decay everywhere in space at the same time rate. However, Keller et al. [13] noted that the disturbances initiating from the nozzle tip actually grow in space and move downstream to break up the jet into drops, leaving a section of jet intact near the nozzle tip. They set k to be complex and allow the disturbance to grow in space as well as in time in a semi-infinite weightless inviscid jet in a vacuum to obtain the following characteristic equation:

$$(\omega + ku_0)^2 = \frac{\sigma}{\rho_l a^3} \frac{kaI_1(ka)}{I_0(ka)} \left(k^2a^2 + n^2 - 1\right) \tag{1.57}$$

They found that Rayleigh's results are relevant only in the case of large Weber numbers. They also showed that in the limit of $We \to \infty$, the spatial growth rate k_i can be inferred from the temporal growth rate, ω_r by the relation $k_i = \omega_r + O(1/We)$, while the disturbance travels at the jet velocity relative to the laboratory frame. For Weber numbers less than the order of one, they found a new mode of faster-growing disturbances whose wavelengths are so long that they may not be actually observable on finite jets.

Using the theory of absolute and convective instability, Leib and Goldstein [15] showed that the new mode actually corresponds to absolute instability arising from a saddle-point singularity in the characteristic equation. The unstable disturbances in an absolutely unstable jet must propagate in both upstream and downstream directions. Thus, the unstable disturbances expand in space over the course of time. This contrasts with what is observed in a Rayleigh jet, wherein unstable disturbances grow over time as they are convected in a wave packet in the downstream direction with the group velocity $d\omega_i/dk_r$.

The critical Weber number We_c, below which an inviscid jet under weightless condition in vacuum is absolutely unstable, and above which the jet is convectively unstable, was found by Leib and Goldstein [45] to be π. When the viscosity of the jet is taken into account, the critical Weber number depends on the Reynolds number Re [15]. For more detailed discussion of spatial instability refer to Refs. [46–59].

Nonlinear Analysis of Capillary Breakup of Liquid Jets

Jet Instability

The linear Rayleigh–Weber theory of capillary breakup developed for small perturbations allows for a rather accurate prediction of the breakup time and length of capillary jets of low-viscosity liquids when it is extrapolated to the nonlinear stage up to the jet breakup. However, it does not allow prediction of the jet profiles at the late nonlinear stage of their evolution. As a result, the linear theory is incapable of predicting the sizes of all droplets originating from the jet breakup. In the experiments, even in the cases with an imposed monochromatic excitation, as a rule, small satellite droplets are formed from liquid threads between the main drops [18, 60–62]. The linear theory obviously predicts only the main drops with the volume equal to the volume corresponding to the fastest growing wavelength. Peculiarities of capillary jet breakup are of significant interest not only from a purely scientific point of view but in a number of important applications. Therefore, there are many works devoted to the analysis of the capillary jet evolution at a later stage, prior to breakup, in the framework of the nonlinear theory. As a rule, the

analytical asymptotic approaches use the method of deformed coordinates or the method of multiple scales applied to the full three-dimensional equations of fluid mechanics [11, 12, 63–66], or to the quasi-one-dimensional equations [14, 60, 67, 68].

The analytical asymptotic solutions allow for a rather accurate prediction of the satellite droplet size [65, 66], and provide with a mostly qualitative description of some of the experimental observations [14, 60, 68]. In particular, in the experiments [61] it was observed that for small initial perturbation amplitude ζ_0 of any wavelength, a satellite droplet does not completely detach from the main drop moving after it, which results in their ultimate merging. At larger initial perturbation amplitude ζ_0, the satellite droplet merges with the main drop moving before it. At a still larger ζ_0, satellite droplets do not form at all, which is sometimes termed as a "print window." The accurate prediction of the peculiarities of the nonlinear capillary breakup is important for the ink-jet printing devices where only the latter situation is acceptable [41, 69].

The quantitative verification of the predictions of the asymptotic nonlinear theory of growth of perturbation modes was achieved using opto-electronic methods to measure jet profile [70]. The experimental data obtained for water jets with the cross-sectional radius of 1.5×10^{-5} m, appeared to be in reasonable agreement with the theory [63].

The idea of control of the nonlinear effects by the energy transfer from the fastest growing mode to the mode with a doubled wavelength is of significant interest. The asymptotic theory of such a process [71] demonstrated satisfactory agreement with the experiments [72, 73] where quantitative characteristics of the energy transfer process were measured.

The asymptotic theories of the nonlinear phenomena characteristic of capillary breakup of liquid jets lead to rather cumbersome expressions, even though they deal with the simplest case of the inviscid liquid. Therefore, direct numerical simulation of the full three-dimensional equations of fluid dynamics or the quasi-one-dimensional equations of the dynamics of thin liquid jets attracted significant attention in the literature. For example, the numerical solution of the quasi-one-dimensional equations in the inviscid case allowed modeling of formation of both main and satellite drops [30]. The investigation of the nonlinear stage of the capillary breakup of low-viscosity liquids in the framework of the quasi-one-dimensional approach is not fully legitimate, since at the later stage a significant non-uniformity of flow should arise in the cross-sections of the growing main drop. The best results for low-viscosity liquids can be obtained using direct numerical simulations of the full three-dimensional equations of fluid dynamics [74]. Several studies have modeled the capillary breakup of jets based on the full Navier–Stokes equations [75–77], which will be discussed later in this chapter.

On the other hand, capillary breakup of sufficiently viscous liquid jets is a long-wave phenomenon, and its description in the framework of the quasi-one-dimensional equations of the dynamics of liquid jets is sufficiently accurate. The effect of the viscosity on the capillary breakup of highly-viscous liquid jets was studied numerically by Yarin [29]. The initial perturbation of the jet surface was imposed as a harmonic

function of small amplitude, with the wavelength corresponding to the fastest growing mode λ_{max} according to the Rayleigh–Weber theory. The non-dimensional group characterizing viscous effects is the Ohnesorge number. As the Ohnesorge number increases, the main drop at the moment of breakup becomes more and more elongated (spindle-like), whereas the volume corresponding to the forming satellite droplet decreases (Figs. 1.6 and 1.7). The predicted breakup time is in good agreement with the experimental data. The results shown in Figs. 1.6 and 1.7 correspond to the infinite, periodically perturbed jets (threads). Capillary breakup of semi-infinite jets issued from a nozzle was numerically modeled in [78] using the quasi-one-dimensional equations of the dynamics of liquid jets. The results of these calculations were in satisfactory agreement with the asymptotical results [14, 68], however, it was impossible to reach full agreement with the experimentally observed breakup pattern in the whole range of the amplitude of the initial perturbation ζ_0.

At the late stage of capillary breakup near the jet cross-section where the breakup will eventually occur, liquid flow completely "forgets" the initial conditions. It is dominated by the local flow conditions and becomes self-similar. The numerical description of the latest stages of capillary breakup is unreliable near the cross-sections where the cross-sectional radius tends to zero. A theoretical description of such self-similar final jet pinching is given in [79–84], assuming either inertia or viscosity dominated flows in the tiny threads and, in particular, using quasi-one-dimensional equations.

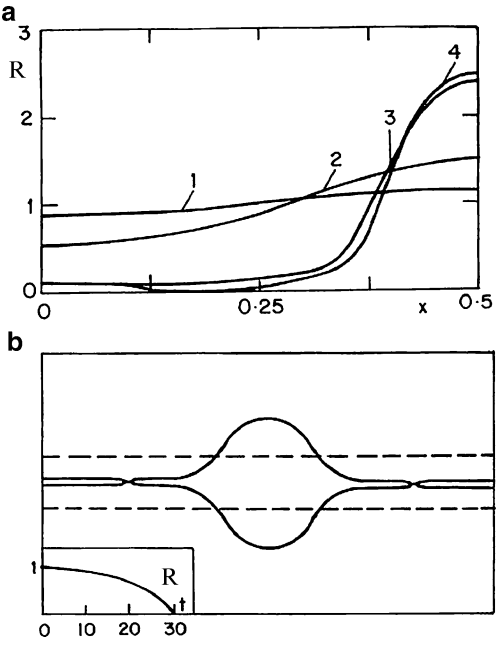


Fig. 1.6 Capillary breakup of a glycerin jet ($Z = 1.755$; Yarin [29]). **(a)** Jet profile corresponding to one half of the perturbation wavelength. The cross-sectional radius R is rendered dimensionless by $a = 6 \times 10^{-5}$ m, the axial coordinate x – by $\lambda_{max} = 1.04 \times 10^{-3}$ m. The dimensionless time $t = 10$ for curve 1, 20 – curve 2, 30 – curve 3, and 30.81 – curve 4 (the time scale is $T = \mu a/\sigma = 0.848 \times 10^{-4}$ s). **(b)** The jet shape at the moment of breakup. In the inset, the radius evolution in the cross-section where the breakup takes place is shown (Courtesy of Pearson Education)

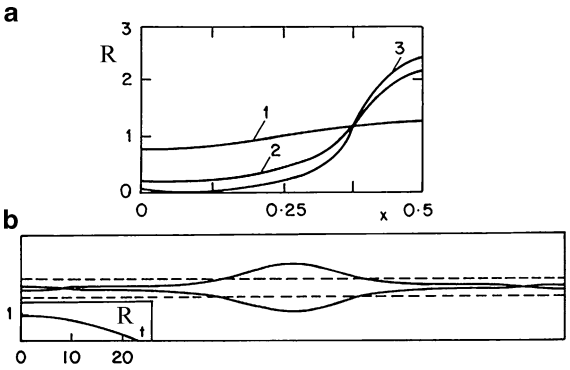


Fig. 1.7 Capillary breakup of a castor oil jet ($Z = 370.3$; Yarin [29]). **(a)** Jet profile corresponding to one half of the perturbation wavelength. The cross-sectional radius R is rendered dimensionless by $a = 6 \times 10^{-5}$ m, the axial coordinate x – by $\lambda_{max} = 3.45 \times 10^{-3}$m. The dimensionless time $t = 10$ for curve 1, 20 – curve 2, and 22.4 – curve 3 (the time scale is $T = \mu a/\sigma = 1.52 \times 10^{-3}$s). **(b)** The jet shape at the moment of breakup. In the inset, the radius evolution in the cross-section where the breakup takes place is shown (Courtesy of Pearson Education)

With the limitations and the problems associated with both the perturbation analysis and the one-dimensional models, the full nonlinear equations of motion for the jet are solved numerically. One such solution is by Ashgriz and Mashayek [75]. They studied the temporal instability of an axisymmetric incompressible Newtonian liquid jet in vacuum and zero gravity. The variables are nondimensionalized by the radius of undisturbed jet, a, and a characteristic time $(\rho a^3/\sigma)^{1/2}$.

An infinitely long cylindrical Newtonian liquid jet, is disturbed with a spatially harmonic surface displacement of a cosine shape: $R = a - \zeta_0 \cos \bar{k}z$, where $\bar{k} = 2\pi a/\lambda$, and a is determined such that the volume of the jet is kept constant when the initial amplitude is changed. Therefore, $a = (1 - \zeta_0^2/2)^{1/2}$. The dynamics of this jet due to capillary forces was investigated for various values of initial disturbance wave number k, and initial amplitude ζ_0, and of the jet Ohnesorge number, Oh.

Their results of the shape evolution of liquid jets with $Oh^{-1} = 200$, 10, and 0.1 and $ka = 0.2$, 0.45, 0.7, and 0.9, are presented in Fig. 1.8. This figure reveals the following characteristics for the breakup of a capillary jet: (1) The breakup point moves towards the swell point of the jet as the jet Oh^{-1} increases. This results in the formation of a ligament in addition to the main drops. The ligament will eventually form a satellite drop. (If the ligament is long enough, it may further break up into even smaller drops.) (2) The length and diameter of the liquid ligament decrease with increasing wave number $\bar{k}$, and, therefore, the satellite size also decreases. (3) The diameter of the liquid ligament and the satellite size increase with increasing Oh^{-1} at a constant wave number. (4) Satellite formation is inhibited at low Oh^{-1}. (5) The breakup time decreases with increasing Oh^{-1}.

The linear theories provide a growth rate for the unstable waves. These growth rates are useful in estimating the breakup length and time. According to the linear

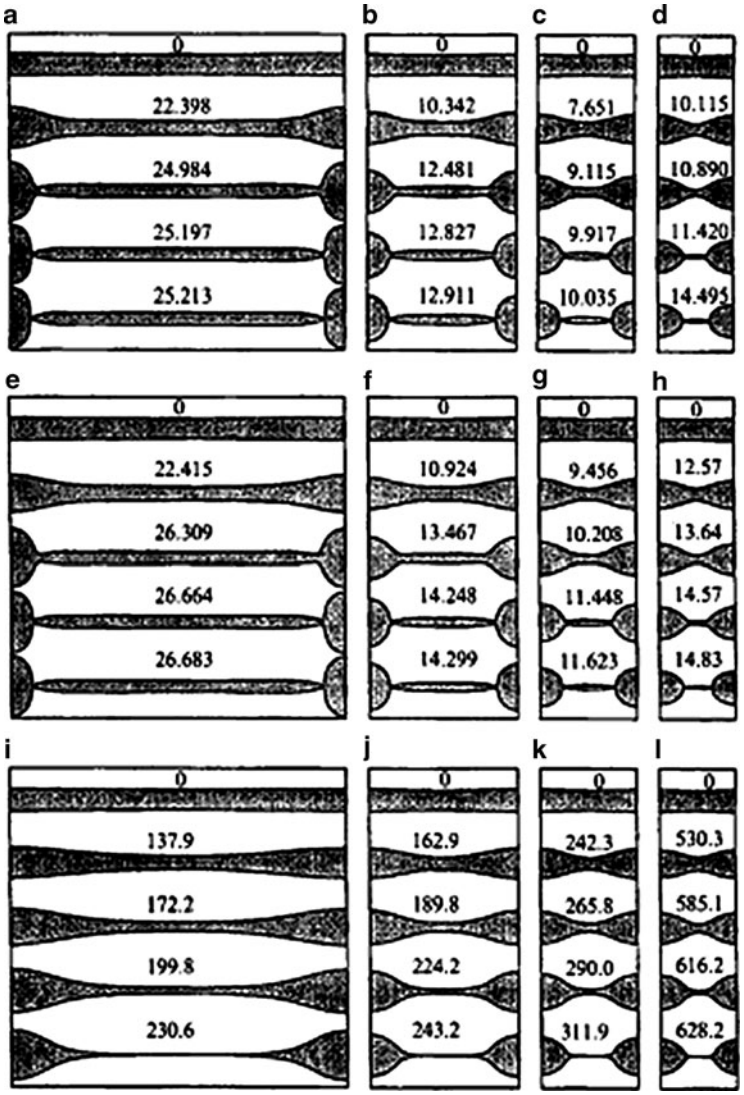


Fig. 1.8 Time evolution of the instability of a capillary liquid jet [75, Fig. 2]. $\zeta_0 = 0.05$: (**a**) $\bar{k} = 0.2$, $Oh^{-1} = 200$, (**b**) $\bar{k} = 0.45$, $Oh^{-1} = 200$, (**c**) $\bar{k} = 0.7$, $Oh^{-1} = 200$, (**d**) $\bar{k} = 0.9$, $Oh^{-1} = 200$, (**e**) $\bar{k} = 0.2$, $Oh^{-1} = 10$, (**f**) $\bar{k} = 0.45$, $Oh^{-1} = 10$, (**g**) $\bar{k} = 0.7$, $Oh^{-1} = 10$, (**h**) $\bar{k} = 0.9$, $Oh^{-1} = 10$, (**i**) $\bar{k} = 0.2$, $Oh^{-1} = 0.1$, (**j**) $\bar{k} = 0.45$, $Oh^{-1} = 0.1$, (**k**) $\bar{k} = 0.7$, $Oh^{-1} = 0.1$, (**l**) $\bar{k} = 0.9$, $Oh^{-1} = 0.1$. The numbers on the figures indicate the corresponding times (Courtesy of Cambridge University Press)

theory the variation of the logarithmic value of the amplitude of the surface disturbances with time is linear. Although, for an actual liquid jet this amplitude variation may not be linear, the experimental results of Goedde and Yuen [18] showed that for water and glycerin-water jets the logarithmic value of the

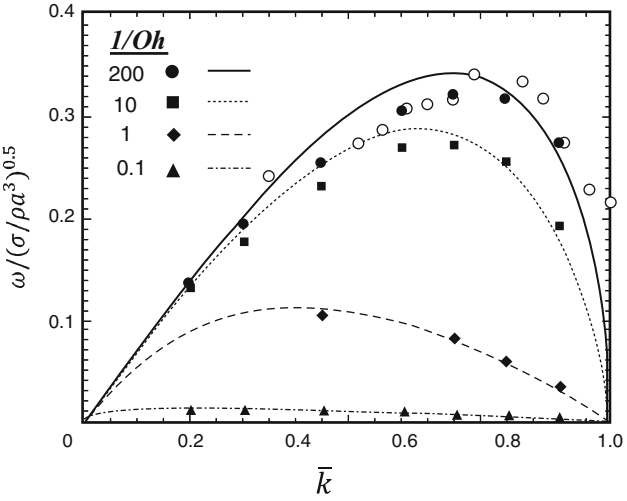


Fig. 1.9 Comparison of the numerically calculated growth rates (symbols) [75, Fig. 5] with those from Chandrasekhar's [23] linear theory, open circles are experimental data from [85] (Courtesy of Cambridge University Press)

difference between the amplitude at the neck and that at the swell varies linearly except close to the breakup moment.

The perturbation spectra are obtained using the calculated values of the growth rate for different wave numbers and for three *Oh* numbers. The data is plotted in Fig. 1.9, along with the corresponding curves from Chandrasekhar's [23] linear theory for a viscous jet equation (1.52). As predicted by the linear theory and observed experimentally, the viscosity reduces the magnitude of the growth rate for all wave numbers. In addition, the maximum growth rate occurs at lower wave numbers (i.e., for longer perturbation waves) for more viscous jets. This is due to the more effective viscous damping at larger wave numbers. The linear theory results in a better prediction at high *Oh* jets. At low *Oh*, the linear theory over-predicts the nonlinear growth rate for lower wave numbers and underpredicts it at higher wave numbers. The largest deviation at $Oh^{-1} = 200$ is approximately 10%. The experimental data of Cline and Anthony [85] for water jets which are also plotted in Fig. 1.9 (open circles) show the same behavior as the nonlinear results.

Again a better understanding of the effect of the nonlinearities on the jet breakup and the mode-coupling, Ashgriz and Mashayek [75] decomposed the jet surface shape into its linear modes by implementing the Fourier expansion:

$$r(z,t) = R + \sum_{n=0}^{\infty} c_n \cos(n\bar{k}z) \tag{1.58}$$

Again, $\bar{k} = 2\pi a/\lambda$ is a reduced wave number. The orthogonality of the cosine functions and numerical integration is used to determine the coefficients c_n.

Figure 1.10 shows the amplitude of the fundamental, zeroth, second, third, and fourth harmonics of the initial disturbance with time. Figure 1.10a shows the fundamental and higher harmonics for a jet with $Oh^{-1} = 200$ and $\bar{k} = 0.2$. Here, the second and third harmonics grow right from the initiation ($t = 0$). However, their amplitudes and growth rates are small at the beginning and become significant only later in time. In Fig. 1.10b, for $Oh^{-1} = 200$ and $\bar{k} = 0.9$, none of the harmonics grow until very close to the breakup time. The higher harmonics in this case do not grow until the formation of the thin ligament close to the breakup time.

The formation of the ligament can be explained by the nonlinear theories. The nonlinear analysis of Yuen [63] and also Chaudhary and Redekopp [71] have revealed that the mode coupling results in a feedback from higher harmonics to the fundamental and vice versa. For instance, the second harmonic generates interactions between the first four harmonics only by considering the second order solution. The summation of all of the fundamentals generated by this mode

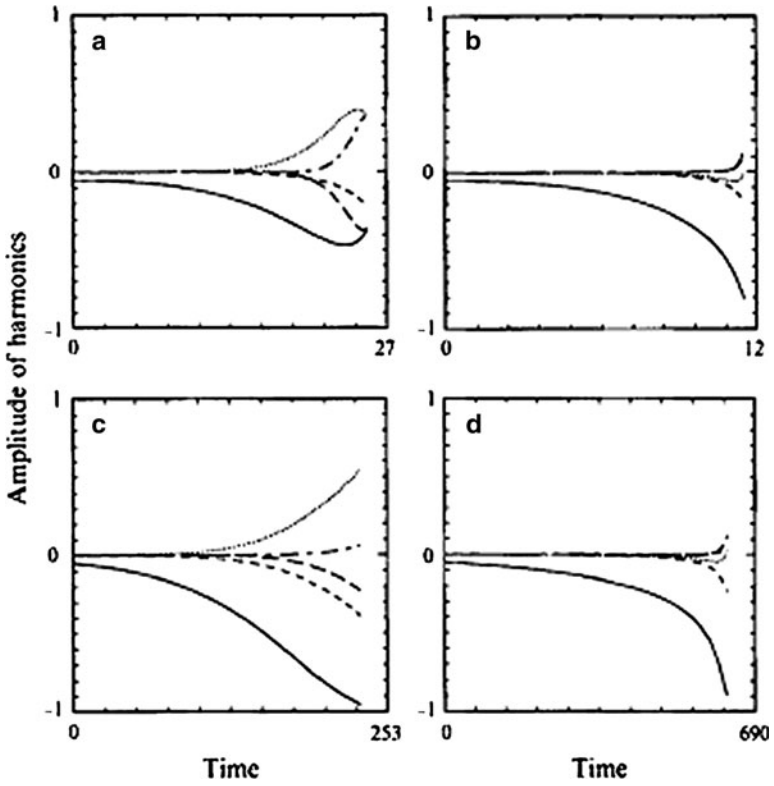


Fig. 1.10 Amplitude of the fundamental (- - -), and zeroth (- - -), second (· · ·), third (-- -- --), and fourth (-- - --) harmonics as a function of time [75, Fig. 6]. $\zeta_0 = 0.05$: (**a**) $\bar{k} = 0.2$, $Oh^{-1} = 200$, (**b**) $\bar{k} = 0.9$, $Oh^{-1} = 200$, (**c**) $\bar{k} = 0.2$, $Oh^{-1} = 0.1$, (**d**) $\bar{k} = 0.9$, $Oh^{-1} = 0.1$ (Courtesy of Cambridge University Press)

coupling results in the nonlinear variation of the fundamental, and the formation of the observed ligament.

As the wave number increases, the higher harmonics do not grow until very close to the breakup time. In addition, for large wave numbers the jet shape remains almost sinusoidal until the last moments of the breakup. This explains the rapid reduction of the ligament length with wave number. For smaller wave numbers, the feedback mechanism from the higher harmonics to the fundamental seems to be small. In fact the energy is mainly transferred from the fundamental to the higher harmonics. Figure 1.10a shows a minimum in the amplitude of the fundamental. Here, significant energy is transferred from the fundamental to the second and third harmonics. Note that the signs of the second harmonic and the fundamental are different for smaller wave numbers, but equal at larger wave numbers. In addition, the study of the harmonics reveals that no significant changes with Oh number occur within the range $Oh^{-1} = 10$–200. Generally, the second harmonic contributes the most to the observed nonlinearity in growth rates.

The breakup times for each wave number and for different Oh are shown in Fig. 1.11. The curves belong to Chandrasekhar's analytical solution, where the breakup times are calculated from the growth rates using the relation $t_b = \ln(a/\zeta_0)/\omega$. The numerically calculated data [75] are shown with symbols on Fig. 1.11 and are in good agreement with the analytical results only around the most unstable wave numbers. For each Oh, as the wave number increases, the breakup time first decreases until it reaches a minimum and then increases.

Linear theories by Rayleigh for inviscid jets and Weber–Chandrasekhar for viscous jets predict that a jet is unstable for disturbances with wave numbers

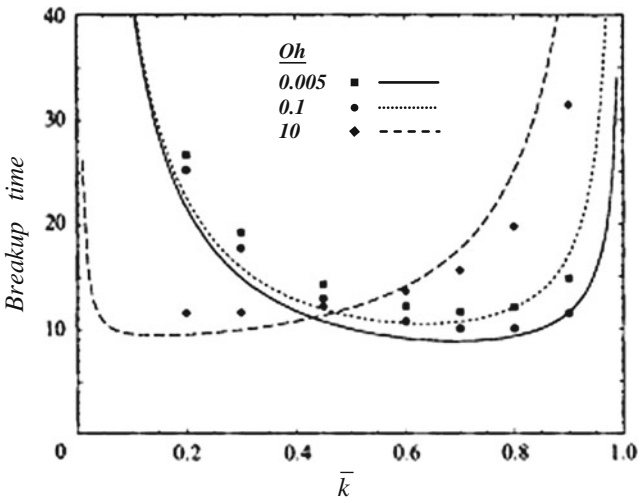


Fig. 1.11 Comparison of the numerically calculated breakup times with $\zeta_0 = 0.05$ (*symbols*) with those from Chandrasekhar's linear theory [75, Fig. 7] (Courtesy of Cambridge University Press)

smaller than one and stable for wave numbers greater than one. The cut-off wave number of $\bar{k}_c = 1$ is found to exist in the limiting case of an infinitesimal initial disturbance. Some nonlinear theories also predict $\bar{k} = 1$ [66]. However, the nonlinear theories by Yuen [63] and Nayfeh [11] predict that the cut-off wave number varies with the initial disturbance amplitude as: $\bar{k}_c = 1 + (9/16)\zeta_0^2$, and $\bar{k}_c = 1 + (3/4)\zeta_0^2$, respectively. Chaudhary and Redekopp's [71] nonlinear analysis results in a transitional zone for the cut-off wave number based on the initial disturbance amplitude. Their analysis shows that in the cut-off zone the growth rate changes from exponential to linear near $\bar{k} = 1$ and finally to an oscillatory solution. Experimental results of Chaudhary and Maxworthy [72, 73] have shown a linear growth rate for large initial inputs and transition toward a higher growth rate (i.e., shorter breakup time) for lower inputs near the cut-off wave number of 1.

Satellite Droplets

The first obvious deviation of the nonlinear instability from the linear theory is the formation of a long ligament between the main (parent) drops after the breakup as shown in Figs. 1.1 and 1.8. This ligament eventually becomes spherical and forms the satellite drop (it may also break up into even smaller drops). Therefore, the volume of the ligament between the main drops after the breakup provides the satellite size. Numerous studies have investigated the satellite droplet [61, 75, 86].

Satellite droplets may merge with the main drops shortly after they are formed. Figure 1.12 [21] shows three types of satellite formation: (a) rear merging; (b) stable; and (c) forward merging satellites. The type of merging depends on whether the satellite droplet is pinched from the front of the ligament or from its rear side.

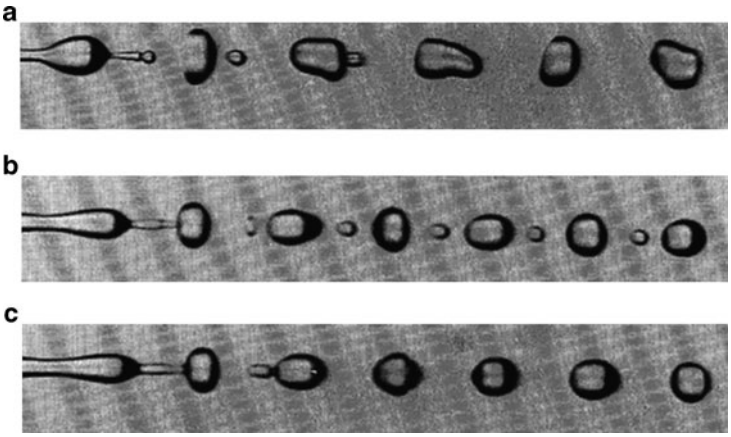


Fig. 1.12 Medium-wavelength Rayleigh breakup. **(a)** Rear merge satellite ($D = 0.34$ mm, $We = 27.3$, $\lambda/D = 5.7$). **(b)** Stable satellite ($D = 0.27$ mm, $We = 30.6$, $\lambda/D = 5.9$). **(c)** Forward merge satellite ($D = 0.27$ mm, $We = 30.6$, $\lambda/D = 5.9$) [21, Fig. 8] (Courtesy of the Royal Society)

Other types of merging droplets, such as reflexive merging are also observed, in which the satellite droplet collides with one of the main drops, but the conditions are such that they do not coalesce. The satellite droplet is then tossed toward the other main droplet for merging.

Figure 1.8 shows that as the wavelength increases, the length of the ligament and, consequently, the satellite size increase. Figure 1.13 shows the variation of the main drop radius as well as the radius of the satellite drop for different wave numbers [75]. Generally for the *Oh* numbers less than 0.1, there is no significant change in sizes with *Oh*. This explains the observed agreement between the results obtained by the inviscid theories (both weakly nonlinear analysis and boundary integral calculations of full nonlinear equations) and the experimental data for water jets ($Oh^{-1} = 200$) [86]. However, for $Oh > 0.1$ the variation becomes more pronounced.

The results show that for the same disturbance wave number the satellite size decreases with increasing *Oh*. For high-*Oh* jets, the viscous damping of the higher harmonics delays the movement of the minimum point and, consequently, results in a reduction of the ligament length. In addition, high-*Oh* jets need a higher pressure difference between the ligament and the drop to overcome the dissipative and inhibiting effects of viscosity in order to cause detachment of the ligament from the drop. This latter effect results in the reduction of the ligament diameter. An increase in viscosity strengthens the inhibiting effects of the fluid, and in order to have detachment, the ligament should become more slender and threadlike. The combined effects of reduced length and diameter of the ligament result in significant reduction of the satellite size for highly viscous liquids. Ashgriz and Mashayek [75] provided marginal jet *Oh* numbers for a range of disturbance wave numbers, below

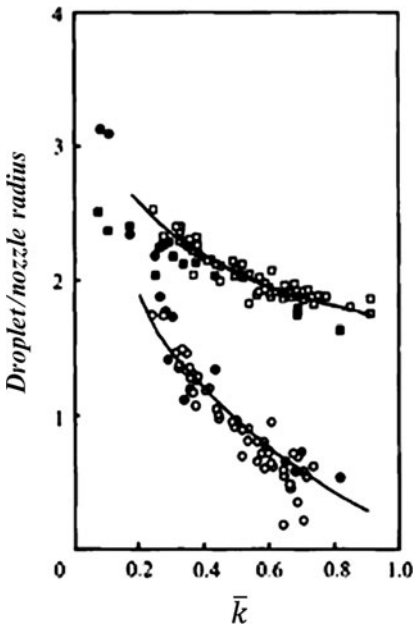


Fig. 1.13 Variation of the main and satellite drop sizes with wave number, prediction and comparison with the experimental data [75, Fig. 8] (Courtesy of Cambridge University Press)

which no satellite is formed. Figure 1.14 shows the satellite/no-satellite regions in terms of Oh and $\bar{k}$ for $\zeta_0 = 0.05$. As Oh decreases, satellite drops are eventually formed for all the unstable wave numbers. An interesting observation made from Fig. 1.14 is that the slope of the limiting Oh^{-1} versus the wave number curve changes significantly around $\bar{k} = 0.7$. For $\bar{k} < 0.7$, much larger Oh jets are needed in order to prevent satellite drop formation. For $\bar{k} > 0.7$, the slope of the curve is drastically increased and the limiting Oh^{-1} increases faster with the wave number.

Based on the nonlinear instability results, the satellite drops are persistently formed after the breakup. Only for very small Oh^{-1} values, the satellite drops are not observed. Also, an increase in the initial disturbance amplitude will shift the no-satellite region to lower Oh numbers. The results show that using jets with Oh^{-1} between 1 and 5 and disturbances with $\bar{k} > 0.8$, the satellite formation can be prevented, even with very small initial disturbance amplitudes.

Hibling and Heister [87] performed a boundary element-based numerical modeling to investigate the influence of unsteady inflow conditions on the nonlinear evolution and droplet formation processes within a low speed, finite-length capillary liquid jet. Their results indicate that modulation of either the amplitude or the frequency (wave number) of the perturbation can affect droplet sizes so as to create a monodisperse droplet train. For fixed orifice radius and liquid density, decreasing the Weber number corresponds to either increasing the surface tension or decreasing the inflow velocity [87]. As the surface tension is increased, the wave formed on the surface of the jet from the unsteady inflow should tend to grow more quickly, leading to shorter breakup lengths. This effect is shown in Fig. 1.15 for a jet that has

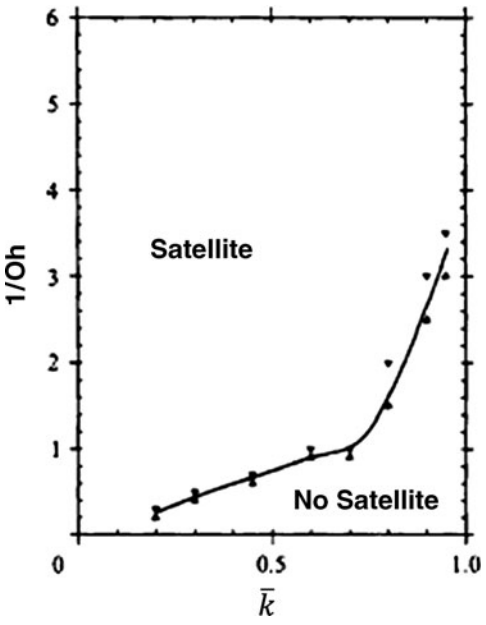


Fig. 1.14 The satellite/no-satellite regions in the Oh-k domain. Δ no satellite is formed, ∇ small satellite is formed [75, Fig. 9] (Courtesy of Cambridge University Press)

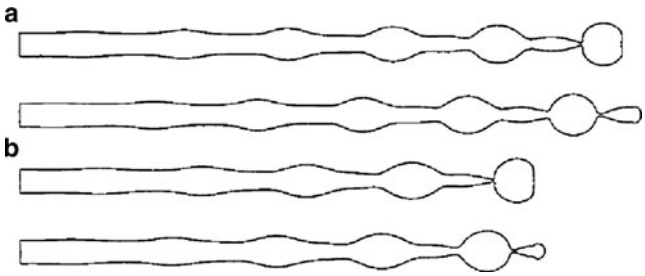


Fig. 1.15 Effect of Weber number on jet profile for $\bar{k} = 0.7$, $u' = 2\%$, (**a**) $We = 100$, (**b**) $We = 50$ [87, Fig. 3] (Courtesy of American Institute of Physics)

an inlet velocity perturbation with $We = 50$ and 100, using $\bar{k} = 0.7$ and velocity perturbation amplitude of $u' = 2\%$. Each pair of profiles shows the jet just before a main droplet and satellite droplet are shed from the calculation. Increasing the Weber number also tends to decrease the size of the satellite droplets for the chosen conditions. Note that the tip of the satellite droplet for the lower Weber number case takes on a more spherical shape before being shed from the calculation. In addition, at lower We values, the pinching event tends to form a series of waves on the parent surface due to the enhanced influence of surface tension.

Controlling Satellite Droplet Formation

It was noted that when a liquid jet is subjected to a monochromatic (single-wave number) disturbance with a wave number less than the cut-off wave number, it becomes unstable and breaks up. Each wavelength of the input disturbance usually generates two types of drops: a large main drop and one or more smaller satellite drops. Generally, the size of the satellite drops reduces with increasing (decreasing) the wave number (wavelength) and increasing the Ohnesorge number.

In order to obtain uniform-size drops, either the larger main drops or the satellite drops are eliminated. This is achieved mainly by three different techniques: (a) preventing the initial formation of the satellite drops; (b) forcing the satellite drops to merge with the main drops; (c) charging and deflecting one of the drops. To prevent satellite formation or forcing it to merge with the main drops, usually a complex wave form, rather than a single period wave, is used to disturb the jet. Therefore, satellite drop formation can be controlled by using frequency modulated disturbances. For instance, by disturbing the jet with two wave numbers, one being the fundamental $\bar{k}$, and the other being its second harmonic $2\bar{k}$, one may be able to reduce the satellite size.

Satellite drops can also be eliminated by increasing the amplitude of the initial disturbance. This reduces the breakup time, and therefore, there is no time for the development of the satellite-forming liquid ligament. For a jet with $Oh^{-1} = 200$ the initial disturbance amplitude has to be very large in order to eliminate the satellites.

Such high amplitudes are impractical in most applications. In practice, however, the change in amplitude results in the forward or backward merging of satellite drops with the main drops and, therefore, the formation of uniform drops shortly after the breakup point. Satellite merging is due to the nonsymmetric breakup of the liquid ligament. Pimbley and Lee [61], Chaudhary and Maxworthy [72, 73], Bousfield et al. [91] and Vassallo and Ashgriz [21] showed experimentally that the forward or backward merging of the satellites with the main drops can occur at various applied disturbance frequencies depending on the amplitude of the disturbance.

A more practical method of eliminating the formation of the satellite drops is by using a modulated disturbance. Chaudhary and Maxworthy [72, 73] provided results of such experiments. They used a modulated velocity disturbance composed of two frequencies, and showed that the satellite drop formation can be most effectively prevented by the superposition of the first and third harmonics for certain ratios of the initial amplitudes of the two harmonics. Modulated disturbances are also used to force the merging of the satellites with the main drops after their formation. Although forward and backward merging occurs even with monochromatic disturbances, the merging can be expedited by using modulated disturbances. Chaudhary and Maxworthy [72, 73] used the two-frequency disturbances and measured the distance it took for the satellite drops to merge with the main drops. They showed that the merging distance depends on the amplitude ratio of the two frequencies and the phase angle between them. In addition, Orme and Muntz [88] studied droplet formation experimentally by perturbing the jet with an amplitude-modulated velocity disturbance. They showed that the small droplets merge into a final configuration where the uniform drops are equally separated by one wavelength of the modulation frequency. Orme et al. [89] further obtained sequences of repeating drop patterns by adding non-integer frequency ratios (the ratio of the high to the low frequency).

Huynh et al. [92] conducted a numerical study of capillary instability of a jet subject to two superposed disturbances. The surface disturbance, ζ was composed of the superposition of two wave numbers:

$$\zeta(x) = \varepsilon_1 \cos(kx) + \varepsilon_n \cos(mkx + \theta)$$

where $\bar{k}$ and ε_1 respectively represent the reduced wave number $(2\pi a/\lambda)$ and the amplitude of the first harmonic (also referred to as the fundamental disturbance). ε_n represents the amplitude of the nth harmonic, and θ is the phase angle between the first and the nth harmonic input. Figure 1.16 presents typical breakup patterns for half of a wavelength obtained with an unstable second harmonic. The wave number considered is 0.45 and the amplitudes of the first and second harmonics are both 0.01. In the following description, the point at $x = 0$ and the point at $x = \lambda/2$ are referred to as the swell and the neck points, respectively (they are respectively the time until a cylindrical thread is formed. A contraction then appears at the joint between the bulbous swell region and the ligament thus creating a local pressure maximum which accelerates the detachment of the ligament by pushing the liquid away from that point. With the second harmonic input (Fig. 1.16b), a contraction is

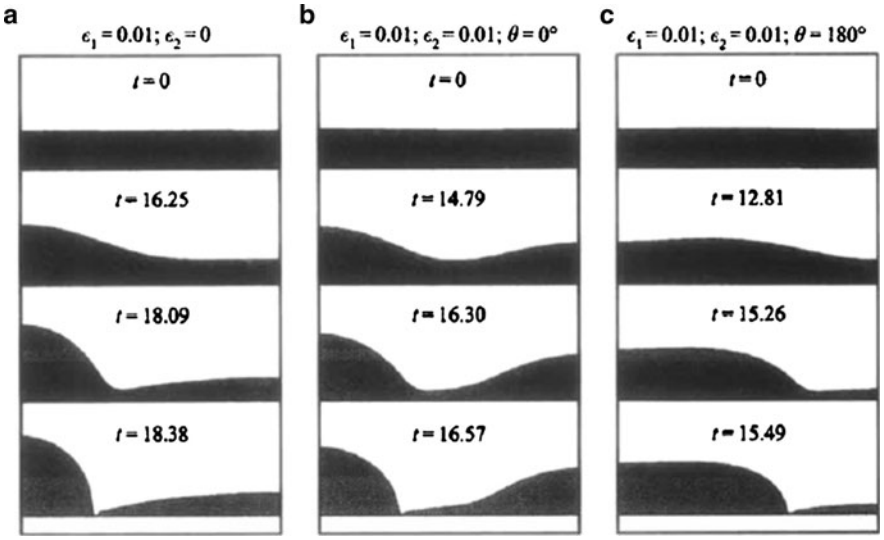


Fig. 1.16 Jet breakup by the addition of an unstable second harmonic, $\bar{k} = 0.45$ and $Oh^{-1} = 200$ [90, Fig. 2] (Courtesy of Elsevier)

formed around $\lambda/4$. The breakup occurs at one end of the ligament, resulting in a large satellite. When a phase angle of 180° is used, an almost opposite evolution of the jet occurs, as shown in Fig. 1.16c. Here, a bulging of the central region is observed and two contractions are formed at the swell and the neck points. The contraction at the neck point leads to the formation of a small ligament, which after pinch-off will produce the satellite drop. Notice that the breakup time is reduced when using an unstable second harmonic.

Figure 1.17 shows the variation of the main and satellite drop sizes versus the wave number of the first harmonic where the initial amplitudes of the sinusoidal disturbances are kept constant at $\varepsilon_1 = 0.01$ and $\varepsilon_2 = 0.05$. Three sets of results are presented in this figure: (a) first harmonic, only; (b) added second harmonic with $\theta = 0$; and (c) added second harmonic with $\theta = 180°$. Two different behaviors are observed. For $\bar{k} < 0.5$, when the added second harmonic is unstable, the breakup is highly dependent on the initial phase of the second-harmonic input. For no phase difference, the initial positive amplitude of the unstable second harmonic leads to satellites much larger than when no second harmonic is added. For very small wave numbers, the satellite drop becomes larger than the main drops. For $\theta = 180°$, which is equivalent to an initial negative amplitude of the second harmonic, the satellite drop sizes are significantly reduced.

Spangler et al. [93] considered nonlinear instability of a straight liquid jet under the influence of both capillary forces and aerodynamic interactions with an external gas. They showed that the gas phase interaction is important even at relatively low jet velocities. The presence of the gas leads to a "swelling" in the trough region of the wave. Aerodynamic interactions had very little effect on predicted droplet sizes

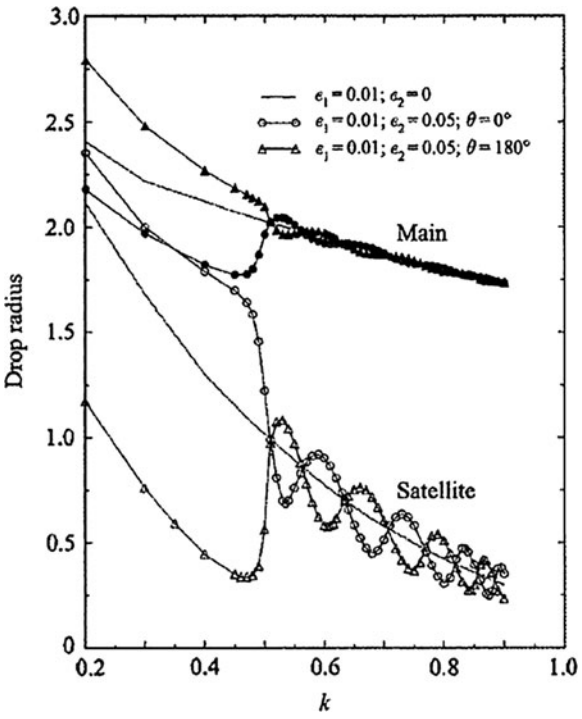


Fig. 1.17 Variations of the main and the satellite drop sizes with the wave number for $Oh^{-1} = 200$ [90, Fig. 5] (Courtesy of Elsevier)

for low speed jets within the Rayleigh regime. At higher velocities, a decrease in main drop size (with an attendant increase in satellite drop size) is predicted by the model. This behavior is attributed to the swelling phenomena which effectively drives the pinch location toward the droplet at higher jet velocities.

Figure 1.18 presents the nonlinear jet evolution in low speed conditions, referred to as the first wind-induced regime. In this figure, the surface shape is given at three different time steps during the evolution, with two complete waves of the disturbance shown. The first surface shape is at $t = 250$, and corresponds to a point just after the jet enters into the nonlinear portion of its growth. At this point, the maximum and the minimum radii of the surface are at the points that correspond to the initial peaks and troughs of the wave. The second surface shape is given at $t = 300$, well into the nonlinear portion of the jet growth. At this time, the minimum radius point on the surface no longer corresponds to the initial trough. The trough area has flattened out and there are now two points of minimum radius per wavelength, one at each end of the flattened trough area. The final surface shape shown is for $t = 312$, just before the pinching process occurs. At this time, the larger main drops are separated by thin ligaments of fluid that make up the satellite drops.

It is shown [93] that below $k = 0.28$ the satellite drops are larger than the main drops, while above this wave number, the main drops are larger than the satellite

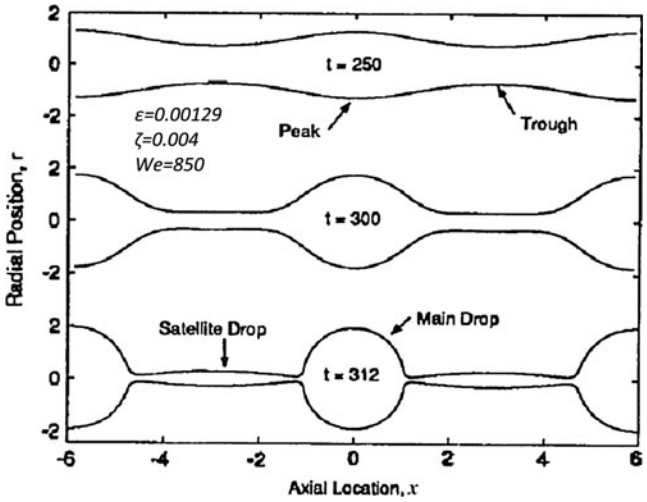


Fig. 1.18 Nonlinear jet evolution in the first wind-induced regime, $\varepsilon = 0.00129$, $k = 1.07$, $\zeta = 0.004$, $We = 850$ [93, Fig. 6] (Courtesy of American Institute of Physics)

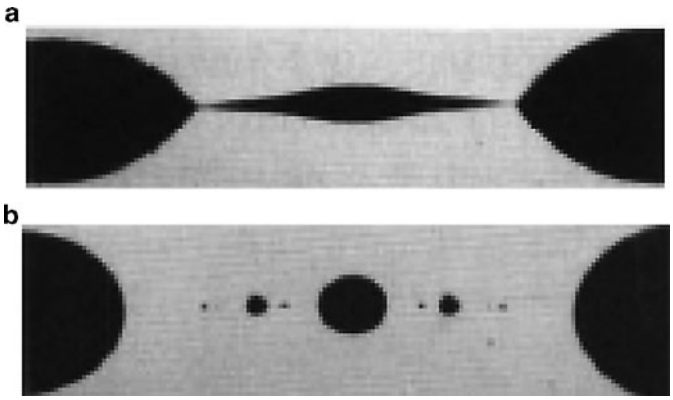


Fig. 1.19 Experiments showing the shape of the filament between the two main drops (satellite droplet) **(a)** before the firtst pinch-off and **(b)** after the last pinch-off, for droplet to surrounding fluid viscosity ratio of 0.4. The initial filament breaks up into more smaller satellite droplets due to the capillary action [94] (Courtesy of Cambridge University Press)

drops. At increased jet velocities (i.e., Weber numbers), the main drop radius decreases and the satellite drop correspondingly increases in size. This effect is attributed to the importance of the swelling phenomena. At higher *We* values, the swelling in the trough region is more dramatic (particularly for lower *k* values), thus moving the pinch location closer to the peak and increasing the size of the satellite droplet. It should be noted that since the initial filament connecting the main drops is highly deformed, it may breakup into several small satellite droplets, as shown in Fig. 1.19 by Tjahjadi et al. [94].

Thermocapillary Instability of a Liquid Jet

There are several studies on the effect of temperature perturbations on the instability of a liquid jet [95–98]. In non-isothermal capillary jets, variation of the surface tension with temperature along the free surface of the liquid results in a tangential shear force on the surface which induces the so-called thermocapillary flows [99, 100]. Thermocapillary effects can, depending on the particular conditions, enhance or retard the instability. It is generally shown that the breakup of a liquid jet may occur not only for surface amplitude disturbances with axial wavelengths larger than the circumference of the jet, but also through oscillatory temperature gradients that excite the otherwise calm and free surface.

Since liquid surface tension is strongly dependent on temperature, it can be controlled by controlling the liquid temperature. This technique was utilized [101, 102] to control the breakup of a water jet. Furlani et al. [103] have conducted a linear analysis of a jet subject to a spatially periodic variation of surface tension imposed along its length. It is shown that as the jet approaches breakup it swells at the points of maximum surface tension, and necks at the points of minimum surface tension. A periodic variation of temperature can induce a time-harmonic modulation of the surface tension σ of the jet, which has an equation of state of the form $\sigma(T) = \sigma_0 - \beta(T - T_0)$ where β is a property constant. Instability of an evaporating jet is considered by Saroka et al. [104], who showed that the evaporation increases the growth rate of instability.

Mashayek and Ashgriz [98] considered effects of the heat transfer from the liquid to the surrounding ambient, the liquid thermal conductivity, and the temperature-dependent surface tension coefficient on the jet instability and the formation of satellite drops. Two different disturbances were imposed on the jet. In the first case, the jet is exposed to a spatially periodic ambient temperature. In addition to the thermal boundary condition, an initial surface disturbance with the same wave number as the thermal disturbance is also imposed on the jet. Both in-phase and out-of-phase thermal disturbances with respect to surface disturbances are considered. For the in-phase thermal disturbances, a parameter set is obtained at which capillary and thermocapillary effects can cancel each other and the jet attains a stable configuration. No such parameter set can be obtained when the thermocapillary flows are in the same direction as the capillary flows, as in the out-of-phase thermal disturbances. In the second case, only an initial thermal disturbance is imposed on the surface of the liquid while the ambient temperature is kept spatially and temporally uniform (Fig. 1.20).

The instability of a liquid jet with thermocapillarity in a dynamically inactive ambient and in the absence of gravity and stationary relative to a moving observer is governed by the following nondimensional parameters: Reynolds, Re_p, Capillary, Ca, Prandtl, Pr, Marangoni, $Ma = Re_p\, Pr$, and Biot, Bi, numbers, defined as:

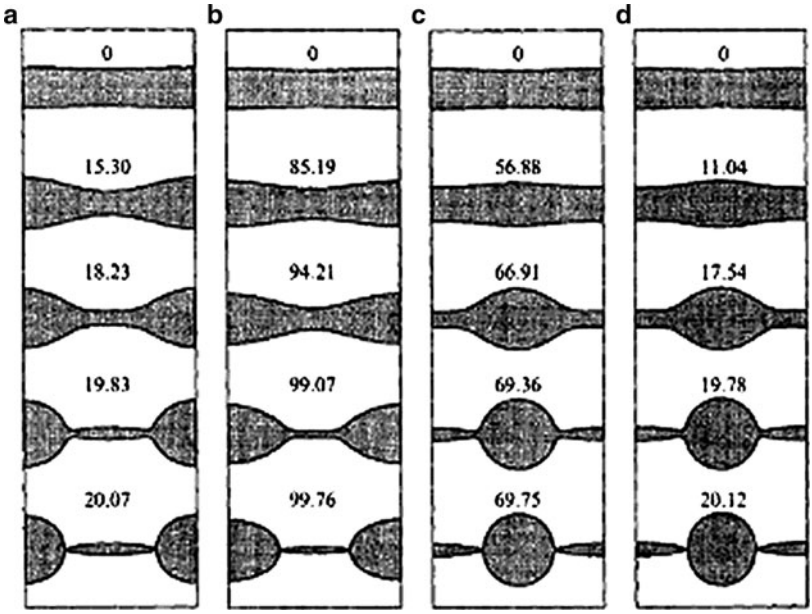


Fig. 1.20 Time evolution of surfaces of four jets with (**a**) $Bi = 0$, (**b**) $Bi = 1.37$, (**c**) $Bi = 1.38$, and (**d**) $Bi = \infty$. For all jets a surface displacement was applied accompanied by a thermal resistance which increased sinusoidally from 0 at the neck to 1 at the swell of the initial surface disturbance. The initial temperature was $T = 1$, $Re_p = 20$, $Ma = 200$, $Ca = 0.2$, $\bar{k} = 0.7$, and $\varepsilon_0 = 0.05$ for all jets. The numbers on the figure represent the time. Critical breakup of the jets occurs in the interval $1.37 < Bi < 1.38$ [98, Fig. 2] (Courtesy of Cambridge University Press)

$$Re_p = \frac{\rho\beta\Delta\widehat{T}a}{\mu^2}, \quad Ca = \frac{\beta\Delta\widehat{T}}{\sigma_0^2}, \quad Ma = Re_p \; Pr, \quad Bi = \frac{h_c a}{\widehat{k}}, \quad Pr = \frac{\mu c_p}{\widehat{k}}$$

where $\widehat{k}$ is thermal conductivity, c_p is the specific heat, h_c is the convective heat transfer coefficient at the surface of the jet, and the liquid surface tension, σ, is assumed to be a linear function of temperature, $\sigma = \sigma_0 - \beta\Delta\widehat{T}$, where $\widehat{T}$ is the liquid temperature, and σ_0 is the surface tension coefficient at a reference temperature $\widehat{T}_0$.

The results clearly show that a small temperature disturbance can quickly induce a surface disturbance which will eventually cause the breakup of the jet. Such temperature disturbances are readily available in most natural processes, since upon exiting from the nozzle the liquid temperature is usually slightly different than the ambient temperature. For the small thermal disturbance amplitudes the results indicate that neither the breakup time nor the satellite size are sensitive to *Bi* and *Ma*; however, they are sensitive to *Ca*. In other words, the initial thermal disturbance only induces a small surface disturbance which basically governs the instability of the jet thereafter.

Capillary Instability of a Swirling Jet

Ponstein [105] provided the following equation for the dispersion relations of a swirling liquid column in gas:

$$\omega^2 = \left[\frac{\sigma}{\rho_l a^3}\left(1-\bar{k}^2\right) + (1-\varepsilon)\left(\frac{\Gamma}{2\pi a^2}\right)^2\right]\bar{k}\frac{I_1(\bar{k})}{I_0(\bar{k})} + \varepsilon U^2 k^2 \frac{I_1(\bar{k})}{I_0(\bar{k})}\frac{K_0(\bar{k})}{K_1(\bar{k})} \tag{1.59}$$

where Γ is the circulation around the ring (or column), which can be estimated as $\Gamma = (2\pi a)U_\theta$ from Saffman [106]. Here U_θ is the tangential velocity of the ring surface. For non-swirling jet (i.e., $\Gamma = 0$) in the absence of the aerodynamic effect (i.e., $U = \varepsilon = 0$), Rayleigh's result is recovered [26]. Here, the centrifugal force (expressed via circulation) has a destabilizing effect as indicated by the positive sign on the Γ term. The faster the column swirls, the more unstable it becomes. Increasing gas density $\varepsilon(\rho_g/\rho_j)$ serves to aid in stabilizing the column circulation-related term, but destabilizes the dominant aerodynamic U^2 term. Considering the non-swirling case with aerodynamic effect, Ponstein's equation (1.59) can be written as [26]:

$$\omega^2 = \frac{\sigma}{\rho_l a^3}\left(1-\bar{k}^2\right)\bar{k}\frac{I_1(\bar{k})}{I_0(\bar{k})} + \varepsilon U^2 k^2 \frac{I_1(\bar{k})}{I_0(\bar{k})}\frac{K_0(\bar{k})}{K_1(\bar{k})} \tag{1.60}$$

For $\bar{k} \ll 1$, it is known that $I_1(\bar{k})/I_0\bar{k} \approx \bar{k}/2$. Applying this identity, (1.60) is re-written as:

$$\omega^2 = \frac{\sigma}{2\rho_l a^3}\left(1-\bar{k}^2\right)\bar{k}^2 + \varepsilon\frac{U^2(\bar{k})^3}{2a^2}\frac{K_0(\bar{k})}{K_1(\bar{k})} \tag{1.61}$$

This result is exactly the same as the inviscid case of the characteristic equation derived by Sterling and Sleicher, (1.45).

Capillary Breakup of Rheologically Complex Liquid Jets

The effects of such physical properties as liquid density, viscosity and surface tension on the capillary jet breakup in the case of Newtonian viscous liquids are discussed in the previous sections of this chapter. In many applications non-Newtonian liquid jet flows are used, which demonstrate very peculiar deviations from the Newtonian behavior. This section is devoted to the discussion of the dominating effects of rheological properties on jet breakup.

A relatively close counterpart of Newtonian liquids is the family of the nonlinear power law liquids, which do not possess any viscoelastic, thixotropic, or rheopectic

effects or yield stresses and behave according to the following rheological constitutive equation:

$$\boldsymbol{\tau} = -p\mathbf{I} + 2K\left[2\,\mathrm{tr}\left(\mathbf{D}^2\right)\right]^{(n-1)/2}\mathbf{D}, \tag{1.62}$$

where p in pressure, $\mathbf{I}$ is the unit tensor, $\boldsymbol{\tau}$ and $\mathbf{D}$ are the stress tensor and the rate of strain tensor, respectively, and K and n are the rheological parameters of the liquids. For $0 < n < 1$, the liquids are termed pseudoplastic, for $n > 1$, dilatant; the linear case of $n = 1$ (with $K = \mu$) corresponds to Newtonian viscous liquid. The effective viscosity of pseudoplastic liquids decreases as the rate of strain increases, whereas for dilatant liquids it increases as the rate of strain increases. Typical representatives of pseudoplastic liquids are various suspensions, whereas dilatant liquids are rather rare, albeit rheological behavior of viscoelastic liquids in some cases mimics that of the dilatant ones, as discussed in the monograph by Yarin [29].

Capillary breakup of free jets of aqueous clay suspensions or of γ-Fe_2O_3 particles in oil moving in air was studied experimentally and theoretically by Yarin and coauthors in [29, 107]. In the experiments the initial perturbations were imposed by a needle periodically touching the jet surface with a frequency of 250 Hz. Such an excitation of purely Newtonian jets frequently led to an irregular breakup. However, jets of sufficiently concentrated suspensions demonstrated a peculiar sausage-like breakup with the length determined by the perturbation frequency (cf. Fig. 1.21). Later on, the sausages shrink in flight under the action of surface tension and recover spherical shape.

The quasi-one-dimensional theory of capillary breakup of pseudoplastic jets provides an explanation of the phenomenon of sausage-like breakup [29, 107]. In the case of the power law liquids, the continuity and momentum balance equations of straight jets have the form (1.49) and (1.50), whereas, based on (1.62), (1.51) is replaced by a more general one:

$$\tau_{xx} = 3^{(n+1)/2}K\left|\frac{\partial U}{\partial x}\right|^{n-1}\frac{\partial U}{\partial x} - \sigma\left\{\frac{1}{R(1+R_x^2)^{1/2}} - \frac{R_{xx}}{(1+R_x^2)^{3/2}}\right\} \tag{1.63}$$

The system of equations (1.49), (1.50), and (1.63) was integrated numerically for the case of an infinite jet (thread), i.e., considering the temporal instability. The results showed that in the case of a sufficiently expressed pseudoplastic behavior (with the exponent n being sufficiently smaller than 1), the time to breakup and the breakup pattern are strongly affected by the amplitude and shape of the initial perturbation. In particular, in the case of a narrow axisymmetric localized depression of the jet surface, which mimics perturbation imposed by a touching needle, the subsequent evolution of the jet profile shows a localized progress of pinching. As a result, the jet breaks up into "sausages" (Fig. 1.22). It is explained by the fact that a sufficient rate of deformation appears only close to the jet necking. For the pseudoplastic rheological behavior, it results in a localized decrease in the effective

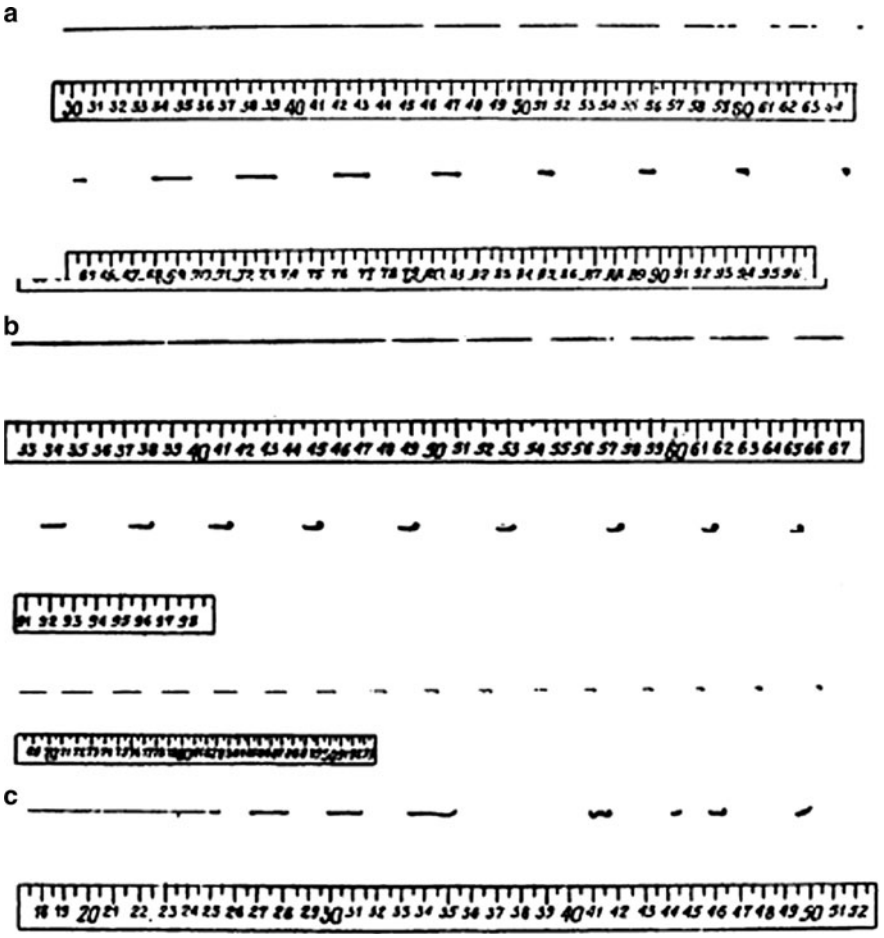


Fig. 1.21 Capillary breakup of pseudoplastic liquid jets [29]. **(a)** Suspension of 25% γ-Fe_2O_3 particles in oil. **(b)** Suspension of 36% γ-Fe_2O_3 particles in oil. **(c)** Aqueous suspension of clay (Courtesy of Pearson Education)

viscosity of the liquid close to the jet necking locations. This, in turn, after a certain delay related to the flow development, leads to a rapid, avalanche-like localized progressing of necking. The duration of the delay depends on the amplitude of the initial perturbation ζ_0. For the values of the exponent n sufficiently lesser than 1, it can be very long for relatively small initial perturbations resulting in small initial rates of deformation near the surface depressions and, hence, in high effective viscosities there. This can extend the duration of the capillary breakup as a whole. On the other hand, relatively large amplitudes of the initial perturbations result in large initial rates of deformation near the surface depressions and, hence, in low effective viscosities there, which decreases the delay time and leads to a rapid jet breakup as a whole.

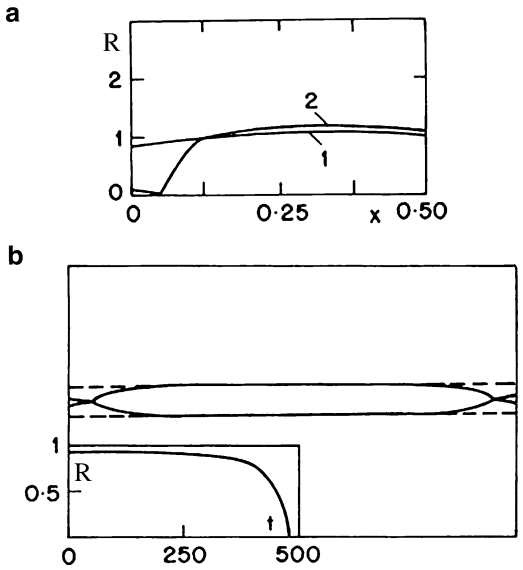


Fig. 1.22 Capillary breakup of a pseudoplastic jet (Yarin [29]). The parameter values are: $K/\rho = 8.18 \times 10^{-4}$ m^2/s$^{1.5}$, $\sigma/\rho = 34.7 \times 10^{-6}$ m^3/s^2, $n = 0.5$, $a = 0.06 \times 10^{-2}$ m, the perturbation wavelength $\lambda = 1.98 \times 10^{-2}$ m. **(a)** The evolution of the jet profile corresponding to a half wavelength of the perturbation (the cross-sectional radius is rendered dimensionless by its unperturbed value a, the longitudinal coordinate x – by λ, time – by $T = 0.229 \times 10^{-3}$ s). **(b)** Shape of the "sausage" emerging at the moment of the breakup corresponding to one perturbation wavelength: $1 - t = 300$, $2 - t = 479.05$. The inset in (b) shows the evolution of the radius in the jet cross-section where the breakup takes place (Courtesy of Pearson Education)

The flow near the necking sections of pseudoplastic liquid jets at the final stages of their capillary breakup "forgets" the global jet configuration and becomes self-similar. This behavior was studied in detail in [108] in the framework of the elongational rheology of gelled propellants and their simulants.

The capillary breakup pattern described above is expressed stronger when the liquid pseudoplasticity manifests itself stronger. Therefore, their most spectacular manifestations are observed in the experiments with sufficiently concentrated suspensions. However, they are also seen in the experiments with jets of polymer gels [109]. The latter work is devoted to the effect of the thixotropic breakup of the internal structure of a gel on capillary jet breakup.

By contrast, it is clear that dilatant liquids should demonstrate an increased stability in the necking sections of capillary jets and a deceleration of the later stages of the capillary breakup. A relatively rapid growth of the initial axisymmetric perturbations leads to an increase of the effective viscosity in the necking sections of the jet and its transformation into a net of practically spherical droplets connected by tiny threads. The results of the numerical calculations for dilatant liquids by Yarin [29] are depicted in Fig. 1.23.

The inset in Fig. 1.23 shows a characteristic deceleration of the later stage of the capillary breakup of a dilatant jet, when significant rates of elongation in the liquid threads connecting the drops are reached, and the corresponding "reinforcement" of the liquid in the threads occurs. At this late stage, the evolution of the jet surface is so slow that the calculations can be made in the inertialess approximation.

The comparison of the results for the capillary breakup of viscous Newtonian (Figs. 1.6 and 1.7), pseudoplastic (Figs. 1.21 and 1.22) and dilatant (Fig. 1.23) liquids demonstrates a very strong influence of the rheological properties of liquid on both the breakup time and the drop shape. Liquid jets with strongly expressed dilatancy are characterized by a relatively rapid transition to a quasi-steady stage with an almost fully developed beads-on-a-string structure of practically spherical drops (in distinction from the pseudoplastic liquid jets whose breakup is completely determined by the magnitude and form of the initial perturbations). The estimate of the breakup time of the beads-on-a-string structure of dilatant jets given in Yarin [29,] reads

$$T_{breakup} = 2n\left(3^{(n+1)/2}\frac{Ka}{\sigma}\right)^{1/n} \tag{1.64}$$

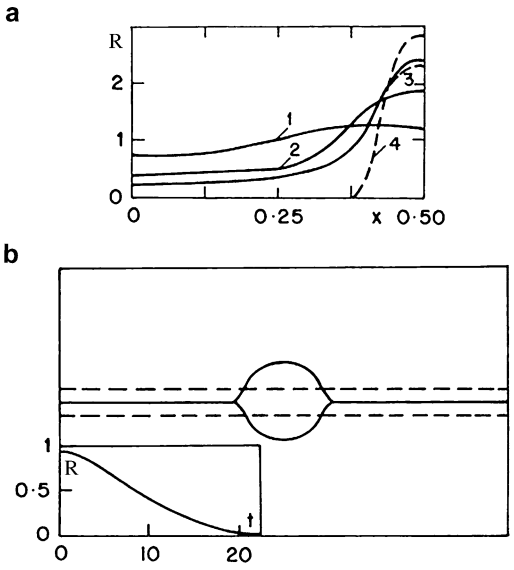


Fig. 1.23 Capillary breakup of a dilatant jet [29]. The parameter values are: $K/\rho = 9.43 \times 10^{-4}$ $m^2/s^{0.5}$, $\sigma/\rho = 34.7 \times 10^{-6}$ m^3/s^2, $n = 1.14$, $a = 0.06 \times 10^{-2}$ m, the perturbation wavelength $\lambda = 1.98 \times 10^{-2}$ m. **(a)** The evolution of the jet profile corresponding to a half wavelength of the perturbation (the cross-sectional radius is rendered dimensionless by its unperturbed value a, the longitudinal coordinate x – by λ, time – by $T = 6.08 \times 10^{-2}$ s); $1 - t = 5$, $2 - t = 10$, $3 - t = 13$, $4 - t = 21.85$. The evolution from curve 3 to the dashed curve 4 was calculated in the inertialess approximation. **(b)** Shape of the jet emerging at the moment of its breakup corresponding to one perturbation wavelength. The inset in (b) shows the evolution of the radius in the jet cross-section where the breakup takes place (Courtesy of Pearson Education)

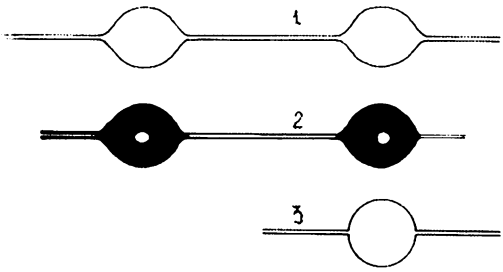


Fig. 1.24 Capillary breakup of a thin jet of 0.02 wt% aqueous solution of poly(oxy ethylene) WSR-301 [29]. The unperturbed cross-sectional jet radius $a = 2.74 \times 10^{-4}$ m. **(1)** The results of the numerical simulations. **(2)** The experimental image. **(3)** The analytical asymptotic solution by Yarin [29, 111] (Courtesy of Pearson Education)

Various liquids (first of all, polymer solutions) demonstrate "memory" effects, i.e., viscoelasticity. Among the experimental works devoted to capillary breakup of dilute polymer solution jets, an important role was played by [110]. In the experiments of [110], the axisymmetric capillary perturbations began to increase similarly to their growth in the corresponding jets of pure solvents. However, at the later stage capillary jets of dilute polymer solutions formed the beads-on-a-string structure (see the photographic image 2 in Fig. 1.24 from Yarin [29]). This structure appears to be amazingly long-living. As a result, the jet length to breakup sharply increases compared to the corresponding jets of pure solvents (with practically the same values of density, surface tension, and the initial cross-sectional radius and velocity). An increase in the polymer concentration results in suppression of the initial fast perturbation growth after a jet is issued from the nozzle. In this case such a jet has an appearance of a smooth cylinder. Only at a significant distance from the nozzle, the visible axisymmetric perturbations become apparent on the jet. This pattern was fully corroborated by the later experiments in [112, 113] and in numerous consequent works.

One of the reasons of the enhanced stability of viscoelastic jets is related to the fact that they can develop significant longitudinal stresses during their flow inside the nozzle or in the transitional zone of the jet formation beyond the nozzle exit, which do not have enough time to relax during capillary breakup of the free jet. The physical reason of the emergence of significant longitudinal stresses is in the coil-stretch transition of polymer macromolecular coils in the converging part of flow near the nozzle entrance or exit. The presence of the longitudinal stresses in polymer liquid jets was experimentally demonstrated in [114, 115] using observations of bending perturbations imposed on straight jets (see some additional detail below). It is emphasized, that this is a nontrivial phenomenon. Indeed, free non-electrified jets are not pulled at their leading edge. Therefore, a jet can continue to be stretched only if the deformation from the unloaded leading edge does not have enough time to reach the nozzle exit [116, 117]. This can happen if the jet velocity is higher than the speed of propagation of waves of the elastic stresses (the elastic "sound"), i.e., the jet is "supersonic" in a sense. On the other hand, if a jet propagates slowly, it will be "subsonic" and completely unloaded. Then, after being issued from a nozzle, a viscoelastic jet abruptly swells, a phenomenon called die swell in the fiber spinning technology.

The appearance of significant longitudinal elastic stresses represents itself only one of the manifestations of stretching of macromolecular coils in jets of polymer solutions. Sometimes the measured stresses are so large (e.g., of the order of 10–100 kPa [115]) that one can speak about an almost complete stretching of macromolecules along the jet. However, this alone does not fully explain the mechanism of stabilization of jets by macromolecular additives. Some additional mechanisms are discussed below.

Formation of the beads-on-a-string structure at the late stage of capillary breakup of dilute polymer solution jets is also directly related to the coil-stretched transition of macromolecular coils in such jets. The very fact of a "long life" of the emerging tiny threads between the growing drops (cf. Fig. 1.24) demonstrates an unusual resistance of liquid in them to any further deformation. A thin thread is squeezed radially by the capillary pressure σ/a. Therefore, liquid in the thread flows axially toward the two ends attached to the neighboring drops. The effective longitudinal stress is also of the order of σ/a. In a viscous Newtonian liquid, such longitudinal stress will result in the following rate of elongation

$$\dot{\varepsilon} = -\frac{2}{R}\frac{dR}{dt} = \frac{\sigma}{3\mu R} \tag{1.65}$$

Therefore, measurements of the rate of thread self-thinning $da/(adt)$ reveal the value of the effective viscosity of liquid μ. The results of such experiments with dilute polymer solution jets and threads [118–120] revealed the values of the effective viscosity that are larger than the solvent viscosity or the shear viscosity of the same solution by 3–4 orders of magnitude. For example, for dilute 0.02 wt% aqueous solution of poly(oxy ethylene) WSR-301, the elongational viscosity was found to be $\mu_{el} = 7$ Pa s, whereas its shear viscosity was $\mu_{sh} = 3 \times 10^{-3}$ Pa s. This approach resulted in the development of a new type of an elongational rheometer for dilute polymer solutions [118–122].

The theoretical studies of the capillary breakup of viscoelastic jets were seemingly in disagreement with the experimental results for quite some time. The linear stability analysis of the effect of the elastic stresses on the capillary instability of capillary jets always (irrespective of the viscoelastic constitutive equation used) leads to a conclusion that small axisymmetric perturbations in viscoelastic liquid jets grow faster than in the corresponding Newtonian jets of the same viscosity [110, 123–128]. The reason of that is quite elementary: in the framework of the linearized small perturbation theory, when the unperturbed state corresponds to an unloaded liquid at rest, the elastic stresses are of the order of the square of the perturbation amplitude, and thus, are negligibly small. As a result, the role of elasticity is reduced to a decrease in the effective viscosity, which makes the jet more unstable. In other words, a Newtonian liquid is rigid, whereas its linearized viscoelastic counterpart is elastic, i.e., weaker than the rigid originator and thus prone to a faster perturbation growth rate. The resolution of the above-mentioned disagreement can be achieved if a jet with significant longitudinal elastic stresses is taken as an unperturbed state [29, 111, 127]. According to the results of these

works, it is possible to state that a fast growth of the axisymmetric perturbations of capillary jets of viscoelastic liquids is possible only after a full relaxation of such longitudinal stresses, i.e., with a delay of the order of the relaxation time of liquid θ. Perhaps that is the reason of a long absence of visible perturbations on the jets of semi-dilute polymer solutions in [110].

Yarin et al. [29, 111] gave a theory of the capillary breakup of thin jets of dilute polymer solutions and formation of the bead-on-the-string structure (some additional later results can be found in [90]). The basic quasi-one-dimensional equations of capillary jets (1.49) and (1.50) are supplemented with an appropriate viscoelastic model for the longitudinal stress. Yarin et al. [29, 111] used the Hinch rheological constitutive model, which yields the following expression

$$\tau_{xx} = 3\mu\left(1 + 5cr^3K_1\right)\frac{\partial U}{\partial x} - \sigma\left(\frac{1}{R(1+R_x^2)^{1/2}} - \frac{R_{xx}}{(1+R_x^2)^{3/2}}\right) + c\kappa K_2\left(L_{xx} - L_{yy}\right) \tag{1.66}$$

The last term on the right hand side in (1.66) expresses the elastic stress through the components of the orientation-deformation tensor **L**. The evolution of this tensor in the jet flow is described by the following equations accounting for macromolecular stretching and relaxation

$$\frac{\partial L_{xx}}{\partial t} + U\frac{\partial L_{xx}}{\partial x} = 2K_1L_{xx}\frac{\partial U}{\partial x} - K_2K_3\left(L_{xx} - \frac{r^2}{3}\right), \tag{1.67}$$

$$\frac{\partial L_{yy}}{\partial t} + U\frac{\partial L_{yy}}{\partial x} = -K_1L_{yy}\frac{\partial U}{\partial x} - K_2K_3\left(L_{yy} - \frac{r^2}{3}\right), \tag{1.68}$$

$$K_1 = \frac{2L_{yy} + L_{xx}}{3r^2 + 2L_{yy} + L_{xx}}, \quad K_2 = \frac{Nb}{Nb - \sqrt{2L_{yy} + L_{xx}}}, \tag{1.69}$$

$$K_3 = \frac{2r}{\theta\sqrt{2L_{yy} + L_{xx}}} \tag{1.70}$$

In (1.66)–(1.70), μ denotes solvent viscosity, c is the number of macromolecules in unit volume, b is the length of Kuhn segments in macromolecule, N is the number of Kuhn segments in macromolecule, $r = bN^{1/2}$ is of the order of the equilibrium macromolecular coil size, $\theta = 6\pi\mu r/\kappa$ is the relaxation time, κ the elasticity of macromolecular coils. According to the second equation (1.69) macromolecules cannot be stretched beyond their fully expended length Nb.

The results of the numerical calculations based on (1.49), (1.50), and (1.66)–(1.70) depicted in Figs. 1.24 and 1.25 reveal the evolution in time of a jet segment corresponding to one wavelength of perturbation. The relevant dimensionless groups for viscoelastic jets are the volume fraction of the macromolecular coils in solution in

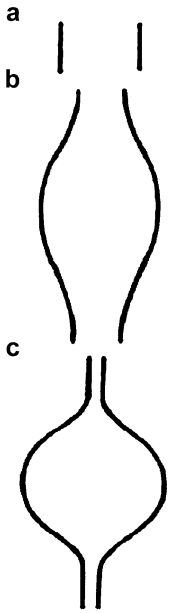


Fig. 1.25 The emergence of the beads-on-a-string structure during capillary breakup of a thin viscoelastic jet (Yarin [29]). The values of the dimensionless groups are $\varphi = 0.419$, $De^{-1} = 0.21 \times 10^{-2}$, $L_0 = 2.5$. (**a**) $t = 0$, (**b**) $t = 0.37 \times 10^{-3}$ s, (**c**) $t = 0.56 \times 10^{-3}$ to 3.04×10^{-2} s (Courtesy of Pearson Education)

equilibrium $\varphi = 4\,\pi cr^3/3$, the inverse Deborah number $De^{-1} = \mu a/(\sigma\theta) = \kappa a/(6\pi r\sigma)$, and L_0 discussed below. The inverse Deborah number represents the ratio of the characteristic time of the capillary breakup affected by viscous forces to the elastic relaxation time. It can also be interpreted as the ratio of the initial modulus of elasticity of macromolecular coils to capillary pressure. The value L_0 represents the initial value of the longitudinal component of the orientation-deformation tensor $\mathbf{L}$, L_{xx}, which characterizes the initial axial elongation of macromolecular coils. The ratio of the initial elastic energy to the surface energy of the jet E_0 can be expressed as $E_0 = 9\,\varphi De^{-1}L_0/8$. The results in Fig. 1.25 correspond to 0.03 wt% aqueous solution of poly(oxy ethylene) WSR-301. In the case of $L_0 = 2.5$, the value of $E_0 = 2.5 \times 10^{-3}$, which shows that the effect of the elastic stresses at the early stage of perturbation growth is small. However, the elongational flow in the emerging thin threads connecting growing drops results in the axial orientation and elongation of macromolecular coils. Such an elongation can reach one third of the fully stretched macromolecular length. The macromolecular stretching at this level appears to be sufficient for such a significant reinforcement of liquid in the threads that the outflow from them into drops abruptly decreases, as the jet evolution decelerates as a whole. As a result, the beads-on-a-string structure forms. It is emphasized that a significant stretching of macromolecular coils in the jet after some delay emerges almost abruptly. In the numerical calculations the beads-on-a-string structure can be observed almost unchanged up to the times, which are fivefold the liquid relaxation time ($\theta = 6.15 \times 10^{-3}$ s). At this moment the calculations were terminated. If the initial axial elongation of macromolecular coils is increased up to $L_0 = 100$ ($E_0 = 0.1$) with the other parameters being unchanged, the initial elastic stresses begin to affect

the initial stage of perturbation evolution. This results in a delay of the order of 2.5θ, during which there is no visible perturbation growth in correspondence with the predictions of the linear stability theory. After a partial relaxation of the longitudinal stress, a relatively slow perturbation growth begins. It results in an increase of the longitudinal stresses in the jet contractions, stretching of macromolecular coils, and the emergence of the beads-on-a-string structure. An increase in the solvent viscosity leads to an increase in the relaxation time, as well as in the delay time. In general, the numerical results confirm the stabilizing effect of the elastic stresses at both the initial stage of the evolution of capillary viscoelastic jets, and at the stage of formation of beads-on-a-string structure. The following numerical works also predicted formation of beads-on-a-string structure in capillary viscoelastic jets using quasi-one-dimensional or three-dimensional (axisymmetric) equations and different viscoelastic rheological constitutive equations [90, 129, 130].

Since the beads-on-a-string structure evolves very slowly, it can be considered as a succession of nontrivial (non-cylindrical) quasi-equilibrium shapes of an elastic material subjected to the action of surface tension and a very slow viscoelastic relaxation. The asymptotic analysis of such jet shapes under the assumption that the material represents itself a neo-Hookean body was conducted by Yarin et al. in [29, 111]. It revealed that the nontrivial quasi-equilibrium jet shapes represent themselves a succession of spherical drops of radius $a = (3\lambda/4a)^{1/3}$ (with λ being perturbation wavelength), which are fully relaxed and practically do not possess any elastic stresses, and strongly stressed thin uniform threads connecting the drops. The cross-sectional radius of these threads is $a(\varepsilon/2)^{1/3}$, where $\varepsilon = 2Ga/\sigma$ is the ratio of the modulus of elasticity to capillary pressure. This analytical solution is compared to the experimental data and the results of the numerical simulations in Fig. 1.24 (curve 3). This analytical solution for beads-on-a-string structure was later confirmed in [131]. The thread stability can be sustained if the gradual thinning would be accompanied by an increase of the longitudinal elastic stress that is faster than the corresponding decrease of the surface tension force $\pi\sigma a$. The initial cylindrical shape would be always stable if the liquid stiffness is sufficiently high, i.e., $\tau_{xx}(t=0)\, a/\sigma >> 1$. In the latter case there is no nontrivial (non-cylindrical) jet shapes.

However, in experiments even beads-on-a-string structure ultimately breaks up. Yarin [29] attributed the weakening and breakup of the beads-on-a-string structure to mechanical degradation of polymer macromolecules in strong elongational flows in the tiny threads between drops. Another possible mechanism of weakening of the threads is related to viscoelastic relaxation leading to a partial unloading there [129]. As a result, new cycles of the capillary instability appear in a cascade-like manner and new drops are formed between the original beads in the structure. These "iterative instabilities" were revealed in the experiments of [132]. It is emphasized that the duration of the uniform stretching in thin threads of dilute polymer solutions is very long. The uniform self-thinning in many cases proceeds to such sizes where the "iterative instabilities" cannot be observed optically. Such threads are the key element of the elongational rheometers for dilute polymer solutions [118–121] where the threads emerge either between the drops in a jet or between small solid

plates. The dynamics of the uniform thread self-thinning under the action of capillary pressure was developed in [118–120, 132–135]. This theory predicts the existence of an intermediate universal regime of thread thinning according to the following exponential law

$$a = a \exp\left(-\frac{t}{3\theta}\right) \tag{1.71}$$

where a is the cross-sectional thread radius at a certain moment of time, i.e., $t = 0$.

Comparing of (1.71) with the experimental data allows for measurements of the viscoelastic relaxation time θ of dilute and semi-dilute polymer solutions.

Straight jets of concentrated polymer solutions and melts typically possess such high elastic stresses that surface tension becomes negligibly small and capillary breakup does not happen. The latter opens doors to such important technologies as melt spinning of man-made polymer fibers, as well as spinning of optical fibers, where the Newtonian viscosity of molten glass dominates surface tension and also suppresses capillary breakup. These are the key technological processes of the textile, non-woven and optoelectronic industries. They demonstrate fascinating dynamics, which are, however, out of scope of the present section. An interested reader is addressed to the following monographs by Yarin, Ziabicki and Kawai discussing these issues: [29, 136, 137].

References

1. Bidone, G. Experiences sur la forme et sur la direction des veines et des courants d'eau lances par diverses ouvertures. *Imprimerie Royale*, Turin, pp. 1–136 (1829).
2. Savart, F. Memoire sur la constitution des veines liquides lancees par des orifices circulaires en mince paroi. *Ann. Chim. Phys.* 53, 337–386 (1833).
3. Plateau, J. Statique experimentale et theorique des liquids soumis aux seules forces moleculaires. Cited by Lord Rayleigh, *Theory of Sound*, Vol. II, p. 363, 1945. New York: Dover (1873).
4. Rayleigh, W.S. On the instability of jets. *Proc. London Math. Soc.* 10, 4–13 (1879).
5. Rayleigh, W. S. On the instability of jets. *Proc. London Math. Soc.* 4, 10 (1878).
6. Rayleigh, W.S. Further observations upon liquid jets. *Proc. London Math. Soc.* 34, 130–145 (1882).
7. Rayleigh, W.S. *Theory of Sound*, 2nd edn, Vol. 2. London: Macmillan (1896). Reprinted in 1945, New York: Dover, 504 pp.
8. Magnus, G. Hydraulische Untersuchungen. *Anne. Phys. Chem.* 95, 1–59 (1855).
9. Boussinesq. J. *Mem. Acad. Sci. Paris* 23, 639 (1877).
10. Weber, C. On the breakdown of a fluid jet, Zum Zerfall eines Flussigkeitsstrahles. *Z. Angew. Math. und Mech.* 11, 136–154 (1931).
11. Nayfeh, A. H. Non-linear stability of a liquid jet. *Phys. Fluids* 13, 841–847 (1970).
12. Nayfeh, A. H. & Hassan, S.D. The method of multiple scales and nonlinear dispersive waves. *J. Fluid Mech.* 48, 463–475 (1971).
13. Keller, J. B., Rubinow, S. I., & Tu, Y. O. Spatial instability of a jet. *Phys. Fluids* 16, 2052–2055 (1973).

14. Bogy, D. B. Drop formation in a circular liquid jet. *Annu. Rev. Fluid Mech.* 11, 207–228 (1979).
15. Leib, S. J. & Goldstein, M. E. The generation of capillary instabilities on a liquid jet. *J. Fluid Mech.* 168, 479–500 (1986).
16. Haenlein, A. Disintegration of a liquid jet. *NACA-TM-659* (1931).
17. Donnelly, R. J. & Glaberson. W. Experiments on the capillary instability of a jet. *Proc. R. Soc. Lond. A* 209. 547–556 (1966).
18. Goedde, E. F. & Yuen, M. C. Experiments on liquid jet instability. *J. Fluid Mech.* 40, 495–511 (1970).
19. McCarthy, M. J. & Molloy, N. A. Review of' stability of liquid jets and the influence of nozzle design. *Chem. Eng. J.* 7, 1–20 (1974).
20. Sirignano, W. A. & Mehring, C. Review of theory of distortion and disintegration of liquid streams. *Prog. Energy Combust. Sci.* 26. 609–655 (2000).
21. Vassallo, P. & Ashgriz, N. Satellite formation and merging in liquid jet breakup. *Proc. R. Soc. Lond. A* 433, 269–286 (1991).
22. Grant, R. P. & Middleman, S. Newtonian jet stability. *AIChE J.* 12, 669–678 (1966).
23. Chandrasekhar, S. *Hydrodynamic and Hydromagnetic Stability*. Oxford: Claredon (1961).
24. Sterling, A. M. & Sleicher, C. A. The instability of capillary jets. *J. Fluid Mech.* 68(3), 477–495 (1975).
25. Reitz, R. D. & Bracco, F. V. Mechanism of atomization of a liquid jet. *Phys. Fluids* 25(10), 1730–1742 (1982).
26. Yoon, S. S. & Heister, S. D. Categorizing linear theories for atomizing round jets, *Atomization and Sprays* (*SCI*), 13(5&6), pp. 499–516 (2003).
27. Batchelor, G. K. *An Introduction to Fluid Dynamics*. New York: Cambridge University Press (1999), pp. 511–517, 521–526.
28. Gordillo, J. M., Perez-Saborid, M., & Ganan-Calvo, A. M. Linear stability of co-flowing liquid–gas jets. *J. Fluid Mech.* 448, 23–51 (2001).
29. Yarin, A. L. *Free Liquid Jets and Films: Hydrodynamics and Rheology*. Harlow/New York: Longman/Wiley (1993).
30. Lee, H. C. Drop formation in a liquid jet. *IBM J. Res. Dev.* 18, 364–369 (1974).
31. Kase, S. & Matsuo, T. Studies on melt spinning. I. Fundamental equations on the dynamics of melt spinning. *J. Polym. Sci., Pt. A* 3, 2541–2554 (1965).
32. Matovich, M. A. & Pearson, J. R. A. Spinning a molten threadline. Steady-state viscous flows. *Ind. Eng. Chem. Fundam.* 8, 512–520 (1969).
33. Eggers, J. Nonlinear dynamics and breakup of free-surface flows. *Rev. Mod. Phys.* 69, 865–929 (1997).
34. Eggers, J. & Villermaux, E. Physics of liquid jets. *Rep. Prog. Phys.* 71, 036601 (2008).
35. Bechtel, S. E., Cao, J. Z., & Forest, M. G. Practical application of a higher-order perturbation-theory for slender viscoelastic jets and fibers. *J. Non-Newton. Fluid Mech.* 41, 201–273 (1992).
36. Pimbley, W. T. Drop formation from a liquid jet: A linear one-dimensional analysis considered as boundary value problem. *IBM J. Res. Dev.* 20, 148–156 (1976).
37. Green, A. E. & Laws, N. Ideal fluid jets. *Int. J. Eng. Sci.* 6, 317–328 (1968).
38. Green, A. E. On the nonlinear behavior of fluid jets. *Int. J. Eng. Sci.* 14, 49–63 (1976).
39. Naghdi, P. M. On the applicability of directed fluid jets to Newtonian and non-Newtonian flows. *J. Non-Newton. Fluid Mech.* 5, 233–265 (1979).
40. Caulk, D. A. & Naghdi, P. M. The influence of twist on the motion of straight elliptical jets. *Arch. Ration. Mech. Anal.* 69, 1–30 (1979).
41. Bogy, D. B. Use of one-dimensional Cosserat theory to study instability of a viscous liquid jet. *Phys. Fluids* 21, 190–197 (1978).
42. Lopez-Herrera, J. M., Ganan-Calvo, A. M., & Perez-Saboird, M. One-dimensional simulation of the breakup of capillary jets of conducting liquids. Application to EHD spraying. *J. Aerosol Sci.* 30, 895–912 (1999).

43. Barrero, A. & Loscertales, I. G. Micro- and nanoparticles via capillary flows. *Annu. Rev. Fluid Mech.* 39, 89–106 (2007).
44. Fernandez de la Mora, J. The fluid dynamics of Taylor cone. *Annu. Rev. Fluid Mech.* 39, 217–243 (2007).
45. Leib, S. J. & Goldstein, M. E. Convective and absolute instability of a viscous liquid jet. *Phys. Fluids* 29, 952–954 (1986).
46. Lin, P. S. & Kang, D. J. Atomization of a liquid jet. *Phys. Fluids* 30, 2000–2006 (1987).
47. Lin, S. P. & Lian, Z. W. Absolute and convective instability of a viscous liquid jet surrounded by a viscous gas in a vertical pipe. *Phys. Fluids. A* 5, 771–773 (1993).
48. Zhou, Z. W. & Lin, S. P. Effects of compressibility on the atomization of liquid jets. *J. Propul. Power* 8, 736–740 (1992).
49. Lin, S. P. Regimes of jet breakup and breakup mechanisms (mathematical aspects). In *Recent Advances in Spray Combustion: Spray Atomization and Drop Burning Phenomena*, Vol. 1, ed. K.K. Kuo. Reston: AIAA Inc. (1996), pp. 137–160.
50. Lin, S. P. & Lian, Z. W. Absolute instability of a liquid jet in a gas. *Phys. Fluids A* 1(3), 490–493 (1980).
51. Lin, S. P. & Chen, J. N. Roles played by the interfacial shears in the instability mechanism of a viscous liquid jet surrounded by a viscous gas in a pipe. *J. Fluid Mech.* 376, 37–51 (1998).
52. Vihinen, I., Honohan, A., & Lin, S. P. Absolute and convective instability of a viscous jet in microgravity. *Phys. Fluids* 9, 3117–3119 (1997).
53. O'Donnel, B., Chen, J. N., & Lin, S. P. Transition from convective to absolute instability in a liquid jet. *Phys. Fluids* 13, 2732–2734 (2001).
54. Lin, S. P. & Reitz, R. D. Drop and spray formation from a liquid jet. *Ann. Rev. Fluid Mech.* 30, 85–105 (1998).
55. Lin, S. P. *Breakup of Liquid Sheets and Jets*. Cambridge: Cambridge University Press, 2003.
56. Gaster, M. Growth of disturbances in both space and time. *J. Fluid Mech.* 11, 723–727 (1968).
57. Lin, S. P. & Woods, D. R. Tailored liquid jets. *Atom. Sprays* 18, 363–374 (2008).
58. Chinn, J. J. An appraisal of swirl atomizer inviscid internal flow analysis, Part 2, Inviscid spray cone angle and comparison of inviscid method with experimental results for discharge coefficient, air core radius, and spray angle. *Atom. Sprays* 19, 283–308 (2009).
59. Craig, L., Barlow, N., Partel, S., Kanya, B., & Lin, S. P. Optimal and non optimal flows in a swirl atomizer. *J. Int. Inst. Liquid Atom. Spray Syst.* 13, 113–1124 (2009).
60. Lafrance, P. & Ritter, R. C. Capillary breakup of a liquid jet with a random initial perturbation. *Trans ASME: J. Appl. Mech.* 44, 385–388 (1977).
61. Pimbley, W. T. & Lee, H.C. Satellite droplet formation in a liquid jet. *IBM J. Res. Dev.* 21, 21–30 (1977).
62. Scarlett, B. & Parkin, C. S. Droplet production on controlled jet breakup. *Chem. Eng. J.* 13, 127–141 (1977).
63. Yuen, M. C. Non-linear capillary instability of a liquid jet. *J. Fluid Mech.* 33, 151–163 (1968).
64. Kakutani, T., Inoue, Y., & Kan, T. Nonlinear capillary waves on the surface of liquid column. *J. Phys. Soc. Jpn.* 37, 529–538 (1974).
65. Lafrance, P. Nonlinear breakup of a liquid jet. *Phys. Fluids* 17, 1913–1914 (1974).
66. Lafrance, P. Nonlinear breakup of a laminar liquid jet. *Phys. Fluids* 18, 428–432 (1975).
67. Bogy, D. B. Break-up of a liquid jet: second perturbation solution for one-dimensional Cosserat theory. *IBM J. Res. Dev.* 23, 87–92 (1979).
68. Bogy, D. B. Break-up of a liquid jet: Third perturbation Cosserat solution. *Phys. Fluids* 22, 224–230 (1979).
69. Bogy, D. B. Wave propagation and instability in a circular semi-infinite liquid jet harmonically forced at the nozzle. *Trans ASME: J. Appl. Mech.* 45, 469–474 (1978).
70. Taub, H. H. Investigation of nonlinear waves on liquid jets. *Phys. Fluids* 19, 1124–1129 (1976).

71. Chaudhary, K. C. & Redekopp, L. G. The nonlinear capillary instability of a liquid jet. Part 1. Theory. *J. Fluid Mech.* 96, 257–274 (1980).
72. Chaudhary, K. C. & Maxworthy, T. The nonlinear capillary instability of a liquid jet. Part 2. Experiments on jet behavior before droplet formation. *J. Fluid Mech.* 96, 275–286 (1980).
73. Chaudhary, K. C. & Maxworthy, T. The nonlinear capillary instability of a liquid jet. Part 3. Experiments on satellite drop formation and control. *J. Fluid Mech.* 96, 287–298 (1980).
74. Mansour, N. N. & Lundgren, T. S. Satellite formation in capillary jet breakup. *Phys. Fluids A* 2, 1141–1144 (1990).
75. Ashgriz, N. & Mashayek, F. Temporal analysis of capillary jet breakup. *J. Fluid Mech.* 291, 163–190 (1995).
76. Ambravaneswaran, B., Phillips, S. D., & Basaran, O. A. Theoretical analysis of dripping faucet. *Phys. Rev. Lett.* 85, 5332–5335 (2000).
77. Basaran, O. A. & Suryo, R. The invisible jet. *Nat. Phys.* 3, 679–680 (2007).
78. Bogy, D. B., Shine, S. J., & Talke, F. E. Finite difference solution of the Cosserat fluid jet equations. *J. Comput. Phys.* 38, 294–326 (1980).
79. Eggers, J. Universal pinching of 3D axisymmetric free-surface flow. *Phys. Rev. Lett.* 72, 3458–3460 (1993).
80. Brenner, M. P., Shi, X. D., & Nagel, S.R. Iterated instabilities during droplet fission. *Phys. Rev. Lett.* 73, 3391–3394 (1994).
81. Eggers, J. Theory of drop formation. *Phys. Fluids* 7, 941–953 (1995).
82. Papageorgiou, D. T. On the breakup of viscous liquid threads. *Phys. Fluids* 7, 1529–1544 (1995).
83. Brenner, M. P., Lister, J., & Stone, H. A. Pinching threads, singularities and the number 0.0304. *Phys. Fluids* 8, 2827–2836 (1996).
84. Brenner, M. P., Eggers, J., Joseph, K., Nagel, S. R., & Shi, X. D. Breakdown of scaling in droplet fission at high Reynolds number. *Phys. Fluids* 9, 1573–1590 (1997).
85. Cline, H. E. & Anthony, T. R. The effects of harmonics on the capillary instability of liquid jets. *J. Appl. Phys.* 49 (6), 3203–3208 (1978).
86. Rutland, D. F. & Jameson, G. J. Theoretical prediction of the sizes of drops formed in the breakup of capillary jets. *Chem. Eng. Sci.* 25(11-E), 1689–1698 (1970).
87. Hibling, J. & Heister, S. D. Droplet size control in liquid jet breakup. *Phys. Fluids* 8(6), 1574–1581 (1996).
88. Orme, M. & Muntz, E. P. The manipulation of capillary stream breakup using amplitude-modulated disturbances: A pictorial and quantitative representation. *Phys. Fluids A* 2(7), 1124–1140 (1990).
89. Orme, M., Willis, K., & Nguyen, T.-V. Droplet patterns from capillary stream breakup. *Phys. Fluids A* 5(1), 80–90 (1993).
90. Bousfield, D. W., Keunings, R., Marrucci, G., & Denn, M. M. Nonlinear analysis of the surface tension driven breakup of viscoelastic filaments. *J. Non-Newtonian Fluid Mech.* 21, 79–97 (1986).
91. Bousfield, D., Stockel, I. H., & Nanivadekar, C. K. The breakup of viscous jets with large velocity modulations. *J. Fluid Mech.* 218, 601–617 (1990).
92. Huynh, H., Ashgriz, N., & Mashayek, F. Instability of a liquid jet subject to disturbances composed of two wave numbers. *J. Fluid Mech.* 320, 185–210 (1996).
93. Spangler, C. A., Hibling, J. H., & Heister, S. D. Nonlinear modeling of jet atomization in the wind-induced regime. *Phys. Fluids* 7 (5), 964–971 (1995).
94. Tjahjadi, M., Stone, H.A., & Ottino, J.M., Satellite and subsatellite formation in capillary breakup. *J. Fluid Mech.* 243, 297–317 (1992).
95. Bauer, H. F. Free liquid surface response induced by fluctuations of thermal Marangoni convection. *AIAA J.* 22, 421–428 (1983).
96. Xu, J. J. & Davis, S. H. Instability of capillary jets with thermocapillarity. *J. Fluid Mech.* 161, 1–26 (1985).

97. Dijkstra, H. A. & Steen, P. H. Thermocapillary stabilization of the capillary breakup of an annular film of liquid. *J. Fluid Mech.* 229, 205–228 (1991).
98. Mashayek, F. & Ashgriz, N. Nonlinear instability of liquid jets with thermocapillarity. *J. Fluid Mech.* 283, 97–123 (1995).
99. Ostrach, S. Low-gravity fluid flows. *Ann. Rev. Fluid Mech.* 14, 13–345 (1982).
100. Davis, S. H. Thermocapillary instabilities. *Ann. Rev. Fluid Mech.* 19, 403–435 (1987).
101. Faidley, R. W. & Panton, R. L. Measurement of liquid jet instability induced by surface tension variations. *Exp. Therm. Fluid Sci.* 3, 383–387 (1990).
102. Nahas, N. M. & Panton, R. L. Control of surface tension flows-Instability of a liquid jet. *J. Fluids Eng. Trans. ASME* 112, 3, 296–301 (1990).
103. Fulnari, E. P. Temporal instability of viscous liquid microjets with spatially varying surface tension. *J. Phys. A: Math. Gen.* 38, 263–276 (2005).
104. Saroka, M., Guo, Y., & Ashgriz, N. Nonlinear instability of an evaporating capillary jet. *AIAA J.* 39(9), 1728–1734 (September 2001).
105. Ponstein, J. Instability of rotating cylindrical jets. *Appl. Sci. Res.* 8(6), 425–456 (1959).
106. Saffman, P. G. The number of waves on unstable vortex rings. *J. Fluid Mech.* 84(4), 625–639 (1978).
107. Entov, V. M., Kordonskii, V. I., Kuz'min, V. A., Shul'man, Z. P., & Yarin, A. L. Investigation of the decomposition of jets of rheologically complex liquids. *J. Appl. Mech. Tech. Phys.* 21, 365–371 (1980).
108. Yarin, A. L., Zussman, E., Theron, S. A., Rahimi, S., Sobe, Z., & Hasan, D. Elongational behavior of gelled propellant stimulants. *J. Rheol.* 48, 101–116 (2004).
109. Goldin, M., Pfeffer, R., & Shinnar, R. Break-up of a capillary jet of a non-Newtonian fluid having a yield stress. *Chem. Eng. J.* 4, 8–20 (1972).
110. Goldin, M., Yerushalmi, J., Pfeffer, R., & Shinnar, R. Breakup of a laminar capillary jet of viscoelastic fluid. *J. Fluid Mech.* 38, 689–711 (1969).
111. Entov, V. M. & Yarin, A. L. Influence of elastic stresses on the capillary breakup of jets of dilute polymer solutions. *Fluid Dyn.* 19, 21–29 (1984).
112. Rubin, H. & Wharshavsky, M. A note on the breakup of viscoelastic liquid jets. *Isr. J. Technol.* 8, 285–288 (1970).
113. Gordon, M., Yerushalmi, J., & Shinnar, R. Instability of jets of non-Newtonian fluids. *Trans. Soc. Rheol.* 17, 303–324 (1973).
114. Goren, S. & Gavis, J. Transverse wave motion on a thin capillary jet of a viscoelastic liquid. *Phys. Fluids* 4, 575–579 (1961).
115. Han, T., Yarin, A. L., & Reneker, D. H. Viscoelastic electrospun jets: initial stresses and elongational rheometry. *Polymer* 49, 1651–1658 (2008).
116. Joseph, D. D. *Fluid Dynamics of Viscoelastic Liquids*. New York: Springer (1990).
117. Entov, V. M. & Kestenboim, Kh. S. Mechanics of fiber formation. *Fluid Dyn.* 22, 677–686 (1987).
118. Reneker, D. H., Yarin, A. L., Zussman, E., & Xu, H. Electrospinning of nanofibers from polymer solutions and melts. *Adv. Appl. Mech.* 41, 43–195 (2007).
119. Bazilevsky, A. V., Voronkov, S. I., Entov, V. M., & Rozhkov, A. N. Orientational effects in capillary breakup of jets and threads of dilute polymer solutions. *Sov. Phys. Doklady* 257, 336–339 (1981) (the English version in Vol. 26).
120. Stelter, M., Brenn, G., Yarin, A. L., Singh, R. P., & Durst, F. Validation and application of a novel elongational device for polymer solutions. *J. Rheol.* 44, 595–616 (2000).
121. Schümmer, P. & Tebel, K. H. A new elongational rheometer for polymer solutions. *J. Non-Newtonian Fluid Mech.* 12, 331–347 (1983).
122. Anna, S. L. & McKinley, G. H. Elasto-capillary thinning and breakup of model elastic liquids. *J. Rheol.* 45, 115–138 (2001).
123. Kroesser, F. W. & Middleman, S. Viscoelastic jet stability. *AIChE J.* 15, 383–386 (1969).
124. Rubin, H. Breakup of viscoelastic liquid jets. *Isr. J. Technol.* 9, 579–581 (1971).

125. Sagiv, A., Rubin, H., & Takserman-Krozer, R. On the breakup of cylindrical liquid jets. *Isr. J. Technol.* 11, 349–354 (1973).
126. Sagiv, A. & Takserman-Krozer, R. Capillary breakup of viscoelastic liquid jet of variable cross-section. *Rheol. Acta* 14, 420–426 (1975).
127. Goren, S. L. & Gottlieb, M. Surface-tension-driven breakup of viscoelastic liquid threads. *J. Fluid Mech.* 120, 245–266 (1982).
128. Lee, W. K., Yu, K. L., & Flumerfelt, R. W. Instability of stationary and uniformly moving cylindrical fluid bodies. *Int. J. Multiphase Flow* 7, 385–400 (1981).
129. Chang, H. C., Demekhin, E. A., & Kalaidin, E. Iterated stretching of viscoelastic jets. *Phys. Fluids* 11, 1717–1737 (1999).
130. Li, J. & Fontelos, M. A. Drop dynamics on the beads-on-string structure for viscoelastic jets: A numerical study. *Phys. Fluids* 15, 922–937 (2003).
131. Clasen, C., Eggers, J., Fontelos, M. A., Li, J., & McKinley, G. H. The beads-on-string structure of viscoelastic threads. *J. Fluid Mech.* 556, 283–308 (2006).
132. Oliveira, M. S. N. & McKinley, G. H. Iterated stretching and multiple beads-on-a-string phenomena in dilute solutions of highly extensible flexible polymers. *Phys. Fluids* 17, 071704 (2005).
133. Renardy, M. Some comments on the surface-tension driven break-up (or lack of it) of viscoelastic jets. *J. Non-Newton. Fluid Mech.* 51, 97–107 (1994).
134. Renardy, M. A numerical study of the asymptotic evolution and breakup of Newtonian and viscoelastic jets. *J. Non-Newton. Fluid Mech.* 59, 267–282 (1995).
135. Bazilevsky, A. V., Entov, V. M., & Rozhkov, A. N. Breakup of an Oldroyd liquid bridge as a method for testing the rheological properties of polymer solutions. *Polym. Sci. Ser. A* 43, 716–726 (2001).
136. Ziabicki, A. *Fundamentals of Fibre Formation*. London: Wiley (1976).
137. Ziabicki, A. & Kawai, H. (editors). *High-Speed Fiber Spinning*. New York: Wiley (1985).

Chapter 2
Bending and Buckling Instabilities of Free Liquid Jets: Experiments and General Quasi-One-Dimensional Model

A.L. Yarin

Abstract This chapter deals with liquid jets bending due to the aerodynamic interaction with surrounding air or buckling due to the impingement on a solid wall. The experimental evidence is considered and linear and nonlinear theories describing perturbation growth developed in the framework of the quasi-one-dimensional equations of the dynamics of liquid jets moving in air are discussed. Jets of viscous Newtonian or rheologically complex liquids (in particular, viscoelastic polymeric liquids) are considered. In addition, bending instability of the electrified liquid jets (in particular, polymeric liquid jets in electrospinning) is considered. In the latter case, both the experimental and theoretical aspects are tackled.

Keywords Bending instability of liquid jets · Buckling of liquid jets · Electrified liquid jets · Electrospinning · Elongational rheology · Newtonian and rheologically complex liquids · Quasi-one-dimensional equations of the dynamics of liquid jets · Small and finite perturbations · Viscoelastic polymeric liquids

Introduction

Thin liquid jets demonstrate not only capillary breakup considered in Chap. 1 but some other regular long-wave forms of instability and breakup, e.g., bending instability of jets moving in air with a relatively high-speed U or of the electrified jets, as well as buckling of thin, highly viscous jets impinging on a wall [1]. Theoretical investigation of the dynamics of bending instability of liquid jets rapidly moving in air began in the seminal works of Weber and Debye and Daen [2, 3]. This leads to a rather complicated coupled problem on a dynamic interaction

A.L. Yarin
Department of Mechanical and Industrial Engineering, University of Illinois at Chicago, Chicago, IL, USA
e-mail: ayarin@uic.edu

N. Ashgriz (ed.), *Handbook of Atomization and Sprays*,
DOI 10.1007/978-1-4419-7264-4_2, © Springer Science+Business Media, LLC 2011

of air flow with a jet when the jet evolution is to be found as well. The linear stability analysis of the temporary planar bending instability of an inviscid jet in [3] resulted in the following characteristic equation for the growth rate γ of bending instability based on the three-dimensional equations of fluid mechanics

$$\gamma = \bar{k}\sqrt{-\frac{\rho_g U^2}{\rho a_0^2}\frac{K_1(\bar{k})I_1'(\bar{k})}{K_1'(\bar{k})I_1(\bar{k})} - \frac{\sigma}{\rho a_0^3}\frac{\bar{k}I_1'(\bar{k})}{I_1(\bar{k})}} \tag{2.1}$$

In (2.1) $\bar{k} = ka_0$ is the dimensionless wave number with k being the dimensional wave number and a_0 the unperturbed jet cross-sectional radius; ρ and σ are the density and surface tension of the jet liquid, respectively; the gas density is denoted by ρ_g; and I_1 and K_1 denote the modified Bessel functions. From several terms in the analysis of [3] describing the dynamic action of air, we keep in (2.1) only the largest one, of the order of $\rho_g U^2$, since $\rho_g << \rho$. The surface tension is a stabilizing factor in the case of the bending instability, since bending results in an increase of the jet surface area $[I_1'(\bar{k}) > 0,\ K_1'(\bar{k}) < 0$ for any $\bar{k}]$. Beginning from a certain critical value of the relative air velocity U, the first (positive) term under the square root on the right hand side in (2.1) acquires a larger magnitude than the second term, which corresponds to the onset of the bending instability and an exponential growth of the bending perturbations. The bending instability is determined by a peculiar pressure distribution in gas over the jet surface: in the framework of the inviscid gas model, gas pressure on convex surface elements is lower than on the concave ones.

General Quasi-One-Dimensional Equations of Dynamics of Free Liquid Jets

The theory of Debye and Daen [3] does not account for a number of important factors. The most important of them is the effect of liquid viscosity, which should counteract to the perturbation growth. In addition, the experiments show that the growing bending perturbations are three-dimensional rather than planar. Also, in the case of low-viscous liquid jets, bending perturbations grow together with the axisymmetric capillary perturbations, which significantly change the cross-sectional sizes and shapes during bending [4]. Moreover, all these factors are dominant in reality. Therefore, the analysis of the dynamics of the bending perturbations in the framework of an inviscid liquid model is intrinsically contradictory. Accounting for these factors in the framework of the Navier–Stokes equations in the context of the bending perturbations of liquid jets is tremendously difficult. However, these difficulties can be relatively easily overcome in the framework of the quasi-one-dimensional description of liquid motion in the bending jets. In the works of Yarin et al. [1, 5, 6], the general quasi-one-dimensional equations of the straight and bending jets were derived from the integral balances of mass, momentum, and moment of momentum,

as well as by averaging the three-dimensional equations of hydrodynamics over the jet cross-section [7]. The quasi-one-dimensional continuity and momentum equations, as well as the moment of momentum equation for the general case of motion of a thin liquid jet in air derived by Yarin et al. [1, 5–7] read

$$\frac{\partial \lambda f}{\partial t} + \frac{\partial W f}{\partial s} = 0, \quad f = \pi a^2, \tag{2.2}$$

$$\frac{\partial \lambda f \vec{V}}{\partial t} + \frac{\partial W f \vec{V}}{\partial s} = \frac{1}{\rho}\frac{\partial}{\partial s}\left(P\vec{\tau} + \vec{\mathrm{Q}}\right) + \lambda \vec{F} f + \vec{q}\frac{\lambda}{\rho}, \tag{2.3}$$

$$\begin{aligned}\frac{\partial \lambda \vec{\mathrm{K}}}{\partial t} + \lambda\left[\vec{\tau} \times \vec{\mathrm{j}}_2 - k\vec{\mathrm{U}} \times \left(\vec{\Omega} \times \vec{\mathrm{j}}_1 + \delta\vec{\mathrm{j}}_1\right)\right] + \frac{\partial}{\partial s}\left(W\vec{\mathrm{K}}_1 + \vec{\mathrm{j}}_3 \times \vec{\mathrm{V}}\right) \\ = \frac{1}{\rho}\frac{\partial \vec{\mathrm{M}}}{\partial s} + \frac{\lambda}{\rho}\vec{\tau} \times \vec{\mathrm{Q}} + \vec{\mathrm{m}}\frac{\lambda}{\rho} - \lambda k\vec{\mathrm{j}}_1 \times \vec{\mathrm{F}}\end{aligned} \tag{2.4}$$

These equations are a close hydrodynamic analog of the equations of the Euler-Bernoulli beam theory [8]. They are related to the three-dimensional equations of hydrodynamics (the Navier–Stokes equations in the case of viscous Newtonian liquids) exactly as the equations of the Euler-Bernoulli beam theory are related to the three-dimensional equations of the theory of elasticity. The hydrodynamics of thin liquid jets is reduced to finding the evolution in time t and over a spatial coordinate s of the "integral" parameters – the cross-sectional area f, the velocity of the center of mass of a liquid cross-section $\vec{\mathrm{V}}$, and the angular velocity of this cross-section $\vec{\Omega}$. Equation (2.2) is the mass balance (the continuity equation). Equation (2.3), the momentum equation, represents itself the balance of forces acting on a jet element, namely, the inertial, internal and external forces. Equation (2.4) represents itself the moment of momentum balance, in particular, its left-hand side expresses the rate of change of the moment of the inertial forces. The following notation is used in (2.2)–(2.4)

$$\vec{\mathrm{K}} = \int\limits_D \left(\vec{\mathrm{x}} \times \vec{\Omega} \times \vec{\mathrm{x}}\right) dS - k\vec{\mathrm{j}}_1 \times \vec{\mathrm{V}}, \quad \vec{\mathrm{K}}_1 = \int\limits_D \left(\vec{\mathrm{x}} \times \vec{\Omega} \times \vec{\mathrm{x}}\right) dS, \tag{2.5}$$

$$\vec{\mathrm{j}}_1 = \int\limits_D y\vec{\mathrm{x}} dS, \quad \vec{\mathrm{j}}_2 = \int\limits_D \left(\vec{\Omega} \times \vec{\mathrm{x}} + \delta\vec{\mathrm{x}}\right)\left[\left(\vec{\Omega} - \vec{\omega}\right) \cdot (\vec{\mathrm{x}} \times \vec{\tau})\right] dS, \tag{2.6}$$

$$\vec{\mathrm{j}}_3 = \int\limits_D \vec{x}\left[\left(\vec{\Omega} - \vec{\omega}\right) \cdot (\vec{\mathrm{x}} \times \vec{\tau})\right] dS, \quad \lambda = \left|\frac{\partial \vec{\mathrm{R}}}{\partial \mathrm{s}}\right| \tag{2.7}$$

$$\vec{\mathrm{U}} = \frac{\partial \vec{\mathrm{R}}}{\partial t}, \quad W = V_\tau - U_\tau, \quad \delta = -\frac{1}{2}\left(\frac{1}{\lambda}\frac{\partial V_\tau}{\partial s} - kV_n\right) \tag{2.8}$$

Here, $\vec{\mathrm{R}}$ and $\vec{\mathrm{x}}$ denote the position vectors of the jet axis, and of a point in the jet cross-section, respectively ($\vec{\mathrm{x}}$ is reckoned from the center of mass of a jet cross-section $D(s, t)$ and belongs to its plane); $\vec{\mathrm{F}}$ is the body force per jet element of unit volume; $\vec{\mathrm{q}}$ and $\vec{\mathrm{m}}$ are the distributed force and moment of force imposed on the jet by the environment, respectively; $\vec{\mathrm{Q}}$ is the shearing force acting in the jet cross-section, which is determined using (2.4); k is the jet axis curvature; ρ is liquid density. Here and hereinafter, $\vec{\mathrm{n}}$, $\vec{\mathrm{b}}$, and $\vec{\tau}$ denote the principal unit normal, unit binormal, and unit tangent to the jet axis, respectively. The angular velocity of the trihedron $\vec{\mathrm{n}}$, $\vec{\mathrm{b}}$ and $\vec{\tau}$ associated with the jet axis is denoted $\vec{\omega}$. Subscripts n, b, and τ denote projections on the principal normal, binormal, and tangent to the jet axis, respectively; y is the coordinate reckoned along the principal normal. In the case of Newtonian viscous liquid, the magnitude of the longitudinal force in the jet cross-section P and the moment of the internal stresses $\vec{\mathrm{M}}$ are related to the kinematic parameters in a cross-section of radius a by the following expressions

$$P = \left[3\mu\left(\frac{1}{\lambda}\frac{\partial V_\tau}{\partial s} - kV_\mathrm{n}\right) - \sigma G\right] f + P_\sigma, \tag{2.9}$$

$$G = \frac{1}{a}\left[1 + \frac{1}{\lambda^2}\left(\frac{\partial a}{\partial s}\right)^2\right]^{-1/2} - \left[1 + \frac{1}{\lambda^2}\left(\frac{\partial a}{\partial s}\right)^2\right]^{-3/2} \frac{1}{\lambda}\frac{\partial}{\partial s}\left(\frac{1}{\lambda}\frac{\partial a}{\partial s}\right), \tag{2.10}$$

$$P_\sigma = 2\pi a\sigma\left[1 + \frac{1}{\lambda^2}\left(\frac{\partial a}{\partial s}\right)^2\right]^{-1/2}, \tag{2.11}$$

$$M_\mathrm{n} = 3\mu I\left(\frac{1}{\lambda}\frac{\partial \Omega_\mathrm{n}}{\partial s} + k\Omega_\tau - \kappa\Omega_\mathrm{b}\right) \tag{2.12}$$

$$\begin{aligned} M_\mathrm{b} = {} & 3\mu I\left(\frac{1}{\lambda}\frac{\partial \Omega_\mathrm{b}}{\partial s} + \kappa\Omega_\mathrm{n} - \frac{3}{2}\frac{k}{\lambda}\frac{\partial V_\tau}{\partial \mathrm{s}} + \frac{3}{2}k^2 V_\mathrm{n}\right) \\ & - \sigma k\frac{I}{a}\left[1 + \frac{1}{\lambda^2}\left(\frac{\partial a}{\partial s}\right)^2\right]^{-3/2} \end{aligned} \tag{2.13}$$

$$M_\tau = \mu I\left(\frac{2}{\lambda}\frac{\partial \Omega_\tau}{\partial s} + \frac{k}{\lambda}\frac{\partial V_\mathrm{b}}{\partial s} + k\kappa V_\mathrm{n} - k\Omega_\mathrm{n}\right), \quad I = \frac{\pi a^4}{4}, \tag{2.14}$$

Here, κ is the geometric torsion of the jet axis, μ and σ are the viscosity and surface tension coefficient, respectively, and I is the moment of inertia of the jet cross-section.

The system of (2.2)–(2.14) describes both the axisymmetric capillary instability of straight jets ((1.49)–(1.51) in Chap. 1 represent its particular case) and bending instability of liquid jets. It is closed if the jet cross-sections possess double symmetry (in particular, it is closed for jets with circular cross-sections). This system of equations was derived by Yarin et al. in [1, 5–7] assuming the jet slenderness and the absence of significant shear tractions at its surface. These assumptions are sufficiently accurate in the case of highly viscous jets moving in air. In the cases of short wavelength perturbations and large axis curvatures, as well as in the case of liquid jets propagating in liquid medium of comparable viscosity, the quasi-one-dimensional description, strictly speaking, is inappropriate. The assumptions of the jet slenderness and of the absence of significant shear tractions at the jet surface lead to the following additional restrictions on the internal kinematics in the jet, namely to

$$\Omega_{\mathrm{n}} = -\frac{1}{\lambda}\frac{\partial V_{\mathrm{b}}}{\partial s} - \kappa V_{\mathrm{n}}, \quad \Omega_{\mathrm{b}} = \frac{1}{\lambda}\frac{\partial V_{\mathrm{n}}}{\partial s} - \kappa V_{\mathrm{b}} + \kappa V_{\tau}, \tag{2.15}$$

The kinematic equation, which should be added to the system of (2.2)–(2.15), determines the location of the jet axis in space in accordance with the velocity field in it

$$\frac{\partial \vec{\mathrm{R}}}{\partial t} = \vec{\mathrm{V}} - (\lambda \vec{\mathrm{V}} \cdot \vec{\mathrm{i}})\vec{\tau} \tag{2.16}$$

Equation (2.16) is written here for the simplest case where the tangent to the jet axis is inclined at any point to a certain straight line $O_1\xi$ by an acute angle and it is possible to introduce a Cartesian coordinate system $O_1\xi\eta\zeta$ with the corresponding unit vectors $\vec{\mathrm{i}}$, $\vec{\mathrm{j}}$ and $\vec{\mathrm{k}}$ and to describe the jet axis using the following equations

$$\xi = s, \quad \eta = H(s,t), \quad \varsigma = Z(s,t), \quad \vec{\mathrm{R}} = \vec{\mathrm{i}}\,\xi + \vec{\mathrm{j}}H + \vec{\mathrm{k}}Z \tag{2.17}$$

In the other cases, the jet axis parameter s can be chosen differently, which leads to changes in the expression for $\partial\vec{\mathrm{R}}/\partial t$.

The distributed force and moment of force imposed on the jet by the environment $\vec{\mathrm{q}}$ and $\vec{\mathrm{m}}$ should be specified separately. In particular, in the case of small spatial perturbations of the jet axis when it rapidly moves in air, the inviscid flow theory yields the following expressions

$$\vec{\mathrm{q}} = -\rho_g U^2 f_0 \left(\vec{\mathrm{j}}\frac{\partial^2 H}{\partial s^2} + \vec{\mathrm{k}}\frac{\partial^2 Z}{\partial s^2}\right), \quad \vec{\mathrm{m}} = 0, \quad f_0 = \pi a_0^2, \tag{2.18}$$

Equation (2.18) for $\vec{q}$ means that it is directed along the normal (as $-\vec{n}$).

For the finite bending perturbations, the drag force imposed by a relative air flow should be accounted in addition. Then, for example, for planar jet bending, (2.18) are generalized by the following expressions

$$\vec{q} = -\rho_g U^2 \left\{ f \frac{\partial^2 H}{\partial s^2} \left[1 + \left(\frac{\partial H}{\partial s} \right)^2 \right]^{-5/2} + a \left(\frac{\partial H}{\partial s} \right)^2 \left[1 + \left(\frac{\partial H}{\partial s} \right)^2 \right]^{-1} \times \operatorname{sgn} \left(\frac{\partial H}{\partial s} \right) \right\} \vec{n}, \quad \vec{m} = 0 \tag{2.19}$$

These expressions close the system of the general quasi-one-dimensional equations of free liquid jets moving in air with arbitrary speeds.

In the context of the electrified jets in electrospraying and electrospinning, the distributed force $\vec{q}$ originates from the Coulomb repulsion of different parts of the jet surface. Then, it is given by the following expression [9–11]

$$\vec{q} = -e^2 \ln \left(\frac{L}{a} \right) k \vec{n} \tag{2.20}$$

where e is the electric charge at the jet surface per unit jet length and L is a cutoff length along the jet axis. Comparison of (2.18) and (2.20) shows that both the aerodynamic and electric bending forces are directed along the normal (as $-\vec{n}$) and should result in a very similar aerodynamically or electrically driven bending instability, as discussed below.

Linear Stability Theory for Bending Breakup of Newtonian Liquid Jets Moving in Air

The solutions of a particular version of the quasi-one-dimensional equations of the jet dynamics in the case of capillary breakup, when they can be reduced to (1.49)–(1.51) of Chap. 1, were discussed there. Here, we discuss the applications of (2.2)–(2.19) to the aerodynamically-driven bending instability of the uncharged liquid jets rapidly moving in air following the work of Yarin [1, 5, 6]. The characteristic equation for the growth rate of small bending perturbations of highly viscous slender liquid jets moving in air in the case of the temporal instability reads

$$\gamma^2 + \frac{3}{4} \frac{\mu \overline{k}^4}{\rho a_0^2} \gamma + \left(\frac{\sigma}{\rho a_0^3} - \frac{\rho_g U^2}{\rho a_0^2} \right) \overline{k}^2 = 0 \tag{2.21}$$

According to (2.21), both planar and three-dimensional (helical) small bending perturbations increase with the same growth rate if the relative velocity of gas flow is

$$U > \sqrt{\frac{\sigma}{\rho_g a_0}} \tag{2.22}$$

when the dynamic action of air can overbear the resistance of surface tension to growth of bending perturbations. The growth rate of the axisymmetric capillary perturbations is much smaller than that of the bending perturbations for sufficiently viscous liquids when the inequality

$$\frac{\mu^2}{\rho a_0^2 \rho_g U^2} \gg 1 \tag{2.23}$$

holds. In this case, deformations of the jet due to the capillary Rayleigh-Weber instability can be neglected during bending.

It is worth noting that at $\mu = 0$ (2.21) coincides with the long-wave limit ($\bar{k} \to 0$) of (2.1).

The breakup length of jets in the case of the aerodynamically-driven bending instability is determined by the following expression [1, 6]

$$L_{\text{breakup}} = \Delta \cdot \left[\frac{3\mu\rho a_0^2 U^3}{\left(\rho_g U^2 - \sigma/a_0\right)^2} \right]^{1/3} \tag{2.24}$$

where $\Delta = \ln(ma_0/\zeta_0)$, $m = 2$–4, ζ_0 is the initial amplitude of bending perturbations. The value of the factor m is chosen in agreement with the experimental data [4] and the energy estimates, which show that as the bending perturbation amplitude reaches the value of the order of a few cross-sectional radii, the jet is almost immediately squeezed by the air pressure difference at its surface. Equation (2.24) predicts a decrease in the jet breakup length at higher flow velocity U, which agrees with the experimental data. (It is emphasized that the breakup length L_{breakup} of straight capillary jets experiencing Rayleigh-Weber instability increases proportionally to U).

Nonlinear Theory of Finite Bending Perturbations of Liquid Jets Moving in Air

In the works of Yarin [1, 6], the aerodynamically-driven nonlinear bending instability of thin jets of highly viscous liquids rapidly moving in air was studied numerically by solving (2.2)–(2.19). It was shown that the nonlinear effects, in

particular, the most important of them – the viscous stresses originating from the elongation of the bending jet axis – decelerate growth of bending perturbations. However, for the estimates of the perturbation amplitudes and timing up to the amplitudes of the order of (2–4)a_0 one may extrapolate the predictions of the linear theory with sufficient accuracy [as it was done in derivation of (2.24)]. The presence in (2.19) for $\vec{q}$ of the quadratic drag force leads to a slow sweep of bending perturbations down the gas flow in addition to growth of their amplitude (the latter is due to the "lift" component of the aerodynamic force $\vec{q}$). The configurations of the jet axis corresponding to one length of the bending perturbation at several consecutive time moments denoted by numerals by the curves are shown in Fig. 2.1. It is seen that the jet axis at the end takes a form of a cliff which leads to an "overturning." At this moment, the amplitude of the bending perturbation is of the order of $4a_0$. Figure 2.2 depicts the corresponding jet section at the moment of "overturning."

The rate of growth of the bending perturbations, as well as its deceleration due to the nonlinear effect (the longitudinal viscous stresses resulting from stretching of the jet axis at the nonlinear stage of bending) can be also calculated based on the energy balance given by Yarin [1]. Namely, the work of the distributed aerodynamic bending force $\vec{q}$ is spent on changes in the kinetic and surface energies and viscous dissipation in the jet. Assuming sinusoidal shape of a bending section of a jet, one arrives at the following equation for the amplitude $H(t)$ of the bending perturbation

$$H'' + \frac{3}{4}\frac{\mu}{\rho a_0^2}\bar{k}^4 H' + \frac{9}{4}\frac{\mu}{\rho a_0^4}\bar{k}^4 H^2 H' + H\bar{k}^2\left(\frac{\sigma}{\rho a_0^3} - \frac{\rho_g U^2}{\rho a_0^2}\right) = 0 \tag{2.25}$$

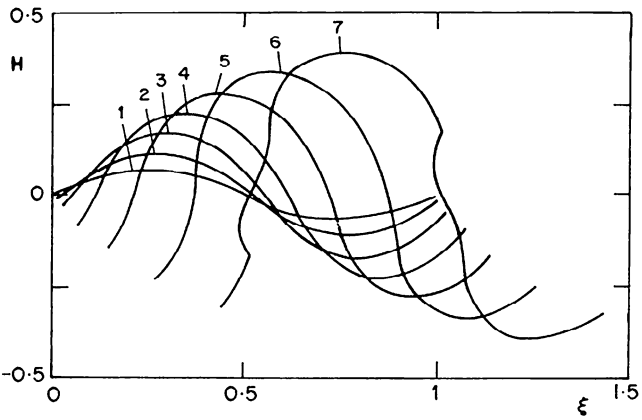


Fig. 2.1 Jet evolution in the case of the bending perturbations of finite amplitude affected by air drag force [1]. All the parameters in the plot are dimensionless. As a length scale, the wavelength of the fastest growing bending mode in the linear approximation $l_* = 2\pi\left[(9/8)\mu^2 a_0^4/\left(\rho\rho_g U^2\right)\right]^{1/6}$ is chosen. Time denoted by the numerals near the curves is rendered dimensionless by the characteristic time of small bending perturbations, $T = \left[\left(\rho\mu a_0^2\right)/\left(\rho_g^2 U^4\right)\right]^{1/3}$ (Courtesy of Pearson Education)

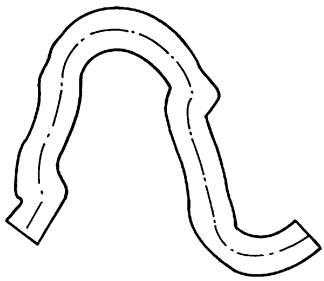


Fig. 2.2 Predicted instantaneous shape of a jet with a large-scale aerodynamically-driven bending instability corresponding to the jet axis configuration at $t = 7$ in Fig. 2.1 [1]. The cross-sectional radius ranging from 65% to 80% of its initial value (Courtesy of Pearson Education)

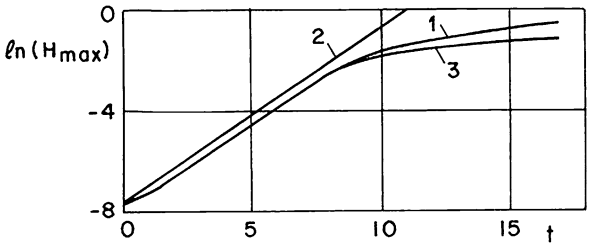


Fig. 2.3 The amplitude of the bending perturbation of a Newtonian liquid jet with $\mu = 1$ Pa s [1]. Curve 1 was obtained by solving the complete system of the quasi-one-dimensional equations of the jet dynamics (2.2)–(2.19). The straight line 2 corresponds to the linear theory: $H = H_0 \exp(\gamma t)$ with γ found from (2.21). Curve 3 was obtained by numerical integration of the nonlinear energy balance, (2.25). The length scale is taken as $l_* = 0.943 \times 10^{-2}$ m and $T = 0.0047$ s is used as a time scale (Courtesy of Pearson Education)

In (2.25) primes denote time differentiation. The above-mentioned nonlinear effect related to stretching of the jet axis by finite bending perturbations is given by the third (nonlinear in H) term on the left-hand side in (2.25). The linearized version of (2.33) corresponds to small bending perturbations and readily admits the solution $H = \exp(\gamma t)$. The amazing fact is that the growth rate γ thus obtained satisfies the exact (2.21). The nonlinear numerical solution of (2.25) is depicted in Fig. 2.3 together with the numerical solution of the quasi-one-dimensional equations and the result of the linear theory.

Bending Instability of Rheologically Complex Liquid Jets

Capillary instability and breakup of thin jets of dilute polymer solutions considered in section Capillary Breakup of Rheologically Complex Liquid Jets of Chap. 1 represents itself an example of the so-called strong flows, in which coil-stretch transition of macromolecular coils can happen because the elongation rate is so

high that viscoelastic relaxation does not succeed to fully unload the liquid. The corresponding presence of significant elastic stresses results in such peculiar non-Newtonian phenomena as formation of the beads-on-a-string structure. Bending instability of non-Newtonian liquids, in particular, of concentrated polymer solutions and melts, also reveals a wide spectrum of nontrivial deviations from the Newtonian behavior, related to a number of important applications. Some of them are discussed below.

The bending instability of jets of power law liquids rapidly moving in air was studied by Yarin [1] in the framework of the energy balance similar to the one which led to (2.25). An equation for the bending amplitude H obtained, which generalizes (2.25) for the power law liquids, reveals that the evolution of the bending perturbations of pseudoplastic jets ($n < 1$) is dominated by an initial stage where the perturbation amplitude and rates of deformation are small (similar to the capillary breakup of pseudoplastic jets discussed in Ch.1). On the other hand, in bending of dilatant ($n > 1$) high-speed jets, an increase of the effective viscosity at a later stage significantly decelerates perturbation growth.

The dynamics of bending perturbations of high-speed viscoelastic jets of uncharged polymer solutions and melts, as well as of concentrated micellar solutions was studied by Yarin [1]. One of the important applications of such jets is in melt blowing – a technology used to produce nonwoven mats of polymer nanofibers [12]. In Yarin [1], it was shown that the growth rate of small bending perturbations is determined by the following characteristic equation

$$\gamma^2 + \frac{3}{4}\frac{\mu\bar{k}^4}{\rho a_0^2(1+\gamma\theta)}\gamma + \left(\frac{\sigma}{\rho a_0^3} - \frac{\rho_g U^2}{\rho a_0^2} + \frac{\sigma_0}{\rho a_0^2}\right)\bar{k}^2 = 0 \tag{2.26}$$

which generalizes (2.21) to the case of viscoelastic liquid jets (the Newtonian case is recovered with the relaxation time $\theta = 0$). In (2.26) the initial longitudinal stress in the jet can either be absent ($\sigma_0 = 0$) or present and "frozen" $\sigma_0 = \text{const} \neq 0$.

If $\sigma_0 = 0$, (2.26) predicts an accelerated growth of small bending perturbations of viscoelastic liquids compared to a corresponding Newtonian liquid (with the same values of ρ, μ, σ, a_0, and U) due to a decrease in the effective viscosity $\mu_{\text{eff}} = \mu/(1 + \gamma\theta)$. The initial stress $\sigma_0 > 0$ is a stabilizing factor, which diminishes the growth rate γ, or can even prevent bending instability if $(\sigma_0 + \sigma/a_0) > \rho_g U^2$. The following dimensionless groups govern the bending perturbations of viscoelastic jets

$$\Pi_1 = \frac{\rho_g}{\rho},\quad \Pi_2 = \frac{\mu^2}{\rho a_0^2 \rho_g U^2},\quad \Pi_3 = \frac{\rho_g U^2}{\mu/\theta},\quad \Pi_4 = \frac{\sigma_0}{\rho_g U^2},\quad \Pi_5 = \frac{\sigma/a_0}{\rho_g U^2}, \tag{2.27}$$

Figure 2.4 depicts the growth rates predicted from (2.26) for two jets of the upper-convected Maxwell liquids, which are shown by curves 1 and 3. They correspond to different values of the relative gas velocity (U for curve 1 is higher

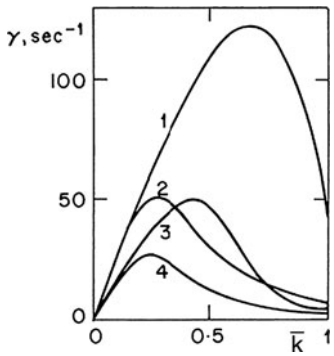


Fig. 2.4 Growth rate of small bending perturbations of viscoelastic jets of the upper-convected Maxwell liquid [1]. For all curves $\Pi_1 = 10^{-3}$, $\Pi_4 = \Pi_5 = 0$. For curves 1 and 2: $\Pi_2 = 0.156 \times 10^4$; for curves 3 and 4 $\Pi_2 = 0.4 \times 10^4$. For curves 2 and 4 $\Pi_3 = 0$. For curves 1 and 3 $\Pi_3 = 0.64$ and $\Pi_3 = 0.25$, respectively (Courtesy of Pearson Education)

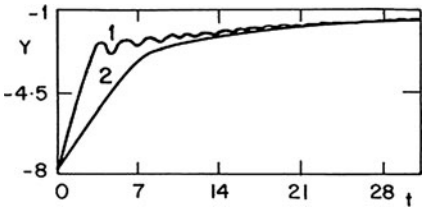


Fig. 2.5 The amplitude Y of the bending perturbations of a jet of the upper-convected Maxwell liquid is shown by curve 1 [1]. The values of the dimensionless groups are: $\Pi_1 = 10^{-3}$, $\Pi_2 = 0.156 \times 10^4$, $\Pi_3 = 0.64$, $\Pi_4 = \Pi_5 = 0$. Curve 2 depicts the amplitude of the corresponding jet of Newtonian liquid ($\Pi_3 = 0$) (Courtesy of Pearson Education)

than for curve 3). Curves 2 and 4 show the results for the corresponding Newtonian liquid jets, with curve 2 corresponding to curve 1, and curve 4 to curve 3.

The nonlinear dynamics of the bending perturbations of high-speed viscoelastic uncharged jets moving in air reveals a new phenomenon found by Yarin [1]. Figure 2.5 shows that at the nonlinear stage the growth of the perturbation amplitude is not only drastically slowed down due to the longitudinal stresses resulting from the jet elongation (similar to Newtonian jets discussed above), but the amplitude can also decrease and oscillate. These latter phenomena result from the competition of the inertial and elastic forces. A jet element undergoing bending misses its "equilibrium" position due to its inertia, and the jet axis becomes overstretched, which produces an extra longitudinal elastic stress. This stress tends to contract the jet element. However, during the contraction stage (when the bending perturbation amplitude decreases), the jet element once more misses its "equilibrium" position due to its inertia and becomes overcompressed. This initiates a new cycle of the oscillations. Viscous stresses gradually dissipate the energy of these oscillations.

Buckling of Thin Liquid Jets

G.I. Taylor in his seminal works [13, 14] discovered a new instability mode of highly viscous jets, namely buckling of slowly moving jets impinging onto a wall when they are subjected to a longitudinal compressive force. In one of his experiments, compressive forces resulted from squeezing the ends of a liquid thread floating on the mercury surface. In another experiment, highly viscous jets were either moving vertically downward in a liquid and passing into a lower layer of higher density, which created a sudden increase in the compressive buoyancy force, or impinging onto a wall. The latter case was experimentally studied in detail in [15, 16]. These works showed that buckling occurs only in very slowly moving highly viscous jets. The jets with the values of the Reynolds number Re exceeding the critical threshold of $\mathrm{Re}_{cr} \approx 1.2$ were stable and straight. Therefore, in this case, the buckling instability emerges when the Reynolds number decreases. On the other hand, there is also a restriction on the jet lengths L from nozzle to wall. If L is less than a certain critical value L_{cr}, there is no buckling. Immediately after the onset of the buckling instability (at $\mathrm{Re} \leq \mathrm{Re}_{cr}$ and $L/d_0 \geq L_{cr}/d_0$ with d_0 being the nozzle diameter) a two-dimensional bucking (folding) sets in, and the jet is deposited on the wall as folds. However, with a further increase of the ratio L/d_0, bucking perturbations become spiral-like. The jet axis becomes three-dimensional, which signifies the bifurcation from folding to coiling, and the jet is deposited on the wall as coils. In the experiments [15], the dependences of L_{cr} and the folding and coiling frequencies on the liquid jet viscosity, its velocity and the nozzle diameter were established. Buckling was also observed in horizontal jets moving over the free surface of a denser liquid (such jets widen beginning from the nozzle, in distinction from gravity-driven jets, which initially become thinner and begin to widen only close to the wall onto which they impinge). All the observations confirmed the idea of Taylor [14] that buckling of liquid jets is determined by the presence of the longitudinal compressive force acting in the jet and in this sense is a direct analog of the elastic buckling of bars and columns studied by Euler [8]. A detailed theory of the onset of buckling instability (folding of highly viscous liquid jets and films-planar jets-impinging on a wall) was given by Yarin et al. in [1, 17, 18] based on the general quasi-one-dimensional equations of jet dynamics (2.2)–(2.19) (see also the later efforts directed on a nonlinear buckling theory in [19]).

Recently, jet buckling on laterally moving solid surfaces nearly perpendicular to the jet axis was reported [20–22], which is of interest, in particular, in relation to writing by short straight electrically driven jets. The stability analysis in that case was also based on the quasi-one-dimensional equations of the dynamics of liquid jets similar to (2.2)–(2.19). It revealed that the characteristic frequencies of buckling are practically unaffected by the lateral motion of the surface and stay the same as in the case of liquid jet impingement on a stationary hard flat surface [21, 22]. Moreover, the deposit morphology at the wall is practically unaffected by the method of jet initiation (gravity-driven jets [20] versus the electrically driven jets

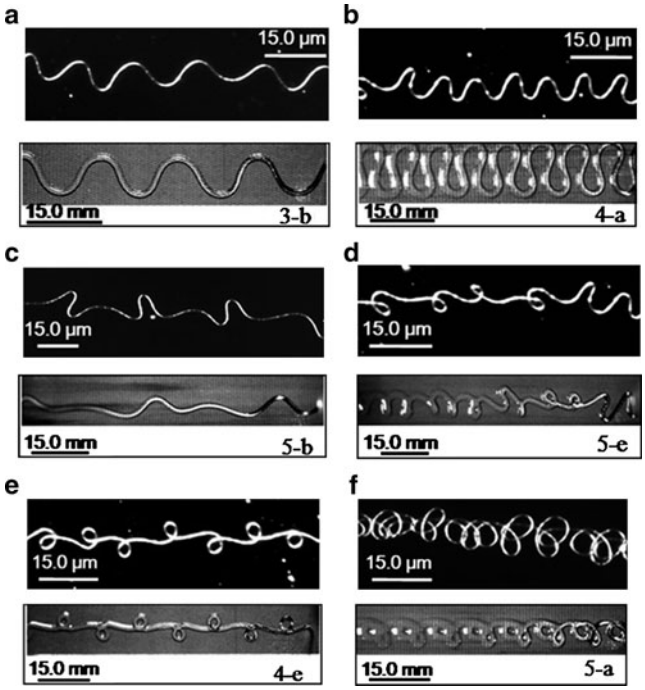


Fig. 2.6 (**a**–**f**) Comparison of the buckled patterns created by electrified jets of polyethylene oxide (*PEO*) in water, collected on glass slides in [22], to patterns produced by the buckling of the uncharged gravity-driven syrup jets [20]. Note that the gravity-driven syrup jets and their buckling patterns are about 1,000 times larger than those of the electrified jets of PEO in water. The upper panel in each pair depicts the results for the electrified PEO jets in [22]. The lower panels show the similar patterns produced by the syrup jets in [20]. The symbols in the lower right corner of each panel are the figure number found in [20] (Courtesy of Elsevier)

[22]) as Fig. 2.6 demonstrates. The buckling frequency ω predicted by the linear stability theory of Yarin et al. [1, 17]

$$\ln\left(\omega\frac{d_0}{V_0}\right) = -0.0194\ln\left(\frac{\mu Q}{\rho g d_0^4}\right) + 0.2582 \tag{2.28}$$

is in reasonable agreement with the experimental data for ω evaluated from the images similar to those in Fig. 2.6 (d_0 denotes the initial cross-sectional jet diameter, Q is the volumetric flow rate in the jet, and g is the gravity acceleration).

Bending Instability of Electrified Liquid Jets

The electrified jets of concentrated polymer solutions move in air with low speeds of the order of 1 m/s. However, they bend due to the Coulombic interactions discussed above in relation with the electric bending force (2.20). Such jets emerge

in electrospinning of polymer nanofibers, one of the nanotechnological processes [9–11, 23, 24]. Comparison of the expressions for the bending forces $\vec{q}$ in the aerodynamic and electric cases, (2.18) and (2.20), respectively, reveals that in the electrically driven bending instability the factor ${e_0}^2\ln(L/a_0)/\pi{a_0}^2$ plays the role of the factor $\rho_g U^2$ in the aerodynamic bending. Accounting for this analogy, it is easy to see that the electrospinning process is enabled by the fact that the viscoelastic stresses dominate the surface tension and prevent capillary breakup when the electric analog of (2.23)

$$\frac{\pi\mu^2}{\rho e_0^2 \ln(L/a_0)} \gg 1 \tag{2.29}$$

holds (e_0 denotes the initial electric charge per unit length of a straight jet). If polymer concentration is too low, capillary perturbations grow on the background of the bending perturbations, since the inequality does not hold, and nanofibers with beads are formed, which is also of interest in certain applications [11]. In the case of electrospinning, the stabilizing role of the viscoelastic stresses in the jet is the key element of the process, since it aims at production of intact nanofibers, in distinction from electrospraying, the process where liquid is fully atomized by the electric forces, which enhances capillary instability.

Several images of bending polymer jets in electrospinning are shown in Fig. 2.7.

The electrospinning jets typically have an almost straight section of the order of several cm followed by a number of bending loops shown in Fig. 2.7. The region near the vertex of the envelope cone about the bending loops in this figure was imaged at 2,000 frames per second. The stereographic images in Fig. 2.7 show the jet shape in three dimensions. The expanding spiral in this figure is a simple example of the kinds of paths that were observed in [9]. After a short sequence of unstable bending back and forth, with growing amplitude, the jet followed a bending, winding, spiraling, and looping path in three dimensions. The jet in each loop grew longer and thinner as the loop diameter and circumference increased. After some time, segments of a primary loop suddenly developed a new bending instability (secondary loops), similar to, but at a smaller scale than, the first

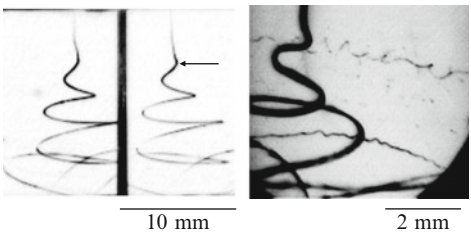


Fig. 2.7 *Left*: Stereographic images of an electrically driven bending instability. The exposure time was 0.25 ms. The *arrow* marks a maximum lateral excursion of a loop. *Right*: An enlarged image of the end of the straight segment of the jet. The exposure time was 0.25 ms (After [9]. Courtesy of AIP)

(cf. the smaller loops on the right-hand side image in Fig. 2.7, where the secondary loops superimposed on the primary ones are clearly seen). Each cycle of bending instability can be described in three steps. (1) A smooth segment that was straight or slightly curved suddenly developed primary bending loops. (2) The segment of the jet in each bend elongated and became a part of spiraling loops with growing diameters. (3) As the loop length increased, the cross-sectional diameter of the jet forming the loop grew smaller, the conditions for step (1) re-established on a smaller scale, and the next cycle of bending instability began resulting in the secondary loops. This cycle of instability was observed to repeat at an even smaller scale resulting in a fractal-like jet. The length of such a fractal jet increased enormously creating nanofibers. In a while, the polymer solution jet lost most of its solvent due to evaporation in flight, solidified as it dried, and electrospun nanofibers were collected at some distance below the envelope cone.

The instability mechanism that is relevant in the electrospinning context is illustrated by the Coulombic interaction of three point-like material elements, each with charge e, moving on a jet and originally in a straight line at A, B, and C as shown in Fig. 2.8. (It is emphasized that charge transport in such a jet is practically purely convective [11]). Two Coulomb forces having magnitudes $F = e^2/r^2$ (in the Gaussian units) push against charge B from opposite directions. If a bending perturbation causes the charged material element B to move off the line by a distance δ to B′, a net force $F_1 = 2F\cos\theta = (2e^2/r^3)\delta$ acts on charge B in the direction perpendicular to the line. This net force tends to cause B to move further in the direction of the bending perturbation away from the line between fixed charges, A and C. Then, the growth of the small bending perturbation that is characterized by δ is governed in the linear approximation by the second law of Newton according to the equation

$$m\frac{d^2\delta}{dt^2} = \frac{2e^2}{l_1^2}\delta \tag{2.30}$$

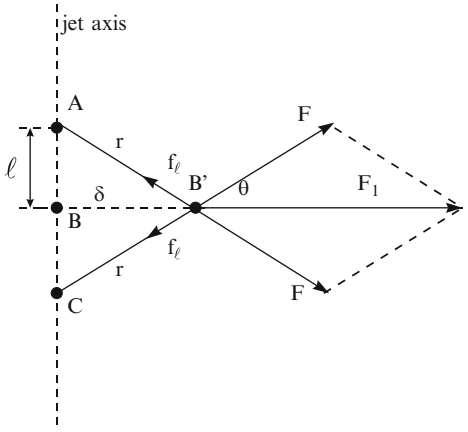


Fig. 2.8 Illustration of the instability, leading to bending of an electrified jet (After [9]. Courtesy of AIP)

where m is the mass, and ℓ is the initial separation between charges A and B in the straight jet.

The growing solution of this equation, $\delta = \delta_0 \exp[(2e^2/ml_1^3)^{1/2}t]$, shows that small perturbations increase exponentially. The increase is sustained because the electrostatic potential energy of the system shown in Fig. 2.8 decreases as e^2/r when the perturbations, characterized by δ and r, grow.

A detailed theory of the bending instability of the electrified polymer jets in electrospinning was given in [9, 10] (see also the reviews [11, 23, 24] and references therein). Recasting the inequality (2.22) for the onset of the aerodynamic bending reveals that the destabilizing electric force overcomes the stabilizing effect of the surface tension if

$$e_0^2 \ln\left(\frac{L}{a_0}\right) > \pi a_0 \sigma \tag{2.31}$$

The equation for the growth rate of small aerodynamic bending perturbations (2.21) is recast in the following equation for the electrically-driven bending [9, 10]

$$\gamma^2 + \frac{3}{4}\frac{\mu \bar{k}^4}{\rho a_0^2}\gamma + \left(\frac{\sigma}{\rho a_0^3} - \frac{e_0^2 \ln(L/a_0)}{\pi \rho a_0^4}\right)\bar{k}^2 = 0 \tag{2.32}$$

The corresponding wavenumber $\bar{k}_*$ and the growth rate γ_* of the fastest growing electrically-driven bending perturbation are given by

$$\bar{k}_* = \left\{\frac{8}{9}\frac{\rho a_0^2}{\mu^2}\left[\frac{e_0^2 \ln(L/a_0)}{\pi a_0^2} - \frac{\sigma}{a_0}\right]\right\}^{1/6} \tag{2.33}$$

$$\gamma_* = \frac{\left[e_0^2 \ln(L/a_0)/\pi a_0 - \sigma\right]^{2/3}}{\left(3\mu\rho a_0^4\right)^{1/3}} \tag{2.34}$$

with $\ln(L/a_0) = \ln(1/\bar{k}_*)$ [10].

The nonlinear stage of the electrically-driven bending instability in electrospinning was studied numerically in [9, 10] using the general quasi-one-dimensional equations of the dynamics of thin liquid jets described in Section "General Quasi-One-Dimensional Equations of Dynamics of Free Liquid Jets." In addition, in [10], the dynamic equations were supplemented by the equations describing solvent evaporation, jet solidification, and the effect of these processes on the rheological behavior of polymeric liquid. Figure 2.9 illustrates the predicted evolution of an electrospun jet.

The fact that strongly stretched polymeric jets are stable relative to bending perturbations demonstrated in [9] means that the electrospun jets possess an initial straight section. It also means that transversal waves can propagate over a stretched jet as over a string [25, 26] (Fig. 2.10). The widening of a lateral displacement pulse

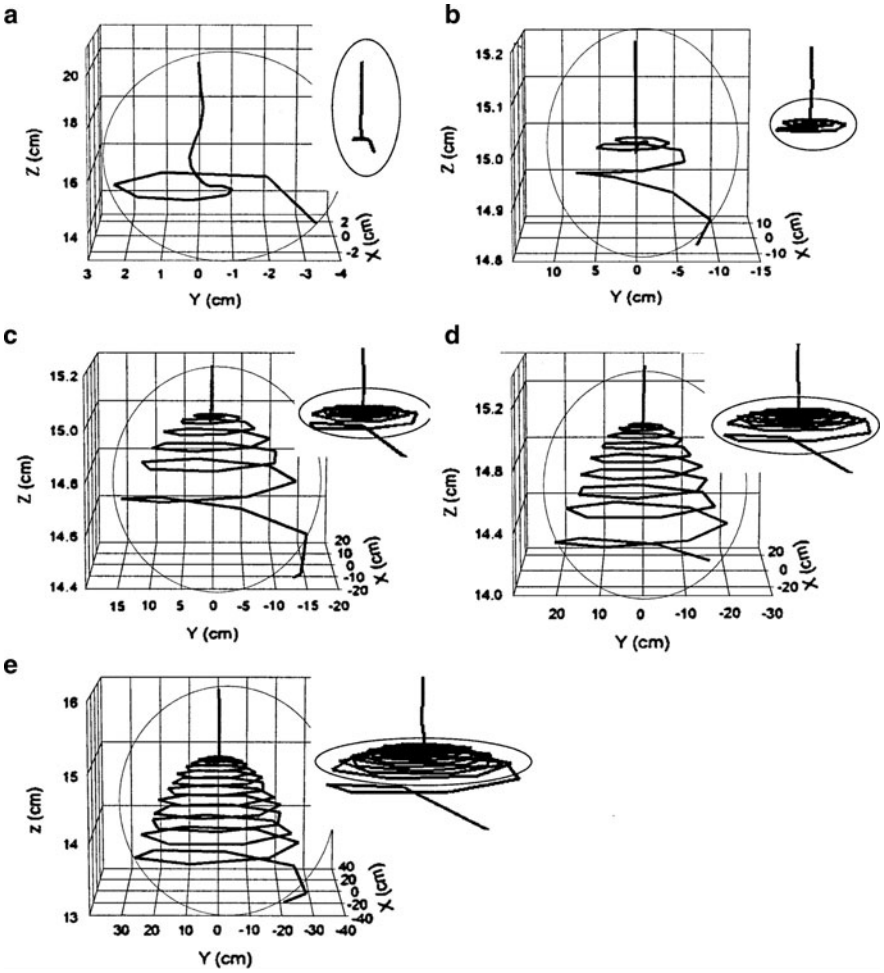


Fig. 2.9 Bending instability of a single jet. Only the jet axis is shown at the dimensionless time moments: (**a**) 0.19, (**b**) 0.39, (**c**) 0.59, (**d**) 0.79, and (**e**) 0.99 (After [9]. Courtesy of AIP)

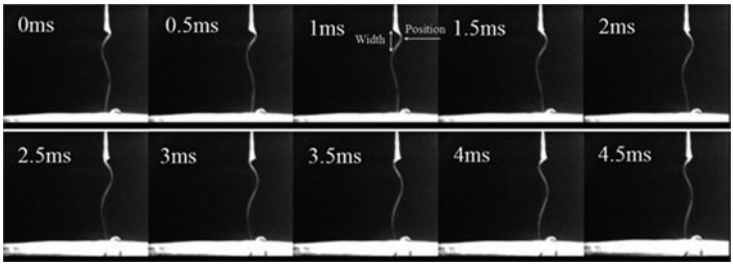


Fig. 2.10 Propagation and widening of a single lateral displacement pulse on an electrically-driven jet of a concentrated polymer solution [26]. The interelectrode distance $L = 5.5$ cm, potential difference of $U = 3$ kV, and the electric current $I = 100$ nA. The jet was straight before the lateral displacement pulse was applied by a plastic impactor (Courtesy of Elsevier)

W between $t = 0$ and $t = \Delta t$ can be measured from such images. Then, the longitudinal stress in the polymeric jet is recovered as

$$\sigma_{xx} = \rho\left(\frac{W}{2\Delta t}\right)^2 \tag{2.35}$$

An elongational rheometer developed in [26] based on this principle revealed that the initial longitudinal stress created by the electric stretching of a polymeric jet as it transforms from the modified Taylor cone to a thin jet, is of the order of 10–100 kPa. These values are one or two orders of magnitude larger than those measured for the uncharged viscoelastic jets. The rheometer also allows evaluation of the modulus of elasticity and relaxation time of concentrated polymer solutions and melts.

References

1. Yarin, A. L. *Free Liquid Jets and Films: Hydrodynamics and Rheology*. Longman, Wiley & Sons; Harlow/New York: Longman/Wiley (1993).
2. Weber, C. On the breakdown of a fluid jet, Zum Zerfall eines Flussigkeitsstrahles, *Z. Angrew. Math und Mech*., 11, 136–154 (1931).
3. Debye, P. & Daen, J. Stability considerations of nonviscous jets exhibiting surface or body tension. *Phys. Fluids* 2, 416–421 (1959).
4. Grant, E. M. & Middleman, S. Newtonian jet stability. *AIChE J*. 12, 669–678 (1966).
5. Entov, V. M. & Yarin, A. L.: Dynamical equations for a liquid jet. *Fluid Dyn*. 15, 644–649 (1980).
6. Entov, V. M. & Yarin, A. L. The dynamics of thin liquid jets in air. *J. Fluid Mech*. 140, 91–111 (1984).
7. Yarin, A. L. On the dynamical equations for liquid jets. *Fluid Dyn*. 18, 134–136 (1983).
8. Landau, L. D. & Lifshitz, E. M. *Theory of Elasticity* Pergamon, New York (1975).
9. Reneker, D. H. Yarin, A. L. Fong, H. & Koombhongse, S. Bending instability of electrically charged liquid jets of polymer solutions in electospinning. *J. Appl. Phys*. 87, 4531–4547 (2000).
10. Yarin, A. L. Koombhongse, S. & Reneker, D. H. Bending instability in electrospinning of nanofibers. *J. Appl. Phys*. 89, 3018–3026 (2001).
11. Reneker, D. H. Yarin, A. L. Zussman, E. & Xu, H. Electrospinning of nanofibers from polymer solutions and melts. *Adv. Appl. Mech*. 41, 43–195 (2007).
12. Bresee R. R. & Ko, W. C. Fiber formation during melt blowing. *Int. Nonwovens J*., 21–28, Summer (2003).
13. Taylor, G. I. Instability of jets, threads and sheets of viscous fluid. In: Proceedings of the 12th International Congress Appl. Mech., Stanford, 1968. Stanford, pp. 382–388 (1969).
14. Taylor, G. I. Electrically driven jets. *Proc. R. Soc. Lond*. A313, 453–475 (1969).
15. Cruickshank J. O. & Munson, B.R. Viscous fluid buckling of plane and axisymmetric jets. *J. Fluid Mech*. 113, 221–239 (1981).
16. Munson, B. R. Viscous buckling of slender horizontal jets. *Phys. Fluids* 24, 1780–1783 (1981).
17. Tchavdarov, B. Yarin, A. L. & Radev, S. Buckling of thin liquid jets. *J. Fluid Mech*. 253, 593–615 (1993).
18. Yarin A. L. & Tchavdarov, B. Onset of folding in plane liquid films. *J. Fluid Mech*. 307, 85–99 (1996).

19. Skorobogatiy M. & Mahadevan, L. Folding of viscous sheets and filaments. *Europhys. Lett*. 52, 532–538 (2000).
20. Chiu-Webster S. & Lister, J. R. The fall of a viscous thread onto a moving surface: a 'fluid-mechanical sewing machine'. *J. Fluid Mech*. 569, 89–111 (2006).
21. Ribe, N. M. Lister, J. R. & Chiu-Webster, S. Stability of a dragged viscous thread: onset of 'stitching' in a fluid-mechanical 'sewing machine'. *Phys. Fluids* 18, 124105 (2006).
22. Han, T. Reneker, D. H. & Yarin, A. L. Buckling of jets in electrospinning. *Polymer* 48, 6064–6076 (2007).
23. Yarin, A. L. Zussman, E. Wendorff, J. H. & Greiner, A. Material encapsulation in core-shell micro/nanofibers, polymer and carbon nanotubes and micro/nanochannels. *J. Mater. Chem*. 17, 2585–2599 (2007).
24. Reneker D. H. & Yarin, A. L. Electrospinning jets and polymer nanofibers. *Polymer* 49, 2387–2425 (2008).
25. Goren S. & Gavis, J. Transverse wave motion on a thin capillary jet of a viscoelastic liquid. *Phys. Fluids* 4, 575–579 (1961).
26. Han, T. Yarin, A. L. & Reneker, D. H. Viscoelastic electrospun jets: initial stresses and elongational rheometry. *Polymer* 49, 1651–1658 (2008).

Chapter 3
Instability of Liquid Sheets

N. Ashgriz, X. Li, and A. Sarchami

Abstract This chapter relates to the liquid sheets and their instability. Liquid sheet instability is due to the interaction between the liquid and its surrounding fluid. When the amplitude of a perturbation grows and reaches a critical value, sheet is disintegrated forming liquid ligaments. Here, the linear and nonlinear instability of an inviscid and viscous liquid sheet is discussed, showing the effect of the aerodynamic forces on the growth rate of the initially small perturbations. Other effects, such as the effect of initial velocity profile on the instability are also discussed.

Keywords Liquid sheet instability · Nonlinear sheet instability · Sinuous and dilational disturbances of a liquid sheet · Thinning liquid sheet · Three dimensional instability of liquid sheets · Viscous sheets

Introduction

In many spray nozzles, the bulk liquid is first transformed into a liquid sheet prior to the atomization process. The liquid sheet exiting a nozzle may go through certain oscillations, which result in the formation of liquid ligaments. The ligaments are then broken into small droplets, forming the spray. The spray droplet sizes are generally in the same order as the liquid sheet thickness. Therefore, by forming a thin liquid sheet one can generate small droplets out of relatively large orifice nozzles. This chapter discusses the mechanism of sheet instability and its breakup as a prerequisite to the understanding of the atomization process.

There have been numerous studies on the temporal and spatial instability of liquid sheet [1–40]. This chapter is mainly on the temporal instability. Among these, Dombrowski and his coworkers [8–16] conducted extensive studies on the factors influencing the breakup of sheets and obtained information on the wave motions of high velocity sheets. More recent analyses are provided by Senecal et al. [20], and Rangel and Sirignano [21]. This chapter provides only

A. Sarchami (✉)
Department of Mechanical and Industrial Engineering, University of Toronto, Canada

N. Ashgriz (ed.), *Handbook of Atomization and Sprays*,
DOI 10.1007/978-1-4419-7264-4_3, © Springer Science+Business Media, LLC 2011

the basic sheet instability theories which are being used to model the atomization process. More detailed review of this topic is provided by Sirignano and Mehring [22] and Lin [24].

Linear Instability of a Liquid Sheet

In a two-dimensional liquid sheet, the sheet instability is mainly due to the aerodynamic interactions between the liquid and its surrounding gas. Contrary to the cylindrical liquid jets, surface tension forces tend to stabilize a planar liquid sheet. Here the instability analysis of a two-dimensional, viscous, incompressible liquid sheet of thickness $2a$ moving with velocity U_1 through a gaseous medium moving with velocity U_2, having a relative velocity of U_0 is considered. The surrounding gas is considered to be inviscid and incompressible. The liquid and gas have densities of ρ_l and ρ_g, respectively, and the viscosity of the liquid is μ_l. The gravitational effects are neglected. The coordinate system is shown on Fig. 3.1. The x-axis is parallel to the direction of the sheet relative velocity, U_0. The y-axis is perpendicular to the x-axis and its origin is located at the mid-plane of the sheet.

The undisturbed sheet has a uniform thickness $2a$, throughout. It is then subject to small disturbances of the following form: $\zeta = \zeta_0 \exp(ikx + \omega t)$ on its upper and lower interfaces ($y = a + \xi_1, y = -a + \xi_2$, respectively) which deform the sheet.

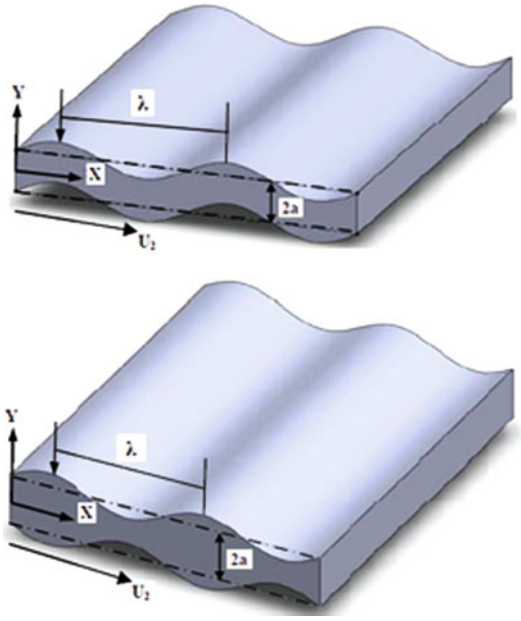


Fig. 3.1 Schematic of a (**a**) sinuous (antisymmetric) disturbance and a (**b**) dilational (symmetric) disturbance

Generally, two modes of oscillations are considered: symmetric and antisymmetric. In the symmetric mode, also referred to as the dilational mode or varicose waves, the middle plane is undisturbed. In the antisymmetric mode, also referred to as sinuous waves, the free surfaces move in the same direction and with the same magnitude. Squire [3] and Hagerty and Shea [4] showed that for the case of inviscid sheets, the antisymmetric mode is the dominant mode of disturbance. However, later studies have revealed that this is not generally the case [22].

Inviscid Liquid Sheet

For an inviscid irrotational flow, $\mathbf{u} = \nabla\varphi$, where $\varphi = \varphi_1$ for $-a < y < a$, and $\varphi = \varphi_2$ for $y > a$ and $y < -a$. The following solution for φ is considered:

$$\varphi = [A\ \cosh(ky) + B\ \sinh(ky)]\exp(ikx - \omega t) \tag{3.1}$$

where k and ω are the disturbance wave number and frequency, respectively. For antisymmetric mode, $A = 0$, and for symmetric mode, $B = 0$. The boundary conditions, similar to the jet instability problem in Chap. 1, includes the kinematic (normal component of the surface velocity is continuous) and dynamic conditions (balance of interface stresses).

The complex frequency, ω has two components: real and imaginary: $\omega = \omega_\mathrm{r} + i\omega_\mathrm{i}$. The real part represents the growth or damping rate of the disturbances, whereas the imaginary part represents the wave velocity of the disturbance. The growth rate is found to be:

$$\frac{\omega_\mathrm{r}}{kU_\mathrm{o}} = \left[\frac{\varepsilon K}{(\varepsilon + K)^2} - \frac{ka}{We}\frac{1}{\varepsilon + K}\right]^{1/2} \tag{3.2}$$

where $K = \tanh(ka)$ for the sinuous mode (antisymmetric) and $K = \coth(ka)$ for the dilational mode (symmetric), $We = \rho_L U_0^2 a/\sigma$, and $\varepsilon = \rho_g/\rho_L$. Figure 3.2, adopted from [22], provides the growth rate for various wave numbers for both sinuous (antisymmetric) and dilational (symmetric) waves and for different Weber numbers and density ratios. The results also show that the varicose mode is more unstable for density ratios near unity. It is clear that for the low Weber number case, the growth of sinuous waves dominate the growth of varicose waves due to the higher growth rates throughout the range of instability.

Sirignano and Mehring [22] summarized the results of the linear sheet instability theory as follows: "For all density ratios, the growth rate for both sinuous and dilational waves increases as the Weber number We is increased. The maximum growth rate for the sinuous disturbances does not significantly change with changes in the density ratio ε. However, the maximum growth rate for the dilational case increases significantly as ε is increased. For low-density ratios,

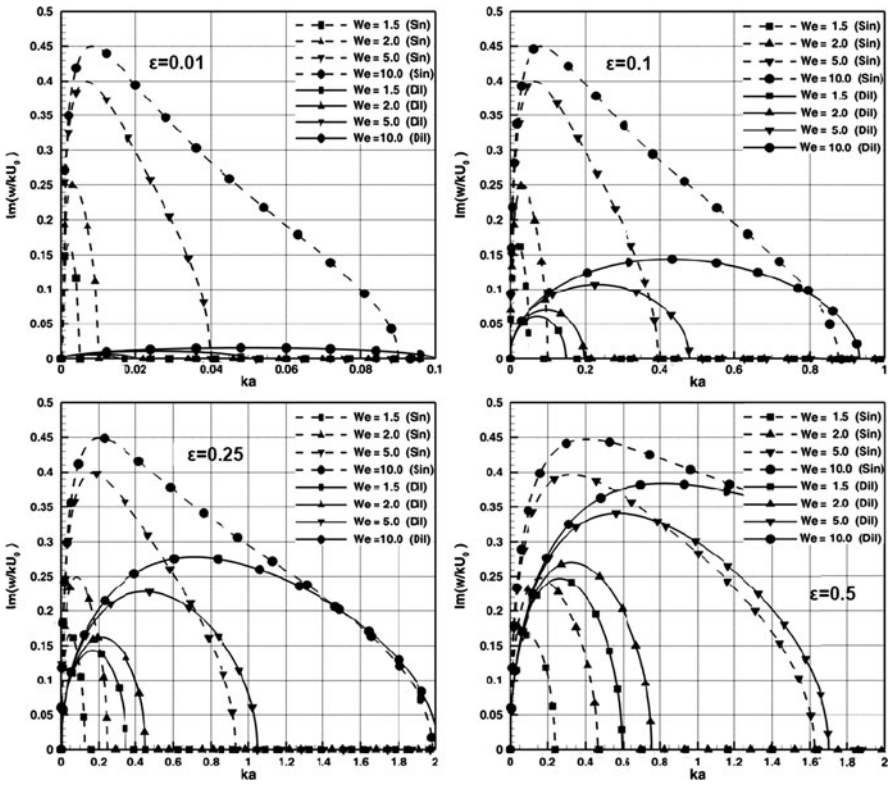


Fig. 3.2 Dimensionless growth rate as a function of ka for different *We* and density [22 Fig. 9] (Courtesy of Elsevier)

the maximum growth rate for the sinuous case is always higher than that for dilational waves. As ε is increased beyond a certain value, the maximum growth rate for dilational waves eventually overcomes the value for sinuous growth. For all density ratios, there exists a region of wave numbers, in which dilational waves are more unstable than the sinuous ones; the latter might even be stable in that region. (6) The disturbance wavelength with maximum growth rate decreases as the density ratio is increased. This is true for both sinuous and dilational waves".

Senecal et al. [20] reduced equation (3.2) to simpler forms for long and short waves. For long waves k is small and $K = \tanh(ka) \approx ka$. Therefore, equation (3.2) for sinous mode becomes:

$$\frac{\omega_r}{kU_o} = \left[\frac{\varepsilon ka}{(\varepsilon + ka)^2} - \frac{ka}{We} \cdot \frac{1}{\varepsilon + ka}\right]^{1/2} \tag{3.3}$$

If $\varepsilon \ll ka$, then:

$$\frac{\omega_r}{kU_o} = \left[\frac{\varepsilon}{ka} - \frac{1}{We}\right]^{1/2} \tag{3.4}$$

For short waves, $K = \tanh(ka) = \coth(ka) \simeq 1$, and equation (3.2) reduces to:

$$\frac{\omega_r}{kU_o} = \left[\frac{\varepsilon}{(\varepsilon+1)^2} - \frac{ka}{We}\cdot\frac{1}{(\varepsilon+1)}\right]^{1/2} \tag{3.5}$$

which reduces to the following for $\varepsilon \ll 1$:

$$\frac{\omega_r}{kU_o} = \left(\varepsilon - \frac{ka}{We}\right)^{1/2} \tag{3.6}$$

Equation 3.2 for the sinuous and varicose growth rates are shown in Figs. 3.3 and 3.4 for gas Weber numbers $We_g = \rho_g U_0{}^2 a/\sigma$ of 0.5 and 5.0, respectively. Each figure also shows the results for the long wave (Equation 3.4), that $\tanh(ka) \approx ka$ and short wave (equation 3.6) approximation. Long wave approximation is similar to that of Hagerty and Shea [4]. For a $We_g = 5.0$, the dimensionless growth rate curves are very similar, except at low values of the dimensionless wave number ka,

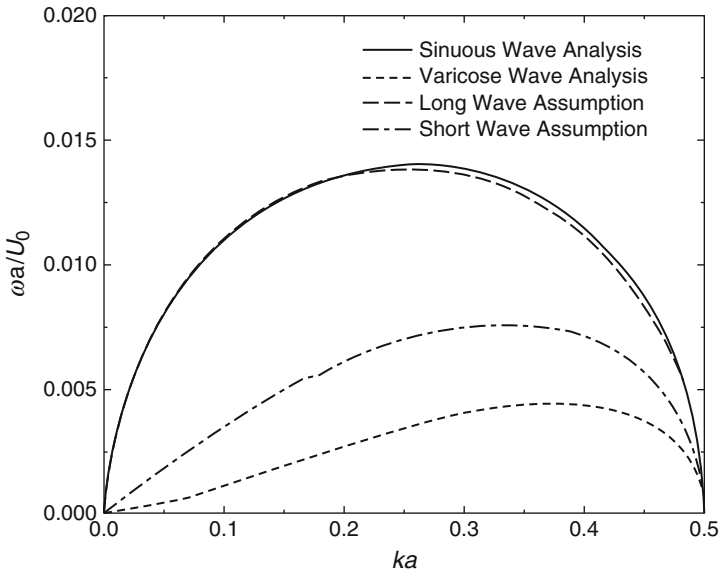


Fig. 3.3 Inviscid dimensionless growth rates $\omega a/U_0$ as functions of dimensionless wave number ka for a gas Weber number of $We_g = 0.5$ [20 Fig. 3] (Courtesy of Elsevier)

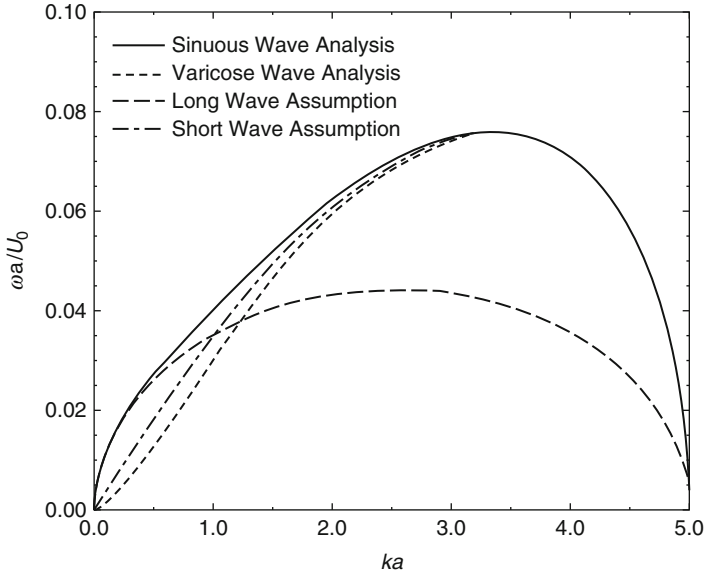


Fig. 3.4 Inviscid dimensionless growth rates $\omega a/U_0$ as functions of dimensionless wave number ka for a gas Weber number of $We_g = 5$ [20 Fig. 4] (Courtesy of Elsevier)

suggesting that the two modes are indistinguishable or that the wave growth on one interface is independent of the growth on the other.

Viscous Liquid Sheets

For a viscous liquid sheet, assuming to have the same pressure distribution as the inviscid liquid, the liquid velocity components can be described as: $u_l = u_I + u_V$ and $v_l = v_I + v_V$. The potential and stream functions that satisfy the continuity equations may have the following forms: $\phi = \varphi(y)\exp(ikx + \omega t)$, $\varphi_1 = \Phi_1(y)\exp(ikx + \omega t)$, and $\psi = \Psi(y)\exp(ikx + \omega t)$. Similar analysis is completed on the gas phase. After substitution, a relation between the complex growth rate and the disturbance wave number k is obtained. Senecal et al. [20] provided the following relation for the growth rate for the sinuous mode:

$$\omega_r = -\frac{2\nu_l k^2 K}{K+\varepsilon} + \frac{\left[4\nu_l^2 k^4 K^2 - \varepsilon^2 {U_0}^2 k^2 - (K+\varepsilon)(\varepsilon {U_0}^2 k^2 + \sigma k^3/\rho_l)\right]^{1/2}}{K+\varepsilon} \tag{3.7}$$

For long waves in the limit of $\varepsilon \ll$ ka, (3.7) reduces to

$$\omega_r = -2\nu_l k^2 + \left[4\nu_l^2 k^4 + \frac{\varepsilon {U_0}^2 k}{a} - \frac{\sigma k^2}{a\rho_l}\right]^{1/2} \tag{3.8}$$

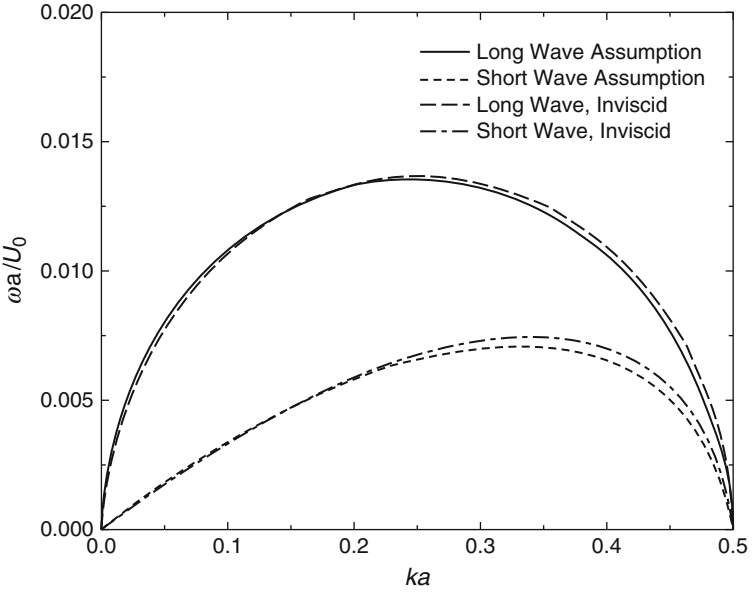


Fig. 3.5 Viscous and inviscid dimensionless growth rates $\omega a/U_0$ as functions of dimensionless wave number ka for a gas Weber number of $We_g = 0.5$ [20 Fig. 7] (Courtesy of Elsevier)

If short waves are assumed for the high speed sheets and $\varepsilon \ll 1$, then

$$\omega_r = -2\nu_l k^2 + \left[4\nu_l^2 k^4 + \varepsilon {U_0}^2 k^2 - \frac{\sigma k^3}{\rho_l}\right]^{1/2} \tag{3.9}$$

which would also be obtained from the dispersion relation for the varicose mode for the same assumptions. Equations (3.8) and (3.9) are presented in Figs. 3.5 and 3.6 with their inviscid counterparts for a We_g of 0.5 and 5.0, respectively [20]. Figure 3.6 shows that the inclusion of viscosity reduces both the maximum growth rate and the corresponding wave number, without altering the instability range of $ka < We$. In addition, the effect of viscosity is minimal for Squire's regime (i.e., for $We < 27/16$ or long wave growth), while the inclusion of the viscous terms are necessary to accurately predict the wave growth of short waves.

Force Balance Model on a Wavy Sheet

Dombrowski and John [12] combined a linear model for temporal instability and a sheet breakup model for an inviscid liquid sheet in a quiescent inviscid gas, to predict the ligament and droplet sizes after breakup. The schematic of their wavy sheet is reproduced in Fig. 3.7. The equation of motion of the neutral axis mid-way

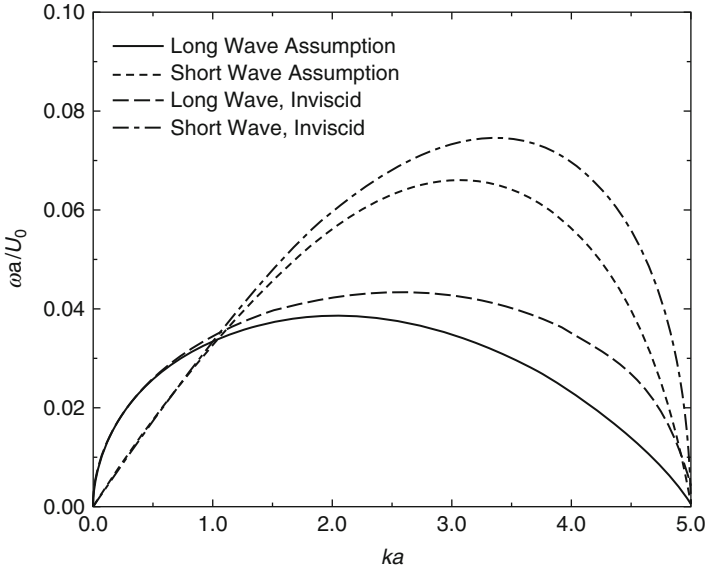


Fig. 3.6 Viscous and inviscid dimensionless growth rates $\omega a/U_0$ as functions of dimensionless wave number ka for a gas Weber number of $We_g = 0.5$ [20 Fig. 8] (Courtesy of Elsevier)

between the two gas/liquid interfaces is obtained for a sheet moving with velocity U_0 through stationary gas. The equation of motion is obtained by considering the forces due to gas pressure, surface tension, liquid inertia, and viscosity on an element of a sheet. The element is defined as $(2a)zdx$, as shown on Fig. 3.7. The four forces are determined as follows:

The total air pressure force on the sheet is obtained by adding the pressure force on the upper and the lower surface of the sheet.

$$F_{\mathrm{p}} = 2k\rho_{\mathrm{g}}U_0^2 yzdx \tag{3.10}$$

where k is the wave number. Force caused by the surface tension along the same element is,

$$F_\sigma = 2\sigma z\frac{\partial^2 y}{\partial x^2}dx \tag{3.11}$$

where the surface tension forces on the top and the bottom surfaces of the sheet are added together. The inertial force can be calculated as,

$$F_I = -\frac{\partial}{\partial t}\left(\rho_l z(2a)dx\frac{\partial y}{\partial t}\right) = -\rho_l\left(2a\frac{\partial^2 y}{\partial t^2} + \frac{\partial(2a)}{\partial t}\frac{\partial y}{\partial t}\right)z\,dx \tag{3.12}$$

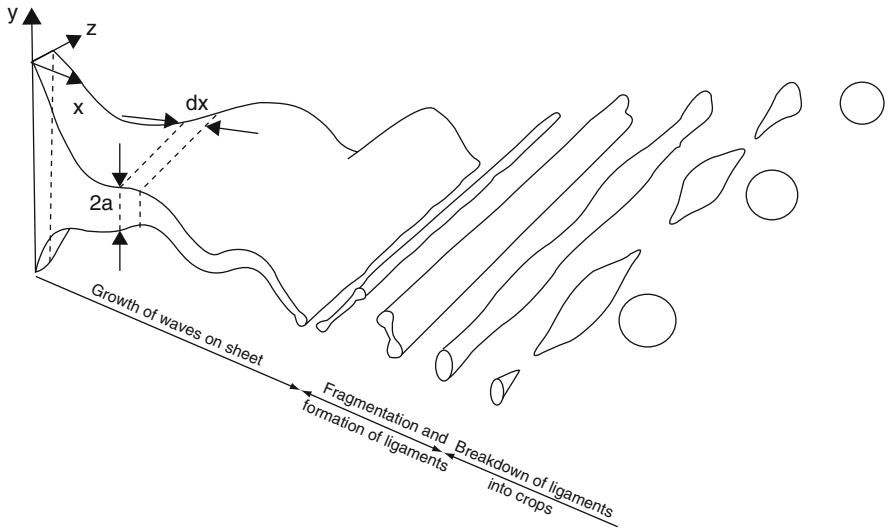


Fig. 3.7 Wave instability of a thinning liquid sheet [12, Fig. 4] (Courtesy of Elsevier)

The viscous force acting upon the sheet is,

$$F_\mu = \mu_l(2a)k^2\frac{\partial h}{\partial t}\sin(kx+\theta) - \frac{\mu_l k}{U}\frac{\partial(2a)}{\partial t}\frac{\partial h}{\partial t}\cos(kx+\theta) \tag{3.13}$$

where h is the wave amplitude (i.e., $h = a + \xi$) which is a function of time and θ is the phase angle. For a constant velocity thinning sheets: $2a = C_t t^{-1}$, where C_t is a constant.

The ratio of the maximum value of the first term to the maximum value of the second term in equation (3.13) is k. Thus, for a sufficiently large wave numbers the second term may be neglected. The total force on the length, dx, is

$$\begin{aligned} F_P + F_\sigma + F_I + F_\mu &= 2\rho_g k U^2 yz\,dx + 2\sigma\frac{\partial^2 y}{\partial x^2}z dx \\ &\quad - \rho_l\left(2a\frac{\partial^2 y}{\partial t^2} + \frac{\partial(2a)}{\partial t}\frac{\partial y}{\partial t}\right)z\,dx + \frac{\mu_l(2a)(\partial^3 y)}{\partial t\partial x^2}z\,dx \\ &= 0 \end{aligned} \tag{3.14}$$

Then,

$$2\rho_g k U^2 y + 2\sigma\frac{\partial^2 y}{\partial x^2} - \rho_l\left(2a\frac{\partial^2 y}{\partial t^2} + \frac{\partial(2a)}{\partial t}\frac{\partial y}{\partial t}\right) + \frac{\mu_l(2a)(\partial^3 y)}{\partial t\partial x^2} = 0 \tag{3.15}$$

or in terms of h,

$$2\rho_g kU^2 h - 2\sigma k^2 h - \rho_l \left(2a \frac{\partial^2 h}{\partial t^2} + \frac{\partial (2a)}{\partial t} \frac{\partial h}{\partial t} \right) - \mu_l (2a) k^2 \frac{\partial h}{\partial t} = 0 \tag{3.16}$$

now, substituting h by $h_0 exp(f)$, equation (3.16) will become

$$2\rho_g kU^2 - 2\sigma k^2 - \rho_l \left((2a) \left(\frac{\partial f}{\partial t} \right)^2 + 2a \frac{\partial^2 f}{\partial t^2} + \frac{\partial (2a)}{\partial t} \frac{\partial f}{\partial t} \right) - \mu_l (2a) k^2 \frac{\partial f}{\partial t} = 0 \tag{3.17}$$

The variable, f, is defined here as breakup parameter and it is $f = \ln(h/h_0)$. It determines when the breakup occurs. The pioneering investigation on this parameter is by Weber [26], who obtained a value of 12 using jet breakup experiments:

$$f = \ln \left(\frac{h}{h_0} \right) = 12 \tag{3.18}$$

Other researchers have reported different but similar numbers. Grant and Middleman [27] proposed a value of 13.4 for jet of glycerol/water solution and Kroesser and Middleman [28] proposed a value of 11 for viscous Newtonian liquid with Ohnserge numbers between 0.28 and 1.03. The latest investigation by Sarchami et al [29] has suggested a correlation for the breakup parameter rather than a constant value. The correlation is based on Reynolds and Weber numbers:

$$f = Re^{0.07} We^{0.37} \tag{3.19}$$

where the Weber and Reynolds numbers are based on injection velocity from the nozzle, nozzle diameter and liquid properties. The final droplet size can be calculated based on, ligament sizes which are produced as a result of the sheet disintegration. The main cause of disintegration is assumed to be the wave instability. Wave amplitude grows until it reaches a critical point which causes the sheet to break. At this point, the tears appear and fragments of sheet (*equal to one-half wavelength*) are broken; then, the surface tension, forces these fragments to become unstable ligaments which finally will break into droplets. Assuming attenuating sheet ($2a = C_t t^{-1}$), the estimate for diameter of a cylindrical ligament is

$$d_L = 2 \left(\frac{4}{3f} \right)^{1/3} \left(\frac{{C_t}^2 \sigma^2}{\rho_g \rho_l U^2} \right)^{1/6} \left[1 + 2.6 \mu_l \sqrt[3]{\left(\frac{C_t {\rho_g}^4 U^8}{6f \rho_l^2 \sigma^5} \right)} \right]^{1/5} \tag{3.20}$$

where C_t, for a radiating sheet of uniform velocity, is:

$$C_t = ht = \frac{C_r t}{r} = \frac{C_r}{U} \tag{3.21}$$

Dombrowski [12] has shown that symmetrical waves are mainly responsible for ligaments break down. Weber et al. [26] have analyzed these waves and assuming that here their results can be applied, we use equation 1.41 to estimate breakup wavenumber:

$$k_L d_L = \left[\frac{1}{2} + \frac{3\mu_l}{2(\rho_l \sigma d_L)^{1/2}}\right]^{-1/2} \tag{3.22}$$

where $k_L = k_{\max}$ representing the wavenumber corresponding to the wave with the maximum growth rate. If it is assumed that the waves grow until their amplitude reaches the ligaments radius, one drop per wave length will be produced. Considering a mass balance, the relation between the drop size and the wave number is given by:

$$d_D^3 = \frac{3\pi d_L^2}{k_L} \tag{3.23}$$

which, combining with (3.22) gives

$$d_D = \left[\frac{3\pi}{\sqrt{(2)}}\right]^{1/3} d_L \left[1 + \frac{3\mu_l}{(\rho_l \sigma d_L)^{1/2}}\right]^{1/6} \tag{3.24}$$

where d_L is the ligament diameter given by (3.20). After simplification we have

$$d_D = 1.882 d_L [1 + 3Oh]^{\frac{1}{6}} \tag{3.25}$$

where Oh is Ohnserge number and is defined based on sheet thickness: $Oh = \mu_l / \sqrt{\rho_l \sigma d_l}$.

Effect of Initial Velocity Profile

Ibrahim [19] developed a power series mathematical solution for the problem of instability of an inviscid liquid sheet of parabolic velocity profile emanated from a nozzle into an inviscid gas. The results show that for both antisymmetrical and symmetrical disturbances departure from uniformity of the velocity profile causes the instability to be reduced. It has been suggested that jet instability may be affected by the relaxation of the velocity profile that takes place once the liquid exits the nozzle and is no longer constrained by its wall. The variation of the growth rate with wave number at $We = 10{,}000$, $\rho = 0.01$, $\beta = 0, 0.1, 0.3, 0.4$, and $n = 96$ are shown in Fig. 3.8 for antisymmetrical disturbances. The results of Fig. 3.8 indicate

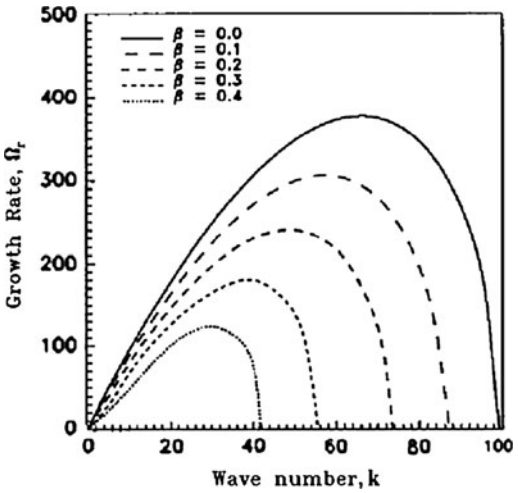


Fig. 3.8 Effect of the velocity profile parameter β on instability at $We = 10{,}000$ and $\rho = 0.01$ [19, Fig. 2], (Courtesy of AIP)

that a sheet of uniform velocity, $\beta = 0$, is more unstable than one with parabolic profile. Both the maximum growth rate and the cutoff wave number of unstable disturbances are reduced. Increasing the parameter β produces a parabolic profile with a higher maximum velocity along the centerline of the sheet and a lower velocity at the liquid–gas interface for a constant mean flow. It is the reduction in the liquid–gas relative velocity across the interface that is thought to be the reason for the decrease in aerodynamic instability as β is increased. Since a uniform velocity profile produces the maximum relative velocity at the liquid gas interface for the same mean flow, it is the most unstable. Therefore, such non-uniformity in the velocity profile (e.g., parabolic) would lead to a reduced instability.

Nonlinear Sheet Instability

The linear theory does not provide a means for the liquid sheet to breakup, because during the sinuous mode of instability, the distance between the two sides of the sheet remains a constant value. Therefore, it is not possible to predict the breakup length of a sheet.

Jazayeri and Li [41] developed up to the third order nonlinear analysis of a liquid sheet to determine the breakup length of the sheet. A typical result of their solution for the surface deformation as a function of distance is shown in Fig. 3.9. This case is for the initial disturbance amplitude of 0.1, the Weber number of 40 and the gas-to-liquid density ratio of 10^{-3}, which approximates the situation of liquid water in ambient air. The wave number of 0.02 is almost equal to the dominant wave number for the sinuous disturbance of the linear theory. It is seen that the surface wave grows in time, and maintains its sinuous character for the majority of its growth

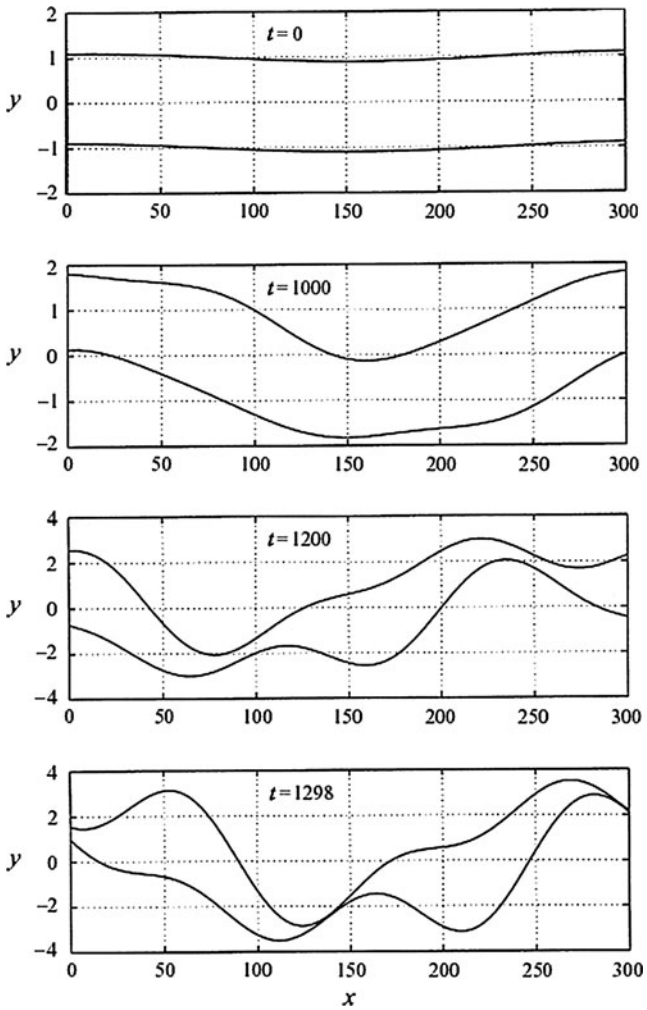


Fig. 3.9 Evolution of the dimensionless surface deformation y as a function of dimensionless distance x for $We = 40$, $\varepsilon = 0.001$, $k = 0.02$, and $\zeta_0 = 0.1$. The dimensionless time t is specified on the figure [41 fig. 3] (Courtesy of Cambridge University Press)

time. As well, the deviation from the linear theory is small, and the distance between the two interfaces is kept almost constant along the wavelength up to the time of 1,000. After that time, the nonlinear effect becomes significant and the waveform is distorted considerably. At $t = 1{,}298$, the distance between the two interfaces vanishes near the half and full wavelength., which is different from the conclusions reached by Clark and Dombrowski [13] and also Dombrowski and Hooper [10] who found that the sheet breakup occurred at positions corresponding to 3/8 and 7/8 of the length of the fundamental wave. However, the liquid sheet breaks off at half-wavelength intervals, a result consistent with that of Clark and Dombrowski.

Figure 3.10 shows the effect of the gas-to-liquid density ratio on the surface wave development for $We = 40$ and $\zeta_0 = 0.1$. The wave number used for each value of the density ratio is the dominant wave number under the given conditions according to the linear theory. The results for $\varepsilon = 10^{-3}$ are given in Fig. 3.10c, whereas Fig. 3.10a–c presents the results for $\varepsilon = 0.01$, 0.02 and 0.05, respectively. As expected, the liquid sheet breaks up considerably earlier for density ratios of large values than for those of small values.

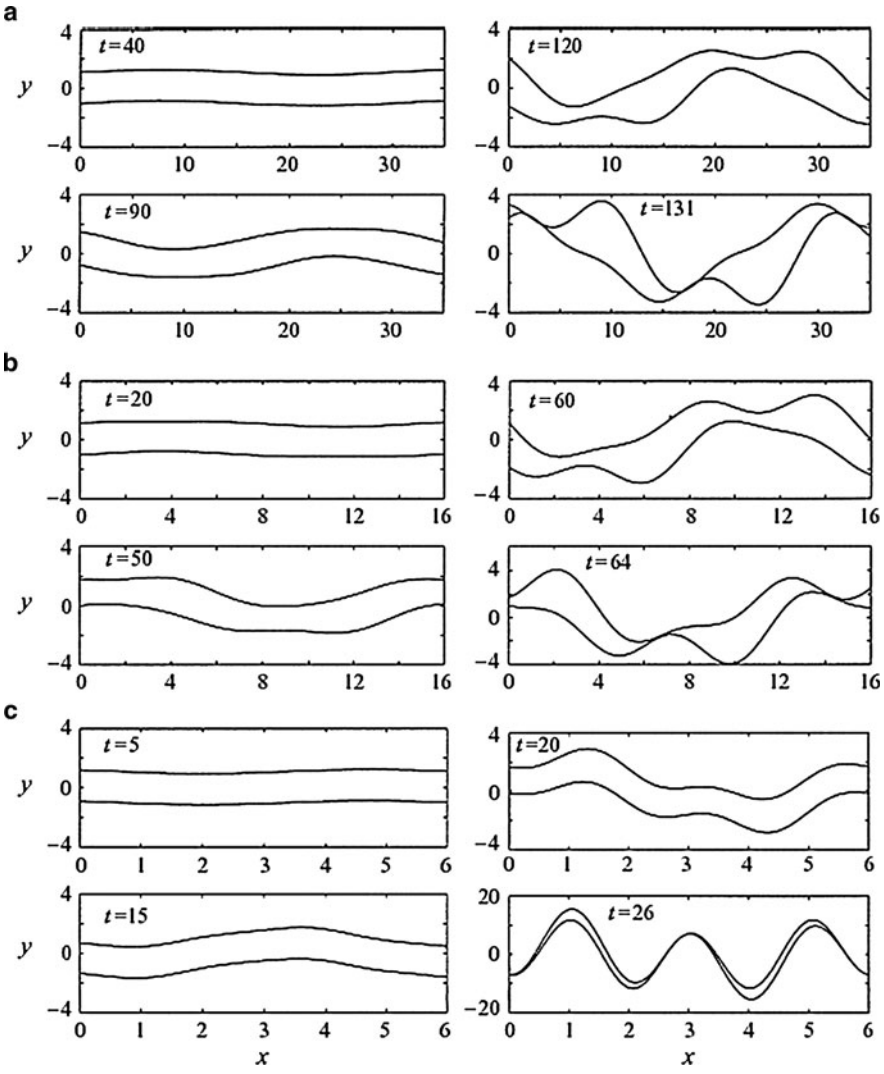


Fig. 3.10 Evolution of the dimensionless surface deformation y as a function of dimensionless distance x for $We = 40$, $k = 0.02$, and $\zeta_0 = 0.1$ and gas-to-liquid density ratio of ε (**a**) 0.01, (**b**) 0.02, (**c**) 0.05 [41 Fig. 6] (Courtesy of Cambridge University Press)

It is observed that the breakup time is reduced as the Weber number is increased, which is expected. It is now evident that the liquid sheet breakup occurs at half-wavelength intervals, as observed earlier, and this parcel of liquid is expected to contract into a ligament under the force of surface tension. There does not exist any indication of "satellite" ligament formation from the liquid sheet breakup.

By replacing the time t by the distance x from the nozzle exit, the present temporal development of the surface wave is transformed into the spatial evolution, and a typical result is shown in Fig. 3.11a for $We = 280.78$, $\varepsilon = 0.00129$, and $k = 0.183$. This figure is contrasted with two other results from directly solving the Navier–Stokes equations in two dimensions. Figure 3.11b shows a result of spatial instability of a 2D sheet with $We = 300$ and density ratio of $\varepsilon = 0.001$ [42]. The results are quite different from the analytical results showing fluid accumulations on the peaks of the sinuous wave. Figure 3.11c is a sheet instability at very high relative velocities, $We = 11{,}400$ [43]. When the relative velocity increases, the liquid is sheared from the surface of the sheet forming small ligaments. These small ligaments generate secondary vorticities as shown in Fig. 3.11d [43], which change the behavior of the sheet even more. Therefore, although sheet instability models are useful in

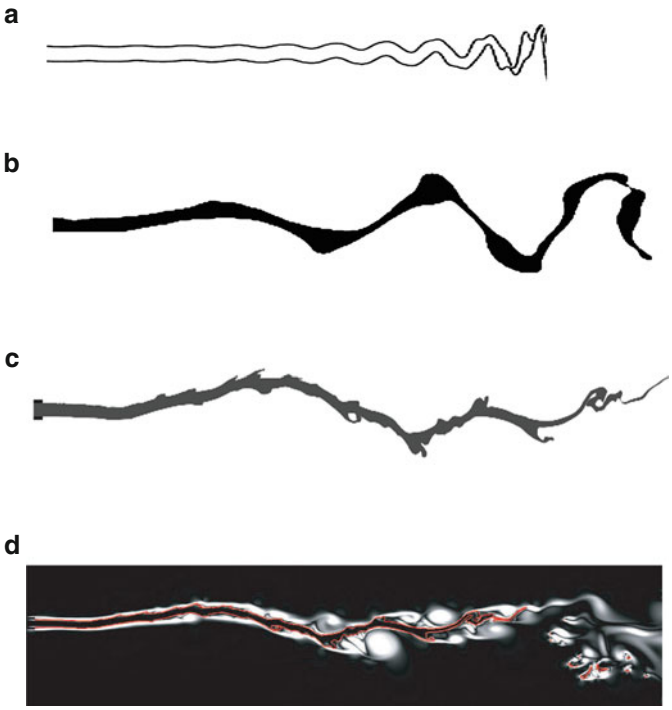


Fig. 3.11 Comparison of spatial surface deformation from analytical (**a**) and numerical (**b**–**d**) results. (**a**) $We = 280.78$, $k = 0.183$, $\varepsilon = 0.00129$, and $\zeta_0 = 0.05$ [41 Fig. 9]. (**b**) $We = 300$, $\varepsilon = 0.001$, and $Oh = 1$ [42]. (**c**) $We = 11{,}400$, $\varepsilon = 0.0015$, and $Oh = 0.015$ [43]. (**d**) Vorticity plot of (**c**) but a different time [43]

predicting the fastest growing wavelengths, they cannot by themselves be used to provide information on the droplet sizes in sprays. These models are used as a first estimate of ligament sizes, and other models (as will be discussed in chapter 9) are used to estimate spray size from these ligament sizes.

It is seen that although the wave remains sinuous for most of the sheet length, nonlinear effects cause the sheet thinning and pinching that lead to the eventual breakup of the sheet. As observed earlier, the breakup time decreases for each initial amplitude ζ_0 until it reaches a minimum value and then approaches infinity when the wave number approaches the cut-off wave number k_c.

The effect of the Weber number on the breakup time (and length) is shown in Fig. 3.12 for several values of initial disturbance amplitude and two values of the density ratio ε. It can be seen that breakup time decreases as the Weber number is increased. This is because the bigger the Weber number, the larger the aerodynamic interactions between the liquid sheet and the surrounding gas, and the latter is what enables the growth of the surface waves and the eventual disintegration of the sheet. In addition, the breakup time is reduced by a larger value of the initial disturbance

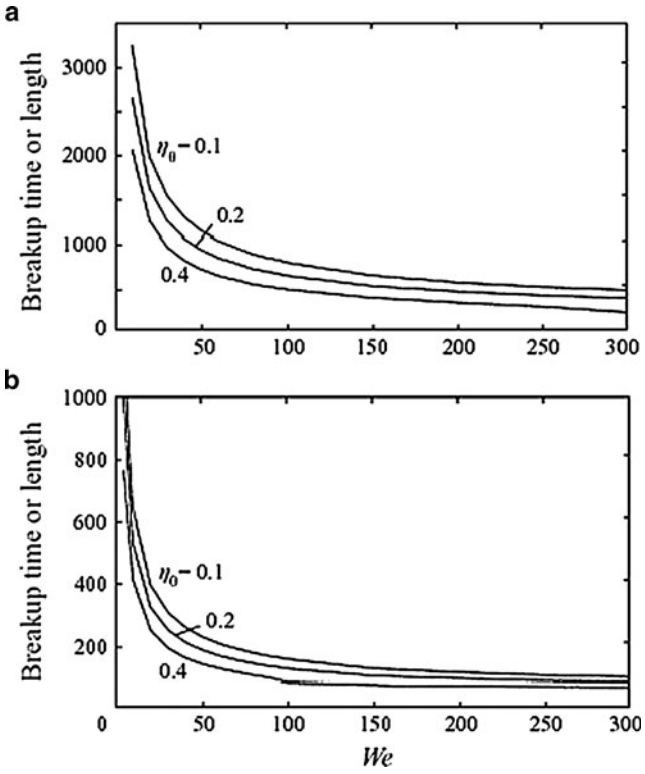


Fig. 3.12 Effect of Weber number on the liquid sheet breakup time for $We = 40$, gas-to-liquid density ratio of $\varepsilon = 0.001$, and 0.005 and ζ_0 of 0.1, 0.2, and 0.4 [41 Fig. 12] (Courtesy of Cambridge University Press)

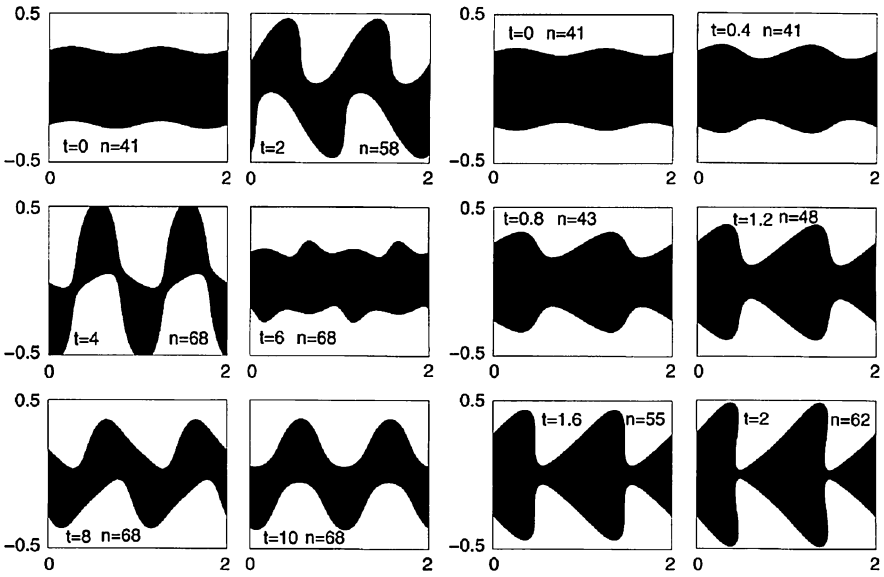


Fig. 3.13 Results of Rangel and Sirignano [21 figs. 13 and 14] for the (**a**) sinuous and (**b**) dilational modes, respectively, in the case where gas and liquid densities are equal and the initial sheet thickness is one quarter of the wavelength of the disturbance (Courtesy of AIP)

amplitude and the density ratio. The breakup time is reduced significantly for an increase in the density ratio when ε is small, and then almost approaches an asymptotic value for larger values of ε.

Rangel and Sirignano [21] assumed periodic spatial behavior on an infinitely long liquid stream and calculated the temporal behavior for both the sinuous and dilational modes. Figure 3.13 is a typical result from Rangel and Sirignano [21] for the sinuous and dilational modes, respectively, in a case where gas and liquid densities are equal and the initial sheet thickness is one quarter of the wavelength of the disturbance.

Three-Dimensional Sheet Instability

Lozano et al. [44] conducted three-dimensional vortex dynamics methods to model instability growth leading to the breakup of a water sheet surrounded by an air co-flow. Figure 3.14 presents the initial and final stages of a case with antisymmetric perturbations (with an amplitude of 25% of the sheet thickness, corresponding to 5% of the wavelength) both in the longitudinal and transverse directions, where surface tension has been included. Both air/liquid interfaces end up touching each other. However, in this case, the first contact does not occur simultaneously on a whole line transverse to the sheet, but in single points of this line. Figure 3.14 represents one of their cases for the Atwood number of $A = (\rho_l - \rho_g)/(\rho_l + \rho_g) = 50.99$ corresponding

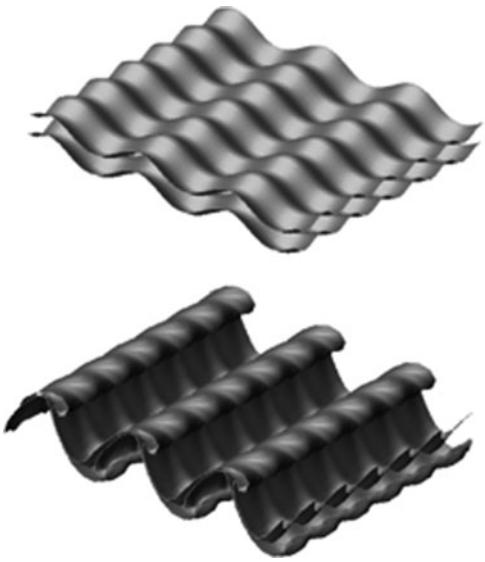


Fig. 3.14 Initial and later stages of a case with antisymmetric perturbations both in the longitudinal and transverse directions, where surface tension has been included [44] (Courtesy of AIP)

to the water/air case. It can be seen that the model reproduces correctly the expected evolution of the Kelvin-Helmholtz instability as described in previously reported 2D simulations. When entering the nonlinear deformation regime, points far away from the axis of symmetry, which will be denoted as maxima, accelerate following the surrounding air, while points close to the axis, which will be denoted as minima, move more slowly. At the same time, there is vorticity advection from minima to maxima, resulting in the generation of rollers in the maxima points that cause the sheet to convolute. As time evolves, the vortex centers assume a saw-tooth configuration. As the vortices rotate, the sheet grows thinner at the initial minima locations. In the final stage, the thinning tends to a limit where the upper and lower interfaces finally touch. As the sheet thickness tends to zero in these points, any perturbation in a real case would cause the sheet to tear. The tear would generate a hole with regions of high curvature, where the effects of surface tension would be very intense. This mechanism explains the generation of span-wise ligaments, oriented parallel to the nozzle.

Figure 3.15 illustrates a case when the initial vortex sheet strength forms an angle of 45° with two perturbations, whose initial amplitudes in this case were 1% of the wavelength (5% of the sheet thickness). This case results in a final situation where the transverse section shows a sinusoidal undulation of finite amplitude. Simulations with initial longitudinal and transverse sinusoidal perturbations indicate that the sheet eventually collapses at discrete points in a transverse cross section. Tearing along these points helped by surface tension effects would explain the formation of the longitudinal filaments. Initial symmetric or antisymmetric transverse perturbation result in very similar final configurations. The presence of

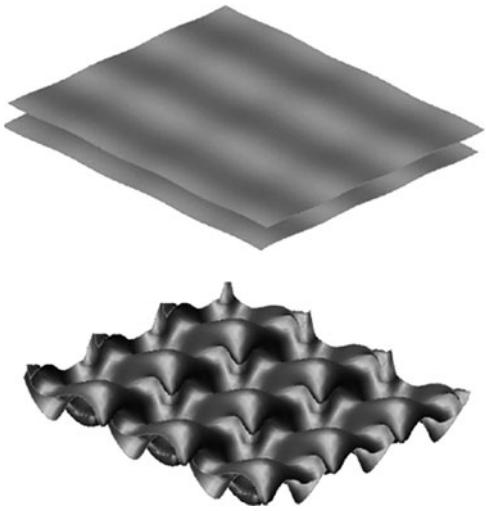


Fig. 3.15 Initial and later stages of a case with antisymmetric perturbations oriented at $\pm$ 45° with the flow direction. Flow direction is towards the viewer [44 Fig. 6] (Courtesy of AIP)

in-phase oblique waves may explain the growth of the transverse wave starting from an infinitesimal perturbation. Edge effects have also been studied, to explain the sack-like structures that can be observed for low air/water velocity ratios.

Three-dimensional dilational and sinuous wave propagation on infinite or semi-infinite thin planar sheets flowing into a gas of negligible density is also given by Kim and Sirignano [45]. The assumption of thin sheets allows the reduction of the problem dimensionality by integration across the sheet thickness. For finite-amplitude disturbances, the strongest nonlinear effects occur when the cross-sectional wave number (l) is close to the stream-wise wave number (k). For, dilational wave propagation, when l is close to k for infinite sheets, higher harmonics are generated in the stream-wise direction, and the standing wave with finite amplitude in the cross-sectional plane becomes flat. As time passes, the waves return to the initial wave shape. This process is repeated in a cycle. A similar phenomenon is found in semi-infinite sheets with low Weber number. When l is close to k for semi-infinite sheets and Weber number is high, fluid accumulates into fluid lumps interspaced by one wavelength in the cross-sectional direction as well as in the stream-wise direction. This leads to the formation of initially non-spherical ligaments or large droplets from the liquid sheet. For, sinuous wave propagation, when l is close to k for semi-infinite sheets and Weber number is high, fluid agglomerates in the edge of the sheet interspaced by half a wavelength in the cross-sectional direction as well as in the stream-wise direction. A three-dimensional visualization of the computational results shows that the disturbance at the nozzle exit induces fluid to agglomerate into half-spherical lumps, which indicate the formation of ligaments or large droplets from the liquid sheet. A similar phenomenon is found in the case of infinite sheets.

References

1. Savart F, Mémoire sar le choc de deux veine liquides, animées de mouvements directement oppose's, Ann. Chim. Phys. 55, 257, 1833.
2. Michell JH, On the theory of free stream lines, Phil. Trans. A 181, 389–431, 1890.
3. Squire H.B, Investigation of the instability of a moving liquid film, Brit. J. Appl. Phys. 4, 167–169, 1953.
4. Hagerty WW, Shea JF, A study of the stability of plane fluid sheets, J. Appl. Mech. 22, 509–514, 1955.
5. Taylor GI, Oblique impact of a jet on a plane surface, Philos. Trans. R. Soc. Lond. Ser. A 260, 96–100, 1966.
6. Taylor GI, Waves on fluid sheets, Pro. Roy. Soc. A, 253, 296–312, 1959a.
7. Taylor GI, Disintegration of fluid sheets, Pro. Roy. Soc. A, 253, 313–321, 1959b.
8. Dombrowski N, Fraser RP, A photographic investigation into the disintegration of liquid sheets, Phil. Trans. 247(924), 101–130, 1954.
9. Dombrowski N, Hasson D, Ward DE, Some aspects of liquid flow through fan spray nozzles, Chem. Eng. Sci. 12, 35–50, 1960.
10. Dombrowski N, Hooper PC, The effect of ambient density on drop formation in sprays, Chem. Eng. Sci. 17, 291–305, 1962.
11. Fraser RP, Eisenklam P, Dombrowski N, Hasson D, Drop formation from rapidly moving sheets, AIChE J 8(5), 672–680, 1962.
12. Dombrowski N, Johns WR, The aerodynamic instability and disintegration of viscous liquid sheets, Chem, Eng. Sci. 18, 203–214, 1963.
13. Clark CJ, Dombrowski N, Aerodynamic instability and disintegration of inviscid liquid sheets, Proc. Roy. Soc. A 329, 467–478, 1972.
14. Crapper GD, Dombrowski N, Jepson WP, Pyott GAD, A note on the growth of Kelvin–Helmholtz waves on thin liquid sheets, J. Fluid Mech. 57(4), 671–672, 1973.
15. Crapper GD, Dombrowski N, Pyott GAD, Large amplitude Kelvin–Helmholtz waves on thin liquid sheets, Proc. R. Soc. London Ser. A Math. Phys. Sci. 342(1629), 209–224, 1975.
16. Crapper GD, Dombrowski N, A note on the effect of forced disturbances on the stability of thin liquid sheets and on the resulting drop size, Int. J. Multiphase Flow 10(6), 731–736, 1984.
17. Weihs D, Stability of thin radially moving liquid sheets, J. Fluid Mech. 87(2), 289–298, 1978.
18. Huang JCP, The breakup of axisymmetric liquid sheets, J. Fluid Mech. 43, 305–319, 1970.
19. Ibrahim EA, Akpan ET, Three-dimensional instability of viscous liquid sheets, Atom. Sprays 6, 649–665, 1996.
20. Senecal PK, Schmidt DP, Nouar I, Ruthland CJ, Reitz RD, Corradini ML, Modeling high-speed viscous liquid sheet atomization, Int. J. Multiphase Flows, 25,1073–1097, 1999.
21. Rangel RH, Sirignano WA, The linear and nonlinear shear instability of a fluid sheet, Phys. Fluids A 3(10), 2392–2400, 1999.
22. Sirignano WA, Mehring C, Review of theory of distortion and disintegration of liquid streams, Prog. Energy Combus. Sci. 26, 609–655, 2000.
23. Mehring C, Sirignano WA, Nonlinear capillary wave distortion and disintegration of thin planar liquid sheets, J. Fluid Mech. 388, 69–113, 1999.
24. Lin SP, Breakup of liquid sheets and jets, Cambridge Publishing, 2003, ISBN: 0521806941.
25. Levitch, VG, Physiochemical Hydrodynamics, Prentice-Hall, 1962.
26. Weber CZ, The break-up of liquid jets, Zeit schrift fur Angewandte Mathematik und Mechanik, 11, 136–154, 1931.
27. Grant RP, Middleman S, Newtonian jet stability, AIChE J. 12(4), 669–678, 1966.
28. Kroesser FW, Middleman S, Viscoelastic jet stability, AIChE J. 15(3), 383, 1969.
29. Sarchami A, Ashgriz N, Tran HN, An atomization model for splash plate nozzles, AICHE J. 56(4), 849–857, 2009.
30. Lin SP, Wang ZL, Three types of linear theories for atomizing liquids, Atom. Sprays 18, 273–286, 2008.

31. Gaster M, Growth of disturbances in both space and time, J. Fluid Mech. 11, 723–727, 1968.
32. Lin SP, Stability of a viscous liquid curtain, J. Fluid Mech. 104, 111–118, 1981.
33. Altimira M, Riras A, Ramos JC, Anton R, Linear spatial instability of viscous flow of a liquid sheet through gas, Physics of Fluids 22, 1–11, 2010.
34. Ramos JI, Planar liquid sheet at low reynolds number, Int. J. Numerical methods, Fluids 22, 961, 1996.
35. Ramos JI, Asymptotic analysis and stability of inviscid liquid sheets, J. Math. Anal. Appl. 250, 512, 2000.
36. de Luca L, Costa M, Instability of spatially developing liquid sheet, J. Fluid Mech. 339, 353–376, 1997.
37. de Luca, Experimental investigation of the global instability of plane flows, J. Fluid Mech. 399, 355–376, 1999.
38. Hauke G, Dopazo C, Lozano A, Barreras F, Hernandez A, Linear stability analysis of a viscous liquid sheet in a High-spped viscous gas, J. flow, Turbulence and Combastion 67, 235–265, 2001.
39. Barreras F, Experimental study of the Break-up and atomization of a liquid sheet, phD Dissertation, University of Zaragoza, 1998.
40. Teng CH, Lin SP, Chen JN, Absolute and convective instability of a viscous liquid curtain in a viscous gas, J. Fluid Mech. 332, 105, 1997.
41. Jazayeri S, Li X, Nonlinear instability of plane liquid sheets, J. Fluid Mech. 406, 281–308, 2000.
42. Movassat M, Maftoon N, Dolatabadi A, A three-dimensional numerical study of the breakup length of liquid sheets, Proceedings of 21th Annual Conference on Liquid Atomization and Spray Systems, Orlando, FL, May 2008.
43. Raessi M, Pitsch H, A level-set based methodology for modeling interfacial flows characterized with large density ratios, ILASS-Americas 22nd Annual Conference on Liquid Atomization and Spray Systems, Cincinnati, OH, May 2010.
44. Lozano A, Garcı'a-Olivares A, Dopazo C, The instability growth leading to a liquid sheet breakup, Phys. Fluids 10(9), 2188–2197, 1998.
45. Kim I, Sirignano WA, Three-dimensional wave distortion and disintegration of thin planar liquid sheets, J. Fluid Mech. 410, 147–183, 2000.

Chapter 4
Dynamics of Liquid Droplets

A. Mashayek and N. Ashgriz

Abstract In this chapter the basic physics and methods of calculation of the effective drag forces acting on drops in isolated-drop and multidrop configurations relevant to sprays are provided. The effect of various physical phenomena such as drop deformation, nonuniformity of the incoming flow, drop–drop interactions, drop–gas interactions, and evaporation on the drag coefficient on the drop, with special focus on the underlying physics, is highlighted.

Keywords Drag coefficient · Drag of deformed drops · Droplet motion · Evaporating droplets · Flow past a droplet · Interacting drops

Droplet Drag Coefficients

Introduction

Lagrangian-Eulerian models, which simulate the motion of drops in different physical configurations, usually employ a drag model to predict the aerodynamic (or hydrodynamic) force acting on the drops. Once the forces on a drop are known, its motion can be calculated by virtue of Newton's second law. Hence, the correct knowledge of the forces interacting between the drop and the surrounding medium is of crucial importance. To model the forces acting on the interface of the two phases, one has to solve (either analytically or numerically) the distribution of the stresses on both sides of the interface. From that, one can calculate the drag and lift forces acting on the drop along with the effect of the drop on the surrounding medium. In multiphase flow simulations, correct calculation of the drag force is a measure of the accuracy of the simulation. Since the mathematical problem of the time evolution of the fully coupled drop-medium system is very complicated, analytical solutions are not possible unless for very limiting cases. Experimental

A. Mashayek (✉)
Department of Physics, University of Toronto

N. Ashgriz (ed.), *Handbook of Atomization and Sprays*,
DOI 10.1007/978-1-4419-7264-4_4, © Springer Science+Business Media, LLC 2011

studies have been employed by following the motion of particles and inferring the effective forces leading to their particular motion. These studies have led to empirical correlations for drag and lift forces acting on particles. However, the physical processes at the interface of the two phases often occur or are initiated at such small time and length scales that experimental apparatus are not capable of fully observing them. Therefore, numerical simulations have become a common practice and probably the best way to gain insight into the details of the small scale physics in interfacial multiphase flows.

It is known that a spherical drop can undergo significant deformation and acceleration and become flattened due to the drag forces. This deformation affects the motion of the drop by increasing the drag forces due to both the larger frontal area and an increase of the drag coefficient. For the cases of drops moving in a stationary medium, the increase in drag due to its deformation slows it down, which decreases the drag force in return. Therefore, predicting the motion of a drop is an inherently time-dependent problem and one that should not be treated as a steady one. Hence, the drag coefficients based on correlations for spheres in steady flows, which are still being used in many multidimensional spray simulations, need to be revised.

Apart from considerations in regard to drop deformation, many empirical and theoretical correlations have been obtained in an isolated-drop configuration. These correlations can be used for simulation of drop motion in very dilute sprays, where each drop can be assumed isolated. In dense sprays, however, the drop spacings are small enough that isolated drop assumption is no longer valid. Therefore, in order to calculate the drop motion in such sprays a group of drops has to be considered as a whole.

In order to calculate the drag force acting on a drop, the stresses on its surface need to be determined and integrated to give the effective forces. In this chapter, we introduce basic concepts on the drag on particles and drops, starting with flows past nondeforming spheres at low Reynolds numbers for which analytical solutions are available. Next, we will consider high Reynolds number flows over solid spheres and liquid drops, which involve flow separation with great implications for the drag force. Effect of small deformation, followed by those with large deformation, on the drag force is discussed next. Finally, a short discussion on the effect of the interaction of drops in multidrop systems is presented.

Flow Around Nondeforming Drops

Consider a flow around a solid nondeforming sphere, as shown in Fig. 4.1a. This case can be relevant to flows around drops which largely do not deform due to high surface tension. When the surface tension on the drop–fluid interface is strong enough to resist the tendency of the aerodynamic force to deform the drop, the drop may either deform very little or have small amplitude oscillations around its spherical shape. For these scenarios, approximating the drop with a solid sphere would be reasonable.

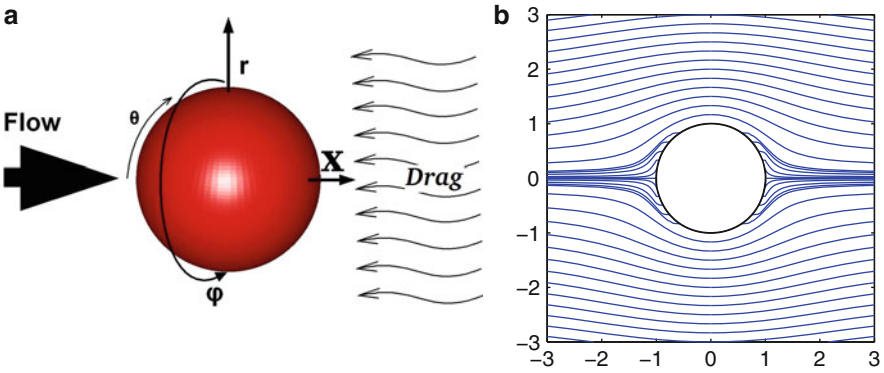


Fig. 4.1 (**a**) Schematic view of a flow past a sphere; (**b**) Streamlines of a Stokes flow past a sphere

For a solid sphere moving through a fluid (or a flow moving past a sphere), the aerodynamic or hydrodynamic force can be broken down into two different parts called the *form drag* and the *skin friction*. The form drag is a resultant of the pressure variations along the sphere's surface induced by its profile. A very thin flat plate parallel to the flow does not experience a considerable amount of form drag. The form drag is also called *pressure drag* or *profile drag*. The second type of force acting on the sphere is the skin friction, which is the result of the friction between the surface of the sphere and the adjacent fluid flow. As one can expect, the flow past a flat surface parallel to the flow would experience this type of resistance as the dominant one.

Let us consider a flow past a sphere with radius a, such as the one shown in Fig. 4.1a. Whether the pressure drag is dominant or the skin drag depends on the relative velocity of the flow with respect to the sphere, U, the diameter of the sphere, $d = 2a$, and the density and dynamic viscosity of the fluid (ρ, μ). These parameters form the Reynolds number $Re = \rho U d/\mu$.

For very small Reynolds numbers, the shear stresses at the surface of the sphere dominate and hence, skin friction is the main contributor to the drag force. For $Re < 1$, the flow falls in the well-known range of Stokes flows, and the drag force on the sphere can be calculated analytically. For very large Reynolds numbers on the other hand, the form drag will be dominant, with the skin friction making a very small contribution. For flows in the mid-range of Reynolds number, both effects have to be accounted for.

When the radius of the particle is very small, or the fluid viscosity is very large, or the relative velocity is very small, or the fluid density is very low, the Reynolds number becomes very small and the flow satisfies the conditions of the *Stokes* or *creeping flow*. In this limit, the inertial forces near the particle are small and can be neglected in the Navier-Stokes equations. The pressure distribution on the drop in this limit takes the form

$$p = \frac{3}{2}\frac{\mu U}{a}\left(\frac{a}{r}\right)^2 \cos\,\theta + c, \tag{4.1}$$

where c is a constant of integration. The traction on the sphere can be written in the form of

$$\hat{f} = \tau_{rr}(r=a)\hat{e}_r + \tau_{r\theta}(r=a)\hat{e}_\theta \tag{4.2}$$

where τ_{rr} and $\tau_{r\theta}$ are the normal and tangent to surface components of the traction and are expressed by

$$\tau_{rr}(r=a) = \left(-p + 2\mu\frac{\partial v}{\partial r}\right)_{r=a} = -\frac{3}{2}\frac{\mu U}{a}\cos\theta - c \tag{4.3}$$

$$\tau_{r\theta}(r=a) = \left(r\frac{\partial}{\partial r}\left(\frac{\partial v}{\partial r}\right) + \frac{1}{r}\frac{\partial u}{\partial \theta}\right)_{r=a} = \frac{3}{2}\frac{\mu U}{a}\sin\theta \tag{4.4}$$

where u and v are the velocity components in the r and θ directions, respectively. Substituting these into (4.2) results in

$$\hat{f} = -\frac{3}{2}\frac{\mu U}{a}\hat{e}_x - c\hat{e}_r \tag{4.5}$$

which can be integrated over the surface of the sphere to give the force on it

$$F_D = \int_0^{2\pi}\int_0^{2\pi} f\,\mathrm{d}S = \int_0^{2\pi}\int_0^{2\pi} fa^2\sin\theta\,\mathrm{d}\theta\,\mathrm{d}\varphi = -6\pi U a\hat{e}_x. \tag{4.6}$$

This is known as the Stoke's law and gives the drag force exerted on a particle with radius a, which is moving with velocity U in a stationary fluid. The negative sign shows that the drag force opposes the motion of the sphere. The drag coefficient C_D is defined as [1]:

$$C_\mathrm{D} = \frac{F_\mathrm{D}}{(1/2)\rho U^2 A}, \tag{4.7}$$

where A is the frontal area of the object. For our case of the spherical drop, $A = \pi a^2$ and so, using (4.7) and the definition of the Reynolds number, we can write

$$C_\mathrm{D} = \frac{24}{Re}. \tag{4.8}$$

Stoke's drag ignores inertial terms in the governing equations. Oseen [2] obtained the first inertial correction to the drag force in the form of

$$C_D = \frac{24}{Re}\left(1 + \frac{3}{16}Re\right), \tag{4.9}$$

which is valid for $Re < 5$, and reduces to Stoke's drag coefficient for $Re \ll 1$. Other approximations are also available with higher order corrections to the Stokes drag. For example, the Voloshuk and Sedunow [3] approximation is

$$C_D = \frac{24}{Re}\left(1 + \frac{3}{16}Re + \frac{9}{160}Re^2 \ln\left(\frac{Re}{2}\right) + \cdots\right), \tag{4.10}$$

which is again valid for $Re < 5$.

At high Re numbers, flow separation occurs when the boundary layer formed on the sphere's surface travels far enough against an adverse pressure gradient (caused by the shape of the sphere) that the speed of the boundary layer becomes almost zero and the fluid becomes detached from the surface. Turbulent boundary layers are known to be more resistant to the adverse gradient and so they separate further downstream compared to laminar boundary layers for the same flow geometries. The *wake* region (the region behind the point of separation) is characterized as a region with high pressure and low velocity. So, if one integrates the pressure over the surface of the object which experiences flow separation, an enhanced form drag is obtained due to the relative higher pressures on the downstream side of the object.

Figure 4.2a and 4.2b show flows past spheres at relatively low Reynolds numbers (from Van Dyke [4]). They show that after Re passes a critical value, the streamlined flow pattern around the sphere (as shown in 4.2a) changes and a doughnut-shaped ring forms behind the sphere (as shown in 4.2b). For Reynolds numbers larger than ~130, the ring vortex behind the drop starts to oscillate while the flow is still laminar. This leads to small vortices being separated from its tail in the form of vortex loops. With further increase in the Reynolds number the length of the recirculating regions and the scales of the detached eddies change considerably. Figure 4.2c shows an instantaneous flow past a sphere at $Re = 15{,}000$. The formation of vortex rings and further breakup of those into smaller structures can be clearly seen in the picture. Figure 4.2d also illustrates the time-averaged streamlines of the same flow, which shows that the flow still possesses a doughnut-shaped structure behind the sphere, in a time-average sense.

Figure 4.3 taken from Kundu and Cohen [5] shows that C_D changes with Re for flows past a solid sphere. As the figure shows, when the Reynolds number is increased beyond unity, Stokes and Oseen's drags cannot properly predict the drag coefficient because of the formation of small recirculating regions in the wake of the drop, which grow in size with the Reynolds number.

Up to the point of $Re \sim 5 \times 10^5$ in Fig. 4.3, the boundary layer formed on the surface of the sphere is laminar even though the wake of the separated flow can be turbulent. The variations in C_D are smooth in this interval, with the drag coefficient having a value close to 4/9. At this point however, a transition of the laminar

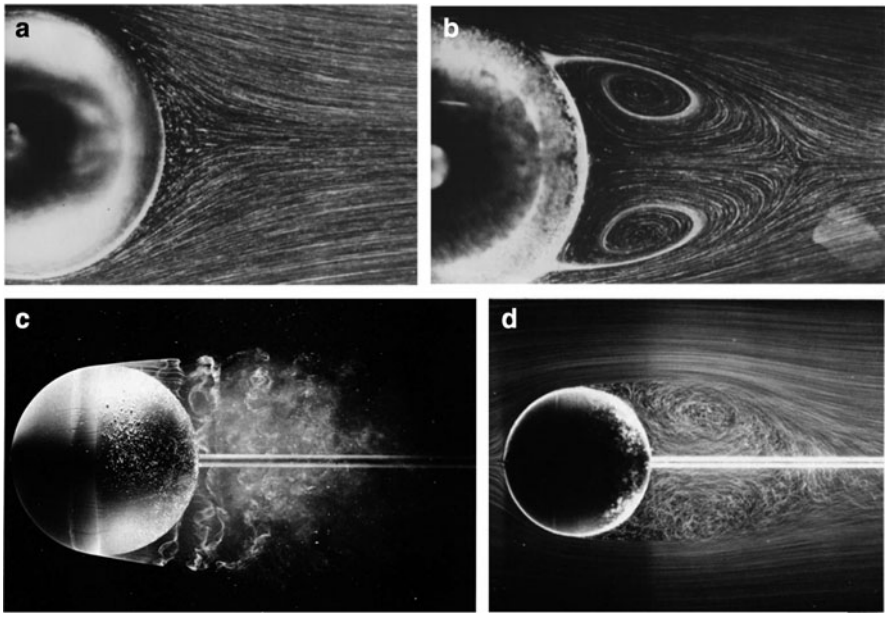


Fig. 4.2 Visualization of an instantaneous flow past a sphere at $Re = 26.8$ in (a), $Re = 73.6$ in (b), $Re = 15{,}000$ in (c), and visualization of the time-averaged streamlines behind the same sphere as panel (c) in (d). (a) and (b) from Taneda (1956) [50], reprinted by permission. (c) and (d) Copyright: ONERA The French Aerospace Lab/Werlé

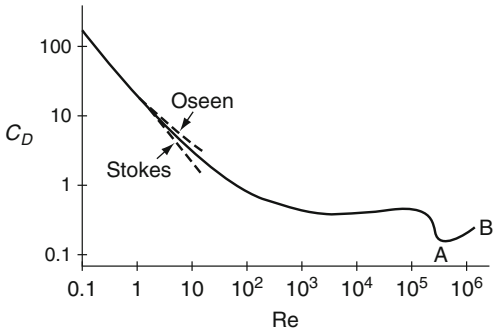


Fig. 4.3 Drag coefficient for a flow past a smooth sphere. The Stokes and the Oseen drags are given by (4.8) and (4.9). From "Fluid Mechanics" by Kundu and Cohen [5] Copyright (2008), Elsevier Inc. Reprinted by permission

boundary layer to a turbulent regime occurs. The turbulent boundary layer can overcome a larger adverse pressure gradient due to its larger energy. Hence, the point of separation is moved further downstream due to this transition and the wake of the sphere becomes thinner. This translates to a sudden decrease in the drag coefficient and is often referred to as the "drag crisis." As the Reynolds number is increased beyond this critical point, the turbulent boundary layer becomes thinner and the separation point slowly moves back upstream, leading to a smooth increase

in the drag coefficient. The sudden decrease at the critical Re followed by the smooth increase leads to the "dip" in the curve of the drag coefficient shown in Fig. 4.3.

Close inspection of Fig. 4.3 shows that the drag coefficient changes very little for Reynolds numbers greater than 2×10^4 and smaller than 5×10^5 and is almost equal to 4/9. There have been various correlations offered for the drag coefficient for flows past solid spheres, each derived for a particular range of the Reynolds number. Some of these relations are

$$C_{\mathrm{D}} = \frac{24}{Re} \quad \text{for} \quad 0.1 \leq Re \leq 0.3 \tag{4.11}$$

$$C_{\mathrm{D}} = \frac{26.5}{Re^{0.9}} \quad \text{for} \quad 0.3 \leq Re \leq 5 \tag{4.12}$$

$$C_{\mathrm{D}} = \frac{18.5}{Re^{0.6}} \quad \text{for} \quad 7 \leq Re \leq 70 \tag{4.13}$$

$$C_{\mathrm{D}} = \frac{4}{9} \quad \text{for} \quad Re > 2 \times 10^4 \tag{4.14}$$

These relations all form tangents to the curve in Fig. 4.3 in their effective range. Kelbaliyev and Ceylan [6] came up with a single correlation, which would fit the drag curve very nicely for Reynolds numbers smaller than that of the drag crisis. Their relation is in the form of

$$C_{\mathrm{D}} = \frac{24}{Re}\left[1 + 18.5Re^{3.6} + \left(\frac{Re}{2}\right)^{11}\right]^{1/30} + \frac{4}{9}\frac{Re^{4/5}}{330 + Re^{4/5}}. \tag{4.15}$$

Flow Around Liquid Drops

One of the earliest works on the flow past a slightly deforming viscous drop in a flow with a large density ratio is that of Hadamard [7], which considers Stokes flows. They offered the following expression for the drag coefficient:

$$C_{\mathrm{D}} = \frac{8}{Re}\left(\frac{3\mu_r + 2}{\mu_r + 1}\right) \tag{4.16}$$

where $\mu_{\mathrm{r}} = \mu_{\mathrm{d}}/\mu_{\mathrm{f}}$ is the ratio of the viscosity of the drop (μ_{d}) to the viscosity of the free stream (μ_{f}). Another theoretical prediction of the drag coefficient for $Re < 1$ is given by Taylor and Acrivos [8]:

$$C_D = \frac{8}{Re}\frac{2+3\mu_r}{1+\mu_r}\left(1+\frac{Re}{16}\frac{2+3\mu_r}{1+\mu_r}+\frac{1}{40}\left(\frac{2+3\mu_r}{1+\mu_r}\right)^2\left(\frac{Re}{2}\right)^2\ln\frac{Re}{2}\right) \quad (4.17)$$

The drag coefficients in (4.16) and (4.17) tend to $24/Re$ for $\mu_r \to \infty$, which is the Stokes drag for flow past a sphere. For $\mu_r \to 0$, C_D tends to $16/Re$, corresponding to flow past a bubble.

Happer and Moore [9] also studied the hydrodynamic forces acting on a spherical viscous drop for Reynolds numbers large enough for boundary layer theory to hold but small enough for surface tension to keep the drop near spherical Re $\propto$ 100). They assumed that the densities of the drop and the incoming flow are comparable and that the surface tension is strong enough to keep the drop's shape near-spherical. They considered the zeroth order flow to be inviscid, corresponding to the Hill's spherical vortex inside the drop (see Fig. 4.4) and a potential flow outside the interface. Then, they considered two boundary layers on each side of the interface as a first approximation and used asymptotic methods to match the exterior solution to that of the interior solution. Using this method they obtained first and second approximations to the drag coefficient and the rate of internal circulation of the drop. Their first order approximation for the drag coefficient is:

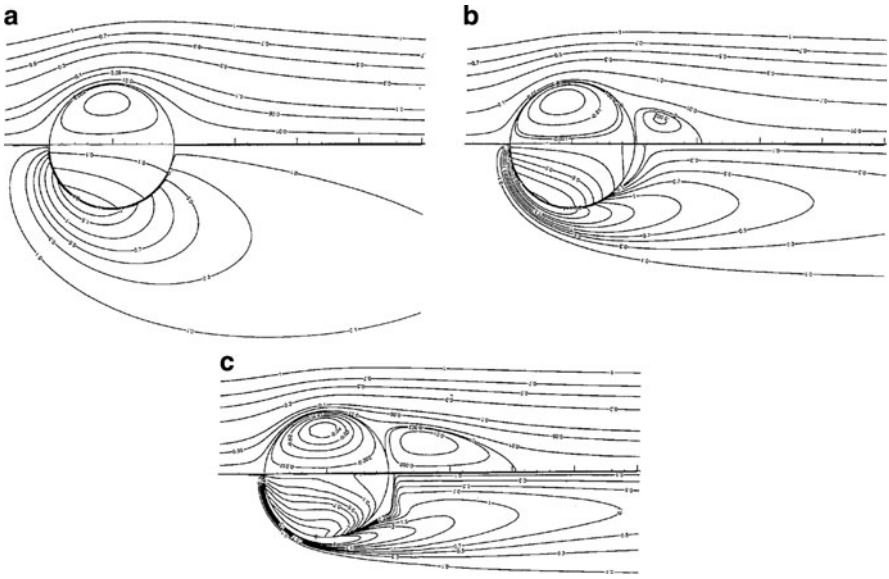


Fig. 4.4 Streamlines (*top half of each figure*) and vorticity field (*bottom half of each figure*) for (**a**) $\mu_r = 7$ and $Re = 10$; (**b**) $\mu_r = 7$ and $Re = 100$; (**c**) $\mu_r = 7$ and $Re = 500$. From Feng and Michaelides [12], Reprinted by permission, Copyright (2001) ASME

$$C_D = \frac{48}{Re}\left(1 + \frac{3}{2}\mu_r\right) \tag{4.18}$$

Rivkind and Ryskin [10] have estimated the drag coefficient as a function of Re and μ_r to be:

$$C_D = \frac{1}{1+\mu_r}\left[\mu_r\left(\frac{24}{Re} + \frac{4}{Re^{1/3}}\right) + \frac{14.9}{Re^{0.78}}\right] \quad \text{for } 0.5 \le Re \le 200 \tag{4.19}$$

Oliver and Chung [11] performed numerical simulations and recommended (4.19) for $2 < Re < 50$ and

$$C_D = C_{Do} + 0.40\left(\frac{2+3\mu_r}{1+\mu_r}\right)^2 \tag{4.20}$$

for $Re < 2$ where C_{Do} is the drag coefficient for Stokes' flow.

Apart from the asymptotic analysis such as those by Happer and Moore [9], numerical methods have been commonly used to resolve the flow structures in the interior and outside of a drop. Even for a nondeforming viscous drop, numerical simulations have helped in understanding the effects of the internal circulation of the drop (which is what makes it different from a rigid sphere) on the drag force it experiences. Moreover, simulations help in investigating the effect of the viscosity ratio and the density ratio on the hydrodynamic force experienced by the drop.

Figure 4.4 from Feng and Michaelides [12] shows the stream function on the top half of each panel and the contours of the vorticity on the bottom half. The viscosity ratio is constant and equal to 7 for all three cases while the Reynolds number is increased from a value of 10 in (a) to 500 in (c). The stream function shows the internal circulation inside each drop (Hill's Vortex) with the strength of the circulation increasing with Reynolds number. For case (a) with a small Re, the exterior flow follows the profile of the drop smoothly. As the Reynolds number is increased to 100, a recirculating region appears in the wake of the drop as shown in panel (b). As expected, the length of this region increases with Re as shown in panel (c). The vorticity fields in the three cases show the formation of the external boundary layer at the upstream stagnation point. Comparing the three cases clearly shows the boundary layer becomes thinner as the Reynolds number is increased. It was found by Feng and Michaelides [12] that the density ratio does not play an important role in their calculation performed for a nondeforming interface. Their study shows that as the viscosity ratio decreases from infinity (for a solid sphere) to zero (for a bubble), the drag coefficient also decreases, which is in agreement with (4.19).

Droplet Motion

The equation of motion for a particle or droplet using the steady-state drag coefficient can be expressed as

$$m\frac{\mathrm{d}v}{\mathrm{d}t} = 3\pi\mu_{\mathrm{c}}Df(u-v) + mg \tag{4.21}$$

where g is the acceleration due to gravity and f is the *drag factor* or the ratio of the drag coefficient to Stokes drag coefficient:

$$f = \frac{C_{\mathrm{D}}\mathrm{Re}_{\mathrm{r}}}{24}. \tag{4.22}$$

Obviously $f \to 1$ for Stokes flow. Assuming a spherical droplet with material density of ρ_{d}, (4.22) can be rewritten as

$$\frac{\mathrm{d}v}{\mathrm{d}t} = \frac{f}{\tau_v}(u-v) + g \tag{4.23}$$

where τ_v is the velocity response time,

$$\tau_v = \frac{\rho_{\mathrm{d}}D^2}{18\mu_{\mathrm{c}}} \tag{4.24}$$

There are several correlations available in the literature for f as a function of Reynolds number. One correlation (Schiller and Naumann [13]) that is reasonably good for Reynolds numbers up to 800 is

$$f = (1 + 0.15Re^{0.687}) \tag{4.25}$$

This correlation yields a drag coefficient that has less than 5% deviation from the standard drag coefficient. A correlation suitable to higher Reynolds numbers has been proposed by Putnam [14],

$$f = 1 + \frac{1}{6}Re^{2/3} \quad Re < 1,000 \tag{4.26}$$

$$f = 0.0183Re \quad 1,000 \le Re < 3 \times 10^5 \tag{4.27}$$

The advantage of this correlation is that the equation for particle motion can be integrated analytically. A shortcoming is the discontinuity in the value for f at $Re = 1,000$. A more accurate correlation over the entire subcritical Reynolds number range is that of Clift and Gauvin [15] which is an extension of Schiller and Naumann's equation.

$$f = 1 + 0.15Re^{0.687} + 0.0175Re(1 + 4.25 \times 10^4 Re^{-1.16})^{-1} \tag{4.28}$$

This correlation provides a fit for f within $\pm 6\%$ of the experimental value over the entire subcritical Reynolds number range. The terminal velocity of a particle is the ultimate velocity a particle achieves in free fall; that is, when the acceleration is zero. From (4.24), for a particle falling in a quiescent environment ($u = 0$), the terminal velocity is

$$v_t = \frac{g\tau_v}{f} \tag{4.29}$$

In Stokes flow, the terminal velocity is simply $g\tau_v$. Otherwise, the value for f has to be obtained iteratively.

Compressibility and Rarefaction Effects

For high Reynolds number gaseous flows around a droplet, the compressibility of the gas phase can play an important role in the drop deformation, the flow structures around the drop, and consequently in the drag force on the drop. To incorporate these effects into drag correlations, the Mach number is often used. The Mach number, M_a, is defined as the ratio of the velocity of the drop relative to its surrounding medium to the speed of sound in that medium.

At a high Reynolds number, the drag coefficient shows an increase with Mach number reaching a maximum value for light supersonic flow. This increase is due to the formation of shock waves on the particle and the attendant wave drag (essentially form drag). Mach number effects become significant for a Mach number of 0.6, which is the *critical Mach number*; that is, when sonic flow first occurs on the sphere.

At a low Reynolds number, the drag coefficient uniformly decreases with increasing Mach number and does not display a maximum value near unity. This is due to the prevalence of rarefied flow.

The importance of rarefaction effects are assessed by the magnitude of the *Knudsen number*, which is the ratio of the mean free path of the molecules to the particle diameter,

$$kn = \frac{\lambda}{D} \tag{4.30}$$

where λ is the mean free path of the molecules. If the Knudsen number is large, the flow cannot be regarded as a continuum. The wave drag due to a shock wave would no longer appear for particles with Knudsen numbers of the order of unity because the thickness of the shock wave would be comparable to the particle size and so, the particles would be engulfed by the wave.

The Knudsen number can be related directly to the Mach number (Ma) and Reynolds number. The viscosity of a gas is proportional to

$$\mu_g \sim c\rho_g\lambda \tag{4.31}$$

where c is the speed of sound in the gas. Thus, the Knudsen number can be written as

$$Kn = \frac{\lambda}{D} \sim \frac{\mu_g}{\rho_g cD} = \frac{Ma}{Re} \tag{4.32}$$

There is no analytic nor numerical model available, which provides the particle drag coefficient for particles over all the regimes of rarefied flows. The earlier methods to correct for rarefied flow effects were based on a correction to Stokes drag, derived by Basset to account for velocity slip at the surface. In that case, the drag coefficient can be expressed as

$$\frac{C_D}{C_{D,\text{Stokes}}} = \frac{1}{1 + Kn[2.49 + 0.84\exp(-1.74/Kn)]} \tag{4.33}$$

which can be regarded as an extension of the Basset correction. This equation has been used for many years as the correction for rarefied flow effects and is commonly referred to as the *Cunningham correction factor*. For large Mach numbers, this equation reduces to

$$C_D \sim \frac{C_{D,\text{Stokes}}}{Ma/Re} \tag{4.34}$$

so

$$C_D \propto \frac{1}{Ma} \tag{4.35}$$

and as $Ma \to \infty$ the drag coefficient approaches zero. Analytic results available for free molecule flows (Schaaf and Chambre [16]) show that the sphere drag coefficient approaches 2 as the Mach number approaches infinity. This is a shortcoming of the Cunningham correction factor but it is still useful for low Mach numbers.

The following empirical equation for drag coefficient proposed by Crowe et al. [17] and simplified by Hermsen [18] has been used extensively in the numerical analysis of the flow in solid propellant rocket nozzles.

$$C_D = 2 + (C_{DM=0} - 2)\exp\left(-3.07\sqrt{kg}(\text{Re})\frac{Ma}{\text{Re}}\right) + \frac{h(Ma)}{\sqrt{k}Ma}\exp\left(-\frac{\text{Re}}{2Ma}\right) \tag{4.36}$$

where k is the ratio of specific heats and g and h are the two functions;

$$g(Re) = \frac{1 + Re(12.278 + 0.548Re)}{1 + 11.278Re} \tag{4.37}$$

and

$$h(Ma) = \frac{5.6}{1 + Ma} + 1.7\sqrt{\frac{T_d}{T_c}} \tag{4.38}$$

and where T_d is the particle temperature and T_c is the temperature of the gas. $C_{D,M=0}$ is the drag coefficient for a Mach number of zero, or the steady-state (standard) drag curve. Note that for large Knudsen numbers (large M_a/Re), the drag coefficient approaches the "standard" drag curve. The model is not valid beyond the Reynolds number where critical Reynolds number effects begin to appear (reduction in drag coefficient).

Drag of Deformed Liquid Drops

Drag of a deforming drop was studied numerically by Wadhwa et al. [19]. Their simulations considered a spherical drop with some initial velocity in a stationary gas and studied the transient response of the drop and its surroundings. Reynolds ($Re = \rho_g\, Ud/\mu_g$), Weber ($We = \rho_g U^2 d/\sigma$), and Ohnesorge ($Oh_l = \mu_l/(\rho_l\, \sigma d)^{1/2}$) numbers based on relative velocity between the drop and the flow are used to describe the drag. The subscript "$_l$" denotes the liquid phase. Wadhwa et al. studied the effect of the Weber number on the drop deformation by keeping Oh_l constant. Figure 4.5 shows their result for $Oh_l = 0.01$ and $We_g = 1$. Panel (a) in the figure shows a snapshot of the streamlines at some fixed time. Panel (b) illustrates the deformation over time (nondimensional time) and panel (c) shows the transient variation in the drag coefficient. Noting that the drop is moving from left to right, the doughnut-shaped vortex is observed behind the drop similar to flow past solid spheres. The deformation plot shows that for this small value of the Weber number the drop deformation is very small and the surface tension can keep the drop in a near-spherical shape. The small oscillations in the drop, however, manifest in the C_D curve, which shows oscillations about the drag force on a solid sphere decelerating in a gas flow at the same flow conditions.

Once the Weber number is increased from 1 to 10, the relative strength of the surface tension to the inertial forces decreases. Hence, less pressure difference across the interface can be tolerated (compared to the $We_g = 1$ case) and the drop starts to deform, as shown in the left column (panel (a)) of Fig. 4.6. The deformed drop almost takes the shape of a flat ellipsoid and hence, the drop recirculating region in the downstream side of the drop grows larger. The enhanced vortex size

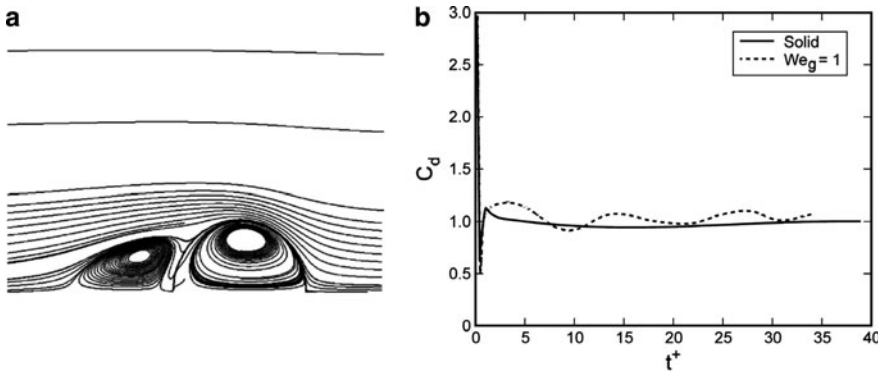


Fig. 4.5 (**a**) Streamlines and (**b**) transient drag coefficient compared to that of a solid sphere, for a viscous drop decelerating in an initially stationary gas. $Oh_l = 0.01, We_g = 1, Re = 150, \rho_l/\rho_g = 50$. Reprinted with permission from Wadha et al., Phys. Fluids, 19, 113301, 2007. Copyright 2007, American Institute of Physics

induces a velocity field which stretches the fluid elements on the drop surface from the axis of symmetry towards its tip. This positive feedback leads to further deformation in the drop. On the other hand, the frontal area of the drop increases through this mechanism leading to an enhanced drag force which slows the drop down significantly and decreases the effective Reynolds number. This slow-down leads to a decrease in the inertial forces. For this particular case with $We_g = 10$, the inertial forces drop down to a level that the surface tension forces can balance them and the drop oscillates back to a more bulky irregular shape, as shown in Fig. 4.6. The transient effect of these processes can be seen in the C_D curve as the drag coefficient increases by a factor of nearly 2.5 when the drop deformation is large. This has great implications for the drop displacement and using a constant drag coefficient (the solid line) for predicting the motion of this drop would lead to an overestimated drift.

Even further increases in the Weber number can lead to a more pronounced deformation in the drop. This is shown in Fig. 4.7 for $We_g = 100$. For this case, there is no returning point and the drop continuously deforms and spreads out into a sheet-like shape. A drop with this much deformation ultimately breaks up into smaller pieces by either particles getting pinched off its tip or the whole flat drop breaking into several pieces. Panel (a) in Fig. 4.7 clearly shows how the enhanced vortex in the leeward side of the jet helps stretching the drop into a thin shape which in turn expands the vortex itself. As expected, the continuous deformation leads to a smooth increase in the drag coefficient.

To investigate the effect of the viscous forces on the drop deformation and the drag coefficient, Wadhwa et al. [19] also performed simulations at fixed Weber numbers but for various Ohsenorge numbers. Their drag results for $We_g = 10^4$ are presented in Fig. 4.8. An increase in the relative strength of the viscous forces adds to the damping of the system. Hence, for drops that undergo some oscillations (reaching a maximum deformation and bouncing back again), this leads to a

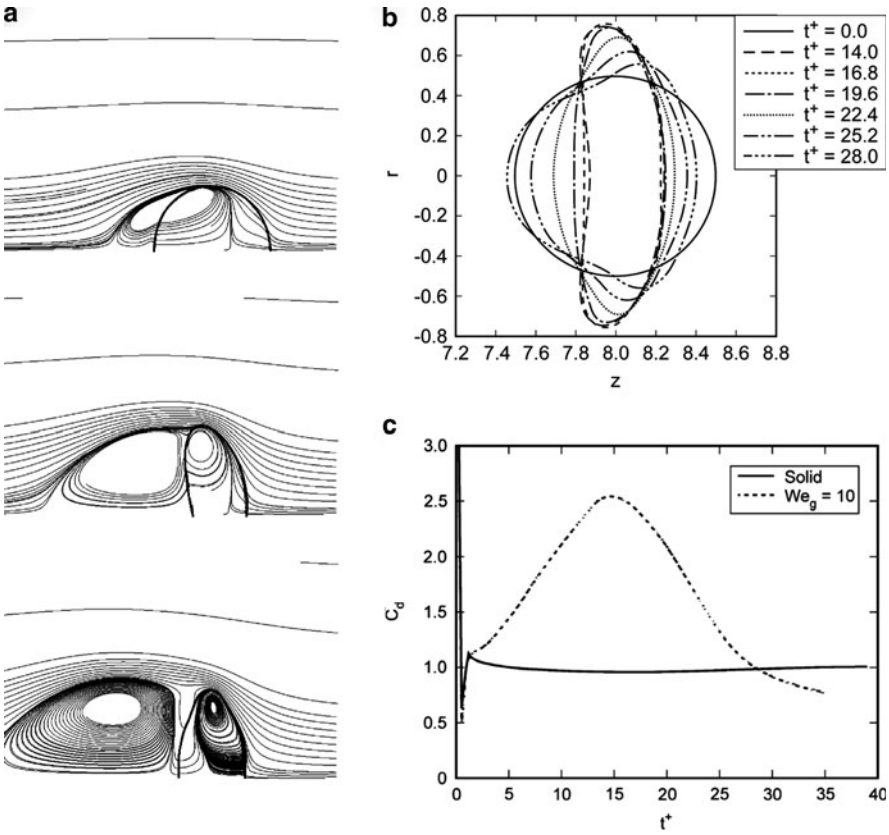


Fig. 4.6 Streamlines for various stages of deformation in (**a**), drop deformation in (**b**), and transient drag coefficient compared to that of a solid sphere in (**c**) for a viscous drop decelerating in an initially stationary gas. $Oh_l = 0.01, We_g = 10, Re = 150, \rho_l/\rho_g = 50$. Reprinted with permission from Wadha et al., Phys. Fluids, 19, 113301, 2007. Copyright 2007, American Institute of Physics

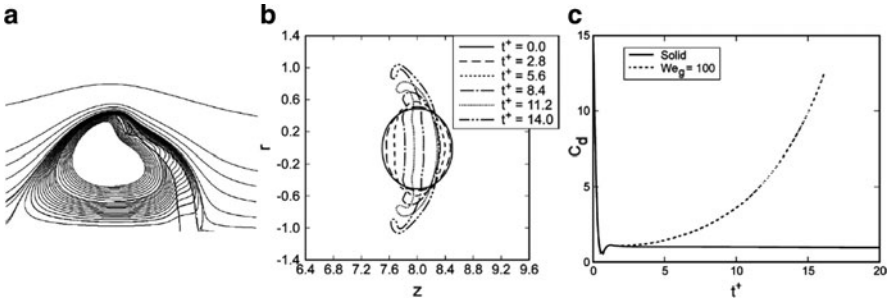


Fig. 4.7 Streamlines (**a**), drop deformation (**b**), and transient drag coefficient compared to that of a solid sphere (**c**) for a viscous drop decelerating in a initially stationary gas. $Oh_l = 0.01$, $We_g = 100$, $Re = 150$, $\rho_l/\rho_g = 50$. Reprinted with permission from Wadha et al., Phys. Fluids, 19, 113301, 2007. Copyright 2007, American Institute of Physics

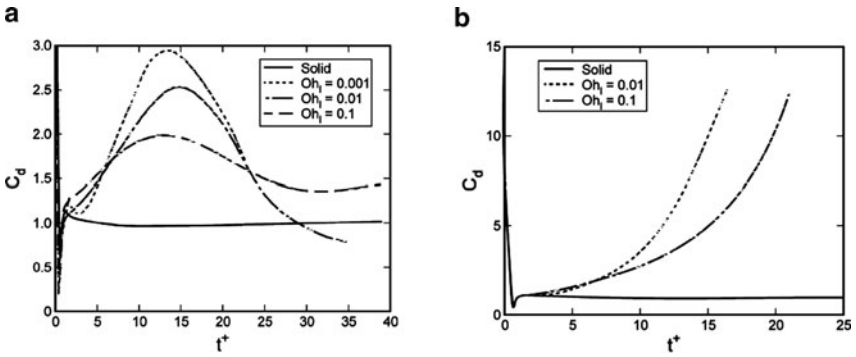


Fig. 4.8 Drag coefficient for various Ohsenorge numbers for (**a**) $We_g = 10$, and (**b**) $We_g = 100$. For both cases $Re = 150$, $\rho_l/\rho_g = 50$. Reprinted with permission from Wadha et al., Phys. Fluids, 19, 113301, 2007. Copyright 2007, American Institute of Physics

decrease in the oscillation amplitude and the drag coefficient, as shown in Fig. 4.8a. For a more severe deformation case such as panel (b) in the figure, increase in viscous forces also decreases the extent to which the drop deforms.

These examples help to illustrate the interplay between the surface tension, viscous forces, and the inertial forces that manifest in the form of pressure variations on the surface of the drop. They show the dependence of the drag force on these parameters through their effects on the drop deformation. In short, they highlight the importance of transient drop responses on the drag force and so, on the drop motion. At higher Reynolds numbers suitable for many real applications, the drop deformation may become more severe and the drop shape can take very irregular profiles, leading to sharp changes in the drag coefficient.

Similar effects are observed on the drag of two-dimensional (2D) and axisymmetric deforming droplets by Mashayek and Ashgriz [20]. To further examine (and emphasize) the importance of extreme drop deformation on the drag force, a set of high resolution numerical simulations for flows past 2D solid drops is performed. The choice of 2D simulations is made to merely focus on the effect of elongation. Moreover, 2D drops are often used as the cross-section of a jet in a flow. We consider steady flows around various deformation levels. Three aspect ratios (AR = minor/major axis of the elliptic cross-section) of 1, 0.5, and 0.25 are considered as shown in Fig. 4.9.

The calculations are performed at equivalent Reynolds numbers $\left(Re_{\text{eq}} = \rho U_\infty d_{\text{eq}}/\mu\right)$ of 150–8,000, where d_{eq} is the equivalent circular diameter for elliptic cross sections defined by $d_{\text{eq}} = (4ab)^{1/2}$, where 2a and 2b are the semimajor and semiminor axes of the ellipse. It is usual to define the Reynolds number based on the major axis of the ellipse in the form of $Re_a = \rho U 2a/\mu$ whereas the choice of d_{eq} can correspond to the same drop but at different deformation levels. So, if we consider the three ellipses of Fig. 4.9(a) as various profiles of the same drop at different times

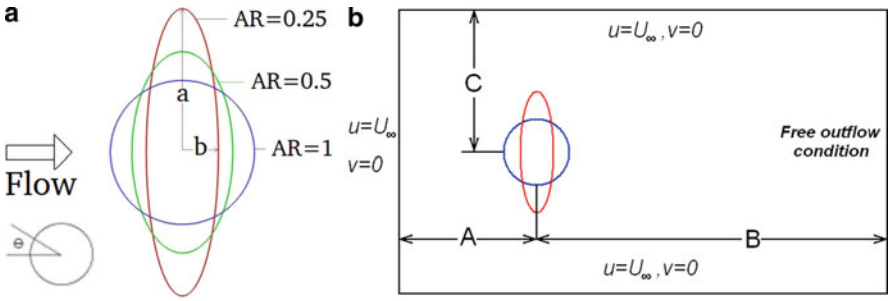


Fig. 4.9 (**a**) Schematic Diagram of the 2D drops with different aspect ratios; (**b**) Geometry and boundary conditions of the computational domain

during its evolution, the Reynolds number for all of them is defined based on the initial diameter of the circular drop.

The simulations are performed for six different Reynolds numbers of 150, 500, 1,000, 2,000, 4,000, and 8,000. As the Reynolds number increases from low values, steady flow occurs around the body without any vortex shedding. Further increase in the Reynolds number causes the formation of a pair of symmetrical counter-rotating vortices about the centerline of the wake for $Re_{eq}<46$ (for AR = 1). At $Re_{eq} \approx 46$, the flow becomes unstable and the Karman vortex street appears in the wake of the ellipse. Experimental studies have shown that at the Reynolds number of 150, the vortex street becomes turbulent in the wake downstream of the 2D drop and at the Reynolds number of 400, the vortices become turbulent. Our results show that for circles with $Re_{eq} = 150$, the wake is very organized and the regular Karman street is observed. As the Reynolds number increases, the separated shear layer formed on the surface of the ellipse becomes unstable and smaller vortices form as a result of this instability, which affects the vortex shedding downstream.

Figure 4.10 shows a close look at the boundary layer for two cases with $Re_{eq} = 500$, but different aspect ratios and Re_a values. Panel (a) shows the start of the formation of smaller vortices due to the growth of the instabilities in the shear layer. It is observed that as the Reynolds number increases (for a constant aspect ratio), the point at which the separated shear layer becomes unstable moves upstream. Panel (b) shows that the distance between the two points of separation on the ellipse are located farther in the vertical direction due to the decrease in the aspect ratio, which creates a wider vortex-shedding area. For AR = 0.25, the shear layers roll up much closer to the tips of the ellipse and occasional interactions between the vortices separated from the upper and lower tips are observed, which is similar to flow past normal plates. At AR = 0.25, shortly downstream of the flow separation point, the shear layer mixing leads to the reattachment of the boundary layer, which is similar to that of higher Reynolds number flows past

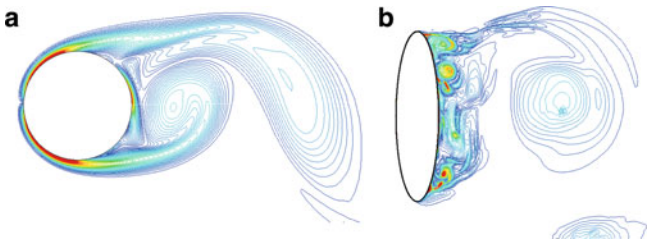


Fig. 4.10 Vorticity contours with contour levels from 0 to 20 in steps of 0.5. (**a**) AR = 1, $Re_{eq} = Re_a = 500$; (**b**) AR = 0.25, $Re_{eq} = 500$, $Re_a = 1000$

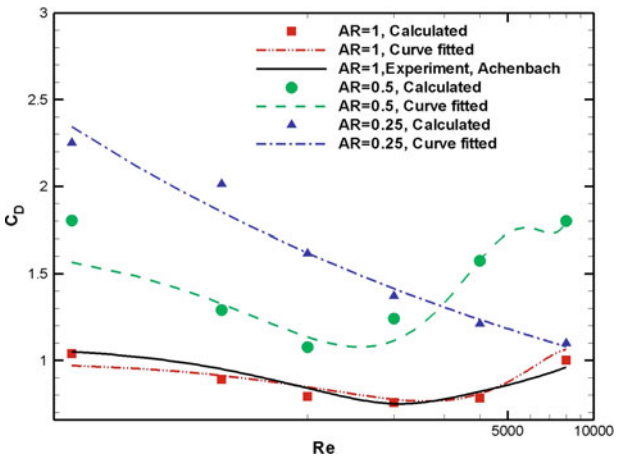


Fig. 4.11 Calculated drag coefficients versus Re_{eq} for all the cases plotted and compared with experiments of Achenbach [22]

circular cylinders with turbulent boundary layers. The formation and separation of the vortices on the leeward of the drop leads to time variations in the drag coefficient. Therefore, for all the simulations, the flow has been given the necessary time to pass the transient phase and to develop the proper statistically steady vortex-shedding pattern. The drag coefficient is then averaged over an adequate amount of time to obtain a statistically valid value for each test case. The final results for all the test cases are plotted in Fig. 4.11 and are compared to experimental results of Achenbach [22] for a circular cylinder. Each line is a polynominal fitted to the results for a specific aspect ratio.

The change in the flow structure around the 2D drop, induced by increasing the aspect ratio, leads to considerable variations in the drag coefficient, as shown in the curves in the figure. Hence, one can expect the change in the drag coefficient to be pronounced as a real drop deforms into elongated ellipsoidal shapes. It should be noted that the flow patterns shown in Fig. 4.10 do not truly correspond to a deforming 2D drop as for each simulation, the drop shape is kept fixed.

However, these simulations help showing the importance of the effect of drop deformation on the drag force. In general, as a drop's deformation becomes larger, one may expect the drag force to become larger due to the increase in its frontal area. This is shown in Fig. 4.11 for most of the Re range. However, this is not true of large Reynolds numbers as the curve for the most elongated ellipse (AR = 0.25) in the simulations dips below that of AR = 0.5. This enforces the importance of the effect of the deformation level on the flow structures and the corresponding drag force.

Drag Coefficient for Sprays

Desantes et al. [21] presented a description of how the effects discussed so far can be incorporated into spray calculations, as also detailed by O'Rourke et al. [23].

The commonly used correlations for drag coefficient used in spray models are

$$\begin{cases} C_{\mathrm{D}} = \dfrac{24}{Re}(1 + 0.15Re^{0.687}) & \text{for} \quad Re \leq 10^3 \\ C_{\mathrm{D}} = 0.44 & \text{for} \quad Re > 10^3 \end{cases} \tag{4.39}$$

The distortion parameter y as defined in Fig. 4.12a can be used to modify the drag coefficient to account for the drop deformation. This can be done using the relation

$$C_{\mathrm{D},y} = C_{\mathrm{D}}(1 + 2.63\mathrm{y}), \tag{4.40}$$

proposed by Liu et al. [24] where $C_{\mathrm{D},y}$ is the drag coefficient for the deformed drop and C_{D} is that of the initially spherical drop. In spray models, the droplet distortion, y, varies between 0 and 1 and the drop is assumed to break down into smaller pieces if y exceeds unity. The logic behind relation (4.40) is very simple. The drag

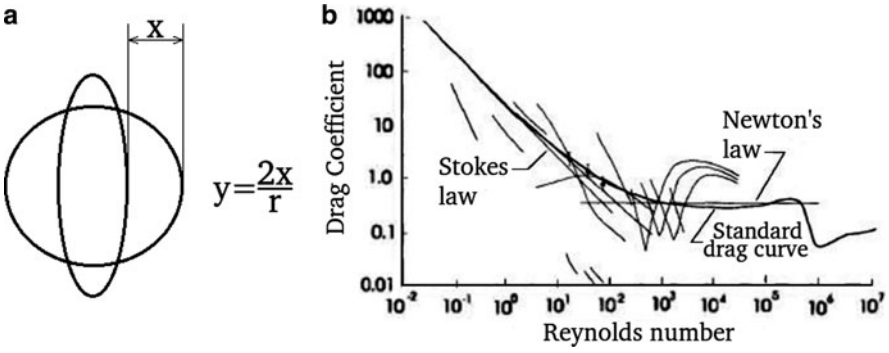


Fig. 4.12 **(a)** Droplet distortion, y, and **(b)** Various experimental drag curves (from Rudinger [47]. Reprinted by permission, Copyright (1980), Elsevier Scientific Publication Company.)

coefficient of a circular disk is about 3.6 times larger than that of a spherical drop at high Reynolds numbers. According to (4.40), as a drop deforms into a flat shape (i.e., $y \rightarrow 1$), its effective drag coefficient becomes 3.6 times its initial drag coefficient.

Drag Coefficient of Interacting Drops

In dense sprays, when the drop spacings are small, the drag coefficient of each drop is significantly altered. The droplet interaction has a leading order effect on the dynamics. Studies on the drag of multiple drops close to each other have shown that the drag ratio (ratio of the drag force modified due to the presence of another drop to the drag force acting on a single drop in the same conditions) is not sensitive to the Reynolds number (for more information see [20–43]). In general, a reduction in drag coefficients for aligned spheres and an increase in drag coefficients for adjacent spheres have been reported by various experimental and numerical studies. Moreover, a decrease in the distance between drops in the normal direction to the free stream tends to increase the drag coefficients; the reverse is true of the parallel direction. The interacting effect in the transversal direction reduces faster than that in the flow direction. The reported numbers indicate that the interaction effect is insignificant for drop spacing larger than 80d in the flow direction and larger than 20d in the transverse direction where d is the drop diameter.

The presence of many drops in a spray can change the effective drag force acting on the drops to a significant extent. This is mainly due to the effect of the drops on the surrounding gas flow through momentum exchange. Various experimental studies (such as Giles [44] and Rhee et al. [45]) have shown that in sprays, some drops move much faster than one would expect if the conventional isolated-drop drag coefficients are used to calculate the drag force. This is even truer of smaller drops and is due to the increased velocity of the surrounding gas resulting from the momentum exchange between the drops and the gas. Hence, the entrainment of the gas flow leads to higher drop velocities. To take this exchange into account in spray models, two approaches have been commonly adopted. The first is modifying the gas velocity by adding a correction to the free stream velocity. The correction is supposed to take into account the momentum exchange between the spray drops and the gas phase. The second approach has been to modify the drag coefficient in such a way that the effect of the enhanced entrained gas velocity is accounted for. This is called the “effective drag” approach. Effective drag models are designed to also take into account the effects of mutual droplet interactions in addition to the gas entrainment. To do so, they often modify the drag coefficient by multiplying it by a function of the local void fraction α in the form of

Table 4.1 Correlations for multiphase flows and interacting particles, drops and bubbles

Drag coefficient	Range	Condition	Investigator
$C_d = \frac{4}{3}\left(1.75 + 150\frac{\alpha_d}{Re}\right)$	$0.7 \leq Re \leq 2,500$	Gas flow through crushed porous solid	Ergun [30]
$C_d = \left(1 + \alpha_d^{\frac{1}{3}}\right)\left(0.63 + 4.\frac{8}{\sqrt{Re_m}}\right)^2$ $Re_m = \frac{\rho_c d U_r}{\mu_m}, \mu_m = \mu_g \exp\left(\frac{K_1 \alpha_d}{1 - K_2 \alpha_d}\right)$ $K_1 = 2.66 \pm 0.20, K_2 = 1.00 \pm 0.03$	$\alpha_d \leq 0.59$	Cloud of Spherical solid particles (fit on published experimental data)	Barnea and Mizrahi [49]
$C_d = \frac{24}{Re_m}\left(1 + 0.1 Re_m^{\frac{3}{4}}\right)$ $Re_m = \frac{\rho_c d U_r}{\mu_m}$ $\mu_m = \mu_g \left(1 - \frac{\alpha_d}{\alpha_m}\right)^{-2.5\alpha_m} \frac{\mu_d + 0.4\mu_g}{\mu_d + \mu_g}$ $0.5 \leq \alpha_m \leq 0.74$ $\alpha_m = 0.62$ for gas-particles flows	Viscous flows $0 \leq \alpha_d \leq 0.55$	Dispersed two-phase flows (spherical solid particle systems)	Ishii and Zuber [34]
$C_d = \frac{4}{3}\alpha_c{}^{-1.8}\left(0.336 + 17.\frac{3}{Re_S}\right)$	Simple cubic array: $0.06 \leq \alpha_c \leq 0.31$ $0.4 \leq Re \leq 11$ And $0.12 \leq a_c \leq 0.5210^3 \leq Re \leq 10^4$ Random Arrarys $0.36 \leq a_c \leq 0.5910^{-2} \leq Re \leq 10^2$	Revisions of experimental correlations by theoretical considerations for fixed beds of spheres	Gibilaro et al. [31]
$C_d = \left(\exp(K_1.\alpha_d) + \alpha_d^{k_2}\right)\frac{24}{Re}\left(1 + 0.15 Re^{0.687}\right)$ $K_1 = 2.68$ *et* $K_2 0.43$	$0.001 \leq Re \leq 1000$	Densely dispersed two phase systems (fit on published experimental data)	Rusche and Issa [46]

$$C_{\mathrm{D},\alpha} = C_{\mathrm{D},y} f(\alpha), \tag{4.41}$$

where $C_{\mathrm{D},y}$ is the drag coefficient, which only takes the drop deformation into account and is defined in (4.36), while $C_{\mathrm{D},\alpha}$ additionally takes the drop interactions into account. Several commonly used drag coefficients for interacting drops and bubbles are provided in Table 4.1. As one example of such relations, Rusche and Issa [46] proposed a linear function of the void fraction in the form of

$$C_{\mathrm{D},\alpha} = C_{\mathrm{D},y}\left[\exp(K_1\alpha) + K_2\alpha^{K_3}\right], \tag{4.42}$$

with the values for the coefficients K_1, K_2, and K_3 being 2.1, 1.0, and 0.249, respectively. Figure 4.12b (Rudinger [47]) shows a summary of the resulting drag curves from various experimental studies performed in wind tunnles and fluidized beds. Although the physical processes discussed in this article explain some of the discrepancies shown in the figure, many discrepancies are still unresolved.

Evaporation

If the heat transfer between the drop surface and the surrounding gas is high enough, the evaporation of liquid from the drop can become an important factor in the calculation of the drag force. This effect goes hand in hand with the deformation factor as a deformed and flattened drop has a higher surface-to-volume ratio, which implies enhanced heat transfer and more evaporation. It is thus necessary for any effective drag correlation to take both of these effects into account. As one example of a correlation that modifies the conventional drag coefficient (drag over a sphere) to take evaporation into account, Eisenklam et al. [48] proposed

$$C_{\mathrm{D,e}} = \frac{C_{\mathrm{D}}}{1 + B_{\mathrm{M}}}, \tag{4.43}$$

where the subscript "e" denotes "evaporation" and B_{M} is the Spalding mass transfer number, which accounts for the vapor mass fraction at the drop surface and is given by

$$B_{\mathrm{M}} = \frac{Y_{\mathrm{fs}}}{1 - T_{\mathrm{fs}}}, \tag{4.44}$$

where Y_{fs} is the vapor mass fraction at the drop surface given by

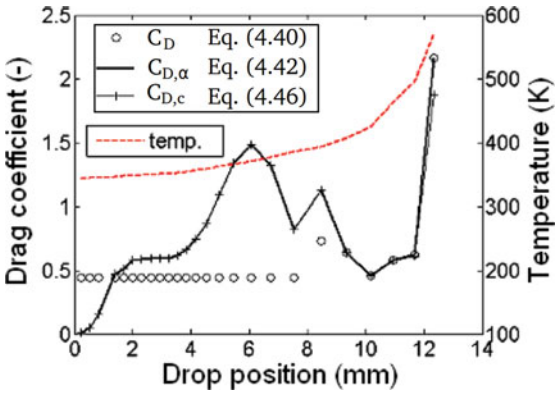


Fig. 4.13 Comparison of drag coefficients. From Desantes et al. [21]. Reprinted by permission, Copyright (2009), American Chemical Society

$$Y_{\mathrm{fs}} = \left[1 + \left(\frac{p_{\mathrm{a}}}{p_{\mathrm{fs}}} - 1\right)\frac{W_{\mathrm{g}}}{W_{\mathrm{l}}}\right]^{-1}, \tag{4.45}$$

where p_{fs} is the surface pressure, p_{a} is the ambient pressure, and W_{g} and W_{l} are the molecular weights of the gas and the liquid phases respectively. As suggested by Desantes et al. [21], combining the three correlations discussed so far leads to the relation for the comprehensive drag coefficient $C_{\mathrm{D,c}}$

$$C_{\mathrm{D,c}} = C_{\mathrm{D},\alpha} f(B_{\mathrm{M}}) = C_{\mathrm{D},y}[\exp(2.1\alpha) + 0.249\alpha^{K_3}]\frac{1}{1 + B_{\mathrm{M}}}. \tag{4.46}$$

Equation (4.47) takes into account the effects of the drop deformation, gas entrainment, drop interactions, and evaporation all based on simplified physical assumptions.

Figure 4.13 (taken from Desantes et al. [21]) plots the variations in the drag coefficients obtained using equations (4.40), (4.42), and (4.46) by following the evolution of a group of drops injected from a nozzle in to a spray model. Also included in the figure is the temperature. As the figure shows, the effects of the drop deformation and their interactions with each other and with their surrounding gas are significant. This can be observed by comparing the C_{D} curve (for spherical drops) to the $C_{\mathrm{D},\alpha}$ curve. However, comparing the curve for $C_{\mathrm{D,c}}$ to that of $C_{\mathrm{D},\alpha}$ shows very little effect of evaporation on the drag coefficie, with the effect becoming more important as the temperature becomes higher. So, for a simulation like the one from which Fig. 4.13 is taken, the effect of evaporation can be neglected. However, this is, true for this particular case, which is for hexadecane drops (used in Diesel engines). For other applications with drops composed of a fluid with different properties, and/or at higher temperatures, the effect of evaporation can be more pronounced.

Nomenclature

$2a$	Semimajor axis of ellipse
$2b$	Semiminor axis of ellipse
A	Frontal area of the object
a	Radius of sphere
B_{M}	Spalding mass transfer number
C	Constant of integration
c	Speed of the sound in the gas
C_{D}	Drag coefficient
$C_{\mathrm{D,o}}$	Drag coefficient for Stokes' flow
$C_{\mathrm{D},\alpha}$	Coefficient of drag, drop interaction accounted
$C_{\mathrm{D,c}}$	Comprehensive drag coefficient
$C_{\mathrm{D,e}}$	Coefficient of drag, evaporation
$C_{\mathrm{D},\ M=0}$	Drag coefficient for a mach number of zero
$C_{\mathrm{D,y}}$	Drag coefficient for the deformed drop
$d = 2a$	Diameter of sphere
d_{eq}	Equivalent circular diameter, elliptic cross section
F_{D}	Drag Force entered on the particle
f	Drag factor, drag coefficient/ Stokes drag
$\hat{f}$	Traction on the sphere
G	Shear rate
g	Acceleration due to gravity
k	Ratio of specific heats
Kn	Knudsen number
Oh_{l}	Ohnesorge
P	Pressure distribution on the drop
P_{a}	Ambient pressure
P_{fs}	Surface pressure
Re	Reynolds number
T_{c}	Temperature of the gas
T_{d}	Particle temperature
U	Relative velocity of flow with respect to sphere
u	Velocity components in r direction
v	Velocity components in θ direction
v_{t}	Terminal velocity
W_{g}	Molecular weight of a gas
W_{l}	Molecular weight of a liquid phase
We	Weber number
Y_{fs}	Vapor mass fraction at drop surface
y	Distortion
ς	Local void fraction
α	Density
ρ_{d}	Material density of a spherical droplet
μ_{c}	Dynamic viscosity
μ_{d}	Viscosity of the drop
μ_{f}	Viscosity of the free stream
μ_{r}	Viscosity of the drop/free stream
τ_{rr}	Normal to surface of the traction

$\tau_{r\theta}$	Tangent to surface of the traction
τ_v	Velocity response time
λ	Mean free path of the molecules

References

1. Batchelor, G. K., An Introduction to Fluid Dynamics, Cambridge University Press, pp. 331–343, 1967.
2. Oseen, C. W., Hydrodynamic, Akademische Verlag, Leipzig, 1927.
3. Voloshuk, V. M. and Sedunow, J. S., The Processes of Coagulation in Dispersed Systems, Nauka, Moscow, 1976.
4. Van Dyke, M., An Album of Fluid Motion, The Parabolic Press, Stanford, (1982).
5. Kundu, P. K. and Cohen, I. M., Fluid Mechanics, Fourth edition, Academic Press, San Diego, 2008.
6. Kelbaliyev, G. and Ceylan, K., Development of new empirical equations for estimation of drag coefficient, shape deformation, and rising velocity of gas bubbles or liquid drops. Chem. Eng. Commun. 194, 1623–1637, 2007.
7. Hadamard, J. S., Mouvement Permanent Lent d'une Sphere Liquid et Visqueuse dans une Liquid Visquese, C.R. Acad. Sci. 152, 1735–1738, 1911.
8. Taylor, T. and Acrivos, A., On the deformation and drag of a falling drop at low Reynolds numbers, J. Fluid Mech., 18, 466–476, 1964.
9. Happer, J. and Moore, D. W., The motion of a spherical liquid drop at high Reynolds number, J. Fluid Mech., 32, part 2, 367–391, 1968.
10. Rivkind, V. Y. and Ryskin, G. M. Flow structure in motion of a spherical drop in a fluid medium at intermediate Reynolds numbers. Fluid Dynamics (English translation of: Izv. Akad. Nauk SSSR Mekh. Zhidk. Gaza), 11, 5–12, 1976.
11. Oliver, D. L. R. and Chung, J. N. Flow about a fluid sphere at low to moderate Reynolds numbers. J. Fluid Mech., 177, 1–18, 1987.
12. Feng, Z. G. and Michaelides, E. E., Drag coefficients of viscous spheres at intermediate and high Reynolds numbers, J. Fluids Eng. 123(Issue), 2001.
13. Schiller, L. and Naumann, A. Über die grundlegenden berechungen bei der schwerkraftaufbereitung. Vereines Deutscher Ingenieure 7, 318, 1933.
14. Putnam, A. Integratable form of droplet drag coefficient. ARS J. 1961.
15. Clift, R. and Gauvin, W. H. The motion of particles in turbulent gas streams. Proc. Chemeca, 1970.
16. Schaaf, S. A. and Chambre, P. L. High speed aerodynamics and jet propulsion VIII, Princeton University Press, Princeton, 1958.
17. Crowe, C. T., Babcock, W., Willoughby, P. G., and Carlson, R. L., Measurement of particle drag coefficient in flow regimes encountered by particles in a rocket nozzle, United Technology Report 2296-FR, 1969.
18. Hermsen, R. W. Review of particle drag models. Subcommittee 12th Meeting Minutes, CPIA Publication, 1979.
19. Wadhwa, A. R., Magi, V., and Abraham, J. Transient deformation and drag of decelerating drops in axisymmetric flows. Phys. Fluids, 19, 113301, 2007.
20. Mashayek, A. and Ashgriz, N., Model or deformation of drops and liquid jets in gaseous crossflows. AIAA J. 47(2) (2009).
21. Desantes, J. M., Margot, X., Pastor, J. M., Chavez, M., and Pinzello, A. CFD-Phenomenological diesel spray analysis under evaporative conditions. Energy Fuels 23, 3919–3929, 2009.
22. Achenbach, E. Distribution of local pressure and skin friction around a circular cylinder in crossflow up to $R_e = 5\times10^6$. Fluid Mechanics 34, 625–639, 1968.
23. O'Rourke, P. J. and Amsden, A. A. The TAB Method for Numerical Calculation of Spray Droplet Breakup, SAE Paper 872089.

24. Liu, A. B., Mather, D., and Reitz, R. D. Modeling the effects of drop drag and breakup on fuel sprays, SAE Paper 930072.
25. Clair, B. L. and Hamielec, A. Viscous flow through particle assemblages at intermediate Reynolds numbers. IεEC Fundam. 7, 308–315, 1968.
26. Poo J. Y. and Ashgriz N. Variation of drag coefficients in an interacting drop stream, Exp. Fluids, 11, 1–8, 1991.
27. Cybulski, A., Dalen, M. V., Verkerk, J., and Berg, P. V. D. Gas-particle heat-transfer coefficients in packed beds. Chem. Eng. Sci. 30, 1015, 1975.
28. Difelice, R. The voidage function for fluid-particle interaction systems. Int. J. Multiph. Flow 20, 153–159, 1994.
29. Dwyer, H., Nirschl, H., Kerschl, P., and Denk, V. Heat, mass and momentum transfer about arbitrary groups of particles. Twenty-Fifth Symposium on Combustion, Irvine, pp. 389–395, 1994.
30. Ergun, S. 1952 Fluid flow through packed columns. Chem. Eng. Prog. 48(2), 89–94, 1952.
31. Gibilaro, L. G., Felice, R. I. D., and Waldram, S. P. Generalized friction factor and drag coefficient correlations for fluid-particle interactions. Chem. Eng. Sci. 40, 1817–1823, 1985.
32. Hill, R. J. Koch, D. L., and Ladd, A. J. C. The first effect of fluid inertia on flows in ordered and random arrays of spheres. J. Fluid Mech. 448, 213–248, 2001a.
33. Hill, R. J. Koch, D. L., and Ladd, A. J. C. Moderate-Reynolds-number flows in ordered and random arrays of spheres. J. Fluid Mech. 448, 243–278, 2001b.
34. Ishii, M. and Zuber, N. Drag coefficient and relative velocity in bubbly, droplet or particulate flows. AIChE J. 25(5), 843–855, 1979.
35. Kim, I., Elghobashi, S., and Sirignano, W. Three-dimensional flow over two spheres placed side by side. J. Fluid Mech. 246, 465–488, 1993.
36. Mulholland, J., Srivastava, R., and Wendt, J. Influence of droplet spacing on drag coefficient in nonevaporating, monodisperse streams. AIAA J. 26(10), 1231–1237, 1988.
37. Poo, J. and Ashgriz, N. Variation of drag coefficients in an interacting drop stream. Exp. Fluids 11, 1–8, 1991.
38. Racmachandran, R., Kleinstreuer, C., and Wang, T.-Y. Forced convection heat transfer of interacting spheres. Numer. Heat Transf. 15, 471–487, 1989.
39. Tal, R., Lee, D., and Siriganano, W. Hydrodynamics and heat transfer in sphere assemblages cylindrical cell models. Int. J. Heat Mass Transf. 26(9), 1265–1273, 1983.
40. Tal, R., Lee, D., and Siriganano, W. Heat and mass momentum transfer around a pair of spheres in viscous flow. Int. J. Heat Mass Transf. 27(11), 1953–1962, 1984.
41. Tal, R. and Sirignano, W. Cylindrical cell model for hydrodynamics of particles assemblages at intermediate Reynolds numbers. AIChE J. 28(2), 233–237, 1982.
42. Zhu, C., Liang, S.-C., and Fan, L.-S. Particle wake effects on the drag force of an interactive particle. Int. J. Multiph. Flow 20(1), 117–129, 1994.
43. Sadhal, S.S., Ayyaswamy, P.S., and Chung, J.N. Transport Phenomena with drops and bubbles, 1997.
44. Giles D. K., Energy conversion and distribution in pressure atomization, Trans. ASAE, 31(6), 1668–1673, 1988.
45. Rhee J.B., Young W., and Bode L. E., Transport of spray droplets from flat-fan nozzles, ASAE paper No. 90–1001, 1990.
46. Rusche, H. and Issa, R. I., The Effects of voidage on the drag force on particles, droplets and bubbles in dispersed two-phase flow, Proceedings of the 2nd Japanese-European Two-Phase Flow Group Meeting, Tsukuba, Japan, 2000.
47. Rudinger, G., Fundamentals of Gas-Particle Flow, Handbook of Powder Technology, Vol. 2, Elsevier Scientific Publishing Co., Amesterdam, 1980.
48. Eisenklam, P., Arunachlaman, S. A., and Weston, J. A., Evaporation rates and drag resistances of burning drops, 11th International Symposium on Combustion, Pittsburgh, pp. 715–728, 1967.

49. Barnea, E. and Mizrahi, J. A. Generalized approach to the fluid-dynamics of particulate systems, part 1: General correlation for fluidization and sedimentation. Chem. Eng. 5, 171–189, 1973.
50. Taned, S. Experimental investigation of the wakes behind cylinders and plates at low Reynolds numbers. Phys. Soc. Jpn. 11, 302–307, 1956.

Chapter 5
Oscillation of Droplets and Bubbles

N. Ashgriz and M. Movassat

Abstract A liquid droplet may go through shape oscillation if it is forced out of its equilibrium spherical shape, while gas bubbles undergo both shape and volume oscillations because they are compressible. This can happen when droplets and bubbles are exposed to an external flow or an external force. Liquid droplet oscillation is observed during the atomization process when a liquid ligament is first separated from a larger mass or when two droplets are collided. Droplet oscillations may change the rate of heat and mass transport. Bubble oscillations are important in cavitation problems, effervescent atomizers and flash atomization where large number of bubbles oscillate and interact with each other. This chapter provides the basic theory for the oscillation of liquid droplet and gas bubbles.

Keywords Bjerknes force · Bubble breakup · Bubble interaction · Bubble oscillation · Chaotic oscillation · Damping rate · Droplet oscillation · Nonlinear oscillation · Oscillation frequency · RPNNP equation · Shape modes · Spherical harmonics · Volume oscillation

Droplet Oscillation

A liquid droplet free from any other forces except its surface tension forces tends to remain in equilibrium, spherical shape. Oscillations occur when a liquid droplet is forced out of its equilibrium shape. An initially spherical inviscid droplet with radius R that is perturbed by ζ will oscillate according to [1]

$$r = R + \zeta = R + S_n \sin(\omega_n t + \hat{\beta}) \tag{5.1}$$

N. Ashgriz (✉)
Department of Mechanical and Industrial Engineering, University of Toronto, CA
e-mail: ashgriz@mie.utoronto.ca

N. Ashgriz (ed.), *Handbook of Atomization and Sprays*,
DOI 10.1007/978-1-4419-7264-4_5, © Springer Science+Business Media, LLC 2011

where S_n is the surface harmonic of order n (consisting of Legendre polynomials), ω_n is the oscillation frequency of the nth mode and $\hat{\beta}$ is the phase shift. For an inviscid drop, the velocity potentials for the droplet and the fluid surrounding it are ϕ_l and ϕ_g, respectively. These potential functions that satisfy the continuity equation in spherical coordinates are:

$$\phi_l = \frac{\omega_n R}{n} = \frac{r^n}{R^n} S_n \cos(\omega_n t + \hat{\beta}) \quad \text{[internal]} \tag{5.2}$$

$$\phi_g = \frac{\omega_n R}{n+1} \frac{R^{n+1}}{r^{n+1}} S_n \cos(\omega_n t + \hat{\beta}) \quad \text{[external]} \tag{5.3}$$

Similar to the jet and sheet instability, the kinematic boundary condition is written to relate the surface deformation ζ to the velocity potentials (i.e., fluid velocity at the surface is equal to the rate of motion of the surface):

$$\frac{\partial \zeta}{\partial t} = -\frac{\partial \phi_l}{\partial r} = -\frac{\partial \phi_g}{\partial r}.$$

Also, the surface pressures can be determined as:

$$p_l = \frac{\rho_l \omega_n^2 R}{n} S_n \sin(\omega_n t + \hat{\beta}) \tag{5.4}$$

$$p_g = \frac{\rho_g \omega_n^2 R}{n+1} S_n \sin(\omega_n t + \hat{\beta}) \tag{5.5}$$

where ρ_l is the density of the liquid droplet and ρ_g is the density of the surrounding fluid. Surface curvature is:

$$\frac{1}{R_1} + \frac{1}{R_2} = \frac{2}{r} + \frac{n(n+1)}{r^2} \zeta_n = \frac{2}{R} + \frac{(n-1)(n+2)}{R^2} S_n \sin(\omega_n t + \hat{\beta}) \tag{5.6}$$

The pressure boundary condition is now applied to determine the frequency. Because $p_l - p_g = \sigma(1/R_1 + 1/R_2)$, we can obtain:

$$\omega_n^2 = n(n+1)(n-1)(n+2) \frac{\sigma}{\Big[(n+1)\rho_l + n\rho_g\Big] R^3} \tag{5.7}$$

where n is the degree of the spherical harmonic, which is also referred to as the "oscillation mode". If $\rho_g = 0$ (i.e., drop oscillation in vacuum)

$$\omega_n^2 = n(n-1)(n+2) \frac{\sigma}{\rho_l R^3} \tag{5.8}$$

The most important mode of oscillation is $n = 2$, which provides:

$$\omega_2^2 = \frac{8\sigma}{\rho_l R^3}. \tag{5.9}$$

For a water drop, the frequency is $\omega_2 = 0.024\,R^{-3/2}$ vibrations per second. If $\rho_l = 0$, we have bubble oscillation in a liquid with $\omega_n^2 = (n-1)(n+1)(n+2)(\sigma/\rho_g R^3)$.

If the droplet is rotating while oscillating, its oscillation frequency is modified. Busse [2] considered this problem and extended Rayleigh solution to rotating flows. He assumed that rotation-induced shape deformation remained small and axisymmetric. His results for the shift in frequency $\Delta\omega_n$ of axisymmetric oscillation of a liquid drop with angular frequency of rotation of Ω are:

$$\frac{\Delta\omega_n}{\omega_n} = \frac{\omega_n^r - \omega_n}{\omega_n} = \frac{R^3\Omega^2}{\sigma}(A + B) \quad \text{for } \omega_n > 2\Omega$$

where

$$A = 2\left[\frac{\rho_l}{n(n+2)(2n-1)} + \frac{\rho_g}{(n^2-1)(2n+3)}\right]$$

and

$$B = \frac{\rho_l - \rho_g}{6(2n-1)(2n+3)}\left[\frac{n^4 + 2n^3 - 4n^2 - 5n + 6}{(n+2)(n-1)} - \frac{n^2(n+4)\rho_l + (n+1)^2(n-3)\rho_g}{4[\rho_l(n+1) + \rho_g n]}\right]$$

The viscous effects are introduced into this problem by Lamb [3] who observed that in the limiting case of small viscosity μ the results are independent of the nature of the forces, which cause the tendency towards a spherical shape. He provided the following decay time constant τ_d:

$$\frac{1}{\tau_d} = \frac{5\mu}{\rho_l R_0^2} \tag{5.10}$$

If a drop carries a uniformly distributed surface charge Q_s, the modified resonant oscillation frequency is given by:

$$\omega_c^2 = \frac{8\sigma}{\rho_l R^3}\left(1 - \frac{Q_s^2}{64\pi^2 R^3 \sigma \varepsilon_o}\right) \tag{5.11}$$

where $\omega_c = 2\pi\nu_c$ is the angular frequency of a charged drop oscillation, and ε_o is the permittivity of vacuum.

Chandrasekhar [4] provided an analytical solution for the attainment of the spherical drop shape due to the gravity forces. Later, Reid [5] showed that for

arbitrary values of viscosity, the results are the same for gravity and surface tension. For the limiting case of small viscosity, he recovered Lamb's result.

Prosperetti [6] applied an alternate technique, based on the use of Laplace transforms, to the initial value problem of infinitesimal-amplitude oscillations of viscous drops. His results show that the motion consists of modulated oscillations with varying frequency and damping parameter. The frequency of oscillations for small viscosity is given by:

$$\omega_{\mathrm{v}}^2 = \omega_n^2 - b_{\mathrm{v}}^2 \tag{5.12}$$

where $b_{\mathrm{v}} = (n-1)(2n+1)\nu/R^2$. Prosperetti's analysis predicts a transition from periodic to aperiodic decay of oscillations as the viscosity is increased. It is also predicted that for certain ranges of viscosities it is possible for the motion to start as an aperiodic oscillation and then evolve into periodic oscillations.

A nonlinear analytical solution for moderate-amplitude oscillations of inviscid drops is provided by Tsamopoulos and Brown [7]. The frequency of oscillation ω_{l} is found to decrease with the square of the initial amplitude, ε_n. For $n = 2$, 3, and 4, the frequency is given by $\omega_l = \omega_n[1 - \gamma\varepsilon_n^2 + O(\varepsilon_n^4)]$, where $\gamma = 0.63876$ for $n = 2$, $\gamma = 1.04496$ for $n = 3$, and $\gamma = 1.45685$ for $n = 4$. The results also show the coupling between the modes through the second-order solution.

Several other studies have considered large amplitude oscillations [8–15]. Figure 5.1 presents results from a second-mode oscillation of a water droplet,

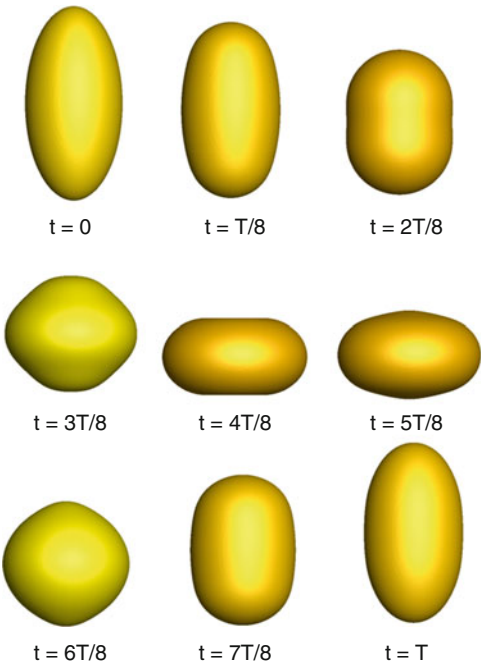


Fig. 5.1 Second mode oscillation of water droplet in air in one period T

which solves the full Navier Stokes equations. The properties are $\rho_1 = 1{,}000$ kg/m^3, $\mu_1 = 10^{-3}$ Pa s, $\rho_g = 1$ kg/m^3, $\mu_g = 2 \times 10^{-5}$ Pa s, and $\sigma = 0.073$ N/m.

Figure 5.2 presents results from a numerical solution of the Navier Stokes equations for a damping oscillation of a viscous droplet released from a third-mode shape, $n = 3$, by Mashayek and Ashgriz [16]. This figure is for a droplet with an Ohnesorge number of $Oh = 0.01$, and the initial amplitude of 0.5, where $Oh = \mu/(\rho\sigma R)^{1/2}$.

Large-amplitude oscillations of a drop subject to the third mode initial deformation exhibit signs of other harmonics. These higher modes can be obtained by decomposing the surface into its harmonics (if a free drop undergoes a small amplitude axisymmetric oscillation in a weak damping limit) as:

$$r(\theta, t) = R + \sum_{n=2}^{\infty} R_n \cos(\omega_n t) P_n(\cos\,\theta) e^{-t/\tau_n} \tag{5.13}$$

where P_n is the Legendre polynomial of order n. The $n = 1$ term was omitted in the equation as it only describes translational movement of the drop. Figure 5.3 shows the temporal evolutions of modes 0–5, for the case considered in Fig. 5.2. During the early stages of oscillation, the primary mode P_3 dominates other modes. In long

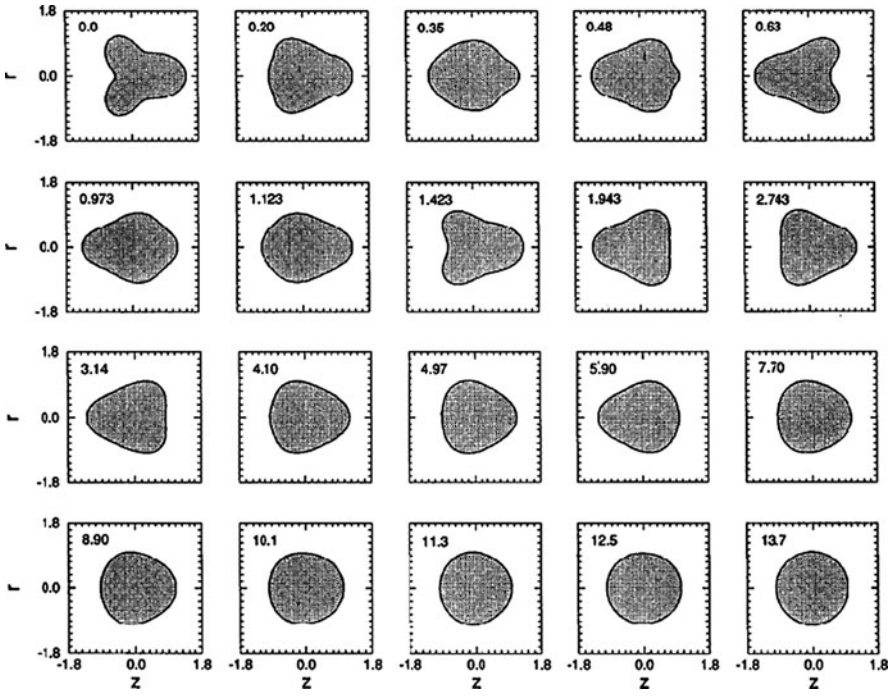


Fig. 5.2 Oscillation of a viscous droplet released from an initial third mode. $Oh = 0.01$, $\varepsilon = 0.5$. Numbers next drops indicate the time [16] (Courtesy of American Institute of Physics)

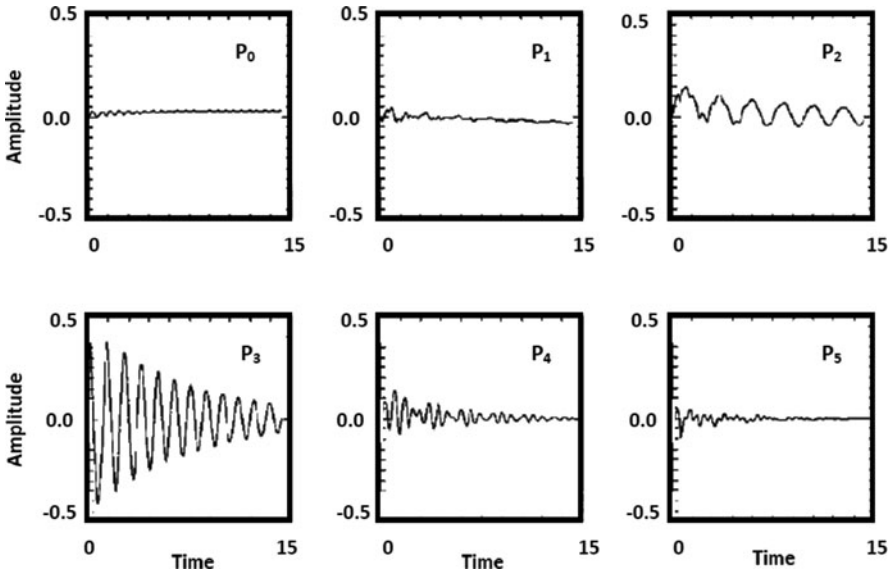


Fig. 5.3 Temporal variation of the amplitude of the fundamental, P_3 and its harmonics for the droplet shown in Fig. 5.2 [16] (Courtesy of American Institute of Physics)

times, the amplitude of all other modes except P_2 is diminished and oscillations are mainly governed by P_2 and P_3. The second mode does not vanish quickly, and, in fact, its amplitude decreases slower than that of the primary third mode. This is due to the irreversible energy transfer between the second and the third modes. During each period of oscillation, part of the surface energy, which is mainly represented by the second and the third modes, is transformed into the kinetic energy. At the end of the period, part of this kinetic energy is dissipated by the viscous effects and the rest is transformed back into the surface energy. It appears that at the end of each surface-to-kinetic-to-surface energy cycle, a larger portion of the energy is restored in the second mode than in the third mode as compared to their corresponding values at the beginning of the cycle.

The studies on the nonlinear oscillation of drops indicate that the second mode oscillation is the dominant mode, and drops released from a static even-mode deformation show an absence of odd harmonics. The effect of viscosity is the damping out of the higher modes faster than the lower ones. The increase in the disturbance amplitude decreases (increases) the frequency (period) of oscillations. The studies [16] have also shown that internal circulations for a drop released from the second spherical harmonic shape results in a small phase shift in the drop oscillation, with frequency remaining almost constant. Relatively large internal circulations, for a drop released from the second spherical harmonic shape results in a significant transfer of energy from the second mode to the fourth mode. For drops released from odd-mode shapes with internal circulations, the energy is mainly transferred to the second mode. Generally, the internal circulation at

"moderate levels" only affects the first few periods, after which the frequency and the decay factor approach those of a drop with no initial internal circulations. Finally, internal circulations tend to transform the drop oscillations initiated from any shape mode to a second-mode oscillation. This may explain why in most practical systems, such as in atomizers, most drops generated by the atomization process attain an ellipsoidal or second-spherical harmonic shapes shortly after detachment from the core liquid.

Other aspects of the drop oscillation problem, such as oscillation of liquid drops immersed in another fluid [17–21], oscillations of pendant drops [22, 23], and oscillations of charged drops [24, 25], have also been considered. In particular, there are numerous works on the oscillation of acoustically levitated drops in acoustic field. In such studies, high-frequency acoustic pressure is required to levitate the droplet and balance the buoyancy force for the experimental studies performed on the Earth. As a result of balance between buoyancy and acoustic forces, the equilibrium shape of the droplet changes from sphere to a slightly flattened oblate shape [26]. Then a modulating force with frequency close to resonant frequencies of different modes is applied to induce small to large amplitude oscillations. Figure 5.4 shows a silicon oil droplet levitated in water and driven to its first three resonant modes by an acoustic force and time evolution for each mode.

Increasing the amplitude of drop oscillation decreases the resonant frequency mainly due to the larger time required between successive oscillations [13, 25]. When the magnitude of the time varying driving force is high enough, in addition

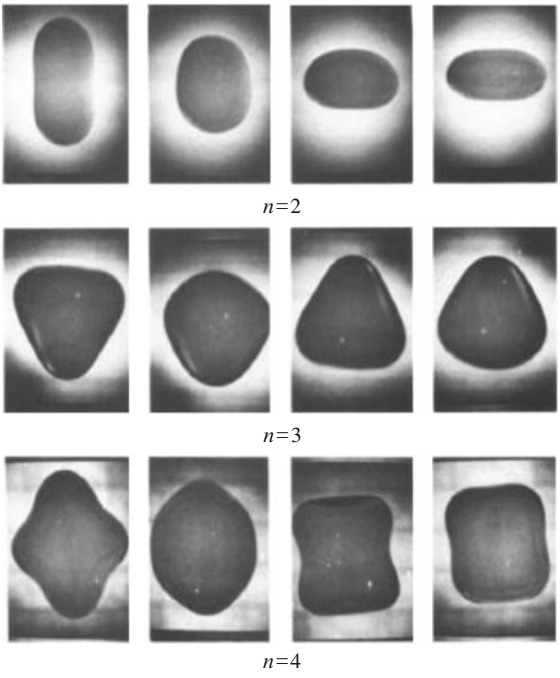


Fig. 5.4 Photographs obtained for a 14 mm diameter silicon oil droplet levitated in water by an acoustic force, first three modes, n = 2, 3, 4 from [21]. 2006 © Cambridge Journals, reproduced with permission

to resonant frequencies coinciding with the forcing frequency, a secondary sub-harmonic resonance is also obtained provided that the forcing frequency is an integer multiple of the resonant frequency. Coupling between modes $n = 2$ and $n = 3$, modes $n = 6$ and $n = 3$, and modes $n = 2$ and $n = 4$ happens due to the energy transfer between these modes [27]. Figure 5.5 illustrates the time variation of the first five harmonics coefficients for a 1.5-cm-diameter silicon oil droplet levitated in water and driven into the $n = 6$ resonant mode of shape oscillation. The sub-harmonic coupling leads to the excitation of the resonant $n = 3$ mode accompanied by a very slight decrease in the amplitude of the response in the $n = 6$ mode. In contrast to free oscillations (Figure 5.3), oscillations do not damp out as long as forcing is applied.

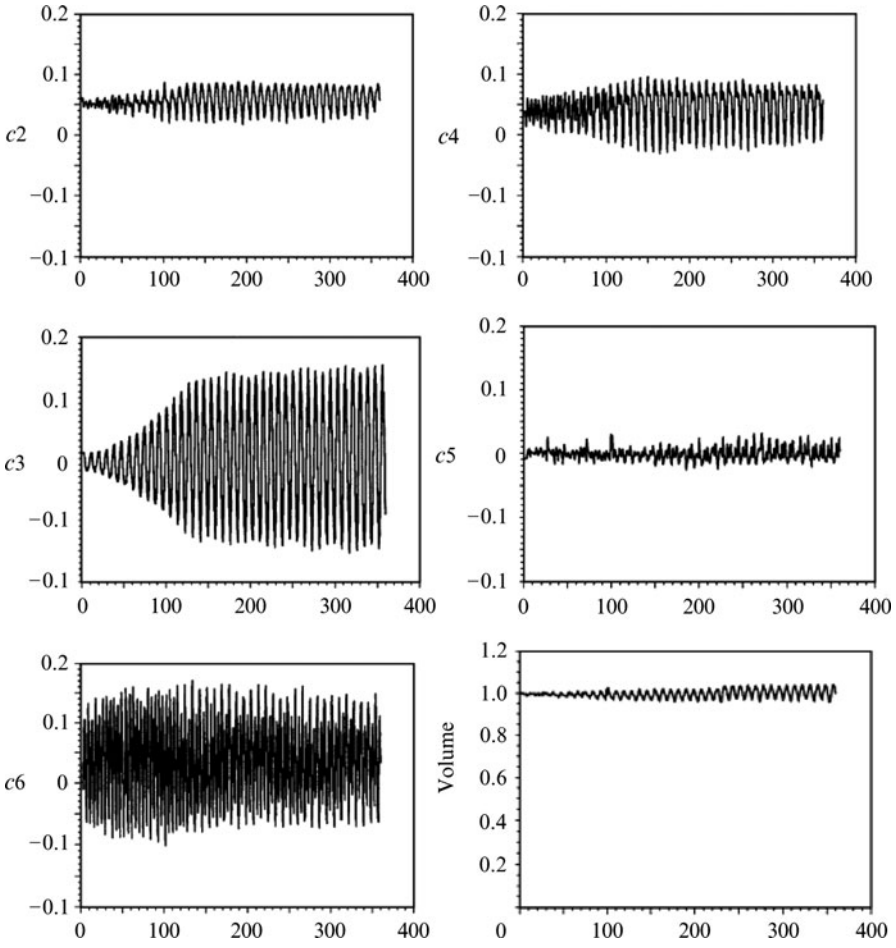


Fig. 5.5 Time variation of first six harmonics coefficients for a 1.5-cm-diameter silicon oil droplet in water driven to its 6th mode by acoustic forcing, the abscissa is time (frame) [27]. 2006 © Cambridge Journals reprinted with permission

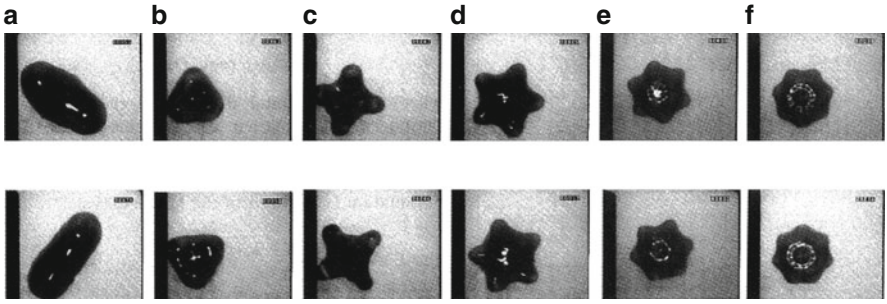


Fig. 5.6 Shape oscillation of a 1 cm diameter water droplet on a vibrating plate. The lower shapes are those after half period. From (**a**) to (**f**) values of n (harmonic mode) increases from 2 to 7 [31] (Courtesy of JPST)

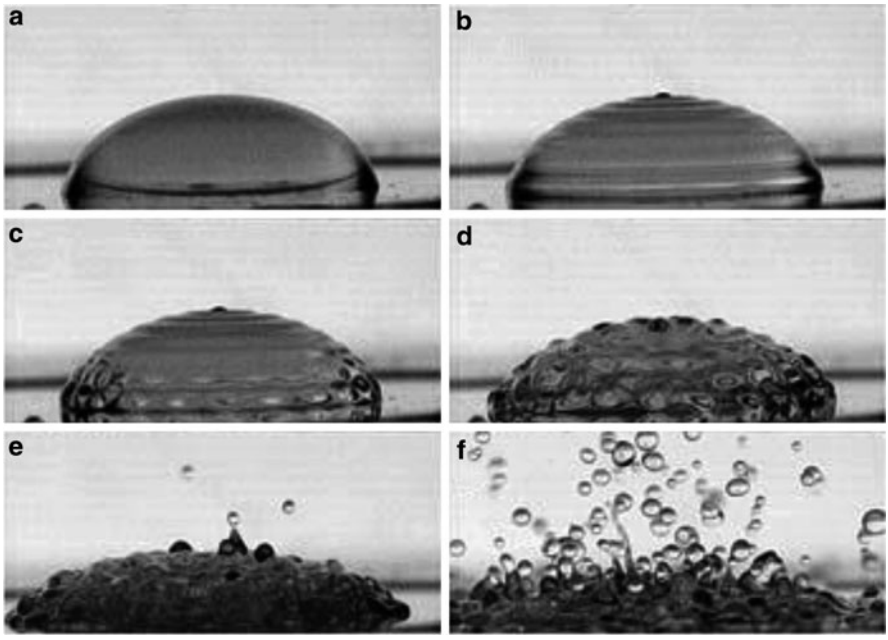


Fig. 5.7 A water drop (8 mm diameter) forced by slowly ramped actuation at frequency of 987 Hz: (**a**) unforced, (**b**) axisymmetric waves, (**c**) coupling of axisymmetric and azimuthal waves, (**d**) pre-ejection state, (**e**) ejection onset, and (**f**) atomization [32], 2003 © Cambridge Journals, reproduced with permission

Other studies have considered oscillations of a liquid droplet placed on a flat plate [28–30]. For instance, Yoshiyasu et al. [31] observed induced polygonal vibrations of a water drop placed on a vertically oscillating plate, relating to the self-induced vibration of a liquid drop as mentioned above (see Figure 5.6). Their study concludes that the axisymmetric polygonal vibration of a drop caused by an oscillating plate is

a kind of parametric vibration, so that the vibration frequency of the drop is half that of the plate. If the vibration amplitude and frequency is above a certain value, depending on droplet properties and size, amplitude of free surface waves grows in time resulting in ejection of smaller droplets from the initial droplet [32]. Figure 5.7 shows the response of a 100 μL water droplet sitting on a vibrating plate with frequency of 987 Hz. In this figure, amplitude of vibration increases from (a) to (f).

Bubble Oscillation

Gas bubbles are relevant to various aspects of the atomization and sprays. In flashing process or flash atomization, bubbles are formed inside the liquid which significantly alter the atomization process (see Chap. 10). Also in effervescent atomizers, high-pressure air is injected inside a liquid and disperses as small bubbles. In addition, bubbles are formed in cavitating nozzles, which significantly alter the atomization process. Gas bubbles go through volume oscillations in addition to shape oscillation discussed in the previous section. In this section, dynamic evolution and stability of a spherical bubble undergoing volume oscillation is discussed.

Rayleigh–Plesset–Noltingk–Neppiras–Poritsky Equation

Consider a single bubble in an infinite liquid which undergoes uniform pressure oscillation. Liquid is assumed to be incompressible and gravity is neglected. Air content of the bubble is assumed to be constant, and heat exchange with the surrounding is neglected. The bubble is saturated with vapor which has the vapor pressure at the liquid temperature. Instantaneous bubble radius is shown by R while the radial distance from the bubble center is denoted by r. Neglecting the mass transfer through the interface, the liquid velocity at the interface is equal to the interface velocity, $u(R,t) = dR/dt = \dot{R}$. The mass and momentum conservation equations in a spherical coordinate system for the liquid yields,

$$u(r,t) = \frac{\dot{R}R^2}{r^2} \tag{5.14}$$

$$\frac{\partial u}{\partial t} + u\frac{\partial u}{\partial r} = -\frac{1}{\rho}\frac{\partial p}{\partial r} \tag{5.15}$$

where p and ρ are liquid pressure and density, respectively. Replacing $u(r,t)$ from (5.14) into (5.15):

$$\frac{\ddot{R}R^2}{r^2} + 2\dot{R}^2\left(\frac{R}{r^2} - \frac{R^4}{r^5}\right) = -\frac{1}{\rho}\frac{\partial p}{\partial r} \tag{5.16}$$

Dynamic boundary condition needed to solve (5.16) is given by the balance of normal forces,

$$p_{\mathrm{v}} + p_{\mathrm{g}}(t) - \frac{2\sigma}{R} = p(R,t) - 2\mu \left.\frac{\partial u}{\partial r}\right|_{r=R} \tag{5.17}$$

where p_{v} is the vapor pressure and p_{g} is the partial pressure of the gas inside the bubble. Assuming adiabatic expansion, instantaneous gas pressure is related to the initial gas pressure by,

$$p_{\mathrm{g}}(t) = p_{\mathrm{g0}} \left(\frac{R_0}{R(t)}\right)^{3\gamma} \tag{5.18}$$

where γ is the ratio of specific heat constants. Replacing (5.18) into (5.17) gives the pressure on the bubble interface,

$$p(R,t) = p_{\mathrm{v}} + p_{\mathrm{g0}} \left(\frac{R_0}{R}\right)^{3\gamma} - \frac{2\sigma}{R} + 2\mu \left.\frac{\partial u}{\partial r}\right|_{r=R} \tag{5.19}$$

Far from the bubble, the liquid is assumed to be at rest ($u_\infty \to 0$), and the liquid pressure is given by $p_\infty(t)$. Integrating (5.16) with respect to r considering the conditions at infinity yields,

$$\frac{p(r,t) - p_\infty(t)}{\rho} = \frac{\ddot{R}R^2}{r} + 2\dot{R}\left(\frac{R}{r} - \frac{R^4}{4r^4}\right) \tag{5.20}$$

On the interface, $r = R$ and equation (5.20) becomes,

$$\frac{p(R,t) - p_\infty(t)}{\rho} = \ddot{R}R + \frac{3}{2}\dot{R}^2 \tag{5.21}$$

Finally, using (5.19) gives the equation for the variation of the bubble radius with the far field pressure change,

$$\rho\left(\ddot{R}R + \frac{3}{2}\dot{R}^2\right) = p_v - p_\infty(t) + p_{go}\left(\frac{R_0}{R}\right)^{3\gamma} - \frac{2\sigma}{R} - 4\mu\frac{\dot{R}}{R} \tag{5.22}$$

Equation 5.22 is known as Rayleigh–Plesset–Noltingk–Neppiras–Poritsky (RPNNP) [33, 34] equation. This equation determines the temporal evolution of the radius of a bubble subjected to a pressure change at infinity. For the case of a nonviscous liquid, the last term on the right-hand side vanishes.

Bjerknes Forces – Application of RPNNP Equation

When a gas bubble is subjected to an acoustic pressure, if the size of the bubble is small enough comparing to the wavelength of the applied pressure, the force on the bubble can be assumed to be symmetric. As a result, bubble responds to such a forcing by symmetric volume oscillations. The time-integral of the pressure force during one period of acoustic oscillation gives the net acoustic force ($F_A = \langle V \times \nabla p \rangle$) which is nonzero because both applied pressure gradient and volume of the bubble oscillate with time. This force is called primary Bjerknes force since it is the primary effect of the external acoustic force on the bubble oscillation. Eller [35] provides the following mathematical description for the primary Bjerknes force,

$$F_A = \frac{2\pi^2 R_0^3 A^2}{3P_0\lambda\left(1-\omega^2/\omega_0^2\right)} \sin\frac{4\pi z}{\lambda} \tag{5.23}$$

where R_0 is the equilibrium radius of the bubble, A is the amplitude of the acoustic pressure, P_0 is the hydrostatic pressure at the location z of the center of bubble, ω is the forcing angular frequency, ω_0 is the resonance angular frequency of the bubble for pure radial pulsation, and λ is the wavelength of the acoustic pressure. In experiments, primary Bjerknes force is used to balance the buoyancy force and trap the bubble inside a liquid. Bjerknes discovered that two pulsating bubbles attract or repel each other when they oscillate, in or out of phase, respectively [36]. The force causing attraction or repulsion is named secondary Bjerknes force. Secondary pressure field produced because of the pulsation of each of the bubbles at the location of the other one is the main source of this force. RPNNP equation is used to derive this force assuming that the bubble is exposed to a periodic pressure field with $p_\infty(t) = P_0 + A\cos(\omega t)$.

Prosperetti [37] has used a linearized form of (5.22) to obtain a harmonic solution for bubble radius variation,

$$R(t) = R_0[1 + \varepsilon\cos(\omega t + \varphi)] \tag{5.24}$$

where the response amplitude, ε, and the response phase shift with respect to the external pressure field, φ, are computed with the following equations,

$$\varepsilon = \frac{A}{\rho\omega_0^2 R_0^2\left(\left(q^2-1\right)^2 + 4\delta^2 q^2\right)^{\frac{1}{2}}} \tag{5.25}$$

$$\varphi = \frac{\arctan\ 2\delta q}{q^2 - 1} \tag{5.26}$$

Here, the frequency index $q = \omega/\omega_0$ and the dimensionless damping coefficient $\delta = \beta/\omega_0$ are defined using the resonance frequency for volume oscillations [38],

$$\omega_0 = \left[3\gamma\left(\frac{p_0}{\rho R_0^2} + \frac{2\sigma}{\rho R_0^3}\right) - \frac{2\sigma}{\rho R_0^3}\right]^{\frac{1}{2}} \tag{5.27}$$

where

$$\beta = \frac{2\mu}{\rho R_0^2} \tag{5.28}$$

Pulsation of a bubble inside a liquid induces a secondary pressure field which can be approximated by [39],

$$p'(r,t) \approx \frac{\ddot{V}}{4\pi r} = \frac{R}{r}(2\dot{R}^2 + R\ddot{R}) \tag{5.29}$$

where V represents the volume of the bubble. To the first order in ε the secondary pressure field induced by bubble pulsation is,

$$p'(r,t) \approx -\frac{\rho\omega^2 R_0^3}{r}\cos(\omega t + \varphi) \tag{5.30}$$

In a two-bubble case, the resulting force on bubble 2 from the pulsation of bubble 1 is calculated from,

$$F_{12} = \langle \nabla p_1'(r,t) \times V_2(t)\rangle = -\frac{2\pi\rho\omega^2 R_{01}^3 R_{02}^3}{r^2}\varepsilon_1\varepsilon_2\cos\varphi\psi(\varepsilon_1,\varepsilon_2,\varphi) \tag{5.31}$$

where $\varphi = \varphi_2 - \varphi_1$ is the phase difference between two pulsations and,

$$\psi(\varepsilon_1,\varepsilon_2,\varphi) = 1 - \frac{\varepsilon_1\varepsilon_2}{\cos\varphi} + \frac{1}{4}(\varepsilon_1^2 + \varepsilon_2^2) + 2\varepsilon_1\varepsilon_2\cos\varphi \tag{5.32}$$

The force on bubble 1 has the same magnitude, but the opposite direction. More details can be found in Barbat et al. [40] and Barbat and Ashgriz [41]. Based on the phase difference between two pulsations, a binary system of bubbles can be classified as:

Nonresonant pair: When φ_1 and φ_2 are both far from $\pi/2$ the interaction force is either attraction or repulsion. There is no equilibrium value for the distance r between the bubbles.

Resonant pair: One phase shift is close to $\pi/2$ and the other approaches π. In this case, the phase difference is $\pi/2$ and attraction force can change to repulsion as the

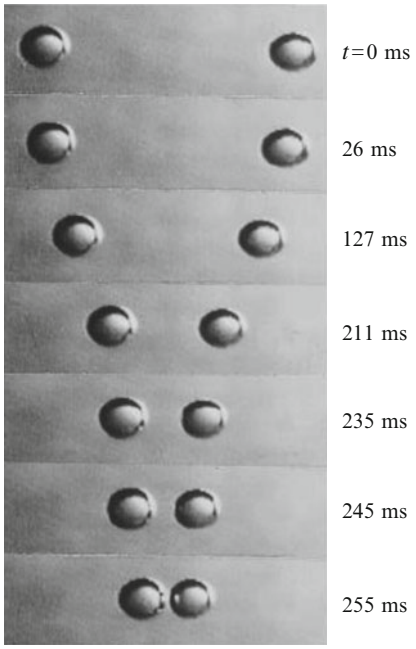


Fig. 5.8 One-dimensional attraction of two oscillating bubbles in acoustic field, $f = 22.5$ kHz, $R_0 = 2$ mm [40]. 2003 © Cambridge Journals, reproduced with permission

bubbles approach each other. Consequently, this case makes it possible to have a stable equilibrium value for bubble separation.

Anti-resonant pair: when for example, $\varphi_1 = \pi/2$ and $\varphi_1 = 0$, if the relative motion starts from an attraction, the attraction pattern is enhanced. If it starts from repulsion, separation force grows.

Two attracting bubbles are shown in Fig. 5.8 [40]. If planar motion of two bubbles is considered based on the interaction force and the relative velocity between two bubbles, closed orbital trajectories are obtained as shown in Fig. 5.9.

Stability of a Spherical Gas Bubble

As the amplitude of the volume oscillation increases, the radial motion of the bubble becomes unstable, and small disturbances cause the bubble to undergo various shape oscillations [42]. As the bubble radius increases, the threshold for the instability decreases. Excitation of different shapes is referenced to as "dancing bubble" motion or "erratic motion".

To analyze the stability of the motion of a pulsating bubble, it is assumed that the bubble with an instantaneous radius of $R(t)$ is distorted slightly by a shape perturbation,

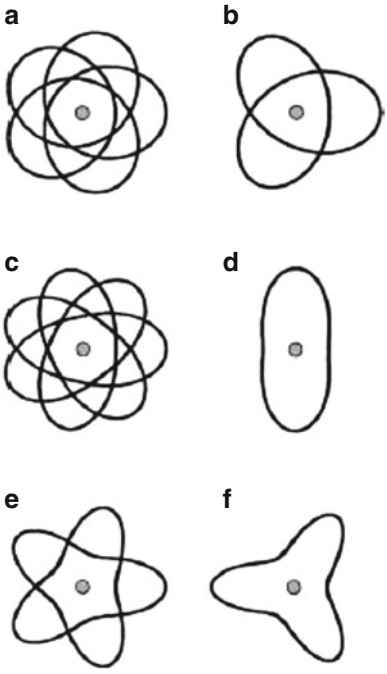


Fig. 5.9 Examples of closed orbital trajectories for a resonant pair of bubbles for different relative velocities [41], (Courtesy of Elsevier)

$$r = r_s(\theta, \phi, t) = R(t) + \sum_{n=2}^{\infty} a_n(t) S_n(\theta, \phi) \tag{5.33}$$

where r, θ, and ϕ are spherical coordinates, r_s is the location of the bubble interface with respect to the center of the bubble, and S_n is a spherical harmonic of order n. The shape distortion consists of a superposition of surface oscillations whose amplitudes are given by $a_n(t)$. The problem is to determine if $a_n(t)$ grows or decays in time. Using (5.33) and RPNNP equation, the following equation is obtained (for details see [42]),

$$\ddot{y}_n + \left[\frac{(n+2)(n^2-1)\sigma}{\rho R^3} - \frac{3}{4}\left(\frac{\dot{R}}{R}\right)^2 - \left(n + \frac{1}{2}\right)\frac{\ddot{R}}{R} \right] y_n = 0 \tag{5.34}$$

where $y_n(t) = R^{3/2} a_n(t)$. Solution for the above equation has the form,

$$y_n = \exp\left(\frac{\tau \omega \mathrm{t}}{2}\right) \sin\left(\frac{jwt}{2} + \varphi\right) \tag{5.35}$$

with $j = 1, 2, 3, \ldots$. This equation describes a shape whose amplitude grows exponentially in time and whose angular frequency is a half integral multiple of the driving angular frequency. The parameter τ is the characteristic exponent, and

φ is a phase angle. Stability analysis shows that the condition for the onset of instability is given by,

$$\tau > \tau_{cr} = \frac{2(n+2)(2n+1)\nu}{\omega R_0^2} \tag{5.36}$$

in which ν is the kinematic viscosity of the liquid. For parameters greater than τ_{cr}, instabilities grow in time leading to excitation of various shapes.

Similar to energy transfer between different shapes of a liquid droplet, coupling between the volume oscillation and different shape oscillations occur for bubbles in acoustic fields [43]. Interaction between modes can lead to chaotic response of the bubble to the external forcing. For a large enough bubble, the spectrum of distortion modes is dense, and several distortion modes attribute to the shape. Development of chaos depends on the number of excited shape modes.

Onset of shape oscillation of a bubble also excites the translational motion of it. Since the forces on the bubble, which govern its translational motion, depend on the shape of the bubble, shape oscillation induces an imbalance on the position of the bubble, and its center of mass starts to move. When equations governing volume oscillations, shape oscillations, and translational motion are solved simultaneously, it reveals that any perturbation in any of these motions, if large enough, can excite other motions. These motions are coupled leading to nonlinear behavior of bubbles under forced oscillation [44]. Excitation of translational motion was also interpreted as "Self-propulsion of asymmetrically vibrating bubbles" by Benjamin and Ellis [45] who used a nonlinear analysis to explain the so-called "erratic motion" of bubble in acoustic fields.

Due to the nonlinear nature of oscillations and translational motion, coupling between these motions makes the behavior of the bubble chaotic. Similar to a double pendulum system which is simply a coupling between two nonlinear motions, coupling between volume oscillations and translational motion, even without considering nonlinear shape oscillations, causes bifurcations in the bubble response. A slight change in the size, frequency, and/or location of the bubble in acoustic field changes the behavior of the bubble drastically. A cascade of bifurcations involving period-doubling bifurcation results in a transition to chaos [46, 47]. Figure 5.10 which is taken from [46] shows the bifurcation cascade and resulting chaotic response of a spherical bubble. R_0 is the equilibrium radius and R_p represents radius of the bubble at integer multiples of oscillation period (T), $R_p = R(t), t = nT$. Oscillation frequency was 20 kHz for an air bubble inside water. When equilibrium radius is small, the bubble response is regular, which means that R_p can be represented by a single point for each R_0. As the equilibrium radius increases, bubble response turns chaotic.

Shape oscillation and translational motion of gas bubbles inside a liquid medium is also achieved in the context of forced vibration of liquid containers with dispersed gas bubbles. Vibration induces an acceleration and effectively a buoyancy force which oscillates in time. Depending on the direction of the applied force, bubbles move in the liquid medium, and since the pressure variation around the bubble is

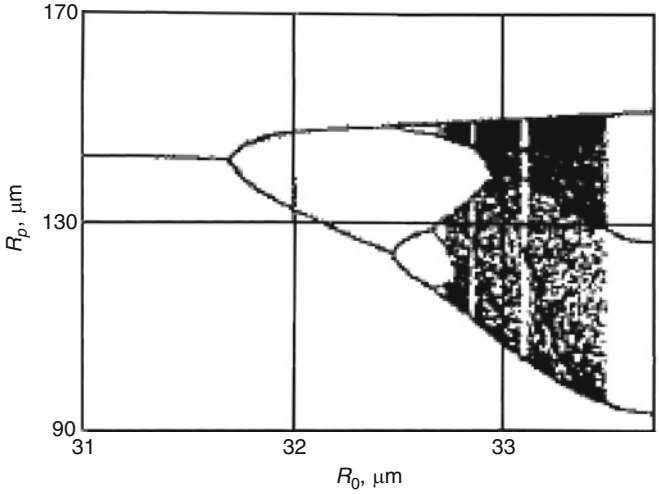


Fig. 5.10 Bubble response to acoustic field, transition from regular to chaotic behavior for an air bubble inside water with an acoustic frequency of 20 kHz [46] (Courtesy of Elsevier)

asymmetric, shape oscillations arise. Similar to what discussed above, coupling between shape oscillation and oscillatory translational motion turns the bubble behavior to chaotic providing that forcing is large enough to excite different harmonics. Since the forcing is applied as a body force, Bond number, $Bo = \rho g D^2/\sigma$, is the proper nondimensional number to describe the ratio of the applied body force to the surface tension force which tends to retain the spherical shape of the bubble. In the above equation, g is the applied acceleration and D is the bubble diameter. As Bo increases, the behavior of the bubble changes from small amplitude regular oscillations to large amplitude chaotic response [48].

If the forcing is large enough, the deformation of bubbles is so large that leads to bubble breakup. This has been observed both in experiments as well as numerical simulations of the bubble motion under forced vibration. Pinching of bubble under forced vibration and its breakup into two parts was reported by Yoshikawa et al [49]. Experiments were done in parabolic flights to reach a microgravity condition to investigate the effect of vibration on bubble deformation. A parametric study was done to investigate the effect of fluid properties and vibration characteristics on the bubble breakup. A study by Movassat et al. [50] showed that under strong forcing, bubble shape changes from an initial sphere, to shapes composed of different harmonics and, finally, a torus shape is achieved. Figure 5.11 illustrates the shape of an air bubble inside water at different times. For this case, $Bo = 0.7$, and the displacement amplitude of oscillations is 4% of the bubble diameter. Inertia force of the water at the bubble centerline is strong enough to penetrate into the bubble ($t = 5T$). Penetration continues so that the bubble shape changes to a torus ($t = 9T$) and the donut-shaped bubble continues to oscillate and its shape changes with the flow field ($t = 11T$).

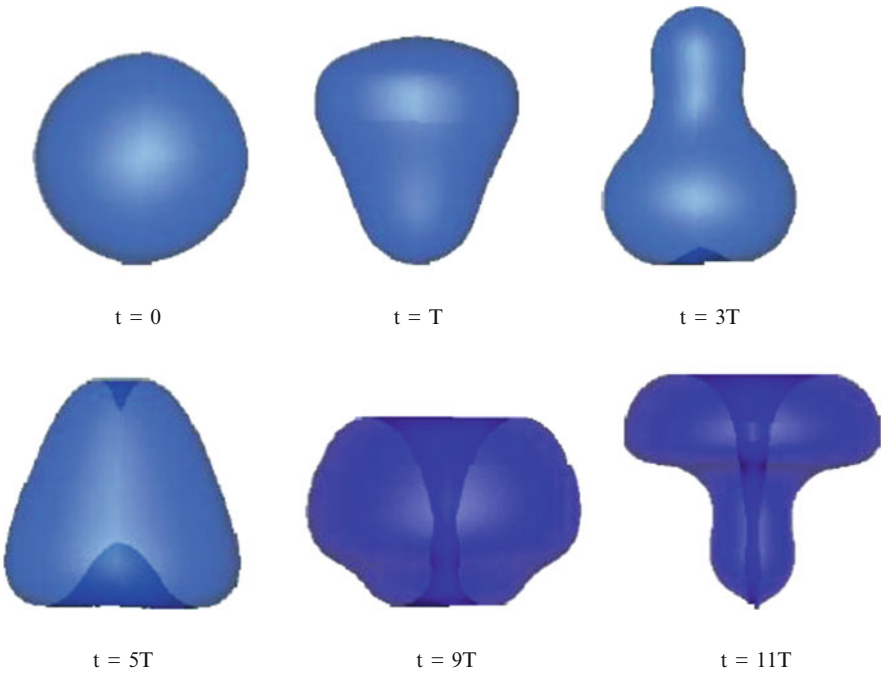


Fig. 5.11 Numerical simulation of bubble under forced vibration. Results for $Bo = 0.7$ based on the imposed acceleration for a 4 mm diameter air bubble inside water. Initial shape is sphere, but different shapes are observed and breakup to a torus shape is achieved

References

1. J. W. S. Rayleigh, On the capillary phenomena of jets, Proc. R. Soc. Lond. **29**, 71, 1879.
2. F.H. Busse, J. Fluid Mech. 142, 1, 1984.
3. H. Lamb, Hydrodynamics, 6th ed. Cambridge University Press, Cambridge, 1932.
4. S. Chandrasekhar, The oscillations of a viscous liquid globe, Proc. Lond. Math. Soc. **9**, 141 1959.
5. W. H. Reid, The oscillations of a viscous liquid drop, Q. Appl. Math. **18**, 86, 1960.
6. A. Prosperetti, Free oscillations of drops and bubbles: the initial-value problem, J. Fluid Mech. **100**, 333, 1980.
7. J. A. Tsamopoulos and R. A. Brown, Nonlinear oscillations of inviscid drops and bubbles, J. Fluid Mech. **127**, 519, 1983.
8. G. B. Foote, A numerical method for studying simple drop behavior: simple oscillation, J. Comput. Phys. **11**, 507, 1973.
9. C. T. Alonso, The Dynamics of Colliding and Oscillating Drops, in Proceedings of the International Colloquium on Drops and Bubbles, edited by D. J. Collins, M. S. Plesset, and M. M. Saffren, Jet Propulsion Laboratory, 1974.
10. T. S. Lundgren and N. N. Mansour, Oscillations of drops in zero gravity with weak viscous effects, J. Fluid Mech. **194**, 479, 1991.
11. T. W. Patzek, R. E. Benner, Jr., O. A. Basaran, and L. E. Scriven, Nonlinear oscillations of inviscid free drops, J. Comput. Phys. **97**, 489 1991.
12. O. A. Basaran, Nonlinear oscillations of viscous liquid drops, J. Fluid Mech. **241**, 169, 1992.

13. E. Trinh and T. G. Wang, Large-amplitude free and driven drop shape oscillations: experimental observations, J. Fluid Mech. **122**, 315, 1982.
14. E. Becker, W. J. Hiller, and T. A. Kowalewski, Experimental and theoretical investigation of large amplitude oscillations of liquid droplets, J. Fluid Mech. **231**, 180, 1991.
15. E. Becker, W. J. Hiller, and T. A. Kowalewski, Nonlinear dynamics of viscous droplets, J. Fluid Mech. **258**, 191, 1994.
16. F. Mashayek and N. Ashgriz, Nonlinear oscillation of liquid drops With internal circulation, Phys. Fluids 10(5), 1071–1082, May 1998.
17. C. A. Miller and L. E. Scriven, The oscillations of a fluid droplet immersed in another fluid, J. Fluid Mech. **32**, 417, 1968.
18. P. L. Marston, Shape oscillation and static deformation of drops and bubbles driven by modulated radiation stresses: theory, J. Acoust. Soc. Am. **67**, 15, 1980.
19. A. Prosperetti, Normal-mode analysis for the oscillations of a viscous liquid drop immersed in another liquid, J. Me´c. **19**, 142, 1980.
20. O. A. Basaran, T. C. Scott, and C. H. Byers, Drop oscillations in liquid-liquid systems, AIChE. J. **35**, 1263, 1989.
21. E. Trinh, A. Zwern, and T. G. Wang, An experimental study of small amplitude drop oscillations in immiscible liquid systems, J. Fluid Mech. **115**, 453, 1982.
22. O. A. Basaran and D. W. Depaoli, Nonlinear oscillations of pendant drops, Phys. Fluids **6**, 2923, 1994.
23. D. W. DePaoli, J. Q. Feng, O. A. Basaran, and T. C. Scott, Hysteresis in forced oscillations of pendant drops, Phys. Fluids **7**, 1181, 1995.
24. J. A. Tsamopoulos and R. A. Brown, Resonant oscillations of inviscid charged drops, J. Fluid Mech. **147**, 373, 1984.
25. E. H. Trinh, R. G. Holt, and D. B. Thiessen, The dynamics of ultrasonically levitated drops in an electric field, Phys. Fluids **8**, 43, 1996.
26. T. Shi and R. E. Apfel, Oscillatiaons of a deformed liquid drop in an acoustic field, Phys. Fluids 7(7), 1545, 1995.
27. E. H. Trinh, D. B. Thiessen, and R. G. Holt, Driven and freely decaying nonlinear shape oscillations of drops and bubbles immersed in a liquid, experimental results, J. Fluid Mech. 364, 253, 1998.
28. N.J. Holter and W.R. Glasscock, Vibrations of evaporating liquid drops, J. Acoust. Soc. Am. **24**, 682, 1952.
29. K. Adachi and R. Takaki, Vibration of a flattened drop. I. Observation, J. Phys. Soc. Jpn. **53**, 4184, 1984.
30. K. Adachi and R. Takaki, Vibration of a flattened drop. II. Normal mode analysis, J. Phys. Soc. Jpn. **54**, 2462, 1985.
31. N. Yoshiyasu, K. Matsuda, and R. Takaki, Self-induced vibration of a water drop placed on an oscillating plate, J. Phys. Soc. Jpn. **65**, 2068, 1996.
32. A. J. James, B. Vukasinovic, M. K. Smith, and A. Glezer, Vibration–induced drop atomization and bursting, J. Fluid Mech. **476**, 1, 2003.
33. L. Rayleigh, The pressure developed in a liquid during the collapse of a spherical cavity, Phil. Mag. **34**, 94, 1917.
34. M. S. Plesset and T. P. Mitchell, On the stability of the spherical shape of a vapor cavity in a liquid, Q. Appl. Math. **13**, 419, 1955.
35. A. I. Eller, Force on a bubble in a standing acoustic wave, J. Acoust. Soc. Am. **43**, 170, 1968.
36. V. F. K. Bjerknes, Fields of Force. Columbia University Press, New York, 1906.
37. A. Prosperetti, Thermal effects and damping mechanisms in the forced radial oscillations of gas bubbles in liquids, J. Acoust. Soc. Am. **61**, 17, 1977.
38. A. Prosperetti, Bubble phenomena in sound fields: part one, Ultrasonics **22**, 69, 1984.
39. A. Prosperetti, Bubble phenomena in sound fields: part two, Ultrasonics **22**, 115, 1984.
40. T. Barbat, N. Ashgriz, and C. Liu, Dynamics of two interacting bubbles in an acoustic field, J. Fluid Mech. **389**, 137, 1999.

41. T. Barbat and N. Ashgriz, Planner dynamics of two interacting bubbles in an acoustic field, Appl. Math. Comput. **157**, 775, 2004.
42. A. I. Eller and L. A. Crum, Instability of the motion of a pulsating bubble in a sound field, J. Acoust. Soc. Am. **47**, 762, 1970.
43. C. C. Mei and X. Zhou, Parametric resonance of a spherical bubble, J. Fluid Mech. **229**, 26, 1991.
44. A. A. Doinikov, Translational motion of a bubble undergoing shape oscillations, J. Fluid Mech. **501**, 1, 2004.
45. T. B. Benjamin and A. T. Ellis, Self-propulsion of asymmetrically vibrating bubbles, J. Fluid Mech. **212**, 65, 1990.
46. I. Sh. Akhatov and S. I. Konovalova, Regular and chaotic dynamics of a spherical bubble, J. Appl. Math. Mech., **69**, 575, 2005.
47. T. Watanabe and Y. Kukita, Translational and radial motions of a bubble in an acoustic standing wave field, Phys. Fluids A. **5**, 2682, 1993.
48. M. Movassat, N. Ashgriz, and M. Bussmann, Bubble dynamics under forced oscillation in microgravity environment, in Proceedings of ASME International Mechanical Engineering Congress and Exposition, November 2009, Lake Buena Vista, FL.
49. H. N. Yoshikawa, F. Zoueshtigh, H. Caps, P. Kurowski, and P. Petitjeans, Bubble splitting in oscillatory flows on ground and in reduced gravity, Eur. Phys. J. E. **31**, 191, 2010.
50. M. Movassat, N. Ashgriz, and M. Bussmann, Three-dimensional numerical simulation of bubble interaction under forced vibration, Presented in COSPAR Meeting, July 2010, Bremen, Germany.

Chapter 6
Droplet Deformation and Breakup

D.R. Guildenbecher, C. López-Rivera, and P.E. Sojka

Abstract Following formation, droplets may enter a region where aerodynamic forces are large enough to cause significant deformation and breakup. When a droplet breaks apart into a multitude of small fragments due to disruptive aerodynamic forces, the process is termed secondary atomization. This has been a rich area of study for many years and a number of in-depth reviews are available [1–4]. Here, the most important findings are discussed. The chapter is divided into two sections: Newtonian and non-Newtonian liquids.

Droplets may be accelerated from rest gently or by a near step change in relative velocity. Experimentation has shown that the breakup is different in each case. The first case is found in nature and plays an important role in rain storms. However, the latter is more likely to occur in sprays. For this reason, this chapter considers only breakup due to step changes in relative velocity.

Keywords: Bag breakup · Breakup mode · Breakup time · Catastrophic breakup · Fragments · Fragment size distribution · Initiation time · Multimode breakup · Newtonian drops · Non-Newtonian drops · Ohnesorge number (*Oh*) · Secondary atomization · Secondary breakup · Sheet-thinning breakup · Total breakup time · Vibrational breakup · Weber number (*We*)

Newtonian Drops

A Newtonian liquid has an approximately linear stress versus strain relation. Many fluids fall in this category including water, alcohol, and most hydrocarbon fuels. Due to their prevalence, the vast majority of secondary atomization studies have been conducted using Newtonian liquids. As a result, most of the available knowledge applies to them.

D.R. Guildenbecher (✉)
Maurice J. Zucrow Laboratories, School of Mechanical Engineering, Purdue University, West Lafayette, IN 47907-2014, USA

N. Ashgriz (ed.), *Handbook of Atomization and Sprays*,
DOI 10.1007/978-1-4419-7264-4_6, © Springer Science+Business Media, LLC 2011

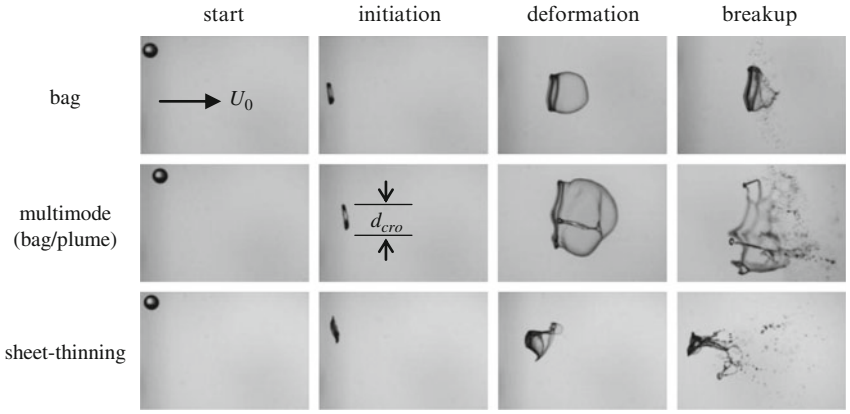


Fig. 6.1 Secondary atomization of Newtonian drops

Figure 6.1 shows typical breakup of Newtonian drops. Time increases from left to right and aerodynamic forces increase from top to bottom. The initial ambient velocity relative to the drop, U_0, acts in the direction shown.

The two most important forces governing the breakup of drops are the disruptive aerodynamic force and the restorative surface tension force. Their ratio results in the nondimensional Weber number:

$$We = \frac{\rho_a U_0^2 d_0}{\sigma} \tag{6.1}$$

Here, ρ_a is the density of the ambient fluid, d_0 is the initial drop spherical diameter, and σ is the surface tension. A larger We indicates a higher tendency toward breakup.

Drop viscosity hinders deformation and also dissipates energy supplied by aerodynamic forces. Both factors reduce the likelihood of fragmentation. This is accounted for by the Ohnesorge number, which represents the ratio of drop viscous forces to surface tension forces:

$$Oh = \frac{\mu_d}{\sqrt{\rho_d d_0 \sigma}} \tag{6.2}$$

Here, ρ_d is the density of the drop and μ_d is the drop viscosity.

Drop viscous forces are found to be significant when $Oh > 0.1$. Below this value, most experimentalists have determined that the process of breakup is essentially independent of Oh.

Many applications of secondary atomization involve air or some other gas of low viscosity as the ambient fluid. Therefore, it is generally found that the resulting phenomena can be explained using the inviscid approximation in the ambient. Such will be assumed here.

Table 6.1 Transition *We* for Newtonian drops with $Oh < 0.1$ [4]

Vibrational (no breakup)	$0 < We < \sim 11$
Bag	$\sim 11 < We < \sim 35$
Multimode	$\sim 35 < We < \sim 80$
Sheet thinning	$\sim 80 < We < \sim 350$
Catastrophic	$We > \sim 350$

Studies involving viscous ambient fluids have been conducted but are not discussed. The interested reader may refer to [1, 3].

The exact manner in which drops fragment is a function of *We*. This is typically represented by a breakup morphology figure as shown in Fig. 6.1, where each row represents a different breakup mode. In the literature, various breakup modes are identified and a wide variety of nomenclature is used. The morphology shown here is a modified version of that proposed in [2].

Although the transition between breakup modes is actually a continuous function of *We*, experimentation and modeling is simplified by assuming the breakup modes occur in the distinct ranges of *We* shown in Table 6.1. The value of *We* demarcating breakup modes is typically referred to as a transitional *We*.

Breakup does not occur instantaneously. Rather the process requires a finite period of time. Knowledge of the breakup time is therefore crucial, especially in rapidly varying processes such as internal combustion engines.

Experimentalists have typically measured two breakup times. Time begins when the drop first enters the disruptive flow field. The initiation time, T_{ini}, is defined at the moment when the deformed drop resembles an oblate spheroid (Fig. 6.1). The total breakup time, T_{tot}, is defined as the moment when the drop and all fragments have reached a stable state and no further breakup occurs.

Time is nondimensionalized by the characteristic transport time given in [5]:

$$T = t\frac{U_0}{\varepsilon^{0.5} d_0} \tag{6.3}$$

Here, T is the nondimensional time, t is the dimensional time, and ε is the drop to ambient density ratio (ρ_d/ρ_a).

Initiation and total breakup times are typically determined from movies of the breakup process. Therefore, judgment is required to identify the appropriate instances. In addition, various definitions for breakup times have been used. As a result, a large amount of scatter is seen in the experimental data and multiple correlations have been proposed [1, 2, 6]. The simplest correlation, which reflects the approximate nature of the results, assumes the nondimensional times are independent of *We* and *Oh* when $Oh < 0.1$ resulting in $T_{ini} \approx 1.5$ and $T_{tot} \approx 5.0$ [4].

As noted by [7], in many high-pressure spray applications, the drop phase approaches the thermodynamic critical point where *Oh* increases rapidly. At elevated *Oh*, the observed breakup modes remain the same, but experiments have shown an increase in the transitional *We* and breakup times.

A few correlations exist for the transitional *We*, although none are known to be accurate much above $Oh > 3$ [4]. One example is given in [8]:

$$We_c = We_{cOh\to 0}\left(1 + 1.077Oh^{1.6}\right) \tag{6.4}$$

Here, $We_{cOh\to 0}$ is the critical We for $Oh < 0.1$. This equation was derived only for the transition from vibrational to bag breakup. However, in [2], the behavior for other transitional We is shown to be similar.

Similarly, no correlation of breakup time is known to be accurate much above $Oh > 0.5$. One example is given in [2]:

$$T_{tot} = \frac{5}{(1 - Oh/7)} \tag{6.5}$$

More work is needed to improve the accuracy of (6.4) and (6.5).

In the pages to follow, each of the breakup modes are discussed in detail. Results and conclusions are presented to aid the designer of spray systems.

Deformation and Vibrational Breakup

When a spherical drop first enters a disruptive flow field, an unequal static pressure distribution over the drop surface causes initial deformation into a shape which resembles an oblate spheroid (Fig. 6.1). Surface tension acts to restore the drop to its initial spherical shape. At low We, this results in droplet oscillation similar to that described in the previous chapter.

In some instances, oscillation may lead to breakup into a few large fragments. This is referred to as vibrational breakup. As noted by [1], this breakup mode does not always occur, proceeds much more slowly than the other modes, and does not lead to small final fragment sizes. As a result, most authors ignore vibrational breakup and consider bag breakup to be the first mode of secondary atomization.

Nevertheless, the study of deformation is important because it has been shown to significantly affect drop drag and hence trajectory. The instantaneous drag force that results in drop deformation can be written as:

$$F_D = \frac{1}{2}\rho_a {U_0}^2 C_D \frac{\pi {d_{cro}}^2}{4} \tag{6.6}$$

where C_D is the instantaneous drag coefficient and d_{cro} is the diameter of the deformed drop in the cross stream direction (Fig. 6.1). Eq. 6.6 requires knowledge of C_D as a function of deformation and d_{cro} as a function of time.

In [2], d_{cro} was found to linearly increase with time until a maximum value is reached at T_{ini}. An approximation for d_{cro} at T_{ini} was given as:

$$\left(\frac{d_{cro}}{d_0}\right)_{max} = 1 + 0.19We^{1/2} \tag{6.7}$$

This equation applies for $We < 10^2$, $Oh < 0.1$.

The drag coefficient of an oblate spheroid has been studied by various researchers and a number of sophisticated correlations have been proposed [2, 9–11]. A simple model derived from linear interpolation between a solid sphere and a solid disk was proposed in [9]:

$$\frac{C_D}{C_{D-sphere}} = (1 + 2.632y) \tag{6.8}$$

Here, $y = 1 - (d_0/d_{cro})^2$ and $C_{D\text{-}sphere}$ is the drag coefficient for a sphere at the same Re.

Equations 6.6, 6.7, and 6.8 can be combined to approximate the deformation and drop trajectory prior to breakup.

Bag Breakup

The goal of atomization is often to create the smallest possible fragment sizes while minimizing energy input. Bag breakup occurs at low We. Therefore, minimal energy is needed to achieve secondary atomization. For this reason, bag breakup is perhaps the most important mode, and the We marking the start of bag breakup has been termed the critical Weber number, We_c. When $Oh < 0.1$, multiple studies have shown that $We_c = 11 \pm 2$ [4].

During bag breakup, separation of the flow around the deformed drop leads to a positive pressure difference between the leading stagnation point and the wake. This tends to blow the center of the drop downstream resulting in the formation of the bag [12]. The outer edge forms a toroidal ring to which the bag is attached.

After some time, the bag bursts into a multitude of fine fragments. Later, the ring breaks up forming a few larger fragments. See the top row of Fig. 6.1.

In one study [13], the mean diameter of the fragments formed from ring breakup was 30% of the original drop diameter while the mean diameter of the fragments formed from breakup of the bag was approximately 4% of the original drop diameter. The larger fragments dominate subsequent evaporation rates, which are crucial to the performance of many spray-related systems.

Sheet-Thinning Breakup

Sheet-thinning breakup occurs at higher relative velocities (We) than bag breakup, and proceeds in a markedly different fashion. Following initial deformation, a sheet is formed at the periphery of the drop. The sheet evolves into ligaments that break up into a multitude of small fragments. The process continues until the drop is completely fragmented, or until it has accelerated to the point at which aerodynamic

forces are negligible. In the latter case, a core drop remains at the completion of secondary atomization [2]. The third row in Fig. 6.1 illustrates typical sheet-thinning breakup.

Early experimentalists observed the stripping of the liquid sheet and hypothesized that this mode was caused by shear due to viscous forces in the ambient [5]. As a result, this mode was called shear stripping. However, this explanation contradicts the inviscid assumption. Nevertheless, the term persists in much of the literature.

An alternative explanation, which is consistent with the inviscid approximation, was given in [14]. It was hypothesized that ambient phase inertia causes the periphery of the deformed drop to be deflected in the direction of the flow, thereby forming a sheet. Following this, the sheet breaks into ligaments and then individual fragments. This mechanism seems to be confirmed by recent numerical simulations [15].

Multimode Breakup

Multimode breakup occurs at values of *We* between those of bag- and sheet-thinning and resembles a combination of the two breakup modes. Bag formation accompanied by the presence of a core drop results in the formation of a long ligament in the center of the bag, which is referred to as a stamen or plume [1, 16]. The third image in the second row of Fig. 6.1 illustrates the bag/plume structure.

Other breakup structures have also been observed to occur in the multimode regime. One example is the plume/sheet-thinning morphology identified in [16]. Nevertheless, all of these structures can be thought of as resembling some combination of bag- and sheet-thinning breakup.

To date, no definitive explanation exists for why bag breakup occurs at low levels of aerodynamic forces and sheet-thinning breakup occurs at higher levels. Some have proposed that unstable surface waves dictate the breakup modes. However, as discussed in [4], this explanation fails to fully explain all of the modes and is not supported by recent numerical simulations. Other possibilities may include a competition between internal flow in the deforming drop and surface tension [4], or strong backflow in the wake at high *We* which prevents bag growth [12]. More research is warranted.

Catastrophic Breakup

At extremely high *We*, some researchers have observed the formation and growth of unstable surface waves on the leading edge of the deformed drop. Eventually, these waves penetrate the drop causing breakup into a multitude of fine fragments.

These waves are hypothesized to be of the Rayleigh–Taylor type, which form due to the acceleration of the dense drop into the lighter ambient. Some authors have had success correlating the predicted wavelength to experimental observations [17, 18].

Catastrophic breakup has only been observed in shock tube experiments where extremely high initial relative velocities are possible. In [7], it is noted that such high velocities are not expected in typical dense sprays. Therefore, the practical applications of this breakup mode are limited.

Fragment Size Distribution

Regardless of breakup mode, the final product of secondary atomization is a collection of fragments with some size distribution, knowledge of which is crucial for determining subsequent evaporation rates and for characterizing target interactions.

Fragment size distributions have been difficult to measure. Among the viable methods are rapid solidification of the fragments and holography. Both are time consuming, difficult to set up, and results are hard to analyze.

Recently, the commercial availability of PDA and other optical drop-sizing methods have resulted in more rapid and accurate measurements. However, to be practical these devices require a continuous spray process so are not handy for single drop experiments. This is because their measurement volumes are typically small compared to the region through which fragments pass. As a result, only limited experimental data exist and more research is warranted.

Drop-size distributions are often described by characteristic diameters [19]:

$$D_{pq} = \left[\frac{\int_0^\infty D^p f_0(D) dD}{\int_0^\infty D^q f_0(D) dD} \right]^{1/p - q} \tag{6.9}$$

where p and q are positive integers and $f_0(D)$ is the number probability density function (PDF). Common characteristic diameters include the arithmetic mean diameter, D_{10}, the volume mean diameter, D_{30}, and the Sauter mean diameter, D_{32}.

Simmons [20, 21] studied drop-size distributions for sprays formed using a large number of aircraft and industrial gas turbine nozzles where secondary atomization is thought to play a crucial role in determining the final size distribution. The fragment mass median diameter (MMD) and D_{32} were found to be related by $\text{MMD}/D_{32} \approx 1.2$. In addition, given either MMD or D_{32}, the fragment volume PDF, $f_3(D)$, could be approximated as root-normal. Finally, the maximum fragment size was found to be approximately three times MMD.

In [2, 22], holography was used to measure drop-size distributions for $Oh < 0.1$. In the bag and multimode regimes, the root-normal distribution with $\text{MMD}/D_{32} \approx 1.2$ fit

the data reasonably well. Furthermore, after removal of the drop core, this same distribution was found to be applicable in the sheet-thinning regime.

The last piece of knowledge needed to determine drop-size distributions a priori is either MMD or D_{32}. In [23], a correlation was proposed based on the analysis of the physics of bag breakup:

$$We_{D_{32}} = C[We(T_{tot} - T_{ini})]^{2/3} \tag{6.10}$$

Here, $We_{D32} = \rho_a D_{32} U_0^2/\sigma$ and $C \approx 0.32$.

As mentioned, the previous correlations were taken from a limited amount of experimental data. Therefore, they should be applied with caution. More work is needed to confirm their accuracy.

Some have attempted to avoid this problem by determining the fragment size distribution from theory. However, these methods are not without problems.

One example is the maximum entropy formalism (MEF), which assumes the final distribution is that which maximizes the entropy production. A detailed discussion is given in [24]. In general, the method is able to calculate the correct shape of the distribution. However, experimental results are needed to obtain the magnitude. At the current time, no method is predictive without some experimental input [4].

In summary, fragment size distributions are crucial to the performance of many spray devices. The correlations given here can be used for estimates. Nevertheless, these estimates should not be used in place of laboratory measurements.

Non-Newtonian Drops

In marked contrast to Newtonian liquids, only a few researchers have considered non-Newtonian drops. This is somewhat surprising since non-Newtonian liquids are encountered as paints, hair care products, foodstuffs, thermal barrier coatings, and, most recently, gelled fuels. They are popular because their rheological behavior can yield low effective viscosity during spray formation (high rate of strain) and a high effective viscosity when on a target (low rate of strain). However, this desirable rheological characteristic adds complexity and causes their secondary breakup behavior to differ from that of Newtonian drops [17, 25–30].

The paucity of non-Newtonian secondary breakup studies means there is not enough data to provide a clear consensus as to either common characteristics (modes) or processes (mechanisms). As a result, the morphology of non-Newtonian liquid drops undergoing secondary breakup is still uncertain.

In addition, transition boundaries between breakup modes have yet to be quantified as functions of We, and the corresponding Oh scaling at these boundaries has not been determined. In fact, only recently has non-Newtonian breakup behavior been related to We [17]. Obviously, these results are preliminary and much work remains to be done.

It also remains unclear as to which dimensionless groups play dominant roles in the purely viscous and viscoelastic cases of non-Newtonian drop breakup. As such, dependence of transition *We* on other nondimensional parameters is unavailable.

The initial and total breakup times also need to be determined, as well as fragment size distribution information. Unanswered questions include: "Does Simmons' scaling rule (MMD/$D_{32} \approx 1.2$) hold for non-Newtonian drop secondary breakup?" and "Will non-Newtonian drop secondary breakup produce a root-normal fragment size distribution?"

The few studies focused on secondary breakup of non-Newtonian drops are reviewed below.

Breakup Modes

The first stage of breakup is deformation of the drop into a shape that resembles an oblate spheroid (see Fig. 6.2). Given the similarity to Newtonian drops, it is reasonable to assume that the same physical mechanisms apply, namely, unequal static pressure distribution over the drop surface.

Note, however, the clear differences observed when comparing Figs. 6.1 and 6.2.

In the bag breakup case, non-Newtonian drops produce both a noticeable rim and a number of stream-wise ligaments. The ligaments are sometimes located on the windward side of the drop core, and sometimes on the leeward side. In the former case, the bag blows out, the rim disintegrates, and the ligaments break up. In the latter case, the bag is blown downstream and disintegrates first, forming a net of filaments. The filaments undergo breakup, as does the toroidal rim [28, 29]. The ligaments always form many large fragments.

The sheet-thinning mechanism observed for non-Newtonian drops resembles that observed for Newtonian liquids in some aspects. For instance, it is found at

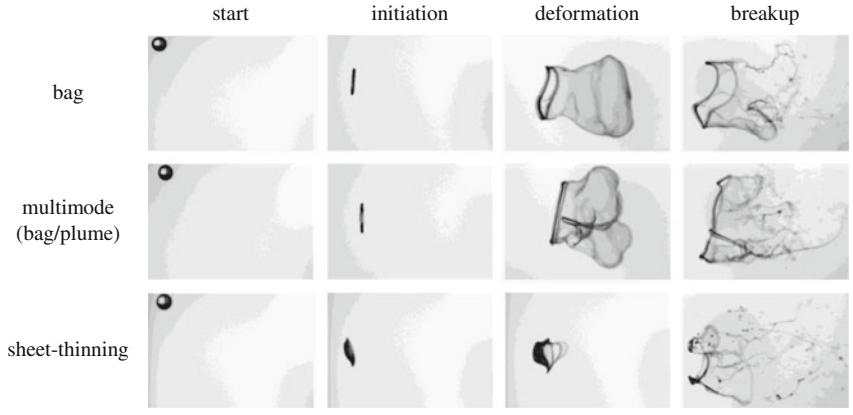


Fig. 6.2 Secondary atomization of non-Newtonian drops

initial relative velocities higher than those necessary to observe multimode breakup. It begins with drop deformation, followed by continuous ligament erosion from the surface of the drop. These ligaments disintegrate rapidly into numerous small fragments.

Contrary to Newtonian drop behavior, [27–28] observed that once ligaments peeled off the drop surface they were joined together by a thin sheet. The sheet expanded and the ligaments elongated and extended downstream undergoing additional splitting.

Increases in non-Newtonian behavior were observed to produce increases in the thickness of the ligaments and sheets [27], and to increase the distance from the main droplet over which ligaments are linked [28]. This distance was also found to decrease with air velocity.

Non-Newtonian liquids also exhibit a transitional multimode regime between bag and sheet-thinning breakup. It is important to note that only bag/plume-type breakup has been observed. Other breakup structures discussed in the Newtonian section have not been observed for non-Newtonian drops. It is unclear if this is due to a lack of available data or some rheological difference.

In the multimode case, non-Newtonian drops form a much more pronounced stamen that has a much longer lifetime. This stamen eventually forms many large fragments when it finally breaks up. In the sheet-thinning case, non-Newtonian breakup proceeds through two steps – the thinning of the sheet followed by the drop core forming a bag that experiences multimode breakup.

Finally, in contrast to Newtonian liquids, catastrophic breakup is particularly important for non-Newtonian drops because extremely high relative velocities are often required for fragmentation to occur. This mechanism has been investigated by [17], where it was concluded that Rayleigh–Taylor instabilities are the cause of non-Newtonian drop catastrophic breakup. Support for this conclusion comes from comparison of experimental results with a (purely viscous) Rayleigh–Taylor analysis for both the critical wavelength and growth rate. The agreement between theory and experiments is within a few percent and is perhaps surprising since their analysis is purely viscous, therefore ignoring elastic effects entirely. This also suggests that their non-Newtonian liquids had characteristic times much greater than those of the breakup events, and so should not be categorized as elastic for the purposes of secondary breakup.

Regardless of breakup morphology, [17] demonstrated that early drop motion obeys a constant acceleration model. Therefore, (6.6) and (6.8) can be applied directly to the calculation of the initial drop trajectory. However, (6.7) requires modification for the case of non-Newtonian liquids. Unfortunately, experimental deformation data is currently unavailable. Analytical models, such as the TAB model or its derivatives, discussed in Chap. 7, could be modified to include purely viscous or viscoelastic non-Newtonian effects. However, this has yet to be done and as a result the accuracy of such a modification is unknown.

There is no information available for non-Newtonian We_c. Groups like [27–28] have declined to correlate their data in terms of We because they claim that We cannot be easily defined due to the shear-dependent viscosity of their fluids.

Breakup Times

No groups are known to have reported T_{ini} for non-Newtonian liquids. Few have reported T_{tot}.

T_{tot} was defined by [27] as the time it takes for a drop to reduce to mist. Their results showed that increases in polymer concentration led to increases in T_{tot}.

A theoretical breakup time, t_b, has been reported by [17]:

$$t_b = \frac{1}{n_t} \ln(M) \tag{6.11}$$

In this expression, n_t is the growth rate and M is given by $M = A(t_b)/A_0$ where A_0 is the initial amplitude of an unstable disturbance, $A(t)$, and $A(t_b)$ is the unstable disturbance at t_b.

Finally, [29] applied the expression reported by [17] and observed that viscoelastic liquids start to break up faster than the purely viscous ones that exhibit similar values of viscosity.

Fragment Size Distribution

One of the few studies supplying non-Newtonian liquid fragment sizes is that performed by [30]. These authors observed that fragments of solutions with polymers added were 1.5 orders of magnitude larger than fragments produced by Newtonian liquids.

Similarly, the experimental results of [25] showed that measured fragment MMD was an order of magnitude larger than values predicted for a Newtonian fluid of similar viscosity magnitude. Their results were found to correlate with a relaxation time obtained from a die swell experiment. From this, it was thought that breakup does not follow a shear mechanism, but an elongation one instead. These findings were supported by [26].

References

1. M. Pilch, C. A. Erdman: Use of Breakup Time Data and Velocity History Data to Predict the Maximum Size of Stable Fragments for Acceleration-Induced Breakup of a Liquid Drop, Intl. J. Multi. Flow 13(6), 741–757 (1987).
2. L. P. Hsiang, G. M. Faeth: Near-Limit Drop Deformation and Secondary Breakup, Intl. J. Multi. Flow 18(5), 635–652 (1992).
3. B. E. Gelfand: Droplet Breakup Phenomena in Flows with Velocity Lag, Prog. Energy Comb. Sci. 22(3), 201–265 (1996).
4. D. R. Guildenbecher, C. López-Rivera, P. E. Sojka: Secondary Atomization, Exp. Fluids 46(3), 371–402 (2009).

5. A. A. Ranger, J. A. Nicholls: Aerodynamic Shattering of Liquid Drops, AIAA J. 7(2), 285–290 (1969).
6. B. E. Gel'fand, S. A. Gubin, S. M. Kogarko, S. P. Komar: Singularities of the Breakup of Viscous Liquid Droplets in Shock Waves, J. Engr. Phys. 25(3), 1140–1142 (1975).
7. G. M. Faeth, L. P. Hsiang, P. K. Wu: Structure and Breakup Properties of Sprays, Intl. J. Multi. Flow 21, 99–127 (1995).
8. R. Brodkey: The Phenomena of Fluid Motions, Addison-Wesley, Reading, MA, Chap. 17-1 C (b) Breakup of Drops (1967).
9. A. B. Liu, D. Mather, R. D. Reitz: Modeling the Effect of Drop Drag and Breakup on Fuel Sprays, SAE 930072 (1993).
10. B. T. Helenbrook, C. F. Edwards: Quasi-Steady Deformation and Drag of Uncontaminated Liquid Drops, Intl. J. Multi. Flow 28(10), 1631–1657 (2002).
11. B. J. O'donnell, B. T. Helenbrook: Drag on Ellipsoids at Finite Reynolds Numbers, Atom. Sprays 15(4), 363–375 (2005).
12. J. Han, G. Tryggvason: Secondary Breakup of Axisymmetric Liquid Drops. II. Impulsive Acceleration, Phys. Fluids 13(6), 1554–1565 (2001).
13. W. H. Chou, G. M. Faeth: Temporal Properties of Secondary Drop Breakup in the Bag Breakup Regime, Intl. J. Multi. Flow 24(6), 889–912 (1998).
14. Z. Liu, R. D. Reitz: An Analysis of the Distortion and Breakup Mechanisms of High Speed Liquid Drops, Intl. J. Multi. Flow 23(4), 631–650 (1997).
15. S. Khosla, C. E. Smith, R. P. Throckmorton: Detailed Understanding of Drop Atomization by Gas Crossflow Using the Volume of Fluid Method, Toronto, Canada (2006).
16. Z. Dai, G. M. Faeth: Temporal Properties of Secondary Drop Breakup in the Multimode Breakup Regime, Intl. J. Multi. Flow 27(2), 217–236 (2001).
17. D. D. Joseph, J. Belanger, G. S. Beavers: Breakup of a Liquid Drop Suddenly Exposed to a High-Speed Airstream, Intl. J. Multi. Flow 25(6–7), 1263–1303 (1999).
18. S. S. Hwang, Z. Liu, R. D. Reitz: Breakup Mechanisms and Drag Coefficients of High-Speed Vaporizing Liquid Drops, Atom. Sprays 6(3), 353–376 (1996).
19. R. A. Mugele, D. H. Evans: Droplet Size Distribution in Sprays, Ind. Engr. Chem. 43(6), 1317–1324 (1951).
20. H. C. Simmons: The Correlation of Drop-Size Distributions in Fuel Nozzle Sprays Part I: The Drop-Size/Volume-Fraction Distribution, J. Engr. Power, 309–314 (1977).
21. H. C. Simmons: The Correlation of Drop-Size Distributions in Fuel Nozzle Sprays Part II: The Drop-Size/Number Distribution, J. Engr. Power, 315–319 (1977).
22. L. P. Hsiang, G. M. Faeth: Drop Properties after Secondary Breakup, Intl. J. Multi. Flow 19(5), 721–735 (1993).
23. K. L. Wert: A Rationally-Based Correlation for Mean Fragment Size for Drop Secondary Breakup, Intl. J. Multi. Flow 21(6), 1063–1071 (1995).
24. E. Babinsky, P. E. Sojka: Modeling Drop Size Distributions, Prog. Energy Comb. Sci. 28(4), 303–329 (2002).
25. J. E. Matta, R. P. Tytus: Viscoelastic Breakup in a High Velocity Airstream, J. Appl. Polym. Sci. 27, 397–405 (1982).
26. J. E. Matta, R. P. Tytus, J. L. Harris: Aerodynamic Atomization of Polymeric Solutions, Chem. Engr. Commun. 19, 191–204 (1983).
27. C. Arcoumanis, L. Khezzar, D. S. Whitelaw, B. C. H. Warren: Breakup of Newtonian and Non-Newtonian Fluids in Air Jets, Exp. Fluids 17, 405–414 (1994).
28. C. Arcoumanis, D. S. Whitelaw, J. H. Whitelaw: Breakup of Droplets of Newtonian and Non-Newtonian Fluids, Atom. Sprays 6, 245–256 (1996).
29. D. D. Joseph, G. S. Beavers, T. Funada: Rayleigh-Taylor Instability of Viscoelastic Drops at High Weber Numbers, J. Fluid Mech. 453, 109–132 (2002).
30. J. D. Wilcox, R. K. June, H. A. Brown, R. C. Kelley: The Retardation of Drop Breakup in High-Velocity Airstreams by Polymeric Modifiers, J. Appl. Polym. Sci. 5(13), 1–6 (1961).

Chapter 7
Droplet Collision

G. Brenn

Abstract We put together the state of knowledge on binary collisional interactions of droplets in a gaseous environment. Phenomena observed experimentally after drop collisions, such as coalescence, bouncing, reflexive separation and stretching separation, are discussed. Collisions of drops of the same liquid and of different – miscible or immiscible – liquids, as well as collisions of drops of equal and different size are addressed. Collisions of drops of immiscible liquids may lead to an unstable interaction which is not observed with drops of equal or miscible liquids. Regimes characterized by the various phenomena are depicted in nomograms of the Weber number and the non-dimensional impact parameter. The state-of-the-art in the simulation of binary droplet collisions is reviewed. Overall three different methods are represented in the literature on these simulations. We discuss models derived from numerical simulations and from experiments, which are presently in use for simulations of spray flows to account for the influence of collisional interactions of the spray droplets on the drop size spectrum of the spray.

Keywords Binary drop collisions · Bouncing · Coalescence · Collision model · Crossing separation · Gaseous environment · Immiscible liquids · Lattice-Boltzmann simulation · Miscible liquids · Navier–Stokes simulation · Reflexive separation · Satellite droplets · Spray flow simulation · SPH simulation · Stretching separation

Introduction

The present chapter puts together the state of knowledge about the collisional interaction of liquid droplets and gives an overview of the literature on experiments, as well as on simulation and modeling of binary liquid droplet collisions, both as an elementary phenomenon and also in the context of spray flows.

G. Brenn
Graz University of Technology, Institute of Fluid Mechanics and Heat Transfer, Graz, Austria
e-mail: brenn@fluidmech.tu-graz.ac.at

N. Ashgriz (ed.), *Handbook of Atomization and Sprays*,
DOI 10.1007/978-1-4419-7264-4_7, © Springer Science+Business Media, LLC 2011

We restrict this review to the case of binary collisions, i.e., to the processes caused by the impact of pairs of liquid droplets. Collisions of three or more droplets are much less investigated, since in spray flows they are much less probable than the binary case. Furthermore, the biggest part of this review will be devoted to droplets of Newtonian liquids. Investigations on collisions of non-Newtonian liquid droplets are very sparse in the literature, as will be discussed in more detail below. Also, since we are in the context of spray flows, we do not discuss collisions of droplets in another immiscible liquid host medium, but take the ambient medium as gaseous.

The importance of droplet collisions in dispersed gas-liquid two-phase flows with the liquid as the dispersed phase has been first recognized in the context of rainfall [1–5]. The first investigations on the effects of droplet collisions on liquid droplet ensembles emerged from the meteorological research on the evolution of clouds. The most important aspect of the collisional interaction of droplets in this context is the stability or instability of a collision, i.e., if the colliding drops merge and form a new stable drop with a volume equal to the sum of the volumes of the two original droplets, or if they separate and either maintain their original volumes or form droplets smaller than the original ones [6–25]. All research on droplet collisions concentrates on the description of the sizes of the droplets after the collision and does not put much emphasis on their velocities, since the velocity may be much more affected by aerodynamic forces from the gaseous host medium than by the collisional interaction itself. Furthermore the droplet size spectrum is the spray property of primary importance for the technological application of the sprays. Our present review therefore concentrates on this aspect.

Experimental Setups Used for Investigations of Drop Collisions

The droplet properties influencing droplet collisions are liquid physical properties as well as the size, velocity and trajectories of the droplets. From this we may conclude on the requirements to an experimental setup suitable for use in experimental studies of drop collisions. The equipment must include:

- Two droplet generators producing drops of controlled size and velocity
- Two reservoirs for supplying the test liquid(s)
- Manipulators allowing for control of the droplet trajectories and, in particular, the impact parameter
- A visualization system with illumination, either synchronized with the drop formation to produce standing pictures of the drops, or providing single short-time pulses for single-shot images
- A technique for measuring droplet diameter, either optical (e.g., phase-Doppler anemometry) or based on image processing

A setup with the essential components mentioned above, enabling experimental studies of droplet collisions, is shown in Fig. 7.1 [26]. In the literature we find

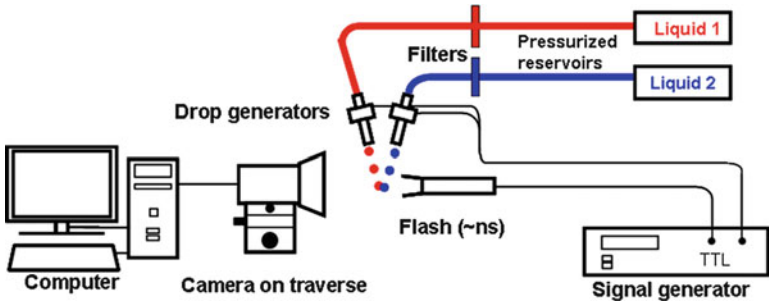


Fig. 7.1 Experimental setup for drop collision studies [26] (Reprinted from Colloids and Surfaces A – Physicochemical and Engineering Aspects. doi 10.1016/j.colsurfa.2009.12.011 (2009), Planchette, Lorenceau, Brenn, Liquid encapsulation by binary collisions of immiscible liquid drops, Copyright 2009, with permission from Elsevier)

a majority of works employing continuous-stream droplet generators for producing the colliding drops [27, 28]. Some researchers produced streams of electrically charged drops, intercepted by drops with different charge. The charged drops were deflected by a plate capacitor into a collector, while the drops with the different charge were removed from the streams and entered the collision region (Adam et al. [29]). The latter method had the advantage that the collision of pairs of single droplets could be realized and observed, without restriction of the largest allowable deformation due to neighboring drops in streams. Droplet generators used in the various studies worked on principles as reviewed in Chap. 10 of this handbook.

An important aspect in the collisional interaction of droplets is the influence of the ambient gaseous medium, which is mostly air. The influence of the gas pressure on the collisions has been subject of some studies (e.g., Qian and Law [30]), extending down to the case of vacuum [31, 32]. This kind of studies requires, of course, a vessel in which the droplet generators are placed, with the possibility to manipulate them from outside.

We now turn to a discussion of knowledge acquired by experiments on binary droplet collisions for various droplet liquids and sizes.

Phenomena in Binary Droplet Collisions

This part of our review summarizes the physical phenomena in binary liquid droplet collisions found in experimental investigations.

The collisional interaction of two liquid droplets, equal or unequal in size, is in general a complicated process, which does not allow for a theoretical description by analytical means. Typically, experimentalists provide insight into the regularities of the phenomena in such processes in the form of flow charts. The flow charts for binary droplet collisions known from the literature are nomograms depicting regimes characterized by certain mechanisms or phenomena occurring after the impact.

The independent variables in these charts emerge from the parameters influencing the collision process: the relative velocity U of the colliding droplets, the sizes d_s and d_l of the smaller and the larger droplet, the impact parameter b (i.e., the distance of closest approach of the centers of mass of the droplets, measured normal to the direction of the relative velocity, as sketched in Fig. 7.2), as well as the density ρ and dynamic viscosity μ of the droplet liquid and its surface tension σ against the ambient gas. This list of seven relevant parameters results in the following set of four characteristic numbers: the non-dimensional impact parameter $X = 2b/(d_s + d_l)$, the drop size ratio $\Delta = d_s/d_l$, the Ohnesorge number $\mathrm{Oh} = \mu/[\sigma\,(d_s + d_l)\,\rho/2]^{1/2}$, and the Weber number $\mathrm{We} = U^2(d_s + d_l)\rho/2\sigma$. Most flow charts represent the flow regimes for a given liquid system with known ρ, μ, and σ, and a given size of the colliding droplets, i.e., for constant Ohnesorge number. For simplicity, in the present section we restrict our discussion to colliding drops of equal (and constant) size d, so that the remaining set of parameters is represented by flow charts with the Weber number $\mathrm{We} = U^2 d\rho/\sigma$ as the abscissa variable and the non-dimensional impact parameter $X = b/d$ as the ordinate variable. A generic form of such a flow chart is shown in Fig. 7.3 [33]. This kind of a nomogram represents the droplet behavior for constant Ohnesorge number, i.e., with a given liquid and for constant drop size. A classification of the regimes of collision mechanisms specifies ranges of values of

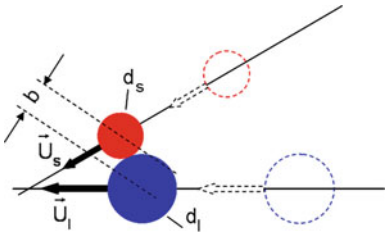


Fig. 7.2 Sketch of a collision of two drops of unequal size. The impact parameter b is measured normal to the direction of the relative velocity $\vec{U} = \vec{U}_s - \vec{U}_l$

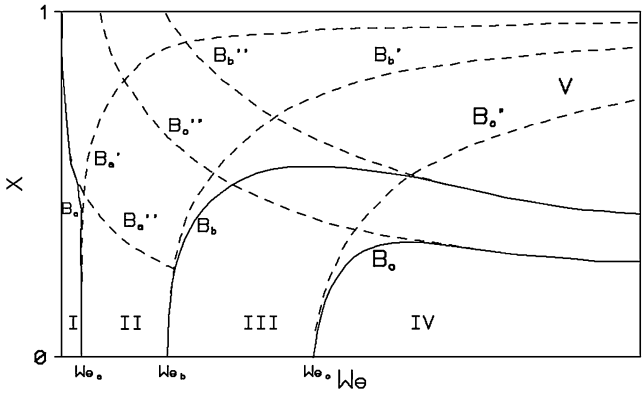


Fig. 7.3 Nomogram for binary collisions of equal-sized droplets for constant Ohnesorge number [33] (Reprinted with permission from [33], Copyright 1997 American Institute of Physics. Adapted from [34])

the Weber number We and the non-dimensional impact parameter X. Collisions with zero or reasonably small impact parameter are called *head-on collisions* or *near-head-on collisions*, respectively. For impacts with sufficiently large non-dimensional collision parameter, which are called *grazing collisions*, the system formed after the encounter is unstable and breaks up into two or more droplets.

We now discuss the phenomena observed after the collision of two droplets, associating typical values of We and X to them. The actual range of values of the characteristic numbers specifying the regimes discussed certainly depends on the pairing of the liquid and its ambient gas investigated, and on the drop size. The values of We and X we name are just typical values. Representative pictures of the processes are displayed in Fig. 7.4 [34]. We discuss the phenomena in the sense of increasing impact Weber number We. Starting at low values of the Weber number less than, say, 4, we find that the result of the drop collision is *coalescence* of the impacting droplets for all values of the impact parameter (Figs. 7.4a and b, regime I in Fig. 7.3). This means that, for this range of Weber numbers, colliding droplets always merge and form one larger drop with a volume equal to the sum of the two colliding droplets' volumes. Such a collision may be termed as stable in the sense that the deformation upon impact does not cause instability and disruption of the newly formed common surface of the liquid system. Collisions of this type have an influence on the drop size spectrum in a spray, since they make drops of given sizes disappear and produce larger drops.

With increasing value of the Weber number, a new phenomenon occurs, which is characterized by *bouncing* back of the drops after the impact (Fig. 7.4c, regime II in Fig. 7.3). This phenomenon occurs for all values of the impact parameter (Fig. 7.4d, regime II in Fig. 7.3). The reason for the occurrence of this mechanism is believed to be the inclusion of portions of the ambient gas between the droplets upon impact, which prevents the formation of a common surface of the colliding droplets. This inclusion of gas becomes possible due to the deformation of the drop surfaces upon approach of the droplets at a kinetic energy which is higher with this mechanism than in the collisions followed by coalescence in regime I. Numerical studies showed that it is the build-up of gas pressure between the two approaching droplets that may flatten the two sides of the droplets facing each other upon approach and cause bouncing. The reason for the pressure build-up is the gas flow resistance against drainage from the gap between the droplets [35]. This interpretation of the findings from the simulations is consistent with the experiments of Willis and Orme in a vacuum, where the build-up of a pressure is impossible and, consequently, bouncing was not observed [31]. It is interesting to note that, in cases of bouncing back of the colliding droplets, there is no mass transfer between the two droplets [36]. Due to obvious methodological difficulties, both in experiments and in numerical simulations, the physical reasons for the occurrence of this mechanism are not clarified in full detail yet. Bouncing of the droplets typically occurs in the range of Weber numbers between 4 and 10. It occurs for all values of the non-dimensional impact parameter X.

In collisions at Weber numbers greater than, say, 10, we observe that, for moderate non-dimensional impact parameter, the droplets merge and form one common drop (Figs. 7.4e and f, regime III in Fig. 7.3). The newly formed drop

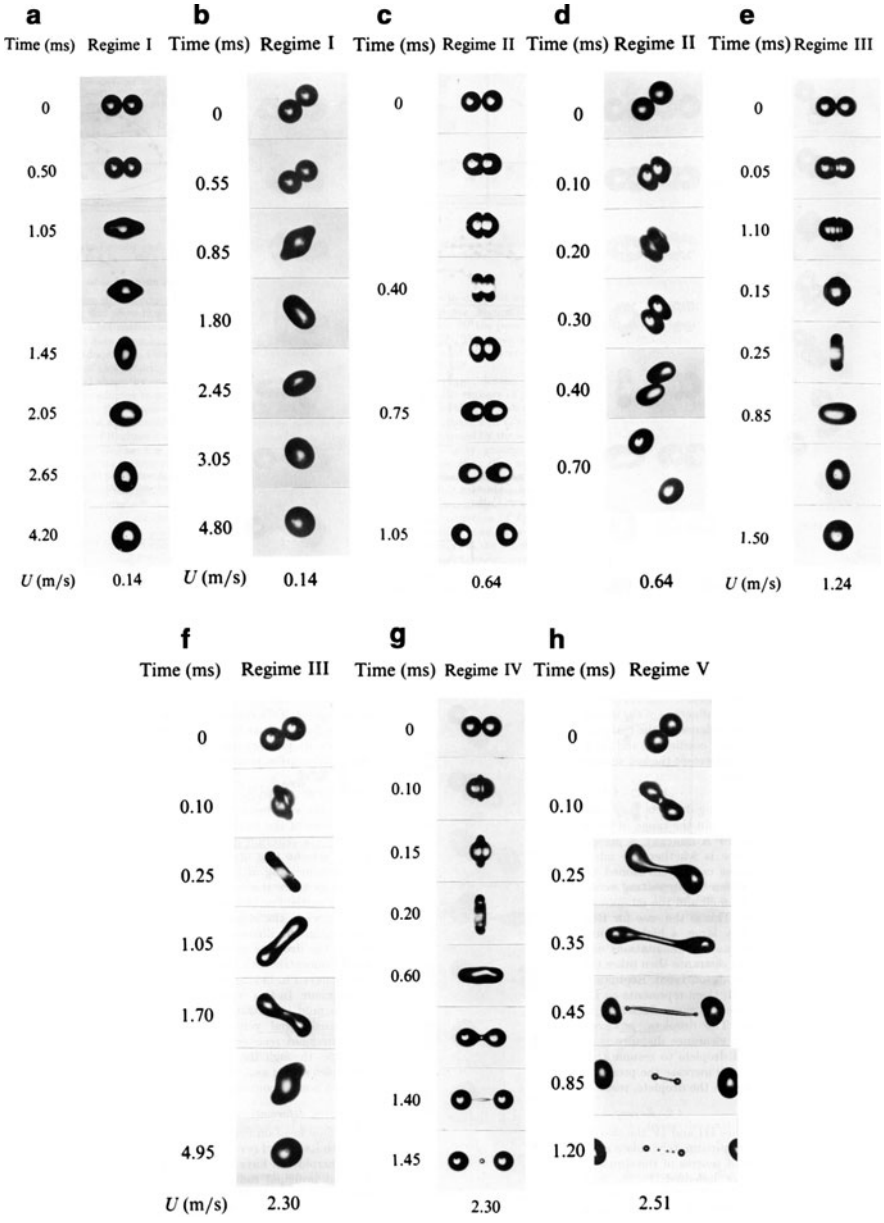


Fig. 7.4 Mechanisms in binary collisions of equal-sized droplets of the same liquid: (**a**) coalescence at low Weber numbers, head-on (regime I); (**b**) coalescence at low Weber numbers, grazing (regime I); (**c**) bouncing, head-on (regime II); (**d**) bouncing, grazing (regime II); (**e**) coalescence at higher Weber number, head-on (regime III); (**f**) coalescence at higher Weber number, grazing (regime III); (**g**) reflexive separation, head-on (regime IV); (**h**) stretching separation (regime V) [34]. Regimes referring to Fig. 7.3 ([34] Copyright, Cambridge Journals, reproduced with permission)

remains stable after the collision. The deformation-induced oscillations of the free surface are dampened, and the result is a spherical merged drop. The stability of this collision, however, is ensured only for sufficiently small non-dimensional impact parameter below, say, 0.5. The mechanism observed for parameters $X > 0.5$, which leads to break-up of the system formed by the collision, is called *stretching separation*, since it includes the formation of a liquid bridge or filament between the bulks of the colliding droplets, which is stretched due to the inertia-dominated motion of the droplets, eventually separates from the remaining portions of the original droplets, and breaks up into satellite droplets (Fig. 7.4h, regime V in Fig. 7.3) [37, 38]. If more than two droplets are formed by this process, all new droplets are smaller than the colliding droplets. The number of (satellite) droplets produced by the break-up of the liquid filament formed in stretching separation depends on the length of the liquid filament, i.e., on the Weber number and non-dimensional impact parameter. The onset value of the non-dimensional impact parameter for stretching separation typically decreases with increasing Weber number. The break-up of the filament into the satellite droplets follows a different mechanism for small and for large values of the impact parameter [38]. At small impact parameters, the mechanism is end-pinching, while it is a mixture of capillary wave growth and end-pinching for large impact parameters. The range of non-dimensional impact parameters leading to stretching separation is wide throughout the relevant range of collision Weber numbers, so that the occurrence of this mechanism is very probable for droplet collisions in sprays. This process influences a spray by making large drops disappear and producing droplets with small sizes, which is an influence on the drop size spectrum contrary to the effect of coalescence.

For still increasing value of the Weber number, a new phenomenon occurs for head-on and near-head-on collisions. A typical value of the onset Weber number for this phenomenon is 30. For these collisions, the stability of the liquid system formed by the encounter is lost, even at very low values of the non-dimensional impact parameter below, say, 0.3. In such collisions, the kinetic energy of the colliding drops is high enough to cause substantial deformations which lead to break-up of the liquid system, often into three droplets. This mechanism is called *reflexive separation* and is restricted to small values of the non-dimensional impact parameter (Fig. 7.4g, regime IV in Fig. 7.3). With increasing non-dimensional impact parameter, the dissipative influence of the increasing shear forces stabilizes the system, so that stable coalescence may occur. For sufficiently high non-dimensional impact parameter, however, stretching separation (regime V) is again observed.

The last mechanism to be discussed is characteristic of encounters of pairs of droplets with very high Weber number. This mechanism leads to large deformations of the drops upon impact, and to irregular break-up of the liquid system formed after the collision. It is called *droplet shattering*. The onset Weber number for this mechanism may be of the order of, say, 400, which is outside the range of Weber numbers investigated in most studies on droplet collisions. Exceptions are, e.g., the studies by Roth et al. [39], and by Willis and Orme [31, 32], where Weber numbers significantly greater than 2,000 are investigated. It is interesting to note that, in the vacuum environment of the experiments by Willis and Orme, shattering

collisions were not observed, despite the large Weber numbers of the collisions. This finding sheds light on the role of the gaseous environment in droplet shattering. Nonetheless, this mechanism is much less investigated than all the others, and, due to the irregular nature of the break-up after impact, its description in terms of drop sizes produced after the collision puts more difficulties than all the other mechanisms found in binary droplet collisions.

Equal and Unequal-Sized Droplets from the Same Liquid

Collisions of equal-sized droplets of the same liquid are the best investigated case in the present context. Regimes of the occurrence of the mechanisms discussed in section Phenomena in Binary Droplet Collisions are well known and explored for various liquids, such as water as well as simple alcohols and hydrocarbons up to the order of hexadecane.

The far more probable case in the collisional interaction of droplets in sprays, however, is the impact of droplets with different sizes. The literature on this case is much more sparse than for equal-sized droplets, but there exist results for certain values of the ratio $\Delta = d_s/d_l$ of the small to the large drop sizes. The most important kind of results are nomograms indicating the various regimes of the above discussed post-collisional mechanisms, which determine the outcome of the collision in terms of drop sizes and velocities. From these charts, mathematical descriptions of the regime boundaries are extracted, which may be used as criteria for the occurrence of the various mechanisms. Important examples for this kind of results are, e.g., the works by Adam et al. [29], Ashgriz and Poo [36], Jiang et al. [34], Qian and Law [30], and Estrade et al. [40, 41]. These authors investigate different liquids, such as water, *n*-alkanes and other hydrocarbons, and ethanol. Figures 7.5a–c show regimes as reported by Ashgriz and Poo [36], Qian and Law [30], and Estrade et al. [40], respectively.

Any mathematical representation of the regime boundaries must necessarily be limited to the liquids and drop sizes investigated, and provides information on the given liquid system in the given gaseous environment only. One model that accounts for the influence of the Ohnesorge number on the stability limit against stretching separation and on the formation of satellite droplets is due to Brenn and Kolobaric [38]. Here we present some equations describing limits between some regimes of different mechanisms. For their water droplets, Ashgriz and Poo [36] described the boundary between coalescence and reflexive separation as

$$We = \frac{3\Delta\left[7\left(1+\Delta^3\right)^{2/3} - 4\left(1+\Delta^2\right)\right]\left(1+\Delta^3\right)^2}{\left(\Delta^6\eta_1 + \eta_2\right)} \tag{7.1}$$

where $\eta_1 = 2(1-\xi)^2\,(1-\xi^2)^{1/2} - 1$, $\eta_2 = 2(\Delta-\xi)^2\,(\Delta^2-\xi^2)^{1/2} - \Delta^3$, with $\xi = 0.5X(1+\Delta)$. This equation was based on a formulation of the reflexive kinetic energy.

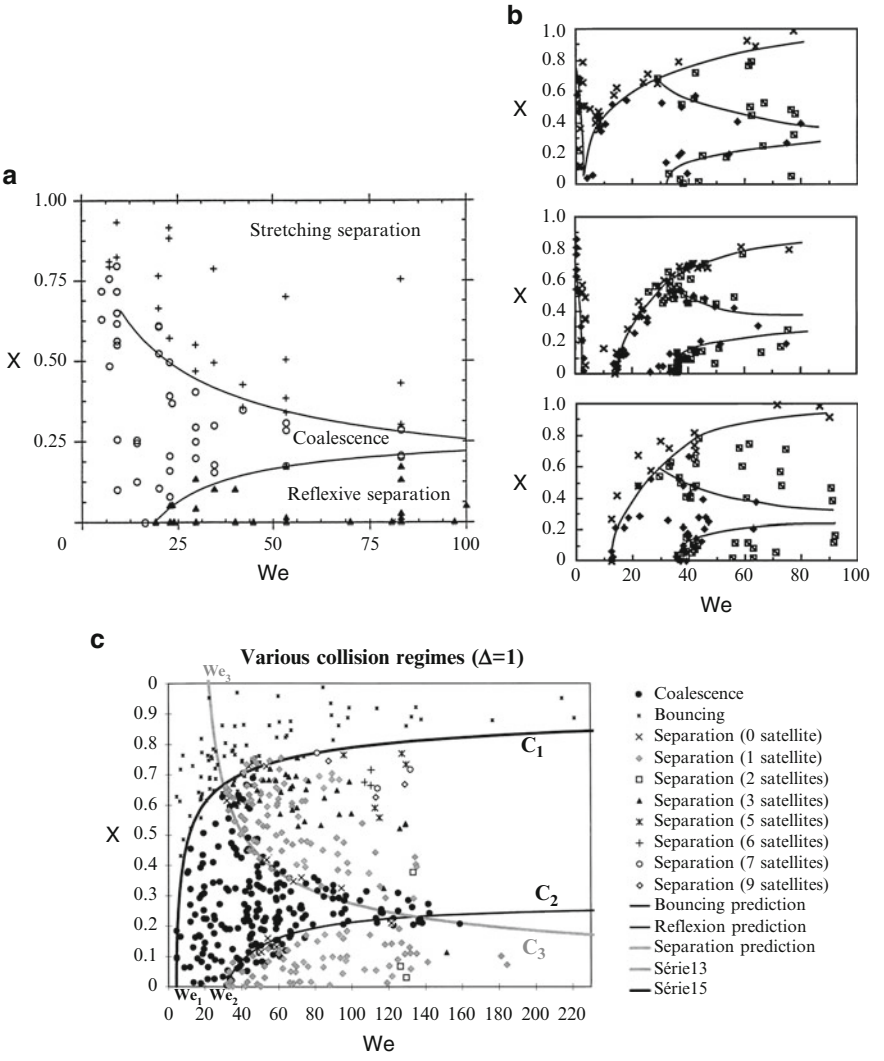


Fig. 7.5 Regimes of mechanisms determining the outcome from binary collisions of equal-sized droplets from various liquids: (**a**) regimes of coalescence, stretching separation and reflexive separation for water drops in air at atmospheric pressure [36]; (**b**) regimes of coalescence, bouncing, and reflexive separation for tetradecane droplets at the ambient nitrogen pressures of 0.6, 1, and 2.4 atm [30]; (**c**) regimes of coalescence, bouncing, reflexive separation and stretching separation for ethanol droplets in air at atmospheric pressure [40] ([30, 36] Copyright, Cambridge Journals, reproduced with permission. Reprinted from [40], Copyright 1999, with permission from Elsevier)

The authors postulate that this energy must be greater than 75% of the nominal surface energy of a nominal spherical combined mass formed after the collision for reflexive separation to occur. The equality in (7.1) represents the case where the 75% threshold is just reached. In an analogous way, Ashgriz and Poo [36]

obtain for the boundary between stable coalescence and stretching separation the criterion

$$We = \frac{4\left(1+\Delta^3\right)^2\left[3(1+\Delta)(1-X)\left(\Delta^3\phi_s+\phi_l\right)\right]^{1/2}}{\Delta^2\left[\left(1+\Delta^3\right)-(1-X^2)\left(\phi_s+\Delta^3\phi_l\right)\right]} \tag{7.2}$$

where

$$\phi_s = \begin{cases} 1-\dfrac{1}{4\Delta^3}(2\Delta-\tau)^2(\Delta+\tau) & \text{for } h>d_s/2 \\ \dfrac{\tau^2}{4\Delta^3}(3\Delta-\tau) & \text{for } h<d_s/2 \end{cases} \tag{7.3}$$

and

$$\phi_l = \begin{cases} 1-\dfrac{1}{4}(2-\tau)^2(1+\tau) & \text{for } h>d_l/2 \\ \dfrac{\tau^2}{4}(3-\tau) & \text{for } h<d_l/2 \end{cases} \tag{7.4}$$

with $\tau = (1 - X)(1 + \Delta)$ and $h = (d_l + d_s)(1 - X)/2$. This boundary compares favorably with experimental data and agrees better than the corresponding relations by Brazier-Smith et al. [42] and Arkhipov et al. [43, 44].

Equal-Sized Droplets from Different Miscible Liquids

Literature on the collision of droplets from different liquids is very sparse to date [45–48]. Gao et al. [45] investigated the collision of equal-sized droplets of water and ethanol, i.e., of two miscible liquids, in monodisperse streams produced by two piezoelectric drop generators. The drop sizes ranged between 400 and 600 μm. The authors provide a flow chart similar to that in Fig. 7.5a, where the Weber number is defined with the relative velocity of the colliding drops and the liquid properties of ethanol. The maximum value of the Weber number realized is 100. Upon contact between the droplet surfaces, the surface tension of the water decreases due to the presence of the ethanol. This leads to a Marangoni effect (called Unbalanced Surface Force [USF]) by Gao et al. [45]. At high non-dimensional impact parameters, this effect elongates the water drop and promotes its break-up into two portions, even at low Weber numbers. At intermediate non-dimensional impact parameters, the formation of a liquid finger is observed, which may pinch off and form a droplet if the impact Weber number is high enough. Finally, for head-on collisions, coalescence of the colliding drops or reflexive separation with formation of at least one satellite due to the "USF" are observed (Fig. 7.6). This field of research is still at its beginning to date.

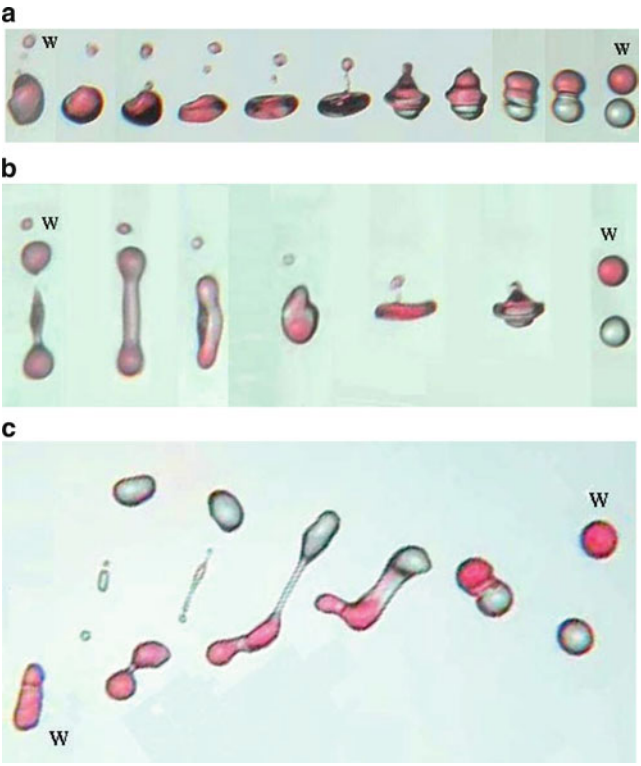


Fig. 7.6 Collisions of a water and an ethanol drop: (**a**) head-on collision with coalescence and separation of one satellite (We = 20, $X = 0$); (**b**) reflexive separation with formation of a small satellite due to Marangoni forces ($We = 38.5, X = 0.02$); (**c**) stretching separation with formation of three satellite droplets ($We = 82.3, X = 0.82$). Droplets move from right to left; the water droplet coming from above is marked with "w" [45] (With kind permission from Springer Science+Business Media: Experiments in Fluids [45], Plates 3, 5 & 6, Copyright Springer-Verlag 2005)

Equal-Sized Droplets from Different Immiscible Liquids

What was said about the state of knowledge on collisions of different miscible liquid drops applies to the case of immiscible liquids also. We find the work by Chen and Chen [49], who investigated the collision of equal-sized droplets of water and Diesel oil. The dynamic viscosities and surface tensions of the two liquids against air at the temperature of the experiments are different by a factor of 3.1 and 2.6, respectively. Drop sizes, produced with the same piezoelectric droplet generators as in Gao et al. [45], ranged between 700 and 800 μm. The result of an experimental survey of the outcome from the collisions for varying impact Weber number and non-dimensional impact parameter is a flow chart similar to that in Fig. 7.5a, where the Weber number is defined with the relative velocity of the colliding drops and the liquid properties of Diesel oil. The boundaries between the

regimes of bouncing, coalescence, reflexive separation, and stretching separation shown in the graph are sharp and convincing (Fig. 7.7). The maximum value of the Weber number realized is 100. What comes in as a new mechanism further to the well known ones with drops of equal or different, but miscible, liquids is a phenomenon called "overlaying action" by Chen and Chen [49]. By that mechanism, the Diesel oil encapsulates the water and forms a thin layer on top of the water drop. Such a process is observed in the head-on configuration ($X = 0$) from Weber numbers of 18.6 on. Three cases of head-on collisions with coalescence are shown in Fig. 7.8 [49]. In their paper, the authors do not undertake any modeling efforts.

One point should be made about the identification of a reflexive separation case in paper [49]. Reflexive separation is defined as an unstable post-collision mechanism that separates the droplets collided at near-head-on impact parameters. In this mechanism, the bulk masses of the colliding droplets remain on the sides of the symmetry plane from where they had approached (therefore "reflexive" separation). In the case shown in Fig. 7.9, however, which is identified as "single reflex separation" by Chen and Chen [49], the dyed drop changes its side from above (before collision) to below the symmetry plane (after collision), and the transparent drop moves vice versa. The actual mechanism therefore implies a mutual penetration of the liquid portions in the collided complex, which is not reflexive separation. This mechanism was called "crossing separation" by Planchette et al. [26] and by Planchette and Brenn [50], since the two liquid portions cross the trajectories of their respective collision partners.

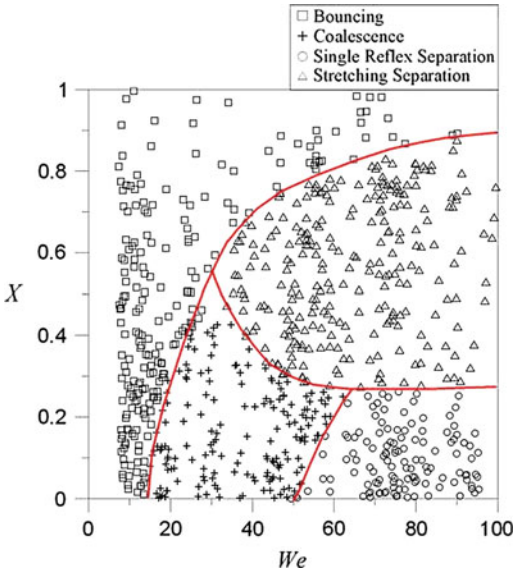


Fig. 7.7 Flow chart for the collision of equal-sized droplets of water and Diesel oil [49] (With kind permission from Springer Science+Business Media: Experiments in Fluids [49] Fig. 3, Copyright Springer-Verlag 2006)

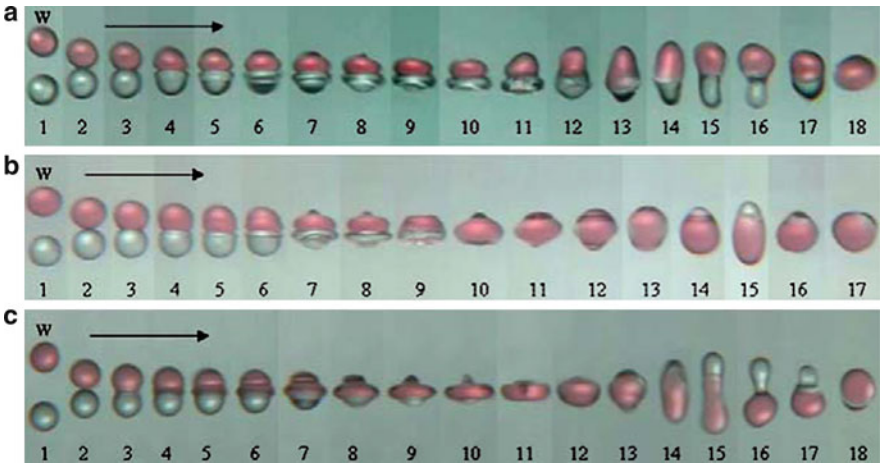


Fig. 7.8 Three cases of coalescence of droplets of water and diesel oil after head-on collisions: (**a**) $We = 18.6$, (**b**) $We = 28.7$, (**c**) $We = 45.3$. Droplets move from left to right; the red incoming water droplet is marked with "w" [49] (With kind permission from Springer Science+Business Media: Experiments in Fluids [49], Fig. 6, Copyright Springer-Verlag 2006)

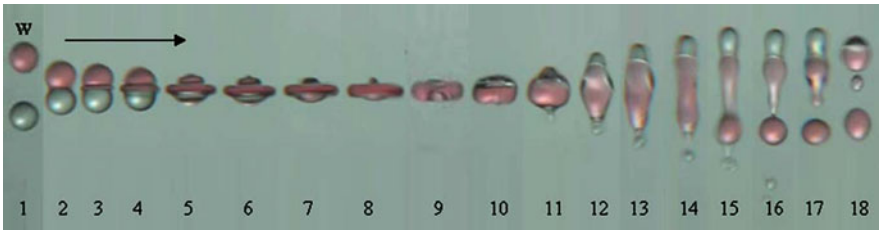


Fig. 7.9 Collision mechanism termed "single reflex separation" in Chen and Chen (2006) at $We = 95.3$, $X = 0$. Note that the colored liquid moves from above (before collision) to below the symmetry plane (after collision) [49]. The mechanism is, therefore, not reflexive (With kind permission from Springer Science+Business Media: Experiments in Fluids [49] Fig. 8, Copyright Springer-Verlag 2006)

Droplets of Non-Newtonian Liquids

A prerequisite for experimental investigations with colliding droplets is the controlled production of the colliding droplets, where the control concerns both the size and the velocity of the droplets. For controlled droplet production in the experiments, researchers employ droplet generators producing jets that are forced to break up into droplets of equal size due to a vibrational excitation. This process works properly – if satellite droplet formation can be suppressed – with Newtonian liquids, even of appreciable dynamic viscosities. Any non-Newtonian flow behavior of the liquids, in particular elasticity, however, makes a difference in this respect. Even small concentrations of, e.g., polymeric substances in Newtonian

solvents lead to the build-up of elastic stresses upon elongational and/or shearing motion of the liquid, which delays the jet break-up and makes the controlled formation of monodisperse streams of droplets very difficult. With strain-hardening elastic liquids, the formation of a beads-on-a-string structure is observed in this process, and the pinch-off of the liquid filaments (strings) between the droplets cannot be controlled by the vibrational excitation. The resulting drop size, which is influenced by the retraction of portions of the filaments into the adjacent droplets, is therefore far less controlled than with Newtonian liquids. This practical experimental difficulty may cause the lack of experiments on viscoelastic liquid droplet collisions in the literature [51].

However, the situation is different for shear-thinning, inelastic liquids. Motzigemba et al. [52] report about experiments and numerical simulations on collisions of droplets with shear-thinning flow behavior. The liquid was an aqueous solution of carboxymethylcellulose (CMC). Head-on collisions of droplets of this liquid with the Weber number of 766, comparable to collisions of droplets of an aqueous glycerol solution with a dynamic viscosity of 100 mPa s (We = 657), showed that the non-Newtonian droplets experienced deformations after the impact that were larger by a factor of ≈ 2 than the Newtonian counterparts. Experiments at different Weber numbers all showed the same trend. A numerical simulation accounting for the non-Newtonian flow behavior of the CMC solution by a modified power law reproduced the maximum deformation of the droplets upon impact well, but showed some delay in the retraction at the later stages of deformation. The simulations also exhibited some shortcomings due to the entrapment of air between the colliding droplets, which was not observed in any of the experiments.

Another kind of non-Newtonian liquid droplets investigated for its collisional behavior are suspension droplets. In these heterogeneous fluids, the mass fraction of the solid matter dispersed in the liquid, the bulk density of the solid, and the solid particle size spectrum come into play as additional parameters influencing the dynamic behavior of the droplets in binary collisions. The group around Schulte and Fritsching reported about experiments on binary suspension droplet collisions. The solid particles consisted of china clay (kaolin), glass and polyamide. Typical ranges of the solid particle sizes were between 4 and 10 μm and between 10 and 15 μm, while the drop sizes were varied between 20 and 500 μm. One finding from the experiments was that the number of satellite droplets formed after grazing collisions decreases with increasing size of the solid particles suspended in the liquid [53]. We may state that this field of research in drop collisions is also still at its beginning.

Simulations of Droplet Collisions

The value of simulations of droplet collisions lies in the potential to analyze the temporal and spatial evolutions of the surface of the liquid system, and of contributions to the energy budget of the system from surface and kinetic energies during

the collision, and in the potential to vary quickly physical parameters of the collision in parameter studies. In particular, properties of the liquid systems, such as velocity fields, which are very difficult to measure, may be quantified by the simulations and related to the respective mechanism, such as, e.g., bouncing, where the velocity field in the liquid may play an essential role.

We report about the computational techniques used for simulations of the elementary process of a binary droplet collision and important results. We find overall three techniques used for the simulations.

Solving the Equations of Change of Continuum Mechanics

The most straight forward approach may be seen in solving the equations of change of continuum mechanics describing the collision process [54–62]. These are the equations of change for mass and momentum, together with the material law quantifying the flow behavior of the liquid. For incompressible Newtonian liquids, the equations to be solved are the Navier–Stokes equations. This approach implies the necessity to describe the dynamics of a liquid system with free surface under the action of inertial, viscous, and capillary forces. For this task, the location and shape of the free surface of the system must be tracked such that the capillary forces may be derived from the curvature of the interface. The biggest challenge is the simulation of the pinch-off of liquid portions from the liquid system, as it takes place, e.g., in stretching separation when the remainders of the original drops pinch off from the liquid filament stretched in the grazing collision. This leads to the need for a high spatial resolution of the numerical grid, and/or spatial adaptivity to avoid excessively large numbers of grid cells. For tracking the interface, most simulations use the Volume-of-Fluid (VoF) or Level-Set methods. Simulations based on these methods are able to reproduce the collision parameters for the onset of reflexive separation and stretching separation found in experiments as functions of the collision Weber number reasonably well. Grid sizes are typically up to 1.6 million cells. Figure 7.10 shows the surface shapes of droplets in a head-on and a grazing collision of two water droplets in air, as simulated by solving the Navier–Stokes equations [54]. The Reynolds and Weber numbers of the collision are 2,500 and 38, respectively, which corresponds approximately to a relative velocity at the impact of $U = 1.1$ m/s and a drop size $d = 2.3$ mm. In the grazing collision, the non-dimensional impact parameter $X = 0.55$.

Lattice-Boltzmann Simulations

One alternative to solving the equations of change of continuum mechanics for simulating droplet collisions is the lattice-Boltzmann approach [63–67]. This technique describes the liquid dynamics on the basis of the dynamics of particle motion, which represents the liquid dynamic behavior and is governed by the lattice-Boltzmann

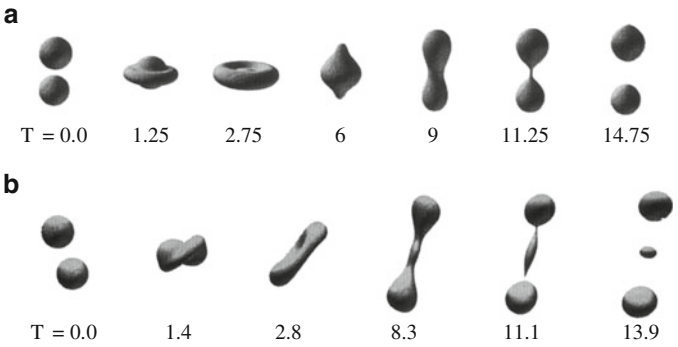


Fig. 7.10 Shapes of droplets produced by an unstable (**a**) head-on and (**b**) grazing collision of two equal-sized water droplets in air, at $Re = 2{,}500$ and $We = 38$, as simulated by solving the Navier–Stokes equations. In (**b**), the non-dimensional impact parameter $X = 0.55$; the non-dimensional time is defined as $T = t\ U/d$ [54] (Reprinted from [54], Copyright 1995, with permission from Elsevier)

equation. The equation allows for discrete directions of motion of the particles only. Various approaches with different numbers of directions of motion are established in the literature. The macroscopic properties of the liquid are derived from probability density functions of particle properties transported in the simulations. Simulations known from the literature use typical grids with 1.4 million cells. Interface shapes simulated for, e.g., grazing binary droplet collisions agree remarkably well with experiments. Also, the non-dimensional impact parameter at the onset of stretching separation as a function of the Weber number is represented well by these simulations. One drawback of this method, however, remains the fact that the physical parameters of the droplet liquid (dynamic viscosity, density, surface tension) represented in these simulations are far from the real values in the experiments. Insofar, the method implies some empiricism which remains unresolved. Figure 7.11 shows the shapes of droplets formed by the grazing collision of two equal-sized droplets at $Re = 100$ and $We = 106$, as observed in an experiment with propanol-2 droplets in air, and simulated with the lattice-Boltzmann method. The data correspond approximately to a relative velocity at the impact of 9.3 m/s and a drop size of 33 μm [63]. The non-dimensional impact parameter $X = 0.484$. The droplets in the experiment were markedly larger than the size corresponding to the characteristic parameters of the simulation.

Simulations Using Smoothed-Particle Hydrodynamics

The smoothed-particle hydrodynamics (SPH) method is an empirical alternative to the two above discussed methods, since it is grid-free and the results are, therefore, independent of a prescribed coordinate system and numerical grid resolution. It is

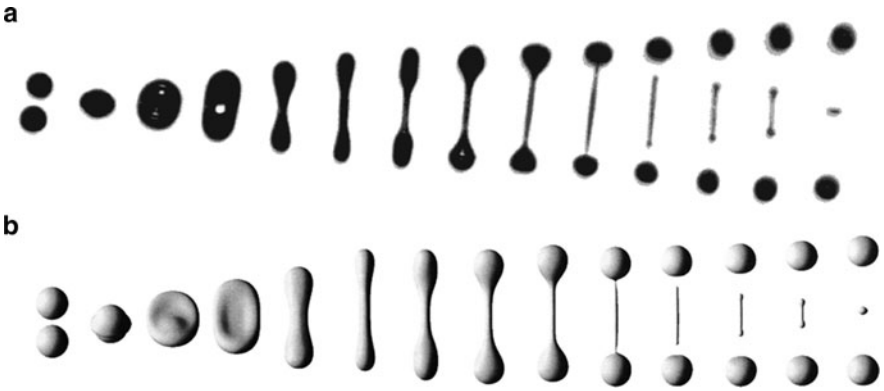


Fig. 7.11 Shapes of droplets produced by an unstable grazing collision of two equal-sized propanol-2 droplets in air at $Re = 100$ and $We = 106$ – (**a**) experiment, (**b**) lattice-Boltzmann simulation. The non-dimensional impact parameter $X = 0.484$ [63] (Reprinted with kind permission from Dr. Markus Schelkle, Immenstaad (Germany) 2010)

therefore suitable for simulating (discontinuous) free-surface flows with large deformations. The method is used to solve the equations of change of continuum mechanics, including the thermal energy equation. A further equation to be included in the formalism is the Lagrangian equation of motion of the particles. The formal discretization of the equations of change is obtained through the use of an interpolating kernel function that provides the estimate of the field variables at a set of particles suitably chosen to represent the fluid elements. The method describes the mean values of macroscopic parameters of a flowing fluid as convolution integrals of the parameter with the kernel function. This integral is approximated as a sum over neighboring particles [68]. The simulation referenced here, however, treats a collision of two-dimensional droplets, i.e., it simulates the collision of two circular cylinders. In the paper by Meleán and Sigalotti [68], only qualitative comparisons between the simulations and experimental results are drawn, without illustrations by diagrams or pictures. This method may be considered as being at its beginning and of limited use for simulating the complicated three-dimensional processes at hand. Figure 7.12 displays the evolution of the shapes of the "drop" cross sections in time, as simulated for a stable grazing collision of two circular cylinders at $X = 0.5$, $Re \approx 31$ and $We \approx 2$.

The overall conclusion from this brief survey is that the state-of-the-art in simulating binary droplet collisions may be considered as well advanced and capable of revealing details of the flow fields in the droplets and representing the sizes of droplets produced, which are difficult to access in the experiment. Nonetheless, the difficulty in correctly representing the process of pinch-off of portions from the liquid system, i.e., the simulation of the decrease of a liquid bridge diameter down to zero, remains unsolved in all methods known from the literature.

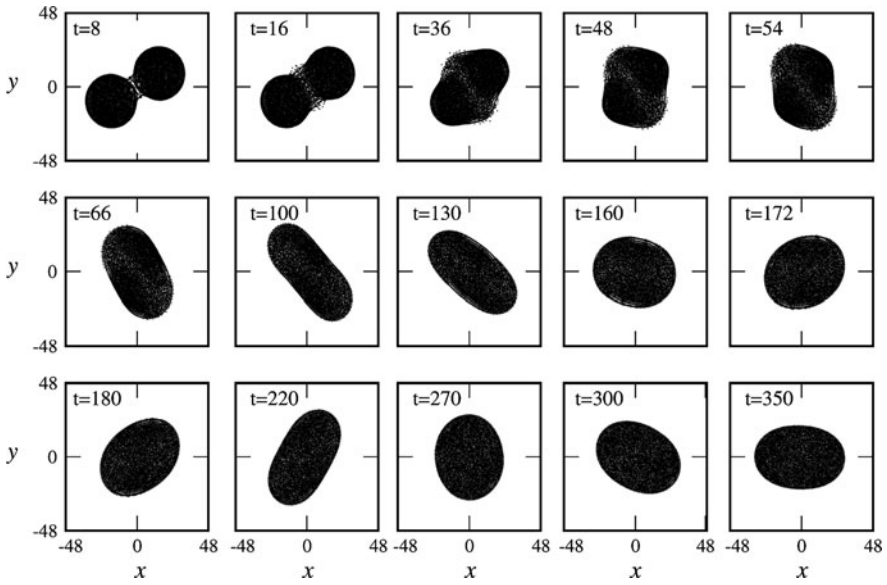


Fig. 7.12 Shapes of droplets produced by a stable grazing collision of two equal-sized two-dimensional droplets at $Re \approx 31$ and $We \approx 2$. The non-dimensional impact parameter $X = 0.5$. The non-dimensional time t is the ratio of the dimensional time to the scale $\mu d/2\sigma$ [68] (Reprinted from [68], Copyright 2005, with permission from Elsevier)

Modeling Binary Droplet Collisions in Spray Simulations

Modeling of the complicated phenomena in binary droplet collisions occurring in spray flows is difficult due to the variety of potential outcomes from a collision [69–71]. The first necessity is to predict the stability against stretching or reflexive separation. Then, for unstable drop collisions, the resulting drop sizes need to be predicted. All predictions should follow from algebraic models without the need to solve additional transport equations in the spray flow code to account for the collisions. Needless to say that it is impossible to simulate the full detail of the processes in droplet collisions, as done in the simulations discussed in section Simulations of Droplet Collisions, in the course of a spray flow simulation [72–82].

The task of modeling binary droplet collisions in Euler–Lagrangian simulations of spray flows was first taken up by O'Rourke and coworkers. Their model in [83] first estimates the coalescence efficiency, which is the probability that coalescence occurs after the collision, once it has taken place:

$$e_{\text{coal}} = \min\left\{1.0, \left[\frac{2.4f(\Delta)}{\text{We}}\right]\right\} \tag{7.5}$$

where the function $f(\Delta)$ reads

$$f(\Delta) = \Delta^{-3} - 2.4\Delta^{-2} + \frac{2.7}{\Delta} \tag{7.6}$$

and Δ is the ratio of sizes of the smaller to the larger droplet. In the model, the non-dimensional impact parameter X is chosen as a random number from the interval between 0 and 1. Collisions with $X<\sqrt{e_{\text{coal}}}$ are taken as stable and assumed to lead to coalescence. Collisions with $X>\sqrt{e_{\text{coal}}}$ are taken as unstable grazing collisions. In the coalescence case, the size and velocity of the new formed drops are computed from algebraic equations of conservation of volume and momentum. In the grazing case, the drops are assumed to conserve their sizes, and the new velocities are computed from an algebraic momentum equation. This means that the formation of satellite droplets by grazing collisions is ignored in this model, and the mechanism of bouncing is not included. Nonetheless, the "O'Rourke model" is termed the standard approach to calculating collisions in Lagrangian spray simulations even today [84].

The model by O'Rourke and coworkers has been extended and improved by several researchers. Schmidt and Rutland [84] developed a new algorithm for drop collision simulations, which is based on the no-time-counter method. The computational cost of this method is proportional to the number of computational particles, while the original algorithm of O'Rourke is proportional to its square. Through this improvement, spray simulations accounting for drop collisions may run several orders of magnitude faster (and slightly more accurate) than the original O'Rourke method. Zhang et al. [85] presented a method for reducing the mesh dependency of the simulation results, which they based on a model called the "cross mesh collision" (CMC) model. The model was implemented into the KIVA code. With three given meshes of different spatial resolution, the original O'Rourke model yielded Sauter Mean Radii of the droplets varying between 35 and 65 μm, while for the same conditions the new CMC model yielded variations only between 30 and 37 μm. Stralin et al. [86] added models based on similar criteria as laid out below to account for the post-collision behavior of the droplets and the formation of small fragments.

Some approaches exist today that identify and account for the various collision mechanisms in Euler–Lagrangian spray simulations. These models achieve best agreement with experimental data on interacting irregular streams of unequal-sized droplets and interacting sprays. Munnannur and Reitz [87] developed such a model, which accounts for the mechanisms bouncing, coalescence, stretching separation, reflexive separation, and separation at high Weber numbers. The regimes are identified according to the Weber number and the non-dimensional impact parameter: for *bouncing*, the criterion

$$We < \frac{\Delta\left(1+\Delta^2\right)(4\Theta' - 12)}{\chi_1[\cos(\arcsin X)]^2} \tag{7.7}$$

developed by Estrade et al. [40] is used, where the shape factor $\Theta' = 3.351$. The function χ_1 depends on the sizes of the smaller and larger colliding drops, and on the impact parameter, and reads

$$\chi_1 = 1 - 0.25(2-\tau)^2(1+\tau) \quad \text{for } (d_s + d_l)(1-X) > d_l \tag{7.8}$$

and

$$\chi_1 = 0.25\tau^2(3-\tau) \quad \text{for } (d_s + d_l)(1-X) \leq d_l. \tag{7.9}$$

Here, $\tau = (1-X)(1+\Delta)$, and d_s and d_l are the sizes of the smaller and the larger colliding drops, respectively. The bouncing of the droplets leaves the drop sizes unchanged. For *coalescence* of the colliding drops, the efficiency is quantified according to (7.5), and the velocity and size of the drop after merging are computed according to the simple volume and momentum balances described above.

Stretching separation is treated accounting for the break-up behavior of the liquid filament formed between the smaller and larger colliding drop bulk masses. The liquid volume in the filament is modeled according to a separation volume coefficient C_{vs} defined as

$$C_{vs} = \frac{E_{strtch} - E_{surten} - E_{dissip}}{E_{strtch} + E_{surten} + E_{dissip}} \tag{7.10}$$

where the energies involved are E_{strtch} – the total effective stretching kinetic energy, E_{surten} – the surface energy in the region of interaction of the two droplets, and E_{dissip} – the viscous dissipation in the interaction region. The first two energies are estimated according to Ashgriz and Poo [36]; the third energy E_{dissip} is assumed to be 30% of the total initial kinetic energy of the droplets for a stretching separation process. The filament formed between the bulbous ends of the liquid system in stretching separation is assumed to be uniform in radius. The length δ and radius r of the filament are time-dependent and inter-related, so that the volume remains constant. The derivative w.r.t. time of an energy balance for the filament results in a differential equation for the radius of the filament as a function of time, which accounts for viscous dissipation. The solution of a simplified version of this differential equation, together with a relation between the time to break-up of the filament and its radius at the instant of break-up, yields a nonlinear algebraic equation for the radius of the filament at break-up, which involves two model constants. The values of these constants are tuned to yield best agreement with experiments. Since the mechanism responsible for the break-up of the filament is assumed to be the Rayleigh mechanism, a simple equation relates the radius of the satellite droplets formed to the radius of the filament at break-up. The dominance of this mechanism in satellite droplet formation, however, depends on the ratio of two time scales: the inverse stretching rate of the filament and the capillary time scale $t_\sigma = \left(\rho r_0^3/\sigma\right)^{1/2}$. This time scale ratio, termed T, is therefore given as $T = t_\sigma \dot{\delta}/\delta$.

For sufficiently small T, the outcome from a stretching separation process is assumed to be the two remaining portions from the smaller and the larger colliding droplets plus one single satellite droplet, since, according to the results of Brenn et al. [33], this is the most probable case for all Weber numbers between 47 and 350. A threshold value of T is found to be 2: for $T \leq 2$, the single satellite is formed. For $T > 2$, the filament is stretched, and the number of satellites is calculated from volume conservation of the ligaments, assuming uniform size of the satellites.

The occurrence of *reflexive separation* is detected using the criterion developed by Ashgriz and Poo [36], which is formulated in (7.1) above. When reflexive separation occurs, again the time scale ratio T is checked against a threshold value, which is 3 for this mechanism. For $T \leq 3$, the ligament formed in reflexive separation contracts into one single "satellite"; the size of this satellite is the volume-equivalent size of the merged collided droplets. For $T > 3$, the ligament is stretched and undergoes break-up. The number and size of the satellites is computed following the same procedure as for stretching separation, but with a different initial length scale r_0 [87]. As an alternative to this model, the one developed by Post and Abraham [88] provides a comparable degree of detail.

Earlier, Georjon and Reitz [89] developed an additional "shattering collision" model that describes the break-up of droplets after collisions with high Weber numbers. As high Weber numbers in the sense of that model, the authors considered values above 100. There is some contradiction of this modelling approach to results, e.g., by Estrade et al. [40] and Brenn et al. [90], who showed that stretching separation with satellite droplet formation, as described in the model of Munnannur and Reitz [87] above, may take place at Weber numbers as high as 130 and 350, respectively. A model for shattering collisions as presented in paper [89] by Georjon and Reitz, is certainly a valuable extension to the drop collision models available in the literature, especially for the simulation of spray flows with high relative drop velocities where shattering collisions are highly probable.

References

1. P. R. Brazier-Smith, S. G. Jennings, J. Latham: Accelerated rates of rainfall, Nature 232, 112–113 (1971).
2. D. M. Whelpdale, R. List: The coalescence process in raindrop growth, J. Geophys. Res. 76, 2836–2856 (1971).
3. R. List, J. R. Gillespie: Evolution of raindrop spectra with collision-induced breakup, J. Atmos. Sci. 33, 2007–2013 (1976).
4. S. G. Bradley, C.D Stow: On the production of satellite droplets during collisions between water drops falling in still air, J. Atmos. Sci. 36, 494–500 (1979).
5. T. B. Low, R. List: Collision, coalescence and breakup of raindrops. Part I: Experimentally established coalescence efficiencies and fragment size distributions in breakup, J. Atmos. Sci. 39, 1591–1606 (1982).
6. D. J. Ryley, B. N. Bennett-Cowell: The collision behaviour of steam-borne water drops, Int. J. Mech. Sci. 9, 817–833 (1967).

7. P. R. Brazier-Smith, S. G. Jennings, J. Latham: An investigation of the behaviour of drops and drop-pairs subjected to strong electrical forces, Proc. R. Soc. Lond. A 325, 363–376 (1971).
8. A. M. Podvysotsky, A. A. Shraiber: Coalescence and break-up of drops in two-phase flows, Int. J. Multiphase Flow 10, 195–209 (1984).
9. N. Ashgriz, P. Givi: Binary collision dynamics of fuel droplets, Heat Fluid Flow 8, 205–210 (1987).
10. N. Ashgriz, P. Givi: Coalescence efficiencies of fuel droplets in binary collisions, Int. Commun. Heat Mass Transfer 16, 11–20 (1989).
11. G. Brenn, A. Frohn: Collision and merging of two equal droplets of propanol, Exp. Fluids 7, 441–446 (1989).
12. G. Brenn, A. Frohn: Collision and coalescence of droplets of various liquids, J. Aerosol Sci. 20, 1027–1030 (1989).
13. A. Menchaca-Rocha, A. Cuevas, M. Chapa, M. Silva: Rotating-liquid-drop model limit tested on macroscopic drops, Phys. Rev. E 47, 1433–1436 (1993).
14. C. K. Law: Dynamics of droplet collision, Proceedings of the IUTAM Symposium Mechanics and Combustion of Droplets and Sprays, Tainan, Taiwan, pp. 99–118 (1994).
15. J. Qian, C. K. Law: Effects of liquid and ambient gas properties on droplet collision, AIAA paper 94–0681 (1994).
16. A. Menchaca-Rocha, F. Huidobro, A. Martinez-Davalos, K. Michaelian, A. Perez, V. Rodriguez, N. Cârjan: Coalescence and fragmentation of colliding mercury drops, J. Fluid Mech. 346, 291–318 (1997).
17. M. Orme: Experiments on droplet collisions, bounce, coalescence and disruption, Prog. Energy Combust. Sci. 23, 65–79 (1997).
18. C. C. Hung, J. K. Martin: Collisional behavior of hydrocarbon droplets, Proceedings of the 10th Annual Conference Liquid Atomization and Spray Systems (ILASS Americas), Ottawa, Ontario (CDN) 1997, pp. 62–66 (1997).
19. J. Eggers, J. R. Lister, H. A. Stone: Coalescence of liquid drops, J. Fluid Mech. 401, 293–310 (1999).
20. L. Duchemin, J. Eggers, C. Josserand: Inviscid coalescence of drops, J. Fluid Mech. 487, 167–178 (2003).
21. F. Mashayek, N. Ashgriz, W. J. Minkowycz, B. Shotorban: Coalescence collision of liquid drops, Int. J. Heat Mass Transfer 46, 77–89 (2003).
22. G. A. Bach, D. L. Koch, A. Gopinath: Coalescence and bouncing of small aerosol droplets, J. Fluid Mech. 518, 157–185 (2004).
23. P. Duru, D. L. Koch, C. Cohen: Experimental study of turbulence-induced coalescence in aerosols, Int. J. Multiphase Flow 33, 987–1005 (2007).
24. C. Gotaas, P. Havelka, H. A. Jakobsen, H. F. Svendsen, M. Hase, N. Roth, B. Weigand: Effect of viscosity on droplet-droplet collision outcome: experimental study and numerical comparison, Phys. Fluids 19, paper 102106 (2007).
25. F.-C. Wang, J.-T. Feng, Y.-P. Zhao: The head-on colliding process of binary liquid droplets at low velocity: high-speed photography experiments and modelling, J. Colloid Interface Sci. 326, 196–200 (2008).
26. C. Planchette, E. Lorenceau, G. Brenn: Liquid encapsulation by binary collisions of immiscible liquid drops, Colloids Surf. A: Physicochem. Eng. Aspects 365, 89–94 (2010).
27. R. W. Park, E. J., Crosby: A device for producing controlled collisions between pairs of drops, Chem. Eng. Sci. 20, 39–45 (1965).
28. J. M. Schneider, N. R. Lindblad, C. D. Hendricks: An apparatus to study the collision and coalescence of liquid aerosols, J. Colloid Sci. 20, 610–616 (1965).
29. J. R. Adam, N. R. Lindblad, C. D. Hendricks: The collision, coalescence, and disruption of water droplets, J. Appl. Phys. 39, 5173–5180 (1968).
30. J. Qian, C. K. Law: Regimes of coalescence and separation in droplet collision, J. Fluid Mech. 331, 59–80 (1997).

31. K. D. Willis, M. Orme: Experiments on the dynamics of droplet collisions in a vacuum, Exp. Fluids 29, 347–358 (2000).
32. K. Willis, M. Orme: Binary droplet collisions in a vacuum environment: an experimental investigation of the role of viscosity, Exp. Fluids 34, 28–41 (2003).
33. G. Brenn, St. Kalenderski, I. Ivanov: Investigation of the stochastic collisions of drops produced by Rayleigh breakup of two laminar liquid jets, Phys. Fluids 9, 349–364 (1997).
34. Y. J. Jiang, A. Umemura, C. K. Law: An experimental investigation on the collision behaviour of hydrocarbon droplets, J. Fluid Mech. 234, 171–190 (1992).
35. Y. Pan, K. Suga: Numerical simulation of binary liquid droplet collision, Phys. Fluids 17, paper 082105 (2005).
36. N. Ashgriz, J. Y. Poo: Coalescence and separation in binary collisions of liquid drops, J. Fluid Mech. 221, 183–204 (1990).
37. A. Y. Tong, Z. Y. Wang: Relaxation dynamics of a free elongated liquid ligament, Phys. Fluids 19, paper 092101 (2007).
38. G. Brenn, V. Kolobaric: Satellite droplet formation by unstable binary drop collisions, Phys. Fluids 18, paper 087101 (2006).
39. N. Roth, M. Rieber, A. Frohn: High energy head-on collision of droplets, Proceedings of the Annual Conference Liquid Atomization and Spray Systems (ILASS Europe), Toulouse, July 1999.
40. J.-P. Estrade, H. Carentz, G. Lavergne, Y. Biscos: Experimental investigation of dynamic binary collision of ethanol droplets – a model for droplet coalescence and bouncing, Int. J. Heat Fluid Flow 20, 486–491 (1999).
41. J.-P. Estrade, P. Berthoumieu, G. Lavergne, Y. Biscos: Experimental investigation of dynamic binary collision of various liquids, Proceedings of the 8th International Symposium Flow Visualization, Sorrento, Italy, September 1998.
42. P. R. Brazier-Smith, S. G. Jennings, J. Latham: The interaction of falling water drops: coalescence, Proc. R. Soc. Lond. A 326, 393–408 (1972).
43. V. A. Arkhipov, G. S. Ratanov, V. F. Trofimov: Experimental investigation of the interaction of colliding droplets, J. Appl. Mech. Tech. Phys. 2, 73–77 (1978).
44. V. A. Arkhipov, I. M. Vasenin, V. F. Trofimov: Stability of colliding drops of ideal liquid, J. Appl. Mech. Tech. Phys. 3, 95–98 (1983).
45. T.-C. Gao, R.-H. Chen, J.-Y. Pu, T.-H. Lin: Collision between an ethanol drop and a water drop, Exp. Fluids 38, 731–738 (2005).
46. R. H. Chen: Diesel-diesel and diesel-ethanol drop collisions, Appl. Thermal Eng. 27, 604–610 (2007).
47. C. H. Wang, W. G. Hung, S. Y. Fu, W. C. Huang, C. K. Law: On the burning and microexplosion of collision-generated two-component droplets: miscible fuels, Combust. Flame 134, 289–300 (2003).
48. S. F. Simpson, J. R. Kincaid, F. J. Holler: Microdroplet mixing for rapid reaction kinetics with Raman spectrometric detection, Anal. Chem. 55, 1420–1422 (1983).
49. R. H. Chen, C. T. Chen: Collision between immiscible drops with large surface tension difference: diesel oil and water, Exp. Fluids 41, 453–461 (2006).
50. C. Planchette, G. Brenn: Liquid encapsulation by binary collisions of immiscible liquid drops, Proceedings of the 11th International Conference Liquid Atomization Spray Systems (ICLASS 2009), Vail, abstract ICLASS2009–243.
51. P. T. Yue, J. J. Feng, C. Liu, J. Shen: Diffuse-interface simulations of drop coalescence and retraction in viscoelastic fluids, J. Non-Newtonian Fluid Mech. 129, 163–176 (2005).
52. M. Motzigemba, N. Roth, D. Bothe, H.-J. Warnecke, J. Prüss, K. Wielage, B. Weigand: The effect of non-Newtonian flow behaviour on binary droplet collisions: vof-simulation and experimental analysis, Proceedings of the 18th Annual Conference Liquid Atomization Spray Systems (ILASS Europe), Zaragoza, Spain, pp. 559–564 (2002).

53. O. Kurt, U. Fritsching, G. Schulte: Secondary droplet formation during binary suspension droplet collision, Atomization Sprays 19, 457–472 (2009).
54. M. Rieber, A. Frohn: Three-dimensional Navier-Stokes simulation of binary collisions between droplets of equal size, J. Aerosol Sci. 26(Suppl. 1), S929–S930 (1995).
55. M. R. Nobari, Y.-J. Jan, G. Tryggvason: Head-on collision of drops – a numerical investigation, Phys. Fluids 8, 29–42 (1996).
56. M. R. H. Nobari, G. Tryggvason: Numerical simulations of three-dimensional drop collisions, AIAA J. 34, 750–755 (1996).
57. M. Rieber, A. Frohn: Navier-Stokes simulation of droplet collision dynamics, Proceedings of the 7th International Symposium CFD, Beijing, China, pp. 520–525 (1997).
58. M. Z. Dai, D. P. Schmidt: Numerical simulation of head-on droplet collision: effect of viscosity on maximum deformation, Phys. Fluids 17, paper 041701 (2005).
59. S. Tanguy, A. Berlemont: Application of a level set method for simulation of droplet collisions, Int. J. Multiphase Flow 31, 1015–1035 (2005).
60. S. P. Decent, G. Sharpe, A. J. Shaw, P. M. Suckling: The formation of a liquid bridge during the coalescence of drops, Int. J. Multiphase Flow 32, 717–738 (2006).
61. X. Jiang, A. J. James: Numerical simulation of the head-on collision of two equal-sized drops with van der Waals forces, J. Eng. Math. 59, 99–121 (2007).
61. N. Nikolopoulos, K.-S. Nikas, G. Bergeles: A numerical investigation of central binary collision of droplets, Comp. Fluids 38, 1191–1202 (2009).
63. M. Schelkle, M. Rieber, A. Frohn: Numerische Simulation von Tropfenkollisionen, Spektrum der Wissenschaft 1, 72–79 (1999).
64. T. Inamuro, S. Tajima, F. Ogino: Lattice Boltzmann simulation of droplet collision dynamics, Int. J. Heat Mass Transfer 47, 4649–4657 (2004).
65. B. Sakakibara, T. Inamuro: Lattice Boltzmann simulation of collision dynamics of two unequal-size droplets, Int. J. Heat Mass Transfer 51, 3207–3216 (2008).
66. M. Schelkle: Lattice-Boltzmann-Verfahren zur Simulation dreidimensionaler Zweiphasenströmungen mit freien Oberflächen, Ph.D. thesis University of Stuttgart, Shaker, Aachen, Germany (1997).
67. M. Schelkle, A. Frohn: Three-dimensional lattice Boltzmann simulations of binary collisions between equal droplets, J. Aerosol Sci. 26(Suppl. 1), S145–S146 (1995).
68. Y. Meleán, L. Di G. Sigalotti: Coalescence of colliding van der Waals liquid drops, Int. J. Heat Mass Transfer 48, 4041–4061 (2005).
69. J. K. Dukowicz: A particle-fluid numerical model for liquid sprays, J. Comp. Phys. 35, 229–253 (1980).
70. G. H. Ko, H. S. Ryou: Modeling of droplet collision-induced breakup process, Int. J. Multiphase Flow 31, 723–738 (2005).
71. L. E. Kollár, M. Farzaneh, A. R. Karev: Modeling droplet collision and coalescence in an icing wind tunnel and the influence of these processes on droplet size distribution, Int. J. Multiphase Flow 31, 69–92 (2005).
72. A. Kitron T. Elperin, A. Tamir: Stochastic modelling of the effects of liquid droplet collisions in impinging streams absorbers and combustors, Int. J. Multiphase Flow 17, 247–265 (1991).
73. M. Gavaises, A. Theodorakakos, G. Bergeles, G. Brenn: Evaluation of the effect of droplet colllisions on spray mixing, Proc. Inst. Mech. Eng. 210, 465–475 (1996).
74. P. Villedieu, J. Hylkema: Une méthode particulaire aléatoire reposant sur une équation cinétique pour la simulation numérique des sprays denses de gouttelettes liquides, C.R. Acad. Sci. Paris vol. 325, Série I, 323–328 (1997).
75. J. Dohmann: Dispersion and coagulation of droplets in intersecting sprays, Chem. Eng. Technol. 21, 341–345 (1998).
76. R. Kaesemann, H. Fahlenkamp: The meaning of droplet-droplet interaction for the wet fluegas cleaning process, Chem. Eng. Technol. 25, 739–742 (2002).
77. D. P. Schmidt, C. J. Rutland: Reducing grid dependency in droplet collision modelling, J. Eng. Gas Turbines Power 126, 227–233 (2004).

78. G. H. Ko, H. S. Ryou: Droplet collision processes in an inter-spray impingement system, J. Aerosol Sci. 36, 1300–1321 (2005).
79. C. Bautsch, H. Fahlenkamp: Detailed simulation of wet flue-gas-desulphurisation scrubbers with CFD, Proceedings of the International Conference on Liquid Atomization Spray Systems (ICLASS 2006), Kyoto, Japan, paper ICLASS06–238.
80. S. Hou, D. P. Schmidt: Adaptive collision meshing and satellite droplet formation in spray simulations, Int. J. Multiphase Flow 32, 935–956 (2006).
81. L. E. Kollár, M. Farzaneh: Modeling the evolution of droplet size distribution in two-phase flows, Int. J. Multiphase Flow 33, 1255–1270 (2007).
82. S. Hou, D. P. Schmidt: Interaction mechanisms between closely spaced sprays, SAE Technical Paper 2008-01-0946 (2008).
83. P. J. O'Rourke, F. V. Bracco: Modelling of drop interactions in thick sprays and a comparison with experiments, Proc. Inst. Mech. Eng. 9, 101–116 (1980).
84. D. P. Schmidt, C. J. Rutland: A new droplet collision algorithm. J. Comp. Phys. 164, 62–80 (2000).
85. H.-Y. Zhang, Y.-S. Zhang, B. Xu, C.-I. Mo: Extension of O'Rourke droplet collision model: application to diesel spray of single-hole injector, SAE Technical Paper 2006-01-3335 (2006).
86. P. Stralin, F. Wahlin, N. Nordin, H.-E. Angström: A Lagrangian collision model applied to an impinging spray nozzle, SAE Technical Paper 2006-01-3331 (2006).
87. A. Munnannur, R. D. Reitz: A new predictive model for fragmenting and non-fragmenting binary droplet collisions, Int. J. Multiphase Flow 33, 873–896 (2007).
88. S. L. Post, J. Abraham: Modeling the outcome of drop-drop collisions in Diesel sprays, Int. J. Multiphase Flow 28, 997–1019 (2002).
89. T. L. Georjon, R. D. Reitz: A drop-shattering collision model for multidimensional spray computations, Atomization Sprays 9, 231–254 (1999).
90. G. Brenn, D. Valkovska, K. D. Danov: The formation of satellite droplets by unstable binary drop collisions, Phys. Fluids 13, 2463–2477 (2001).

Chapter 8
Droplet Impact on a Solid Surface

Abstract This chapter considers droplet-wall interaction and droplet impact and splashing on a solid surface. The discussion on droplet-wall interaction considers thermo-fluid-dynamic processes associated with droplet impact onto solid surfaces. The emphasis is put on the disintegration mechanisms as an introduction to the intricate interaction phenomena occurring at spray impingement. The analysis starts with the simplest situation of single droplet impacts onto non-heated and dry surfaces; further complexities are then introduced which consider the interaction with a liquid film and the combined effects of heat transfer. The discussion on droplet impact and splashing on a solid surface includes splashing and fragmentation of molten metal and other liquid droplets landing on a solid surface. Issues such as different types of splashing, corona splashes, freezing induced splashing are considered from an experimental point of view.

Keywords Contact angle · Corona splashes · Disintegration · Disintegration limits · Droplet impact · Drop surface energy · Heat transfer regimes · Leidenfrost point · Molten metal droplet impact · Rupture · Secondary atomization · Spread · Surface topography · Thermal induced atomization · *Wettability*

N. Ashgriz (ed.), *Handbook of Atomization and Sprays*,
DOI 10.1007/978-1-4419-7264-4_8, © Springer Science+Business Media, LLC 2011

Droplet–Wall Interactions

António L.N. Moreira and A.S. Moita

Single Droplet Impingement onto Non-heated Dry Surfaces

The Impact Regimes

When a droplet impacts onto a solid surface, different outcomes may arise depending on the dynamics of the interactions occurring at the liquid-solid interface which, for impacts onto cold, rigid and dry surfaces, include: (1) stick, (2) spread, (3) disintegration or (4) rebound. Prediction of the exact mechanism involves accounting for the relative magnitude of the forces acting upon the droplet at impact, usually grouped in dimensionless numbers as in Table 8.1 There, the Mach number is not included, as it is associated with compressible effects, an issue not addressed here and for which the reader is referred to the various reviews on the subject, e.g., [1].

Surface boundary conditions (either geometrical or chemical) also alter the physics of the problem, but cannot be accurately included in any dimensionless parameter. Their effects are usually accounted by the topography of the surface and by the *wettability* of the surface to the liquid. The topography is characterized by the roughness amplitude (mean roughness, R_a or mean peak-to valley roughness, R_z), by its fundamental wavelength (i.e., average distance between consecutive rough peaks) and shape of the asperities. The latter is difficult to quantify in practical surfaces, as their roughness profiles are stochastic, but it can be defined for custom made targets. After the pioneering work by Range and Feuillebois [2], who speculate on the relevance of these parameters, a renewed interest has recently been shown on the development of tailored surfaces in several practical situations (e.g., [3]), which thus confirm the relevant role of the geometrical relations between the topographical characteristics. However, it is essential to use a common terminology when referring to these parameters, to define all these quantities accurately, as well

A.L.N. Moreira (✉) and A.S. Moita
Department of Mechanical Engineering, Technical University of Lisbon – Instituto Superior Técnico, Lisbon, Portugal
e-mail: anamoita@dem.ist.utl.pt, moreira@dem.ist.utl.pt

Table 8.1 Most relevant dimensionless numbers used in the analysis of droplet/(cold) surface interactions. ρ, μ and σ_{lv} stand for liquid specific mass, dynamic viscosity and surface tension, respectively and g is the gravitational acceleration constant

Dimensionless number	Definition	Relations
Weber number Inertial forces/surface tension forces	$We = \frac{\rho U_0^2 D_0}{\sigma_{lv}}$	
Reynolds number Inertial forces/viscous forces	$Re = \frac{\rho U_0 D_0}{\mu}$	
Capillary number Viscous forces/surface tension forces	$Ca = \frac{\mu}{\sigma_{lv}} U_0$	
Froude number Inertial forces/gravitational forces	$Fr = \frac{U_0}{(gD_0)^{1/2}}$	
Ohnesorge number Viscous forces/surface tension forces	$Oh = \frac{\mu}{(\rho\sigma_{lv}D_0)^{1/2}}$	$Oh = \frac{We^{1/2}}{Re}$
Laplace number Surface tension forces/momentum transport (dissipation)	$La = \frac{\rho\sigma_{lv}}{\mu^2} D_0$	$La = \frac{Re^2}{We} = \frac{We}{Ca^2} = \frac{Re}{Ca} = Oh^{-2}$
Bond number Body (gravitational) forces/surface tension forces	$Bo = \frac{\rho g D_0^2}{\sigma_{lv}}$	$Bo = \frac{We}{Fr}$

as standards to determine R_a and R_z (e.g., [4]) to avoid misleading interpretation of the results reported by different authors.

Wettability is a thermodynamic property of the interface solid-liquid–vapor, defined by the equilibrium contact angle θ, given by the Young's equation:

$$\sigma_{ly} \cos\theta + \sigma_{ls} = \sigma_{sy} \tag{8.1}$$

where σ_{lv}, σ_{ls} and σ_{sv} are the interfacial tensions at the boundaries of the system liquid-surface-vapor. For low wetting surfaces, the contact angle varies in the range $90° < \theta < 180°$, while for partial wetting surfaces it is smaller than 90°, $0° < \theta < 90°$. Values of the contact angle $\theta = 0°$ and $\theta = 180°$ correspond to complete wetting or non-wetting, respectively.

However, the contact angle measured on a real surface, θ_R, does not obey to Young's equation as this applies only to theoretically smooth surfaces. In general, the extent of liquid penetration into the roughness grooves is unknown and two extreme situations may occur: (1) the liquid penetrates completely within the grooves – the so called homogeneous wetting or (2) the liquid does not penetrate into the roughness grooves so that air pockets are entrapped between the liquid and the surface, which alters viscous dissipation – heterogeneous wetting.

The homogeneous wetting regime is accurately described by the classical theory of Wenzel, which relates the measured angle, $\theta_R = \theta_w$ with the Young angle, θ_Y:

$$\cos\theta_w = r_f \cos\theta_Y \tag{8.2}$$

where r_f is a roughness factor representing the ratio of the true wetted area to the correspondent apparent area. The heterogeneous regime is described by the

equation of Cassie and Baxter, where an apparent contact angle, $\theta_R = \theta_{CB}$ is defined as

$$\cos\theta_{CB} = -1 + f_w(r_f \cos\theta_Y + 1) \tag{8.3}$$

where f_w is the fraction of the projected area of the solid surface that is wetted by the liquid. It is worth noting that the equation of Wenzel is a particular case of that of Cassie and Baxter for homogeneous wetting ($f_w = 1$). Transition between the homogeneous and the heterogeneous wetting regimes is not clear, though it is known to depend on surface chemistry and roughness, e.g., [5]. However, the equilibrium contact angle does not accurately represent the dynamic effects of the surface on droplet spread upon impact, and the dynamic contact angle is found to be more appropriate (e.g., [6]), though it has not been possible to obtain functional relations yet (e.g., [2]).

Regarding the outcomes of the impact, the spreading mechanism and their governing parameters are extensively described in the literature. This phenomenon is characterized by four stages, namely the *kinematic phase*, the *spreading phase*, the *recoiling phase* and the *equilibrium phase* (see [6], for the characterization of each phase). Inertial forces dominate the initial kinematic phase where the diameter of the spreading lamella increases with the square root of time

$$d(t) = CD_0\tau^{1/2} \tag{8.4}$$

where $\tau = t/(D_0/U_0)$). The spreading phase follows right after and is where the lamella expands up to its maximum diameter. Most approaches reported in the literature to describe this phase derive expressions for the maximum diameter and the time taken to reach it from the application of the conservation principles to the spreading lamella. Neglecting variations of the potential energy, the energy conservation principle gives:

$$E_{Ki} + E_{Si} = E_{Kf} + E_{Sf} + E_{diss} \tag{8.5}$$

where E_K and E_S refer to the kinetic and surface energy, respectively; E_{diss} refers to the energy dissipated by viscous effects; subscripts i and f stand for the initial and final states, respectively. The initial kinetic energy is computed as:

$$E_{Ki} = (1/2)\rho U_0^2 Vol = (1/2\rho U_0^2)(1/6\pi D_0^3) \tag{8.6}$$

and the initial surface energy is computed considering the droplet spherical before impact:

$$E_{Si} = \int_0^{Vol} \Delta p dVol = 4\sigma_{lv}\pi R_0^2 = \sigma_{lv}\pi D_0^2 \tag{8.7}$$

The final state *f* is usually taken at the position where the diameter of the lamella is maximum, where E_{diss} and E_{Sf} can be easily determined. Major differences between the various existing models lay in the assumptions regarding the shape of the lamella, the estimation of E_{Kf} and E_{diss} and the way to account for *wettability* effects. Regarding the shape of the lamella, most models consider it as a cylindrical disk with instantaneous diameter $d(t)$ and height $h(t)$, so that relations between $d(t)$ and D_0 can be easily determined by mass conservation laws. Only recent models, e.g., [7] assume a more complex shape, in which the lamella is a thin film bounded by a thicker rim. Also, most of these models consider $E_{\mathrm{Kf}} = 0$ at maximum spread, which is not entirely correct, although it leads to good agreement with the experiments, probably because most are validated for impacts at small or moderate velocities. Again, few exceptions have been observed in recent works such as in Roisman et al. [7]. Though the energy dissipated, E_{diss} is also disregarded by some authors, it can be computed as:

$$E_{\mathrm{diss}} = \int_0^{t_2} \int_{Vol} \phi dVol dt \approx \phi Vol t_2 \tag{8.8}$$

where $\phi = \mu\left(\partial U_i/\partial x_j + \partial U_j/\partial x_i\right)\partial U_i/\partial x_j$ is the dissipation function and t_2 is a known time period after impact, for which the effect of viscous dissipation is expected to be relevant. The viscous dissipation function is subsequently scaled based on different assumptions. For instance, Pasandideh-Fard et al. [8] scale it with the impact velocity and with the boundary layer thickness, δ. According to this, $\phi \approx \mu(U_0/\delta)^2$, for the boundary layer thickness estimated as in White [9], $\delta = 2D_0/(Re)^{1/2}$.

Further differences are found in the way the models account for *wettability* effects. These effects can be explicitly accounted in the spreading diameter by introducing the contact angle in the term of the surface energy of the spreading droplet, E_{Sf} as (e.g., [8]), $E_{\mathrm{Sf}} = (1/4)\pi d_{\max}^2 \sigma_{\mathrm{lv}}(1 - \cos\theta)$, where some authors use the equilibrium angle θ, while others, particularly in more recent work, rather use the dynamic contact angle.

The *recoiling phase* occurs for partial wetting systems, while for complete wetting systems the lamella continues to spread over a long period after impact, clearly dominated by capillary forces, governed by the power law $d(t)/(D_0) = Ct^{1/10}$, as early proposed by Tanner [6].

Disintegration Mechanisms

Contrary to spreading, the disintegration mechanisms are not so well documented in the literature. Several disintegration mechanisms can be identified: (a) prompt splash, (b) corona splash, (c) receding break-up (d) partial rebound, (e) finger break-up [10, 11].

The prompt splash is the mechanism usually addressed in the criteria for the spread/disintegration limits. The roughness amplitude, usually quantified by the mean roughness R_a, promotes the occurrence of such phenomenon at two different scales. Small roughness amplitudes ($R_a/R_0 < 3.4E - 4$) destabilize the lamella, while large roughness amplitudes ($R_a/R_0 > 2.5E - 3$) govern the disintegration mechanism [11]. Prompt splash takes place within the early instants after impact, being dominated by inertial forces. *Wettability* effects are observed only in extreme opposite situations: in low wetting systems ($\theta > 90°$), receding break-up and partial rebound are more likely to occur, while in complete wetting systems, ($\theta \approx 0°$), such as those formed by fuel droplets onto smooth surfaces, disintegration occurs after the formation of a crown (e.g., [10–12]), which destabilizes, disrupts into jets and further break up into secondary droplets. Despite some authors (e.g., [13]) state that the crown is induced by a kinematic discontinuity of the flow as proposed by Yarin and Weiss [14] for wetted surfaces, experimental studies show that such models do not predict accurately the growth rate of the crown (e.g., [11, 12]).

The development of the crown can be described as in Cossali et al. [14]. Referring to Fig. 8.1, crown diameters grow according to a power law:

$$\frac{D_c}{D_0} = C.(\tau - \tau_0)^n \tag{8.9}$$

where $0.41 < n < 0.45$ and C is weakly dependent on liquid properties. This is in agreement with the theory proposed by Yarin and Weiss [15]. However, crown height and angle (and consequently the ejection angle of the secondary droplets) cannot be accurately described by this theory, since they are known to strongly depend on viscosity and aerodynamic forces. An alternative theory considers that the crown formation is driven by aerodynamic forces, according to the process described in Moita and Moreira [11] and Xu et al. [12]. This should be accounted in future models which consider the physical mechanisms of crown formation as performed, for instance, by Han et al. [16].

From the aforementioned, it is clear that the mechanisms of droplet disintegration depend in a complex way on the combination of the diverse conditions (e.g., droplet size, velocity and impact angle, surface topography and surface forces). The results of the systematic investigations reported by Rioboo et al. [10] and Moita and Moreira [11] are summarized in Table 8.2, where the arrows indicate the direction of change necessary to promote the occurrence of a particular mechanism. Dashed

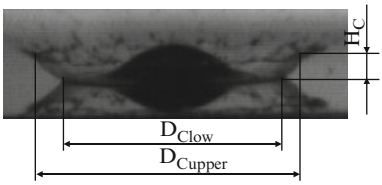


Fig. 8.1 Crown morphology: H_C crown height, D_{Clow} crown lower diameter, D_{Cupper} crown upper diameter

Table 8.2 Effect of the various parameters to promote each disintegration mechanism: summary of the results reported by Rioboo et al. [10] and by Moita and Moreira [11]

Increase of	Prompt splash	Corona splash	Receding break-up	Finger break-up	Partial rebound
U_0	↑	↑	↑	↑	↑
D_0	↑				
σ	↓	↓	↑		↑
μ	↓	↓	↓	↓	
R_a	↑	↓		↑	↓
λ_R	↓	↓			
θ		↓	↑	↓	↑

arrows indicate the additional contributions from the work which has been developed by Moita and Moreira [11].

Secondary Atomization

Besides, it is necessary to be able to predict which regime occurs at droplet impact. Threshold criteria are then defined which establish the boundaries between the four basic outcomes (stick, spread, rebound and disintegration). Particular emphasis is given here to the transition from spread to disintegration, due to its relevance to model the secondary spray generated at spray impact (e.g., [17]). Most criteria make use of the Weber number (e.g., [18]). However, care must be taken to assure that viscous effects are negligible (e.g., [2]), otherwise the Weber number alone does not describe the phenomenon. Prompt splash is then predicted to occur when inertial forces overcome capillary effects, i.e., when:

$$\rho U_0^2 > \frac{\sigma_{lv} h_L}{D_0^2} \tag{8.10}$$

where $h_L \sim (\nu D_0/U_0)^{1/2} = D_0 Re^{-1/2}$ is the thickness of the lamella (e.g., [15, 19]). If this relation is rewritten in terms of the dimensionless groups in Table 8.1, a "splashing parameter" is defined as

$$K_c = AOh^a We^b \tag{8.11}$$

This parameter, introduced by Stow and Hadfield [20] and later confirmed by Mundo et al. [21], is currently used in most correlations reported to predict the onset of splash. Although some of those correlations consider the effect of roughness amplitude (e.g., [20]), they still do not account for the complex mechanisms arising from the influence of other topographical parameters (e.g., [10–22]). This is the main reason for the discrepancies observed when the various criteria are compared and fitted to a diversity of experimental results. It is, therefore, unlikely that a unique criterion can accurately describe disintegration induced by any mechanism.

Given that impacting droplets may disintegrate by diverse mechanisms, secondary droplets are thus generated with dissimilar characteristics. Research efforts have also been put on the development of empirical sub-models to predict the size, velocity and number of secondary droplets. There are relatively few models valid for impacts onto dry surfaces. This must be taken into account, since major limitations to the use of these sub-models lies in the inaccurate consideration of the disintegration limits and in disregarding the boundary conditions for which they were validated.

The Presence of a Liquid Film

The presence of a liquid film over the surface alters the boundary conditions, as the impact event now involves liquid/liquid interactions, though surface characteristics may still be important, depending on the thickness of the film. Based on the dimensionless roughness, $R_{ND} = R_a/D_0$ and on the dimensionless film thickness $\delta = h_f/D_0$ one may classify the impacts [23] as follows:

- Very thin film ($L_R/D_0 < \delta_f < 3R_{ND}^{0.16}$): droplet behavior at impact depends on surface topography. (In the absence of any other parameters besides R_a, Tropea and Marengo [23] define a "length scale of roughness"-L_R).
- Thin film ($3R_{ND}^{0.16} < \delta_f < 1.5$): the dependence of droplet behavior on surface topography becomes weaker.
- Thick film ($1.5 < \delta_f < 4$): droplet impact no longer depends on surface topography, but only on the film thickness.
- Deep pool ($\delta_f > 4$): droplet impact does not depend either on surface topography or on film thickness.

Here we focus on the impacts onto films with $\delta < 2$ since this condition is often satisfied in most practical spray applications. Similarly to droplet impingement on dry targets, diverse outcomes may occur: deposition and coalescence, bounce, formation of a crater, corona splash or uprising of a central jet. Most studies reported in the literature consider corona splash and focus on three issues: (1) characterization of crown morphology, (2) establishment of threshold criteria for disintegration and (3) characterization of secondary atomization.

Morphological Characterization

The morphology of the crown is described with the temporal evolution of its diameter and height, as for impacts onto dry surfaces. Empirical laws for the diameter, valid for normalized film thickness $\delta \leq 1.13$ have been proposed (e.g., [14, 15]), which are similar to (8.9) but where $n = 0.5$ and the constant C now depends on impact conditions:

$$C = 2.\left(\frac{2}{3}\right)^{0.25} U_0^{0.5} \cdot (D_0 h_0)^{-0.25} f^{-0.375} \tag{8.12}$$

where f is the impact frequency, which for single droplets is taken as D_0/U_0.

The crown height is described by diverse expressions, depending on the relevant physical parameters of the phenomena. When the impact is governed by inertial forces and either viscous or compressibility effects are considered, after droplet impact, a kinematic discontinuity appears in the velocity distribution, due to the presence of the free surface of the pre-existing film. The liquid from the central spot spreads and forces the outward quiescent liquid, which is propelled upward and forms the crown. The formulation proposed by Roisman et al. [19] is found to be the most appropriate to describe crown formation and its evolution in the starting phase. At later stages, the discontinuity propagates towards the thicker section of the film and detaches part of it and propels it into the crown. In this case, the shape of the crown rim, $Y = Y(x, t)$, is governed by the eikonal equation which is useful to describe the cusp formation:

$$\frac{\partial Y}{\partial t} = V_{\text{rim}} \left[1 + \left(\frac{\partial Y}{\partial x}\right)^2\right]^{1/2} \tag{8.13}$$

here V_{rim} is the velocity of the free rim propagating over the crown wall, Y is the coordinate along the crown surface and x is the circumferential coordinate over the crown. Although of relative minor importance for impacts onto wetted targets, the surface topography may not negligible, although studies on its effects are quite sparse (e.g., [13]). These studies mainly report that increasing roughness amplitude promotes crown disturbances and further disintegration, which is understandable, based on the discussion for impacts onto dry surfaces.

Impact Regimes and Secondary Atomization

As for the impacts onto dry surfaces, the most straightforward and usual approach is to distinguish between the four basic impact outcomes (stick, spread, rebound and disintegration) by establishing straight boundaries. The boundaries stick/spread, spread/rebound, are often defined by threshold values of the Weber number. For instance, the limit for stick/spread is often set at $We < 5$, while the limit for spread/rebound is usually given as $We < 10$ (e.g., [16, 17]). Concerning the limits for spread/disintegration the force balance in (8.10) is still valid here, although the boundary conditions are different. In line with this, the group $K_c = Oh^{-0.4}We$ is still of major importance, but then, the empirical correlations have to be adjusted by including other parameters such as the film thickness. Hence, correlations for the spread/disintegration limits are of type: $K_{c,\text{wet}} = f(K_c, \delta)$ (e.g., [15, 22]).

Secondary droplet characteristics can also be predicted from semi-empirical models. This subject is not addressed here but the reader is referred to the various reviews (e.g., [24]) which analyze the models proposed for impacts onto wetted and cold surfaces (e.g., [16, 17, 19]).

The Additional Effects of Heat Transfer

Depending on the surface temperature, diverse heat transfer mechanisms may develop when a droplet impacts onto a heated surface, which can be described by the classical boiling curve of a droplet gently deposited on a heated surface (see Fig. 8.2: (1) film evaporation ($T_W \leq T_{sat}$, where T_{sat} is the liquid saturation temperature), (2) bubble boiling ($T_{sat} \leq T_w \leq T_{Nukiyama}$), (3) transition ($T_{Nukiyama} \leq T_W \leq T_{Leidenfrost}$) and (4) film boiling ($T_W \geq T_{Leidenfrost}$).

For the case of an impacting droplet, the critical temperatures establishing the transition between these regimes, particularly the Leidenfrost temperature, depend on the impact conditions, as well as on the properties of the system liquid-surface-vapor. An extensive review on the Leidenfrost temperature and their influencing parameters is presented by Bernardin and Mudawar [25, 26]. Also, though the heat transfer regimes for an impacting droplet ($U_0 \neq 0$) are qualitatively similar to those for a sessile droplet, they are quantitatively different. For example, while for a sessile droplet the film boiling regime is characterized by the formation of a vapor layer, which precludes the contact between the droplet and the surface, the dynamic analog is the reflection (rebound) of the impinging droplet from the surface.

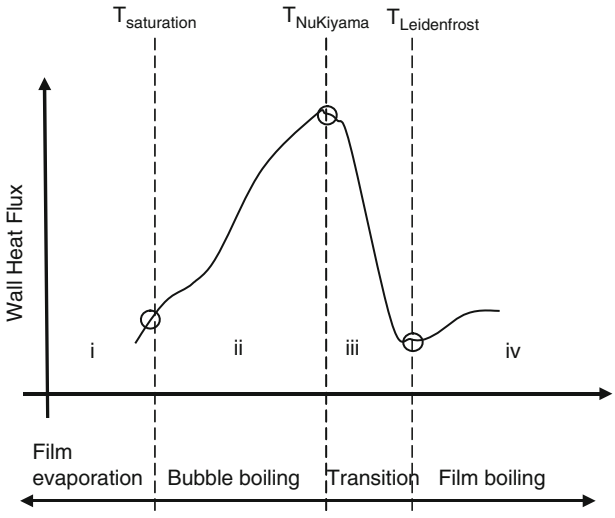


Fig. 8.2 Heat transfer regimes, as described by the classical boiling theory

However, in the latter case, the temperature at which there is in fact no contact between the droplet and the surface, (the so called dynamic Leidenfrost temperature) is very high and it depends on the Weber impact number (e.g., [27]). To avoid misleading, many authors identify the film boiling regime based on a morphological analysis and consider that the droplet falls within the film boiling regime at the so called reflection or pure rebound temperature [17], which is slightly below the dynamic $T_{\text{Leidenfrost}}$.

Morphological Characterization

Figure 8.3 depicts the various outcomes of a droplet impacting with velocity U_0 onto a smooth surface at increased surface temperatures T_W. The images evidence that the relative importance of the effects governing droplet break-up depends on the heat transfer regime.

Within the bubble boiling regime, the secondary atomization occurs within a time scale long enough to allow phase transition of the liquid. Hence, the disintegration occurs at later stages of spreading as the vapor pressure forces disrupt the thin surface area of the lamella. Consistently, the secondary droplets are mainly ejected upwards and droplet morphology is not much influenced by the impact velocity.

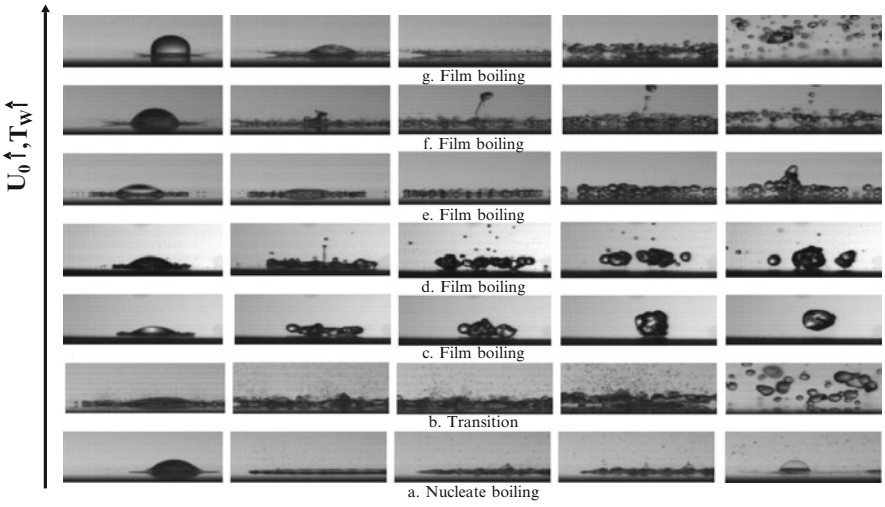


Fig. 8.3 Morphology of an ethanol droplet ($D_0 = 2.4$ mm) impacting onto a smooth stainless steel surface ($R_a = 0.311$ μm, $R_z = 2.32$ μm) at different surface temperatures and impact velocities: (a) $T_w = 115°C$, $U_0 = 2.5$ ms^{-1}, (b) $T_w = 150°C$, $U_0 = 2.5$ ms^{-1}, (c) $T_w = 300°C$, $U_0 = 0.5$ ms^{-1}, (d) $T_w = 300°C$, $U_0 = 0.8$ ms^{-1}, (e) $T_w = 300°C$, $U_0 = 1.3$ ms^{-1}, (f) $T_w = 300°C$, $U_0 = 2.5$ ms^{-1} (formation of the central jet), (g) $T_w = 300°C$, $U_0 = 2.5$ms^{-1} (crown formation)

As the droplet impacts the surface within the film boiling regime, the lamella disintegrates almost immediately after impact, mainly in the radial direction, at the edge of the lamella as for prompt splash onto cold surfaces. Then, a number of large droplets are generated after the levitation of the lamella. The inertial forces dominate the disintegration mechanism within this short time period and droplet morphology is very sensitive to impact velocity. Viscous dissipation is of minor importance but, instead, the vapor film is responsible for the dissipation of kinetic energy.

Impact Regimes and Secondary Atomization

When the impact occurs onto a heated surface, besides the disintegration mechanisms described for impacts onto cold surfaces, disintegration may also occur by thermal induced mechanisms.

Rebound (with or without disintegration), prompt disintegration, (at low U_0) and corona splash are the mechanisms observed at the film boiling regime. Few authors proposed a global representation to explain all possible impact outcomes within the various heat transfer regimes as a function of the Weber number and of the surface temperature (e.g., [17]). Although this approach provides a good qualitative interpretation, the background physics is quite complex. Therefore, most authors rather prefer to analyze the disintegration regimes and the secondary droplet characteristics within each regime, separately (e.g., [28]). Thermal-induced disintegration has been addressed in recent researches (e.g., [29–31]) from which correlations can be devised to predict secondary droplet characteristics within the various boiling regimes. Here the emphasis is given to droplet size.

Within the bubble boiling regime, thermal induced disintegration occurs when the vapor pressure unbalances the equilibrium between surface tension, viscous forces and inertial forces. The nature of this mechanism is different from those observed onto cold surfaces, as it is triggered by combined effects induced by the liquid surface tension and the latent heat of evaporation, h_{fg}, and the analysis requires the use of dimensionless groups complementary to those in Table 8.1. The most important is the Jakob number, defined as $Ja = C_{\mathrm{p}}(T_{\mathrm{W}} - T_{\mathrm{sat}})/h_{\mathrm{fg}}$ where C_{p} is the specific heat of the liquid.

The Jakob number is relevant within the transition regime given the violent boiling occurring within the early instants after impact, before the lamella levitates. On the other hand, there is an evident relation of droplet morphology with the Weber number, as shown in Fig. 8.3.

Within the film boiling regime, the disintegration is clearly dominated by inertial effects and the size of secondary droplets correlate with the thickness of the lamella as defined for the impact onto a dry wall, $h_{\mathrm{L}} \sim (\nu D_0/U_0)^{1/2} = D_0 \mathrm{Re}^{-1/2}$ (e.g., [19]). The following relation is suggested by Moita and Moreira [32] to predict the size of secondary droplets:

$$\frac{\mathrm{SMD}}{D_0} = f(We, Re) \sim A_2 We_N^{-0.6} Re^{-0.23} \tag{8.14}$$

It is worth mentioning that any of the proposed relations accounts with surface topography (the relation suggested by Moita and Moreira (2009) [32] is valid only for $R_a/D_0 < 2E - 3$). The role of surface topography is far more complex than promoting droplet disintegration, especially when dealing with heated targets as it significantly alters the fluid dynamic and thermal behavior of the impinging droplets. Tailored surfaces have quite different wetting behaviors and may be used to enhance liquid/surface contact or, instead to produce hydrophobic behaviors. Distinct results can be obtained in terms of secondary atomization and thermal behavior, depending, once again on the heat transfer regime which is being considered. In line with this, surface topography may even degrade the thermal behavior of the droplet. Optimization of the topographical parameters, based on the relations between R_a/λ_R, is therefore a compromising solution of endorsing liquid–solid contact without promoting an excessively intense thermal induced atomization.

Final Remarks

Droplet/wall interactions were described for impacts onto non-heated dry surfaces to which further complexities were gradually added considering, first the presence of a liquid film and then surface heating. Diverse outcomes develop from droplet impact, depending on impact conditions and surface boundary conditions (e.g., *wettability* and topography). The onset of disintegration depends on the competition between inertial and capillary effects and is shown to scale with a splashing parameter $K_c = AOh^a We^b$. A variety of disintegration mechanisms have been identified, within very dissimilar time scales, so that the relative importance of the governing parameters is different. Therefore, though it is possible to identify general trends, different relations must be considered to predict the secondary droplet characteristics for each mechanism.

References

1. M. Lesser: The impact of a compressible liquid, In Drop-surface interactions, M. Rein (Ed.), Springer Wien, New York, p. 39 (2002).
2. K. Range, F. Feuillebois: Influence of surface roughness on liquid drop impact, J. Col. Int. Sci., 203, 16–30 (1998).
3. D. Sivakumar: Spreading behaviour of an impacting drop on a structured rough surface, Phys. Fluids, 17, 100608 (2005).
4. T. Thomas (Ed.): Rough surfaces, Longman Group Limited (1982).
5. C. W. Extrand: Criteria for ultralyphobic surfaces, Langmuir, 20, 5013–5018 (2004).

6. R. Rioboo, M. Marengo, C. Tropea: Time evolution of liquid drop impact onto solid, dry surfaces, Exp. Fluids, 33(1), 112–124 (2002).
7. I. V. Roisman, R. Rioboo, C. Tropea: Normal impact of a liquid drop on a dry surface: model for spreading and receding, Proc. R. Soc. Lond. Ser. A, 458, 1411–1430 (2002).
8. M. Pasandideh-Fard, Y. M. Qiao, S. Chandra, J. Mostaghimi: Capillary effects during droplet impact on a solid surface, Phys. Fluids, 8(3), 650–658 (1006).
9. M. White: Viscous fluid flow, 2nd edn., McGraw-Hill, New-York (1991).
10. R. Rioboo, C. Tropea, M. Marengo: Outcome from a drop impact on solid surfaces, Atom. Sprays, 11, 155–165 (2001).
11. S. Moita, A. L. N. Moreira: Drop impacts onto cold and heated rigid surfaces: Morphological comparisons, disintegration limits and secondary atomization, Int. J. Heat Fluid Flow, 28(4), 735–752(2007).
12. L. Xu, W. W. Zahang, S. R. Nagel: Drop splashing onto a dry smooth surface, Phys. Rev. Lett., 94, 184505 (2005).
13. L. Randy, G. Vander Wall, G. M. Berger, S. D. Mozes: The combined influence of a rough surface and thin fluid film upon the splashing threshold and splash dynamics of a droplet impacting onto them, Exp. Fluids, 40, 23–32 (2006).
14. G. E. Cossali, M. Marengo, A. Coghe, S. Zhdanov: The role of time in single droplet splash on thin film, Exp. Fluids, 36(6), 888–900 (2004).
15. L. Yarin, D. A. Weiss: Impact of drops on solid surfaces: Self-similar capillary waves and splashing as a new type of kinematic discontinuity, J. Fluid Mech., 283, 141–173 (1995).
16. Z. Han, Z. Xu, N. Trigui: Spray/wall interaction models for multidimensional engine simulation, Int. J. Eng. Res., 1(1), 127–146 (2000).
17. C. X. Bai, A. D. Gosman: Development of a methodology for spray impingement simulation, SAE Paper 950283 (1995).
18. M. Gavaises, A. Theodorakakos, G. Bergeles: Modeling wall impaction of diesel sprays, Int. J. Heat Fluid Flow, 17(2), 130–138 (1996).
19. V. Roisman, K. Horvat, C. Tropea: Spray impact: Rim transverse instability initiating fingering and splash: Description of a secondary spray, Phys. Fluids, 18, 102104 (2006).
20. D. Stow, M. G. Hadfield: An experimental investigation of fluid flow resulting from the impact of a water drop with an unyielding dry surface, Proc. R. Soc. Lond. Ser. A, 373, 419–441 (1981).
21. C. Mundo, C. Tropea, M. Sommerfeld: On the modelling of liquid sprays impinging on surfaces, Atom. Sprays, 8, 625–652 (1998).
22. G. E. Cossali, A. Coghe, M. Marengo: The impact of a single drop on a wetted solid surface, Exp. Fluids, 22, 463–472 (1997).
23. Tropea, M. Marengo: The impact of drops on walls and films, Multiphase Sci. Tech., 11(1), 19–36 (1999).
24. S. Y. Lee, S. U. Ryu: Recent progress of spray-wall interaction research, J. Mech. Sci. Tech., 20(8), 1101–1117 (2006).
25. J. D. Bernardin, I. Mudawar: The Leidenfrost point: Experimental study and assessment of existing models, Trans. ASME, 121, 894–903 (1999).
26. J. D. Bernardin, I. Mudawar: A Leidenfrost point model for impinging droplets and sprays, ASME J. Heat Transfer, 126, 272–278 (2004).
27. H. Xie, Z. Zhou: A model for droplet evaporation near Leidenfrost point, Int. J. Heat Mass Transfer, 50, 5238–5333 (2007).
28. S. W. Akhtar, A. J. Yule: Droplet impaction on a heated surface at high Weber numbers, In: Proceedings of the ILASS-Europe 2001, Zurich (2001).
29. J. D. Naber, P. Farrel: Hydrodynamics of droplet impingement on a heated surface, SAE Paper 930919 (1993).
30. G. E. Cossali, M. Marengo, M. Santini: Secondary atomization produced by single drop vertical impacts onto heated surfaces, Exp. Thermal Fluid Sci., 29, 937–946 (2005).

31. A. L. N. Moreira, A. S. Moita, E. Cossali, M. Marengo, M. Santini: Secondary atomization of water and isooctane drops impinging on tilted heated surfaces, Exp. Fluids, 43, 297–313 (2007).
32. S. Moita, A. L. N. Moreira: Development of correlations to predict the secondary droplet size of impacting droplets onto heated surfaces, Exp. Fluids, 47, 755–768 (2009).

Splashing and Fragmentation of Droplets Landing on a Solid Surface

S. Chandra

Introduction

Driving through rain you can observe water drops hitting the windscreen and splashing, fragmenting into smaller droplets. The sight is fascinating, but the moment too fleeting to observe the details of how a liquid drop splashes. It was not until Worthington [1] built an ingenious apparatus that used the spark from an electric capacitor discharge to illuminate impacting droplets and freeze their motion long enough to take photographs that the details of fluid motion during droplet impact became visible. Decades later, when electronic flash became widely available, Edgerton [2] took pictures of splashing milk droplets that have since been widely reproduced so that the crown-like shape of a splashing droplet is instantly recognizable.

Figure 8.4 shows photographs of successive stages during the impact of a 2.7 mm diameter molten tin droplet impacting with a velocity of 4 m/s on a stainless steel plate [3]. Both drop and plate are at a temperature of 240°C, above the melting point of tin (232°C) so that impact is isothermal. The drop, initially spherical, begins to deform very rapidly upon contact and a thin liquid sheet begins to spread radially under it. The liquid–solid contact line edge of this sheet becomes unstable as it advances and a periodic disturbance is visible around it. Once the droplet reaches its maximum extension surface tension, which is very strong in molten metals, begins to pull it back. Because the molten metal does not wet the steel substrate well the fingers grow longer and break-up into smaller satellite droplets. The remaining liquid bounces off the substrate.

Since early photographic studies first revealed the complex dynamics of droplet impact, splashing has been studied intensively. It is fascinating from the view of fundamental fluid mechanics since many of the phenomena involved, such as the rapid deformation of free liquid surfaces, the motion of liquid–solid contact lines,

S. Chandra
Department of Mechanical and Industrial Engineering, University of Toronto, Toronto, Ontario, Canada
e-mail: Chandra@mie.utoronto.ca

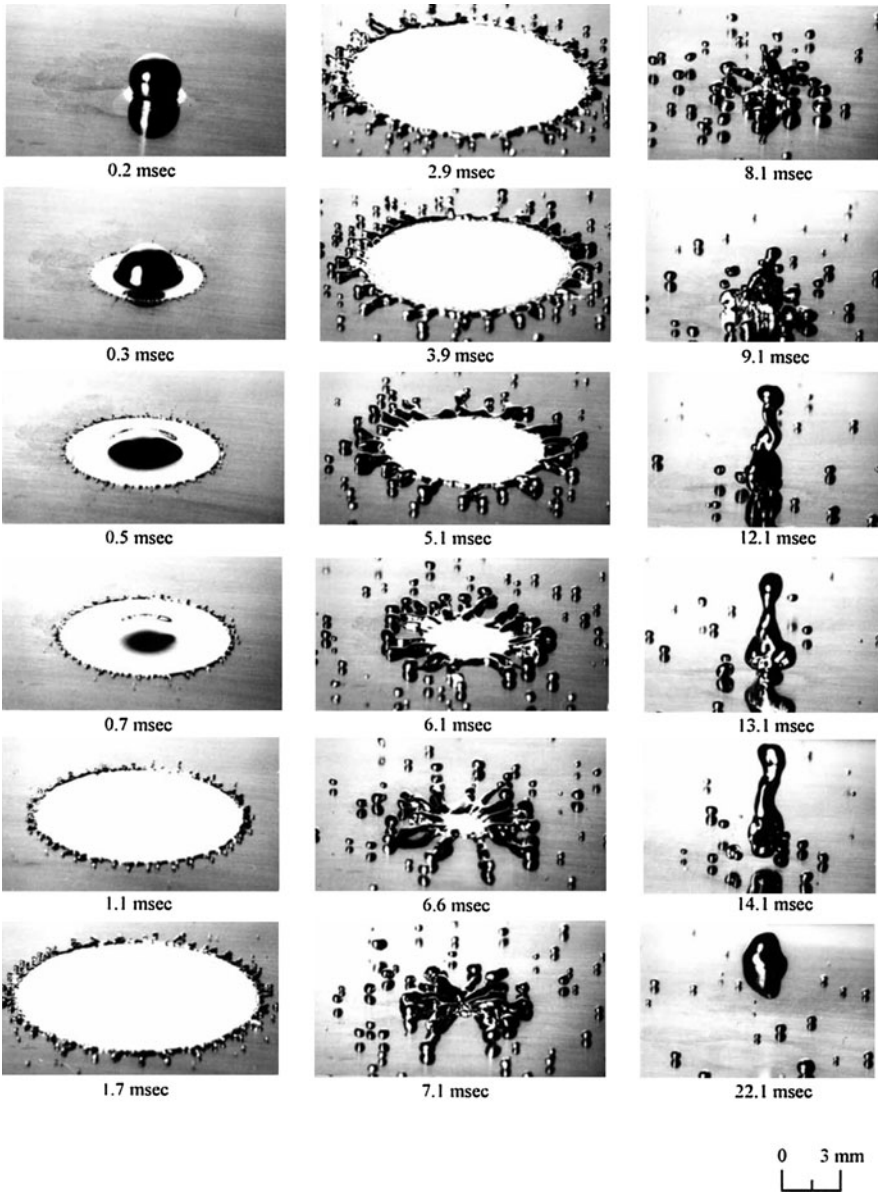


Fig. 8.4 Splashing of a 2.7 mm diameter molten tin droplet during impact with velocity 4 m/s on a stainless steel surface at temperature 240°C. The droplet and substrate are both above the melting point of tin (232°C) so there is no freezing [3]

and the onset of fluid instabilities are not still well understood. There are, in addition, a host of industrial technologies where droplet splashing is important. In spray coating and painting, pesticides application or spray quenching of hot

surfaces it is important to prevent droplet fragmentations since satellite droplets bounce off the surface, reducing the sprayed material that stays on the surface [4]. The quality of pictures printed using an ink-jet technique depend on the accuracy with which droplets are placed on paper: splashing results in random deposition of ink and degrades the image [5]. Splashing may be helpful in preventing accumulation of water on surfaces, which can freeze and lead to ice accretion on aircraft and buildings [6]. The shape of splashes can provide information in forensic studies of blood splatter, from which the size and velocity of droplets can be deduced [7]. As a consequence of this interest a large number of studies of droplet splashing have been carried out and the early literature has been reviewed in detail by Rein [8] and Yarin [9].

When a droplet collides with a surface, there are three phases involved: liquid (the droplet), solid (the substrate) and gas (the surrounding atmosphere). A droplet is described by two impact parameters, diameter (D_d) and impact velocity (V_d), and three physical properties: liquid density (ρ_l), viscosity (μ), and liquid–gas surface tension (γ_{lg}). Combining these into non-dimensional groupings we obtain the Reynolds number ($Re = \rho_l V_d D_d/\mu$) and Weber number ($We = \rho_l V_d{}^2 D_d/\gamma_{lg}$). The Weber number is a ratio comparing inertial forces, which drive splashing, to surface forces that hold the droplet intact. Similarly, the Reynolds number is a ratio of the droplet inertia to viscous forces that damp out motion. Droplets are more likely to splash when Re and We are large. However these two parameters alone do not provide adequate information to predict if splashing will always occur since they do not describe the effect of the substrate and surrounding gas.

The topology of the substrate affects fluid flow and this is typically described by specifying the average surface roughness (R_a). Stow and Hadfield [10] studied the effects of surface roughness on spreading and splashing of water droplets and established that splashing was promoted by increasing drop diameter (D_d), impact velocity (V_d), and surface roughness (R_a). They combined the Reynolds and Weber numbers to define a dimensionless "splash factor" equal to $ReWe^2$ and droplet splashing was observed if this parameter exceeded a critical value, whose value depended on surface roughness. Subsequent studies developed empirical correlation between the splash factor and surface roughness [11–14] but these have been of limited use in predicting whether splashing will occur in impacts that are not very close to the conditions for which experiments were conducted.

Droplet properties and surface roughness alone are not sufficient to account for splashing. Once liquid contacts the solid surface the total surface energy of the system is determined by the surface tension of liquid–solid (γ_{ls}), liquid–gas (γ_{lg}) and solid–gas (γ_{sg}) interfaces. Since γ_{ls} and γ_{sg} are usually not well known it is convenient to replace them with the equilibrium contact angle (θ) using Young's equation:

$$\gamma_{lg} \cos\theta = \gamma_{sg} - \gamma_{ls}$$

The wettability of the surface, characterized by θ, is therefore important in modelling droplet impact. Since the contact line is moving the dynamic advancing

(θ_a) and receding (θ_r) contact angles also have to be considered, depending on whether the droplet edge is spreading outwards or retreating.

As the droplet approaches the substrate, the gas between them has to be expelled and its density and viscosity determine how rapidly this occurs [15, 16]. The gas film trapped at the liquid–solid interface forms a bubble [17]. Then as the edges of the droplet spread out they face resistance from the surrounding atmosphere that has to be pushed back. Xu, Zhang and Nagel [18] demonstrated that lowering the pressure of the surrounding atmosphere suppresses splashing. Figure 8.5 shows photographs of alcohol droplets landing on a smooth glass plate. At atmospheric pressure the droplet splashes, but when pressure is reduced no splashing is seen.

Some of the difficulty in predicting when splashing will occur can be attributed to uncertainties about surface wettability and the effect of the surrounding atmosphere. However, there is a certain ambiguity about the concept of "splashing" itself. Several different break-up modes are grouped under the same term, even though the mechanism of each may be quite different. Rioboo et al. [19] identified three different types of splashing, shown in Fig. 8.6 Immediately after impact, as the liquid sheet under the droplet spreads out, its edge becomes unstable and fingers around the edge begin to break off and form small droplets. This has been termed "prompt splash" and occurs when the edge of the lamella is still in contact with the

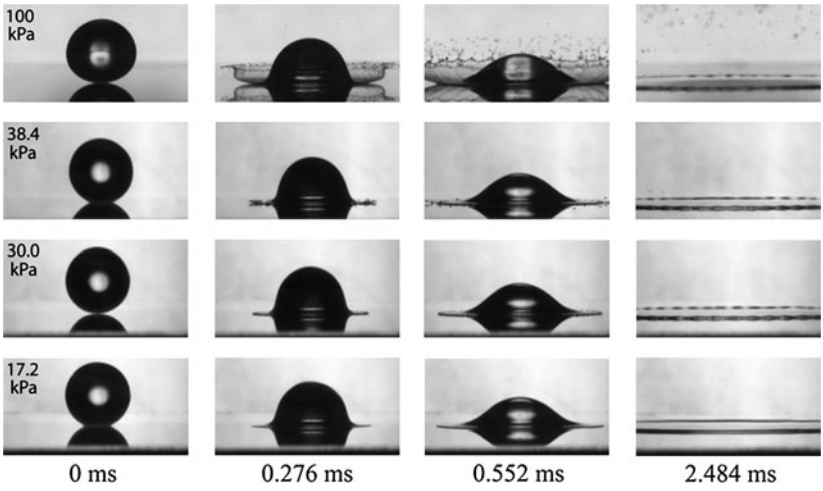


Fig. 8.5 Photographs of a liquid drop hitting a smooth dry substrate. A 3.4 mm diameter alcohol drop hits a smooth glass substrate at impact velocity 3.74 m/s in the presence of different background pressures of air. Each row shows the drop at four times. The first frame shows the drop just as it is about to hit the substrate. The next three frames in each row show the evolution of the drop at 0.276, at 0.552, and at 2.484 ms after impact. In the top row, with the air at 100 kPa (atmospheric pressure), the drop splashes. In the second row, with the air just slightly above the threshold pressure, 38:4 kPa, the drop emits only a few droplets. In the third row, at a pressure of 30.0 kPa, no droplets are emitted and no splashing occurs. However, there is an undulation in the thickness of the rim. In the fourth row, taken at 17.2 kPa, there is no splashing and no apparent undulations in the rim of the drop [18]

surface. The second type of splashing has been termed "corona" splashing: the liquid lamella lifts off the surface, the edge becomes unstable so that fingers grow at regular spaced intervals and the tips of these break off in the crown-like shape characteristic of splashing drops. The third row in Fig 8.6. shows "receding break-up," in which the droplet remains intact until it has spread to its maximum extent and then, as surface tension forces pull it back, the fingers formed due to instabilities around its periphery grow longer and begin to breakup into smaller droplets.

Apart from these three mechanisms, there are two others that can cause break-up of impacting droplets. If a droplet impacts on a substrate that is cold enough to cause freezing, the solid layer formed at the liquid–substrate interface acts as a barrier. The spreading liquid hits the solid mass obstructing its path, jets upwards and disintegrates. This is known as freezing-induced splashing [20] and whether it occurs depends on the rate of heat transfer between the droplet and substrate, which is controlled by the substrate temperature, substrate thermal properties, and the thermal contact resistance at the liquid–solid interface.

There is yet one more mechanism that leads to droplet fragmentation, when impact velocities are very high so that the liquid film becomes very thin and air bubbles trapped under it break through. These punctures in the liquid grow larger and can eventually lead to complete disintegration of the droplet [21].

Prompt Splashing

Prompt splashing is observed immediately after a droplet impacts on a surface and is promoted by increasing impact velocity, droplet diameter and surface roughness [19]. Immediately after impact a very thin liquid lamella emerges from below the droplet and expands radially outwards. The thickness of the liquid sheet, initially a few microns, increases as it spreads [22]. Initially, if the liquid thickness is small and its velocity high, if it hits any obstruction on the surface it is diverted upwards, becoming airborne [23]. The edge of the liquid film becomes unstable as it continues to rise up and disintegrate, releasing satellite droplets. Satellite droplets are shed continuously from the advancing contact line (see Fig. 8.6). Similarly,

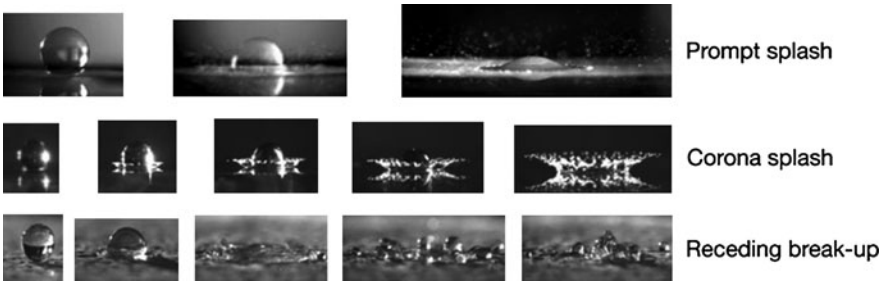


Fig. 8.6 Different types of splashing during droplet impact [19]

a droplet deposited inside a rectangular slot splashes when the spreading liquid hits the vertical walls of the slot and rises upwards [24].

A rough surface has a large number of surface asperities that act as obstacles, promoting prompt splashing [25]. If the surface has asperities that are significant in height, compared to the thickness of the liquid film the edges of the film become unstable and disintegrate releasing small satellite droplets. For splashing to occur, the liquid must have enough momentum so that it rises over the obstructions rather than being halted by them. Xu Barcos and Nagel [25] postulated that prompt splashing occurs if the average surface roughness R_a is greater than Ch, where h is the liquid lamella thickness and C is a function of Re and We. In their experiments they found that $h = 50$ μm and $R_a = 5$ μm, and concluded that $C \sim 0.1$.

Once prompt splashing occurs the liquid lamella thickness continues to increase as more liquid flows from the droplet into the spreading film, while its velocity diminishes [22]. Both of these factors combine to suppress edge instabilities and therefore prompt splashing is typically seen only briefly during droplet impact, during the earliest stages of collision. During experiments carried out at high impact velocities ~40 m/s) it becomes more difficult to differentiate between prompt splashes and corona splashes [21, 26] since the rapidly spreading liquid lamella quickly overruns the thin liquid ligaments that are formed during prompt splashing.

On artificially textured surfaces, where pillars are etched in a square array, splashing occurs along the diagonals, where the liquid meets more resistance, but not along the channels between pillars where it can flow easily [27]. Prompt splashing is sensitive to the spacing, height and arrangement of pillars [28].

Corona Splashes

When a droplet spreads into a thin liquid film the surrounding gas pushes against it, creating an adverse pressure gradient that eventually lifts the edge of the liquid lamella off the surface. The edge of the liquid sheet becomes unstable so that undulations begin to form, grow into long fingers and then detach in the form of satellite droplets (see Fig. 8.5). Schroll et al. [29] numerically simulated the impact of a viscous liquid drop onto a smooth dry solid surface, including the effect of the surrounding air. The no-slip boundary condition at the wall produces a boundary layer inside the liquid. As the radial expansion slows the pressure gradient within the liquid sheet drops to zero and the boundary layer is not securely attached to the wall. An adverse pressure gradient, created by resistance from the surrounding airflow, can cause the boundary layer to separate from the wall so that the liquid layer rises up to form a corona. Much more prominent corona splashes are seen when a droplet lands on a thin liquid film since the surrounding quiescent liquid offers strong resistance to the spreading. The adverse pressure gradient creates a corona that breaks up [30, 31].

Many studies have been devoted to predicting when corona splashes will occur. Mundo, Sommerfeld, and Tropea [11] found that droplets splashed only if the

so-called "splash parameter" $K = We^{1/2}Re^{1/4}$ exceeds a critical value $K = 57.7$. Cossali, Coghe and Marengo [30] developed an empirical correlation between K, R_a and the liquid lamella thickness h.

The nature of the instability that initiates formation of fingers around the edges of the spreading droplet has been the subject of much debate [9]. Allen [32] suggested that fingering is initiated by a Rayleigh-Taylor instability that occurs at the interface between liquid and surrounding gas when the lighter gas pushes the heavier liquid. Linear instability analysis predicts that the fastest growing disturbances at a planar liquid–gas interface will have a wavelength:

$$\lambda = 2\pi\sqrt{\frac{3\gamma_{lg}}{a(\rho_l - \rho_g)}}$$

where a is the deceleration of the interface and ρ_l and ρ_g the densities of the liquid and surrounding gas respectively. Allen [32] estimated $a = V_d^2/(D_{max}/2)$, with D_{max} the diameter of the droplet at its maximum extension, so that the number of fingers $N = \pi D_{max}/\lambda$. He demonstrated reasonable agreement between predictions and the number of fingers around ink blots formed by drops falling on a piece of paper. Bhola and Chandra [33] proposed that $a = V_d^2/D_d$, and using a simple energy balance model to calculate D_{max}, obtained:

$$N = \frac{\left(We^{1/2}Re^{1/4}\right)}{\left(4\sqrt{3}\right)} = \frac{K}{\left(4\sqrt{3}\right)}$$

Range and Feuillebois [34] studied splashing of droplets of water–glycerin and water–ink mixtures and found that the number of fingers was sensitive to the surface tension of the liquid, but not its viscosity. Kim, Feng and Chun [35] presented a Rayleigh-Taylor instability analysis of the liquid sheet emerging from under the drop, solving the potential flow equation. They neglected the effect of viscosity, arguing that formation of fingers is initiated immediately after droplet impact, when viscous forces are negligible. They solved the governing equations numerically, to obtain the fastest growing wavelength as a function of We. Since viscous effects were neglected, the solution was independent of Re. Mehdizadeh, Chandra, Mostaghimi [21] found an analytical solution to the equations governing the Rayleigh-Taylor instability and found that $N = 1.14\ We^{1/2}$ predicted reasonably the number of fingers formed around water droplets over a wide range of We. Fedorchenko and Chernov [36] claimed the initial radial liquid velocity equals the sonic velocity in the liquid therefore the liquid lamella experiences very high deceleration, sufficient to trigger the Rayleigh–Taylor instability. Pepper, Courbin and Stone [37] measured lamella deceleration as high as $10^3 g$.

The air film trapped under the impacting droplet plays an important role in creating instabilities. Xu, Zhang, Nagel [18] demonstrated that if the pressure in the atmosphere surrounding an impacting drop is reduced corona splashes are

suppressed. Prompt splashing, however, persists even in the absence of surrounding gas [25]. Thoroddsen and Sakakibara [38] photographed water droplets landing on a glass plate, viewed from below during very early stages of impact and showed that the instability begins immediately at the first contact of the drop with the solid surface. The bottom of the droplet becomes flattened as the droplet approaches the surface due to the increase in pressure in the air gap between the liquid and solid surface. Thoroddsen and Sakakibara [38] proposed that fingering is initiated by a Rayleigh–Taylor instability of the annular ring of fluid that first touches the surface, which is then propagated over to the radially expanding sheet of liquid.

Yoon et al. [39] also emphasized the importance of the air trapped between the droplet and substrate. They pointed out that the Rayleigh-Taylor instability should continue to occur even if the density of the surrounding gas goes to zero, which contradicts the findings of Xu, Zhang and Nagel [18] that splashing disappeared when gas pressure was reduced. They proposed instead that fingering is initiated by a Kelvin-Helmholtz instability that occurs when the heavier liquid spreads over a thin gas film that is trapped between the droplet and substrate.

The dominant wavelength for a Kelvin-Helmhotz instability is [40]

$$\lambda = 2\pi\sqrt{\frac{3\sigma}{a\rho_g V_{diff}^2}}$$

where V_{diff} is the velocity difference between the liquid and gas layers. In the limit that $\rho_g \rightarrow 0$ the instability is suppressed, which agrees with the observations of Xu, Zhang and Nagel [18]. Yoon et al. [40] have proposed that it is the Kelvin-Helmholtz, rather than the Rayleigh-Taylor, instability that leads to initiation of fingers around the edges of spreading drops.

When droplets impact on an elastic membrane splashing can be suppressed by reducing the tension of the substrate [37]. The flexible substrate absorbs some energy, but it also makes it easier for air to escape from below the droplet, which reduces splashing.

Receding Breakup

Once a droplet has reached its maximum extension after impact, surface tension forces pull its edges back. If the liquid-solid contact angle is small, less than 90°, neighboring fingers along the edges of the spreading liquid sheet tend to merge with each other [38] and disappear. However, if the contact angle is large, as is the case with droplets of molten metal [3] or for impact on super-hydrophobic surfaces [41] the fingers stay well defined and grow longer as the liquid recedes. The cylindrical fingers become unstable and begin to break-up into become so long that they disintegrate (see Fig. 8.4).

Freezing Induced Splashing

The presence of solid asperities on the substrate promotes splashing since it obstructs the flow of the spreading droplet. In the case that the droplet spreads on a substrate at a temperature lower than the freezing point of the liquid, it will begin to solidify. If heat transfer from the spreading droplet to the substrate is rapid, the rate of solidification in the droplet becomes sufficiently fast that its edges begin to freeze and form a solid ring while liquid is still flowing radially outwards. If the droplet Weber number is low the solid layer will stop liquid motion and suppress splashing since the impacting liquid does not have enough momentum to jet over the solidified layer near the edges of droplets and splash [3]. If the Weber number is high the solid layer acts as a surface asperity that promotes splashing: the radially spreading liquid will hit the obstruction, become unstable, and break into satellite droplets.

Mehdizadeh et al. [21] built an apparatus in which molten tin droplets impinged on a steel plate mounted on the rim of a rotating flywheel, giving impact velocities of up to 40 m/s and $We \sim 10^3$. Photographs of splashing droplets were compared with predictions from computer simulations that showed that freezing around the edges of a spreading droplet obstructs liquid flow and causes splashing. Dhiman and Chandra [20] photographed impact of molten tin droplets on solid plates for a range of impact velocities (10–30 m/s), substrate temperature (25°C–200°C) and substrate materials (stainless steel, aluminum and glass). Figure 8.7 shows images of 0.6 mm diameter tin droplets impacting on a mirror-polished stainless steel substrate with 20 m/s velocity. Each column shows successive stages of droplet impact on a substrate at initial temperature ($T_{s,i}$) varying from 25°C to 200°C (indicated at the top of the column). The first picture in each sequence shows a droplet prior to impact, and the last shows the final splat shape. Droplets hitting a cold substrate ($T_{s,i} = 25°C$ –150°C) splashed extensively, producing small satellite droplets and leaving a splat with irregular edges. The extent of splashing decreased and eventually disappeared as substrate temperature was increased. No splashing was visible on a surface at 180°C. Solidification did not start until fairly late during spreading; localized freezing at several spots acted to obstruct spreading of the splat and produced an irregular shaped splat even though there was no splashing. At $T_{s,i} =$ 200°C solidification was sufficiently delayed that droplets spread to form thin discs. Computer simulations [42] have shown that freezing around the droplet periphery during spreading on a substrate at low temperature obstructs liquid flow and triggers splashing. When substrate temperature is increased, freezing is slowed down and the droplet spreads in the form of a thin liquid sheet without any splashing.

Dhiman and Chandra [20] developed an analytical model to predict the substrate temperature at which splashing would occur by using a one-dimensional model for solidification of a molten metal droplet in contact with a semi-infinite substrate. They assumed that splashing occurred if the thickness of the solid layer reached that of the splat by the time the droplet had finished spreading. The thermal contact resistance between the droplet and surface was found to play a critical role in

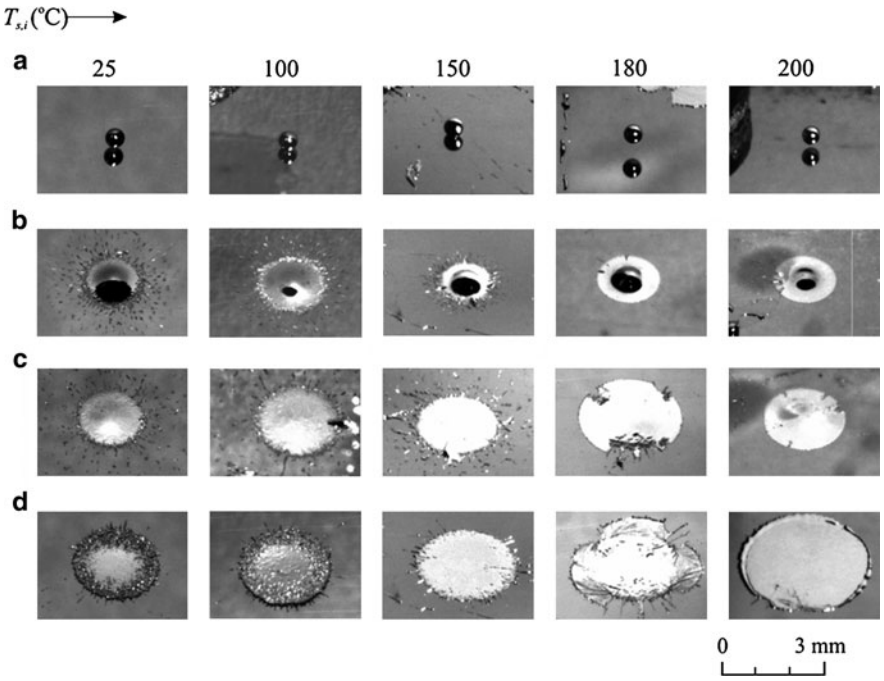


Fig. 8.7 Impact of molten tin drops with velocity 20 m/s on a stainless steel surface at temperature, $T_{s,i}$ (1) 25°C, (2) 100°, (3) 150°C, (4) 180°C and (5) 200°C. The last picture in each column is the final solidified shape of the droplet. $Re = 43{,}636$, $We = 3{,}180$

determining whether splashing occurred, especially for high temperature melting point materials [43, 44]. Thermal resistance is created by imperfect contact at the droplet-substrate interface, and may be due to trapped air or the presence of contaminants such as adsorbed water vapor or oxide layers on the surface. The transition temperature at which splashing occurs therefore depends on the condition of the surface substrate.

Droplet Rupture

Studies on splashing have largely focused on instabilities along the edges of the thin film created by the impacting droplet. Most of these studies have been conducted at relatively low impact velocities (1–10 m/s), where fluid instabilities around the edge of the spreading droplet caused the formation of long fingers that detached to form satellite droplets [3, 4]. At higher impact velocities, up to 40 m/s, photographs of water droplets impacting a polished stainless steel surface showed that the liquid became so thin that it ruptured internally and then, as the holes expanded due to surface tension the film disintegrated completely. Most practical spray applications

use high impact velocities and it is likely that a major cause of droplet break-up is internal rupture rather than edge instabilities.

Dhiman and Chandra [41] photographed impact of water droplets on surfaces of different wettability at impact velocities up to 30 m/s. Figure 8.8 shows three different sequences of the impact of water droplets on a wax surface at three different impact velocities: 10 m/s, 20 m/s and 30 m/s. Each vertical column shows successive stages of impact at one of the velocities, which yielded Reynolds numbers (*Re*) of 5,800, 11,600, and 17,400 respectively. Droplets flattened into a thin film after impact as they reached their maximum extension, followed by retraction until they eventually attained equilibrium. The diameter of the films at maximum extension increased with *Re* and hence their thickness decreased. Holes were formed in each film that grew larger, rendering the film unstable.

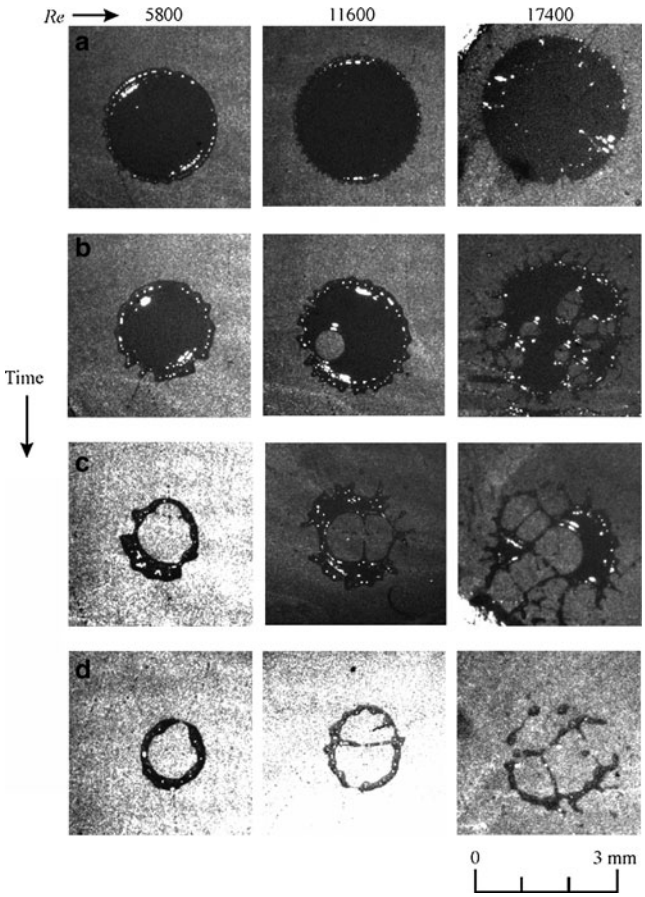


Fig. 8.8 Impact of 580 μm diameter water droplets with different *Re* on smooth wax surfaces. Each column shows successive stages of impact [41]

Dhiman and Chandra [41] used a simple thermodynamic model to predict whether holes in a thin film would grow or not, comparing the surface energy of the intact liquid film resting on a surface with the energy of the same film with a hole in it. If the addition of the surface area of the hole decreased the total energy of the system, the hole would continue to grow, whereas, if it increased the energy the hole would close. In general, holes in a liquid film on a solid surface with very small or large contact angles have a large surface area and hence close up [41]. An intermediate contact angle produces a meniscus with small surface area, and such holes tend to expand. Experimentally, it was found that water films on hydrophilic or superhydrophobic surfaces remain stable, whereas those on surfaces with contact angles $\sim 90^\circ$ are the most likely to rupture.

For film rupture to commence a hole must be initiated in the liquid film. In practice, air bubbles trapped between the impacting droplet and substrate break through the liquid film and create holes. Increasing surface roughness promotes surface rupture since it increases the amount of air trapped at the interface. Similarly, raising the temperature of the substrate above the liquid boiling point also creates bubble and causes the film to fragment [45].

References

1. A. M. Worthington: A study of splashes. Longmans, Green, London, 129 pp. (1908).
2. H. E. Edgerton, J. R. Killian: Flash! Seeing the unseen by ultra-high-speed photography. Branford, Boston, 215 pp. (1954).
3. S. D. Aziz, S. Chandra: Impact, recoil and splashing of molten metal droplets, Int. J. Heat Mass Transfer, 43, 2841–2857 (2000).
4. S. Chandra, P. Fauchais: Formation of solid splats during thermal spray deposition, J. Thermal Spray Technol., 18, 148–180 (2009).
5. R. Li, N. Ashgriz, S. Chandra, J. R. Andrews: Shape and surface texture of molten droplets deposited on cold surfaces, Surface Coatings Technol., 202, 3960–3966 (2008).
6. R. W. Gent, N. P. Dart, J. T. Cansdale: Aircraft icing, Philos. Trans. R. Soc. Lond. A, 358, 2873–2911 (2000).
7. L. Hulse-Smith, N. Z. Mehdizadeh, S. Chandra: Deducing droplet size and impact velocity from circular bloodstains, J. Forensic Sci., 50, 1–10 (2005).
8. M. Rein: Phenomena of liquid drop impact on solid and liquid surfaces, Fluid Dyn. Res., 12, 61–93 (1993).
9. A. L. Yarin: Drop impact dynamics: Splashing, spreading, receding, bouncing. . ., Annu. Rev. Fluid Mechanics, 38, 159–192 (2006).
10. C. D. Stow, M. G. Hadfield: An experimental investigation of fluid flow resulting from the impact of a water drop with an unyielding dry surface. Proc. R. Soc. Lond. Ser. A, 373, 419–441 (1981).
11. C. Mundo, M. Sommerfeld, C. Tropea: Droplet-wall collisions: experimental studies of the deformation and breakup process, Int. J. Multiphase Flow, 21, 151–173 (1995).
12. G. E. Cossali, A. Coghe, M. Marengo: The impact of a single drop on a wetted solid surface, Exp. Fluids, 22, 463–72 (1997).
13. K. Range, F. Feuillebois: Influence of surface roughness on liquid drop impact, J. Colloid Interface Sci., 203, 16–30 (1998).

14. R. L. Vander Wal, G. M. Berger, S. D. Mozes: The combined influence of a rough surface and thin fluid film upon the splashing threshold and splash dynamics of a droplet impacting onto them, Exp. Fluids, 40, 23–32 (2006).
15. M. Mani, S. Mandre, M. P. Brenner: Precursors to splashing of liquid droplets on a solid surface, Phys. Rev. Lett., 102, 134502 (2009).
16. M. Mani, S. Mandre, M. P. Brenner: Events before droplet splashing on a solid surface, J. Fluid Mech., 647, 163–185 (2010).
17. V. Mehdi-Nejad, J. Mostaghimi, S. Chandra: Air bubble entrapment under an impacting droplet, Phys. Fluids, 15, 173–183 (2003).
18. L. Xu, W. W. Zhang, S. R. Nagel: Drop splashing on a dry smooth surface, Phys. Rev. Lett., 94, 184505 (2005).
19. R. Rioboo, C. Tropea, M. Marengo: Outcomes from a drop impact on solid surfaces, Atomization Sprays, 11, 155–165 (2001).
20. R. Dhiman, S. Chandra: Freezing-induced splashing during impact of molten metal droplets with high Weber numbers, Int. J. Heat Mass Transfer, 48, 5625–5638 (2005).
21. N. Z. Mehdizadeh, S. Chandra, J. Mostaghimi: Formation of fingers around the edges of a drop hitting a metal plate with high velocity, J. Fluid Mechanics, 510, 353–373 (2004).
22. J. de Ruiter, R. E. Pepper, H. A. Stone: Thickness of the rim of an expanding lamella near the splash threshold, Phys. Fluids, 22, 022104 (2010).
23. C. Jossrand, L. Lemoyne, R. Troeger, S. Zaleski: Droplet impact on a dry surface: Triggering the splash with a small obstacle, J. Fluid Mechanics, 524, 47–56 (2005).
24. H. J. Subramani, T. Al-Housseiny, A. U. Chen, M. Li, O. A. Basaran: Dynamics of drop impact on a rectangular slot, Ind. Eng. Chem. Res., 46, 6105–6112 (2007).
25. L. Xu, L. Barcos, S. R. Nagel: Splashing of liquids: Interplay of surface roughness with surrounding gas, Phys. Rev. E, 76, 066311 (2007).
26. K. L. Pan, K. C. Tseng, C. H. Wang: Breakup of a droplet at high velocity impacting a solid surface, Exp. Fluids, 48, 143–156 (2010).
27. L. Xu: Liquid drop splashing on smooth, rough, and textured surfaces, Phys. Rev. E, 75, 056316 (2007).
28. P. Tsai, S. Pacheco, C. Pirat, L. Lefferts, D. Lohse: Drop impact upon micro- and nanostructured superhydrophobic surfaces, Langmuir, 25, 12293–12298 (2009).
29. R. D. Schroll, C. J. S. Zaleski, W. W. Zhang: Impact of a viscous liquid drop, Phys. Rev. Lett., 104, 034504 (2010).
30. G. E. Cossali, A. Coghe, M. Marengo The impact of a single drop on a wetted solid surface, Exp. Fluids, 22, 463–472 (1997).
31. G. E. Cossali, M. Marengo, A. Coghe, S. Zhdanov: The role of time in single drop splash on thin film, Exp. Fluids, 36, 888–900 (2004).
32. R. F. Allen: The role of surface tension in splashing, J. Coll. Interface Sci., 51, 350–351 (1975).
33. R. Bhola, S. Chandra: Parameters controlling solidification of molten wax droplets falling on a solid surface, J. Mater. Sci., 34, 4883–4894 (1999).
34. K. Range, F. Feuillebois: Influence of surface roughness on liquid drop impact, J. Colloid Interface Sci., 203, 16–30 (1998).
35. H. Y. Kim, Z. C. Feng, J. H. Chun: Instability of a liquid jet emerging from a droplet upon collision with a solid surface. Phys. Fluids, 12, 531–541 (2000).
36. A. I. Fedorchenko, A. A. Chernov: Formation of fingers at the front of an axially symmetric film of liquid upon the impact of a drop with a solid surface, Doklady Phys., 44, 570–572 (1999).
37. R. E. Pepper, L. Courbin, H. A. Stone: Splashing on elastic membranes: The importance of early-time dynamics, Phys. Fluids, 20, 082103 (2008).
38. S.T. Thoroddsen, J. Sakakibara: Evolution of the fingering pattern of an impacting drop, Phys. Fluids, 10, 1359–74 (1998).

39. S. S. Yoon, R. A. Jepsen, M. R. Nissen, T. J. O'Hern: Experimental investigation on splashing and nonlinear fingerlike instability of large water drops, J. Fluids Struct., 23, 101–115 (2007).
40. S. S. Yoon, R. A. Jepsen, S. C. James, J. Liu, G. Aguilar: Are drop-impact phenomena described by Rayleigh-Taylor or Kelvin-Helmholtz theory?, Drying Technol., 27, 316–321 (2009).
41. R. Dhiman, S. Chandra: Rupture of thin films formed during droplet impact, Proc. R. Soc. A, 466, 1229–1245 (2010).
42. N. Z. Mehdizadeh, M. Raessi, S. Chandra, J. Mostaghimi: Effect of substrate temperature on splashing of molten tin droplets, J. Heat Transfer, 126, 445–452 (2004).
43. A. McDonald, C. Moreau, S. Chandra: Thermal contact resistance between plasma sprayed particles and flat surfaces, Int. J. Heat Mass Transfer, 50, 1737–1749 (2007).
44. R. Dhiman, A. McDonald, S. Chandra: Predicting splat morphology in a thermal spray process, Surface Coatings Technol., 201, 7789–8801 (2007).
45. N. Z. Mehdizadeh, S. Chandra: Boiling during high velocity impact of water droplets on a hot stainless steel surface, Proc. R. Soc. Lond. A, 462, 3115–3131 (2006).

Part II
Atomization and Spray Models

Chapter 9
Atomization Models

C.A. Chryssakis, D.N. Assanis, and F.X. Tanner

Abstract In an effort to characterize fuel sprays using Computational Fluid Dynamics (CFD) codes, a number of spray breakup models have been developed. The primary atomization of liquid jets and sheets is modeled considering growing wave instabilities on the liquid/gaseous interface or a combination of turbulence perturbations and instability theories. The most popular approaches for the secondary atomization are the Taylor Analogy Breakup (TAB) model, the Enhanced-TAB (E-TAB) model, and the WAVE model. Variations and improvements of these models have also been proposed by other researchers. In this chapter, an overview of the most representative models used nowadays is provided.

Keywords Atomization · Breakup · CAB model · KH-RT model · LISA · TAB model · USB model

Primary Atomization of Liquid Jets

A commonly used primary atomization model for liquid jets has been developed by Huh et al. [1]. The model considers the effects of both infinitesimal wave growth on the jet surface and jet turbulence including cavitation dynamics. Initial perturbations on the jet surface are induced by the turbulent fluctuations in the jet, originating from the shear stress along the nozzle wall and possible cavitation effects. This approach overcomes the inherent difficulty of wave growth models, where the exponential wave growth rate becomes zero at zero perturbation amplitude.

C.A. Chryssakis (✉)
National Technical University of Athens, School of Naval Architecture & Marine Engineering, Division of Marine Engineering, Heroon Polytechniou 9, GR-15773, Zografou, Athens, Greece
e-mail: cchryssa@naval.ntua.gr

N. Ashgriz (ed.), *Handbook of Atomization and Sprays*,
DOI 10.1007/978-1-4419-7264-4_9, © Springer Science+Business Media, LLC 2011

The model is based on two main assumptions: (1) The length scale of turbulence is the dominant length scale of atomization:

$$L_A = C_1 \cdot L_t = C_2 \cdot L_w \tag{9.1}$$

where L_t and L_w are the turbulence length scale and the wavelength of surface perturbations respectively.

(2) The time scale of atomization is the linear sum of the turbulence and wave growth time scales:

$$\tau_A = C_3 \cdot \tau_t + C_4 \cdot \tau_w \tag{9.2}$$

where τ_t is the turbulence time scale and τ_w the wave growth time scale that determines the exponential growth rate. The empirical constants C_1 to C_4 are set to 2.0, 0.5, 1.2 and 0.5 respectively.

The initial turbulence length and time scale are calculated using average quantities for the turbulent kinetic energy and energy dissipation rate as:

$$\begin{aligned} L_t^0 &= C_\mu \frac{k_{avg}^{3/2}}{\varepsilon_{avg}} \\ \tau_t^0 &= C_\mu \frac{k_{avg}}{\varepsilon_{avg}} \end{aligned} \tag{9.3}$$

where $C_\mu = 0.09$ and the average quantities are estimated as:

$$\begin{aligned} k_{avg} &= \frac{U^2}{8(L/D)} \left[\frac{1}{c_d^2} - K_c - \left(1 - s^2\right) \right] \\ \varepsilon_{avg} &= K_\varepsilon \frac{U^2}{2L} \left[\frac{1}{c_d^2} - K_c - \left(1 - s^2\right) \right] \end{aligned} \tag{9.4}$$

where L, D are the nozzle length and diameter, c_d the nozzle discharge coefficient, K_c is a constant taking into account losses in the contraction corner (typically set to 0.45), K_ε is a constant for average turbulent energy dissipation, set to 0.27, and s is the area ratio at the nozzle contraction.

The resulting turbulence length and time scale are given as a function of the time and the initial turbulence conditions as:

$$\begin{aligned} L_t(t) &= L_t^0 \left(1 + \frac{0.0828t}{\tau_t^0} \right)^{0.457} \\ \tau_t(t) &= \tau_t^0 + 0.0828t \end{aligned} \tag{9.5}$$

The wave growth timescale is approximated by neglecting the surface tension and viscous effects and maintaining only the aerodynamic destabilizing term:

$$\tau_w = \frac{L_w}{U} \sqrt{\frac{\rho_L}{\rho_G}} \tag{9.6}$$

The liquid jet can be represented in the form of computational parcels (blobs) with breakup rate proportional to the ratio of the atomization length over the time scale:

$$\frac{dD_p}{dt} = k_1 \frac{L_A}{t_A} \tag{9.7}$$

where the constant k_1 is subject to calibration, and is expected to obtain values of the order of 1. The resulting drop size is assumed to be equal to the atomization length scale, L_A, as calculated with Eq. 9.1. When the reduced primary parcel reaches the size of the secondary droplet, the primary atomization process for this parcel is assumed to be completed and the secondary atomization model is engaged to model its behavior.

In order to take into account the aerodynamic forces on the liquid core, it can be assumed that the liquid core is wedge-shaped, with an aerodynamic drag coefficient of $C_D = 0.3$, according to [2]. This assumption may have to be corrected by increasing the drag coefficient to take into account the instabilities on the liquid/gas interface that disturb the liquid surface and the gas flow around the liquid core.

Primary Atomization of Liquid Sheets (LISA Model)

The Linearized Instability Sheet Atomization (LISA) model has been developed by Schmidt et al. [3, 4] in order to model the primary breakup of the liquid film emerging from outwardly opening high-pressure swirl injectors, typically used in Gasoline Direct Injection engines. It is based on simple fluid mechanics principles, in an attempt to eliminate the required experimental data. Due to the centrifugal forces developed as a result of the swirl component of the velocity, at the exit of the orifice a liquid film is formed on the nozzle walls. The thickness of this film, h_o, is calculated from the mass flow rate equation:

$$\dot{m}_l = \pi \rho_l u h_o (d_o - h_o) \tag{9.8}$$

where u is the axial component of velocity at the nozzle exit, which can be calculated if the spray cone angle is known.

The model assumes two-dimensional, viscous, incompressible liquid sheet with thickness of $2h$ and velocity U, moving through a quiescent, inviscid, incompressible gas medium. The breakup occurs due to wave disturbances, with a growth rate approximated by Eq. 3.2.7:

$$\omega_r = -2\nu_l k^2 + \sqrt{4\nu_l^2 k^4 + \rho_r U^2 k^2 - \frac{\sigma k^3}{\rho_l}}, \tag{9.9}$$

where ρ_r is the air-fuel density ratio and k the wave number. This expression is numerically maximized to calculate the maximum growth rate, $\omega_{\max}$, which is then used for the evaluation of breakup time and length:

$$\tau = \frac{1}{\omega_{\max}} \ln\left(\frac{\zeta_b}{\zeta_o}\right) \tag{9.10}$$

and

$$L = U \cdot \tau = \frac{U}{\omega_{\max}} \ln\left(\frac{\zeta_b}{\zeta_o}\right), \tag{9.11}$$

where $\ln\,(\zeta_b/\zeta_o) = 12$. The sheet half-thickness at L is given by:

$$h = \frac{2h_o[d_o - h_o]/\cos\theta}{2L\sin\theta + d_o - h_o} \tag{9.12}$$

where h_o is the film thickness, measured perpendicular to the injector axis, at the nozzle exit. At the point of breakup, fluid ligaments are formed, with diameter calculated from the mass balance, as:

$$d_L = \sqrt{\frac{16h_b}{k_{\max}}} \tag{9.13}$$

where $k_{\max}$ is the wave number corresponding to the maximum growth rate $\omega_{\max}$ and h_b the sheet thickness at the breakup location. The ligaments break up once the amplitude of the unstable waves is equal to the radius of the ligaments, giving droplets with diameter:

$$d_D = \left(\frac{3\pi d_L^2}{K_L}\right)^{1/3} \tag{9.14}$$

with

$$K_L = \left[\frac{1}{2} + \frac{3\mu_l}{2(\rho_l \sigma d_L)^{1/2}}\right]^{-1/2} \cdot \frac{1}{d_L} \tag{9.15}$$

which is the Weber result for the wave number corresponding to the maximum growth rate for the breakup of a cylindrical, viscous liquid column (the ligament in this case). After the end of primary breakup, the TAB model (described in the next section) can be used for the secondary breakup of the occurring droplets, which have sizes according to the Rosin–Rammler distribution.

TAB and E-TAB Models

The TAB (Taylor Analogy Breakup) breakup model has been developed by O'Rourke and Amsden [5] and is considered one of the standard models used for spray breakup calculations. The model is based on an analogy between an oscillating and distorting droplet, and a spring–mass system. The restoring force of the spring corresponds to the surface tension forces, while the external force on the mass is equivalent to the gas aerodynamic force and the damping force represents the liquid viscosity effects.

The main limitation of the TAB model is that it can only keep track of one oscillation mode, while in reality more than one mode exists. The model keeps track only of the fundamental mode, corresponding to the lowest order harmonic whose axis is aligned with the relative velocity vector between droplet and gas. This is the most important oscillation mode, but for large Weber numbers other modes are also contributing significantly to drop breakup. Despite this limitation, a rather good agreement is achieved between the numerical and experimental results for low Weber numbers.

The equation of a damped, forced harmonic oscillator is given by:

$$m\ddot{x} = F - k_s x - d\dot{x}, \tag{9.16}$$

where x is the displacement (corresponding to the displacement of the equator of the droplet from its equilibrium position), F are the external forces (corresponding to aerodynamic drag), k_s the spring's constant (corresponding to surface tension) and d the damping parameter (corresponding to viscous forces). In accordance with the Taylor analogy, the physical dependencies of the coefficients in this equation are:

$$\frac{F}{m} = C_F \frac{\rho_g u^2}{\rho_l r}, \quad \frac{k_s}{m} = C_k \frac{\sigma}{\rho_l r^3}, \quad \frac{d}{m} = C_d \frac{\mu_l}{\rho_l r^2} \tag{9.17}$$

where C_f, C_k, and C_d are dimensionless numbers. In addition, C_b is used to non-dimensionalize x, by defining $y = x/(C_b r)$. Now, the equation of the oscillator can be written as:

$$\ddot{y} = \frac{C_f}{C_b} \frac{\rho_g}{\rho_l} \frac{u^2}{r^2} - \frac{C_k \sigma}{\rho_l r^3} y - \frac{C_d \mu_l}{\rho_l r^2} \dot{y} \tag{9.18}$$

with breakup occurring if and only if $y > 1$. Also, it is assumed that breakup occurs if and only if the amplitude of oscillation of the north and south poles equals the drop radius. The dimensionless constants C_f, C_k, and C_d are determined by comparing with experimental and theoretical results and have the following values: $C_k = 8$, $C_d = 5$, $C_b = 0.5$ and $C_f = 1/3$ [3]. It has been proposed by Grover et al. [6] that a value of $C_k = 6$ may be more appropriate for sprays used in Gasoline Direct Injection applications.

In order to predict the drop sizes after breakup, an equation based on energy conservation analysis is derived. The analysis equals the energy of the parent drop before breakup with the energies of the subsequent product drops after breakup and it yields:

$$\frac{r}{r_{32}} = 1 + \frac{8K}{20} + \frac{\rho_l r^3}{\sigma}\dot{y}^2\left(\frac{6K-5}{120}\right), \tag{9.19}$$

where r_{32} is the Sauter Mean Radius (SMR) of the parent droplet and K a constant that must be evaluated experimentally by measuring drop sizes. O'Rourke and Amsden suggest a value of $K = 10/3$ [5].

The Enhanced-TAB Model (E-TAB) has been developed by Tanner in 1997 [7] and reflects a cascade of droplet breakups, in which the breakup condition is determined by the Taylor droplet oscillator dynamics (this method is further described in the next section). The droplet size is reduced in a continuous manner, until the product droplets reach a stable condition. The model maintains the droplet deformation dynamics of the TAB model [5]. According to this approach, the droplet distortion is described by a forced damped harmonic oscillator, in which the forcing term corresponds to the aerodynamic droplet-gas interaction, the restoring force is due to surface tension, while damping is attributed to the liquid's viscosity.

Breakup occurs when the normalized (with respect to the initial radius) droplet distortion exceeds the critical value of 1. The rate of droplet creation is

$$\frac{d}{dt}m(t) = -3K_{br}m(t) \tag{9.20}$$

where $m(t)$ is the mean mass of a droplet's product distribution, and K_{br} a constant that depends on the breakup mechanism [8]. This correspondingly leads to an exponential relation between the product and parent droplet radius, r and α, respectively:

$$\frac{r}{\alpha} = e^{-K_{br}t} \tag{9.21}$$

Droplets are initialized with a "negative" deformation velocity in order to avoid the almost immediate breakup of highly unstable initial ligaments, and to extend their lifetime to levels comparable with experimentally observed jet breakup lengths [8].

KH-RT Model

The Kelvin–Helmholtz (KH) breakup model, developed by Reitz and Diwakar [9] and further improved by Reitz [10], is based on a linearized analysis of a KH instability of a stationary, round liquid jet immersed into a quiescent,

incompressible gas. The result is a general dispersion equation, which relates the growth rate of an initial surface perturbation to its wavelength. From numerical solutions it is shown that the maximum growth rate, $\omega_{\max}$, and its corresponding wavelength, $k_{\max}$, are approximated by:

$$\frac{k_{\max}}{r_o} = 9.02 \frac{\left(1 + 0.45Oh^{0.5}\right)\left(1 + 0.4(Oh \cdot {We_g}^{0.5})^{0.7}\right)}{(1 + 0.87We^{1.67})^{0.6}} \tag{9.22}$$

$$\omega_{\max}\left[\frac{\rho_L r_o^3}{\sigma}\right]^{0.5} = \frac{0.34 + 0.38We^{1.5}}{(1 + Oh)\left(1 + 1.4(Oh \cdot {We_g}^{0.5})^{0.6}\right)} \tag{9.23}$$

where Oh is the Ohnesorg number based on liquid properties. Under the assumption that the size of the stripped off product droplets are proportional to the length of the fastest growing surface wave, and that the rate of droplet generation is proportional to the maximal jet disturbance growth rate, $\omega_{\max}$, one obtains the expression for the radius, r, and the time constant, τ, of the stripped off product droplet as:

$$r = \begin{cases} B_o\lambda_{\max} & \text{for } B_o\lambda_{\max} \le r_o \\ \min\begin{bmatrix} (3\pi r_o^2 u_r/2\omega_{\max}) & \text{for } B_o\lambda_{\max} > r_o \text{ once} \\ (3r_o^2\lambda_{\max}/4)^{0.33} & \end{bmatrix} \end{cases}$$

$$\tau = 3.726 \cdot B_1 \frac{r_o}{k_{\max} \cdot \omega_{\max}} \tag{9.24}$$

where the constants $B_o = 0.61$ and B_1 is subject to further debate but suggested values are in the range 1.73–60 [11]. It is shown that in the limits $We \to 0$ and $We \to \infty$ the characteristic breakup time, τ, takes the form:

$$\tau = \begin{cases} 0.82B_1\sqrt{\frac{\rho_l r_o^3}{\sigma}}, & \text{for bag breakup} \\ B_1\sqrt{\frac{\rho_l}{\rho_g}}\frac{r_o}{|U|}, & \text{for shear breakup} \end{cases} \tag{9.25}$$

The conditions for bag and shear breakup are taken from experiments to be $We > 6$ and $We/\sqrt{\mathrm{Re}_G} > 0.5$, respectively, with the Weber and Reynolds numbers based on the drop radius. The rate of change of the radius of the parent drop, r_o, is given by an exponential law so that the parent drop approaches the stripping drop size asymptotically:

$$\frac{dr_o}{dt} = -\frac{r_o - r}{\tau}, \; r \le r_o \tag{9.26}$$

The difference of the models presented by Reitz and Diwakar [9] and Reitz [10] lies in the handling of the product droplets. In the first approach, no distinction is made between the parent and product drops when their size is updated. In fact, the parent drop decays into products of identical size and no small drops are created. In the second approach, the product droplets and the parent droplets are treated differently: while the size of the parent drop is still governed by the same rate equation, its mass decrease is compensated by the creation of product droplets of size r. With this breakup strategy there are more small droplets produced.

The Rayleigh–Taylor (RT) component has been added to the breakup model by Patterson et al. [11] to improve predictions of the secondary breakup of the droplets. The RT model predicts instabilities on the surface of the drop that grow until a certain characteristic breakup time is reached, when the drop finally breaks up. The RT waves are only allowed to form on droplets with diameters larger than the wavelength of the fastest growing disturbance. When the disturbances exceed the elapsed breakup time, the droplet is split into smaller droplets, with diameters proportional to the wavelength of the disturbances.

This component of the breakup model results in reduced overall breakup rate and dispersion of the droplets. Adjusting the effective wavelength of the RT waves can affect the time between breakup events, and, consequently, the breakup rate and the resulting droplet size.

Droplet Deformation Breakup (DDB) Model

Ibrahim et al. [12] proposed the Droplet Deformation Breakup (DDB) model, which is based on the drop's dynamics in terms of the motion of the center-of-mass of the half-droplet. It is assumed that the liquid drop is deformed due to a pure extensional flow from an initial spherical shape of radius r_o into an oblate spheroid having an ellipsoidal cross-section with major semi-axis a and minor semi-axis b. The internal energy of the half-drop comes from the sum of its kinetic and potential energies, $\dot{E}$, expressed as follows:

$$\dot{E} = \frac{2}{3}\pi r_o^3 \rho_L \dot{y}_1 \ddot{y}_1 + \frac{9\pi^2\sigma}{8} y_1 \left[1 - 2\left(\frac{c y_1}{r_o}\right)^{-6}\right] \dot{y}_1 \tag{9.27}$$

where $c = 3\pi/4$ and y_1 is the distance from the center-of-mass of the deforming half-droplet to its pole. It is assumed that $\dot{E}$ is equal to the work done by pressure and viscous forces, $\dot{W}$, which can be expressed as follows:

$$\dot{W} = -\frac{\pi}{4} r_o^2 \rho_G u^2 \dot{y}_1 + \frac{8}{3}\pi r_o^3 \mu_L \left(\frac{\dot{y}_1}{y_1}\right)^2 \tag{9.28}$$

Letting $y^*_1 = y_1/r_o$ to non-dimensionalize and dropping the asterisk, the above equations yield:

$$\ddot{y}_1 + \frac{4N}{\mathrm{Re}\rho_r}\frac{1}{y_1^2}\dot{y}_1 + \frac{27\pi^2}{16We\rho_r}y_1\left[1 - 2(cy_1)^{-6}\right] = \frac{3}{8\rho_r} \tag{9.29}$$

where ρ_r is the liquid–gas density ratio, N the liquid–gas viscosity ratio and Re and We numbers are based on the drop radius. By solving this equation the major and minor semi-axes of the droplet can be obtained as:

$$a = 3\pi r_o\frac{y_1}{4},\ b = \frac{r_o^3}{a^2} \tag{9.30}$$

The DDB model is applicable to the shear breakup regime, assumed to start at $We > 40$.

Unified Spray Breakup (USB) Model

In the Unified Spray Breakup (USB) model, the spray breakup has been divided into three distinct sub-processes, namely, primary atomization, drop deformation due to aerodynamic drag, and secondary atomization [13, 14].

The primary atomization is modeled based on the Huh et al. approach [1], as described in Sect. 9.1.

The drop deformation and secondary atomization model builds on top of already existing drops, generated by primary atomization. The secondary atomization has been further divided into four breakup regimes, based on experimental observations reported in the literature [15]. In accordance with the findings of [15], determination of the appropriate secondary atomization regime depends only on the *Weber number* of the droplets, defined as: $We = \rho_G U^2 d_o/\sigma$, where ρ_G is the density of the ambient gas, U the droplet velocity, d_o the droplet initial diameter upon its creation, and σ the surface tension. For low Weber numbers (less than 12), atomization does not occur, and only droplet deformation takes place. For higher values of Weber number, the following regimes are identified in [15] and are shown in Fig. 9.1:

- Bag breakup, $12 < We < 20$
- Multimode breakup, $20 < We < 80$
- Shear/stripping breakup, $80 < We < 800$
- Catastrophic breakup, $800 < We$

In [13, 14], the breakup times and resulting droplet sizes are estimated from experimentally verified correlations for each breakup regime. Once a droplet's secondary breakup has been completed, further disintegration (tertiary breakup) is not possible [16], and droplets reach a stable condition.

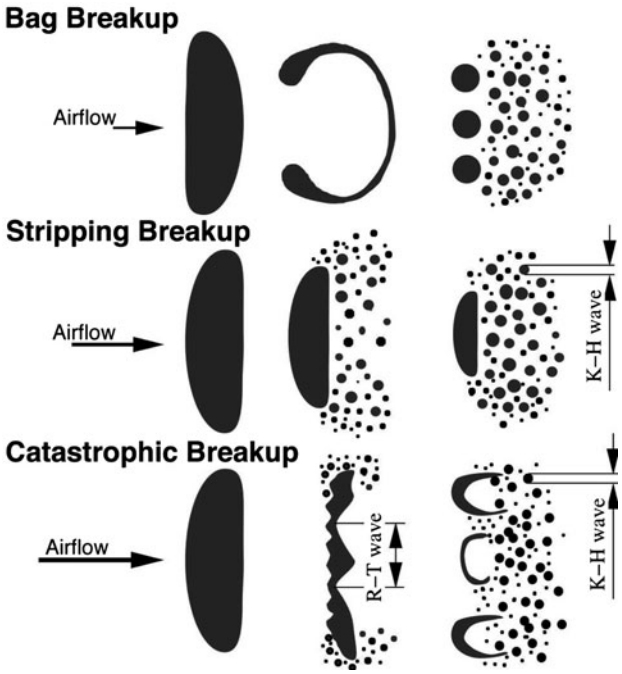


Fig. 9.1 Schematic illustration of a drop breakup caused by Kelvin–Helmholtz (KH) or Rayleigh–Taylor (R-T) instabilities. The breakup mechanisms are classified with respect to the (increasing) Weber number as bag, stripping (shear) and catastrophic breakup

In experiments with isolated droplets, Faeth and coworkers [15, 16] observed that, for sufficiently high values of the liquid's viscosity, the limits of breakup regimes are affected. The effect of the liquid's viscosity is accounted for in the *Ohnesorge number*, defined as: $Oh = \mu_L/(\rho_L d_o \sigma)^{1/2}$, where μ_L, ρ_L are the dynamic viscosity and density of the droplet, respectively. As the viscosity increases, the value of Weber number required for the onset of breakup increases. As a consequence, the transitions between the four above-mentioned regimes occur at higher Weber numbers; thus, breakup of the liquid droplets takes place at a slower pace. This is illustrated in Fig. 9.2, where a map of the breakup regimes is presented, based on the findings of [15], as compiled by Chryssakis and Assanis [13, 14]. On this map, the areas of typical gasoline and diesel sprays for automotive applications are identified. As illustrated in Fig. 9.2, the dependence of breakup on Ohnesorge number is important only for values higher than order 1.

The Cascade Atomization and Drop Breakup (CAB) Model

The CAB model is a further development of the ETAB model (see Refs. [7, 8]). The main motivation for the development of the ETAB and CAB model was the

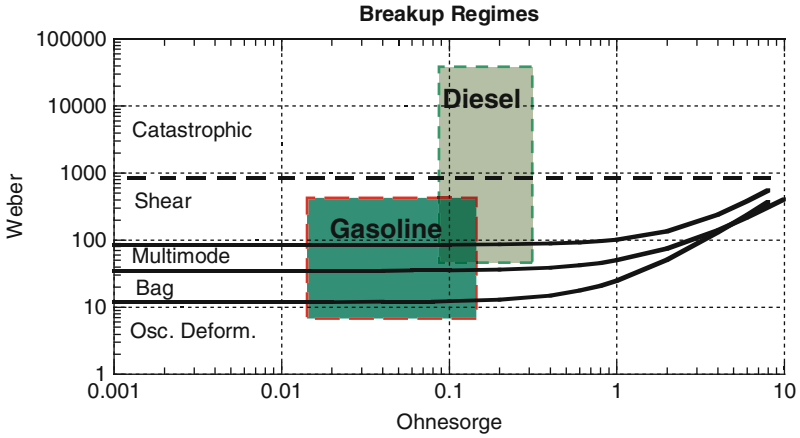


Fig. 9.2 Map of secondary atomization regimes as functions of Ohnesorge and Weber numbers, in which the areas representative of automotive gasoline and diesel sprays are identified

simulation of a fragmented liquid core at the nozzle exit in high-pressure-driven liquid jets. This fragmented liquid core has been observed experimentally by various investigators, using optical and X-ray-based techniques (cf. Refs. [17–19]).

A fragmented liquid core is simulated by injecting large drops which break up into smaller and smaller product droplets, until the latter reach a stable condition. The primary breakup, that is, the first drop breakup after injection, is modeled by delaying the initial drop breakup in accordance with experimental correlations. The drop distortion and the breakup criterion are obtained from Taylor's drop oscillator. The properties of the product droplets are derived from principles of population dynamics and are modeled after experimentally observed droplet breakup mechanisms.

Drop Breakup Modeling

In the CAB model the breakup condition is determined by means of the drop deformation dynamics of the standard Taylor analogy breakup model [5] (cf. TAB model above). In this approach, the drop distortion is described by a forced, damped, harmonic oscillator in which the forcing term is given by the aerodynamic droplet-gas interaction, the damping is due to the liquid viscosity and the restoring force is supplied by the surface tension. More specifically, the drop distortion is described by the deformation parameter, $y = 2x/r$, where x denotes the largest radial distortion from the spherical equilibrium surface, and r is the drop radius. The deformation equation in terms of the normalized distortion parameter, y, as provided in Eq. 9.29 is

$$\ddot{y} + \frac{5\mu_d}{\rho_d r^2}\dot{y} + \frac{8\sigma}{\rho_d r^3}y = \frac{2\rho_g \|v_r\|^2}{3\rho_d r^2} \tag{9.33}$$

where $\mathbf{v}_r$ is the relative drop-gas velocity, and the subscripts g and d denote the gas and droplet/liquid properties, respectively.

As discussed in the original TAB article, a necessary condition for drop breakup has been established from shock wave experiments such that the drop Weber number (based on relative velocity) satisfies $We > We_{crit} = 12$, where d denotes the drop diameter.

The creation of the product droplets is based on the assumption that for each breakup event, the number of product droplets is proportional to the number of critical parent drops, where the proportionality constant depends on the drop breakup regime. From this, one can define the rate of droplet creation, which, in conjunction with the mass conservation principle between parent and product droplets, leads to the basic cascade breakup law

$$\frac{d}{dt}\bar{m}(t) = -3K_{bu}\bar{m}(t) \tag{9.34}$$

where $\bar{m}(t)$ denotes the mean mass of the product drop distribution, and the breakup frequency K_{bu} depends on the drop breakup regimes.

As is illustrated in Fig. 9.1, the breakup regimes are classified with respect to increasing Weber number into the bag breakup regime ($We_{crit} < We \leq We_{b,s}$), into the stripping breakup regime ($We_{b,s} < We \leq We_{s,c}$) and into the catastrophic breakup regime ($We > We_{s,c}$), where the regime-dividing Weber numbers are taken to be $We_{b,s} = 80$ and $We_{s,c} = 350$, as suggested in Liu and Reitz [20].

More formally, the breakup frequency can be expressed as

$$K_{bu} = \begin{cases} k_1\omega & if \quad We_{crit} < We \leq We_{b,s} \\ k_2\omega\sqrt{We} & if \quad We_{b,s} < We \leq We_{s,c} \\ k_3\omega We^{3/4} & if \quad We_{s,c} < We \end{cases} \tag{9.35}$$

where the drop oscillation frequency ω follows from Eq. 9.33 and is given by

$$\omega^2 = \frac{8\sigma}{\rho_d r^3} - \frac{25\mu_d^2}{4\rho_d^2 r^4}.$$

The breakup parameter, K_{bu}, in the bag breakup and the stripping breakup regime is proportional to the characteristic breakup frequencies suggested by [5]. The characteristic breakup frequency for the catastrophic breakup regime is derived from the study of the RT instability by Bellman and Pennington [21] as reported by Patterson and Reitz [11]. The constant $k_1 = 0.05$ has been determined such that the drop radii match the phase Doppler measurements of Schneider [22], whereas the values for the constants k_2 and k_3 are chosen such that K_{bu} is continuous at the regime-dividing Weber numbers, $We_{b,s}$ and $We_{s,c}$.

Note that except for the mean mass $\bar{m}(t)$, the actual size distribution of the product droplet has not been specified yet. For high-velocity sprays, where drops

are subject to several breakups, a uniform product drop size distribution has been assumed, by which Eq. 9.27 becomes

$$\frac{r_{bu}}{r} = e^{-K_{bu}t_{bu}} \tag{9.36}$$

where r and r_{bu} are the radii of the parent and product drops, respectively, and t_{bu} is the breakup time.

After the breakup of a parent drop, the initial drop deformation of the product droplets is assumed to be zero, i.e., the drop deformation parameters are taken to be $y(0) = \dot{y}(0) = 0$. In addition, the product droplets are initially supplied with a velocity component perpendicular to the path of the parent drop given by $v_{\perp} = A\dot{x}$, where A is a constant determined from the following energy conservation consideration[1]. It should be noted that this radial velocity contributes to the radial expansion of the spray.

The energy of the parent drop is the sum of the surface energy and the energy stored in the drop deformation. The drop deformation is estimated from the aerodynamic drag and is expressed in terms of the stagnation point displacement from its equilibrium, which is $5r/9$. This follows from a volume conservation argument and the fact that drop breakup occurs for $y(t_{bu}) = 1$, i.e., when $x = r/2$. More precisely, assuming that the shape of the deformed parent drop is an axisymmetric ellipsoid with volume $V = 4\pi abc/3$, where a, b and c denote the lengths of the semi-axes, then at breakup the semi-axes satisfy $a = b = 3r/2$ and $c = 4r/9$, which leads to the stagnation point displacement of $5r/9$. Consequently, the energy conservation equation becomes

$$E_{parent} = 4\pi\sigma r^2 + 5\pi C_D \rho_g r^3 ||\mathbf{v}_r||^2/18, \tag{9.37}$$

where C_D is the aerodynamic drag coefficient. The energy of the product droplets (in the reference frame of the parent drop), is given by

$$E_{product} = 4\pi\sigma r^3/r_{32} + A^2\pi\rho_d r^5\dot{y}^2/6, \tag{9.38}$$

where r_{32} is the SMR of the product droplets given by

$$r_{32} = \sum r_{bu}^3 / \sum r_{bu}^2 = r^3 / \sum r_{bu}^2$$

and $r^3 = \sum r_{bu}^3$ because of volume conservation. From Eqs. 9.37 and 9.38 one obtains the expression

$$A^2 = 3[1 - r/r_{32} + 5C_D We/72]\omega_o^2/\dot{y}^2 \tag{9.39}$$

where $\omega_o^2 = 8\sigma/(\rho_d r^3)$.

[1] An analogous energy conservation argument, but using the drop oscillation energy instead of the drop deformation energy, is used in the original TAB model to determine the product drop sizes.

For inviscid, large Weber number drops with initial deformations $y(0) = \dot{y}(0) = 0$, Eq. 9.39 becomes

$$A^2 = 5C_D/4 + 18(1 - r/r_{32})/We. \tag{9.40}$$

For a breakup of a drop with $We = 250$, $C_D = 0.5$ and $r_{32}/r = 0.65$, Eq. 9.40 yields $A \approx 0.77$.

Jet Breakup Modeling

The simulation of a fragmented liquid core at the nozzle exit is achieved by injecting large drops of the size of the nozzle orifice. These drops eventually break up into smaller product droplets until they reach a stable condition, thus forming a breakup cascade where each breakup event is governed by the basic cascade breakup law given in Eq. 9.34, or, with the uniform product droplet assumption, in Eq. 9.36.

The *primary breakup* of these highly unstable initial drops is modeled by artificially prolonging their lifetime such that they agree with experimentally observed breakup lengths. More precisely, the value for the breakup time, t_{bu}, is obtained from the experimental jet breakup length correlation of Levich [23]

$$L = u_o t_{bu} = C_\lambda \sqrt{\frac{\rho_d}{\rho_g}} d_o, \tag{9.41}$$

where d_o is the nozzle diameter and u_o the nozzle exit speed. The constant C_λ is nozzle dependent and a value of $C_\lambda = 5.5$ was found to give good results for sprays used in the validation process.

In addition, to account for the droplet surface stripping near the nozzle exit, the initially injected drops have been equipped with an initial drop size distribution (IDSD) such that the small droplets reflect the surface stripping and the large drops yield good penetration and simulate a fragmented liquid core. This drop size distribution (actually a probability density function) is formally given by the power law

$$f(r) = \begin{cases} \dfrac{n+1}{r_o}\left(\dfrac{r}{r_o}\right)^n & \text{if} \quad 0 \le r \le r_o \\ 0 & \text{otherwise} \end{cases} \tag{9.42}$$

where $n \ge 0$, and r and r_o are the drop and nozzle radii, respectively.

Model tuning has lead to a value of $n = 0.5$ in Eq. 9.42. In fact, sensitivity studies have shown (cf. Ref. [24]) that the spray behavior is not very sensitive with respect to changes in the exponent n. Also, the main influence of the IDSD is on reacting sprays, in particular on the ignition delay and location.

In the CAB model, the initial spray angle, θ, is prescribed as an initial condition. The values used in this study have been obtained from the experimental correlation of Naber and Siebers [25]

$$\tan(\theta/2) = 0.31\left(\frac{\rho_g}{\rho_d}\right)^{0.19}. \tag{9.43}$$

The jet breakup modeling is illustrated in Fig. 9.3 for a non-evaporating spray. This figure illustrates the drop breakup cascade, which results in a fragmented liquid core at the nozzle exit.

Model Validation

The tuning of the model constants is detailed in Ref. [24], and the model constants used in the validation process are the ones listed in Table 9.1. Note that the initial spray angle θ and the breakup constant C_λ depend on the nozzle- and injection-system-specific properties and, in general, need to be adjusted in order to compensate for such influences.

The validation of the CAB model has been performed by means of experimental data for non-evaporating, evaporating and reacting sprays under controlled conditions in either a constant-volume or a constant-pressure combustion vessel. Particular attention has been given to the spray structure in the near-nozzle region by comparing the mass distribution with data from X-ray measurements reported in Ref. [19].

Details of these model validations can be found in the original CAB model paper, Ref. [24], and in Ref. [26]. In addition, the CAB model has been successfully

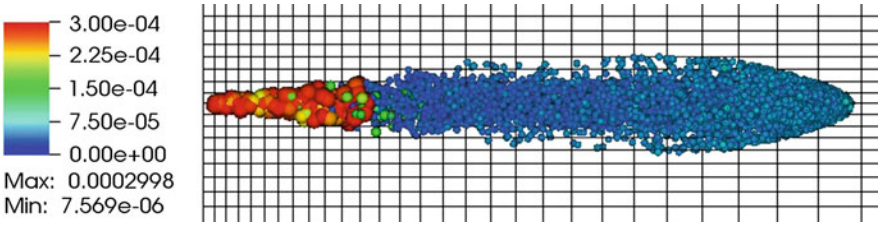


Fig. 9.3 Simulation of a fragmented liquid core for a non-evaporating spray ($d_o = 0.3$ mm; $t_{inj} = 1.2$ ms; $p_g = 1.1$ MPa). The scale represents the drop radii in meters

Table 9.1 Standard CAB model constants

C_λ	jet breakup length	5.5
θ	spray angle [deg]	Eq. 9.43
k_1	breakup regime constant	0.05
n	exponent of IDSD	0.5

employed in many diesel engine simulations of various size and speed (cf. Refs. [27–29]). More recently, the model has been extended to accommodate an air-assist atomization process for low-pressure food sprays (cf. Ref. [31]), and it has been successfully utilized in the simulation of freezing sprays for the production of cocoa butter powder (cf. Ref. [30]).

References

1. K.Y. Huh, E. Lee, J.-Y. Koo, Diesel spray atomization model considering nozzle exit turbulence conditions, Atomization and Sprays, 8:453–469, 1998.
2. B.R. Munson, D.F. Young, T.H. Okiishi, Fundamentals of Fluid Mechanics, 2nd Edition, Wiley, 1994.
3. D.P. Schmidt, I. Nouar, P.K. Senecal, C.J. Rutland, J.K. Martin, R.D. Reitz, Pressure-swirl atomization in the near field, SAE Technical Paper Series 1999-01-0496, 1999.
4. P.K. Senecal, D.P. Schmidt, I. Nouar, C.J. Rutland, R.D. Reitz, M.L. Corradini, Modeling high-speed viscous liquid sheet atomization, International Journal of Multiphase Flow, 25:1073–1097, 1999.
5. P.J. O'Rourke, A.A. Amsden, The TAB method for numerical calculation of spray droplet breakup, SAE Technical Paper 872089, 1987.
6. R.O. Grover, D.N. Assanis, A.M. Lippert, S.H. El Tahry, M.C. Drake, T.D. Fansler, D.L. Harrington, A critical analysis of splash criteria for GDI spray impingement, ILASS Americas, 15th Annual Conference on Liquid Atomization and Spray Systems, Madison, May 2002.
7. F.X. Tanner, Liquid jet atomization and droplet breakup modeling of non-evaporating diesel fuel sprays, SAE Technical Paper Series 970050, 1997.
8. F.X. Tanner, G. Weisser, Simulation of liquid jet atomization for fuel sprays by means of a cascade drop breakup model, SAE Technical Paper Series 980808, 1998.
9. R.D. Reitz, R. Diwakar, Structure of high-pressure fuel sprays, SAE Technical Paper Series 870598, 1987.
10. R.D. Reitz, Modeling atomization processes in high-pressure vaporizing sprays, Atomisation and Spray Technology, 3:309–337, 1987.
11. M.A. Patterson, R.D. Reitz, Modeling the effects of fuel spray characteristics on diesel engine combustion and emissions, SAE Technical Paper 980131, 1998.
12. E.A. Ibrahim, H.Q. Yang, A.J. Przekwas, modeling of spray droplets deformation and breakup, Journal of Propulsion Power, 9(4):651–654, 1993.
13. C. Chryssakis, D.N. Assanis, A unified fuel spray breakup model for internal combustion engine applications, Atomization and Sprays, 18(5):375–426, 2008.
14. C. Chryssakis, D.N. Assanis, C. Bae, Development and validation of a comprehensive CFD model of diesel spray atomization accounting for high weber numbers, SAE Technical Paper Series 2006-01-1546, 2006.
15. G.M. Faeth, L.-P. Hsiang, P.-K. Wu, Structure and breakup properties of sprays, International Journal of Multiphase Flow, 21: (Suppl.) 99–127, 1995.
16. L.-P. Hsiang, G.M. Faeth, Drop properties after secondary breakup, International Journal of Multiphase Flow, 19(5):721–735, 1993.
17. Ö.L. Gülder. Temporally and spatially resolved drop sizing of dense diesel sprays. In Proc. 2nd ILASS-Americas Annual Meeting, pp. 78–81, Pittsburgh, May 1988.
18. T.-W. Lee and A. ∼Mitrovic. Liquid core structure of pressure – atomized sprays via laser tomographic imaging, Atomization and Sprays, 6:111–126, 1996.
19. Y. Yue, C.F. Powell, R. Poola, J. Wang, and J.K. Schaller. Quantitative measurements of diesel fuel spray characteristics in the near-nozzle region using X-ray absorption. Atomization and Sprays, 11(4):471–490, 2001.

20. A.B. Liu and R.D. Reitz. Mechanisms of air-assisted liquid atomization. Atomization and Sprays, 3:55–75, 1993.
21. R. Bellman and R.H. Pennington. Effects of surface tension and viscosity on Taylor instability. Quarterly of Applied Mathematics, 12(2), 1954.
22. B. Schneider. Experimental investigation of diesel sprays. CRFD and Laser Diagnostic Workshop, 21st CIMAC Congress 1995, Interlaken, May 1995.
23. V.G. Levich. Physicochemical Hydrodynamics. Prentice–Hall, Englewood Cliffs, pp. 639–650, 1962.
24. F.X. Tanner. Development and validation of a cascade atomization and drop breakup model for high-velocity dense sprays. Atomization and Sprays, 14(3):211–242, 2004.
25. J.D. Naber and D.L. Siebers. Effects of gas density and vaporization on penetration and dispersion of diesel sprays. SAE Paper 960034, 1996.
26. F.X. Tanner, K.A. Feigl, S.A. Ciatti, C.F. Powell, S.-K. Cheong, J. ∼Liu, and J. ∼Wang, Structure of high-velocity dense sprays in the near-nozzle region, Atomization and Sprays, 16:579–597, 2006.
27. O. Kaario, M. Larmi, and F.X. Tanner. Non-evaporating liquid spray simulations with the ETAB and wave droplet breakup models. In Proc. 18th ILASS-Europe Annual Conference, pp. 49–54, Zaragoza, September 2002.
28. S. Srinivasan, J. Macek, M. Polacek, and F.X. Tanner. Computational optimization of a split injection system with EGR and boost pressure/compression ratio variations in a diesel engine. SAE Paper 2007-01-0168, 2007.
29. F.X. Tanner and S. Srinivasan. CFD-based optimization of fuel injection strategies in a diesel engine using an adaptive gradient method. Journal of Applied Mathematical Modelling, 33:1366–1385, 2009.
30. F.X. Tanner, K.A. Feigl, T.O. Althaus, and E.J. Windhab. Modeling and simulation of an air-assist atomizer for food sprays. In Proc. 21st ILASS-Americas Annual Conference, Orlando, May 2008. CD ROM Publication.
31. F.X. Tanner, S. Srinivasan, T.O. Althaus, K.A. Feigl, and E.J. Windhab. Modeling and validation of the crystallization process in food sprays. In Eleventh Triennial International Conference on Liquid Atomization & Spray Systems, ICLASS 2009, Vail, July 2009. CD-ROM Publication.

Chapter 10
Flashing Sprays

R. Karami and N. Ashgriz

Abstract This chapter discusses flashing in spray nozzles. Different physical aspects involved in flashing such as phase change, bubble nucleation, bubble growth, internal two-phase flow and flash atomization are discussed. The effect of flashing on droplet size and velocity are also discussed.

Keywords Boiling evaporation · Bubble growth · Droplet size · Flashing · Flash atomization · Jet breakup · Nucleation

Flashing

Introduction

Flashing in spray nozzles is generally referred to as significant void development in the flow due to depressurization and phase change. This phenomenon occurs often in nozzles working at either high temperatures or large pressure drops. An initially subcooled liquid may become saturated if the pressure drop is large enough to reduce the substance pressure below the saturation pressure corresponding to its temperature. This results in formation of large number of bubbles, which may grow rapidly in both number and size.

Depending on the condition of the flow and the geometry of the system and the nozzle, flashing can occur either inside or outside of the nozzle. The phase change itself can occur in different ways depending on the conditions and the delivery system, which will be discussed later in this chapter.

Flashing can be desirable or undesirable depending on the application. In some spray systems, unpredicted flashing may dramatically reduce droplet sizes. Since the small hot droplets evaporate rapidly, flashing may disturb performance

N. Ashgriz (✉)
Department of Mechanical and Industrial Engineering, University of Toronto, Toronto, Ontario, Canada
e-mail: ashgriz@mie.utoronto.ca

N. Ashgriz (ed.), *Handbook of Atomization and Sprays*,
DOI 10.1007/978-1-4419-7264-4_10, © Springer Science+Business Media, LLC 2011

of the system. On the other hand, flashing may be desirable to attain small droplet size for more efficient combustion. In some fuel injecting nozzles flashing can reduce the size of the droplets and hence reduce the inertia of the droplets, which decreases the penetration of the fuel. In recovery boilers of pulp and paper industry, flashing is a method to decrease the droplet size when required.

Flashing process can be studied from different points of view including nucleation and phase change, internal two-phase flow, atomization and droplet size and velocity outcome. This chapter provides a brief overview of these topics, in practical flash atomization.

When the jet is released into the ambient medium, a combination of hydrodynamic instabilities and thermal non-equilibrium conditions in the flow expands the jet. Violent and explosive characteristics of the jet cause its break-up into smaller droplets. This process is referred to as flash atomization.

Phase Change

When subcooled liquid faces a sudden drop in the pressure it goes through metastable state. Bubbles form inside the liquid consuming latent heat which is provided by the surrounding fluid and cools down the fluid. This process continues until the temperature of the liquid equals the saturation temperature of the liquid in the ambient pressure.

Figure 10.1 shows the fluid behavior during a transitional state. In this figure the van der Waals equation of state has been plotted in a *p-v* diagram at constant

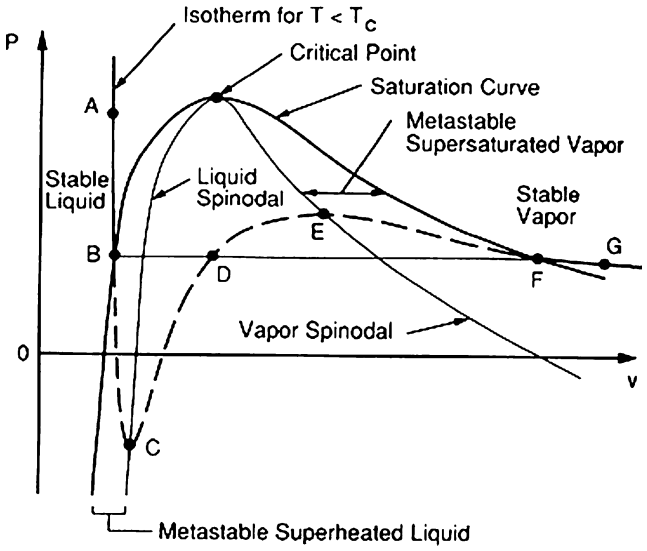


Fig. 10.1 Metastable state and spinodal line in a *p-v* diagram [1]

temperature. If the pressure on a liquid is decreased keeping the temperature constant, the liquid can maintain its form at even lower pressures than the saturation pressure. As shown in Fig. 10.1, after this point the liquid is inside the vapor dome and the slope of the *p*-*v* diagram starts to decrease, which means the liquid is less stable.

When a system is held at a fixed pressure P, temperature T and chemical potential μ, statistical thermodynamics predicts the following equation describing the variance of the number of the molecules:

$$\sigma_{\mathrm{N}}^2 = K_{\mathrm{B}} T \left(\frac{\partial N}{\partial \mu} \right) \tag{10.1}$$

where N is the mean value of the number of the molecules in the system. Using Maxwell relation, equation (10.1) can be written in the following form:

$$\sigma_{\mathrm{N}}^2 = \frac{N^2 k_{\mathrm{B}} T}{-(\partial P / \partial V)_{N,T} V^2} \tag{10.2}$$

which can be used to obtain the variance in the internal energy of the system:

$$\sigma_U^2 = \frac{N k_{\mathrm{K}} T^2 \hat{c}_v}{N_{\mathrm{A}}} + \sigma_{\mathrm{N}}^2 \left(\frac{\partial U}{\partial N} \right)_{V,T}^2 \tag{10.3}$$

The last equation represents the fluctuation of the energy of a subsystem within a control volume. In order for the system to be stable, the fluctuation in the energy and the number of the molecules inside the system must be finite and hence $\hat{c}_v$ and $-(\partial P / \partial / V)_{N,T}$ must be positive and finite. In both of the above equations the definitions of σ_N^2 and σ_U^2 imply that these variables are positive, therefore $\hat{c}_v$ and $-(\partial P / \partial V)_{N,T}$ are positive. Adding heat to a realistic material always increases the temperature, therefore $\hat{c}_v$ is always positive. However, in some conditions, the value of $-(\partial P / \partial V)_{N,T}$ can become small and very close to zero, which increases the fluctuation in the number of the molecules in the control volume. Therefore, the liquid density fluctuates in small control volume. This shows the fact that in some conditions, although the material is stable and the requirements for stability are met, fluctuations in some properties of the material may be large enough to shift the substance into a new phase.

A thermodynamic system is at equilibrium when the entropy of the system is maximum:

$$dS = 0 \tag{10.4}$$

For two systems to be in thermodynamic equilibrium the above equation leads to the following condition [1]:

$$\partial S = [T_{\mathrm{I}} - T_{\mathrm{II}}]\delta U_{\mathrm{I}} + \left[\frac{\mu_{\mathrm{II}}}{T_{\mathrm{II}}} - \frac{\mu_{\mathrm{I}}}{T_{\mathrm{I}}}\right]\delta N_{\mathrm{I}} \tag{10.5}$$

$$\hat{c}_v > 0 \tag{10.6}$$

$$\left(\frac{\partial \mu}{\partial N}\right)_{V,T} > 0 \tag{10.7}$$

Equations 10.6 and 10.7 are necessary and sufficient for stability of a pure fluid and the system at these conditions is called "intrinsically stable." Now consider, the following equation from thermodynamics:

$$\left(\frac{\partial \mu}{\partial N}\right)_{V,T} = -\frac{V^2}{N^2}\left(\frac{\partial P}{\partial v}\right)_{N,T} \tag{10.8}$$

When the liquid state is close to point A, $-(\partial P/\partial V)_{\mathrm{N,T}}$ becomes close to zero and according to (10.2) the liquid is very close to unstable condition. At this stage any perturbation can shift the liquid to another phase. Point A is where $-(\partial P/\partial V)_{N,T}$ becomes zero and it is called the "limit of intrinsic instability" or "spinodal limit." From point A to point B $-(\partial P/\partial V)_{N,T}$ is positive and the material cannot physically be stable. Notice between these two points the liquid is supposed to expand when the pressure is increased. Any slight expansion due to the local density fluctuation generates more pressure itself and hence larger volume. This effect continues until the specific volume exceeds point B. A similar process can be described to decrease the specific volume below point A. Therefore, the material cannot stay at any point between A and B. The locus of the limit of intrinsic stability in the vapor dome is called "spinodal curve." In order to find the spinodal curve equation, $\partial P/\partial v$ is set equal to zero in the van der Waals equation.

Homogeneous Nucleation

When a liquid is heated to the metastable state, bubbles form everywhere inside the liquid. This is referred to as "homogeneous nucleation." The same term is used when liquid droplets are formed in supercooled metastable vapor. "Heterogeneous nucleation" is a condition, in which bubbles form on the interfacial regions between the liquid and another phase (normally a solid).

In the metastable condition, an embryo bubble may be formed inside the liquid. Whether this embryo collapses after formation or grows depends on the size of the embryo and the conditions of the liquid.

Chemical potential and pressure balances must be applied for a bubble at equilibrium with its surrounding liquid:

$$\mu_l = \mu_v \tag{10.9}$$

$$P_{ve} = P_l + \frac{2\sigma}{r_e} \tag{10.10}$$

The second equation is Young–Laplace equation for a bubble and P_{ve} is the vapor pressure of an embryo in equilibrium with the liquid. Using the above equation along with Gibbs–Duhem equation it can be shown that the radius of an embryo at equilibrium conditions are:

$$r_e = \frac{2\sigma}{P_{sat}(T_l)\exp\{v_l[P_l - P_{sat}(T_l)]/RT_l\} - P_l} \tag{10.11}$$

and the pressure inside the embryo is

$$P_{ve} = P_{sat}(T_l)\exp\left\{\frac{-2v_l\sigma}{r_e RT_l}\right\} \tag{10.12}$$

The next question is whether this bubble is stable or not. The following equation shows the variation of the Gibbs free energy with bubble radius for an embryo formed in a superheated liquid due to a density fluctuation:

$$\frac{\Delta G}{\Delta G_e} = \frac{\Delta G}{(4/3)\pi\sigma_i r_e^2} = 1 - \left[2 + \frac{1}{1 + 2\sigma_i/r_e P_l}\right]\left(\frac{r}{r_e} - 1\right)^2 + \cdots \tag{10.13}$$

In the above equation ΔG_e is the Gibbs free energy of formation of an embryo of size r_e. Since ΔG approaches zero as the bubble radius, r, approaches zero or infinity, the Gibbs free energy decreases (the free energy is consumed because of vaporization).

Figure 10.2 represents the variation of Gibbs free energy. If an embryo of equilibrium size is formed, gaining even one molecule will increase the radius slightly and the embryo will grow to decrease Gibbs free energy, and bubble nucleation will take place. If the embryo looses one molecule, the bubble radius will decrease, reducing the Gibbs free energy. Thus, the bubble will shrink until the embryo is completely collapsed [1].

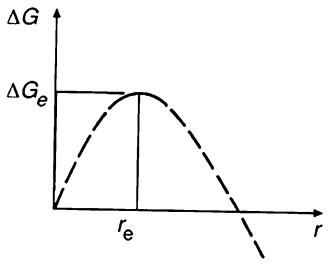


Fig. 10.2 The change in Gibbs free energy versus the diameter of the embryo formed in superheted liquid [1]

From statistical thermodynamics, it is possible to estimate the number of embryos formed in a liquid in terms of fluid properties. The following relation is derived for the number of embryos formed [1]:

$$J = 1.44 \times 10^{40} \left(\frac{\rho_l^2 \sigma}{\overline{M}^3} \right)^{1/2} \exp \left[\frac{-1.213 \times 10^{24} \sigma^3}{T_l [\eta P_{sat}(T_l) - P_l]^2} \right] \tag{10.14}$$

where

$$\eta = \exp \left\{ \frac{v_l [P_l - P_{sat}(T_l)]}{R T_l} \right\} \tag{10.15}$$

This equation shows that the number of embryos formed is an exponential function of temperature. Therefore, a small change in temperature may increase the number of embryos. Hence, the probability that some of bubbles become larger than r_e is increased. In typical conditions, increasing the temperature by only 1°C can change J by three to four orders of magnitude. This means that there is a threshold temperature above which the number of embryos formed rises rapidly. This threshold can be considered as the temperature at which homogenous nucleation occurs. The median of the temperature range where the number of embryos grows rapidly is referred to as the "kinetic limit of superheat." Assuming a threshold value of $J = 10^{12}$ m^{-3} s^{-1}, the kinetic limit of superheat for pure water is 308°C.

Heterogeneous Nucleation

In many cases, the nucleation in a superheated liquid at metastable state is more likely to occur adjacent to the solid surface of the container depending on the condition of the fluid and solid surface. A similar approach used in homogeneous nucleation can be used to determine the criterion for heterogeneous nucleation on a flat surface.

Assuming the embryo formed is spherical we can obtain the change in the Gibbs free energy due to the formation of an embryo. Gibbs free energy is the sum of the free energy of the liquid, vapor and all interfaces, which itself is the sum of the interfacial energy of the liquid–vapor, liquid–solid and solid–vapor interfacial region. It can be shown that Taylor series expansion of ΔG about the equilibrium condition of $r = r_e$ is:

$$\Delta G = \frac{4}{3} \pi r_e^2 \sigma_{lv} F - \left(\frac{4 \pi \sigma_{lv} F}{3} \right) \left(2 + \frac{P_l}{P_{ve}} \right) (r - r_e)^2 + \cdots \tag{10.16}$$

where

$$F = F(\theta) = \frac{1}{2} + \frac{3}{4}\cos\theta - \frac{1}{4}\cos^3\theta \tag{10.17}$$

Similar to the homogeneous nucleation, there is a threshold temperature, at which the number of embryos increases rapidly. This is referred to as the heterogeneous nucleation temperature. Equation 10.18 represents the number of embryos formed close to an interface. It indicates that the threshold temperature depends on the contact angle of the liquid and solid wall:

$$J = \frac{\rho_l^{2/3}(1+\cos\theta)}{2F}\left(\frac{3F\sigma_{lv}}{\pi m}\right)^{1/2}\exp\left\{\frac{-16\pi F\sigma_{lv}^3}{3k_B T_l[\eta P_{sat}(T_l - P_l)]^2}\right\} \tag{10.18}$$

Note that if θ is taken to be zero (which means the embryo is completely surrounded by the liquid) and $\rho_l^{2/3}$ is replaced by ρ_l, 10.18 becomes the same as (10.14) for the homogeneous nucleation. This expression shows that the contact angle can reduce the kinetic limit of superheat. For example, the contact angle of water on common materials may vary between 0°C to 108°C which may reduce the limit of superheat by more than 20°C.

In the above analysis, it was assumed that the surface of the wall is perfectly smooth and there are no scratches or irregularities in the shape of the surface. However, in reality most of the containers have scratches on their inner walls. If these scratches are filled with water they may not change the nucleation temperature. Therefore the nucleation temperature for pure water at atmospheric pressure is about 300°C if the container wall is fully wetted. However when a container is being filled with a liquid, small air bubbles may become trapped in the cavities of the container walls. The condition for gas entrapment by an advancing liquid front in a conical cavity is:

$$\theta > 2\gamma \tag{10.19}$$

where θ is the advancing contact angle and 2γ is the cone angle of the cavity.

Experiments have shown that in such systems, nucleation starts on the walls at temperatures slightly above the saturation temperature. After nucleation, the resulting bubble may grow to a specific size and may leave the cavity due to its buoyancy. This may occur repeatedly. Each bubble may take away some of the initial gas in the cavity. After a while, the gas inside the cavity is replaced by the vapor. This means that if the system is cooled down, the vapor is condensed and the cavity is filled with liquid. The next time the system is heated it will require a higher temperature for heterogeneous, because there are less nucleation spots. Also if the liquid rests at the pressurized container for a long time before being heated, all the entrapped gas may dissolve in the liquid and deactivate many nucleation spots.

In most of the experiments, flashing starts when the temperature is raised by only a few degrees above the saturation temperature. This may occur either inside the reservoir, the connecting pipe, or the nozzle itself.

There are numerous studies of the heterogeneous nucleation, considering bubble density and vapor generation rate [2], the critical flow rates for nucleation [3], thermal mechanic condition for the inception of flashing [4], and bubble size, velocity and concentration in flashing flow behind a sudden constriction in vertical flow in a pipe [5].

Bubble Growth in a Superheated Liquid

The equilibrium bubble size can be determined based on applying the pressure balance at the bubble interface. Gibbs–Duhem equation and Young–Laplace equation are written for the bubble [1],

$$P_{\mathrm{v}} = P_{\mathrm{sat}} \exp\left[\frac{v_{\mathrm{l}}}{RT}\left(P_{\mathrm{l}} - P_{\mathrm{sat}}\right)\right] \tag{10.20}$$

$$r^* \cong \frac{2\sigma v_{\mathrm{l}}}{RT \ln\left(\frac{P_{\mathrm{sat}}}{P_{\mathrm{v}}}\right)} \tag{10.21}$$

Hence it is assumed that the vapor inside the bubble is an ideal gas, liquid is incompressible and the temperature inside the bubble is uniform.

The bubbles larger than r^* will grow, while the bubbles smaller than r^* will collapse. In equilibrium condition, the pressure inside the bubble is greater than the pressure outside the bubble. The difference is compensated by the surface tension as shown in Fig. 10.3. The temperature of the liquid on the other hand is greater than that of the vapor inside the bubble (i.e., the liquid is superheated but the vapor is at saturation temperature).

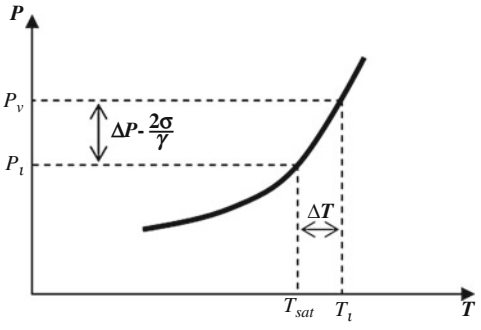


Fig. 10.3 Temperature and pressure of the bubble and liquid in the saturation line

The degree of superheat required for a liquid to be able to keep a bubble at equilibrium is:

$$\Delta T = \frac{2RT_{\text{sat}}^2\sigma}{h_{\text{lv}}P_{\text{l}}r} \tag{10.22}$$

For instance, if the bubble size is 0.005 mm and the pressure is atmospheric pressure and the liquid is water, the degree of superheat for the bubble to survive is 6.6°C, which means that the water temperature must be 106.6°C.

As the bubble grows, the pressure difference between the inside and the outside of the bubble reduces.

Therefore, the surrounding liquid temperature reduces approaching the saturation temperature. The bubble growth continues until evaporation at the interface stops.

Bubbles can grow in two ways. First possible process is that the pressure inside the bubble is great enough that it can push the liquid aside and increase the size of the bubble. This type of bubble growth is called "inertia controlled growth." The second method occurs when the heat from surrounding liquid is transferred to the liquid adjacent to the interfacial region of the liquid and vapor, and changes the phase of liquid to vapor. This growth mechanism is referred to as "heat transfer controlled growth."

Assuming a spherical bubble and an incompressible, inviscid liquid, it can be shown that the inertia controlled growth is linearly dependent on time, t.

However, in the heat transfer controlled growth the radius changes with $\sqrt{t}$. The following graph shows that in the very first moments after the bubble is formed, heat transfer controlled growth is dominant and after the bubble grows gradually the inertia controlled growth becomes the main growth mechanism (Fig. 10.4).

Bubble generation and bubble growth turns the liquid flow into a bubbly two-phase flow. Depending on the amount of bubble the flow regime can differ from one to another before emerging from the nozzle orifice. The following section briefly introduces different flow regimes in a pipe.

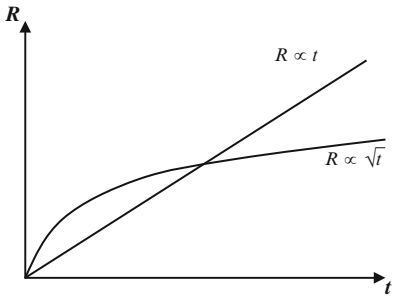


Fig. 10.4 Inertial (curve) and thermal (line) growth of a bubble: First the Inertial growth is dominant and then the growth continues due to thermal effects

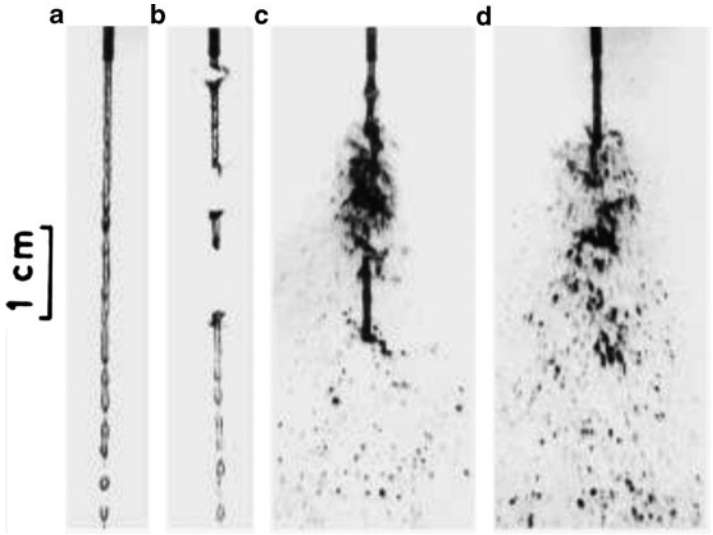


Fig. 10.5 Breakup pattern of superheated water jet, (A) Cold jet, (B) Bubbles are formed and break the jet due to the superheat, (C) higher superheat at which the jet explodes but the segments are still observed, (D) Complete flashing without any jet segments (courtesy of Elsevier)

Bubble growth rate is more complex for free jets issuing from nozzles. For instance, Kitamura et al. [6] found the following relation for a bubble growth rate in a flashing water and ethanol jet issuing into a vacuum, as shown in Fig. 10.5:

$$R = \phi Ja[\pi\alpha\Delta T]^{1/2} \tag{10.23}$$

where Jacob number is defined as:

$$Ja = \frac{\rho_{\mathrm{l}} C_{\mathrm{p}} \Delta T}{\rho_{\mathrm{v}} h_{\mathrm{lv}}} \tag{10.24}$$

where ϕ is:

$$\phi = 1 - \exp(-2,300\rho_{\mathrm{v}}/\rho_{\mathrm{L}}) \tag{10.25}$$

They [6] also provide the following relation for the critical superheat for flashing in terms of Weber number and density ratio:

$$Ja\phi = 100We^{-1/7} \tag{10.26}$$

A model for flash atomization is proposed by Razzaghi [7]. In this model, each droplet is assumed to form a nucleate bubble inside. This bubble grows bursting the drop. The secondary droplets each go through the same process forming the spray. The process is also referred to as microexplosion in drops (Fig. 10.6).

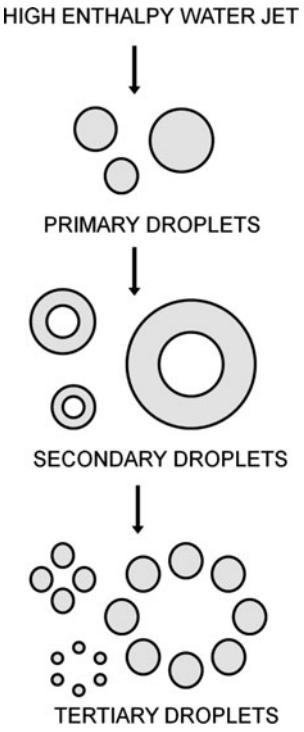


Fig. 10.6 Scheme of the modelling: The primary superheated droplets are formed by hydrodynamic process and due to excess heat the bubble is formed inside the droplets and after the explosions the tertiary droplets are formed [7] (courtesy of Elsevier)

In this study a frozen model is recognized as the best model to calculate velocity which assumes zero vaporization during primary breakup.

The condition for internal boiling of the droplet is:

$$T_{\text{cen}} > T_{\text{l}} = \frac{T_{\text{amb}}}{0.9}\left[1 + \frac{1}{C}\left(1 + K_{\text{e}}\frac{\rho_{\text{l}}}{\rho_{\text{amb}}}\right)\right] \tag{10.26}$$

where C and K_{e} are dimensionless Kelvin and Clausius-Clapeyron numbers respectively defined by equations $C \equiv L\{T_{\text{amb}}\}M_{\text{w}}/(T_{\text{amb}}R)$ and $K_{\text{e}} \equiv 4\sigma\{T_{\text{amb}}\}$ $M_{\text{w}}/(D_{\text{p}}\rho_{\text{l}}RT_{\text{amb}})$.

In the above equations, L is latent heat of vaporization and M_{w} is the molecular weight.

In this study, the tertiary droplets are assumed to be all the same size, thus according to mass conservation of liquid:

$$D_{\text{t}} = \sqrt[3]{\frac{D_{\text{s}}^3 - D_{\text{b}}^3}{n}} \tag{10.27}$$

where n is the number of tertiary droplets from bursting bubble and it is a random number between 1 to 10 and the probability of all the numbers are equal.

It is shown by [3] that the excess pressure (the difference between the pressure and the saturation pressure) decreases at high pressures, due to evaporation inside the drop. In these conditions the bubble growth is thermally controlled and flashing is reduced.

Owen [3] studied the evaporation of superheated water droplets in saturated steam at pressures up to 900 kPa. The droplets were superheated by depressurizing the vessel at different rates. He observed that if the excess temperature was below 5°C, the evaporation was on the surface; between 5°C and 18°C the droplets started to boil internally, however they did not disintegrate. Above 18°C the droplets flashed, and disintegrated.

Flow Regimes in a Two Phase Pipe Flow

In a flashing nozzle, it is likely that evaporation starts before the liquid reaches the nozzle exit. Depending on the amount of vapor, liquid and vapor characteristics, velocity, and pipe geometry different flow regimes may be observed in a pipe leading to a nozzle. The flow regime inside a pipe depends on the flow quality x, defined as the ratio of vapor mass flow rate, $\dot{m}_\mathrm{v}$, to the total mass flow rate $\dot{m}$:

$$x = \frac{\dot{m}_v}{\dot{m}} \tag{10.28}$$

The mass flux in the pipe is:

$$G = \frac{\dot{m}}{A} \tag{10.29}$$

where A is the cross-sectional area of the pipe. It is also dependent on the void fraction α, defined as the ratio of the cross-sectional area of pipe occupied by vapor A_v to total cross-sectional area A:

$$\alpha = \frac{A_\mathrm{v}}{A} \tag{10.30}$$

And superficial fluxes of gas and liquid, j_v and j_l, respectively are:

$$j_\mathrm{v} = \frac{G_x}{\rho_\mathrm{v}} \tag{10.31}$$

$$j_l = \frac{G(1-x)}{\rho_l} \tag{10.32}$$

When the quality is low, the bubbles are normally small and separately travel in the flow. This type of flow is called bubbly flow. At higher void fractions, the bubbles join together and generate large bubbles that occupy almost the entire

cross-section. This flow regime is referred to as slug flow. Increasing the quality changes the flow type to a regime called the annular flow. In the annular flow, the liquid travels on the inner wall and vapor moves in the core. If the vapor part carries the droplets, the flow is called "wispy annular." The regime between the annular and the slug, which resembles both and has a very irregular interface compared to slug flow, is called churn flow. Figure 10.7 schematically shows these flow regimes.

Different flow regimes in vertical pipe are mapped in Fig. 10.8 [1].

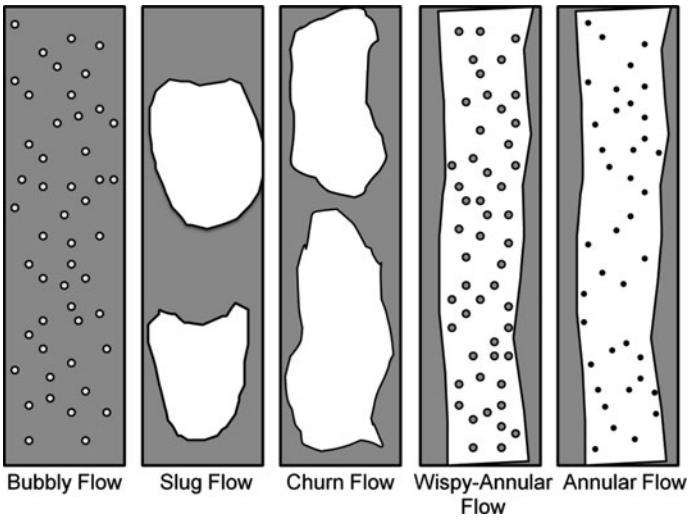


Fig. 10.7 Flow regimes in a vertical pipe

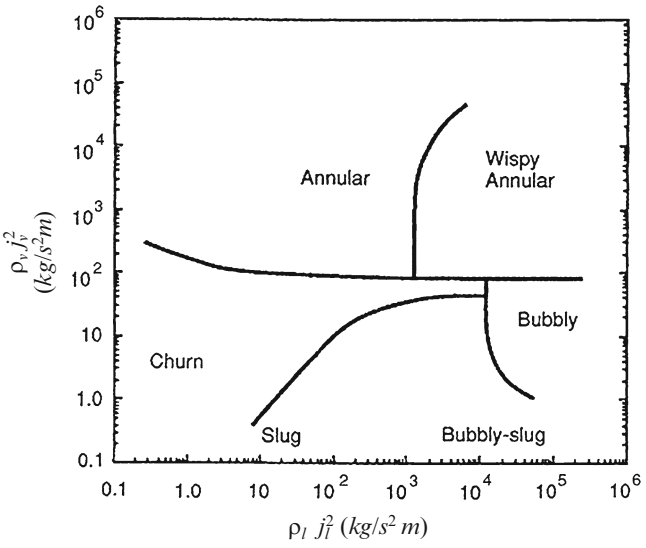


Fig. 10.8 Flow regime map in a vertical pipe [1]

Effect of Flashing on Choking

When the flow velocity reaches the sound velocity in the fluid, (i.e., the Mach number is one) the flow becomes choked, and the mass flow through the nozzle cannot be raised further by decreasing the back pressure. Flash evaporation in the nozzle can affect choking of the nozzle.

The sonic speed in a two-phase flow depends on the void fraction of the flow:

$$\frac{1}{c^2} = \frac{\alpha}{kp}[\rho_l(1-\alpha) + \rho_v \alpha] \tag{10.33}$$

where c is the sonic speed and k is polytropic coefficient.

Therefore, a flashing nozzle may choke at much lower flow velocities as compared to the non-flashing nozzles.

Flash Atomization

There are several different methods governing the flash atomization processes include: bubble growth in a superheated and two-phase superheated flow. Studies show that when flashing occurs it becomes the dominant breakup mechanism. Figure 10.9 shows how disintegration mechanism changes when the liquid temperature is raised above the flashing temperature. The jet cone angle increases by increasing the temperature.

Figure 10.10 shows the change in disintegration process with changing the temperature in a splash-plate nozzle. In this case, a liquid jet impinges on a solid plate, forming a spreading liquid sheet, which breaks up into droplets. In the first image, the sheet is intact since flashing has not started yet. Increasing the temperature to 107°C increases the jet velocity and the number of the perforations in the sheet. Above 108°C the sheet disappears and the spray is interconnected ligaments, which break into droplets.

Oza and Shinnamon [8] showed that external flashing occurs at lower degree of superheat where the jet is intact when leaving the nozzle and suddenly breaks due to rapid bubble growth. Internal flashing in the nozzle occurs when higher degree of superheat is applied and the two-phase flow generated a large cone angle

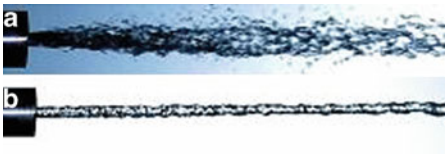


Fig. 10.9 (**a**) The temperature is below the boiling point and the jet breaks due to instability of a circular jet. (**b**) The temperature is 10°C degrees above the boiling point. The jet is not intact anymore

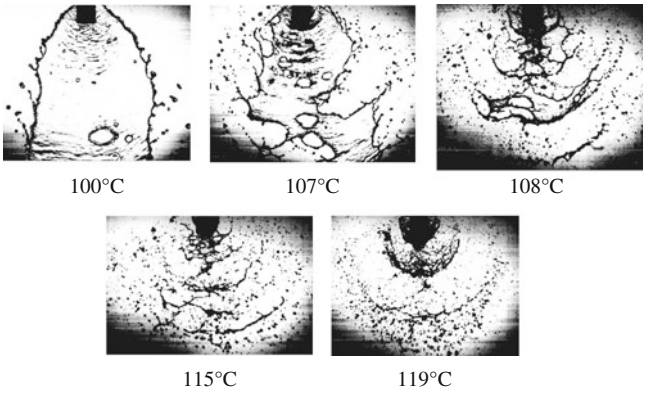


Fig. 10.10 Different spray formation observed by increasing the temperature above the flashing temperature for water in Splash-Plate nozzle

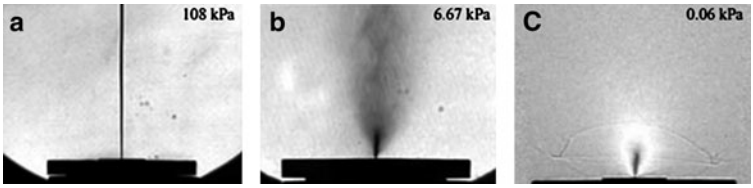


Fig. 10.11 The effect of discharge pressure on spray formation [9] (courtesy of Cambridge University Press)

Viera and Moreira [9] conducted experiments on flashing mechanisms in different injection-to-discharge pressure ratios for iso-octane liquid jets. Figure 10.11 shows the jet at three different discharge pressures and the injection pressure of 250 kPa. Shock-waves are seen in case c, which is a result of sudden liquid evaporation in a discontinuous process. In this experiments iso-octane was the liquid and it was observed that downstream of the discontinuity, the two-phase flow reaches high velocities, up to the local sonic speed.

Effect of Flashing on Droplet Size

Generally, increasing the liquid temperature above the flashing point, reduces the droplet size. This can be due to void development that increases the velocity and turbulence inside and outside of the jet, which breaks the jet violently and generates a finer spray. Droplet size in non-flashing conditions are mostly affected by nozzle geometry, liquid properties, and flow velocity. Reitz [10] conducted a photographic study of flash boiling atomization. He divided the atomizing jet into intact inner

core and its surrounding small ligaments and subjets. He observed that flashing reduces the size of the inner core as well as the surrounding droplets.

Brown and York [11] investigated many aspects of flashing phenomenon. He used Freon-11 and water as the working liquids. He measured droplet sizes at different flashing conditions, and predicted the following correlation for the droplet size with degree of superheat and Weber number.

$$\bar{D}_{30\mu} = \frac{1840 - 5.18T(^{\circ}\mathrm{F})}{We} \tag{10.1.34}$$

In this study, a critical superheat temperature was found above which the jet was totally shattered because of high number of growing bubbles. The bubble growth rate was correlated with the Weber number as:

$$r = r_1 + Ct^{1/2} \tag{10.1.35}$$

where:

$$C = 19.7 - 0.58We \quad \text{for} \quad We < 12.5$$

$$C = 11.5 - 0.42We \quad \text{for} \quad We > 12.5$$

Sher and Elata [12] proposed a theory to predict the droplet size of flashing using a propellant as bubble generator. He assumed that the energy of the bubbles generated by the propellant will be transformed to surface energy of the droplets.

While the pressurized solution is discharged from the container into the atmosphere, vapor bubbles are produced. These bubbles grow rapidly through evaporation of the propellant. When they touch each other, flashing is assumed to occur-the bubbles "explode" and an aerosol is formed. The energy contained in these exploding bubbles is, in part, transformed into surface energy of the droplets of the aerosol. On the basis of this model of the flashing process, a mathematical derivation is presented, expressing the average spray droplet diameter in terms of the physical properties of the binary fluid system.

Solving the equation of motion of a droplet, Sher and Elata [11] used the following for the bubble growth shown in Fig. 10.4:

$$R = Ct^{1/2} \tag{10.36}$$

where C is a growth rate coefficient defined by

$$C = 2\left(\frac{3}{\pi}\right)^{1/2} \psi \frac{C_p \overline{T}^3 R'^2 D_{th}^{1/2}}{L^2 \overline{P} M^2} \Delta P \tag{10.37}$$

where ψ is assumed to be 1. D_{th} is the thermal diffusion coefficient. R' is the universal gas constant, and ΔP is the pressure difference between inside and outside of the bubble.

The bubble growth and bursting process eventually transforms the flow from a liquid flow with separate bubbles to a vapor flow with separate droplets. Assuming closed pack array of vapor bubbles, the volumes occupied by vapor and liquid per unit volume are $\pi/6$ and $1 - \pi/6$, respectively. Based on this assumption and log normal size distribution, the number of droplets created from unit volume of initial liquid is:

$$n = \frac{1 - \pi/6}{(\pi/6) d_{50}^3 \exp(4.5 \ln^2 \sigma_g)} \tag{10.38}$$

where σ_g is the geometric deviation.

The availability E_b for the irreversible bursting of bubbles was assumed to be isothermal mechanical work. Assuming that bubble pressure to be very close to ambient pressure and neglecting the surface energy E_b is found as:

$$E_b \approx m\left(1 - \frac{\pi}{6}\right)\frac{4}{3}\pi R^{*3}(P_b^3 - P_a) \tag{10.39}$$

The energy required to generate n bubbles whose diameter is the log normal distribution is:

$$E_d = n\sigma\pi\bar{d}^2 = n\sigma\pi\bar{d}_{50}{}^2 \exp(2\ln^2\sigma_g) \tag{10.40}$$

He proposed the following relation for the mass median droplet size, d_{50}.

$$d_{50} = \frac{\alpha\sigma}{\rho_1}\left[\frac{L^2\bar{P}^2M^2}{C_p\rho_1\bar{T}^3R'^2D^{1/2}}\right]^4 \frac{\exp(-2.5\ln^2\sigma_g)}{\psi^4(\Delta P)^4} \tag{10.41}$$

In this equation $\alpha = 1.226/\eta m^{2/3}$ where μ is the efficiency defined as the ratio between the energy required to generate the surface of the droplets to the energy contained in the bubbles.

Cleary et al. [13] proposed the following correlation to predict the Sauter mean diameter (SMD) in subcooled condition. Reynolds number, Weber number and L/d of the nozzle were used in this correlation.

$$\frac{\text{SMD}}{d_0} = 64.73\left(\frac{L}{d_0}\right)^{0.114} - 0.014We_L{}^{-0.533} \tag{10.42}$$

In another work by the same authors [14], a new correlation was proposed for subcooled jets (mechanical breakup):

$$\frac{\text{SMD}}{d_0} = 64.73We^{-0.533}Re^{-0.014}\left(\frac{L}{d_0}\right)^{0.114} \tag{10.43}$$

Witlox proposed a transitional model for the flash atomization as depicted in Fig. 10.12 and 10.13. For Fig. 10.12 the following correlations where proposed to find the degrees of superheat at which points A and C occur:

$$\text{Point A}: Ja\phi = 55We_{\text{V}}^{-1/7} \text{ with } \phi = 1 - e^{-2{,}300(\rho_{\text{V}}/\rho_{\text{L}})} \tag{10.44}$$

$$\text{Point C}: Ja\phi = 150We_{\text{V}}^{-1/7} \tag{10.45}$$

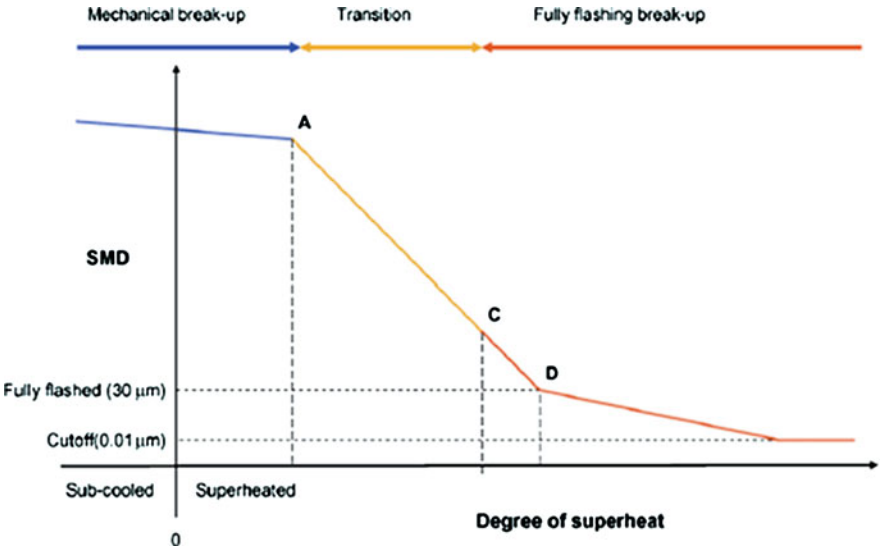


Fig. 10.12 Variation of SMD with increasing the degree of superheat [13] (courtesy of Elsevier)

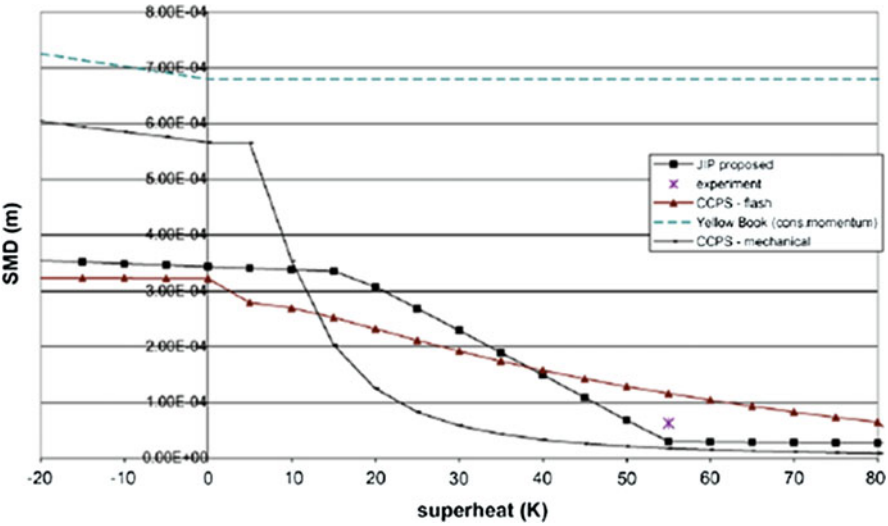


Fig. 10.13 Comparing different results on SMD versus Superheat [13] (courtesy of Elsevier)

where

$$Ja = \frac{C_{pL}\Delta T_{sh}}{h_{fg}}\frac{\rho_L}{\rho_v}, \quad We_V = \frac{\rho_v u_0^2 d_0}{\sigma_L}$$

Jacob number, Ja, represents the degree of superheat.

Another model by Johnson and Woodward [15] in CCPS book is displayed in Fig. 10.13. This model, which is for aerosol accidental rainout release, assumes the droplets size to be the minimum of mechanical or aerodynamic breakup and flashing breakup:

$$d_d = \min\{d_{da}, d_{df}\} \tag{10.46}$$

in which d_{da} is a function of critical Weber number:

$$d_{da} = \frac{\sigma_L We_{crit}}{u_f^2 \rho_a} \tag{10.47}$$

where u_f is the post-expansion velocity, the surface tension is the surface tension of the liquid after the expansion and density is the air density. We_{crit} is the value of gas Weber number which according to the literature can taken to be 12.5.

The best correlation matching the data of flashing droplet size in CCPS Book is noted to be:

$$d_{df} = 0.883 \times 10^{-3} - 0.0734 \times 10^{-3} \ln(E_p) \tag{10.48}$$

where E_p is the partial expansion energy and is given by:

$$E_p = -\Delta h - \left[P_v^{sat}(T_{st}) - P_a\right] v_{st} + \left[P_{st} - P_v^{sat}(T_{st})\right] v_{st} \quad \text{if} \quad P_a < P_v^{sat}(T_{st}) \tag{10.49}$$

and

$$E_p = (P_{st} - P_a) v_{st} \quad \text{if} \quad P_a > P_v^{sat}(T_{st}) \tag{10.50}$$

where Δh is the change in the enthalpy of material from stagnation to final condition, "st" subscript stands for stagnation value and a stands for ambient value respectively.

The correlation recommended in *Yellow Book* (Fig. 10.13) by van den Bosch and Duijm [16] is:

$$d_d = 1.89 d_f \sqrt{1 + 3\frac{We_{LF}^{0.5}}{Re_{LF}}} \tag{10.51}$$

if $We_{Lf} < 10^6 Re_{Lf}^{-0.45}$

and

$$T_o < 1.11 T_v^{sat}(P_a)$$

or

$$d_d = \frac{\sigma_L We_{crit}}{u_f^2 \rho_a} \tag{10.52}$$

T_o is the liquid temperature at the nozzle exit and the liquid Reynolds and Weber numbers are:

$$We_{Lf} = \frac{\rho_L u_f^2 d_f}{\sigma_L}$$

$$Re_{Lf} = \frac{\rho_L u_f d_f}{\mu_L}$$

Gemci et al. [17] investigated flash atomization of hydrocarbon solutions containing n-hexadecane and *n*-butane, with nitrogen as the propellant gas. The variable parameters were nitrogen flow rate, injection temperature and butane concentration. The droplet size measurement was based on image analysis and based on the results, the following correlation was suggested for the SMD:

$$\text{SMD}(\mu\text{m}) = 118.4 - 28.3(\Delta T^* - K) \tag{10.53}$$

$$K = \frac{P_o - P_v}{1/2 \rho_l U^2} \tag{10.54}$$

where ΔT^* is the dimensionless degree of superheat and K is the dimensionless cavitation number, which represents the pressure difference. The breakup pattern under the effect of degree of superheat, butane concentration and nitrogen flow was also studied based the images obtained. The following image shows a sample of flashing jet at different temperatures in this study.

Nomenclature

c	Speed of sound
$\hat{c}_v$	Heat capacity
g	Gibbes free energy
G	Mass flux
ΔG	Change in Gibbs energy of formation of an embryo
ΔG_e	Change in Gibbs energy of formation of an embryo of critical size
h_{lv}	Latent heat of evaporation

H	Enthlpy
j	Superficial mass flux
$_J$	Number of embryos
Ja	Jacob number
k	Polytropic coefficient
k_B	Boltzmann constant
$\dot{m}_v$	Gas mass flow rate
$\dot{m}$	Mass flow rate
$\overline{M}$	Molecular weight
$_N$	Number of molecules
$_{NA}$	Avogadro number
P	Pressure
$_{Pl}$	Liquid pressure
$_{Pve}$	Vapor pressure in equilibrium
$_{Psat}$	Saturation pressure
$_R$	Ideal gas constant
Re	Reynolds number
r^*	Critical bubble size
$_{re}$	Bubble radius in equilibrium
S	Entropy
T	time
ΔT	Degree of superheat
ΔT^*	Dimensionless degree of superheat
$_T$	Temperature
$_U$	Internal Energy
$_v$	Specific Volume
V	Volume
We	Weber number
x	Quality
σ_N	Variance of the number of the molecules
σ	Surface tension
ρ_l	Liquid density
σ_{lv}	Surface tension between liquid and vapor
θ	Contact angle
γ	Cone angle of a cavity
μ	Chemical potential
α	Void fraction

References

1. Van P. Carey, (2007) Liquid-Vapor Phase Change Phenomena, 2nd edn., Taylor & Francis Group, Boca Raton.
2. Riznic, J. R. & Ishii, M. (1989). Bubble number density and vapor generation in flashing flow. Int. J. Heat Mass Transfer, 32(10), 1821–1833. doi: 10.1016/0017-9310(89)90154-3.

3. Yildiz, D. & Rambaud, P. (2002). Study on Dynamics of a Flashing Jet. von Karman Institute of Fluid Dynamics, Belgium.
4. Elias, E. & Chambre, P. L. (1993). Flashing inception in water during rapid decompression. J. Heat Transfer, 115(1), 231–238. doi: 10.1115/1.2910654.
5. Domnick, J. & Durst, F. (1995). Measurement of bubble size, velocity and concentration in flashing flow behind a sudden constriction. Int. J Multiphase Flow, 21(6), 1047–1062. doi: 10.1016/0301-9322(95)00045-Y.
6. Kitamura, Y., Morimitsu, H., & Takahashi, T. (1986). Critical superheat for flashing of superheated liquid jets. Ind Eng Chem Fundamentals, 25(2), 206–211. doi:10.1021/i100022a005.
7. Razzaghi, M. (1989). Droplet size estimation of two-phase flashing jets. Nucl. Eng. Des., 114(1), 115–124.
8. Oza, R. D. & Sinnamon, J. F. (n.d.). An Experimental and Analytical Study of Flash-Boiling Fuel Injection.
9. Viera, M. M. & Simoes-Moreira, J. R. (2007). Low-pressure flashing mechanisms in isooctane liquid jets. J. Fluid Mech., 572(1), 121–144.doi: 10.1017/S0022112006003430.
10. Reitz, R. D. (1990). A photographic study of flash-boiling atomization. Aerosol Sci. Technol., 12(3), 561. doi: 10.1080/02786829008959370.
11. Brown, R. & York, J. L. (1962). Sprays formed by flashing liquid jets. AIChE J., 8(2), 149–153. doi: 10.1002/aic.690080204.
12. Sher, E. & Elata, C. (1977). Spray formation from pressure cans by flashing. Ind. Eng. Chem. Process Des. Dev., 16(2), 237–242. doi: 10.1021/i260062a014.
13. Cleary, V., Bowen, P., & Witlox, H. (2007). Flashing liquid jets and two-phase droplet dispersion: I. Experiments for derivation of droplet atomisation correlations. Journal of Hazardous Materials, 142(3), 786–796. doi:10.1016/j.jhazmat.2006.06.125.
14. Witlox, H., Harper, M., Bowen, P., & Cleary, V. (2007). Flashing liquid jets and two-phase droplet dispersion: II. Comparison and validation of droplet size and rainout formulations. Journal of Hazardous Materials, 142(3), 797–809. doi:10.1016/j.jhazmat.2006.06.126.
15. Johnson, D. W., & Woodward, J. L. (1999). A Model with Data to Predict Aerosol Rainout in Accidental Releases, Center of Chemical Process Safety (CCPS), New York.
16. van den Bosch, C. J. H., & Duijm, N. J. (1997). Sections 2.3.4.6, 2.4.3.5, 2.5.3.7 on 'Finite-duration spray releases' in Outflow and Spray Release, Chapter 2 in "Methods for the calculation of physical effects—TNO Yellow Book", CPR14E, Third Edition, Committee for the Prevention of Disasters, SDU, The Hague.
17. Gemci, T., Yakut, K., Chigier, N., & Ho, T. C. (2004). Experimental study of flash atomization of binary hydrocarbon liquids. Int. J. Multiphase Flow, 30(4), 395. doi: 10.1016/j.ijmultiphaseflow.2003.12.003.

Chapter 11
Supercritical and Transcritical Injection

P. Seebald and P.E. Sojka

Introduction

A supercritical fluid is defined as one that is above its thermodynamic critical point, as identified by the critical pressure (p_c) and critical temperature (T_c). Supercritical fluid behavior can be peculiar because of the variation of thermophysical properties such as density and specific heat near and at the critical point. Supercritical fluids have some properties similar to liquids (e.g., density), and some properties that are comparable to those of gases (e.g., viscosity). Thus, they cannot be considered either a liquid or a gas.

An important spray-related property that changes near the critical point is surface tension. A supercritical fluid lacks surface tension, which means that ligaments and droplets do not form upon injection of this type of fluid.

It should also be noted that specific heat grows without bound at the critical point. Density also becomes very sensitive to small changes in temperature, as the gradients become very steep.

As a result of the significant variation in thermodynamic properties near and at the critical point, it is difficult to use Computational Fluid Dynamics (CFD) when modeling supercritical flows. Also, since small changes in temperature and pressure can have large effects on the structure of a fluid near the critical point, local property values are very important.

The critical properties relating to injection are well defined for simple fluids, such as N_2 or CO_2, and even some single component hydrocarbon fuels (such as JP-10). However, critical conditions for complex hydrocarbons, and for most mixtures, are not well-known. Finding these properties is important, since the critical temperature or pressure of a mixture may be well above the critical point of each of the separate species in that mixture, especially at increased pressures. This is just one more reason why local conditions are extremely important, as mixing may determine if a small, local volume of fluid is subcritical or supercritical.

P.E. Sojka (✉)
Maurice J. Zucrow Laboratories, School of Mechanical Engineering, Purdue University, IN, USA
e-mail: sojka@purdue.edu

N. Ashgriz (ed.), *Handbook of Atomization and Sprays*,
DOI 10.1007/978-1-4419-7264-4_11, © Springer Science+Business Media, LLC 2011

Definition

The term supercritical injection can refer to several different types of processes. There are four classes (note that T_r is reduced absolute temperature and p_r is reduced absolute pressure; the subscript inj refers to injection, and env represents the environment):

I. A fluid that is above the supercritical point is injected into an environment at conditions above the critical point of the injectant ($T_{r,inj}$ and $p_{r,inj} > 1$, $T_{r,env}$ and $p_{r,env} > 1$)
II. The injectant is at a subcritical temperature, but supercritical pressure prior to injection, and is injected into an entirely supercritical environment ($T_{r,inj} < 1$ and $p_{r,inj} > 1$, $T_{r,env}$ and $p_{r,env} > 1$),
III. A supercritical fluid is injected into subcritical surroundings (relative to the injectant critical point) ($T_{r,inj}$ and $p_{r,inj} > 1$, $T_{r,env}$ and $p_{r,env} < 1$),
IV. A fluid with a temperature below the critical point, and a pressure above the critical point, is injected into an environment where the pressure is subcritical, but the temperature is supercritical ($T_{r,inj} < 1$ and $p_{r,inj} > 1$, $T_{r,env} > 1$ and $p_{r,env} < 1$), and generally passes through the supercritical region.

Injections of types II, III, and IV are typically labeled transcritical, since they cross the injectant critical conditions at some point during the injection process.

Depending on the conditions of the initial fluid and the environment, many different changes to the fluid can occur. Figure 11.1, similar to one provided by [1], illustrates the different classes of supercritical injection.

Why should injection near the critical point be studied? Perhaps the most long-lasting application is high-speed flight, where the fuel is used as a heat sink. This can cause the fluid to become supercritical.

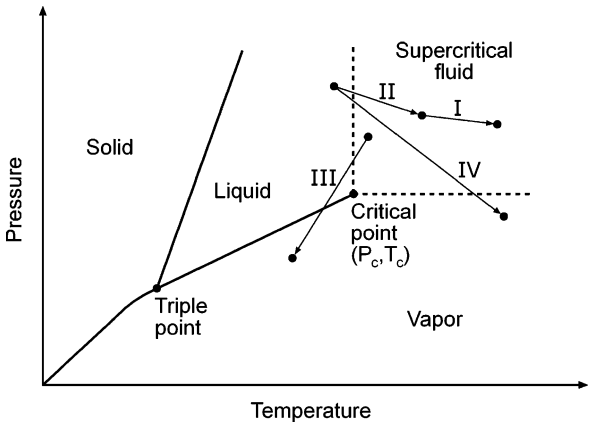


Fig. 11.1 The supercritical region and definitions of various injection processes on a pressure–temperature diagram

Transcritical injection, particularly Type II, is also becoming increasingly important in research related to rocket combustors. It has been studied more than any other type, with cryogenic liquids as the fuel. In addition, the higher chamber pressures being used for gas turbine and diesel engines to increase efficiency and performance often increase the pressure above the fuel's critical value. This happens if the fuel is injected into an environment where combustion raises the temperature above critical conditions for the fuel. Thus, a subcritical temperature, supercritical pressure fuel is injected into a supercritical chamber.

Literature Results

Of the many studies on super- or transcritical injection, Newman and Brzustowski [2] were the first to observe how an injected fluid behaves near the critical point. They noted the decreased effect of surface tension.

Mayer et al. [3] described Type II injection as a mixing between two fluids rather than a spray entering a gas. They also observed that surface tension vanished at transcritical (subcritical temperature, but supercritical pressure) conditions.

Woodward and Talley [4] and Mayer et al. [5] observed the significant effect of mixture critical properties on transcritical jets. The former group saw no drops for a nitrogen-nitrogen system, except when small amounts of helium were added. The latter group observed surface tension in a multi-component transcritical spray. It was theorized that surface tension was present due to the temperature being below the mixture critical property, even though the pressure was supercritical.

Much of the available research agrees that supercritical jets typically behave similar to turbulent gas jets, specifically variable-density gas injection. Chehroudi et al. [6] first found favorable comparison between measured transcritical (Type II or IV) jet spreading angles and those of variable-density gas jets. Barata et al. [7] used numerical variable-density gas jet models to predict experimental results, and found good agreement.

Branam and Mayer [8] have compared supercritical core length measurements to those of variable-density gas jets, and found that the two matched well. However, the authors believed that more parameters were needed to be able to accurately predict transcritical core lengths, as Reynold's number was the sole parameter used in their gas jet model. They considered quantities such as the density ratio and reduced temperature and pressure to be important.

Zong and Yang [9] performed a numerical study, using a coaxial injector geometry, and found that the calculated turbulent kinetic energies matched variable-density jet data in the self-similar region of the flow, but not elsewhere. The differences outside of the self-similar regime were ascribed to critical property variations. Their computations also confirmed the spreading angle correlation proposed by Chehroudi et al. [10], and presented as Eq. 11.1.

$$\theta = 0.27\left[F\left(\frac{\rho_\infty}{\rho_{\text{inj}}}\right) + \left(\frac{\rho_\infty}{\rho_{\text{inj}}}\right)^{0.5}\right] \tag{11.1}$$

where $F(\rho_\infty/\rho_{\text{inj}}) = 5.325 \times (\rho_\infty/\rho_{\text{inj}}) + 0.0288$ when $\rho_\infty/\rho_{\text{inj}} < 0.0885 = 0.5$ when $\rho_\infty/\rho_{\text{inj}} < 0.0885$

The Zong et al.[11] numerically determined density profiles at various axial locations matched the Chehroudi et al. [10] measured values to within ±5%.

Oschwald and Micci [12] found spreading angles similar to those of Chehroudi et al. [10], but centerline densities differed from variable-density gas jet data in their study.

Mayer and Telaar [13] also compared supercritical injection to gas–gas mixing. They noted that transcritical injection forms a regime that lies between subcritical spray breakup and supercritical jet breakup.

With regards to maximum specific heat at the critical point, several researchers have observed that heat input to the fluid goes into expansion of the jet near the critical point and the disappearance of surface tension, instead of raising the temperature. Oschwald and Schik [14] first mentioned this behavior. It was confirmed by Mayer et al. [13, 15], who noted that this expansion affects atomization and mixing.

Recent research has also investigated which independent variables (e.g., density ratio, temperature, mass flow rate) significantly affect jet structure and mixing. The quantities measured include penetration length, concentration or density profiles, spreading angles, velocity, and core lengths.

Chen [16] found that the penetration length of a supercritical jet was affected by injection temperature and chamber pressure. Doungthip et al. [17] observed that changing flow rate and/or temperature affected both penetration length and spreading angle.

Interestingly, both Oschwald and Schik [14] and Branam and Mayer [8] observed that velocity and momentum flux had little impact on jet behavior, with both groups determining that thermodynamic conditions were dominant instead. Wakashima and Umemura [18] also concluded that mixing depended on jet pressures, which affected the jet transition to a supercritical state.

Two research groups, Zeaton et al. [19] and Zong and Yang [20], studied supercritical injection through a simplex swirl injector. The former showed that swirl number greatly affects quantities such as spreading angle and penetration length, while density ratio and mass flow rate have slight effect on them. Zong and Yang's [20] numerical studies also showed that swirl strength affected spreading angle, but it also moved the recirculation zone closer to the injector. Zeaton et al.'s [19] experimental results showed self-similarity in concentration profiles, similar to the Chehroudi et al. [21] self-similar density profiles. Meanwhile, Zong and Yang [20] numerically found three regions similar to liquid jets: potential core, transitional region, and self-similar zone. They also observed that increasing chamber pressure moved the self-similar region closer to the injector.

Rachedi et al. [22] continued Zeaton et al.'s work by examining the behavior of a real jet fuel (JP-10), and compared it to Zeaton et al.'s carbon dioxide data. Their results showed that carbon dioxide could be used as a surrogate fluid for JP-10, since their behaviors were very similar. Both Rachedi et al. and Zeaton et al. found that the injected fluid radial concentration profile was well described by a Gaussian profile when the radius was normalized by the jet half-radius. The jet half-radius was defined as the radius where the concentration is half of the maximum (centerline) value.

Seebald and Sojka [23] reported transcritical (Type III injection) concentration profiles with a maximum concentration that was offset from the centerline. They attributed this to a temperature gradient across their jet, which affected density calculations.

Most recently, Segal and Polikhov [1] performed Type II and Type IV studies to characterize the mixing processes of transcritical jets. They found that "transitional mixing" occurred when only one condition (temperature or pressure) was supercritical, even if the other was subcritical. They also saw density gradients that were similar to laminar jets at standard temperature and pressure, which have also been seen in numerical studies before, but not in experimental research.

Several Type III studies were performed at very high injectant-to-chamber pressure ratios to imitate SCRAMJET conditions. Wu and Chen [24, 25] and Lin and Cox-Stouffer [26] studied the location of shock structures resulting from this type of injection. Far from the critical point, jet behavior resembled ideal-gas expansion. In contrast, homogeneous droplet nucleation was observed near the critical point. Locations of the observed shock structures, i.e. Mach disks, matched well with those from under-expanded ideal-gas jet predictions. However, the Mach disks disappeared as the injectant-to-chamber pressure ratio decreased.

It should also be mentioned that Bellan [27] discusses the use of numerical models for supercritical flow. In particular, she notes that a computationally expensive system of Direct Numerical Simulations (DNS) is able to model supercritical fluids (especially mixing layers) quite well.

In contrast, current Large Eddy Simulations (LES) are not able to reproduce supercritical mixing. This is mainly because the small-grid scales used for subcritical conditions are not applicable to the anisotropic supercritical mixing processes. Due to sharp density gradients that greatly affect supercritical flow, numerical resolution must be advanced, also.

Several important conclusions can be drawn from the research that has been conducted over the past 20 years:

1. Supercritical and transcritical jets can be structurally similar to variable-density gas jets, typically in the self-similar regime
2. Transcritical injection is mainly dependent on thermodynamic conditions
3. Mixing is affected by significant property variations near the critical point
4. Surface tension can play a role in transcritical injection, depending on mixture critical properties.

Supercritical injection is still being studied. However, it is clear that there are many considerations that need to be accounted for when designing an injector for

supercritical or transcritical injection. For example, density differences between a liquid and a supercritical fluid may cause dramatic changes in flow rates through a fixed nozzle area.

References

1. Segal, C. & Polikhov, S. (2008). Subcritical to supercritical mixing. Phys. Fluids, 20, 052101.
2. Newman, J. & Brzustowski, T. (1971). Behavior of a liquid jet near the thermodynamic critical region. AIAA J., 9, 1595–1602.
3. Mayer, W., Schik, A., Talley, D., &Woodward, R. (1998). Atomization and breakup of cryogenic propellants under high-pressure subcritical and supercritical conditions. J. Prop. Power, 14, 835–842.
4. Woodward, R. & Talley, D. (1996). Raman imaging of transcritical cryogenic propellants, AIAA 34th Aerospace Sciences Meeting and Exhibit, Reno, IV. AIAA-1996-468.
5. Mayer, W., Ivancic, B., Schik, A., &Hornung, U. (2001). Propellant atomization and ignition phenomena in liquid oxygen/gaseous hydrogen rocket combustors. J. Prop. Power, 17, 794–799.
6. Chehroudi, B., Talley, D., & Coy, E. (2002). Visual characteristics and initial growth rates of round cryogenic jets at subcritical and supercritical pressures. Phys. Fluids, 14, 850–861.
7. Barata, J., Gokalp, I., &Silva, A. (2003). Numerical study of cryogenic jets under supercritical conditions. J. Prop. Power, 19, 142–147.
8. Branam, R. &Mayer, W. (2003). Characterization of cryogenic injection at supercritical pressure. J. Prop. Power, 19, 342–355.
9. Zong, N. & Yang, V. (2006). Cryogenic fluid jets and mixing layers in transcritical and supercritical environments. Comb. Sci. Tech., 178, 193–227.
10. Chehroudi, B., Cohn, R., &Talley, D. (2002). Cryogenic shear layers: experiments and phenomenological modeling of the initial growth rate under subcritical and supercritical conditions. Int. J. Heat Mass Transfer, 23, 554–563.
11. Zong, N., Meng, H., Hsieh, S., & Yang, V. (2004). A numerical study of cryogenic fluid injection and mixing under supercritical conditions. Phys. Fluids, 16, 4248–4261.
12. Oschwald, M. & Micci, M. (2002). Spreading angle and centerline variation of density of supercritical nitrogen jets. Atom. Sprays, 11, 91–106.
13. Mayer, W. & Telaar, J. (2002). Investigation of breakup of turbulent cryogenic variable-density jets. Atom. Sprays, 12, 651–666.
14. Oschwald, M. & Schik, A. (1999). Supercritical nitrogen free jet investigated by spontaneous Raman scattering. Exp. Fluids, 27, 497–506.
15. Mayer, W., Telaar, J., Branam, R., Schneider, G., & Hussong, J. (2003). Raman measurements of cryogenic injection at supercritical pressure. Heat Mass Transfer, 39, 709–719.
16. Chen, L. Heat transfer, fouling and combustion of supercritical fuels. Def. Tech. Info. Center, Report # 940321.
17. Doungthip, T., Ervin, J., Williams, T., &Bento, J. (2002). Studies of injection of jet fuel at supercritical conditions, Ind. Eng. Chem. Res., 41, 5856–5866.
18. Wakashima, Y. & Umemura, A. (1999). Linear stability analysis of axisymmetric fuel jet issued into supercritical ambient. JSME J. Ser. B, 42, 539–546.
19. Zeaton, G., Crook, L., Guildenbecher, D., &Sojka, P. E. (2005). An experimental study of supercritical fluid jets. Proceedings of the 19th European Conference on Liquid Atomization and Spray System, Toronto, Ontario, Canada.
20. Zong, N. & Yang, V. (2004). Dynamics of simplex swirl injectors for cryogenic propellants at supercritical conditions. 42nd AIAA Aerospace Sciences Meeting and Exhibit, Reno, IV. AIAA 2004–1332.

21. Chehroudi, B., Cohn, R., Talley, D., & Badakhshan, A. (2000). Raman scattering measurements in the initial region of sub- and supercritical jets. 36th AIAA/ASME/SAE/ASEE Joint Propulsion Conference and Exhibit, Huntsville, AL. AIAA 2000–3392.
22. Rachedi, R., Crook, L., &Sojka, P. E. (2007). A study of supercritical fuel injection. Proceedings of the ASME IMECE, Seattle, WA, pp. 837–845.
23. Seebald, P. &Sojka, P. E. (2008). An experimental study of transcritical CO2 injection, ILASS-Europe 2008 Conference, Italy. ILASS08-A055.
24. Wu, P., Chen, T., Nejad, A., &Carter, C. (1996). Injection of supercritical ethylene in nitrogen. J. Prop. Power, 12, 770–777.
25. Wu, P., Shahnam, M., Kirkendall, K., Carter, C., &Nejad, A. (1999). Expansion and mixing processes of underexpanded supercritical fuel jets injected into superheated conditions, J. Prop. Power 15, 642–649.
26. Lin, K., Cox-Stouffer, S., &Jackson, T. (2006). Structures and phase transition processes of supercritical methane/ethylene mixtures injected into a subcritical environment. Comb. Sci. Tech., 178, 129–160.
27. Bellan, J. (2006). Modeling and analysis of turbulent supercritical mixing. Comb. Sci. Tech., 178, 253–281.

Chapter 12
Evaporating Sprays

F.X. Tanner

Abstract Evaporation of multi-component liquid droplets is reviewed, and modeling approaches of various degrees of sophistication are discussed. First, the evaporation of a single droplet is considered from a general point of view by means of the conservation equations for mass, species and energy of the liquid and gas phases. Subsequently, additional assumptions and simplifications are discussed which lead to simpler evaporation models suitable for use in CFD spray calculations. In particular, the heat and mass transfer for forced and non-forced convection is expressed in terms of the Nusselt and Sherwood numbers. Finally, an evaporation model for sprays that is widely used in today's CFD codes is presented.

Keywords Dufour effect · Evaporation · Frössling correlation · Heat transfer · Latent heat · Mass transfer · Nusselt number · Ranz-Marshall correlation · Soret effect · Stefan flow

Introduction

Evaporation is a phase transition process by which molecules in a liquid overcome their intermolecular attraction forces and escape into the surrounding gaseous environment. When heat is supplied to a liquid, its temperature, and hence the kinetic energy of the liquid molecules, are increased, which results in an increased evaporation activity. Also, a decrease in the ambient pressure increases the chances of the liquid molecules near the surface to overcome their intermolecular attraction potential, which results in an increased evaporation rate.

The description of the evaporation process on the molecular level is an emerging subject in the computational sciences and, no doubt, will play an increasingly

F.X. Tanner
Department of Mathematical Sciences, Michigan Technological University, USA
e-mail: tanner@mtu.edu

N. Ashgriz (ed.), *Handbook of Atomization and Sprays*,
DOI 10.1007/978-1-4419-7264-4_12, © Springer Science+Business Media, LLC 2011

important role in the future. Pioneering articles along these lines are authored by Consolini et al. [9], Yasuoka and Matsumoto [32, 33] and Walther and Koumoutsakos [29], just to name a few. In this exposition, the evaporation process is discussed from a continuum point of view using the conservation equations for mass, momentum and energy that take discontinuities in the density at the phase boundary into consideration.

A comprehensive discussion of droplet vaporization can be found in the books of Sirignano [25] and Crowe et al. [10], and in the article of Sazhin [24]. Evaporation models of various degrees of complexity, with different applications in mind, are described in the texts of Glassman [11], Heywood [13], Lefebvre [16], Stiesch [28], Williams [31], and others. In addition, there is a multitude of papers on the subject, each addressing different aspects of the evaporation process, including the effect of multi-component liquids, fuel in particular. A few examples of such investigations are by Abraham and Magi [1], Abramzon and Sirignano [2], Aouina et al. [4], Ayoub and Reitz [5], Brenn et al. [7], Lippert and Reitz [17], Pagel et al. [19], Renksizbulut et al. [22, 21], Zhu et al. [34].

According to Sirignano [25], continuum-based evaporation models can be classified into the following six categories, which are listed in order of increasing complexity:

1. Constant droplet temperature models where the drop temperature is constant throughout the evaporation process
2. Infinite liquid-conductivity models, where the drop temperature is time-varying but uniform
3. Conduction limit models which consider the transient heating process in the droplet
4. Effective conductivity models which take the internal drop re-circulation into account via adjustment of the internal liquid conductivity
5. Vortex models which describe the drop heating by considering the internal flow, i.e., the Hill vortex
6. Models based on the full solution of the Navier–Stokes equations.

With increasing complexity of the models, one gets more accurate predictions but also the computation times become considerably larger. Keeping in mind that many of these evaporation models have been developed for use in CFD spray simulations, where hundreds of thousands of droplets have to be considered, computational costs become a primary issue. Therefore, the models discussed in this chapter are limited to the second and third category. The presentation starts with the general conservation equations for mass, species and energy, from which the simplified models are derived.

Single Drop Evaporation

Experimental observations in moderate pressure environments show that a drop is initially subject to a transient heating process until it reaches steady-state vaporization. The latter is described by the well-known *d-squared law*, which gives the square of the drop diameter as a function of time, t, by the relation

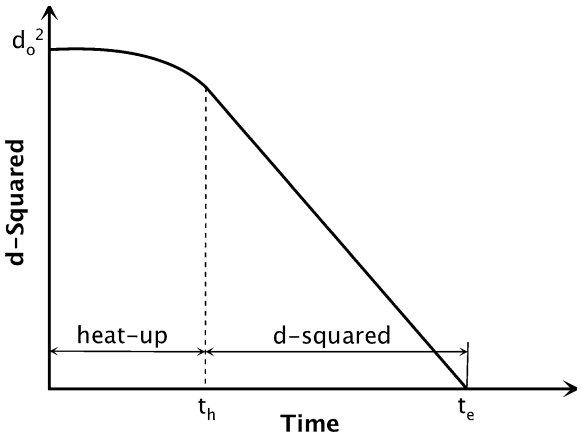


Fig. 12.1 D-squared evaporation law with initial heat-up period

$$d^2(t) = d_o - \beta_v t, \tag{12.1}$$

where d is the drop diameter, d_o is the initial diameter, and β_v is the *evaporation coefficient*. This behavior is illustrated in Fig. 12.1. It will be shown later, that under the proper assumptions, this law can be recovered from theoretical considerations.

Basic Considerations and General Assumptions

The equations that govern the evaporation process of a drop are the conservation equations for mass, species and energy/enthalpy for the gas and liquid phases, together with boundary conditions and compatibility conditions at the liquid-gas interface. The momentum conservation is neglected since drop drag is not considered in this chapter. The conservation equations for both the gas and liquid phases, are given by (cf. Byron Bird et al. [8])

$$\frac{\partial \rho}{\partial t} + \operatorname{div}(\rho \mathbf{u}) = 0 \tag{12.2}$$

$$\frac{\partial (\rho Y_i)}{\partial t} + \operatorname{div}(\rho Y_i \mathbf{u}) = -\operatorname{div}\, \mathbf{j}_i \tag{12.3}$$

$$\frac{\partial (\rho h)}{\partial t} + \operatorname{div}(\rho h \mathbf{u}) = \frac{\mathrm{d}p}{\mathrm{d}t} - \operatorname{div}\, \mathbf{q} + \sigma : \operatorname{grad}\, \mathbf{u}. \tag{12.4}$$

In these equations, the symbols have respective interpretations for either the gas or the liquid phase. Specifically, ρ denotes the mass density and **u** is the velocity.

$Y_i = \rho_i/\rho$ is the mass fraction of species i and $\mathbf{j}_i$ is its diffusion mass flux, where the subscript i, $i = 1,\ldots, N$, denotes species i. The specific enthalpy is $h = e + p/\rho$, where e denotes the specific internal energy and p is the pressure; $\mathbf{q}$ is the mass specific heat flux, $\boldsymbol{\sigma}$ is the extra stress tensor and $\mathrm{d}/\mathrm{d}t$ denotes the material or substantial derivative.

Observe that the sum over all the species equations leads to the mass conservation equation, or, equivalently, $\sum_i \mathbf{j}_i = 0$. Further, it should be noted that the species include F fuel species and $N-F$ species from the surrounding gas.

The liquid phase quantities are identified with a subscript l or d, the gas phase quantities have no subscript, or when necessary to avoid confusion, a subscript g is used. Vapor quantities use the subscript v. Quantities just on the liquid side of the phase-dividing interface are subscripted with ls and on the gas side with either s or, if necessary to distinguish between fuel vapor and gas, with vs or gs. Further, the following general assumptions are made throughout this chapter, unless stated otherwise.

- There are no energy contributions due to external forces such as gravity, or due to radiation. Therefore, there is no gravity-induced diffusion or convection.
- In the enthalpy equation, (12.4), the term $\boldsymbol{\sigma}$:grad $\mathbf{u}$ accounts for the internal energy generated by the viscous stresses and is neglected.
- The total pressure change during the evaporation process is taken to be zero and, therefore, $\mathrm{d}p/\mathrm{d}t = 0$ in (12.4).

The Liquid Phase

The liquid phase is described by (12.2)–(12.4) subject to the general assumptions listed above. As shown in the appendix, integration of these equations over the droplet volume, using the generalized Reynolds transport theorem for the left-hand integrals, and the divergence theorem for the right-hand integrals, yields the liquid phase governing equations

$$\frac{\mathrm{d}m}{\mathrm{d}t} = -\rho_s u_s S_d \tag{12.5}$$

$$\frac{\mathrm{d}m_i}{\mathrm{d}t} = -\rho_{is} u_{is} S_d, \quad i = 1,\ldots,F \tag{12.6}$$

$$m\frac{\mathrm{d}(\overline{C}_{pl}\overline{T}_l)}{\mathrm{d}t} = \left[q_s - \rho_s u_s \overline{C}_{pl}(T_s - \overline{T}_l)\right] S_d. \tag{12.7}$$

In these equations, m is the droplet mass and m_i is the mass of species i, ρ_n is the density of the vapor at the drop surface, $u_s = \mathbf{u}_s \cdot \mathbf{n}$ is the normal component of the vapor velocity, where $\mathbf{n}$ denotes the droplet outward unit normal vector, and S_d is the droplet surface. Further, $\bar{C}_{pl}$ and $\bar{T}_l$ denote the mass-averaged liquid heat

capacity and drop temperature, respectively, q_s is the surface heat flux from the gas to the droplet and T_s is the temperature at the drop surface. Note that (12.5)–(12.7) reflect the fact that the rate of change of the liquid quantities (total mass, species mass and enthalpy) are balanced by their respective fluxes through the drop surface.

The following additional assumptions for the liquid phase have been made implicitly or follow from the derivation in the appendix.

- The solubility of the ambient gas species in the liquid phase is neglected. Therefore, the liquid phase consists of only $F \leq N$ species.
- The internal flow in the drop, known as the Hill vortex, is neglected.

The Gas Phase

In addition to the general assumptions stated previously, the gas phase of the evaporation process is assumed to satisfy the *quasi-steady* condition. This means that the system responds quickly to changes in the gas and vapor flow conditions. Consequently, the partial derivatives of the gas phase variables with respect to time are zero. Under these assumptions the gas phase conservation equations become

$$\mathrm{div}(\rho \mathbf{u}) = 0 \tag{12.8}$$

$$\mathrm{div}(\rho \mathrm{Y_i} \mathbf{u}) = -\mathrm{div}\ \mathbf{j_i}, \quad i = 1, \ldots, N \tag{12.9}$$

$$\mathrm{div}(\rho h \mathbf{u}) = -\mathrm{div}\ \mathbf{q}. \tag{12.10}$$

Observe that there are a total of N species including $F \leq N$ fuel species.

The flow induced by evaporating molecules is called *Stefan flow*. The contribution of the ith evaporating species to the Stefan flow is given by the convection term, $\rho Y_i \mathbf{u}$, for $i = 1,\ldots, F$, in (12.9), and the total Stefan flow is obtained as the sum over the evaporating species, namely $\sum_{i=1}^{F} \rho Y_i \mathbf{u}$, $F \leq N$.

In general, the species flux $\mathbf{j}_i$ is the sum of various sub-fluxes, including the diffusion due to the concentration gradient, which is given by Fick's law

$$\mathbf{j}_{D_i} = -\rho D_{ig}\, \mathrm{grad} Y_i. \tag{12.11}$$

Here, D_{ig} is the mass diffusivity of species i in the surrounding gas. (D_{ig} is often taken to be the same for all species and is then denoted by D_v). Additional sub-fluxes that can play a role are due to a possible partial pressure gradient of species i, and the mass flux caused by the temperature gradient, also called the *Soret effect*.

Similarly, the heat flux $\mathbf{q}$ is composed of various sub-fluxes which include the heat conduction from the gas to the droplet, given by Fourier's law as

$$\mathbf{q} = -K_g \, \mathrm{grad} T, \tag{12.12}$$

where K_g is the conduction coefficient. Depending on the situation, additional sub-fluxes that may play a role can include the heat exchange due to molecular diffusion, or the heat flux caused by concentration gradients, called the *Dufour effect*.

Instead of modeling each of these sub-fluxes separately, which can lead to complex models that can be computationally very expensive, the entire fluxes, $\mathbf{j}_i$ and $\mathbf{q}$, are expressed in terms of transfer coefficients. These transfer coefficients depend on the various flow and thermodynamic conditions, as will be discussed in more detail later.

Interface and Boundary Conditions

On the drop surface, the continuity of the evaporating mass must be imposed on the total vapor mass flux, which is given via (12.5) by

$$\dot{m}_{vl} = \dot{m}_{vg} = \dot{m}_v = \rho_s u_s S_d \tag{12.13}$$

and on each fuel species, $i = 1, \ldots, F$, which is given via (12.6) by

$$\dot{m}_{vil} = \dot{m}_{vig} = \dot{m}_{vi} = \rho_{is} u_{is} S_d. \tag{12.14}$$

In addition, the scalar heat transfer rates must satisfy

$$q_{sg} = q_{sl} + \dot{m}_v L, \tag{12.15}$$

where L is the (averaged) latent heat, obtained from the partial specific latent heats L_i of species i, given by

$$L = \sum_{i=1}^{F} \frac{\dot{m}_{vi}}{\dot{m}_v} L_i. \tag{12.16}$$

The gas phase boundary conditions for the far field are T_∞ and $Y_{i\infty}$, $i = 1, \ldots, N$. Further, it is assumed that the temperature is continuous on the drop surface, that is,

$$T_{sl} = T_{sg} = T_s, \tag{12.17}$$

and that phase equilibrium holds, that is, the Clausius–Clapeyron equation applies.

In order to determine the temperature, T_s, and the fuel mass fraction, Y_{is}, on the drop surface, an additional relation is needed, which is obtained from Raoult's law

$$Y_{is} = \frac{W_i}{W} \frac{p_i}{p} \tag{12.18}$$

where p_i is the partial pressure, W_i is the molecular weight of the fuel species i, and p and W are the total gas pressure and the molecular weight of the gas mixture, respectively. The fuel vapor pressure, p_i, can be determined from tables or from the generalized Clausius–Clapeyron equation

$$p_i = p_{i0} \exp\left(\frac{L_i}{R_i}\left(\frac{1}{T_{i0}} - \frac{1}{T_s}\right)\right). \tag{12.19}$$

Here, the index $i0$ indicates a reference state of species i and R_i is its gas constant.

Heat and Mass Transfer Numbers

The ith species mass flux, $\mathbf{j}_i$, and the total heat flux, $\mathbf{q}$, can be expressed in terms of transfer coefficients. This is useful in situations where the liquid or gas phase is not completely resolved, or when the flow conditions are not exactly known. Often, these transfer coefficients are determined experimentally for a particular flow situation. For instance, different expressions are used, depending on whether the transfer is due to pure conduction or whether it is dominated by convection. Also, the type of convection plays a role, that is, if the convection is forced or non-forced. A forced convection has a non-zero relative velocity between droplet and environment, whereas for a non-forced convection, the relative drop-gas velocity is zero and only the Stefan flow dominates. Note that the natural convection due to gravity is taken to be zero since gravity is an external force, and external forces are neglected in this article. In addition, in forced convection, the nature of the flow, that is, whether the flow is laminar or turbulent, plays an important role. These issues will be discussed in more detail in the following subsections.

The gas phase species transfer coefficient, h_j, is assumed to be the same for all species and is defined via the scalar expression

$$j_i = ||\mathbf{j}_i|| = h_j(\rho_{is} - \rho_{i\infty}) = h_j\rho(Y_{is} - Y_{i\infty}), \tag{12.20}$$

where $||\cdot||$ denotes the Euclidean norm. Note that j_i is the rate of mass per unit area transferred to the gas. Likewise, the gas phase heat transfer coefficient, h_q, is given by the scalar expression for the rate of heat per unit area transferred to the droplet, namely,

$$q = ||\mathbf{q}|| = h_q(T_\infty - T_s). \tag{12.21}$$

The non-dimensional mass transfer number, the *Sherwood number*, is defined by

$$Sh = \frac{h_j d}{D_v} = \frac{d}{D_v\rho(Y_s - Y_\infty)} j_i \tag{12.22}$$

where D_v is the mass diffusivity of the vapor in the gas, and d is the drop diameter. In an analogous fashion, one defines the non-dimensional heat transfer number, called the *Nusselt number*, by

$$Nu = \frac{h_q d}{K_g} = \frac{d}{K_g(T_\infty - T_s)} q_s, \tag{12.23}$$

where K_g denotes the thermal conductivity of the gas.

Transfer Numbers for Non-forced Convection

For a drop in a quiescent atmosphere, that is, a drop under non-forced convection, exact expressions for the Nusselt and Sherwood numbers can be derived under the assumption that the problem is spherically symmetric. The initial derivation for a single species drop is due to Spalding [26, 27]. An insightful presentation of this approach can be found in Kuo [15]. Essentially the same methodology can also be applied to multi-species droplets and the resulting expressions for the Sherwood and Nusselt numbers are formally the same as for a single species drop. For more details see Gradinger [12].

The Sherwood number that results from this derivation can be expressed as

$$Sh_0 = 2\frac{\ln(1 + B_m)}{B_m}, \tag{12.24}$$

and the Nusselt number is

$$Nu_0 = 2\frac{\ln(1 + B_h^*)}{B_h^*}, \tag{12.25}$$

where the *Spalding mass transfer number*, B_m, is

$$B_m = \frac{Y_{Fs} - Y_{F\infty}}{1 - Y_{Fs}}, \tag{12.26}$$

and the adjusted heat transfer number, B_h^*, is given by

$$B_h^* = C_{pg}(T_\infty - T_s)/L^*. \tag{12.27}$$

In the last equation, L^* is the adjusted latent heat, which is related to the actual latent heat via

$$L^* = \frac{q_s}{q_s - q_{ls}} L,$$

where q_s is the heat transferred from the gas to the droplet surface, and q_{ls} is the heat transferred from the drop surface to the inside of the drop. (q_{ls} is usually expressed in terms of the liquid Nusselt number, Nu_l, whose value, according to Renksizbulut et al. [21], is $Nu_l = 22$.)

The condition $q_{sl} = 0$ means that there is no droplet heating, so that all the heat from the surrounding gas is used for evaporation. This situation occurs when the drop surface temperature is close to the boiling point, which is often the case when drops heat up quickly in a hot environment.

Note that for *zero convection*, the mass and heat transfer numbers B_m and B_h^* are zero and, therefore, the expressions for the Sherwood and Nusselt numbers reduce to

$$Sh_0 = Nu_0 = 2,$$

The d-squared law, discussed in (12.1), can now be recovered under the assumption that $q_{ls} = 0$, i.e., no droplet heating, and when the Lewis number[1] is unity. It follows that the Spalding transfer numbers, given in (12.26) and (12.27), satisfy $B = B_m = B_h^*$. Under these assumptions, the *d-squared evaporation law* can be written as

$$d^2 = d_o^2 - \left[8\alpha_s \frac{\rho_s}{\rho_d} \ln(1 + B_m)\right] t, \tag{12.28}$$

where the quantity in the brackets represents the evaporation coefficient β_v in (12.1).

Transfer Numbers for Forced Convection

There are various expressions for the Sherwood and Nusselt numbers if the relative drop-gas velocity is nonzero, i.e., for forced convection. Widely used correlations are those by Ranz and Marshall [20]. These were obtained from experiments of vaporizing single-component drops at atmospheric pressure and moderate ambient temperatures with low transfer rates, that is, when $B_m = B_h^* \approx 0$ and, therefore, $Nu_0 = Sh_0 = 2$. These correlations are given by

$$Sh_1 = 2 + 0.6\,\mathrm{Re}_d^{1/2} Sc_d^{1/3} \tag{12.29}$$

$$Nu_1 = 2 + 0.6\,\mathrm{Re}_d^{1/2}\,\mathrm{Pr}_d^{1/3} \tag{12.30}$$

[1]The Lewis number is the ratio of the mass diffusivity and the heat diffusivity.

and hold for $2 \leq \mathrm{Re}_d \leq 200$, where

$$\mathrm{Re}_d = \frac{\rho_g ||\mathbf{v}_{rel}|| d}{\mu_g}, \quad Sc_d = \frac{\mu_g}{\rho_g D_v}, \quad \mathrm{Pr}_d = \frac{\mu_g C_{pg}}{K_g}$$

denote the droplet Reynolds number, the droplet Schmidt number and the droplet Prandtl number, respectively. For forced convection with high transfer rates, the Ranz-Marshall correlations are often combined to get (cf. [3])

$$Sh = (2 + 0.6\mathrm{Re}_d^{1/2} Sc_d^{1/3}) \frac{\ln(1 + B_m)}{B_m} \tag{12.31}$$

$$Nu = (2 + 0.6\mathrm{Re}_d^{1/2}\, \mathrm{Pr}_d^{1/3}) \frac{\ln(1 + B_h^*)}{B_h^*}. \tag{12.32}$$

A more refined approach has been taken by Abramzon and Sirignano [2] based on film theory (cf. Bird et al. [8]). The expressions for the transfer numbers they obtained are

$$Sh = 2\frac{\ln(1 + B_m)}{B_m} + (Sh_1 - 2)(1 + B_m)^{-0.7} \tag{12.33}$$

$$Nu = 2\frac{\ln(1 + B_h^*)}{B_h^*} + (Nu_1 - 2)(1 + B_h^*)^{-0.7}, \tag{12.34}$$

where Nu_1 and Sh_1 are given by (12.29) and (12.30). Renksizbulut et al. [22] proposed similar expressions based on their experimental work [23].

High Pressure Effects

In many technical applications, droplet evaporation takes place at high pressures and high temperatures. This is particularly true in combustion devices such as diesel engines and gas turbines, where droplets can reach their critical states. In such circumstances, the ideal gas law predictions become inaccurate and real gas effects have to be considered. Also, the effect of high pressure on the liquid properties and the transport coefficients needs to be taken into account. An overview of high pressure vapor-liquid equilibrium effects is given by Ohe [18], and a discussion in terms of combustion devices, together with additional references, can be found in Gradinger [12].

Evaporation in Sprays

For a collection of droplets, the evaporation process of one particular drop can be influenced by the neighboring droplets depending on their distance and relative location. The study of Bellan and Harstad [6] concluded that in a dense droplet cluster, evaporation occurs primarily due to diffusion effects (that is when $\mathrm{Sh} \approx 2$), while convection plays a dominant role in the more dilute regions of a spray. A detailed discussion of the mass and heat transfer of a collection of drops, together with appropriate references, can be found in the text of Sirignano [25].

One of the most widely used approaches for the simulation of sprays is the stochastic discrete droplet model introduced by Williams [30]. In this approach, the droplets are described by a probability density function (PDF), $f(t,\mathbf{X})$, which represents the probable number of droplets per unit volume at time t and in state $\mathbf{X}$. The state of a droplet is described by its parameters that are the coordinates in the particle state space. Typically, the state parameters include the location $\mathbf{x}$, the velocity $\mathbf{v}$, the radius r, the temperature T_d, the deformation parameter y, and the rate of deformation $\dot{y}$. As discussed in more detail in Chapter 16, this spray PDF is the solution of a spray transport equation, which in component form is given by

$$\frac{\partial f}{\partial t} + \mathrm{div}_{\mathbf{x}}(f\mathbf{v}) + \mathrm{div}_{\mathbf{v}}(f\dot{\mathbf{v}}) + \frac{\partial}{\partial r}(f\dot{r}) + \frac{\partial}{\partial T_d}(f\dot{T}_d) + \frac{\partial}{\partial y}(f\dot{y}) + \frac{\partial}{\partial \dot{y}}(f\ddot{y}) = \dot{f}_{coll} + \dot{f}_{bu} \tag{12.35}$$

where $\mathrm{div}_{\mathbf{x}}$ and $\mathrm{div}_{\mathbf{v}}$ indicate the divergences with respect to the droplets' spatial and velocity coordinates, and the source terms on the right-hand side are due to droplet collision and droplet breakup, respectively. In order to be able to solve (12.35), expressions for $\dot{\mathbf{v}}$, $\dot{r}$, $\dot{T}_d$, $\dot{y}$, and $\ddot{y}$ need to be specified. This is done via modeling of the individual spray subprocesses.

The mass and heat transfer of an evaporation process determine the drop size and drop temperature. Both of these quantities require a description that is numerically efficient but sufficiently accurate so that averages taken over the chosen sampling sizes reflect realistic values. In order to be able to compute drop sizes and temperatures for millions of droplets (or, after discretization of the PDF, for tens of thousands of parcels), various simplifying assumptions have to be made. One of the most common assumptions is the *lumped capacitance* assumption which states that the temperature within the droplet is spatially uniform and only depends on time. This assumption is satisfied if the Biot number, defined as the ratio of heat transferred to the droplet over heat conducted inside the droplet, is small. More formally, this is expressed as (cf. Incropera and DeWitt [14])

$$Bi = \frac{h_q d}{K_l} < 0.1$$

where h_q is the heat transfer coefficient, d is the characteristic length and K_l is the liquid thermal conductivity. For sprays with drop sizes at most a couple of hundred micrometers, the Biot number criterion is usually satisfied.

For a single liquid species, the governing equations, (12.5)–(12.7), lead to the simplified system

$$\frac{\mathrm{d}r^2}{\mathrm{d}t} = \frac{\rho_v}{\rho_d} D_v B_m Sh_d \tag{12.36}$$

$$C_{pl} m_d \frac{\mathrm{d}T_d}{\mathrm{d}t} = q_s S_d + L(T_d) \frac{\mathrm{d}m_d}{\mathrm{d}t}, \tag{12.37}$$

where r is the drop radius and B_m is the mass transfer number given by (12.26).

In order to solve this system efficiently, additional correlations and simplifications are used. The drop surface temperature T_s is not solved for explicitly, but instead, the temperature-dependent vapor and gas properties are determined by using the two-thirds weighted temperature

$$\breve{T} = (T_g + 2T_d)/3 \tag{12.38}$$

Typically, the vapor diffusivity in air is given by the relation

$$\rho_v D_v(\breve{T}) = D_1 \breve{T}^{D_2},$$

where D_1 and D_2 are species dependent constants. The temperature dependence of the viscosity (in [g/(cm s)]) and the heat conduction coefficients (in [erg/(s cm K)]) in air can be obtained from the Sutherland relations

$$\mu_g(\breve{T}) = \frac{A_1 \breve{T}^{1.5}}{\breve{T} + A_2}$$

and

$$K_g(\breve{T}) = \frac{K_1 \breve{T}^{1.5}}{\breve{T} + K_2}$$

where the constants A_1, A_2, K_1 and K_2 are given by $A_1 = 1.45710^{-5}$, $A_2 = 110$, $K_1 = 252$ and $K_2 = 200$.

The fuel mass fraction at the drop surface, needed to compute B_m, is obtained from

$$Y_{Fs}(T_d) = \left[1 + \frac{W_\infty}{W_v}\left(\frac{p_g}{p_v(T_d)} - 1\right)\right]^{-1},$$

and the gas-liquid heat transfer, which follows from (12.23), is

$$q_s = K_s(\breve{T})Nu(T_\infty - T_d)/d$$

Note that the Sherwood and Nusselt numbers are obtained from correlations discussed in the previous section, e.g., the Ranz-Marshal correlations given in (12.31) and (12.32).

Finally, the latent heat of vaporization, $L(T_d)$, is given by the difference of the vapor enthalpy h_v and the liquid enthalpy, h_l, as

$$L(T_d) = h_v(T_d) - h_l(T_d, p_v(T_d)) = [e_v(T_d) + R_0 T_d/W_v] - [e_d(T_d) + p_v(T_d)/\rho_d]$$

where e is the mass specific internal energy, R_0 is the universal gas constant, W_v is the molecular weight of the vapor, and $p_v(T_d)$ is the equilibrium vapor pressure.

The equations for multi-species drops are obtained in an analogous way. More details can be found in Ref. [25] or in the cited references.

Appendix

Divergence Theorem

Let Ω be a region in $\mathbf{R}^3$ with a piecewise smooth boundary $\partial\Omega$ and outward normal vector $\mathbf{n}$. Further, assume that $\boldsymbol{\phi}(\mathbf{x}, t)$ is a piecewise continuous vector field (or tensor field) on an open set containing Ω. Then

$$\int_{\partial\Omega} \phi(\mathbf{x}, t) \cdot \mathbf{n} \mathrm{d}A = \int_{\Omega} \mathrm{div}\phi(\mathbf{x}, t) \mathrm{d}V.$$

In general, Ω and $\partial\Omega$ can depend on time, and the vector field $\boldsymbol{\phi}(\mathbf{x},t)$ denotes the surface flux of an appropriate physical quantity, such as mass, species or heat.

Generalized Reynolds Transport Theorem

Reynolds' transport theorem is a differentiation rule for integral expressions whose integration limits depend on the variable of differentiation. This theorem is the generalization to higher dimensions of the Leibnitz formula. The generalized Reynolds transport theorem accounts, in addition, for jump discontinuities of the integrand inside the region of integration. More formally, this is expressed as follows.

Let $\Omega(t)$ be a region in $\mathbf{R}^3$ with the piecewise smooth boundary $\partial\Omega(t)$ depending on time t, and let $S(t) \subset \Omega(t)$ be a *singular surface* across which the volume density of a physical quantity, γ, experiences the *jump discontinuity* $[\gamma]_S = \gamma^+ - \gamma^-$. The superscripts $+$ and $-$ indicate the different sides of $S(t)$. Further, assume that $S(t)$ is moving with the displacement velocity $\mathbf{w}$, and that $\mathbf{n}_s$ is the unit normal vector on S. Then

$$\frac{\mathrm{d}}{\mathrm{d}t}\int\limits_{\Omega(t)} \gamma \mathrm{d}V = \int\limits_{\Omega(t)} \left(\frac{\partial \gamma}{\partial t} + div(\gamma u)\right)\mathrm{d}V - \int\limits_{S(t)} [\gamma(\mathbf{w}-\mathbf{u})\cdot\mathbf{n}_s]_S \mathrm{d}A.$$

Note that if γ is continuous across S, then $[\gamma]_S = 0$ and the second integral on the right is zero; thus the statement reduces to the usual Reynolds transport theorem.

Derivation of Equations 12.5–12.7

Equation 12.5 gives the total rate of evaporation of the droplet. It has been obtained by integrating (12.2) over the droplet volume and applying the generalized Reynolds transport theorem. Note that the velocity of the moving drop surface has been set to zero, that is, $\boldsymbol{w} = 0$ in the generalized Reynolds transport theorem. Therefore, assuming that $\rho_s u_s = \rho_s \mathbf{u}_s \cdot \mathbf{n}$ is constant on the drop surface, or that $\rho_s u_s$ denotes the surface-averaged normal vapor flow, one obtains

$$\dot{m}_v = \int\limits_{S_d(t)} \rho_s \mathbf{u}_s \cdot \mathbf{n} \mathrm{d}A = \rho_s u_s S_d,$$

where $\mathbf{u}_s$ is the vapor velocity.

The evaporation rate for each species is given in (12.6) which has been obtained by integrating (12.3) over the droplet volume and invoking the generalized Reynolds transport theorem. The resulting surface integral, which corresponds to the mass evaporation rate of species i, can be simplified to give

$$\dot{m}_{vi} = \int\limits_{S_d(t)} (\mathbf{j}_i + \rho_{is}\mathbf{u}_s)\cdot\mathbf{n}\mathrm{d}A = (j_i + \rho_{is}u_s)S_d = \rho_{is}u_{is}S_d,$$

under the assumption that $(j_i + \rho_{is}u_s) = (\mathbf{j}_i + \rho_{is}\mathbf{u}_s)\cdot\mathbf{n}$ is constant on the drop surface, or that $(j_i + \rho_{is}u_s)$ denotes the average over the drop surface S_d. Note that the total evaporating mass flux of species i is the sum of the convecting flux, $\rho_{is}\mathbf{u}$, plus the "diffusion" flux, $\mathbf{j}_i$. More formally, this can be expressed as

$$\rho_{is}\mathbf{u}_{is} = \rho_{is}\mathbf{u}_s + \mathbf{j}_i$$

Since there are only liquid species involved in the mass transfer, there is no mass flux from the gas to the droplet, that is, the solubility of the ambient gas species in the liquid phase is neglected.

The enthalpy equation, (12.7), is obtained by writing the heat flux as $\mathbf{q} = -\mathbf{q}_s + h\rho_s\mathbf{u}_s$. Assuming a uniform radial heat flux $q_s = \mathbf{q}_s \cdot \mathbf{n}$ to the droplet, and a uniform evaporation speed $u_s = \mathbf{u}_s \cdot \mathbf{n}$, leads to

$$\int_{\Omega(t)} div\mathbf{q}\mathrm{d}V = \int_{\partial\Omega(t)} (-\mathbf{q}_s + h\rho_s\mathbf{u}_s) \cdot \mathbf{n}\mathrm{d}S = [-q_s + \rho_s u_s \overline{C}_{pl} T_s] S_d.$$

In addition, applying Reynolds transport theorem to the left-hand side of (12.4), and using the fact that

$$\frac{\mathrm{d}}{\mathrm{d}t} \int_{\Omega(t)} \rho h \mathrm{d}V = \frac{\mathrm{d}}{\mathrm{d}t} \left(m \overline{C}_{pl} \overline{T}_l \right) = m \frac{\mathrm{d}(\overline{C}_{pl} \overline{T}_l)}{\mathrm{d}t} + \dot{m} \overline{C}_{pl} \overline{T}_l$$

leads to (12.7).

References

1. J. Abraham and V. Magi. A model for multicomponent droplet vaporization in sprays. SAE Paper 980511, 1998.
2. B. Abramzon and Sirignano. Droplet vaporization model for spray combustion calculations. *International Journal of Heat and Mass Transfer*, 32(9):1605–1618, 1989.
3. A. A. Amsden, P. J. O'Rourke, and T. D. Butler. KIVA II: A computer program for chemically reactive flows with sprays. Technical Report LA-11560-MS, Los Alamos National Laboratory, May 1989.
4. Y. Aouina, E. Gutheil, U. Maas, U. Riedel, and J. Warnatz. Mathematical modeling of droplet heating, vaporization, and ignition including detailed chemistry. *Combustion Science and Technology*, 173:1–29, 2001.
5. N. S. Ayoub and R. D. Reitz. Multidimensional computation of multicomponent spray vaporization and combustion. SAE Paper 950285, 1995.
6. J. Bellan and K. Harstad. The details of convective evaporation of dense and dilute clusters of droplets. *International Journal of Heat and Mass Transfer*, 30:1083, 1987.
7. G. Brenn, L. J. Deviprasath, and F. Durst. Computations and experiments on the evaporation of multicomponent droplets. In *Proceedings of the Ninth International Conference on Liquid Atomization & Spray Systems*, Sorrento, July 2003. CD-ROM Publication.
8. R. Byron Bird, W. E. Stewart, and E. N. Lightfoot. *Transport Phenomena*. Wiley, New York, second edition, 2002.
9. L. Consolini, S. K. Aggarwal, and S. Murad. A molecular dynamics simulation of droplet evaporation. *International Journal of Heat and Mass Transfer*, 46(10):3179–3188, 2003.
10. C. T. Crowe, M. Sommerfeld, and Y. Tsuji. *Multiphase Flows With Droplets and Particles*. CRC Press, New York, 1998.
11. I. Glassman. *Combustion*. Academic, San Diego, third edition, 1996.
12. T. B. Gradinger. *Spray Modeling with Application to Fuel-Air Premixing*. PhD thesis, ETH Zurich, Diss. ETH Nr. 13497, 2000.

13. J. B. Heywood. Engine combustion modeling – an overview. In J. N. Mattavi and C. A. Amann, eds., *Combustion Modeling in Reciprocating Engines*. Plenum Press, New York, 1980.
14. F. P. Incropera and D. P. DeWitt. *Introduction to Heat Transfer*. Wiley, New York, fourth edition, 2002.
15. K. K. Kuo. *Principles of Combustion*. Wiley, New York, first edition, 1989.
16. A. H. Lefebvre. *Atomization and Sprays*. Hemisphere Publishing Corporation, Bristol, first edition, 1989.
17. A. M. Lippert and R. D. Reitz. Modeling of multicomponent fuels using continuous distributions with applications to droplet evaporation and sprays. SAE Paper 972882, 1997.
18. S. Ohe. *Vapor-Liquid Equilibrium at High Pressure*. Elsevier, New York, 1st edn., 1990.
19. S. Pagel, G. Stiesch, and G. P. Merker. Modeling the evaporation of a multicomponent fuel. In *Proceedings of 12th International Heat Transfer Conference*, pp. 899–904, Grenoble, 2002.
20. W. E. Ranz and W. R. Marshall. Evaporation from drops (parts I and II). *Chemical Engineering Progress*, 48:141–146, 173–180, 1952.
21. M. Renksizbulut, M. Bussmann, and X. Li. A droplet vaporization model for spray calculations. *Particle & Particle Systems Characterization*, 9:59–65, 1992.
22. M. Renksizbulut, R. Nafziger, and X. Li. A mass transfer correlation for droplet evaporation in high-temperature flows. *Chemical Engineering Science*, 46(9):2351–2358, 1991.
23. M. Renksizbulut and M. C. Yuen. Experimental study of droplet evaporation in a high-temperature air stream. *Journal of Heat Transfer*, 105:384–388, 1983.
24. S. S. Sazhin. Advanced models of fuel droplet heating and evaporation. *Progress in Energy and Combustion Science*, 32:162–214, 2006.
25. W. A. Sirignano. *Fluid Dynamics and Transport of Droplets and Sprays*. Cambridge University Press, New York, 1999.
26. D. B. Spalding. The combustion of liquid fuels. In *Fourth Symposium (International) on Combustion*, pp. 847–864, Williams and Wilkins, Baltimore, 1953.
27. D. B. Spalding. *Some Fundamentals of Combustion*. Butterworth, London, 1955.
28. G. Stiesch. *Modeling Engine Spray and Combustion Processes*. Springer, Berlin, 2003.
29. J. H. Walther and P. Koumoutsakos. Molecular dynamics simulation of nanodroplet evaporation. *Journal of Heat Transfer*, 123(4):741–748, 2001.
30. F. A. Williams. Spray combustion and atomization. *Physics of Fluids*, 1(6):541–545, 1958.
31. F. A. Williams. *Combustion Theory*. Benjamin/Cummings Publishing, Menlo Park, second edition, 1985.
32. K. Yasuoka and M. Matsumoto. Molecular dynamics of homogeneous nucleation in the vapor phase. I. Lennard-Jones fluid. *Journal of Chemical Physics*, 109:8451, 1998.
33. K. Yasuoka and M. Matsumoto. Molecular dynamics of homogeneous nucleation in the vapor phase. II. water. *Journal of Chemical Physics*, 109:8464, 1998.
34. G. S. Zhu, R. D. Reitz, J. Xin, and T. Takabayashi. Characteristics of vaporizing continuous multi-component fuel sprays in a port fuel injection gasoline engine. SAE Paper 2001-01-1231, 2001.

Chapter 13
Reacting Sprays

F.X. Tanner

Abstract The classification regimes for premixed and non-premixed combustion processes are discussed in terms of the Damköhler and Karlovitz numbers. Dec's diesel spray combustion concept is introduced, followed by a short review of chemical kinetics. The ignition process together with appropriate models is then discussed. Subsequently, various combustion models are presented, including mixing-controlled, flamelet and PDF combustion models. The chapter ends with a discussion of pollutant modeling for nitric oxides (NO) and particulates.

Keywords Borghi diagram · Combustion · Chemical reactions · Chemical kinetics · Damköhler number · Flamelets · Ignition · Karlovitz number · Mixing-controlled combustion · PDF combustion models · Pollution modeling

Introduction

Sprays are an important means of supplying fuel to a combustion process, for example in engines, turbines, rocket motors, furnaces, and boilers. The central issues associated with spray combustion include fuel economy and pollution formation, both of which have been major driving forces in the past and the current spray combustion research. The vast amount of literature on the subject is a reflection of its complexity. There are many texts on combustion at various levels of difficulty and with different applications in mind (cf. [9, 17, 20, 23, 28, 29, 30, 37, 52, 56]). In addition, various modeling approaches are discussed in the articles of Pope [41], Borghi [6] and, more recently, in Veynante and Vervisch [51].

F.X. Tanner
Department of Mathematical Sciences, Michigan Technological University, Houghton, MI, USA
e-mail: tanner@mtu.edu

N. Ashgriz (ed.), *Handbook of Atomization and Sprays*,
DOI 10.1007/978-1-4419-7264-4_13, © Springer Science+Business Media, LLC 2011

The detailed chemical reaction mechanism of a hydrocarbon combustion process can involve thousands of reactions among hundreds of species (cf. [11, 18, 52, 55]). Since for each species, there is a species transport equation that needs to be solved, this would lead to huge systems of partial differential equations, whose computing demands lie far beyond the capacities of today's computers. Therefore, only the process-domineering reactions and species are considered, and when necessary, the reaction rates are determined from empirical and/or flow determining quantities. In practice, often only three phenomena are of interest when dealing with reacting sprays, namely, ignition, heat release, and pollutant formation. These three phenomena occur on different length and time scales, and therefore, they are often decoupled and modeled separately.

Combustion processes are determined by the interaction of flow properties and chemistry and can be subdivided into premixed and non-premixed regimes for either laminar or turbulent flows. In premixed combustion, the fuel and the oxidizer are fully mixed at the time the chemical reactions take place. In contrast, in non-premixed combustion processes, the fuel and the oxidizer are separated until mixing and chemical reactions take place almost simultaneously. Non-premixed combustion is also referred to as diffusion combustion and is typically encountered in sprays. Note that spray combustion is almost always turbulent because the interaction between the spray droplets and the surrounding air induces a turbulent flow. Also, as discussed below in more detail, in transient spray processes such as those encountered in diesel engines, both premixed and non-premixed combustion take place.

Combustion Regimes

The classification of flames depends on the mixture characteristics of the fuel and oxidizer, and on the interaction between the flow properties and the chemistry. This classification is done by means of dimensionless quantities, namely, the turbulent Reynolds number, the turbulent Damköhler number, and the turbulent Karlovitz number, respectively defined by

$$Re_\mathrm{t} = \frac{u' L_\mathrm{I}}{\nu_\mathrm{o}}, \quad Da = \frac{\tau_\mathrm{I}}{\tau_\mathrm{c}}, \quad Ka = \frac{\tau_\mathrm{c}}{\tau_\eta} \tag{13.1}$$

In these formulae, $u' = \sqrt{2k/3}$ is the turbulence intensity (or the root mean square turbulence fluctuation) where k is the (specific) turbulent kinetic energy, L_I is the turbulence integral length scale (a measure for the largest turbulent eddies), and ν_0 is the kinematic molecular viscosity. Further, $\tau_\mathrm{I} = L_\mathrm{I}/u'$ is the turbulence integral time scale and $\tau_\mathrm{c} = L_\mathrm{F}/u_\mathrm{F}$ is the chemical or laminar flame time scale, where L_F is a characteristic laminar flame thickness, and u_F is a characteristic laminar flame speed. Finally, $\tau_\eta = \sqrt{\nu_0/\varepsilon}$ is the Kolmogorov time scale, where ε is the turbulence dissipation (rate).

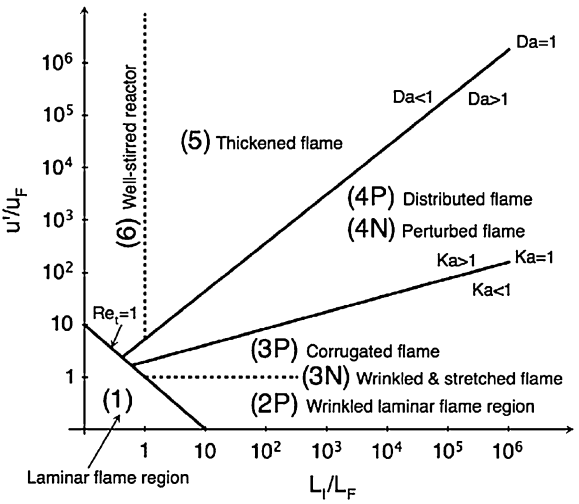


Fig. 13.1 Borghi diagram showing the different combustion regimes. The (*P*) applies to premixed combustion and (*N*) applies to non-premixed combustion

Note that *Da* is a measure for the importance of the turbulent mixing in comparison with the chemical reactions, and *Ka* is a measure for the local stretching or distortion of a laminar flame due to turbulence. More precisely, the smaller *Da*, the more dominant is the turbulent mixing, and the larger *Ka*, the more distorted or fragmented is the structure of the flame front.

The characterization of flames can be represented in the Borghi diagram (cf. [6]) shown in Fig. 13.1. In this diagram, the velocity ratio u'/u_F is plotted against the length scale ratio $L_\mathrm{I}/L_\mathrm{F}$ in a double logarithmic plot. Constant values of *Da* and *Ka* appear as straight lines, as do constant values of Re_t, since $v_0 \approx u_\mathrm{F} L_\mathrm{F}$ for laminar flames. The different regions in Fig. 13.1 are labeled with a P or a N, depending on whether they apply to premixed (P) or non-premixed (N) combustion. Regions without this distinction apply to both types of flames. Obviously, the boundaries of these regions are not strict; when moving from one combustion regime to another, the change in the flame behavior is not sudden but rather gradual.

Premixed Flames

In premixed combustion, the characteristic laminar speed, u_F, is the laminar flame propagation speed and the characteristic length scale, L_F, corresponds to the flame thickness. The laminar flame regimes are confined to regions (1) and (2P), where in the latter the turbulence intensity, u', is less than the laminar flame speed, u_F. Region (1) is defined by $Re_\mathrm{t}<1$ and the flame front is essentially a thin planar

reacting sheet that can be treated as a one-dimensional object. In region (2P), the wrinkled laminar flame region, the interaction of large eddies with the laminar flame front leads to a distorted, hence wrinkled, laminar flame. In region (3P), the corrugated flame region, u' exceeds u_F, which leads to a more intense flame front distortion where the flame front can fold over itself, forming isolated (laminar) flames, called corrugated flamelets. Also, the Karlovitz number is less than unity which indicates that, locally, the laminar flame structure still dominates the turbulent flow. In region (4P), the distributed reaction zone where the Karlovitz number is larger than unity, the turbulence dominates the flame front distortion. This leads to a fragmentation (or distribution) of the flame front into many small laminar flamelets and hence a widening of the reaction zone. Finally, in region (5), the thickened flame region, $Da < 1$ and the flame front becomes more and more dominated by turbulent mixing. With progressive mixing, the chemical reactions increasingly resemble the ones of a well-stirred reactor, as is indicated in region (6).

In summary, the Borghi diagram illustrates how a one-dimensional laminar flame front in region (1) becomes increasingly three-dimensional through the interaction between turbulence and chemistry.

Non-premixed Flames

For non-premixed combustion processes, the flame classification is done analogously, but with different meanings for the various flame regimes. The most obvious difference is the fact that there is no moving flame front for non-premixed combustion, hence no obvious laminar flame speed u_F. Also, the flame thickness depends on the local mixing properties, and therefore, it is more difficult to identify an appropriate characteristic length scale. Nevertheless, if $\gamma = grad_n\ u$ denotes the gradient of the oxidizer or fuel speed normal to the laminar flame sheet, and D is the diffusion coefficient, then the laminar diffusion flame thickness can be defined as

$$L_F = L_D \approx \sqrt{\frac{D}{\gamma}},$$

and the laminar diffusion flame speed can be taken to be

$$u_F = u_D \approx \sqrt{D\gamma}.$$

With these identifications, according to Borghi [6], one obtains a diagram with almost identical regions as for premixed combustion. In Fig. 13.1, the non-premixed regions are identified with the letter N. Note that the basic turbulence-chemistry interactions which define these regions, that is $Re_t = 1$, $Da = 1$, and $Ka = 1$, also define the different regions for the non-premixed flame structures.

As in the premixed case, the line $Re_t = 1$ separates the laminar and the turbulent non-premixed flames. In analogy to the premixed flames, region (3N), which coincides with regions (2P) and (3P), corresponds to the wrinkled and stretched flamelet regime. The stretching and wrinkling of the flame is determined by the Kolmogorov time scale τ_η, and the rate of combustion is determined by τ_c. When τ_η becomes too small, that is, the wrinkling or stretching of the flame is too large, then flame quenching occurs. In this situation, a stable reaction sheet cannot be sustained and the flame extinguishes itself. This occurs in region (4N), the perturbed flame region, where the Karlovitz number is above its critical value, i.e., $Ka > 1$. In addition, the interaction of unsteady flamelets causes overall flame instabilities which contribute to the self-extinction. These phenomena lead to an unstable reaction region where flame extinction is followed by mixing of products, fuel, and oxidizer. Subsequently, this leads to spontaneous re-ignition in a partially premixed medium. For very large τ_c, the time delay between flamelet extinction and re-ignition becomes large, which increases the degree of this local premixing. If, at the same time, the characteristic turbulent mixing time, τ_I, becomes small enough compared to τ_c, then the ensuing non-premixed flame resembles locally a well-stirred premixed flame. This happens in region (5) where $Da = \tau_I/\tau_c < 1$, and is called the thickened flame region.

For spray combustion in diesel engines and gas turbines, the flame types for premixed and non-premixed combustion fall mainly into the wrinkled and stretched flame regime in region (3), and into the distributed or perturbed flames in region (4).

Spray Combustion

Because of its highly nonstationary nature, diesel combustion is one of the most challenging spray combustion processes to understand. It consists of a premixed combustion phase followed by a non-premixed combustion phase. The premixed combustion is a consequence of the ignition delay. More precisely, when fuel is injected into a combustion chamber, it atomizes into tiny droplets that evaporate and mix with air to form a reactive compound. This reactive compound is well mixed by the time ignition takes place, thus initiating the premixed combustion process. This premixed combustion results in a sharp increase in pressure and temperature and results in the first local maximum in the heat release curve, as is illustrated for a medium-speed direct injection (DI) diesel engine in Fig. 13.2. Subsequently, when all the premixed fuel mixture is consumed, the non-premixed or diffusion-controlled combustion takes over, which leads to the second local maximum of the heat release. Observe that there is a small negative heat release just after the start of injection. This occurs because the evaporation of fuel uses energy from the surrounding gas.

The detailed structure of the non-premixed portion of a spray combustion has not been well understood until recently. Various theories had been proposed, which

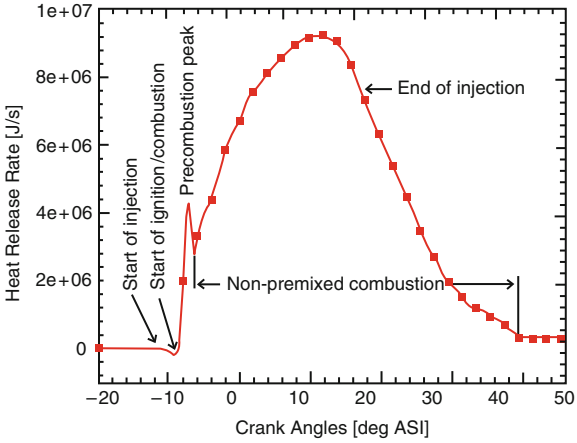


Fig. 13.2 Rate of heat release of a medium-speed DI diesel engine at full load

attributed the non-premixed flame either to a collection of individual droplet diffusion flames, or to a sheath-type combustion at the spray periphery, or to a combination of the two. A relatively recent conceptual model of diesel spray combustion has been proposed by Dec [12] as a result of an extensive experimental research program, using data from laser sheet imaging techniques. Figure 13.3 illustrates a schematic of this model for the mixing-controlled, that is the non-premixed, combustion phase, just before the end of injection. It is seen that the liquid portion of the fuel reaches a maximum penetration after which the fuel is completely evaporated. The fuel vapor mixes with the entrained air and is convected downstream to form a relatively uniform, fuel-rich mixture. This mixing region is engulfed by a sheath of a high-temperature, fast-chemistry diffusion flame which burns under near stoichiometric conditions. This flame begins at a certain distance downstream from the nozzle exit, called the flame lift-off length. The flame lift-off region itself is surrounded by a low-temperature, slow-chemistry combustion sheath. Soot, which is a consequence of fuel pyrolysis, is produced over the entire region inside the diffusion flame, but the main soot concentration is found near the head vortex of the spray. The reason for this soot accumulation at this location is that soot particles, which have been generated earlier, have time to grow and are convected towards the head of the spray. This soot is then transported out to the diffusion flame where most of it oxidizes.

Because of the relatively low temperatures in the fuel-air mixing zone near the flame lift-off, the experimentally observed soot formation cannot be explained in terms of fuel pyrolysis. To account for the soot observed in this zone, Dec and Coy [13] hypothesize that there is a standing fuel-rich premixed flame just upstream from the liquid phase, where the fuel vapor and air mixture reaches an equivalence ratio between two and five. Such a fuel-rich combustion zone is ideal for soot production, because the combustion products contain an abundance of excess fuel

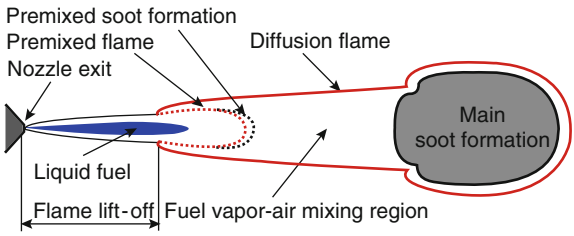


Fig. 13.3 Conceptual model of diesel spray combustion according to Dec [12]

and are sufficiently hot for fuel pyrolysis to take place. This standing premixed combustion zone, together with its soot formation region, is indicated by dashed lines in Fig. 13.3.

Finally, the experiments show that the early thermal nitric oxide (NO) production occurs on the lean side of the diffusion flame. As pointed out in the paper by Dec [12], and observed by other researchers (e.g., [46]), the bulk of the thermal NO production occurs after the end of fuel injection and away from the actual spray combustion zone. The reason for this behavior can be attributed to the fact that the thermal NO production is relatively slow, and that hot pockets of gases are convected into air-rich regions where plenty of nitrogen is available for NO formation.

A Brief Review of Chemical Kinetics

Chemical reactions occur over a wide range of time scales and have a considerable influence on the flow and transport processes in a particular problem. The reaction rates, which are governed by chemical kinetics, are essential in predicting the outcome of many turbulent reacting flows.

Chemical reactions are symbolically denoted by

$$\sum_{\mathrm{m}} a_{\mathrm{mr}} \chi_{\mathrm{m}} \longleftrightarrow \sum_{\mathrm{m}} b_{\mathrm{mr}} \chi_{\mathrm{m}}, \tag{13.2}$$

where χ_{m} represents 1 mol of species m, and a_{mr} and b_{mr} are the integral stoichiometric coefficients for reaction r. The forward and backward directions are indicated with the double arrow. The species conservation in each chemical reaction r dictates that

$$\sum_{\mathrm{m}} (a_{\mathrm{mr}} - b_{\mathrm{mr}}) W_{\mathrm{m}} = 0,$$

where W_{m} is the molecular mass of species m. The rate at which the rth kinetic reaction proceeds is given by the reaction rate

$$\dot{\omega}_{\mathrm{r}} = k_{\mathrm{f}} \prod_{\mathrm{m}} \left(\frac{\rho_{\mathrm{m}}}{W_{\mathrm{m}}} \right)^{a'_{\mathrm{mr}}} - k_{\mathrm{b}} \prod_{\mathrm{m}} \left(\frac{\rho_{\mathrm{m}}}{W_{\mathrm{m}}} \right)^{b'_{\mathrm{mr}}}, \tag{13.3}$$

where ρ_{m} is the density of species m. The reaction orders a'_{mr} and b'_{mr} need not equal their stoichiometric counterparts a_{mr} and b_{mr}, so that empirical, possibly noninteger, reaction orders can be used. The coefficients k_{f} and k_{b} are the specific forward and backward reaction rates given by the generalized Arrhenius law

$$k_{\mathrm{f}} = A_{\mathrm{f}} T^{\zeta_{\mathrm{f}}} \exp\left(-\frac{E_{\mathrm{f}}}{T} \right) \tag{13.4}$$

$$k_{\mathrm{b}} = A_{\mathrm{b}} T^{\zeta_{\mathrm{b}}} \exp\left(-\frac{E_{\mathrm{b}}}{T} \right), \tag{13.5}$$

where A_{f}, A_{b}, ζ_{f}, and ζ_{b} are constants, and E_{f} and E_{b} are the forward and backward activation temperatures.

With the reaction rates determined by (13.3), the chemical source terms in the gas phase conservation equations for species and energy can respectively be written as

$$\dot{\rho}^{\mathrm{c}}_{\mathrm{m}} = W_{\mathrm{m}} \sum_{\mathrm{r}} (b_{\mathrm{mr}} - a_{\mathrm{mr}}) \dot{\omega}_{\mathrm{r}} \tag{13.6}$$

$$\dot{Q}^{\mathrm{c}} = \sum_{\mathrm{r}} \dot{\omega}_{\mathrm{r}} \sum_{\mathrm{m}} (a_{\mathrm{mr}} - b_{\mathrm{mr}}) (\Delta h^0_{\mathrm{f}})_{\mathrm{m}} \tag{13.7}$$

where $(\Delta h^0_{\mathrm{f}})_{\mathrm{m}}$ is the heat of formation of species m at absolute zero. These source terms form the main interaction between chemistry and fluid flows. Note that (13.6) is a manifestation of *the law of mass action*.

Fast chemical reactions, usually at high temperatures, are often assumed to be in equilibrium. This means that the forward and backward reaction rates are the same, hence $\dot{\omega}_{\mathrm{r}} = 0$. Therefore, (13.3) becomes the constraint condition

$$\prod_{\mathrm{m}} \left(\frac{\rho_{\mathrm{m}}}{W_{\mathrm{m}}} \right)^{b_{\mathrm{mr}} - a_{\mathrm{mr}}} = \frac{k_{\mathrm{f}}}{k_{\mathrm{b}}} = K^{\mathrm{r}}_{\mathrm{c}}(T), \tag{13.8}$$

where the concentration equilibrium constant, $K^{\mathrm{r}}_{\mathrm{c}}(T)$, is of the form

$$\ln K^{\mathrm{r}}_{\mathrm{c}}(T) = A_{\mathrm{r}} \ln T_{\mathrm{A}} + \frac{B_{\mathrm{r}}}{T_{\mathrm{A}}} + C_{\mathrm{r}} + D_{\mathrm{r}} T_{\mathrm{A}} + E_{\mathrm{r}} T^2_{\mathrm{A}}. \tag{13.9}$$

In this equation, $T_{\mathrm{A}} = T/1000$ and A_{r}, B_{r}, C_{r}, D_{r} and E_{r} are reaction-specific constants. Therefore, if $K^{\mathrm{r}}_{\mathrm{c}}(T)$ and the reactant concentrations are known for each reaction r, then the product concentrations can be obtained from (13.8).

Ignition Modeling

Spray combustion is initiated by an ignition process, which occurs at relatively low temperatures and, therefore, its chemical time scales are comparable with the ones of the flow. Consequently, fluid dynamics effects play an important role, and species transport equations are essential for monitoring the ignition progress. Also, the chemical reactions are dominated by various reaction paths, which lead to a large number of intermediate species that can exhibit unexpected behavior. The ignition delay characteristics are illustrated for different gas pressures of a *n*-heptane fuel in Fig. 13.4. The data in this figure has been obtained from computations based on a detailed reaction mechanism as reported by Inhelder et al. [25].

As shown in Fig. 13.4, after the initial low temperature reactions, which are mainly due to chain-branching, there is a temperature region, called the *cool-flame region*, where reverse reactions lead to a very slow burning process. This can result in a small temperature increase and hence in an increase of the ignition delay. Subsequently, after the cool-flame regime, other reaction paths dominate the chemical processes and release sufficient heat such that the associated temperature increase leads to the high-temperature reactions, that is, the actual combustion process.

Detailed reaction mechanisms that describe the ignition process of hydrocarbon fuels involve thousands of chemical reactions among hundreds of species, as is for instance reported by Chevalier et al. [11] or Pilling et al. [38]. In computational fluid dynamics (CFD) it is impossible to take all of these reaction mechanisms into account. A common approach to the modeling of the ignition process is to derive a reduced reaction mechanism from a set of detailed

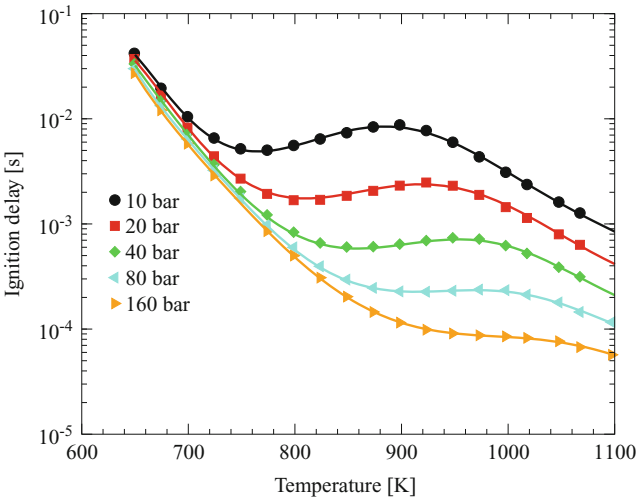


Fig. 13.4 Ignition delay of *n*-heptane as a function of temperature for different gas pressures

chemical reactions (cf. [15, 32]). A widely used auto-ignition model that is utilized in the CFD simulations of diesel combustion processes is the Shell ignition model of Halstead et al. [22], or any of its many variants (e.g., [2, 26]). The Shell ignition model is based on eight global chemical reactions involving six representative species, where the kinetic parameters have been determined from fitting experimental data. Technically, the Shell model is not a reduced reaction mechanism; it rather represents a virtual mechanism among generic species that can be used to model the ignition behavior of many hydrocarbon fuels. The Shell model computes the heat release due to the chemical reactions, and it requires an additional transport equation for each intermediate species in order to describe its flow behavior.

Another approach to the modeling of the ignition process is the least-square-fitted ignition transport (LIT) model of Tanner [45], which is a further development of the simplified kinetic ignition (SKI) model developed by Weisser et al. [54]. The LIT model is based on a concept utilizing a single transport progress variable, C_{ig}, which describes the progress of the physical and chemical processes governing the ignition delay, τ. This quantity is formally equivalent to the concentration of an intermediate species, nondimensionalized by its critical value and subject to the conservation equation

$$\frac{\partial(\rho C_{\mathrm{ig}})}{\partial t} + \nabla \cdot (\rho C_{\mathrm{ig}} \mathbf{u}) = \nabla \cdot (\rho D \nabla C_{\mathrm{ig}}) + \frac{\rho}{\tau(p, T, \Phi, \ldots)},$$

where ρ, $\mathbf{u}$, p, T are the gas density, velocity, pressure, and temperature, respectively, Φ represents the local fuel-air equivalence ratio, and D is the effective diffusivity. Note that the nondimensionalization of C_{ig}, mentioned above, leads to the critical value $C_{\mathrm{crit}} = 1$. Therefore, if $C_{\mathrm{ig}} > 1$ at some point, then ignition has occurred and the actual combustion model takes over at that location.

The performance of the LIT model has been evaluated by simulating the ignition experiments of Reuter [42] in a constant pressure combustion chamber for diesel fuel. The ignition delay and the ignition location (axial distance from the nozzle orifice) have been investigated for a range of temperatures from 750 to 900 K and a range of gas pressures from 40 to 50 bar. The results of these investigations are shown in Fig. 13.5 for the gas pressure of 45 bar. It can be seen that there is good agreement between the simulations and experiments. Additional details are presented in [45].

Combustion Modeling

The heat release in a combustion process can be determined with as few as one reaction equation using empirical reaction rate coefficients and activation temperatures. This drastic reduction in the number of chemical reactions is justified by Hess' law, which states that the net heat of reaction of a set of chemical reactions

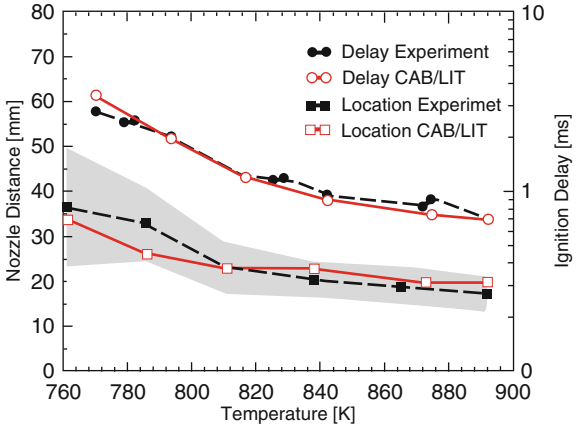


Fig. 13.5 Ignition locations (*left scale*) and ignition delays (*right scale*) as a function of temperature at the gas pressure $p_g = 4.5$ MPa for CAB/LIT computations and the experiments of Reuter [42]. The *shaded region* indicates the experimental ignition location fluctuations

depends only on the initial and final states. To illustrate this point, the heat release of an idealized hydrocarbon fuel, say C_nH_m, can be modeled with a global one-step reaction mechanism

$$C_nH_m + \left(n + \frac{m}{4}\right)O_2 \rightarrow nCO_2 + \frac{m}{2}H_2O,$$

where the specific reaction rates are determined from the generalized Arrhenius relation in (13.4) using empirical coefficients and activation temperatures.

The length and time scales of chemical reactions are generally much smaller than the ones of the underlying flow. In fact, with today's computers, CFD computations cannot resolve all the scales in technically relevant combustion problems. Consequently, modeling is required to make meaningful combustion predictions. Since for fuel sprays the gas flow is usually turbulent, the fuel-air mixing process depends on the turbulence parameters from which the chemical reaction rates are determined.

Mixing-controlled Combustion Models

Mixing-controlled reaction models are probably the most widely used spray combustion models. Different methods have been proposed by various researchers, including Spalding [43], Borghi [5], Magnussen and Hjertager [31], Bray and Moss [7], Gosman et al. [21], Abraham et al. [1], and others. All of these approaches relate the average eddy turnover time $\tau = k/\varepsilon$ to the reaction rate. As a representative of these mixing-controlled reaction models, the characteristic time combustion

model of Abraham et al. [1], as adapted to diesel engine combustion by Kong and Reitz [27], is discussed here. This model also accounts for the initial premixed reaction phase that occurs in diesel combustion, because the fuel of the early injection phase has already vaporized and mixed with air, before the onset of combustion.

In the *characteristic time combustion model*, the rate of change of the mass fraction, Y_m, of species m due to chemical reaction, is given by

$$\frac{\mathrm{d}Y_\mathrm{m}}{\mathrm{d}t} = -\frac{Y_\mathrm{m} - Y_\mathrm{m}^*}{\tau_\mathrm{r}},$$

where Y_m^* denotes the local equilibrium mass fraction and τ_r is the characteristic time of combustion. The latter is the weighted sum of a laminar time scale, τ_l, used for the premixed combustion phase, and a turbulent time scale, τ_t, and is given by

$$\tau_\mathrm{r} = \tau_\mathrm{l} + f\tau_\mathrm{t}.$$

The weight function f simulates the transition from the premixed to turbulence-controlled combustion after ignition has taken place. More precisely, it can be expressed as

$$f = \frac{1 - e^{-p}}{0.632},$$

where the combustion progress parameter p satisfies $0 < p < 1$, and is computed as the ratio of the amount of products to the amount of the total reactive species (except N_2), i.e.

$$p = \frac{Y_{\mathrm{CO}_2} + Y_{\mathrm{H}_2\mathrm{O}} + Y_\mathrm{CO} + Y_{\mathrm{H}_2}}{1 + Y_{\mathrm{N}_2}}.$$

The laminar time scale is derived from a global one-step Arrhenius reaction rate and is given by

$$\tau_\mathrm{l} = A^{-1}[\mathrm{C}_{14}\mathrm{H}_{30}]^{0.75}[\mathrm{O}_2]^{-1.5}\exp\left(\frac{E}{RT}\right),$$

where $A = 1.54 \times 10^{10}$, $R = 8.3143$ J/(mol K) is the universal gas constant, the activation energy is taken to be $E = 77.3$ kJ/mol, and the brackets denote the molar concentrations. The turbulent time scale is proportional to the eddy turnover time

$$\tau_\mathrm{t} = \frac{C_\mathrm{M} k}{\varepsilon},$$

where the constant C_M serves as a parameter to adjust the reaction rate to engine specific conditions (cf. [47]).

Flamelet Models

The flamelet assumption (cf. Peters [35, 36]) states that in regions of large Damköhler numbers, a wrinkled, turbulent flame front behaves locally like a laminar flame, provided that the turbulent length and time scales are larger and slower than the ones of the chemical reactions. The validity of this assumption can be justified by the fact that for turbulent eddies larger than the flame thickness, the flame front is not yet fragmented into a wide-distributed reaction zone. In the Borghi diagram shown in Fig. 13.1, the flamelet region covers regions (2), (3), and the lower part of region (4). It should be noted that if the turbulence Reynolds number Re_t approaches zero, then the flamelet model reduces to a laminar flame description.

For a non-premixed flame, the relatively thin reaction zone is viewed as a collection of laminar flamelets subject to turbulence fluctuations. The chemical reactions within a flamelet can be treated as a locally one-dimensional phenomenon that depends on the fuel-oxidizer mixture. This mixture is expressed in terms of the mixture fraction

$$Z = \frac{\dot{m}_{\text{fuel}}}{\dot{m}_{\text{fuel}} + \dot{m}_{\text{oxidizer}}},$$

where $Z = 1$ in a pure fuel stream and $Z = 0$ in a pure oxidizer (air) stream. The variable Z is a conserved quantity and it is proportional to the mass fraction of the involved chemical elements. Therefore, it is not affected by chemical reactions but only by (turbulent) mixing. The effects of the turbulent flow on the flamelets are accounted for by introducing the instantaneous scalar dissipation rate defined by

$$\chi = 2D||grad\ Z||^2,$$

where D is the species diffusion coefficient. χ can be interpreted as a characteristic diffusion rate, which increases due to turbulent straining and decreases due to diffusion.

As a consequence of this one-dimensional description of the flamelets, the flamelet chemistry can be separated from the three-dimensional flow field properties, which allows a decoupled evaluation of the two. The big advantage of this decoupling is that more detailed reaction mechanisms can be considered without the drawback of excessive additional CPU times.

In particular, the chemistry can be computed independently of the flow field for different values of Z and the other flamelet parameters such as temperature, pressure, and the scalar dissipation rate χ. The results of such computations can then be stored in look-up tables, called flamelet libraries, and are readily available when the actual flow computations are performed (cf. [19]).

Instead of look-up tables, another approach consists of deriving simple algebraic relations from these computations, which require insignificant additional computation

times when integrated into a CFD code. This approach is known as coherent flamelet modeling and is documented in [14, 33].

However, in highly transient flows, as for instance encountered in diesel engines, the scalar dissipation rate is too slow to adjust to the changing flow conditions and, therefore, steady flamelet solutions are a source of inaccuracies. In order to account for such highly unsteady flows, the research group of Peters (e.g., [39, 40]) introduced the concept of Representative Interactive Flamelets (RIF), where the flamelet code is coupled to the CFD code and the combustion rates are determined interactively.

The details of flamelet modeling is quite complex and beyond the scope of this chapter. For more detailed insight into the topic, there is vast literature including the texts of Cant and Mastorakos [9], Peters [37], Stiesch [44], Warnatz et al. [52], and the article by Bray and Peters [8].

PDF Combustion Models

The variables that govern turbulent reacting flows have large, random fluctuations. This suggests a statistical treatment of the variables which leads to the use of multivariable joint probability density functions (PDF) $P(\xi;\mathbf{x}, t)$. $P(\xi;\mathbf{x}, t)$ denotes the probability that a system at location $\mathbf{x}$ and time t is in a state between ξ and $\xi + d\xi$, where ξ denotes a particular state in the underlying sample space Ω. In this notation, for instance, $\xi = (\rho, p, T, \mathbf{u}, Y_1, \ldots, Y_N)$ denotes a vector whose components are flow and thermo-chemical random variables. More precisely, ρ denotes the density, p the pressure, T the temperature, $\mathbf{u}$ the velocity, and $Y_1, \ldots, Y_N$ the N species mass fractions.

A direct consequence of the PDF description is that for each pair $(\mathbf{x}, t)$

$$1 = \int_{\Omega} P(\xi;\mathbf{x}, t)\, d\xi$$

$$\langle f(\mathbf{x}, t)\rangle = \int_{\Omega} f(\xi) P(\xi;\mathbf{x}, t) d\xi,$$

where $f(\xi)$ is a physical quantity defined on Ω and $\langle\cdots\rangle$ denotes the average. For example, if $f(\xi) = ||\mathbf{u}'||^2$ denotes the square of the velocity fluctuation, then $\langle||\mathbf{u}'||^2\rangle$ is the mean square of this fluctuation.

The central issue with the PDF approach is the prediction of the PDF itself. In general, a PDF-transport equation needs to be solved, which can be quite challenging and computationally very expensive. However, the universality of the method,[1] together with the ever increasing computing speeds of new computers, promise to

[1] cf. the stochastic particle model used for the spray description in Chap. 19.

make this subject more and more popular. There is vast literature on PDFs, and more detailed accounts for turbulent reacting flows can be found, for example, in the texts of Libby and Williams [29, 30] or in the article of Pope [41].

Pollutant Modeling

Hydro-carbon-based spray combustion is associated with pollutant formation. These pollutants include the NO and NO_2 (referred to as NOx), carbon monoxide (CO), particulate matter (soot), unburned hydrocarbons (HC), and others such as sulfur oxides. Although pollutants form a small part of the overall exhaust gas composition, they are produced in such large quantities that they have become considerable environmental and health hazards. Therefore, pollution reduction has become one of the most important aspects of spray combustion research. A very effective approach to achieve this objective is to reduce pollutants at their source, and thereby contribute directly to the production of cleaner and more efficient spray combustion devices.

In the following, a few models are discussed which are used to predict pollutants, and at the same time serve in the efforts to reduce and/or eliminate them. The relationship between engine input variables and their influence on the emissions and fuel economy is very complex, and in general, is not explicitly known. Typically, a reduction in NO is associated with an increase in the soot formation, known as the soot-NOx trade-off, which usually occurs at the expense of fuel consumption. One approach is the optimization of the combustion devices by minimizing the fuel efficiency and keeping the pollution formation within mandated boundaries. Such optimization processes for diesel engines are presented in [3, 50].

Only relatively simple pollution models are discussed here. All these models are decoupled from the main combustion process. Also, the models may require additional tuning when the involved time and length scales change, as for instance is the case when they are applied to different-sized engines (cf. [48]).

Prompt Nitric Oxide Formation

In spray combustion, the prompt NO formation is initiated by HC radicals, which are present in fuel-rich regions. Therefore, prompt NO is generated directly in the main reaction zone. This mechanism has first been described by Fenimore [16] and, subsequently, has been refined by various other researchers. For a more detailed account of prompt NO formation, together with additional references (see [20, 52]).

In diesel engines, where the combustion temperatures are generally very high, prompt NO is negligible in comparison to the thermal NO discussed next. However, in relatively low-temperature spray combustion, for instance, encountered in gas turbines, the main source of NOx production is usually the prompt NO.

Thermal Nitric Oxide Formation

Diesel engines have a high fuel efficiency because the combustion process occurs at high pressures and temperatures. Unfortunately, the drawback of this high-temperature combustion is the formation of nitric oxides, the so-called secondary or thermal NO. One of the simplest ways to model this thermal NO is with the extended Zeldovich mechanism (cf. [20, 57]), which involves the three kinetic reactions

$$\mathrm{O} + \mathrm{N_2} \leftrightarrow \mathrm{N} + \mathrm{NO}$$

$$\mathrm{N} + \mathrm{O_2} \leftrightarrow \mathrm{O} + \mathrm{NO}$$

$$\mathrm{N} + \mathrm{OH} \leftrightarrow \mathrm{H} + \mathrm{NO}$$

and the five equilibrium reactions

$$\mathrm{H_2} \rightarrow 2\mathrm{H}$$

$$\mathrm{O_2} \rightarrow 2\mathrm{O}$$

$$\mathrm{O_2} + \mathrm{H_2} \rightarrow 2\mathrm{OH}$$

$$\mathrm{O_2} + 2\mathrm{H_2O} \rightarrow 4\mathrm{OH}$$

$$\mathrm{O_2} + 2\mathrm{CO} \rightarrow 2\mathrm{CO_2}.$$

These equilibrium reactions are needed to generate the H, O, N, and OH radicals at high temperature, before the slower kinetic reactions can be initialized. The coefficients and activation temperatures used in (13.4) and (13.9) for a medium-speed DI diesel engine are summarized in a study by Tanner and Srinivasan [49].

Many different reaction mechanisms for thermal NO formation have been proposed by various research groups. For an example and additional references see Weisser [53]. Also, an application of Weisser's NO mechanism to large-bore marine diesel engines is presented in [46].

The experimental NOx values, usually obtained from measurements made in the exhaust pipe, consist mainly of the more stable compound NO_2, but the Zeldovich mechanism produces exclusively NO. Therefore, in order to compensate for this additional later conversion into NO_2, the NO mass predicted at the end of each simulation is converted to NO_2 by multiplying its mass by 1.53. This factor is the ratio of the molecular weights of NO_2 and NO.

Soot Modeling

As discussed in the context of the conceptual spray combustion model of Dec [12], illustrated in Fig. 13.3, soot tends to form in fuel-rich regions at relatively low temperatures. The exact soot formation process is a rather complex topic; more details can be found in the texts of Refs. [4, 23, 44]. In the following, a relatively simple production-oxidation soot model, used in the prediction of particle emissions in diesel engines, is outlined.

The net soot density, ρ_s, is governed by the species transport equation

$$\frac{\partial \rho_s}{\partial t} + div(\rho_s \mathbf{u}) = div\left(\rho D \left(\frac{\rho_s}{\rho}\right)\right) + \dot{\rho}_s$$

where ρ, ρ_s, $\mathbf{u}$, D are the gas density, the net soot density, the gas velocity, and the effective diffusivity, respectively. The interaction between the flow properties of the net soot and its generation or depletion, is described by means of the source term $\dot{\rho}_s$. This source term is modeled according to Hiroyasu and Kadota [24] by

$$\frac{d\rho_s}{dt} = \frac{d\rho_{sf}}{dt} - \frac{d\rho_{so}}{dt},$$

where ρ_{sf} is the density of soot formed and ρ_{so} is the density of soot oxidized.

The soot formation is modeled according to (cf. [24])

$$\frac{d\rho_{sf}}{dt} = C_f \rho_v p^{0.5} \exp\left(-\frac{E_f}{RT}\right),$$

where ρ_v is the fuel vapor density, p is the pressure in bar, T is the temperature in Kelvin, $E_f = 52{,}300$ J/mol is the activation energy, and $R = 8.3143$ J/(mol K) is the universal gas constant, and C_f is a tuning constant.

The oxidation model used is the one by Nagle and Strickland-Constable [34], as presented in Chan et al. [10]. In this model, the oxidation of carbon takes place by two mechanisms whose rates are dependent on the surface chemistry involving the more reactive form of carbon, C_A, and the less reactive form of carbon, C_B. This mechanism is expressed by the chemical reactions

$$C_A + O_2 \rightarrow C_A + 2CO$$

$$C_B + O_2 \rightarrow C_A + 2CO$$

$$C_A \rightarrow C_B$$

together with the overall oxidation rate

$$\frac{d\rho_{so}}{dt} = C_o \frac{m_c}{\sigma D} R_t \rho_s,$$

where C_o is a tuning constant, $m_c = 12$ g/mol is the molecular weight of carbon, $\sigma = 2$ g/cm is the density of a soot particle, and $D = 3 \times 10^{-6}$ cm is the average diameter of a soot particle; R_t represents the overall reaction rate of this system whose value is given by

$$R_t = \left(\frac{p_{O_2} K_A}{1 + K_Z p_{O_2}} \right) x + K_B p_{O_2} (1 - x),$$

where p_{O_2} is the oxygen partial pressure and x is the proportion of carbon C_A determined from

$$x = \left(\frac{p_{O_2}}{p_{O_2} + (K_T / K_B)} \right).$$

The rate expressions K_A, K_B, K_T, and K_Z, together with the constants C_f and C_o used for the simulation of a medium-speed DI diesel engine, are given in a study by Tanner and Srinivasan [49].

References

1. J. Abraham, F. V. Bracco, and R. D. Reitz. Comparisons of computed and measured premixed charge engine combustion. *Combust. Flame*, 60:309–322, 1985.
2. M. Astarita, F. E. Corcione, M. Costa, A. De Maio, and B. M. Vaglieco. Application of the Shell ignition model and comparison with spectroscopic measurements of a high swirl diesel combustion. In *Proceedings of the ASME Fall Technical Conference*, *ICE*, Vol. 33–3, pp. 27–34, Oct. 1999.
3. M. J. Bergin, R. P. Hessel, and R. D. Reitz. Optimization of a large diesel engine via spin spray combustion. SAE Paper 2005-01-0916, 2005.
4. H. Bockhorn. *Soot Formation in Combustion: Mechanisms and Models*. Springer-Verlag, Berlin, 1994.
5. R. Borghi. Chemical reactions calculations in turbulent flows: application to a co-containing turbojet plume. *Adv. Geophys.*, 18(part II):349–365, 1974.
6. R. Borghi. Turbulent combustion modelling. *Prog. Energy Combust. Sci.*, 14:245–292, 1988.
7. K. N. C. Bray and J. B. Moss. *Acta Astronautica*, 4:291–304, 1977.
8. K. N. C. Bray and N. Peters. Laminar flamelets in turbulent flames. In P. A. Libby and F. A. Williams, editors, *Turbulent Reacting Flows*, Academic, San Diego, 1994, pp. 63–113.
9. R. S. Cant and E. Mastorakos. *An Introduction to Turbulent Reacting Flows*. Imperial College Press, London, 2008.
10. M. Chan, S. Das, and R. D. Reitz. Modeling multiple injection and EGR effects on diesel engine emissions. SAE Paper 972864, 1997.

11. C. Chevalier, P. Loussard, U. C. Müller, and J. Warnatz. A detailed low-temperature reaction mechanism of n-heptane auto-ignition. In *Second International Symposium, COMODIA*, pp. 93–97, Kyoto, Japan, 1990.
12. J. E. Dec. A conceptual model of DI diesel combustion based on laser-sheet imaging. SAE Paper 970873, 1997.
13. J. E. Dec and E. B. Coy. OH radical imaging in a DI diesel engine and the structure of the early diffusion flame. SAE Paper 960831, 1996.
14. B. Dillies, K. Marx, J. Dec, and C. Espey. Diesel engine combustion modeling using the coherent flame model in Kiva II. SAE Paper 930074, 1993.
15. M. Elsden, E. Gutheil, M. Nehse, and J. Warnatz. Auto-ignition modeling in diesel engines. In *Proceedings of the 3rd International ICE Conference*, Capri, Italy, September 1997.
16. C. P. Fenimore. Formation of nitric oxide in premixed hydrocarbon flames. In *Thirteenth Symposium (International) on Combustion*, pp. 373–380, The Combustion Institute, Pittsburgh, 1971.
17. R. O. Fox. *Computational Models for Turbulent Reacting Flows*. Cambridge University Press, Cambridge, 2003.
18. M. Frenklach, H. Wang, and M. J. Rabinowitz. Optimization and analysis of large chemical kinetics mechanisms using the solution mapping method – combustion of methane. *Prog. Energy Combust. Sci.*, 18:47–73, 1992.
19. A. Gill. Modellierung der Verbrennung in einem Schichtlade-Motor unter Verwendung detaillierter chemischer Reaktionsmechanismen. Ph.D. thesis, Universität Stuttgart, 1995.
20. I. Glassman. Combustion, 3rd edn. Academic, San Diego, 1996.
21. A. D. Gosman, F. C. Lockwood, and A. P. Salooja. The prediction of cylindrical furnaces gaseous fueled with premixed and diffusion burners. In *Seventeenth Symposium (International) on Combustion*, pp. 747–760, The Combustion Institute, Pittsburgh, 1979.
22. M. Halstead, L. Kirsh, and C. Quinn. The autoignition of hydrocarbon fuels at high temperatures and pressures – fitting of a mathematical model. *Combust. Flame*, 30:45–60, 1977.
23. J.B. Heywood. *Internal Combustion Engine Fundamentals*. McGraw-Hill, New York, 1988.
24. H. Hiroyasu and T. Kadota. Models for combustion and formation of nitric oxide and soot in direct injection diesel engines. SAE Paper 760129, 1976.
25. J. Inhelder, C. E. Frouzakis, and K. Boulouchos. A discussion of approaches for predicting end–gas autoignition in homogeneous charge engines. LVV Internal Report 93/20, ETHZ, 1993.
26. S.-C. Kong, Z. Han, and R. D. Reitz. The development and application of a diesel ignition and combustion model for multidimensional engine simulation. SAE Paper 950278, 1995.
27. S.-C. Kong and R. D. Reitz. Multidimensional modeling of diesel ignition and combustion using a multistep kinetics model. *J. Eng. Gas Turbines Power*, 115:781–789, 1993.
28. K. K. Kuo. *Principles of Combustion*, 1st edn. Wiley, New York, 1989.
29. P. A. Libby and F. A. Williams. *Turbulent Reacting Flows*. Springer-Verlag, Berlin, 1980.
30. P. A. Libby and F. A. Williams. *Turbulent Reacting Flows*. Academic, San Diego, 1994.
31. B. F. Magnussen and B. H. Hjertager. On mathematical modeling of turbulent combustion with special emphasis on soot formation and combustion. In *Sixteenth Symposium (International) on Combustion*, pp. 719–729, The Combustion Institute, Pittsburgh, 1976.
32. U. C. Müller. Reduzierte Reaktionsmechanismen für die Zündung von n–Heptan und ISO–Oktan unter motorrelevanten Bedingungen. PhD thesis, RWTH, Aachen, 1993.
33. M. P. Musculus and C. J. Rutland. Coherent flamelet modeling of diesel engine combustion. Combust. *Sci. Technol.*, 104:295–337, 1995.
34. J. Nagle and R. F. Strickland-Constable. Oxidation of carbon between 1000–2000 C. In *Proceedings of the Fifth Carbon Conference*, vol. 1, pp. 154. Pergammon Press, 1962.
35. N. Peters. Laminar diffusion flamelet models in non-premixed turbulent combustion. *Prog. Energy Combust. Sci.*, 10:319–339, 1984.
36. N. Peters. Laminar flamelet concepts in turbulent combustion. In *Twenty-First Symposium (International) on Combustion*, pp. 1231–1250, The Combustion Institute, Pittsburgh, 1986.

37. N. Peters. *Turbulent Combustion*. Cambridge University Press, Cambridge, 2000.
38. M. J. Pilling, S. H. Robertson, and P. W. Seakins. Elementary radical reactions and autoignition. *J. Chem. Soc. Faraday Trans.*, 91:4179–4188, 1995.
39. H. Pitsch, H. Barth, and N. Peters. Three-dimensional modeling of NOx and soot formation in DI diesel engines using detailed chemistry based on the interactive flamelet approach. SAE Paper 962057, 1996.
40. H. Pitsch, Y. P. Wan, and N. Peters. Numerical investigation of soot formation and oxidation under diesel engine conditions. SAE Paper 952357, 1995.
41. S. B. Pope. PDF methods for turbulent reactive flows. *Prog. Energy Combust. Sci.*, 11:119–192, 1985.
42. U. Reuter. Kammerversuche zur Strahlausbreitung und Zündung bei dieselmotorischer Einspritzung. Ph.D. thesis, RWTH, Aachen, 1989.
43. D. B. Spalding. In *Thirteenth Symposium (International) on Combustion*, pp. 649–657, The Combustion Institute, Pittsburgh, 1971.
44. G. Stiesch. *Modeling Engine Spray and Combustion Processes*. Springer-Verlag, Berlin, 2003.
45. F. X. Tanner. Validation of an auto-ignition model based on a transport equation of a characteristic ignition progress variable. In *Proceedings of the 15th ILASS-Americas Annual Conference*, pp. 98–102, Madison, May 2002.
46. F. X. Tanner, M. Brunner, and G. Weisser. A computational investigation of water injection strategies for nitric oxide reduction in large-bore DI diesel engines. SAE Paper 2001-01-1069, 2001.
47. F. X. Tanner and R. D. Reitz. The spray-induced flow and its effect on the turbulent characteristic combustion time in DI diesel engines. Atomization Sprays, 12(1–3):187–208, 2002.
48. F. X. Tanner, G. S. Zhu, and R. D. Reitz. A non-equilibrium turbulence dissipation correction and its influence on pollution predictions for DI diesel engines. *J. Eng. Gas Turbines Power*, 125(2):534–540, 2003.
49. F. X. Tanner and S. Srinivasan. Optimization of an asynchronous fuel injection system in diesel engines by means of a micro-genetic algorithm and an adaptive gradient method. SAE Paper 2008-01-0925, 2008.
50. F. X. Tanner and S. Srinivasan. CFD-based optimization of fuel injection strategies in a diesel engine using an adaptive gradient method. *J. Appl. Math. Model.*, 33:1366–1385, 2009.
51. D. Veynante and L. Vervisch. Turbulent combustion modeling. *Prog. Energy Combust. Sci.*, 28:193–266, 2002.
52. J. Warnatz, U. Maas, and Dibble R. W. Combustion: Physical and Chemical Fundamentals, Modeling and Simulation, Experiments, Pollutant Formation, 3rd edn. Springer-Verlag, Berlin, 2001.
53. G. Weisser. Modelling of combustion and nitric oxide formation for medium-speed DI diesel engines: zero and three-dimensional approaches. Ph.D. thesis, Swiss Federal Institute of Technology (ETH), Diss. ETH Nr. 14465, 2001.
54. G. Weisser, F. X. Tanner, and K. Boulouchos. Modeling of ignition and early flame development with respect to large diesel engine simulation. *SAE Trans.: J. Fuels Lubricants*, 107 (4):802–811, 1999.
55. C. K. Westbrook and F. L. Dryer. Simplified reaction mechanisms for the oxidation of hydrocarbon fuels in flames. *Combust. Sci. Technol.*, 27:31–45, 1981.
56. F. A. Williams. *Combustion Theory*, 2nd edn. Addison-Wesley, Redwood City, 1985.
57. Y. B. Zeldovich. The oxidation of nitrogen in combustion and explosions. *Acta Physicochimica, USSR*, 21:577–628, 1946.

Chapter 14
Spray Group Combustion

A. Umemura

Abstract Starting from a consideration of microscopic flame propagation modes between neighboring droplets and macroscopic flame propagation modes in spray elements, the excitation mechanism of group combustion (diffusion flame enclosing droplets) is described for an example of atomizing liquid fuel jet issuing into an otherwise stagnant oxidizing atmosphere.

Keywords Diffusion flame · Droplet evaporation · Droplet interaction · Flame propagation · Group combustion number · Penetration distance

Introduction

Spray combustion takes a distinct combustion feature [1, 2] called group combustion. Figure 14.1 illustrates the steady burner flame structure proposed by Chiu [3, 4] who developed group combustion theory based on continuum theory. Characteristic is the appearance of diffusion flames enclosing a large number of droplets. In this section, the underlying physics of spray group combustion are described in the light of the current understanding of spray combustion.

Since a great number of small liquid droplets are involved in spray combustion, it is impossible to understand the whole detailed structure of spray combustion by tracing every microscopic process associated with each droplet which interacts with its surrounding gas. Only averaged quantities are meaningful from a practical point of view. It is usual to describe spray combustion in the framework of two-phase flow theories. Including the KIVA code used for engineering design purposes, there are several numerical simulation schemes available for analysis [5–7]. The Eulerian description of a reactive gas flow is common in these approaches. The effects of interactions with droplets are incorporated in the source terms of the conservation equations. These source terms are expressed as the droplet-number-density-weighted

A. Umemura
Department of Aerospace Engineering, Nagoya University, Nagoya, Japan
e-mail: akira@prop.nuae.nagoya-u.ac.jp

N. Ashgriz (ed.), *Handbook of Atomization and Sprays*,
DOI 10.1007/978-1-4419-7264-4_14, © Springer Science+Business Media, LLC 2011

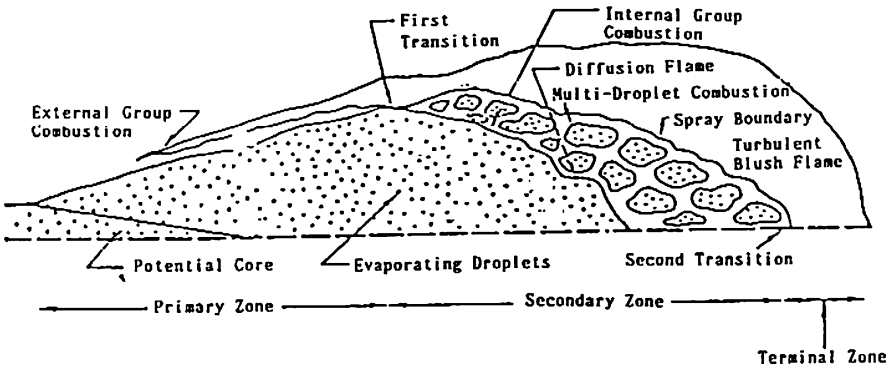


Fig. 14.1 Spray group flame structure [3] (Courtesy of AIAA 2010)

superposition of individual droplet contributions, which are derived from the single droplet vaporization characteristics by identifying the ambient gas state of the single droplet vaporization problem as the local gas-phase state in a continuum medium coexisting with the droplets. Since chemical reactions take place in the gas phase, the gas-phase governing equations are especially important for adequately describing the spray combustion. Using the same single-droplet vaporization characteristics as used in the gas-phase governing equations, the spray equations, which govern the movement, evaporation, and heating of each droplet or droplet ensemble, are formulated by regarding a spray as either a coexisting continuum medium in the Eulerian description or particle points treated in a Lagrangian scheme.

These approaches are especially useful for dilute sprays consisting of very small or volatile droplets, because the region where droplet evaporation occurs can be completely separated from the region where chemical reactions take place. In fact, if the evaporation time of every droplet is very short compared to the characteristic flame time, obtained by dividing the flame thickness $\delta_f = D/S_L$ (including preheating zone) by the burning speed of the gaseous reaction S_L, then the droplets can evaporate completely before they reach the reaction zone where purely gaseous combustion occurs. The combustion of such a spray is similar to that of a reacting gas, except that the reaction zone may be deformed by local variations of the equivalence ratio due to dispersed vaporizing droplets. A numerical simulation under this limiting case is conducted by Reveillon and Vervisch [8] to explore the features strongly influenced by fluid dynamics. However, we do not consider such a case any more in detail, because we are interested in much denser sprays.

One-dimensional Flame Propagation Problem

The most important characteristic quantity of combustion is burning speed. Following methodologies developed for gaseous combustion, burning speed in a spray has been measured and analyzed for a uniform spray produced from a supercooled

vapor in a bomb [9], evaporation tube [10], spray jet [11], and counterflow set-up [12]. Figure 14.2 shows two photos of flame fronts propagating in a spray in microgravity experiments. We consider a spray element, which is much smaller than the radius of curvature of a macroscopic flame front but much larger than the constituent droplets. Flame propagation into such a spray element can be theoretically treated as a one-dimensional problem of a macroscopic planar flame with an irregular microscopic structure propagating through an infinite-extent of uniform air-fuel spray with prescribed properties [13]. The purpose of this approach is to characterize both the burning speed and flame structure in terms of the prescribed spray properties. However, the burning speed has not been satisfactorily characterized, because the measured values include the effects of volumetric expansion by evaporated fuel and turbulence, which vary depending on the flow configuration. Therefore, in the following, we focus on the topological aspect under a strong assumption that the droplets and gas have no velocity difference, for simplicity. Recent advances in the direct numerical simulation approach will reveal the details in more realistic situations in future studies.

Figure 14.3 illustrates microscopic flame propagation [14], showing the possible modes of flame propagation between neighboring droplets in a plot of local

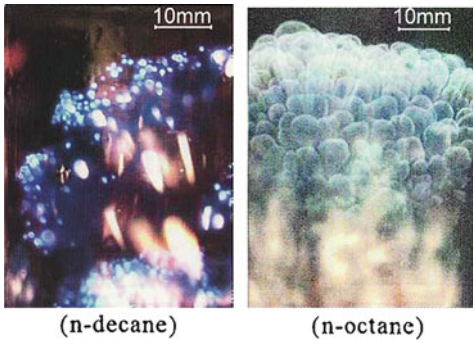


Fig. 14.2 Photos of flame fronts propagating in a spray in microgravity [10] (Courtesy of Elsevier 2010)

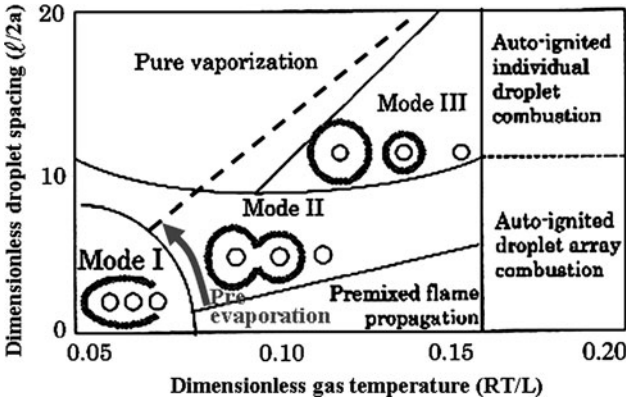


Fig. 14.3 Interdroplet flame propagation model map [14] (Courtesy of Elsevier)

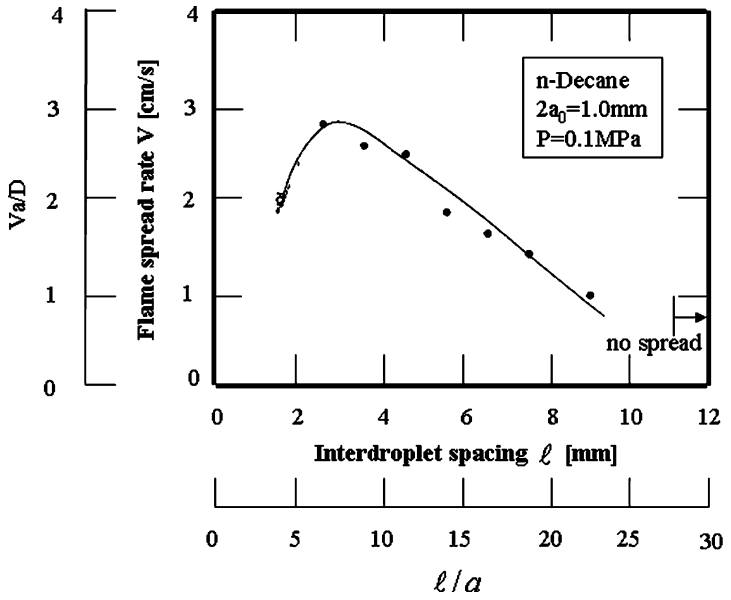


Fig. 14.4 Dependence of interdroplet flow propagation speed on interdroplet spacing, measured in microgravity experiments for a linear array of n-decane droplets in standard atmosphere [15] (Courtesy of JSME 2010)

surrounding gas temperature and interdroplet spacing. The map is made, assuming that the gas surrounding each droplet initially has the same composition as the air at different temperatures. Therefore, the presence of pre-evaporated fuel vapor in the surrounding gas will shift each boundary line upward in the figure. It has been found from linear droplet array experiments [15, 16] that the flame propagation speed maximizes at a certain interdroplet spacing at each gas temperature (see Fig. 14.4). At small interdroplet spacings, the flame spreading speed is reduced by the cooling effect of droplets.

Premixed Flame Propagation

When a microscopic flammable gas mixture formed between neighboring droplets is connected throughout the spray element, a premixed flame can propagate along this corridor and consume oxygen contained in the spray element. It should be noted that the flame propagation, which can be described by the conventional two-phase flow theories is restricted to this case.

In Fig. 14.3, the upper boundary of the premixed flame propagation mode corresponds to the point where fuel vapor concentration becomes equal to the lower flammability limit at the mid-point between neighboring droplets. Since

the heat capacity of a droplet is large, the droplet temperature slowly increases towards a wet-bulb or saturation temperature. Therefore, even if an initially cold droplet is exposed to a high-temperature gas, it will have a small surface fuel vapor concentration and evaporation rate, implying that the Stefan flow effect is negligible. As the droplet temperature rises, the Stefan flow moves fuel vapor far away from the droplet surface. The two upper boundaries (the solid line and broken line in the figure) of the premixed flame propagation mode are derived using the single-droplet evaporation solution without and with the Stefan flow effect, respectively. The transition from the solid line to the broken line expresses the effect of pre-evaporation [17]. Correspondingly, the spray number density range for which the conventional numerical simulation scheme can be applied is enlarged. Borghi's diagram [18] classifies possible submodes caused by a premixed flame front in terms of the ratios of the droplet evaporation time to the characteristic flame time and of interdroplet spacing to flame thickness.

Interdroplet Flame Propagation Caused by Diffusion Flame Expansion

When evaporation of liquid fuel before atomization is negligible, the fuel vapor concentration at mid-points between neighboring droplets initially takes such a small value that continuum theory does not allow a premixed flame to propagate in the spray element. However, even in this case, it is possible that a microscopic spherical layer of flammable gas mixture surrounds each droplet. Therefore, once a part of the flammable layer is somehow ignited, a microscopic premixed flame propagates around the droplet surface and eventually results in a spherical diffusion flame enclosing the droplet. Then, the diffusion flame enhances evaporation of the burning droplet and expands its size. At the same time, the outward heat flux from the diffusion flame heats the neighboring droplets and their surrounding gas. Thus, it is possible that the nearest droplet is ignited by the expanding diffusion flame. Three types of such interdroplet flame propagations can be distinguished, as illustrated in Fig. 14.3.

Mode I is excited when the expanding diffusion flame can swallow at least the nearest neighboring droplet. This type of interdroplet flame propagation takes place for relatively low gas temperature and small interdroplet spacing.

For larger interdroplet spacings, for which the expanding diffusion flame of an ignited droplet no longer reaches any neighboring droplets, we can consider two cases: (1) the diffusion flame reaches the flammable gas mixture of a neighboring droplet, resulting in an enclosed diffusion flame (Mode II) and (2) the diffusion flame cannot reach the flammable gas mixture of a neighboring droplet but the heat flux from the diffusion flux ignites the flammable gas mixture, resulting in separate diffusion flames or later a merged diffusion flame (Mode III).

Since the rules of these interdroplet flame propagations can be easily formulated into a simple algorithm, the sequence of interdroplet flame propagation in a spray

element can be simulated on computer for randomly distributed droplets [14]. Applying percolation theory to an ensemble of spray elements, the characteristic properties of interdroplet flame propagation have been examined, showing that the tip of the diffusion flame propagates by selecting the fastest propagating route and forms a larger merged diffusion flame, which encloses a cluster of droplets depending on the droplet distribution. Then, the expansion of the large merged diffusion flame can ignite a droplet belonging to another distant cluster. Therefore, the average interdroplet spacing for which a diffusion flame can spread through the spray element becomes larger than that predicted in Fig. 14.4.

In any case, after the passage of a premixed/diffusion flame, droplet evaporation is enhanced because droplets are exposed to a high-temperature burnt gas. Thus, the spray element behind the propagating flame becomes a source of fuel vapor.

Spray Combustion Structure

Since each element of a real spray changes its state with time or along its path line, the possible mode of flame penetration into the spray element changes depending on when a part of the spray element boundary is ignited. Combining the temporal change of the spray element state and the possible flame penetration mode, we can determine the structure of the spray combustion. In this section, we consider the temporal evolution of the spray element.

Specification of Initial Spray Element State

The characteristics of a spray depend on the atomization process. The state of each spray element is characterized by its statistical quantities such as droplet number density and radial distribution function, which generally vary both spatially and temporally. We may consider that each spray element (corresponding to the physically infinitesimal volume when the spray is described in the framework of continuum theory) consists of statistically uniformly distributed identical droplets with number density n_0 and droplet radius a_0 in a gas of uniform state (density ρ_0, oxygen concentration $Y_{o,0}$, and temperature T_0 in particular) at an initial time. We assume that the evaporation before atomization is negligible. Then, we have the following expression

$$\left(\frac{a_0}{\ell_0}\right)^3 = \frac{3}{4\pi}\phi_0\frac{\rho_0}{\rho_*}Y_{o,0}\frac{W_o\nu_o}{W_F\nu_F} \tag{14.1}$$

where ϕ_0 denotes the overall equivalence ratio of a spray element, ρ_* is the liquid fuel density, W_i is the molecular weight of chemical species i, and ν_i is the

stoichiometric coefficient. As a simple spray element model, we consider a cubic lattice on which identical droplets of radius a_0 are located regularly at a separation of $\ell_0 = n_0^{-1/3}$.

Evolution of Spray Element State Before Combustion

Each droplet of an initial spray element interacts with its surrounding gas and evaporates. Since the total surface area of the liquid is extremely enlarged through the atomization process, the effect of droplet evaporation is significant. This droplet evaporation proceeds independent of the external gas condition until the influence of the external gas reaches the spray element under consideration. When the state change between neighboring spray elements is small (this condition is required so that the gas phase of the spray might be described in terms of conventional continuity theory), the presence of relative velocities between droplets and the gas only contributes to an enhanced droplet evaporation rate and gaseous mixing (if unknown complexities caused by fluctuating motions of droplets are neglected). Therefore, the occupation space assigned to each droplet tends to expand isotropically due to droplet evaporation because the density ratio of liquid to gas is very large. An estimation of the velocity at which the boundary of a typical spray expands due to internal droplet evaporation shows that this expanding velocity is usually much smaller than the sound velocity. This implies that the expansion of each droplet occupation space takes place isobarically. Therefore, the interdroplet spacing ℓ increases according to

$$\frac{\ell}{a} = \frac{a_0}{a}\left[\frac{4\pi}{3}\left(1 - \left(\frac{a}{a_0}\right)^3\right)\left(\frac{\rho_*}{\rho} - 1\right) + \left(\frac{\ell_0}{a_0}\right)^3\right]^{\frac{1}{3}} \tag{14.2}$$

where a denotes the radius of a droplet reduced by evaporation. If we assume for simplicity that the evaporated vapor is uniformly distributed over the gas phase of the droplet occupation space (see Fig. 14.5), the gas-phase equivalence ratio ϕ of spray element is expressed as

$$\phi = \frac{1 - (a/a_0)^3}{(3/4\pi)(\ell/a_0)^3 - 1}\frac{W_\mathrm{o}\nu_\mathrm{o}}{W_\mathrm{F}\nu_\mathrm{F}}\frac{\rho_*}{\rho Y_{\mathrm{o},0}} \tag{14.3}$$

Figure 14.6 shows the variation of ℓ/a and ϕ against a/a_0 for given values of ℓ_0/a_0. *n*-Decane is adopted as a fuel. The gaseous mixture becomes flammable at the grey zone for which premixed flame propagation is possible. It is found from this figure that interdroplet flame propagation may occur only at an early stage of droplet evaporation. Note that there exists a lower limit of droplet radius, which depends on the initial gas temperature, because droplet evaporation stops when the droplet occupation space reaches a saturation state [19].

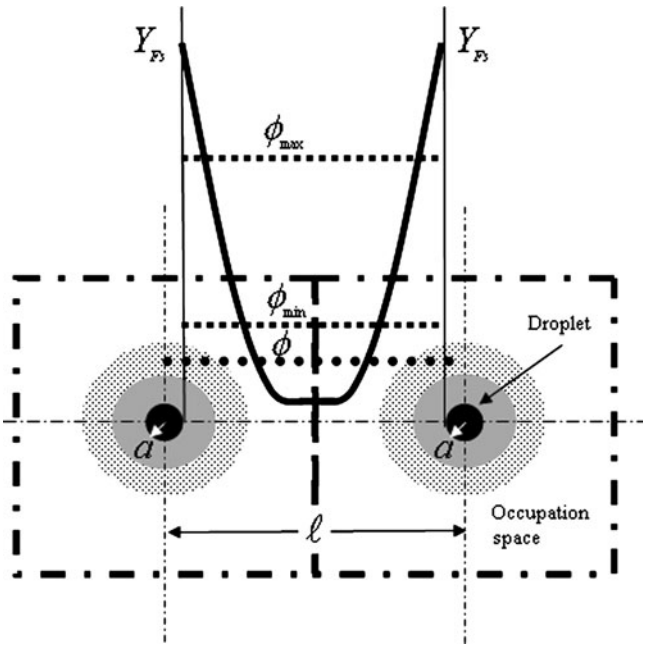


Fig. 14.5 Fuel vapor concentration distribution between neighboring droplets

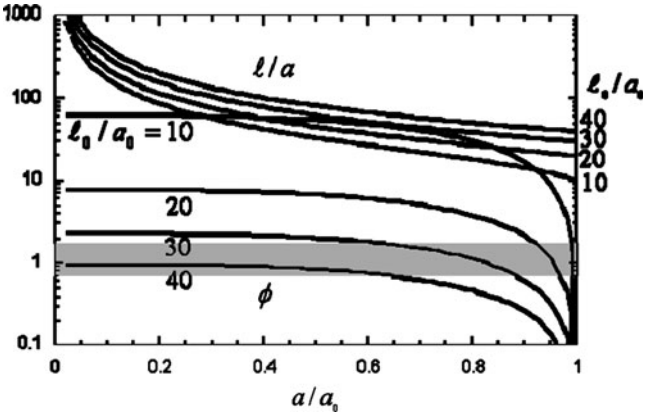


Fig. 14.6 Change of interdroplet spacing and gas phase equivalence ratio

Flames Developing from Flame Holding Location

From which part of a spray stream combustion starts, or in what state a spray element is at the flame holding location depends on the atomizer and combustor used. We consider the combustion of a spray stream issuing from a pre-evaporation tube into an otherwise quiescent oxidizing gas. In this system, the state of a spray

element (L/a, ϕ; T) at the outlet of the pre-evaporation tube is arbitrarily adjustable by changing the pre-evaporation tube length. Also, the formation of vortices attached to the tube rim can anchor the flame tip.

With reference to the arguments of flame penetrating into a spray discussed above, the type of inner flame extending from the flame holding location can be classified as shown in Fig. 14.7. A monodispersed spray issued at a uniform speed is considered for simplicity. Each macroscopic flame tends to propagate normal to the spray stream. A difference from the one-dimensional flame propagation problem

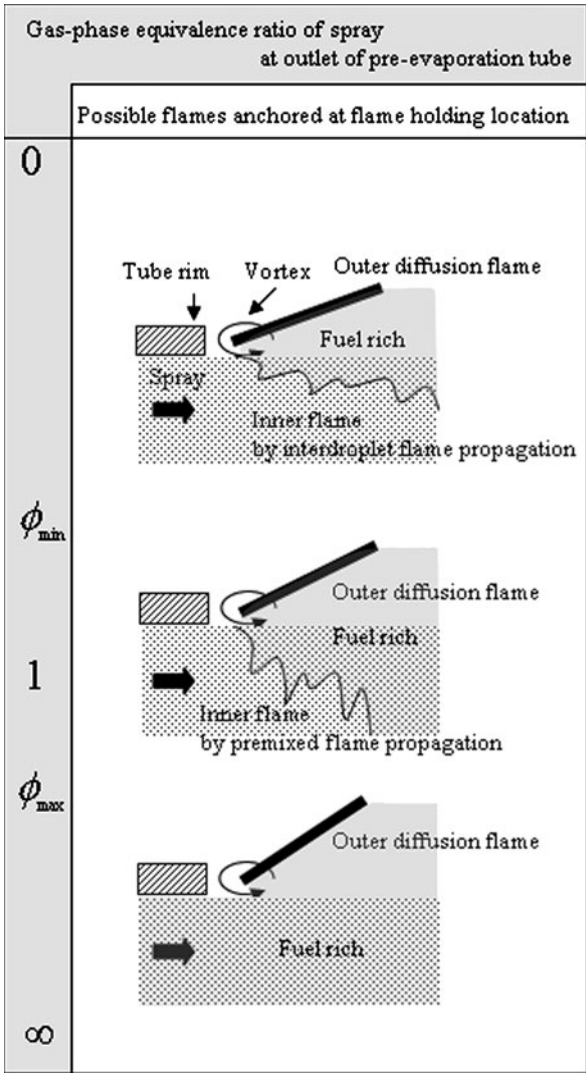


Fig. 14.7 Classification of inner flame for a dense spray stream

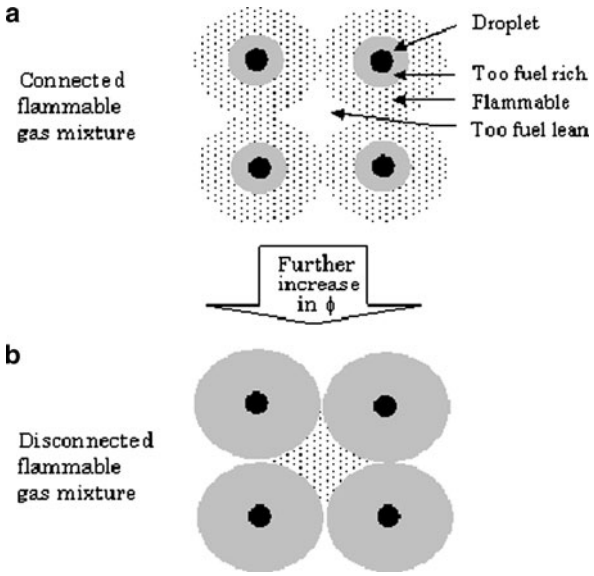


Fig. 14.8 Topological change of flammable gas mixture region

mentioned in Fig.14.2 is that, besides the inward-propagating flame which constitutes the inner flame at an angle to the spray stream, there exists a diffusion flame outside the spray stream. At the diffusion flame, which also extends from the flame holding location, the fuel vapor supplied from droplets whose evaporation is enhanced by the passage of the inner flame reacts with the outer oxidizing gas. The type of inner flame that is realized depends on the state of the spray at the outlet of the pre-evaporation tube.

Under the condition of $\phi < \phi_{\min}$, the only possible inner flame is due to interdroplet flame propagation for sprays with ℓ smaller than a certain value. The angle of this inner flame to the spray stream is a small value. No flame can be held near the pre-evaporation tube rim for larger interdroplet spacing. As the gas-phase equivalence ratio is increased, the inner flame angle increases to the maximum value in the regime of premixed flame propagation, or Mode II. A further increase in gas-phase equivalence ratio beyond a certain value less than $\phi_{\max}$ causes the blowoff of the inner flame because, as illustrated in Fig. 14.8, the flammable region between droplets becomes disconnected in the microscopic picture. Therefore, only the outer diffusion flame remains.

Behavior of Outer Diffusion Flame

The previously mentioned droplet evaporation effect and inner flame development are caused by the presence of heat and oxygen in the gas phase of a spray stream.

This implies that the spray tends to approach a saturation state unless additional heat and oxygen are supplied from the outside of the spray stream. It also implies that the behavior of the outer diffusion flame dominates the subsequent evolution of spray combustion from the spray boundary side. In real spray combustion, this boundary-layer type of change occurs dynamically because the boundary of the spray stream is located in the coherent vertical structure of the shear layer. In addition, turbulent effects are inevitable. However, such fluid dynamic effects have not yet been well characterized. Therefore, we focus on the behavior of the outer diffusion flame based on a quasi-steady continuum spray model. Chiu's theory is developed on this basis to classify the combustion modes excited by the penetration of the outer diffusion flame into the spray region.

In the steady combustion of a high-speed spray stream depicted in Fig. 14.1, the axial change of the spray state is gradual compared to the radial change. Neglecting the influence of the outer flame on the geometrical characteristics ($\ell = n^{-1/3}$and a) of the internal spray, the radial transport of heat and mass within the spray stream may be described by the Helmholtz type of equation

$$\frac{d^2\beta}{dy^2} - 4\pi na\beta = 0 \tag{14.4}$$

for an appropriately chosen coupling function β such as

$$\beta_{\mathrm{F}} = (Y_{\mathrm{F}} - Y_{\mathrm{F}\infty}) - \left(\frac{W_{\mathrm{F}}\nu_{\mathrm{F}}}{W_{\mathrm{o}}\nu_{\mathrm{o}}}\right)(Y_{\mathrm{o}} - Y_{\mathrm{o}\infty}) \tag{14.5a}$$

or

$$\beta_{\mathrm{T}} = \frac{\left\{c_{\mathrm{p}}(T - T_\infty) + H(W_{\mathrm{F}}\nu_{\mathrm{F}}/W_{\mathrm{o}}\nu_{\mathrm{o}})(Y_{\mathrm{o}} - Y_{\mathrm{o},\infty})\right\}}{L}, \tag{14.5b}$$

where y denotes the inward normal distance from the spray boundary and the subscript ∞ refers to the internal spray state, which is not influenced by the outer flame. For example, heat conducted from the outer flame is absorbed by droplet evaporation according to (14.4) with $\beta = \beta_{\mathrm{T}}$. The solution of (14.4), which decays at a distance y from the spray boundary, is given by

$$\beta = \beta_0 \exp\left(-\sqrt{4\pi na}y\right) \tag{14.6}$$

which defines the shielding length or penetration length as

$$L_{\mathrm{s}} = \frac{1}{\sqrt{4\pi an}} \tag{14.7}$$

The effect of the outer diffusion flame can effectively penetrate only within this distance. In the inner region beyond this distance, the spray state is independent of the outer gas condition and develops as described in the previous sections. Note that the penetration length is determined by the geometrical quantities which characterize the droplet occupation space. This property is attributed to the quasi-steady analysis.

The ratio of penetration length L_s to spray radius R expresses how deep the influence of the outer diffusion flame can penetrate into the spray region by diffusion. It is equal to the inverse of the square root of the group combustion number $G = 4\pi anR^2$ introduced by Chiu, i.e.,

$$\frac{R}{L_s} = R\sqrt{4\pi an} = \sqrt{G} \tag{14.8}$$

According to Chiu's theory, the group combustion modes which are excited downstream of the flame holding location are classified in terms of the magnitude of G on the plots of total droplet number $N = (R/\ell)^3$ against droplet spacing ℓ/a as shown in Fig. 14.9. The boundary values of G were derived from the analysis of quasi-steady combustion of spherical droplet clouds, but it is believed to be applicable to other cases as well. In the problem under consideration, the penetration length increases from a small value to a large value along the spray stream because the droplet spacing increases downstream. As a result, the combustion mode changes from external sheath combustion to external group combustion, internal group combustion, and individual droplet combustion in turn. This explains the group combustion feature depicted in Fig. 14.1. The following is the physical explanation of these mode changes.

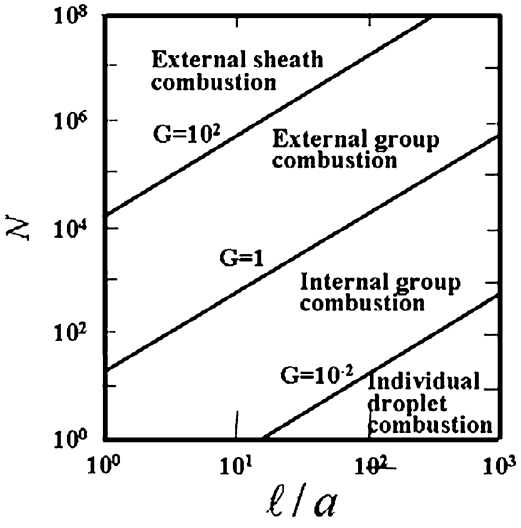


Fig. 14.9 Group combustion modes [21] (Courtesy of Elsevier 2010)

If the issued spray is very dense, then the penetration length (comparable to the interdroplet spacing) is much smaller than the spray radius ($G > 10^2$). Receiving heat flux from the outer diffusion flame, droplets located near the spray boundary evaporate intensively and supply fuel vapor. Therefore, the diffusion flame initially moves outward from the spray boundary and then moves inward as the boundary droplets evaporate completely (a reduction of the spray radius R). Sickel [20] treated the thin layer of enhanced droplet evaporation as a singular vaporization wave ahead of which the spray is in a saturation state. If the speed of the inward moving vaporization wave exceeds the inward propagating speed of the inner flame, the inner flame merges with the outer diffusion flame downstream. Such a phenomenon will occur when the inner flame is due to interdroplet flame propagation.

As the interdroplet spacing increases, the penetration distance reaches a value comparable to the spray radius at a certain distance downstream of the flame holding station ($G = 1$). Then, oxygen can reach the center line of the spray steam, provided that the geometrical characteristics of the internal spray are unchanged. Therefore, for $1 < G < 10^2$, the boundary droplets whose evaporation is enhanced by the outer flame have larger interdroplet spacings and smaller droplet radii. As a result, the outer diffusion flame front penetrates into the spray region, and behind it there remain separate diffusion flames enclosing clusters of droplets due to fluctuations of droplet number density and other factors. This combustion mode is external group combustion.

When the group combustion number exceeds unity due to a reduction of the spray radius, the influence of the outer diffusion flame on the opposite side overlaps near the center line of the spray stream. Thus, the diffusion flame front rapidly approaches the center line and burning of clustered droplets occurs near the center line as well (internal group combustion).

It is important to note that similar arguments can be made for the burning of clustered droplets by replacing the spray size by the cluster size and modifying the ambient oxygen concentration, as experimentally documented by Akamatsu et al. [21]. Enhanced droplet evaporation due to envelope diffusion flames decreases the droplet radius significantly. Since the evaporation rate of a small droplet is small, the interdroplet spacing is almost unchanged. Therefore, further reduction of the droplet radius causes the envelope diffusion flames to move close to the small droplet surfaces, leading to the individual combustion mode [22].

Summarizing, enlarged interdroplet spacing and reduced droplet radius by evaporation and a reduction of droplet ensemble size cause the envelop diffusion flame to penetrate into the droplet ensemble. This is the basic concept of Chiu's theory and has much in common with the diffusion flame behaviors observed in the combustion of a single droplet and a finite number droplet ensemble immersed in an infinite oxidizing gas. For this reason, many investigations [23–25] have been made on various finite systems to gain deeper insights into the detailed droplet interaction effects involved in the group combustion of spray. The next challenge is to develop a numerical simulation scheme incorporating the droplet interaction effects as well as various fluid dynamic contributions in order to describe the dynamic features of spray combustion.

References

1. C.G. McCreath, N.A. Chigier: Liquid-spray burning in the wake of a stabilizer disc, Fourteenth symposium (international) on combustion, The Combustion Institute, Pittsburgh, 1973, pp. 1355–1363.
2. Y. Onuma, M. Ogasawara, T. Inoue: Further experiments on the structure of a spray combustion flame, Sixteenth symposium (international) on combustion, The Combustion Institute, Pittsburgh, 1976, pp.561–567.
3. H.H. Chiu, R.K. Ahluwalia, B. Koh, E.J. Croke: Spray group combustion, AIAA 16th aerospace science meeting, Paper No. 78-75, 1978.
4. H.H. Chiu, T.M. Liu: Group combustion of liquid droplets, Combust. Sci. Technol., 17, 127–142 (1971).
5. W.A. Sirignano: Fuel droplet vaporization and spray combustion theory, Proc. Energy Combust. Sci., 9, 291–322 (1983).
6. R. Miller, J. Bellan: Direct numerical simulation of a confined three-dimensional gas mixing layer with one evaporating hydrocarbon-droplet-laden stream, J. Fluid Mech., 384, 293–338 (1999).
7. H. Watanabe, R. Kurose, S.-M. Hwang, F. Akamatsu: Characteristics of flamelets in spray flames formed in a laminar counterflow, Combust. Flame, 148, 234–248 (2007).
8. J. Reveillon, L. Vervisch: Analysis of weakly turbulent dilute-spray flames and spray combustion regimes, J. Fluid Mech., 537, 317–347 (2005).
9. H. Nomura, M. Koyama, H. Miyamoto, Y. Ujiie, J. Sato, M. Kono, S. Yoda: Experiments of flame propagation in ethanol droplet-vapor-air mixture, Proc. Combust. Inst., 28, 999–1005 (2000).
10. Y. Nunome, S. Kato, K. Maruta, H. Kobayashi, T. Niioka: Flame propagation of n-decane spray in microgravity, Proc. Combust. Inst., 29, 2621–2626 (2002).
11. K. Nakabe, Y. Mizutani, T. Hirano, S. Tanimura: Burning characteristics of premixed sprays and gas-liquid coburning mixtures, Combust. Flame, 74, 39–51 (1988).
12. J.B. Greenberg, N. Sarig: An analysis of multiple flames in counterflow spray combustion, Combust. Flame, 104, 431–459 (1996).
13. F.A. Williams: Combustion theory (2nd edn.), Addison-Wesley, Reading, MA (1995), p. 446.
14. A. Umemura, S. Takamori: Percolation theory for flame propagation in non-or less-volatile fuel spray: a conceptual analysis to group combustion excitation mechanism, Combust. Flame, 141, 336–349 (2005).
15. S. Kato, H. Mizuno, H. Kobayashi, T. Niioka: Experiments on flame spread of fuel. droplet array in a high-pressure ambience, JSME Int. J., B41, 322–330 (1998).
16. M. Kikuchi, T. Arai, S. Yoda, A. Umemura, M. Uchida, M. Kakei, T. Niioka: Numerical study on flame propagation on a fuel droplet array in a high-temperature environment under microgravity, Proc. Combust. Inst., 29, 2611–2619 (2002).
17. M. Mikami, H. Oyagi, N. Kojima, Y. Wakashima, M. Kikuchi, S. Yoda: Microgravity. Experiments on flame spread along fuel-droplet arrays at high temperatures, Combust. Flame, 146, 391–406 (2006).
18. . R. Borghi: Background on droplets and sprays, In Combustion and Turbulence in Two-Phase Flows, Lecture series 1996–02, Von Karman Institute for Fluid Dyanamics.
19. J. Bellan, K. Harstad: Analysis of the convective evaporation of non-dilute clusters of drops, Int. J. Heat Mass Transfer, 30, 125–136 (1987).
20. S.M. Correa, M. Sichel: The group combustion of a spherical cloud of monodisperse fuel droplets, Nineteenth symposium (international) on combustion, The Combustion Institute, Pittsburgh (1982), pp. 981–991.
21. F. Akamatsu, Y. Mizutani, M. Katsuki, S. Tsushima, Y.D. Cho: Measurement of local group combustion number of droplet clusters in a premixed spray stream, Proc. Combust. Inst., 26, 1723–1729 (1996).

22. G. Chen, A. Gomez: Dilute laminar spray diffusion flames near the transition from group combustion to individual droplet burning, Combust. Flame, 110, 392–404 (1997).
23. M. Labowsky, D.E. Rosner: Group combustion of droplets in fuel. Clouds, I. Quasi-steady predictions, in Evaporation-Combustion of Fuels (J.T. Zung, Ed.) American Chemical Society (1978), pp. 63–79.
24. K. Annamalai, W. Ryan: Interactive processes in gasification and combustion, i: liquid. drop arrays streams and clouds, Proc. Energy Combust. Sci., 18, 221–295 (1992).
25. A. Umemura: Interactive droplet vaporization and combustion: approach from asymptotics, Proc. Energy Combust. Sci., 20, 325–372 (1994).

Chapter 15
Droplet Evaporation in the Non-continuum Regime

E.J. Davis

Abstract At low pressures, the evaporation rate of a droplet is not adequately described by the equations of continuum mechanics, that is, by mass diffusion and conduction heat transfer. When the mean free path of the evaporated molecules is large compared with the droplet radius, the kinetic theory of gases can be applied to determine the evaporation rate. In this limit, the free-molecule regime, it is assumed that the molecules have a Maxwell-Boltzmann distribution of molecular velocities. In the intermediate regime, the Knudsen regime, molecular collisions distort the Maxwell-Boltzmann distribution and reduce the rate of transport of the molecules leaving and arriving at the droplet surface. This chapter reviews the theory and measurements of droplet evaporation in the free-molecule and Knudsen regimes.

Keywords Accommodation coefficients · Condensation · Evaporation · Free-molecule regime · Gas phase transport · Knudsen regime · Non-continnum regime

Introduction

At atmospheric pressure and higher pressures, the rate of droplet evaporation is usually governed by the rate of diffusion of the evaporating species i in the surrounding carrier gas j, and the heat and mass transport equations of continuum mechanics apply. For quasi-steady isothermal evaporation in a stagnant gas, the well-known Maxwell [1] formula has been extensively used, that is,

$$j_{\text{cont}} = \frac{D_{\text{ij}}}{a} m_{\text{i}} (n_{\text{s}} - n_{\infty}), \tag{15.1}$$

E.J. Davis
Department of Chemical Engineering, Box 351750, University of Washington, Seattle, WA 98195-1750, USA
e-mail: davis@cheme.washington.edu

N. Ashgriz (ed.), *Handbook of Atomization and Sprays*,
DOI 10.1007/978-1-4419-7264-4_15, © Springer Science+Business Media, LLC 2011

in which j_{cont} is the mass flux, D_{ij} is the gas phase diffusion coefficient, a is the droplet radius, m_i is the mass of a molecule of species i, and n_s and n_∞ are the number densities of molecules at the gas/liquid interface and far from that interface, respectively. The number densities may be written in the form

$$n_s = \frac{p^o(T_s)}{kT_s} \quad \text{and} \quad n_o = \frac{p(T_\infty)}{kT_\infty}, \tag{15.2}$$

where $p^o(T_s)$ is the vapor pressure at interfacial temperature T_s, k is Boltzmann's constant, and $p(T_\infty)$ is the partial pressure of the evaporating component in the bulk carrier gas. If the evaporation rate is sufficiently slow, $T_s \simeq T_\infty$, but for highly volatile species the interfacial temperature is reduced. In this case, it is necessary to introduce heat conduction equations for the liquid and gas phases and solve the coupled system of heat and mass transfer equations to obtain the evaporation rate. Davis and Schweiger [2] discussed this procedure in their monograph, and Taflin et al. [3] presented data and analysis for the nonisothermal evaporation of water droplets.

For quasi-steady heat transfer from the gas phase to the droplet surface the heat flux for the continuum regime is given by

$$q_{cont} = -\frac{\kappa}{a}(T_\infty - T_s), \tag{15.3}$$

where κ is the gas thermal conductivity. As discussed by Taflin et al., higher order quasi-steady state solutions for the mass flux and heat flux introduce correction factors in (15.1) and (15.3) taking into account complicating factors of Stefan flow (convective flow associated with vapor transport from the surface to the gas), thermal diffusion, and the energy of the diffusing species; but, for many systems, these correction factors are nearly unity. They will be neglected here.

If the energy required for droplet evaporation is provided by heat conduction from the gas phase, the heat and mass fluxes are coupled because the vapor pressure is a strong function of the interfacial temperature, and the flux equations must satisfy the energy balance,

$$q = \lambda_{vap}\, j_i, \tag{15.4}$$

in which λ_{vap} is the heat of vaporization.

The droplet mass change for a constant density droplet is related to the mass flux of the evaporating species by

$$j_i = -\frac{1}{4\pi a^2}\frac{dm}{dt} = -\rho\frac{da}{dt}, \tag{15.5}$$

where m is the droplet mass, and ρ is its density.

Continuum theory is applicable when the mean free path, ℓ, of the diffusing species is small compared to the droplet radius, that is, when the Knudsen number, Kn, is sufficiently small ($Kn \ll 1$). The Knudsen number is defined by

$$Kn = \frac{\ell}{a}. \tag{15.6}$$

As discussed below, several definitions of the mean free path appear in the literature, so some care should be taken in interpreting the results of various authors.

In the limit of large Knudsen number ($Kn \gg 1$) the kinetic theory of gases is applied to determine the molecular flux. This is the free-molecule regime.

The Free-molecule Regime

For a Maxwell-Boltzmann distribution of molecular velocities, the number of molecules of species i crossing a unit area per unit time is

$$N_\mathrm{i} = \frac{n_\mathrm{i}\bar{c}_\mathrm{i}}{4}, \tag{15.7}$$

where n_i is the number density of molecules of species i, and $\bar{c}_\mathrm{i}$ is the mean molecular speed given by

$$\bar{c}_\mathrm{i} = \sqrt{\frac{8kT}{\pi m_\mathrm{i}}}. \tag{15.8}$$

The mass flux of molecules emerging from a surface, assuming the surface acts as a reservoir of an equilibrium gas at surface temperature T_s, is given by

$$j_\mathrm{i}^{(\mathrm{e})} = \frac{m_\mathrm{i}\bar{c}_{\mathrm{i,s}}}{4} n_\mathrm{s}, \tag{15.9}$$

where $\bar{c}_{\mathrm{i,s}}$ is the mean molecular speed at surface temperature T_s. This result is often multiplied by a factor ε, the evaporation coefficient, to account for deviations from the equilibrium gas velocity distribution. Similarly, the mass flux of molecules impinging on the surface, in the absence of bulk flow, is

$$j_\mathrm{i}^{(\mathrm{i})} = \frac{m_\mathrm{i}\bar{c}_{\mathrm{i},\infty}}{4} n_\infty, \tag{15.10}$$

in which $\bar{c}_{\mathrm{i,s}}$ is the mean molecular speed at bulk temperature T_∞. This result is often multiplied by a factor α_m, the mass accommodation coefficient

(or condensation coefficient), to take into account molecular reflections from the surface, that is, failure to accommodate to the surface. Thus, in the free-molecule regime, the net mass flux of molecules between a droplet surface and the surroundings is given by the Hertz-Knudsen equation,

$$j_{\mathrm{fm}} = j_{\mathrm{i}}^{(\mathrm{e})} - j_{\mathrm{i}}^{(\mathrm{i})} = \frac{m_{\mathrm{i}}}{4}\left(\varepsilon \bar{c}_{\mathrm{i,s}} n_{\mathrm{s}} - \alpha_m \bar{c}_{\mathrm{i},\infty} n_\infty\right); \quad \frac{m_{\mathrm{i}}\alpha_m}{4}\bar{c}_{\mathrm{i},\infty}(n_{\mathrm{s}} - n_\infty), \tag{15.11}$$

where it is assumed that $\varepsilon = \alpha_{\mathrm{m}}$ since the emerging flux must equal the impinging flux at equilibrium.

For a mass accommodation coefficient of unity, the mass flux ratio $j_{\mathrm{cont}}/j_{\mathrm{fm}}$, which appears in some theoretical analysis, is

$$\frac{j_{\mathrm{cont}}}{j_{\mathrm{fm}}} = \frac{4D_{\mathrm{ij}}}{a\bar{c}_{\mathrm{i}}}. \tag{15.12}$$

For a dilute vapor/gas mixture ($n_{\mathrm{i}}/n_{\mathrm{j}} \ll 1$) the heat flux is given by

$$q_{\mathrm{fm}} = \frac{\kappa_{\mathrm{j}}\alpha_{\mathrm{th}}}{2}\left(\bar{c}_{\mathrm{j,s}} n_{\mathrm{j,s}} T_{\mathrm{s}} - \bar{c}_{\mathrm{j},\infty} n_{\mathrm{j},\infty} T_\infty\right); \quad \frac{\kappa_{\mathrm{j}}\alpha_{\mathrm{th}}}{2}\bar{c}_{\mathrm{j},\infty} n_{\mathrm{j},\infty}(T_{\mathrm{s}} - T_\infty), \tag{15.13}$$

where α_{th} is the thermal accommodation coefficient, and κ_{j} is the thermal conductivity of the gas.

For a thermal accommodation coefficient of unity, the heat flux ratio $q_{\mathrm{cont}}/q_{\mathrm{fm}}$ is given by

$$\frac{q_{\mathrm{cont}}}{q_{\mathrm{fm}}} = \frac{2\kappa_{\mathrm{j}}}{akn_\infty \bar{c}_{\mathrm{j}}}. \tag{15.14}$$

As indicated in a review by Davis [4], accommodation coefficients and evaporation coefficients are usually determined from experimental data, but a limited amount of information has been obtained from theoretical considerations such as molecular dynamics computations. Davidovits et al. [5] reviewed experimental techniques and results for mass accommodation coefficients and chemical reactions at gas–liquid interfaces. Simultaneous measurements of mass and thermal accommodation coefficients for water vapor condensation on droplets using an expansion cloud chamber reported by Winkler et al. [6, 7] indicate that $\alpha_{\mathrm{th}} > 0.8$ and $\alpha_{\mathrm{m}} > 0.4$. Zientara et al. [8] used electrodynamic levitation to measure mass and thermal accommodation coefficients for evaporating water droplets, reporting $\alpha_{\mathrm{m}} = 0.12 \pm 0.02$ and $\alpha_{\mathrm{th}} = 0.65 \pm 0.09$ at room temperature ($T_\infty \approx 286$ K).

Molecular dynamics simulations have been performed by numerous investigators, including Tsuruta and Nagayama [9], Vieceli et al. [10], and Morita et al. [11]. Most of these theoretical studies address the issue of the condensation coefficient. The simulations of Morita et al. yielded $\alpha_{\mathrm{m}} \sim 1$ for the condensation coefficient of water vapor on liquid water at 273 K, and Tsuruta and Nagayama reported mean

values of condensation coefficients for water ranging from 0.286 at 550 K to 0.961 at 330 K. Experimental data for condensation coefficients of water from several investigations range from 0.10 to 1.00 (see Table 1 of Tsuruta and Nagayama). Vieceli et al. determined α_m and α_{th} to be 0.99 and 1.0, respectively.

The Knudsen Regime

In the intermediate regime between the two limiting cases of large and small Knudsen numbers, transport theory is much more complicated than either continuum theory or the simple kinetic theory of gases. Fuchs [12] attempted to fill the gap between continuum theory and free molecule theory by introducing flux-matching at some point between the region near the droplet surface and the outer region. In the region extending about a mean free path from the surface, he applied the kinetic theory of gases, and in the outer region he applied diffusion theory. The fluxes based on the two theories were matched at some arbitrary distance from the surface.

Sahni [13] analyzed the Knudsen regime problem of neutron transport to a black sphere by solving the Boltzmann equation, the integro-differential equation describing the velocity distribution of a nonuniform gas. Sahni's problem is analogous to that of condensation on a sphere for the limiting case of $\alpha_m = 1$ and molecular weight ratio $z_{ij} = m_i/m_j = 0$. Based on Sahni's result, Fuchs and Sutugin [14] recognized that flux-matching leads to the wrong dependence on the Knudsen number, so they proposed an interpolation formula that has been widely used for evaporation and condensation in the Knudsen regime. A modified form that includes the mass accommodation coefficient is

$$\frac{j_i}{j_{fm}} = \frac{(4/3)Kn_{FS}}{1 + \left[\frac{(4/3)Kn_{FS} + 0.71}{1 + Kn_{FS}} + \frac{4}{3}\frac{(1-\alpha_m)}{\alpha_m}\right]Kn_{FS}}. \tag{15.15}$$

The mean free path used in the Knudsen number in (15.15) is given by

$$l_{FS} = \frac{3D_{ij}}{\bar{c}_i}, \tag{15.16}$$

which is based on the simplest approximation from the kinetic theory of gases for hard sphere molecules of the same size. As we shall show, different authors use different definitions of the mean free path, so some care should be taken in applying various transport theories. The classical mean free path for a dilute gas ($n_i \ll n_j$) composed of hard sphere molecules with diameters σ_i and σ_j (Jeans [15]) is

$$l_{HS} = \frac{1}{\pi n_j \sigma_{ij}^2 \sqrt{1 + z_{ij}}}, \tag{15.17}$$

in which $\sigma_{ij} = (\sigma_i + \sigma_j)/2$, and $z_{ij} = m_i/m_j$. This result can be related to the diffusion coefficient for a hard-sphere gas (Davis and Schweiger [2]) given by

$$D_{ij}^{(0)} = \frac{1}{3p\sigma_{ij}^2}\sqrt{\frac{2(1+z_{ij})}{m_i}\left(\frac{kT}{\pi}\right)^3}, \tag{15.18}$$

where p is the pressure, which is given by $p = n_j kT$ for a dilute ideal gas. Using (15.8), (15.17), and (15.18), one obtains the relationship

$$l_{HS} = \frac{6D_{ij}^{(0)}}{\bar{c}_i(1+z_{ij})}, \tag{15.19}$$

which reduces to the formula used by Fuchs and Sutugin when $z_{ij} = 1$. It is convenient to use this result to define a standard Knudsen number based on the hard sphere gas model by

$$Kn_0 = \frac{l_{HS}}{a} = \frac{6D_{ij}^{(0)}}{a\bar{c}_i(1+z_{ij})}. \tag{15.20}$$

Sahni's work stimulated Loyalka and others to develop theory for the Knudsen regime by solving the Boltzmann equation. Loyalka developed a number of different approaches, and he and his co-workers (Loyalka et al. [16]) revisited the problem of isothermal condensation for arbitrary z_{ij}, tabulating the results for various models and approximations, assuming the accommodation coefficient to be unity. Some of these results are discussed by Williams and Loyalka [17] in their monograph. Figure 15.1 shows the results obtained by Loyalka et al. by solving the linearized Boltzmann equation. The flux ratio is seen to be a weak function of the molecular weight ratio, z_{ij}.

Because of the extensive use of the Fuchs-Sutugin equation, Loyalka et al. used the form of the equation to correlate the solution of the linearized Boltzmann equation. The result is

$$\frac{j_i}{j_{fm}} = \frac{\sqrt{\pi}Kn_L}{1 + \left[\frac{\sqrt{\pi}Kn_L\xi_c + \zeta_c}{1 + Kn_L\xi_c}\right]Kn_L}, \tag{15.21}$$

in which Kn_L is defined by

$$Kn_L = \frac{4}{\sqrt{\pi}}\frac{D_{ij}}{a\bar{c}_i}, \tag{15.22}$$

αvδ ζ_c is a dimensionless jump distance, and $\xi_c = 1.3333$. For the black sphere considered by Sahni, the value of the jump distance is $\zeta_c = 0.9444$. For the BGK

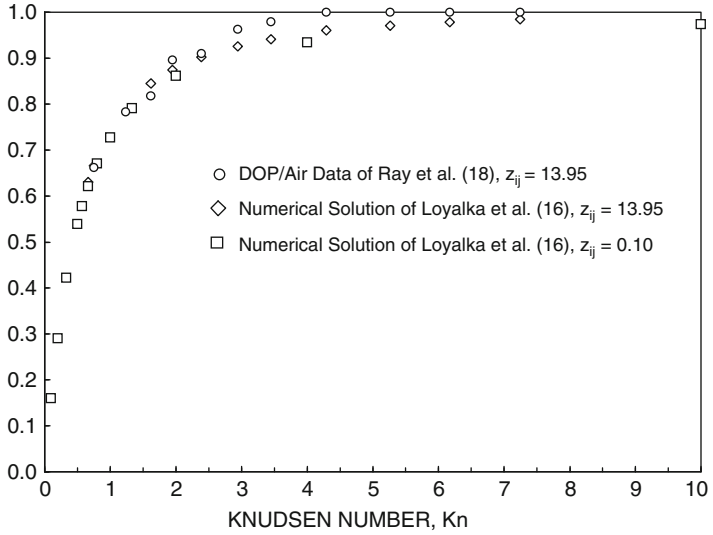


Fig. 15.1 The effect of the mass ratio z_{ij} on the mass flux ratio j_i/j_{fm} based on the solution of the Boltzmann equation by Loyalka et al. [16] and a comparison with data of Ray et al. [18] assuming $\alpha_m = 1$

model of the Boltzmann equation, Williams and Loyalka reported $\zeta_c = 1.0161$. Loyalka et al. [16] obtained an expression for ζ_c that depends on the mass ratio z_{ij}, which is

$$\zeta_c = 0.9769 - 0.0518Z + 0.0018Z^2 + 0.0196Z^3, \tag{15.23}$$

where Z is a function of z_{ij} given by $Z = \log_{10}(1/z_{ij})$.

Figure 15.1 shows the mass flux ratios computed by Loyalka et al. for $z_{ij} = 0.10$ and $z_{ij} = 13.95$. The latter mass ratio corresponds to the evaporation of a dioctyl phthalate (DOP) in air. Also shown in the figure are the evaporation data of Ray et al. [18] for DOP/air at relatively large Knudsen numbers. The Knudsen numbers shown in the figure are given by (15.22). The fact that the mass flux ratio is a weak function of z_{ij} justifies to some extent the use of the Fuchs-Sutugin equation, which should apply only to systems with $z_{ij} \ll 1$. Because DOP has a very low vapor pressure at room temperature, the droplet evaporation process is very nearly isothermal, that is, the interfacial temperature is approximated closely by the bulk gas temperature.

For the heat flux ratio q/q_{fm} in the Knudsen regime, Williams and Loyalka reported an expression analogous to (15.21),

$$\frac{q}{q_{fm}} = \frac{(5/4)\sqrt{\pi}Kn_H}{1 + \left[\frac{(5/4)\sqrt{\pi}Kn_H\zeta_H + \zeta_H}{1 + Kn_H\zeta_H}\right]Kn_H}, \tag{15.24}$$

where the Knudsen number for heat transfer is

$$Kn_{\mathrm{H}} = \frac{8}{5\sqrt{\pi}} \frac{\kappa_{\mathrm{j}} T_{\infty}}{a p_{\infty} \bar{c}_{\mathrm{j}}} = \frac{8}{5\sqrt{\pi}} \frac{2\kappa_{\mathrm{j}}}{a n_{\infty} k \bar{c}_{\mathrm{j}}}, \tag{15.25}$$

κ_{j} is the thermal conductivity of the gas, and the constants ξ_{H} and ζ_{H} are 1.9234 and 1.3026, respectively.

Sitarski and Nowakowski [19] relaxed the assumption of $\alpha_{\mathrm{m}} = 1.0$, and used the 13-moment method of Grad [20] to solve the Boltzmann equation for isothermal condensation. This method is less accurate than the methods applied by Loyalka and his colleagues, but it yields good results in the near-continuum regime. They assumed hard sphere molecules in their treatment of molecular interactions. Their result is

$$\frac{j_{\mathrm{i}}}{j_{\mathrm{fm}}} = \frac{Kn_{\mathrm{SN}} \left[1 + \frac{3\beta(1+z_{\mathrm{ij}})^2}{4(3+5z_{\mathrm{ij}})} Kn_{\mathrm{SN}} \right]}{\frac{4(9+10z_{\mathrm{ij}})}{15\pi(1+z_{\mathrm{ij}})^2} + \left[\frac{\beta(1+2z_{\mathrm{ij}})}{\pi(3+5z_{\mathrm{ij}})} + \frac{1}{2\beta} \right] Kn_{\mathrm{SN}} + \frac{9(1+z_{\mathrm{ij}})^2}{8(3+5z_{\mathrm{ij}})} Kn_{\mathrm{SN}}^2}, \tag{15.26}$$

where β is related to the mass accommodation coefficient by

$$\beta = \frac{\alpha_{\mathrm{m}}}{(2 - \alpha_m)}, \tag{15.27}$$

and the Knudsen number is defined by

$$Kn_{\mathrm{SN}} = \frac{32\left[1 - 0.1/(1 + z_{\mathrm{ij}})\right]}{3\pi(1 + z_{\mathrm{ij}})} \frac{D_{\mathrm{ij}}}{a\bar{c}_{\mathrm{i}}}. \tag{15.28}$$

Qu and Davis [21] carried out a similar solution of the Boltzmann equation using Maxwell's molecular interaction force, which is inversely proportional to the molecular interaction distance to the power 5. Their result has a form similar to that of Sitarski and Nowakowski, and, as we shall show, yields almost identical numerical results. They obtained the expression

$$\frac{j_{\mathrm{i}}}{j_{\mathrm{fm}}} = \frac{2Kn_{\mathrm{QD}} \left[1 + \frac{8\beta(1+z_{\mathrm{ij}})^2}{5A_1 \left(3\frac{A_2}{A_1} + 4z_{\mathrm{ij}} \right)} Kn_{\mathrm{QD}} \right]}{\frac{2A_1}{\pi(1+z_{\mathrm{ij}})} + \left[\frac{16\beta(1+z_{\mathrm{ij}})}{5\pi \left(3\frac{A_2}{A_1} + 4z_{\mathrm{ij}} \right)} + \frac{1}{2\beta} \right] Kn_{\mathrm{QD}} + \frac{24(1+z_{\mathrm{ij}})^2}{\left(3\frac{A_2}{A_1} + 4z_{\mathrm{ij}} \right)} Kn_{\mathrm{QD}}^2}, \tag{15.29}$$

where A_1 and A_2 are numerical values of integrals having the values 0.42194 and 0.43619, respectively. In this case, the Knudsen number is given by

$$Kn_{\mathrm{QD}} = \frac{4A_1}{\pi(1 + z_{\mathrm{ij}})} \frac{D_{\mathrm{ij}}}{a\bar{c}_{\mathrm{i}}}. \tag{15.30}$$

The equations of Sitarski and Nowakowski and Qu and Davis fail to yield the correct result in the free-molecule regime. For $Kn \gg 1$ and $\alpha_m = 1$, (15.26) and (15.29) both give $j_i/j_{fm} = 2/3$ rather than unity, but they show explicitly the dependence on z_{ij} and the accommodation coefficient.

Nowakowski and Popielawski [22] and Qu et al. [23] extended the method of Grad to nonisothermal droplet evaporation and condensation, but the lower accuracy of the method leads one to favor the correlation of Loyalka and his co-workers.

Figures 15.2 and 15.3 compare the various mass flux equations with experimental data for the evaporation of low volatility species. Figure 15.2 shows the data for dibutyl sebacate (DBS) droplets evaporating in nitrogen obtained by Davis and Ray

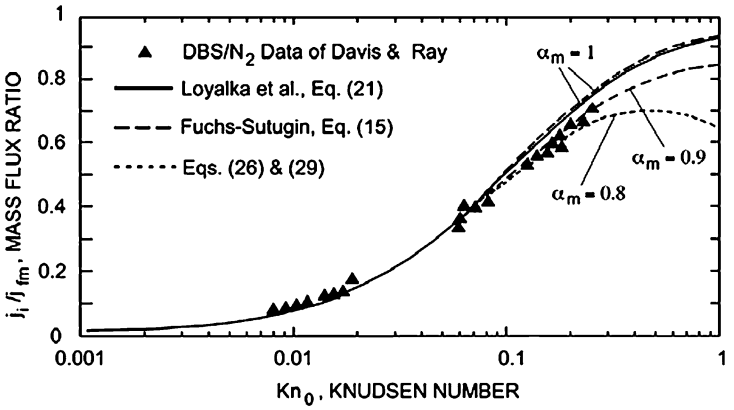


Fig. 15.2 A comparison of the various formulas for the flux ratio j_i/j_{fm} compared with the droplet evaporation data of Davis and Ray [24] (Reproduced with permission of Elsevier Publishing Company)

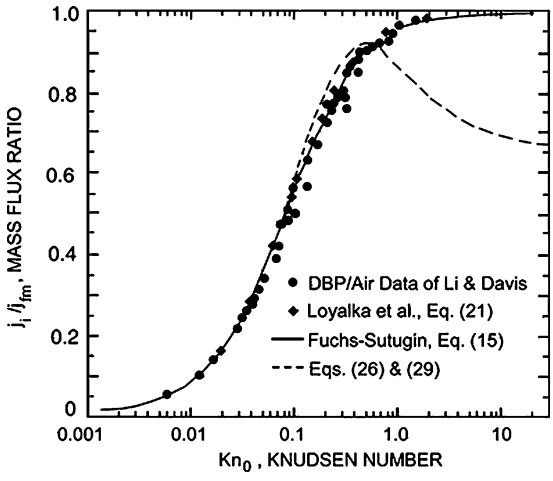


Fig. 15.3 A comparison of the various formulas for the flux ratio j_i/j_{fm} compared with the data of Li and Davis [25] assuming $\alpha_m = 1$ ([25]. Copyright 1996. Mount Laurel, N.J. Reprinted with permission)

[24], and Fig. 15.3 presents the data of Li and Davis [25] and theoretical results for dibutyl phthalate (DBP) droplets evaporating in air. The Knudsen numbers associated with the various correlations and theories have all been converted to Kn_0 given by (15.20) for Figs. 15.2 and 15.3.

All of the formulas yield the same results in the near-continuum regime ($Kn_0 < 0.1$ when $\alpha_m = 1$, and the Fuchs-Sutugin equation gives flux ratios very close to the results of Loyalka et al. [16] for all mass accommodation coefficients. The formulas of Sitarski and Nowakowski and Qu and Davis deviate from the other formulas for $Kn_0 > 0.1$ and fail completely for $Kn_0 > 1$.

The data presented in Fig. 15.2 agree with the Fuchs-Sutugin and Loyalka et al. correlations assuming $\alpha_m = 0.9$, and appear to agree with (15.26) and (15.29) assuming $\alpha_m = 0.8$. The DBP/air data of Li and Davis shown in Fig. 15.3 are in good agreement with (15.15) and (15.21) assuming $\alpha_m = 1$, and they agree with all of the formulas for $Kn_0 < 0.1$.

Because of the low vapor pressures of DOP, DBP, and DBS the prediction of droplet evaporation rates for these species does not require simultaneous solution of the mass flux and heat flux equations. For more volatile species evaporating in the Knudsen regime, (15.4), (15.21), and (15.24) must be satisfied.

References

1. J. C. Maxwell: Diffusion. In Encyclopedia Britannica, 9th edn., Vol. 7, p. 214 (1878).
2. E. J. Davis, G. Schweiger: The Airborne Microparticle, Springer, Heidelberg (2002).
3. D. C. Taflin, S. H. Zhang, T. Allen, E. J. Davis: Measurement of droplet interfacial phenomena by light-scattering techniques, AIChE J. 34, 1320–1320 (1988).
4. E. J. Davis: A history and state-of-the-art of accommodation coefficients, Atmos. Res., 82, 561–578 (2006).
5. P. Davidovits, C. E. Kolb, L. R. Williams, J. T. Jayne, D. R. Worsnop: Mass accommodation and chemical reactions at gas-liquid interfaces, Chem. Rev. 106, 1323–1354 (2006).
6. P. M. Winkler, A. Vrtala, P. E. Wagner, M. Kulmala, K. E. J. Lehtinen, T. Vesala: Mass and thermal accommodation during gas-liquid condensation of water, Phys. Rev. Lett. 93, 075701-1-075701-4 (2004).
7. P. M. Winkler, A. Vrtala, R. Rudolf, P.E. Wagner, I. Riipinen, T. Vesala, K. E. J. Lehtinen, Y. Viisanen, M. Kulmala: Condensation of water vapor: experimental determination of mass and thermal accommodation coefficients. J. Geophys. Res. D: Atmos. 111, D19202 (2006).
8. M. Zientara, D. Jakubczyk, G. Derkachov, K. Kolwas, M. Kolwas: Determination of mass and thermal accommodation coefficients from evolution of evaporating water droplet, Proc. SPIE 5849, 162–165 (2005).
9. T. Tsuruta, G. Nagayama: Molecular dynamics studies on the condensation coefficient of water, J. Phys. Chem. B 108, 1736–1743 (2004).
10. J. Vieceli, M. Roeselova, D. J. Tobias: Accommodation coefficients for water vapor at the air/water interface, Chem. Phys. Lett. 393, 249–255 (2004).
11. A. Morita, M. Sugiyama, H. Kameda, S. Koda, D. R. Hanson: Mass accommodation coefficient of water: molecular dynamics simulation and revised analysis of droplet train/flow reactor experiment, J. Phys. Chem. B 108, 9111–9120 (2004).
12. N. A. Fuchs: Über die Verdampfungsgeschwindigkeit Kleiner Tröpfchen in Einer Gasatmosphäre, Phys. Z. Sowjet 6, 225–243 (1934).

13. D. C. Sahni: The effect of a black sphere on the flux distribution in an infinite moderator, J. Nucl. Energy 20, 915–920 (1966).
14. N. A. Fuchs, A. G. Sutugin: Highly Dispersed Aerosols, Ann Arbor Science, Ann Arbor, MI (1970).
15. J. Jeans: The Dynamical Theory of Gases, Dover, New York (1954).
16. S. K. Loyalka, S. A. Hamoodi, R. V. Tompson: Isothermal condensation on a spherical particle, Phys. Fluids 14, 358–362 (1989).
17. M. M. R. Williams, S. K. Loyalka: Aerosol Science Theory and Practice, Pergamon, Oxford (1991).
18. A. K. Ray, A. J. Lee, H. L. Tilley: Direct measurements of evaporation rates of single droplets at large Knudsen numbers, Langmuir 4, 631–637 (1988).
19. M. Sitarski, B. Nowakowski: Condensation rate of trace gas vapor on Knudsen aerosols from the solution of the Boltzmann equation, J. Colloid Interface Sci. 72, 113–122 (1979).
20. H. Grad: On the kinetic theory of rarefied gas, Commun. Pure Appl. Math. 2, 331–407 (1949).
21. X. Qu, E. J. Davis: Droplet evaporation and condensation in the near-continuum regime, J. Aerosol Sci. 32:861–875 (2001).
22. B. Nowakowski, J. Popielawski: Nonisothermal condensation on spherical aerosol particles from the Grad solution of the Boltzmann equation, J. Colloid Interface Sci. 122, 299–307 (1988).
23. X. Qu, E. J. Davis, B. D. Swanson: Non-isothermal droplet evaporation and condensation in the near-continuum regime, J. Aerosol Sci. 32:1315–1339 (2001).
24. E. J. Davis, A. K. Ray: Submicron droplet evaporation in the continuum and non-continuum regimes, J. Aerosol Sci. 9, 411–422 (1978).
25. W. Li, E. J. Davis: Aerosol evaporation in the transition regime, Aerosol Sci. Technol. 25, 11–21 (1996).

Chapter 16
Droplet Freezing and Solidification

F.X. Tanner

Abstract Freezing and solidification processes are discussed and modeled for liquid droplets which undergo first-order phase transitions. First, a four-stage model is presented which accounts for supercooling, nucleation, recalescence, and crystallization. Subsequently, a more detailed discussion of a three-stage solidification model for droplets that do not exhibit supercooling is given. Aspects of the three-stage model validation are presented for a single cocoa butter drop and for a cocoa butter spray.

Keywords Cocoa butter · Crystallization · Freezing · Latent heat · Nucleation · Nusselt number · Ranz–Marshall correlation · Recalescence · Schmidt number · Sherwood number · Solidification · Supercooling

Introduction

Freezing and melting are complex phase transition phenomena whose modeling poses a considerable challenge. For most common substances below the critical pressure, solidification is a first-order phase transition, that is, solidification occurs via a crystallization process where liquid and solid states coexist. This is in contrast to second-order phase transitions that occur continuously as the temperature changes. Such materials have an amorphous structure and include glass and many polymers. The phase transitions considered in this article are first order and focus on the freezing of liquid droplets. A more detailed and general discussion of these phase transition phenomena can be found in [1].

The crystallization process consists of a nucleation phase followed by crystal growth. Nucleation is the process where, at random locations throughout the liquid,

F.X. Tanner
Department of Mathematical Sciences, Michigan Technological University, Houghton, MI, USA
e-mail: tanner@mtu.edu

N. Ashgriz (ed.), *Handbook of Atomization and Sprays*,
DOI 10.1007/978-1-4419-7264-4_16, © Springer Science+Business Media, LLC 2011

molecules start clustering in a well-defined manner to form tiny crystals. Subsequently, during the crystal growth phase, these tiny crystal structures grow until the entire substance is solidified.

During a crystallization process, molecules arrange themselves into more ordered, lower energy states, and in the process, release energy called latent heat. In the reverse process, when a solid turns into liquid, the latent heat is the energy that is needed to elevate the molecules into higher-energy states, thus reducing the inter-molecular forces, which then leads to the melting of the substance. The presence of latent heat in phase changes is characteristic for first-order phase transitions.

For many liquids, especially for pure substances that lack nucleation agents, crystallization can begin at temperatures that lie far below the material's melting point. This phenomenon is called supercooling or undercooling, and the subsequent solidification process is often referred to as flash-freezing. In fluids with plenty of irregularities or impurities, or in vibrating fluids, supercooling is less likely and the freezing and melting temperatures are almost the same. Also, polymorphous materials, that is, materials that produce different types and sizes of crystals, tend not to exhibit supercooling, and the solidification process can occur while the temperature is decreasing.

The type and size of crystals in polymorphous materials depend on the crystallization process itself. In particular, the cooling conditions will affect the crystal size and shape and can produce substances with different properties. This topic is of particular interest for manufacturing processes of pharmaceutical and food products, as is discussed in more detail in [3, 8, 11, 15].

Freezing is a common method for food preservation because it limits food decay and the growth of harmful microorganisms. In particular, spray-freezing is a method to realize stable forms of food products in powder form that undergo no, or only extremely slow, structural changes after the crystallization process. Further, spray-freezing provides fast cooling rates via rapid convective heat transfer, primarily due to the high surface/volume ratio of the liquid phase. Therefore, small droplet sizes allow for more homogeneous temperature fields for freezing, which results in a more uniform microstructure of the powder products.

A Four-stage Freezing Model

Many pure substances, water in particular, experience supercooling before the solidification process starts. Of particular interest is the freezing process of a droplet, which, according to Hindmarsh et al. [6], can be described in the following four stages, and is illustrated in Fig. 16.1.

1. The supercooling stage, during which the droplet cools from its initial temperature to the nucleation temperature, T_n, which lies below the equilibrium freezing temperature, T_f.

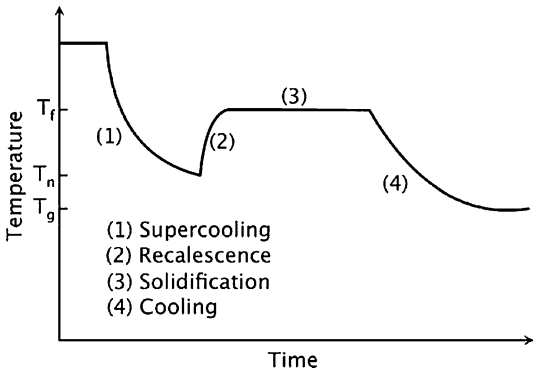


Fig. 16.1 Temperature profile of a four-stage freezing process for a single droplet

2. The recalescence stage, during which the supercooling-induced, rapid crystal growth releases latent heat, which results in a temperature increase until the droplet has reached its equilibrium freezing temperature, T_f.
3. The solidification or freezing stage, during which crystal growth takes place at the constant equilibrium freezing temperature, T_f, until the droplet is completely solidified.
4. The cooling or tempering stage, during which the solidified droplet cools down to the temperature of the ambient gas, T_g.

Cooling Stages

The cooling of the liquid or solid particles in stage one or stage four is determined by the energy exchange of the particles with the environment. Assuming that the particles have a uniform temperature distribution, the rate of temperature change is described by

$$\rho_d V_d C_{pd} \frac{dT_d}{dt} = -S_d(q_h + q_m + q_r), \tag{16.1}$$

where the subscript d denotes the particle properties (liquid or solid), C_{pd} the heat capacity, ρ_d the density, T_d the temperature, V_d the volume, and S_d the surface. The symbols q_h, q_m, and q_r denote the heat fluxes (per unit area) caused by the convective heat transfer, the convective mass transfer, and the thermal radiation, respectively.

The convective heat flux, q_h, from the particle surface to the ambient gas is given by

$$q_h = h_0(T_d - T_g), \tag{16.2}$$

where T_g is the temperature of the ambient gas and h_0 is the convective heat transfer coefficient. The latter is determined from the Ranz–Marshall [12] correlation via the Nusselt number

$$Nu = \frac{h_0 d}{K_g} = 2 + 0.6 \mathrm{Re}_d^{1/2} \mathrm{Pr}_d^{1/3}. \tag{16.3}$$

Here, d is the drop diameter, K_g the thermal conductivity of the ambient gas, Re_d the droplet Reynolds number, and Pr_d the droplet Prandtl number. The latter two are given by

$$\mathrm{Re}_d = \frac{\rho_g ||\mathbf{v}_r|| d}{\mu_g} \quad \text{and} \quad \mathrm{Pr}_d = \frac{C_{pg} \mu_g}{K_g},$$

where $\mathbf{v}_r$ is the relative droplet-gas velocity, $||\cdot||$ denotes the norm, ρ_g and μ_g are the density and viscosity of the surrounding gas, and C_{pg} is the gas heat capacity at constant pressure.

The heat flux due to the convective mass transfer is given by

$$q_m = L h_m (\rho_v - \rho_g), \tag{16.4}$$

where L is the latent heat of phase change (vaporization or sublimation), ρ_v the vapor density, and h_m the convective mass transfer coefficient determined from the Frössling [4] correlation via the Sherwood number

$$Sh = \frac{h_m d}{D_{vg}} = 2 + 0.6 \mathrm{Re}_d^{1/2} Sc_d^{1/3}. \tag{16.5}$$

Here, D_{vg} is the vapor-gas diffusivity and Sc_d is the droplet Schmidt number given by

$$Sc_d = \frac{\mu_g}{\rho_g D_{vg}}.$$

The heat flux due to thermal radiation is given by

$$q_r = \varepsilon \sigma (T_d^4 - T_g^4), \tag{16.6}$$

where ε is the emissivity for thermal radiation and σ is the Stefan–Boltzmann constant of radiation.

The dimensionless quantities, Re_d, Pr_d, and Sc_d, depend on the material properties μ_g, K_g, and D_{vg} of the surrounding gas, which in turn depend on the gas temperature near the particle surface. Since the gas temperature on the particle surface is in general different from its far field value, this difference is accounted for

by using the two-third temperature average, $\breve{T}$, in the calculation of these material coefficients, that is,

$$\breve{T} = \frac{T_g + 2T_d}{3}.$$

For example, the temperature dependence of the viscosity (in [g/(cm s)]) and the heat conduction coefficients (in [erg/(s cm K)]) in air are given by the Sutherland relations

$$\mu_g(\breve{T}) = \frac{A_1 \breve{T}^{1.5}}{\breve{T} + A_2}$$

and

$$K_g(\breve{T}) = \frac{K_1 \breve{T}^{1.5}}{\breve{T} + K_2}$$

where the constants A_1, A_2, K_1, and K_2 are given by $A_1 = 1.457 \times 10^{-5}$, $A_2 = 110$, $K_1 = 252$, and $K_2 = 200$.

Recalescence Stage

As indicated in Fig. 16.1, a droplet that exhibits supercooling, once the nucleation starts, experiences a rapid temperature increase until it reaches the equilibrium freezing temperature, T_f. The portion of the droplet volume that is solidified during this recalescence stage, V_f, can be estimated from the heat balance equation

$$V_f = V_d \frac{\rho_d C_{pd}(T_f - T_n)}{\rho_s L_f}, \tag{16.7}$$

where the nucleation temperature, T_n, is usually an empirical value, L_f the latent heat due to crystallization, and ρ_s the solid particle density. Further, the droplet is assumed to change its temperature instantly, thus neglecting the recalescence time.

Freezing Stage

After nucleation produces the partially frozen volume fraction, V_f, the freezing of the remaining liquid is controlled by the heat transfer from the droplet to the surrounding gas at the constant equilibrium freezing temperature, T_f. Assuming that the nucleation is uniformly spread throughout the droplet, the latent heat due to

crystallization, L_f, is removed by the external heat fluxes, which, by means of (16.1), leads to the expression for the droplet temperature

$$\rho_d V_d C_{pd} \frac{dT_d}{dt} = -S_d(q_h + q_m + q_r) + L_f \rho_s \frac{dV_f}{dt}. \tag{16.8}$$

Assuming that the temperature remains constant during this solidification stage, that is, $dT_d/dt = 0$, the rate at which the volume of solid is produced follows from (16.8) and is given by

$$L_f \rho_s \frac{dV_f}{dt} = S_d(q_h + q_m + q_r), \tag{16.9}$$

where the initial value of V_f is obtained from (16.7). In order to still allow mass transfer via evaporation during this stage, it has to be assumed that the outer surface of the droplet remains liquid during this process. If the outer surface is assumed to be solid, then the mass transfer is due to sublimation.

The assumption of a uniform droplet temperature is only justified if the Biot number,

$$Bi = \frac{h_0 d}{2K_d},$$

is small, typically $Bi \leq 0.1$ (cf. Incropera and DeWitt [7]). In this equation, K_d denotes the heat conduction coefficient inside the droplet. In a spray, the drop diameters are typically below 200 μm, and therefore, the Biot number criterion is usually satisfied. In a situation where $Bi > 0.1$, the temperature profile within the particle should be taken into consideration. A heat conduction model that accounts for such temperature gradients, together with a moving boundary model for the tracking of the solidification process, is presented in Hindmarsh et al. [6].

A Three-Stage Freezing Model

Many materials of interest do not experience supercooling and, therefore, they do not show recalescence when they start to solidify. This means that as soon as the freezing temperature, T_f, is reached, the nucleation, and hence the crystallization, begins. The release of latent heat is slow enough that it does not lead to a temperature increase, but to a significant decrease in the droplet cooling rate. Therefore, a model that describes the freezing process of a material with no significant recalescence can be reduced to three stages: the initial cooling stage of the liquid, the crystallization or solidification stage, and the cooling stage of the solid particle. One such material is cocoa butter (CB), which is a basic ingredient in the manufacturing process of chocolate (cf. [9, 10]). With a clearly defined crystalline structure of CB

powder, products with improved qualities, such as storage stability, melting behavior, and consistency, can be obtained [15].

In addition, radiation is usually not an issue in a freezing spray, and nor is the mass flux because droplets are small and freeze rapidly. Therefore, the radiation heat flux, q_r, and the mass heat flux, q_m, in (16.1) and (16.9) can be neglected. Such a model has been developed by Srinivasan et al. [13] for the simulation of freezing CB sprays.

Cooling Stages

The liquid and solid cooling stages, that is, stage one and stage three, are described by a convective heat transfer process. Since the heat exchange due to mass transfer and radiation is neglected, these two stages can be described by means of (16.1)–(16.3), with $q_m = q_r = 0$.

Crystallization Stage

Once the droplet reaches the freezing temperature, T_f, the crystallization process begins. It is assumed that the droplet starts solidifying from the outer surface toward the center. The beginning of the crystallization process is identified by a drastic decrease in the droplet freezing rate, which leads to a flatter freezing curve, as is shown in Fig. 16.2. This is a consequence of the release of the latent heat due to the

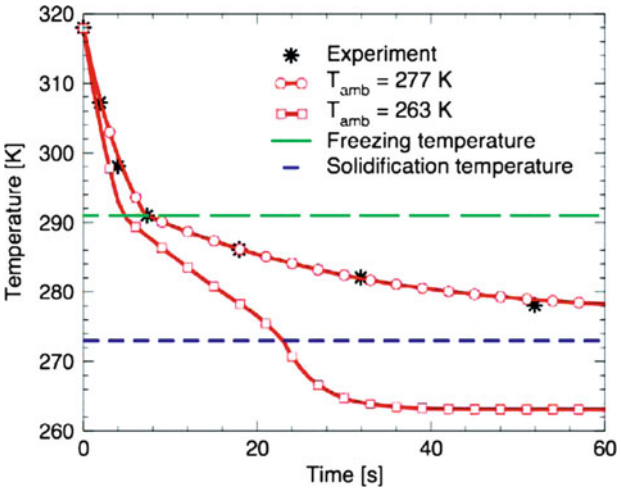


Fig. 16.2 Temperature profiles of a 2 mm cocoa butter (*CB*) droplet, initially at 318 K, for the two different ambient temperature of 263 and 277 K

crystallization process. Since the temperature of polycrystalline materials, such as CB, does not necessarily remain constant during this stage, this process is described by (16.8). Under the stated assumptions that $q_m = 0$ and $q_r = 0$, (16.8) becomes

$$\rho_d V_d C_{p\gamma} \frac{dT_d}{dt} = -S_d h_0 (T_d - T_g) + L_f \rho_d \frac{dV_f}{dt}. \tag{16.10}$$

In this equation, $C_{p\gamma}$ is the heat capacity of the semisolid droplet which is assumed to vary linearly from the liquid value, C_{pl}, down to its solid value of C_{ps}. For CB, $C_{pl} = 2.2\ \mathrm{kJ/kg\,K}$ and $C_{ps} = 1.25\ \mathrm{kJ/kg\,K}$. More precisely, the heat capacity during this phase is given by

$$C_{p\gamma} = (1 - \gamma) C_{pl} + \gamma C_{ps}, \tag{16.11}$$

where γ is a progress variable that varies linearly from 0 to 1 and is given by

$$\gamma = \frac{T_f - T_d}{T_f - T_s}. \tag{16.12}$$

Here, T_s is the solidification temperature, that is, the temperature at which the particle is completely solidified.

In order to solve (16.10), an additional relation is needed to express dV_f/dt. This is achieved by linearly interpolating the diameter of the liquid portion of the droplet, d_l, by

$$d_l = (1 - \gamma) d, \tag{16.13}$$

where γ is the progress variable given in (16.12). Since the droplet solidifies from the surface towards the center, it follows that the frozen volume, V_f, can be expressed as

$$V_f = \frac{\pi d^3}{6} [1 - (1 - \gamma)^3],$$

and its derivative with respect to time is given by

$$\frac{dV_f}{dt} = -\frac{\pi d^3}{2} \frac{(1 - \gamma)^2}{T_f - T_s} \frac{dT_d}{dt}. \tag{16.14}$$

Substitution of (16.14) into (16.10) gives an expression for the crystallization phase that depends only on the droplet temperature, namely

$$\rho_d d \left[C_{p\gamma} + 3 L_f \frac{(1 - \gamma)^2}{T_f - T_s} \right] \frac{dT_d}{dt} = -6 h_0 (T_d - T_g). \tag{16.15}$$

This equation can now be solved for the droplet temperature, T_d, keeping in mind that γ and $C_{p\gamma}$ depend on T_d as well.

Model Validation for a Single CB Drop

The three-stage freezing model described in this subsection has been implemented into a modified version of the computational fluid dynamics code, *KIVA-3* [2]. The model has been validated for a single drop according to the experiments of Gwie et al. [5]. In these experiments, a CB droplet with a diameter of 2 mm is suspended in an airflow through an open cylinder of 2 cm in diameter and 5 cm in height with a conical diffuser at the bottom. The air inflow occurs through an orifice at the center of the diffuser, resulting in a relative droplet-air velocity of 83 cm/s. The droplet is held stationary on the cylinder axis, thus experiencing the relative droplet-gas velocity responsible for the convective heat transfer. Additional experimental details are summarized in Table 16.1.

Two simulations have been performed, the first at the ambient air temperature of $T_g = 277$ K, and the second at $T_g = 263$ K. The temperature freezing profiles are shown in Fig. 16.2, together with the experimental data for the 277 K case. Additional comparisons with experimental data are shown in Table 16.2. As these comparisons show, there is good agreement between experiment and simulation.

The change in the rate of decrease of temperature at the freezing point of $T_f = 291$ K, observed in both simulations (cf. Fig. 16.2), is due to the onset of crystallization. As discussed previously, the crystallization process releases latent heat, which contributes toward heating the droplet. Since the heat convected away from the droplet is still greater than the contribution due to latent heat, there is a net decrease in the droplet temperature.

For the 277 K ambient temperature case, the simulations and the experiments show that after 60 s the CB droplet has almost reached the ambient temperature of 277 K. However, the droplet is not completely solidified yet. This can be concluded because once the droplet is completely solid, there is a distinct decrease in the

Table 16.1 Data used in the three-stage freezing model validation for a single CB droplet

Parameter	Value
Droplet diameter, d (mm)	2
Droplet density, ρ_d (g/cm^3)	0.894
Initial droplet temperature (K)	318
Freezing temperature, T_f (K)	291
Solidification temperature, T_s (K)	273
Latent heat of crystallization, L_f (kJ/kg)	157
Ambient air temperature, T_g (K)	277/263
Ambient air pressure (bars)	1.0
Inflow air velocity (cm/s)	83.0

Table 16.2 Comparison between the simulation and experimental values [5] for the single CB droplet case at 277 K

Parameter	Sim.	Exp.
Stage 1 cooling rate (K/s)	6.3	7–9
Initial stage 2 cooling rate (K/s)	0.5	0.2–0.4
Nusselt number (stage 2)	6.2	7–8
Heat transfer coefficient, (W/m^{2}K)	101	93–95

temperature profile, which indicates the beginning of stage three. This decrease, however, was not observed in the simulation or the experiment.

In order to observe the abrupt change in the droplet cooling rate after the solidification process, the ambient temperature would need to be decreased. Therefore, a simulation was performed with $T_g = 263$ K. As the temperature profile in Fig. 16.2 shows, this change in the cooling rate occurs after the droplet has reached a temperature of 273 K at about 23 s. In view that the current sample size is relatively small and that for spray investigations the droplets are even smaller (in the micron range), it is reasonable to assume that the droplet is completely frozen once it reaches a temperature of 273 K. Beyond this point, stage three of the freezing model is initiated, where the solid droplet cools to the ambient temperature of 263 K.

Model Validation for a CB Spray

The three-stage freezing model has been used to simulate a freezing spray for CB. The liquid CB is initially at a temperature of 318 K and has been injected with a pressure of 6 bar into the spray tower by means of a hollow cone nozzle with an orifice of 0.5 mm and cone angles of 80° and 12.5°. The ambient gas temperature is 223 K and the pressure is 1 bar.

The simulation duration was 40 ms, which is sufficient for most of the spray droplets away from the nozzle to reach the freezing temperature. This is illustrated in Fig. 16.3, which shows the spray at 40 ms in a vertical cross-sectional plane through the nozzle. It can be seen that most of the droplets in the lower half of the spray have already reached the freezing temperature and thus do not break up or coalesce anymore. In fact, as shown in Fig. 16.4, the average temperature of the entire spray has reached the freezing temperature of 291 K after 23 ms, whereas the average spray temperature is 283 K at the end of the simulation. In the same figure, the maximum and minimum drop temperatures are also shown. The maximum

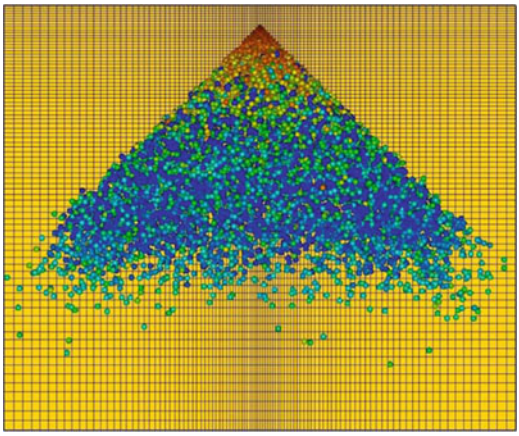


Fig. 16.3 Cocoa butter (*CB*) spray at an injection time of 40 ms. The particle temperature scale ranges from 290 K (*bottom*) to 320 K (*top*), and the gas temperature is 223 K

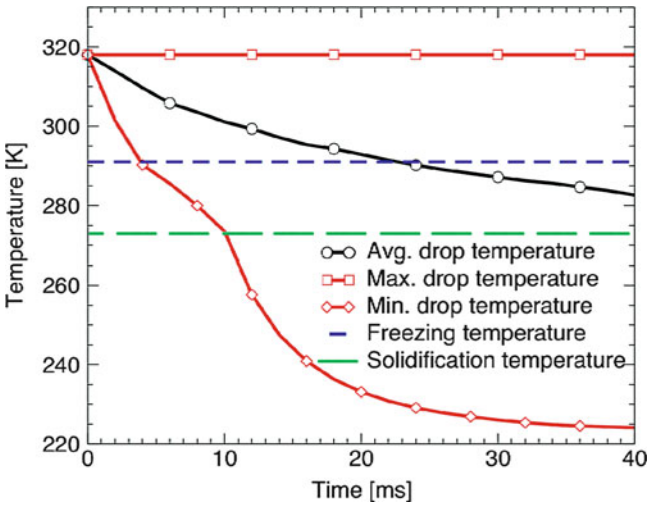


Fig. 16.4 Cocoa butter (*CB*) spray temperatures. The average spray temperature reaches the freezing temperature at 23 ms

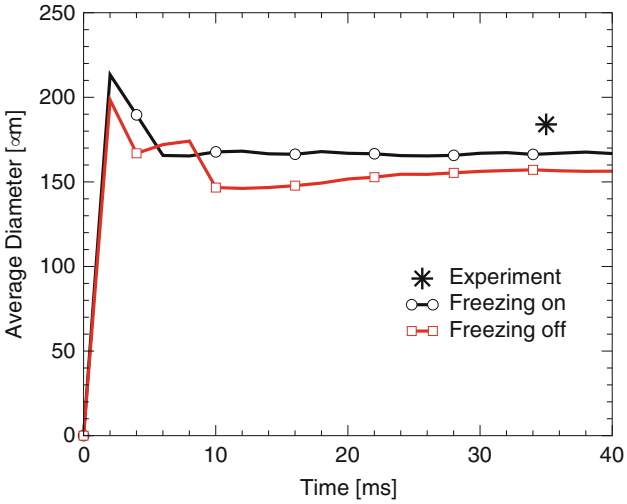


Fig. 16.5 Average droplet sizes of a cocoa butter (*CB*) spray with and without the freezing model

temperature of the droplets corresponds to the liquid temperature of 318 K. The minimum temperature, which presumably arises from one particular drop, reflects the nature of the temperature profile of the 263 K single droplet case in Fig. 16.2; it clearly shows the three freezing stages but at much higher freezing rates.

The average droplet sizes are shown in Fig. 16.5 for simulations with the freezing model switched on and off. Also shown is an experimental data point.

The agreement between the experimental value and the freezing simulation is quite good. Further, it is seen that the average drop size without the freezing model is smaller than with the freezing model switched on. This is because once the droplets reach the freezing temperature, they no longer break up, and hence tend to be larger. Note that the droplet coalescence plays a less important role, because hollow cone sprays are not very dense away from the nozzle, and therefore, the coalescence activity is small. Additional details of this investigation are documented in Ref. [14].

References

1. Alexiades, V. and A.D. Solomon. *Mathematical modeling of melting and freezing processes*. Hemisphere Publishing, Washington, 1993.
2. Amsden, A.A. KIVA–3: A KIVA program with block-structured mesh for complex geometries. Technical Report LA-12503-MS, Los Alamos National Laboratory, March 1993.
3. Constantino, H.R., L. Firouzabadian, K. Hogeland, Wu C., C. Beganski, K.G. Carrasquillo, M. Cordova, K. Griebenow, S.E. Zale, and M.A. Tracy. Protein spray freeze drying. Effect of atomization conditions on particle size and stability. *Pharmaceutical Research*, 17 (11):1374–1383, 2000.
4. Frössling, N. Über die Verdunstung fallender Tropfen. *Gerlands Beiträge zur Geophysik*, 52:170–216, 1938.
5. Gwie, C.G., R.J. Griffiths, D.T. Cooney, M.L. Johns, and D.I. Wilson. Microstructures formed by spray freezing of food fats. *American Oil Chemists Society*, 83:1053–1062, 2006.
6. Hindmarsh, J.P., A.B. Russell, and X.D. Chen. Experimental and numerical analysis of the temperature transition of a suspended freezing water droplet. *International Journal of Heat and Mass Transfer*, 46:1199–1213, 2003.
7. Incropera, F.P. and D.P. DeWitt. *Introduction to heat transfer*, 4th edn. Wiley, New York, 2002.
8. Leach, W.T., D.T. Simpson, T.N Val, Z. Yu, K.T. Lim, E.J. Park, R.O. Williams III, and K.P. Johnston. Encapsulation of protein nanoparticles into uniform-sized microspheres formed in a spinning oil film. *AAPS PharmSciTech*, 6(4):605–617, 2005.
9. Loisel, C., G. Keller, G. Lecq, C. Bourgaux, and Ollivon M. Phase transition and polymorphism of cocoa butter. *American Oil Chemists Society*, 75:425–439, 1998.
10. Metin, S. and R.W. Hartel. Crystallization behavior of blends of cocoa butter and milk fat or milk fat fractions. *Thermal Analysis*, 47:1527–1544, 1996.
11. Nguyen, X.C., J.D. Herberger, and P.A. Burke. Protein powders for encapsulation: a comparison of spray-freeze drying and spray drying of darbepoetin alfa. *Pharmaceutical Research*, 21(3):507–514, 2004.
12. Ranz, W.E. and W.R. Marshall. Evaporation from drops (parts I and II). *Chemical Engineering Program*, 48:141–146, 173–180, 1952.
13. Srinivasan, S., F.X. Tanner, K.A. Feigl, T.O. Althaus, and E.J. Windhab. Development of a freezing model for food sprays. In *Proceedings of the 8th World Congress of Chemical Engineering*, Montreal, CA, August 2009.
14. Tanner, F.X., S. Srinivasan, T.O. Althaus, K.A. Feigl, and E.J. Windhab. Modeling and validation of the crystallization process in food sprays. In *Proceedings of the Eleventh Triennial International Conference on Liquid Atomization & Spray Systems*, Vail, CO, July 2009. CD-ROM Publication.
15. Windhab, E.J. New developments in crystallization processing. *Thermal Analysis and Calorimetry*, 57:171–180, 1999.

Chapter 17
Numerical Techniques for Simulating the Atomization Process

N. Ashgriz

Abstract This chapter provides an overview of the techniques available to deal with flows having liquid-gas interfaces. These techniques are categorized based on the type of flow modeling (Eulerian, Lagrangian, or mixed), type of interface modeling (capturing or tracking), flow–interface coupling (integrated or segregated), and the type of spatial discretization (meshless, finite difference, finite volume, finite element [FE], or others).

Keywords: Finite element · Finite volume · Finite difference · Volume of fluid · Level set · Interface tracking · Free surface flows · Fixed mesh · Boundary-fitted coordinates · Boundary integral · Marker and cell · Immersed boundary · Volume tracking · Surface tracking · Surface capturing · Interfacial flow modeling

Introduction

Numerical simulation of the atomization process requires accurate capturing of the complex deforming liquid–gas interfaces. Special types of numerical techniques are needed for this type of flows, which have sharp moving and deforming interfaces. The solution of these types of flows is complex since the boundary between the two phases is not known *a priori* and it is part of the solution. In addition, the problem usually involves fluid flows with very large density, viscosity, and velocity ratios. This makes the solution of the governing partial differential equations (PDEs) very difficult. Several numerical techniques are developed to tackle this complex fluid flow. They can be categorized based on the type of flow modeling (Eulerian, Lagrangian,

N. Ashgriz
Department of Mechanical and Industrial Engineering, University of Toronto, Toronto, ON, Canada
e-mail: ashgriz@mie.utoronto.ca

N. Ashgriz (ed.), *Handbook of Atomization and Sprays*,
DOI 10.1007/978-1-4419-7264-4_17, © Springer Science+Business Media, LLC 2011

or mixed), type of interface modeling (capturing or tracking), flow– interface coupling (integrated or segregated), and the type of spatial discretization (meshless, finite difference, finite volume, finite element [FE], or others).

Generally, standard numerical techniques, which are used for confined flows, such as the finite element (FE), finite volume (FV), and finite difference (FD) methods, can also be used to simulate interface flows. However, special techniques have to be used to deal with the unknown location of the fluid interfaces. There are two main categories of the interface solvers. The first category of methods involves mesh motion and deformation while the second group is based on fixed grids. In the moving mesh methods, the grid points move according to the local flow characteristics. In most cases where all grid points are moved, the method is Lagrangian; otherwise, it is a mixed Lagrangian–Eulerian approach. This includes methods such as FE-based Lagrangian [1], interface fitting (or boundary-fitted coordinate) [2], and boundary integral (BI) [3] methods. In these methods, the grid points near the interface essentially play the role of marker points. Thus, these techniques are confronted with difficulties when applied to large surface deformations, surface breaking, and merging.

In the interface fitting methods (Fig. 17.1a), the mesh is fit on the interface and it is moved in time using some iterative methods for the convergence of the conservation equations. These methods are mainly applicable to interfaces with small deformations, and are difficult to use in flows with large interface deformations. Mesh regenerations are necessary when mesh cells and elements become highly skewed, to prevent computational failures. This can make the interface fitting scheme and other moving mesh techniques very complicated and inefficient.

The fixed grid methods have been more successful and, therefore, more commonly used in flows with large interface deformations. Fixed grid methods can have pure Eulerian or combined Lagrangian–Eulerian framework. In the fixed grid method, an extra indicator is introduced in order to track the interface. These methods are characterized based on the type of indicator used and are divided into three main categories: interface capturing (Fig. 17.1b), interface tracking

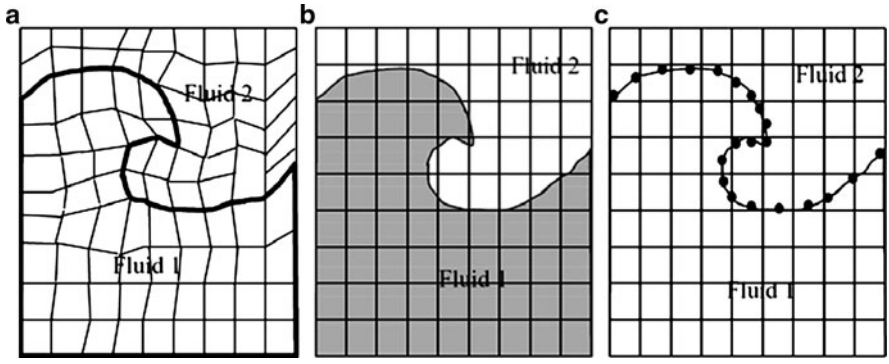


Fig. 17.1 Different interfacial flow solution methodologies: (**a**) interface fitting, (**b**) interface capturing, and (**c**) interface tracking [4] (Recopied from [4] with permission)

(Fig. 17.1c), and combined interface capturing–interface tracking techniques. Examples of interface capturing methods include marker and cell (MAC) [5], volume of fluid (VOF) [6, 7], level set (LS) [8], and diffuse interface (DI), or phase field [9] methods. The most widely used interface tracking method is Glimm's front tracking method [10]. The notable combined techniques which inherit both from interface capturing and interface tracking methods are Tryggvason's front tracking [11], sharp interface (SI) [12], immersed boundary (IB) [13] and immersed interface (II) [14] methods.

In general, interface capturing methods can handle complex interfacial regions more easily, but interface tracking methods give a more accurate description of the free surface because of their Lagrangian nature. In interface tracking methods, the position of the free surface is described in a direct way, either by specifying a set of marker points located on the free surface [10] or by introducing a height function which explicitly describes the free surface position [15]. Furthermore, in interface tracking schemes, implementation of the surface tension force is straightforward given the location and curvature of the free surface. The limitation of these methods, unlike interface capturing methods, is their inability to cope naturally with folding or rupturing interfaces.

In the interface capturing techniques, the interface motion can be reproduced using different approaches. In MAC, hundreds of massless marker particles are added to the fluid. These particles are then advected in the Lagrangian sense using the average of Eulerian velocities in their vicinity. In the VOF method, the use of volume fractions to mark the fluid regions is adopted because of its efficiency and simplicity and the natural way in which complex interfaces can be treated as internal moving boundaries. The volume fractions are convected through the flow domain by solving a scalar convection equation. In the LS method, a smooth distance function is used as the indicator function for the interface. A similar approach is taken in the DI method, by devising an equation which governs the continuity of mass concentration. The methods of using volume fractions, LS, or mass concentration are robust enough to handle the breakup and coalescence of fluid masses.

The advantage of LS and DI techniques over the VOF method is that their indicator functions are smooth, rather than discontinuous, and are easier to solve. Another advantage of LS and DI over MAC method is that these two techniques do not suffer from the lack of divisibility that discrete particles exhibit. There are highly accurate numerical schemes that can be applied to the LS equation. The disadvantage of the LS method, however, is that the LS needs to be reset periodically, which is not strictly mass-conservative. The DI method models interfacial forces as continuum forces by smoothing interface discontinuities and forces over thin but numerically resolvable layers. This smoothing allows the use of conventional numerical approximations, sometimes even central differencing, of interface kinematics on fixed grids with acceptable accuracy. This is because the DI method relies on physical mechanisms it is based upon rather than special numerical schemes to capture the interface.

Given the shortcoming of different interface solution techniques such as interface tracking and capturing methods and considering their strengths, progress has been made by combining different methods and taking advantage of the best features of each technique while removing or alleviating their drawbacks. A class of promising techniques is the combined Eulerian–Lagrangian methods which have the potential to deliver both accuracy and efficiency. The interface is tracked explicitly as curves (or surfaces in 3D). The computations are performed on fixed meshes whose topology is independent of that of the interface. One example of this type of method is the IB technique used for a range of multi-fluid problems [11, 12] and for fluid–structure interaction problems. While explicitly tracking the interface, this method transmits the information regarding the discontinuity across the interface to the grid in much the same way as purely Eulerian methods, i.e., by casting the surface forces into a body force term in the governing equations. Therefore the solution reverts to a single-fluid approach, i.e., the solver does not see a discontinuity at the location of the interface, but experiences distributed forces and material properties in the vicinity of the interface. On the other hand, the cut-cell treatment [12] proceeds to reconstruct the domain on either side of the interface with attention to the IB and its geometry overlying the grid. Phases are treated separately and no smearing of the interface takes place at the formulation level.

In the following sections, different formulations of some popular interfacial flows are presented.

Fluid Flow Formulations

Consider an arbitrary control volume Ω having two sub-volumes Ω_1 and Ω_2 separated by an interface Γ. The flow equations can be written in two different forms: two-fluid and single-fluid.

The two-fluid formulation consists of solving the governing equations in both fluids independently and then matching the interfacial boundary conditions at the interface, which usually requires an iterative algorithm. This approach keeps the interface as a discontinuity, consistent with the continuum mechanics concept. For each phase, we can write the following momentum equation along with the incompressibility constraint:

$$\begin{aligned} &\frac{D(\rho_i \mathbf{u}_i)}{Dt} = \nabla \cdot \Pi_i + \rho_i \mathbf{g} \\ &\nabla \cdot \mathbf{u}_i = 0 \quad \mathrm{x} \in \Omega_i, \quad i = 1, 2 \end{aligned} \tag{17.1}$$

where D/Dt is the material derivative $\partial/\partial t + u_i \cdot \nabla$. The subscript i denotes fluids 1 and 2, respectively. The stress tensor is defined as:

$$\Pi_i = -p_i \mathbf{I} + \mu_i (\nabla \mathbf{u}_i + (\nabla \mathbf{u}_i)^T) \tag{17.2}$$

where ρ and μ are density and viscosity, respectively. The last term in (17.1) is the body force due to gravity and buoyancy effects. For a liquid–gas interface of the type observed in atomization processes, the fluid interface Γ is impermeable and assuming no mass transfer between the two fluids yields a continuous velocity condition at the interface

$$\mathbf{u}_1 = \mathbf{u}_2 \quad \text{for} \quad x \in \Gamma. \tag{17.3}$$

The jump in normal stresses along the fluid interface is balanced with the surface tension. Neglecting the variations of the surface tension coefficient, σ, gives the following Laplace–Young boundary condition for momentum conservation at the interface:

$$\Pi_1 - \Pi_2 = \sigma\kappa\mathbf{n} \quad \text{for} \quad x \in \Gamma \tag{17.4}$$

where σ is surface tension coefficient and $\mathbf{n}$ is the unit normal vector along the interface pointing outwards from fluid 2 into fluid 1. The curvature κ of the interface is given as $-\nabla \cdot \mathbf{n}$.

The two-fluid formulation requires computationally demanding iteration between the two fluids to satisfy the boundary conditions between them. Instead, a single-fluid approach can be used, in which one set of equations is solved in the whole domain making use of appropriate physical properties of each phase. The conservation of total momentum for the body of fluid in control volume Ω can be written as:

$$\int_{\Omega} \frac{D(\rho\mathbf{u})}{Dt}\, dx = \int_{\Omega} \nabla \cdot \Pi\, dx + \int_{\Gamma} \sigma\kappa\mathbf{n}\, ds + \int_{\Omega} \rho\mathbf{g}\, dx. \tag{17.5}$$

It is assumed that the velocity field is continuous across the interface and the interface boundary conditions are implicitly contained within the equation of motion.

In order to properly solve (17.5), sharp changes in the properties as well as pressure forces due to surface tension effects have to be resolved. In particular, surface tension results in a jump in pressure across a curved interface. The pressure jump is discontinuous and located only at the interface. This singularity creates difficulties when deriving a continuum formulation of the momentum equation. The interfacial conditions should be embedded in the field equations as source terms. Once the equations are discretized in a finite-thickness interfacial zone, the flow properties are allowed to change smoothly. It is therefore necessary to create a continuum surface force (CSF) equal to the surface tension at the interface, or in a transitional region, and zero elsewhere. Therefore, the surface integral term in (17.5) could be rewritten into an appropriate volume integral

$$\int_{\Omega} \sigma\kappa\delta(\chi)\nabla\chi\, dx \tag{17.6}$$

where χ is an indicator (or color) function which represents the location of the interface and $\delta(\chi)$ is a 1D Dirac delta function, which is equal to 1 at the interface and 0 elsewhere. After replacing the surface integral with obtained volume integral, the final form of the unsteady Navier–Stokes equations for a system consisting of two incompressible phases is

$$\frac{\partial(\rho\mathbf{u})}{\partial t} + \nabla\cdot(\rho\mathbf{u}\mathbf{u}) = \nabla\cdot\mathbf{\Pi} + \sigma\kappa\delta(\chi)\nabla\chi + \rho\mathbf{g} \tag{17.7}$$

with the incompressibility constraint

$$\nabla\cdot\mathbf{u} = 0. \tag{17.8}$$

The single-fluid approach has been undertaken utilizing Eulerian methods such as VOF, LS, and the mixed Eulerian–Lagrangian methods [11, 12]. For most interface capturing schemes, which use single-fluid formulation, an additional equation is solved to obtain the interface evolution and topology. This equation governs the advection of a variable that can be attributed to the interface. The equation of interface motion is

$$\frac{\partial\chi}{\partial t} + \mathbf{u}\cdot\nabla\chi = 0 \tag{17.9}$$

The scalar χ is defined differently in different interface capturing techniques. For example, χ is volume fraction in the VOF volume tracking method, a distance function in the LS method, or a Heaviside (step) function in the front tracking method.

The normal vector and curvature are computed from the indicator function using the following formulas:

$$\mathbf{n} = \frac{\nabla\chi}{|\nabla\chi|}, \quad \kappa = -\nabla\cdot\mathbf{n}. \tag{17.10}$$

The physical properties, such as density and viscosity, used in the single-fluid approach are dependent on the value of χ in the cells throughout the computational domain. For example, if χ is a normalized color function such as volume fraction in the VOF method which changes between 0 and 1 throughout the domain, the following formulas determine the density and viscosity:

$$\rho = \rho_2 + (\rho_1 - \rho_2)\chi \tag{17.11}$$

$$\mu = \mu_2 + (\mu_1 - \mu_2)\chi \tag{17.12}$$

where subscripts 1 and 2 refer to the first and second fluids respectively.

Lagrangian Methods

Finite Element Methods

FE performs on either fixed or deforming spatial meshes (see Fig. 17.2a). Deforming meshes are more popular and are divided into three subcategories. One is based on a three-stage iterative cycle by guessing the location of the free surface, solving the governing equations, and updating the free surface. Iterations are repeated until the difference between the two successively updated free surface locations becomes less than some desired convergence tolerance. The second approach eliminates the iterations by introducing the position of the nodes on the free surface as a degree of freedom. The third technique is the height flux (HF) method. In this technique, neither are iterations involved for locating the free surface nor is one degree of freedom added to the set of the unknowns. The free surface is found by using the VOF inside the sub-volumes which are updated at any time step using the velocity field.

Interface Fitting Method

In the interface fitting, or boundary-fitted method (Fig. 17.1a), the interface is tracked by attaching it to a mesh surface which is forced to move with the interface.

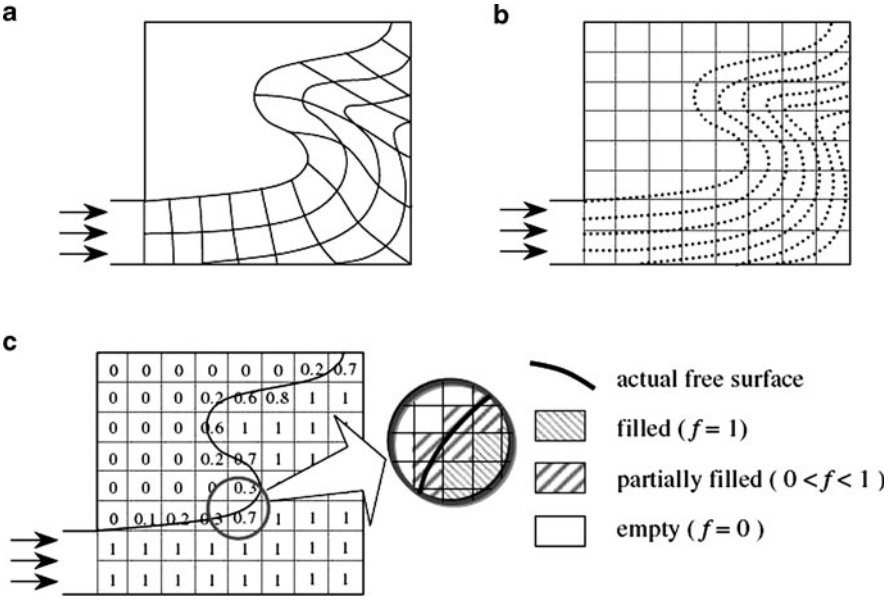


Fig. 17.2 Numerical methods for the fluid flow with moving free surface. Moving grids: (**a**) Lagrangian FE method, and fixed grids: (**b**) MAC method and (**c**) VOF method [16] (Courtesy of John Wiley and Sons)

This can be considered a Lagrangian mesh method. The motion of the free surface is accounted for by a coordinate transformation which maps the moving, body-fitted coordinate system in physical space to a uniformly spaced coordinate system in computational space. If the free surface becomes highly distorted, a new mesh may have to be generated in order to prevent both grid singularities and highly skewed grid point distributions.

Boundary Integral Method

The low Reynolds number approximation of the Navier–Stokes equations (also known as Stokes equations) is an acceptable model for a number of interfacial flow problems. For instance, the typical example of drop coalescence belongs to this case. A BI method [3] arises from a reformulation of the Stokes equations in terms of BI expressions and the subsequent numerical solution of the integral equations. This technique is further described in chapter 18.

Interface Capturing

Marker and Cell Method

The first method capable of modeling gas–liquid flows, separated by a moving interface, was the MAC method of Harlow and Welch [5]. In MAC method, as shown in Fig. 17.2b, the massless markers are used to define the location and track the movement of free surface. This is in fact a combination of an Eulerian solution of the basic flow field, with Lagrangian tracking of marker particles. The computational cycle in the MAC method consists of the advancement of discrete field variables from an initial time t_0 to the subsequent time $t_0 + \Delta t$ by accomplishing the steps below. The computation starts with a predictor–corrector algorithm for the determination of the velocity field at $t_0 + \Delta t$. In the predictor stage of the solution algorithm, the pressure is replaced by an arbitrary pseudo-pressure β (which in most cases is set equal to zero at full cells), and tentative velocities are then calculated. A pseudo-pressure boundary condition is applied in surface cells to satisfy the normal stress condition. Since pressure has been ignored in the full cells, the tentative velocity field does not satisfy the incompressible continuity equation. The deviation from incompressibility is used to calculate a pressure potential field ψ, which is then used to correct the velocity field [17]. In the final steps, the velocity boundary conditions are calculated, the new location of free surface is determined by tracking the markers, and the velocity boundary conditions associated with the new fluid cells are assigned (Fig. 17.3).

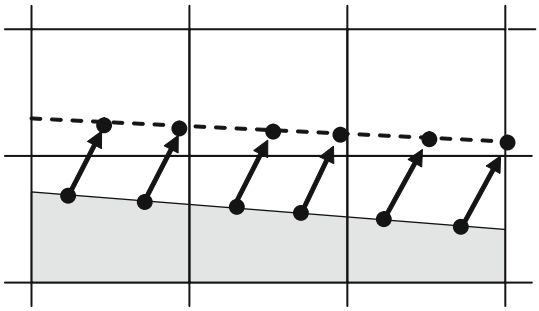


Fig. 17.3 Free surface in MAC family of interface tracking schemes. The circles represent surface markers. The interface is moved to a new location (dotted line) by first moving the marker particles and then reconstructing the interface using the new location of the markers

The MAC method, which allows arbitrary free surface flows to be simulated, is widely used and can be readily extended to three dimensions. Its drawback lies in the fact that it is computationally demanding to trace a large number of particles, especially in 3D simulation. In addition, it may result in some regions void of particles because the density of particles is finite. The impact of the MAC method is much beyond its interface capturing scheme. The staggered mesh layout and other features of MAC have become a standard model for many other Eulerian codes (even numerical techniques involving mono-phase flows).

Volume of Fluid (VOF) Technique

In the VOF method [6, 7], free surface is represented on the fixed grids using fractional fluid volume in a cell. Each rectangle in Fig. 17.2c denotes a unit cell. The fractional VOF, C, is defined such that it is equal to unity at any point occupied by the heavier fluid, and zero elsewhere. As the free surface moves, the fractional VOF of each cell is updated. In a numerical sense, every cell is classified into three categories according to the value of C (see Fig. 17.2c). If a cell is completely filled with fluid, the fractional VOF of the cell is unity ($C = 1$) and the cell is considered to be in the main flow region. If a cell is empty ($C = 0$), it belongs to an empty region and its contribution to the computation of flow field is excluded. A cell is considered to be on the free surface when the values of C lies between 0 and 1 ($0 < C < 1$). Discontinuity in C propagates according to equation 17.9, where χ is replaced with C [6, 7]:

$$\frac{\partial C}{\partial t} + \mathbf{u} \cdot \nabla C = 0. \tag{17.13}$$

By solving (17.13), the distribution of C is obtained and thus free surface location can be identified. In a physical sense, the equation implies mass conservation of one phase in the mixture. Numerically, this equation is characterized as a hyperbolic or pure convection equation.

The formulation of the VOF model requires that the convection and diffusion fluxes through the control volume faces be computed and balanced with source terms within the cell itself. The interface will be approximately reconstructed in each cell by a proper interpolating formulation, since interface information is lost when the interface is represented by a volume fraction field. The application of (17.13) to the interface cells is not trivial and requires certain knowledge of the interface shape. The problem of reconstructing an interface by using the volume fraction field data (updated or given at the start) has generated a multitude of approaches and methods. The geometric piecewise linear interface calculation (PLIC) scheme is commonly employed because of its accuracy and applicability for complex flows, compared to other methods such as the donor–acceptor, Euler explicit, and implicit schemes. An interface is viewed as comprised of line segments. This is acceptable when the grid system is fine enough. Inside of each cell, this line segment determines uniquely what the volume fraction inside that cell is. However, the reverse correlation is not unique, since more than one location of the interface may determine the same volume fraction in the cell. One has to take into account a group of neighboring cells in order to reconstruct the interface accurately.

A VOF geometric reconstruction scheme is divided into two parts: a reconstruction step and a propagation step. The key part of the reconstruction step is the determination of the orientation of the segment. This is equivalent to the determination of the unit normal vector $\mathbf{n}$ to the segment. Then, the normal vector $\mathbf{n}_{i,j}$ and the volume fraction $C_{i,j}$ uniquely determine a straight line. Once the interface has been reconstructed, its motion by the underlying flow field must be modeled by a suitable algorithm.

In the PLIC method, the interface is approximated by a straight line of appropriate inclination in each cell. A typical reconstruction of the interface with a straight line in cell (i,j), which yields an unambiguous solution, is perpendicular to an interface normal vector $\mathbf{n}_{i,j}$ and delimits a fluid volume matching the given $C_{i,j}$ for the cell. A unit vector $\mathbf{n}$ is determined from the immediate neighboring cells based on a stencil $C_{i,j}$ of nine cells in 2D. The normal vector $\mathbf{n}_{i,j}$ is thus a function of $C_{i,j}$, $\mathbf{n}_{i,j} = \nabla C_{i,j}$.

Surface Tension Calculation in VOF Method

Modeling interfacial tension effects are important because it is a potentially large force which is concentrated on the interface. There are two different approaches to modeling surface tension forces. The first one is CSF defined as

$$F^{st} = \sigma\kappa\mathbf{n}\delta_s = \sigma\nabla\cdot\left(\frac{\nabla C}{|\nabla C|}\right)\frac{\nabla C}{[C]} \tag{17.14}$$

where the normal vector and curvature are calculated from (17.10). The Delta function is approximated as $\delta_s = |\nabla C|/[C]$ and $[C] = C_1 - C_2$ is the difference between maximum and minimum values of C.

The second approach is continuous surface stress (CSS) model where the surface force is expressed as the divergence of a surface tension tensor:

$$T = -\sigma(\mathbf{I} - \mathbf{n} \otimes \mathbf{n})\,|\nabla c|, \quad F^{st} = -\nabla \cdot T = \sigma \nabla \cdot \left(|\nabla c| \mathbf{I} - \frac{\nabla c \otimes \nabla c}{|\nabla c|} \right). \quad (17.15)$$

An advantage of the CSS model is that it does not explicitly contain the curvature term since curvatures calculated from VOF method are less accurate than those calculated from other methods such as LS. This is because curvature evaluation in effect requires the second derivative of the discontinuous volume fraction field. Therefore, care must be given in order to avoid errors in curvature calculations.

Since the movement of free surface is accomplished by solving (17.13) in the VOF method, instead of deforming the mesh as in the Lagrangian method or tracing marker particles as in the MAC method, an overall solution algorithm becomes simple and efficient. Combined with advantages of fixed grids which can accommodate complex geometry, the VOF method is adaptable to any existing CFD codes regardless of the solution methods such as FD, FV, or FE. For this reason, the VOF-based methods have been used extensively in the simulation of general free surface flow problems. There are several extended or modified versions of the VOF method [18]. If mass conservation is a design constraint, geometrically based algorithms tend to result rather than simpler algebraically based techniques. Geometrically based algorithms, on the other hand, tend to exhibit "numerical surface tension" when interface features are not resolved [19].

The basic idea behind the VOF method is to discretize the equations for conservation of volume in either conservative flux or equivalent form resulting in near perfect volume conservation except for small over- and undershoots. The main disadvantage of the VOF method, however, is that it suffers from the numerical errors typical of Eulerian schemes such as the LS method. The imposition of a volume preservation constraint does not eliminate these errors, but instead changes their symptoms replacing mass loss with inaccurate mass motion leading to small pieces of fluid nonphysically being ejected as flotsam or jetsam, artificial surface tension forces that cause parasitic currents, and an inability to accurately calculate geometric information such as normal vector and curvature. Due to this deficiency, most VOF methods are not well suited for surface tension-driven flows unless some improvements are made [20].

Level Set Method

In the LS method, the interface between the two phases is represented by a continuous scalar function $\phi(\mathbf{x}, t)$, which is set to zero at the interface, is positive on one side, and negative on the other. This way both phases are identified, and the

location of the physical interface is associated with the surface $\phi = 0$. The function ϕ is called the LS function and is typically defined as the signed distance to the interface; i.e., $\phi = -d(\mathbf{x}, t)$ on one side of the interface and $\phi = +d(\mathbf{x}, t)$ on the other, where $d(\mathbf{x}, t)$ is the shortest distance from the point $\mathbf{x}$ to the interface.

When the interface is advected by the flow, the evolution of the LS function is given by equation (17.10), in which χ is replaced with ϕ:

$$\frac{\partial \phi}{\partial t} + \mathbf{u} \cdot \nabla \phi = 0. \tag{17.16}$$

The LS (17.15) moves the interface along its normal vector field with the normal speed $v^n = \mathbf{u} \cdot \mathbf{n}$. Note that any tangential component will have no effect on the position of the front. Using the normal vector $\mathbf{n}$ given as $\nabla\phi/|\nabla\phi|$ we can rewrite (17.15) as

$$\frac{\partial \phi}{\partial t} + v^n |\nabla \phi| = 0. \tag{17.17}$$

This is called the *Hamilton–Jacobi* formulation and yields the motion of the front $\Gamma(t)$ with normal velocity v^n on the zero LS, $\phi = 0$.

In the LS formulation, the density and viscosity are typically interpolated across the interface as follows:

$$\rho(\mathbf{x}, t) = \rho_2 + (\rho_1 - \rho_2) H_\varepsilon(\phi(\mathbf{x}, t)) \tag{17.18}$$

$$\mu(\mathbf{x}, t) = \mu_2 + (\mu_1 - \mu_2) H_\varepsilon(\phi(\mathbf{x}, t)) \tag{17.19}$$

where subscripts 1 and 2 denote the values corresponding, respectively, to the two different phases. Here, $H_\varepsilon(\phi)$ is a smoothed Heaviside function, which is defined as:

$$H_\varepsilon(\phi) = \begin{cases} 0 & \text{if } \phi < -\varepsilon \\ (\phi + \varepsilon)/(2\varepsilon) + \sin(\pi\phi/\varepsilon)/(2\pi) & \text{if } |\phi| \le \varepsilon \\ 1 & \text{if } \phi > \varepsilon \end{cases} \tag{17.20}$$

where ε is a small parameter on the order of the size of a mesh cell close to the interface. By using the smoothed Heaviside function, one effectively assigns the interface a fixed finite thickness of 2ε, over which the phase properties are interpolated. Hence, the value of ε can be considered to be the half-thickness of the numerical interface.

The LS function will not necessarily remain a distance function as the front propagates. For large time computations this distortion will give a nonuniform thickness of the interface randomly causing distance over which fluid properties change and surface tension forces are distributed.

There are basically two reasons for this distortion. Standard differencing schemes introduce numerical diffusion to the initial distance function. This problem

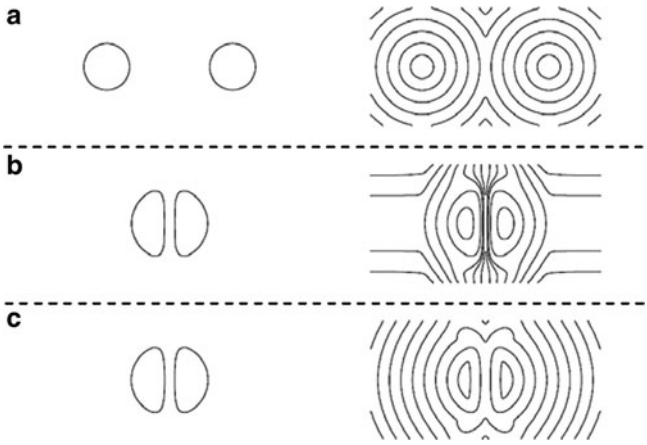


Fig. 17.4 Effect of reinitialization for two merging bubbles. *Left columns* show the interface and *right columns* show the contours of the LS function ϕ. (**a**) Initial configuration, (**b**) just before merging (time step $n = 100$) with no reinitialization, (**c**) just before merging ($n = 100$) with reinitialization back to a distance function [21]

can be reduced by using higher-order numerical methods. The second reason is that the flow field is very rarely of that character so that the LS function ϕ would be kept as a distance function. For example, the maximum and minimum values of the LS function will remain the same throughout the computations. For two merging interfaces (e.g., two bubbles) this will cause a steep gradient and an impenetrable sheet between the two merging interfaces (see Fig. 17.4). It is therefore necessary to reinitiate the distance function after each time step.

Reinitialization Procedure

Maintaining ϕ as a distance function becomes important for providing a uniform thickness at the interface with a fixed width in time and to avoid steep gradients. It is also essential that the LS function is reinitialized to a distance function without changing its zero LS. An iterative procedure is used to maintain ϕ as a distance function.

Immersed Boundary and Immersed Interface Techniques

The IB technique [22] is a combined Eulerian–Lagrangian method, in the sense that the flow is solved using a Eulerian approach on a fixed Cartesian mesh, and the interface is represented by a discrete set of points and advected in a Lagrangian

way. In this method, a single set of conservation equations valid for both phases is solved. The interface conditions are incorporated into the governing field equation as source terms using the CSF method [18]. As a result, the interface is considered to be of small nonzero thickness within which the values of the properties change smoothly. The IB method tracks the interface explicitly instead of reconstructing it as a posteriori measure. Furthermore, the fluid properties are not advected but prescribed based on the known interface position, therefore keeping the transitional zone on both parts of the interface constant and avoiding any numerical diffusion. This method is suitable for solving bubble and drop dynamics that often encounter large deformation, as has been proved in the existing literature.

In the IB method, the information between the moving interface and the field variables is exchanged through interpolation. Since the locations of the marker points in general do not coincide with the underlying grid points employed to solve the field equations, the velocity of the field equation, defined according to the Cartesian grid system, is interpolated to obtain the marker velocity. Furthermore, the interfacial force acting on the marker points is spread to the nearby grid points. The concept is illustrated in Fig. 17.5 [13]. The interpolations are performed via a discrete Dirac delta function taken in this study where the interface half-thickness of $\varepsilon = 2h$ with h as grid size is used.

The IB or II denoted by $C(t)$ (a curve in two dimensions or a surface in three dimensions) (see Fig. 17.5a) is represented by K markers of coordinates $\mathbf{x}_k(s)$ with $k = 1, 2, \ldots, K$. The markers are uniformly distributed along $C(t)$ at some fraction of the grid spacing, $0.5h < ds < 1.5h$. The interface is parameterized as a function of the arc length s by fitting quadratic polynomials $\mathbf{x}_k(s) = \mathbf{a}_k s^2 + \mathbf{b}_k s + \mathbf{c}_k$ through three consecutive marker points of coordinates $\mathbf{x}_{k-1}$, $\mathbf{x}_k$, $\mathbf{x}_{k+1}$.

The II method [23] is similar to the IB technique with some differences. The IB method uses a set of discrete delta functions to spread the entire singular force exerted by the IB to the nearby fluid grid points. However, the II method instead incorporates part of this force into jump conditions for the pressure, avoiding discrete dipole terms that adversely affect the accuracy near the IB.

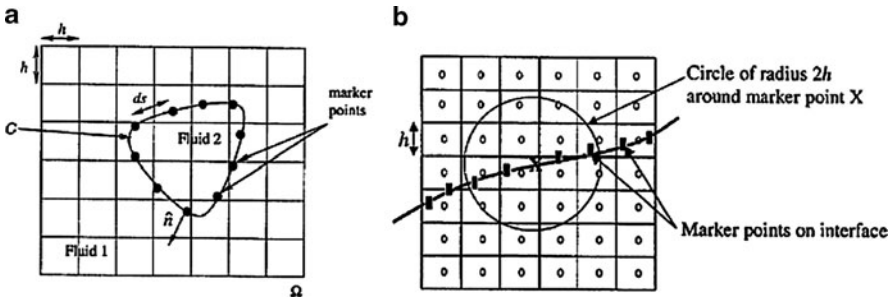


Fig. 17.5 IB method. (**a**) Illustration of a computational domain composed of two immiscible fluids. (**b**) Grid points considered for the interface velocity around the marker X [13] (Courtesy of Taylor & Francis)

Other Methods

There are other methods which are used in some studies of multiphase and interfacial flows. These include interface tracking methods, such as those of Glimm's front tracking method [10], where the discrete representation of the flow is based on a composite grid that consists of a spatial grid representing the flow field in the bulk fluid, together with a lower dimension grid that represents the fronts; combined interface capturing and interface tracking method, such as that of Tryggvason's hybrid method; and SI methods, which use two sets of equations to resolve the interface [24]. There are also a number of hybrid techniques which integrate different methodologies. These include (a) coupled LS–VOF (CLSVOF), which combines mass-conserving properties with accurate normal and curvature calculation of LS; (b) particle LS, which uses particles to enhance mass conservation; (c) mixed markers and VOF obtains a smooth motion of the interface, typical of the marker approach, with a good volume conservation, as in standard VOF methods; and (d) hybrid II–LS, where instead of tracking the interface explicitly, it captures the interface similar to the LS method (purely Eulerian technique). There are a number of other hybrid techniques which have been limitedly used.

Other methods include particle-based methods and also techniques that do not rely on the Navier–Stokes equation for flow solution. Particle-based methods are roughly divided into two main categories: those that use particles in conjunction with a grid, namely, particle-in-cell (PIC) methods, and those that are massless, such as the smoothed particle hydrodynamics (SPH). The most striking feature of particle-based methods is their ease of implementation. They are essentially as easy to implement on 3D unstructured meshes as on 2D structured meshes. However, they are very demanding in terms of memory and processing power, which has caused their limited use in interfacial flows so far.

There are methods which are not based on Navier–Stokes equations. These include molecular dynamics (MD) and lattice Boltzmann (LB) applied to two-phase flows. An MD study of any physical phenomena attempts to simulate the real behavior of nature by identifying each molecule and following their motion in time through the basic laws of classical mechanics. The system behavior and temporal evolution of its thermodynamic and transport properties are, therefore, nothing more than the cumulative result of individual molecular motion. The simulation of macroscopic multiphase flow phenomena such as droplet evaporation using MD is not yet possible due to the prohibitively large computational requirements both in terms of central processing unit (CPU) time and memory. However, a system involving a submicron droplet is small enough to successfully apply MD. Consolini et al. [25] studied evaporation of submicron droplets in a gaseous surrounding using MD.

The LB method [26] is a relatively new computational method for fluid dynamics. It is based on the foundations of kinetic theory and involves the solution of a kinetic equation, a simplified form of the Boltzmann equation.

This equation describes the evolution of the distribution of the population of particles whose collective behavior reproduces fluid behavior. The distribution of the population of particles is modified by the movement and collisions of the particles simulated on a lattice. This lattice restricts the movement and interaction of particles to selected discrete directions such that in the continuum, i.e., longer length and time scales, the collective behavior of the particle populations correspond to the dynamics of fluid flow described by the Navier–Stokes equations. In contrast to the conventional computational methods for fluid dynamics, which solve macroscopic equations, the LB method effectively simulates macroscopic fluid flow by solving the kinetic equations at the mesoscopic level. This modeling of physics at a smaller scale relative to the macroscopic scale enables it to naturally incorporate physical properties needed to compute complex flows. In the case of multiphase flows, phase segregation and interfacial dynamics can be simulated by incorporating appropriate intermolecular attraction forces or by employing concepts based on the free-energy approach. LB-based methods do not track interfaces, but can maintain SIs without any artificial treatments. Also, the LB method is accurate for the mass conservation of each component fluid. Recently, Inamuro et al. developed an LB method which is applicable to real interfacial flows with density ratios as high as 1,000 [27].

Numerical Modeling of Atomization Process

The atomization process requires capturing of the highly turbulent liquid–gas interfaces. The application of free surface flows to the atomization process is still at its infancy and, here, only some of the recent works are presented.

A method based on both VOF and LS techniques in combination with large eddy simulation for the turbulent flows is used to simulate the atomization of a liquid jet exiting a nozzle [28, 29]. The following figures show a jet exiting a nozzle with a 2.2 mm diameter at various velocities. Figure 17.6 shows a turbulent jet with an initial velocity of 9 m/s entering into a stagnant ambient. Figure 17.7 shows the atomization of a jet discharging into high-pressure air. The nozzle diameter is 150 μm, with injection velocities of 250 m/s and air pressure of 3 MPa. Figure 17.8 shows the liquid core for the same jet but at a higher velocity of 500 m/s.

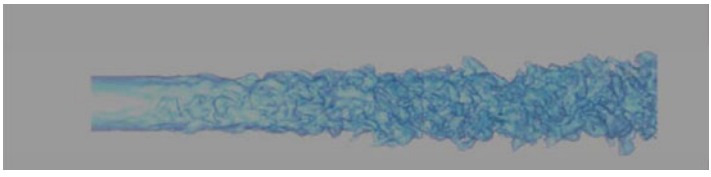


Fig. 17.6 A turbulent jet with exit velocity of 90 m/s injected into stagnant ambient air [28]

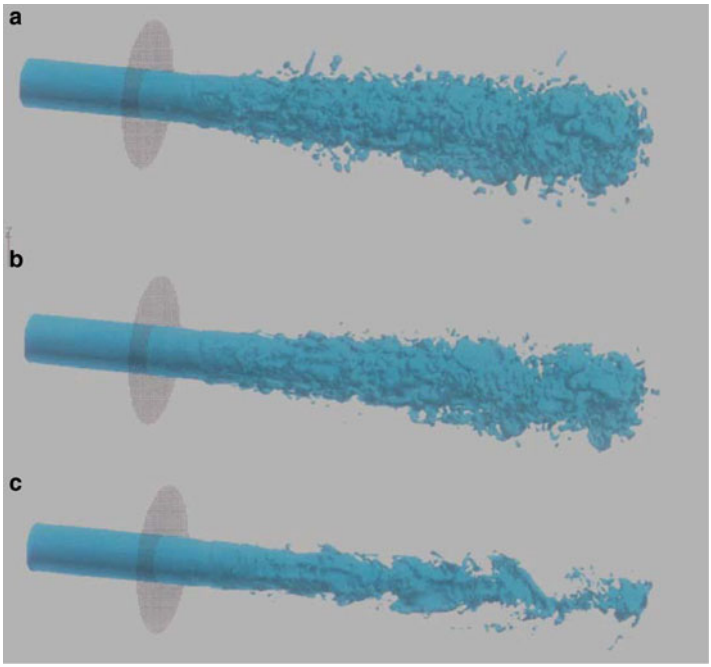


Fig. 17.7 Turbulent liquid jet entering high-pressure air at exit velocity of 250 m/s. (**a**) atomized mass, (**b**) liquid interface, and (**c**) liquid core

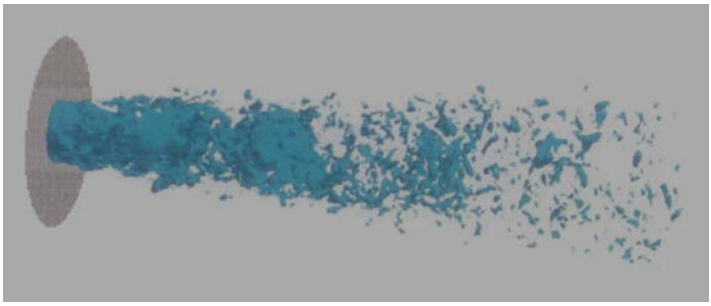


Fig. 17.8 Turbulent liquid jet entering high-pressure air at exit velocity of 500 m/s

In this figure the small separated droplets are removed and only the liquid core is shown.

Finally, with the aid of supercomputers, it is now becoming possible to simulate the process of atomization directly. One such simulation is provided in Fig. 17.9 by Shinjo and Umemura [30]. They used direct numerical simulation with up to 6 billion grid points to obtain a grid resolution of 0.35 μm. They simulated the

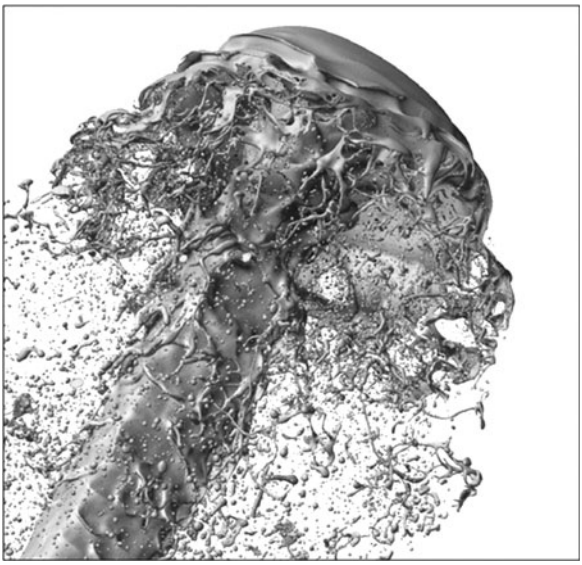


Fig. 17.9 Direct numerical simulation of a liquid jet at high speed injected into still air [30] (Courtesy of Elsevier)

primary atomization of a jet liquid injected at high speed into still air by direct numerical simulation. With sufficient grid resolution, ligament and droplet formations were captured as shown in Fig. 17.9.

References

1. Fukai J, Zhao Z, Poulikakos D, Megaridis CM, Miyatake O (1993) Modeling of the deformation of a liquid droplet impinging on a flat surface. Physics of Fluids A 5(11):2588–2599
2. Raymond F, Rosant JM (2000) A numerical and experimental study of the terminal velocity and shape of bubbles in viscous liquids. Chemical Engineering Science 55:943–955
3. Pozrikidis C (1992) Boundary-integral and singularity methods for linearized viscous flow. Cambridge University Press, Cambridge
4. Veldman AEP (1979) Liquid sloshing under low-g conditions: mathematical model and basic numerical method. NLR Report TR 79057 U, National Aerospace Laboratory, The Netherlands
5. Harlow FH, Welsh JE (1965) Numerical calculation of time dependent viscous incompressible flow with a free surface. Physics of Fluids 8:2182–2189
6. Hirt CW, Nicholls BD (1981) Volume of fluid (VOF) method for the dynamics of free boundaries. Journal of Computational Physics 39:201–225
7. Ashgriz N, Poo JY (1991) FLAIR: flux line-segment advection and interface reconstruction. Journal of Computational Physics 93(2):449–468
8. Osher S, Fedkiw RP (2001) Level set methods. Journal of Computational Physics 169:463–502
9. Anderson DM, McFadden GB, Wheeler AA (1998) Diffuse-interface methods in fluid mechanics. Annual Review of Fluid Mechanics 30:139–165

10. Glimm J, Grove JW, Li XL, Shyue KM, Zhang Q, Zeng Y (1998) Three-dimensional front tracking. SIAM Journal of Scientific Computing 19:703–727
11. Tryggvason G, Bunner B, Esmaeeli A, Juric D, Al-Rawahi N, Tauber W, Han J, Nas S, Jan YJ (2001) A front tracking method for the computations of multiphase flow. Journal of Computational Physics 169:708–759
12. Udaykumar HS, Mittal R, Shyy W (1999) Computation of solid-liquid phase fronts in the sharp interface limit on fixed grids. Journal of Computational Physics 153:535–574
13. Francois M, Shyy W (2003) Computations of drop dynamics with the immersed boundary method, part 1: numerical algorithm and buoyancy-induced effect. Numerical Heat Transfer, Part B 44:101–118
14. Lee L, Leveque RJ (2003) An immersed interface method for incompressible Navier-Stokes equations. SIAM Journal of Scientific Computing 25:832–856
15. Zhao Y, Tan HH and Zhang B (2002) A high-resolution characteristics-based implicit dual time-stepping VOF method for free surface flow simulation on unstructured grids. Journal of Computational Physics 183:233–273
16. Kim MS, Lee W (2003) A new VOF-based numerical scheme for the simulation of fluid flow with free surface. Part I: new free surface-tracking algorithm and its verification. International Journal for Numerical Methods in Fluids 42:765–790
17. Chen S, Johnson DB, Raad PE (1995) Velocity boundary conditions for the simulation of free surface fluid flow. Journal of Computational Physics 116:262–276
18. Scardovelli R, Zaleski S (1999) Direct numerical simulation of free-surface and interfacial flow. Annual Review of Fluid Mechanics 31:567–603
19. Kothe DB (1997) Perspective on Eulerian finite volume methods for incompressible interfacial flows. LANL Report LA-UR-97–3559, Los Alamos National Lab., Albuquerque, NM
20. Jafari A, Shirani E, Ashgriz N (2006) An improved three-dimensional model for pressure calculation in volume tracking methods. International Journal of Computational Fluid Dynamics 21(2):87–97
21. Berthelsen PA (2002) A short introduction to the level set method and incompressible two-phase flow: a computational approach, NTNU Report, Norway
22. Peskin CS (1977) Numerical analysis of blood flow in the heart. Journal of Computational Physics 25:220–252
23. Li Z (1997) Immersed interface methods for moving interface problems. Numerical Algorithms 14:269–293
24. Ye T, Shyy W, Chung JN (2001) A fixed-grid, sharp-interface method for bubble dynamics and phase change. Journal of Computational Physics 174:781–815
25. Consolini L, Aggarwal SK, Murad S (2003) A molecular dynamics simulation of droplet evaporation. International Journal of Heat and Mass Transfer 46:3179–3188
26. Succi S (2001) The lattice Boltzmann equation for fluid dynamics and beyond. Clarendon Press, Oxford
27. Inamuro T, Ogata T, Tajima S, Konishi N (2004) A lattice Boltzmann method for incompressible two-phase flows with large density differences. Journal of Computational Physics 198: 628–644
28. Jafari A, Ashgriz N (2005) Turbulence effects on the interface evolution for high velocity liquid jets, Invited paper. In International Symposium on Heat Mass Transfer Spray Systems, Antalya, Turkey, Jun. 5–10
29. Jafari A, Ashgriz N (2005) A new formulation of interface equation for volume tracking on arbitrary meshes. In 18th Annual Conference on Liquid Atomization and Spray Systems, Irvine, CA, May 22–25
30. Shinjo J, Umemura A (2010) Simulation of liquid jet primary breakup: Dynamics of ligament and droplet formation, Int. J. Multiphase Flow 36:513–532

Chapter 18
Modeling Atomization Using Boundary Element Methods (BEM)

S.S. Yoon and S.D. Heister

Abstract This chapter reviews atomization modeling works that utilize boundary element methods (BEMs) to compute the transient surface evolution in capillary flows. The BEM, or boundary integral method, represents a class of schemes that incorporate a mesh that is only located on the boundaries of the domain and hence are attractive for free surface problems. Because both primary and secondary atomization phenomena are considered in many free surface problems, BEM is suitable to describe their physical processes and fundamental instabilities. Basic formulations of the BEM are outlined and their application to both low- and high-speed plain jets is presented. Other applications include the aerodynamic breakup of a drop, the pinch-off of an electrified jet, and the breakup of a drop colliding into a wall.

Keywords Bond number · Boundary element method · Drop impact · Electrified jet · Liquid jet · Pinch-off · Primary and secondary atomization

Introduction

The boundary element method (BEM) is among a class of modeling schemes that provide a Lagrangian tracking of a deforming free surface. In contrast to volume-based meshing schemes such as finite element methods, the BEM formulation results in a computational grid that lies entirely on the free surface (as well as any inflow and outflow boundaries demanded by a given topology) [1]. Because the computational nodes of the interior domain do not need to be tracked (interior fluxes are available through applications of appropriate kernels [2, 3]), computational cost is drastically reduced. The dimension of the computational mesh is reduced by one by the application of BEM, but not by the more traditional

S.S. Yoon (✉)
School of Mechanical Engineering, Korea University, South Korea
e-mail: skyoon@korea.ac.kr

N. Ashgriz (ed.), *Handbook of Atomization and Sprays*,
DOI 10.1007/978-1-4419-7264-4_18, © Springer Science+Business Media, LLC 2011

computational fluid dynamic calculation; for two-dimensional geometries, the BEM grid is simply a curved line. In problems with variable surface topology (such as atomization), this simplification becomes quite valuable because it reduces the number of computational nodes inside the surface.

Numerical approaches using the volume of fluid (VOF) method have also been applied to atomization problems [4, 5]. While these VOF-based approaches continue to improve their surface tracking capabilities with the aid of powerful computers, their inherent interpolative nature can introduce substantial inaccuracies in surface curvature estimations (and hence, capillary forces). As an example, a typical VOF calculation of a sloshing fluid in a tank [6] exhibits 1% error in preserving the liquid volume, while a BEM calculation has 0.01% volume error with a similar level of grid resolution [7]. Using 45 nodes, a typical BEM calculation involving nonlinear oscillations of a droplet gives a maximum volume error of 0.04%, while a comparable finite element method (FEM) calculation [8] using over 1,600 nodes produces a volume error of 0.8%.

Given its efficiency, BEM has been applied to a variety of problems involving large deformations of a free surface. Several solutions have been developed for problems related to the nonlinear evolution of water waves, [9–11] and for problems related to nonlinear deformations of both viscous and inviscid drops [12, 13]. BEM has been applied to several applications of creeping (Stokes) flows in liquid columns [14–16] and in annular layers [16]. Inviscid solutions have also been obtained for both infinite [16] and finite-length [13] liquid jet problems, as well as for dripping flows [13], fountains [13], and fluid sloshing problems [17].

For atomization processes in particular, BEM can be used to model the interaction between flows of fluids with different characteristics (e.g., liquid and gas) or energies. In most cases, this interaction flow physics is well explained by the inviscid instability theory of Kelvin–Helmholtz or Rayleigh–Taylor [18]. Because these instability theories are based on potential flow, inviscid-based BEM can be very effective in modeling such systems [11]. Although weak viscous effects can also be modeled by BEM [12], viscosity is typically neglected under the assumptions that surface tension forces are predominant and that boundary layers are thin. While there are fully viscous formulations of the BEM approach [19], these formulations necessitate volume integrals, and hence, a full volumetric mesh, thereby detracting from one of the main advantages of the technique. For these reasons, the majority of BEM solutions in atomization problems have employed the inviscid fluid assumption.

The BEM has been applied to many atomization/breakup regimes including Rayleigh, first wind-induced, second wind-induced, and atomization regimes [20] such as in the calculation of the dominant wave or drop sizes and their distributions. BEM enables nonlinear tracking of a jet in the Rayleigh regime where some infinitesimal disturbance within the jet is sufficient to form primary and satellite drops. For wind-induced waves where interfacial effects are important, BEM can account for the gas pressure effect on the shape of the interface using a standard two-phase flow formulation [1]. BEM can be extended even to the atomization regime where the surface topology is extremely complex [21–24].

Atomization of electrified jets has also been the subject of much attention by BEM modelers. A pinch-off [3] or explosive behavior [25] of an electrified droplet that exceeds the Rayleigh limit [26] is an important field of science, and BEM is a superior and efficient modeling tool. Instead of the gas phase, the electrostatic phase is generally considered the destabilizing force competing against surface tension. Normally, viscosity is neglected, though there are applications where viscosity is important [27]. As for other practical applications, BEM is commonly applied to describe the dynamics of cavitation bubbles [28–40], which erode ship propellers, pumps, pipelines, and turbines, and can be applied to modern medical technologies including ultrasonic cleaning, salmonella destruction, and treatment of kidney stones [41]. In terms of numerical computation, the dynamics of these bubbles, such as their growth, deformation, collapse, and jetting, is no different from that of an atomizing liquid. Similarly, the drop impact phenomenon can also be considered as an atomizing phenomenon in splashing, which occurs after the snap-off of the rising corona from a spreading rim following an impact. Relevant BEM applications were provided by Yarin and Weiss [42], Weiss and Yarin [43], Davidson [44, 45], and Park et al. [46].

Despite some unique computational issues and assumptions, BEM computation appears to accurately predict many of the physical phenomena that were observed in experiments. In this article, we provide a standard description of the BEM formulation and review several applications of BEM to typical atomization scenarios.

Model Development

Governing Equations

Our interest lies in developing a model which can address capillary (surface tension) forces at the interface. By choosing the liquid density (ρ_l), the size/height of the liquid body (a) and the farfield velocity (U) as dimensions, the gas/liquid density ratio

$$\varepsilon = \frac{\rho_g}{\rho_l} \tag{18.1}$$

and the Bond and Weber numbers based on gas and liquid densities, respectively

$$Bo = \frac{\rho_l g a^2}{\sigma}, \quad We_g = \frac{\rho_g U^2 a}{\sigma}, \quad We_l = \frac{\rho_l U^2 a}{\sigma}, \tag{18.2}$$

become the three dimensionless parameters characterizing the flowfield. Here, the Weber number measures the ratio of the inertial forces imposed by the gas and liquid phase to the surface tension (σ) forces. In the following development, we presume that the non-dimensionalization described above has been applied.

We assume that both phases can be represented as incompressible, inviscid fluids. In this case, a velocity potential (whose gradient is simply the velocity) exists. Let ϕ and ϕ_g represent the velocity potentials in the liquid and gaseous phases, respectively. Continuity requires that both the velocity potentials satisfy the Laplace equation:

$$\nabla^2\phi = \nabla^2\phi_g = 0. \tag{18.3}$$

BEM formulation begins with an integral form of (18.3). For the liquid domain we obtain

$$\alpha\phi(\vec{r}_i) + \int_\Gamma \left[\phi\frac{\partial G}{\partial n} - qG\right]d\Gamma = 0 \tag{18.4}$$

where $\phi(\vec{r}_i)$ is the value of the potential at a point $\vec{r}_i$, Γ denotes the boundary of the domain, and G is the free-space Green's function corresponding to the Laplace equation. An analogous form of (18.4) can also be derived for the gas phase potential. For a well-posed problem, either ϕ or $q = \partial\phi/\partial n$ must be specified at each "node" on the boundary. Here n is the outward normal to the boundary, so q represents the velocity normal to the boundary. The quantity α in (18.4) results from singularities introduced as the integration passes over the boundary point $\vec{r}_i$.

Models have been developed for 2D, 3D, and axisymmetric flowfields. If we let r and z denote the radial and axial coordinates, respectively, and we denote the base point with subscript "i," Green's function solution to the axisymmetric Laplacian can be written as

$$G = \frac{4rK(p)}{\sqrt{(r+r_i)^2 + (z-z_i)^2}} \tag{18.5}$$

where

$$p = \frac{(r-r_i)^2 + (z-z_i)^2}{(r+r_i)^2 + (z-z_i)^2} \tag{18.6}$$

and $K(p)$ is the complete elliptic integral of the first kind. For computational efficiency, this quantity is calculated using a curve fit [47], which has an accuracy to 10^{-8}.

In the case of a 2D flow (letting x and y represent the coordinates), we have

$$G = \frac{1}{2\pi}\ln|\vec{r} - \vec{r}_i| = \frac{1}{4\pi}\ln\left[(x-x_i)^2 + (y-y_i)^2\right]. \tag{18.7}$$

A 3D description is provided in Chao [48]. To integrate G and $\partial G/\partial n$ over the surface Γ, the behavior of ϕ and q must be approximated along the length of each of

the elements within the integration path. Linear elements that assume linear variation in these quantities along a given segment are typically employed by most researchers.

For 2D flows, integration across a linear element segment can be carried out analytically. Singularities resulting from integration across a segment containing the base point are also integrable. In the case of axisymmetric flow, the integrations must be carried out numerically. In this case, we choose a four-point Gaussian quadrature for the evaluation of the integrals. Logarithmic singularities, which arise in the elliptic integral when the segment contains the base point, are treated with a special Gaussian integration designed to accurately treat this condition. Additional details regarding the numerical implementation can be found in Refs. [13, 49] for the axisymmetric and 2D cases, respectively.

Free Surface Treatment

The main challenge in developing models capable of tracking large deformations of an interface lies in the treatment of the free surface itself. Since capillary forces at the interface are important, it is crucial to develop a treatment capable of accurately determining the large deformations or curvature at all times during the simulation. For this reason, many models employ fourth-order centered differencing (on a generalized, variable spacing mesh) to determine surface curvature. The curvature is calculated based on coordinate derivatives as a function of the distance along the surface using the parametric representation of Smirnov [50].

The modeler has a choice between tracking the motion of the free surface nodes in a variety of directions [10]. In current models, we have opted to track the surface nodes along the local liquid velocity vector. Under this tracking assumption, for an axisymmetric situation, flow kinematics requires

$$\frac{Dz}{Dt} = \frac{\partial \phi}{\partial z} \quad \frac{Dr}{Dt} = \frac{\partial \phi}{\partial r} \tag{18.8}$$

where the notation $D(\,)/Dt$ implies a Lagrangian derivative for points on the surface moving at the local liquid velocity.

Recognizing that our BEM solver will return velocities normal to the surface, we employ the velocity transformations

$$\frac{\partial \phi}{\partial r} = \frac{\partial \phi}{\partial s}\sin(\beta) + q\cos(\beta), \quad \frac{\partial \phi}{\partial z} = \frac{\partial \phi}{\partial s}\cos(\beta) - q\sin(\beta), \tag{18.9}$$

where β is the local wave slope and $\partial\phi/\partial s$ is the velocity tangential to the local surface.

The dynamics of the interface is described by the unsteady Bernoulli equation. In an Eulerian system where time derivatives are assumed to occur at a fixed

spatial location, the dimensionless form of this Bernoulli relation for the liquid surface is

$$\frac{\partial \phi}{\partial t} + \frac{1}{2}(\nabla \phi)^2 + P_g + \frac{\kappa}{We} = 0 \tag{18.10}$$

where P_g is the gas pressure at the interface and κ is the surface curvature. The Eulerian–Lagrangian transformation for nodes on the interface moving at the liquid velocity is

$$\frac{D(\ )}{Dt} = \frac{\partial(\ )}{\partial t} + \nabla \phi \cdot \nabla(\ ). \tag{18.11}$$

Using this transformation, the Bernoulli equation in the liquid becomes

$$\frac{D\phi}{Dt} = \frac{1}{2}(\nabla \phi)^2 - P_g - \frac{\kappa}{We} \tag{18.12}$$

and an analogous treatment for the gas phase gives

$$\varepsilon \frac{D\phi}{Dt} = \varepsilon \nabla \phi \cdot \nabla \phi_g - \frac{\varepsilon}{2}\left(\nabla \phi_g\right)^2 - P_g. \tag{18.13}$$

Time Integration Scheme

Mathematically, (18.8), (18.12), and (18.13) provide a system of relations that describes the evolution of the surface shape (z,r or x,y) and velocity potentials for the unsteady motion of an interface. These equations are integrated in time using a fourth-order Runge–Kutta scheme [51]. This scheme has the advantage of a full fourth-order accuracy without the requirement of a knowledge of the *history* for a given nodal location; i.e., information at previous time levels is not required in the integration algorithm. This feature can be advantageous in calculations where a variable time step is employed or where the number of nodes along the free surface is not constant (caused by atomization events or surface re-gridding).

As mentioned, the main challenge in this problem is the development of a stable, consistent procedure to handle the coupled, nonlinear boundary conditions at the interface ((18.12) and (18.13)). More specifically, if we regard (18.13) as an expression for P_g, then an approximation for the derivative $D\phi_g/Dt$ is required. We have found that for a wide array of problems, it is adequate to approximate this derivative using a first-order forward difference scheme

$$\frac{D\phi_g}{Dt} = \frac{\phi_g^{i+1} - \phi_g^i}{Dt} \tag{18.14}$$

where superscript "i" denotes the time level.

The following procedure is implemented for the nodes on the free surface:

- At the start of a given time step, the value of ϕ is known. Using this value as a boundary condition on the interface, the liquid velocity of q can be determined by solving the Laplace equation (18.4).
- Since the gas nodes on the interface are fixed to move with the liquid nodes, this liquid velocity is used as the gas phase boundary condition $(q_g = -q)$ to calculate ϕ_g, value on the gas side of the interface.
- This gas phase velocity potential is then used in (18.13) to determine the gas pressure at the new time step using the approximation $D\phi_g/Dt$ given in (18.14).
- The gas pressure at the new time is then used in (18.12) to calculate the current $D\phi/Dt$, which is then integrated in time.

Since the nodes on the interface are allowed to move at their local velocity, over time they will tend to group themselves in regions of high curvature. This phenomenon leaves regions of lower curvature poorly defined. To alleviate this problem, the surface mesh is re-gridded using a series of cubic splines (for surface coordinates ϕ and ϕ_g) at each time to keep the spacing between the nodes constant along the surface. The Runge–Kutta integration scheme is well suited to this type of re-meshing, since it does not require information on the node positions at the previous time to predict the subsequent motion of the surface. Also, the surface can be "re-gridded" in this case since the approximation for $D\phi_g/Dt$ (18.14) involves only two time levels. If more accurate representations of this derivative are required, then re-gridding tends to destroy information about previous ϕ_g at given nodal locations.

Lastly, re-gridding does provide a natural "smoothing" of the surface. Many previous authors [10, 11, 47, 51] have been forced to implement the smoothing procedures to alleviate *zigzag* instabilities which develop on the surface after a large number of time steps. Often, the re-gridding procedure by itself provides smoothing of the surface (or any other functions associated with the surface). For these reasons, calculations using the methodology described above have very little numerical dissipation. In the following sections, we provide several examples to illustrate the results of the free surface treatment described above.

Examples

As mentioned, the distortion of the free surface in all primary breakup regimes can be modeled using BEM. Here we distinguish all of the primary breakup regimes into three major categories, namely, low-speed regime, moderate-speed regime, high-speed regime. Here, the "speed" implies the relative speed, and its quantity within a medium in which the liquid presides (i.e., gas) determines the regime change. By that it means that the gas/liquid density ratio is an important parameter, which essentially determines the rate of the destabilization of the jet; this fact is universally applicable to both flow situations of Kelvin–Helmholtz and

Rayleigh–Taylor. Also, BEM modeling of the secondary breakup of a primarily atomized droplet is briefly reviewed. Furthermore, the BEM modeling of atomization processes of electrified jets is discussed. The BEM modeling for a snap-off or atomization of the rising liquid rim from the drop impact phenomenon, known as the "crown," is also discussed.

Low-Speed Jet in Rayleigh Regime

Because of low speed, the relative velocity between the liquid and its surrounding gas is not sufficient enough to cause ripples on the free surface of liquid; thus, the aerodynamic effect is not important in the Rayleigh regime. The linear analysis by Lord Rayleigh [52] for low-speed jets predicts that the most dominant wave number and wavelength are $ka \sim 0.7$ and $\lambda \sim 9a$, respectively, given infinitesimal disturbances. Assuming that the cylinder length of $9a$ becomes a spherical drop, the radius of the drop is estimated around $R \sim 1.9a$, which is predicted by BEM [53]. In fact, BEM prediction is more accurate as it addresses the nonlinear effect which produces multiple crests per the dominant wave, eventually yielding satellites droplets whose radius is about $R \sim 0.67a$, according to the nonlinear analysis by Lafrance [54]. Figure 18.1 shows the BEM predictions for the main and satellite droplets, which are consistent with the experimental data of Rutland and Jameson [55] and Moses [56] and the analytic solution of Lafrance [54]. Mansour and

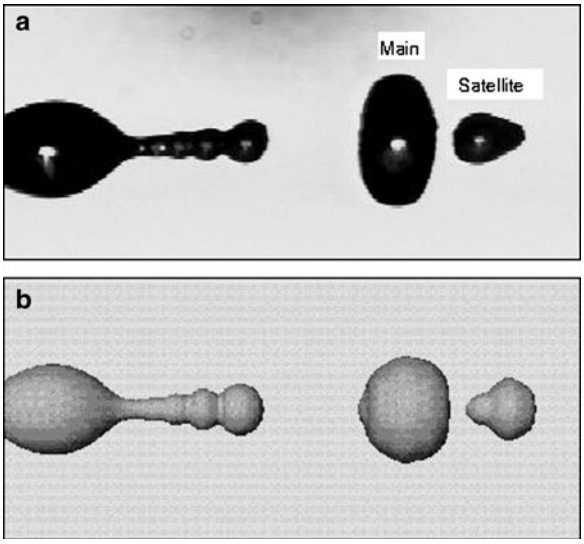


Fig. 18.1 Jet profile comparison near the pinch location in the Rayleigh regime. (**a**) Experiment of Moses, (**b**) BEM result, $We_1 = 17.6$, $Bo = 0.0109$, $ka = 0.447$ [53] (Courtesy of American Institute of Physics)

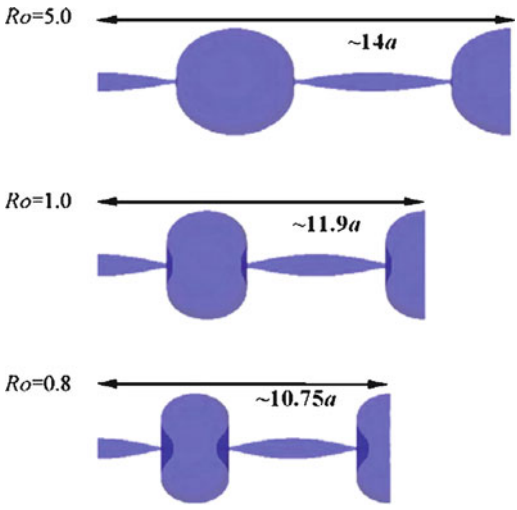


Fig. 18.2 Rotating liquid column jet profiles at the pinching condition for various Rossby numbers [57] (Courtesy of Elsevier)

Lundgren also utilized a similar BEM technique to model the nonlinear effect of a column jet subject to infinitesimal disturbances in the Rayleigh regime [51].

BEM was also applied to a study of a swirling column jet [57]. It appears that Ponstein [58] was the first author who considered the effect of swirl on the stability of a classical liquid jet/column. Ponstein's [58] analysis was so complete and original that his dispersion equation is deemed to be equivalent to the dispersion equations of Rayleigh [52], Weber [59], Levich [60], and Reitz and Bracco [61] for their specific cases when considering the non-swirling case. Ponstein's equation can also recover the Kelvin–Helmoltz and the Taylor equation for the limiting case of $ka \rightarrow \infty$, where the relevant wavelengths are much smaller than the jet diameter. Ibrahim [62] solved 1D unsteady Navier–Stokes equations for the swirling jet and showed that his numerical solutions were in agreement with Ponstein's linear theory. Figure 18.2 shows perspective views of the droplet formation condition at various Rossby numbers, Ro. The droplet shape is far from spherical at the pinch-off condition as the swirl strength increases. The main droplet deforms like a disk near $Ro = 0.8$, and finally becomes a doughnut shape because the droplet stretches in the radial direction by the centrifugal force.

Moderate-Speed Jet in Wind-Induced Regime

As the relative speed between the liquid and gas phases becomes large, the effect from this increased relative speed is reflected in the rapid destabilization of the liquid jet, generally with smaller length scale of atomized droplets. The relevant BEM simulation was carried out by Spangler et al. [63], who predicted the sizes of

the main and the satellite droplets for the liquid-based Weber numbers of 2, 850, 1,500; these results are shown in Fig. 18.3.

Figure 18.3 depicts the radii of the main and satellite drops versus the wave number of the disturbance for $\varepsilon = 0.00129$ and $We_l = 2$, 850, and 1,500. For $We_l = 2$, the main and satellite drops are of equal size for $k = 0.28$. Below this wave number, the satellite drops are larger than the main drops, and above this wave number, the main drops are larger than the satellite drops. At increased jet velocities (i.e., Weber numbers), the main drop radius decreases and the satellite drop correspondingly increases in size; this effect is attributed to the swelling phenomenon: at higher We_l values, the swelling in the trough region is more dramatic (particularly for lower k values), moving the pinch location closer to the peak and increasing the size of the satellite droplets. The study noted that the transition from the Rayleigh to the first wind-induced, and then the transition from the first wind-induced to the second wind-induced regimes occur at $We_g = 1.0$ and 2.5 (based on gas density, ρ_g, and jet radius, a), respectively. The study also confirmed that the aerodynamic forces become more important as the density ratio increases ($0.001 \leq \varepsilon \leq 0.1$) and that the jet becomes more unstable and has a shorter length upon breakup, results of which are consistent with the linear theory.

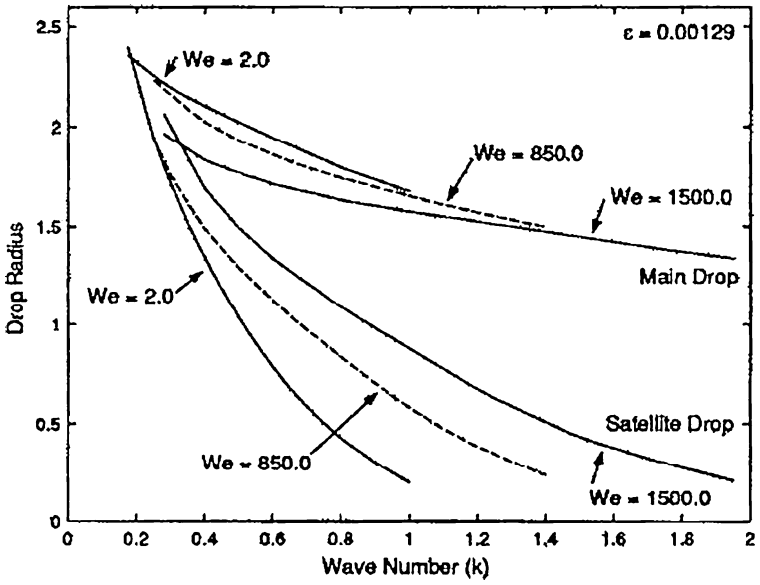


Fig. 18.3 Drop size versus wave number for gas/liquid density ratio of $\varepsilon = \rho_g/\rho_l = 0.00129$ and $We_l = 2$, 850, and 1,500 (based on liquid density, ρ_l, and jet radius, a) [63] (Courtesy of American Institute of Physics)

High-Speed Jet in Atomization Regime

Modeling a complex surface shape of liquid jets in the atomization regime via BEM was first performed by Heister's group [21, 64]. The model presumes that the internal flow condition prior to injection inside the nozzle, rather than the shear force due to the presence of gas outside, is the fundamental destabilizing source for causing atomization. This destabilizing source is modeled with an axisymmetric vortex ring causing a rollup motion at an emanating free surface. While providing a drastic simplification of the flowfield, the axisymmetric ring treatment is clearly the weak link in comparing results from this model with reality. Disturbances on high-speed jets tend to begin axisymmetrically, but will take on 3D azimuthal modes prior to the pinching of the axisymmetric waveforms. Current computational resources do not permit treatment of this more complex physics at the present time.

To further investigate this fundamental instability, the water jet case of Hoyt and Taylor [65] was benchmarked because their high-speed laminarized jet was immediately destabilized by the rollup motion due to the boundary layer instability [21]. Brennen's [66] inviscid solution for the Orr–Sommerfeld equation offered the dominant wavelength proportional to the momentum thickness $\lambda = (2\pi/\gamma)\ \delta_2$, where γ is the dimentionless frequency of 0.175 by Brennen [66]. The theory suggests that the wavelength should be $\lambda = d/14.8$ (note: d is the nozzle diameter) but experiments gave $\lambda_{exp} = d/13.8$ and the BEM predicted $\lambda_{exp} = d/19.4$, as shown in Fig. 18.4. Although the wavelength of the BEM simulation is somewhat smaller than the experimental result, it is evident that there is considerable difficulty in

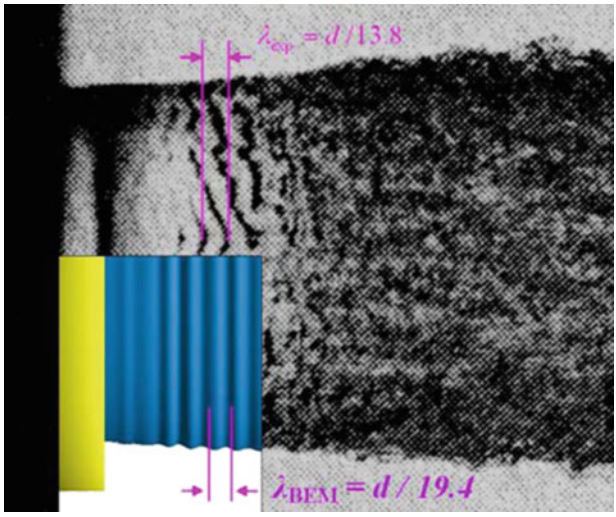


Fig. 18.4 Comparison of Hoyt–Taylor's experiment [65] and BEM simulation, the wavelengths of experiment and simulation are $\lambda_{exp} = d/13.8$ and $\lambda_{BEM} = d/19.4$, respectively (Courtesy of Elsevier)

assigning a single wavelength to the latter due to the 3D nature of the wave structure. Figure 18.5 provides a series of quasi-3D images produced by the BEM simulation [64] for the three different velocities studied previously. The nonlinear wave growth in the near orifice exit region shows a character similar to the experimental results.

When these ripples grow and eventually detach from the main liquid core/stream, they are considered *atomized*. The morphology of these individual droplets is unique and their initial shape has a profound effect on their subsequent secondary atomization, discussed in the following section.

Figure 18.6 provides a side-by-side comparison of an inviscid jet and a weakly viscous jet [64]. The BEM simulation [64] indicates that, though the diameter of the ligament is changed slightly, the viscosity does not have much influence on the statistical properties such as Sauter mean diameter (SMD), velocity, etc. At the droplet pinching level, viscosity is destabilizing, and many more drops are produced by the weak viscous model than by the inviscid result.

Another BEM modeling of a jet in the atomization regime was done by Park and Heister [24]. They simulated a swirling jet by using the superposition theory, which implements a complex potential containing a vortex. This potential vortex provides a vortical flow that acts as the circumferential pressure caused by the swirling. Annular ligaments pinched from the parent surface are presumed to break into the

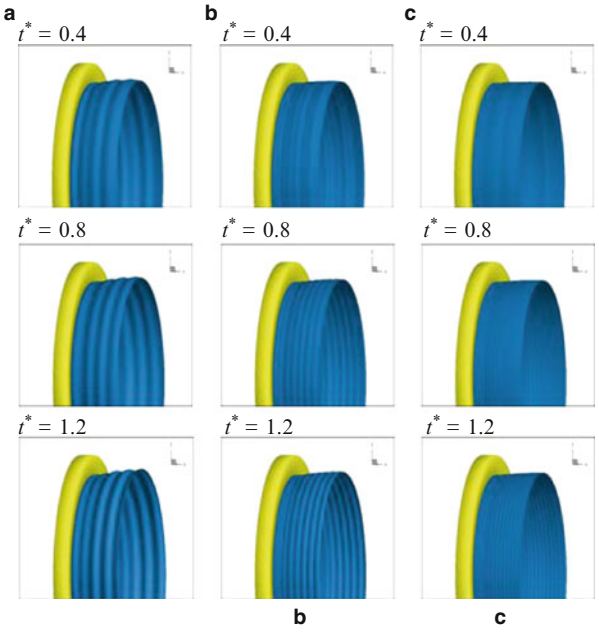


Fig. 18.5 Primary instability of high-speed water jet at various flow velocities [64]. (**a**) $U = 7$ m/s, (**b**) $U = 21$ m/s, and (**c**) $U = 63$ m/s for the nozzle diameter of $d = 2a = 6.35$ mm. Here dimensionless time is defined as $t^* = (U/a)\, t$ (Courtesy of Elsevier)

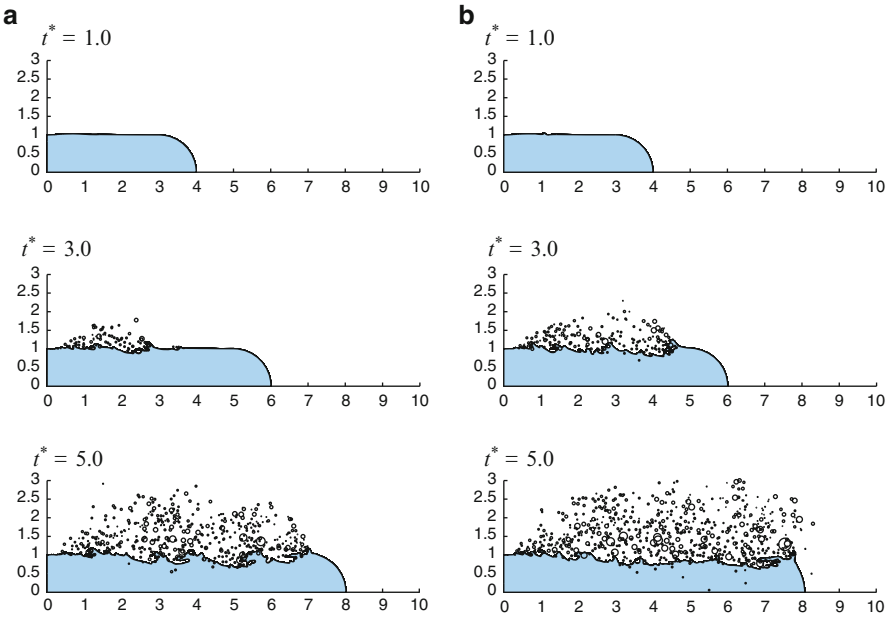


Fig. 18.6 BEM simulation [64] of Hoyt–Taylor water jet for (**a**) an inviscid case and (**b**) a viscous case (Courtesy of Elsevier)

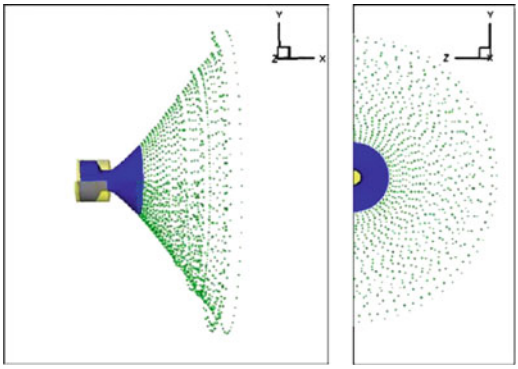


Fig. 18.7 Three-dimensional view of spray at $t^* = 10$ showing parent surface and atomization region for baseline case conditions noted in Bayvel and Orzechowski [67] (Courtesy of American Institute of Physics)

droplets, according to the linear stability analysis of Ponstein [58]. Droplets are tracked in a Lagrangian fashion according to their size, initial velocity, and atmospheric drag. In this fashion, a quasi-3D representation of the spray can be developed. Figure 18.7 shows the images from BEM simulations for a typical swirl injector designed by the monopropellant swirl injector design procedure outlined by Bayvel and Orzechowski [67]. The images assume that the droplets are uniformly distributed circumferentially from a given ring atomization event. The development

of the film breakup into shed droplets is accurately modeled, and the results are qualitatively similar with those of actual experimental images.

Secondary Atomization

In relatively high-speed atomization, the secondary breakup of a droplet is always followed by the primary breakup. This secondary breakup can also be modeled by a standard two-phase flow procedure of BEM [68]. Murray and Heister [68] identified the three major modes for the secondary breakup, namely, *nipple* ($1.1 < We_g < 2.5$), *kidney* ($2.5 < We_g < 3.0$), and *toroidal* ($We_g > 3.0$) mode. The time required for the breakup of these modes reduces substantially as We_g increases. For the *toroidal* mode, the droplet rapidly flattens in a plane perpendicular to the imposed acoustic disturbance. With increasing We_g, the overall diameter of the droplet (at the atomization point) increases, while the inner diameter of the torus decreases, as shown in Fig. 18.8. Here, the $We_g = 5.78$ case is shown at a reduced scale for display purposes. The droplet shapes at high We_g values are consistent with those at aerodynamic shattering, which has been documented by observing the response of a droplet to a shock wave [69].

Figure 18.9 shows another BEM simulation of the secondary breakup inside vacuum [23]. Because of the absence of gas, the nonlinearity in the initial shape of the shed droplet became a sufficient condition for the secondary atomization of the droplet without any external disturbances like air drag, as the simulation showed. The initial kinetic energy was large enough to overcome the surface tension.

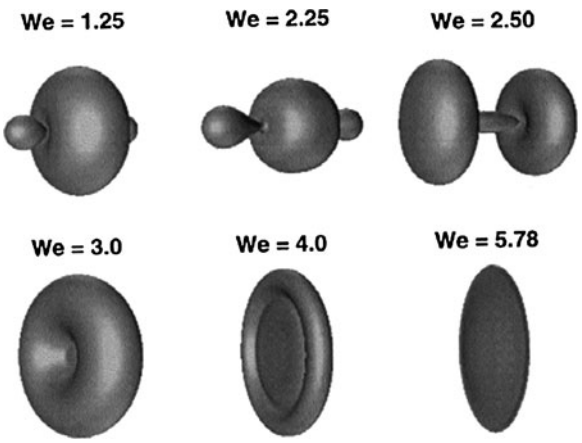


Fig. 18.8 Various breakup modes of a droplet exposed to acoustic disturbance at $\varepsilon = \rho_g/\rho_l = 0.00123$ and $\omega = \omega_n$. The Weber number is based on gas, We_g (Courtesy of Elsevier)

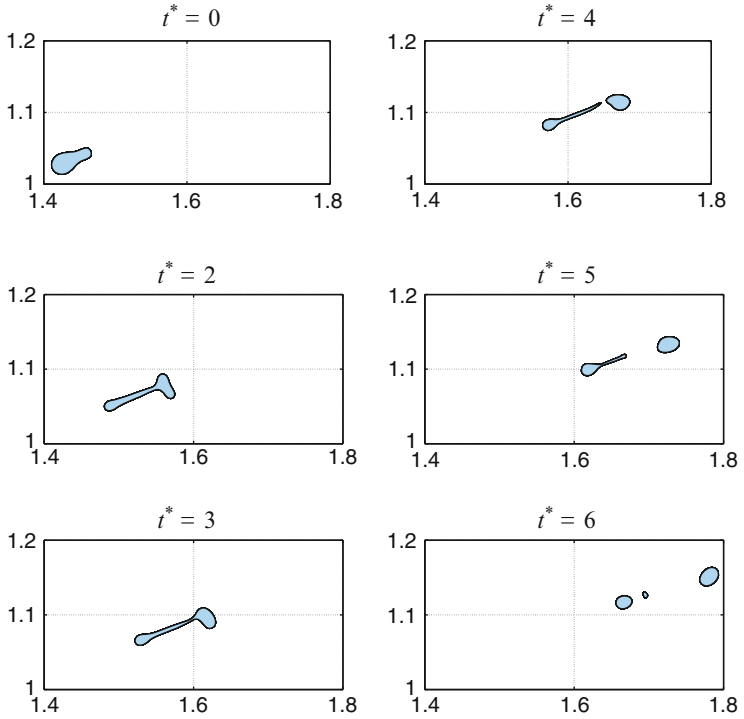


Fig. 18.9 Typical secondary breakup process of pinch-off ligament [23] (Courtesy of John Wiley & Sons)

Electrified Jet Atomization

Because of several distinctive advantages of an electrified jet (i.e., first, the droplet size of monodispersity can be easily manipulated by controlling voltage, flowrate, and conductivity; second, droplets are extremely fine and self-dispersive, which prevents droplet agglomeration but enhances wettability against the substrate adherence), it is used in many practical industrial applications ranging from agriculture to electric propulsion, bio-science such as in mass spectrometry, pharmaceutical powder coating, micro-fluidic technology, and nano-science. In these electrified jets, the ionization on the liquid free surface is the source of destabilization, which eventually leads to atomization. A few BEM simulations have been conducted for electrified liquid columns [3, 70] and droplets [71–75].

Setiawan and Heister [70] computed the nonlinear surface shape of an electrified axisymmetric column at various charging levels, as shown in Fig. 18.10. Because the voltage potential also obeys Laplace's equation for cases where charge migration to the body of the fluid is negligible, the BEM approach provides an elegant and efficient treatment of problems of this nature. The Setiawan and Heister simulations

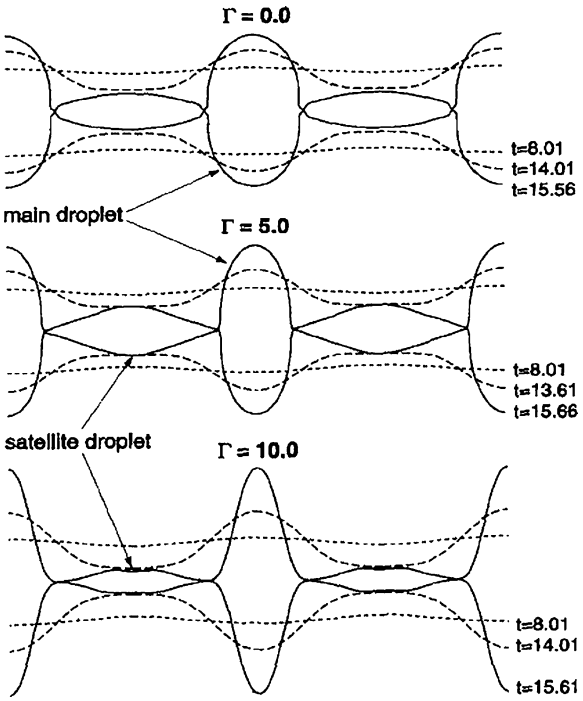


Fig. 18.10 Nonlinear jet evolution for various dimensionless charging levels, Γ ($ka = 0.6$, $b/a = 10$, where b is the ground location) [70] (Courtesy of Elsevier)



Fig. 18.11 (*Above*) Axisymmetric breakup of a weakly electrified jet in the experiments compared to (*below*) the results of the corresponding numerical simulation using a 1D model [76, 77] (Courtesy of Elsevier)

are consistent with the experiment and 1D simulation of Lopez-Herrera et al. shown in Fig. 18.11 [76, 77]. When the jet is uncharged, a flattening and broadening of the trough occurs in the nonlinear deformation range, followed by atomization of the wave into two droplets (typically termed "main" and "satellite" drops). This well-known process has been observed experimentally, and confirmed by nonlinear BEM simulations [51, 63]. The comparison of this result to the cases with electrostatic forces ($\Gamma_e = \epsilon_0 V^2/(\sigma a) = 5, 10$) shows the definite influence of the charging level on the shape of the surface in the nonlinear deformation range.

As for a charged droplet, probably the most striking phenomenon is the "spike" behavior at the pole of a stretching droplet that ejects atomized droplets whose mass constitutes less than 1% of the parent droplet, but carrying more than one third of the total charges. This "jetting" of the spike occurs when the droplet charge exceeds

the Rayleigh limits [26], $Q = 8\pi^2 \in_0 \sigma D^3$, that is, when the fissility $X = Q^2/(64\pi^2 \in_0 \sigma a^3)$ is greater than unity, where D and $\in_0$ are the droplet diameter and permittivity of free surface, respectively [25].

Betelu et al. [78] simulated, by using BEM, the changing topology of a charged droplet stretching to be an ellipsoid, as shown in Fig. 18.12. The shape of the jetting tip is somewhat similar to the Taylor cone [79], but its cone angle [25] was slightly narrower than the typical angle of the Taylor cone [79]. Figure 18.13 also shows the BEM simulations [3, 70] for the similar spike produced at the dominance of the electrostatic forces at relatively high charging levels. Depending on the level of initial deformation and the charging level, the shapes formed at this spike event vary. In these cases, capillary forces, which tend to broaden the sharp surface features, are overcome by Coulomb forces. For cases of larger Γ_e, the node at the

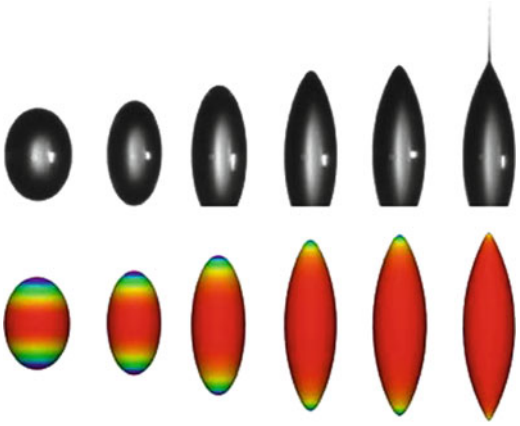


Fig. 18.12 An electrified droplet stretches into an ellipsoid and charge agglomeration at the tip/pole causes a spike to appear, eventually leading to jetting of atomized droplets [25, 78] (Courtesy of American Institute of Physics)

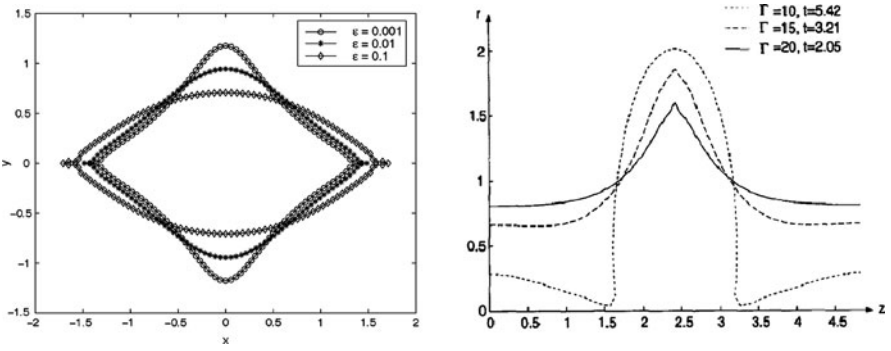


Fig. 18.13 Spike behavior at the tip of an electrified column. (**a**) Cross-sectional view of a 2D jet [3] showing the effect of initial deformation and (**b**) side view of an axisymmetric jet [70] showing the effect of charging level. The jet is disturbed at $ka = 1.3$ and $b/a = 10$ (Courtesy of Elsevier)

peak is traveling outward, while its nearest neighbors are traveling inward (toward the symmetry axis), and this behavior creates a tendency to shear off a tiny ring of fluid at the tip of the peak, whose phenomenon was experimentally observed by Cloupeau [80] and Kelly [81].

BEM can be extended to compute interior fluxes by taking the derivative of the velocity potential from the governing equation (18.4). Yoon et al. [3] computed the interior fluxes of the electrostatic field outside an electrified jet whose symmetric *sector* configuration is shown in Fig. 18.14. Assuming symmetry, they computed a sector of the multi-jets, which can produce extremely small (a few or sub-micron) droplets. The multi-jet mode enables multiple cone-jet operation (about 5–40 jets), which in turn increases the flow rate without sacrificing basic features of the eletrospray's cone-jet mode [82].

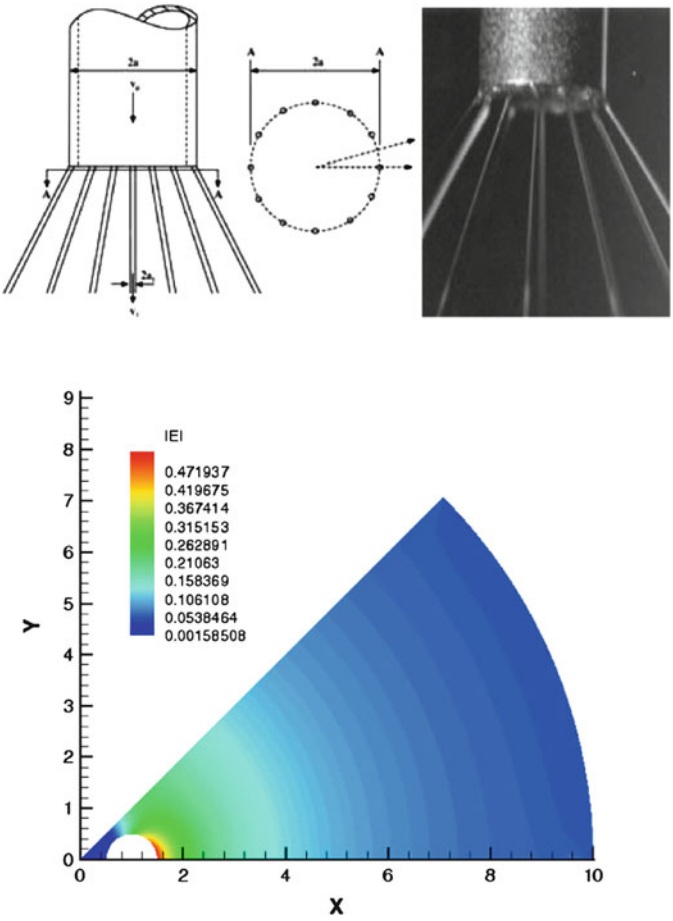


Fig. 18.14 Multiple cone-jet mode, its symmetric sector, and the interior electric field computation using the BEM [3] (Courtesy of Elsevier)

Atomization of Splashing Drop

BEM is also suitable for droplet splash modeling because it accurately tracks the changing morphology of the impacting drop, while the VOF approach tends to smear out the interface between the liquid and the gas. The pioneering BEM work for the droplet splash study was conducted by Yarin and Weiss [42] with subsequent relevant work by Weiss and Yarin [43], Davidson [44, 45], and Park et al. [46]. In most BEM modeling efforts, a droplet is initially assumed to be in contact with the impacting substrate or liquid film, which in turn precludes the compressed air effect [83]. Bang et al. [84] attempted to address air effects on droplet splashing. They introduced a quasi-3D model, [21–24] that is, application of the vortex ring instability analysis to the snap-off ring or rising corona to predict the number of splashed droplets. They qualitatively showed that the newly implemented quasi-3D model produced seemingly plausible results when their splash model predicted 56 atomized or splashed droplets while the corresponding experimental images indicated approximately 52 ± 2 splashed droplets at the rim of the crown, indicating a fairly good comparison between the model's prediction and the experiment (see Fig. 18.15).

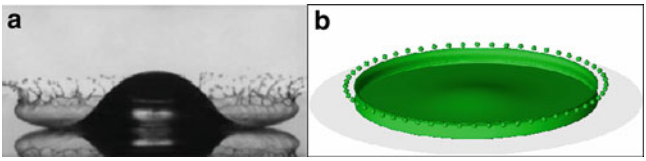


Fig. 18.15 (**a**) A snapshot of the splashing from zu et al.'s experiment. (**b**) Formation of the rising corona and the subsequent splashed droplets, whose number is predicted by the vortex ring instability theory of Ponstein [58]. The impact condition at which this simulation was carried out is based on the operating condition of Xu et al. [83] experiment: impact speed, $U = 3.74$ m/s; droplet radius, $a = 1.7$ mm; Weber number, $We_l = 838$; Bond number, $Bo = 0.998$

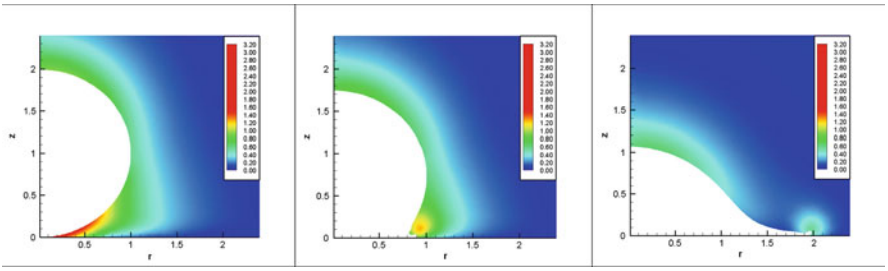


Fig. 18.16 The time series variation ($t^* = 0$, 0.25, and 1) of the gas flux contour outside the splashing droplet at $We_l = 200$. The induced gas flux reaches up to three times the drop's falling or impact speed (which is unity at the reference speed). The dimensionless time is defined as $t^* = (U/a)t$

They also computed the interior gas fluxes by taking derivatives of the velocity potential, which comprises the integral of the derivatives of Green's function of (18.4). The BEM computations showed that the escaping air velocity was more than triple the drop's impact speed. This escaping air provides sufficient destabilizing force to rupture the drop into splashing.

Figure 18.16 shows the induced speed of gas surrounding the collapsing drop. For high computational resolution, enough random points (5,000) were seeded into the region of interest. As consistent with the experiment [83], at the instant of impact (i.e., $t^* = 0$), the air is accelerated to a maximum speed of about $3.3U$ right beneath the droplet's bottom surface. This high air speed, suddenly generated at the drop surface, yields sufficient vorticity to provide the disturbance that eventually leads to splashing or atomization.

Acknowledgment This work was supported by the NRF Grant of Korea (2010-D00013 and 2010-0010217).

Nomenclature

a	Orifice or column radius
G	Free space Green's functions
k	Wave number
$K(p)$	Complete elliptic integral of the first kind
n	Coordinate normal to local
P	Pressure
q	Velocity normal to local boundary
r	Radial coordinate (axisymmetric flow)
s	Coordinate aligned with local surface
t	Time
We	Weber number
x	Axial coordinate (2D flow)
y	Transverse coordinate (2D flow)
z	Axial boundary singularity contribution
α	Boundary point singularity contribution
β	Surface slope
ε	Gas/liquid density ratio
$\in_0$	Permittivity of free space
V	Applied voltage
Γ	Domain boundary
κ	Surface curvature
ϕ	Velocity potential
ρ	Density
σ	Surface tension
ω	Frequency

Subscripts

$( )_g$	gas phase
$( )_l$	liquid phase

References

1. Heister, S. D.: Boundary element methods for two-fluid free surface flows, Eng. Anal. Boundary Elements 19, 309–317 (1997).
2. Yoon, S. S., S. D. Heister: Analytic solution for fluxes at interior points for the 2D laplace equation, Eng. Anal. Boundary Elements 24, 155–160 (2000).
3. Yoon, S. S., S. D. Heister, J. T. Epperson, P. E. Sojka: Modeling multi-jet mode electrostatic atomization using boundary element methods, J. Electrostat. 50, 91–108 (2001).
4. Gorokhovski, M., M. Herrmann: Modeling primary atomization, Ann. Rev. Fluid Mech. 40, 343–366 (2008).
5. Lebas, R., T. Menard, P. A. Beau, A. Berlemont, F. X. Demoulin: Numerical simulation of primary break-up and atomization: DNS and modeling study, Int. J. Multiphase Flow 35, 247–260 (2009).
6. Hung, R. J., C. C. Lees: Effect of a baffle on slosh waves excited by gravity-gradient acceleration in microgravity, Z Spacecraft Rockets 31, 1107–1114 (1994).
7. Class Project, A and AE 630, Stability of Free Surfaces, Purdue University School of Aeronautics and Astronautics, Professor Heister, 1994.
8. Foote, G. B.: A numerical method for studying drop behavior: simple oscillation, J. Comput. Phys. 11, 507–530 (1973).
9. Dold, J. W., D. H. Peregrine: Steep unsteady water waves, an efficient computational scheme. In Proceedings of the 19th Coastal Engineering Conference 1, Houston, ASCE (1984).
10. Ligguet, J. A., P. L. F. Liu: The boundary integral equation method for porous media flow, Allen & Unwin, London (1983).
11. Longuet-Higgins, M. S., E. D. Cokelet: The deformation of steep surfaces waves on water. I. A numerical method of computation, Proc. R. Soc. Lond. A 350, 1–26 (1976).
12. Lundgren, T. S., N. N. Mansour: Oscillations of drops in zero gravity with weak viscous effects, J. Fluid Mech. 194, 479–510 (1988).
13. Hilbing, J. H., S. D. Heister, C. A. Spangler: Boundary element method for atomization of a finite liquid jet, Atomization Sprays 5, 621–638 (1995).
14. Kelmanson, M. A.: Boundary integral equation solution of viscous flows with free surfaces, J. Eng. Math. 17, 329–343 (1983).
15. Tjahjadi, M., H. A. Stone, J. M. Ottino: Satellite and subsatellite formation in capillary breakup, J. Fluid Mech. 243, 297–317 (1992).
16. Newhouse, L. A., C. Pozrikidis: The capillary instability of annular layers and liquid threads, J. Fluid Mech. 242, 193–209 (1992).
17. Nakayama, T., K. Washizu: The boundary element method applied to the analysis of two-dimensional nonlinear sloshing problems, Int. J. Numer. Methods, Eng. 17, 1631–1646 (1982).
18. Chandrasekhar, S.: Hydrodynamic and hydromagnetic stability, Dover, New York (1981).
19. Pozrikidis, C.: Boundary integral and singularity methods for linearized viscous flow, Cambridge University Press, New York (1992).
20. Reitz, R. D., F. V. Bracco: Mechanism of atomization of a liquid jet, Phys. Fluids 25, 1730–1742 (1982).
21. Yoon, S. S., S. D. Heister: A nonlinear atomization model based on a boundary layer instability mechanism, Phys. Fluids 16, 47–61 (2004).
22. Yoon, S. S.: Droplet distributions at the liquid core of a turbulent spray, Phys. Fluids, 035103 (2005).
23. Park, H., S. S. Yoon, S. D. Heister: A nonlinear atomization model for computation of drop-size distributions and complete spray simulation, Int. J. Numer. Methods Fluids, 48, 1219–1240 (2005).
24. Park, H., S. D. Heister: Nonlinear simulation of free surfaces and atomization in pressure swirl atomizers, Phys. Fluids 18, 052103 (2006).

25. Duft, D., T. Achtzehn, R. Muller, B. A. Huber, T. Leisner: Rayleigh jets from levitated microdroplets, Nature 42, 128 (2003).
26. Rayleigh, L.: On the equilibrium of liquid conducting masses charged with electricity, Philos. Mag. 14, 184–186 (1882).
27. Reznik, S. N., A. L. Yarin, A. Theron, E. Zussman: Transient and steady shapes of droplets attached to a surface in a strong electric field, J. Fluid Mech. 516, 349–377 (2004).
28. Blake, J. R., D. C. Gibson: Cavitation bubbles near boundaries, Ann. Rev. Fluid Mech. 19, 99–123 (1987).
29. Sato, K., Y. Tomita, A. Shima: Numerical analysis of a gas bubble near a rigid boundary in an oscillatory pressure field, J. Acoust. Soc. Am. 95, 2416–2424 (1994).
30. Wang, Q. X., K. S. Yeo, B. C. Khoo, K. Y. Lam: Nonlinear interaction between gas bubble and free surface, Comput. Fluids 25, 607–628 (1996).
31. Yuan, H., A. Prosperetti: Gas-liquid heat transfer in a bubble collapsing near a wall, Phys. Fluids 9, 127–142 (1997).
32. Blake, J. R., M. C. Hooton, P. B. Robinson, R. P. Tong: Collapsing cavities, toroidal bubbles, and jet impact, Philos. Trans. R. Soc. Lond. A 355, 537–550 (1997).
33. Tong, R. P.: A new approach to modelling an unsteady free surface in boundary integral methods with applications to bubble-structure interactions, Math. Comput. Simul. 44, 415–426 (1997).
34. Tong, R. P., W. P. Schiffers, S. J. Shaw, J. R. Blake, D. C. Emmony: The role of 'splashing' in the collapse of a laser-generated cavity near a rigid boundary, J. Fluid Mech. 380, 339–361 (1999).
35. Zhang, Y. L., K. S. Yeo, B. C. Khoo, W. K. Chong: Simulation of three-dimensional bubles using desingularized boundary integral method, Int. J. Num. Methods Fluids 31, 1311–1320 (1999).
36. Tomita, Y., P. B. Robinson, R. P. Tong, J. R. Blake: Growth and collapse of cavitation bubbles near a curved rigid boundary, J. Fluid Mech. 466, 259–283 (2002).
37. Yasuda, A., H. Takahira, Numerical analysis of the dynamics of toroidal bubbles considering the heat transfer of internal gas, JSME Int. J. Ser. B 46, 600–609 (2003).
38. Xiao, Z., R. B. H. Tan: An improved model for bubble formation using the boundary integral method, Chem. Eng. Sci. 60, 179–186 (2005).
39. Makuta, T., F. Takemura: Simulation of micro gas bubble generation of uniform diameter in an ultrasonic field by a boundary element method, Phys. Fluids 18, 108102 (2006).
40. Tsiglifis, K., N. A. Pelekasis: Nonlinear oscillations and collapse of elongated bubbles subject to weak viscous effects: effect of internal overpressure, Phys. Fluids 19, 072106 (2007).
41. Obreschkow, D., P. Kobel, N. Dorsaz, A. Bosset, C. Nicollier, M. Farhat: Cavitation bubble dynamics inside liquid drops in microgravity, Phys. Rev. Lett. 97, 094502 (2006).
42. Yarin, A. L., D. A. Weiss: Impact of drops on solid surfaces: self-similar capillary waves, and splashing as a new type of kinematic discontinuity, J. Fluid Mech. 283, 141–173 (1995).
43. Weiss, D. A., A. L. Yarin: Single drop impact onto liquid films: neck distortion, jetting, tiny bubble entrainment, and crown formation, J. Fluid Mech. 385, 229–254 (1999).
44. Davidson, M. R.: Boundary integral prediction of the spreading of an inviscid drop impacting on a solid surface, Chem. Eng. Sci. 55, 1159–1170 (2000).
45. Davidson, M. R.: Spreading of an inviscid drop impacting on a liquid film, Chem. Eng. Sci. 57, 3639–3647 (2002).
46. Park, H. B., S. S. Yoon, R. A. Jepsen, S. D. Heister, H. Y. Kim: Droplet bounce simulations and air pressure effects on the deformation of pre-impact droplets using a boundary element method, Eng. Anal. Boundary Elements 32, 21–31 (2008).
47. Abramozwitz, M., F. A. Stegun (eds.): Handbook of mathematical functions, 9th edn., Dover, New York (1970).
48. Chao, C. C.: Boundary element modeling of 2d and 3d atomization, Ph.D. thesis, Purdue University (1999).

49. Rutz, M. W.: Boundary element model for the semi-infinite liquid jet, Masters thesis, Purdue University (1995).
50. Smirnov, V. I.: A course of higher mathematics, Volume II, Pergamon, New York (1964).
51. Mansour, N. N., T. S. Lundgren: Satellite formation in capillary jet break-up, Phys. Fluids A 2, 1141–1144 (1990).
52. Rayleigh, W. S.: On the instability of jets, Proc. Lond. Math. Soc. 10(4), 4–73 (1878).
53. Hilbing, J. H., S. D. Heister: Droplet size control in liquid jet breakup, Phys. Fluids 8, 1574–1580 (1996).
54. Lafrance, P.: Nonlinear breakup of a laminar liquid jet, Phys. Fluids 18, 428–432 (1975).
55. Rutland, D. F., G. J. Jameson: Theoretical prediction of the sizes of drops formed in the breakup of capillary jets, Chem. Eng. Sci. 25, 1689–1698 (1970).
56. Moses, M. P.: Visualization of liquid jet breakup and droplet formation, MS thesis, Purdue University (1995).
57. Park, H., S. S. Yoon, S. D. Heister: On the nonlinear stability of a swirling liquid jet, Int. J. Multiphase Flow 32, 1100–1109 (2006).
58. Ponstein, J.: Instability of rotating cylindrical jets, Appl. Sci. Res. 8, 425–456 (1962).
59. Weber, C.: Zum zerfall eines flussigkeitsstrahles, Z. Angew. Math. Mech. 11, 138–145 (1931).
60. Levich, V. G.: Physicochemical hydrodynamics, Prentice Hall, New Jersey, 639–646 (1962).
61. Reitz, R. D., F. V. Bracco: Mechanism of atomization of a liquid jet, Phys. Fluids 25, 1730–1742 (1982).
62. Ibrahim, E. A.: Effect of swirl on jet atomization, AIAA J. 31, Technical notes (1993).
63. Spangler, C. A., J. H. Hilbing, S. D. Heister: Nonlinear modeling of jet atomization in the wind-induced regime, Phys. Fluids 7, 964–971 (1995).
64. Park, H., S. D. Heister: A numerical study of primary instability on viscous high-speed jets, Comput. Fluids 35, 1033–1045 (2006).
65. Hoyt, J. W., J. J. Taylor: Waves on water jets, J. Fluid Mech. 83, 119–127 (1977).
66. Brennen, C.: Cavity surface wave patterns and general appearance, J. Fluid Mech. 44.
67. Bayvel, L., Z. Orzechowski: Liquid Atomization Taylor and Francis, Washington, DC (1993).
68. Murray, I. F., S. D. Heister: On a droplet's response to acoustic excitation, Int. J. Multiphase Flow 25, 531–550 (1999).
69. Hsiang, L. P., G. M. Faeth: Near-limit drop deformation and secondary breakup, Int. J. Multiphase Flow 18, 635–652 (1992).
70. Setiawan, E. R., S. D. Heister: Nonlinear modeling of an infinite electrified jet, J Electrostat. 42, 243–257 (1997).
71. Pelekasis, N. A., J. A. Tsamopoulos: Equilibrium shapes and stability of charged and conducting drops, Phys. Fluids A 2, 1328–1340 (1990).
72. Basaran, O. A., T. W. Patzek, R. E. Benner, L. E. Scriven: Nonlinear oscillations and breakup of conducting, inviscid drops in an externally applied electric field, Ind. Eng. Chem. Res. 34, 3454–3465 (1995).
73. Feng, Z. C., L. G. Leal: Numerical simulation of the dynamics of an electrostatically levitated drop, Int. J. Multiphase Flow 22, 93–120 (1996).
74. Feng, Z. C.: Instability caused by the coupling between non-resonant shape oscillation modes of a charged conducting drop, J. Fluid Mech. 333, 1–21 (1997).
75. Feng, Z. C., Y. H. Su: Numerical simulations of the translational and shape oscillations of a liquid drop in an acoustic field, Phys. Fluids 9, 519–529 (1997).
76. Lopez-Herrera, J. M., A. M. Ganan-Calvo, M. Perez-Saborid: One-dimensional simulation of the breakup of capillary jets of conducting liquids. Application to EHD spraying, J. Aerosol Sci. 30, 895–912 (1999).
77. Lopez-Herrera, J. M., A. M. Ganan-Calvo: A note on charged capillary jet breakup of conducting liquids: experimental validation of a viscous one-dimensional model, J. Fluid Mech. 501, 303–326 (2004).

78. Betelu, S. I., M. A. Fontelos, U. Kindelan, O. Vantzos: Singularities on charged viscous droplets, Phys. Fluids 18, 051706 (2006).
79. Taylor, G. I.: Disintegration of water drops in an electric field, Proc. R. Soc. Lond., Ser. A 280, 383 (1964).
80. Cloupeau, M., B. Prunet-Foch: Electrostatic spraying in cone-jet mode, J. Electrostat. 22, 135–159 (1989).
81. Kelly, A. J.: On the statistical quantum and practical mechanics of electrostatic atomization, J. Aerosol Sci. 25, 1159–1177 (1994).
82. Duby, M. H., W. Deng, K. Kim, T. Gomez, A. Gomez: Stabilization of monodisperse electrosprays in the multi-jet mode via electric field enhancement, J. Aerosal Sci. 37, 306–322 (2006).
83. Xu, L., W. W. Zhang, S. R. Nagel: Drop splashing on a dry smooth surface, Phys. Rev. Lett. 94, 184505 (2005).
84. Bang, B. H., Yoon, S. S., Kim, H. Y., Heister, S. D., James, S. C.: Assessment of gas and liquid velocities induced by an impacting liquid drop, Int. J. Multiphase Flow 37, in press (2011)

Chapter 19
Continuum-Based Methods for Sprays

F.X. Tanner

Abstract In this chapter, the mathematical description of spray processes is presented. After a brief summary of the basic mathematical concepts used, a discussion of the conservation equations is given, followed by a brief introduction to turbulence. Subsequently, a discussion of turbulence modeling is presented including Reynolds-averaged Navier–Stokes (RANS) and large eddy simulation (LES) modeling. Once this basic background is established, the discussion of the averaged or filtered conservation equations in conjunction with the liquid phase equations is given. The chapter ends with a discussion of the discretization of the equation system and the main algorithms used for the numerical solutions.

Keywords Atomization · Chemical reactions · Conservation equations · Constitutive equations · Drop breakup · Drop deformation · Drop collisions · Evaporation · LES · Newtonian fluids · RANS · Spray modeling · Spray PDF · Stochastic discrete particle method · Source terms · Turbulence

Introduction

Advances in computational technology have made continuum-based methods one of the most widely used approaches for the description of sprays. In this approach, the gas phase is formulated by conservation equations for mass, momentum, and energy, and the dispersed or liquid phase is described by a multidimensional distribution function. In most applications, the gas phase is turbulent and, therefore, plays an important role in almost every aspect of a spray.

The main purpose of this chapter is to give the mathematical formulation of spray processes, including reacting sprays. After a brief summary of the basic

F.X. Tanner
Department of Mathematical Sciences, Michigan Technological University, USA
e-mail: tanner@mtu.edu

N. Ashgriz (ed.), *Handbook of Atomization and Sprays*,
DOI 10.1007/978-1-4419-7264-4_19, © Springer Science+Business Media, LLC 2011

mathematical concepts required for the formulation of sprays, the general form of the conservation equations is introduced. This then leads to the specific field equations for isotropic Newtonian fluids considered in this chapter.

Due to the importance of turbulence in spray systems, this topic is treated in some detail. It includes a summary of time averaging and spatial filtering, followed by a description of RANS and LES turbulence modeling. The RANS model that is presented is the $k-\varepsilon$ turbulence model, and the LES SGS models that are outlined include the Smagorinsky model and the one-equation subgrid scale (SGS) model.

The remainder of the chapter focuses on the actual spray modeling. The exposition is primarily done for the RANS method, but with the indicated modifications, the methodology also applies to LES. The liquid phase is described by means of a probability density function (PDF). The various submodels needed to determine this PDF are derived from drop-drop and drop-gas interactions. These submodels include drop collisions, drop deformation, and drop breakup, as well as drop drag, drop evaporation, and chemical reactions. Also, the interaction between gas phase, liquid phase, turbulence, and chemistry is examined in some detail. Further, a discussion of the boundary conditions is given, in particular, a description of the wall functions used for the simulations of the boundary layers and the heat transfer between the gas and its confining walls.

Finally, computational aspects and numerical issues are considered. This includes a short description of the finite difference, the finite volume, and the finite element discretization methods. The chapter ends with some general comments.

The discussions in this chapter are far from comprehensive. Virtually every aspect of spray simulation is the subject of on-going theoretical, experimental, and computational investigations. Many of the topics are treated in more depth in individual chapters, as for instance, the atomization and drop breakup phenomena in Chap. 9. The evaporating model presented here applies only to one-component fluids. Multicomponent fluid evaporation is discussed in more detail in Chap. 12. Also, reacting sprays are discussed only at a rudimentary level in this chapter. In general, reacting sprays are very complex and there are different modeling approaches of various degrees of complexity. A more detailed discussion of combustion applied to sprays is given in Chap. 13.

Preliminaries

Notations, Definitions, and Basic Theorems

The *dot product* or *scalar product* of two vectors $\mathbf{a}, \mathbf{b} \in \mathbf{R}^n$, $\mathbf{a} = (a_1, \ldots, a_n)^T$ and $\mathbf{b} = (b_1, \ldots, b_n)^T$, is the scalar defined by

$$\mathbf{a} \cdot \mathbf{b} = \sum_{i=1}^{n} a_i b_i.$$

The superscript T denotes the transpose. The *Euclidean norm* of a vector $\mathbf{a} \in \mathbf{R}^n$ is given by

$$\|\mathbf{a}\| = \sqrt{\mathbf{a} \cdot \mathbf{a}} = \sqrt{\sum_{i=1}^{n} a_i a_i}.$$

Similarly, if $\mathbf{A}, \mathbf{B} \in \mathbf{R}^{n \times n}$ are matrices (or tensors of order two) with components A_{ij} and B_{ij}, then the *dot product* or *single contraction product* between a second-order tensor and a vector is the vector defined by

$$(\mathbf{a} \cdot \mathbf{B})_j = \sum_{i=1}^{n} a_i B_{ij} \text{ or } (\mathbf{A} \cdot \mathbf{b})_i = \sum_{j=1}^{n} A_{ij} b_j.$$

Note that the latter is just the usual matrix-vector multiplication.

The *dot product* between two tensors of order two is a tensor of order two defined by

$$(\mathbf{A} \cdot \mathbf{B})_{ij} = \sum_{k=1}^{n} A_{ik} B_{kj},$$

which corresponds to the usual matrix multiplication. Further, the *double contraction product* between two second-order tensors, also called the *scalar product*, is a scalar defined by

$$\mathbf{A}{:}\mathbf{B} = \sum_{i,j} A_{ij} B_{ji} = \text{tr}(\mathbf{A} \cdot \mathbf{B}),$$

where tr denotes the trace defined by $\text{tr}(\mathbf{A}) = \sum_i A_{ii}$.

The *tensor product* of two vectors, also called the *dyadic product*, is denoted by $\mathbf{a} \otimes \mathbf{b}$ or just $\mathbf{ab}$, and is an order two tensor with components

$$(\mathbf{a} \otimes \mathbf{b})_{ij} = (\mathbf{ab})_{ij} = a_i b_j.$$

The *gradient*, grad, of a multi-dimensional map, $\mathbf{f}: \mathbf{R}^n \to \mathbf{R}^m$ is the linear operator, grad $\mathbf{f} \in \mathbf{R}^{m \times n}$, with components

$$(\text{grad}\, \mathbf{f})_{ij} = \frac{\partial f_i}{\partial x_j} = \partial_j f_i = f_{i,j},$$

and the *divergence*, div $\mathbf{f}$, is the scalar-valued function

$$\text{div}\ \mathbf{f} = \sum_{i=1}^{n} \frac{\partial f_i}{\partial x_i}.$$

There are two basic mathematical facts that play a fundamental role in the derivation and understanding of the continuum formulation of sprays. The first is the divergence theorem, which relates surface integrals to volume integrals. The second is the Reynolds transport theorem, which shows that the time derivative of a volume integral with time-dependent boundary is equivalent to the same volume integral but of the convective derivative of the integrand.

More formally, let $\Omega(t)$ be a region in a body B with a piece-wise smooth boundary $\partial\Omega(t)$ and the outward unit normal vector $\mathbf{n}$. Further, denote by $\boldsymbol{\phi}(\mathbf{x}, t)$ a piece-wise continuous vector or tensor field defined on an open set containing Ω. Then the *Divergence Theorem* states that

$$\int_{\partial\Omega} \phi(\mathbf{x}, \mathrm{t}) \cdot \mathbf{n} \mathrm{d}A = \int_{\Omega} \mathrm{div}\phi(\mathbf{x}, t) \mathrm{d}V \tag{19.1}$$

where dA and dV denote the respective surface and volume elements. Further, let $G(t) = \int_{\Omega(t)} \gamma(\mathbf{x}, t) \mathrm{d}V$ be an additive physical quantity such as mass, momentum or energy, where the volume density $\gamma(\mathbf{x}, t)$ is defined on Ω. Then, the *Reynolds Transport Theorem* states that

$$\frac{\mathrm{d}G(t)}{\mathrm{d}t} = \int_{\Omega(t)} \left(\frac{\partial \gamma}{\partial t} + \mathrm{div}(\gamma \mathbf{u}) \right) \mathrm{d}V \tag{19.2}$$

where $\mathbf{u} = \mathbf{u}(\mathbf{x}, t) = \mathrm{d}\mathbf{x}/\mathrm{d}t$ is the velocity of the point $\mathbf{x}$. Note that by means of the vector identity

$$\mathrm{div}(\gamma \mathbf{u}) = \gamma \,\mathrm{div}\, \mathbf{u} + \mathbf{u} \cdot \mathrm{grad}\, \gamma \tag{19.3}$$

and the material derivative discussed in (19.5), the Reynolds transport theorem in (19.2) can be written as

$$\frac{\mathrm{d}G(t)}{\mathrm{d}t} = \int_{\Omega(t)} \left(\frac{\mathrm{d}\gamma}{\mathrm{d}t} + \gamma \,\mathrm{div}\, \mathbf{u} \right) \mathrm{d}V. \tag{19.4}$$

Lagrangian and Eulerian Representations

If a body is in motion, its physical properties, such as temperature, velocity or stress, can change with time. These changes are often described in two different ways, the Lagrangian or the Eulerian formulation. In the Lagrangian formulation,

the changes are described with a coordinate system that moves with the body, the material coordinates, whereas in the Eulerian formulation, the physical properties of the body are described with respect to a fixed location in space.

More formally, in the Lagrangian formulation, each point in a body is represented with respect to a *reference coordinate system* with the *material* coordinates $\mathbf{X} = (X_1, X_2, X_3)$ for all times t. The *motion* of a material point is described by the vector $\mathbf{x} = \mathbf{r}(\mathbf{X}, t)$, and a change in the physical variable G at the material point $\mathbf{X}$ is given as a function of time as $G = G(\mathbf{X}, t)$.[1] In the Eulerian formulation, at time t, the material point in the *present coordinate system* has the spatial coordinates $\mathbf{x} = \mathbf{r}(\mathbf{X}, t)$ and a physical variable G at the material point $\mathbf{X}$ is $G = g(\mathbf{x}, t)$. Obviously, $G(\mathbf{X}, t) = g(\mathbf{x}, t)$.

The transformation between Lagrangian and Eulerian variables is determined by the *motion* vector $\mathbf{x} = \mathbf{r}(\mathbf{X}, t)$. Considering the rate of change of a physical variable G at a fixed material point, $\mathbf{X}$, leads to the *material* or *substantial* derivative

$$\frac{\mathrm{d}G}{\mathrm{d}t} = \frac{\partial G(\mathbf{X}, t)}{\partial t} = \frac{\mathrm{d}g(\mathbf{x}, t)}{\mathrm{d}t} = \frac{\partial g(\mathbf{x}, t)}{\partial t} + \mathbf{u} \cdot \mathrm{grad} g(\mathbf{x}, t) \tag{19.5}$$

where $\mathbf{u} = \mathrm{d}\mathbf{x}/\mathrm{d}t$ is the material velocity at the point $\mathbf{x}$. Informally, this means that the time derivative following a particle is equal to the local rate of change plus the convective change.

General Conservation Equations

The basic structure of a conservation or balance equation is independent of the specific quantity that is considered. Therefore, in this subsection, the general form of the conservation principle for a physical quantity is derived from an Eulerian point of view. This principle is then applied to specific conservation quantities such as mass, species, momentum, energy, etc.

The rate of change of a physical variable $G(t)$ over a domain $\Omega(t)$ with boundary $\partial\Omega(t)$, subject to the production $P(t)$, the supply $S(t)$, and the flux $F(t)$ through $\partial\Omega(t)$ is

$$\frac{\mathrm{d}G}{\mathrm{d}t} = P + S + F. \tag{19.6}$$

The production terms are often referred to as sources or sinks, and the supply terms are sometimes called body forces.

[1] The same symbols are used for a physical properties and its Lagrangian representation.

The physical variable G with volume density γ is obtained from

$$G = \int_{\Omega(t)} \gamma(\mathbf{x}, t) \mathrm{d}V. \tag{19.7}$$

The production P is due to the generation or depletion of the physical quantity within the domain $\Omega(t)$, caused by sources and sinks. Typically, this can occur because of the creation or depletion of species due to chemical reactions, the addition or removal of mass and energy due to sprays, the heat production due to radioactive decay, etc. The production term is given by

$$P = \int_{\Omega(t)} \pi(\mathbf{x}, t) \mathrm{d}V, \tag{19.8}$$

where $\pi(\mathbf{x}, t)$ is the production density.

The supply S is the contribution to the physical quantity G from forces acting from a far distance onto every point in $\Omega(t)$. These forces are also called body forces and can be due to gravity, radiation or electromagnetic interactions. The supply term is given by

$$S = \int_{\Omega(t)} \varsigma(\mathbf{x}, t) dV, \tag{19.9}$$

where $\varsigma(\mathbf{x}, t)$ is the supply density.

The flux F through $\partial\Omega(t)$ is obtained from

$$F = -\int_{\partial\Omega(t)} \phi(\mathbf{x}, t) \cdot \mathbf{n} \, \mathrm{d}A. \tag{19.10}$$

Here, the vector $\mathbf{n}$ denotes the outward unit normal on $\partial\Omega$ and $\boldsymbol{\phi}(\mathbf{x}, t)$ denotes the flux density vector. Fluxes through a surface can arise, for example, from stresses acting on the surface or from a heat or species flux through the surface.

Substitution of (19.7)–(19.10) into (19.6) leads to the *general conservation equation* in integral form

$$\frac{\mathrm{d}G}{\mathrm{d}t} = \int_{\Omega(t)} (\pi(\mathbf{x}, t) + \varsigma(\mathbf{x}, t)) \mathrm{d}V - \int_{\partial\Omega(t)} \phi(\mathbf{x}, t) \cdot \mathbf{n} \mathrm{d}A \tag{19.11}$$

where the left-hand side is given by (19.2) or (19.4).

The conservation equation in differential form is obtained from the general balance equation, (19.11), by use of the divergence theorem, (19.1) and the Reynolds transport theorem, (19.2), and by the fact that the resulting equation must hold on all subsets of the domain $\Omega(t)$. Consequently, the *local conservation equation* is given by

$$\frac{\partial \gamma}{\partial t} + \mathrm{div}(\gamma \mathbf{u}) = -\mathrm{div}\phi + \pi + \varsigma, \tag{19.12}$$

or, utilizing the vector identity in (19.3), by

$$\frac{\mathrm{d}\gamma}{\mathrm{d}t} + \gamma \,\mathrm{div}\,\mathbf{u} = -\mathrm{div}\,\phi + \pi + \varsigma. \tag{19.13}$$

It should be noted that if γ is a vector-valued function, as is the case for the momentum density, then the above equations are formally the same, but with appropriate vector or tensor interpretations for the other variables.

Specific Conservation Equations

The conservation equation for a specific physical density, γ, is obtained by determining the appropriate expressions for the production, supply, and flux densities in either (19.12) or (19.13). For example, using the terms given in Table 19.1 leads to the following gas-phase equations:

Mass conservation

$$\frac{\partial \rho}{\partial t} + \mathrm{div}(\,\rho \mathbf{u}) = \dot{\rho}^{\mathrm{s}} \tag{19.14}$$

Momentum conservation

$$\frac{\partial (\rho \mathbf{u})}{\partial t} + \mathrm{div}(\rho \mathbf{u}\mathbf{u}) = \mathrm{div}\,\boldsymbol{\tau} + \rho \mathbf{g} + \dot{\mathbf{M}}^{\mathrm{s}} \tag{19.15}$$

Energy conservation

$$\frac{\partial (\rho e)}{\partial t} + \mathrm{div}(\rho e \mathbf{u}) = -\mathrm{div}\,\mathbf{q} + \mathrm{grad}\,\mathbf{u} : \boldsymbol{\tau} + \dot{Q}^{\mathrm{s}}. \tag{19.16}$$

In these equations, ρ denotes the mass density and $\dot{\rho}^{\mathrm{s}}$ the production term due to a spray; $\mathbf{u}$ is the velocity, $\boldsymbol{\tau}$ is the Cauchy stress tensor, $\mathbf{g}$ is the constant of gravity, and $\dot{\mathbf{M}}^{\mathrm{s}}$ is the spray momentum production; e denotes the specific internal energy, $\mathbf{q}$ is the mass specific heat flux vector, and $\dot{Q}^{\mathrm{S}}$ is the energy contribution due to the spray.

Note that in order to obtain the above form of the energy equation, the mass and momentum conservation equations, (19.14) and (19.15), were used. In addition,

Table 19.1 Physical quantities used in the derivation of the specific local balance equations

Variable G	Density γ	Production π	Supply ς	Flux $\boldsymbol{\phi}$
Mass	ρ	$\dot{\rho}^{\mathrm{s}}$	0	0
Momentum	$\rho\mathbf{u}$	$\dot{\boldsymbol{M}}^{\mathrm{s}}$	$\rho \boldsymbol{g}$	$-\boldsymbol{\tau}$
Energy	$\frac{1}{2}\rho \boldsymbol{u}\cdot\boldsymbol{u} + \rho \boldsymbol{e}$	$\dot{\boldsymbol{Q}}^{\mathrm{s}}$	$\rho \boldsymbol{g}\cdot\boldsymbol{u}$	$\boldsymbol{q} - \boldsymbol{U}\cdot\boldsymbol{\tau}$

using the symmetry property of $\boldsymbol{\tau}$ and the fact that the trace of a symmetric and antisymmetric tensor is zero, yields the commonly used expression

$$\operatorname{grad}\mathbf{u} : \boldsymbol{\tau} = \frac{1}{2}[(\operatorname{grad}\mathbf{u} + (\operatorname{grad}\mathbf{u})^T] : \boldsymbol{\tau}.$$

The actual conservation equations used for the description of a turbulent, reacting spray are obtained in a similar fashion and are discussed in more detail in the section "Gas Phase".

Material Equations for Newtonian Fluids

In the specific conservation equations for mass, momentum, and energy given in (19.14)–(19.16), there are material-dependent expressions such as the Cauchy stress tensor $\boldsymbol{\tau}$, the specific heat flux vector **q,** and the specific internal energy e. The expressions for these quantities are called the *constitutive equations*.

The most commonly encountered fluids are Newtonian fluids, that is, fluids whose stress tensor depends linearly on its rate-of-strain tensor (at a fixed temperature). For isotropic Newtonian fluids, the Cauchy stress tensor is given by

$$\boldsymbol{\tau} = -p\mathbf{I} + \mu[\operatorname{grad}\mathbf{u} + (\operatorname{grad}\mathbf{u})^T - \frac{2}{3}\operatorname{div}\mathbf{u}\mathbf{I}], \tag{19.17}$$

where $p = p(\rho, T)$ is the pressure, $\mu = \mu(\rho, T)$ is the viscosity, T is the temperature, and $\mathbf{I}$ is the identity tensor. For a single-component system, the specific heat flux vector $\mathbf{q}$ is given by the Fourier law of heat conduction

$$\mathbf{q} = -K \operatorname{grad} T, \tag{19.18}$$

where K is the thermal conductivity. Further, the expression for the internal energy in thermodynamic equilibrium is given by Gibbs' law in differential form as

$$\mathrm{d}e = T\mathrm{d}s + \frac{p}{\rho^2}\mathrm{d}\rho, \tag{19.19}$$

where ds denotes the differential of the entropy.

Introduction to Turbulence

When a liquid is injected into a gaseous environment, it exchanges momentum with the gas and thus induces a flow. This flow is usually turbulent and strongly influences the liquid-gas interactions, such as liquid breakup, phase changes, and mixing. Consequently, turbulence plays a fundamental role in spray phenomena.

Basic Concepts of Turbulence

The effects of turbulence are nicely illustrated by the classical experiment of Reynolds, where a dye is carefully added to a liquid in the center of a simple flow through a pipe of constant diameter. Reynolds discovered that the flow behavior depends on a dimensionless number, the *Reynolds number*, defined as the ratio of characteristic inertial forces, $\rho||\mathbf{u}||$, over characteristic viscous forces, μ_g/d, given by

$$Re = \frac{\rho\|\mathbf{u}\|d}{\mu_g} = \frac{\|\mathbf{u}\|d}{\nu_g}. \tag{19.20}$$

Here, d is a characteristic length scale of the flow, that is, the diameter for a pipe flow, and $\nu_g = \mu_g/\rho$ is the *kinematic viscosity*. If the Reynolds number of the flow lies below a critical value, say $Re_c \approx 2,000$, then the flow is laminar and the dye follows the stream lines along the axis of the cylinder. If $Re > Re_c$, then the flow turns turbulent, that is, the dye mixes very rapidly with the liquid and fills the entire cross-section of the pipe. This behavior is typical for turbulent flows. In fact, turbulent flows are highly diffusive, allowing for rapid mixing of mass, momentum, and heat. In addition, turbulent flows are dissipative and occur at high Reynolds numbers. The observation that a turbulent flow exhibits greatly enhanced mass, momentum, and heat diffusion suggests that the flow properties behave as if they were material properties. This, as discussed later, is the key observation for turbulence models using the eddy viscosity approach.

The cause of turbulence is the nonlinear interaction between inertial and viscous forces which, for high Reynolds numbers, amplifies small disturbances and results in a highly irregular, random flow. This process is explained in more detail by the Kolmogorov–Richardson turbulence cascade, which states that disturbances of the mean flow induce local swirling motions, called eddies. These eddies produce smaller and smaller eddies via a vortex-stretching mechanism. When the smallest eddies cannot sustain a coherent flow structure anymore, they start dissipating into heat. Therefore, a turbulent flow exhibits eddy length scales that range from the integral length scale, determined by the geometry of the flow, down to the smallest eddies at the Kolmogorov dissipation scale.

A summary of the commonly used scalar turbulence length and time scales is given in Table 19.2. Most of these scales can be obtained by means of dimensional analysis. The integral length scale, L_I, is determined by a characteristic dimension of the flow, and the associated time scale is $\tau_I = L_I^2/\nu_g$. The length and time scales that are computed from turbulence models, called the macro or model scales, are given by $L_M = C_\varepsilon k^{3/2}/\varepsilon$ and $\tau_M = \tau = k/\varepsilon$, respectively. Here, C_ε is a model constant, k is the turbulent kinetic energy (per unit mass), and ε is the turbulence dissipation (per unit mass), that is, the rate at which turbulent kinetic energy is

Table 19.2 Scalar turbulence length and time scales

	Length Scale	Time Scale
Integral (I)	L_I	$\tau_\mathrm{I} = L_\mathrm{I}^2/\nu_0$
Macro (model) (M)	$L_\mathrm{M} = C_\varepsilon k^{3/2}/\varepsilon$	$\tau_\mathrm{M} = \tau = k/\varepsilon$
Taylor (λ)	$L_\lambda^2 = 10\nu_0 k/\varepsilon$	$\tau_\lambda = L_\lambda/q_\mathrm{t} = \sqrt{15\nu_0/\varepsilon}$
Kolmogorov (η)	$L_\eta = (\nu_0^3/\varepsilon)^{1/4}$	$\tau_\eta = \sqrt{\nu_0/\varepsilon} \propto \tau_\lambda$

converted into thermal energy. The Taylor length scale separates the small scales from the large scales and relates the *turbulence intensity*

$$q_\mathrm{t} = \|u'\|/\sqrt{3} = \sqrt{\frac{2k}{3}}$$

to the turbulence dissipation ε. Here, $\boldsymbol{u}'$ is the turbulence fluctuation vector. Finally, the Kolmogorov scale is the smallest length scale that can sustain a coherent flow structure. Eddies whose sizes fall below the Kolmogorov scales dissipate into heat.

Because the larger eddies are determined by the geometry of the flow, they depend on direction (nonisotropic) and location (nonhomogeneous). The structure of the smaller eddies is much more uniform. In fact, smaller eddies are self-similar, meaning that their flow patterns are essentially the same at all the different scales.

The prediction of turbulent flows by computational means requires that the smallest spatial and temporal length scales associated with a flow are resolved. These types of computations are referred to as direct numerical simulations (DNS). Because of computational limitations, such fully resolved turbulence computations can only be obtained for simple flows at relatively low Reynolds numbers. For technically relevant flows, that is, flows with complex geometries at high Reynolds numbers, not all length and time scales can be resolved. In fact, the flow variables are averaged or filtered, and then the problem is solved for the averaged or filtered set of variables. As is discussed in more detail below, this averaging or filtering process leads to the use of turbulence models.

Averages and Filters

The random nature of turbulence suggests that flow quantities can be described as the superposition of a mean flow quantity plus its fluctuation. More formally, this means that an instantaneous flow variable, $\hat{f}$, can be written as

$$\hat{f} = f + f' = \langle \hat{f} \rangle + f', \tag{19.21}$$

where $f = \langle \hat{f} \rangle$ is the average or filtered part, $\langle \hat{f} \rangle$ denotes the averaging or filtering process, and f' denotes the turbulent fluctuation. Typical instantaneous flow variables

are the velocity $\hat{\mathbf{u}}$, the density $\hat{\rho}$, the pressure $\hat{p}$, and the temperature $\hat{T}$. Note that for clarity and simplicity of notation, the symbols without diacritical marks denote the filtered or averaged quantities.

The filtering process is used to separate mean flow variables from their turbulence fluctuations. There are three different types of filters: the time filters, which result in the Reynolds-averaged conservation equations, also called the RANS; the spatial filters, which lead to LES; and the statistical filters, which reflect ensemble-averaged quantities from experiments. Statistical filters are not discussed here any further.

Time filters are defined by

$$\langle \hat{f} \rangle_{T_0}(\mathbf{x}, t) = \frac{1}{W} \int_{t-T_0/2}^{t+T_0/2} w(\mathbf{x}, s)\hat{f}(\mathbf{x}, s)\mathrm{d}s, \tag{19.22}$$

where $W = \int_{t-T_0/2}^{t+T_0/2} w(\mathbf{x}, s)\mathrm{d}s$, $w(\mathbf{x}, t)$ is a weight function, and T_0 is an appropriate time interval. Time filters satisfy the following properties.

- Linearity:

$$< \alpha\hat{f} + \beta\hat{g} >_{T_0} = < \alpha\hat{f} >_{T_0} + < \beta\hat{g} >_{T_0} = \alpha f + \beta g,$$

  where $\hat{f}$ and $\hat{g}$ are instantaneous flow quantities and α, β are scalars.

- Commutativity with differentiation:

$$< \partial\hat{f} >_{T_0} = \partial < \hat{f} >_{T_0} = \partial f,$$

  where ∂ represents any spatial or temporal differential operator such as ∂_x, ∂_t, grad or div.

- Filter invariance:

$$\langle \langle \hat{f} \rangle_{T_0} \rangle_{T_0} = \langle \hat{f} \rangle_{T_0} = f. \tag{19.23}$$

Note that this has the important consequence that $\langle f' \rangle_{T_0} \equiv 0$, a property that is not necessarily satisfied by spatial filters.

Spatial filters are, in general, defined by a convolution integral over the entire domain Ω by

$$\langle \hat{f} \rangle_{\Delta}(\mathbf{x}, t) = \int_{\Omega} K(\mathbf{x} - \xi; \Delta)\hat{f}(\xi, t)\mathrm{d}\xi, \tag{19.24}$$

where $K(\mathbf{x} - \xi; \Delta)$ is the filter function with the filter size Δ, and satisfies the normalization condition

$$\int_{\Omega} K(\mathbf{x} - \xi; \Delta) d\xi = 1. \tag{19.25}$$

The linearity and differential commutativity properties, which are satisfied by time filters, also hold for spatial filters. However, the filter invariance is, in general, not satisfied for spatial filters. More precisely,

$$\langle \langle \hat{f} \rangle_{\Delta} \rangle_{\Delta} \neq \langle \hat{f} \rangle_{\Delta},$$

which has the important implication that, in contrast to time filters, the spatial average of the fluctuation terms is, in general, not zero, that is, $\langle f' \rangle_{\Delta} \neq 0$. More details on the spatial filtering are discussed in the context of LES in the section "LES Turbulence Modeling".

Averaging or filtering of a system of conservation equations leads to an identical set of equations for the filtered variables, plus additional, unknown expressions which involve averaged fluctuation terms. This constitutes the notorious closure problem, namely, there are more unknowns than equations, which leaves the system of equations underdetermined. In order to resolve this closure problem, additional relations are required that describe the new unknown fluctuation variables and thereby close the system. These relations are called turbulence models. If the averaging process is done with a time filter then one obtains RANS equations, whereas a spatial filtering leads to LES.

RANS Turbulence Modeling

For technically relevant flows at high Reynolds numbers, the most commonly used approach to turbulence is via the time-filtered conservation equations. In this approach, the conservation equations are averaged by means of (19.22) using weight functions w(**x**, t) = 1, called Reynolds averaging, or $w(\mathbf{x}, t) = \hat{\rho}$, called Favre[2] averaging. Applying a combination of Reynolds and Favre averaging to the conservation equations for the instantaneous mass, momentum, and energy yields an identical system of equations for the filtered variables, plus additional expressions involving the averaged fluctuation terms, namely, the *Reynolds stress tensor*

$$\mathbf{R} = -\langle \hat{\rho} \boldsymbol{u}' \otimes \boldsymbol{u}' \rangle_{T_0} = -\langle \hat{\rho} \boldsymbol{u}' \boldsymbol{u}' \rangle_{T_0} \tag{19.26}$$

[2]Favre averaging applied to the compressible mass conservation equation avoids the generation of fluctuation terms that otherwise might have to be modeled.

in the momentum equation, and the *Reynolds heat flux*

$$\mathbf{T} = -\langle \hat{\rho} T' \boldsymbol{u}' \rangle_{T_0} \tag{19.27}$$

in the energy equation. In the derivation of (19.26) and (19.27), the filter invariance property, (19.23), has played an important role. If this property is not satisfied, as is the case with most LES filters, then the fluctuation terms are more complicated.

The averaging process introduces the additional unknown fluctuation terms, $\boldsymbol{u}'$ and T', for which no additional information is available. Consequently, there are more unknowns than equations, which is the reason why these expressions need to be modeled. The modeling of the Reynolds stress tensor is the focus of RANS-based turbulence models.

The basic idea of RANS models is to account for the change in the fluid transport properties by introducing an *eddy viscosity*, μ_t, also called *turbulence viscosity*, which relates the Reynolds stress tensor $\mathbf{R}$ to the fluid deformation. Such a relationship was first proposed by Boussinesq in the nineteenth century. More formally, this *Boussinesq assumption* can be written as

$$\mathbf{R} = \mu_t \mathbf{S} - 2\rho k/3 \mathbf{I}, \tag{19.28}$$

where $k = <\mathbf{u}' \cdot \mathbf{u}'>_{T_0}/2$ is the turbulent kinetic energy, and $\mathbf{S}$ is the rate-of-strain tensor given by

$$\mathbf{S} = \left[\left(\operatorname{grad} \mathbf{u} + (\operatorname{grad} \mathbf{u})^{\mathrm{T}} \right) - \frac{2}{3} \operatorname{div} \mathbf{u} \mathbf{I} \right]. \tag{19.29}$$

Analogously, the Reynolds heat flux, T, is obtained by postulating that

$$\mathbf{T} = \rho \kappa_{\mathrm{t}} \operatorname{grad} T,$$

where the turbulent heat diffusivity, κ_{t}, is related to the eddy viscosity via

$$\kappa_{\mathrm{t}} = \frac{\mu_{\mathrm{t}}}{\rho Pr_{\mathrm{t}}},$$

and Pr_{t} is the turbulent Prandtl number. It follows that once an expression for μ_{t} has been found, the Reynolds stress tensor and the Reynolds heat flux can be determined.

The first successful eddy viscosity turbulence model, referred to as an *algebraic mixing length model*, was introduced by Prandtl in the 1920s [43]. Prandtl postulated that

$$\mu_{\mathrm{t}} = \rho L_{\mathrm{mix}} u_{\mathrm{mix}} = \rho L_{\mathrm{mix}}^2 \|\operatorname{grad} \mathbf{u}\|, \tag{19.30}$$

where L_{mix} is a mixing length that depends on the flow, and the mixing velocity is related to the gradient of the mean flow via $u_{\text{mix}} = ||grad\ \mathbf{u}||L_{\text{mix}}$. In a further attempt, Prandtl [44] developed the *one-equation turbulence model*, where a transport equation for the specific turbulent kinetic energy, k, is utilized (cf. (19.34)) to obtain the eddy viscosity from

$$\mu_{\text{t}} = \rho\sqrt{k}\, L_{\text{mix}}. \tag{19.31}$$

A drawback of the one-equation model is the determination of L_{mix}, which, in general, is not a constant of the flow. Dimensional analysis suggests that the mixing length can be expressed as

$$L_{\text{mix}} = C_{\mu}\frac{k^{3/2}}{\varepsilon}, \tag{19.32}$$

where C_{μ} is a model constant, usually taken to be $C_{\mu} = 0.09$. This leads to the well-known expression for the eddy viscosity, namely

$$\mu_{\text{t}} = C_{\mu}\rho k^2/\varepsilon. \tag{19.33}$$

Equation 19.33 plays a key role in the development of *two-equation turbulence models*. This relationship suggests that besides the k-equation, an additional transport equation for the dissipation, ε, is required to make predictions for the mixing length L_{mix}.

The need for two-equation turbulence models had already been recognized by Kolmogorov in the 1940s, but it is only the advances in computer technology that have allowed their realization. Among the two-equation turbulence models that have emerged over the last few decades, the most popular ones are the $k-\varepsilon$ *turbulence models*. In this type of models, two transport equations are solved, one for the turbulent kinetic energy, k, and the other for the turbulence dissipation, ε. The eddy viscosity is then obtained from (19.33). A more detailed discussion of the standard $k-\varepsilon$ turbulence model is given below.

In contrast to the eddy viscosity approach, the Reynolds stress tensor, R, can be modeled directly by introducing one transport equation for each term. Such models are called *Reynolds stress models*, *second-order closure models* or *second-moment closure models* and have been pioneered by Rotta [47]. Since R is a symmetric second-order tensor, this requires six transport equations, and an additional three transport equations are needed to model $\mathbf{T}$. Obviously, the predictive capabilities of the Reynolds stress models over the two-equation models are improved, but these models are significantly more complex and there is a considerable additional computational cost. A Reynolds stress model for spray applications has been developed and tested by Yang et al. [63].

The $k-\varepsilon$ Turbulence Model

The $k-\varepsilon$ model has been pioneered by various researchers including Harlow and Nakayama [21], Jones and Launder [26], Launder and Spalding [29, 31] and others. The standard form of the $k-\varepsilon$ two-equation model for an incompressible flow is given by (cf. Refs. [26, 30])

$$\frac{\partial k}{\partial t} + \operatorname{div}(k\mathbf{u}) = \operatorname{div}\left[\left(\frac{\nu_t}{Pr_k} + \nu_g\right)\operatorname{grad} k\right] + P_k - \varepsilon \tag{19.34}$$

$$\frac{\partial \varepsilon}{\partial t} + \operatorname{div}(\varepsilon\mathbf{u}) = \operatorname{div}\left[\left(\frac{\nu_t}{Pr_\varepsilon} + \nu_g\right)\operatorname{grad} \varepsilon\right] + C_1\frac{\varepsilon}{k}P_k - C_2\frac{\varepsilon^2}{k} \tag{19.35}$$

where the kinematic eddy viscosity is given by

$$\nu_t = C_\mu \frac{k^2}{\varepsilon}.$$

In these equations, the term P_k determines the turbulence production and is given by

$$P_k = \boldsymbol{\sigma} : \operatorname{grad} \boldsymbol{u} = \sum_{i,j} \sigma_{ij}\frac{\partial u_j}{\partial x_i},$$

where $\sigma = (\mu_g + \mu_t)\mathbf{S}$, and $\mathbf{S}$ is the rate-of-strain tensor given in (19.29). The molecular viscosity, μ_g, is usually neglected in a fully developed turbulent flow. The values for the standard model constants Pr_k, Pr_ε, C_1, and C_2 are listed in Table 19.3. These values were determined from experiments and theoretical considerations.

Observe that (19.34) and (19.35) reflect the basic structure of the local conservation equation given in (19.12): the flux density vectors are given by the gradients of k and ε; the source terms are P_k and ε in (19.34), and $C_1\varepsilon P_k/k$ and $C_2\varepsilon^2/k$ in (19.35).

The transport equation for k, (19.34), is obtained by first deriving an equation for the momentum of the fluctuation velocity, $\mathbf{u}'$, that is, the transport equation obtained by taking the difference between the momentum balance equation for the instantaneous variables and the one for the filtered variables. The dot product of this fluctuation momentum equation with the fluctuating velocity, $\mathbf{u}'$, is then time-averaged, which, after simplifications, leads to (19.34).

In a similar way, the transport equation for ε, (19.35), is derived by taking the curl with the fluctuation momentum equation, followed by the dot product with curl $\mathbf{u}'$

Table 19.3 k–ε turbulence model constants. (C_3 and C_s are for the compressible form)

Pr_k	Pr_ε	C_1	C_2	C_3	C_S
1.0	1.3	1.44	1.92	1.96	1.5

and a subsequent time-averaging process. After a considerable amount of simplification and empirical consideration, (19.35) is obtained. Details of these derivations and additional references can be found in many text books on turbulence; for example, in Wilcox [61] or Pope [41].

LES Turbulence Modeling

In a turbulent flow, the large eddies transport the principal turbulent momentum and energy, and they are determined by the geometry of the flow. Small eddies, on the other hand, are self-similar, and therefore, are more universal in character. They are mainly responsible for the dissipation of turbulent kinetic energy. These facts are the motivation for the underlying principles of LES, namely, the large eddies are resolved by a filtered set of conservation equations, whereas the small eddies are modeled with so-called SGS models.

The filter scale determines the smallest turbulence scale that is resolved, and hence the resolution needed in the computations. As a general rule, the filter is much larger than the Kolmogorov scale, but it is still much smaller than the spatial resolutions used in RANS simulations. Therefore, LES is computationally cheaper than DNS, but it is still much more expensive than RANS simulations.

The general definition of the spatial filtering process is given in (19.24). Commonly used filters in LES are the box filter, $B(\mathbf{x} - \boldsymbol{\xi}; \Delta)$, the Fourier cutoff filter, $F(\mathbf{x} - \boldsymbol{\xi}; \Delta)$, and the Gaussian filter, $G(\mathbf{x} - \boldsymbol{\xi}; \Delta)$. These filters are defined by

$$B(\mathbf{x} - \boldsymbol{\xi}; \Delta) = \begin{cases} 1/\Delta^3 & \text{if } |x_i - \boldsymbol{\xi}_i| < \Delta_i/2 \\ 0 & \text{otherwise} \end{cases}$$

$$F(\mathbf{x} - \boldsymbol{\xi}; \Delta) = \prod_{\mathbf{i}=\mathbf{1}}^{\mathbf{3}} \frac{\sin[(\mathbf{x_i} - \boldsymbol{\xi_i})/\Delta_\mathbf{i}]}{(\mathbf{x_i} - \boldsymbol{\xi_i})}$$

$$G(\mathbf{x} - \boldsymbol{\xi}; \Delta) = \left(\frac{6}{\pi\Delta^2}\right)^{3/2} \exp\left(-6\frac{\|\mathbf{x} - \boldsymbol{\xi}\|^2}{\Delta^2}\right),$$

where $i \in \{1, 2, 3\}$ denotes the ith spatial direction and $\Delta = (\Delta_1\Delta_2\Delta_3)^{1/3}$ is the representative filter width. Note that all three filters satisfy the normalization condition given in (19.25).

A box-filtered quantity is simply the volume average of this quantity over the box. It provides a sharp cutoff for values in the physical space that lies outside the box. In contrast, however, the cutoff of the wave numbers in the Fourier space is gradual. Further, the box filter is the only LES filter that satisfies the invariance property given in (19.23). Box filters have been used by Deardorff [12] in his pioneering LES investigations.

The Fourier cutoff filter has the property of being able to provide a sharp cutoff of the wave lengths in Fourier space, but the cutoff in the physical space follows a hyperbolic decay. In this sense, the Fourier cutoff filter is the dual of the box filter (see Ref. [41]). Fourier cutoff filters are widely used in spectral methods (see Ref. [14]).

Gaussian filters reflect a Gaussian distribution with mean x and variance $\Delta^2/12$. They are the most widely used filters in present-day LES research, because they provide a good balance for transforming between the physical space and the Fourier space (see Ref. [41]).

Subgrid Scale (SGS) Models

In an analogy to the RANS approach, spatial filtering of the conservation equations for the instantaneous variables leads to an identical system of equations, but for the resolved (filtered) variables, plus an additional expression, the (mass specific) SGS stress tensor, $\boldsymbol{\tau}^{\mathrm{SGS}}$. But unlike the Reynolds stress tensor in the RANS approach, $\boldsymbol{\tau}^{\mathrm{SGS}}$ has, in general, a different form because the filter invariance property in (19.23) is not satisfied. More precisely, for an incompressible flow, the specific SGS stress is given by

$$\boldsymbol{\tau}^{\mathrm{SGS}} = \langle \hat{\mathbf{u}} \otimes \hat{\mathbf{u}} \rangle - \mathbf{u} \otimes \mathbf{u} = \mathbf{L} + \mathbf{C} + \mathbf{R}, \tag{19.36}$$

where, for simplicity of notation, the subscript Δ in $\langle\rangle$ is omitted for the remainder of this section. (Recall that according to (19.21), the averaged quantities are without accents.) In (19.36), $\mathbf{L}$ is called the *Leonard stress*, $\mathbf{C}$ is the *cross-term stress*, and $\mathbf{R}$ is the *SGS Reynolds stress*. The expressions for these individual stresses are given by

$$\mathbf{L} = \langle \mathbf{u} \otimes \mathbf{u} \rangle - \mathbf{u} \otimes \mathbf{u}$$

$$\mathbf{C} = \langle \mathbf{u} \otimes \mathbf{u}' \rangle + \langle (\mathbf{u} \otimes \mathbf{u}')^{\mathrm{T}} \rangle$$

$$\mathbf{R} = \langle \mathbf{u}' \otimes \mathbf{u}' \rangle.$$

The Leonard stress term can be computed directly and does not need to be modeled. However, as shown by Shaanan et al. [50], the Leonard stresses are of the same order as the truncation errors of a second-order discretization scheme, and therefore, $\mathbf{L}$ can be implicitly accounted for. Consequently, a computed solution may depend on the numerical scheme that is used.

The terms that do require modeling are the subgrid stresses, $\mathbf{C}$ and $\mathbf{R}$. In fact, most SGS models account for the entire SGS stress $\boldsymbol{\tau}^{\mathrm{SGS}}$ given in (19.36). Consequently, LES modeling is formally similar to the modeling of the Reynolds stress tensor in the RANS approach and, therefore, analogous methods are used for LES

subgrid modeling. In particular, eddy viscosity models, as motivated by the Boussinesq hypothesis in (19.28), are also widely used in LES. The two models discussed here are the Smagorinsky model [51] and the one-equation model of Schumann [49]. A more comprehensive account of SGS modeling, together with additional references, can be found in the text of Pope [41].

The *Smagorinsky Model* (cf. Ref. [51]) is an algebraic model in the same spirit as the Prandtl mixing length model discussed in section "RANS Turbulence Modeling." In the Smagorinsky model, the SGS stresses are assumed to be proportional to the rate of strain, that is, $\boldsymbol{\tau}^{\mathrm{SGS}} = \nu_{\mathrm{t}}\mathbf{S}$, and the kinematic eddy viscosity is determined from the expression

$$\nu_{\mathrm{t}} = (C_{\mathrm{s}}\Delta)^2\sqrt{\mathbf{S}:\mathbf{S}}. \tag{19.37}$$

Here, C_{s} is the Smagorinsky coefficient with a range of $0.1 < C_{\mathrm{s}} < .24$, Δ is the representative filter width, and $\mathbf{S}$ is the rate-of-strain tensor given in (19.29). The expression $C_{\mathrm{s}}\Delta$ is called the Smagorinsky length scale and plays the same role as L_{mix} in (19.30).

The advantage of the Smagorinsky model is that it is numerically inexpensive. However, the coefficient C_{s} is not universal and depends on the flow regime. An improvement of this shortcoming is provided by the dynamic Smagorinsky model proposed by Germano et al. [17], where the coefficient C_{s} is computed according to different flow conditions.

The *One-Equation Model* (cf. Ref. [49]) is the analog of the Prandtl one-equation model used in RANS simulations. It utilizes a transport equation for the SGS turbulent kinetic energy, k^{SGS}. The SGS stress tensor is modeled in analogy to (19.28), that is,

$$\boldsymbol{\tau}^{\mathrm{SGS}} = \nu_t\mathbf{S} - \frac{2}{3}k^{\mathrm{SGS}}\mathbf{I}, \tag{19.38}$$

where $\mathbf{S}$ is the rate of strain tensor defined in (19.29), and the eddy viscosity is determined by

$$\nu_{\mathrm{t}} = C_k\Delta\sqrt{k^{\mathrm{SGS}}} \tag{19.39}$$

where C_k is a constant.

The transport equation for k^{SGS} is formally identical to (19.34), but with different interpretations as follows: The production term P_k can be written as

$$P_k = \nu_{\mathrm{t}}(\mathbf{S}:\mathbf{S})$$

and the expression for the SGS dissipation rate is analogous to (19.32); it is obtained from

$$\varepsilon^{\mathrm{SGS}} = C_\varepsilon(k^{\mathrm{SGS}})^{3/2}/\Delta$$

where the constant $C_\varepsilon = 0.916$.

Spray Modeling

Sprays involve many subprocesses, which occur over a wide range of length and time scales. As discussed in the previous section, due to the lack of computational capacities of present-day computers, an averaging or filtering of the conservation equations for the gas phase is required. Time averaging of the governing equations leads to RANS simulations, whereas spatial filtering results in LES. The difference between the two approaches lies in the treatment of the turbulence and its interaction with the liquid phase. The description presented in this section is given for the RANS approach, but it applies equally well to LES when appropriate modifications are made. These modifications are discussed in the corresponding subsection. Despite the fact that much of the two approaches is formally the same, LES require considerably higher spatial and temporal resolutions, and consequently, they are computationally much more expensive.

The first spray phenomenon that needs to be modeled is the atomization process, that is, the disintegration of the bulk liquid into tiny droplets. The atomization process can be separated into inner-nozzle and outer-nozzle effects. The forces that govern the inner-nozzle atomization include cavitation-induced and turbulence-induced disturbances of the liquid. Once the liquid exits the nozzle, it interacts with the gaseous environment that induces disturbances on the liquid-gas interface caused by aerodynamic and inertial forces. Also, when the liquid exits the nozzle, it experiences a discontinuity in the boundary condition, namely, from the fixed boundary of the nozzle orifice to a free surface boundary. This abrupt change in the boundary condition leads to disturbances of the liquid that influence the atomization process. In general, the atomization of a bulk liquid is a very complex process and is still the subject of intensive research.

In addition to the atomization process, there are drop-drop and drop-gas interactions to be considered. The drop–drop interactions include drop collisions, which lead to drop coalescence and possible subsequent drop breakups. The drop–gas interactions lead to liquid-gas momentum and energy transfer, phase changes such as drop evaporation or solidification, vapor-gas mixing as well as secondary drop breakup. Further, for fuel sprays in engines and turbines, chemical reactions play a dominant role, and processes such as ignition, heat release, and pollutant formation need to be described.

Moreover, equations of state for gas, internal energy, enthalpy and heat capacities are required, and the transport coefficients for mass, momentum, and heat diffusion need to be determined. Finally, as the description of the above processes leads to a large system of differential and algebraic equations for multifluids and multiphases, initial and boundary conditions are needed to obtain a solution.

Gas Phase

In the RANS approach, the gas phase is modeled with the Reynolds–Favre-averaged conservation equations for a compressible fluid. For a reacting spray,

this is achieved with the conservation equations for mass, species, momentum, and energy, shown in Table 19.4. The turbulence is taken into account with the k–ε model for a compressible fluid. The equations are given in Table 19.5. The basic structure of the transport equations in Tables 19.4 and 19.5 is the same as for the local conservation equation in (19.12), that is, the left-hand sides of the equations are convective derivatives, which are balanced on the right-hand side by the divergence of the appropriate flux densities, plus production and supply terms. Note that the only supply term is the gravity term $\rho\mathbf{g}$ in the momentum equation.

The production or source terms are due to the spray droplets and the chemical reactions, as well as to turbulence production and dissipation. The spray source terms are identified with a superscript, s, and the chemical source terms with a superscript c. In the mass and species equations, the spray source term is $\dot{\rho}^S$ which indicates the mass transfer between the liquid and gas phases, e.g., due to evaporation. The Kronecker delta, $\delta_{m,\upsilon}$ in the species equation indicates when fuel vapor is transferred to the gas phase, i.e., $\delta_{m,\upsilon} = 1$ if m is a fuel species and $\delta_{m,\upsilon} = 0$ if otherwise. The spray contributions in the momentum and energy equations are given by $\dot{\boldsymbol{M}}^{\mathrm{S}}$ and $\dot{Q}^{\mathrm{S}}$, respectively. There is also a spray source

Table 19.4 Reynolds–Favre-averaged gas-phase conservation equations

Mass:

$$\frac{\partial \rho}{\partial t} + \operatorname{div}(\rho \mathbf{u}) = \dot{\rho}^s$$

Species:

$$\frac{\partial \rho_m}{\partial t} + \operatorname{div}(\rho_m \mathbf{u}) = \operatorname{div}\left[\rho D \operatorname{grad}\left(\frac{\rho_m}{\rho}\right)\right] + \dot{\rho}^s \delta_{m,\upsilon} + \dot{\rho}^c_m$$

Momentum:

$$\frac{\partial (\rho \mathbf{u})}{\partial t} + \operatorname{div}(\rho \mathbf{u}\,\mathbf{u}) = \operatorname{div}\left[\boldsymbol{\sigma} - (p + \frac{2}{3}\rho k)\mathbf{I}\right] + \dot{\mathbf{M}}^s + \rho \mathbf{g}$$

$$\boldsymbol{\sigma} = \mu\left[\left(\operatorname{grad}\mathbf{u} + (\operatorname{grad}\mathbf{u})^T\right) - \frac{2}{3}\operatorname{div}\mathbf{u}\mathbf{I}\right]$$

Energy:

$$\frac{\partial (\rho e)}{\partial t} + \operatorname{div}(\rho e \mathbf{u}) = -\operatorname{div}\mathbf{q} - p \operatorname{div}\mathbf{u} + \rho\varepsilon + \dot{Q}^s + \dot{Q}^c$$

$$\mathbf{q} = -K \operatorname{grad} T - \rho D \sum_m h_m \operatorname{grad}\left(\frac{\rho_m}{\rho}\right)$$

Table 19.5 Compressible k–ε turbulence model equations

$$\frac{\partial (\rho k)}{\partial t} + \operatorname{div}(\rho k \mathbf{u}) = \operatorname{div}\left[(\mu_{\mathrm{g}} + \frac{\mu_{\mathrm{t}}}{\mathrm{Pr_k}})\operatorname{grad} k\right] + \boldsymbol{\sigma} : \operatorname{grad}\mathbf{u} - \rho\varepsilon - \frac{2}{3}\rho k \operatorname{div}\mathbf{u} + \frac{\mathrm{d}W^s}{\mathrm{d}t}$$

$$\frac{\partial (\rho \varepsilon)}{\partial t} + \operatorname{div}(\rho \varepsilon \mathbf{u}) = \operatorname{div}\left[(\mu_g + \frac{\mu_t}{\mathrm{Pr}_\varepsilon})\operatorname{grad}\varepsilon\right] + C_1 \frac{\varepsilon}{k}\boldsymbol{\sigma} : \operatorname{grad} u - C_2 \rho \frac{\varepsilon^2}{k} - C_3 \rho\varepsilon \operatorname{div}\mathbf{u} + C_s \frac{\varepsilon}{k}\frac{\mathrm{d}W^s}{\mathrm{d}t}$$

term, $\dot{W}^{\mathrm{S}}$, in both turbulence model equations, which is always negative because the turbulence fluctuations perform work on the spray droplets. The expressions for the spray source terms are given by (19.53)–(19.56) and are discussed later in more detail.

For an LES approach, the k–ε model has to be replaced with an appropriate SGS model discussed in the section "LES Turbulence Modeling." The important difference between RANS and LES for sprays is that the LES models do not require a spray source term. This is because the large eddies, which contain most of the turbulent energy, are resolved and, therefore, the work done by the turbulence on the droplets is taken into account by the droplet energy source term $\dot{Q}^{S}$.

The source terms due to chemical reactions are $\dot{\rho}_m^c$ in the species equation, and $\dot{Q}^{\mathrm{C}}$ in the energy equation. These expressions are given later in (19.61) and (19.62).

Note that for each species m, there is one transport equation for its density ρ_m. The species flux is given by Fick's law of diffusion,

$$\mathbf{j}_m = \rho D_m \,\mathrm{grad}\left(\frac{\rho_m}{\rho}\right), \tag{19.40}$$

where D_m is the vapor mass diffusivity of species m in the surrounding gas. (D_m is usually taken to be the same for all species and is then denoted by D).

In the energy equation, the heat flux vector $\mathbf{q}$ accounts for the heat conduction via $-K\mathrm{grad}\ T$, and, because of the different species, the enthalpy diffusion via

$$\rho D \sum_m h_m \,\mathrm{grad}(\rho_m/\rho),$$

where K is the heat conductivity and h_m is the specific enthalpy of species m. The term $-p$ div $\mathbf{u}$ accounts for compressibility effects and ρε for the turbulence dissipation.

The k–ε model equations, given in Table 19.5, are for a compressible fluid. In comparison with the standard k–ε model for incompressible flows, given in (19.34) and (19.35), there are additional terms due to compressibility, involving div $\mathbf{u}$, and due to the multiphase nature of the flow, given by the spray source term $\dot{W}^{\mathrm{S}}$. The constants used in this model are summarized in Table 19.3. As mentioned above, there is no spray source term $\dot{W}^{\mathrm{S}}$ necessary when LES is used instead of RANS.

Transport Coefficients

The transport coefficients, that is, the mass diffusivity D, the *effective viscosity* μ, and the heat conductivity K, can be determined once the turbulence quantities k and ε

are known. The effective viscosity is the sum of the molecular viscosity for the gas phase, μ_g, and the turbulent viscosity μ_t in (19.33), and is given by

$$\mu = \mu_g + C_\mu \frac{\rho k^2}{\varepsilon}. \tag{19.41}$$

The temperature dependence of μ_g is given by the Sutherland formula

$$\mu_g = \frac{A_1 T^{3/2}}{T + A_2},$$

where A_1 and A_2 are constants. Once the value for μ is known, the mass diffusivity and the heat conductivity follow from

$$D = \frac{\mu}{\rho Sc_t} \tag{19.42}$$

$$K = \frac{\mu C_p}{Pr_t} \tag{19.43}$$

where Sc_t and Pr_t are the turbulent Schmidt and Prandtl numbers, which are of the order of unity, and C_p is the heat capacity at constant pressure.

State Relations

The equations of state are assumed to be the ones for an ideal gas and are given by

$$p = R_0 T \sum_m \frac{\rho_m}{W_m}$$

$$e(T) = \sum_m \left(\frac{\rho_m}{\rho}\right) e_m(T)$$

$$C_p(T) = \sum_m \frac{\rho_m}{\rho} C_{pm}(T)$$

$$h_m(T) = e_m(T) + \frac{R_0 T}{W_m}$$

where, $R_0 = 8314$ J/kmol-K denotes the universal gas constant, W_m is the molecular weight of species m, $e_m(T)$ the specific internal energy, $C_{pm}(T)$ the specific heat at constant pressure, and $h_m(T)$ the specific enthalpy. The values for $h_m(T)$ and $C_{pm}(T)$ are usually taken from tables.

For high gas pressures, ideal gas law predictions can become inaccurate and real gas effects have to be taken into account. More details on high-pressure effects can be found in Ohe [34].

Liquid Phase

A spray is a collection of dispersed liquid droplets moving in a gaseous environment. Typically, there are a huge number of droplets whose behavior is influenced by drop–drop and drop–gas interactions. Different regions of the spray can have various drop number densities, that is, in the near nozzle region, the drop number density is much larger than further downstream. A mathematical formulation that is capable of describing the complex nature of spray processes is the probability density approach pioneered by Williams [62]. In this approach, the spray droplets are represented by a PDF, $f(t, \mathbf{X})$, which represents the probable number of droplets per unit volume at time t and in state $\mathbf{X}$. The state of a droplet is described by its parameters that are the coordinates in the particle state space. Typically, the particle parameters include the location x, the velocity v, the radius r, the temperature T_d, the deformation parameter y, and the rate of deformation $\dot{y}$. This leads to the spray PDF $f(t, x, v, r, T_\mathrm{d}, y, \dot{y})$

Note that the liquid or droplet properties are identified with a subscript d in order to distinguish them from the gas-phase properties. In accordance with the previous sections, the latter are either not subscripted, or whenever necessary to avoid confusion, are indicated with a subscript g. A subscript v is used to indicate the vapor properties associated with the droplet species in order to distinguish them from the continuum gas phase properties. The droplet velocity is denoted by $\mathbf{v}$ to distinguish it from the gas phase velocity $\mathbf{u}$.

In an analogy to the derivation of the specific conservation equations in section "Specific Conservation Equations," setting $\gamma = f(t, \mathbf{X})$ in (19.12), leads to the spray transport equation

$$\frac{\partial f}{\partial t} + \mathrm{div}_{\mathbf{X}}(f\dot{\mathbf{X}}) = \dot{f}_{\mathrm{coll}} + \dot{f}_{\mathrm{bu}}. \tag{19.44}$$

Here, $\mathrm{div}_{\mathbf{X}}$ indicates that the divergence is taken over all the state variables, and the source terms on the right-hand side are due to droplet collision and droplet breakup. In component form, (19.44) becomes

$$\begin{aligned}\frac{\partial f}{\partial t} + \mathrm{div}_{\mathbf{X}}(f\mathbf{v}) + \mathrm{div}_{\mathbf{V}}(f\dot{v}) + \frac{\partial}{\partial r}(f\dot{r}) + \frac{\partial}{\partial T_\mathrm{d}}(f\dot{T}_\mathrm{d}) \\ + \frac{\partial}{\partial y}(f\dot{y}) + \frac{\partial}{\partial \dot{y}}(f\ddot{y}) = \dot{f}_{\mathrm{coll}} + \dot{f}_{\mathrm{bu}}\end{aligned} \tag{19.45}$$

where $\mathrm{div}_{\mathbf{X}}$ and $\mathrm{div}_{\mathbf{V}}$ indicate the divergences with respect to the droplets' spatial and velocity coordinates, respectively.

In order to be able to solve (19.45), expressions for the individual terms, $\dot{\mathbf{v}}$, $\dot{r}$, $\dot{T}_\mathrm{d}$, $\dot{y}$, and $\ddot{y}$ need to be specified. This is done via modeling of the individual spray subprocesses as, following the exhibition of Amsden et al. [4], is discussed next.

Drop Acceleration

The drop acceleration has contributions due to aerodynamic drag and gravitation, and is given by

$$\frac{\mathrm{d}}{\mathrm{d}t}\mathbf{v} = \frac{3}{8} C_\mathrm{D} \frac{\rho_\mathrm{g}}{\rho_\mathrm{d}} \frac{\|\mathbf{v}_\mathrm{r}\|}{r} \mathbf{v}_\mathrm{r} + \mathbf{g}, \tag{19.46}$$

where C_D is the drag coefficient; ρ_g , the gas density; ρ_d , the drop density; $\mathbf{v}_\mathrm{r} = \mathbf{u} + \mathbf{u}' - \mathbf{v}$, the relative drop velocity with $\mathbf{u}'$ the turbulence fluctuation; and **g,** the constant of gravity. The drag coefficient is given by the formula of Putnam as

$$C_\mathrm{D} = \begin{cases} \dfrac{24}{Re_\mathrm{d}}(1 + Re_\mathrm{d}^{2/3}/6) & \text{if } Re_\mathrm{d} \leq 1,000 \\ 0.424 & \text{if } Re_\mathrm{d} > 1,000 \end{cases}$$

Here, Re_d is the droplet Reynolds number defined by

$$Re_\mathrm{d} = \frac{2r\rho_\mathrm{g}\mathbf{v}_\mathrm{r}}{\mu_\mathrm{g}(\breve{T})}, \tag{19.47}$$

where the viscosity μ_g depends on the weighted gas temperature given by the two-thirds law

$$\breve{T} = (T + 2T_\mathrm{d})/3. \tag{19.48}$$

Note that for LES, the fluctuation term $\mathbf{u}'$ is usually neglected in the computation of $\mathbf{v}_\mathrm{r}$.

Drop Radius

The drop radius is determined by the mass rate of change due to evaporation or condensation. Taking the convective mass transfer into account, these phenomena can be described by the Frössling correlation [16],

$$\frac{\mathrm{d}}{\mathrm{d}t} r^2 = \frac{\rho_\upsilon}{\rho_\mathrm{d}} D_\upsilon B_\mathrm{d} Sh_\mathrm{d}. \tag{19.49}$$

Here, D_υ is the vapor diffusivity in the gas and is determined from the empirical relation

$$\rho_v D_v = D_1 \breve{T}^{D_2},$$

where D_1 and D_2 are constants, and $\breve{T}$ is given by (19.48). The term B_d is the Spalding mass transfer number defined as

$$B_\mathrm{d} = \frac{Y_v^* - Y_v}{1 - Y_v^*}$$

where $Y_v = \rho_v/\rho_\mathrm{g}$ is the vapor mass fraction, and Y_v^* is the vapor mass fraction on the drop surface computed from

$$Y_v^*(T_d) = \left[1 + \frac{W_0}{W_v}\left(\frac{p_\mathrm{g}}{p_v(T_\mathrm{d})} - 1\right)\right]^{-1}.$$

In this formula, W_v is the molecular weight of the vapor and W_0 is the molecular weight of the surrounding gas, but excluding the fuel vapor. $p_v(T_d)$ is the equilibrium vapor pressure and p_g is the gas phase pressure.

The *Sherwood number* is given by

$$Sh_\mathrm{d} = (2.0 + 0.6\, Re_\mathrm{d}^{1/2} Sc_\mathrm{d}^{1/3}) \ln\frac{(1 + B_\mathrm{d})}{B_\mathrm{d}},$$

where the droplet Schmidt number is defined by

$$Sc_\mathrm{d} = \frac{\mu_\mathrm{g}(\breve{T})}{\rho_\mathrm{g} D_\mathrm{g}(\breve{T})}$$

and $\breve{T}$ is given by (19.48).

Drop Temperature

The rate of change of the drop temperature is determined by an energy balance equation, where the energy supplied to the drop raises the temperature or supplies heat for evaporation. Formally, this is expressed as

$$C_\mathrm{d} m_\mathrm{d} \frac{\mathrm{d}T_\mathrm{d}}{\mathrm{d}t} = q_\mathrm{h} S_\mathrm{d} + L(T_\mathrm{d}) \frac{\mathrm{d}m_\mathrm{d}}{\mathrm{d}t}, \tag{19.50}$$

where C_d is the droplet specific heat, m_d is the droplet mass, S_d is its surface, q_h is the convective heat flux to the drop (per unit area), and $L(T_\mathrm{d})$ is the latent heat of evaporation. In analogy to the Frössling correlation for describing the change in the drop radius, the change in the drop temperature heat conduction rate, q_h, is given by the Ranz-Marshall correlation [45]

$$q_{\mathrm{h}} = K_{\mathrm{g}}(\breve{T}) Nu_{\mathrm{d}} (T - T_{\mathrm{d}})/2r. \tag{19.51}$$

In this equation, the conductivity of the gas is given by the empirical relation

$$K_{\mathrm{g}}(\breve{T}) = \frac{K_1 \breve{T}^{3/2}}{\breve{T} + K_2}$$

where K_1 and K_2 are constants and $\breve{T}$ is given by (19.48). The convective heat transfer is governed by the *Nusselt number*

$$Nu_{\mathrm{d}} = (2.0 + 0.6\, Re_{\mathrm{d}}^{1/2} Pr_{\mathrm{d}}^{1/3}) \ln \frac{(1 + B_{\mathrm{d}})}{B_{\mathrm{d}}},$$

where Re_{d} is given in (19.47) and the droplet Prandtl number is defined by

$$\mathrm{Pr}_{\mathrm{d}} = \frac{\mu_{\mathrm{g}}(\breve{T}) C_p(\breve{T})}{K_{\mathrm{g}}(\breve{T})}.$$

Finally, the latent heat of vaporization, $L(T_{\mathrm{d}})$, is the energy required to convert liquid to vapor at the constant vapor pressure. This latent heat is the difference between the vapor enthalpy h_{υ} and the liquid enthalpy, h_{d}, and is given by

$$L(T_d) = h_{\upsilon}(T_{\mathrm{d}}) - h_{\mathrm{d}}(T_{\mathrm{d}}, p_{\upsilon}(T_{\mathrm{d}})) = \left[e_{\upsilon}(T_d) + \frac{R_0 T_d}{W_{\upsilon}} \right] - \left[e_d(T_d) + \frac{p_{\upsilon}(T_d)}{\rho_d} \right],$$

where e is the specific internal energy, R_0 is the universal gas constant, W_{υ} is the molecular weight of the vapor, and $p_{\upsilon}(T_d)$ is the equilibrium vapor pressure.

Drop Deformation

The drop deformation is modeled by Taylor's drop oscillator [56], as introduced by O'Rourke and Amsden [37] into the context of sprays. In this approach, the drop distortion is described by a forced, damped, harmonic oscillator in which the forcing term is given by the aerodynamic drag, the damping is due to the liquid viscosity, and the restoring force is supplied by the surface tension. More specifically, the drop distortion is described by the deformation parameter, $y = 2x/r$, where x denotes the maximum radial distortion from the spherical equilibrium surface, and r is the drop radius. The deformation equation in terms of the normalized distortion parameter, y, is

$$\ddot{y} + \frac{5\mu_d}{\rho_d r^2}\dot{y} + \frac{8\gamma}{\rho_d r^3} y = \frac{2\rho_g \|\boldsymbol{v}_r\|^2}{3\rho_d r^2} \tag{19.52}$$

where ρ denotes the density, μ_d is the drop viscosity, γ is the surface tension, and $\mathbf{v}_r$ is the relative drop-gas velocity.

Note that the drop distortion parameters can influence the drop drag via its change of the cross-section and the drag coefficient because of the change of shape. Such investigations have been reported by Hwang et al. [23]. More importantly, the drop distortion parameters play a fundamental role in the determination of drop breakup and in the modeling of the atomization process.

Atomization and Drop Breakup

Drop breakup enters the spray equation via the source term $\dot{f}_{bu}$ in (19.45). There are various ways of accounting for drop breakup, most of which are also used for a rudimentary description of the atomization process. Some of these approaches are discussed in more detail in Chap. 9, and include the TAB model of O'Rourke and Amsden [37], the Wave Breakup model of Reitz and coworkers [46, 40], the Unified Spray Breakup model of Chryssakis and Assanis [10], and the Cascade Atomization and Drop Breakup model of Tanner [54].

Drop Collisions

In (19.45), the drop collisions are accounted for via the source term, $\dot{f}_{coll}$. One of the most widely used collision models is the one *developed* by O'Rourke [36]. In this model, the probability for a drop with index 1 to undergo n collisions with a drop of index 2 in a given volume V during the time interval Δt is given by the Poisson distribution

$$P_n = \bar{x}^n \exp(-\bar{x})/n!$$

where $\bar{x} = v\Delta t$ is the mean and

$$v = \frac{N_2}{V}\pi(r_1 + r_2)^2 ||\mathbf{v}_1 - \mathbf{v}_2||$$

is the collision frequency, with N_2 being the number of drops in volume V and drop state 2. A collision has two possible outcomes, depending on the collision impact parameter b. If b is less than a critical value b_{cr}, then the drops coalesce, and if b exceeds b_{cr}, then the drops undergo an elastic collision, that is, they exchange their momentum but maintain their size and temperature. The critical impact parameter $b_{crit} = b_{crit}(r_1, r_2, \gamma)$ depends on the collision drop sizes and the surface tension γ.

There are other approaches that model drop collisions, one of which is the no-time counter (NTC) model of Schmidt and Rutland [48], and another is due to Post and Abraham [42].

Spray Source Terms

The spray source terms in the gas phase equations, shown in Table 19.4, can be computed when all the spray submodels are in place, and the drop PDF $f(t, \mathbf{x}, \mathbf{v}, r, T_\mathrm{d}, y, \dot{y})$ in (19.45) is determined. These source terms are obtained by summing up the rates of change of mass, momentum, and energy of all droplets at a fixed location $\mathbf{x}$ and time t. This leads to the expressions

$$\dot{\rho}^s = -\int \frac{\mathrm{d}}{\mathrm{d}t}\left[\frac{4\pi}{3}\rho_\mathrm{d} r^3\right] f \,\mathrm{d}\Omega \tag{19.53}$$

$$\dot{\mathbf{M}}^s = -\int \left[\frac{\mathrm{d}}{\mathrm{d}t}\left(\frac{4\pi}{3}\rho_\mathrm{d} r^3 \mathbf{v}\right) - \frac{4\pi}{3}\rho_\mathrm{d} r^3 \mathbf{g}\right] f \,\mathrm{d}\Omega \tag{19.54}$$

$$\begin{aligned}\dot{Q}^\mathrm{s} = -\int \Bigg\{ & 4\pi\rho_\mathrm{d} r^2 \frac{\mathrm{d}r}{\mathrm{d}t}\left[e_\mathrm{d}(T_\mathrm{d}) + 0.5(\mathbf{v}-\mathbf{u})^2\right] \\ & + \frac{4\pi}{3}\rho_\mathrm{d} r^3 \left[C_\mathrm{d}\frac{\mathrm{d}T_\mathrm{d}}{\mathrm{d}t} + (\mathbf{F}-\mathbf{g})\cdot\mathbf{v}_\mathrm{r}\right]\Bigg\} f \,\mathrm{d}\Omega\end{aligned} \tag{19.55}$$

$$\dot{W}^\mathrm{s} = -\int \frac{4}{3}\pi\rho_\mathrm{d} r^3 [(\mathbf{F}-\mathbf{g})\cdot\mathbf{u}'] f \,\mathrm{d}\Omega \tag{19.56}$$

where the integrals are taken over all droplets at location $\mathbf{x}$ and time t, and $f\,\mathrm{d}\Omega = f(t, \mathbf{X})\mathrm{d}v\mathrm{d}r\mathrm{d}T_\mathrm{d}\mathrm{d}y\mathrm{d}\dot{y}$. As mentioned earlier, there is no spray source term $\dot{W}^\mathrm{s}$ necessary when LES is used instead of RANS.

Chemical Reactions

In this subsection, a brief exposition of chemical reactions related to spray combustion modeling is presented. More details, together with additional references, can be found in Chap. 10.

The detailed chemical reaction mechanism of a combustion process can involve thousands of reactions between hundreds of species (cf. Refs. [9, 15, 57, 60]). Since for each species, there is a species transport equation that needs to be solved, this would lead to enormously large systems of PDEs, whose computing demands lie far beyond the capacities of today's computers. Therefore, only the process-domineering

reactions and species are considered, and when necessary, the reaction rates are determined from empirical and/or flow determining quantities.

There are essentially three phenomena of interest when dealing with reacting sprays, namely, ignition, heat release, and pollutant formation. Before discussing these three phenomena, a review of chemical kinetics is presented.

Chemical Kinetics

Chemical reactions are symbolically denoted by

$$\sum_m a_{mr}\chi_m \leftrightarrow \sum_m b_{mr}\chi_m, \tag{19.57}$$

where χ_m represents one mole of species m, and a_{mr} and b_{mr} are the integral stoichiometric coefficients for reaction r. The forward and backward directions are indicated with the double arrow. The species conservation in each chemical reaction r dictates that

$$\sum_m (a_{mr} - b_{mr})W_m = 0,$$

where W_m is the molecular mass of species m. The rate at which the rth kinetic reaction proceeds is given by the reaction rate

$$\dot{\omega}_r = k_\mathrm{f} \prod_m \left(\frac{\rho_m}{W_m}\right)^{a'_{mr}} - k_\mathrm{b} \prod_m \left(\frac{\rho_m}{W_m}\right)^{b'_{mr}}, \tag{19.58}$$

where the reaction orders a'_{mr} and b'_{mr} need not equal their stoichiometric counterparts a_{mr} and b_{mr}, so that empirical, possibly noninteger, reaction orders can be used. The coefficients k_f and k_b are the specific forward and backward reaction rates given by the generalized Arrhenius law

$$k_\mathrm{f} = A_\mathrm{f} T^{\zeta_\mathrm{f}} \exp\left(\frac{-E_\mathrm{f}}{T}\right) \tag{19.59}$$

$$k_\mathrm{b} = A_\mathrm{b} T^{\zeta_\mathrm{b}} \exp\frac{-E_\mathrm{b}}{T}, \tag{19.60}$$

where A_f, A_b, ζ_f, and ζ_b are constants, and E_f and E_b are the forward and backward activation temperatures.

With the reaction rates determined by (19.58), the chemical source terms in the gas phase conservation equations for species and energy can be written as

$$\dot{\rho}_m^{\mathrm{c}} = W_m \sum_r (b_{mr} - a_{mr})\dot{\omega}_r \tag{19.61}$$

$$\dot{Q}^c = \sum_r \dot{\omega}_r \sum_m (a_{mr} - b_{mr})(\Delta h_{\mathrm{f}}^0)_m \tag{19.62}$$

respectively, where $(\Delta h_{\mathrm{f}}^0)_{\mathrm{m}}$ is the heat of formation of species m at absolute zero. Note that (19.61) is a manifestation of *the law of mass action*.

Fast chemical reactions, usually at high temperatures, are often assumed to be in equilibrium. This means that the forward and backward reaction rates are the same; hence, $\dot{\omega}_r$. Therefore, (19.58) becomes the constraint condition

$$\prod_m \left(\frac{\rho_m}{W_m}\right)^{b_{mr}-a_{mr}} = \frac{k_{\mathrm{f}}}{k_{\mathrm{b}}} = K_{\mathrm{c}}^r(T), \tag{19.63}$$

where the concentration equilibrium constant, $K_{\mathrm{c}}^r(T)$, is of the form

$$\ln K_{\mathrm{c}}^r(T) = A_r \ln T_A + \frac{B_r}{T_A} + C_r + D_r T_A + E_r T_A^2.$$

In this equation, $T_A = T/1,000$ and A_r, B_r, C_r, D_r, and E_r are reaction specific constants. Therefore, if $K_{\mathrm{c}}^r(T)$ and the reactant concentrations are known for each reaction r, then the product concentrations can be obtained from (19.63).

Ignition

The first chemical reactions associated with a spray occur at relatively low temperatures and are referred to as the auto-ignition or pressure ignition process. This ignition process is important in diesel engines because it influences the subsequent high-temperature combustion and pollution formation.

When fuel is injected into a combustion chamber, it atomizes into tiny droplets that evaporate and mix with air to form a reactive compound. Under increased temperature and pressure, this compound starts reacting, and in the process, releases heat to initiate the actual combustion process. The initial stage of this reaction process, called ignition, occurs at relatively low temperatures and therefore, its chemical time scales are comparable to the ones of the flow. Also, the chemical reactions are dominated by various reaction paths, which lead to a large number of intermediate species that can exhibit unexpected behavior. In fact, after the initial reactions, which are mainly due to chain-branching, there is a temperature region, called the *cool-flame region*, where reverse reactions lead to a very slow burning process, hence a small temperature increase. As a consequence, this can result in an increase of the ignition delay. This reverse ignition delay characteristic is illustrated for three different gas pressures of an *n*-heptane fuel in Fig. 19.1. Subsequently,

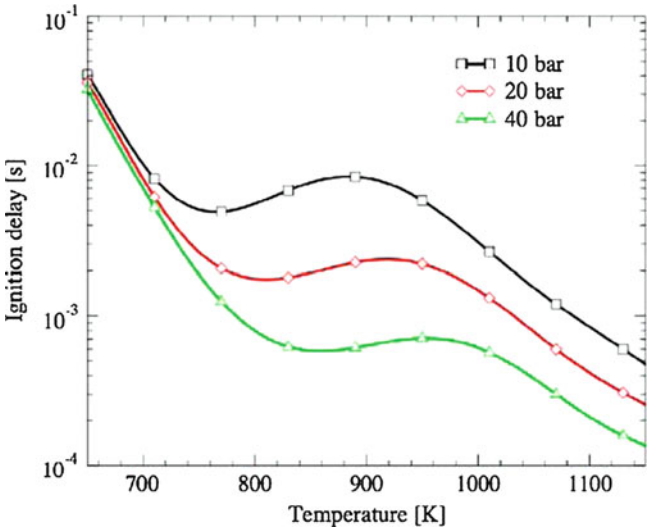


Fig. 19.1 Ignition delay of n-heptane as a function of temperature for three different gas pressures

after the cool-flame regime, other reaction paths are dominating the chemical processes and release sufficient heat such that the associated temperature increase leads to the high-temperature reactions, that is, the actual combustion process.

Detailed reaction mechanisms that describe the entire ignition process are very extensive and computationally expensive. A common approach to the modeling of the ignition process is to derive a reduced reaction mechanism from a set of detailed chemical reactions (cf. [13, 33]). A widely used auto-ignition model utilized in CFD simulations of diesel combustion processes is the Shell ignition model of Halstead et al. [20], or any of its many variants (e.g. [5, 27]). The Shell ignition model is based on eight global chemical reactions involving six representative species, where the kinetic parameters have been determined from fittings to experimental data. The Shell model computes the heat release due to chemical reactions, and it requires an additional transport equation for each intermediate species in order to describe its flow behavior.

Another approach to the modeling of the ignition process is the Least-Square-Fitted Ignition Transport (LIT) model of Tanner [53], which is a further development of the simplified kinetic ignition (SKI) model developed by Weisser et al. [59]. The LIT model is based on a concept utilizing a single transport progress variable, C_{ig}, which describes the progress of the physical and chemical processes governing the ignition delay, τ. This quantity is formally equivalent to the concentration of an intermediate species, nondimensionalized by its critical value and subject to the transport equation

$$\frac{\partial(\rho C_{\mathrm{ig}})}{\partial t} + \operatorname{div}(\rho C_{\mathrm{ig}}\mathbf{u}) = \operatorname{div}(\rho D \operatorname{grad} C_{\mathrm{ig}}) + \frac{\rho}{\tau(p,T,\Phi)},$$

where ρ is the density of the gas; $\mathbf{u}$, p, and T are the gas velocity, pressure, and temperature, respectively; Φ represents the local fuel equivalence ratio; and D, is the effective diffusivity. Note that the nondimensionalization of C_{ig}, mentioned above, leads to the critical value $C_{\text{crit}} = 1$. Therefore, if $C_{\text{ig}} > 1$ in some cell, then ignition has occurred and the actual combustion model takes over at that location. Additional details of ignition modeling are given in Chap. 13.

Combustion and Emissions

The heat release in a combustion process can be determined with as few as one reaction equation using empirical reaction rate coefficients and activation temperatures. This drastic reduction in the number of chemical reactions is justified by Hess' law, which states that the net heat of reaction of a set of chemical reactions depends only on the initial and the final states. To illustrate this point, the heat release of an idealized hydrocarbon fuel, say C_nH_m, can be modeled with the following global one-step reaction mechanism

$$C_nH_m + \left(n + \frac{m}{4}\right)O_2 \rightarrow nCO_2 + \frac{m}{2}H_2O,$$

where the specific reaction rates are determined from the generalized Arrhenius relation in (19.59), using empirical coefficients and activation temperatures.

Another illustration of a reduced set of chemical reactions is the extended Zeldovich mechanism (cf. [18, 64]) used to predict thermal nitric oxide formation in high-temperature diesel combustion. This reaction mechanism involves the three kinetic reactions

$$O + N_2 \leftrightarrow N + NO$$

$$N + O_2 \leftrightarrow O + NO$$

$$N + OH \leftrightarrow H + NO$$

and the five equilibrium reactions

$$H_2 \rightarrow 2H$$

$$O_2 \rightarrow 2O$$

$$O_2 + H_2 \rightarrow 2OH$$

$$O_2 + 2H_2O \rightarrow 4OH$$

$$O_2 + 2CO \rightarrow 2CO_2$$

The equilibrium reactions are needed to generate the O, N, and OH radicals at high temperature, before the slower kinetic reactions can be initialized. The coefficients and activation temperatures used for a specific diesel engine computation are listed in Ref. [55]. There have been many different reaction mechanisms developed for the prediction of nitric oxides by various research groups. For an example and additional references, see Weisser [58].

In *premixed combustion*, that is, in a reaction system where the reactants, usually fuel and oxygen, are mixed before reactions take place, the kinetic or equilibrium reaction rates obtained via (19.58) or (19.63) represent the relevant physics of the problem. In spray combustion, however, the reactants are initially separated, often referred to as *nonpremixed reactions* or *diffusion reactions*, and only after several processes such as liquid atomization, fuel evaporation, and fuel-air mixing, do they form a flammable mixture. The region of flammable mixture is usually a very thin reacting sheet whose geometric properties are determined by the gas flow, which for fuel sprays, is usually turbulent. Therefore, the mixing process itself is determined by the turbulence properties of the flow, which in turn determines the speed of the chemical reactions, i.e., the reaction rates.

A number of modeling approaches that take turbulent mixing into account when computing chemical reaction rates have been proposed by various researchers, including Spalding [52], Borghi [7], Magnussen and Hjertager [32], Bray and Moss [8], Gosman et al. [19], Abraham et al. [1], Kong and Reitz [28], and others. All these approaches relate the average eddy turn-over time $\tau = k/\varepsilon$ to the reaction rate. Further details of mixing-controlled reaction models are given in Chap. 13.

Gas, Liquid, Turbulence, and Chemistry Interactions

The direct interactions between the gas phase, the liquid phase, the chemical reactions, and the turbulence effects are illustrated in the diagram in Fig. 19.2. In order to solve the gas phase conservation equations for mass, species, momentum,

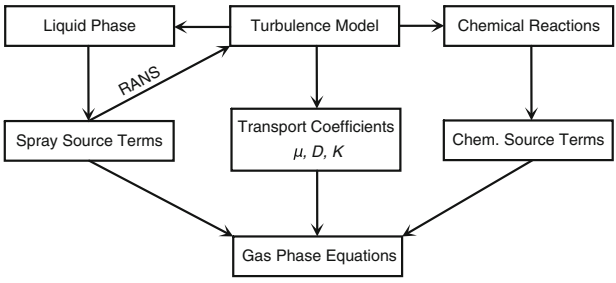


Fig. 19.2 Interaction diagram for gas, turbulence, liquid, and chemical reactions

and energy given in Table 19.4, the source terms from the liquid phase and the chemical reactions need to be known. The liquid or spray source terms, given in (19.53)–(19.56), are determined from the solution of the spray equation, (19.45), and the chemical source terms in (19.61) and (19.62) are obtained via the appropriate chemical reaction mechanisms. The flux densities in the gas conservation equations depend on the transport coefficients, that is, on the effective viscosity μ, the mass diffusivity, D, and the heat conductivity, K, given in (19.41)–(19.43). These material coefficients are obtained from the turbulence model equations for k and ε given in Table 19.5. For RANS simulations, the latter two also depend on the spray source term $\dot{W}^{S}$ given in (19.56), which helps deplete the turbulence kinetic energy and contributes to its dissipation.

The diagram shows only the direct interdependence between the various phenomena. Of course, as presented, all the flow, spray, and combustion processes are coupled at many levels. For example, in order to compute the spray properties via the spray submodels, the gas variables including turbulence quantities, need to be known, and the same is true for solving the chemical reaction equations. Since all these phenomena have their own characteristic length and time scales, and these scales range over a wide spectrum, the solution of this system of equations poses a real challenge.

Boundary and Initial Conditions

The description of a dispersed multiphase flow with chemical reactions leads to a complex system of differential and algebraic equations, which can only be solved by specifying appropriate boundary and initial conditions. For the gas phase equations, the boundary conditions are imposed on the gas velocity **u**, the temperature T, the turbulent kinetic energy k, and its dissipation ε. The spray equations require conditions at the nozzle exit and for the interactions of the droplets with the walls.

For the gas velocity **u**, the wall boundary conditions can be of free slip, no-slip, or turbulent law-of-the-wall type. The free-slip condition demands that the normal velocity components of the fluid and the wall coincide, while the tangential components of the stress tensor satisfy $\boldsymbol{\sigma}_{\mathrm{w}} = \boldsymbol{\sigma} \cdot \mathbf{t} = 0$, where **t** is the unit tangential vector to the wall. The no-slip boundary conditions require the fluid velocity to coincide with the wall velocity. No-slip boundary conditions impose large velocity gradients, which, because of lack of sufficient computational resources, cannot be resolved. Therefore, wall functions are used. The following discussion reflects the exhibition given by Amsden et al. [4].

The turbulent law-of-the-wall, as in the case of the free-slip conditions, has its normal velocity component equal to the normal wall speed. The tangential components

are determined by matching the velocity component to the empirically determined logarithmic profile

$$\frac{||\mathbf{u}_r||}{u^*} = \begin{cases} \dfrac{7}{8\kappa}\ln(\zeta/R_c) + \sqrt{R_c} & \zeta > R_c \\ \sqrt{\zeta} & \zeta < R_c \end{cases} \tag{19.64}$$

$$\rho(u^*)^2 \frac{\mathbf{u}_r}{||\mathbf{u}_r||} = \boldsymbol{\sigma}_w - (\boldsymbol{\sigma}_w \cdot \mathbf{n})\mathbf{n} \tag{19.65}$$

where $\mathbf{u}_r = \mathbf{u} - \mathbf{u}_w$ is the relative gas-wall velocity; $\zeta = (\rho y||\mathbf{u}_r||)/\mu_g(T)$, the Reynolds number based on the relative gas/wall velocity evaluated a distance y from the wall, $\dot{u}^*$, the shear speed defined by (19.65); R_c, the Reynolds number defining the boundary between the laminar and logarithmic regions in the turbulent boundary layer; and $\kappa = \sqrt{C_\mu^{1/2}(C_2 - C_1)\mathrm{Pr}_\varepsilon}$ is determined by the k–ε model constants in Table 19.3.

The isothermal or adiabatic boundary conditions for the heat transfer can be specified with the wall temperature T or the normal heat flux $\mathbf{q}_w = -K\mathrm{grad}\, T \cdot \mathbf{n}$. Isothermal boundary conditions in conjunction with the law-of-the-wall are modeled as

$$\frac{\mathbf{q}_w}{\rho u^* C_p(T - T_w)} = \begin{cases} 1/\left(Pr_{lam}\dfrac{||\mathbf{u}_r||}{u^*}\right) & \zeta \le R_c \\ \left\{Pr\left[\dfrac{||\mathbf{u}_r||}{u^*} + \left(\dfrac{Pr_{lam}}{Pr} - 1\right)R_c^{1/2}\right]\right\}^{-1} & \zeta > R_c \end{cases} \tag{19.66}$$

where T_w is the wall temperature and Pr_{lam} is the Prandtl number of the laminar fluid.

For the k–ε turbulence model, the boundary conditions for the turbulent kinetic energy k and its dissipation rate ε are specified as

$$\mathrm{grad}\, k \cdot \mathbf{n} = 0$$

$$\varepsilon = \sqrt{\frac{C_\mu}{Pr_\varepsilon(C_2 - C_1)}}\left(\frac{k^{3/2}}{y}\right)$$

with k and ε evaluated at a distance y from the wall.

The boundary conditions for the spray equations specify the droplet-wall interactions, as well as the mass flow rate and the droplet distribution function at the nozzle exit. Additional details and references can be found in Ref. [4].

Computational Aspects

The three-dimensional description of a turbulent spray combustion problem leads to a complex system of differential and algebraic equations together with boundary and initial conditions. The phenomena involved occur over a wide range of time and length scales that poses a substantial challenge for finding a solution. The solution approaches are often highly specialized and are realized via complex computer programs. In this subsection, only an overview of the solution approaches is given; the details can be found in the literature referred to.

One of the pioneering computer programs that has made a significant contribution to the three-dimensional simulation of sprays is the *Kiva* family of open source codes [2–4], developed primarily for reacting sprays in engine and turbine applications. More recently, the C++ open source computing environment, OpenFoam [35], is providing spray libraries as part of its standard packages. Many research groups use these codes as their modeling and simulation platforms to improve the art of spray simulations. Also, there are many well developed commercial CFD codes available that allow the simulation of sprays under various conditions.

System Discretization

In order to solve numerically a continuum-based description of a dispersed multiphase flow, the system has to be discretized appropriately. First, the physical domain is subdivided into simple, nonoverlapping subregions, called cells, with the intention of solving the system of equations on each cell. Typically, these cells are hexahedra or tetrahedra and contain the nodes, that is, the set of points on which the unknown variables are approximated. The collection of nodes form the computational mesh or grid. This domain subdivision demands that the system is discretized appropriately and that the boundary conditions are properly specified. The commonly used discretization methods for RANS-type continuum descriptions are the finite difference method (FDM), the finite volume method (FVM), and the finite element method (FEM). The discretization of the system leads to a large system of algebraic equations, whose solution is obtained by various, often highly specialized, computational methods. The solution approach just outlined is schematically shown in the diagram of Fig. 19.3.

In the FDM, the differential form of the conservation equations (cf. (19.12) or (19.13)) are discretized by approximating the spatial and temporal derivatives by means of an appropriate difference quotient, such as a forward, central, or backward difference. The spatial derivatives utilize the cell nodes in one form or the other to achieve this discretization, while the temporal derivatives use a given time step. FDMs require a structured grid, that is, meshes that are topologically equivalent[3] to a right hexahedron in integer space, called the logical space, where the nodes

[3]Equivalent under a bi-continuous bijection.

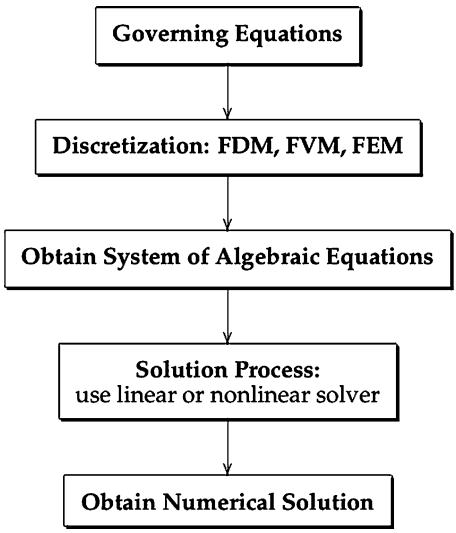


Fig. 19.3 Overview of the computational solution process

correspond to points with integer coordinates. This has the disadvantage that surfaces need to be mapped topologically into a Cartesian space, which can be difficult in general.

In the FVM, a *control volume* is associated with each node, usually in such a way that the node becomes the center of the control volume. The integral equations are then solved over each control volume that guarantees that the physical quantities are conserved. In contrast to the FDM, the FVM utilizes the integral form of the conservation equation, (19.11), together with the Reynolds transport theorem, to obtain

$$\int_{\Omega(t)} \left[\frac{\partial \gamma}{\partial t} - \pi(\mathbf{x}, t) - \varsigma(\mathbf{x}, t) \right] \mathrm{d}V = - \int_{\partial\Omega(t)} [\gamma \mathbf{u} + \phi(\mathbf{x}, t) \cdot \mathbf{n}] \mathrm{d}A$$

In FVMs, the evaluation of divergences is avoided by computing the convective and diffusion fluxes over the control volume surfaces. This avoids the evaluation of difference operators and hence the transformation into the Cartesian integer space. The FVM method is much more flexible than the FDM; it can be used for complex geometries and unstructured grids.

In the FEM, the conservation equations are reformulated as a weighted residual problem. More precisely, the residual of a local conservation equation, represented by (19.12), is defined as

$$R(\gamma) = \frac{\partial \gamma}{\partial t} + \mathrm{div}(\gamma \mathbf{u}) + \mathrm{div}\, \phi - \pi - \varsigma,$$

and the physical property, $\gamma(\boldsymbol{x}, t)$, is obtained by solving

$$\int_{\Omega} w(\mathbf{x}) R(\gamma) \mathrm{d}x = 0,$$

where the integral is taken over the entire domain and for all admissible weighting or test functions $w(\boldsymbol{x})$. The spatial discretization is obtained by approximating the solution γ on each element by a piecewise smooth polynomial $\gamma^e(\boldsymbol{x}, t)$, that is,

$$\gamma(\boldsymbol{x}, t) \approx \gamma^e(\boldsymbol{x}, t) = \sum_{j}^{N} \gamma_j^e(t) \psi_j^e(\boldsymbol{x}),$$

where the $\psi_j^e(\boldsymbol{x})$ are the shape (basis, interpolation, trial) functions computed on each cell, and the superscript e indicates the particular element (cell). The polynomials are interpolation polynomials (Lagrange, Hermite, Chebychev) that are computed at the element nodes and satisfy smoothness conditions across the element boundaries. Substitution of the approximations into the weighted residual problem, along with a weight function $w(\boldsymbol{x})$ for each node, yields a large system of ordinary differential equations in time, which is then solved using the FDM. The FEM method is less intuitive than the FDM or FVM, but it is more flexible and can be more easily used for complex geometries and unstructured grids.

The discretization of the conservation equations via FDM, FVM or FEM leads to a large system of algebraic equations in each time step which, in order to be solved, is usually linearized. Thus, the problem of solving a complex multiphase flow, with possibly chemical reactions, is reduced to the solutions of large linear systems. Further details for the various solution approaches, together with additional references, can be found in Chung [11].

The discretization of the liquid phase is achieved by the discrete particle method (c.f. Ref. [4]). In this method, the domain, $\mathbf{X}$, of the spray PDF, $f(t, \mathbf{X})$, is subdivided into hyper-rectangles, and all droplets that fall within one particular hyper-rectangle are identified as one representative particle. In other words, the spray PDF $f(t, \mathbf{X})$ is approximated with a discrete PDF, where each discretization point corresponds to a representative particle consisting of droplets of identical states. The evolution of the spray PDF is then determined in analogy to the Monte Carlo method by using a sampling process on these particles.

Solution Algorithms

The actual solution algorithm is often based on the arbitrary Lagrangian-Eulerian (ALE) method of Hirt et al. [22]. In this method, in order to make the solution computationally more efficient, a decoupling of the convective and nonconvective gas-phase terms in each time step is introduced. In the Lagrangian phase, where the computational cells move with the fluid flow, the spray PDF is updated and the source terms due to liquid and chemistry are evaluated. Also, the nonconvective

terms, that is, the diffusion terms on the right-hand side of the conservation equations, are computed. After the Lagrangian computations are completed for a given time step, the convective terms are computed via the Eulerian approach. This is achieved by freezing the flow field and then mapping the distorted mesh onto its original shape. More details of the ALE approach for specific spray computations are given in Amsden et al. [4].

The computations of the flux densities in the Lagrangian phase are performed with specialized pressure-correction methods based on a SIMPLE-type [38, 39] or a PISO-type [24, 25] algorithm. (For a comparison of the two algorithms see Barton [6].) Both type of solution approaches are predictor-corrector methods that are usually applied on a staggered grid. The convective terms, solved during the Eulerian phase, are computed by means of an explicit upwinding scheme, and need to be subcycled in order to meet the CFL-stability criterion. More details of these algorithms can be found in the respective references.

General Comments

Intermittent sprays, such as those encountered in engine applications, are transient processes whose computations require a tracking of the time variable. The complexity of the solution algorithm outlined above requires that the time steps are determined from accuracy and stability criteria that include the change in cell size and the cell distortion as well as the strength of the chemical and liquid source terms.

In addition, tabulated quantities for the internal energies and heat capacities of the various species in the gas and liquid phases are necessary to complete the computations. Further, special attention is required to accommodate moving boundaries that account for piston and valve movements in engine applications.

References

1. J. Abraham, F. V. Bracco, and R. D. Reitz. Comparisons of computed and measured premixed charge engine combustion. Combustion and Flame, 60:309–322, 1985.
2. A. A. Amsden. KIVA–3V: a block–structured KIVA program for engines with vertical or canted valves. Technical Report LA-13313-MS, Los Alamos National Laboratory, Los Alamos July 1997.
3. A. A. Amsden, T. D. Butler, P. J. O'Rourke, and J. D. Ramshaw. KIVA – a comprehensive model for 2-D and 3-D engine simulations. SAE Paper 850554, 1985.
4. A. A. Amsden, P. J. O'Rourke, and T. D. Butler. KIVA II: A computer program for chemically reactive flows with sprays. Technical Report LA-11560-MS, Los Alamos National Laboratory, Los Alamos, May 1989.
5. M. Astarita, F. E. Corcione, M. Costa, A. De Maio, and B. M. Vaglieco. Application of the shell ignition model and comparison with spectroscopic measurements of a high swirl diesel combustion. In Proceedings of the ASME Fall Technical Conference, ICE–vol. 33-3, pp. 27–34, October 1999.

6. I. E. Barton. Comparison of SIMPLE- and PISO-type algorithms for transient flows. International Journal for Numerical Methods in Fluids, 26:459–483, 1998.
7. R. Borghi. Chemical reactions calculations in turbulent flows: Application to a co-containing turbojet plume. Advances in Geophysics, 18(pt II):349–365, 1974.
8. K. N. C. Bray and J. B. Moss. A unified statistical model of the premixed turbulent flame. Acta Astronautica, 4:291–319, 1977.
9. C. Chevalier, P. Loussard, U. C. Müller, and J. Warnatz. A detailed low-temperature reaction mechanism of n-heptane auto-ignition. In Second International Symposium, COMODIA, pp. 93–97, Kyoto, Japan, 1990.
10. C. Chryssakis and D. Assanis. A unified fuel spray breakup model for internal combustion engine applications. Atomization and Sprays, 18(5):375–426, 2008.
11. T. J. Chung. Computational Fluid Dynamics. Cambridge University Press, Cambridge, 2002.
12. J. W. Deardorff. A numerical study of three-dimensional turbulent channel flow at large Reynolds numbers. Journal of Fluid Mechanics, 41:453–480, 1970.
13. M. Elsden, E. Gutheil, M. Nehse, and J. Warnatz. Auto-ignition modeling in diesel engines. In Proceedings of the Third International ICE Conference, Capri, September 1997.
14. J. H. Ferziger. Large eddy numerical simulations of turbulent flows. AIAA Paper 76–347, San Diego, 1976.
15. M. Frenklach, H. Wang, and M. J. Rabinowitz. Optimization and analysis of large chemical kinetics mechanisms using the solution mapping method – combustion of methane. Progress in Energy and Combustion Science, 18:47–73, 1992.
16. N. Frössling. Über die Verdunstung fallender Tropfen. Gerlands Beiträge zur Geophysik, 52:170–216, 1938.
17. M. Germano, U. Piomelli, P. Moin, and W. Cabot. A dynamic subgrid-scale eddy viscosity model. Physics of Fluids, 3:1760–1765, 1991.
18. I. Glassman. Combustion, 2nd edn. Academic, Orlando, 1987.
19. A. D. Gosman, F. C. Lockwood, and A. P. Salooja. The prediction of cylindrical furnaces gaseous fueled with premixed and diffusion burners. In Seventeenth Symposium (International) on Combustion, pp. 747–760, The Combustion Institute, Pittsburgh, 1979.
20. M. Halstead, L. Kirsh, and C. Quinn. The autoignition of hydrocarbon fuels at high temperatures and pressures – fitting of a mathematical model. Combustion and Flame, 30:45–60, 1977.
21. F. H. Harlow and P. I. Nakayama. Transport of turbulence energy decay rate. Technical Report LA-3854, Los Alamos National Laboratory, Los Alamos, 1968.
22. C. W. Hirt, A. A. Amsden, and J. L. Cook. An arbitrary Lagrangian-Eulerian computing method for all flow speeds. Journal of Computational Physics, 14:227–253, 1974.
23. S. S. Hwang, Z. Liu, and R. D. Reitz. Breakup mechanisms and drag coefficients of high-speed vaporizing liquid drops. Atomization and Sprays, 6:353–376, 1996.
24. R. J. Issa. Solution of implicitly discretized fluid flow equations by operator-splitting. Journal of Computational Physics, 62:40–65, 1986.
25. R. J. Issa, A. D. Gosman, and A. P. Watkins. The computation of compressible and incompressible recirculating flows by a non-iterative scheme. Journal of Computational Physics, 62:66–82, 1986.
26. W. P. Jones and B. E. Launder. The prediction of laminarization with a two-equation model of turbulence. International Journal of Heat Mass Transfer, 15:301–314, 1972.
27. S.-C. Kong, Z. Han, and R. D. Reitz. The development and application of a diesel ignition and combustion model for multidimensional engine simulation. SAE Paper 950278, 1995.
28. S.-C. Kong and R. D. Reitz. Multidimensional modeling of diesel ignition and combustion using a multistep kinetics model. Journal of Engineering for Gas Turbines and Power, 115: 781–789, 1993.
29. B. E. Launder and D. B. Spalding. Lectures in Mathematical Models of Turbulence. Academic, London, 1972.
30. B. E. Launder and B. I. Sharma. Application of the energy dissipation model of turbulence to the calculation of flow near a spinning disk. Letters in Heat and Mass Transfer, 1(2):131–138, 1974.

31. B. E. Launder and D. B. Spalding. The numerical computation of turbulent flows. Computer Methods in Applied Mechanics and Engineering, 3:269–89, 1974.
32. B. F. Magnussen and B. H. Hjertager. On mathematical modeling of turbulent combustion with special emphasis on soot formation and combustion. In Sixteenth Symposium (International) on Combustion, pp. 719–729, The Combustion Institute, Pittsburgh, 1976.
33. U. C. Müller. Reduzierte Reaktionsmechanismen für die Zündung von n–Heptan und ISO–Oktan unter motorrelevanten Bedingungen. PhD thesis, RWTH, Aachen, 1993.
34. S. Ohe. Vapor-Liquid Equilibrium at High Pressure, 1st edn. Elsevier, New York, 1990.
35. OpenFOAM. The open source CFD toolbox. OpenCFD Ltd., http://www.opencfd.co.uk/openfoam/, 2004–2008.
36. P. J. O'Rourke. Collective Drop Effects in Vaporizing Sprays. PhD thesis, Princeton University, 1981. PhD thesis 1532-T.
37. P. J. O'Rourke and A. A. Amsden. The TAB method for numerical calculation of spray droplet breakup. SAE Paper, 872089, 1987.
38. S. V. Patankar. Numerical Heat Transfer and Fluid Flow. Hemisphere, New York, 1980.
39. S. V. Patankar and D. B. Spalding. A calculation procedure for heat, mass and momentum transfer in three-dimensional parabolic flows. International Journal of Heat and Mass Transfer, 15:1787–1806, 1972.
40. M. A. Patterson and R. D. Reitz. Modeling the effects of fuel spray characteristics on diesel engine combustion and emission. SAE Paper 980131, 1998.
41. S. B. Pope. Turbulent Flows, 2nd edn. Cambridge University Press, New York, 2000.
42. S. L. Post and J. Abraham. Modeling the outcome of drop-drop collisions in diesel sprays. International Journal of Multiphase Flow, 28:997–1019, 2002.
43. L. Prandtl. Bericht über Untersuchungen zur ausgebildeten Turbulenz. Zeitschrift für angewandte Mathematik und Mechanik (ZAMM), 5(2):136–139, 1925.
44. L. Prandtl. Über ein neues Formelsystem für die ausgebildete Turbulenz. In Nachrichten der Akademischen Wissenschaften, Math.-Phys. Klasse, pp. 6–19, Göttingen, Deutschland, 1945.
45. W. E. Ranz and W. R. Marshall. Evaporation from drops (parts I and II). Chemical Engineering Progress, 48:141–146, 173–180, 1952.
46. R. D. Reitz. Modeling atomization processes in high-pressure vaporizing sprays. Atomization and Spray Technology, 3:309–337, 1987.
47. J. C. Rotta. Statistische Theory nichthomogener Turbulenz. Zeitschrift für Physik, 129: 547–572, 1951.
48. D. P. Schmidt and C. J. Rutland. A new droplet collision algorithm. Journal of Computational Physics, 164:62–80, 2000.
49. U. Schumann. Realizability of Reynolds-stress turbulence models. Physics of Fluids, 20: 721–725, 1977.
50. S. Shaanan, J. H. Ferziger, and W. C. Reynolds. Numerical simulation of turbulence in the presence of shear. Department of Mechanical Engineering Technical Report No. TF-6, Stanford University, Stanford, 1975.
51. J. Smagorinsky. General circulation experiments with the primitive equations, part I: the basic experiment. Monthly Weather Review, 91:99–164, 1963.
52. D. B. Spalding. In Thirteenth Symposium (International) on Combustion, pp. 649–657, The Combustion Institute, Pittsburgh, 1971.
53. F. X. Tanner. Validation of an auto-ignition model based on a transport equation of a characteristic ignition progress variable. In Proceedings of the 15th ILASS-Americas Annual Conference, pp. 98–102, Madison, May 2002.
54. F. X. Tanner. Development and validation of a cascade atomization and drop breakup model for high-velocity dense sprays. Atomization and Sprays, 14(3):211–242, 2004.
55. F. X. Tanner and S. Srinivasan. Optimization of an asynchronous fuel injection system in diesel engines by means of a micro-genetic algorithm and an adaptive gradient method. SAE Paper 2008-01-0925, 2008.

56. G. I. Taylor. The shape and acceleration of a drop in a high speed air stream. In G. K. Batchelor, editor, The Scientific Papers of Sir Geoffrey Ingram Taylor, vol. 3, pp. 457–464. Cambridge University Press, New York, 1963.
57. J. Warnatz, U. Maas, and R. W. Dibble. Combustion: Physical and Chemical Fundamentals, Modeling and Simulation, Experiments, Pollutant Formation, 3rd edn., Springer-Verlag, Berlin, 2001.
58. G. Weisser. Modelling of combustion and nitric oxide formation for medium-speed DI diesel engines: Zero and three-dimensional approaches. PhD thesis, Swiss Federal Institute of Technology (ETH), Zurich, 2001. Diss. ETH Nr. 14465.
59. G. Weisser, F. X. Tanner, and K. Boulouchos. Modeling of ignition and early flame development with respect to large diesel engine simulation. SAE Transactions: Journal of Fuels and Lubricants, 107(4):802–811, 1999.
60. C. K. Westbrook and F. L. Dryer. Simplified reaction mechanisms for the oxidation of hydrocarbon fuels in flames. Combustion Science and Technology, 27:31–45, 1981.
61. D. C. Wilcox. Turbulence Modeling for CFD, 2nd edn. DCW Industries, La Canada, 1993.
62. F. A. Williams. Spray combustion and atomization. Physics of Fluids, 1(6):541–545, 1958.
63. S. L. Yang, B. D. Peschke, and K. Hanjalic. Second-moment closure model for IC engine flow simulation using KIVA code. Journal Engineering for Gas Turbines and Power, 122:355–363, 2000.
64. Y. B. Zeldovich. The oxidation of nitrogen in combustion and explosions. Acta Physicochimica, USSR, 21:577–628, 1946.

Chapter 20
Lattice Boltzmann Method for Sprays

K.N. Premnath and J. Abraham

Abstract Among the noncontinuum-based computational techniques, the lattice Boltzman method (LBM) has received considerable attention recently. In this chapter, we will briefly present the main elements of the LBM, which has evolved as a minimal kinetic method for fluid dynamics, focusing in particular, on multiphase flow modeling. We will then discuss some of its recent developments based on the multiple-relaxation-time formulation and consistent discretization strategies for enhanced numerical stability, high viscosity contrasts, and density ratios for simulation of interfacial instabilities and multiphase flow problems. As examples, numerical investigations of drop collisions, jet break-up, and drop impact on walls will be presented. We will also outline some future directions for further development of the LBM for applications related to interfacial instabilities and sprays.

Keywords Interfacial instabilities · Lattice Boltzmann method · Sprays

Introduction

In recent years, there has been great interest in developing physically inspired computational models based on the idea that the dynamics of the motion of fluid and interfaces can be represented in terms of the collective behavior of interactions of quasi-particle populations at scales smaller than macroscopic, but larger than molecular scales. These models fall in the class of mesoscopic methods – the LBM [6, 42, 45] being one. The LBM is generally based on minimal discrete kinetic models whose emergent behavior, under appropriate constraints, corresponds to the

K.N. Premnath (✉)
Mechanical Engineering, University of Wyoming, USA
e-mails: knandhap@uwyo.edu, jabraham@purdue.edu

N. Ashgriz (ed.), *Handbook of Atomization and Sprays*,
DOI 10.1007/978-1-4419-7264-4_20, © Springer Science+Business Media, LLC 2011

dynamical equations of fluid flows. It involves the solution of the lattice-Boltzmann equation (LBE) that represents the evolution of the distribution of particle populations due to their collisions and advection on a lattice. When the lattice, which represents the discrete directions for propagation of particle populations, satisfies sufficient rotational symmetries, the LBE recovers the weakly compressible Navier–Stokes equations (NSE) in the continuum limit. The LBE can be constructed to simulate complex flows by incorporating additional physical models, either based on force interactions [38] or free-energy considerations [43].

Though its origins can be traced to the lattice gas cellular automata as one of its computationally efficient forms, it was well established about a decade ago that the LBE is actually a much simplified form of the continuous Boltzmann equation [11]. As a result, several previous developments in kinetic theory could be directly applied to the LBE. This has led to, for example, improved physical modeling in various situations, such as multiphase flows [10, 12], multicomponent flows [2], incorporation of rarefaction effects [39], and in an asymptotic approach suitable for numerical analysis [17]. As a result of features of the stream-and-collide procedure of the LBE, such as the algorithmic simplicity, amenability to parallelization with near-linear scalability, the ability to represent complex boundary conditions, and incorporate physical models more naturally, LBM has rapidly found a wide range of applications. It may be noted that direct comparison of the solution of the LBM with that of more conventional methods such as the front-tracking method has shown to yield similar results for complex temporal interfacial dynamics [36]. Thus, the LBM can be considered to be a reliable and accurate approach for direction simulation of multiphase flows. Recent reviews of the multiphase flow applications of the LBM are presented by Nourgaliev et al. [28] and Premnath et al. [32]. In this chapter, we will focus on some new developments in the LBM for multiphase flows and their applications to fundamental investigations of various interfacial instabilities relevant to spray processes.

Lattice Boltzmann Method (LBM)

The starting point of the LBM is the continuous Boltzmann equation [5, 9]

$$\frac{\partial f}{\partial t} + \vec{\xi} \cdot \vec{\nabla}_{\vec{x}} f + \frac{\bar{F}}{\rho} \cdot \vec{\nabla}_{\vec{\xi}} f = \Omega(f, f) \tag{20.1}$$

where f is the single-particle density distribution function, i.e., probability of locating a particle in a given region of space around location $\vec{x}$, moving with a microscopic velocity $\vec{\xi}$ at time t, which is subjected to an external force $\vec{F}$. In (20.1), $\vec{\xi} \cdot \vec{\nabla}_{\vec{x}} f$ and $\bar{F}/\rho \cdot \vec{\nabla}_{\vec{\xi}} f$ represent the changes in distribution function due to the advection of particle populations and the external forces, respectively. On the other hand, the term $\Omega(f,f)$ in (20.1) represents the cumulative effect of the collision of

particles on the distribution function. It is generally given in terms of a formidable collision integral [9], which is extremely difficult to use for practical purposes. Hence, it is often modeled. One such commonly used model considers the effect of collision as a relaxation process, where the distribution function relaxes to its local equilibrium at a certain characteristic rate [3]. According to this model, also termed as the BGK model,

$$\Omega(f, f) = -\frac{(f - f^M)}{\lambda} \tag{20.2}$$

where f^M is the Maxwell–Boltzmann equilibrium distribution function. Considering isothermal flows for simplicity, it is given by

$$f^M = \frac{\rho}{2\pi c_s^2} \exp\left[-\frac{(\vec{\xi} - \vec{u})^2}{c_s^2}\right] \tag{20.3}$$

Here, ρ is the fluid density, $\vec{u}$ is the macroscopic or fluid velocity, and c_s is the speed of sound. The macroscopic fluid properties can be obtained by taking various weighted moments of the distribution function, where the weights are components of the particle velocities of various orders. For example, the fluid density and velocities are obtained by

$$\begin{aligned} \rho &= \int f \, d\vec{\xi} \\ \rho\vec{u} &= \int f\vec{\xi} \, d\vec{\xi} \end{aligned} \tag{20.4a, b}$$

These quantities satisfy compressible fluid motion equations, whose kinematic viscosity ν is related to the relaxation parameter λ in the BGK model (20.2) through $\nu = c_s^2\lambda$ [5].

The lattice Boltzmann equation (LBE) is obtained as a dramatic simplification of the Boltzmann equation, (20.1) along with its associated equations, (20.2–20.4). In particular, it was discovered that the roots of the Gauss–Hermite quadrature used to exactly and numerically represent the moment integrals in (20.4), corresponds to a particular set of few discrete particle velocity directions $\vec{e}_\alpha$ in the LBE [11]. Furthermore, the continuous equilibrium distribution (20.3) is expanded in terms of the fluid velocity $\vec{u}$ as a polynomial, where the continuous particle velocity $\vec{\xi}$ is replaced by the discrete particle velocity set $\vec{e}_\alpha$ obtained as discussed above, i.e., f^{M} becomes f_α^{eq}. After replacing the continuous distribution function $f = f(\vec{x}, \vec{\xi}, t)$ in (20.1) by the discrete distribution function $f_\alpha = f(\vec{x}, \vec{e}_\alpha, t)$, (20.1) is integrated by considering particle advection from one lattice node to its adjacent location along the characteristic of $\vec{e}_\alpha$ during a time step δ_t. In this process, the collision term is treated explicitly in time for simplicity, while the forcing term is treated semi-implicitly for improved accuracy, after approximating $\vec{F}/\rho \cdot \vec{\nabla}_{\vec{\xi}} f$ in (20.1) by $\vec{F}/\rho \cdot \vec{\nabla}_{\vec{\xi}} f^{\mathrm{M}}$ and

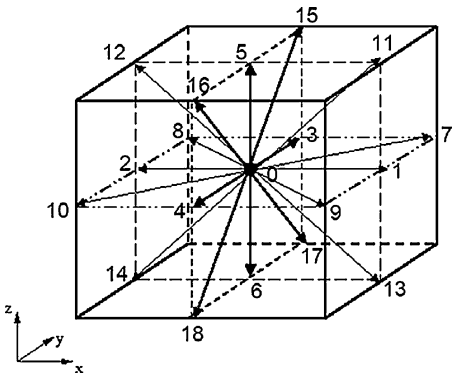


Fig. 20.1 Three-dimensional, nineteen velocity (D3Q19) lattice

then replacing $\vec{\xi}$ by $\vec{e}_\alpha$ [12]. The implicitness present in the forcing term is then effectively removed by applying a transformation to the discrete distribution function. A typical example of a lattice representing $\vec{e}_\alpha$ is the three-dimensional, nineteen velocity (D3Q19) model, which is shown in Fig. 20.1. The LBE resulting from all these steps may be written as

$$f_\alpha(\vec{x}+\vec{e}_\alpha\delta_t, t+\delta_t) - f_\alpha(\vec{x},t) = \Omega_\alpha + \left(1-\frac{1}{2\tau}\right)S_\alpha\delta_t \tag{20.5}$$

where Ω_α is the discrete collision term given by

$$\Omega_\alpha = -\frac{1}{\tau}\left[f_\alpha(\vec{x},t) - f_\alpha^{eq}(\vec{x},t)\right], \quad f_\alpha^{eq} = w_\alpha\left\{1+\frac{\vec{e}_\alpha\cdot\vec{u}}{c_s^2}+\frac{(\vec{e}_\alpha\cdot\vec{u})^2}{2c_s^4}-\frac{\vec{u}\cdot\vec{u}}{2c_s^2}\right\} \tag{20.6}$$

where w_α is a weighting factor; the forcing term S_α in (20.5) can be written as

$$S_\alpha = \frac{(\vec{e}_\alpha-\vec{u})\cdot\vec{F}}{\rho c_s^2} f_\alpha^{eq} \tag{20.7}$$

In the above, τ is the nondimensional relaxation time, i.e., $\tau = \lambda/\delta_t$. The LBE simulates weakly compressible Navier–Stokes equations for the density and fluid velocity that satisfy

$$\rho = \sum_\alpha f_\alpha, \quad \rho\vec{u} = \sum_\alpha f_\alpha\vec{e}_\alpha + \frac{1}{2}\vec{F}\delta_t \tag{20.8}$$

The kinematic viscosity of the fluid is related to the relaxation parameter through the relation $\nu = c_s^2(\tau - 1/2)\delta_t$, which is obtained by means of a multiscale Chapman–Enskog analysis [5].

In order to represent multiphase flows in the LBE framework, different approaches are possible. One of the earliest efforts in this regard is by Gunstensen et al. [8], who proposed a color-gradient method. This is essentially a heuristic approach and limited to varying its characteristic parameters to within a narrow range. Moreover, it requires a computationally intensive recoloring step to maintain phase segregation. Nevertheless, this pioneering effort has motivated searches for physically inspired approaches for multiphase flows based on the LBM. As a consequence, Shan and Chen [38] developed a pseudo-potential approach to model phase-segregation based on local particle interactions. While it is able to represent complex features of interfacial dynamics, it has certain limitations such as surface tension emerging as a numerical artifact, which cannot be independently varied with equation of state (EOS) and small contrasts in phase density. There have been continuous efforts to mitigate some of these limitations. Perhaps one of the most notable in this regard is the recent work of Sbragaglia et al. [37], who developed an extended pseudo-potential approach that also included additional number of near-neighbor interactions.

Swift et al. [43] developed multiphase modeling in the LBE framework based on different considerations. They derived the equilibrium distribution in the collision term of the LBE from the minimization of a free-energy functional, which gives rise to phase-segregation and surface tension effects. While this approach is endowed with interesting features, it has certain nonphysical artifacts such as not being Galilean invariant, amongst others. Some of these limitations have been partially addressed by Holdych et al. [14] and Inamuro et al. [15].

He et al. [12] developed a more physically consistent LBM approach based on Enskog theory of dense fluids [5], in which the force interactions are represented by van der Waals theory [35]. In the following, we will briefly summarize this approach. As before, we start with continuous Boltzmann equation, but now for the nonideal fluids, which may be written as [12]

$$\frac{\partial f}{\partial t} + \vec{\xi} \cdot \vec{\nabla}_{\vec{x}} f = -\frac{(f - f^M)}{\lambda} + \frac{(\vec{\xi} - \vec{u}) \cdot (\vec{F} + \vec{F}_{ext})}{\rho c_s^2} f^M \tag{20.9}$$

where $\vec{F}$ represents the effective molecular interaction force between particles and $\vec{F}_{\text{ext}}$, which represents external forces such as gravity. The intermolecular force is modeled as a function of density following van der Waals [35] and including the exclusion volume effect [5] to give

$$\vec{F} = -\vec{\nabla}\psi + \vec{F}_s \tag{20.10}$$

where ψ is the nonideal part of the EOS given by

$$\psi = p - \rho c_s^2 \tag{20.11}$$

We employ the Carnahan–Starling–van der Waals EOS [4]. ψ plays an important role in phase segregation as its $p - 1/\rho$ curve shows regions where $\mathrm{d}p/\mathrm{d}\rho < 0$.

This represents an unstable physical situation and is the driving mechanism for keeping the phases segregated. The term $\vec{F}_s$ in (20.10) represents the surface tension force given by

$$\vec{F}_s = \kappa\rho\vec{\nabla}\nabla^2\rho \tag{20.12}$$

where κ is a surface tension parameter. It is related to the surface tension of the fluid σ by [35]

$$\sigma = \kappa\int\left(\frac{\partial\rho}{\partial n}\right)^2 dn \tag{20.13}$$

where n is the normal to the interface. In practice, to alleviate the numerical stiffness associated with the intermolecular forces, a suitable transformation is applied to the distribution function and an index function is employed in place of density to determine different phases [13]. An important issue of these various LBE approaches for multiphase flow is their thermodynamic consistency, which has been analyzed by various authors in recent years [10, 18, 21, 44].

While the above multiphase model provides a physically consistent approach, there are some limitations which need to be addressed. Prior LBE-based approaches were found to have a narrow limit on the minimum kinematic viscosity that can be employed to be numerically stable. One of the reasons for this is the fact that the BGK model for the collision term employed uses a single relaxation time (SRT) for the distribution functions in all particle velocity directions, which is insufficient in suppressing grid-scale numerical oscillations that induce numerical instability.

On the other hand, an equivalent representation of distribution functions is in terms of their moments, such as various hydrodynamic variables including density, momentum, and stress tensor. The relaxation process due to collisions can more naturally be described in terms of a space spanned by such moments, which can in general relax at different rates. This forms the basis of the LBE based on multiple relaxation times (MRT) [7, 19]. By carefully separating the time scales of various hydrodynamic and kinetic modes through a linear stability analysis, the numerical stability of the MRT-LBE can be significantly improved compared to the SRT-LBE, particularly for more demanding problems at high Reynolds numbers. The MRT-LBE has been extended for multiphase flows in two-dimensions by McCracken and Abraham [22] and in three-dimensions by Premnath and Abraham [31]. It was found that the improvements achieved with the MRT-LBE can be as much as an order of magnitude compared to the SRT-LBE. As a result of the superior stability characteristics of the multiphase MRT-LBE, it can be employed for interfacial flows related to sprays at relatively higher viscosity ratios and wider variation of Ohnesorge numbers than what is possible with the use of SRT-LBE.

Moreover, standard LBE is strictly formulated either in two- or three-dimensions. On the other hand, there is a large class of problems related to interfacial flows and instabilities in sprays that can be considered to have an axial symmetry. Such symmetries should be fully exploited for computationally efficient

implementation of the LBE. In fact, Premnath and Abraham [29] developed an axisymmetric LBE for multiphase flows by incorporating geometric source terms, representing inertial, viscous, and surface tension forces due to axial symmetry, in a two-dimensional LBE, effectively achieving a dimensional reduction. This axisymmetric multiphase LBE was further extended to incorporate the MRT formulation of the collision term for enhanced numerical stability [30].

Another important issue related to multiphase flow simulation using the LBE is that they are generally restricted to simulation of relatively low or moderate density ratios, unless appropriate numerical strategies are devised to circumvent it. In this regard, Inamuro et al. [16] developed a formulation of the LBE with a projection step, which enforces strict incompressibility, overcoming numerical instability problems at high density ratios. However, this entails the use of a Poisson-type equation to obtain the pressure field, which undermines the inherent parallelization properties of the LBE. Hence, there has been search for other more efficient approaches to tackle the density ratio problem with the LBE. In particular, Lee and Lin [20] developed a set of consistent discretization strategies and suitable transformations of the distribution function for stabilizing the LBE at high density ratios. Mukherjee and Abraham [24] developed an MRT formulation of the LBE with such consistent set of discretization strategies for simulation of multiphase flows at high density ratios. By employing such a formulation, they also further extended the axisymmetric multiphase LBE [29] to simulate high density ratio problems [25]. It may be noted that within a free-energy formulation of the LBE, high density ratios can be achieved for multiphase flow simulations using the recent approach of Zheng et al. [46]. An important class of multiphase flows relevant to sprays is related to the impingement of drops on solid walls and the instabilities arising as a result of such interactions due to wetting effects. Mukherjee and Abraham [26] developed a model to study the drop impact on walls and contact angle dynamics in the LBE framework. For additional details, the original references of Premnath, McCracken, Mukherjee and Abraham may be consulted. In the next section, we will present a few illustrative applications of the LBE as applied to multiphase flows related to atomization and sprays.

Examples

Three illustrative examples of the application of LBM to simulate drops and sprays will now be shown. Other examples may be seen in the references cited above. Note that all dimensions below are given in lattice units.

Binary Drop Collisions

An important phenomenon, particularly in the dense region of the spray, is the collision of drops. A canonical example is the head-on collision of binary drops,

which have been studied in the LBM context by Premnath and Abraham [30] under different conditions. Here, we present results from one such simulation. Figure 20.2. shows the temporal evolution of interfaces of equal size colliding

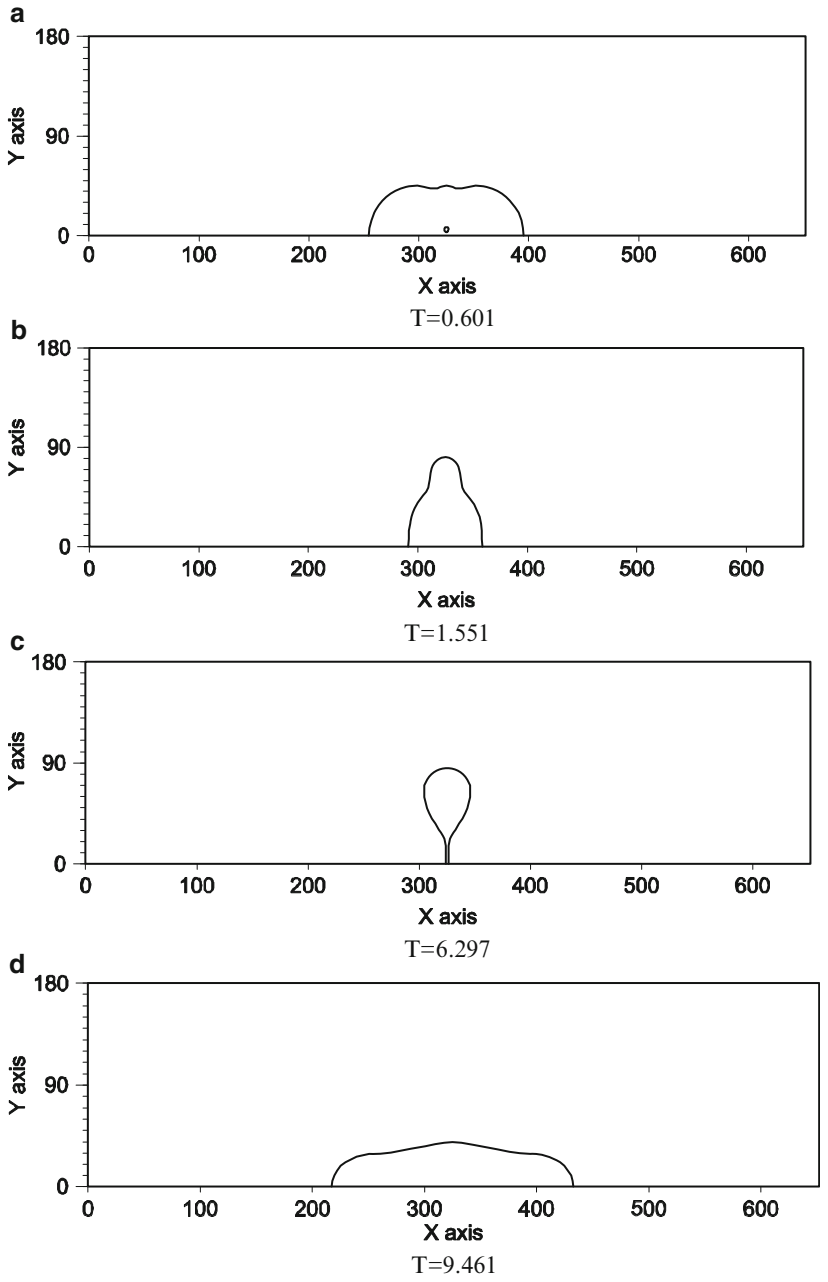


Fig. 20.2 (continued)

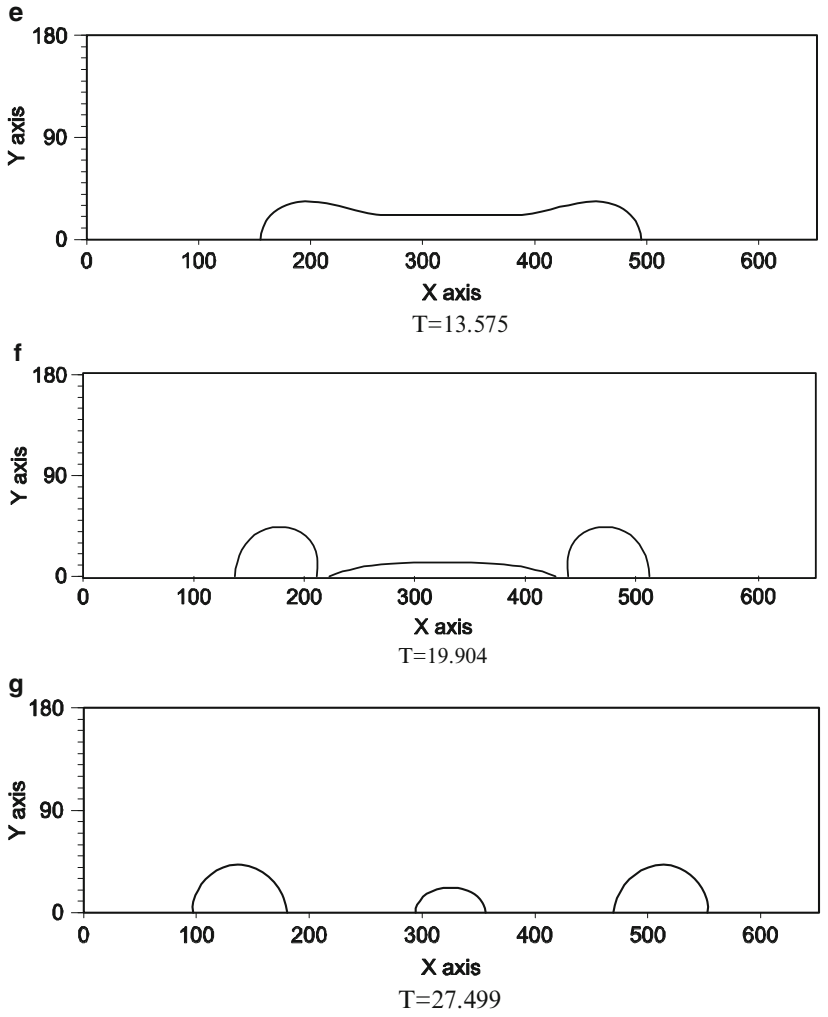


Fig. 20.2 Colliding drops at different times, T; $We = 100$, $Re = 384.5$, $B = 0$, $Oh = 0.589$, $r = 4$, $\lambda = 4$, $\gamma = 1$ [30] (**a**) $T = 0.601$, (**b**) $T = 1.551$, (**c**) $T = 6.297$, (**d**) $T = 9.461$, (**e**) $T = 13.575$, (**f**) $T = 19.904$, (g) $T = 27.499$

drops at a Weber number of 100, Reynolds number of 384.5, Ohnesorge number of 0.59 and density ratio of 4, and dynamic viscosity ratio of 4. In these simulations, the Reynolds number noted above is obtained by considering liquid drops with a kinematic viscosity of 0.067. Time T is the nondimensional time obtained by $T = tU/(R_1 + R_2)$, where R_1 and R_2 are the radii of the colliding drops and U is their relative velocity. For such high Weber numbers, it is expected that the colliding drops separate after stretching [1, 33].

The collision dynamics exhibit the different phases of deformation and internal flow as pointed out by Roisman [34]. Upon initial deformation of the temporarily

coalesced drop, shown at $T = 0.601$ in Fig. 20.4, it undergoes radial stretching shown at times $T = 1.551$. The rim recedes at $T = 6.297$. It then undergoes axial stretching (see $T = 9.4610$ and $T = 13.575$). Such stretching results subsequently in bulbous ends which break up through the well-known "end-pinching" mechanism observed experimentally and computationally by Stone and coworkers [40, 41] when drops are subjected to axial stretching. Thus, the LBM approach is capable of reproducing some of the key features in collision dynamics of drops. In addition, Premnath and Abraham [29] demonstrated using their approach that Rayleigh break-up of liquid column and satellite drop formation could be computed in a quantitatively accurate manner in close agreement with those using other approaches.

Transient Liquid Jet Breakup

As another important application directed towards simulation of atomization problems, McCracken and Abraham [23] employed LBM to study transient liquid jet break-up. In the transient liquid jet computations, liquid is injected at the centerline of the domain along the axial direction into an ambient with lower density. Initially, the domain is filled with quiescent gas except at the inlet near the orifice where a small amount of liquid is placed for numerical stability. An initial plug flow velocity profile is employed for the jet. The inlet liquid density is perturbed using two harmonics given by $h_l = R + 2\sin(2\pi u_l t/\lambda_1) + 3\sin(2\pi u_l t/\lambda_2)$, where h_l is the radial height of the liquid, the unperturbed radius of the jet R is 60, and u_l is velocity of the liquid jet. The perturbation wavelength $\lambda_1 = 226$ corresponds to an unstable wavelength for Rayleigh instability, while the wavelength $\lambda_2 = 50$ corresponds to Kelvin–Helmholtz instabilities.

Figure 20.3. illustrates the evolution of the liquid jet with a liquid viscosity of 0.005, an injection velocity, u_l of 0.1, and a surface tension of 0.000308. These conditions give a Reynolds number of 2400 and an Ohnesorge number of 0.0116. A head region forms at the front of the jet. As the jet penetrates into the domain, the head region sheds "drops" from its downstream edges and begins to breakup even in the downstream region near the stagnation point.

In general, increased liquid viscosity reduces deformation and tendency for liquid break-up. Figure 20.4. illustrates the evolution of the liquid jet with a liquid viscosity of 0.003, and injection velocity of 0.1, and a surface tension of 0.000308. These conditions give a Reynolds number of 4,000 and an Ohnesorge number of 0.00698. The head region at the front of the jet begins to disintegrate by $t = 6{,}000$. Shorter wavelength instabilities grow and shed "drops." As these instabilities grow, they eventually break off into larger ligaments. These ligaments then undergo secondary break-up apparently from instabilities growing on their upstream interface. This type of instability is often accredited to the acceleration of the gas around the ligament (Rayleigh–Taylor type). These

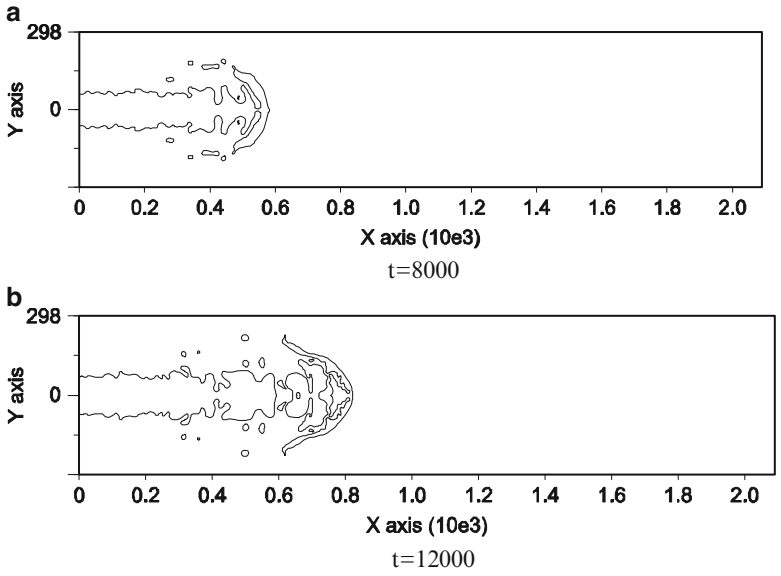


Fig. 20.3 Density profiles for axisymmetric liquid jet with $v_1 = 0.005$, $\sigma = 0.000308$, and $u_1 = 0.1$ at several times (Reprinted with permission from [23]. World Scientific Publishing Company). (**a**) $t = 8{,}000$, (**b**) $t = 12{,}000$

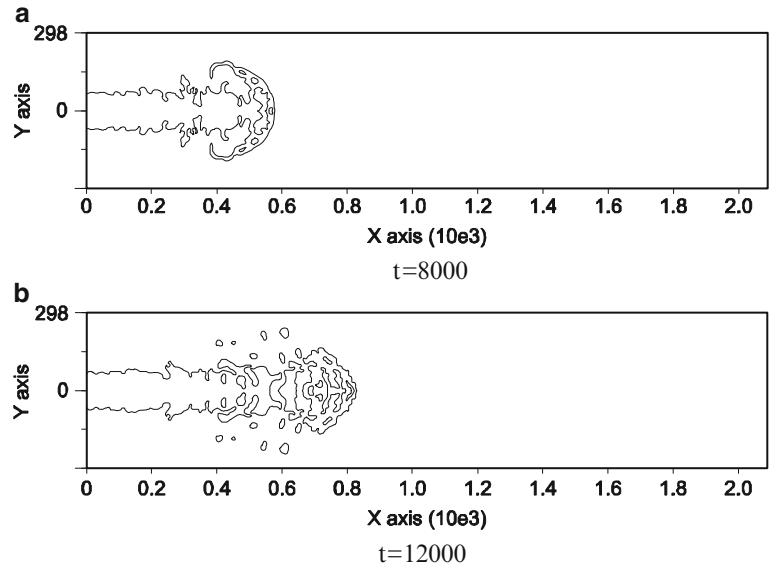


Fig. 20.4 Density profile for axisymmetric liquid jet with $v_1 = 0.003$, $\sigma = 0.000308$, and $u_1 = 0.1$ (Reprinted with permission from [23]. World Scientific Publishing Company). (**a**) $t = 8{,}000$, (**b**) $t = 12{,}000$

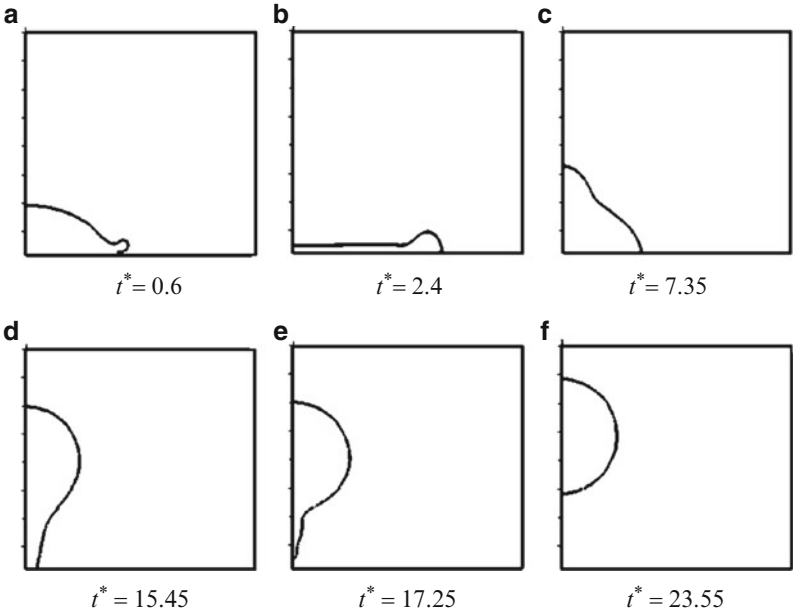


Fig. 20.5 Snapshots of drop rebound; $We = 137$, $Oh = 0.026$ [26]. (**a**) $t^* = 0.6$, (**b**) $t^* = 2.4$, (**c**) $t^* = 7.35$, (**d**) $t^* = 15.45$, (**e**) $t^* = 17.25$, (**f**) $t^* = 23.55$

results show that the LBM is capable of simulating certain basic features of the break-up process in transient liquid jets.

Drop Impact on Walls

Figure 20.5 shows an example of a rebounding drop following impact with a dry wall computed with the method [26]. The method has also been employed to study drop impact on wet walls [27].

Concluding Remarks

In this chapter, we have provided a brief introduction to the LBM for computation of multiphase flows of relevance to atomization and sprays. Since its inception, the LBM has come a long way, especially in overcoming some of the early challenges. In particular, the use of MRT formulation for multiphase flows has been a major step in maintaining numerical stability at lower viscosities or higher Reynolds numbers; the use of consistent discretization approaches in the LBM has enabled simulation of high density ratio problems. During the last few years,

there has been a rapid increase in the number of publications on the LBM related to its further development and applications. Results accumulated thus far have demonstrated that the LBM is an accurate approach for computation of complex interfacial flows and instabilities. Nevertheless, several challenges remain that need to be addressed for the application of the LBM to realistic engineering problems involving multiphase flows. In the following, we point out some directions for further research.

Current LBM approaches largely consider the interfaces to be diffuse in nature, with certain thickness. However, for improved accuracy, it is highly desirable to maintain sharp interfaces. This could also enable computation of interfacial transport/phase change such as evaporation problems. Thus, it is highly desirable to develop a sharp interface-based LBM for multiphase flows. In conjunction, an approach based on more conventional approaches could be developed to introduce energy transport in the LBM for multiphase flows. For further improvements in the fidelity of solutions, adaptive grid refinement strategies could be introduced in the multiphase LBM approaches. It is known that around interfaces, small but finite velocity currents are established by numerical artifacts and whose magnitude is dependent on surface tension and viscosities. While there have been some recent efforts to mitigate or eliminate such issues in the LBM, robust strategies that apply under a wide range of conditions are desirable. In the case of interfacial instabilities arising from interactions with solid walls, wetting effects and contact angle dynamics play a crucial role. While there have been considerable efforts to incorporate such effects in the LBM, they have largely been confined to problems with flat walls. It is thus desirable to develop LBM approaches for simulation of contact line dynamics for complex solid boundaries in a reliable way.

For practical applications, it is important to further broaden the parameter ranges, such as Weber numbers, Ohnesorge numbers, Reynolds numbers, and density and viscosity ratios, currently accessible by the LBM. In this regard, advances in the classical numerical methods should be extended to the LBM. From a physical point of view, there are certain classes of interfacial flow problems, where macroscopic or continuum considerations have not been fully satisfactory. This includes, for example, the phenomenon of bounce that could occur for two drops approaching at slow speeds under certain conditions. Currently, they have been modeled in a semiempirical manner in macroscopic-based approaches. On the other hand, the LBM, being based on kinetic theory, has the potential to be further developed to incorporate the relevant physics for such problems in a more consistent manner. Last, but not the least, the present authors and their collaborators have made some of the initial efforts to apply the LBM for interfacial flow problems related to atomization and sprays. In our opinion, more focus should be given for application of the LBM for fundamental studies of interfacial break-up problems in the atomization regime, and eventually under turbulent conditions. As many of the above mentioned challenges are resolved, the LBM, with its excellent parallelization characteristics, is ideally perched at the dawn of petascale computing and appears to be a promising computational tool for fundamental investigations of multiphase flows of practical interest.

References

1. Ashgriz, N. and Y. Poo. Coalescence and Separation in Binary Collisions of Liquid Drops. *J. Fluid Mech.* **221**: 183–204 (1990).
2. Asinari, P. Viscous Coupling based Lattice Boltzmann Model for Binary Mixtures. *Phys. Fluids* **067102**: 1–22 (2005).
3. Bhatnagar, P., E. Gross, and M. Krook. A Model for Collision Processes in Gases, I. Small Amplitude Processes in Charged and Neutral One-Component Systems. *Phys. Rev.* **94**: 511–525 (1954).
4. Carnahan, N. and K. Starling. Equation of State for Nonattracting Rigid Spheres. *J. Chem. Phys.* **51**: 635–636 (1969).
5. Chapman, S. and T. Cowling. *Mathematical Theory of Non-Uniform Gases*. Cambridge University Press, London (1964).
6. Chen, S. and G. Doolen. Lattice Boltzmann Method for Fluid Flows. *Annu. Rev. Fluid Mech.* **30**: 329–364 (1998).
7. d'Humieres, D., I. Ginzburg, M. Krafczyk, P. Lallemand, and L.-S. Luo. Multiple-Relaxation-time Lattice Boltzmann Models in Three Dimensions. *Phil. Trans. Roy. Soc. Lond. Ser. A* **360**: 437–351 (2002).
8. Gunstensen, A.K., D.H. Rothman, S. Zaleski, and G. Zanetti. Lattice Boltzmann Model of Immiscible Fluids. *Phys. Rev. A* **43**: 4320–4327 (1991).
9. Harris, S. *An Introduction to the Theory of the Boltzmann Equation*. Dover Publications, New York (2004).
10. He, X. and G. Doolen. Thermodynamic Foundations of Kinetic Theory and Lattice Boltzmann Models for Multiphase Flows. *J. Stat. Phys.* **107**: 1572–4996 (2002).
11. He, X. and L.-S. Luo. Theory of the Lattice Boltzmann Method: From the Boltzmann Equation to the Lattice Boltzmann Equation. *Phys. Rev. E* **56**: 6811–6817 (1997).
12. He, X., X. Shan, and G. Doolen. Discrete Boltzmann Equation Model for Nonideal Gases. *Phys. Rev. E* **57**: R13–R16 (1998).
13. He, X., S. Chen, and R. Zhang. A Lattice Boltzmann Scheme for Incompressible Multiphase Flow and its Application in Simulation of Rayleigh–Taylor Instability. *J. Comput. Phys.* **152**: 642–663 (1999).
14. Holdych, D.J., D. Rovas, J.G. Georgiadis and R.O. Buckius. An Improved Hydrodynamic Formulation for Multiphase Flow Lattice Boltzmann Models. *Int. J. Modern Phys. C* **9**: 1393–1404 (1998).
15. Inamuro, T., N. Konishi, and F. Ogino. A Galilean Invariant Model of the Lattice Boltzmann Method for Multiphase Fluid Flows Using Free-Energy Approach. *Comput. Phys. Commun.* **129**: 32–45 (2000).
16. Inamuro, T., T. Ogata, S. Tajima, and N. Konishi. A Lattice Boltzmann Method for Incompressible Two-phase Flows with Large Density Ratios. *J. Comput. Phys.* **198**: 628–644 (2004).
17. Junk, M., A. Klar, and L.-S. Luo. Asymptotic Analysis of the Lattice Boltzmann Equation. *J. Comput. Phys.* **210**: 676–704 (2005).
18. Kikkinides, E.S., A.G. Yiotis, M.E. Kainourgiakis, and A.K. Stubos. Thermodynamic Consistency of Liquid-Gas Lattice Boltzmann Methods. *Phys. Rev. E* **78**: 036702 (2008).
19. Lallemand, P. and L.-S. Luo, Theory of the Lattice Boltzmann Method: Dispersion, Isotropy, Galilean Invariance, and Stability. *Phys. Rev. E* 61: 6546–6562 (2000).
20. Lee, T. and C.-L. Lin. A Stable Discretization of the Lattice Boltzmann Equation for Simulation of Incompressible Two-Phase Flows at High Density Ratio. *J. Comput. Phys.* **206**: 16 (2005).
21. Luo, L.-S. Theory of the Lattice Boltzmann Method: Lattice Boltzmann Models for Nonideal Gases. *Phys. Rev. E* **62**: 4982–4996 (2000).
22. McCracken, M.E. and J. Abraham. Multiple-Relaxation-Time Lattice-Boltzmann Model for Multiphase Flow. *Phys. Rev. E* **71**: 036701 (2005a).

23. McCracken, M.E. and J. Abraham. Simulations of Liquid Break up with an Axisymmetric, Multiple Relaxation Time, Index-Function Lattice Boltzmann Model. *Int. J. Mod. Phys. C* **16**: 1671–1682 (2005b).
24. Mukherjee, S. and J. Abraham. A Pressure-Evolution-Based Multi-Relaxation-Time High-Density-Ratio Two-Phase Lattice-Boltzmann Model. *Comput. Fluids* **36**: 1149–1158 (2007a).
25. Mukherjee, S. and J. Abraham. Lattice Boltzmann Simulations of Two-Phase Flow with High Density Ratio in Axially Symmetric Geometry. *Phys. Rev. E*. **75**: 026701 (2007b).
26. Mukherjee, S. and J. Abraham. Investigations of Drop Impact on Dry Walls with a Lattice Boltzmann Model. *J. Colloid Interface Sci*. **312**: 341–354 (2007c).
27. Mukherjee, S. and J. Abraham. Crown Behavior in Drop Impact on Wet Walls. *Phys. Fluids* **19**: 052103 (2007d).
28. Nourgaliev, R., T.N. Dinh, T.G. Theofanous, and D. Joseph. The Lattice Boltzmann Equation Method: Theoretical Interpretation, Numerics and Implications. *Int. J. Multiphase Flow* **29**: 117–169 (2003).
29. Premnath, K.N. and J. Abraham. Lattice Boltzmann Model for Axisymmetric Multiphase Flows. *Phys. Rev. E*, **71**: 056706 (2005a).
30. Premnath, K.N. and J. Abraham. Simulations of Binary Drop Collisions with a Multiple-Relaxation-Time Lattice-Boltzmann Model. *Phys. Fluids* **17**: 122105 (2005b).
31. Premnath, K.N. and J. Abraham. Three-Dimensional Multi-Relaxation Time (MRT) Lattice-Boltzmann Models for Multiphase Flow. *J. Comput. Phys.* **224**: 539–559 (2007).
32. Premnath, K.N., McCracken, M.E. and J. Abraham. A Review of Lattice Boltzmann Methods for Multiphase Flows Relevant to Engine Sprays. *SAE Trans: J. Engines*, **114**: 929–940 (2005).
33. Qian, J. and C. Law. Regimes of Coalescence and Separation in Droplet Collision. *J. Fluid Mech.* **331**: 59–80 (1997).
34. Roisman, I. Dynamics of Inertia Dominated Binary Drop Collisions. *Phys. Fluids* **16**: 3438–3449 (2004).
35. Rowlinson, J. and B. Widom. *Molecular Theory of Capillarity*. Clarendon Press, Oxford (1982).
36. Sankaranarayanan, K., I.G. Kevrekidis, S. Sundaresan, J. Lu and G. Tryggvason. A Comparative Study of Lattice Boltzmann and Front-Tracking Finite-Difference Methods for Bubble Simulations. *Int. J. Multiphase Flow* **29**: 109–116 (2003).
37. Sbragaglia, M., R. Benzi, L. Biferale, S. Succi, K. Sugiyama, and F. Toschi. Generalized Lattice Boltzmann Method with Multirange Pseudopotential. *Phys. Rev. E* **75**: 026702 (2007).
38. Shan, X. and H. Chen. Lattice Boltzmann Model of Simulating Flows with Multiple Phases and Components. *Phys. Rev. E* **47**: 1815–1819 (1993).
39. Shan, X., X.-F. Yuan, and H. Chen. Kinetic Theory Representation of Hydrodynamics: A Way Beyond the Navier-Stokes Equation. *J. Fluid Mech.* **550**: 413–441 (2006).
40. Stone, H. and L. Leal. Relaxation and Breakup of an Initially Extended Drop in an Otherwise Quiescent Fluid. *J. Fluid Mech.* **198**: 399–427 (1989).
41. Stone, H., B. Bentley, and L. Leal. An Experimental Study of Transient Effects in the Breakup of Viscous Drops. *J. Fluid Mech.* **173**: 131–158 (1986).
42. Succi, S. *The Lattice Boltzmann Equation for Fluid Dynamics and Beyond*. Oxford University Press, New York (2001).
43. Swift, M., S. Orlandini, W. Osborn, and J. Yeomans. Lattice Boltzmann Simulations of Liquid-Gas Binary-fluid Systems. *Phys. Rev. E* **54**: 5041–5042 (1996).
44. Wagner, A.J. Thermodynamic Consistency of Liquid-Gas Lattice Boltzmann Simulations. *Phys. Rev. E* **74**: 056703 (2006).
45. Wolf-Gladrow, D. *Lattice-Gas Cellular Automata and Lattice Boltzmann Models*, *Lecture Notes in Mathematics*, No. 1725. Springer, Berlin (2000).
46. Zheng, H.W., C. Shu, and Y.T. Chew. A Lattice Boltzmann Model for Multiphase Flows with Large Density Ratio. *J. Comput. Phys.* **218**: 353–371 (2006).

Chapter 21
Spray-Wall Impact

A.L.N. Moreira and M.R. Oliveira Panão

Abstract Spray-wall impact is an important process in numerous applications such as internal combustion (IC) engines, spray cooling, painting, metallurgy, and many others. This chapter reviews the main challenges in this dynamic thermofluid event and attempts to systematize the knowledge developed in the hydrodynamics of multiple drop impacts and liquid deposition, the statistical analysis of secondary atomization after impact, and the thermodynamics underlying heat transfer processes in spray impaction onto heated surfaces.

Keywords Atomization · Correlations · Deposition · Drop Interaction · Heat transfer · Impinging spray · Liquid deposition · Multiple drop impacts · Secondary thermodynamics · Spray · Spray-wall impact · Statistics

Introduction

Spray impingement is a dynamic thermofluid process present in many industrial applications such as IC engines, spray painting and coating, microelectronic cooling, fire extinguishment, cooling and quenching in metal foundries, ice chiller and air-conditioning systems, medical inhalators, and dermatological surgery. Besides, some of these applications consider intermittent spraying, such as fuel injection in IC engines and cryogen spraying for cooling in dermatological surgery, where the impingement process is dominated by the transient characteristics of the spray.

Numerous studies are described in the literature, which address the process at a very fundamental level considering the dynamic phenomena involved at the impact of each single drop of the spray – a comprehensive and systematic review has been reported by Yarin [32]. However, the interaction between droplets in the vicinity of each other alter those phenomena and does not allow to describe the spray as the

A.L.N. Moreira (✉)
Instituto Superior Técnico, IN+ Centro de Estudos em Inovação Tecnologia e Políticas de Desenvolvimento, Lisboa, Portugal
e-mail: moreira@dem.ist.utl.pt

N. Ashgriz (ed.), *Handbook of Atomization and Sprays*,
DOI 10.1007/978-1-4419-7264-4_21, © Springer Science+Business Media, LLC 2011

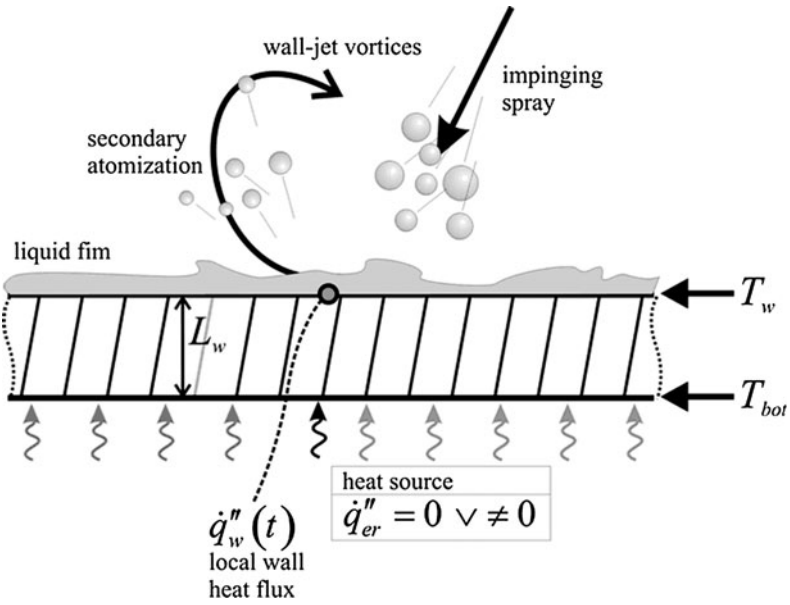


Fig. 21.1 Illustration of spray-wall impact with heat transfer

summation of individual impacts [25, 27], except when it is sufficiently dilute at the moment of impact. Those phenomena include (1) partial deposition of the impinging mass; (2) emergence of secondary droplets due to hydrodynamic or thermally induced break-up mechanisms; and (3) heat extraction and vaporization, as illustrated in Fig. 21.1. Together with multiple drop interactions, these are the issues addressed in the present chapter.

Meeting the challenges of integrating the current available physical information into a tool, which can accurately describe the resulting complex flow is both technically interesting and intellectually stimulating. For example, research in fuel sprays has significantly contributed to the emergence of innovative technological solutions to meet the increasingly stringent regulations imposed by environmental policies and are referred to by most researchers in this field as the main motivation for studying spray impingement; also important is the research related to spray impingement for thermal management. Both areas provided the context for the systematic knowledge reported here.

Multiple Drop Interactions

Despite single drop impact experiments providing understanding on the fundamental mechanisms eventually present on spray impaction, when interaction phenomena occurs between drops with quite dissimilar diameters, impact velocities, and

directions, some hydrodynamic structures are produced, leading to secondary atomization, but with a morphology that is quite different from the splash and rebound observed on the impact of single droplets. Roisman et al. [27] identified those structures as asymmetric corona splash, uprising central jet break-up, splash from an uprising lamella resultant from multiple drop interactions and film jetting with subsequent break-up.

The experiments reported in the literature explore the outcome of those interactions studying the influence of length and time scales associated with multiple drop impacts on the outcome, as described in Fig. 21.2.

The length scale corresponds to the spacing between droplets striking the impinging surface $\left(l_{\text{spacing}} = |r_{i+1} - r_i|\right)$ while the normalized time scale between consecutive impacts (ci) is expressed as

$$\tau_{\text{ci}} = \frac{t_{i+1} - t_i}{t_{i+2} - t_i} = \frac{l_{i+1,i}}{l_{i+1,i} + l_{i+2,i+1}} \frac{|\vec{u}_{i+2}| \cos\left(\gamma_{i+2}\right)}{|\vec{u}_{i+1}| \cos\left(\gamma_{i+1}\right)} \tag{21.1}$$

where $\vec{u}$ and γ refer to the velocity and angle of impact, respectively; i corresponds to the droplet striking the wall, $(i + 1)$ and $(i + 2)$ corresponds to the subsequent ones. From the reported literature, another parameter can be introduced, expressed as $\phi = 2\pi\tau_{\text{ci}}$, which describes the phase between multiple and consecutive drop impacts. When multiple impacts are made simultaneously $t_{i+1} = t_i$ and $\phi = 0°$ [7, 8], and if droplets impact on the same point and, thus are consecutive, $r_{i+1} = r_i$, $l_{\text{spacing}} = 0$, and $\phi = 180°$ [33].

For impacts with $l_{\text{spacing}} > 0$, the interaction occurs between spreading lamellae, which give rise to asymmetric uprising sheets. In a complete wetting system, where each spreading lamella may form a crown, the interaction arises between uprising crowns, though Barnes et al. [5] observed that, for $l_{\text{spacing}} < 2D_0$ there is no time for crown formation before interaction occurs, while for $l_{\text{spacing}} < D_0$ droplets coalesce. According to Barnes et al. [5], the height of those liquid sheets depends mainly on

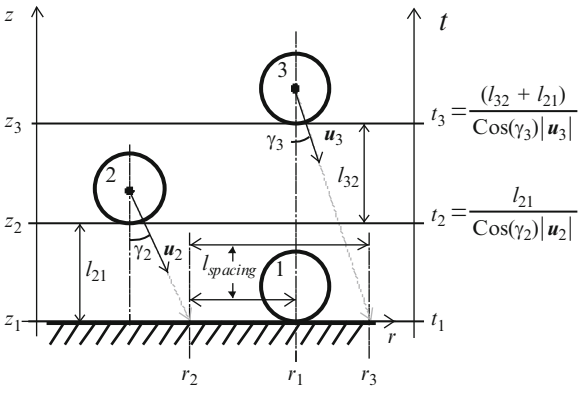


Fig. 21.2 Scale parameters involved in multiple drop impacts

drop spacing ($l_{spacing}$) and the interaction phase (ϕ) (it would be maximum with $l_{spacing} = 2D_0$ for $\phi = 0°$ and $l_{spacing} = 2.5D_0$ for $\phi = 180°$). In an attempt to improve the description of such structures, Roisman et al. [26] report an approach to estimate the velocity, shape, and thickness of the uprising sheet, the collision line and the rim motion taking into account the influence of both drop spacing and interaction phase.

The uprising sheets may further break up into secondary droplets which are, in general, larger and slower than those generated at single impacts [5, 7]. Despite the evidence that drop spacing ($l_{spacing}$) is an important parameter triggering break-up [7, 8], the establishment of transition criteria has not been an easy task. Only Kalb et al. [12] address the development of such criteria, though their experiments consider the interaction of a droplet impacting onto one previously deposited on the surface. The main difficulties may be attributed to the effects that other impact parameters have on the length and time scales or even altering the physics of the interaction. For example, the experiments of Cossali et al. [7] show a strong influence of the impact velocity on the interaction-driven liquid sheet break-up. The liquid film thickness influences the size of secondary droplets and slightly reduces their number, but not the morphological structures formed by interaction phenomena. Roisman and Tropea [24] further show that crown formation is inhibited in dense sprays and that multiple drop impacts interacting with a dynamic liquid film generating finger-like jets, later disrupting into secondary droplets with size and velocity similar to the characteristic scales of the film's fluctuations. The integration of interaction phenomena in submodels for spray impingement is still far from being achieved with accuracy, which means that investigations on this topic are still at their early stage, and one cannot but realize that multiple drop interaction phenomena are one of the most prominent subjects open for creative research.

Liquid Deposition upon Spray Impact

In the case of spray impact without heat transfer, the deposited mass fraction and the mass ratio of secondary to impinging drops are related as

$$\frac{m_{dep}}{m_b} = 1 - \frac{m_a}{m_b} \tag{21.2}$$

where m_b is the mass of droplets impacting onto the surface, m_a is the mass of droplets issuing from the surface due to disintegration mechanisms, and m_{dep} is the mass of deposited liquid. When the surface is wetted, the liquid film may contribute to the generation of secondary droplets and the ratio m_a/m_b can be larger than 1, as observed by Panão and Moreira [20]. Then, the submodel would not apply because it ceases to depend solely on m_a/m_b, otherwise $m_{dep} < 0$. In this case, the approach of Samenfink et al. [28] can be quite useful because m_a/m_b depends on the spray characteristics before impact, though experiments are limited to the range $m_a/m_b \in [0.26–1]$ and cases where $m_a/m_b > 1$ are not considered (see Table 21.1).

Table 21.1 Submodels to predict the mass ratio between secondary (a – after) and primary droplets (b – before)

Reference	m_a/m_b	Subparameters and validation domain
Mundo et al. [18]	$\begin{cases} 3.9869 \times 10^{-21} K^{9.2133} \text{(smooth)} \\ 8.0350 \times 10^{-11} K^{4.1718} \text{(rough)} \end{cases}$	$K = We^{0.5} Re^{0.25}$
Bai et al. [4]	$0.2 + 0.6 \cdot \text{rnd}(0..1)$	
Kuhnke [13]	$\min\left[1, \frac{T^* - 0.8}{1.1 - 0.8}(1 - B) + B\right]$	$\begin{cases} B = 0.2 + 0.6 \cdot \text{rnd}(0.1) \\ T^* = T_w/T_b \end{cases}$
Samenfink et al. [28]	$0.0866(s_{cd} - 1)^{0.3188} \times (90 - \alpha_b)^{0.1223} \delta_f^{-0.9585}$	$s_{cd} = 24^{-1} Re_b\, La_b^{-0.4189} \in [1, 5]$, $La \in [5,000, 20,000]$, $\alpha_b \in [0°, 85°]$, $\delta_f = \bar{h}_f/d_b \in [0.3, 3]$
Bai et al. [4]	$0.2 + 0.9 \cdot \text{rnd}(0..1)$	
Stanton and Rutland [31]	$-27.2 + 3.15u - 0.1164u^2 + 1.4 \times 10^{-3} u^3$	$u = U_b(\rho/\sigma)^{1/4} \nu^{-1/8} f^{3/8}$, $f = U_b/d_b$
Han et al. [10]	$0.75\left(1 - \exp\left(-10^{-7}(H - H_{cr})^{1.5}\right)\right)$	$H = We \cdot Re^{0.5}$, $H_{cr} = K_H\left[1 + 0.1 Re^{0.5} \cdot \min\{\delta_f, 0.5\}\right]$, $K_H = \left(1{,}500 + 650(R_a/D_{iD})^{-0.42}\right)$
Senda and Fujimoto [29]	For $We \le 300$ $0.423 - 0.096\delta_f + 1.61\delta_f^2 - 1.47\delta_f^3 + 0.367\delta_f^4$ For $We > 300, 0.8$	
Kuhnke [13]	$\min\left\{1 + \frac{m_{lf}}{m_b}, \frac{T^* - 0.8}{1.1 - 0.8}(1 - B) + B\right\}$	$B = 0.2 + 0.9 \cdot \text{rnd}(0..1)$, $T^* = T_w/T_b$
Kalantari and Tropea [11]	For $\lambda_{We_b} < 0.1$ $6.74 \times 10^{-3} We_{nb} - 0.204$ For $\lambda_{We_b} \ge 0.1$ $35 We_{nb}^{-1.63}$	$\lambda_{We_b} = We_{tb}/We_{nb}$

Condition: Dry/wetted

The various submodels proposed in the literature are summarized in Table 21.1, where R_a is the average surface roughness; ρ, σ, and ν are the liquid density, surface tension, and kinematic viscosity, respectively; We_{nb} and We_{tb} are the Weber numbers ($=\rho U_b{}^2 D/\sigma$) based on the normal (U_{nb}) and tangential (U_{tb}) velocity components of impinging droplets, respectively.

Statistical Description of Secondary Atomization

Secondary atomization upon spray impact can be generated by diverse mechanisms. Models have been devised from experiments with single droplet impacts, which give the number, velocity, and direction of secondary droplets. Incorporation

of these models on CFD codes gives innumerable secondary droplets, such that tracking them all becomes prohibitive. To resolve this issue a stochastic approach is usually followed by calculating a statistical sample of the full population, where each computational secondary droplet actually represents a parcel of real droplets. Some older models originally assigned number mean values to these parcels within an appropriate range, which were randomly selected. However, experiments indicate that secondary droplets are better described by characteristic probability density functions (PDF).

Basically, the distributions reported by several authors for secondary atomization processes depend on a curve fit to data collected for a wide range of operating conditions and atomizer designs, which is designated as the empirical approach. Babinsky and Sojka [3] have reviewed also two other methods or approaches for predicting size distributions: (1) the maximum entropy (ME); and (2) the discrete probability function (DPF). Although these methods rely on a physical interpretation of the droplet generation process as nondeterministic (ME method), or as an ensemble of deterministic and nondeterministic portions (DPF method), one may question whether the resulting distributions fully capture the true nature of the atomization process. Moreover, even within the common empirical approach, what is the reason for stating that a Weibull, χ^2, Rosin–Rammler, Nukiama–Tanasawa, or a Log-normal distribution function is more suitable for describing, or predicting, secondary atomization?

Liquid atomization is a process for converting a bulk liquid volume of fluid into a myriad of single particle elements of multiple sizes (drops), which can be statistically described. Therefore, it is worth synthesizing the underlying statistical principles associated with a certain distribution function and the atomization process itself.

When we do this, the distributions usually considered for describing secondary atomization could be encompassed in two groups. One purely empirical, concerned about the shape and scale of the secondary drop size distribution (Weibull, χ^2, Rosin–Rammler, Nukyiama–Tanasawa), and the second, a semiempirical group associated with the multiplicative meaning of the Log-normal distribution function.

The distribution function for the first group could be generally expressed as

$$f(d) = \left[\frac{q}{\bar{d}}\left(\frac{d}{\bar{d}}\right)^{p}\right] \exp\left[-\left(\frac{d}{\bar{d}}\right)^{q}\right] \tag{21.3}$$

where p is a shape parameter, $\bar{d}$ and q are the scale parameters. While $\bar{d}$ clearly shifts the size distribution within its range because it is intrinsically linked with a characteristic drop size, q appears to affect, mainly, the frequency range and, consequently the size range for "conservation" reasons since the integral of $f(d)$ must equal 1 (see Fig. 21.3), and p, as seen on the top left plot in Fig. 21.3, affects the distribution shape. In the case of Weibull or Rosin–Rammler, the shape and scale parameters are the same as in (21.3), with $p = q - 1$; and the χ^2 case is similar, but with $q = 1$.

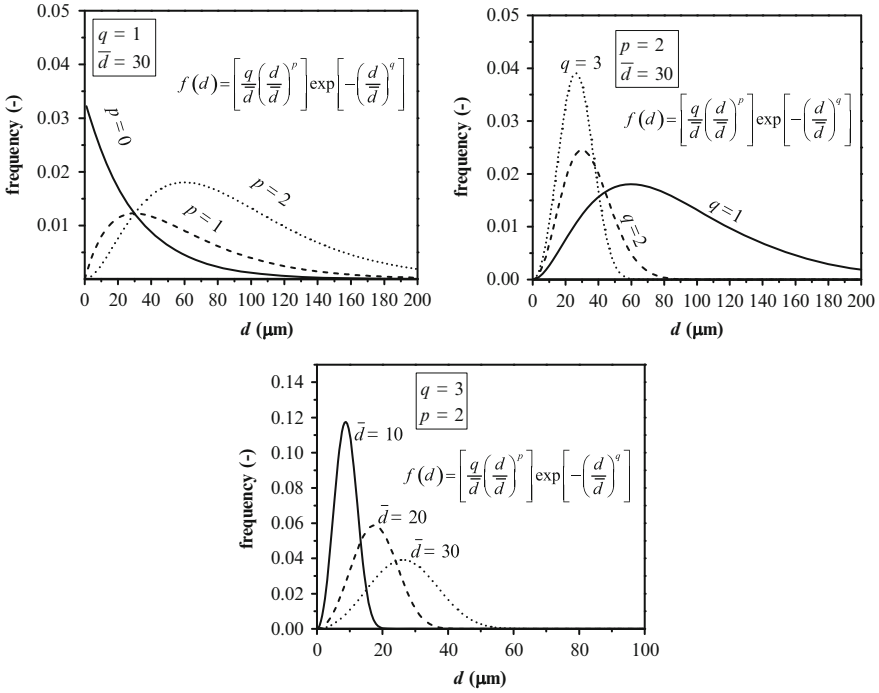


Fig. 21.3 Effect of shape and scale parameters on drop size distributions

The known Nukiama–Tanasawa empirical function, expressed as:

$$f(D) = \alpha \cdot D^p \exp[-\beta \cdot D^q] \tag{21.4}$$

can be considered a particular case of the general form written in (21.3), with $\alpha = q/\bar{d}^q$; $p = q - 1$; $\beta = \bar{d}^{-q}$, but is unable to independently control the shape and scale parameters of the distribution, given that α and β are nonlinearly dependent on both q and $\bar{d}$. The distribution functions for secondary drop size reported in the literature are summarized in Table 21.2.

In Stanton and Rutland [31], the shape and scale parameters depend on the Weber number, using the axial component of the impinging drop velocity in the calculations, but the authors are unclear about the characteristic mean size, whether it is arithmetic (AMD), volumetric (VMD, or D_{30}) or Sauter (SMD). The approach in Bai et al. [4] depends on the mass ratio between secondary and primary drops, which is randomly determined, thus introducing some nondeterminism into the formulation. In his approach, Lemini [14] fitted three polynomial functions f_1, f_2, f_3 to the data reported in Mundo et al. [18], with the objective of establishing different scale parameters q_1 and q_2, aiming at an independent control of the frequency and size range of the distribution, respectively.

Table 21.2 Distribution functions for secondary drop size reported in the literature

Reference	d	q	$\bar{d}$	P	Other parameters
Stanton and Rutland [31]	d_a/d_b	$2.71-9.25\times10^{-4}\,We_b$	$0.21-7.69\times10^{-5}\,We_b$	$q-1$	$We_b=\rho U_b{}^2 d_b/\sigma$
Han et al. [10]	d_a	3/2	$0.463d_{32}$	2	d_{32} is the Sauter mean diameter
Bai et al. [4]	d_a	1	$\bar{d}_{30}$	0	$\bar{d}_{30}=0.3218\left(\frac{6\cdot m_a/m_b}{\mathrm{We}_b/\mathrm{We}_{bc}-1}\right)^{1/3} d_b$ m_a/m_b is on Table 21.1 and the critical Weber We_{bc} on Bai et al. [4]
Lemini [14]	d_a	q_i	$\bar{d}_i$	1	$f(d_a)=\left[\frac{q_1}{\bar{d}_1}\left(\frac{d}{\bar{d}_1}\right)^p\right]\exp\left[-\left(\frac{d}{\bar{d}_2}\right)^{q_2}\right]$ $\bar{d}_1=f_1(K)d_b;\ q_1=\Gamma(2/f_3(K))/[f_3(K)\cdot f_1(K)/f_2(K)]$ $\bar{d}_2=f_2(K)d_b;\ q_2=f_3(K)$ $f_1(K)=1.96602\times10^{-4}K^2-9.1349\times10^{-2}K+10.419257$ $f_2(K)=-5.3313\times10^{-5}K^2+1.53062\times10^{-2}K-0.936192$ $f_3(K)=-1.05522\times10^{-3}K^2+0.34599K-26.130703$ and $K=We_b{}^{0.5}Re_b{}^{0.25}$ with $K\in[133;187]$
Roisman et al. [27]	d_a/D_{a30}	1.94	0.813	$q-1$	$D_{a30}=\begin{cases}24D_{b30}Re_b^{-1/2} & \text{for } Re_b>500\\ D_{b30}\left(0.65+0.017\cdot\exp\left[\frac{\mathrm{Re}_b-252}{73.5}\right]\right) & \text{for } Re_b>500\end{cases}$ $Re_b=\rho U_b d_b/\mu$ and D_{b30} is the Volumetric Mean Diameter

Acronyms: a = secondary drops (after impact); b = primary drops (before impact). In Lemini [14] q_1 is equal to 1, but the expression presented is the result of the PDF normalization

The second group of distributions, which describes secondary atomization is based on the Log-normal distribution function, expressed as:

$$f(d_a) = \frac{1}{d_a \gamma_g \sqrt{2\pi}} \exp\left(- \frac{\left(\ln(d_a) - \ln\left(\bar{d}_g\right)\right)^2}{2\gamma_g^2} \right) \tag{21.5}$$

where $\bar{d}_g$ and γ_g are the geometric mean diameter and standard deviation, respectively. As earlier mentioned, the Log-normal is related to the multiplicative nature of the statistical process involved. In fact, it is not hard to imagine such multiplicative nature within the disintegration process itself, for example, one large droplet could split into two smaller ones, these two into four and so on. However, since the Log-normal distribution is being applied to describe secondary drop sizes, the fact that some authors found a good fitting to their measurement data using it, means that secondary atomization triggered by hydrodynamic impact mechanisms (e.g., rebound, splash), has also a multiplicative physical nature. In fact, mechanisms such as splash will produce a certain number of droplets on the impact of a single one. Even with some degree of interaction on multiple impacts, this multiplicative factor remains. Nevertheless, as reviewed in the "Introduction" section, the knowledge on multiple drop impacts is still in its early stages, justifying that integrating the statistical description of secondary atomization with its physical interpretation remains open for further research.

Heat Transfer on Spray Impact

Heat transfer can be analyzed based on the rate form of the conservation of energy equation for the open thermodynamic system depicted in Fig. 21.4, where liquid vaporization occurs with the extraction of a heat flux $\dot{q}''_w$ from the surface. The mass flux of impinging droplets ($\dot{m}''_{in}$) may deposit and accumulate on the surface in the form of a liquid film (Dm''/Dt with temperature T_{LF}); move away from the surface in the form of secondary droplets ($\dot{m}''_s$); or, vaporize and mix with the surrounding environment ($\dot{m}''_{vap}$) with an average temperature between the wall and boiling values.

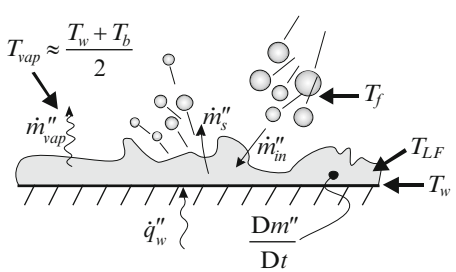


Fig. 21.4 Open system considered in the analysis of heat transfer at spray impact

One of the key parameters in the analysis is the initial surface temperature as, according to the classical boiling theory, it establishes the regime by which a liquid removes heat from a heated surface. In the film evaporation and boiling regimes, a liquid film forms onto the surface, and these are, therefore, jointly considered as a *wetting regime*. In vaporization/boiling, bubbles emerge from the surface due to nucleation, which may result in thermo-induced secondary atomization mechanisms [9, 16, 17]. In the transition regime, the liquid is in contact with the surface only intermittently, due to separations from the surface caused by vapor expelled from the liquid. Above the temperature of the local minimum in the boiling curve, occurs the Leidenfrost phenomenon, characterized by the appearance of a thin vapor layer between the liquid and the surface, being thus referred to as a *nonwetting regime*. Though these heat transfer regimes can be applied to the impact of a spray, the temperature values defining the transition between regimes depend on the impact conditions. Moreover, if the spray is intermittent, transition criteria are dynamic and multiple regimes can be simultaneously present within the entire impact area [15, 20].

Also, heat transfer must be analyzed either locally or globally within the entire area where the liquid is in contact with the surface because, depending on the flow conditions, initial surface temperature and its geometry, or roughness and heat sources, the heat fluxes can either be enhanced or inhibited, at a local or overall perspective.

From a local heat-transfer perspective, the outcome of this characterization is mainly in the form of empirical correlations for the Nusselt dimensionless number ($Nu = hD_d/k$), summarized in Table 21.3. Most correlations were derived from experiments within the context of IC engines, except for the dynamic correlation reported in Panão and Moreira [21], which considers the transient characteristics of droplets of an intermittent spray along an injection cycle, and a newly introduced dimensionless parameter λ corresponding to the average number of droplets impinging in the vicinity of each other [24].

An important issue concerns the evaluation of the cooling performance. Usually, the first-law of thermodynamics is used to compare the amount of heat extracted by the impinging spray with the total amount of heat that would be removed if all the mass impinging on the surface vaporized (sensible and latent heat components):

$$\varepsilon = \frac{\dot{q}''_{\mathrm{w}}}{\dot{m}''_{\mathrm{f}}\left(c_p \Delta T_{\mathrm{wb}} + h_{\mathrm{fg}}\right)} \tag{21.6}$$

where $\dot{m}''_{\mathrm{f}}$ is the mass flux rate of impinging droplets, ΔT_{wb} is the superheating degree, and c_p and h_{fg} are the specific heat and latent heat of vaporization, respectively. It has been recently argued in Panão and Moreira [22] that a performance analysis should also include the point of view of the second-law of thermodynamics. Basically, the best performance is achieved with the lowest production of irreversibility in the process, or else, the main sources should be identified in order to act accordingly. Assuming that a liquid film, regardless of its thickness, is present and that χ represents the mass faction of fluid vaporized, according to the analysis in Panão and Moreira [22], the rate of entropy generation is given by

Table 21.3 Heat transfer correlations for spray impingement

Reference/liquid	Correlation	Obs.
Arcoumanis and Chang [1]/diesel	$Nu = 0.34\dfrac{We^{0.94}}{Re^{0.53}Pr^{0.33}}$	Local correlation
Arcoumanis et al. [2]/diesel	$Nu = 0.0012\dfrac{Pr^{3.94}We^{1.59}}{Re^{1.89}}\left(\dfrac{U}{U+V_c}\right)^{-1.08}\left(\dfrac{d_{b32}}{d_{b32}+Z_{imp}}\right)^{-0.057}$	Local correlation in cross-flow conditions
Moreira et al. [16, 17]/gasoline	$Nu = 3.4\times10^{-5}\dfrac{Re^{1.51}}{Ja^{0.254}}$	Local correlation
Panão and Moreira [21]/HFE-7100 and acetone	$Nu = \begin{cases} 4.283\times10^{-37}\lambda^{1.028}La^{9.287}Ca^{-0.984}, & t_{impact}<t\le t_{impact}+\Delta t_{LFS} \\ 5.8\times10^{-5}\lambda^{0.581}Ja^{0.137}La^{1.11}Ca^{-0.745}, & t_{impact}+\Delta t_{LFS}<t\le t_{EOI} \\ 4.191\times10^{-4}\lambda^{0.272}Ja^{-0.365}La^{1.085}Ca^{0.901}, & t>t_{EOI} \end{cases}$	Local dynamic correlation

For the definition of dimensionless parameters, see Chap. 3, section "Three dimensional sheet instability"
Acronyms: *LFS*, leading front of the spray; *EOI*, end-of-injection

$$\dot{S}''_{\text{gen}}(\chi) = \underbrace{[\varphi_{\text{L}}(\chi)s_{\text{L}} + \varphi_{\text{V}}(\chi)s_{\text{V}}]\Delta\dot{m}''}_{\dot{S}''_{\text{gen},\Delta\dot{m}''}} + \underbrace{\dot{q}''_{\text{w}}\left(\frac{1}{T_{\text{LF}}} + \frac{1}{T_{\text{w}}}\right)}_{\dot{S}''_{\text{gen},\dot{q}''_{\text{w}}}}$$

$$\begin{cases} \varphi_L(\chi) = \chi\left(3\chi - \chi^2 - 3\right) \\ \varphi_V(\chi) = \chi\left(\chi^2 - 2(\chi - 1)\right) \\ \Delta\dot{m}'' = \dot{m}''_{\text{in}} - \dot{m}''_{\text{s}} \end{cases} \tag{21.7}$$

where the first parcel of the right-hand side corresponds to the irreversibility associated with evaporation ($\dot{S}''_{\text{gen},\Delta\dot{m}''}$) and the second parcel corresponds to the irreversibility associated with the heat extracted from the surface ($\dot{S}''_{\text{gen},\dot{q}''_{\text{w}}}$). The ratio between the former and the latter gives the irreversibility distribution ratio ϕ_{sc}.

Application of the entropy generation minimization (EGM) method to (21.7) allows identifying the optimal parameters to be considered in the optimization [6]. Concerning the entropy generated by the evaporated mass flux, that parameter is the fraction χ of evaporated mass and its optimal value is found by equating to zero the partial derivative of (21.7) with respect to χ. The optimal evaporated mass fraction is thus found to be

$$\chi_{\text{opt}} = \frac{3s_{\text{L}} - 2s_{\text{V}} - \sqrt{3s_{\text{L}}s_{\text{V}} - 2s_{\text{V}}^2}}{3(s_{\text{L}} - s_{\text{V}})} \tag{21.8}$$

which requires a positive term inside the square root, such that $s_{\text{L}} \geq (2/3)s_{\text{V}}$. The equality in the former expression sets the lower limit optimal value, $\chi_{\text{opt}} = 0$. The upper-limit of the inequality is $s_{\text{L}} \rightarrow s_{\text{V}}$, which could only occur near the critical temperature of the cooling liquid and implies that only half of the impinging mass is vaporized ($\chi_{\text{opt}} = 0.5$). This analysis indicates that energy losses should be minimum if the cooling liquid vaporization is minimized, favoring the presence of a liquid film on the surface, as in some continuous spray cooling concepts (see [23, 30]).

Application of the EGM method to the entropy generated by heat transfer at the surface (which should be maximum in a spray-cooling application), identifies the temperature as the parameter to be accounted for in the optimization process. Here, the derivative of (21.7) produces a single solution for the optimization of the wall temperature as $T_{\text{w,opt}} = T_{\text{b}} + 2T_{\text{f}}$, which can be interpreted with respect to the superheating degree ($\Delta T_{\text{wb,opt}} = T_{\text{w,opt}} - T_{\text{b}}$) as

$$\Delta T_{\text{wb,opt}} = 2T_{\text{f}} \tag{21.9}$$

This simple criterion based on the least irreversibility is technically interesting for choosing the most adequate fluid in the optimal design of a certain spray-cooling application. It should be stressed that the optimal wall temperature corresponds to the working temperature of the heat-dissipating surface, which the spray-cooling system is required to maintain at a constant value.

When designing a spray-cooling system, the optimization analysis should consider the relative importance of each term in (21.7) to the irreversibility distribution ratio $\phi_{sc.}$

Concluding Remarks

The application of spray-wall impact to engineering systems relies on the accurate knowledge of four research subjects: (1) multiple drop impacts; (2) liquid deposition; (3) secondary atomization; and (4) heat transfer on spray impaction.

Research on multiple drop impacts evidences that hydrodynamic structures depend on interdrop length and time scales, having a different morphology from that commonly found in single drop impacts, such as splash with crown development. Secondary droplets produced by uprising liquid sheets resulting from multiple drop interaction on the impact site are larger and slower than those usually generated by single impacts.

The deposition of liquid by spray-wall impact can be positive in thermal management systems, or spray-painting applications, but it can be negative in IC engines, since it is directly related to the emission of pollutants. Several methods, deterministic and nondeterministic, have been reviewed.

A systematic analysis has been made for the statistical approach to describe secondary drop size distributions. Two groups were identified. An empirical one based on the Weibull distribution where the scale and shape parameters can change according to the degree of control desired over the size and frequency range. The second group is semiempirical and is associated with a log-normal distribution function. The statistical meaning of the log-normal expresses the multiplicative nature of the secondary atomization process.

The heat transfer process on spray-wall impact can be viewed at from a local, or an overall perspective. From a local perspective, a synthesis has been made of the correlations found between energy exchanges and the characteristics of the impinging spray. From an overall perspective, the analysis argues that the performance can be improved if, besides taking into account the efficiency based on the first-law of thermodynamics, it also takes into account the second-law. The insights given by the EGM method can be useful not only to physically interpret heat transfer on spray impact, but also to provide criteria for optimizing the performance of the system from the viewpoint of cooling.

References

1. Arcoumanis C, Chang J-C (1993) Heat transfer between a heated plate and an impinging transient diesel spray. Experiments in Fluids 16:105–119.
2. Arcoumanis C, Cutter PA, Whitelaw DS (1998) Heat transfer processes in diesel engines. Chemical Engineering Research and Design 76:124–132.

3. Babinsky E, Sojka PE (2002) Modeling size distributions. Progress in Energy and Combustion Science 28:303–329.
4. Bai CX, Rusche H, Gosman AD (2002) Modeling of gasoline spray impingement. Atomization and Sprays 12:1–27.
5. Barnes HA, Hardalupas Y, Taylor AMKP, Wilkins JH (1999) An investigation of the interaction between two adjacent droplets. In: ILASS-Europe'99, Toulouse
6. Bejan A (1995) Entropy generation minimization. CRC Press, Boca Raton.
7. Cossali GE, Marengo M, Santini M (2004a) Impact of single and multiple drop array on a liquid film. In: Proceedings of the 19th ILASS-Europe, Nottingham.
8. Cossali GE, Marengo M, Santini M (2004b) Drop array impacts on heated surfaces: secondary atomization characteristics. In: Proceeding of the 19th ILASS-Europe, Nottingham.
9. Cossali GE, Marengo M, Santini M (2008) Thermally induced secondary atomization produced by single drop impact onto heated surfaces. International Journal of Heat and Fluid Flow 29:167–177.
10. Han Z, Xu Z, Trugui N (2000) Spray/wall interaction models for multidimensional engine simulation. International Journal of Engine Research 1(1):127–146.
11. Kalantari D, Tropea C (2007) Spray impact onto flat and rigid walls: Empirical characterization and modelling. International Journal of Multiphase Flow 33:525–544.
12. Kalb T, Kaiser H-G, Chaves H, Obermeier F, Ebert F (2000) Splashing due to neighbouring droplet impact. In: Proceedings of the ILASS-Europe, Darmstadt.
13. Kuhnke D (2004) Spray/Wall-Interaction Modelling by Dimensionless Data Analysis, PhD Thesis, Darmstadt University of Technology, Darmstad.
14. Lemini E (2004) A New Methodology for Modelling Impinging Sprays Based on Drop Size Moments, PhD Thesis, University of Manchester, Manchester.
15. Moreira ALN, Panão MRO (2006) Heat transfer at multiple-intermittent impacts of a hollow cone spray. International Journal of Heat and Mass Transfer 49:4132–4151.
16. Moreira ALN, Carvalho J, Panão MRO (2007) An experimental methodology to quantify the spray cooling event at intermittent spray impact. International Journal of Heat and Fluid Flow 28:191–202.
17. Moreira ALN, Moita AS, Cossali GE, Marengo M, Santini M (2007) Secondary atomization of water and isooctane drops impinging on tilted heated surfaces. Experiments in Fluids 43:297–313.
18. Mundo CHR, Sommerfeld M, Tropea C (1995) Droplet-wall collisions: experimental studies of the deformation and break-up processes. International Journal of Multiphase Flow 21(2): 151–173.
19. Panão MRO, Moreira ALN (2005a) Flow characteristics of spray impingement in PFI injection systems. Experiments in Fluids 39:364–374.
20. Panão MRO, Moreira ALN (2005b) Thermo- and fluid dynamics characterization of spray cooling with pulsed sprays. Experimental Thermal and Fluid Science 30:79–96.
21. Panão MRO, Moreira ALN (2009a) Heat transfer correlation for intermittent spray impingement: a dynamic approach. International Journal Thermal Science 48(10):1853–1862.
22. Panão MRO, Moreira ALN (2009b) Intermittent spray cooling: a new technology for controlling surface temperature. International Journal of Heat and Fluid Flow 30:117–130.
23. Pautsch A, Shedd T (2005). Spray impingement cooling with single- and multiple-nozzle arrays. Part II: visualization and empirical models. International Journal of Heat and Mass Transfer 48:3176–3184.
24. Roisman I V, Tropea C (2005) Fluctuating flow in a liquid layer and secondary spray created by an impacting spray. International Journal of Multiphase Flow 31:179–200.
25. Roisman I, Araneo L, Marengo M, Tropea C (1999). Evaluation of drop impingement models: experimental and numerical analysis of a spray impact. In: Proceedings of the 15th Annual Conference on Liquid Atomization and Spray Systems, Toulouse.
26. Roisman I V, Prunet-Foch B, Tropea C, Vignes-Adler M (2002) Multiple drop impact onto a dry solid substrate. Journal of Colloid and Interface Science 256:396–410.
27. Roisman I, Horvat K, Tropea C (2006). Spray impact: rim transverse instability initiating fingering and splash, and description of a secondary spray. Physics of Fluids 18:102104, 1–19.

28. Samenfink W, Elsäβer A, Dullenkopf K, Wittig S (1999) Droplet interaction with shear-driven liquid films: analysis of deposition and secondary droplet characteristics. International Journal of Heat and Fluid Flow 20:462–469.
29. Senda J, Fujimoto H (1999) Multidimensional modeling of impinging spray on the wall in diesel engines. ASME Applied Mechanical Review 52(4):119–138.
30. Shedd T, Pautsch A (2005) Spray impingement cooling with single- and multiple-nozzle arrays. Part II: heat transfer data using FC-72. International Journal of Heat and Mass Transfer 48:3167–3175.
31. Stanton D, Rutland C (1996) Modeling fuel film formation and wall interaction in diesel engines. SAE Technical Paper 960628.
32. Yarin AL (2006) Drop impact dynamics: splashing, spreading, receding, bouncing . . .. Annual Review of Fluid Mechanics 38:159–192.
33. Yarin AL, Weiss DA (1995) Impact of drops on solid surfaces: self-similar capillary waves and splashing as a new type of kinematic discontinuity. Journal of Fluid Mechanics 283:141–173.

Chapter 22
Interacting Sprays

J.B. Greenberg

Abstract In many disparate engineering systems, ranging from cooling systems for microelectronics to jet engines, multiple sprays are utilized and the way they interact with one another is the subject matter of this chapter. A general overview of published research on interacting sprays is presented. Both experimental and theoretical or numerical investigations of combusting or noncombusting systems are covered. The nature of the interactions may be either direct (with actual contact between the sprays) or indirect (with no contact between the sprays). It is found that, despite the underlying common physics which reflects the mutual interaction between the sprays and their surroundings and between themselves, with few exceptions the material in the literature tends to relate to the impact of spray interactions *in specific systems* rather than on the fundamentals of the interaction. The question that is addressed is: is the use of multiple sprays more effective than the use of a single spray, or is it possibly detrimental? And, if the latter is true, can the situation be ameliorated by manipulation of the physics through geometric and other factors that relate to the sprays? Surveying the sparse literature on this subject gives some inkling of the important features that are relevant at a basic level. But much remains to be done, both experimentally and theoretically, in order to fully elucidate the complexities of spray interactions.

Keywords Coalescence · Collisions · Combustion · Entrainment · Included angle · Interactions · Nozzles · Interacting sprays

Introduction

The predominance of nozzles in a wide variety of practical engineering applications has been responsible for the enormous effort invested theoretically, computationally, and experimentally in unraveling the way in which sprays behave under

J.B. Greenberg
Faculty of Aerospace Engineering, Technion, Israel Institute of Technology, Haifa, Israel
e-mail: aer9801@aerodyne.technion.ac.il

N. Ashgriz (ed.), *Handbook of Atomization and Sprays*,
DOI 10.1007/978-1-4419-7264-4_22, © Springer Science+Business Media, LLC 2011

widely differing sets of operating conditions. However, a cursory glance at books on sprays as well as published research literature reveals that interest is generally focused on a *single* spray of droplets in a two- or three-phase system. Indeed, it is natural to ask as to how an individual spray will respond to a given environment or, more generally, what mutual interaction can be expected between an individual spray and its surroundings. Historically speaking, in the past such questions were posed in the context of individual droplets, then, subsequently, in connection with pairs of droplets, arrays of droplets and, ultimately, for single sprays of droplets.

However, in many practical systems more than one single spray is employed. Is the use of multiple sprays more effective than the use of a single spray, or is it possibly detrimental? The answer to this question will presumably depend on the particular application involved and on the ability to choose suitable operating conditions. Yet, remarkably, there is a relative paucity of material on research on multiple sprays and the way in which they interact not only with their surroundings but also with one another. Of course, the degree of complexity that already exists when investigating the behavior of single sprays of droplets is compounded when multiple sprays are to be considered. In this chapter some of the sparse material on this topic will be briefly surveyed. It is somewhat notable that despite the many varied applications in which multiple sprays are utilized, from cooling systems for microelectronics to jet engines, there does not seem to be a large body of basic work dedicated to defining the fundamental principles involved in spray interaction under controlled experimental conditions, accompanied by appropriate theory. This is not to say that *no* basic research has been carried out. But that which has been performed understandably tends to reflect those particular problems which are of concern to the researchers involved.

In the following sections emphasis will be placed on giving a general overview of published material devoted to different aspects of interacting sprays. These can either be in a noncombusting or a combusting context. A further categorization will be made in terms of whether the sprays interact directly or indirectly. By direct interaction will be meant whether, in a given system, there is some *direct* contact at some stage between the droplets of the initially separate sprays. Indirect interaction will refer to a situation in which the presence of initially separated sprays exerts some sort of mutual influence on the surrounding medium in which they are found, without any physical contact between the sprays.

As will be seen, a basic configuration of directly interacting sprays will be one in which at least two sprays will issue from separate orifices. The relative size and location of the orifices to one another as well as the included angle between the orifices and central axes will be of importance in their subsequent downstream interaction (see the sketches in Fig. 22.1a,b). Some typical triple spray configurations are drawn in Fig. 22.2. Note that although these figures show the nozzles pointing downwards they do not necessarily always do so and the actual configuration of the nozzles can be obtained by simply rotating the figures through the appropriate angle. In addition, the nozzles in the figures are illustrated pointing inwards towards one another. This, too, is a specific case and other instances in which the nozzles are tilted away from each other can be also expected.

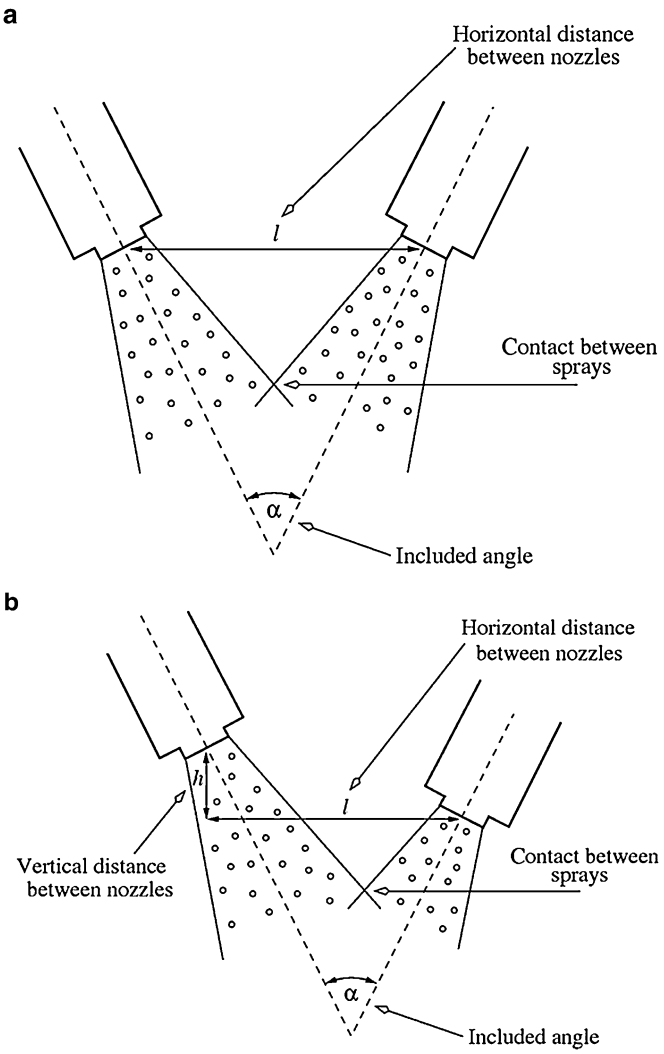


Fig. 22.1 Sketch of the configuration of typical double interacting sprays with (**a**) no vertical displacement between them and (**b**) with both horizontal and vertical displacements between them

Some further parameters that can be envisioned as impacting (to a greater or lesser extent) on spray interaction are the sort of atomizers producing the sprays of droplets (e.g., pressure atomizers, pressure-swirl atomizers, rotary atomizers, etc.), the spray angle, the actual droplet size distributions produced by the atomizers, and the liquid flow rates. Yet, as will become apparent, there does not seem to be any uniformity in the operating conditions of reported studies of interacting sprays. The emphasis has been almost exclusively on the influence of spray interaction *in a given system* under appropriate operating conditions.

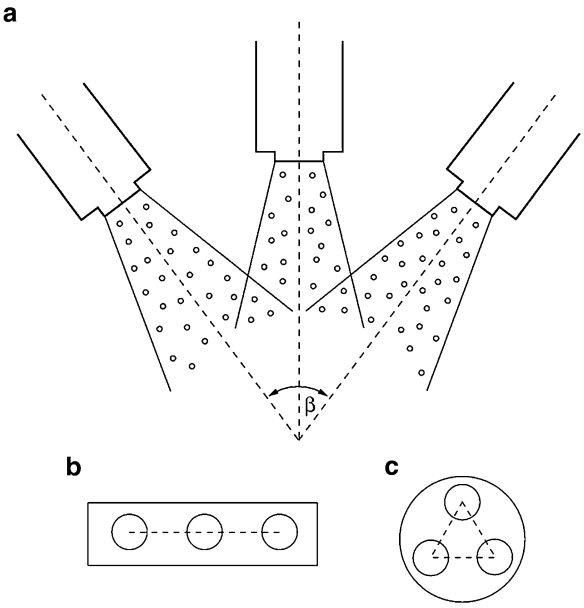


Fig. 22.2 Sketch of the configurations of (**a**) typical triple interacting sprays; in (**b**), the alignment is linear whereas in (**c**), it is triangular

Interacting Sprays – Experimental Studies

In this section, an overview of experimental studies involving interacting sprays will be given, mainly arranged chronologically.

An early pioneering experimental investigation into the characteristics of multiple diesel sprays was given by Fujimoto et al. [1]. Using a high-pressure chamber of size 200 mm in diameter, 500 mm in height with a volume of 15.7×10^{-3} m^3 they injected JIS heavy fuel oil through three fixed injection nozzle holes aligned such that the central spray emerged along the axis of the vertical chamber whereas the axis of each of the other two sprays was at an angle of 33° to the central one. Because of the spherical shape of the atomizer tip the off-center sprays were located at horizontal and vertical distances of 1.08 and 0.324 mm, respectively, from the central spray. The central axes of the three sprays were all located in the same plane. Fuel was not injected continuously; rather, the injection period was up to 9 ms. Data was primarily collected using a high-speed 35 mm camera and 16 mm high-speed photography. It was found that spray tip penetration, the overall spray cone angle, and the equivalent spray angle of the central spray were negligibly influenced by the off-center sprays, for the range of operating conditions considered (i.e., initial pressures in the range of 0.098–9.89 MPa and initial temperatures of about 300–600 K). However, it was observed that the axes of the two off-center sprays were attracted to the axis of the central spray. The attraction increased with an

increase in initial pressure. It was suggested that this interaction between the sprays is related to the Coanda effect [2]. Using a smoke tracer, the air movement between adjacent sprays was found to be in the direction of the nozzle tip with subsequent normal entrainment into the spray. Although the latter phenomenon occurs in single sprays the initial air movement in the nozzle tip direction is peculiar to the multiple spray system. In fact, further data on what the authors term "flame growth" during the period of liquid fuel injection (i.e., the extent of combustion in the direction of the spray nozzle) strongly suggests that the aforementioned air movement enhances mixing and heat exchange between the spray and its surroundings thereby leading to an increased region of flammable mixture. This was clearly illustrated as a function of the number of nozzle holes (which was increased to 11). No droplet size or velocity measurements are reported so that the structure of the merging sprays is not known other than in some general qualitative way.

Of slight relevance to controlled experiments aimed at characterizing spray interaction in the noncombusting context is the work of Snarski and Dunn [3] who carried out experiments with electrically charged liquid droplets, of size 50 μm. Correlation of droplet size with lateral velocity was used to detect the presence of droplets from the two sprays in the region of spray interaction. However, in these experiments the behavior of the droplets is primarily dictated by the electrical forces at play, thus making the results of limited applicability.

Dombrowski and Singh [4] looked into the influence of multiple spray nozzles in the context of a forced-draft water cooling tower. They were particularly concerned with gas entrainment relative to the water flow rate per unit cross-sectional area and the effect of spray separation and drop size on entrainment efficiency. In their experimental configuration, they utilized a nozzle manifold with the nozzles arranged along the manifold such that the spray of water emerged vertically downwards (similar to the configuration of Fig. 22.2a). The manifold was installed in a rectangular duct with an adjustable width and/or length of spray penetration. However, the breadth of the duct was fixed (at 0.465 m). The air flow in the duct was controlled to be almost uniform for all experiments conducted. Fan spray nozzles were used, produced from single-orifice pressure nozzles. The droplets produced by the different nozzles had Sauter mean diameters of 265, 405, and 456 μm. The entrainment efficiency was defined as the gas to liquid mass ratio. The main conclusion drawn was that entrainment is reduced as the nozzles were brought closer together. For a single unconstrained spray, air is entrained along the length of the spray. However, for sprays confined to a duct, the air outside the spray envelope is forced to flow parallel to it so that the relative drop-air velocity within each spray envelope decreases. This reduces the drag between the air and the spray droplets, resulting in lower momentum transfer, and hence, lower entrainment.

In contrast to the work of Dombrowski and Singh [4] who, due to the particular problem they considered, were interested in the impact which an array of sprays has on its surroundings rather than intraspray interaction, Hardalupas and Whitelaw [5] specifically addressed the latter issue quantitatively. They investigated the interaction between three sprays from coaxial airblast atomizers in a noncombusting context and made detailed comparisons with data for a single atomizer and, for

the air flow, with a single-phase flow. The triplet consisted of three identical nozzles in a triangular arrangement with jet axes equidistant (by two jet diameters) from one another and parallel to each other (similar to Fig. 22.2c). The liquid (water) jet diameters were 2.3 mm centered in an 8.95 mm diameter air stream. Phase Doppler measurements of size, velocity, liquid flux, and average mass fractions were made. Cases of two liquid flow rates were examined, keeping the air flow rate fixed. It was observed that up to 10 air jet diameters from the nozzle exit each spray retained its individuality with the maximum Sauter mean diameters (of the order of 150 μm) and liquid fluxes on the geometrical axes of the nozzles. However, spray merging was also strongly present between the nozzle axes. This merging exhibited itself through a reduction in the Sauter mean diameter accompanied by an increase in the liquid flux, the mean and RMS of the fluctuations of the droplets axial velocity of both the droplets and the air flow relative to a single spray. At 25 air jet diameters from the nozzle exit merging of the sprays was such that a single spray-like flow was produced as if from a nozzle at the center of the triangular region between the nozzles. Reducing the liquid flow rate by 50% shortened the distance at which the merging occurred by 30% and increased the air flow turbulence by 20%. In addition, it was noted that the Sauter mean diameter increased by 15% with axial distance giving a clear indication that, under the specific operating conditions, droplet coalescence, due to collisions between droplets from the three sprays, assumed importance. A major effect of the spray merging was to increase the air flow turbulence and the local mass fraction distribution of the air between the nozzle axes by 40–50% relative to the situation with a single spray. In a combustion context, this would result in a more fuel rich region with increased gas flow turbulence thereby enhancing ignition. Interestingly, this conclusion can be understood to be borne out qualitatively by Fujimoto et al.'s [1] earlier observations about "flame growth" using rather less sophisticated experimental equipment than those employed by Hardalupas and Whitelaw [5]. Similarly, their recommendation to use an increased number of nozzles (with reduced diameter and distance between the axes) to increase the spray interaction also overlaps with the earlier work.

Brenn and coworkers [6, 7] presented a number of experimental investigations into the details of the interaction between two noncombusting binary sprays. In [6], they treated the interaction between two hollow-cone sprays of different liquids (as per a configuration shown in Fig. 22.1a) in order to enable identification of the droplets from the different sprays through their refractive index. The work actually concentrated on evaluation of the extended phase-Doppler anemometry as a measuring technique in this context rather than on detailed effects of the actual spray interaction. In [7], details of the actual interaction of [6] were given. The PDA system used for the measurements was able to supply information about the size and two velocity components of drops at each measurement location and comparisons were made between flows with single sprays and double sprays. The demineralized water sprays used were injected downwards from two semi-hollow cone pressure swirl atomizer nozzles that were arranged so that the intersection angle between them could be adjusted. The cone angle of the nozzles was 60°. From the data given, the distance between the nozzles can be deduced to be about 20–25 mm.

Droplet sizes were in the range of 10 to about 70 μm. Measurements were made from the level of first contact of the sprays, which was held fixed at 20 mm from the nozzles. Size/velocity correlations of the droplets showed clearly that the droplets were accelerated by the spray interaction in the downstream direction. Droplet motion in the lateral direction was induced by the airflow caused by the sprays interaction. The integrated mean droplet size, D_{10}, across the spray increased with downstream distance and this increase was greater for the interacting sprays than for a single spray. Droplet coalescence was also noted as being important in the center of the combined flow field where the mean droplet size increased. In contrast to what might be anticipated, this was found to be due to the increased relative velocity of colliding droplets rather than a higher droplet concentration.

Valencia-Bejarano et al. [8] carried out similar experiments to those of Brenn et al. [7] with two full cone polydisperse water sprays produced by a pair of two fluid-atomizing nozzles. The sprays were directed towards each other at 45° to the center line with a horizontal distance of 40 mm between them. As in [7], a PDA system was used for measuring droplet diameter and droplet mean axial and radial velocities. SMD radial distributions were reported for various downstream locations both upstream and downstream of the first contact point between the sprays. Droplet diameters (in terms of SMD) were in the range of 30 to about 70 μm. These were preferred to the mean droplet size of [7] as the latter is more sensitive to smaller droplets. Droplet trajectories were also examined beyond the crossover point of the two sprays and it was concluded that the primary mechanism for droplet coalescence was the differential velocity between large and small droplets due to inertia and the eddying motion of air. However, coalescence was greater when small droplets were generated compared with larger droplets because of the larger number density and droplet velocity in the smaller droplet case. An important observation was that coalescence events are predominantly caused by droplets from one spray penetrating the other spray and colliding with droplets encountered on their trajectory from the other nozzle, rather than by droplets of the same spray overtaking one another and colliding en route.

Motivated by increasingly stringent government requirements for pollutant emissions in the automotive industry, Chehroudi et al. [9, 10] suggested an interacting sprays injection concept for use in diesel engines in order to attempt to reduce both NO_x and smoke production. A single cylinder compression-ignition two-stroke research engine was used. Two fuel injector nozzles were used 6.4 mm apart with an impinging angle of one on the other at 12–14°. The spray injection system produced two separate independently controlled liquid fuel spray injections with flexibility with regard to the injection timing and the quantity of supplied fuel. The interaction of the sprays was controlled via the way in which injection from the two nozzles was performed. Instead of using continuous injection the concept of split injection was adopted (see Tow et al. [11] who explain that the advantage of this idea lies in the enhancement of the mixing caused by the delayed last subinjection).The basic idea was to try to exploit the flexibility of the double fuel injectors so as to optimize the spray interaction at the right time and location within the chamber to achieve the desired reduction in pollutant production. The details of the

actual interaction (droplet distributions, velocities, coalescence, etc.) were not measured as it was the *result* of the interaction that was of prime interest. The fuel utilized was commercial #2 diesel fuel with an additive of 3% isopropyl nitrate (an ignition enhancer). A number of possibilities were investigated and the influence on pollutant production was compared: (1) a single continuous injection of 30 mm^3 of fuel, (2) coincident interacting sprays injection with an equal amount of fuel, 15 mm^3, injected from each nozzle starting simultaneously, (3) interacting sprays injection (15 mm^3) but with the second pulse end completed near the end of the ignition delay period, and (4) interacting sprays injection but with the start of the second injection at about 2.5 ms from the start of the first one so that the time between the end of the first injection and the start of the second one was 1.8 ms. The measured NO_x and smoke showed quite dramatically that all the interacting sprays cases were more effective in reducing the pollutants than the single injection case. Moreover, the optimal case was found to be number (2) above. This was in contrast to the findings of Tow et al. [11], although this is probably explicable in view of the fact that the latter researchers used a single spray but with split injection rather than two injectors. The reduction in soot production was explained as follows. Soot formation is initiated in the dense regions of diesel fuel spray. Heywood [12] suggests that these dense local regions of soot are formed early on in the combustion process. Subsequently, much of this soot is oxidized during later stages of combustion with emissions made up of the remnants of incompletely oxidized particles. Chehoudri et al. [10] proposed that their reduced soot production is due to interactions between the injection pulses, which disrupt and disperse the dense spray regions thereby eliminating some of the potential sites of nucleation within which soot particles are formed. The NO_x reduction is particularly effective when the second injection pulse is close to or slightly after the ignition delay period so that the local burned and burning gases temperatures are lowered with the NO_x chemistry thereby quenched.

Parvez and Gollahalli [13, 14] performed basic experiments in a laboratory scale combustion chamber (164 cm tall, 76 cm squared cross section) to investigate the effects of inter-jet spacing on multiple spray flames. They studied single, double, and triple sprays arranged in a line (as in Fig. 22.2b), with the interjet distance presented in the form of the ratio of the interjet spacing to the atomizer exit diameters (the latter being identical and equal to 1.622 mm). The sprays of liquid Jet-A fuel were injected vertically from the bottom of the combustion chamber using twin fluid atomizers. A comprehensive set of experimental data was obtained for which flame length, merging length and lift-off heights, droplet size and velocity distributions, radiative fraction of heat release and temperature profiles, soot concentration and emission indices of carbon monoxide (CO), NO, and NO_x were measured for all the aforementioned spray flames and for varying interspray distances. Details of the experimental facilities that provided the measurements are given in [13, 14]. Measured droplet Sauter mean diameters were in the range of about 10–60 μm with mean droplet velocities reaching about 12 m/s. The main conclusions of the study are that increasing the interspray spacing permits greater penetration of oxygen to the space between the jets, thereby producing a higher

temperature, lower CO formation, higher NO formation, higher carbon dioxide concentrations, and lower soot formation. In addition, a decrease in flame length, an increase in merging length and lift-off height, and a small decrease in radiative fraction of heat release result. Also, emission indices of CO, NO, and NO_x increase with an increase in interspray spacing. The authors found no indication of spray interaction effects on the atomization process in the near nozzle region, except for the case of the smallest interspray spacing of 18.5 (=an actual distance of almost 30 mm). This latter conclusion can explain the seeming discrepancy between these experimental results and those reported by Fujimoto et al. [1], Hardalupas and Whitelaw [5], and Chehoudri et al. [10]. Each of these latter works considered a different geometrical configuration of spray nozzles. However, more importantly, even the smallest interspray spacing considered by Parvez and Gollohali [13] is considerably larger than the equivalent spacing of the other works which range from about 1 mm [1] up to 18 mm [5]. It may be surmised that had Parvez and Gollohali considered values of the interspray distances in this range, a much stronger spray interaction would have been noted, with its attendant influence on the combustion characteristics of the spray flames formed.

A further application in which multiple interacting sprays are to be found is in the context of spray cooling of systems in which large heat fluxes exist, such as aerospace and space-based applications as well as other applications that incorporate microelectronic devices. However, it seems that spray interaction can be disadvantageous in these contexts due to excess fluid getting trapped in between sprays (flooding). Glassman et al. [15], using pressure-atomized sprays, suggested what they term a "fluid management system" for overcoming inefficiencies resulting from spray overlap. Essentially, the system suctions away excess fluid thereby increasing the heat flux and the heat transfer coefficient. Details of the actual spray interaction (such as droplet collisions, etc.) were not reported as they were of secondary interest in relation to the main aim of cooling a large area. Pautsch and Shedd [16] performed a comprehensive study of multiple spray cooling using swirl chamber type pressure atomizers. They too concluded that spray interactions can degrade performance. Although multiple nozzles permitted higher peak heat fluxes they used fluid inefficiently due to spray interaction. Some form of optimization is necessary in terms of nozzle geometry and where the nozzles are located relative to one another. Once again, since the heat transfer was of prime importance, measurements of spray properties were not reported.

The notion of group-hole nozzle sprays was proposed by Tokudo et al. [17] with subsequent studies appearing in [18–21]. The basic idea was motivated by the need for an enhanced fuel/air mixing in high-efficiency diesel engines in order to achieve improved ignition, combustion, and exhaust emissions. Ensuring combustion of available oxygen during the process of mixing controlled combustion the fuel sprays must exhibit adequate penetration with a small droplet SMD for satisfactory evaporation. Since a small SMD spray generally has a shorter penetration distance, some balance between these two factors is necessary. Conventional nozzles involve a single orifice through which the fluid to be atomized flows. In practice, a number of single-hole orifices are used. Tokudo et al. [17] suggested the use of what is

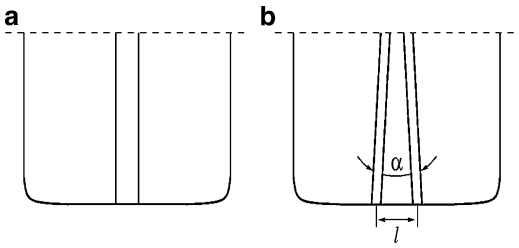


Fig. 22.3 (**a**) Conventional nozzle exit and (**b**) group-hole nozzle exit

termed a group-hole nozzle (see the sketch in Fig. 22.3). This involves replacing single-hole orifices in the nozzle tip by a pair of micro-orifices located in close proximity to one another. These group-holes may have the channels preceding the orifices parallel to one another or with some nonzero included angle. In [18], an experimental comparison was made between the performance of a single-hole nozzle and several double-orifice group-hole nozzles under noncombusting conditions. Using a common rail-type diesel injection system the sprays were injected into nitrogen, and impinged on a flat wall, thus simulating, to a certain extent, wall interaction in the fuel-air mixing process in a direct injection diesel engine. The flat wall was located at 31 mm below the nozzle tip and the diameter of the orifice for the single hole was 0.160 mm whereas that of the group-hole orifice was 0.113 mm with a constant distance of 0.1 mm between the two orifices.

Included angles of 0°, 5°, and 10° were considered. Measurements were made using a laser absorption scattering technique in order to determine such features as vapor concentration and droplet density, spray angle, and penetration of the vapor and liquid phases. It was found that for a group-hole nozzle (with included angle 0°), there was no significant difference in the spray shape, spray tip penetration or spray angle when compared to a single-hole nozzle. However, improvement was noted in fuel atomization (a smaller SMD was obtained – about 20 μm as opposed to about 24 μm for a single-hole nozzle), evaporation (a greater vapor mass fraction), as well as air entrainment. For group-hole nozzles with a nonzero included angle, faster penetration along the wall was observed when viewed along the line of orientation of the holes to one another. The penetration was slower when viewed along a line at right angles to the aforementioned orientation. The authors also relate to the actual interaction of the sprays and the question of droplet collision and coalescence. They argue that, for the group-holes with nonzero included angles, there is less coalescence than for a single-hole nozzle due to the diverging angle between the orifices. Thus, smaller size droplets are likely to be produced because of the smaller orifice diameters as compared to a single-hole nozzle.

More recently, Gao et al. [20] used basically the same experimental set-up and apparatus together with direct flame imaging and OH chemiluminescence imaging to examine the flame structure induced by utilization of group-hole nozzles. In terms of spray penetration, their results echoed those of Zhang et al. [18]. However, they were also able to deduce that the ignition delay of group-hole nozzles was shortened when the included angle and the injection pressure were

increased because of improved evaporation and fuel/air mixing. Other results pointed to improved combustion characteristics. Moreover, the observed flame structure seemed to imply that the group-hole configuration can be critical in ensuring proper air utilization in the combustion chamber, thereby ameliorating soot formation.

An independent investigation of group-hole nozzles was performed by Pawlowski et al. [21] under noncombusting conditions. The diameter of the single orifice case (used for comparison) was 0.131 mm whereas that of the group-hole orifice was 0.093 mm. The distance between the orifices was 0.6 mm. Configurations of included angles of 0°, 5°, 10°, and 20° were examined. The sprays were injected for a short period of time and their development was recorded. Unlike the impinging sprays of Zhang et al. [18], the sprays used by Pawlowski et al. [21] were injected freely into a pressurized chamber. A combined set of experimental techniques, consisting of simple Schlieren imagery and Phase Doppler Anemometry, were employed to visualize the spray and to measure droplet velocities and sizes, respectively. The results indicate that for an included angle of 10° the sprays merge, which is in agreement with Zhang et al. [18]. However, for a 20° angle, the sprays do not merge. This is also borne out by the phase Doppler measurements of axial velocity in the radial direction, which exhibit two peaks with a minimum in between. It was found in general that the group-hole nozzle sprays penetrated significantly slower than those of a conventional nozzle.

Interacting Sprays – Theoretical and Numerical Studies

Attention is now directed to basic theoretical and numerical studies of interacting sprays, which appear to have received less attention in the literature than experimental studies.

As far as it can be seen, the first ground-breaking theoretical treatment of direct spray interaction was given by Tambour and Portnoy [22]. They considered a simple model of the interaction of two combined jet atomizers. Their motivation stemmed from an understanding of afterburners in jet engines in which spray characteristics are controlled through the injectors geometry via their being located at certain positions relative to one another. The media into which the two sprays were injected were two parallel streams having dissimilar free-stream velocities, $U_1 \neq U_2$. In order to describe the flow field, use was made of Prandtl's theory of the smoothing of an initial velocity discontinuity between two parallel streams via turbulent mixing (see Fig. 22.4).

The width of the mixing region, b, increases with time and Prandtl's mixing length theory is such that the turbulent mixing length, $l_t = \beta b$, where β is constant. Assuming that the developing velocity profiles are similar, and introducing the nondimensional stream-wise coordinate $\eta = y/b(t)$, where t represents time, it can be shown that the axial velocity is given by

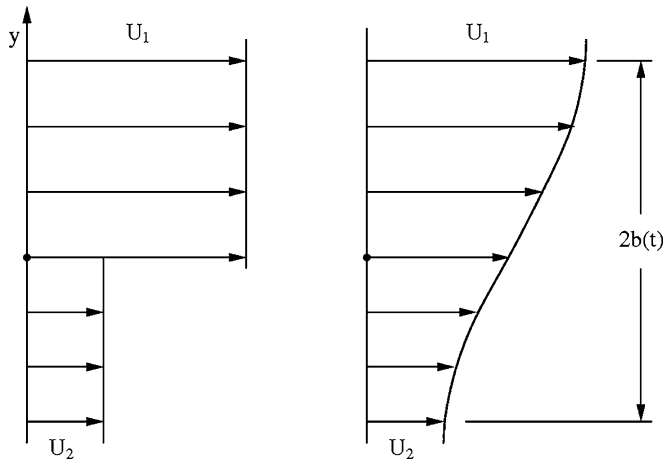


Fig. 22.4 Development of two parallel streams having dissimilar free-stream velocities

$$u(\eta, t) = U_{\mathrm{m}} + Af(\eta) \tag{22.1}$$

where

$$U_{\mathrm{m}} = \frac{1}{2}(U_1 + U_2); \quad A = \frac{1}{2}(U_1 - U_2); \quad f(\eta) = \frac{3}{2}\eta - \frac{1}{2}\eta^3 \tag{22.2}$$

Tambour and Portnoy [22] made use of the sectional method [23, 24] to describe the sprays of kerosene or di-methyl butane they considered. The evaporating droplets were assumed to move along streamlines (defined via the aforementioned velocity field) and, given the initial location of any group of droplets at time $t = 0$ straightforward integration of the sectional spray equations was performed to track their downstream evolution. For the baseline case, the vertical distance between the two atomizers was taken as 18 mm with a downstream displacement of 20 mm of one relative to the other (refer to Fig. 22.1b but with the two nozzles parallel to one another and orientated horizontally). Droplet sizes ranged from 1–150 μm and 1.5–26.5 μm in the two sprays. The initial conditions for the sprays and the surroundings were taken from experimental work by Yule et al. [25]. Radial profiles of the normalized volume distribution of droplets in a 293 K environment and a 450 K environment show the way in which the temperature of the surroundings effects the interaction between two sprays as they move downstream. Although the authors could not make a comparison with experimental data it is interesting to note the *qualitative* similarity of their prediction of the merging of the sprays with (a) the data of Brenn et al. [7] for downstream evolution of transverse profiles of the integral mean droplet size D_{10} and, (b) the measurements of Hardalupas and Whitelaw [5] (although the latter are admittedly for triple sprays) and Valencia-Bejarano et al. [8] of Sauter mean diameters. Nevertheless, the deficiencies of this

pioneering theoretical work should not be overlooked. The description of the host flow field is somewhat simplified in that the transverse velocity component is absent. The sprays are modeled as having already been formed and are taken to be located in the far-field region relative to the atomizers producing them. This eliminates the need to consider droplet momentum since the droplets are in dynamical equilibrium with their surroundings, which is clearly not the case in Brenn et al. [7], Valencia-Bejarano et al. [8], and Hardalupas and Whitelaw [5]. In addition, droplet collisions of any nature, whether coalescing or otherwise, were not accounted for, whereas in the aforementioned experimental works the occurrence of droplet coalescence was noted to be quite significant in the overlap region of the interacting sprays. Thus, despite the (limited) qualitative resemblance with later experimental data, it is clear that any theoretical modeling of even noncombusting spray interaction will require a more substantial treatment of the two-phase fluid dynamical situation than that given in Tambour and Portnoy [22] and will probably necessitate a full numerical solution.

Greenberg [26] carried out a theoretical/computational study of the characteristics of arrays of spray diffusion flames. The model did not consider direct interaction between sprays but rather the way in which fuel sprays, injected into a combustion chamber through parallel ducts separated by ducts through which an oxidant flowed, impact on the characteristics of the spray diffusion flames that are formed. A number of simplifications were made in order to enable a certain degree of tractability. The flow was taken to be laminar with a constant velocity thereby divorcing the flow field from the heat and mass transfers. The gas-phase conservation equations were solved numerically. The spray was modeled using the sectional approach [23, 24] and, for additional ease in trying to isolate the relevant critical parameters, was considered to be monosectional and located in the far-field relative to the spray source so that it was in dynamic equilibrium with its host gas environment. The entrance conditions for the sprays were allowed to be dissimilar in their respective ducts in order that a situation of (partial) fuel feeds and/or distortion of fuel spray patterns brought on by nozzle spray imperfections (see, for example, [27–29]) could be modeled. Configurations in which either four- or six-spray diffusion flames existed were considered. The results pointed to the strong coupling between the geometric (i.e., relative location and size of the entrance orifices), spray and flow parameters of the system that are called into play in the subtle interaction between adjacent spray flames through modification of the heights, shapes, and types (i.e., under- or over-ventilated) of flames formed.

More recently, this problem was revisited extending and expanding some of the previous assumptions [30, 31]. Velocity differences between the droplets in the spray and the host gas were permitted and the role of the associated drag parameters was looked into. Under certain operating conditions, two flame fronts would merge at their tips into a single front. However, under other operating conditions (such as appreciable asymmetry in the location of the oxidant orifice relative to the neighboring fuel orifices), a bifurcation into two separate flame fronts could occur. These relatively simple models of multiple co-flow spray diffusion flames offer some insight into the way several sprays can lead to downstream indirect interaction of

their combustion even if there is no initial direct interaction between them at their sources.

Spray interaction is also utilized in wet flue gas-cleaning processes. In large coal-fired power plants, the flue gas flows upwards through a series of sprays that introduce a liquid flux of droplets made up of water with a limestone suspension that is used as an absorbent. The droplets have a large mass transfer surface area whereby a high degree of success in removing sulfur dioxide may be achieved. In order to attempt to optimize this process via spray- related control, it is desirable to be able to model the spray interaction correctly. Kaesemann and Fahlenkamp [32] used a computational model to examine the influence of collisions between droplets in overlapping sprays such as those found in a realistic gas-flue scrubber. The computation was three-dimensional and two different configurations of the two hollow cone nozzles inserting the sprays were investigated: (1) nozzles at the same horizontal level at a typical distance of 1,200 mm apart, and (2) nozzles separated vertically by a distance of 1,500 mm. The mean droplet diameter reported was 1,600 μm. The sparse results given in [32] for case (1) clearly show appreciably higher droplet concentrations in regions of spray overlap resulting from the break-up of colliding droplets (which was computed using a break-up coefficient based on matching with experimental data). In contrast, the results for case (2) showed fairly insignificant influence of droplet collisions compared to case (1). The authors suggest that this is a consequence of the distance from the nozzles to the over-lapping region. For case (1), this was 700 mm whereas for case (2), it was 1,500 mm. Interestingly, the possibility of droplet coalescence was not discussed – possibly, it is not significantly achievable under the operating conditions examined.

An example of a more detailed theoretical approach to directly interacting sprays can be found in the context of computational fluid dynamics (CFD) modeling of water spray barriers in which Gant [33] refers to spray interaction. He was concerned with the prediction of how such barriers could be effectively utilized for slowing the progress of smoke in tunnels under construction in the event of a fire breaking out. Water spray barriers generally consist of a ring of piping around the circumference of the tunnel with a large number of nozzles directing water sprays radially inwards. In the presence of a fire, the fan-shaped water sprays from the nozzles combine and interact to produce a sort of barrier to smoke penetration. The purpose of the work described in [33] was to develop a CFD capability for predicting the behavior of a water barrier and amongst the trial computer runs was one of interacting sprays at an angle of 45° to one another – one spray injected vertically downwards with the other discharging towards it at 45° to the vertical. The distance between the sprays was not specified. Droplet diameters were of the order of 0.4 mm. Details of the CFD code employed, such as the turbulence model implemented, do not appear in the report. Both an Eulerian and a Lagrangian approaches were adopted for modeling the sprays and results predicted by these two approaches were compared. The Lagrangian approach seemed to predict more realistic flow behavior although no droplet–droplet interactions, such as coales-cence, were accounted for, so that the results must be interpreted accordingly. Owing to this particular applied interest in spray interaction, the details of

downstream droplet size and velocity distributions were not discussed. However, considerable influence of the interacting spray barrier on the flow field in a tunnel was predicted but the discrepancy between the Eulerian predictions and the Lagrangian ones prevents drawing specific conclusions about the actual spray interaction other than the fact that the interacting sprays do exert a considerable influence on the surrounding air flow field.

In a similar vein to [26], indirect spray interaction was investigated in the context of flame extinction using water sprays [34–36]. In their comprehensive review of the use of water sprays for fire suppression Grant et al. [37] write of the rebirth that took place in this field as a result of certain global legislative acts. These acts have led to a surge of interest in the use of water mists (roughly speaking, water sprays made up of small size droplets with a mean diameter of the order of 50–200 μm) as an effective method for fire fighting. In an attempt to gain a detailed understanding of the mechanisms by which water sprays suppress flames, one approach that has been adopted involves examining geometrically simple configurations. In these, the situation is stripped of the complexities of reality; yet, the essential physics is retained in such a way that it can be investigated both experimentally and theoretically under well-controlled conditions. This, then, enables different features of the system to be isolated. A map of the realm of relevance of the different controlling mechanisms can then be traced and conclusions can be drawn therefrom for practical application. Water spray extinction studies have almost exclusively dealt with gaseous fires. Dvorjetski and Greenberg [34–36] presented the first theoretical study of liquid spray flame extinction using a water spray. This was motivated by the statement of Grant et al. [37] that Mawhinney and Solomon's [38] "Class 1" water sprays (i.e., sprays for which 90% of the volume is contained in droplets less than 200 μm in diameter) are well suited to the suppression of spray fires. Dvorjetski and Greenberg [34] considered a counterflow situation (see Fig. 22.5) in which a liquid spray of evaporating polydisperse droplets impinges on an opposing flow of oxidant. Under appropriate conditions, a spray diffusion flame can be maintained either to the left or the right of the stagnation plane. If a polydisperse spray of water droplets is also introduced in the oxidant stream the strong heat absorption of the water droplets can lead to a sufficiently large drop in temperature so that the spray flame is extinguished. Thus, a situation exists in which although the liquid fuel and water sprays do not interact directly there is indirect interaction between them. It was demonstrated that the endothermicity of both the fuel and water sprays has a paramount influence in lowering the flame temperature. In addition, the water spray tends to shift the flame towards the water source whereas the fuel spray has the opposite effect. Flame extinction was analyzed. It is found that the water spray's initial polydispersity has a profound effect on spray flame suppression. In particular, it was shown that there exists a set of conditions that delineates between effective and ineffective uses of the water droplets for suppression. For the data used in the work these conditions favor use of an initial quasi-monodisperse water spray rather than a bimodal spray having the same SMD. This indicates the difficulty in utilizing the SMD to characterize a polydisperse spray and for drawing conclusions therewith in this context. It is interesting to note

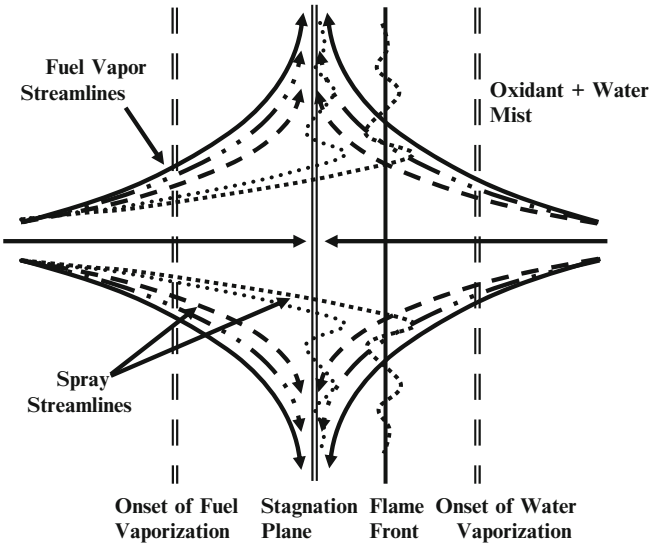


Fig. 22.5 Counter-flow spray diffusion flame configuration with a water spray in the oxidant stream

that other authors [39, 40] have observed the possibility of some sort of optimal drop size for extinction, both experimentally and numerically, in monodisperse sprays. Lentati and Chelliah [39] suggested that the phenomenon is associated with droplet dynamics. The results of Dvorjetski and Greenberg [34] imply that, even within the framework of a model in which droplets are in dynamic equilibrium with their surroundings, "optimal" conditions for flame suppression are sensitive to spray polydispersity.

Returning to noncombusting directly interacting sprays Park and Reitz [41] carried out a numerical simulation of a group-hole nozzle spray (see [17–21] and the previous associated discussion) using the KIVA CFD code [42], modified to remove the grid size dependency that often plagues numerical simulations of sprays. The code accounts for droplet collisions and coalescence. Experimental validation of the code was executed using a phase Doppler particle analyzer (PDPA) and a spray-visualization system. The PDPA system provided characterization of the spray in terms of SMD and the visualization system was used to deduce spray penetration measurements. There was good agreement between the computed predictions and the experimental data of spray penetration. However, there was no notable difference between the group-nozzle's spray penetration and that of an equivalent single-hole nozzle having the same overall nozzle area. The computations also revealed that the group-hole nozzle reduces spray droplet sizes in the near-field region and the predicted SMD of the spray was in general agreement with the measured values.

Concluding Summary and Remarks

In this chapter, a review was given of some of the major contributions to the understanding of how different combinations of interacting sprays influence their surroundings and downstream features of the systems in which they are found, as well as what happens to the sprays themselves as they come in contact with one another. The wide variety of applications that attempt to take advantage of spray interactions in some optimal manner has spawned both application-orientated and more basic research. This research was mainly experimental although some theoretical/numerical modeling was also undertaken. The physics of the interaction is complex. It can be broadly viewed as twofold involving (a) the influence of the sprays on one another and (b) the mutual influence between the sprays and their host environment. In the case of intrasprays phenomena, details of droplet size and droplet velocity distributions help to characterize the nature of the interaction, which inevitably will involve droplet–droplet collisions and possible merging of droplets, as well as momentum and energy transfer within the sprays. In terms of the mutual influence between the interacting sprays and their environment, entrainment of surrounding air/gases, the movement of air/gases in between the interacting sprays, mixing and transport of vapors from evaporating sprays and downstream effects, possibly on combustion, are of relevance.

For application-orientated research, it is not surprising that focus has only been on those aforementioned interactions that are of practical interest, so that operating conditions considered by different researchers seldom overlap or are comparable. However, even in the case of more basic research, the wide range of configurations utilized (i.e., type of atomizers, location of spray nozzles in relation to one another, droplet size distributions, etc.) usually enables nothing more than general qualitative conclusions to be drawn. This is particularly true of the experimental efforts. For theoretical/numerical modeling, there is also a lot that needs to be done. Consider the question of droplet collisions alone. There is a body of research on binary droplet collisions and the different scenarios that can result from them, viz. coalescence after minor deformation, bouncing, coalescence after substantial deformation, coalescence for near head-on collisions or coalescence followed by separation (see, for example, [43, 44] and references therein). However, a comprehensive theory of such collisions is required and, indeed, a recent suggestion for such a theory was given by Zhang and Law [45]. Any modeling of direct spray interaction ought to incorporate the most advanced theories of droplet collisions. In the modeling reviewed here, it was found that either no droplet collisions were accounted for at all or that collisions were dealt with using O'Rourke's collision model [46], which exhibits serious numerically related problems when included in a CFD code, and is not as comprehensive as the model in [45].

In fact, even if one were to put aside the question of droplet collisions, an accurate CFD modeling of single sprays can be fraught with problems due, to a great extent, to the way in which the entire collection of droplets is to be described. Modeling approaches range from the use of statistically representative droplets

[42], through the spray equation [47], the sectional method [23, 24], Beck's method [48], and the use of the direct quadrature method of moments [49], to name but a few. Tied in with the choice of a modeling approach is the decision as to whether to adopt an Eulerian–Eulerian or an Eulerian–Lagrangian description of the coupled two-phase turbulent flow under consideration. Massot [50] gave a broad overview of the ramifications of using an Eulerian description of the liquid spray phase whereas an accurate use of a Lagrangian description can be found, for example, in [51], or via a stochastic approach [52, 53]. However, it would appear that an accurate computation of two interacting evaporating sprays even in a noncombusting system is yet to be made.

In view of the aforementioned remarks and, despite the important information supplied by the material that has been detailed here, the subject of characterization of interacting sprays remains a formidable challenge. It would appear that a solid database of experimental measurements made under a comprehensive set of well-defined operating conditions is very much needed. This database will serve a dual purpose. On the one hand, it will help to gain a deeper understanding of the relative importance of the physical mechanisms at play as a result of the interaction. On the other hand, it will serve as a source of initial/boundary conditions for theoretical and computer simulations and will be an excellent reference for validating such simulations.

Acknowledgments The author acknowledges the Lady Davis Chair in Aerospace Engineering and the Technion Fund for the Promotion of Research for their partial support of this work. Thanks are also due to my graduate students Dr. Ariel Dvorjetski and Liron Hamelnick, and to Yonit Mindelis for her dedicated professional technical assistance.

References

1. H. Fujimoto, H. Tanabe, H. Kuniyoshi, G.T. Sato: Investigation on the characteristics of diesel spray (shape of multiple diesel sprays and air movement between neighbouring sprays), Bulletin of the JSME, 25(200), 249–256 (1982).
2. C. Bourque, B.G. Newman: Reattachment of a two-dimensional, incompressible jet to an adjacent flat plate, The Aeronautical Quarterly, XI, 201–232 (1960).
3. S.R. Snarski, P.F. Dunn: Experiments characterizing the interaction between two sprays of electrically charged liquid droplets, Experiments in Fluids, 11, 268–278 (1991).
4. N. Dombrowski, J. Singh: Ducted air flow induced by multiple spray nozzles, Atomization and Sprays, 5, 123–135 (1995).
5. Y. Hardalupas, J.H. Whitelaw: Interaction between sprays from multiple coaxial airblast atomizers, Journal of Fluids Engineering, Transactions of the ASME, 118, 762–771 (1996).
6. G. Brenn, A. Selbach: Experimental investigation of polydisperse spray interaction, International Journal of Fluid Mechanics Research, 24, 534–543 (1997).
7. G. Brenn, F. Durst, A. Selbach: Experimental investigations of the binary interaction of polydisperse sprays, Particle and Particle Systems Characterization, 15, 263–273 (1998).
8. M. Valencia-Bejarano, J.J. Nijdam, T.A.G. Langrish: Experimental investigation of coalescence and droplet trajectories between two polydisperse sprays, Atomization and Sprays, 16, 265–278 (2006).
9. K. Sinko, D. Pushka, B. Chehroudi: Visualization of interacting pilot and main diesel-type sprays in an engine, Journal of Flow Visualization and Image Processing, 2, 93–112 (1995).

10. B. Chehroudi, K.M. Sinko, W.J. Minkowycz, S. Shih: Interacting-spray injection: a new concept for NOx and smoke reduction in diesel engines, Atomization and Sprays, 8, 673–690 (1998).
11. T.C. Tow, D.A. Pierpont, R.D. Reitz: Reducing particulate and NO_x emissions by using multiple injections in a heavy duty D.I. Diesel engine, SAE Paper 940897, 1994.
12. J.B. Heywood: Internal Combustion Engine Fundamentals, McGraw-Hill, New York, 1988.
13. K. Parvez, Studies on interacting multiple burning liquid sprays, PhD dissertation, School of Aerospace and Mechanical Engineering, University of Oklahoma, Norman, April 1995.
14. K. Parvez, S.R. Gollahalli: Effects of interjet spacing on burning multiple sprays, AIAA Journal of Propulsion and Power, 17(1), 169–174 (2001); also appeared as AIAA Paper No. 99-0460, 1999.
15. B. Glassman, S. Kuravi, J. Du, Y. Lin, G. Zhao, L. Chow: A fluid management system for a multiple nozzle array spray cooler, AIAA Paper No. 2004-2574, 37th AIAA Thermophysics Conference, Portland, June 28–July 1, 2004.
16. A.G. Pautsch, T.A. Shedd: Spray impingement cooling with single- and multiple-nozzle arrays. Part 1: Heat transfer data using FC-72, International Journal of heat and Mass Transfer, 48, 3167–3175 (2005).
17. H. Tokudo, S. Itoh, M. Kinugawa: Denso common rail technology to successfully meet future emission regulation, Proceedings of the 26th Vienna Motor Symposium, Vienna, 2005.
18. Y.Y. Zhang, K. Nishida, S. Nomura, T. Ito: Spray characteristics of a group-hole nozzle for direct injection diesel engines, Atomization and Sprays, 16, 35–49 (2006).
19. K. Nishida, S. Nomura, Y. Matsumoto: Spray and mixture properties of group-hole nozzle for D.I. diesel engine, Proceedings of ICLASS 2006, ICLASS06-171, Kyoto, 2006.
20. J. Gao, S. Moon, Y.Y. Zhang, K. Nishida, Y. Matsumoto: Flame structure of wall impinging diesel fuel sprays injected by group-hole nozzles, Combustion and Flame, 156(6), 1263–1277 (2009).
21. A. A. Pawlowski, R. Kneer, A.M. Lippert, S.E. Parrish: Investigation of the interaction of sprays from clustered orifices under ambient conditions relevant for diesel engines, SAE International Journal of Engines, 1(1), 514–527, (2008).
22. Y. Tambour, D. Portnoy: Spray characteristics of two combined jet atomizers, International Journal of Turbo- and Jet Engines, 2, 263–271 (1985).
23. J.B. Greenberg, I. Silverman, Y. Tambour: On the origins of spray sectional conservation equations, Combustion and Flame, 93, 90–96 (1993).
24. F. Laurent, M. Massot: Multi-fluid modeling of laminar polydispersed spray flames: origin, assumptions and comparison of the sectional and sampling methods, Combustion Theory and Modelling, 5, 537–572 (2001).
25. A.J. Yule, Ah. Seng, P.G. Felton, A. Ungut, N.A. Chigier: A study of vaporizing fuel sprays by laser techniques, Combustion and Flame, 44, 71–84 (1982).
26. J.B. Greenberg: Characteristics of arrays of spray diffusion flames, AIAA Paper No.1997-3184 33rd AIAA/ASME/SAE/ASEE Joint Propulsion Conference and Exhibit, Seattle, July 6–9, 1997.
27. J. Ortman, A.H. Lefevbre: Fuel distributions from pressure-swirl atomizers, AIAA Journal of Propulsion and Power, 1, 11–15 (1985).
28. T.J. Rosfjord, S. Russell: Nozzle design and manufacturing influences on fuel spray circumferential uniformity, AIAA Journal of Propulsion and Power, 5(2),144–150 (1989).
29. T.J. Rosfjord, W.A. Eckerle: Nozzle airflow influences on fuel patternation, AIAA/ASME/ASEE 24th Joint Propulsion Conference, Boston, AIAA Paper AIAA-88-3140, 1988.
30. L. Hamelnick, J.B. Greenberg: Influence of inlet asymmetries on the characteristics of multiple spray flames, 49th Israel Annual Conference on Aerospace Sciences, Tel-Aviv, March 2009.
31. L. Hamelnick, J.B. Greenberg: Multiple spray diffusion flames – effects of dissimilar fuel feed patterns, 23rd Israel Combustion Symposium, Haifa, December 2008

32. R. Kaesemann, H. Fahlenkamp: The meaning of droplet-droplet interaction for the wet flue-gas cleaning process, Chemical Engineering Technology, 25(7), 739–742 (2002).
33. S.E. Gant: CFD modeling of water spray barriers, Report HSL/2006/79, Health and Safety Laboratory, Harper Hill, Buxton, Derbyshire, 2006.
34. A. Dvorjetski, J.B. Greenberg: Analysis of extinction of counterflow polydisperse spray diffusion flames by a polydisperse water spray, Proceedings of the Combustion Institute, 29, 385–392 (2002).
35. A. Dvorjetski, J.B. Greenberg: Lewis number and droplet slip effects in water spray suppression of opposed flow diffusion flames, 19th Annual Symposium of the Israeli Section of the Combustion Institute, Haifa, December 2003.
36. A. Dvorjetski, J.B. Greenberg: Effects of water-mist dynamics and droplet size in suppression of counterflow diffusion flames, Seventh Asian-Pacific Conference on Combustion (ASPACC 09), Tapei, May 2009.
37. G. Grant, J. Brenton, D. Drysdale: Fire suppression by water sprays, Progress in Energy and Combustion Science, 26, 70–130 (2000).
38. J.R. Mawhinney, R. Solomon: Section 6/chapter 15, in Fire Protection Handbook, 18th edition, A.E. Cote (ed.), National Fire Protection Association, Quincy, pp. 6/216–6/248, 1997.
39. A.M. Lentati, H.K. Chelliah: Dynamics of water droplets in a counterflow field and their effect on flame extinction, Combustion and Flame, 115, 158–179 (1998).
40. E.J.P. Zegers, B.A. Williams, E.M. Fisher, J.W. Fleming, R.S. Sheinson: Suppression of non-premixed flames by fluorinated ethanes and propanes, Combustion and Flame, 121, 471–487 (2000).
41. S.W. Park, H.K. Suh, C.S. Lee, N. Abani, R.D. Reitz: Modeling of group-hole-nozzle sprays using grid-size-, hole location- and time-step-independent models, Atomization and Sprays, 19(6), 567–582 (2009).
42. A.A. Amsden: KIVA-3V Release 2, Improvement to KIVA-3V, Los Alamos National Laboratory, LA-UR-99-915, Los Alamos, 1999.
43. Y.J. Jiang, A. Umemura, C.K. Law: An experimental investigation on the collision behaviour of hydrocarbon droplets, Journal of Fluid Mechanics, 234, 171–190 (1992).
44. J. Qian, C.K. Law: Regimes of coalescence and separation in droplet collision, Journal of Fluid Mechanics, 331, 59–80 (1997).
45. P. Zhang, C.K. Law: Theory of bouncing and coalescence in droplet collision, Paper # G16, 5th US Combustion Meeting, University of California at San Diego, San Diego, March, 2007.
46. P.J. O'Rourke: Collective drop effects on vaporizing liquid sprays, PhD thesis, Princeton University, Princeton, 1981.
47. F.A. Williams: Combustion Theory, The Benjamin/Cummings Publishing Company, Menlo Park, 1985.
48. J.C. Beck: Computational modeling of polydisperse sprays without segregation into droplet size classes, PhD thesis, Department of Mechanical Engineering, University of Manchester Institute of Science and Technology, Manchester, September 2000.
49. R.O. Fox, F. Laurent, M. Massot: Numerical simulation of spray coalescence in an Eulerian framework: direct quadrature method of moments and multi-fluid method, Journal of Computational Physics, 227, 3058–3088 (2008).
50. M. Massot: Eulerian multi-fluid models for polydisperse evaporating sprays, in multiphase reacting flows: modeling and simulations, in CISM – International Centre for Mechanical Sciences – Courses and Lecture Series, vol. 492, D.L. Marchisio and R.O. Fox (eds), Springer, Wien, 2007.
51. J. Reveillon, L. Vervisch: Analysis of weakly turbulent diluted-spray flames and spray combustion regimes, Journal of Fluid Mechanics, 537, 317–347 (2005).
52. M.A. Gorokhovski: The stochastic Lagrangian model of drops breakup in the computation of liquid sprays, Atomization and Sprays, 11, 505–520 (2001).
53. S.V. Apte, M.A. Gorokhovski, P. Moin: LES of atomizing spray with stochastic modeling of secondary breakup, International Journal of Multiphase Flow, 29, 1502–1522 (2003).

Part III
Atomizers and Spray Generators

Chapter 23
Drop Size Distributions

A. Déchelette, E. Babinsky, and P.E. Sojka

Abstract Drop size distributions are at least as important as mean drop sizes. Some spray applications require narrow size distributions (paint and respirable sprays), while some need wide ones (gas turbine engines). Other spray processes require very few small drops (agricultural or consumer product sprays) or very few large ones (waste incineration, IC engines). In this section, we discuss the concepts of drop size distributions, moments of those distributions, and characteristic drop diameters computed from them. This is followed by a summary of methods available for describing drop size distributions.

Keywords Characteristic drop diameter · Cumulative volume fraction · Discrete probability function (DPF) · Drop size distribution · Empirical drop size distribution · Log-hyperbolic distribution · Log-normal distribution · Maximum entropy formalism (MEF) · Nukiyama–Tanasawa distribution · Number distribution function · Probability density function (pdf) · Representative diameter · Root-normal distribution · Rosin–Rammler distribution · Upper limit distribution · Volume distribution

Basic Spray Characterization

Drops are described by their diameter, velocity, temperature, and composition. The diameter is the most common measure and is the focus here.

We begin by separating drops into groups whose diameters are between $D - \Delta D/2$ and $D + \Delta D/2$. We make a histogram of drop sizes by counting the number of drops in each group. The continuous version of the discrete histogram is the

P.E. Sojka (✉)
Maurice J. Zucrow Laboratories, School of Mechanical Engineering, Purdue University, West Lafayette, IN, USA
e-mail: sojka@ecn.purdue.edu

N. Ashgriz (ed.), *Handbook of Atomization and Sprays*,
DOI 10.1007/978-1-4419-7264-4_23, © Springer Science+Business Media, LLC 2011

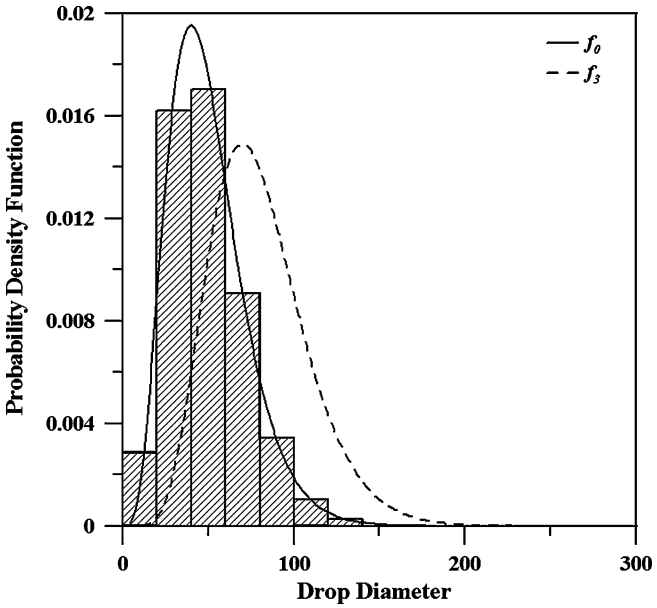


Fig. 23.1 Discrete number probability function, its corresponding continuous *number* PDF, $f_0(D)$, and its corresponding continuous *volume* PDF, $f_3(D)$ (PDF's in μm^{-1}, D in μm)

probability density function (PDF), or more correctly the *number* distribution $f_0(D)$. $f_0(D)$ gives the probability of finding a drop whose diameter lies in the $D - \Delta D/2$ to $D + \Delta D/2$ group, divided by the width of that group (ΔD). $f_0(D)$ has dimensions of 1/diameter. Figure 23.1 provides illustrations.

Number distributions are not the only type of PDF. Area and volume distributions are also used, with volume distributions being by far the more popular of the two. The volume distribution, $f_3(D)$, gives the fraction of a spray's volume for drops in group $D - \Delta D/2$ to $D + \Delta D/2$ and has dimensions of 1/diameter (see Fig. 23.1).

Actual sprays contain drops having finite maximum and minimum sizes. For convenience sake, it is commonly assumed that $0 < D < \infty$. Common sense tells us that the probability of finding a drop in each group must be greater than or equal to zero, and that the probability of finding a drop in any of the groups must total 100%:

$$f(D) \geq 0 \tag{23.1}$$

$$\int_0^\infty f(D)\,\mathrm{d}D = 1 \tag{23.2}$$

These are the positivity and normalization conditions, and hold for both $f_0(D)$ and $f_3(D)$.

The spray literature often reports drop size distribution information via a single number, or "representative drop diameter." In effect, the actual (polydisperse) distribution is replaced by the same number of drops that all have the same representative size (monodisperse). Representative drop diameters were standardized by Mugele and Evans [1]:

$$D_{pq} = \left[\frac{\int_0^\infty D^p f_0(D)dD}{\int_0^\infty D^q f_0(D)dD}\right]^{\frac{1}{p-q}} \tag{23.3}$$

where p and q are positive integers, and D_{pq} has the units of diameter. Commonly used representative diameters include: D_{10}, the arithmetic mean diameter, D_{30}, the volume mean diameter, D_{32}, the Sauter mean diameter, and D_{43}, the de Brouckere mean diameter.

As Sowa [2] points out, the PDF is a statistical entity so has a set of moments:

$$M_n = \int_0^\infty D^n f_0(D)dD \tag{23.4}$$

Moments can be used to calculate any D_{ij}, and should be positive and finite. For example, $D_{32} = (D_{30})^3/(D_{20})^2$. Note that characteristic diameters are not necessarily the same as the common statistical moments: mean, standard deviation, coefficient of skewness, and coefficient of kurtosis. The exception is D_{10}, which is the statistical mean of $f_0(D)$, and D_{43}, which is the statistical mean of $f_3(D)$.

Drop size distributions are typically described using one of four methods: empirical, maximum entropy formalism (MEF), discrete probability function (DPF) method, or stochastic. The empirical method was most popular before about the year 2000, when drop size distributions were usually determined by fitting spray data to predetermined mathematical functions. Problems arose when extrapolating to regimes outside the range of experimental data. Two analytical approaches were proposed to surmount this, MEF and DPF, as well as one numerical approach, the stochastic breakup model.

The MEF [3, 4] assumes spray formation is a random process that can be described using the principle of entropy maximization subject to a set of global constraints.

The DPF method [5–7] assumes spray formation is a combination of random and nonrandom processes. An instability analysis is used to describe primary breakup, which is uniquely determined for a given set of initial conditions (fluid physical properties and atomizer parameters) and a model of the breakup mechanism. The drop size distribution arises from fluctuations in the initial conditions due to such factors as gas and liquid turbulence, atomizer passage surface roughness, vortex shedding, liquid mixture composition, etc.

The stochastic breakup model assumes that the spray fragments following a cascade for which the probability of forming a daughter drop via breakup is independent of its parent drop size.

Empirical Methods

Some common empirical size distributions are listed below. Their discussion closely follows that of Paloposki [8].

The log-normal *number* distribution is:

$$f_0(D) = \frac{1}{D(\ln \sigma_{\mathrm{LN}})\sqrt{2\pi}} \exp\left\{ -\frac{1}{2}\left[\frac{\ln(D/\bar{D})}{\ln \sigma_{\mathrm{LN}}}\right]^2 \right\} \tag{23.5}$$

where $\bar{D}$ is the logarithmic mean diameter of the distribution and σ_{LN} the distribution width. A log-normal distribution results from continuous random partitioning of drops, as shown by Kolmogorov [9] when studying the continuous grinding of coal.

The upper-limit distribution is a modified version of the log-normal distribution. It is a *volume* distribution, and a maximum drop size is introduced:

$$f_3(D) = \frac{\delta D_{\max}}{\sqrt{\pi} D(D_{\max} - D)} \exp\left\{ -\delta^2 \left[\ln\left(\frac{aD}{D_{\max} - D}\right)\right]^2 \right\} \tag{23.6}$$

$$a = \frac{D_{\max}}{\bar{D}}, \quad \delta = \frac{1}{\sqrt{2}(\ln \sigma_{UL})} \tag{23.7}$$

Here, σ_{UL} is the distribution width, $D_{\max}$ the maximum diameter, and $\bar{D}$ a representative diameter.

The root-normal *volume* distribution is:

$$f_3(D) = \frac{1}{2\sigma_{RN}\sqrt{2\pi D}} \exp\left\{ -\frac{1}{2}\left[\frac{\sqrt{D} - \sqrt{\bar{D}}}{\sigma_{RN}}\right]^2 \right\} \tag{23.8}$$

where σ_{RN} is the distribution width and $\bar{D}$ the mean diameter. Tate and Marshall [10] proposed it to describe sprays. It was later shown by Simmons and Faeth and coworkers to accurately describe the results of secondary drop breakup.

The Rosin–Rammler is a *cumulative* volume fraction distribution:

$$F_3(D) \equiv \int_0^D f_3(D)dD = 1 - \exp\left\{-(D/\bar{D})^q\right\} \tag{23.9}$$

$\bar{D}$ is the distribution mean and q an indicator of the distribution width. Small q corresponds to a wide spray distribution while large q indicates a narrow spray

distribution. It was developed to describe the cumulative volume distribution of coal particles after grinding.

The Nukiyama–Tanasawa *number* distribution is:

$$f_0(D) = aD^p \exp(-bD^q) \tag{23.10}$$

Here b, p, and q are adjustable coefficients, and a is a normalizing constant. The distribution width and location of the mean are controlled by b, p, and q. It was developed to describe sprays from pneumatic atomizers by Nukiyama and Tanasawa [11]. Meaningful results require $p > 1$ and $q > 0$ or $p < -4$ and $q < 0$.

The log-hyperbolic distribution was first applied to sprays by Bhatia et al. [12–14]:

$$f_0(x;\alpha,\beta,\delta,\mu) = a(\alpha,\beta,\delta)\exp\left\{-\alpha\sqrt{\delta^2+(x-\mu)^2}+\beta(x-\mu)\right\} \tag{23.11}$$

Here a is a normalizing constant, given by

$$a = \frac{\sqrt{\alpha^2-\beta^2}}{2\alpha\delta K_1\left(\delta\sqrt{\alpha^2-\beta^2}\right)} \tag{23.12}$$

and K_1 is the modified Bessel function of the third kind and first order. Requirements include: $-\infty < x < \infty$, $\alpha > 0$, $|\beta| < \alpha$, $\delta > 0$, and $-\infty < \mu < \infty$. δ is the scale parameter, μ the location parameter, while α and β describe the shape.

A key question is which of these distributions is best? Paloposki [8] provided an answer by performing χ^2 tests on 22 sets of data that came from seven experimental studies. His analysis showed that the Nukiyama–Tanasawa and log-hyperbolic distribution functions provided the best fits, that the upper-limit and log-normal distributions were clearly inferior to these two, and that the Rosin–Rammler distribution gave poor results. Paloposki [8] also determined the mathematical stability of distribution parameters. The Nukiyama–Tanasawa and log-hyperbolic distribution functions both had problems, while the log-normal distribution was more stable.

Regardless of which distribution is best, Paloposki's [8] work underscores the key issue when using empirical distributions – no single distribution accurately fits even a large fraction of the available drop size data. This necessitates trial-and-error use of several distributions to determine which one best fits a particular data set.

A further problem with the empirical approach is the difficulty of extrapolating the data to operating regimes outside the experimental range. Without additional experimentation, one can never be certain whether the extrapolated empirical correlation applies to the new regime of interest; unfortunately, additional experimentation is often impractical, impossible, or prohibitively expensive.

Maximum Entropy Formalism (MEF)

The maximum entropy formalism (MEF) treats atomization as a "black box" that transforms bulk liquid into a particular drop size distribution. Because the procedure is analogous to statistical thermodynamics the transformation details are assumed to be irrelevant.

The transformation process is subject to physical constraints, such as the conservation of mass, energy, momentum, etc. The MEF assumes that the drop size distribution is the one that maximizes the entropy of the spray subject to the constraint(s).

According to Paloposki [8], Griffith [15] was probably the first to develop a PDF based on the concept of maximum entropy when he applied it to the grinding of solids. Sellens and Brzustowski [3] and Li and Tankin [4] were the first to use MEF to predict drop size distributions.

Sellens and Brzustowski [3] treated the breakup of a liquid sheet having velocity V and thickness τ. The products were assumed to be spherical drops. Constraints were:

$$\text{Normalization:} \quad \iint_{\psi} f d\delta_* dv_* = 1 \tag{23.13}$$

$$\text{Mass conservation:} \quad \iint_{\psi} f \delta_*^3 d\delta_* dv_* = 1 + S_{\text{m}} \tag{23.14}$$

$$\text{Momentum conservation:} \quad \iint_{\psi} f \delta_*^3 v_* d\delta_* dv_* = 1 + S_{\text{mv}} \tag{23.15}$$

$$\text{Surface energy conservation:} \quad \iint_{\psi} f \delta_*^2 d\delta_* dv_* = \frac{1}{3\tau_*} + S_{\text{s}} \tag{23.16}$$

$$\text{Kinetic energy conservation:} \quad \iint_{\psi} f \delta_*^3 v_*^2 d\delta_* dv_* = 1 + S_{\text{ke}} \tag{23.17}$$

Here δ_* is the dimensionless drop diameter, v_* is the dimensionless drop velocity, τ_* is the dimensionless sheet thickness, and S_{xx} are source terms. The source terms describe evaporation and condensation, aerodynamic drag, and the conversion of surface and kinetic energy into other forms of energy.

The resulting PDF for drop size and velocity takes the form:

$$f_0 = \exp\left(-\lambda_0 - \lambda_1 \delta_*^2 - \lambda_2 \delta_*^3 - \lambda_3 \delta_*^3 v_* - \lambda_4 \delta_*^3 v_*^2\right) \tag{23.18}$$

and is obtained by maximizing the Shannon entropy

$$S = -k \int_{\psi} f_0(\delta_*, v_*) \ln[f_0(\delta_*, v_*)] \mathrm{d}\delta_* \, \mathrm{d}v_* \tag{23.19}$$

A drop size distribution is obtained by integrating over the velocity:

$$f_0 = \left(\frac{\pi}{4\lambda_4 \delta_*^3}\right)^{1/2} \left\{ erf\left(v_{*\max}\sqrt{\lambda_4 \delta_*^3} + \frac{\lambda_3}{2}\sqrt{\frac{\delta_*^3}{\lambda_4}}\right) - erf\left(\frac{\lambda_3}{2}\sqrt{\frac{\delta_*^3}{\lambda_4}}\right)\right\} \times \exp\left\{-\lambda_0 - \lambda_1 \delta_*^2 - \left(\lambda_2 - \frac{\lambda_3^2}{4\lambda_4}\right)\delta_*^3\right\} \tag{23.20}$$

This early work, and those that followed, illustrated issues that arise when using the MEF to predict drop size distributions: formulating the constraints is not trivial because it is difficult to determine a priori which ones should be included and which ones omitted; the presence of source terms, which are difficult to evaluate; and the fact that f_0 does not always approach zero at small diameters. The latter issue was overcome by invoking an additional constraint:

$$\text{Partition of surface energy: } \iiint_{\psi} f \delta_*^{-1} d\delta_* du_* dv_* = K_p \tag{23.21}$$

Regardless of which constraints are chosen, it is necessary to estimate the parameters that appear there. When this is done, there is similarity between predicted and measured drop size distributions, and the predicted drop velocity distribution is consistent with measured profiles. However, agreement with experimental data is achieved by adjusting the source term magnitudes. Hence, the MEF is similar to curve fitting.

Li and Tankin [4] independently used MEF to predict $f_3(D)$ for spherical drops, instead of $f_0(D)$:

$$f_3 = 3\left(\frac{\pi}{6}\frac{\rho_1 \dot{n}}{\dot{m}_1}\right)^2 D^5 \exp\left(-\frac{\pi}{6}\frac{\dot{\rho}_1 \dot{n}}{\dot{m}_1} D^3\right) \tag{23.22}$$

Their constraints were:

$$\text{Normalization}: \sum_i P_i = 1 \tag{23.23}$$

$$\text{Mass conservation: } \sum_i P_i v_i \rho_i \dot{n} = \dot{m}_1 \tag{23.24}$$

where P_i is the probability of finding a drop with volume v_i and density ρ_i, $\dot{n}$ is the total number of drops produced per unit time, and $\dot{m}_1$ is the liquid mass flow rate. Note

that (20.22) is a Nukiyama–Tanasawa function with distribution parameter equal to 3. Li and Tankin [16] intended to set all of the source terms in their constraints to zero, but could not obtain a solution, so the momentum source term was set to –0.05. The calculated number distribution does go to zero for small drop sizes.

Because of identified limitations, Ahmadi and Sellens [17] used the MEF to predict drop size distributions independently of velocity distributions. A simplified set of constraints results:

$$\text{Normalization}: \int_{\delta_{\min}}^{\delta_{\max}} f \, \mathrm{d}\delta_* = 1 \tag{23.25}$$

$$\text{Conservation of surface energy}: \int_{\delta_{\min}}^{\delta_{\max}} f\delta_*^2 \, \mathrm{d}\delta_* = \frac{D_{30}}{D_{32}} \tag{23.26}$$

$$\text{Conservation of mass}: \int_{\delta_{\min}}^{\delta_{\max}} f\delta_*^3 \, \mathrm{d}\delta_* = 1 \tag{23.27}$$

$$\text{Partition of surface energy}: \int_{\delta_{\min}}^{\delta_{\max}} f\delta_*^{-1} \, \mathrm{d}\delta_* = K_p \tag{23.28}$$

The energy partition constraint is required to ensure that f_0 vanishes as the drop size approaches zero. The resulting PDF is:

$$f_0 = \exp\left(-\lambda_0 - \lambda_1\delta_*^2 - \lambda_2\delta_*^3 - \lambda_3\delta_*^{-1}\right) \tag{23.29}$$

The primary inputs are D_{30}, D_{32}, and K_p; they were obtained from experiments. Note that it is possible to cast K_p in terms of a mean diameter:

$$K_p = \int_0^\infty f\delta_*^{-1} \, d\delta_* = D_{30} \int_0^\infty f'\delta^{-1} \, d\delta = D_{30}D_{-10} \tag{23.30}$$

This suggests that constraints can be expressed solely in terms of representative diameters, a vast improvement over the source terms appearing in prior formulations, because it is possible to use other means to predict representative diameters.

Van der Geld and Vermeer [18] used a simplified MEF to investigate satellite drop formation. They were the first to point out that the Shannon entropy is not the proper measure if drop volume is used instead of drop diameter. This point was best addressed by Cousin et al. [19], who rigorously derived the proper application of the MEF. They pointed out that MEF should be used to predict either $f_0(D)$ or $f_3(D)$. $f_3(D)$ can be used if information that the drops are spherical is included.

Cousin et al. [19] also advocated new approaches for choosing constraints, based on some representative diameter(s) of the resulting distribution. The first approach was to calculate $f_0(D)$ for an ensemble of spherical drops from one constraint based on some representative drop diameter and normalization:

$$\int_0^\infty f_0 \, dD = 1 \tag{23.31}$$

$$\int_0^\infty f_0 D^q \, dD = D_{q0}^q \tag{23.32}$$

Here D_{q0}^q is a representative drop diameter. This yields:

$$f_0 = \exp(-\lambda_0 - \lambda_1 D^q) \tag{23.33}$$

and

$$f_3 = q \frac{(q-4)}{q} \frac{D^3}{D_{q0}^4 \Gamma(4/q)} \exp\left(\frac{-D^q}{q D_{q0}^q}\right) \tag{23.34}$$

The parameter q, the order of the constraint, is analogous to the Rosin–Rammler distribution spread parameter.

The second approach was to consider an ensemble of drops and apply the MEF to predict $f_3(D)$ directly. The relationship between drop diameter and volume must be introduced to ensure that a meaningful $f_3(D)$ is produced. The constraint equations are:

$$\int_0^\infty f_3 \, \mathrm{d}D = 1 \tag{23.35}$$

$$\int_0^\infty f_3 D^{p-3} \, dD = D_{p3}^{p-3} \tag{23.36}$$

and the volume distribution is:

$$f_3 = \frac{|p-3|^{p-7/p-3}}{\Gamma[4/p-3]} \frac{D^3}{D_{p-3,0}^4} \exp\left(\frac{-D^{p-3}}{|p-3| D_{p-3,0}^{p-3}}\right) \tag{23.37}$$

where the order of the constraint, $p - 3$, is similar to the parameter q. When both approaches are applied to the same spray, $p - 3 = q$.

To predict drop size distributions, it is first assumed that D_{32} can be obtained in some manner. D_{32} is related to D_{q0} by:

$$D_{32} = D_{q0} \sqrt[q]{q} \frac{\Gamma(4/q)}{\Gamma(3/q)} \tag{23.38}$$

so D_{q0} can be determined, given the order of the constraint, q. Cousin et al. [19] indicate that q may be constant for each disintegration process (one for pressure atomizers, another for pressure-swirl atomizers, etc.).

Cousin et al.'s [19] work was a major step forward in using the MEF to predict drop size distributions. However, while the source terms were eliminated, the value for q still had to be determined. At this time, it is not clear whether it is possible to predict q a priori. In addition, $f_0(D)$ does not vanish as the diameter goes to zero. This supports the introduction of information related to small drops in order to have a reasonable distribution, as shown by Ahmadi and Sellens [17].

Dumouchel [20] generalized the work of Cousin et al. [19] by introducing a new a priori probability function to account for the non-equal probability of diameter classes (i.e., existence of a diameter $D_{\min} > 0$). Under these assumptions:

$$f_0(D) = \frac{q}{\Gamma(\alpha/q)} \left(\frac{\alpha}{q}\right)^{\frac{\alpha}{q}} \frac{D^{\alpha-1}}{D_{q0}^{\alpha}} \exp\left(-\frac{\alpha}{q}\frac{D^q}{D_{q0}^q}\right) \tag{23.39}$$

This is a Nukiyama–Tanasawa type distribution. The parameter $\alpha > 1$, guarantees that the number distribution vanishes at small D, as opposed to the expression derived by Cousin et al. [19] which corresponds to $\alpha = 1$. Unfortunately this introduces a third parameter that needs to be determined. Lecompte and Dumouchel [21] suggest that there may be a unique pair q and α that can represent all drop size distributions for a specific atomization process (ultrasonic atomization, twin-fluid atomization, etc.). This could transform the MEF into a pseudo-predictive method.

In an attempt to make the MEF predictive, Li et al. [22] proposed a scheme based on the maximization of entropy generation under a set of two constraints (conservation of mass and normalization). Li et al.'s approach [22] reduces to MEF for an extended set of constraints expressed in terms of characteristic diameters that are usually difficult to predict a priori.

In summary, advances have been made in using the MEF to predict drop size distributions. Guidelines have been put forth:

1. Constraints should be formulated in terms of representative diameters of the distribution. These diameters must be obtained by some other means.
2. A single constraint that involves one representative diameter evidently results in unrealistic $f_0(D)$. A second constraint (the partition of surface energy, as used by Ahmadi and Sellens [16]) or an a priori probability function (as used by

Dumouchel [20]), must be used to ensure that $f_0(D)$ vanishes as the drop diameter approaches zero.
3. The representative diameters should be some measure of the distribution sought, i.e., the mean, variance, etc.
4. It appears that at least two representative diameters or parameters are required as inputs to produce a realistic f_0. It is possible to predict one diameter by using a stability analysis for liquid breakup. However, it appears impossible to predict more than one diameter. This seriously hampers the utility of MEF as a method to predict drop size distributions from first principles.

The Discrete Probability Function (DPF) Approach

The DPF approach treats spray formation in stages, beginning with breakup of the bulk liquid, which separates into ligaments. The ligaments break up into fragments that then evolve into drops. A geometrical model is often used to describe ligament formation, and an instability analysis models ligament breakup.

The ligament breakup model predicts drop diameter given a set of initial conditions. A distribution of drop sizes results because the initial conditions fluctuate, due to vibration of the atomizer, variations in liquid delivery rate, unsteady exit velocity, inhomogeneous liquid physical properties, cavitation-induced pulsations, turbulent flow fields, etc. PDFs are required for all fluctuating quantities.

Fluctuating quantities are discretized into a number of bins, with each bin characterized by the value at the bin midpoint and the corresponding probability. Bin midpoints are used in the drop formation model to predict the drop size. The probability of occurrence of that drop size is the same as the probability of the bin being populated.

When several initial conditions fluctuate simultaneously, the procedure is virtually identical to that used in the single fluctuation case, the only difference being that the probability of a given drop size occurring is equal to either the product of the probabilities of each fluctuating input (if the varying initial conditions are independent), or, to the product of probabilities multiplied by a correlation factor (if the varying initial conditions are not independent).

The DPF method has been used by Sovani et al. [5, 6] for Newtonian liquids and Babinsky and Sojka [23] for non-Newtonian ones. Sovani et al. [5] discovered that relative velocity fluctuations have the greatest effect on f_0, while fluctuations in fluid physical properties (density, surface tension and viscosity) have a negligible effect. Sovani et al. [6] demonstrated that 1% fluctuations in liquid physical properties have no effect on f_0, and that larger fluctuations in fluid physical properties only widen f_0 slightly at low velocities.

Babinsky and Sojka [23] used DPF to study non-Newtonian liquid drop size distributions. For a single fluctuation, their results showed that fluctuations in ALR and interphase velocity slip ratio have the largest effect on effervescent atomizer f_0. For two simultaneously fluctuating quantities, the influence on f_0 is found by adding

the influence of each fluctuation considered separately when the fluctuation levels for both are low. When the fluctuation level of one quantity is large, the effect of the second set of fluctuations on f_0 is negligible.

The DPF method does have limitations. They are:

1. It is limited to treating primary atomization.
2. DPF results haven't been compared to experimental data because measurements for fluctuating quantities don't exist.
3. DPF requires a ligament instability model. The computational complexity can become unwieldy if a nonlinear or multidimensional breakup model is employed.
4. DPF requires input PDFs of fluctuating input quantities. Since they likely depend on atomizer geometry and operating conditions, they are required for each case. Unless a theoretical method can be found to predict them, they will have to be measured.

Stochastic Breakup Models

Numerical models try to accurately predict the behavior of a jet breaking up. If one wants to exactly solve the full set of equations (Navier–Stokes, energy, etc.) one needs to perform direct numerical simulations (DNS), which requires tremendous computational power. The computational power available today only allows modeling of simple flow with low spatial and temporal resolution. Researchers are therefore required to make approximations that simplify the governing equations and thereby reduce the complexity of the system.

One recent approach is the stochastic modeling of droplet breakup. It was developed by Apte et al. [24], Gorokhovski and Saveliev [25], Rimbert and Sero-Guillaume [26], and Vinkovic et al. [27] for secondary air-blast atomization (high Weber number) for which the drop breakup frequency can be considered high enough to guarantee a fragmentation cascade. It has also been applied to primary atomization [28].

Regardless of the breakup mechanism, for a constant fragmentation frequency the kinetic fragmentation equation takes the form:

$$\frac{1}{v}\frac{\partial f(r,t)}{\partial t} = \int_0^1 \frac{1}{\alpha} f\left(\frac{r}{\alpha}\right) q(\alpha)\, d\alpha - f(r,t) \tag{23.40}$$

where v is the breakup frequency, $q(\alpha)$the fragmentation spectrum, f the probability density function, and α a random multiplier such that $r \rightarrow \alpha r$ after breakup. At intermediate time, solution of this equation reduces to the log-normal asymptotic shape of the size distribution developed by Kolmogorov. At later time, the particle-size distribution becomes a power law, which implies it should be a fractal

distribution. At very long times under scaling symmetries, (20.40) reduces to the Fokker–Plank equation.

Fragment size after droplet breakup is governed by f, the solution of (20.40). The solution is implemented as a numerical code that tracks the droplet and that models the gas phase using LES. Apte et al. [24] showed that the f_0 generated by this technique is in agreement with available experimental data.

When modeling high Weber number secondary atomization, the probability of breakup is first applied to a parent drop of the size of the nozzle diameter. Once the first daughter drop(s) is(are) formed, time is reinitialized and the daughter drop becomes a parent drop (with the probability for second daughter drop breakup independent of the original parent drop size). This breakup cascade occurs until the drop critical radius (a function of the local Weber number) is reached.

Fractal scaling of breakup has been observed by several authors when using the stochastic approach, and was observed when measuring drop size distributions for pre-filming atomizers [29]. The drop size distribution after primary atomization was assumed to be a Gamma distribution, and a droplet was assumed to break up into at most two daughter drops only if its diameter was above the critical diameter. In addition, the daughter-to-parent mass ratio was a random variable between $[a, 1 - a]$, $0 \leq a \leq 0.5$. Zhou [30] assumed a takes the value 0, while Liu et al. [29] determined it experimentally. Liu et al.'s predictions were fitted to a Rosin–Rammler distribution that was also fitted to experimental data. The two sets of parameters were compared and good agreement was noted.

For extended information regarding stochastic breakup modeling, refer to the review of Gorokhovski and Herrman [28].

Summary

Four methods of modeling drop size distributions, empirical, maximum entropy formalism (MEF), Discrete Probability Function (DPF), and stochastic were reviewed. Key conclusions are:

- The empirical method is flexible; it can be used to model virtually any non-pathological data set. However, its predictive power is severely limited. If it is found that an atomizer operating under certain conditions produces drops described by a given empirical distribution, it is possible to establish a relationship between atomizer geometry and operating conditions and the parameters of the distribution. This can't necessarily be applied to predict the drop size distribution produced by a different atomizer, or for the same atomizer operating in a different regime, because there is no guarantee that the empirical relationships (or the empirical distribution function) will remain the same. Furthermore, it is difficult to select an empirical distribution function that fits a wide range of actual drop size distributions. Those that do work well (such as the log-hyperbolic distribution) suffer from numerical stability problems and are difficult to handle

Table 23.1 Summary of the advantages and disadvantages of the three available methods for predicting drop size distributions (MEF, DPF, stochastic)

	ME	DPF	Stochastic
Inputs required (in addition to fluid physical properties and atomizer parameters)	At least two representative drop diameters	Probability density function of the fluctuating quantity	None
Inputs that can be computed now	One representative diameter (from instability analysis)	No experimental PDFs exist	N/A
Can the lack of necessary inputs be overcome?	Unclear	In principle, CFD advances will provide the required information	N/A
Are there predictions that agree with experiments?	No. Agreement reached only after adjusting source terms or measuring the representative diameter directly	No. No experimental PDFs exist	Yes. Full numerical simulations produce satisfactory results
Computational complexity	Satisfactory. Requires the minimization of a multidimensional function. The number of dimensions is proportional to the number of constraints	Simple if CFD is not involved and 1-dimensional liquid breakup model is used. Requires the minimization of a 1-dimensional function. Not at all simple if multidimensional liquid breakup models are used	Quite complex. Requires numerical simulation of coupled equations
Can it be applied to fluids with complex rheology or different atomization modes?	Unknown. Unclear whether it would be possible to formulate the appropriate constraints for complex liquids	Yes	Yes

mathematically. The proliferation of parameters that invariably accompanies flexible distribution functions is concomitant with relatively complex computer algorithms required to estimate the value of the parameters.

- The Maximum Entropy Formalism (MEF) has worked well in a number of situations. It appears to be a reasonable approach to modeling drop size distributions, and, in particular, would be useful for processes dominated by secondary atomization where the breakup physics are stochastic in nature. Experience with using the MEF has shown it requires more information about the resulting drop size distribution than is possible to predict using other representative diameters. Specifically, it appears that at least two representative diameters are required for accurate predictions (or a representative diameter and the spread parameter q), while only a representative diameter can currently be obtained (by using an instability analysis). Attempts to remedy this situation have required modeling the details of the breakup process, which should be ignored in a proper application of the ME method.
- The discrete probability (DPF) method attempts to resolve difficulties encountered when using the MEF by mathematically describing the details of the breakup process and then introducing probabilistic effects to account for the inherent randomness. It can be applied to a variety of atomizer configurations and operating conditions simply by selecting an appropriate instability model for breakup. However, it is limited to primary atomization; for secondary atomization the MEF is more appropriate. The DPF method has not been validated because of the difficulties involved in obtaining experimental data (it requires the PDFs of the fluctuating initial conditions as inputs). If the PDF is obtained experimentally, the DPF method loses its predictive power, since PDFs are likely to vary under different conditions. Therefore, future work on the DPF method may well involve the use of CFD to predict the input PDFs.
- Stochastic methods have been successfully introduced into numerical models applied to primary and secondary atomization. Unfortunately their use is restricted to high-Weber number situations so they cannot accurately predict drop sizes in sprays for which fragmentation cascade cannot be assumed. These models can be considered as fully predictive.

Of the four available methods, only the MEF, the DPF approach, and the stochastic method can possibly be considered "predictive." Table 23.1 summarizes their advantages and disadvantages.

References

1. R. A. Mugele, H. D. Evans: Droplet Size Distributions in Sprays, Ind. Eng. Chem. 43(6), 1317–1324 (1951).
2. W. A. Sowa: Interpreting Mean Drop Diameters Using Distribution Moments, Atomization Sprays 2, 1–15 (1992).

3. R. W. Sellens, T. A. Brzustowski: A Prediction of the Drop Size Distribution in a Spray from First Principles, Atomization Spray Technol. 1, 89–102 (1985).
4. X. Li, R. S. Tankin: Droplet Size Distribution: A Derivation of a Nukiyama–Tanasawa Type Distribution Function, Combust. Sci. Technol. 56, 65–76 (1987).
5. S. D. Sovani, P. E. Sojka, Y. R. Sivathanu: Prediction of Drop Size Distributions from First Principles: The Influence of Fluctuations in Relative Velocity and Liquid Physical Properties, Atomization Sprays 9, 113–152 (1999).
6. S. D. Sovani, P. E. Sojka, Y. R. Sivathanu: Prediction of Drop Size Distributions from First Principles: Joint-PDF Effects, Atomization Sprays 10, 587–602 (2000).
7. Y. R. Sivathanu, J. P. Gore: A Discrete Probability Function Method for the Equation of Radiative Transfer, J. Quant. Spectrosc. Radiat. Transfer 49(3), 269–280 (1993).
8. T. Paloposki: Drop Size Distributions in Liquid Sprays, Acta Polytechnica Scandinavica, Mech. Eng. Series 114, Helsinki, Finland (1994).
9. E. L. Crow, K. Shimizu: Lognormal Distributions: Theory and Applications, Marcel Dekker, New York (1988).
10. R. W. Tate, W. R. Marshall Jr.: Atomization by Centrifugal Pressure Nozzles, Chem. Eng. Prog. 49, 169–174 (1953).
11. S. Nukiyama, Y. Tanasawa: Experiments on the Atomization of Liquids in an Air Stream. Report 3: On the Droplet-Size Distribution in an Atomized Jet. Trans. Soc. Mech. Eng. Jpn. 5, 62–67 (1939).
12. J. C. Bhatia, J. Dominick, F. Durst: Phase-Doppler-Anemometry and the Log-Hyperbolic Distribution Applied to Liquid Sprays, Part. Part. Syst. Char. 5, 153–164 (1988).
13. J. C. Bhatia, F. Durst: Comparative Study of Some Probability Distributions Applied to Liquid Sprays, Part. Part. Syst. Char. 6, 151–162 (1989).
14. J. C. Bhatia, F. Durst: Description of Sprays Using Joint Hyperbolic Distribution in Particle Size and Velocity, Combust. Flame 81, 203–218 (1990).
15. L. Griffith: A Theory of the Size Distribution of Particles in a Comminuted System, Can. J. Res. 21(A), 57–64 (1943).
16. X. Li, R. S. Tankin: Derivation of Droplet Size Distribution in Sprays by Using Information Theory, Combust. Sci. Technol. 60, 345–357 (1988).
17. M. Ahmadi, R. W. Sellens: A Simplified Maximum-Entropy-Based Drop Size Distribution, Atomization Sprays 3, 291–310 (1993).
18. C. W. M. van der Geld, H. Vermeer: Prediction of Drop Size Distributions in Sprays Using the Maximum Entropy Formalism: The Effect of Satellite Formation, Int. J. Multiphase Flow 20 (2), 363–381 (1994).
19. J. Cousin, S. J. Yoon, C. Dumouchel: Coupling of Classical Linear Theory and Maximum Entropy Formalism for Prediction of Drop Size Distribution in Sprays: Application to Pressure-Swirl Atomizers, Atomization Sprays 6, 601–622 (1996).
20. C. Dumouchel: A New Formulation of the Maximum Entropy Formalism to Model Liquid Spray Drop-Size Distribution, Part. Part. Syst. Char. 23, 468–479 (2006).
21. M. Lecompte, C. Dumouchel: On the Capability of the Generalized Gamma Function to Represent Spray Drop-Size Distribution, Part. Part. Syst. Char. 25, 154–167 (2008).
22. X. Li, M. Li, H. Fu: Modeling the Initial Droplet Size Distribution in Sprays Based on the Maximization of Entropy Generation, Atomization Sprays 15, 295–321 (2005).
23. E. Babinsky, P. E. Sojka: Modeling Drop Size Distributions from First Principles for Non-Newtonian Fluids, Atomization Sprays 11, 597–617 (2001).
24. S. Apte, M. Gorokhovski, P. Moin: LES of Atomizing Spray with Stochastic Modeling of Secondary Break-Up, Int. J. Multiphase Flow 29, 1503–1522 (2003).
25. M. Gorokhovski, V. Saveliev: Further Analyses of Kolmogorov's Model of Breakup, Phys. Fluids 15, 184–192 (2003).
26. N. Rimbert, O. Sero-Guillaume: Log-Stable Laws as Asymptotic Solutions to a Fragmentation Equation: Application to the Distribution of Droplet in a High-Weber-Number Spray, Phys. Rev. E: Stat. Nonlinear Soft Matter Phys. 69, 056316 (2004).

27. I. Vinkovic, C. Agguire, S. Simoens, M. Gorokhovski: Large Eddy Simulations of Droplet Dispersion for Inhomogeneous Turbulent Wall Flow, Int. J. Multiphase Flow 32, 344–364 (2006).
28. M. Gorokhovski, M. Herrman: Modeling Primary Atomization, Annu. Rev. Fluid Mech. 40, 343–366 (2008).
29. H. F. Liu, X. Gong, W. F. Li, F. C. Wang, Z. H. Yu: Prediction of Droplet Size Distribution in Sprays of Prefilming Air-Blast Atomizers, Chem. Eng. J. 61, 1741–1747 (2006).
30. W. X. Zhou, T. J. Zhao, T. Wu, Z. H. Yu: Application of Fractal Geometry to Atomization Process, Chem. Eng. J. 78, 193–197 (2000).

Chapter 24
Spray Nozzles

K. Omer and N. Ashgriz

Abstract Spray nozzles are used in many applications such as cleaning, cutting, and spraying. Spray nozzles come in many varieties, and are usually classified according to the specific mode of atomization they employ. In this chapter, twin fluid, swirl, hydraulic, ultrasonic, rotary, and electrostatic nozzles are discussed. First, their specific mode of atomization is explained, followed by a brief description on the variation on each type of nozzle. Next, a comprehensive list of performance correlations for each type of nozzle is compiled from various sources. Finally, these correlations are explored in more detail for each type of nozzle.

Keywords Air blast · Air assist · Discharge coefficient · Effervescent · Electrostatic · Flat fan nozzles · Full cone · Hydraulic · Hollow cone · Rotary · SMD · Spray angle · Spray impact · Spray pattern · Swirl · Twin fluid · Ultrasonic

Introduction

There are a wide variety of spray nozzles, each developed for a special application and a particular range of flows, and to generate a desired droplet size and velocity distribution. For instance, Fig. 24.1 shows a series of nozzles employed for cleaning purposes.

Spray nozzles can be categorized based on mass flow rate, liquid mass distribution, spray pattern, spray angle, spray impact, and droplet size.

The flow rate is dependent on the nozzle area, nozzle geometry, nature of the fluid and the feed pressure. In twin-fluid nozzles, there are two mass flows, one for the liquid and one, usually, for the gas. For the same nozzle, a higher liquid flow rate tends to lead to larger droplet sizes, whereas a higher gas flow rate leads to smaller

N. Ashgriz (✉)
Department of Mechanical and Industrial Engineering, University of Toronto, Toronto, Ontario, Canada
e-mail: ashgriz@mie.utoronto.ca

N. Ashgriz (ed.), *Handbook of Atomization and Sprays*,
DOI 10.1007/978-1-4419-7264-4_24, © Springer Science+Business Media, LLC 2011



Fig. 24.1 A series of spray nozzles performing a cleaning operation (Courtesy of Lechler, Inc.)

droplets. The type of application will determine the appropriate nozzle flow rate, depending upon how much fluid is needed to achieve the desired goal, as well as other operating attributes of the nozzle.

Similarly, the spray angle is a function of the feed pressure and the fluid characteristics. Higher feed pressures lead to larger spray angles. The appropriate spray angle for a nozzle depends on the area needed to be covered by the spray. A higher spray angle can also reduce the spray impact of a nozzle.

Spray impact is the impingement of a spray upon its target. It is a factor of droplet size, the feed pressure, the flow rate and the gas velocity in the case of twin-fluid atomizers. While impact is quantitatively measurable, it is more typically qualitatively measured. That is, testing with various nozzles and operating conditions can determine what impact is most effective for that spray application.

The droplet size of a spray is some average droplet size as discussed in Chap. 23. A commonly reported droplet size is the Sauter mean diameter, SMD or D_{32}. Droplet size depends on the type of nozzle, flow rate, feed pressure and spray pattern.

Liquid distribution refers to the amount of liquid being distributed at different areas of the spray impact. Some applications use multiple nozzles at once where an even liquid distribution is critical, while others use only one nozzle, where an even liquid distribution is not required. Designing nozzles to evenly distribute liquid is a challenge, since most nozzles do not have even liquid distribution. Figure 24.2 shows a patternator (composed of a series of vials) which is used to measure the mass distribution across the spray. It is evident from it that the vials near the edges do not collect as much liquid as those at the center.

The last nozzle attribute to be discussed is spray pattern, which refers to the shape in which the liquid droplets are distributed rather than the amount of liquid itself. Many different spray patterns exist, such as the hollow cone, full cone and flat fan. These are discussed in more detail in the next section.



Fig. 24.2 A diagram showing liquid distribution in a spray. A patternator, comprising a series of vials, is used to collect the spray. As can be seen by white floats, the liquid is evenly distributed in the centre, but slowly disperses near the edges (Courtesy of Lechler, Inc.)

Spray nozzles can be classified as: twin-fluid, swirl, hydraulic, rotary, ultrasonic, electrostatic, and many more. Often a single nozzle may fall under more than one category due to its design. For example, a swirl nozzle may be based on twin-fluid swirl atomization.

Numerous experiments have been conducted to determine the droplet size distribution and the mean drop size for various spray nozzles and for different operating conditions. Also, different methods have been used to measure the droplet size. Early studies used photography and direct imaging of droplets to determine the droplet size. This used to be a very cumbersome process, requiring manual measurement of the size of each droplet from an image. However, recently, the same direct imaging is being done automatically using image processing techniques, providing fast and accurate results. In addition, more advanced optical techniques, such as phase Doppler anemometry have allowed measurement of tens of thousands of droplet sizes (and simultaneously droplet velocities) in a short time, resulting in statistically better mean droplet sizes.

Lefebvre [1] has compiled droplet size correlations for variety of spray nozzles. The present chapter extends the same compilation to include more recent correlations. The correlations provided are by no means exhaustive, yet they provide commonly used correlations. These correlations are provided in Tables 24.1–24.12 at the end of this chapter. The correlations are mainly based on the (i) fluid properties (mainly density, viscosity, and surface tension), (ii) nozzle geometry, such as the exit orifice diameter, impinging angle of the air on the liquid, etc., and (iii) operational parameters such as the flow rates of the liquid or gas. While some experiments have been conducted to consider the effects of all these three types of variables, many simply choose only to deal with a handful of them, and neglect the effects of others. Obviously, the more the experimental variables, the more difficult it is to obtain an accurate correlation for the droplet size.

Furthermore, while some correlations were derived theoretically, others used curve-fitting techniques. It should be noted that while these correlations can give fairly accurate results if applied correctly, they are only approximations. They do not necessarily give exact results, as was shown by Gosman and Clerides in their study [2].

Twin-Fluid Nozzles

Twin-fluid atomizing nozzles, shown in Fig. 24.3, can generate fine droplets at low liquid flow rates. In these nozzles, a high velocity gas stream is brought in contact with a liquid stream. Applications for this family of nozzles include humidification, dust control, gas cooling, precision coating and spray drying. Twin-fluid atomizing nozzles are available in various designs. Some employ the pressure principle, where the liquid is supplied from a pressurized source. Others use the gravity principle, where the liquid supply is located above the nozzle, invoking gravity for the liquid flow. The siphon principle is also used in some twin-fluid atomizing nozzles where the liquid source is self-aspirating. Figure 24.4 shows two different

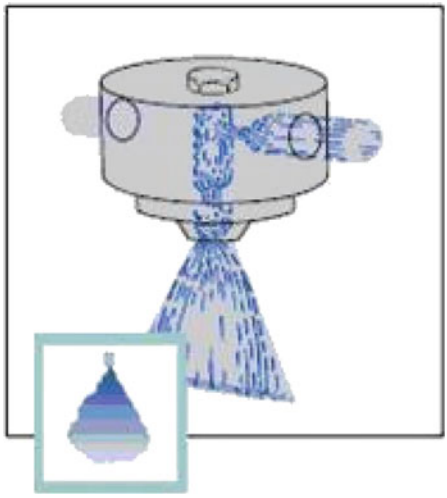


Fig. 24.3 A schematic representation of a twin fluid atomizing nozzle (Courtesy of Lechler, Inc.)



Fig. 24.4 Examples of air atomizing nozzles found in industry (Courtesy of Lechler, Inc.)



Fig. 24.5 Three common spray shapes: full cone (*left*), flat fan (*center*), hollow cone (*right*) (Courtesy of Lechler, Inc.)

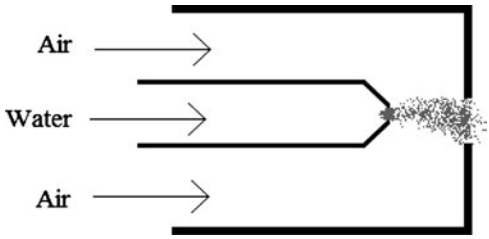


Fig. 24.6 A schematic for a simple airblast nozzle design

atomizing nozzles. These nozzles can generate different spray patterns, such as those shown in Fig. 24.5. They are flat fan, full cone and hollow cone sprays. Spray angles typically range from 20° to 60°. The spray impact, flow rate and droplet size distribution vary for each nozzle. However, many twin-fluid nozzles are capable of producing very fine droplets. The liquid distribution of the sprays tends to be uneven for full cone sprays. Flat fan sprays are available in both even and uneven distributions

Gas and liquid can be brought in contact either within the nozzle (internal mix) or outside of the nozzle (external mix). In addition, nozzles can be categorized based on the flow rate of the atomizing gas and the way the gas is brought into contact with the liquid. These variations are airblasting, air-assisting, and effervescent nozzles. The main difference between each of the three is the velocity and quantity of air used in the atomizing process. Another difference relates to when the air is mixed with the liquid stream.

Airblast Nozzles

Figure 24.6 shows a schematic for a simple airblast nozzle. An inner liquid-carrying tube is surrounded by an annular gas flow tube. The liquid is released into the gas chamber, causing atomization. The air is normally injected at low velocities, but there

is a limiting value to this velocity. The limiting value depends on the pressure gradient in the nozzle chamber. Because the velocity is limited to a finite amount, a fairly large amount of air is needed to fully atomize the liquid stream. This is a disadvantage in most cases. These nozzles are commonly used in combustion systems.

Prefilming Airblast Nozzle

Prefilming airblast nozzles are the most popular type of twin-fluid nozzle [1]. In this design, the liquid is first spread into a very thin sheet, or a film. The film is then exposed to air operating at a high velocity causing atomization. By spreading the liquid into a thin sheet or film, the contact area between the liquid and gas increases. Therefore, gas energy is more efficiently transferred to the liquid. In addition, the film thickness is usually smaller than the original jet exiting the liquid orifice, therefore, the characteristic length of the liquid reduces, reducing the average droplet size produced. A sketch of a typical prefilming airblast nozzle is provided in Fig. 24.7 [3]. An important design consideration here is that the thickness of the liquid film should be kept as consistent as possible, because an inconsistent liquid film will create a spray with inconsistent droplet sizes, which can lead to a number of problems downstream in the application. Prefilming nozzles are more difficult to manufacture, and they are less accurate over longer distances than non-prefilming nozzles.

Correlations for the mean droplet sizes produced by prefilming airblast nozzles are summarized in Table 24.1. In general, the similar correlations are grouped together. The first few equations are the ones derived using experimental data, whereas the ones at the end of the table were derived from theory. All tables presented at the end of this chapter follow this format. For convenience, each equation is given a reference number.

An important parameter in most twin-fluid nozzles is the gas-to-liquid mass flow rate ratio:

$$m = \frac{\dot{m}_g}{\dot{m}_l} = \text{GLR} \tag{24.1}$$

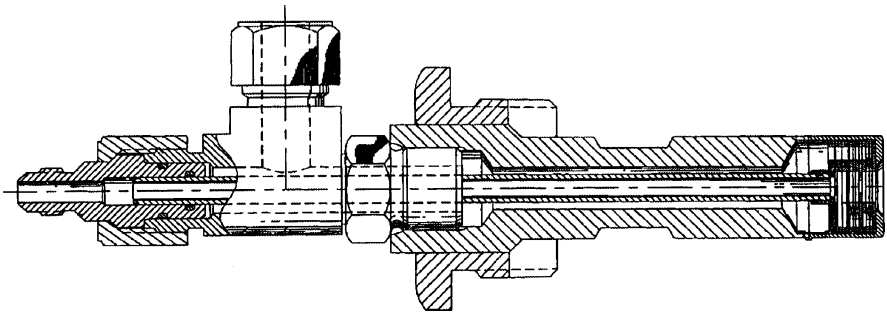


Fig. 24.7 A prefilming airblast nozzle [3]

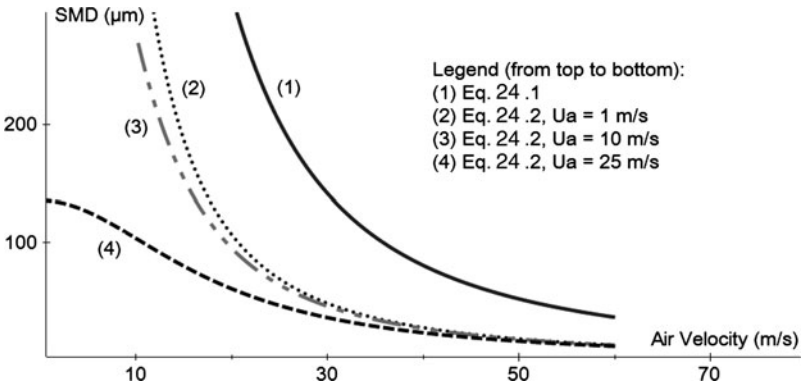


Fig. 24.8 Comparison of 24.1.i and 24.1.ii at different values of liquid velocity, GLR = 0.5, and properties of water are used

Based on energy analysis, Lefebvre [4] derived equation 24.1.i for the SMD of a nozzle where the liquid velocities are not too high. His result was later improved by Barreras and Eduardo [5], in 24.1.ii, to include the effects of the kinetic energy of the liquid. Figure 24.8 shows SMD plots 24.1.i and 24.1.ii. For these plots, t, C, ρ_L, and σ are kept constant, the mass flow rate ratio is set to 0.5, U_A is kept as the variable, for several values of U_L. It is evident from the graph that as U_L reduces, Barreras and Eduardo's equation approaches that of Lefebvre. As U_L increases, the curves become more flat, implying that air velocity has less effect at higher liquid velocities. Therefore, an airblast nozzle tends to perform like a plain orifice hydraulic nozzle (discussed in "Swirl Nozzles" section) at high liquid velocities.

Figure 24.9a and c show variations on 24.1.i at different film thicknesses. Water was once again used for the liquid properties, and the discharge coefficient was selected to be 0.07. Figure 24.9b and d show variations on the same formula at different discharge coefficients. In this case, the film thickness was set to 0.1 mm, as was done in Lefebvre's [4] experiment. In Fig. 24.9b and d, GLR was set to 1. In both situations, the SMD appears to be approaching a "limiting value." In other words, there seems to be a point on the graph beyond which the GLR has negligible impact on the SMD.

Another very important parameter that often plays a role in the performance of a nozzle is its discharge coefficient. A discharge coefficient is defined as the ratio of the theoretical mass flow in a nozzle to the actual mass flow. Nozzle geometry plays a huge role in determining this. Ganippa et al. [6] derived, from theory, the following formula:

$$C_d = \left[\frac{F}{2A_0\Delta P}\right]^{0.5} \tag{24.2}$$

where F denotes the impingement of the spray at the nozzle exit, A_0 denotes the nozzle orifice area, and ΔP represents the pressure difference across the orifice.

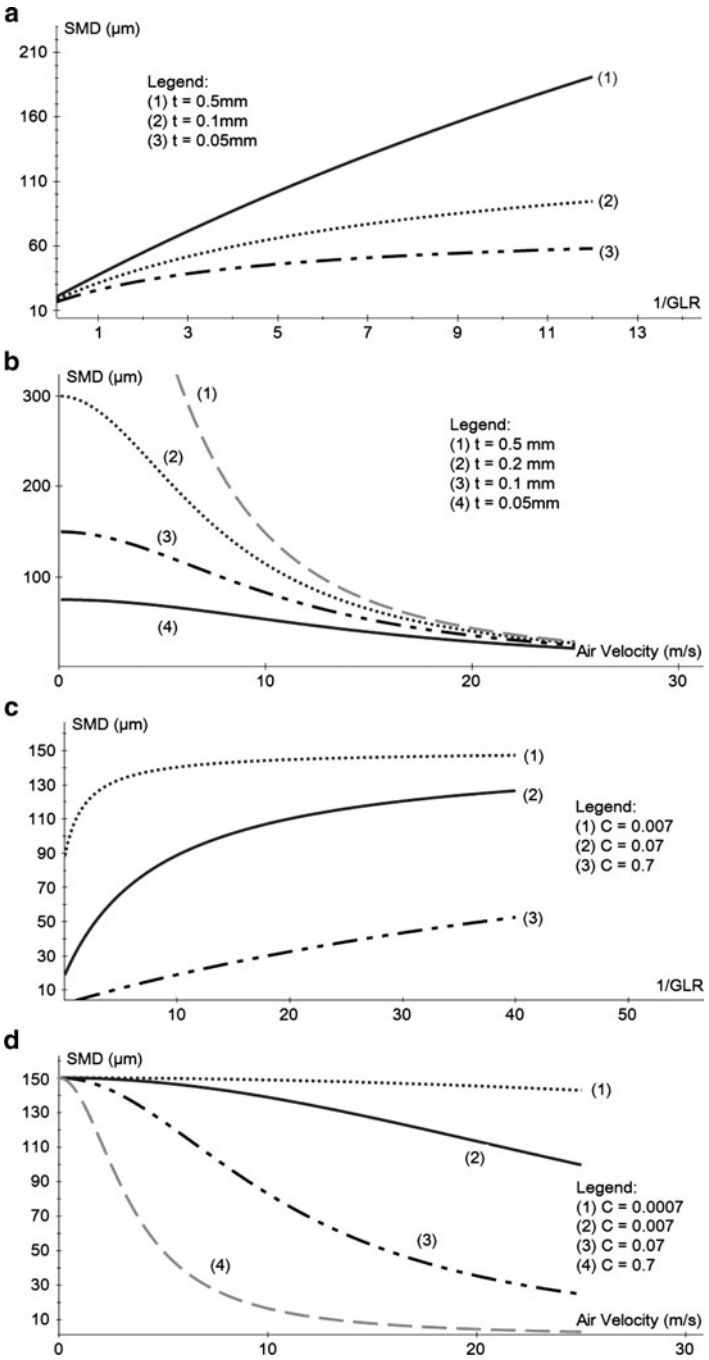


Fig. 24.9 Variations on the equation derived by Lefebvre [4], plotted against 1/GLR (**a**) with changes in t, (**b**) changes in C, and plotted against U_A (**c**) with changes in t and (**d**) changes in C; Values used were: $C_d = 0.07$, $t = 0.1$ mm, GLR = 1, σ, ρ, μ were same as water

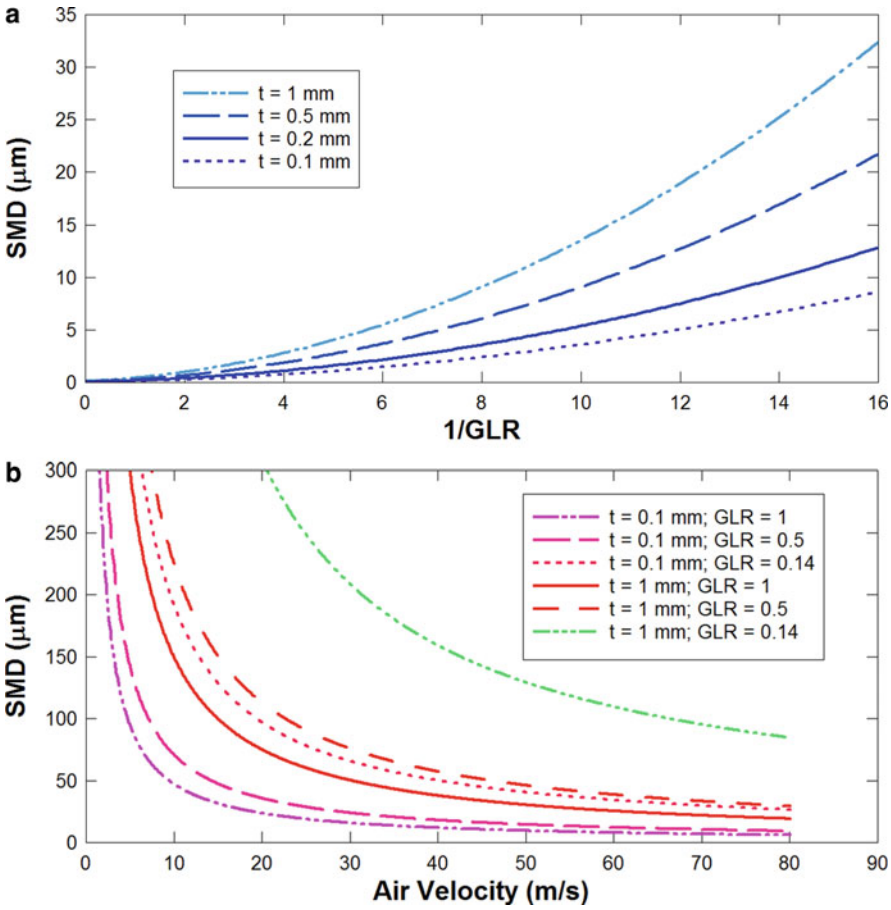


Fig. 24.10 A plot of (**a**) SMD vs. 1/GLR at different values of film thickness and (**b**) SMD vs. U_A at different values of GLR and film thickness, in 24.1.iii for water [7]

Equation 24.1.iii, by Rizkalla and Lefebvre [7], contains one term for the surface tension effects and another for viscous effects. The viscous effects appear to have stronger influence on the drop size as the exponent of viscosity is 0.85, whereas that for surface tension is 0.5.

Figure 24.10 shows SMD predictions given from 24.1.iii at various film thicknesses. In this case, the properties of water were used, U_A was set to 50 m/s and GLR to 1. As is evident from the equation and theory, an increase in film thickness leads to coarser atomization, while an increase in GLR leads to finer atomization.

Equation 24.1.iv by Jasuja [8] is very similar to 24.1.iii. However, one key factor is that it is missing the effect of film thickness. The layout of the equation is the same; it contains two terms, and the exponents on most of the variables are identical. The difference is in the GLR ratio, where the exponent is equal only to 0.5, as opposed to 2 in 24.1.iii. The equation predicts very coarse atomization. The difference can

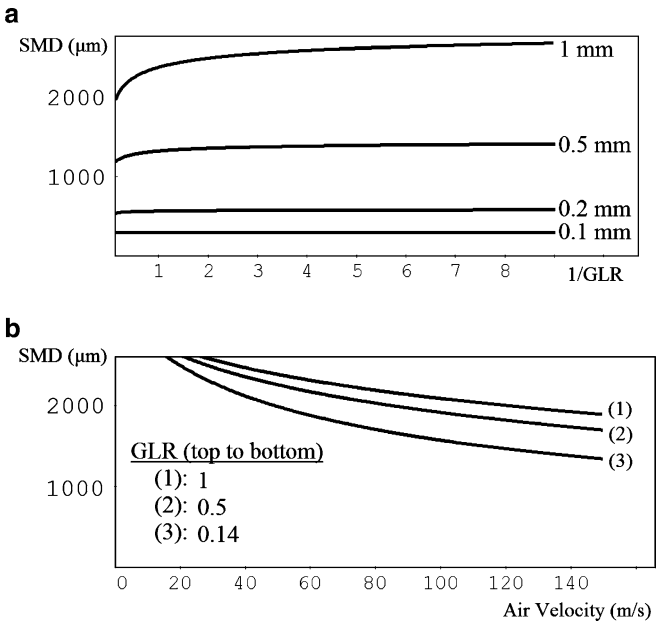


Fig. 24.11 A plot of 24.1.vii with SMD plotted against (**a**) 1/GLR at different film thicknesses and (**b**) against U_A at different values of GLR

be attributed to the fluids used. Rizkalla and Lefebvre [7] used a wide variety of liquids, while Jasuja's [8] experiments were confined only to different types of fuel, such as kerosene. Also, Jasuja used only one kind of nozzle that contained a pintle and the air was injected tangentially.

When comparing 24.1.ii by Barreras and Eduardo [5] to 24.1.vii by Knoll and Sojka [9] we note that 24.1.ii does not contain liquid viscosity, and both equations put an exponent of -1 on the liquid density. Both equations also contain very complex effects of surface tension. Equation 24.1.vii also introduces a new variable, which is the air slot thickness. Figure 24.11 plots this equation in much the same way as Fig. 24.10 plots the 24.1.iii. There is indeed a marked contrast between both the equations. This may be due to the uncertainties in the size measurement.

Plain Jet Airblast Nozzle

Non-prefilming nozzles, called plain jet nozzles, come in a wide variety; however, their basic design consists of a chamber containing liquid, which is externally mixed with air. These are used only in low-to-moderate pressure environments, as the spray tends to break in high pressure environments.

The liquid jet cannot be atomized at low gas velocities and breaks into droplets mainly through capillary action. This is the Rayleigh mode. At higher velocities, the

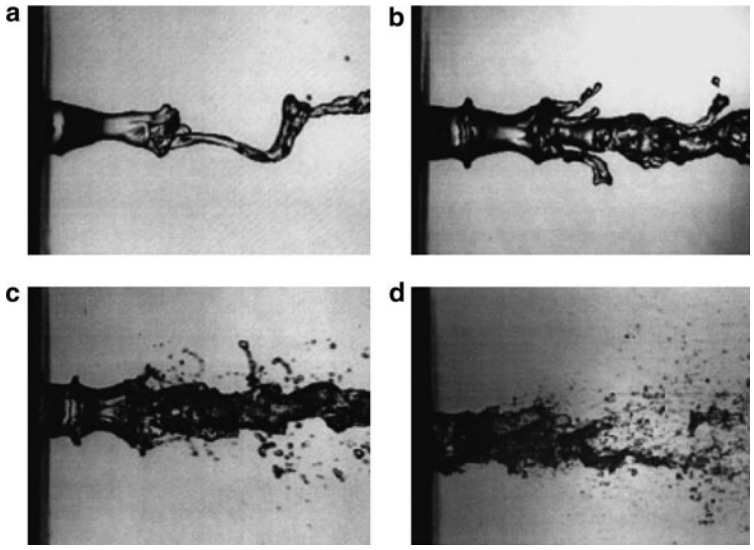


Fig. 24.12 Images of jet breakup by a coaxial gas flow. The nozzle contraction ratio is 7:1, and liquid and gas diameters are $D_l = 7.6$ mm and $D_g = 11.3$ mm, respectively. (**a**) $U_l = 0.16$ m/s and $U_g = 19$ m/s, (**b**) $U_l = 0.55$ m/s and $U_g = 21$ m/s, (**c**) $U_l = 0.86$ m/s and $U_g = 30$ m/s, and (**d**) $U_l = 0.26$ m/s and $U_g = 50$ m/s [12] (Courtesy of Annual Reviews, Inc.)

jet stretches forming ligaments, which later break into drops. This is called membrane regime. At even higher gas velocities, the atomization is termed as being by fiber mode and by the superpulsating mode, in which the liquid fragments into small fibers. Figure 24.12 shows images of jet breakup by coaxial gas flow and figure 24.13 shows breakup regimes in the parameter space $Re_l - We$ [12].

The momentum ratio is very important in determining the type of atomization that will occur [13]. This is shown in Fig. 24.14. Three situations are exemplified, and as can be seen, the size of the droplets varies considerably when the momentum ratio is changed. Both front and side views are shown in the figure for all three cases.

This superpulsating mode is believed to be due to the onset of a gaseous recirculation on the central jet and occurs at

$$\frac{\sqrt{We_g}}{Re_l} = \frac{\sqrt{\rho_g (U_g - U_l)^2 D/\sigma}}{\rho_l U_l D/\mu_l} > 0.01 \tag{24.3}$$

This equation can also be written in terms of the gas to liquid momentum ratio: $qOh^2 > 10^{-4}$, where

$$q = \frac{\rho_g U_g^2}{\rho_l U_l^2} \tag{24.4}$$

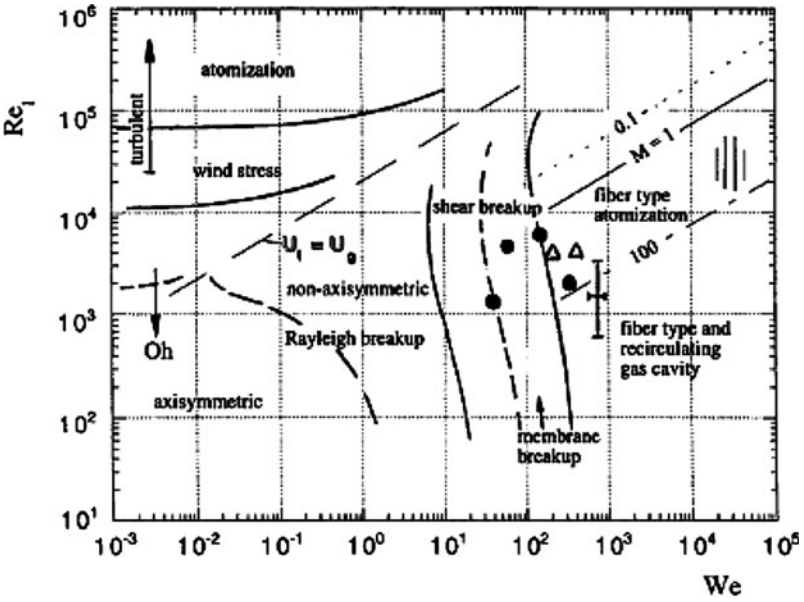


Fig. 24.13 Breakup regimes in the parameter space $Re_l - We$. Lines of constant M are calculated for water–air and $D_l = 7$ mm. For full experimental conditions, refer to [12] (Courtesy of Annual Reviews, Inc.)

Correlations for plain jet airblast nozzles are summarized in Table 24.2.

Kim and Marshall [14] derived two separate correlations for plain jet airblast nozzles. Equation 24.1.i was derived for the convergent kind, and 24.2.ii for the double concentric type. Their equations consider many different variables including liquid properties and nozzle geometry.

Equation 24.1.iii by Nukiyama and Tanasawa [15] is one of the most commonly used correlations for plain jet nozzles. However, it neglects the effect of the diameter of the discharge orifice. In their experiment though, Nukiyama and Tanasawa did investigate the effects of the exit orifice diameter, but concluded that its effect was negligible.

A study conducted by Browner [16] found that the Nukiyama–Tanasawa equation was in fact a very poor correlation. In his experiment, he obtained experimental values that were considerably smaller than those predicted by the equation. He attributed this error to the poor technique used by Nukiyama and Tanasawa, which was not able to detect the finer droplets produced. Kahen et al. [17] came up with 24.2.iv in Table 24.2, which is a modified version of 24.2.iii. They state that the modified version is valid for all conventional twin fluid nozzles, and not just for the concentric type. Figure 24.15 shows comparisons for the original and modified equations, using the properties of water, and setting Q_A/Q_L to 400 and U_R to 10. What is interesting is that 24.2.iv actually predicts higher SMD values than the original equation when plotted against Q_A/Q_L.

Lorenzetto and Lefebvre [18] and Rizk and Lefebvre [19] also derived two similar equations containing the same variables. One primary difference between

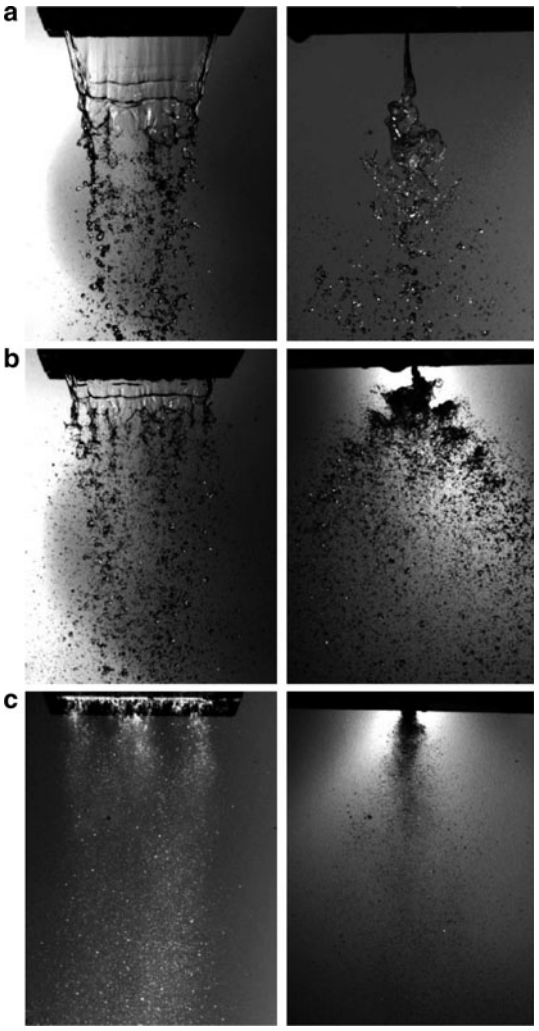


Fig. 24.14 Example of the air-blasted liquid sheet oscillation regimes [13]. Field of view, 10.4 × 14 cm. (**a**) Zone C: air velocity, 17 m/s, water velocity, 2.1 m/s. (**b**) Zone B: air velocity, 20 m/s, water velocity, 1.7 m/s. (**c**) Zone A: air velocity, 60 m/s, water velocity, 0.6 m/s (Courtesy of Springer)

the two was that Lorenzetto and Lefebvre's equation 24.2.v suggested that d_0 only had an impact on low viscosity fluids, while Rizk and Lefebvre's equation 24.2.vi stated that d_0 always played a major role. Lefebvre [1] pointed out that it was in fact Rizk and Lefebvre whose equation was the more accurate one, especially for low viscosity fluids.

Thus far, all the graphs provided have compared SMD with regards to some nozzle attribute. Figure 24.16 plots 24.2.v and 24.2.vi as a function of various liquid properties. The constants used were as follows: $\mu = 0.1$ Pa s, $\rho = 1{,}000$ kg/m^3, $\sigma = 0.05$ N/m, GLR $= 1$, liquid mass flow rate $= 50$ g/s, $d_0 = 0.5$ mm and $U_R = 1$.

Kahen et al. [17] found that 24.2.vi, by Rizk and Lefebvre [19] often underestimated the SMD from its actual value. So they proposed a modification

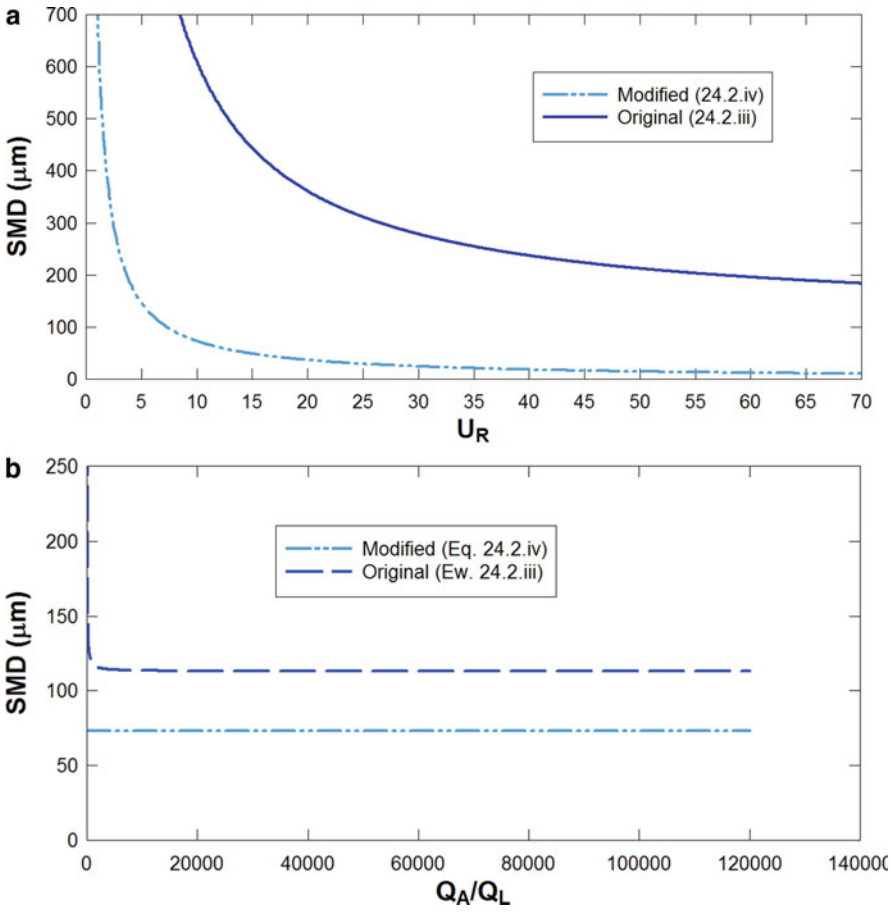


Fig. 24.15 The original and modified versions of the Nukiyama–Tanasawa equation using properties of water with $Q_A/Q_L = 400$, $U_2 = 10$, when (**a**) plotted against U_R and (**b**) against Q_A/Q_l

to it. This modified version proves to be the most accurate when predicting the size of the droplets of a generic twin-fluid nozzle. Comparisons between the modified 24.2.vii and original 24.2.vi equations can be found in Fig. 24.17. Equation 24.2.vii does not make any significant changes. Instead, it just adjusts the exponents and the coefficients for better accuracy. It predicts a slightly higher influence of the GLR, and a slightly lower influence of U_R.

Ingebo and Foster [20] and Ingebo [21] derived 24.2.viii and 24.2.ix, which are two similar equations, for two separate conditions. Both equations relate SMD to U_R^3, while all the other equations put the exponent at 1 or 2. Also, while $We \cdot Re < 10^6$, SMD is related to d_0^2, but when $We \cdot Re > 10^6$, SMD is related to $d_0^{0.5}$. Figure 24.18 shows that at some point or another, the two equations do intersect with each other, assuming all variables are equal.

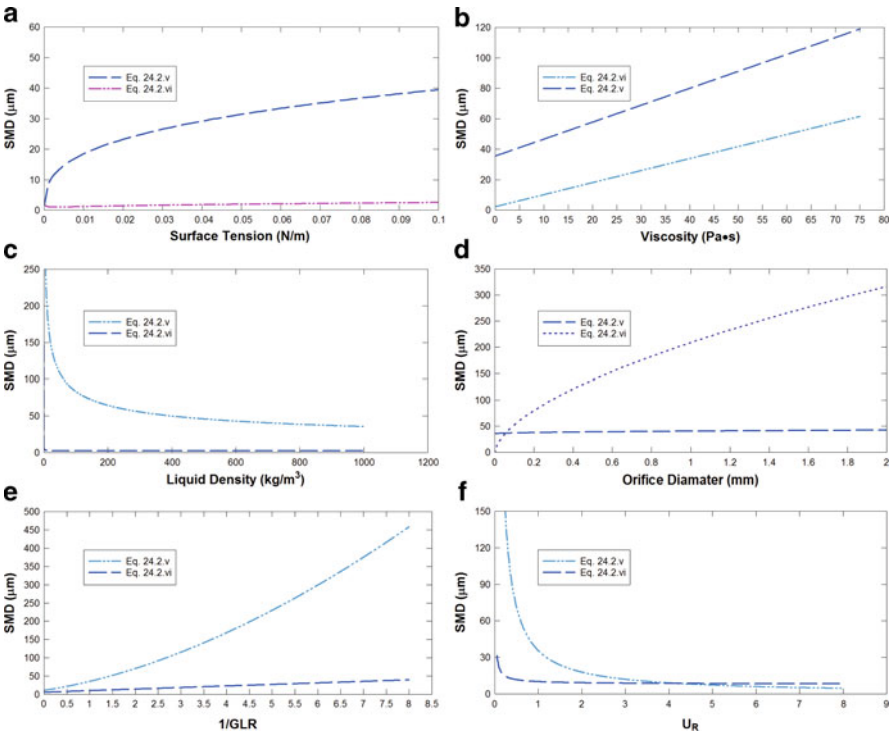


Fig. 24.16 Comparisons of 24..2.v [18] and (24.21) using $\mu = 0.1$ Pa·S, $\rho = 1000$ kg/m^3, $\sigma = 0.05$ N/m, GLR $= 1$, $m_L^a = 50$ g/s, $d_0 = 0.5$ mm, $U_R = 1$. [19] plotted against (**a**) surface tension, (**b**) viscosity, (**c**) liquid density, (**d**) orifice diameter, (**e**) GLR, and (**f**) velocity ratio

Many of the more recent SMD correlations for plain jet nozzles contain nozzle constants, such as those derived by Barreras and Eduardo [5] 24.2.x, Harari and Sher [22] 24.2.xi and Broniarz-Press et al. [23] 24.2.xii. The equation for minimum diameter derived by Isaac et al. [24] also contains a constant. In a sense, these constants indicate that the correlations are not complete, as the constants can only be determined experimentally. At the same time, the constants also ensure that the correlations are valid for a wide range of properties, and not just for a specific type of nozzle. This turns out to be true in the case of Harari and Sher. They proposed their correlation as a generic one valid for all plain jet nozzles. Their formula was later modified by Mulhem et al. [25] in 24.2.xiii, for a suspension type of spray, where they found that the constant $B = 0.21 d_l Oh^{0.0622}$.

Of the correlations mentioned above, (24.2.x) found that SMD was a function of a nozzle constant, its exit orifice diameter and the liquid's Reynolds number. Another unusual equation is 24.2.xi. It is the first formula that extensively covers the properties of air, rather than neglecting them. Both equations can be found in Fig. 24.19, where Fig. 24.19a shows 24.2.x plotted as a function of Reynolds

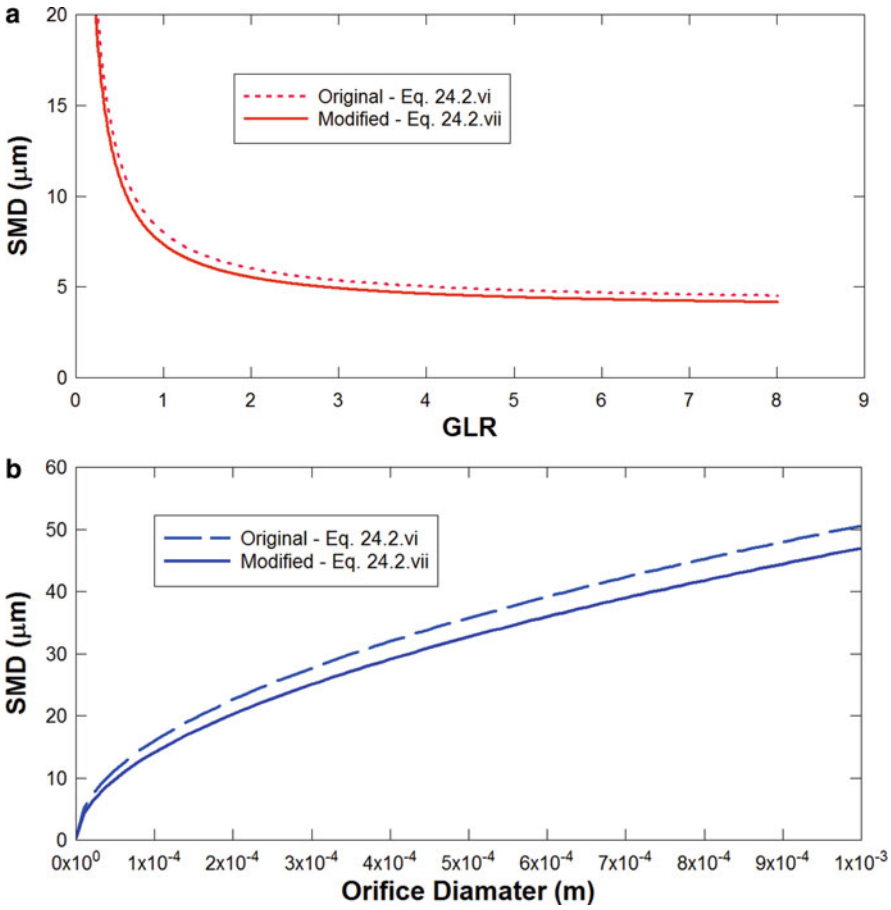


Fig. 24.17 The original and modified versions of the Rizk–Lefebvre equations plotted against (**a**) GLR, (**b**) orifice diameter

number at various nozzle diameters. The nozzle constant was set to its ideal value of 1,267. Figure 24.19b shows 24.2.xi plotted as a function of Weber's number at various values for B and GLR.

The remaining correlations from Table 24.2 which have not been discussed are the ones by Liu et al. [26] 24.2.xv and Antkowiak and Heim [27] (24.2.xvi). These two equations are derived for very specific cases. Liu et al. introduced a new variable in their correlation, the ratio of the liquid/gas mass flux. Because of this, comparison between other equations becomes difficult. In contrast, the Antkowiak–Heim equation considers no liquid properties, since it is valid only for water. This makes it very hard to compare as well.

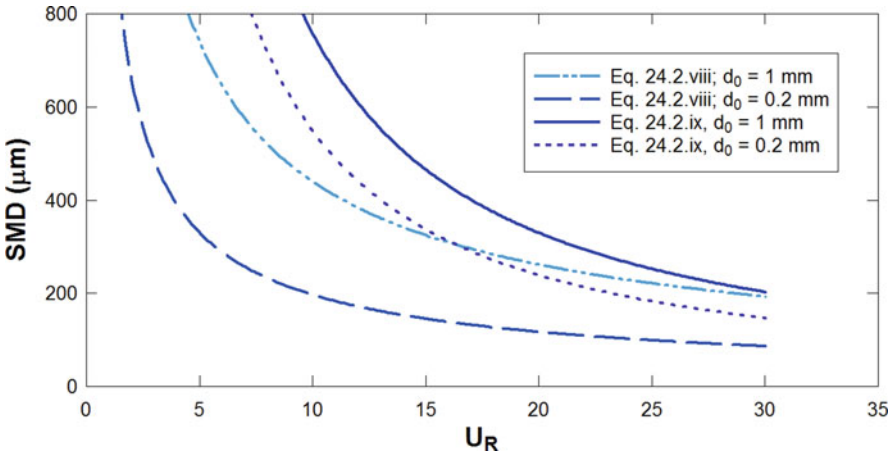


Fig. 24.18 Equations 24.2.viii and 24.2.ix at different values of film thickness

Air-Assist Nozzles

Unlike airblast nozzles, air-assist nozzles operate at low flow rates, but the air supply is kept under pressure. However there is no restriction on the velocity of the air or liquid. Because the air is kept under a pressurized source, it must only be supplied when it is needed, and not continuously. As the name suggests, in *air-assist* nozzles, air is supplied only when needed, whereas in *airblast* nozzles, the air is supplied continuously. Performance correlations can be found in Table 24.3.

The SMD correlations in Table 24.3 for air-assist nozzles contain at least one condition that makes it difficult to compare them with each other. For example, 24.3.i derived by Sakai et al. [28] contains restrictions on the liquid, and 24.3.v by Wu et al. [29] assumes that there are no aerodynamic effects on the liquid. The most generic equation in Table 24.3 is 24.3.vii derived by Simmons [30]; however, even it contains a restriction that the nozzle must be of the externally mixing type. Also, due to the constant C present, the equation has very limited applicability. The reason on these conditions was explained, in part, by Lefebvre [1]. He said that differentiating between an air-assist and an airblast nozzle is often arbitrary. And many times, a nozzle classified as one may be the other. In other words, a nozzle may be both air-assist and airblast.

The two most similar equations in Table 24.3 are 24.3.ii and 24.3.iii, derived by Inamura and Nagai [31] and Elkotb et al. [32], respectively. However 24.3.ii contains film thickness as a variable, while 24.3.iii contains the discharge orifice diameter. Since the two variables are different, the equations cannot be compared. However, the effects of each variable individually are considered in Fig. 24.20. The constants were set as follows: $We = 10{,}000$, $Re = 10{,}000$ and GLR $= 10$. By inspection it is obvious that this formula is not dimensionally correct. Reynolds number is said to have a larger impact on SMD than the Weber number. This implies that liquid viscosity is more crucial than surface tension.

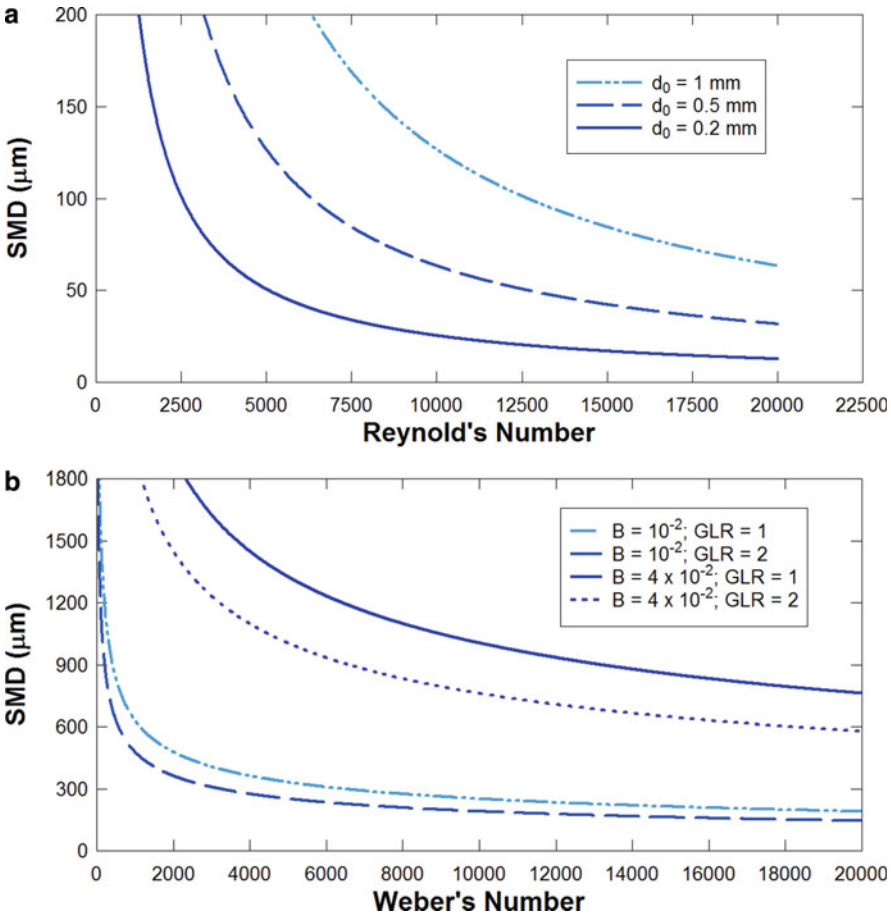


Fig. 24.19 (**a**) Equation 24.2.x at different nozzle diameters, (**b**) (24.26) at different values of the constant B and GLR

Hewitt [34] derived formulas for Mass Mean Diameter (MMD) and Number Mean Diameter (NMD) for air-assist nozzles. He claims that SMD is primarily a function of liquid density and air velocity. The effects of nozzle geometry are neglected from his study, as his study was aimed more at rotary nozzles (as explained later in "Rotary Nozzles" section).

Effervescent Nozzles

Effervescent atomization is a special form of the twin-fluid atomization in which a small amount of gas is used to generate bubbles inside the body of the nozzle and then the resultant bubbly flow is forced through an orifice [1]. Effervescent

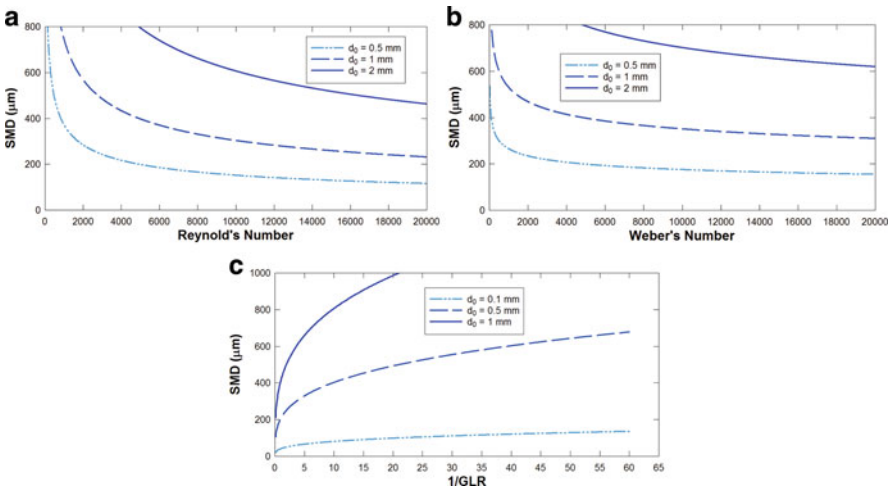


Fig. 24.20 The equation of Elkotb et al. [32] plotted at different values of nozzle diameter with $We = 10{,}000$, $Re = 10{,}000$ and GLR = 10. (**a**) Reynolds number, (**b**) Weber number, (**c**) GLR

atomization is highly effective, although the amount of gas that is used is substantially less than that used in the air-blast atomizers. When the bubbly flow exits the nozzle, the liquid pressure drops and the bubbles expand through the outlet orifice and cause the liquid to squeeze into thin ligaments, which are subsequently broken up by the combined effect of the liquid velocity and the expansion of the gas bubbles. The bubbles can be generated by forcing air through small holes into the liquid flow, or by liquid flashing in which the expansion of the vapor phase inside the liquid breaks up the liquid into small droplets.

Effervescent atomizers are already employed or may potentially be used in various spray systems such as, the gas turbine combustors, furnaces, and boilers [10], combustion of diesel or gasoline fuel containing dissolved CO_2 [11], atomization of viscoelastic liquids [13], atomization of liquids containing nanoparticles [35], etc.

A typical effervescent atomizer is shown in Fig. 24.21. It consists of liquid and gas supply ports, a mixing chamber where the gas is bubbled into the liquid stream, and an exit orifice. Liquid is supplied to the atomizer through a port at the top and flows down inside a perforated central tube to the exit orifice. The gas, which is at a pressure slightly higher than that of the liquid, is supplied to an annular chamber surrounding the perforated central tube, and generates bubbles in the liquid. The generated bubbly flow exits the orifice.

The successful operation of effervescent atomizers has been dependent on the ability to maintain a stable uniform sized bubble flow. Bubbly flows depend on nozzle geometry, air and liquid flow rates, and they become influenced by pressure and velocity instabilities. The stability of bubbly flows depends upon two factors: (1) bubble coalescence and (2) characteristics of the bubble formation, which may affect their coalescence. The bubble formation may occur at various regimes, which

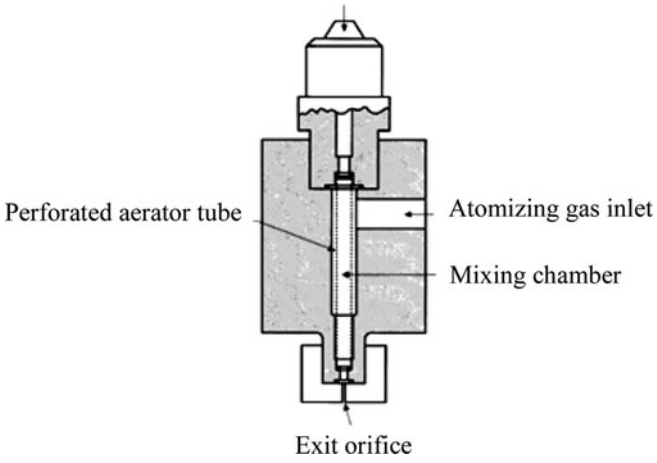


Fig. 24.21 Schematic design of a typical effervescent atomizer (From [10]. With permission from Elsevier)

depend on the velocity of the gas phase through the orifice. The size of these bubbles affects their transport in the liquid flow and also the interaction between the bubbles. Contact between the bubbles leading to coalescence disrupts the stability of the bubbly flow regime. The very large difference in density between the gas and the liquid causes a delay in the acceleration of the newly injected bubbles, which enhances the possibility of bubble coalescence.

The mechanism of liquid atomization has been systematically studied by several workers such as Lefebvre and Sojka and coworkers, e.g., [36–39]. At the right conditions, where a bubbly two-phase mixture forms in the mixing chamber and flows toward the exit orifice, the bubbles experience a sudden pressure relaxation and expand rapidly, thereby shattering the liquid into drops, as shown schematically in Fig. 24.22.

Effervescent atomization uses the atomizing gas to perform two separate functions that lead to enhanced liquid atomization. The gas-phase forces the liquid to flow through a small fraction of the discharge orifice cross section leading to a decrease in the size of the liquid shreds and ligaments and thus the formed droplets. Also, the momentum of the rapidly expanding gas has a shattering effect on the liquid flow leaving the nozzle exit, which enhances the liquid atomization.

Huang et al. [40] investigated the effects of the internal flow patterns on droplet characteristics. They visualized the bubble forming process with a high-speed camera and measured the droplet size using phase Doppler anemometry. They identified three regimes of the two-phase flows inside the discharge orifice: bubbly flow, annular flow and the intermittent flow. The flow patterns transferred from bubbly flow to intermittent flow and then to annular flow with decreasing water flow rate. In addition, with increasing working pressure or decreasing water flow rate, the SMD of the droplets decreased and the axial mean velocity increased. Figure 24.23 shows their photographs of the water flow in the bubbly-flow regime at four conditions.

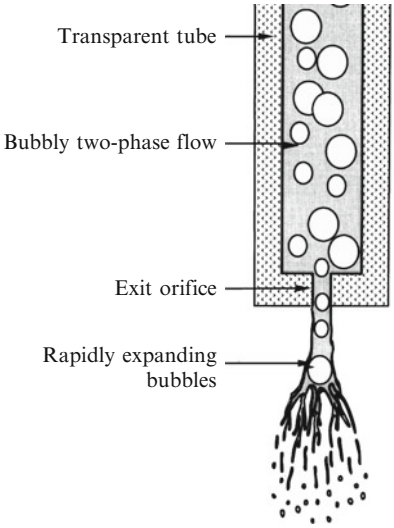


Fig. 24.22 Mechanism of liquid atomization through the bubbly flow and bubble expansion in effervescent atomization. (From [10]. With permission from Elsevier)



Fig. 24.23 Visualization of the bubbly flow in effervescent atomization under various conditions. (From [40]. With permission from the Visualization Society of Japan)

There are various experimental and numerical works that address spray characteristics in effervescent nozzles (e.g., [10, 37]). For instance, the variation of the droplet SMD versus the GLR at various injection pressures is shown in Fig. 24.24 [37]. The experimental data shown in Fig. 24.24 were obtained at the relatively low injection pressures that are of interest to gas turbine and spray coating applications.

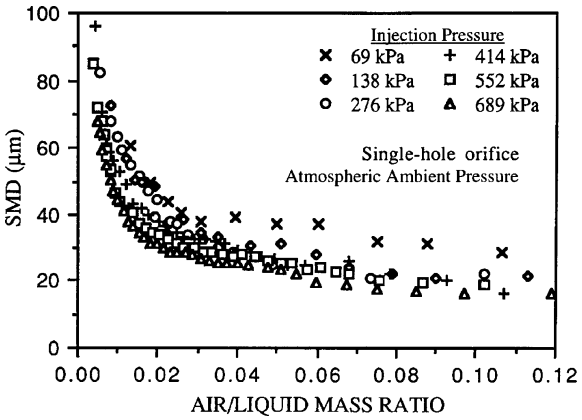


Fig. 24.24 Spray SMD versus the air/liquid mass ratio at various injection pressures. (From [37]. With permission from Begell House Inc.)

There are also few numerical and theoretical studies on the effect of various parameters on the effervescent spray characteristics. Neglecting the secondary atomization and following a stability analysis, Lund et al. [36] obtained the following theoretical correlation for the spray SMD

$$\mathrm{SMD} = \left[\frac{3}{2}\sqrt{2}\pi {d_1}^3\left(1+\frac{3\mu_1}{\sqrt{\rho_1\sigma_1 d_1}}\right)^{1/2}\right]^{1/3} \tag{24.5}$$

where d_1 represents the ligament diameter and ρ_1, μ_1, and σ_1 are the liquid density, viscosity, and surface tension, respectively. Equation 24.5 does not take into account the aerodynamic effect of the gas surrounding a ligament. Therefore, other workers have improved the Lund's model by incorporating other effects, such as the relative velocity between the gas and ligaments [38] and also considering the effervescent atomization as a stochastic process that produces a droplet size distribution [39]. The correlation by Buckner and Sojka [41] assumes that energy, mass, and momentum are conserved during atomization. This is not true in practice, as energy, mass, and momentum can be lost due to various effects. Lin et al. [42] derived a formula that did consider secondary atomization, but once again their formula contains variables and constants which make its applicability very limited.

In order to obtain a correlation, the outflow of the effervescent spray was simulated by a numerical model based on the Navier–Stokes equations and the particle tracking method. The external gas flow was considered turbulent. In droplet phase modeling, Lagrangian approach was followed. Droplet primary and secondary breakup were considered in their model. Secondary breakup consisted of cascade atomization, droplet collision, and coalescence. The droplet mean diameter under different operating conditions and liquid properties were calculated for the spray SMD using the curve fitting technique [43]:

The SMD (cm) correlation right at the nozzle exit is as follows:

$$\text{SMD}\,(y \to 0) = 0.00505\left(\frac{\text{GLR}}{0.12}\right)^{-0.4686}\left(\frac{P_{\text{in}}}{5\times 10^6}\right)^{-0.1805}\left(\frac{D_{\text{noz}}}{0.2}\right)^{0.6675} \times \left(\frac{\mu_{\text{l}}}{0.2}\right)^{0.1714}\left(\frac{\sigma_{\text{l}}}{46}\right)^{0.1382} \tag{24.4.iv}$$

For distances close to the nozzle exit ($0 < y < 1$ cm), the following correlation best fits the data:

$$\begin{aligned}\text{SMD}\ \ (0 < y < 1\text{cm}) = 10^{-4}y\Bigg\{&1.103\left(\frac{\text{GLR}}{0.12}\right)^{-0.218} \\ &+ 14.72\left(\frac{\text{GLR}}{0.12}\right)^{-0.3952}\left(\frac{\mu_{\text{l}}}{0.2}\right)^{0.1571}\left(\frac{\sigma_{\text{l}}}{46}\right)^{0.8199}\Bigg\} \\ &+ 0.00505(1-y)\left(\frac{\text{GLR}}{0.12}\right)^{-0.4686}\left(\frac{P_{\text{in}}}{5\times 10^6}\right)^{-0.1805} \\ &\times\left(\frac{D_{\text{noz}}}{0.2}\right)^{0.6675}\left(\frac{\mu_{\text{l}}}{0.2}\right)^{0.1714}\left(\frac{\sigma_{\text{l}}}{46}\right)^{0.1382}\end{aligned} \tag{24.4.v}$$

And finally for the droplet SMD (cm) downstream of the nozzle the following correlation is obtained:

$$\begin{aligned}\text{SMD}\ (1\text{cm} < y < 20\text{cm}) = 10^{-4}\Bigg\{&1.103y\left(\frac{\text{GLR}}{0.12}\right)^{-0.218} \\ &+ 14.72\left(\frac{\text{GLR}}{0.12}\right)^{-0.3952}\left(\frac{\mu_{\text{l}}}{0.2}\right)^{0.1571}\left(\frac{\sigma_{\text{l}}}{46}\right)^{0.8199}\Bigg\}\end{aligned} \tag{24.4.vi}$$

In above equations GLR is the gas (air) to liquid mass ratio, P_{in} (g/cm s^2) is the injection pressure, D_{noz} is the nozzle diameter (cm), μ_{l} (g/cm s) is the liquid dynamic viscosity, σ_{l} (g/s^2) is liquid surface tension. Note that all parameters in Qian et al. correlation are expressed in CGS units.

Xiong et al. [44] developed a three-dimensional model of droplet-gas two-phase flow and studied the evolution of spray downstream along the exit orifice in an effervescent atomizer. The model was used to calculate the mean size and statistical distributions of atomized droplets under various operating conditions. Their key results show that the gas to liquid mass ratio is one of the most important control parameters and increasing this parameter will decrease the droplet size gradually and finally tend to a certain limitation. They also found that a decreasing nozzle exit favors primary breakup, while high injection pressure has more influence on the secondary atomization.

Table 24.4 shows performance correlations for effervescent nozzles. In general, effervescent nozzles exhibit a low SMD if the air to liquid mass flow rate is high [45].

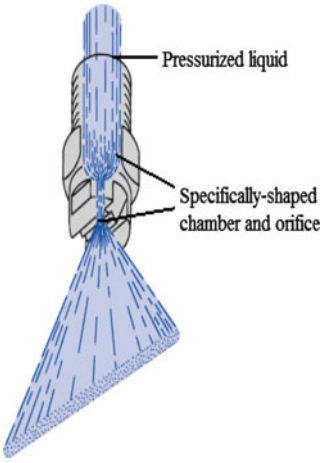


Fig. 24.25 The basic mechanism in hydraulic nozzles (Courtesy of Lechler, Inc.)

Hydraulic Nozzles

Hydraulic atomization involves the use of pressurized liquid, where the liquid is forced through a specifically shaped chamber and orifice. This increases the velocity of the liquid and breaks it into droplets. This is pictured in Fig. 24.25. There are many possible shapes that could be created using a hydraulic nozzle. As mentioned before, a full cone and hollow cone spray could be produced if a swirl insert is added. Asides from this, hydraulic nozzles can also produce flat fan sprays, with spray angles ranging from 15° to 110°, and also solid streams, as shown in Fig. 24.26. These types of nozzles can be used in a wide range of applications, varying from home use such as showers and lawn sprinklers, to industrial applications such as concentrated cleaning, cutting, and product cooling.

The primary variable in the design of hydraulic nozzles is the geometry, shape, and arrangement of the orifice through which the fluid flows before exiting the nozzle. A proper design to these types of nozzles is paramount since the higher pressures which the orifice will be subjected to can quickly erode the nozzle surface and function. In their simplest form, hydraulic nozzles are known as plain orifice nozzles. Their design is very similar to simplex swirl nozzles; however, these atomizers do not rely on the swirling action of the liquid. Instead, they use hydraulic pressure to insert kinetic energy into the particles. The discharge orifice length is the most important design parameter here. The finest atomization is achieved when the discharge orifice is not very large. However, a limiting factor on the orifice length is the difficulty of shorter orifices in keeping foreign particles out of the liquid. For this reason most orifices will not be larger than 0.33 mm. The shape produced by this type of nozzle resembles a round jet of liquid. It is similar to a solid stream pictured in Fig. 24.26b, but a solid stream does not contain any droplets. Plain orifice nozzles do produce droplets, and discharge them into a jet

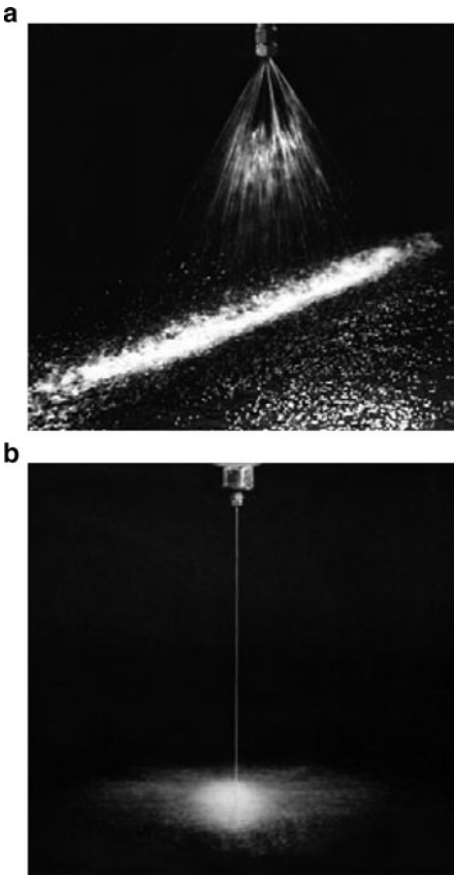


Fig. 24.26 (**a**) A flat fan shape, (**b**) a solid stream shape (Courtesy of Lechler, Inc.)

of liquid droplets. Predicting the performance of this category of nozzles is rather complex, given the simplicity of the design. Many attempts have been made in the past, yielding different formulas. Table 24.5 compiles some of these formulas.

Flat fan nozzles are another type of hydraulic nozzle. Like their name indicates, these nozzles produce a flat fan spray hydraulically. These were briefly discussed in the twin-fluid nozzles section. It was mentioned that the flat fan spray is produced by a specially shaped orifice. The same is true for hydraulic nozzles. Liquid is pushed out using pressure, and the flat fan shape is achieved by inserting a V-shaped groove at the liquid inlet. The V-shaped groove intersects with a hemispheric cavity, causing the liquid stream to atomize and form a rectangular or elliptical shape. The liquid stream will then be discharged out of the nozzle. This method is known as the axial flow method, since the liquid will flow parallel to the orifice after hitting the V-shaped groove.

Another method for producing flat fans exists, and is known as the tangential flow, or the deflector method. In it, a liquid is discharged through a hole onto a curved



Fig. 24.27 Examples of flat fan nozzles. The two on the left use axial flow, while the two on the right use tangential flow (Courtesy of Lechler, Inc.)

deflector plate. The water hits the deflector plate and assumes the shape of a flat fan. This method does not produce atomization as fine as the axial method, but it can achieve very high spray angles. The risk of clogging is also minimized here since the flow passageways are large here. Examples of flat fan nozzles are found in Fig. 24.27.

Asides from the method in which flat fan sprays are produced, another factor differentiating them is their liquid distribution. This can be divided into either even or parabolic. In even distribution, the liquid exiting the nozzle is spread out with the same concentration throughout the entire spray. Evidently, this type of distribution is difficult to achieve so most flat fan sprays do not utilize this. Even sprays are generally used when there is only one nozzle present, and the impinging surface requires the same amount of liquid throughout. If there is more than one nozzle, then a parabolic distribution is acceptable since the nozzles can be arranged so that the sprays overlap. In parabolic distribution, the liquid is deliberately concentrated more heavily at its centre. Figure 24.28a shows parabolic distribution in a flat fan spray. When a series of nozzles are placed together, it is important to offset the sprays by 5°–15° to the horizontal axis so that each spray does not interfere with each other, which can also be seen in Fig. 24.28a. The difference between even and parabolic distributions can be seen in Fig. 24.28b. Performance correlations for flat fan nozzles are found in Table 24.6.

Solid stream nozzles are another type of hydraulic nozzle, in that they use hydraulic pressure to push the liquid out. However, it is important to note that these nozzles are specifically designed to not produce any droplets, but to keep the liquid stream intact. The main advantage offered by these nozzles is their highly concentrated impact, which can be used for cleaning, cutting, and liquid recycling. Figure 24.29 shows some solid stream nozzles. The spray angle for these nozzles is considered to be 0°. In practice though, the liquid jet may disperse slightly after being discharged, leading to a spray angle of slightly greater than zero. Asides from their concentrated impact, these nozzles can operate in environments of extremely large pressures, where other types of sprays would otherwise break and not offer

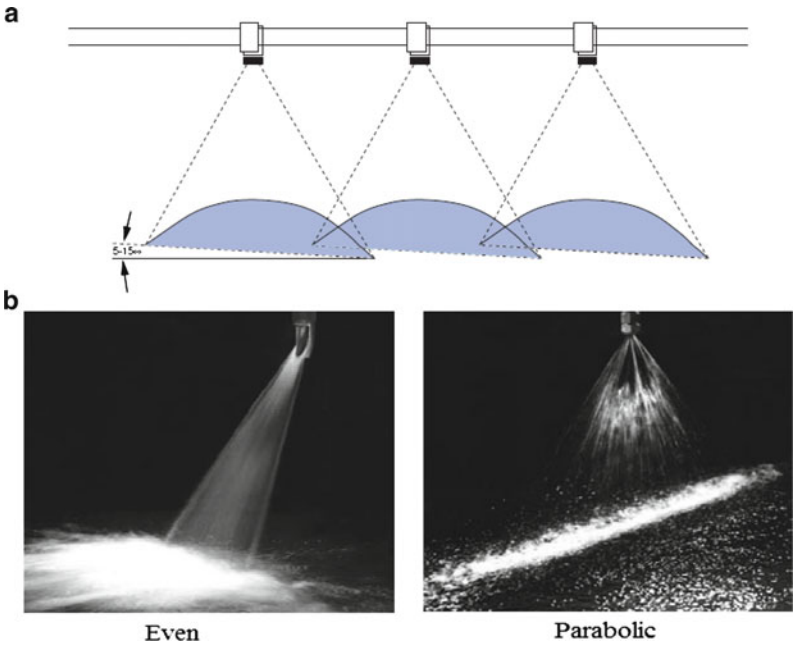


Fig. 24.28 (**a**) Flat fan sprays exhibiting parabolic distribution; (**b**) even vs. parabolic distribution in flat fan sprays (Courtesy of Lechler, Inc.)

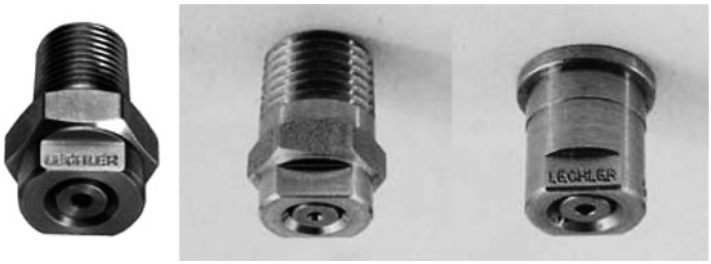


Fig. 24.29 Examples of solid stream nozzles (Courtesy of Lechler, Inc.)

any impact on the landing surface. Even among other hydraulic nozzles, which can handle large pressures compared to non-hydraulic nozzles, solid stream nozzles can withstand the largest pressures.

The solid stream shape from a given nozzle can be achieved in multiple ways. One of them involves having special chambers with contours and grooves before the discharge orifice. Another method is through adding internal vanes, similar to the axial swirl nozzle design. The internal vanes however are designed to stabilize liquid flow rather than to swirl or break it. These can be seen in Fig. 24.30.

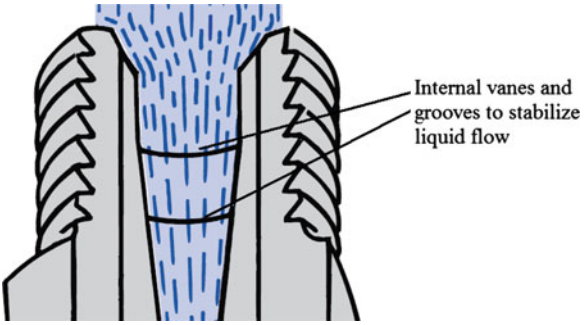


Fig. 24.30 Internal vanes and grooves to achieve a solid stream (Courtesy of Lechler, Inc.)

Plain Orifice Nozzles

The main application for plain orifice nozzles is in fuel combustion [1]. Therefore most correlations have been developed for this application [46–51]. Tanasawa and Toyoda [46] derived 24.5.i for diesel sprays in still air. Harmon [47] derived a correlation 24.5.ii that considered many different properties for both the liquid and the gas. In (24.52), liquid viscosity has very little impact on the SMD. Also, it predicts that an increase in surface tension will lead to finer atomization. This is contrary to the findings of most other experiments. Figure 24.31 shows a graph with both equations plotted plus (24.5.iii) by Merrington and Richardson [48], where d_0 was set to 0.2 mm and U_L to 50 m/s. The diesel properties were taken from [50] as follows: $\rho = 826$ kg/m^3, $\mu = 2.744$ mPa s and $\sigma = 0.0286$ N/m.

Miesse [49] predicted a formula for the $D_{0.999}$, also known as the D_{max} for plain orifice nozzles. The equation was derived using second hand data and best-fitting it. The D_{max} is related to both the Weber's number and the Reynolds number, as well as the exit orifice diameter. Weber's number is said to be less significant than Reynolds number. To observe this, the equation has been plotted in Fig. 24.32 as a function of both Weber's and Reynolds number.

Hiroyasu and Katoda [50] and Elkotb [51] provided equations by changing injection pressure rather than inlet velocity. Their correlations were derived on the basis of diesel fuel atomization, where the droplets were injected into stagnant air. The equation by Hiroyasu and Katoda (24.5.viii) considers the volumetric flow rate of the liquid, but does not consider any liquid properties. Thus the equation is not useful for liquids other than diesel. According to their equation, the injection pressure, air density and volumetric flow rate have the same effect on SMD, as can be seen from the exponents. Figure 24.33 shows a graphic representation of the formula, using an air density of 1.2 kg/m^3.

Equation 24.5.ix by Elkotb [51] considers liquid density, surface tension, kinematic viscosity, air density and injection pressure. The air density is said to have little to no impact on the SMD. Both surface tension and liquid density are raised to the exponent of 0.737, while the kinematic viscosity is raised only to 0.385.

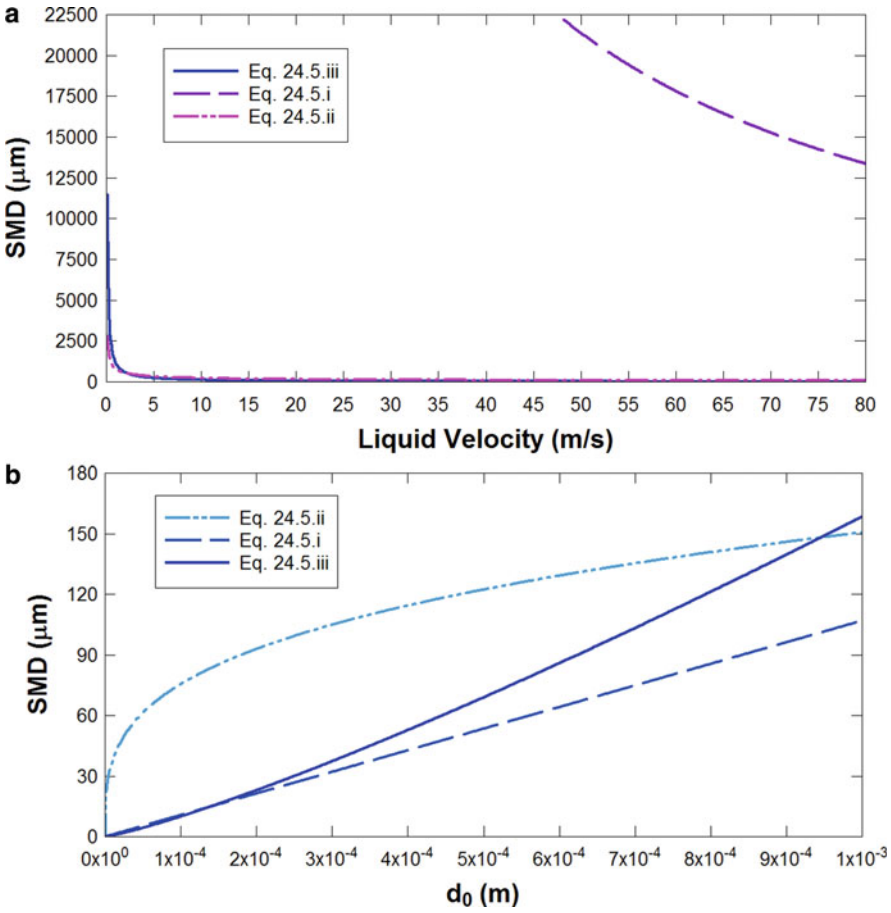


Fig. 24.31 Comparison of 24.5.i, 24.5.ii, and 24.5.iii for plain orifice nozzles using $\rho = 826$ kg/m^3, $\mu = 2.744$ mPa s, $\sigma = 0.0286$ N/m, $d_0 = 0.2$ mm, $U_L = 50$ m/s, plotted against (**a**) liquid velocity, (**b**) orifice diameter

This equation is plotted in Fig. 24.34a and b, as a function of injection pressure and liquid density respectively. The properties of diesel and air were used, and the injection pressure was set to 1.5 MPa.

At the end, Table 24.5 contains a series of similar equations in which the variable Λ constantly appears. As explained in the table, Λ represents the radial spatial integral scale of turbulence. In practice, the five formulas are very hard to apply because of the recurring presence of the Λ variable. However, when put together, they offer a very complete way of theoretically determining the SMD of plain orifice nozzles. Equation 24.5.x by Dumouchel's [52] formula applies only for cylindrical liquid jets of a high Weber number. Equation 24.5.xi by Sallam et al. [53] applies for all liquid jets injected into still air. Sallam and

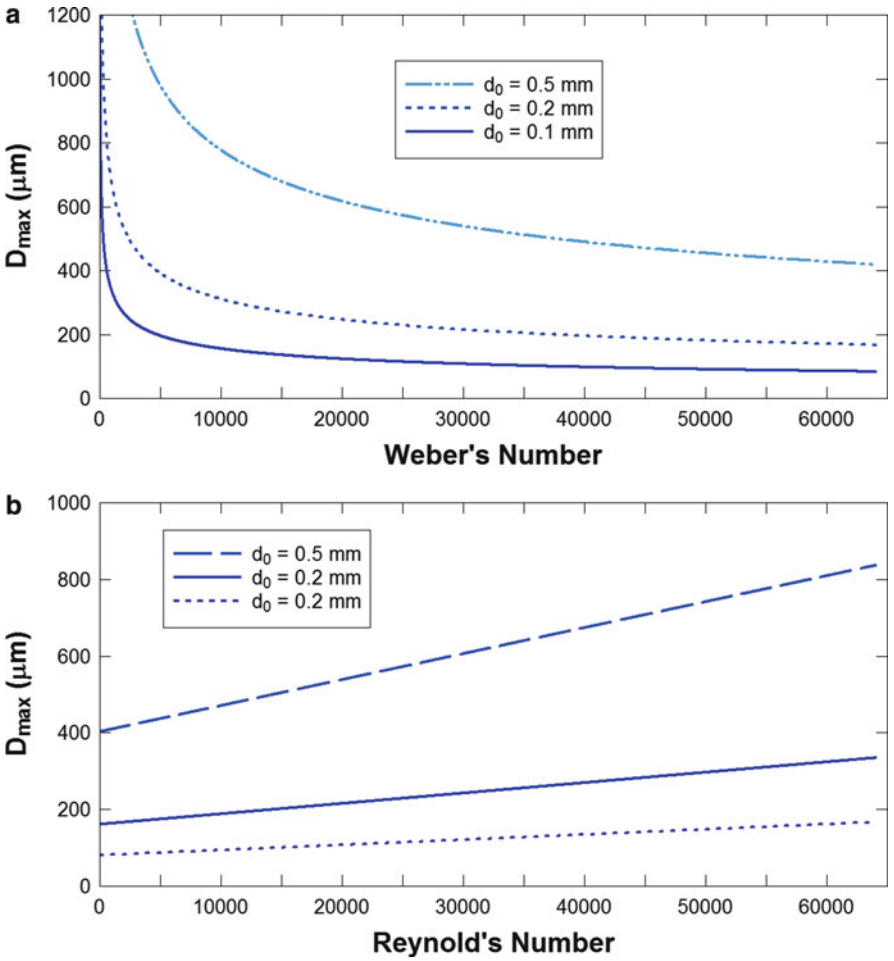


Fig. 24.32 Equation 24.5.vii plotted against (**a**) Weber's number, (**b**) Reynolds numbers, at different values of d_0

Faeth [54] derived two different equations; each of them for turbulent and round water jets injected into still air. Equation 24.5.xii was derived based on ligament properties, while (24.5.xiii) was derived based on droplet properties. Lastly, 24.5.xiv by Lee et al. [55] derived an equation for round liquid jets injecting into cross-flowing air.

Figure 24.35 shows a plot with three of the five equations plotted. Equation 24.5.x was excluded to avoid arbitrarily selecting a value for Λ, and 24.5.xii was excluded to avoid arbitrarily selecting a value for We_l. Water was used as the liquid, where $U_l = 40$ m/s and $D_n = 5$ mm. These values were selected so that the

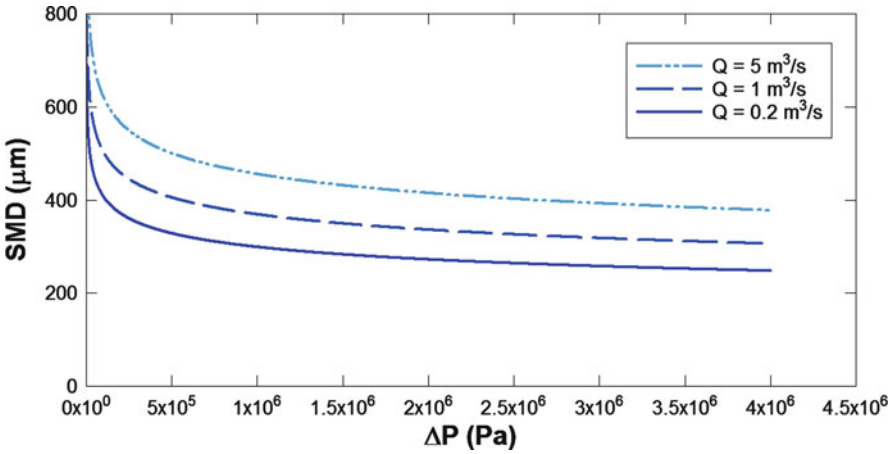


Fig. 24.33 Equation 24.5.viii plotted against ΔP at different values of Q, using $\rho = 1.2$ kg/m^3

conditions stated for all five formulas could be met. The graph itself plotted SMD/Λ against x/Λ.

Cleary et al. [56] came up with another expression for plain orifice nozzles. What is interesting about their formula is that it works only when the liquid has been subcooled (i.e., it is incompressible). It considers many relevant liquid properties, and also the nozzle's geometrical attributes. The velocity of the liquid is also considered in Reynolds and Webers numbers.

A specialized case of when two liquid jets of the same substance impinge each other to atomize was investigated by Bayvel and Orzechowski [57]. The angle between the two jets and the diameter of the liquid jets play an important role in the degree of atomization. It is predicted that the mass median droplet diameter will be proportional to $We^{-0.25}$.

Flat Fan Spray Nozzles

Table 24.6 shows correlations for various flat fan hydraulic nozzles that do not quite fall into the plain orifice category. The first three equations [58–60] are fairly old, and contain conditions and variables in them that render them incomparable to each other. Equation 24.6.i assumes that the air is still, 24.6.ii has a very small range of viscosity, and 24.6.iii completely neglects viscosity, rendering it useless for all liquids except water and oil. Equation 24.6.i, as quoted from Kreith and Goswami [58] is plotted in Fig. 24.36 as a function of injection pressure.

The last four equations listed in Table 24.4 are not actual formulas, but proportionality statements. Originally, Dombrowski and Hooper [61] derived two such proportionality statements; one for low injection pressures 24.6.iv and one for

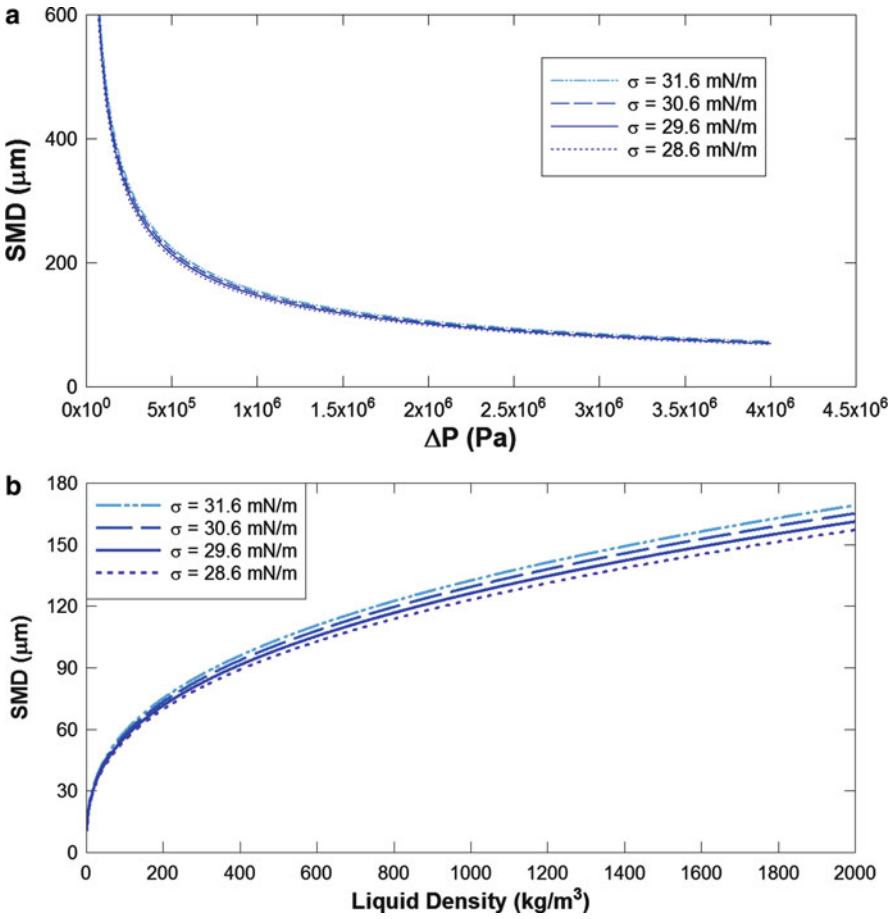


Fig. 24.34 Equation 24.5.ix plotted against (**a**) injection pressure, (**b**) liquid density, at different values of surface tension, using properties of diesel and air, and P = 1.5 MPa

high injection pressures 24.6.v. However, they neglected the effects of secondary atomization in their experiments. Later on, Kawamura et al. [62] modified the equations while considering secondary atomization effects. In 24.6.iv, the original Dombrowski–Hooper equation for low pressures, SMD is said to be a factor of slit thickness, injection pressure and air density. In the modified version 24.6.vi by Kawamura et al., air thickness is not part of the correlation. Also, while the original Dombrowski–Hooper equation for high injection pressures only considers the effects of slit thickness and air density, the modified version by Kawamura et al. 24.6.vii also adds the effect of injection pressure. Kawamura et al. attributed this to the fact that under lower injection pressures, atomization is dominated by the instability of the liquid film. At higher pressures, the injection pressure governs atomization.

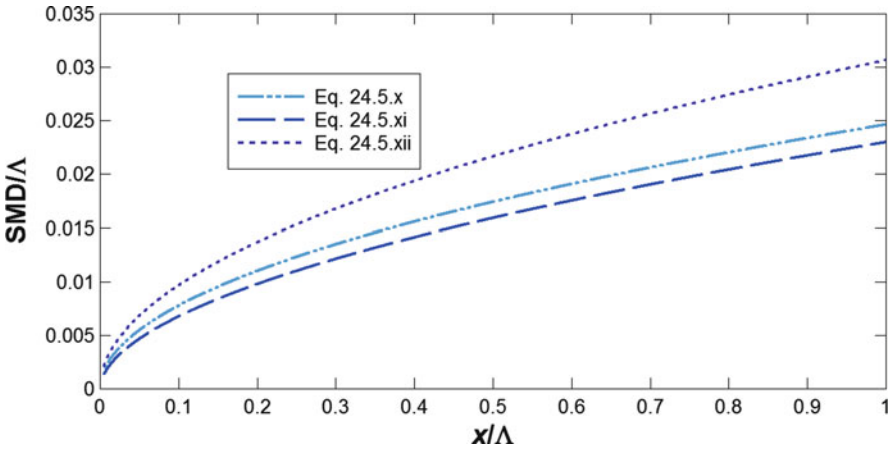


Fig. 24.35 Comparison of three recent equations for plain orifice nozzles by Lee et al. [55], Sallam and Faeth [54], and Sallam et al. [53]. Properties used were that of water, and $U_l = 40$ m/s, $D_n = 5$ mm

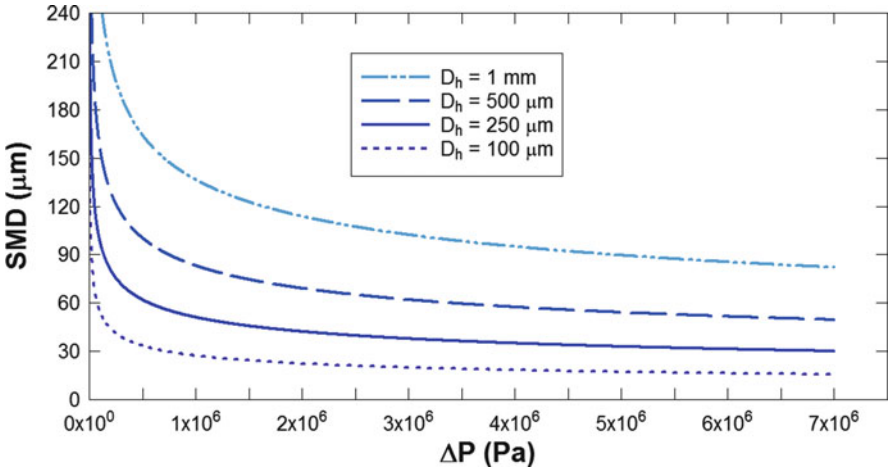


Fig. 24.36 Equation 24.6.i plotted against injection pressure at different values of hydraulic diameter

Swirl Nozzles

In swirl nozzles, a fast-swirling fluid experiences a centrifugal force as it rotates in the nozzle chamber. This centrifugal force results in the formation of a liquid sheet which later breaks into droplets. The two most common spray shapes that result from this are the hollow cone design and the full cone design. The hollow cone design is employed more frequently for its ability to create fine droplets rather than the shape of the spray. Applications for this single fluid atomizing spray include

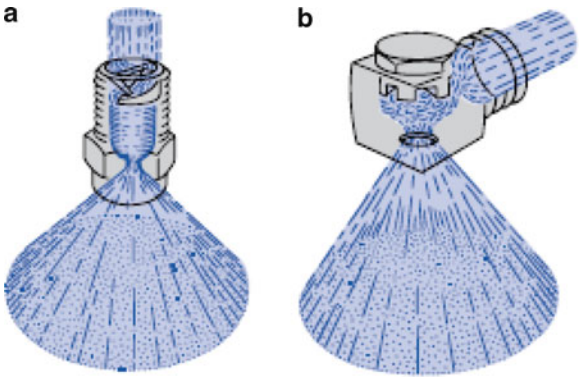


Fig. 24.37 (**a**) A schematic of a swirl nozzle with axial flow, (**b**) a schematic of a swirl nozzle with tangential flow (Courtesy of Lechler, Inc.)

scrubbers, chemical reactors, gas cooling, and dust control. The full cone spray uses internal swirling action to create a cone with uniform distribution throughout. Applications for the full cone spray include product cooling, washing, and conveyor cleaning. Swirl nozzles are the most common type of nozzles found in use today, with their uses ranging from industrial applications to aerosol cans.

Swirl nozzles come in many different designs. One variation is the direction in which to feed the liquid. The two different variations are the axial flow and the tangential flow designs. In axial flow (Fig. 24.37a), an internal vane (swirl insert) creates a conical spray that could be either hollow or filled. The small droplets created tend to be quite similar in size and relatively evenly distributed throughout the area of the spray. Spray angles for axial designs can be as high as 90°. They also offer a very large area of contact on the impact surface due to the very fine droplets of which the spray is composed. However, one very big problem with such nozzles is that the swirl insert through which the liquid flows can get clogged very easily. With regards to this, tangential flow should be used. In tangential flow (Fig. 24.37b), the liquid enters the nozzle on a path perpendicular to the output cone to generate swirling action without an internal vane. Although the droplets are not as small, they also provide a very uniform cone spray, and because there is no internal vane, clogging is very rare. Another advantage that the tangential design has is that it offers stable spray angles. In axial flow, the spray angle of the nozzle tends to fluctuate slightly; however this is not an issue in tangential flow.

Swirl nozzles that incorporate tangential flow are considered to be the "true" swirl nozzles, since nozzles with axial flow require a special vane to swirl the liquid. Also, designs with axial flow are often used in twin-fluid or hydraulic nozzles, since the swirl action alone is rarely enough to fully atomize the fluid. Axial designs are really used to complete the atomization rather than to fully perform it. On the other hand, tangential designs can atomize on their own due to the perpendicular nature of their fluid flow. The incoming liquid stream hits the wall of the nozzle, which immediately has an impact on its surface tension, and the additional swirling action that follows breaks the stream into droplets.

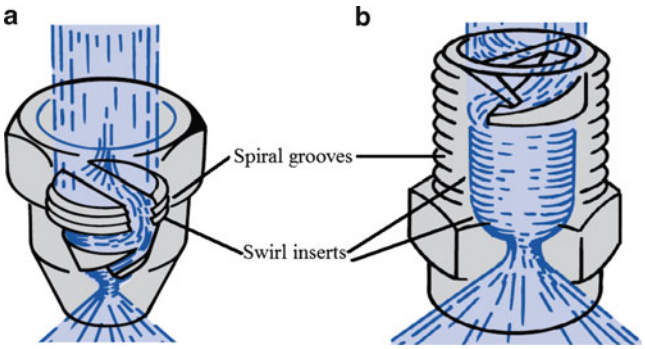


Fig. 24.38 The swirl inserts in a swirl nozzle with axial flow, for (**a**) hollow cone spray, and (**b**) a full cone spray (Courtesy of Lechler, Inc.)

The two spray shapes that swirl nozzles can produce are full and hollow cones. While the basic design outline is the same for both shapes, there are minor differences. Both shapes can be produced either tangentially or axially. In axial flow for hollow cones, a swirl insert in the nozzle chamber is added, and this swirl insert contains spiral grooves. The spiral grooves cause the incoming liquid to rotate around, creating a centrifugal force, as shown in Fig. 24.38a. And the centrifugal force causes the liquid to move away from the center, and as close as possible to the edge. Thus, when it comes out of the nozzle, the liquid exhibits a hollow cone shape. To ensure that the liquid is spread evenly throughout the ring, the spiral grooves in the swirl insert are specially positioned. This controls the liquid flow, and makes sure that its distribution remains fluid. In axial flow for full cones, a similar design, with swirl inserts and spiral grooves, exists. However in this design, the spiral grooves themselves are positioned differently, and unlike the hollow cone spray, where one swirl insert is sufficient, a full cone spray contains many swirl inserts. These can be seen in Fig. 24.38b. The purpose of these multiple swirl inserts is to break up the fluid flow internally, and to make sure that enough fluid comes from the outer edges of the hollow cone towards the centre to create a full cone. Both the swirl inserts and the spiral grooves help in making sure that the liquid is spread evenly throughout the spray.

In tangential flow, the design mechanism is also slightly different in producing a full cone and hollow cone spray. For both spray shapes, a swirl insert is not needed, as a swirl can be created without it. To produce a hollow cone spray, not much needs to be done asides from getting the liquid into the chamber. Here, it will start to swirl on its own, and the mechanism for creating a hollow cone shape is the same as that of axial flow. This mechanism is illustrated in Fig. 24.39a. To produce a full cone spray, much of the same technique is applied; however additional spiral grooves must be milled into the nozzle chamber. These grooves are located at the bottom, and are especially designed to disrupt the liquid flow, and to force enough of the liquid towards the centre to achieve a uniform full cone spray. This mechanism is outlined in Fig. 24.39b.

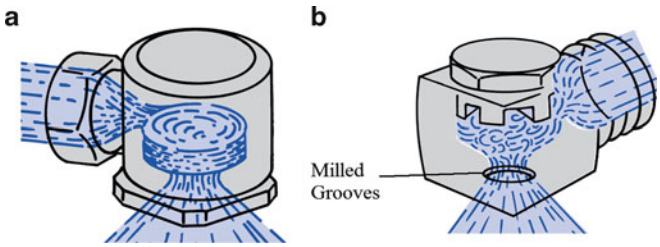


Fig. 24.39 The design mechanism inside a swirl nozzle with tangential flow. (**a**) Shows a nozzle that produces a hollow cone, and (**b**) shows a nozzle that produces a full cone (Courtesy of Lechler, Inc.)

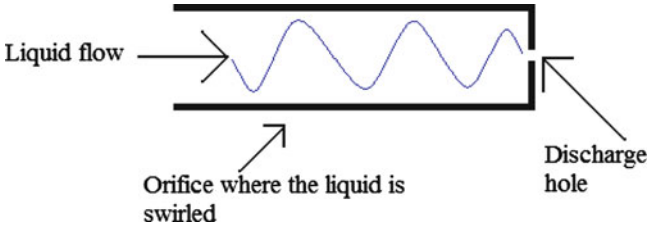


Fig. 24.40 A diagram showing the design of a typical pressure swirl chamber

The swirl nozzle comes in three varieties: Simplex, dual orifice or duplex, and spill-return [63]. In its simplest form, the swirl nozzle is known as a simplex swirl nozzle. In it, a liquid is pushed via pressure into a round-shaped orifice, where it performs swirling action, until it reaches the discharge hole. Here, the kinetic energy from the swirling action will atomize the liquid. Figure 24.40 shows a diagram outlining this design. The two main design variables in simplex swirl nozzles are the length of the swirl chamber, and the diameter of the discharge hole. A longer swirl chamber length allows the liquid to reach higher velocity, attaining very fine atomization. However, too much swirling action may lead to droplets that are too small and do not make an impact on the landing surface. On the other hand, a swirl chamber length that is too small may not achieve proper atomization. The discharge hole diameter of the nozzle should generally be kept small, since a large hole will not produce a spray. But a hole that is too small will not discharge enough liquid for impact.

Dual orifice or duplex swirl nozzles consist of two simplex nozzles placed inside one chamber. In the chamber, one nozzle surrounds the other, where the surrounding nozzle is called the secondary nozzle, and the inside nozzle is called the primary nozzle. The underlying idea behind a dual orifice design is that if the supply of liquid is low, it will flow entirely through the primary nozzle, and the resulting spray will not be any less diluted. Once the spray starts to increase, some of the liquid will flow through the secondary nozzle, increasing the coverage of the spray. The mechanism is outlined in Fig. 24.41.

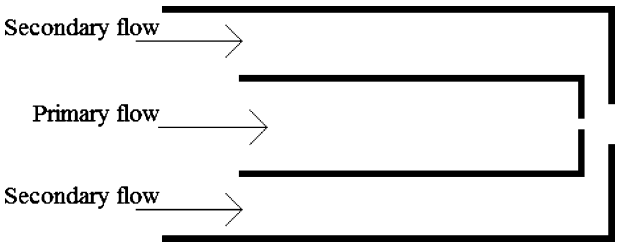


Fig. 24.41 The design of a typical dual-orifice swirl nozzle

Spill return nozzles are almost the same as the simplex types; however they contain a passageway from which any surplus liquid not atomized can make its way back to the supply source. Hollow cone shapes are the most common shapes produced from this. They tend to yield a very high quality spray since exactly the right amount of liquid is atomized, while the rest is sent back to the supply source.

Many investigations have been done on the performance of swirl nozzles. And yet, due to the complex physics in swirl atomization, much has yet to be discovered [64]. This text attempts to compile drop size correlations for the three types of swirl nozzles mentioned, and they are shown in Table 24.7. From the correlations shown below, it can be concluded that the performance of swirl nozzles depends largely on the liquid properties, and very little on the nozzle geometry.

Swirl nozzles are often used in twin-fluid nozzles, to enhance the overall atomization process in them. In some cases, the air is swirled before it comes in contact with the liquid. In other cases, both the air and liquid are swirled. An important design consideration in nozzles where both the liquid and gas are swirled is whether the gas should be swirled in the same direction, or in the opposite directions. Rotation in the same direction provides a strong circulation of fluid, while rotation in the opposite direction creates opposing shear forces, which helps in mixing the liquid and gas, and also in the atomization. Airblast, air-assist, and effervescent nozzles often contain swirling chambers.

Both prefilming and non-prefilming airblast nozzles often contain pressure swirl nozzles within their internal structures. Prefilming nozzles often contain a pair of pressure swirl chambers, each at one side of the surface where the liquid has been spread onto a film. The swirl chambers swirl the air within them before impinging it upon the liquid film. The two chambers may swirl the air in the same direction or in opposite directions. This would depend on the specific nozzle design and application, and advantages to both co-rotation and counter-rotation are the same as already outlined. Asides from the air, the liquid in the nozzle may also be swirled in some designs. Non-prefilming nozzles, as mentioned earlier, can have a variety of designs. One of these variations is that often the air, liquid, or both are swirled prior to contacting each other. Pressure swirl nozzles are sometimes found within air assist nozzles as well. Just like in the airblast nozzles, the swirl chambers may be used to swirl either liquid or gas, or both.

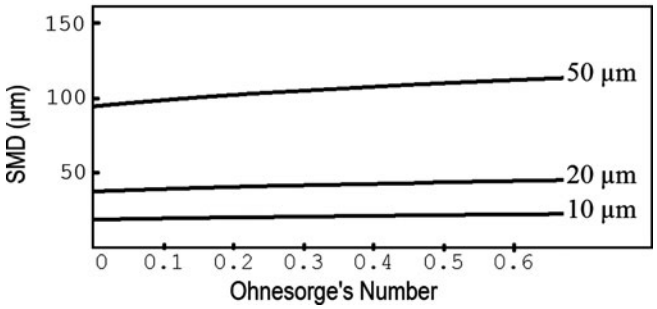


Fig. 24.42 The plot of 24.4.i, plotted against Ohnesorge's number at various ligament diameters

The first equation in Table 24.7, 24.7.i, considers all the relevant variables in swirl atomization, plus the spray angle. It was derived by Wang and Lefebvre [65]. It is very similar to the two general equations proposed by Khavkin [64], 24.7.xvi and 24.7.xvii. But their results were confined to a certain range of viscosities and surface tensions. Equation 24.75 also bears a resemblance to some of the equations in Table 24.2, such as 24.2.v and 24.2.vi.

In the section on "Twin-Fluid Nozzles," it was shown that Lund et al. [36] derived 24.4.i for effervescent nozzles. This same equation is valid for swirl nozzles. The only difference lies in the method by which the ligament diameter is determined. A formula was derived by Couto et al. [66] 24.7.ii, and can be used in conjunction with 24.4.i. The spray angle is considered in this formula as well. Equation 24.4.i is plotted in Fig. 24.42 as a function of the Ohnesorge number at different ligament diameters.

Lefebvre [63] derived 24.7.v for simplex swirl nozzles using a wide range of surface tensions. He equated SMD to be a function of injection pressure, mass flow rate, surface tension, and dynamic viscosity. Additionally, he also included the effect of air density. In his equation, he gave surface tension a smaller influence, and injection pressure a larger influence.

Equation 24.7.vi, derived by Radcliffe [70], is a function of the surface tension, liquid kinematic viscosity, liquid mass flow rate and the injection pressure of the liquid. In his experiment though, Radcliffe did not alter the value of surface tension too much. His results were focused primarily to fuel combustion, and thus his equation does not yield good values when used for other liquids like water. Jasuja [8] modified this to 24.7.vii later on, using the same experimental conditions. In his equation, mass flow rate and kinematic viscosity are slightly less significant, while the injection pressure is slightly more significant.

Kennedy [71] used six different nozzles and 25 different fuels to derive a formula 24.7.iii. His formula is a function of mass flow rate, surface tension and injection pressure. However, this is only true if $We > 10$, and assuming that the critical dimension in the Weber number is the film thickness. To get an idea of this inaccuracy, 24.7.v is plotted against 24.7.iii7, 24.7.iv, and 24.7.vi in Fig. 24.43.

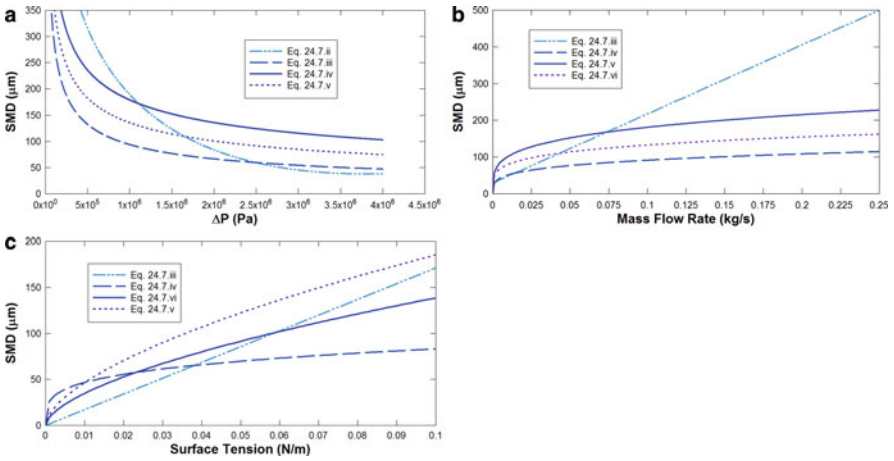


Fig. 24.43 Comparisons between four correlations for simplex swirl nozzles with $\dot{m}_c = 50$ g/s, $\Delta P = 1.5$ MPa plotted against (**a**) injection pressure, (**b**) mass flow rate, (**c**) surface tension

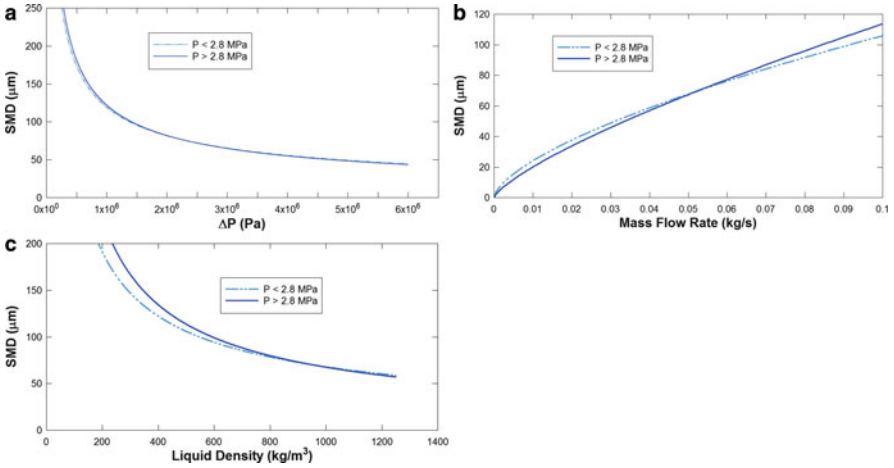


Fig. 24.44 A comparison of 24.7.iii and 24.7.iv derived by Babu et al. [67], plotted against (**a**) injection pressure, (**b**) liquid density, (**c**) mass flow rate. Properties used $\dot{m}_c = 50$ g/s, $\rho_L = 1000$ kg/m^3, ΔP = MPa

The mass flow rate of the water is set to 50 g/s, injection pressure to 1.5 MPa, and the properties of water were used.

Babu et al. [67] derived two separate equations for SMD prediction 24.7.vii and 24.7.viii. Their equations neglect many liquid properties that others do not; therefore, comparison of the equations becomes difficult. However, Fig. 24.44a does provide the two equations plotted side by side. What separates the two equations is that one is valid only when $\Delta P > 2.8$ MPa, and the other when $\Delta P < 2.8$ MPa. Figure 24.44b and c plot SMD against mass flow rate and liquid

density respectively. Mass flow rate was set to 50 g/s and liquid density was set to 1,000 kg/m^3. For the purposes of comparison, injection pressure was set to 2.8 MPa. Both equations yield almost the same results at a pressure of 2.8 MPa, meaning that the transition from one to the other is smooth.

Park et al. [68] derived 24.7.ix for duplex swirl nozzles. It is very similar to 24.5.i–24.5.iii; however it does not contain any effect of liquid mass flow rate. The formula was derived based on variations in temperature only, which caused the liquid properties to change; independent changes were not applied. The correlation indicates that surface tension has a much smaller impact on SMD in duplex nozzles than simplex nozzle. It also shows that the viscosity plays a much larger role in the atomization process, while the effect of the injection pressure is the same as in simplex nozzles. Figure 24.45 plots this equation as a function of viscosity and injection pressure at various surface tensions, using $\Delta P = 300$ kPa and mass flow rate = 50 g/s. As expected, an increase in injection pressure leads to a decrease in SMD, and an increase in viscosity leads to an increase in SMD.

Orzechowski [69] derived many different formulas, not just for swirl nozzles, but rotary nozzles too. Four correlations are accredited to him in the area of swirl nozzles. The first one presented in Table 24.4, 24.7.x, is very similar to 24.7.iii–24.7.vi. Due to the absence of surface tension in the formula, it is not fair to compare it with the other four equations mentioned.

Equation 24.92 is a formula for spill-return type of swirl atomizers, as derived by Orzechowski [69]. He attributes $D_{\max}$ to be a function of exit orifice diameter, injection pressure, surface tension and liquid density and viscosity.

Orzechowski derived two more correlations, one for kerosene 24.7.x, and the other for a water-glycerin mixture 24.7.xi. The correlations are said to be a function of film thickness, Weber number and Ohnesorge's number. The effect of film thickness and Weber number remains unchanged on both liquids. The difference arises in Ohnesorge's number, where the exponent is slightly lower for kerosene. Figure 24.46 shows a comparison of the two equations, using $t = 0.1$ mm.

Equation 24.7.xiii, derived by Jones [72], is a lengthy one, and it relates to the volume mean diameter (VMD). It considers various different liquid properties and nozzle geometry attributes, such as the nozzle length and diameter, and orifice length and diameter. It also considers flow properties such as the liquid mass flow rate and the injection pressure of the liquid. Given the completeness of the formula, there are also many conditions that must be met if the equation is to yield accurate results.

Petela and Zajdel [73] and Zajdel [74] conducted experiments on coal slurry atomization where coal particles of diameters up to 385 μm were mixed in a solution of benzoic acid and atomized using a swirl nozzle. The experiment by Petela and Zajdel [73] was conducted on monodispersed coal particles. In their experiment, 140 atomization processes were conducted; however only 74 of them were used to derive the formula given. Zajdel [74] later conducted a similar experiment using polydispersed coal particles. The resulting equations, 24.7.xiv and 24.7.xv, are shown in Table 24.7. An interesting aspect about both equations is that only ratios are considered instead of individual variables. It should be noted

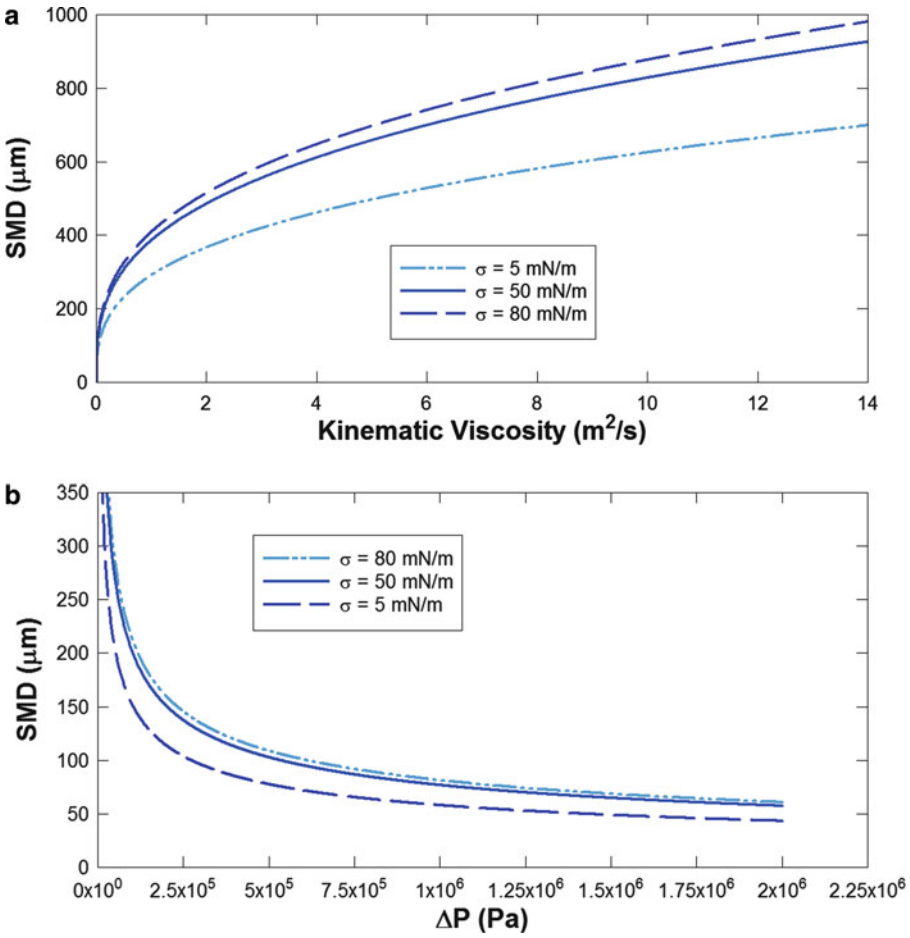


Fig. 24.45 Equation 24.7.v plotted against (**a**) kinematic viscosity, (**b**) injection pressure at the following values of surface tension (from top to bottom): 0.08, 0.05, 0.005 N/m. Properties: $\dot{m}_c$ = 50 g/s, $\Delta P = 300$ kPa

here that even though film thickness is used in the formulas presented in Table 24.7, Petela and Zajdel said that for practical purposes, using the exit orifice diameter may be better.

A more recent study on swirl nozzles was conducted by Khavkin [64]. In his book, he went into great detail on the mechanism and theory of swirl nozzles, and presented the findings of his own research. He proposed two equations for all swirl nozzles, 24.7.xvi and 24.7.xvii. Equation 24.7.xvi considers the effect of the liquid film thickness, while 24.7.xvii considers the effect of nozzle diameter. In both cases, Khavkin proposes that SMD is proportional to either $t^{1/2}$ or $(D_n)^{1/2}$. Three more constants are present within the formula. What is more important is that the

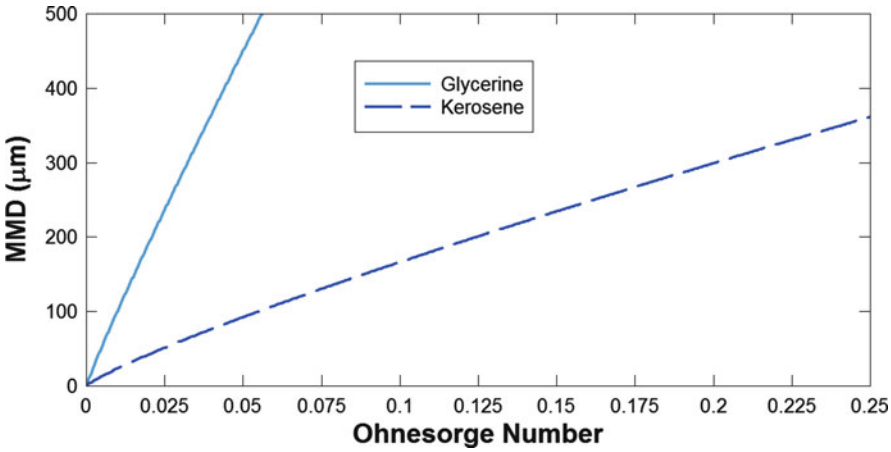


Fig. 24.46 Equations 24.7.vi and 24.7.vii for kerosene (*top curve*) and glycerin (*bottom curve*) plotted against Ohnesorge's number, $t = 0.1$ mm



Fig. 24.47 Examples of rotary nozzles (Courtesy of Lechler, Inc.)

equation considers all the relevant liquid properties, nozzle geometry and also the injection pressure.

Rotary Nozzles

Rotary nozzles employ the use of centrifugal force similar to swirl nozzles; however unlike swirl nozzles, rotary nozzles contain a disk or a plate that also rotates. The liquid to be atomized is poured from above onto the rotating surface, and the rotating disk or plate spins at very high velocities, forcing the liquid stream to break into droplets. After atomizing and leaving the nozzle surface, the spray comes in contact with the surrounding gas. Figure 24.47 shows some examples of rotary nozzles. The main advantage this type of nozzle offers is that it does not clog. Other than this, rotary nozzles are also good for their ability to create uniform

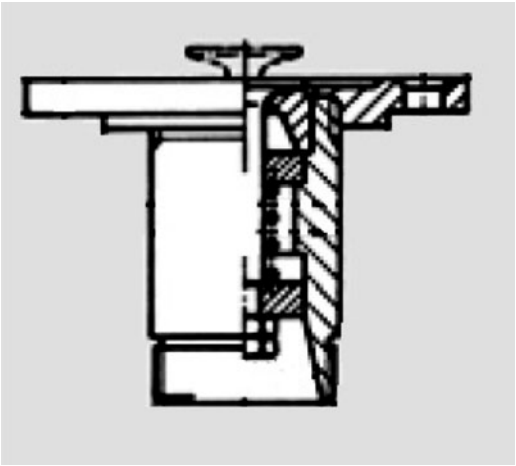


Fig. 24.48 Design of a typical flat disk rotary nozzle (Courtesy of Lechler, Inc.)

droplet sizes. Often this family of nozzles is used in boilers, fire extinguishing and more obviously, in lawn sprinklers.

The way in which rotary nozzles are classified usually relates to the type of surface the liquid will be rolled on. These include flat disk, disk with vanes, windmill (slotted wheel) and rotating cups. Often rotary nozzles mix the liquid with gas to improve the atomization, creating a twin fluid rotary nozzle.

In flat disk nozzles, the liquid is poured from the top, and since the disk is bare with no grooves or edges, the liquid spreads uniformly throughout it. As the disk spins, centrifugal force is created, causing the liquid to burst out in droplets. Figure 24.48 shows a flat disk nozzle design. At this stage, each droplet contains a ligament behind it, which will break after a while into tiny droplets. If the liquid is poured at high rates then instead of the ligaments forming behind the droplets, the ligaments will form continuously along the entire edge of the disk. Here the ligaments will stick out, and bit by bit, droplets will break off them. However the ligament size will remain steady because after each droplet breaks away, the liquid on the disk causes the ligament to enlarge to its original length.

Another problem encountered when dealing with disk rotary nozzles is that when extremely high rotational speeds are reached, ligaments are unable to accommodate the liquid flow rate. And so instead of a series of ligaments forming at the edge of the disk, a solid sheet of liquid is formed from which droplets break apart. There is nothing wrong with this in that the nozzle still functions; however the droplet size distributions are more random and more spread out. The solution to this problem is to use a windmill-type nozzle. In this type of nozzle, cuts are made at the edge of the disk, with the remaining teeth twisted. This variation in the overall radius of the rotary surface increases the rotational speed which the ligaments can accommodate.

Unlike in ultrasonic nozzles (discussed in "Ultrasonic Nozzles" section), the atomization process on rotary nozzles is random, and can occur at any time at any

point on the rotating surface. The theoretical performance correlations of vaneless rotary nozzles can be found in Table 24.8, as compiled by Lefebvre [1].

A common issue encountered with all flat disk rotary nozzles is that the liquid often tends to slip from the solid surface. The solution to this is to add vanes or inserts onto the rotating channel. This design is called the vaned disk design. This type of nozzle is used at high rotating speeds, since slippage does not usually occur at low rotating speeds. The slippage of liquid is prevented in this because the spiral or radial vanes contain the liquid inside. However, the vanes are designed to direct the liquid towards the periphery of the disk. At some point before reaching the edge, the liquid will in itself reach the velocity equivalent to the rotation speed of the disk. Table 24.9 shows empirical correlations for the mean drop sizes of vaned disks.

Rotary nozzles are most effective when being used on low to medium viscosity liquids. When dealing with high viscosity liquids, atomization becomes very coarse and this is not good for most applications. The solution to this is to use the rotating cup nozzle. In this nozzle, instead of a flat, vaned, or radially cut surface being used as the rotary surface, a cup with a certain depth is used. The walls of the cup are usually inclined by 5–6° [42]. Their performances can be determined by equations found in Table 24.10.

The last major type of rotary nozzles is the twin-fluid rotary nozzle. Its main application is combustion for various devices. The air (or another gas) is supplied with a spinning fan, at a flow rate much greater than that of the liquid. Once the air comes in contact with the liquid, the droplets produced become smaller and the spray is finer. This type of atomization is also very good for high viscosity liquids. Table 24.11 shows some mean drop size correlations for twin fluid rotary nozzles.

Vaneless Disk Nozzles

Table 24.9 presents ten correlations for vaneless rotary nozzles. The three equations for $D_{0.999}$, as derived by Bar [75], Walton and Prewett [76], and Fraser and Eisenklam [77] are very similar to each other, with the only difference being in their coefficients. The equations were derived for atomization by droplet formation, ligament formation and sheet formation respectively. From the coefficients, it can be said that the coarsest atomization occurs during droplet formation, followed by ligament formation, and finally sheet formation. It should be noted though that while sheet formation exhibits the lowest $D_{0.999}$, it also exhibits the highest drop size distribution, as already mentioned. The three equations mentioned are plotted in Fig. 24.49 for the purposes of comparison.

Two equations have been compiled for rotary atomizers exhibiting droplet atomization. Tanasawa et al. [78] proposed 24.8.iv that considered the relevant liquid properties, volumetric flow rate, rotational speed and disk diameter. The formula does include liquid viscosity but the viscosity does not have a very large impact on the SMD. Matsumoto et al. [79] proposed a much simpler equation 24.8.vii, and related SMD to only the disk diameter and the liquid's Weber number.

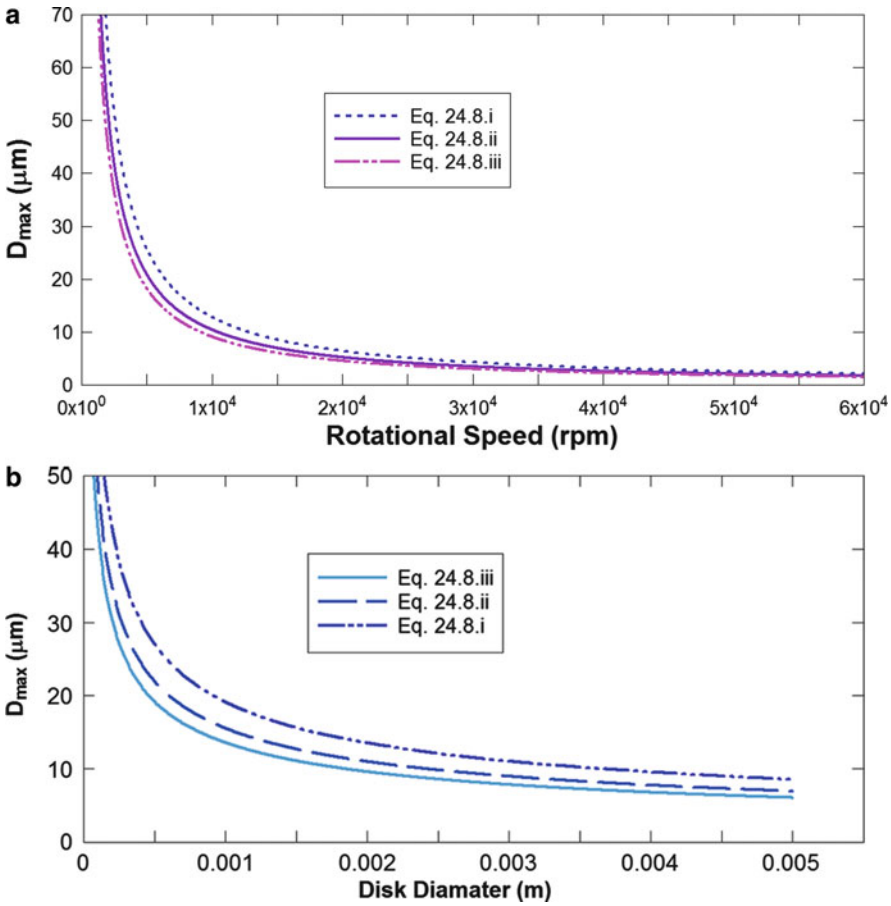


Fig. 24.49 A comparison for three equations for the $D_{0.999}$ of a flat, vaneless rotary atomizer, plotted against (**a**) rotational speed, (**b**) disk diameter

The Weber number is said to be inversely proportional to the SMD, raised to the exponent −0.523. Troshkin [80] proposed a similar equation 24.8.viii for the median diameter of the droplets.

Oyama and Endou [81] were the first to derive an SMD equation for a rotary nozzle undergoing ligament formation 24.8.ix. Though their experiments were restrained only to water, they did draw some very useful conclusions. Figure 24.50 plots this equation, using N = 15,000 rpm and Q =.05 m^3/s. As was the case with droplet formation, we see that in ligament formation, a higher disk diameter leads to finer atomization, higher rotational speed leads to finer atomization, and a higher volumetric flow rate leads to coarser atomization.

Hege [82] derived 24.8.v for the MMD of a spray. His formula applied for sheet disintegration only, and is a function of angular velocity, surface tension, liquid density and disk diameter.

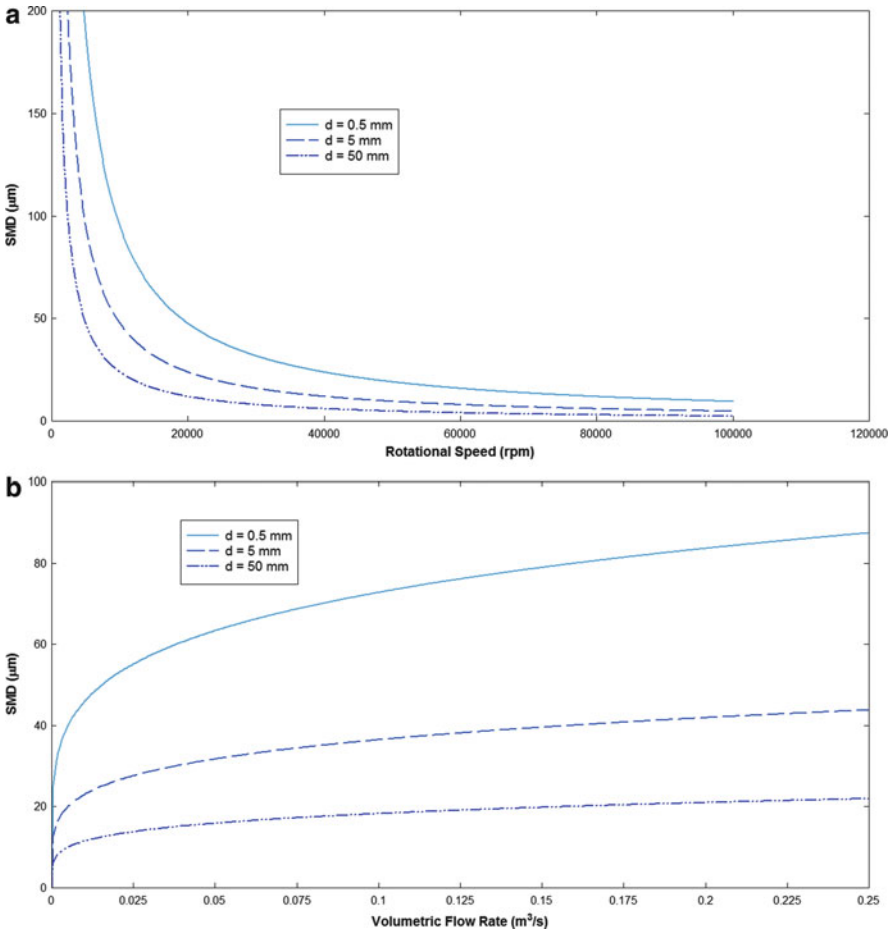


Fig. 24.50 Plot of 24.8.v for ligament formation atomization, plotted at different values of disk diameter against (**a**) rotational speed, (**b**) volumetric flow rate. Properties: $N = 15{,}000$ rpm, $Q = 0.05$ m^3/s

Matsumoto and Takashima [83] proposed an equation for ligament formation, in which the diameter of the ligament is also considered. Equation 24.4.i for effervescent and swirl nozzles greatly resembles this correlation.

Kayano and Kamiya [84] derived an equation 24.8.x where all relevant geometrical, liquid, and flow properties were considered. Figure 24.51 plots their equation using the same values as Figs. 24.49 and 24.50.

The only available formula for the SMD of a rotary nozzle undergoing sheet disintegration is by Tanasawa et al. [78] 24.8.vi, which is plotted in Fig. 24.52. The equation is not too dissimilar to the equation derived by the same author for droplet formation. The $\sigma/(\rho_l d)$ ratio exists in both; however in droplet formation, it is raised to 0.5, while in sheet formation, it is raised to 0.4. The major difference between the

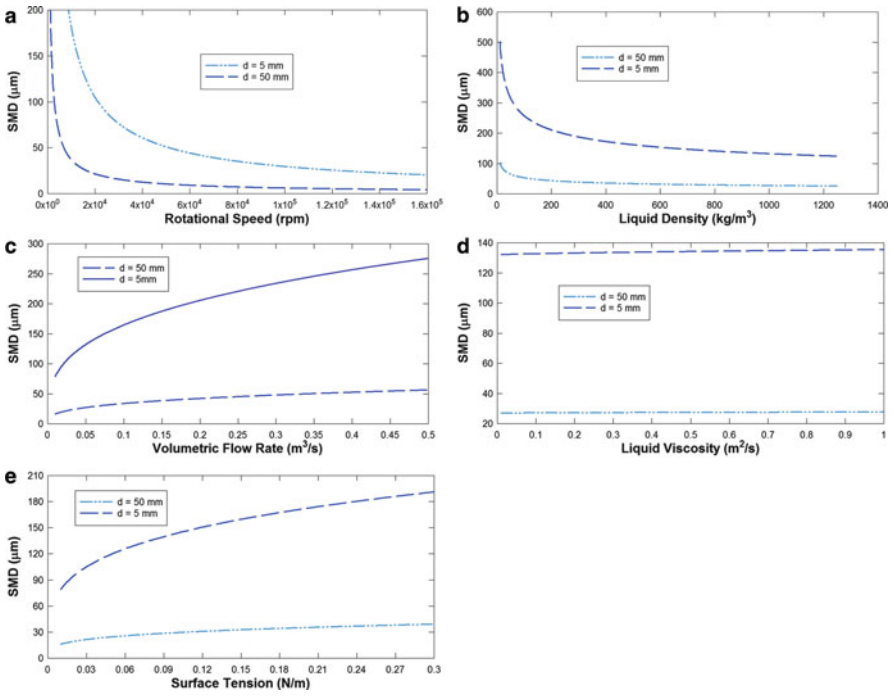


Fig. 24.51 Equation 24.8.vi plotted using water properties at different values of disk diameter against (**a**) rotational speed, (**b**) liquid density, (**c**) liquid viscosity, (**d**) volumetric flow rate of the liquid, and (**e**) surface tension

two correlations is that the liquid viscosity does not appear in sheet formation, while it does in ligament formation.

Vaned Disk Nozzles

SMD correlations for this subfamily of nozzles can be found in Table 24.10. There are six correlations in total. The first three [85–87] are similar to each other in the sense that they contain the same variables. All three relate SMD to be a function of number of vanes, height of vanes, disk diameter, liquid mass flow rate, liquid density, rotational speed, liquid viscosity and surface tension. The fourth equation [88] relates SMD to liquid mass flow rate, number of vanes, disk diameter, rotational speed and liquid viscosity.

The equations by Friedman et al. [85] 24.9.i and Fraser et al. [87] 24.9.iii are almost the same. If one reduces the equations, the exponents on each of the terms work out to be the same, with the exception of nh. The Friedman equation states SMD is proportional to $(nh)^{0.1}$, while the Fraser equation states that the SMD is proportional to $(nh)^{-0.1}$. Figure 24.53 plots the two mentioned equations against

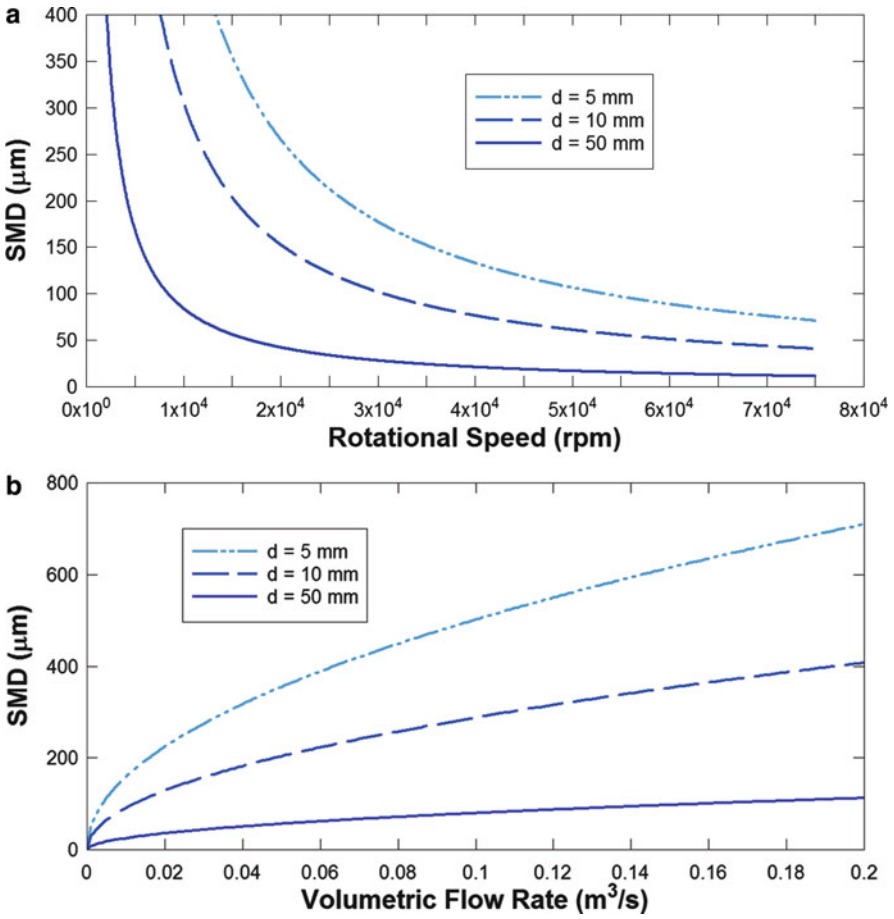


Fig. 24.52 A plot of 24.8.ii for sheet disintegration at various values of disk diameter, plotted against (**a**) rotational speed and (**b**) volumetric flow rate

each other, as a function of *nh*. The properties of water were used, mass flow rate was 50 g/s, *d* was set to 5 mm, and *N* to 15,000 rpm.

Herring and Marshall [86] proposed an equation 24.9.ii that did not consider any liquid properties. Instead, they added a constant A to their equation, which would vary according to the properties of the liquid. Their equation is characteristically different from the two compared in Fig. 24.53. The exponents are higher on the *d* and the *N*, while lower on the *nh* product.

Scott et al. [88] proposed another correlation for the SMD. In their formula, they neglected the effect of liquid density and viscosity, vane height and surface tension.

The last two correlations in Table 24.10, derived by Willauer et al. [89] are very different from the first four. They equate SMD only to Weber number and the disk diameter, much the same way as Matsumoto et al. [79] did in 24.8.vii.

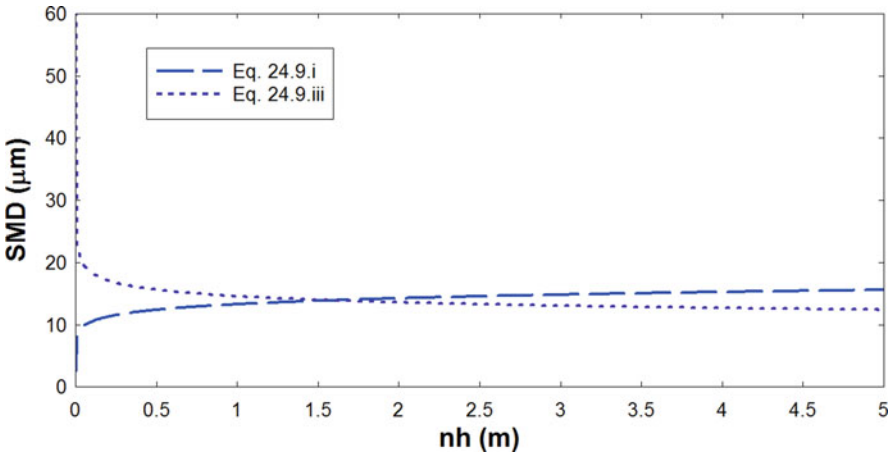


Fig. 24.53 A comparison of 24.9.i and 24.9.iii for rotary nozzles with vaned disks, using properties of water with $\dot{m}_c = 50$ g/s, $d = 5$ mm, $N = 15{,}000$ rpm

Their equation contains two constants: a coefficient and an exponent on the Weber number. They depend on the flow rate and the properties of the liquid to be used. According to Willauer et al., the constants a and b are numerical. The constant b was found to be greater than -0.5, which is contrary to prior experiments which found it to be around -0.5.

Rotary Cup Nozzles

When searching for mean drop size correlations for cup atomizers, the same difficulty arises as in air-assist nozzles. The way in which one distinguishes cup vs. disk atomizers can also be arbitrary. In the literature, Fraser et al. [87], Hinze and Milborn [90], and Hewitt [34] were the only ones that could be found to have comprehensively explored rotary cup atomization. Both of them explored the atomization process in a cup that is vaneless. No equation for the SMD could be found; the only equations found were for NMD and VMD. Fraser et al. [87] equated NMD to be proportional to $Q^{0.333}$ in 24.10.i, while Hinze and Milborn [90] equated it to $Q^{0.5}$ in 24.10.ii. Figure 24.54 shows a comparison of the two equations, using the same properties as Fig. 24.53. Equation 24.10.ii is plotted at different values of θ.

A more recent equation was developed by Hewitt [34] for VMD 24.10.iii. He equated VMD to be proportional to $Q^{0.58}$; however his equation only works for a certain amount of liquids. He states that the VMD of a rotating cup nozzle is only a function of its rotational speed and volumetric flow rate. There are also various restraints on the formula, which are stated in Table 24.10. This formula is explored in Fig. 24.55.

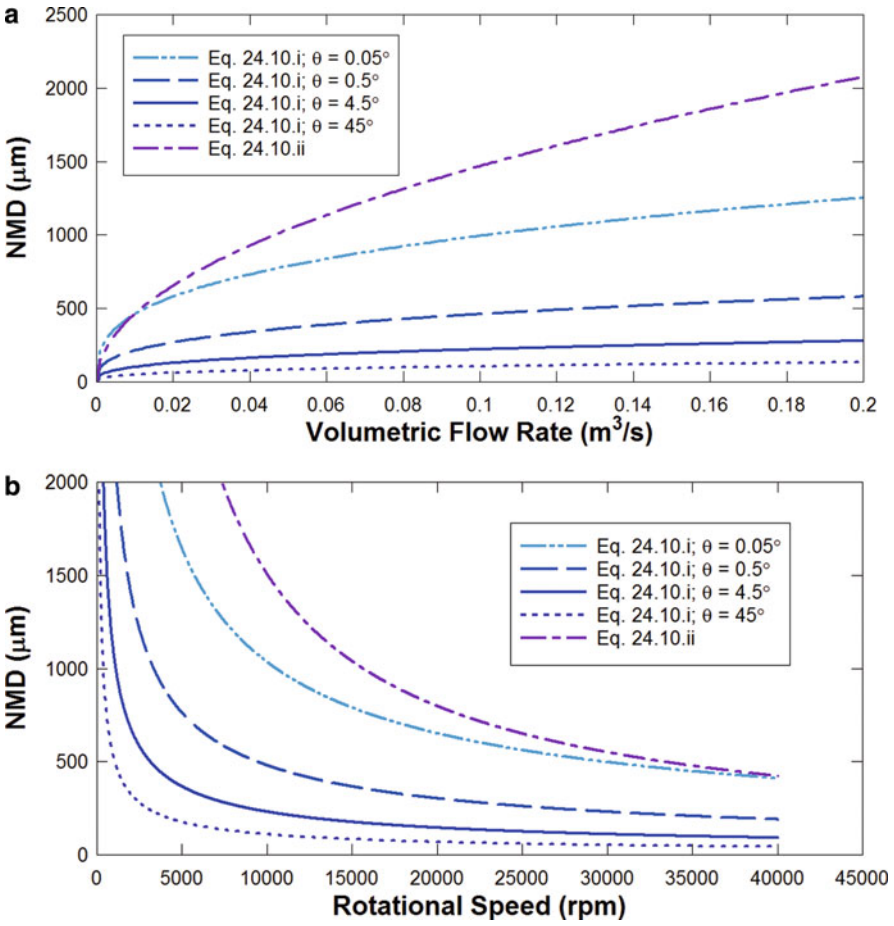


Fig. 24.54 A comparison 24.10.i and 24.10.ii for rotating cup performance. The Hinze–Milborn equation has been plotted at various spray angles, and both equations plotted against (**a**) volumetric flow rate, and (**b**) rotational speed

Figure 24.56 shows an equation for rotary cup atomizers that relates the SMD to the maximum droplet diameter. The equation was derived by Orzechowski [69] 24.10.iv, and applies only for a small margin of data. But nevertheless, it is important in establishing the fact that there is a relationship between different types of drop sizes.

Twin-Fluid Rotary Nozzles

Several correlations for mean drop sizes of twin-fluid rotary nozzles have been developed by Hewitt [34], and are presented in Table 24.11. In his experiments, all

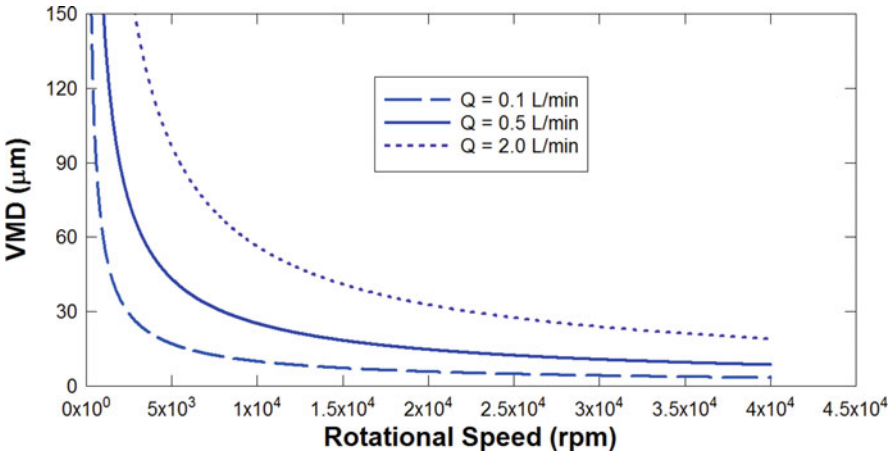


Fig. 24.55 Equation 24.10.iii for rotary cup nozzles plotted against rotational speed at different values of Q

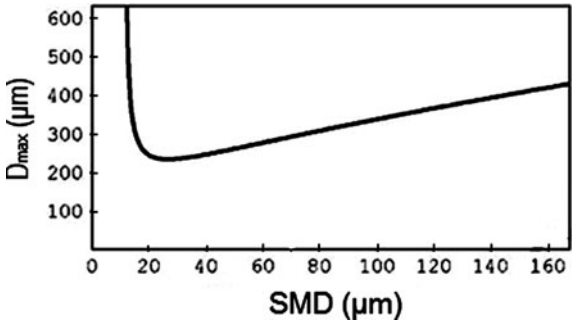


Fig. 24.56 Equation 24.10.v that relates SMD to D_{max} for a cup atomizer

the nozzles were of the external mixing type. In total there are four correlations, three for VMD and one for NMD. Hewitt proposed that the atomization process for rotating cups was not dependent on the liquid properties, as was the case in his formula in Table 24.11. He derived two formulas for twin fluid rotary cup nozzles, one for the VMD and one for the NMD. He proposed that mean drop size was a function of volumetric flow rate, rotational speed and air velocity.

For the rotating cage type of nozzle, Hewitt found two correlations for the VMD; one for when atomization was achieved by drop formation 24.11.iii, and one for ligament formation 24.11.iv. The formula for droplet formation is the only one of the formulas derived by Hewitt that considers the liquid properties. It considers the effect of surface tension and liquid viscosity. According to Hewitt, liquid properties become insignificant at higher modes of atomization. It is interesting to note that under droplet formation, Hewitt states that the volumetric flow rate has very little

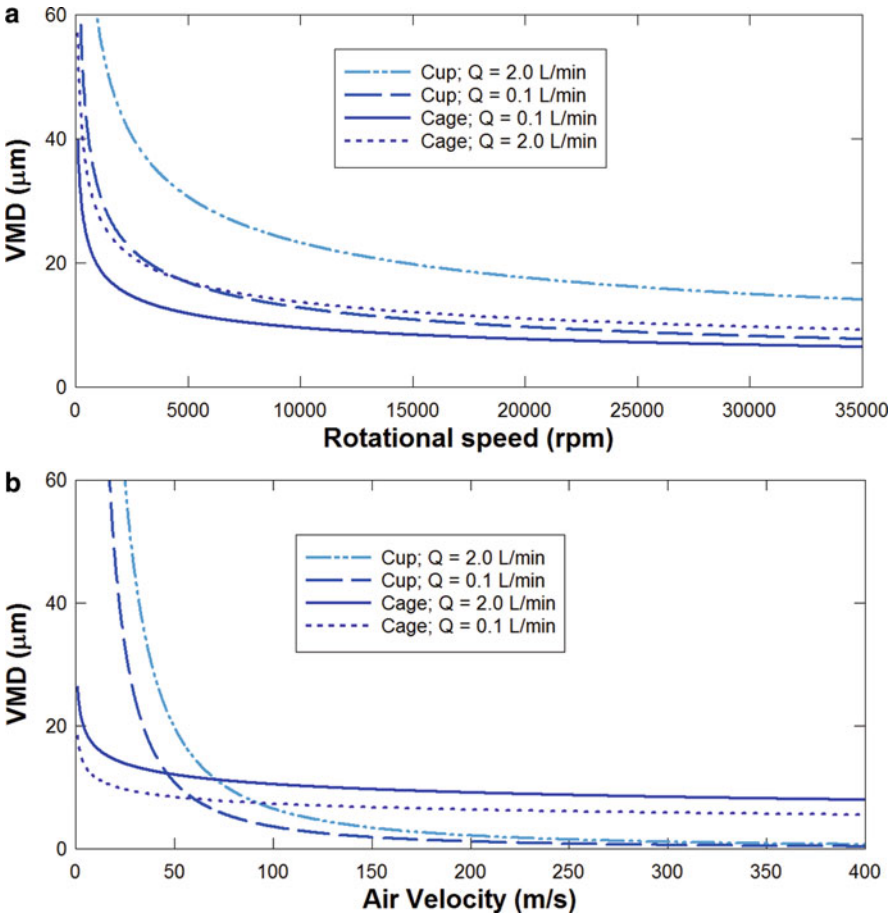


Fig. 24.57 A plot of 24.10.i and 24.10.iv, both plotted at different values of Q against (**a**) rotational speed and (**b**) air velocity

impact on the atomization, while in ligament and sheet formation, the effect of the flow rate is significantly higher. The effect of air velocity on the other hand is prevalent in drop formation, but it significantly decreases in the ligament and sheet formation modes of atomization.

Figure 24.57 shows a comparison between Hewitt's VMD equation for rotary cup 24.11.i and rotary cage 24.11.iv nozzles undergoing ligament or sheet formation atomization. From the graph, it can be seen that the cage atomizer gives finer atomization for the range in which the formula is applicable. However, if one goes outside the $U_A < 116$ m/s range, the cup atomizer tends to have better atomization.

Tumanovski et al. [91] investigated a rotary atomizer of an air-assist type. They found MMD to be proportional to $We^{-1.5}$, and to $\text{GLR}^{-0.5}$. They also found that the rotational speed had a pretty small impact on the drop sizes.

A great deal of work was done by Orzechowski [69] for twin fluid rotary atomizers under very well defined conditions (see Table 24.11). He proposed two correlations; one for when the atomizing surface was a disk with no rims 24.11.vi, and one for when the atomizing surface was a cup with rims 24.11.vii. In the latter case, the rim properties are also taken into account. One key difference between the two formulas is that for rotating disks, liquid film thickness is said to have an effect and SMD proportional to U_l^{-3}. In the case of rotating cups, liquid film thickness is said to have no effect on the atomization, and instead the volumetric flow rate of the liquid does. Also, U_l is raised to the power of -2 instead of -3.

Ultrasonic Nozzles

Ultrasonic atomization uses mechanical vibrations generated via a piezoceramic element, which distribute liquid across its surface without pressure or compressed air. The energy from the vibrations gets transferred to the liquid, creating capillary waves. Once enough energy is added, these capillary waves will no longer be able to remain stable, and this will cause the liquid stream to break into smaller droplets. The vibrations in an ultrasonic nozzle are created by the piezoceramic element, which converts electrical energy being fed into the nozzle into mechanical energy in the form of vibrations. These types of nozzles are primarily used in the biomedical and electronic industry for coating purposes [92]. They are employed for this because of their ability to create very fine droplets travelling at a relatively low velocity. They also do not consume a lot of fluid. Figure 24.58 shows an example.

The basic design in most ultrasonic nozzles comprises a liquid inlet and feeding tube, and a piezoceramic element that is used to create capillary waves. In many nozzles an additional component is added whose function is to amplify the waves created by the piezoelectric element. This greatly reduces the amount of energy



Fig. 24.58 Examples of ultrasonic nozzles, along with their energy source (Courtesy of Lechler, Inc.)

needed for the atomizer. Two different methods exist for categorizing ultrasonic nozzles. They can either be classified based on the method by which capillary waves are created, or by spray angles. The major types based on the wave generation method are the transducer and horn, vibrating capillary and ultrasonic twin fluid [58].

In the transducer and horn design, also known as the standing wave design, two transducers are placed around a pair of horns. The transducers convert inputted electrical energy into kinetic energy in the form of vibrating oscillations. The transducers are made of a piezoelectric material. Each transducer either contracts or expands at the same time as the other one, and by the same amount, and keeps doing so as long as the source of electric energy is available. This repeated action results in waves being created. The nozzle is designed to be equal in length to the pressure wavelength. This results in resonance, which will eventually break the liquid stream flowing within the horns, creating sprays. Usually these nozzles contain a wave amplifier a little before the discharge orifice because otherwise ultrasonic atomization would consume a lot of energy. A schematic drawing of standing wave ultrasonic nozzles can be seen in Fig. 24.59.

The capillary wave design consists of a vibrating surface, which basically replaces the two transducers in the previous design. The vibrations in the liquid will increase surface tension forces, and small, uniform droplets will eject one by one from the liquid stream to relieve the stream from the surface tension. This mechanism can be seen in Fig. 24.60. This process will continue as long as the surface below keeps vibrating. The energy source from which the vibrations originate is usually electricity, much like the standing wave design. Table 24.12 shows drop size correlations for the capillary wave and standing wave designs. As compared to other nozzles, predicting their performance is very simple.

Ultrasonic twin fluid nozzles are the last major category of ultrasonic nozzles. The fundamental design in them is the same as it is for a general twin fluid nozzle. However, in this case the gas is transported through the passageway into the liquid stream ultrasonically. This creates a fluctuating gas flow, both in terms of velocity

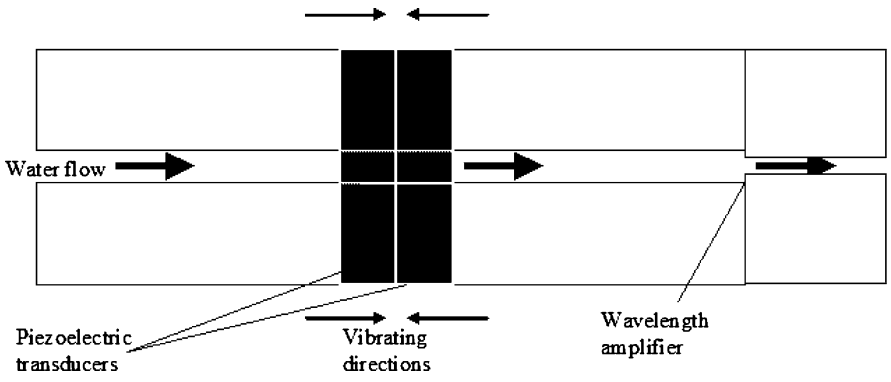


Fig. 24.59 A schematic drawing of an ultrasonic nozzle that uses standing waves

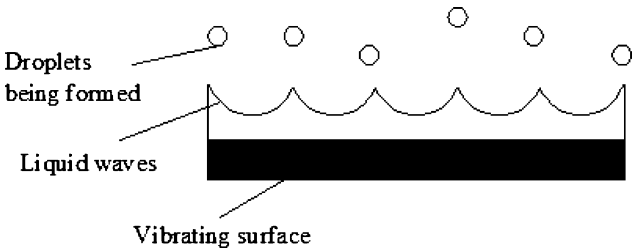


Fig. 24.60 The basic working mechanism in a vibrating capillary nozzle

and pressure. The fluctuations in the gas flow are beneficial to the atomization process since the main fluctuating frequency could correspond to the fastest instability wave in the liquid stream.

Table 24.12 shows mean drop size correlations for the ultrasonic nozzle design. Equations 24.12.i–24.12.iv were compiled by Lefebvre [1], while the rest are more recent correlations.

Ultrasonic nozzles are still largely in their development and research phase. And yet despite this, all the droplet size correlations that could be found in existing literature can be readily used without the need for further experiments. That is, none of them contain experimental constants or any properties that would be hard to determine. The three formulas presented for standing wave ultrasonic nozzles contain different variables and relationships. And yet the formulas obtained for the capillary wave design are very similar to each other.

The earliest known formula for the standing wave ultrasonic nozzle was derived by Mochida [93]. He found that the SMD of a nozzle was a function of the volumetric flow rate, liquid density, viscosity, and surface tension. His results were confined to only a single frequency of 26 kHz. A limitation on the volumetric flow rate also exists of up to 50 L/h, and there is a limitation of the liquids that may be used.

More recently, another correlation was derived by Hansmann [94]. In his experiment, Hansmann was primarily concerned with the effects of operating parameters and the type of liquid used in the nozzle. It should be noted that even though Hansmann experimented with more than one transducer frequency, he did not include it in his equation. Several plots are provided in Fig. 24.61, using the properties of liquid and air, and by setting C_0 to 0.005, Q_l to 4 m^3/s and d_0 to 0.5 mm.

Baukhage et al. [95] also derived an equation considering various liquid, nozzles, and operating attributes. They also did not include the frequency in their results, even though their experiment was conducted over a frequency range of 100 kHz. Various conditions apply for their formula, which are listed in Table 24.8.

Lang [96] was one of the first investigators to come up with any form of correlation for an ultrasonic nozzle. He stated that the NMD of a nozzle was a function of surface tension, liquid density and frequency. Later investigations done by Peskin and Raco [97] and Dobre and Bolle [98] adhered to this result.

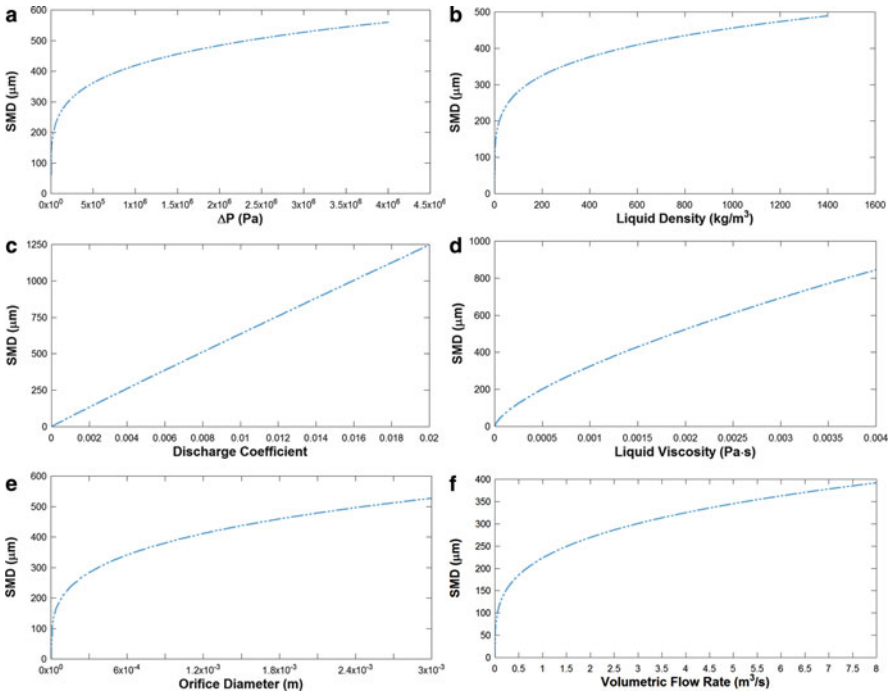


Fig. 24.61 Equation 24.12.ii plotted against (**a**) injection pressure, (**b**) liquid density, (**c**) discharge coefficient, (**d**) liquid viscosity, (**e**) orifice diameter, (**f**) volumetric flow rate; with the following properties: $C_0 = 0.005$, $Q_l = 4$ m^3/s, $d_0 = 0.5$ mm

Electrostatic Nozzles

Electrostatic nozzles operate by creating an electric potential around the nozzle and impact surface. A like electric charge is induced onto the surface of the liquid to be atomized, and an opposite electric charge is induced on the impact surface. The like charges created on the liquid surface severely increase its surface tension, causing the film to break into ligaments. As the charge is continuously applied, the ligaments atomize into droplets. The degree to which atomization occurs depends on the strength of the electric potential created per unit area, also known as the electric pressure (units: V/m^2) [99]. As the liquid surface becomes more charged, the repulsive forces between the molecules increase, causing the droplets to move away from each other. As the droplets move away from each other, they will get attracted to the opposite charge induced on the impact surface. The attractive force between the two opposite charges accelerates the droplets towards their destination, creating a spray. Not a lot of literature exists to predict the mean drop size of this family of nozzles. Table 24.13 does have the few correlations available.

Electrostatic nozzles are particularly advantageous because their droplet sizes are more uniform than any other type of nozzle, and they offer a greater degree of

control on the droplet size. However, their relatively low liquid flow rates have prevented these nozzles from widespread use. The main application for these nozzles is paint spraying. Use of electrostatic nozzles in inkjet printing is being investigated in research.

The basic principle is the same here, but the process is done on a much smaller scale. The advantages of inkjet printing are the same as the advantages found in electrostatic paint spraying. An additional advantage found in inkjet printing is that once the droplets land on the paper, they do not spread and instead they penetrate onto the paper. Such technology is slowly finding applications in food, paper, and package industries [100] due to its good print quality.

In electrostatic paint spraying, the paint particles are electrically charged and the paint surface is oppositely charged or kept grounded. Either way, the charged paint droplets will be attracted towards the body to be painted. Once they reach the body, they have a greater chance of sticking to the body than they would in conventional spraying where the droplets are sprayed onto the body by pressure. They are also able to stick at hard-to-reach places. Their last main advantage is that droplets produced by electrostatic spray painting create a very uniform layer of paint.

References

1. Lefebvre, Arthur, *Atomization and Sprays*, Hemisphere, 1989.
2. Gosman, A. D., and Clerides, D., Diesel Spray Modelling: A Review, *Conference of Liquid Atomization and Spray Systems*, 1998.
3. Mansour, A. B., Buca, P. V., Harvey, R. J., Aiken, K. L., and Duncan, J. F., Multi-function Simplex/Prefilmer Nozzle. U.S. Patent 6 920 749, July 26, 2005.
4. Lefebvre, A. H., Energy Considerations in Twin-Fluid Atomization, ASME Paper, Vol. 114, GTP000089, 1992, pp. 89–96.
5. Barreras, F., and Eduardo, L., Experimental Characterization of Industrial Twin-Fluid Atomizers, *Atomization Sprays J. Inst. Liq. Atomization Spray Syst*, Vol. 16, No. 2, 2006, pp. 127–145.
6. Ganippa, L. C., Andersson, S., and Chomiak J., Combustion Characteristics of Diesel Sprays from Equivalent Nozzles with Sharp and Rounded Inlet Geometries, *Combust. Sci. Technol.*, vol. 175, 2003, pp. 1015–1032.
7. Rizkalla, A., and Lefebvre, A. H., The Influence of Air and Liquid Properties on Air Blast Atomization, *ASME J. Fluids Eng.*, Vol. 97, No. 3, 1975, pp. 316–320.
8. Jasuga, A. K., Atomization of Crude and Residual Fuel Oils, *ASME J. Eng. Power*, Vol. 101, No. 2, 1979, pp. 250–258.
9. Knoll, K. E., and Sojka, P. E., Flat-Sheet Twin-Fluid Atomization of High-Viscosity Fluids, Part I: Newtonian Fluids, *Atomization Sprays*, Vol. 2, 1992, pp. 17–36.
10. Sovani, S. D., Sojka, P. E., and Lefebvre, A. H., Effervescent Atomization, *Prog. Energy Combust.*, Vol. 27, 2001, pp. 483–521.
11. Rashkovan, A., Kholmer, V., and Sher, E., Effervescent Atomization of Gasoline Containing Dissolved CO_2, *Atomization Sprays*, Vol. 14, No. 4, 2004, pp. 341–354.
12. Lasheras, J.C., and Hopfinger, E.J., Liquid Jet Instability and Atomization in a Coaxial Gas Stream, Annu. Rev. Fluid Mech. 2000, pp. 32:275–308.
13. Lozano A., and Barreras F., Experimental Study of the Gas Flow in an Air-Blasted Liquid Sheet, *Exp. Fluids*, Vol. 31, 2001, pp. 367–376.

14. Kim, K. Y., and Marshall, W. R. Jr., Characteristics of Pneumatic Atomizers, *AIChE J*., Vol. 17, No. 3, 1971, pp. 575–584.
15. Nukiyama, S., and Tanasawa, Y., Experiments on the Atomization of Liquids in an Air-stream, *Trans. Soc. Mech. Eng. Jpn*., Vol. 5, 1939, pp. 68–75.
16. Browner, R. F., Experimental Evaluation of the Nukiyama-Tanasawa Equation for Pneumatic Nebulisers Used in Plasma Atomic Emission Electroscopy, *J. Anal. Atom. Spectrosc*., Vol. 6, February 1990, pp. 61–66.
17. Kahen, K., Acon, B. W., and Montaser, A., Modified Nukiyama-Tanasawa and Rizk-Lefebvre Models to Predict Droplets Size for Microconcentric Nebulizers with Aqueous and Organic Solvents. vol. 33, Issue 6, pp. 455–962.
18. Lorenzetto, G. E., and Lefebvre, A. H., Measurements on Drop Size on a Plain jet Air Blast Atomizer, *AIAA J*., Vol. 15, No. 7, 1977, pp. 1001–1010.
19. Rizk, N. K., and Lefebvre, A. H., Spray Characteristics of Plain Jet Airblast Atomizers, *Trans. ASME J. Eng. Gas Turbines Power*, Vol. 106, July 1984, pp. 639–644.
20. Ingebo, R. D., and Foster, H. H., Drop Size Distribution for Cross-Current Breakup of Liquid Jets in Air Streams, NACA TN 4087, 1957.
21. Ingebo, R. D., Capillary and Acceleration Wave Breakup of Liquid Jets in Axial Flow Air-Streams, *NASA Technical Paper*, 1981, p. 1791.
22. Harari, R., and Sher, E., Optimization of a Plain-Jet Atomizer, *Atomization Sprays J. Inst. Liq. Atomization Spray Syst*., Vol. 7, No. 1, 1997, pp. 97–113.
23. Broniarz-Press, L., Ochowiak, M., Rozanski, J., and Woziwodzki, S., The Atomization of Water-Oil Emulsions, *Exp. Thermal Fluid Sci*., J. Anal. At. Spac from., vol. 20, 2009, pp. 631–637.
24. Issac, K., Missoum, A., Drallmeier, J., and Johnston, A., Atomization Experiments in a Coaxial Coflowing Mach 1.5 Flow, *AIAA J*. Vol., 32, No. 8, 1994, pp. 1640–1646.
25. Mulhem, B., Schulte, G., and Fritsching U., Solid-Liquid Separation in Suspension Atomization, *Chemical Engineering Science*, Vol. 61, 2006, pp. 2582–2589.
26. Liu H. F., Li, W. F., Gong, X., Cao, X. K., Xu, J. L., Chen, X. L., Wang, Y. F., Yu, G. S., Wang, F. C., and Yu, Z. H., Effect of Liquid Jet Diameter on Performance of Coaxial Two-Fluid Airblast Atomizers, *Chemical Engineering and Processing*, Vol. 45, No. 4, 2006, pp. 240–245.
27. Antkowiak, W., and Heim, A., Investigation of Pneumatic Spray Nozzle for Wetting Granulate Fine Material, *Inzynieria Chemiczna i Procesowa (Chem. Process Eng.)*, Vol. 8, No. 1, 1987, pp. 57–65 (in Polish).
28. Sakai, T., Kito M., Saito M., and Kanbe T., Characteristics of Internal Mixing Twin-Fluid Atomizers, *Proceedings of the 1st International Conference on Liquid Atomization and Sprays*, Tokyo, 1978, pp. 235–241.
29. Wu, P. K., Miranda, R. F., and Faeth, G. M., Effects of Initial Flow Conditions on Primary Breakup of Nonturbulent and Turbulent Round Liquid Jets. *Atom. Sprays*, Vol. 5, 1995, pp. 176–196.
30. Simmons, H. C., The Prediction of Sauter Mean Diameter for Gas Turbine Fuel Nozzles of Different Types, ASME Paper 79-WA/GT-5, 1979.
31. Imamura T., and Nagai, N., The Relative Performance of Externally Mixed Twin Fluid Atomizers, Proceedings of the 3rd International Conference on Liquid Atomization and Sprays, London, July 1985.
32. Elkotb, M. M., Madhy, M. A., and Montaser, M. E., Investigation of External-Mixing Airblast Atomizers, *Proceedings of the 2nd International Conference on Liquid Atomization and Sprays*, Madison, 1982, pp. 105–115.
33. Levy, Y., Sherbaum, V., Ovcharenko, V., Sotsenko, Y., and Zlochin, I., Study and Field Tests of the Novel Low Pressure Fogger System for Industrial Gas Turbine, *J. Eng. Gas Turbines Power*, Vol. 130, No. 1, 2008. pp. 012002.1–012002.7
34. Hewitt, A. J., Droplet Size Spectra Produced by Air-Assisted Atomizers, *J. Aerosol Sci*., Vol. 24, No. 2, 1993, pp. 155–162.

35. Esfarjani, S. A. and Dolatabadi, A., A 3D Simulation of Two-Phase Flow in an Effervescent Atomizer for Suspension Plasma Spray, *Surf. Coat. Technol*., Vol. 203, No. 15, 2009, pp. 2074–2080.
36. Lund, M. T., Sojka, P. E., Lefebvre, A. H., and Gosselin, P. G.. Effervescent Atomization at Low Mass Flow Rates. Part 1: The Influence of Surface Tension, *Atomization Sprays*, Vol. 3, 1993, pp. 77–89.
37. Whitlow, J. D., Lefebvre, A. H., Effervescent Atomizer Operation and Spray Characteristics, *Atomization Sprays*, Vol. 3, 1993, pp. 137–156.
38. Sutherland, J. J., Sojka, P. E., and Plesniak, M. W., Ligament Controlled Effervescent Atomization. *Atomization Sprays*, Vol. 7, No. 4, 1997, pp. 383–406.
39. Sovani, S. D., Sojka, P. E., and Sivathanu, Y. R., Predictions of Drop Size Distributions from First Principles: Joint-PDF Effects, *Atomization Sprays*, Vol. 10, No. 6, 2000, pp. 587–602.
40. Huang, X., Wang, X., and Liao, G., Visualization of Two Phase Flow Inside an Effervescent Atomizer, *J. Visual*., Vol. 11, No. 4, 2008, pp. 299–308.
41. Buckner, H. E., and Sojka, P. E., Effervescent Atomization of Higher Viscosity Fluids. Part 2: Non-Newtonian Fluids, *Atomization Sprays*, Vol. 3, 1993, pp. 157–170.
42. Lin, J., Qian, L., and Xiong, H., Relationship Between Deposition Properties and Operating Parameters for Droplet onto Surface in the Atomization Impinging Spray, *Powder Technology*, Vol. 191, No. 3, April 2009, pp. 340–348.
43. Qian, L., Lin, J., and Xiong, H., A Fitting Formula for Predicting Droplet Mean Diameter for Various Liquid in Effervescent Atomization Spray, *J. Thermal Spray Technol*., 2009, pp. 1–16, DOI: 10.1007/s11666-009-9457-4.
44. Xiong, H.-B., Lin, J.-Z., and Zhu, Z.-F., Three-Dimensional Simulation of Effervescent Atomization Spray, *Atomization Sprays*, Vol. 19, No. 1, 2008, pp. 75–90.
45. Kim, H. G., Yano, T., Song, K. K., and Shuichi, T., Microscopic Spray Characteristics in the Effervescent Atomizer with Two Aerator Tubes, *KSME Int. J*., Vol. 18, No. 9, 2004, pp. 1661–1667.
46. Tanasawa, Y., and Toyoda, S., On the Atomization of Liquid Jet Issuing from a Cylindrical Nozzle, Tech. Report of Tohuku University, Japan, No. 19-2, 1955, p. 135.
47. Harmon, D. B., Drop sites from Low Speed Jets. *J. Franklin Inst*., Vol. 259, 1955, p. 519.
48. Merrington, A. C., and Richardson, E. G., The Break-up of Liquid Sheets, *Proc. Phys. Soc. London*, Vol. 59, No. 33, 1947, pp. 1–13.
49. Miesse, C. C., Correlation of Experimental Data on the Disintegration of Liquid jets, *Ind. Chem. Eng*., Vol. 47, No. 9, 1955, pp. 1690–1701.
50. Hiroyasu, H., and Katoda, T., Fuel Droplet Size Distribution in a Diesel Combustion Chamber, *SAE Trans*., Paper 74017, 1974.
51. Elkotb, M. M., Fuel Atomization for Spray Modeling, *Prog. Energy Combust. Sci*., Vol. 8, No. 1, 1982, pp. 61–91.
52. Dumouchel, C., On the Experimental Investigation on Primary Atomization of Liquid Streams, *Exp. Fluids*, Vol. 45, 2008, pp. 371–422.
53. Sallam, K. A., Dai, Z., and Faeth, G. M., Drop Formation at the Surface of Plane Turbulent Liquid Jets in Still Gases, *Int. J. Multiphase Flow*, Volume 25, No. 6–7, September 1999, pp. 1161–1180.
54. Sallam, K. A., and Faeth, G. M., Surface Properties During Primary Breakup of Turbulent Liquid Jets in Still Air, *AIAA Journal*, Vol. 41, No. 8, August 2003, pp. 1514–1524.
55. Lee, K., Aalburg, C., Diez, F. J., Faeth, G. M., and Sallam, K. A., Primary Breakup of Turbulent Round Jets in Uniform Crossflows, *AIAA Journal*, Vol. 45, No. 8, August 2007, pp. 1907–1916.
56. Cleary, V., Bowen, P., and Witlox, H., Flashing Liquid Jets and Two-Phase Droplet Dispersion: 1. Experiments for Derivation of Droplet Atomization Correlations, *J. Hazard. Mater*., Vol. 142, No. 3, April 2007, pp. 786–796.
57. Bayvel, L., and Orzechowski, Z., *Liquid Atomization*, Taylor & Francis, Washington, 1993.

58. Kreith, F. and Goswami, D. Y., *The CRC Handbook of Mechanical Engineering*, CRC Press, Boca Raton, 2004.
59. Hasson, D., and Mizrahi, J., The Drop Size of Fan Spray Nozzle, Measurements by the Solidifying Wax Method Compared with Those Obtained by Other Sizing Techniques, *Trans. Inst. Chem. Eng*., Vol. 39, No. 6, 1961, pp. 415–422.
60. Dombrowski, N., and Munday, G., *Spray Drying*, *Biochemical and Biological Engineering Science*, Vol. 2, Chapter 16, Academic, New York, pp. 209–320, 1968.
61. Dombrowski, M., and Hooper, P. C., The Effect on Ambient Density on Drop Formation in Sprays, *Chem. Eng. Sci*., Vol. 17, 1962, pp. 291–305.
62. Kawamura, K., Saito, A., Kanda, M., Kashiwagura, T., and Yamamoto, Y., Spray Characteristics of Slit Nozzle for DI Gasoline Engines, *JSME Int. J*., Series B, Vol. 46, No. 1, 2003, pp. 10–16.
63. Lefebvre, Arthur, *Gas Turbine Combustion*, Taylor & Francis, Boca Raton, 1998.
64. Khavkin, Y. I., *Theory and Practice of Swirl Atomizers*, Taylor & Francis, New York, 2004.
65. Wang, X. F., and Lefebvre, A. H., Atomization Performance of Pressure Swirl Nozzles, *AIAA Paper*, 1986.
66. Couto, H. S., Carvalho, J. A., and Bastos-Netto, D., Theoretical Formulation for Sauter Mean Diameter of Pressure Swirl Atomizers, *J. Propul. Power*, Vol. 13, No. 5, 1997, pp. 691–696.
67. Babu, K. R., Narasimhan, M. V., and Narayanaswamy, K., Prediction of Mean Drop Size of Fuel Sprays from Swirl Spray Atomizers, *Proceedings of the 2nd International Conference on Liquid Atomization and Sprays*, Madison, 1982, pp. 99–106.
68. Park, B. S., Kim, H. Y., Kim, Y., and Chung, T. K., An Experimental Study on the Spray Characteristics of a Dual-Orifice Type Swirl Injector at Low Fuel Temperatures, *KSME Int. J*., Vol. 18, No. 7, 2004, pp. 1187–1195.
69. Orzechowski, A., *Liquid Atomization*, WNT, Warsaw, 1976 (in Polish).
70. Radcliffe, A., Fuel Injection, *High Speed Aerodynamics and Jet Propulsion*, Vol. X1, Sect. D, Pinceton University Press, Princeton, N. J., 1960.
71. Kennedy, J. B., High Weber Number SMD Correlations for Pressure Atomizers, ASME Paper 85-GT-37, 1985.
72. Jones, A.R., Design Optimization of a Large Pressure-Jet Atomizer for Power-Plant, Proceedings of the 2nd International Conference on Liquid Atomization and Sprays, Madison, WI, 1992, pp. 181–185.
73. Petela, R., and Zajdel, A., Atomization of Coal-Liquid Mixtures, *Fuel*, Vol. 59, No. 7, July 1980. pp. 495–498.
74. Zajdel, A., Investigation of Dust-Liquid Fuel. Ph.D. Thesis, Silesian Polytechnic, Gliwice, Poland, 1979 (in Polish).
75. Bär, P., Dr. Eng. Dissertation, Technical College, Karlsruhe, Germany, 1935.
76. Walton, W. H., and Prewett, W. G., The production of sprays and mists of Unifrom Prof sites by means fo spinning Disc Type Sprauers. *Proc. Phys. Soc. London Sect. B*, Vol. 62, 1949, p. 341.
77. Fraser, R. P., and Eisenklam, P., Liquid Atomization on the Drop Size of Sprays, *Trans. Inst. Chem. Eng*., Vol. 34, 1956, pp. 294–319.
78. Tanasawa, Y., Miyasaka, Y., and Umehara, M., Effect of Shape of Rotating Disks and Cups on Liquid Atomization, *Proceedings of the 1st International Conference on Liquid Atomization and Spray Systems*, Tokyo, 1978, pp. 165–172.
79. Matsumoto, S., Saito, K., and Takashima, Y., J. Phenomenal Transition of liquie Atortation form Disk. *Chem. Eng. Jpn*., Vol. 7, 1974, p. 13.
80. Troshkin, O. A., Hydraulic Design of the Centrifugal Cylindrical Sprayer, *Khim. Nett. Mashinostr*., No. 5, 1984 (in Russian). Vol. 20, no. 5, pp. 252–254.
81. Oyama, Y., and Endou, K., On the Centrifugal Disk Atomization and Studies on the Atomization of Water Droplets, *Kagaku Kagaku*, Vol. 17, 1953, pp. 256–260, 269–275 (in Japanese, English summary).

82. Hege, H. *Aufbereit. Tech.*, Die Aufiusung von Flvissigaeiten in tropten. 1969, Vol. 10, no. 3, pp. 142–147.
83. Matsumoto, S., and Takashima, Y., Droplet size Distribution in sprcy. *Kagaku Kagaku*, no. 4, Vol. 33, 1969, pp. 357–360.
84. Kayano, A., and Kamiya, T., Calculation of the Mean Drop Size of the Droplets Purged from the Rotating Disks, *Proceedings of the 1st International Conference on Liquid Atomization and Sprays*, Tokyo, 1978, pp. 133–143.
85. Friedman, S. J., Gluckert, F. A., and Marshall, W. R., *Chem. Eng. Prog.*, Vol. 48, No. 4, 1952, p. 181.
86. Herring, W. H., and Marhsall, W. R., Performance fo Vuned-Disk Atomiters. *J. Am. Inst. Chem. Eng.*, Vol. 1, No. 2, 1955, p. 200–209.
87. Fraser, R. P., Dombrowski, N., and Routley, J. H., The Production of Uniform Liquid Sheets from Spinning Cups; The Filming by Spinning Cups; The Atomization of a Liquid Sheet by an Impinging Air Stream, *Chem. Eng. Sci.*, Vo. 18, 1963, pp. 315–321, 323–337, 339–353.
88. Scott, M. N., Robinson, M. J., Pauls, J. F., and Lantz, R. J., *J. Pharm. Sci.*, Vol. 53, No. 6, 1964, p. 670.
89. Willauer, H. D., Mushrush, G. W., and Williams, F. W., Critical Evaluation of Rotary Atomizer, *Petrol. Sci. Technol.*, Vol. 24, 2006, pp. 1215–1232.
90. Hinze, J. O., and Milborn, H., Atomization of Liquids by Means of a Rotating Cup, *ASME J. Appl. Mech.*, Vol. 17, No. 2, 1950, pp. 145–153.
91. Tumanovski, A. G., Semichastnyi, N. N., and Akhrameev, V. I., Application of Air-Assisted Atomizers for Fuel Atomizers in Stationary Gas Turbines, *Teploenergetika*, No. 11, 1984 (in Russian).
92. Berger, H., *Ultrasonic Liquid Atomization: Theory and Application*, 2nd ed., Hyde Park: Partrige Hill, 2006.
93. Mochida, T., Ultrasonic Atomization of Liquids, *Proceedings of the 1st International Conference on Liquid Atomization and Sprays*, Tokyo, 1978, pp. 193–200.
94. Hansmann, S., Einfluss von Stoff- und Betriebsparametern auf die Zerstäubung hochviskoser Flüssigkeiten im Ultraschall-Stehwellenfeld, Disseration, Universität Bremen, 1996.
95. Bauckhage, K., Andersen, O., Hansmann, S., Reich, W., and Schreckenberg, P., Production of Fine Powders by Ultrasonic Standing Wave Atomization, *Powder Technol.*, Vol. 86, No. 1, 1996, pp. 77–86.
96. Lang, R. S. J., Ultrasonic Atomization of Liquids, *J. Acoust. Soc. Am.*, Vol. 34, No. 1, 1962, pp. 6–8.
97. Peskin, R. L., and Raco, R. J., Ultrasonic Atomization of Liquids, *J. Acoust. Soc. Am.*, Vol. 25, No. 9, September 1963, pp. 1378–1381.
98. Dobre, M., and Bolle, L., Practical Design of Ultrasonic Spray Devices: Experimental Testing of Several Atomizer Geometries, *Exp. Thermal Fluid Sci.*, Vol. 26, No. 2–4, June 2002, pp. 205–211.
99. Graf, P. E., Breakup of Small Liquid Volume by Electrical Charging, *Proceedings of API Research Conference on Distillate Fuel Combustion*, API Publication 1701, Paper CP62-4, 1962.
100. Nasr, Y., and Bendig, L., *Industrial Sprays and Atomization*, Springer, London, 2002.
101. El-Shanawany, M. S. M. R., and Lefebvre, A. H., Airblast Atomization: The Effect of Linear Scale on Mean Drop Size, *J. Energy*, Vol. 4, No. 4, 1980, pp. 184–189.
102. Jasuja, A. K., and Lefebvre, A. H., Influence of Ambient Pressure on Drop Size and Velocity Distributions in Dense Sprays. *Twenty-Fifth Symposium (International) on Combustion*, The Combustion Institute, Pittsburg, pp. 345–352.
103. Fraser, R. P., Eisenklam, P., and Dombrowski, N., Liqued Atomitation in Chemical Engineering. *Br. Chem. Eng.*, Vol. 2, No. 9, 1957, pp. 414–417, 491–501, 536–543, 610–613.
104. Valeev, R. S., Kudryavtstev, A. V., and Kuntsev, G. M., Experimental Investigation of Atomization of a Liquid Jet Fed Perpendicularly to the Gas Jet, *Izv. Vyssh. Uchebn. Zaved.* "Aviatsionnoya Tetkhnika," No. 3, 1984 (in Russian). pp. 87–88.

105. Baik, S., Blanchard, J. P., and Carradini, M. L., Development of Micro-Diesel Injector Nozzles via Microelectromehcanical Systems Technology and Effects on Spray Characteristics, *J. Eng. Gas Turbines Power*, vol. 125, April 2003, pp. 427–434.
106. Panasenkov, N. J., *Zh. Tekh. Fiz*., Vol. 21, 1951, p. 160.
107. Mori, Y., Hijikata, K., and Nagasaki, T., Electrostatic Atomization for Small Droplets of Uniform Diameter, *Trans. Jpn. Soc. Mech. Eng. Ser. B*, 1981, Vol. 47, pp. 1881–1890.
108. Bandyopadhyay, A., and Biswas, M. N., Spray Scrubbing of Particulates with a Critical Flow Atomizer, *Chem. Eng. Technol*., Vol. 30, No. 12, 2007, pp. 1674–1685.
109. Dickerson, R., Tate, K., and Barsic, N., Correlation of Spray Injector Parameters with Rocket Engine Performance, Technical Report AFRPL-TR-68-147, Rocketdyne Division of North American Rockwell Corporation, Canoga Park, Calif., June, 1968.
110. Zajac. L., Correlation of Spray Drop size Distribution and Injector Variables, Rocketdyne Report R-8455, Contract NAS7-726, February 1971.
111. Nonnenmacher, S., and Piesche, M., Design of Hollow Cone Pressure Swirl Nozzles to Atomize Newtonian Fluids, Chemical Engineering Science, Vol. 55, 2000, pp. 4339–4348.

Table 24.1 Prefilming airblast nozzles

Equation number	Correlation	Conditions for use/nomenclature	Investigator(s)
24.1.*i*	$D_{32} = \dfrac{3}{\dfrac{2}{t} + \dfrac{C\rho_l U_A^2}{4\sigma(1 + \dot{m}_l/\dot{m}_A)}}$	C: discharge coefficient Liquids used must be either water or heating oil Ideal when C is around 0.007 Drag of the air flow on the liquid film is neglected and also viscosity Effect of kinetic energy of the liquid is also neglected (i.e., $U_l = 0$)	Lefebvre [4]
24.1.*ii*	$D_{32} = \dfrac{3}{\dfrac{1}{t} + \dfrac{C\rho_l}{4\sigma}\left[U_{a_0}^2\left(\dfrac{\dot{m}_A}{\dot{m}_l}\right) + U_{l_0}^2\right]}$	U_{a0}: air velocity at the exit hole U_{l0}: liquid velocity at the exit hole Same as above; includes effect of kinetic energy	Barreras and Eduardo [5]
24.1.*iii*	$D_{32} = 3.33 \times 10^{-3}\dfrac{(\sigma\rho_l t)^{0.5}}{\rho_A U_A}\left(1 + \dfrac{\dot{m}_l}{\dot{m}_A}\right) + 13 \times 10^{-3}\left(\dfrac{\mu_L^2}{\sigma\rho_L}\right)^{0.425} t^{0.575}\left(1 + \dfrac{\dot{m}_L}{\dot{m}_A}\right)^2$	D_{32}: SMD t: film thickness U_a: air velocity First term is governed by surface tension, and the second term is governed by viscosity. So both properties independently affect the outcome of the formula	Rizkalla and Lefebvre [7]
24.1.*iv*	$D_{32} = 10^{-3}\dfrac{(\sigma\rho_l)^{0.5}}{\rho_A U_A}\left(1 + \dfrac{\dot{m}_l}{\dot{m}_A}\right)^{0.5} + 6 \times 10^{-5}\left(\dfrac{\mu_L^2}{\sigma\rho_L}\right)^{0.425}\left(1 + \dfrac{\dot{m}_L}{\dot{m}_A}\right)^{0.5}$	The liquid should be either kerosene, gas oil, or a gas oil–residual oil mix	Jasuja [8]
24.1.*v*	$D_{32} = D_h\left(1 + \dfrac{\dot{m}_l}{\dot{m}_A}\right)\left[0.33\left(\dfrac{\sigma}{\rho_A U_A t}\right)^{0.6}\left(\dfrac{\rho_l}{\rho_A}\right)^{0.1} + 0.068\left(\dfrac{\mu_L^2}{\sigma\rho_L t}\right)^{0.5}\right]$	D_h: hydraulic diameter Liquid used should be water or kerosene	El-Shanawany and Lefebvre [101]

(*continued*)

Table 24.1 (continued)

Equation number	Correlation	Conditions for use/nomenclature	Investigator(s)
24.1.*vi*	$D_{32} = 48P^{-0.05}\left(1+\frac{\dot{m}_l}{\dot{m}_A}\right)^{0.5}$	P: ambient air pressure 1 Bar $< P <$ 12 bar Liquid must be kerosene Kerosene flow rate $<$ 75 g/s Temperature is around 323 K $1.1 < \dot{m}_a/\dot{m}_l < 7.8$	Jasuja and Lefebvre. [102]
24.1.*vii*	$D_{32} = \frac{12\sigma}{\left(\frac{\rho_l U_g^2}{U_l^2}\right)} \times \frac{}{\left(1+\frac{U_g^{1.3}\,\mu_l^{0.3}\,\dot{m}_l^{0.39}}{1.62\,\dot{m}_g^{0.39}}\right)} + \frac{4\sigma}{t_s}$	t_s: thickness of the slot from which air impinges on the liquid film Liquids used should be glycerin, water, or a mixture of the two	Knoll and Sojka [9]
24.1.*viii*	$D_{32} = 6\times10^{-6} + 0.019 \times \left(\frac{\sigma^{0.5}\nu_r^{0.21}}{\rho_A^{0.5}(rD_c+r^2)^{0.25}}\right)\left(1+0.065\left(\frac{\dot{m}_l}{\dot{m}_a}\right)^{1.5}\right) \times \frac{Q_L}{U_P^2\left(0.5\left[\frac{U_a}{U_l}\right]^2 - \frac{U_a}{U_l}+1\right)}$	D_c: diameter of the cup at the lip ν_r: kinematic viscosity ratio relative to water U_p: cup peripheral velocity r: radial distance from cup at lip Formula works for a nozzle where a spinning cup is used to create a thin sheet of liquid with uniform thickness	Fraser at al. [103]
24.1.*ix*	$D_m = 0.91 d_0 We^{-0.5}$	D_m: median diameter of droplets Both liquid and gas jets must be flat The gas and liquid jets must impinge perpendicularly	Valeev et al. [104]
24.1.*x*	$D_{32} = \left(2.67\times10^4 U_l P_a^{-0.33} + 4.11\times10^6 \rho_a U_a P_a\right)^{-1}$	U_l: liquid velocity 0.1 MPa $< P_A <$ 2.1 MPa Only valid for nozzles that have a splash plate injector where a round fuel jet is arranged to impinge at the centre of a small plate [2]	Ingebo [21]
24.1.*xi*	$D_{10} = 1.88\sqrt{\frac{8t}{k}}(1+3Oh)^{1/6}$	D_{10}: number mean diameter k_s: wave number corresponding to the maximum growth rate 2 mm $< t <$ 7 mm The liquid used is water	Liu et al. [26]

Table 24.2 Plain jet airblast nozzles

Equation number	Correlation	Conditions for use; nomenclature	Investigator(s)
24.2.*i*	$D_{10} = 5.36 \times 10^{-3} \frac{\sigma^{0.41}\mu_l^{0.32}}{\rho_a^{0.57} U_r^{1.14} A_a^{0.36} \rho_l^{0.16}} + 3.44 \times 10^{-3} \left(\frac{\mu_l^2}{\rho_l \sigma}\right)^{0.17} \times \left(\frac{\dot{m}_A}{\dot{m}_L}\right)^m \left(\frac{U_L}{U_A}\right)^{0.54}$	A_A: area of the air flow m: a constant; $m = -1$ when $\dot{m}_L/\dot{m}_A < 3$, and $m = -0.5$ when $\dot{m}_L/\dot{m}_A > 3$ Works for a convergent nozzle where the air expands around a liquid nozzle 0.001 kg/m^3 $< \mu_L <$ 0.05 kg/m^3 75 m/s $< U_A/U_L <$ 393 m/s $0.06 < \dot{m}_L/\dot{m}_A < 40$ 800 kg/m^3 $< \rho_L <$ 960 kg/m^3 0.93 kg/m^3 $< \rho_A <$ 2.4 kg/m^3	Kim and Marshall [14]
24.2.*ii*	$D_{10} = 2.62 \frac{\sigma^{0.41}\mu_L^{0.32}}{\rho_A^{0.72} U_R^{1.44} \rho_L^{0.16}} + 1.06 \times 10^{-3} \left(\frac{\mu_L^2}{\rho_L \sigma}\right)^{0.17} \times \left(\frac{\dot{m}_A}{\dot{m}_L}\right)^m \times \left(\frac{U_L}{U_A}\right)^{0.54}$	Conditions same as above; except this formula works for an axially inserted nozzle such that the air swirls around the liquid, creating a double concentricity	Kim and Marshall [14]
24.2.*iii*	$D_{32} = 0.585 \left(\frac{\sigma}{\rho_L U_R^2}\right)^{0.5} + 53 \left(\frac{\mu_L^2}{\sigma \rho_L}\right)^{0.225} \left(\frac{Q_L}{Q_A}\right)^{1.5}$	Q: volumetric flow rate Air density should be at its atmospheric value Browner [37] found it to be a poor correlation Valid for a concentric nozzle	Nukiyama and Tanasawa [15]
24.2.*iv*	$D_{32} = \frac{86.4}{U_R} \left(\frac{\sigma}{\rho_L}\right)^{0.5} + 105.4 \times \left(\frac{\mu_L^2}{\sigma \rho_L}\right) \exp\left(\frac{-Q_A}{10^6 Q_L}\right)$	Modified version of the Nukiyama–Tanasawa [14] equation. 0.2 L/min $< Q_A <$ 1.0 L/min 10 μL/min $< Q_L <$ 500 μL/min Valid for all conventional twin fluid nozzles	Kahen et al. [17]
24.2.*v*	$D_{32} = 0.95 \left[\frac{(\sigma \dot{m}_L)^{0.33}}{\rho_L^{0.37} \rho_A^{0.3} U_R}\right] \left(1 + \frac{\dot{m}_L}{\dot{m}_A}\right)^{1.7} + 0.13 \left(\frac{\mu_L^2 d_0}{\sigma \rho_L}\right)^{0.5} \left(1 + \frac{\dot{m}_L}{\dot{m}_A}\right)^{1.7}$	d_0: discharge orifice diameter Valid to within 8% over a very large range of liquid and air properties	Lorenzetto and Lefebvre [18]

(*continued*)

Table 24.2 (continued)

Equation number	Correlation	Conditions for use; nomenclature	Investigator(s)
24.2.*vi*	$D_{32} = 0.48d_0\left(\frac{\sigma}{\rho_A U_R^2 d_0}\right)^{0.4}\left(1+\frac{\dot{m}_L}{\dot{m}_A}\right)^{0.4} + 0.15d_0\left(\frac{\mu_L^2}{\rho_L \sigma d_0}\right)^{0.5}\left(1+\frac{\dot{m}_L}{\dot{m}_A}\right)$	0.55 mm $< d_0 <$ 0.75 mm; the formula may be accurate outside of this range; however it was not shown in the experiment	Rizk and Lefebvre [19]
24.2.*vii*	$D_{32} = 0.54d_0\left(\frac{\sigma}{\rho_A U_R^2 d_0}\right)^{0.31}\left(1+\frac{\dot{m}_L}{\dot{m}_A}\right)^{05} + 0.16d_0\left(\frac{\mu_L^2}{\rho_L \sigma d_0}\right)^{0.48}\left(1+\frac{\dot{m}_L}{\dot{m}_A}\right)$	Modified version of (24.20) Conditions same as above	Kahen et al. [17]
24.2.*viii*	$D_{32} = 5.0\left(\frac{\sigma\mu_L d_0^2}{\rho_A \rho_L U_R^3}\right)^{0.25}$	Liquids should be: water, JP 5, benzene, CCl_4, or isooctane Only valid for nozzles containing cross-current air injection $We * Re < 10^6$	Ingebo and Foster [20]
24.2.*ix*	$D_{32} = 37\left(\frac{\sigma\mu_L d_0^{0.5}}{\rho_A \rho_L U_R^3}\right)^{0.4}$	Conditions same as above, but $We * Re > 10^6$	Ingebo [21]
24.2.*x*	$D_{32} = \frac{kd_0}{Re}$	k: a nozzle constant d_0: diameter of the exit hole Works best when $k = 1267$ Liquid exit velocity must be between 10 and 40 m/s Air exit velocity must be between 160 and 325 m/s	Barreras and Eduardo [5]

24.1.*xi*	$D_{32} = B\left(We_A \frac{\dot{m}_A}{\dot{m}_L}\right)^{-0.4}$	We_A: Weber number for the air B: characteristic nozzle constant Reynolds' number must be between 1236 and 3540 Weber's number must be between 65 and 595 $15 < U_A/U_L < 110$ Nozzle must be external mixing	Harari and Sher [22]
24.2.*xii*	$D_{32} = Ad_0{}^{0.12} d_{in}{}^{0.56} \frac{\mu_L^{0.12}}{\mu_A} \left(\frac{\dot{m}_L}{\dot{m}_A}\right)^{0.3}$	A: an experimental constant d_{in}: diameter of the nozzle entrance $1.4 \times 10^{-6} < Q_L < 11 \times 10^{-6}$ m^3/s $280 \times 10^{-6} < Q_A < 1.4 \times 10^{-3}$ m^3/s Liquid used must be water, oil, or a mixture	Broniarz-Press et al. [23]
24.2.*xiii*	$D_{32} = 0.21 d_l (Oh)^{0.0622} \left(We_A \frac{\dot{m}_A}{\dot{m}_L}\right)^{-0.4}$	d_l: liquid jet diameter Ideal for sprays containing small solid particles mixed inside liquid (a suspension spray)	Mulhem et al. [25]
24.2.*xiv*	$D_{\min} = \frac{4\sigma}{C_f \rho_A U_A^2}$	C_f: a constant Works for a nozzle where liquid is injected into a co-flowing stream Mach number of the nozzle must be around 1.5 $C_f \approx 0.0196$	Isaac et al. [24]
24.2.*xv*	$D_{32} = 685.8(U_A - 3.297U_L)^{-0.4813} M^{0.3665} + 0.1824dM$	M: ratio of the liquid/gas mass flux $0.137 < M < 15.6$ Valid only for a coaxial flow nozzle containing a round liquid jet Water must be the liquid used	Liu et al [26]
24.2.*xvi*	$D_{32} = 1.06 \times 10^5 U_A^{-3} \left(\frac{P}{P_A}\right)^{-4.1} \dot{m}_L^{0.83}$	Studied for a nozzle used in dust granulation Gas must be air, liquid must be water	Antkowiak and Heim [27]

Table 24.3 Air-assist nozzles

Equation number	Correlation	Conditions for use; nomenclature	Investigator(s)
24.3.*i*	$D_{32} = 14 \times 10^{-6} d_0^{0.75} \left(\frac{\dot{m}_L}{\dot{m}_A}\right)^{0.75}$	The liquid used is water, and the gas is air 30 kg/h $< \dot{m}_L <$ 100 kg/h $5 < \dot{m}_A/\dot{m}_L <$ 100 Nozzle must be internal mixing	Sakai et al. [28]
24.3.*ii*	$D_{32} = t\left[1 + \frac{16850Oh^{0.5}}{We(\rho_L/\rho_A)}\right]\left[1 + \frac{0.065}{(\dot{m}_L/\dot{m}_A)^2}\right]$	The liquid film thickness, t, must be less than 0.7 mm Ideal liquids are ethanol or glycerin Nozzle must be external mixing	Inamura and Nagai [31]
24.3.*iii*	$D_{32} = 51 d_0 Re^{-0.39} We^{-0.18} \left(\frac{\dot{m}_L}{\dot{m}_A}\right)^{0.29}$	Ideal for kerosene, or a liquid with liquid properties similar to kerosene Nozzle must be external mixing	Elkotb et al. [32]
24.3.*iv*	$D_{30} = 9.6 \times 10^{10} Q_L^{0.097} U_A^{-5.04} \mu_L^{-0.59} \rho_L^{2.4}$	D_{30}: volume mean diameter 87 m/s $< U_A <$ 116 m/s 6.5 m^3/s $< Q_L <$ 10.5 m^3/s Air should be injected tangentially	Hewitt [34]
24.3.*v*	$D_{10} = 457.1 Q_L^{-0.003} U_A^{-0.62} \mu_L^{-0.01} \rho_L^{0.72}$	Conditions are the same as above	Hewitt [34]
24.3.*vi*	$D_{32} = \frac{7D_n}{We_A}\left[\left(\frac{L_p}{D_n}\right)^{0.5} \frac{We_A}{Re_L^{0.5}}\right]^{0.87}$	L_p: liquid–air boundary layer length D_n: nozzle diameter Aerodynamic effects must be negligible (i.e., $\rho_L/\rho_A > 500$)	Wu et al. [29]
24.3.*vii*	$D_{32} = C\left(\frac{\rho_L^{0.25}\mu_L^{0.06}\sigma^{0.375}}{\rho_A^{0.375}}\right)\left(\frac{\dot{m}_L}{\dot{m}_L U_L + \dot{m}_A U_A}\right)$	C: nozzle constant Nozzle must be external mixing, and operating at room temperature	Simmons [30]
24.3.*viii*	$D_{\max} = \frac{\sigma We_{L-cr}}{\rho_A U_A^2}$	$D_{\max}$: maximum diameter achieved by any droplet $We_{L\text{-}cr}$: critical Weber number $13 < We_{L\text{-}Cr} < 22$	Levy et al. [33]
24.3.*ix*	$D_{32} = \frac{3M_f \overline{RQ_{ext}}}{2a_p \rho \sum_{j=1}^{P} (-\ln \tau_j)}$	M_f: total fuel mass a_p: cross-sectional area of each exit orifice τ_j: transmittance for the jth exit orifice RQ_{ext}: average extinction coefficient Valid for a micro-fabricated nozzle injector with P numbers of exit orifices Valid only for fuel atomization	Baik et al. [105]

Table 24.4 Effervescent nozzles

Equation number	Correlation	Conditions for use; nomenclature	Investigator(s)
24.4.*i*	$D_{32} = \left[1.5\sqrt{2}\pi d_l^3 (1+3Oh)^{0.5}\right]^{1/3}$	d_l: ligament diameter $\dot{m}_A, \dot{m}_L < 1.5$ g/s $P < 336$ kPa $\dot{m}_A/\dot{m}_L < 0.02$ Secondary atomization is neglected	Lund et al. [36]
24.4.*ii*	$D_{32} = 12\sigma\left[\rho_l\left\{U_l^2 + \varepsilon(\dot{m}_A/\dot{m}_L)U_A^2 - \frac{(U_L + \varepsilon(\dot{m}_A/\dot{m}_L)U_A)^2}{1+\varepsilon(\dot{m}_A/\dot{m}_L)}\right\}\right]$	ε: specific nozzle coefficient Mass, momentum, and energy must be conserved Energy entering the nozzle is assumed to be the kinetic energies of the liquid and the gas; similar assumption for exiting energy	Buckner and Sojka [41]
24.4.*iii*	$D_{32} = 0.0038\left(\frac{\dot{m}_A}{0.12\dot{m}_L}\right)^{-0.4787}\left(\frac{P_{in}}{4\times10^6}\right)^{-0.1639} \times \left(\frac{D_n}{0.2}\right)^{0.7039} + k\left(y\times10^{-4} + 1 - (1.5t^3\lambda)^{1/3}\right)$, Where $\lambda = \pi\sqrt{2}t(1+2Oh)$	y: axial distance between the two flows k: nozzle constant P_{in}: injection pressure λ: breakup wavelength First term considers secondary atomization; second term considers primary atomization	Lin et al. [42]
24.4.*iv*	$\mathrm{SMD}(y\to 0) = 0.00505\left(\frac{GLR}{0.12}\right)^{-0.4686}\left(\frac{P_{in}}{5\times10^6}\right)^{-0.1805} s \times \left(\frac{D_{noz}}{0.2}\right)^{0.6675}\left(\frac{\mu_l}{0.2}\right)^{0.1714}\left(\frac{\sigma_l}{46}\right)^{0.1382}$	y: distance from nozzle exit Derived based on curve-fitting using a numerical model based on the Navier–Stokes equation The liquid must be very close to the nozzle exit	Qian et al. [43]

(*continued*)

Table 24.4 (continued)

Equation number	Correlation	Conditions for use; nomenclature	Investigator(s)
24.4.*v*	$\text{SMD} = 10^{-4} y \left\{ 1.103 \left(\frac{GLR}{0.12} \right)^{-0.218} + 14.72 \left(\frac{GLR}{0.12} \right)^{-0.3952} \left(\frac{\mu_l}{0.2} \right)^{0.1571} \left(\frac{\sigma_l}{46} \right)^{0.8199} \right\} + 0.00505(1-y) \left(\frac{GLR}{0.12} \right)^{-0.4686} \left(\frac{P_{in}}{5 \times 10^6} \right)^{-0.1805} \times \left(\frac{D_{\text{noz}}}{0.2} \right)^{0.6675} \left(\frac{\mu_l}{0.2} \right)^{0.1714} \left(\frac{\sigma_l}{46} \right)^{0.1382}$	Derived the same way as above $0 < y < 1$ cm	Qian et al. [43]
24.4.*vi*	$\text{SMD} = 10^{-4} \left\{ 1.103 y \left(\frac{GLR}{0.12} \right)^{-0.218} + 14.72 \left(\frac{GLR}{0.12} \right)^{-0.3952} \left(\frac{\mu_l}{0.2} \right)^{0.1571} \left(\frac{\sigma_l}{46} \right)^{0.8199} \right\}$	Derived the same way as above $1 < y < 20$ cm	Qian et al. [43]

Table 24.5 Plain orifice nozzles

Equation number	Correlation	Conditions for use; nomenclature	Investigators
24.5.*i*	$D_{32} = \dfrac{47\, d_0 \sigma^{0.25}(1 + 331Oh)}{U_L \rho_G^{0.25}}$	Liquid used in experiments was diesel fuel Applicable only to injector-type nozzles $U_A = 0$	Tanasawa and Toyoda [46]
24.5.*ii*	$D_{32} = 3330\, d_0^{0.3} \mu_L^{0.07} \rho_L^{-0.648} \sigma^{-0.15}\ U_L^{-0.55} \mu_G^{0.78} \rho_G^{-0.052}$	Liquid used in experiments was diesel fuel Both liquid and gas properties are considered $U_A = 0$	Harmon [47]
24.5.*iii*	$D_{32} = \dfrac{500\, d_0^{1.2} \nu_L^{0.2}}{U_L}$	Used for a plain circular orifice $U_A = 0$ Valid only for low viscosity fluids	Merrington and Richardson [48]
24.5.*iv*	$D_{30} = 6\, d_0 Re^{-0.15}$	$1{,}000 < Re < 12{,}000$	Panasenkov [106]
24.5.*v*	$D_{32} = 64.73\, d_0 Re \left(\dfrac{L}{d_0}\right)^{0.114} - 0.014 d_0 We^{-0.533}$	L: axial length of nozzle liquid must be subcooled (compressed) water	Cleary et al. [56]
24.5.*vi*	$D_{0.5} = 1.22 \dfrac{d_L \sin(90 - \alpha)}{We^{0.25}}$	α: the angle of impingement between the two jets d_L: diameter of the liquid jet Formula derived for the case of two liquid jets impinging with each other The two jets must be of the same liquid	Bayvel and Orzechowski [57]
24.5.*vii*	$D_{0.999} = d_0 We_L^{-0.333}(23.5 + 0.000395\, Re_L)$	$D_{0.999}$: 99.9% of droplets in the spray are below this diameter Based on second-hand experimental data from various sources The equation was "best-fitted" onto the existing data $U_A = 0$	Miesse [49]
24.5.*viii*	$D_{32} = 2330 \rho_A^{0.121} Q^{0.131} \Delta P_L^{-0.135}$	Same as above	Hiroyasu and Katoda [50]
24.5.*ix*	$D_{32} = 3.08 \nu_L^{0.385} (\sigma \rho_L)^{0.737} \rho_A^{0.06} \Delta P_L^{-0.54}$	Same as above	Elkotb [51]
24.5.*x*	$D_{32} = 0.69\Lambda \left(\dfrac{x/\Lambda}{(We\Lambda/D_n)^{0.54}}\right)^{0.57}$	x: distance from nozzle Λ: the radial spatial integral scale of turbulence Applies only for cylindrical liquid jets of a high Weber number	Dumouchel [52]

(*continued*)

Table 24.5 (continued)

Equation number	Correlation	Conditions for use; nomenclature	Investigators
24.5.*xi*	$D_{32} = 0.45\Lambda\left(\frac{x}{\Lambda We_{ex}^{0.5}}\right)^{0.5}$	We_{ex}: Weber number at nozzle exit Works for liquid jets injected into still air Temperature and pressure must be at standard levels $91{,}000 < Re < 424{,}000$ at nozzle exit $13{,}000 < We < 151{,}000$ at nozzle exit $0.0009 < Oh < 0.0012$ at nozzle exit	Sallam et al. [53]
24.5.*xii*	$D_{32} = 0.5\Lambda\left(\frac{x}{\Lambda We_{ex}^{0.5}}\right)^{0.53}$	Applies for turbulent, round, and annular water jets injected into still air $6{,}000 < Re < 424{,}000$ at nozzle exit $200 < We < 300{,}000$ at nozzle exit $Oh < 0.0053$ at nozzle exit	Sallam and Faeth [54]
24.5.*xiii*	$D_{32} = 0.72\Lambda\left(\frac{x}{\Lambda We_{l}^{0.5}}\right)^{\frac{2}{3}}$	We_l: Weber number based on ligament (primary atomization) properties *Re*, *We*, *Oh* conditions same as above Incorporates the effect of non-turbulent ligaments	Sallam and Faeth [54]
24.5.*xiv*	$D_{32} = 0.56\Lambda\left(\frac{x}{\Lambda We_{ex}^{0.5}}\right)^{0.5}$	Conditions same as above; however the air is not still, but in cross-flow $36 \text{ m/s} < U_A < 90 \text{ m/s}$	Lee et al. [55]
24.5.*xv*	$D_{32} = 0.45\Lambda\left(\frac{x}{\Lambda We_{ex}^{0.5}}\right)^{0.5}$	We_{ex}: Weber number at nozzle exit Works for liquid jets injected into still air Temperature and pressure must be at standard levels $91{,}000 < Re < 424{,}000$ at nozzle exit $130{,}00 < We < 151{,}000$ at nozzle exit $0.0009 < Oh < 0.0012$ at nozzle exit	Sallam et al. [53]
24.5.*xvi*	$D_{32} = 0.5\Lambda\left(\frac{x}{\Lambda We_{ex}^{0.5}}\right)^{0.53}$	Applies for turbulent, round, and annular water jets injected into still air $6{,}000 < Re < 424{,}000$ at nozzle exit $200 < We < 300{,}000$ at nozzle exit $Oh < 0.0053$ at nozzle exit	Sallam and Faeth [54]
24.5.*xvii*	$D_{32} = 0.72\Lambda\left(\frac{x}{\Lambda We_{l}^{0.5}}\right)^{\frac{2}{3}}$	We_l: Weber number based on ligament (primary atomization) properties *Re*, *We*, *Oh* conditions same as above Incorporates the effect of non-turbulent ligaments	Sallam and Faeth [54]
24.5.*xviii*	$D_{32} = 0.56\Lambda\left(\frac{x}{\Lambda We_{ex}^{0.5}}\right)^{0.5}$	Conditions same as above; however the air is not still, but in cross-flow $36 \text{ m/s} < U_A < 90 \text{ m/s}$	Lee et al. [55]

Table 24.6 Flat fan nozzles

Equation number	Correlation	Conditions for use; nomenclature	Investigators
24.6.*i*	$D_{32} = 2.83 D_h \left(\frac{\sigma \mu_L^2}{\rho_g D_h^3 \Delta P_L^2}\right)^{0.25} + 0.26 D_h \left(\frac{\sigma \rho_L}{\rho_g D_h \Delta P_L}\right)^{0.25}$	D_h: hydraulic diameter of the liquid in the nozzle Assumes air is still	Found in Kreith and Goswami [58] who referenced it from Lefebvre [1]
24.6.*ii*	$D_{32} = 0.071 \left(\frac{tx\sigma \mu_L^{0.5}}{\rho_L^{0.5} U_L^2}\right)^{\frac{1}{3}}$	$0.003 \text{ kg/m s} < \mu_L < 0.025 \text{ kg/m s}$	Hasson and Mizrahi [59]
24.6.*iii*	$D_{32} = 4.78 \times 10^{-6} \left(\frac{A_L^3 \sigma}{\sin\theta \rho_L Q_L^2}\right)^{\frac{1}{3}}$	Neglects liquid viscosity effects Liquids used must be water or oil	Dombrowski and Munday [60]
24.6.*iv*	$D_{32} \propto \Delta P_L^{-0.33} H^{0.33} \rho_A^{-0.17}$	H: slit thickness Secondary atomization is neglected Intended for an injector nozzle to carry gasoline ΔP must be low	Dombrowski and Hooper [60]
24.6.*v*	$D_{32} \propto H^{0.5} \rho_A^{-0.25}$	Secondary atomization is neglected Intended for an injector nozzle to carry gasoline ΔP must be high	Dombrowski and Hooper [61]
24.6.*vi*	$D_{32} \propto \Delta P_L^{-0.25} H^{0.3}$	Secondary atomization is considered Intended for an injector nozzle to carry gasoline $0.1 \text{ MPa} < \Delta P < 0.3 \text{ MPa}$	Kawamura et al. [62]
24.6.*vii*	$D_{32} \propto \Delta P_L^{-0.5} H^{0.1} \rho_A^{-0.33}$	Secondary atomization is considered Intended for an injector nozzle to carry gasoline $6 \text{ MPa} < \Delta P < 12 \text{ MPa}$	Kawamura et al. [62]

Table 24.7 Swirl nozzles

Equation number	Correlation	Conditions for use; nomenclature	Investigators
24.7.*i*	$D_{32} = 4.52\left(\frac{\sigma\mu_L^2}{\rho_A P_{in}^2} t\cos\frac{\theta}{2}\right)^{0.25} + 0.39\left(\frac{\sigma\rho_L}{\rho_A P_{in}}\left(t\cos\frac{\theta}{2}\right)^3\right)^{0.25}$	θ: spray cone angle 3×10^{-6} m^2/s $< \mu_L < 18 \times 10^{-6}$ m^2/s 27 dyne/cm $< \sigma <$ 73.4 dyne/cm	Wang and Lefebvre [65]
24.7.*ii*	$D_l = 0.9615\cos\theta \times \left(\frac{t^4\sigma^2\cos^2\theta}{U_L^4\rho_A\rho_L}\right)^{1/6} \times \left[1 + 2.6\mu_L\cos\theta\left(\frac{t^2\rho_A^4 U_L^7}{72\rho_L^2\sigma^5\cos^8\theta}\right)^{1/3}\right]^{0.2}$	The equation is used to determine ligament diameter as the liquid exits the nozzle To be used in conjunction with the next equation listed	Couto et al. [66]
24.7.*iii*	$D_{32} = 10^{-3}\sigma(6.11 + 32{,}000\frac{\dot{m}_L}{\Delta P_L^{0.5}} - 6.973 \times 10^{-3}\Delta P_L^{0.5} + 1.89 \times 10^{-6}\Delta P_L)$	Weber's number is greater than 10 The $\dot{m}_L/(\Delta P_L\rho_L)$ ratio (flow number) must be large Valid only for simplex swirl nozzles	Kennedy [71]
24.7.*iv*	$D_{32} = 2.25\sigma^{0.25}\mu_L^{0.25}\dot{m}_L^{0.25}\Delta P_L^{-0.5}\rho_A^{-0.25}$	Same as above; however this equation was derived over a broad range of surface tension values	Lefebvre [63]
24.7.*v*	$D_{32} = 7.3\sigma^{0.6}\upsilon_L^{0.2}\dot{m}_L^{0.25}\Delta P_L^{-0.4}$	υ_L: kinematic viscosity of liquid ΔP_L: injection pressure differential across nozzle Variation in surface tension was very small in the experiments conducted Results compiled empirically from second-hand data Valid only for simplex swirl nozzles	Radcliffe [70]
24.7.*vi*	$D_{32} = 4.4\sigma^{0.6}\upsilon_L^{0.16}\dot{m}_L^{0.22}\Delta P_L^{-0.43}$	Same as above	Jasuja [8]
24.7.*vii*	$D_{32} = 133\frac{\dot{m}_L{}^{0.64291}}{\Delta P_L^{0.547105}\rho_L^{0.642955}}$	Liquid used was kerosene Formula obtained from linear regressions used from second-hand data $\Delta P_L < 2.8$ MPa Valid only for simplex swirl nozzles	Babu et al. [67]
24.7.*viii*	$D_{32} = 607\frac{\dot{m}_L{}^{0.75344}}{\Delta P_L^{0.57608}\rho_L^{0.75342}}$	Same as above; $\Delta P > 2.8$ MPa	Babu et al. [67]

24.7.*ix*	$D_{32} = 111.3\sigma^{0.122}{\nu_L}^{0.331}\Delta P_L^{-0.42}$	Liquid used should be fuel The formula was derived based on variations in temperature only, which cause liquid properties to change; independent changes to liquid properties were not applied Valid only for duplex swirl nozzles $D_n = 1.9$ mm 0.29 MPa $< \Delta P <$ 0.69 MPa	Park et al. [68]
24.7.*x*	$D_{0.5} = 269tWe^{-0.35}Oh^{0.846}$	Liquid must be kerosene $\mu_G \approx 0.01\mu_L$ $\rho_G \approx 0.0015\rho_L$	Orzechowski [69]
24.7.*xi*	$D_{0.5} = 1415tWe^{-0.35}Oh^{0.926}$	Liquid must be water, glycerin, or a mixture of the two $\mu_G \approx 0.018\mu_L$ $\rho_G \approx 0.0012\rho_L$	Orzechowski [69]
24.7.*xii*	$D_{32} = 52\dot{m}_L\Delta P_L^{-0.397}\upsilon_L^{0.204}$	Neglects atomizer dimensions Very similar to the equations derived by Babu et al. [42], Radcliffe [41], Jasuja [4], and Lefebvre [39]	Orzechowski [69]
24.7.*xiii*	$D_{0.5} = 2.47\frac{\dot{m}_L^{0.315}\mu_L^{0.16}\sigma^{0.25}}{\Delta P_L^{0.47}\mu_A^{0.04}\rho_L^{0.22}} \times \left(\frac{l_0}{d_0}\right)^{0.03}\left(\frac{L_n}{D_n}\right)^{0.07} \times \left(\frac{D_n d_0}{A_i}\right)^{0.13}\left(\frac{D_n}{d_0}\right)^{0.21}$	$D_{0.5}$: mass mean diameter l_0: discharge orifice length A_i: total area of the inlet ports L_n: nozzle chamber length $11{,}500 < We < 355{,}000$ $1{,}913 < Re < 21{,}140$ $0.1 < l_0/d_0 < 0.9$ $0.31 < L_n/D_n < 1.26$ $0.19 < A_p/(d_0 D_n) < 1.21$ Air density and viscosity must be negligible compared to the liquid $1.41 < D_n/d_0 < 8.13$	Jones [72]

(*continued*)

Table 24.7 (continued)

Equation number	Correlation	Conditions for use; nomenclature	Investigators
24.7.*xiv*	$D_{0.5} = 9.129 \times 10^{-5} tWe^{-0.159} \times Oh^{1.396} \left(\frac{\rho_A}{\rho_L}\right)^{-3.17} \left(\frac{\mu_A}{\mu_L}\right)^{1.204} \times \left(1 - \frac{d_{sl}}{d_0}\right)^{-6.41g}$	d_{sl}: median diameter of the coal particles in the slurry g: the mass mean fraction of dust in the mixture Valid for coal slurry mixtures where the liquid is benzoic acid 0.17 MPa < P_{in} < 0.8 MPa 0 < d_{sl} < 385 μm 0.033 < g < 0.287 Discharge orifice diameter must be around 1.05 mm Particles must be monodispersed The formula was derived based on results from 74 of 140 tests conducted	Petela and Zajdel [73]
24.7.*xv*	$D_{0.5} = 5.13 \times 10^{-6} tWe^{-0.68} h^{1.396} \left(\frac{\rho_A}{\rho_L}\right)^{-3.17} \left(\frac{\mu_A}{\mu_L}\right)^{1.204} \times \left(1 - \frac{d_{sl}}{d_0}\right)^{-0.545g}$	Conditions same as above; however the particles must be polydispersed instead of monodispersed	Zajdel [74]
24.7.*xvi*	$D_{32} = at \left(\frac{\sqrt{2P_{in}\rho_L}t}{\mu_L}\right)^{-m} \left(\frac{\mu_A}{\mu_L}\right)^{n}$	a, m, n: constants t: film thickness Acts as a general equation for all swirl nozzles	Khavkin [64]
24.7.*xvii*	$D_{32} = aD_n \left(\frac{\sqrt{2P_{in}\rho_L}D_n}{\mu_L}\right)^{-m} \left(\frac{\mu_A}{\mu_L}\right)^{n}$	Conditions same as above	Khavkin [64]
24.7.*xviii*	$D_{0.999} = 3.72 \times 10^6 \frac{\left(\frac{d_0}{2}\right)^{0.56} E^{0.11}}{\left(\frac{\Delta P_L \sqrt{1-\varepsilon}}{\sigma}\right)^{0.33}}$	$E = 10^6 \mu_L{}^2/(2\sigma\rho_L)$ ε: experimental constant Valid only for a spill-return type of swirl nozzle Re > 1,200	Orzechowski [69]
24.7.*xix*	$D_{32} = 0.5 d_0 \sqrt{[3]{\frac{3\pi d_l^2}{k_{cr}}}}$	k_{cr}: wave number of disturbing wave Use for hollow cone sprays (both axial and tangential) Valid only for simplex swirl nozzles	Nonnenmacher and Piesche [111]

Table 24.8 Vaneless rotary nozzles

Equation number	Correlation	Conditions for use; nomenclature	Investigators
24.8.*i*	$D_{0.999} = \frac{1.07}{N}\left(\frac{\sigma}{d\rho_L}\right)^{0.5}$	d: disk diameter N: rotational speed Disk must be flat and vaneless Neglects effect of liquid viscosity Atomization must occur by droplet formation	Bar [75]
24.8.*ii*	$D_{0.999} = \frac{0.87}{N}\left(\frac{\sigma}{d\rho_L}\right)^{0.5}$	Disk must be flat and vaneless; atomization must occur by ligament formation Very similar to (24.94)	Walton and Prewett [76]
24.8.*iii*	$D_{10} = \frac{0.76}{N}\left(\frac{\sigma}{d\rho_L}\right)^{0.5}$	Very similar to (24.94) and (24.95); suggests a similarity in rotary nozzle performance regardless of the mechanism Neglects liquid flow rate and liquid viscosity Atomization must occur by sheet formation	Fraser and Eisenklam [77]
24.8.*iv*	$D_{32} = \frac{27}{N}\left(\frac{\sigma}{d\rho_L}\right)^{0.5}\left(1 + 0.003\frac{Q}{d\nu_L}\right)$	Viscosity is considered; conditions same as those of (24.94)	Tanasawa et al. [78]
24.8.*v*	$D_{10} = 4.42\left(\frac{\sigma}{\omega^2\rho_L d}\right)$	Disk must be vaneless; but not necessarily smooth or flat Atomization must occur by sheet formation	Hege [82]
24.8.*vi*	$D_{32} = 15.6\frac{Q^{0.5}}{N}\left(\frac{\sigma}{d^2\rho_L}\right)^{0.4}$	Includes liquid flow rate but still neglects liquid viscosity Atomization must occur by sheet formation	Tanasawa et al. [78]
24.8.*vii*	$D_{32} = 1.6dWe^{-0.523}$	Disk must be flat and vaneless Atomization must occur by droplet formation All liquid properties are considered	Matsumoto et al. [79]
24.8.*viii*	$D_{20} = 19.7d_0We^{-0.5}$	D_{20}: mean surface area diameter Very similar to (24.100); conditions are also similar to that equation	Troshkin [80]
24.8.*ix*	$D_{32} = \frac{0.177Q^{0.2}}{Nd^{0.3}}$	Disk must be flat and vaneless; atomization must occur by ligament formation Valid only when water is used as the liquid to be atomized	Oyama and Endou [81]
24.8.*x*	$D_{32} = \frac{0.26Q^{0.32}\sigma^{0.26}}{N^{0.79}d^{0.69}\rho_L^{0.29}}\left(1 + 0.027\mu_L^{0.65}\right)$	Includes all relevant geometrical and liquid properties Atomization must occur by ligament formation	Kayano and Kamiya [84]
24.8.*xi*	$D_{32} = d_l(1.5\pi)^{\frac{1}{3}}\left(1 + \frac{3We}{Re^2}\right)^{\frac{1}{6}}$	Disk must be flat and vaneless; atomization must occur by ligament formation Considers the effects of ligament diameter	Mastsumoto and Takashima [83]

Table 24.9 Vaned rotary nozzles (atomizer wheels)

Equation number	Correlation	Conditions for use; nomenclature	Investigators
24.9.*i*	$D_{32} = 0.44d\left(\frac{\dot{m}_L}{\rho_L N d^2}\right)^{0.6} \times \left(\frac{\mu_L}{\dot{m}_L}\right)^{0.2}\left(\frac{\sigma\rho_L nh}{\dot{m}_L^2}\right)^{0.1}$	n: number of vanes h: height of vanes All factors are considered	Friedman et al. [85]
24.9.*ii*	$D_{32} = \frac{3.3\times10^{-9}A\dot{m}_L^{0.24}}{(Nd)^{0.83}(nh)^{0.12}}$	A: a constant, ranging from 850,000 to 950,000	Herring and Marshall [86]
24.9.*iii*	$D_{32} = \frac{0.483}{N^{0.6}\rho_L^{0.5}}\left(\frac{\mu_L\dot{m}_L}{d}\right)^{0.2}\left(\frac{\sigma}{nh}\right)^{0.1}$	All relevant factors considered; however the counter-intuitive natures of the formula derived by Friedman et al. [69] is remedied	Fraser et al. [87]
24.9.*iv*	$D_{32} = \frac{6.3\times10^{-4}\dot{m}_L^{0.171}}{(ndN)^{0.537}\mu_L^{0.017}}$	Surface tension and vane properties are ignored	Scott et al. [88]
24.9.*v*	$D_{32} = adWe^b$	a, b: constants Similar to the equation derived by Matsumoto et al. [64], however more generalized a and b depend on flow rate and the liquid used b was found to be greater than −0.5, which is contrary to prior experiments which found it to be around −0.5	Willauer et al. [89]
24.9.*vi*	$D_{0.999} = 0.33dWe^{-0.5}$	Rearranged version of the formula derived by Walton and Prewett [65] Conditions same as above	Willauer et al. [89]

Table 24.10 Rotary cup nozzles

Equation number	Correlation	Conditions for use; nomenclature	Investigators
24.10.*i*	$D_{10} = \left(\frac{3Q\mu_L}{2\pi\rho_L[\pi dN]^2 \sin\theta}\right)^{1/3}$	Disk must be vaneless; but not necessarily smooth or flat Atomization must be achieved by direct drop formation No effect of surface tension	Fraser et al. [87]
24.10.*ii*	$D_{10} = \left(0.77\frac{Q}{Nd}\left[\frac{\rho_L N^2 d^3}{\sigma}\right]^{-5/12} \times \left[\frac{\rho_L \sigma d}{\mu_L^2}\right]^{-1/16}\right)^{0.5}$	Disk must be vaneless; but not necessarily smooth or flat Atomization must be achieved by ligament formation	Hinze and Milborn [90]
24.10.*iii*	$D_{30} = 7215 Q_L^{0.58} N^{-0.78}$	6.5 $m^3/s < Q_A < 10.5$ m^3/s 2,500 rpm $< N <$ 19,000 rpm 100 mL/min $Q_L <$ 2,000 mL/min $U_A = 0$ Liquid must be either water with 0.1% w/w Argal, or kerosene, or Risella oil	Hewitt [34]
24.10.*iv*	$D_{0.999} = D_{32}\left(0.6 + 43(D_{32} - 11.5)^{-0.612}\right)$	Relates two different types of drop sizes Applies for a very small margin of conditions: $N \approx$ 3,000 rpm, $v_L \approx 0.000045$ m^2/s, $U_G \approx 29$ m/s, $\dot{m}_L \approx 256$ kg/h	Orzechowski [69]

Table 24.11 Twin-fluid rotary nozzles

Equation number	Correlation	Conditions for use; nomenclature	Investigators
24.11.*i*	$D_{30} = 1.8 \times 10^6 \frac{Q_L^{0.2}}{N^{0.4} U_{\mathrm{A}}^{1.6}}$	6.5 $m^3/s < Q_A < 10.5$ m^3/s 2,500 rpm $< N <$ 19,000 rpm 100 mL/min $Q_L <$ 2,000 mL/min Nozzle must be of the rotating cup type Nozzle must be external mixing	Hewitt [34]
24.11.*ii*	$D_{10} = 11,392 \frac{Q_L^{0.08}}{N^{0.14} U_{\mathrm{A}}^{0.96}}$	Conditions same as above	Hewitt [34]
24.11.*iii*	$D_{30} = 3.1 \times 10^{10} \frac{Q_{\mathrm{L}}^{0.03} \mu_{\mathrm{L}}^{0.26} \sigma^{1.62}}{N^{0.4} U_{\mathrm{A}}^{2.32}}$	6.5 $m^3/s < Q_A < 10.5$ m^3/s 5,500 rpm $< N <$ 13,000 rpm 87 m/s $< U_A <$ 116 m/s 100 mL/min $Q_L <$ 2,000 mL/min Nozzle surface must be a rotating cage with mesh sizes of 20, 30, 40, and 60 Atomization must be achieved by drop formation Nozzle must be external mixing	Hewitt [34]
24.11.*iv*	$D_{30} = 1,300 \frac{Q_{\mathrm{L}}^{0.12}}{N^{0.31} U_{\mathrm{A}}^{0.2}}$	6.5 $m^3/s < Q_A < 10.5$ m^3/s 50 rpm $< N <$ 5,500 rpm 0 m/s $< U_A <$ 116 m/s 100 mL/min $Q_L <$ 2,000 mL/min Nozzle surface must be a rotating cage with mesh sizes of 20, 30, 40, and 60 Atomization must be achieved by ligament/sheet formation Nozzle must be external mixing	Hewitt [34]
24.11.*v*	$D_{0.5} = 15.3 \times 10^3 \frac{D_{\mathrm{n}} \sqrt{1 + \frac{\dot{m}_{\mathrm{L}}}{\dot{m}_{\mathrm{G}}}}}{We^{1.5} N^{0.065}}$	Nozzle must be an air-assist type 40 m/s $< U_G <$ 90 m/s 100 kg/h $< \dot{m}_L <$ 500 kg/h $\nu_L \approx 12 \times 10^{-6}$ m^2/s	Tumanovski et al. [91]

24.11.*vi*	$D_{32} = 6 \times 10^{-4} + \frac{1.4\sigma^{0.5}\upsilon_{\mathrm{L}}^{0.21}}{\rho_{\mathrm{G}}^{0.5}}\left(1 + 0.065\frac{\dot{m}_{\mathrm{L}}}{\dot{m}_{\mathrm{G}}}\right) \times \frac{t}{U_{\mathrm{L}}^2\left[0.5\left(\frac{U_{\mathrm{G}}}{U_{\mathrm{L}}}\right)^2 - \frac{U_{\mathrm{G}}}{U_{\mathrm{L}}} + 1\right]}$	110 kg/h $< \dot{m}_L <$ 450 kg/h 5×10^{-6} m^2/s $< \nu_{\mathrm{L}} < 165 \times 10^{-6}$ m^2/s 30 m/s $< U_{\mathrm{G}} <$ 200 m/s 23 kg/h $< \dot{m}_G <$ 450 kg/h $0.17 <$ GLR$^{-1} < 3.8$ 1,500 rpm $< N <$ 1,600 rpm Axial distance = 5 mm Radial distance = 14 mm Atomizing surface must be a disk t and D_{32} in cm, U_{L} and U_{G} in cm/s, and σ in mN/m	Orzechowski [69]
24.11.*vii*	$D_{32} = 6 \times 10^{-4} + \frac{1.4\sigma^{0.5}\upsilon_{\mathrm{L}}^{0.21}}{\rho_{\mathrm{G}}^{0.5}\left(l_{\mathrm{n}}d_{\mathrm{c}} + l_{\mathrm{n}}^2\right)^{0.25}} \times \times \left(1 + 0.065\frac{\dot{m}_{\mathrm{L}}}{\dot{m}_{\mathrm{G}}}\right)\frac{Q_L}{U_{\mathrm{L}}^3\left[0.5\left(\frac{U_{\mathrm{G}}}{U_{\mathrm{L}}}\right)^2 - \frac{U_{\mathrm{G}}}{U_{\mathrm{L}}} + 1\right]}$	d_{c}: the cup rim diameter l_{n}: nozzle length Conditions same as above; however the rotating surface must be a cup	Orzechowski [69]

Table 24.12 Ultrasonic nozzles

Equation number	Correlation	Conditions for use; nomenclature	Investigators
24.12.*i*	$D_{32} = 0.158\left(\frac{\sigma}{\rho_L}\right)^{0.354} \mu_L^{0.303} Q_L^{0.139}$	Frequency is 26 kHz Flow rates up to 50 L/h Liquids used must be either distilled water or solutions of water with methanol and glycerin Valid for standing wave design	Mochida [93]
24.12.*ii*	$D_{32} = 0.53 \frac{Q_L^{0.27} d_0^{0.27} \mu_L^{0.69} \rho_g^{0.48} C_0^{0.97}}{\rho_L^{-0.21} \Delta P_L^{-0.21}}$	C_0: discharge coefficient of the nozzle Valid for standing wave design	Hansmann [94]
24.12.*iii*	$D_{10} = 0.53\left(\frac{d_0 \rho_g U_s^2 \rho_L^2 U_L^2}{P_{max}^2 Re^{0.69}}\right)$	D_s: diameter of active surface of transmitter 20 kHz $< F <$ 120 kHz 360 cm^3/h $< Q <$ 7,200 cm^3/h 65.25 kPa $< P_{max} <$ 167.27 kPa Valid for a standing wave design $0.01 < Re < 1$ $0.1 < We < 200$	Bauckhage et al. [95]
24.12.*iv*	$D_{10} = 0.34\left(\frac{8\pi\sigma}{\rho_L F^2}\right)$	F: vibrating frequency Valid for the capillary wave design 10 kHz $< F <$ 800 kHz Film thickness must be small	Lang [96]
24.12.*v*	$D_{10} = \left(\frac{4\pi^3\sigma}{\rho_L F^2}\right)^{\frac{1}{3}}$	Valid for the capillary wave design It is assumed that SMD will increase proportionally with wavelength	Peskin and Raco [97]
24.12.*vi*	$D_{30} = 0.73\left(\frac{\sigma}{\rho_L F^2}\right)^{\frac{1}{3}}$	Similar to the above equation, with a difference in coefficient Conditions same as for above equation	Dobre and Bolle [98]

Table 24.13 Electrostatic nozzles

Equation number	Correlation	Conditions for use; nomenclature	Investigators and equation Ref. number
24.13.*i*	$D_{32} = 5.39 d_0 \left(\frac{\varepsilon E^2 d_0}{\sigma}\right)^{-0.255} \times \left(\frac{\rho_L Q^2 d_0^3}{\sigma}\right)^{-0.277} \left(\frac{Q}{\mu_L d_0}\right)^{-0.124}$	ε: dielectric constant E: electric field intensity Generally true for all electrostatic nozzles, and the most popular one	Mori et al. [107]
24.13.*ii*	$D_{32} = 3.78934 \times 10^7 \frac{Q_L^{0.48657}}{P_A^{1.82414}}$	P_A: atomizing air pressure Correlation works for an electrostatic twin fluid nozzle (ideally in a wet scrubber)	Bandyopadhyay and Biswas [108]

Chapter 25
Drop-on-Demand Drop Generators

M. Eslamian and N. Ashgriz

Abstract This chapter provides information on different types of drop-on-demand drop generators. It starts with thermal or bubble jets, in which a nucleation bubble is used to eject a droplet out of an orifice. This is followed by piezoelectric, pneumatic, microfluidic, electrohydrodynamics (EHD) and aerodynamic droplet generators. For each droplet generator, the principle of operation and major features and characteristics are described.

Keywords Droplet-on-demand (DOD) droplet generators · Electrohydrodynamics (EHD) droplet generators · Microfluidic droplet generators · Piezoelectric droplet generators · Pneumatic droplet generators · Thermal or bubble jet droplet generators

Introduction

The most natural way of the formation of single droplets is through droplet dripping from a needle in the absence of any disturbances or instabilities. In this process, a drop is detached from a capillary such as a needle, when it is large enough so that the droplet weight overcomes the liquid surface tension holding on to the needle. Owing to the relatively large surface tensions in liquids, droplets that are formed by dripping are much larger than the capillary diameter. In order to produce smaller droplets, instabilities must be present to facilitate and trigger the droplet formation in a controlled manner. In the following sections, major methods of droplet on-demand and controlled formation of droplet streams using various kinds of single droplet generators are described.

M. Eslamian (✉) and N. Ashgriz (✉)
Department of Mechanical and Industrial Engineering, University of Toronto, Toronto, ON, Canada
e-mail: m.eslamian@utoronto.ca; ashgriz@mie.utoronto.ca

N. Ashgriz (ed.), *Handbook of Atomization and Sprays*,
DOI 10.1007/978-1-4419-7264-4_25, © Springer Science+Business Media, LLC 2011

Thermal Ink-Jet or Bubble Jet Drop Generators

Principle of Operation

Perhaps, the most commonly used drop-on-demand (DOD) drop generator is the thermal drop generator. This method is used in most inkjet printers and is referred to as thermal inkjet or bubble jet. The first commercially successful thermal inkjet was introduced by Hewlett-Packard and Canon. Since then, thermal inkjet technology has been improved significantly by increasing the resolution and speed. In a thermal inkjet, a short duration electric pulse (1–5 μs) is applied to a resistive heater to generate a high heat flux. Thus, the ink becomes highly superheated and reaches meta-stable state, forming a vapor bubble. Sudden formation of the vapor bubble generates a pressure impulse, which, in turn, results in the growth of the bubble. The rapid growth of the bubble ejects a small drop of ink out of a nozzle located close to the heater. Once the bubble collapses, the nozzle refills due to capillary forces, becoming ready for the next pulse.

Thermal inkjet technology can also be used whenever pico-jetting of droplets are needed, such as in the bio-medical industry, flat-panel display (liquid crystal and plasma TV) industry, and micro-droplet injector industry [1]. For instance, in the bio-medical industry, it can be used in DNA synthesis that requires dosing of micro-drops with high accuracy [2, 3]. Application to flat-panel display industry is also prominent because of its uniform coating capability [4]. In addition, micro-droplet injectors can be used for controlling the mixing in the combustion chambers of jet engines [5].

The liquid must be superheated to form a vapor bubble. The degree of superheat depends on the properties of the liquid, such as surface tension, viscosity, and the conditions of the heating process. For conventional boiling process at low heating rate, the superheat is only a few degrees above the boiling point of the liquid. However, the superheat can approach 90% of the critical temperature of the liquid with high heat flux [6, 7]. Bubble nucleation occurs when the liquid is sufficiently superheated. As discussed in chapter 10 there are two classes of bubble formation mechanisms [6, 8, 9]. One is based on the heterogeneous nucleation, which occurs when small gas bubbles trapped in minute cracks or crevices on the heated surface become the initiation sites for bubble growth when the liquid is superheated at the liquid/solid interface. Heterogeneous nucleation depends strongly on the properties and the geometry of the heater surface. The other is based on the homogeneous nucleation, which is the result of thermally driven density fluctuations within the liquid. When the density fluctuation is sufficiently large, the low density volume can seed bubble growth. Therefore, homogeneous nucleation depends primarily on the liquid properties. The liquid properties, heated surface properties, and the heating kinetics can determine which of these mechanisms is dominant.

Process Modeling and Experimental Studies

A theoretical model for the heterogeneous nucleation was proposed by Hsu [10] for the growth of pre-existing nuclei in a cavity on a heated surface. The model included the effect of non-uniform superheated liquid. The equation for the activation curve of bubble nucleation was derived by combining the Clausius–Clapeyron and the Young–Laplace equations. Then, by substituting the linear temperature profile into the equation, the range of active cavity sizes on the heated surface was obtained.

The theory of bubble nucleation in a superheated liquid was first applied to the concept of thermal inkjet by Allen et al. [7]. They were able to determine the minimum conditions for the first bubble nucleation by applying Hsu's theory [10]. Time dependent temperature profiles above a heater surface were obtained. By superimposing the activation curve with the thermal boundary layer, the initial bubble size and the minimum temperature for nucleation were determined. Based on a one-dimensional model and by assuming the nucleation temperature to be the superheat limit of the liquid at 330°C transient temperature profiles for the heater structure and the bubble surface after nucleation were obtained. It was noticed that the decay time to ambient temperature from its initial state was only several microseconds after 6 μs heating pulse. The thermal effects of the passivation (protective coating) layer on the heater surface were also analyzed. The results showed that the effective pulse energy required for bubble nucleation increases with the thickness of the passivation layer.

Asai [8, 11, 12] conducted a series of numerical and theoretical studies on the bubble nucleation and growth in thermal inkjets. A one-dimensional numerical model of bubble growth and collapse and the resulting flow motion was presented [11]. The model is divided into two phases. The first phase is for the state before bubble nucleation. The heat transfer process in this phase is approximated by a one-dimensional heat conduction equation from which nucleation temperature is estimated to be 270°C. The second phase describes the bubble generation, growth, and collapse. The temperature and pressure in the bubble are assumed to be uniform and to be related by Clausius–Clapeyron equation and the equation of state. Their results show that the initial pressure is around 4.5 MPa, but it decreases to less than 10 kPa in 10 μs. In addition, effects of viscosity of the ink, the nozzle outlet length, and three different operating voltages on the bubble formation were investigated. A theoretical model was also developed to predict the nucleation process. Nucleation probability was derived from the classical nucleation theory and was used to simulate the initial bubble growth process. It was concluded that the incipient boiling time is not a point value but a stochastic variable and as the heat input increases the initial bubble growth process becomes more reproducible and less random [8]. Another theoretical model of bubble dynamics was proposed by Asai [12]. The nucleation temperature as a function of heat flux was obtained from the classical nucleation theory. The result showed that the nucleation temperature increased linearly with the heat flux. An analytical expression for the time

dependent bubble pressure was developed. The bubble growth process was described as an impulsive motion of a thin vapor film caused by initial bubble pressure.

An empirical equation for the nucleation criterion was derived from the experimental results by Runge [13]. A linear dependency between nucleation temperature and temperature gradient was observed.

Avedisian et al. [14] measured the bubble nucleation temperature by measuring the electrical resistance. The measured resistance was converted into temperature using a calibration heater. An aluminum-tantalum heater with thickness of 0.2 μm, and width of 64.5 μm was used. The bubble nucleation temperature was found by identifying the inflection point from time dependent temperature profiles. Their results were in good agreement with the homogeneous nucleation theory. Therefore, they concluded that homogeneous nucleation governs the boiling process in micro-heaters at high heating rates. They also noted that the nucleation temperature increased with heating rate.

Chen et al. [15] performed a numerical study on the bubble growth and ink ejection process of a thermal inkjet printhead. Based on a one-dimensional unsteady heat conduction model and theories presented by Asai [12], the bubble volume, temperature, and pressure at various operating voltages were obtained [12, 15]. It was found that the bubble volume decreases with increasing voltage. The relationship between threshold voltage and the pulse width was also presented. The threshold voltage was taken to be the minimum value that could generate enough heat for bubble nucleation at the end of the heating pulse.

Lin et al. [16] conducted an experimental study on the bubble formation on a line shaped polysilicon micro-resistor, which was immersed in the sub-cooled liquids such as Fluorinert fluids (inert and dielectric fluids from 3M Company), water, and methanol. Three different types of input currents were applied after initial nucleation. First, a bubble grew and departed when the input current was constant or increased. Second, a bubble collapsed when the current was turned off abruptly. Third, the size of the bubble decreased and stayed on the top of the heater when the current was reduced gradually. Some important bubble formation phenomena such as Marangoni effects on a microscale, controllability of the size of the microbubbles, and bubble nucleation hysteresis were reported.

In an experimental study of explosive vaporization of the bubble on a microheater, by detecting acoustic emissions during explosive vaporization process of the bubble, the bubble volume and the bubble expansion velocity and acceleration was reconstructed [17]. The vapor pressure inside the bubble was also calculated using the Rayleigh–Plesset equation.

Measuring the nucleation temperature directly is not a simple task because of the limited physical size of the heater and extremely small time scale. Avedesian et al. [14] have measured bubble nucleation temperatures on the surface of inkjet heater by identifying an inflection point on the temperature profile of the heater surface.

Droplet Ejection Characteristics

A detailed experimental and numerical investigation of bubble nucleation, growth and collapse in thermal inkjets is conducted by Hong et al. [18, 19]. A typical result of their experiments showing the top and the front views of the explosive boiling for a thermal jet is shown in Fig. 25.1 [18]. The process consists of isolated bubble nucleation, formation of the vapor sheet, growth and collapse of the bubble, and bubble rebound. The first nucleation of the bubble starts at $t = 2.8$ μs into the heater pulse (Fig. 25.1a). Only few nucleate bubbles appear at this stage. While the initial bubbles are still growing, more nucleation sites are observed at $t = 3.2$ μs into the heater pulse (Fig. 25.1b). The location of nucleation sites and the size of bubbles for each event are almost identical over long period of time until the surface geometry and/or the material property of the heater change due to the hours of thermal stresses and cavitation processes. Figure 25.1 clearly shows the identical nucleation sites for two different events at 45 V. Identical nucleation events occurred for all voltages tested here. Coalescence of the small bubbles leads to the formation of a vapor sheet, which covers the entire heater surface, as seen at $t = 3.6$ μs into the

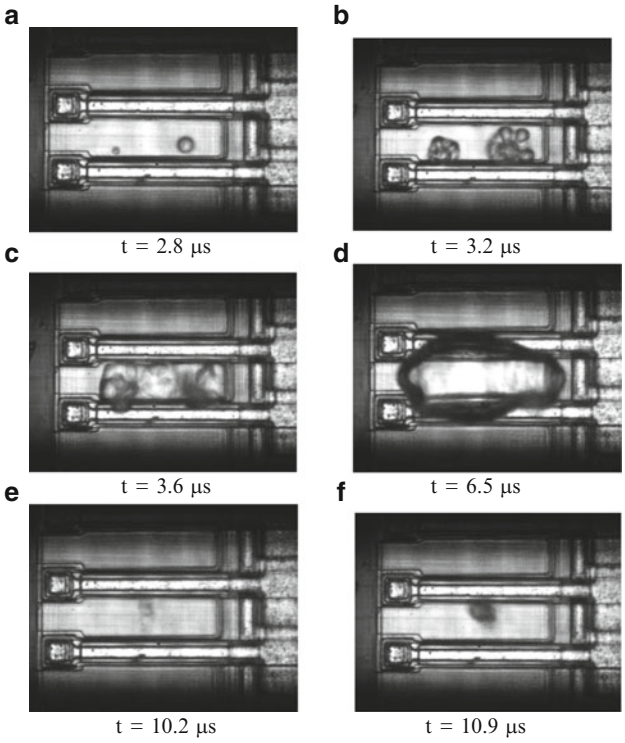


Fig. 25.1 Bubble growth and collapse (**a**) and (**b**) Nucleation and Growth, (**c**) Vapor sheet formation, (**d**) Maximum size, (**e**) Collapse, (**f**) Rebound

heating pulse in Fig. 25.1c. The bubble grows to a maximum size around $t = 6.5$ μs (Fig. 25.1d). It then starts shrinking until it reaches to a minimum size around $t = 10.2$ μs (Fig. 25.1e). A small rebounding bubble follows around $t = 10.9$ μs (Fig. 25.1f) before it collapses completely around $t = 12.0$ μs. Unlike the nucleation stage, in the rebound stage the process is not very repeatable. Although the location of the rebound is almost consistent, the formation of the rebounding bubble is different. Sometimes only a small spherical bubble is observed, whereas, other times several attached bubbles are seen. The shape of the bubble does not stay the same at the same time delay during the rebound phase. The radius of the re-growing bubble is around 10 μm and its life time is about 1.5 μs. The main cause of this rebound can be attributed to the compression of non-condensable gas within the bubble during bubble collapse.

Hong et al. [18] provided the following information on thermal inkjets: The maximum size of the bubble does not change above a threshold pulse duration. This threshold value corresponds to the time of vapor sheet formation. The initial liquid temperature does affect the time of nucleation and the maximum size of the bubble increases with increasing the initial liquid temperature. Times to reach the phase of nucleation, vapor sheet formation, maximum bubble size, and bubble collapse decrease linearly with an increasing input voltage. Experimentally determined nucleation temperatures for a given heating rate are slightly below the limit of superheat of water and show a weak linear dependency on the heating rate. Since the nucleation temperature is close to the super heat limit of the liquid and the dependency of the heating rate is weak, the mechanism of the bubble formation is the homogeneous nucleation. The maximum size of the bubble decreases with an increasing input voltage since the energy transferred and the pressure impulse during pulse heating decreases. The time evolution of the bubble wall velocity and acceleration are determined throughout the process. Both the velocity and acceleration show abrupt changes near the point of the collapse. The pressure inside the bubble remains below the atmospheric pressure until it bounces back near the collapse point.

Piezoelectric Droplet Generators

Piezoelectric Printhead

Piezoelectric droplet generators have also been mainly developed for the inkjet printing, but are now being used in a wide variety of industries for micro-droplet generation [20]. Starting with continuous (or pressurized) jetting, ink jetting has entered the age of DOD (or pulsed jetting) technique [21], which can be divided into thermally and piezo-electrically driven DOD methods [22].

Figure 25.2 schematically shows the inner structure of an inkjet printer with "bend mode" [22] piezoelectric DOD technique. Due to the pressure generated by a voltage-pulse driven piezoelectric actuator, liquid is ejected out of small orifices

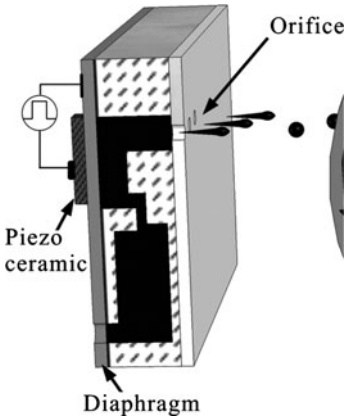


Fig. 25.2 A "bend mode" piezoelectric DOD printhead

(diameter $d \sim 20$ μm) with pulsed flow rates to form pulsed jets. The pulsed jetting and droplet generation processes are sensitive to waveform [23], nozzle structure [24] and liquid (e.g., ink) properties [25]. There are a few published studies on the jetting process; however, there are numerous unpublished industrial research works in the field. Yang et al. [26] numerically investigated the formation of droplets by changing nozzle dimensions, ejection time and fluid properties. Meinhart and Zhang [27] used a PIV (particle image velocimetry) system to examine the instantaneous velocity field and evolution of meniscus in an inkjet printhead. The flow field of ejected ink was found to be strongly coupled to the evolution of meniscus during ejection process. Gans et al. [25] also showed that different fluids exhibited varied jetting behaviors. Bogy and Talke [24] experimentally and theoretically studied the ink jetting characteristics in relation to the propagation and reflection of acoustic waves inside inkjet chamber.

Other parameters that affect the jetting process are the voltage amplitude of electric pulses applied to the piezoelectric and the jetting frequency. Low working voltages generate droplets with low velocities, and droplet trajectory, therefore, become vulnerable to convective flows outside of the generator. For instance, in inkjet printers, in order to accurately place droplets on print target, high working voltages are usually preferred. In addition, depending on the jetting frequency, a pulsed jet, where fluid is supplied with pulsed flow rates, can behave in two modes: low frequency mode and high frequency mode. In the low frequency mode, liquid inside the nozzle comes to rest before the next pulse is applied. Consequently, each pulse generates a ligament that detaches from the remaining liquid in the orifice. In the high frequency mode, a jet with periodic perturbations on its surface is formed, and droplets break up from the jet at the applied frequency. In practice, high ejection frequencies are required for high printing speed.

There is often a trade-off between high working voltage and high frequency on one hand, and droplet consistency and nonexistence of satellite droplets on the other hand. When the frequency of applied pulse signal is low, liquid inside the nozzle has enough time to come to rest before the next pulse is applied. Therefore, the

jetting process of each pulse is not affected by the previous one, and it does not affect the next one.

Typical images of the time evolution of droplet formation upon application of a pulsed force on the liquid chamber in a typical inkjet printer are shown in Figs. 25.3 and 25.4 [28, 29]. The jetting process starts with the appearance of outward moving meniscus ($t = 0$ μs), which keeps growing into a ligament connected to the orifice. After reaching a limiting length (L_m), the ligament separates from the remaining liquid in the orifice. For low working voltages (Fig. 25.3), ligaments contract and eventually form spherical droplets. For large voltages (Fig. 25.4) satellite droplets are observed.

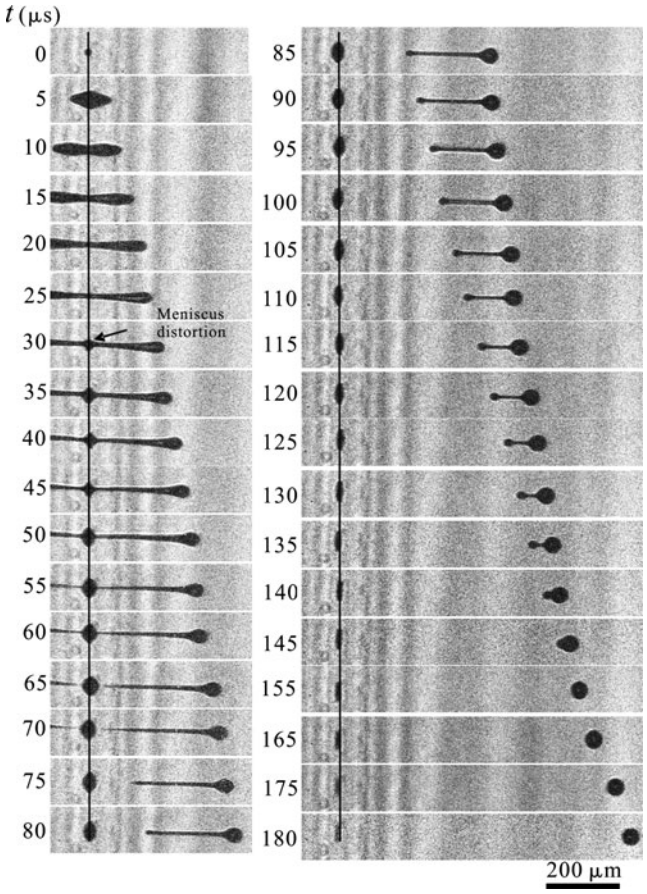


Fig. 25.3 Time sequence of droplet formation in response to one pulse ($V_p = 29$ V). The ink is ejected rightward, and the vertical line shows the location of orifice. Meniscus distortion appears at $t \sim 30$ μs. Mirror images due to reflection from the printhead are visible on the right side of the orifice. Images from a solid ink printhead (Phaser 860 provided by Xerox Corporation, Rochester, NY) with orifice diameter of $d \sim 20$ μm (Reproduced from [28]. With permission. Copyright 2008)

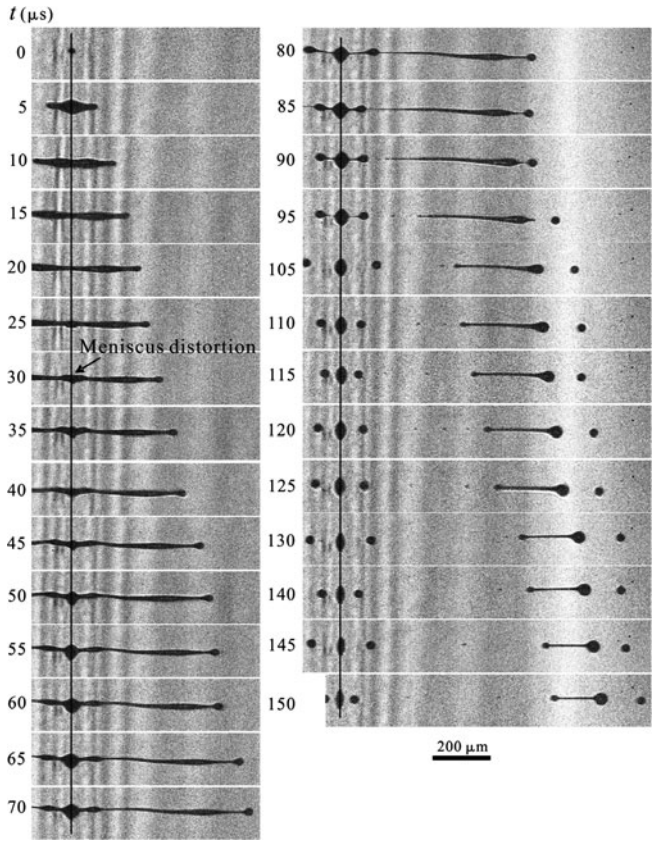


Fig. 25.4 Time sequence of droplet formation in response to one pulse ($V_p = 32$ V). The ink is ejected rightward, and the vertical line shows the location of orifice. Meniscus distortion appears at $t \sim 30$ μs. Images from a solid ink printhead (Phaser 860 provided by Xerox Corporation, Rochester, NY) with orifice diameter of $d \sim 20$ μm (Reproduced from [28]. With permission. Copyright 2008)

For continuous jets with low flow rates, it has been found that the limiting length increases with increasing fluid velocity [30], increasing viscosity [31] and decreasing surface tension [32]. The limiting length also depends critically on a viscous length scale [33] given by $L_v = \mu^2/\rho\sigma$. All these effects can be combined to obtain the limiting length of the jet formed through the following nondimensional form:

$$\frac{L_m}{d} \propto Oh_o Ca \tag{25.1}$$

where Oh_o and Ca are the Ohnesorge and capillary numbers defined as $Oh_o = \mu/\sqrt{\rho\sigma d}$ and $Ca = U_j\mu/\sigma$. The experimentally obtained constant for this relation is around 23: $L_m/d = 23 Oh_o Ca$.

Figures 25.3 and 25.4 show that liquid ligaments detach from the remaining liquid in the orifice with a conical tip. This is due to the abrupt stop of liquid motion inside the nozzle. This conical point quickly forms a round end, due to local sharp curvature. The ligaments formed in Fig. 25.3 contract into droplets without breakup, while the jet in Fig. 25.4 breaks into a ligament and satellite droplets.

The pinch-off time scale of inviscid jets is in the order of $\sim 5(\rho R^3/\sigma)^{0.5}$, where R is jet radius [34]. And the Rayleigh instability time scale is $\sim 10(\rho R^3/\sigma)^{0.5}$ for the initial disturbance amplitude as large as $0.2R$ [35]. Therefore, unless a disturbance with even larger initial amplitude was created with wavelengths larger than the circumference of undisturbed jet, the Rayleigh instability would be slower than the pinch-off process [34].

General Purpose Piezoelectric Droplet Generators

Droplet Generators that Use Disk-Type Piezoelectric Ceramics

A disk-type piezoelectric ceramic and some sequential pictures of droplet ejection from this droplet generator are shown in Fig. 25.5 [36]. The piezoelectric buzzer is constructed of a 0.2 mm piezoelectric ceramic layer, which sticks on a vibration diaphragm with a 27 mm diameter. It is fixed within the main body and bends when a voltage pulse is applied. The pressure is generated in the liquid flow channel and pushes the liquid out of the glass nozzle.

Fan et al. [36] studied the effect of various parameters on droplet size and velocity. The droplet size almost linearly increases with the nozzle diameter. Pulse voltage and pulse width has also a linear effect on the droplet volume. They also identified four types of droplet formation.

Type 1, the desired type, is when only one main drop forms and flies straight. In other types, a satellite droplet also forms in addition to the main droplet. In type 2, the satellite and the mother droplets combine and form one single droplet after ejection. In type 3, the satellite droplet will be sucked back to the nozzle before ejection. Type 4, is the unstable mode in which a satellite and a mother droplet form, disperse, and fly randomly.

Droplet Generators That Use Tubular Piezoelectric Ceramics

Tubular piezoelectric ceramics have been also used to generate droplets on demand [37]. Figure 25.6 shows a (glass) capillary in the core coupled with a piezoelectric ceramic. Almost the entire inner and outer surface of the piezoceramic tube has an electrode. A voltage between the inner and outer electrode causes the tube to contract in a longitudinal direction, thereby reducing its diameter. The piezoelectric tube is driven by a pulse generator.

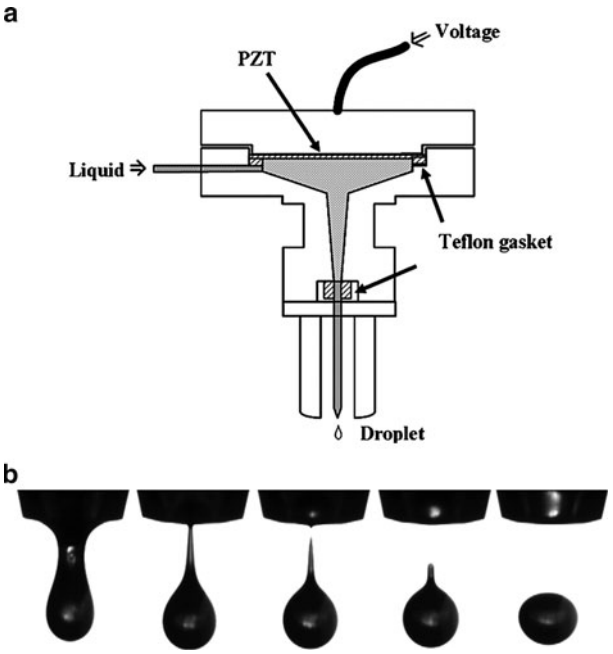


Fig. 25.5 (**a**) Schematic of a piezoelectric droplet generator; (**b**) sequences of droplet ejection from the droplet generator (Reproduced from [36]. With permission. Copyright 2008 Elsevier)

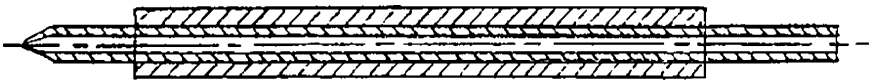


Fig. 25.6 Drawing of a piezoceramic tube with imbedded capillary (Reprinted from [37]. With permission. Copyright 2001 Wiley)

The diameter of the droplet produced by the electromechanical pulse is approximately equivalent to the diameter of the capillary orifice. By varying the pulse amplitude it is possible to alter this value by approximately 10%.

Acoustic Droplet Generators

Principle of Operation

Loudspeakers may be employed as a source of disturbance generation in droplet on demand or continuous droplet stream generators [38]. An acoustic droplet generator is shown in Fig. 25.7 [39]. Typically, these droplet generators consist of a

loudspeaker, a thin membrane, and a liquid chamber with an orifice. Figure 25.7b shows several sequential images of droplet formation using the described acoustic generator. As seen, due to the nature of the disturbance generation, it seems that

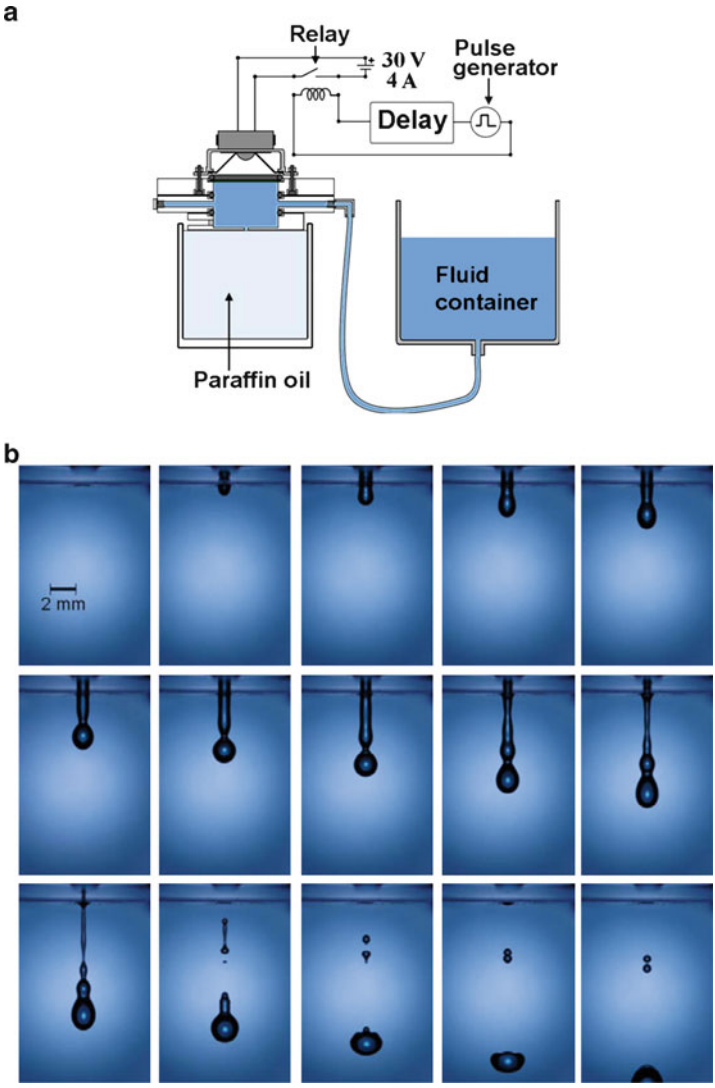


Fig. 25.7 (**a**) Schematic of the acoustic droplet generator. The paraffin oil container may be used for experiments in which jets of one liquid are to be projected into another and can be removed for experiments in air. (**b**) Photographic sequence showing the formation and ejection of an equimass water/glycerol droplet into air. The drive voltage was a square pulse of 10 V amplitude and 15 ms duration. Frames are 2 ms apart. Drop velocity is 0.54 m/s (Reprinted from [39]. With permission. Copyright 2008 American Institute of Physics)

achieving a controllable droplet generation pattern is more challenging compared to the piezoelectric droplet generators. Also, the scale bar shows that the generated droplets are large.

Pneumatic Droplet Generators

Principle of Operation

Another type of droplet generator is based on applying a gas or liquid pressure pulse on a liquid to be ejected. These are referred to as pneumatic droplet generators [40, 41].

A typical pneumatic drop generator is shown in Fig. 25.8 [40]. It consists of a robust steel chamber, a nozzle at the bottom, and a T-junction arrangement at the top. Instead of using a piezoelectric ceramic and a pulse generating device, it works based on applying pulses of a pressurized gas to the liquid contained in the chamber, forcing out droplets through the nozzle in the bottom plate of the generator. A solenoid valve is rapidly opened and closed to create pressure pulses. In each pulse, one or more droplets emerge from the nozzle exit. The nozzle is a cylindrical

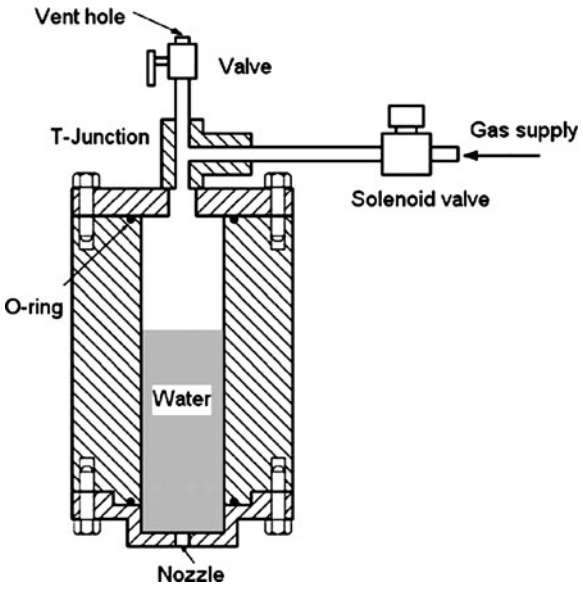


Fig. 25.8 Schematic of a pneumatic droplet generator (Reprinted from [40]. With permission. Copyright 2003 of Elsevier)

synthetic sapphire nozzle of about 0.1 mm diameter. Owing to this small size, droplets only may be ejected if a gas pressure pulse is applied.

Droplet generation in this technique is controlled by the gas pulse duration (solenoid valve duration), the vent-hole diameter, and the gas supply pressure. By proper adjustment of these parameters, single droplets are ejected per gas pulse.

Figure 25.9 shows the pressure variation in the cavity of the droplet generator during the formation of a single water droplet. The supply pressure is 138 kPa, the width of the pulse used to open the solenoid valve is 4.61 ms and the release needle valve is kept fully open. The timing of the electrical pulse sent to open the solenoid valve is also shown in the figure (dashed line). Time $t = 0$ corresponds to the start of the pulse. Using these conditions, only a single droplet forms. It is seen that the pressure in the cavity oscillates at a constant frequency while its amplitude gradually decreases.

Note that in Fig. 25.9 at some times the cavity pressure becomes negative, meaning that the emerging liquid is pulled back to the chamber. This effect has been used to generate droplets that are even smaller than the orifice size [41], provided that the negative pressure is sufficiently large. Small droplets may not form when liquid viscosity is too low or too high. For pure water, droplet diameters were several times that of the nozzle. Using more viscous glycerin mixtures, droplets with diameters as small as 65% of the nozzle diameter were produced using this pneumatic droplet generator. Figure 25.10 shows the picture of emerging liquid and droplet formation for 85 wt% water-glycerin solution. A droplet has

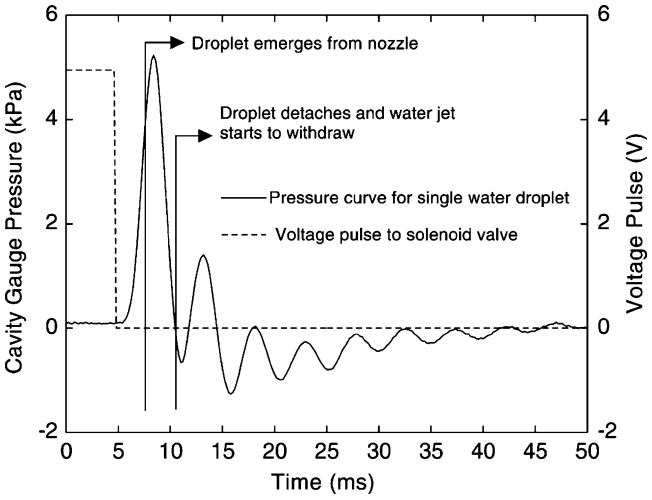


Fig. 25.9 Measured pressure variation (*solid line*) inside the droplet generator cavity when a 4.61 ms pulse was used to trigger the solenoid valve. The applied pulse is also shown (*dashed line*). In this case, a single droplet is emerged (Reprinted from [40]. With permission. Copyright 2003 of Elsevier)

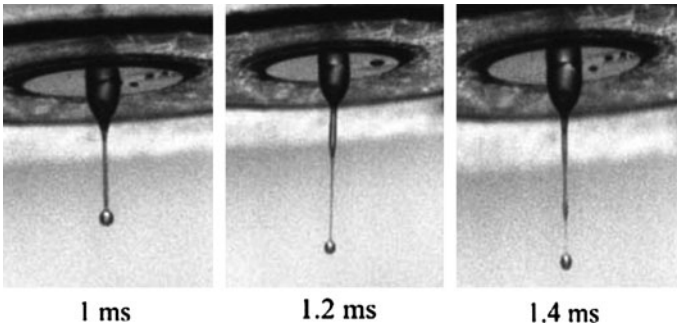


Fig. 25.10 Emerging single small droplet from a 204 lm diameter nozzle at a 5.937 ms pulse width; liquid: mixture with 85 wt% glycerin, supply pressure is 69 kPa, exit vent tube length is 24.5 cm (Reprinted from [41]. With permission. Copyright 2008 of Elsevier)

formed at the tip of the emerging liquid tongue and then, as the filament or ligament becomes thinner, a small droplet is emerged.

Microfluidic Droplet Generators

Principle of Operation

Microfluidic generation of droplets is a method of droplet formation in microfluidic channels. It works by combining two or more streams of immiscible fluids and generating a shear force on the discontinuous phase causing it to break up into discrete droplets. In contrast to piezoelectric, pneumatic and acoustic forms of droplet generation, in this method, there is no need for an actuator to impose instabilities on the liquid jet. In the absence of an actuator, the size and polydispersity of the droplets are determined by the dimensions of microchannels, the flow rates of liquids, wetting properties of microchannels, etc.

This method is able to produce droplets with controlled sizes, shapes, and internal structures. It is particularly used to produce single or multi-component liquid emulsion droplets, in which droplets are formed and dispersed in another immiscible liquid to form an emulsion, such as water in oil emulsions.

The capillary number, Ca, is used to predict droplet behavior:

$$Ca = \mu u/\sigma$$

where μ and u are the viscosity and velocity of the continuous phase, and σ is the interfacial tension between the two immiscible phases. Above a critical capillary number, which depends on the channel geometry, droplet formation starts.

T-junction and flow-focusing design/device (FFD) are the two main and traditional methods of droplet formation in microfluidic applications. Other emerging methods include dielectrophoresis and electrowetting on dielectric [42].

In the T-junction channel layout, a fluid flows through the inlet channel and perpendicularly intersects the main channel. The two phases form an interface at the junction, and as the fluid flow continues, the tongue of the dispersed phase enters the main channel due to the shear forces generated by the continuous phase and the subsequent pressure gradient. As the result, the neck of the dispersed phase thins and eventually breaks the stream into a droplet.

In the flow-focusing configuration, the dispersed and continuous phases are forced through a narrow region in the microfluidic device. The design employs symmetric shearing by the continuous phase on the dispersed phase which enables more controlled and stable generation of droplets. The main difference between the two configurations is that a sheet flow is created ahead of the restriction in case of the focused-flow droplet generator whereas the T-junction droplet generator solely relies on the shear force at the channel Tee.

Figure 25.11 schematically shows the process of droplet formation suspended in another liquid (emulsification) in a single planar flow using the focusing design (FFD). Liquid A and liquid B, are supplied to the central and the side channels, respectively. A pressure gradient along the long axis of the device forces two liquids through the narrow orifice of the FFD. In Fig. 25.11, liquid A does not wet the walls of the microchannels. Liquid B surrounds the inner stream of liquid A so that the thread becomes unstable and breaks up in a periodic manner to release droplets of liquid A into the downstream channel. Droplets may form in the dripping, flow-focusing, or jetting regimes. Each regime produces droplets with a characteristic size and size distribution. When liquid A wets the material of FFD, emulsification occurs in a manner resembling the formation of droplets at a T-junction, as shown in Fig. 25.11b. In the orifice, liquid A adheres to the wall of the microchannel while a stream of liquid B is sheared off to produce droplets. Thus instead of the emulsion of liquid A, as in Fig. 25.11a, the process of emulsification yields an emulsion of liquid B [43].

In addition to the formation of single-component droplets in another liquid, multi-component droplets dispersed in another liquid may also be formed using microchannels. This process is schematically illustrated in Figure 25.12. Two

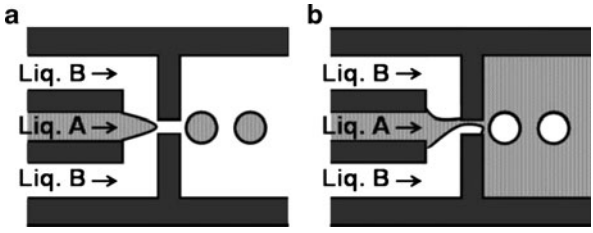


Fig. 25.11 Schematics depicting two mechanisms of droplet formation in a microfluidic flow focusing device (FFD) (Reprinted from [43]. With permission. Copyright 2007 the Royal Society of Chemistry)

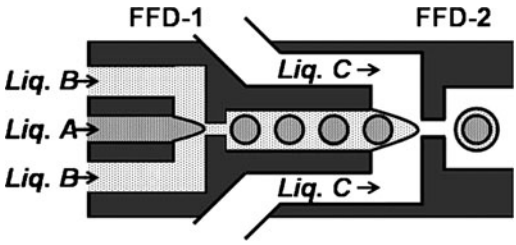


Fig. 25.12 Schematics of consecutive flow-focusing double droplet generator producing double emulsions (Reprinted from [43]. With permission. Copyright 2007 the Royal Society of Chemistry)

immiscible liquids, A and B, are introduced in the first FFD (FFD-1) in a manner similar to that shown in Fig. 25.11. Liquid B wets the FFD-1 and forms a continuous phase while the thread of liquid A (not wetting FFD-1) breaks up and releases droplets. In the second flow focusing device (FFD-2), liquid C, immiscible with B, is introduced in the two outermost channels. Liquid C has a higher affinity for the FFD-2 than liquid B. A thread of the primary emulsion generated in FFD-1 is focused in the second orifice by liquid C, where it collapses and releases droplets with a core of liquid A engulfed by a shell of liquid B [43].

Electro-Hydrodynamic Droplet Generators

Electro-hydrodynamic (EHD) droplet generation has been theoretically studied by Crowley [44, 45]. He presented a theory of EHD exciters that predicts the breakup length of the jet in terms of the geometry and physical properties of the droplet generator. It seems that he has made an EHD droplet generator, but the details of the device was not available to the authors; also to our knowledge, no further investigation has been performed on EHD droplet generation.

In an EHD droplet generator, an electric field acts directly on the surface of an electrically conducting jet after it has been formed and ejected from the nozzle. At proper electric field frequency, it disturbs the jet by inducing compression and expansion of the jet, which will eventually cause the jet to break up into droplets.

In contrast to other types of droplet generators, such as acoustic and vibrating orifice droplet generators, in EHD droplet generator, the initial disturbance is physically separated from the nozzle, and directly acts on the liquid jet.

Aerodynamics Droplet Generator

Aerodynamics droplet generators use a coaxial air to separate a slow forming droplet at a tip of a capillary tube (Fig. 25.13). Having no moving parts and no electronic parts, the technique has the advantage of being simpler than those described in previous sections. As originally developed [46], the gas outlet was located just above the tip of the liquid tube.

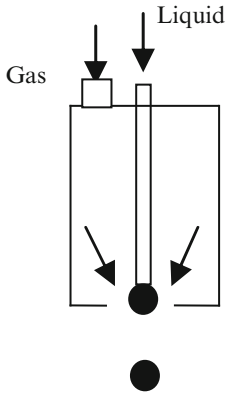


Fig. 25.13 Schematic of an aerodynamics droplet generator

Later work [47] improved the design by placing the liquid tip fully inside a long gas flow tube and demonstrating that the droplets would be swept along the centerline of the gas tube while accelerating to exit velocities of up to 10 m/s. Another design [48] of this type places the tip of the liquid tube at the throat of a venturi through which the gas flows. One difficulty with the designs employing gas flow tubes or venturies is positioning the liquid tube tip (100–200 μm diameter) within the gas tube – whose inner diameter is typically less than 1 mm. Adequate alignment was achieved in prior designs by adjusting small positioning screws that moved the liquid tip radially [47], and by employing a three axis micrometer stage [48].

When a liquid flows out of a small tube at a very low flow rate, it forms a pendant droplet at its tip. As the droplet grows it effectively blocks the flow of gas in the annulus which surrounds it. Pressure difference between the upstream and downstream sides of the pendant droplet, in addition to viscous fluid drag, provides the force that strips the liquid droplet from its tube-ejecting it from the generator. Since, typically, the droplet occupies a large fraction of the hole area, a rather short length of hole is sufficient to establish a very stable exit trajectory.

Figure 25.14 shows the variation of droplet diameter with the diameter of the gas flow hole at the minimum and maximum pressures. This plot defines the attainable range of droplet diameters corresponding to a given gas flow hole size. It can be used as a guide in selecting dimensions for a particular application.

The linear behavior of Figure 25.14 makes it extremely easy to predict the performance of the droplet generator once the flow rates, diameters, and velocities corresponding to the critical pressures are known. Equations which correlate these quantities to the gas flow hole size can be obtained empirically.

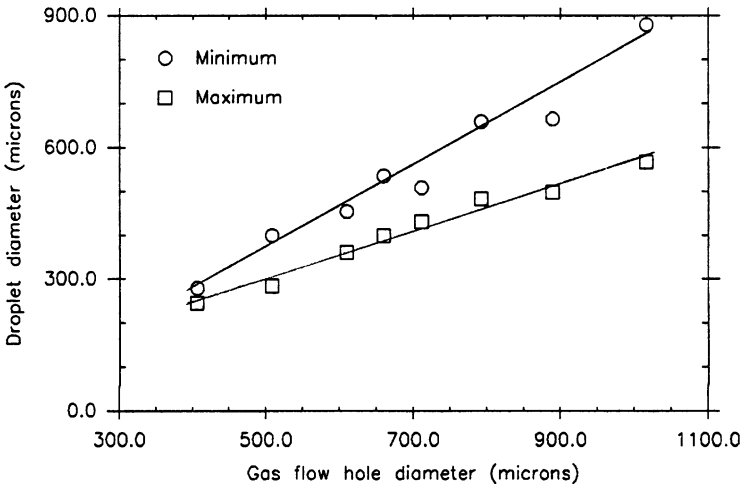


Fig. 25.14 Droplet diameter versus the gas hole diameter for both the minimum and maximum critical pressures

References

1. J.-T. Yeh: Simulation and industrial Applications of Inkjet, Presented at the Seventh National Computational Fluid Dynamics Conference, August 2000, Kenting (2000).
2. T. Goldmann and J. S. Gonzalez: DNA printing: utilization of a standard inkjet printer for the transfer of a nucleic acid to solid supports, Journal of Biochemical and Biophysical Methods, 42, 105–110 (2000).
3. C. Maier, S. Wiesche, and E. P. Hofer: Impact of microdrops on solid surfaces for DNA-synthesis (2000), Available online at: http://www.comppub.com/publications/MSM/2000/pdf/T42.07.pdf
4. M. Grove, D. Hayes, R. Cox, and D. Wallace: Color flat panel manufacturing using inkjet technology, Display Works'99, San Jose (1999).
5. F. Tseng: A micro droplet injector system, Ph.D. thesis, University of California, Los Angeles (1998).
6. M. Blander and J. L. Katz: Bubble nucleation in liquids, AIChE Journal, 21(5), 833–848 (1975).
7. R. R. Allen, J. D. Meyer, and W. R. Knight: Thermodynamics and hydrodynamics of thermal ink jets, Hewlett-Packard Journal, 36, 21–27 (1985).
8. A. Asai: Application of the nucleation theory to the design of bubble jet printers, Japanese Journal of Applied Physics, 28(5), 909–915 (1989).
9. J. R. Andrews and M. P. O'Horo: Initial stages of vapor bubble nucleation in thermal inkjet processes, Proceedings of SPIE – The Internation Society for Optical Engineering, 2413, 182–188 (1995).
10. Y. Y. Hsu: On the size range of active nucleation cavities on the heating surface, Journal of Heat Transfer, 84, 207–216 (1962).
11. A. Asai, T. Hara, and I. Endo: One-dimensional model of bubble growth and liquid flow in bubble jet printers, Japanese Journal of Applied Physics, 26(10), 1794–1801 (1987).
12. Asai: Bubble dynamics in boiling under high heat flux pulse heating, Journal of Heat Transfer, 113, 973–979 (1991).

13. W. Runge: Nucleation in thermal ink-jet printers, IS&T's Eighth International Congress on Advances in Non-Impacting Technologies, Springfield, 299–302 (1992).
14. C. T. Avedisian, W. S. Osbourne, F. D. McLeod, and C. M. Curley: Measuring bubble nucleation temperature on the surface of a rapidly heated thermal inkjet heater immersed in a pool of water, Proceedings of the Royal Society of London, Series A, 455, 3875–3899 (1999).
15. P. Chen, W. Chen and S. H. Chang: Bubble growth and ink ejection process of a thermal ink jet print head, International Journal of Mechanical Sciences, 39 (6), 683–695 (1997).
16. L. Lin, A. P. Pisano, and V. P. Carey: Thermal bubble formation on polysilicon micro resistor, Journal of Heat Transfer, 120, 735–742 (1998).
17. Z. Zhao, S. Glod, D. Poulikakos: Pressure and power generation during explosive vaporization on a thin film microheater, International Journal of Heat and Mass Transfer, 43, 281–296 (2000).
18. Y. Hong, N. Ashgriz, and J. Andrews: Experimental study of bubble dynamics on micro heaters induced by pulse heating, ASME Journal of Heat Transfer, 126(2), 259–271 (2004).
19. Y. Hong, N. Ashgriz, J. Andrews and H. Parizi: Numerical simulation of growth and collapse of a bubble induced by a pulsed micro-heater, Journal of Microelectromechanical Systems, 13(5), 857–869 (2004).
20. J. Krestschmer, C. Tille, and I. Ederer: A drop-on demand inkjet printhead for a wide range of applications, IS&Ts NIP 14: International Conference on Digital printing technologies, Seattle, pp. 343–347 (1997).
21. M. Döring: Ink-jet printing, Philips Technical Review, 40, 192–198 (1982).
22. H. P. Le: Progress and trends in ink-jet printing technology, Journal of Imaging Science and Technology, 42, 49–62 (1998).
23. R. G. Self and D. B. Wallace: Method of drop size modulation with extended transition time waveform, US Patent No. 6029896 (2000).
24. D. B. Bogy and P. E. Talke: Experimental and theoretical study of wave propagation phenomena in drop-on-demand ink jet devices, IBM Journal of Research and Development, 28(3), 314–321 (1984).
25. B. J. Gans, L. Xue, U. S. Agarwal, and U. S. Schubert: Ink-jet printing of linear and star polymers, Macromolecula Rapid Communications, 26, 310–314 (2005).
26. A. S. Yang, J. C. Yang, and M. C. Hong: Droplet ejection study of a picojet printhead, Journal of Micromechanics and Microengineering, 16, 180–188 (2006).
27. C. D. Meinhart and H. Zhang: The flow structure inside a microfabricated inkjet printhead, Journal Microelectromechanical Systems, 9(1), 67–75 (2000).
28. R. Li, N. Ashgriz, and S. Chandra: Droplet generation from pulsed micro-jets, Journal of Experimental Thermal and Fluid Science, 32, 1679–1686 (2008a).
29. R. Li, N. Ashgriz, S. Chandra, and J. R. Andrews: Contraction of free liquid ligaments, AIChE Journal, 54(12), 3084–3091 (2008b).
30. X. Zhang and O. A Basaran: An experimental study of dynamics of drop formation, Physics of Fluids, 7, 1184–1203 (1995).
31. D. M. Henderson, W. G. Pritchard, and L. B. Smolka: On the pinch-off of a pendant drop of viscous fluid, Physics of Fluids, 9(11), 3188–3200 (1997).
32. X. D. Shi, M. P. Brenner, and S. R. Nagel: A cascade of structure in a drop falling from a faucet, Science, 265, 219–222 (1994).
33. D. H. Peregrine, G. Shoker, and A. Symon: The bifurcation of liquid bridges, Journal of Fluid Mechanics, 212, 25–39 (1990).
34. R. M. S. M. Schulkes: The contraction of liquid filaments, Journal of Fluid Mechanics, 309, 277–300 (1996).
35. P. Lafrance: Nonlinear breakup of a laminar liquid jet, Physics of Fluids, 18(4), 428–432 (1975).
36. K-C. Fan, J.-Y. Chen, C.-H. Wang, and W.-C Pan: Development of a drop-on-demand droplet generator for one-drop-fill technology, Sensors and Actuators A, 147, 649–655 (2008).

37. H. Ulmke, T. Wriedt, and K. Bauckhage: Piezoelectric droplet generator for the calibration of particle-sizing instruments, Chemical Engineering and Technology, 24(3), 265–268 (2001).
38. C. O. Pedersen: An experimental study of the dynamic behavior and heat transfer characteristics of water droplets impinging upon a heated surface, International Journal of Heat and Mass Transfer, 13(2), 369–381 (1970).
39. J. R. Castrejón-Pita, G. D. Martin, S. D. Hoath, and I. M. Hutchings: A simple large-scale droplet generator for studies of inkjet printing, Review of Scientific Instruments, 79, 075108 (2008).
40. S. Cheng and S. Chandra: A pneumatic droplet-on-demand generator, Experiments in Fluids, 34, 755–762 (2003).
41. A. Amirzadeh Goghari and S. Chandra: Producing droplets smaller than the nozzle diameter by using a pneumatic drop-on-demand droplet generator, Experiments in Fluids, 44, 105–114 (2008).
42. S.-Y. Teh, R. Lin, L.-H. Hungb and A. P. Lee: Droplet microfluidics, Lab Chip, 8, 198–220 (2008).
43. M. Seo, C. Paquet, Z. Nie, S. Xu and E. Kumacheva: Microfluidic consecutive flow-focusing droplet generators, Soft Matter 3, 986–992 (2007).
44. J. M. Crowley: Electrohydrodynamic droplet generators, Journal of Electrostatics, 14, 121–134 (1983).
45. D. W. Hrdina and J. M. Crowley: Drop-on-demand operation of continuous jets using EHD techniques, IEEE Transactions on Industry Applications, 25(4), 705–710 (1989).
46. R. Lane: A Microburette for producing small liquid drops of known size, Journal of Scientific Instruments, 24, 98–101 (1947).
47. R. B. Peterson: Characterization of a simple, high Reynolds number droplet generator for combustion studies, Review of Scientific Instruments, 59(6), 960–966 (1988).
48. G. J. Green, F. Takahashi, D. E. Walsh, and F. L. Dryer: Aerodynamic device for generating mono-disperse fuel droplets, Review of Scientific Instruments, 60(4), 646–652 (1989).

Chapter 26
Droplet Stream Generator

G. Brenn

Abstract The working principle and the functioning of droplet stream generators are discussed. The essential feature of these generators is that the size of the droplets produced can be accurately controlled. This makes the generators important tools for setting initial or boundary conditions of the droplets in transport processes. Droplet sizes may range between 10 μm and the order of millimeters. Droplet streams and sprays produced with this technique may be very accurately monodispersed. Devices suitable for producing such droplet streams and sprays are presented and discussed. Ranges of the relevant operation parameters and spray properties are specified. Electric charging of the droplets allows the droplet trajectories to be controlled. Fields of application of the droplet stream generators, ranging from packaging to rapid prototyping and space applications, are addressed.

Keywords Discrete polydisperse spray · Electric droplet charging · Extension nozzle · Ink-jet printing · Monodisperse droplet stream · Monodisperse spray · Multihole orifice · Modulated jet excitation · Nozzle hole shapes · Rapid prototyping · Rayleigh-type jet break-up · Solder ball production

Introduction

This section puts together the state-of-the-art of the technology for producing streams of droplets with controlled size by means of droplet stream generators. The purpose of using such devices is to produce droplets with controlled size as boundary or initial conditions for transport processes, such as in research on mechanical droplet-droplet interactions, on the impact of droplets on solid surfaces

G. Brenn
Institute of Fluid Mechanics and Heat Transfer, Graz University of Technology, Graz, Austria
e-mail: brenn@fluidmech.tu-graz.ac.at

N. Ashgriz (ed.), *Handbook of Atomization and Sprays*,
DOI 10.1007/978-1-4419-7264-4_26, © Springer Science+Business Media, LLC 2011



Fig. 26.1 Stream of monodisperse propanol-2 droplets with highly controlled size, as produced with a droplet stream generator of the presently discussed kind. The oscillations are caused by the deformations upon pinch-off from the jet

or liquid films and sheets, on droplet evaporation, etc. Another wide field of applications in research is the validation of particle sizing techniques. In production technology, discontinuous coating of solid substrates with droplets, continuous spray coating, ink jet printing, particle production, etc., are fields of application of controlled drop formation. For all named processes in research and production, it is of advantage to produce droplets with controlled size in a continuous way, which is possible with droplet generators of the presently described kind. A typical stream of droplets achievable with these generators is shown in Fig. 26.1.

Physical Principle

This part of our review reports about the physical working principle of generators producing controlled streams of droplets. We restrict our discussion to droplet stream generators working on the principle of controlled Rayleigh-type jet break-up, since essentially all known continuous-stream techniques that allow for a high level of control on the drop size rely on this principle. Break-up of liquid sheets and jets by different (e.g., Kelvin-Helmholtz-type) instability mechanisms does not allow for the same accuracy of control of the drop size. We therefore restrict the entire discussion of this section to the Rayleigh regime of jet break-up. The physical basics to be discussed therefore relate to the capillary instability of liquid jets, which are treated elsewhere in this book and are, therefore, not presented in detail here.

Droplet production by droplet stream generators takes place by pinch-off of liquid portions from jets. A trivial prerequisite for the application of this technique of drop production is, therefore, the formation of a laminar liquid jet from a round orifice or nozzle. The conditions of liquid flow through the orifice required to form a laminar jet are discussed in Sect. 26.3 below. Once the laminar jet is formed, its linear temporal instability against a disturbance with a non-dimensional wave number $ka = 2\pi a/\lambda$ (with the wavelength λ of the disturbance and the jet radius a) in a gaseous ambient medium under the action of surface tension, neglecting both the liquid viscosity and the dynamic interaction with the ambient gas, is described by the dispersion relation

$$\omega_r^2 = \frac{\sigma}{\rho a^3} ka\left(1 - k^2 a^2\right) \frac{I_1(ka)}{I_0(ka)} \tag{26.1}$$

In this relation, ω_r is the growth rate of a disturbance, σ and ρ are the surface tension of the liquid against the ambient gas and the liquid density, respectively,

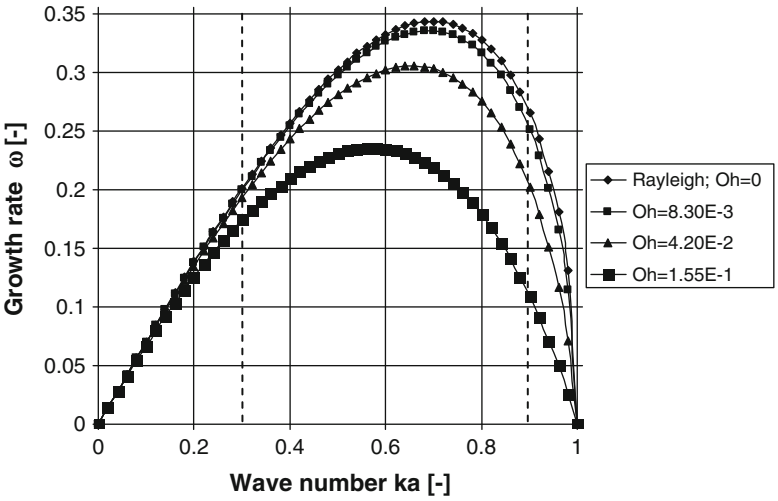


Fig. 26.2 The dispersion relations of an inviscid laminar jet in a vacuum [1] and of viscous jets with different Ohnesorge numbers $Oh = \mu/\sqrt{\sigma d \rho}$ for the jet diameter d [4]: the non-dimensional growth rate $\omega = \omega_r(\rho a^3/\sigma)^{1/2}$ as a function of the non-dimensional wave number ka. The jet diameter is 200 µm. The case $Oh = 8.3{\cdot}10^{-3}$ is for water (and close to the inviscid case), $Oh = 4.2{\cdot}10^{-2}$ for propanol-2, and $Oh = 0.155$ for a silicon oil at 20°C. Disturbances with wave numbers between the dashed lines produce monodisperse droplets

and I_0 and I_1 modified Bessel functions of the first kind [1, 2]. The function in (26.1) is displayed as the curve with the highest maximum ($Oh = 0$) in Fig. 26.2. The relation shows that disturbance wavelengths must exceed the jet circumference to destabilize the jet. Yet, it is seen that disturbances with very large wavelengths do not grow appreciably. The disturbance with the maximum growth rate exhibits the non-dimensional wave number $(ka)_{opt} = 0.697$. It is labeled as an "optimum" in the sense that it produces the droplets in shortest time. This non-dimensional wave number corresponds to the wavelength of $\lambda_{opt} = 4.508{\cdot}2a$ and yields the droplet size $D_{opt} = 1.891{\cdot}2a$. When a Rayleigh-type jet breaks up without forced excitation, this size is close to the mean drop size formed. The size D_{opt} is a good estimate for the order of magnitude of the droplet size formed by this process, which is about twice the diameter of the jet.

The dispersion relation of an incompressible viscous Newtonian liquid jet in an inviscid ambient medium was derived by Rayleigh [3], and, more widely recognized in the literature, by Weber [4], relating to experiments by Haenlein [5]. The dispersion relation for this case reads

$$\omega_r^2 + \omega_r \frac{3\mu}{\rho a^2} k^2 a^2 = \frac{\sigma}{2\rho a^3} k^2 a^2 \left(1 - k^2 a^2\right) \tag{26.2}$$

and does not account for the dynamic interaction with the ambient medium. In this equation, the number 3 on the left-hand side represents a lengthy expression with modified Bessel functions of the first and second kinds to a good approximation for

non-dimensional wave numbers $ka < 1$. The ratio of modified Bessel functions on the right-hand side of (26.1) is approximated in (26.2) by the value of $ka/2$. We do not present the version of this dispersion relation accounting for the dynamic interaction of the jet with the ambient medium, which was also derived by Weber [4], since we are restricted to capillary instability. Equation (26.2) is plotted in Fig. 26.2 for three different values of the Ohnesorge number $Oh = \mu/\sqrt{\sigma\,\mathrm{d}\rho}$. Both the maximum of the growth rate and the corresponding disturbance wave number $(ka)_{\mathrm{opt}}$ decrease with increasing Oh. The cutoff wave number $(ka)_{\max} = 1$, however, does not change with Oh. The non-dimensional wave number of the fastest growing disturbance is $(ka)_{\mathrm{opt}} = (2 + 6Oh)^{-1/2}$, which corresponds to the optimum wavelength $\lambda_{\mathrm{opt}} = 2\pi a(2 + 6Oh)^{1/2}$. This yields the drop size $D_{\mathrm{opt}} = [44.4(1 + 3Oh)]^{1/6}.2a$, which clearly depends on the liquid properties.

As the most general case of a liquid jet in a fluid ambient medium, the instability of a viscous column of liquid in another immiscible incompressible viscous Newtonian host medium was analyzed by Tomotika [6] as a generalization of the works by Rayleigh [3] and Weber [4]. It has the form of a determinant that equals zero and reads

$$\begin{vmatrix} I_1(ka) & I_1(k_1'a) & K_1(ka) & K_1(k_1a) \\ kaI_0(ka) & k_1'aI_0(k_1'a) & -kaK_0(ka) & -k_1aK_0(k_1a) \\ 2\frac{\mu'}{\mu}k^2a^2I_1(ka) & \frac{\mu'}{\mu}\left(k^2a^2+k_1'^2a^2\right)I_1(k_1'a) & 2k^2a^2K_1(ka) & \left(k^2a^2+k_1^2a^2\right)K_1(k_1a) \\ F_1 & F_2 & F_3 & F_4 \end{vmatrix} = 0 \tag{26.3}$$

In this equation, the terms F_1 through F_4 read

$$\left.\begin{aligned} F_1 &= 2i\frac{\mu'}{\mu}k^2a^2I'_1(ka) - \frac{\omega\rho'a^2}{\mu}I_0(ka) + \frac{\sigma(k^2a^2-1)}{a^2}\frac{k^2a^2}{\omega\mu}I_1(ka) \\ F_2 &= 2i\frac{\mu'}{\mu}kak_1'aI'_1(k_1'a) + \frac{\sigma(k^2a^2-1)}{a^2}\frac{k^2a^2}{\omega\mu}I_1(k_1'a) \\ F_3 &= 2ik^2a^2K'_1(ka) + \frac{\omega\rho a^2}{\mu}K_0(ka) \\ F_4 &= 2ikak_1aK'_1(k_1a) \end{aligned}\right\} \tag{26.4}$$

The quantities with the primes are for the jet liquid, and the quantities without prime for the ambient liquid. A prime at the modified Bessel functions denotes the derivative with respect to the argument. Furthermore, the definition $k_1^2 = k^2 + i\omega/\nu$ is used. The quantity k_1 exists for both liquids. It is therefore also distinguished by the prime. For this case of the instability of a liquid filament in an immiscible viscous host medium, an analytical expression for the non-dimensional wave number of the disturbance maximizing the growth rate does not exist. With simple numerical procedures, however, this growth rate may be easily obtained. We present this dispersion relation for completeness, but do not use it here, since we are interested in droplet formation in a gaseous medium.

Ranges of Operation Parameters

The production of droplets by means of droplet stream generators relies on the growth of deformations of laminar Rayleigh-type liquid jets from an infinitesimal level to a value that equals the jet radius, so that droplets pinch off. The trivial prerequisite for the application of this technique is that a liquid jet emerging from a nozzle orifice is formed. For the jet to be produced, a sufficiently large Weber number of the liquid flow, with the diameter d of the nozzle hole as the length scale, is needed. The condition for the Weber number ensuring jet formation, as derived by Walzel [7] on the basis of experiments, reads

$$We > We_0 = 14.5\, Oh^{0.08} \tag{26.5}$$

where $We = U^2\, \mathrm{d}\rho/\sigma$ and U is the jet velocity. The stability behavior of the jets discussed in the present context is characterized by the Rayleigh regime of break-up, as identified by v. Ohnesorge [8]. The Rayleigh regime is defined for jets in practical situations (involving viscous liquids) by the inequality

$$Oh \leq 132.3 Re^{-1.259}, \text{or, equivalently,} We \leq 2345.46\, Oh^{0.412} \tag{26.6a, b}$$

Having thus defined the operation window for producing laminar liquid jets to run droplet stream generators in the Rayleigh regime as

$$14.5 Oh^{0.08} \leq We \leq 2345.46\, Oh^{0.412} \tag{26.7}$$

we can now specify the range of frequencies suitable for producing monodisperse droplets. The range of suitable wave numbers was specified empirically by Schneider and Hendricks [9] as $0.45 \leq ka \leq 0.95$. Brenn found for his nozzles the range $0.3 \leq ka \leq 0.9$ [10]. The actual ranges allowing for monodisperse drop formation may depend on the nozzle hole profile and shape. The latter range may be rewritten as

$$0.3 \leq ka = \frac{\pi}{\sqrt{We}} \sqrt{\frac{\rho d^3}{\sigma}} f \leq 0.9 \tag{26.8}$$

With the excitation frequency f, the drop size is also known as

$$D = \left(\frac{3\pi}{2}\frac{1}{ka}\right)^{1/3} d = \left(\frac{3}{2}\sqrt{We}\sqrt{\frac{\sigma}{\rho d^3}}\frac{1}{f}\right)^{1/3} d \tag{26.9}$$

The droplet concentration in the single drop streams or sprays depends on the geometrical arrangement of the nozzle holes in the orifice plate. The concentration of the drops may be expressed as a linear concentration for single drop streams, an area concentration for a linear arrangement of nozzle holes in the orifice, and

a spatial concentration for multi-hole nozzles with two-dimensional arrangements of the holes. For droplet streams from a single-hole orifice, one drop per wavelength of the deformed jet shape is produced. This results in the linear droplet number concentration

$$c_{\mathrm{n,lin}} = \frac{1}{\sqrt{We}}\sqrt{\frac{\rho d^3}{\sigma}}\frac{f}{d} = \left(\frac{3}{2\pi^2}\right)^{1/3}(ka)^{2/3}\frac{1}{D} \tag{26.10}$$

Accounting for the variability of the non-dimensional wave number ka between 0.3 and 0.9, the reciprocal non-dimensional inter-drop spacing corresponding to this linear concentration may be expressed as

$$0.239 \leq c_{\mathrm{n,lin}}D = D/\lambda \leq 0.497 \tag{26.11a}$$

and as

$$0.095 \leq c_{\mathrm{n,lin}}d = d/\lambda \leq 0.286 \tag{26.11b}$$

In sprays produced by multihole nozzle orifice plates, the droplet concentration depends on the arrangement of the holes in the orifice. Taking a two-dimensional hexagonal nozzle hole arrangement with the constant spacing s, the spatial droplet number concentration reads

$$c_{\mathrm{n,hex}} = \frac{2}{\sqrt{3}}\frac{1}{s^2\lambda} = \frac{2}{\sqrt{3}}\frac{ka}{\pi\,\mathrm{d}s^2} \tag{26.12}$$

The corresponding spatial droplet volume concentration is

$$c_{v,hex} = \frac{\pi}{3\sqrt{3}}\frac{D^3}{s^2\lambda} = \frac{\pi}{2\sqrt{3}}\frac{1}{s^2/d^2} \tag{26.13}$$

Equation (26.13) reveals the interesting result that the volume concentration in a monodisperse spray of the given kind depends only on the ratio of the spacing s of the nozzle holes to the hole diameter d. It should be emphasized that these concentrations are typically realized at small distances from the nozzle exit, where the momentum exchange with the ambient air has not caused much displacement of the droplets from their regular positions in the streams [11]. With increasing distance from the orifice, the drop positions in the streams tend to fluctuate more strongly [12]. This loss of coherence of the drop positions in the streams goes along with the risk of coalescence and, therefore, with the loss of monodispersity of the drop size spectra. It is therefore desirable to stabilize monodisperse sprays, once they are produced. Methods for stabilizing the sprays are

- Electrical charging of the droplets in the streams. The repulsive forces between the droplets keep them apart and prevents coalescence.

- Use of an air stream in a direction transverse to the direction(s) of the drop stream(s) to drag the droplets apart and thus prevent coalescence.

Both the electrical and aerodynamic methods are well established and effective in maintaining the monodispersity of drop ensembles, once they are produced.

Techniques and Devices for Controlled Droplet Formation

This part of this review reports about techniques for enforcing monodisperse droplet formation. The techniques must essentially allow for the formation of droplets with controlled sizes. One requirement may be that the droplet generators produce monodisperse streams of droplets. However, essentially the same technique appropriate for this purpose may be used for the controlled formation of sprays with discrete polydisperse drop size spectra also. We will also account for techniques that achieve the monodispersity of the drop streams at least approximately.

It has been some decades before the theoretical works by Rayleigh, when Savart discovered in his experiments that periodic vibrations may influence the break-up of a capillary jet such that the frequency of the vibrations may control the formation of droplets, and, therefore, for a given liquid flow rate, their size [13]. The technique to control the break-up of laminar liquid jets in the Rayleigh regime by mechanical vibrations is well established, and there are many devices available on the market and used in research that work on this principle.

One class of drop stream generators use capillary tubes to produce the liquid jets and vibrate the tubes to control the jet break-up by the vibrations. One of the first devices working with vibrating capillaries may be the one due to Dimmock [14]. Another early device of this kind was reported by Schneider and Hendricks [9], which vibrated the capillary tube in its axial direction with a piezoelectric transducer. For ensuring disturbance-free operation of the stainless-steel capillary tubes, their tips were etched to remove irregularities. The further devices by Lindblad and Schneider [15, 16] and Schneider et al. [17] emphasized the inclusion of a ring electrode in the device downstream from the exit of the capillary for charging the liquid – and thus the droplets formed – electrically. This charge enables the experimenter to deflect single droplets from their original directions of motion by a plate capacitor. A temporal variation of the electric voltage used for charging the droplets, while the electric field in the plate capacitor is kept constant, allows for controlled variation of the droplet trajectories. Thus, by applying pulses of voltage to the ring electrode, single droplets may be removed from the continuous stream of droplets with smaller charge. This feature of the droplet generator is of particular interest for droplet collision experiments.

As an alternative to the drop stream generators working with capillary tubes, a type of generator using thin orifice plates with nozzle holes was developed. A well-known device of this kind is the “vibrating orifice droplet generator” by TSI Inc.,

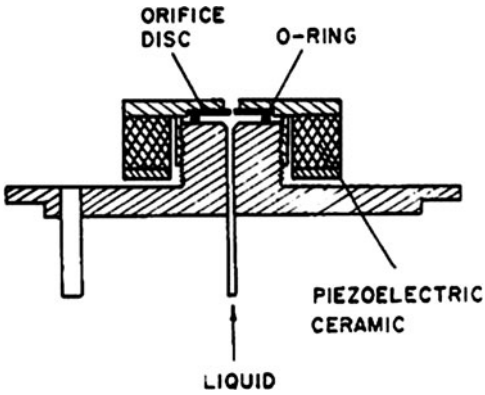


Fig. 26.3 Sketch of the vibrating orifice droplet generator by Berglund and Liu [18], commercialized by TSI Inc (Reprinted from [18]. With permission. Copyright 1973 American Chemical Society)

which was developed based on the work by Berglund and Liu [18]. This device, which is sketched in Fig. 26.3, vibrates an orifice plate with a single nozzle hole, using a piezoelectric vibrator with approximately 30 mm diameter, mounted directly around the nozzle plate. The droplet generator is equipped with a syringe pump for adjusting the liquid flow rate and a signal generator for exciting the piezoelectric vibrator. The piezoelectric ring is mounted at the orifice of this droplet generator. Therefore, the droplet generator cannot be exposed to air flows with elevated temperature, and the device is not suitable for research with combusting droplets in a hot environment. Also, investigations on collisions of droplet pairs are problematic, since the spacing of the droplet generators required leads to long traveling distances of the droplets to the point of impact.

An alternative version of a droplet generator producing monodisperse droplets from excited capillary jets was used by the group around Frohn at the University of Stuttgart in Germany [19]. This droplet generator, which is shown in Fig. 26.4, introduces the vibrations into the liquid, about 100 mm upstream from the orifice plate, so that the downstream end of the drop generator is small in diameter and makes the use of this device more flexible than the TSI generator. Additional features of this drop generator are an option for heating or cooling of the generator body, and a built-in thermocouple for measuring the liquid temperature.

The drop generator established by Yim et al. for producing solder balls is shown in Fig. 26.5 as an example for a device suitable for use with melts [20]. This device combines a heatable reservoir for the metal melt with a solenoid-driven vibrator, which transmits oscillations by a disk mounted at the end of a shaft to the molten metal bath. The orifice piece is manufactured from ruby. The solidification of the solder drops is controlled by immersing them into a silicone oil bath. Particles produced with this device are nicely spherical, with typical diameters of 780 μm and a standard deviation of 26 μm. Apart from the spherical particles, irregular shapes are also observed, which are due to coalescence of the drops, either in the drop stream before entry into the oil bath, or in the oil bath prior to formation of a solid shell on their surface.

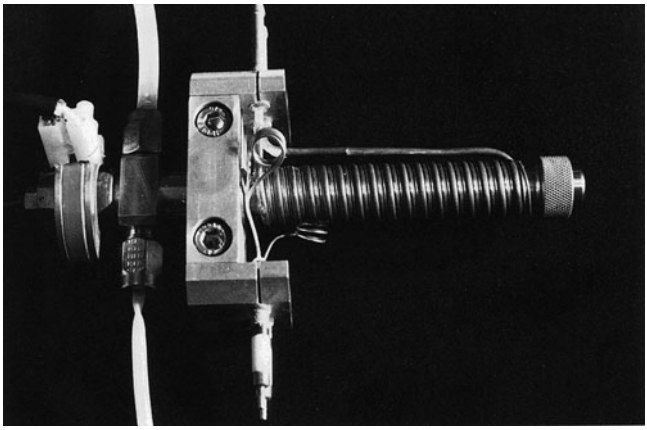


Fig. 26.4 Drop generator of the group around Frohn at Stuttgart University, Germany [19] (With kind permission from Springer Science + Business Media: Frohn and Roth, Dynamics of Droplets. Springer, Berlin, Heidelberg. © Springer-Verlag 2000)

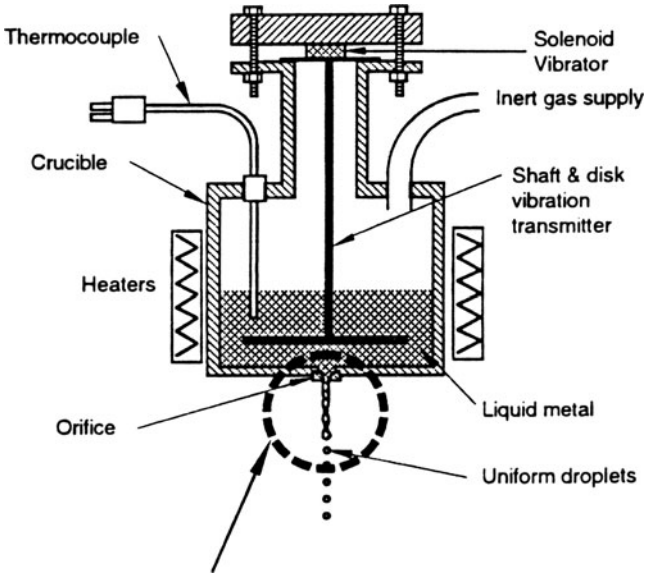


Fig. 26.5 Drop generator for manufacturing solder balls by solidification of melt droplets [20] (Reprinted from [20]. With kind permission from Prof. Chun, MIT, 2010)

An early attempt to establish a device that produces monodisperse sprays is due to Dabora [21]. He proposed to use the principle of liquid jet formation by capillary tubes for producing a spray generator by mounting more than one capillary needle in the nozzle plate of the spray generator. Devices with 9–25 needles were realized. Internal diameters of the needles varied between 150 and 500 μm. Vibrations

applied to the capillaries from a loudspeaker produced spray drops with sizes between 290 and 950 μm. The formation of drops smaller than 290 μm is not reported. The monodispersity of the sprays produced by these devices is not quantified in Dabora's paper [21]. The photographs of the drop streams, however, are convincing and show regular drop configurations.

A shower-head monodisperse spray generator allowing for large liquid flow rates was developed by Brenn et al. [22]. The device applies the working principle of the single-hole droplet stream generators to nozzle plates with very large numbers of nozzle holes. The device showed that the vibrations produced by a single piezoceramic vibrator were effective for forcing monodisperse droplet formation from more than 600 liquid jets. The device is shown in Fig. 26.6. Liquid mass flow rates of the order of 300 kg/h were realized. Nozzle plates producing 613 streams with droplet sizes of about 80 and 150 μm were manufactured for testing the device. Earlier versions of such shower-head spray generators were put forward by *P*. Walzel in Germany and used, e.g., in nuclear industries [23]. Several other devices were developed in various research groups.

It is common to the above devices that single- or multi-hole orifice disks are used for producing the laminar liquid jets forming the droplets by controlled

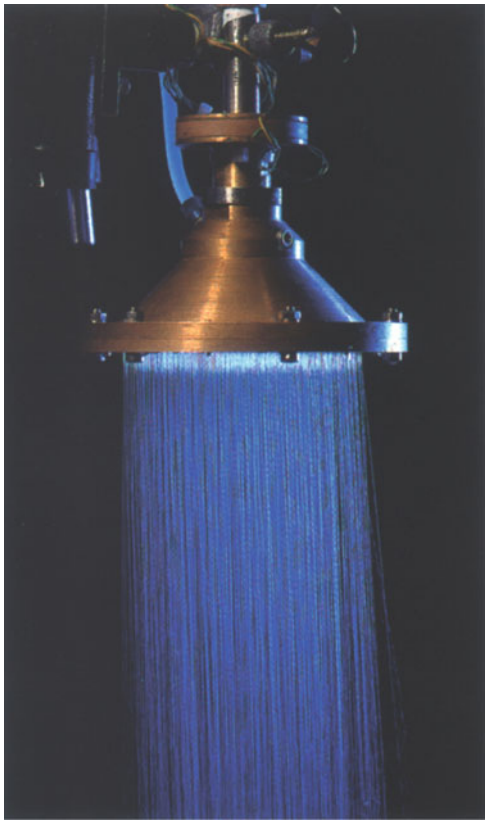


Fig. 26.6 Monodisperse spray generator by Brenn et al. [22]. Liquid feed from the top, drainage line at the left-hand side on top of the conical distribution chamber. The jets emerge from the nozzle plate vertically downwards. Two nozzle plates tested exhibit 613 holes each, with hole diameters of 41 and 76 μm (photograph © LSTM of the University of Erlangen-Nürnberg, Germany, reprinted with kind permission)

Rayleigh-type break-up. From (26.1) above it followed that the droplets formed by this mechanism exhibit typical diameters which are about twice the jet diameter, i.e., approx. twice the nozzle hole diameter. This means that, for producing small droplets, which are of interest for, e.g., fuel injection research, orifice disks with very small nozzle holes are needed: typically we need a 10 μm nozzle hole diameter for producing 20 μm droplets. Such small holes, however, are very sensitive against particulate impurities in the liquid and, therefore, clog very easily, even if the liquid feed is filtered properly. In most cases, this practical problem restricts the use of droplet generators of the above kind to drop sizes above, say, 60 μm. Weierstall et al., however, showed that stable conditions of droplet formation by Rayleigh-type liquid jet break-up may be achieved with glass capillaries with diameters as small as 4 μm, producing 8 μm droplets, when high purity (HPLC grade) water is used [24]. To a bigger part, nozzle clogging may be due to impurities precipitating from the liquid, such as silicates from glass nozzle walls.

There exist a couple of drop generators that also produce reasonably monodisperse droplets and circumvent the problem of nozzle clogging. This is achieved by allowing for the use of liquid feed tubes with inner diameters of the order of 1 mm. Appropriate stretching of the liquid jet emerging from such wide tubes still enables the production of quite small droplets. Basically two methods may be mentioned:

1. Stretching of the thick jet from a millimeter tube by an accompanying gas flow (called capillary flow focusing, CFF). The gas flow stretches the jet, thereby reducing its diameter. The break-up of this elongated jet into droplets may then be controlled by mechanical vibrations. This kind of "extension nozzle" was put forward by Walzel and co-workers [25, 26]. It produces reasonably monodisperse streams of drops with sizes of about one tenth of the inner diameter of the jet producing tube, with the obvious advantage that clogging of the tube is not very likely with this device. A sketch of the device is shown in Fig. 26.7. Extensive studies on the stability behavior of liquid jets and droplet formation in CFF are, e.g., due to the group around Gañán-Calvo, Gordillo, and Perez-Saborid in Sevilla (Spain) [27–29].
2. Use of the interaction of the liquid with an electrostatic field. For electrically conducting liquids, applying an electrostatic field enforces mechanisms of jet break-up very different from those of jets without electrical influences. There exist modes of jet break-up under the influence of an electrostatic field that form very thin jets emerging from the Taylor cone attached to the end of the feed tube (e.g., Cloupeau and Prunet-Foch [30–32]). These jets may also break up according to the Rayleigh mechanism and form very small (and electrically charged) droplets with very low size fluctuations, so that they may be very nearly monodisperse. The regime of operation of an electrospraying device may be defined for a given liquid by the flow rate of the liquid and the electric voltage applied. Cloupeau and Prunet-Foch point out that the parameter space determining the regimes is quite large [30–32]. An effort to represent the regimes in terms of non-dimensional numbers is not made.

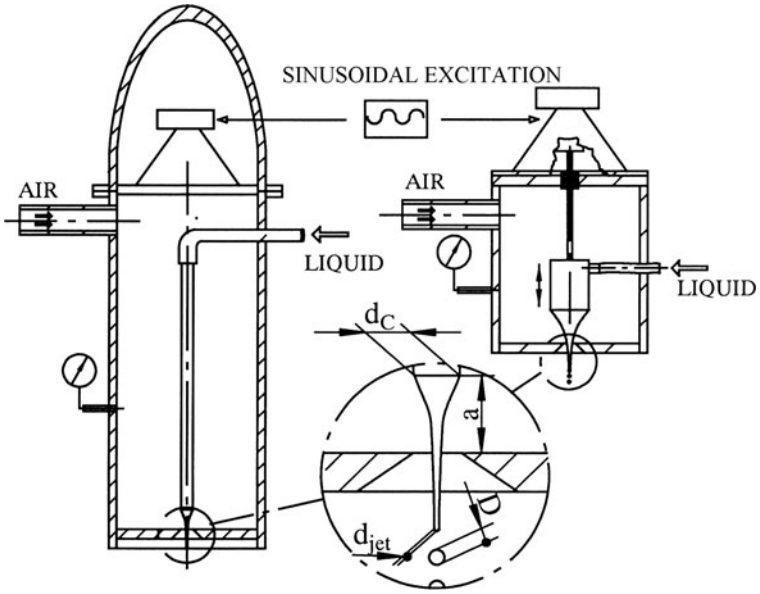


Fig. 26.7 Extension nozzle for flow focusing, developed by the group around Walzel at Dortmund University of Technology, Germany [25] (Reprinted with kind permission from the Institute SLA of Darmstadt University of Technology, Prof. C. Tropea, 2010)

Other methods, such as aerodynamic techniques to extract droplets of certain size fractions from polydisperse sprays in order to produce narrow drop size spectra, are established in inhalation technology to provide sprays with very small droplets. This and other comparable methods are not addressed here, since the related devices are no droplet stream generators.

Signals for Exciting the Vibrator

The vibrators used in the Rayleigh-type devices employed for controlled droplet formation are excited to apply the vibrations to the liquid jets and produce controlled disturbances of the jets. The disturbances result in the formation of drops with volumes that correspond to liquid jet portions with lengths equal to the wavelength of the disturbance. Typical frequencies to be realized strongly depend on the size of the drops (i.e., on the jet diameter d), and on the velocity U of the jet. They are proportional to U/d and may range well in the higher kHz regime, so that the vibrators must be able to perform vibrations at such frequencies. Most vibrators are therefore based on piezoelectric devices, which make use of an inverse piezoelectric effect, i.e., they are deformed upon application of an electric voltage. The corresponding electric signals may be quite variable in shape, frequency, and

amplitude. The steepness of the flanks of the signals proved important for a good transfer efficiency of the disturbances to the jets. Signals are typically sinusoidal or rectangular in shape.

Generally, the formation of drops by break-up of laminar jets controlled by the above techniques leads to a narrow spacing of the drops in the streams. Typical is an inter-drop distance of 4.5 diameters. For many applications this is a disadvantage. Orme and Muntz [33, 34], Orme [35, 36], and Orme et al. [37] came up with a technique that avoided this limitation by excitation of the liquid jets with modulated signals. The (amplitude) modulation produced deformations of the liquid jets such that the drops pinched off were in relative motion that made them merge to form larger drops with larger spacing. Hilbing and Heister presented a simulation of the effects of amplitude-modulated signals on liquid jet break-up, which agreed well with the experimental findings of Orme and Muntz [38]. Brenn and Lackermeier showed that, further to amplitude modulation, frequency modulation may also be applied [39]. The effect of the modulated signals depends on the ratio N of carrier to modulation frequencies, the modulation depth m, and the wave numbers k_C and k_M of the carrier and modulation signals. Minimum and maximum applicable wave numbers k_C and k_M were quantified in a non-dimensional form for varying liquids. Examples of drop systems formed by modulated excitation are shown in Fig. 26.8.

One interesting technique proposed by Frohn and Roth is to use the drop stream itself for producing the signal for the excitation of the liquid jet, rather than taking the signal from a signal generator [19]. This is achieved by using a signal from a light barrier detecting the droplets passing by and – after amplification – feeding it into the piezoceramic vibrator of the droplet generator. This technique may ensure stable states of operation of the droplet generator close to the optimum frequency providing fastest growth of the disturbances. Due to the convergence of the system towards this frequency, however, the variability in choosing different states of operation is limited.

Another device well known to the community is the one from the group around Dressler [40], which is capable of introducing large-amplitude velocity perturbations into the liquid jet. Depending on the perturbation amplitude, the result may be a monodisperse stream of droplets or a polydisperse spray. Round and rectangular orifice geometries are used. In our present context, this device does not differ significantly from the one by Frohn and Roth [19], except in its ability to induce atomization due to the high perturbation amplitudes. This feature, however, is not of interest in the present context.

Nozzle Design for Monodisperse and Discrete Polydisperse Sprays

In the present section, we restrict ourselves to the version of droplet generators working with (mostly metal) nozzle plates carrying the orifice hole(s). The design of the nozzle plate concerns both the diameter and the shape of the

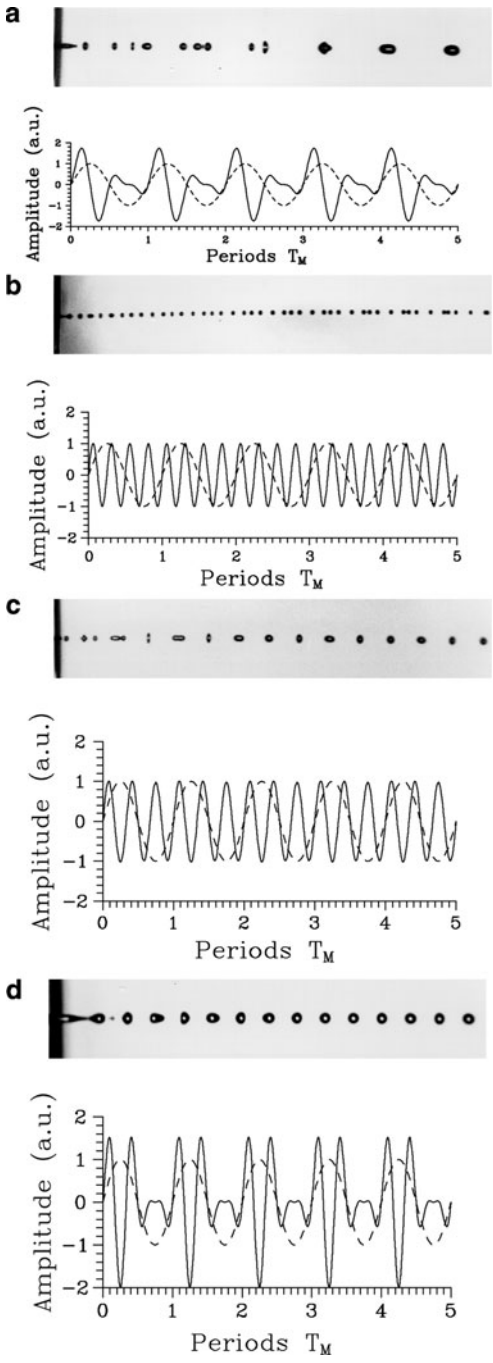


Fig. 26.8 Drop streams produced by the modulated signals shown: (**a**) Multiple drop formation, frequency modulation, $N = 2$, $m = 1.0$, $k_M = 0.15$, $d_M = 84.9$ µm; (**b**) formation of N carrier drops, frequency modulation, $N = 4$, $m = 0.02$, $k_M = 0.152$, $d_C = 53.3$µm; (**c**) formation of 2 carrier drops, amplitude modulation, $N = 3$, $m = 0.02$, $k_M = 0.267$, $d_M = 70.1$ µm; (**d**) direct formation of modulation drops, amplitude modulation, $N = 3$, $m = 1.0$, $k_M = 0.54$, $d_M = 55.4$ µm (Reprinted from [39]. With permission. Copyright 1997 American Institute of Physics)

nozzle hole(s) across the orifice plate, and also the number and geometrical arrangement of the holes in the plate. The technologies used for producing the holes range from lithography through mechanical drilling to laser drilling. Companies providing nozzle plates suitable for controlled droplet formation with droplet stream generators are typically found in the industry producing spinnerets for fiber spinning. The following requirements are to be fulfilled for a good nozzle plate:

- Accurate placement of the nozzle holes in the disk
- High repeatability and precision of the diameter and axially symmetric geometry of the hole
- Low flow resistance
- Sharp edges at the entrance and exit cross sections
- Axis of symmetry of the nozzle hole directed normal on the orifice disk

As single-hole nozzle plates, circular orifice disks, typically 200 μm thick, with the nozzle hole in the center, are equally suitable as thin metal sheets, as used, e.g., for spatial filtering in optical setups. Thicker disks are best suitable as orifice plates if the hole exhibits a tapered (inlet) region on one side and has its nominal diameter only on a short part of the plate thickness. This feature ensures low flow resistance and good directional stability of the jet. Figure 26.9 shows typical shapes of nozzle cross section profiles [41].

The diameter of the nozzle hole required for a given application may be roughly chosen as half the diameter of the droplets to be produced. Given this, the variability of the excitation frequency between the wave numbers of 0.45 and 0.95 (Schneider and Hendricks [9]) corresponds to a variability of the drop size of $\pm 12.4\%$ around the value produced with the mean wave number of 0.639.

Further to single-hole orifice plates for droplet generators, multi-nozzle or multi-capillary devices were already used by Dabora [21], as discussed above, for producing sprays of monodisperse droplets. For producing separate liquid jets from "showerhead" nozzles with nozzle holes in thin orifice plates, a minimum spacing s of the nozzle holes with diameter d must be exceeded to avoid coalescence of the jets at the downstream side of the orifice plate. According to Walzel, this distance is ensured by the relation [7]

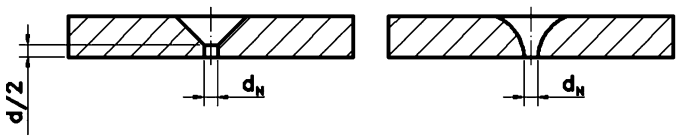


Fig. 26.9 *Left*: Shape of a typical nozzle hole for spinnerets with tapered inlet region. *Right*: Nozzle hole with curved shape, as typically obtained by laser drilling. Simple cylindrical holes in thin metal sheets are also suitable for producing liquid jets of good quality [41] (Reproduced from [41]. With kind permission. Copyright Wiley-VCH Verlag GmbH and Co. KGaA)

$$s/d \geq 1 + \left(\frac{C}{We - We_0}\right)^{1/n} \tag{26.14}$$

where both the coefficient C and the exponent n depend on the Ohnesorge number as per

$$\log C = 2 - 2.7Oh^{0.48} \quad \text{and} \quad n = 1 + 1.6Oh^{0.4} \tag{26.15}$$

While practically all devices known from the literature using multiple nozzle hole or capillary tube arrangements produce monodisperse sprays, the multi-hole nozzles by Brenn [10] are the only ones known for their potential to produce discrete polydisperse sprays. Brenn developed a semi-empirical method that enables the design of multi-hole orifice plates for producing sprays with predetermined discrete polydisperse drop size spectra at a given mass flow rate of a given liquid [10]. The nozzle holes arrangement ensures that the flows through the various holes do not influence each other. The flow through each hole is therefore equivalent to the flow through a single-hole orifice with the given hole diameter. The non-dimensional empirical correlation

$$\frac{\dot{m}_i}{\mu d_i} = C_1 \left(\frac{\Delta p \rho d_i^2}{\mu^2}\right)^{C_2} \tag{26.16}$$

determined by dimensional analysis, represents the discharge behavior of nozzle holes with diameter d_i very well. In paper [10], $C_1 = 0.3601$ and $C_2 = 0.5774$. This equation allows for the calculation of the velocities of the liquid jets emerging from each nozzle hole. Based on the empirical finding that non-dimensional wave numbers of disturbances controlling the jet break-up in the range between 0.3 and 0.9, i.e., $0.3 \leq ka \leq 0.9$, lead to the formation of monodisperse drop streams, an inequality for a frequency band for suitable disturbances is derived. The case when this frequency band degenerates to a single point, i.e., when there is no freedom left for variation of the frequency of excitation of the jets, represents the case of the largest allowable ratio of the largest to the smallest nozzle hole diameter in the orifice plate. This value puts limitations to the span of drop sizes that can be produced with a single multi-hole orifice plate. In paper [10], the ratio $d_{\max}/d_{\min} = 3.669$. The corresponding maximum value of the ratio of the largest to the smallest drop size in the spray produced equals 2.544. The sprays produced by this technique are easy to characterize with analytical relations for mean drop sizes and velocities, etc. Figure 26.10 shows results of the design of a discrete polydisperse water spray with a predetermined drop size spectrum, using an 11-holes orifice plate. The total liquid mass flow rate was about 1 kg/h, and the corresponding driving pressure difference was 1.1 bar. Drop sizes produced ranged between 66 and 139 μm.

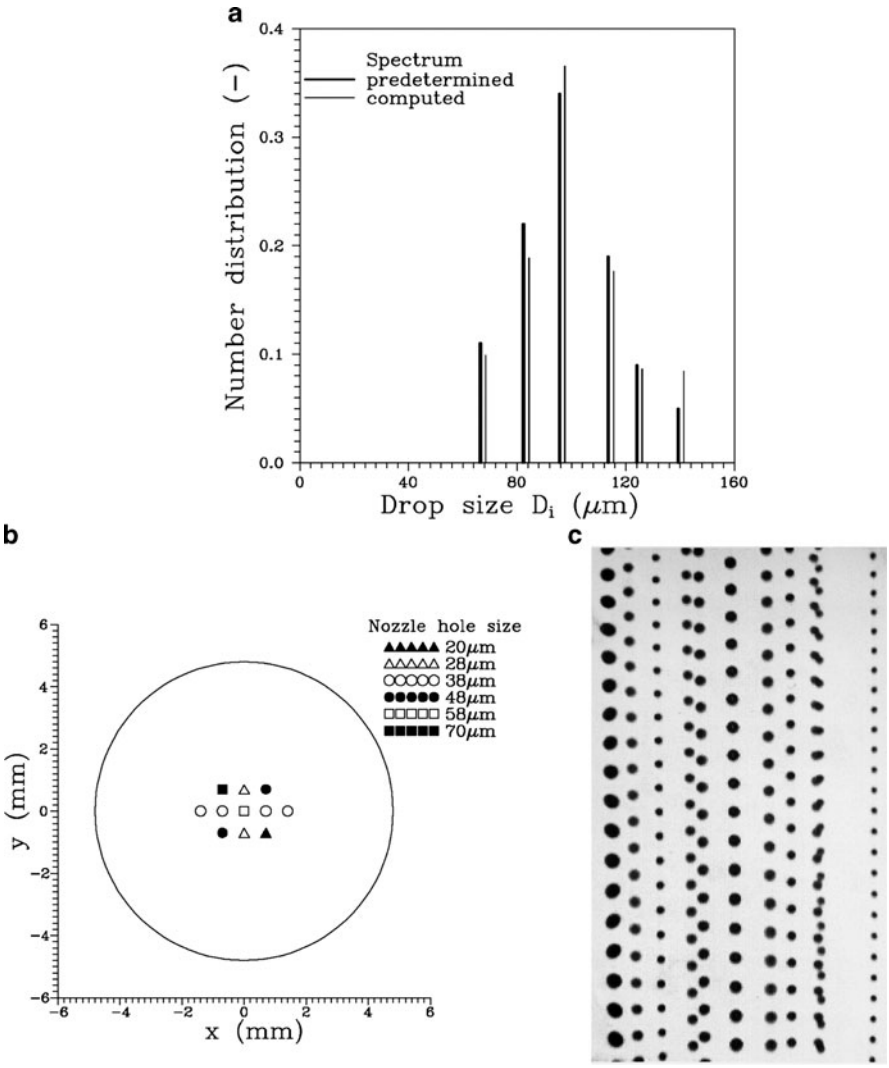


Fig. 26.10 (**a**) Required and designed discrete polydisperse drop size spectra, (**b**) nozzle hole arrangement in the 11-holes orifice disk designed, (**c**) resultant discrete polydisperse spray produced at an excitation frequency of 47.3 kHz. Drop sizes range between 66 and 139 μm [10] (Reprinted from [10]. Copyright 2000. With permission from Elsevier)

Electric Charging and Deflection of the Drops

This section provides insight into techniques for conditioning and treatment of the drops, which essentially rely on the electric charging of the drops and their deflection in the electrostatic field of a capacitor. The purpose followed by this

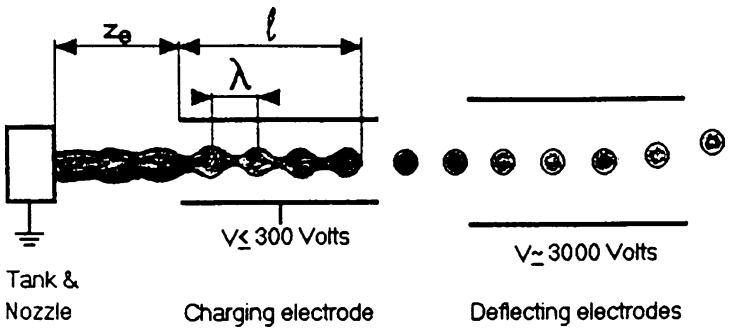


Fig. 26.11 Device for electrical charging and deflection of liquid droplets [42] (Reprinted from [42]. Copyright 1992. With permission from Elsevier)

method is to enforce trajectories of the droplets suitable for a given application, which may be, e.g., ink jet printing with continuous streams of ink droplets, and research on the collisional interaction of droplets.

A prerequisite for electric charging of droplets is the presence of mobile charges in the liquid phase. A ring electrode is placed close enough to the nozzle orifice of the droplet generator, so that the liquid passes the ring as a coherent jet, which is not disintegrated into droplets. A sketch of this arrangement is shown in Fig. 26.11 [42]. The electric field of the ring electrode shifts the (negative) electric charges in the liquid upstream, so that the liquid portions detached from the jet carry a resultant (positive) charge. The charged droplets can therefore be deflected in the electric field of a capacitor.

The placement of the droplets on a target, or their arrival at a point of intersection with the trajectory of a second stream of droplets, may be varied by varying the strength of field of the ring electrode and/or the capacitor. Both of them may be either steady or pulsed in time, so that different droplets may be produced with different charges and/or be deflected by different fields, so that their trajectory and, consequently, their point of arrival in the intended plane may be varied. This variation may be achieved accurately enough to be able to, e.g., print with the droplets and/or place the (solidified) droplets on the grid of a soldering array.

Fields of Applications of Droplet Stream Generators

The fields of applications of droplet stream generators are predominantly research and development [43–48]. They are typically used for investigations of transport phenomena with liquid drops, where the good control of the drop size provides a means to adjust initial or boundary conditions of the process. Examples are evaporation of droplets and their transport in gas flows. In the development of new sizing techniques for liquid droplets, the availability of a calibration or validation standard is essential. Drop stream generators were important experimental means for verifying

new measuring techniques, such as extended and dual-burst phase-Doppler anemometry, and, in the version producing discrete polydisperse sprays [10], also for testing the ability of established sizing techniques based on laser-light diffraction of capturing the correct Sauter-Mean Diameter of droplets in polydisperse sprays.

One field of application in production technologies that is well established is the printing of data on packages of, e.g., groceries and pharmaceuticals. The black ink droplets are charged and deflected for the printing by a capacitor. When the continuously running drop stream is not used for printing, the drops enter into a dump tank from where the ink is returned to the feed. Another application in production processes is the formation of spheres from molten metals to achieve a form suitable for long-term storage. Also, solder tin, a metal with a low melting point, may be turned into droplets in the production of electronic devices.

One wide field of applications of droplet stream generators is the production of monodisperse metal spheres for various purposes by solidification of streams of melt droplets. Metals often used are tin alloys, such as solder (60Sn40Pb). These alloys exhibit relatively low melting points and are convenient to handle for producing monodisperse spheres by the method presently discussed. The results are typically ensembles of monosized spheres which can be used, e.g., for manufacturing ball grid array-type multi-module integrated-circuit packaging. Due to the high degree of control on the spheres produced, they may be subjected to rapid solidification from the molten state, e.g., by oil baths, to achieve a desired grain structure [20, 49–54].

Another example is rapid prototyping with build-up of the desired parts from molten metal droplets impacting on a target. This process is, in principle, equivalent to a printing process, since the droplets are produced with electrical charges and then deflected by a plate capacitor to be deposited at a desired position on the target. The build-up of the target is achieved by solidification of the droplets (or splats), which may take place at high cooling rates and produce advantageous material properties [36, 55–57].

Applications of droplet stream generators for transfer processes in space have been considered and discussed since a long time [58, 59]. Certainly the present summary cannot claim completeness.

References

1. J. W. S. Lord Rayleigh: On the instability of jets, Proc. Lond. Math. Soc.10, 4–13 (1878).
2. J. W. S. Lord Rayleigh: On the capillary phenomena of jets, Proc. R. Soc. Lond. 29, 71–97 (1879).
3. J. W. S. Lord Rayleigh: On the instability of a cylinder of viscous liquid under capillary forces, Philos Mag. 34, 145–154 (1892).
4. C. Weber: Zum Zerfall eines Flüssigkeitsstrahles (On the break-up of a liquid jet), Zeitschr. Angew. Math. Mech. (J. Appl. Math. Mech.) 11, 136–154 (1931).

5. A. Haenlein: Über den Zerfall eines Flüssigkeitsstrahles (On the break-up of a liquid jet), Forsch. Geb. Ing.-Wesens (Res. Eng. Sci.) 2, 139–149 (1931).
6. S. Tomotika: On the instability of a cylindrical thread of a viscous liquid surrounded by another viscous fluid, Proc. R. Soc. Lond. A 150, 322–337 (1935).
7. P. Walzel: Koaleszenz von Flüssigkeitsstrahlen an Brausen (Coalescence of liquid jets at shower-head atomizers), Chem.-Ing.-Tech. 52, 652–654 (1980).
8. W. v. Ohnesorge: Die Bildung von Tropfen an Düsen und die Auflösung flüssiger Strahlen (The formation of drops at nozzles and the break-up of liquid jets), Zeitschr. Angew. Math. Mech. (J. Appl. Math. Mech.) ZAMM 16, 355–358 (1936).
9. J. M. Schneider, C. D. Hendricks: Source of uniform-sized liquid droplets, Rev. Sci. Instrum. 35, 1349–1350 (1964).
10. G. Brenn: On the controlled production of sprays with discrete polydisperse drop size spectra, Chem. Eng. Sci. 55, 5437–5444 (2000).
11. G. Brenn: Die gesteuerte Sprayerzeugung für industrielle Anwendungen (Controlled spray production for industrial applications), Habilitation thesis, Friedrich-Alexander University of Erlangen-Nürnberg, Department of Chemical Engineering, 193 pp (1999).
12. K. Anders, N. Roth, A. Frohn: Operation characteristics of vibrating-orifice generators: the coherence length, Part. Part. Syst. Charact. 9, 40–43 (1992).
13. F. Savart: Mémoire sur la constitution des veines liquides lancées par des orifices circulaires en mince paroi, Ann. Chim. Phys. 53. 337–386 (1833).
14. N. A. Dimmock: Production of uniform droplets, Nature 166, 686–687 (1950).
15. N. R. Lindblad, J. M. Schneider: Production of uniform-sized liquid droplets, J. Sci. Instrum. 42, 635–638 (1965).
16. N. R. Lindblad, J. M. Schneider: Method of producing and measuring charged single droplets, Rev. Sci. Instrum. 38, 325–327 (1967).
17. J. M. Schneider, N. R. Lindblad, C. D. Hendricks: An apparatus to study the collision and coalescence of liquid aerosols, J. Coll. Sci. 20, 610–616 (1965).
18. R. N. Berglund, B. Y. H. Liu: Generation of monodisperse aerosol standards, Environ. Sci. Technol. 7, 147–153 (1973).
19. A. Frohn, N. Roth: Dynamics of droplets, Springer, Berlin, 65–80 (2000).
20. P. W. Yim, J.-H. Chun, T. Ando, V. K. Sikka: Production and characterization of mono-sized Sn-Pb alloy balls, Int. J. Powder Metall. 32, 155–164 (1996).
21. E. K. Dabora: Production of monodisperse sprays, Rev. Sci. Instrum. 38, 502–506 (1967).
22. G. Brenn, T. Helpiö, F. Durst: A new apparatus for the production of monodisperse sprays at high flow rates, Chem. Eng. Sci. 52, 237–244 (1997).
23. P. Naefe, H. Ringel, E. Zimmer: Erzeugung gleichförmiger Tropfen aus Flüssigkeitsstrahlen (Uniform droplet formation from liquid jets), Chem.-Ing.-Tech. 50, 321 (1978).
24. U. Weierstall, R. B. Doak, J. C. H. Spence, D. Starodub, D. Shapiro, P. Kennedy, J. Warner, G. G. Hembree, P. Fromme, H. N. Chapman: Droplet streams for serial crystallography of proteins, Exp. Fluids 44, 675–689 (2008).
25. F. Schmelz, S. Schneider, P. Walzel: Production of monosized droplets in pneumatic extension nozzles, Proceedings of the 16th Annual Conference on Liquid Atomization and Spray Systems (ILASS Europe), Darmstadt, paper II.2 (2000).
26. P. Walzel, F. Schmelz, S. Schneider: Herstellen monodisperser Tropfen mit pneumatischen Ziehdüsen (production of monodisperse droplets with pneumatic extension nozzles), Chem. Ing. Tech. 73, 1599–1602 (2001).
27. A. M. Gañán-Calvo: Generation of steady liquid microthreads and micron-sized monodisperse sprays in gas streams, Phys. Rev. Lett. 80, 285–288 (1998).
28. L. Martín-Banderas, M. Flores-Mosquera, P. Riesco-Chueca, A. Rodríguez-Gil, Á. Cebolla, S. Chávez, A. M. Gañán-Calvo: Flow focusing: a versatile technology to produce size-controlled and specific morphology microparticles, Small 1, 688–692 (2005).

29. L. Martín-Banderas, A. Rodríguez-Gil, Á. Cebolla, S. Chávez, T. Berdún-Álvarez, J. M. Fernandez Garcia, M. Flores-Mosquera, A. M. Gañán-Calvo: Towards high-throughput production of uniformly encoded microparticles, Adv. Mater. 18, 559–564 (2006).
30. M. Cloupeau, B. Prunet-Foch: Electrostatic spraying of liquids in cone-jet mode, J. Electrostat. 22, 135–159 (1989).
31. M. Cloupeau, B. Prunet-Foch: Electrostatic spraying of liquids: main functioning mode, J. Electrostat. 25, 165–184 (1990).
32. M. Cloupeau, B. Prunet-Foch: Electrohydrodynamic spraying functioning modes: a critical review, J. Aerosol Sci. 22, 1021–1036 (1994).
33. M. Orme, E. P. Muntz: New technique for producing highly uniform droplet streams over an extended range of disturbance wavenumbers, Rev. Sci. Instrum. 58, 279–284 (1987).
34. M. Orme, E. P. Muntz: The manipulation of capillary stream breakup using amplitude-modulated disturbances: a pictorial and quantitative representation, Phys. Fluids A2, 1124–1140 (1990).
35. M. Orme: On the genesis of droplet stream microspeed dispersions, Phys. Fluids A3, 2936–2947 (1991).
36. M. Orme: A novel technique of rapid solidification net-form materials synthesis, J. Mater. Eng. Perform. 2, 399–405 (1993).
37. M. Orme, K. Willis, T.-V. Nguyen: Droplet patterns from capillary stream breakup, Phys. Fluids A5, 80–90 (1993).
38. J. H. Hilbing, S. D. Heister: Droplet size control in liquid jet breakup, Phys. Fluids 8, 1574–1581 (1996).
39. G. Brenn, U. Lackermeier: Drop formation from a vibrating orifice generator driven by modulated electrical signals, Phys. Fluids 9, 3658–3669 (1997).
40. F. Takahashi, W. J. Schmoll, J. L. Dressler: Characterization of a velocity-modulation atomizer, Rev. Sci. Instrum. 65, 3563–3569 (1994).
41. G. Brenn, F. Durst, C. Tropea: Monodisperse sprays for various purposes – their production and characteristics, Part. Part. Syst. Charact. 13, 179–185 (1996).
42. A. Atten, S. Oliveri: Charging of drops formed by circular jet breakup, J. Electrostatics 29, 73–91 (1992).
43. R. W. Park, E. J. Crosby: A device for producing controlled collisions between pairs of drops, Chem. Eng. Sci. 20, 39–45 (1965).
44. P. Schümmer, K. H. Tebel: Production of monodispersed drops by forced disturbance of a free jet, Ger. Chem. Eng. 5, 209–220 (1982).
45. H. Ulmke, T. Wriedt, K. Bauckhage: Piezoelectric droplet generator for the calibration of particle-sizing instruments, Chem. Eng. Technol. 24, 265–268 (2001).
46. P. Walzel: Zertropfen von Flüssigkeiten mittels Druckschwingungen, Chem.-Ing.-Tech. 51, 525 (1979).
47. K.-J. Choi, B. Delcorio: Generation of controllable monodispersed sprays using impulse jet and charging techniques, Rev. Sci. Instrum. 61, 1689–1693 (1990).
48. H. Huynh, F. Mashayek, N. Ashgriz: Satellite size control in liquid jets using modulated amplitude disturbances, Proceedings of the Seventh Annual Conference on Liquid Atomization and Spray Systems (ILASS Americas), Bellevue, pp. 60–64 (1994).
49. M. Asano, N. Nagai, A. Kawasaki, R. Watanabe: Optimization of process parameters for preparing honodisperse (sic!) particles by pulsated orifice injection method, J. Jpn. Soc. Powder Powder Metall. 43, 1273–1278 (1996) (in Japanese).
50. K. Ichiki, M. Asano, A. Kawasaki, R. Watanabe, M. Miyajima: Preparation of monodisperse spherical particles of Bi-Sb system for thermoelectric microdevices, J. Jpn. Soc. Powder Powder Metall. 44, 700–705 (1997) (in Japanese).
51. A. Kawasaki, R. Watanabe, Y. Kuroki: Preparation of monosized spherical powders of Pb-Sn alloy by pulsated orifice injection method, Proceedings of the Powder Metallurgy World Congress, Paris, vol. 1, pp. 365–368 (1994).

52. M. Orme, C. Huang: Phase change manipulation for droplet-based solid freeform fabrication, Trans. ASME – J. Heat Transf. 119, 1–6 (1997).
53. M. Orme, Q. Liu, R. Smith: Molten aluminum micro-droplet formation and deposition for advanced manufacturing applications, Alumin. Trans. 3, 95–103 (2000a).
54. M. Orme, R. F. Smith: Enhanced aluminum properties by means of precise droplet deposition, Trans. ASME – J. Manuf. Sci. Eng. 122, 484–493 (2000).
55. M. Orme, C. Huang, J. Courter: Precision droplet-based manufacturing and material synthesis: fluid dynamics and thermal control issues, Atomization Sprays 6, 305–329 (1996).
56. M. Orme, J. Courter, Q. Liu, J. Zhu, R. Smith: Charged molten metal droplet deposition as a direct write technology, Mater. Res. Soc. Symp. Proc. 624, 17–22 (2000b).
57. B. M. Michaelis, D. Dunn-Rankin, R. F. Smith Jr., J. E. Bobrow: In-flight thermal control of molten metal droplet streams, Int. J. Heat Mass Transf. 50, 4554–4558 (2007).
58. K. Anders: Monodisperse droplet streams and their application in space, Proceedings of the Symposium on Fluid Dynamics and Space, VKI, Rhode-Saint-Genèse, pp. 119–125 (1986).
59. E. P. Muntz, M. Orme: Characteristics, control, and uses of liquid streams in space, AIAA J. 25, 746–756 (1987).

Chapter 27
Plain Orifice Spray Nozzles

S.D. Heister

Abstract Plain orifice, or "pressure atomizers" are the most commonly used atomizers due primarily to their simplicity and ease of manufacture. This chapter provides background on the characteristics of these devices in terms of spray production and general behavior. Classical linear theories are reviewed to provide a basis for theoretical droplet size predictions. More recent developments assessing the unsteadiness within these devices, and its role in spray production, is also provided in subsequent discussion. The chapter closes with modern nonlinear simulations of spray production using modern numerical techniques.

Keywords Boundary element method · Cavitation · Discharge coefficient · Hydrodynamic instability · Jet instability · Liquid jet · Pressure atomizer · Satellite droplets

Background/Introduction

The plain orifice or "pressure atomizer" is ubiquitous in our society due to its inherent simplicity and practicality of use. Applications include garden hose and shower nozzles in the home, to industrial spraying and spray drying operations, to inkjet printers in the office and in diesel and rocket engine propulsion devices. The device can be manufactured by a mechanical drilling operation or more advanced techniques such as laser or electron discharge machining. In this context, practical issues are raised relative to the length of hole that can be drilled or machined with a tiny drill bit, and the higher precision techniques are often required.

Figure 27.1 highlights external flow structures that may be observed at various operational conditions and flow properties. At very low velocities, the stream exiting

S.D. Heister
School of Aeronautics and Astronautics, Purdue University, West Lafayette, Indiana, USA
e-mail: heister@purdue.edu

N. Ashgriz (ed.), *Handbook of Atomization and Sprays*,
DOI 10.1007/978-1-4419-7264-4_27, © Springer Science+Business Media, LLC 2011

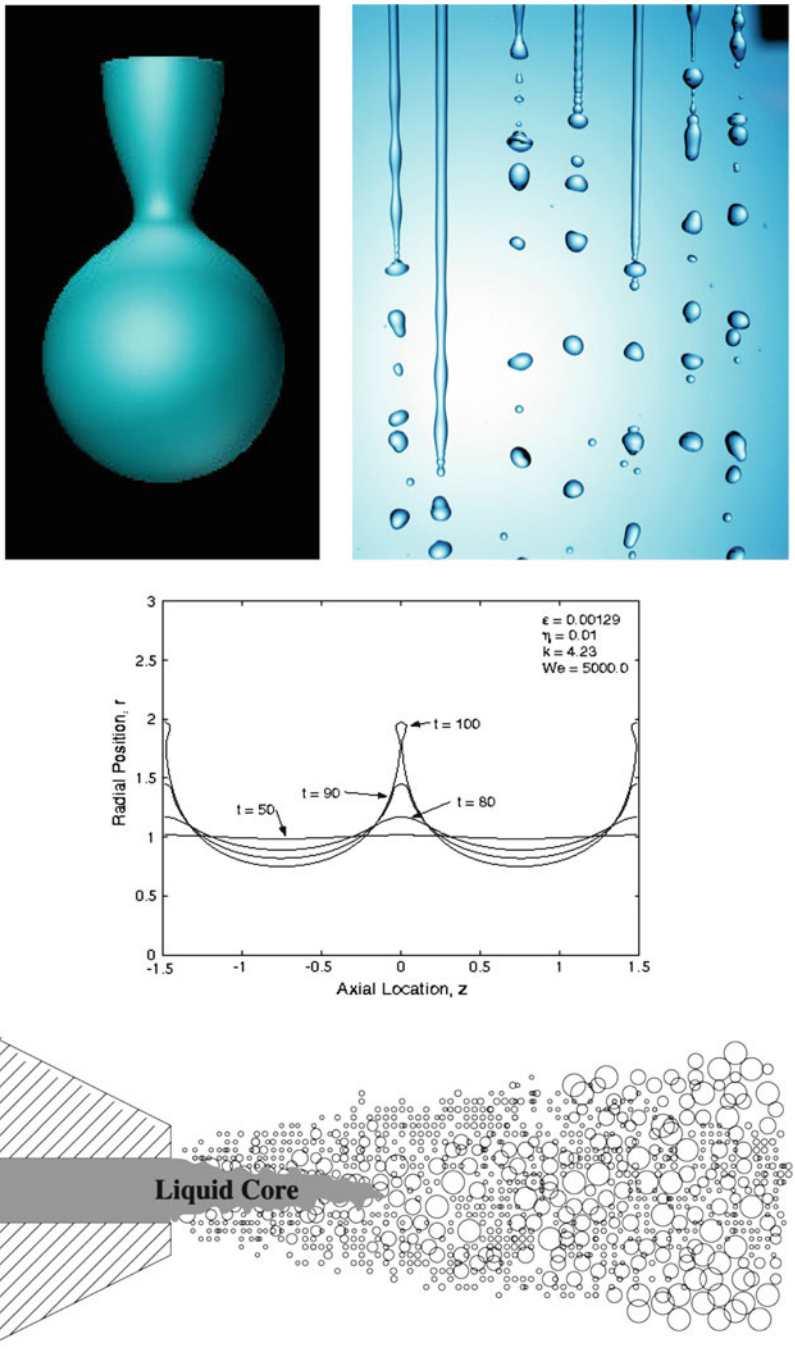


Fig. 27.1 External flow structures pertinent to plain orifice atomizers

the orifice is substantially affected by gravitational acceleration and the *dripping flow* regime results. As jet speed increases, capillary forces dominate the atomization process in a regime typically referred to as the *Rayleigh breakup* regime. For both dripping and Rayleigh regimes, droplet pinching occurs in a reasonably axisymmetric fashion at the centerline of the jet thereby producing drops that are comparable in size to the orifice diameter. At higher velocities, aerodynamic interactions with the ambient gas lead to additional instability of the surface in what is termed the *wind-induced* regime. Within the wind-induced regime, we see the first instances of droplet pinchoff at locations other than the centerline of the jet thereby providing the opportunity to form drops substantially smaller than the diameter of the orifice. At still higher velocities, we enter the *atomization* regime characterized by the appearance of a spray; i.e. a collection of very small drops around a liquid core that vanishes at some distance downstream of the orifice. Observations of the atomization regime are challenging in that the liquid core tends to be obscured by the dense droplet cloud emanating from its periphery.

The length of the liquid jet or the liquid core is of fundamental interest in many applications and is characterized schematically in Fig. 27.2 in what is often called the *jet stability curve*. The overall length to the breakup point increases monotonically with jet speed as one moves from the dripping flow into the wind-induced flow regimes and reaches a maximum as the aerodynamic interactions begin to destabilize the column. Further increases in jet velocity actually lead to decreased jet length as one enters the atomization regime. Depending on fluid properties and orifice design, the intact core length may either decrease or increase with further

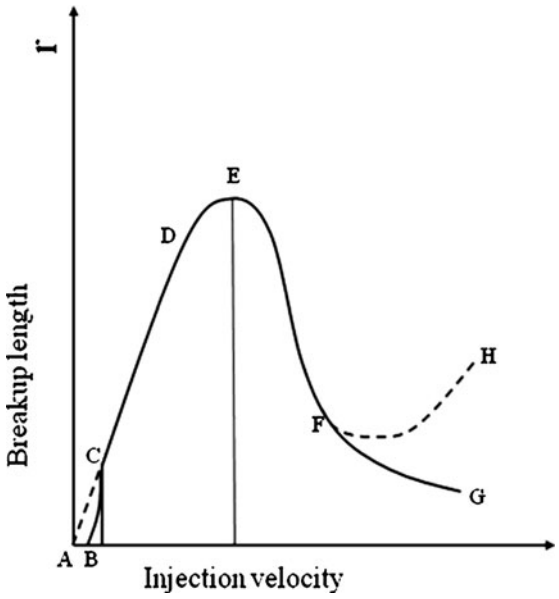


Fig. 27.2 Jet stability curve; dripping flow (*A–B–C*), Rayleigh breakup (*C–D*), wind-induced regime (*D–F*), atomization regime (*F–G* or *H*)

increases in jet speed within the atomization regime (as noted by points G and H in Fig. 27.2).

Our ability to understand the behavior of the resultant spray produced by the pressure atomizer has largely been governed by observations of the external flow structures as highlighted in Figs. 27.1 and 27.2. However, our ability to influence the formation of jets/sprays is entirely dependent on the design of the orifice passage and the inherent internal flow structures resulting from a given passage shape. The practical difficulties associated with observing small scale internal flows has definitely limited understanding, but there is a general agreement that the types of processes noted in Fig. 27.3 are potential contributors to the resultant spray formation. As the flow nears the orifice entry, a tremendous acceleration occurs due to the highly favorable pressure gradients in this region. Disturbances from upstream flow features or manifold crossflow may affect the overall spatial distribution of flow entering the orifice. Even under conditions where the orifice is fed in an axisymmetric fashion, there is a separation zone that develops near the inlet. The stability of this separation zone has not been studied in earnest, but as velocities in this region tend to be low it may not contribute substantially to the overall flow pattern at the exit.

Under high inlet velocities pertinent to most atomization regime operations, any small disturbance at the inlet lip (burrs from machining for example) may be convected downstream for substantial distances. Because of the high gradients and thin boundary layers in the inlet lip region, the performance of high-speed atomizers can be greatly affected by small geometrical changes in this region.

Depending on the overall pressure drop, orifice inlet shape, and flow velocity, a vena-contracta region may be formed downstream of the inlet corner. At high jet

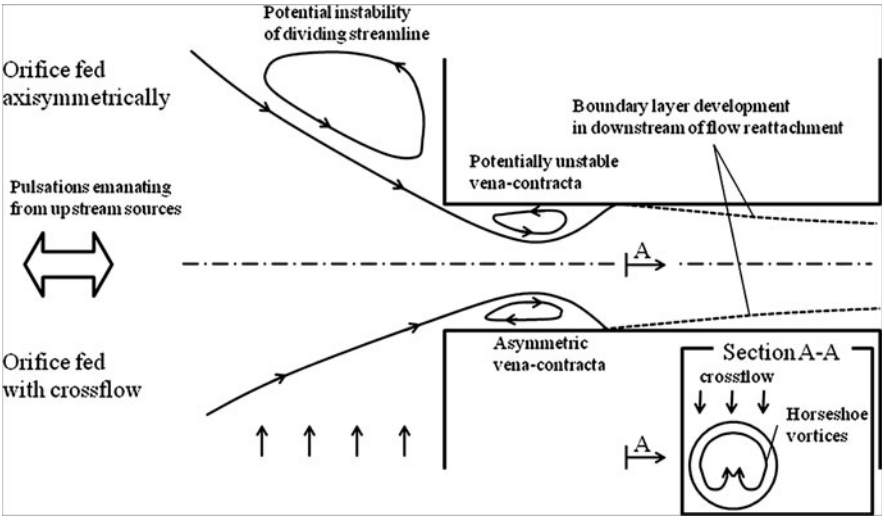


Fig. 27.3 Flow phenomena and forces within a pressure atomizer nozzle

velocities, the local pressure within the vena-contracta region may be low enough to cause local cavitation of the flow. Downstream of the reattachment point, a boundary layer will begin to form along the wall and any turbulence-related development will become pertinent. When the Reynolds number based on orifice diameter exceeds 5,000 or so, the vena-contracta becomes hydrodynamically unstable due to the adverse pressure gradient present on the aft portion of this structure. This instability leads to periodic shedding of vortices from the trailing edge of the vena-contracta and produces unsteadiness in the massflow production of the device.

The thickness of the boundary layer at the orifice exit is determined by the length of the passage downstream of the attachment point and the character of the flow (laminar vs turbulent). At the exit plane, strong gradients are placed on this boundary layer as we transition from a no-slip wall to a free-surface condition at the edge of the boundary layer. The boundary layer thickness at the exit plane is tremendously important for high-velocity injectors as the vorticity convected from the boundary layer leads to unbalanced radial forces on the free surface immediately downstream of the orifice exit. An orifice passage that promotes a very thin boundary layer will result in a highly stable jet – such an approach is used in water jet cutters for example. A design that leads to a thick (and unsteady) boundary layer will provide for large amounts of atomization such as to produce a fine mist or spray.

Due to the huge number of applications of the device and its geometric simplicity, the literature pertaining to the analysis of pressure atomizers is immense.

Historically, practical analysis of pressure atomizers has focused on experimental characterization of the discharge coefficient (C_d) that represents the ratio of measured and theoretical flowrates under an imposed pressure drop condition:

$$C_d = \frac{\dot{m}_m}{\rho V_B A} \tag{27.1}$$

where $\dot{m}_m$ is the measured massflow rate, ρ is the liquid density, $A = \pi D^2/4$ is the orifice cross-sectional area and V_B is the "Bernoulli" velocity computed assuming inviscid flow with the imposed pressure drop ($V_B = \sqrt{2\Delta p/\rho}$). For a given orifice design, discharge coefficient can be correlated with Reynolds number, desired massflow, or imposed pressure drop. Typical values range from 0.6 for a sharp-edged short orifice to values in excess of 0.95 for rounded/chamfered inlet designs with reasonable lengths ($3 < L/D < 6$).

Plain orifice atomizer discharge coefficient data are available in Lefebvre [1] as well as other published sources [2–4] but in general the data must be gathered experimentally for a particular design and range of flow conditions. There tends to be a strong variation of C_d with Re at low flow (laminar) conditions, but at high Re turbulent conditions, C_d shows only minor variations over a large Reynolds number range. Data typically show a strong variation of C_d with inlet roundness or chamfer. Longer nozzles display lower discharge coefficients due to additional viscous losses downstream of the flow reattachment point. At high pressure drop conditions for injection into ambient pressure air, cavitation is likely on some of the internal passages.

The mechanisms for primary instability of a liquid emanating from a simple round orifice passage represents one of the most fundamental problems in two-phase flow. Chapter 1 provides an overview of jet instability theories. As noted there, a number of theories have been advanced over the years as to the underlying mechanism leading to instability and the subsequent primary atomization of the jet. At injection speeds below a few m/s, the capillary instability developed by Lord Rayleigh [5] has been shown to be dominant. Weber [6] provided corrections to Rayleigh's linear theory to account for finite liquid viscosity, but this correction did not alter the predicted wavelengths substantially. Modern computational analyses [7–9] have recently been applied to the capillary jet and have demonstrated the formation of satellite droplets created via nonlinear interactions not considered in Rayleigh's or Weber's analyses. The linear theories cannot predict the formation of satellite droplets as these structures form during the nonlinear evolution of the capillary instability.

The droplet sizes from these nonlinear processes have been shown to be in agreement with experimental observations and entire industries such as ink-jet printing have capitalized on the ability to understand and control primary atomization within this low-speed regime. Electrostatic charging of the jet is also used to provide precise control of droplet sizes in many of these applications. For these reasons, it could be argued that the mechanisms for primary atomization in the low-speed jet are well understood. For example, a comparison of a computed and observed jet shape in the breakup region is highlighted in Fig. 27.4. By introducing a known wavelength disturbance (λ) in the jet, both main and satellite droplet sizes can be measured under a variety of conditions. Figure 27.5 depicts the comparison of experimental measurements and computed results for this case; please see Chap. 15 for a discussion of the modeling approach using boundary element methods (BEM). In general, as the wavenumber $k = 2\pi/\lambda$ is increased, the satellite drop shrinks in size. Rayleigh's result predicts that in nature, $k = 2 \times 0.707/D$ which implies main and satellite drop sizes of approximately $2.1D$ and $0.6D$ accordingly.

At higher jet speeds (generally above 15–20 m/s for low viscosity liquids), there are many more potential contributors to the atomization process. A number of linear models appeared in the latter half of the last century that served as extensions of the Rayleigh theory to account for such processes as aerodynamic interaction with the gas phase, velocity profiles within the liquid/gas phase, and boundary layer relaxation from a no-slip condition to a free-surface condition at the orifice exit plane. Many of the analyses presume an initially undisturbed liquid column subjected to aerodynamic, viscous, and capillary forces. These "column-based" linear analyses due to Levich [12], Sterling and Sleicher [13], and Reitz and Bracco [14] began to emphasize the importance of the gas-phase interactions at the higher jet speeds. For the most part, these models neglected the flow processes within the orifice passage itself and most models did not account for the boundary layer profile at the exit plane as a potential contributor via the relaxation mechanism. More recently, spatial analyses with a similar column-based assumption [15, 16] have also become available for prediction of linear instabilities.

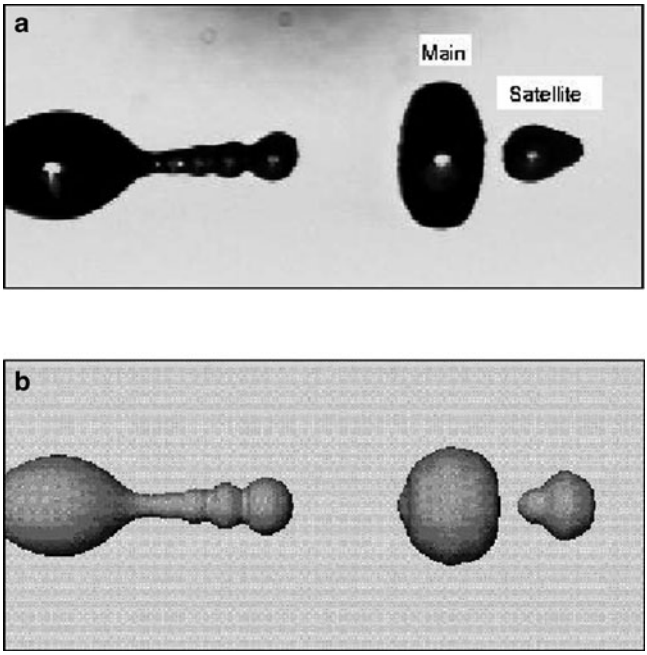


Fig. 27.4 Experimental photo [10] (**a**) compared with boundary element computation (**b**) [11] for a liquid jet within Rayleigh breakup regime

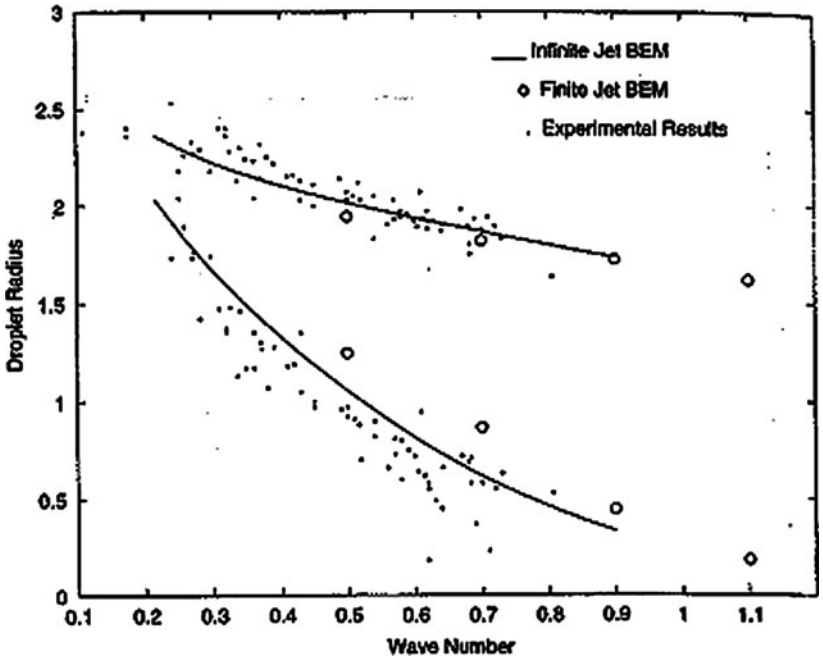


Fig. 27.5 Comparison of measured and computed main/satellite drop sizes in Rayleigh regime [11]

The Sterling-Sleicher [13] result is often used in current approaches as it incorporates aerodynamic effects. Chapter 3 provides a detailed description of the analytic technique employed for these linear stability analyses, only a final result (dispersion equation) relating the growth rate of disturbances given a certain wavenumber (k) will be provided here. The inviscid form of Sterling and Sleicher's result may be written (see (1.4.2)):

$$\left(\frac{\bar{k}I_o(\bar{k})}{2I_1(\bar{k})}+\varepsilon\frac{\bar{k}K_o(\bar{k})}{2K_1(\bar{k})}\right)w^2+\left(i\varepsilon\frac{U\bar{k}^2K_o(\bar{k})}{aK_1(\bar{k})}\right)w=\frac{\sigma}{2\rho_l a^3}(1-\bar{k}^2)\bar{k}^2 +\varepsilon\frac{U^2\bar{k}^2}{2a^2}\frac{K_o(\bar{k})}{K_1(\bar{k})} \tag{27.2}$$

In (27.2), capillary forces account for the first term on the RHS while aerodynamic interactions with the gas account for the second term on the RHS. This latter term is equivalent to a classical Kelvin-Helmholtz instability resulting from aerodynamic destabilization of a wavy liquid interface.

In the 1970s, a number of groups began to focus attention on the boundary layer instability (BLI) mechanism beginning with the ground-breaking experiments of [17–19] and McCarthy and Molloy [20] and complementary linear stability analyses emanating from the Orr-Sommerfield equation due to Skhadov [21] and Brennen [22]. This mechanism focuses on free surface instabilities attributed to vorticity convected from the orifice exit as the boundary layer on the orifice wall is ejected into the chamber.

Shkadov [21] provides the solution of the Rayleigh's equation (limiting form of the Orr-Sommerfield Equation for high Reynolds numbers) and proves that the amplitude of surface waves grows in the downstream direction, as the jet velocity profile relaxes. Brennen [22] extended Shkadov's result to solve for frequencies of formation of instability waves. He considered separated boundary layer flow over the planar plate using Gaussian velocity profile. This resulted in:

$$\gamma=2\pi f\frac{\delta_2}{U} \tag{27.3}$$

where γ is the nondimensional frequency, f is the dimensional frequency in (Hz), δ_2 is the momentum thickness in (m), and U is the speed of the uniform flow in (m/s). Brennen concluded that $\gamma=0.175$ was to be the nondimensional frequency which would give maximum amplification at the flow separation point. Using this result, we arrive at a very simple prediction for the wavelength of the instability ($\lambda=U/f$):

$$\lambda=\frac{2\pi\delta_2}{0.175} \tag{27.4}$$

thus indicating the tremendous importance the boundary layer thickness at the exit plane plays in this theory. Some researchers have approximated the boundary layer

momentum thickness, δ_2, using Blasius solution [11] for laminar flow assuming that $\delta_2 \ll a$:

$$\frac{\delta_2}{x} = \frac{0.664}{\sqrt{\mathrm{Re}_x}} \tag{27.5}$$

where $\mathrm{Re}_x = \rho \mathrm{Ux}/\mu$. While in many cases, a turbulent boundary layer growth would be more appropriate, this methodology provides a simple approach toward estimating the length of waves from the boundary layer instability mechanism.

McCarthy and Molloy [20]'s experiment provides further confirmation of the role of the momentum thickness in wave formation at the orifice exit plane. They varied the nozzle-to-diameter ratio (i.e., *L*/*D*) while keeping the flowrate fixed and therefore observed the effect of *L*/*D* on "laminar" jet structure. In their paper [23], it was not mentioned that the jets had distinctive axisymmetric waves for different orifice designs, yet the experimental images do contain these structures as shown in Fig. 27.6 excerpted from their paper. Farther downstream, the jets become chaotic/turbulent in appearance (see Case $L/D = 5$ and 10 in Fig. 27.6) and result in the primary atomization.

To compare the McCarthy and Molloy results with Brennan's theory, we assume boundary layer development inside the passage can be approximated by boundary layer growth on a flat plate. Clearly, this assumption becomes poor when the boundary layer is a substantial fraction of the orifice radius, but one could use a numerical analysis or more elaborate theory to more accurately ascertain momentum thicknesses at the orifice exit plane. The errors result from freestream pressure gradients which develop as the boundary layer builds in the passage. Given this caveat, the predicted δ_2 values using this technique, when implemented in Brennen's equation, show good agreement with the observed wavelengths from the McCarthy and Molloy experiments as presented in Table 27.1. One can also note from Table 27.1 that the δ_2 values are all quite small relative to the orifice radius, thereby

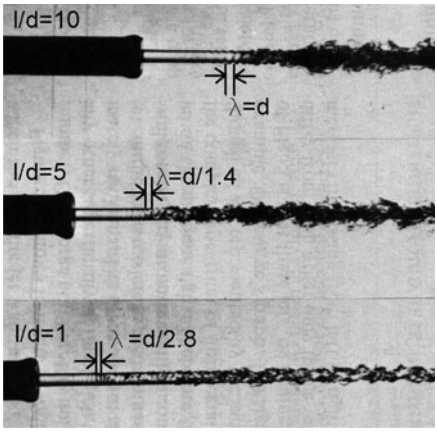


Fig. 27.6 McCarthy and Molloy's experiment [20]. The most dominant wavelength appears subsequent to laminar region which can be scaled by the Brennen's [17] theory (Printed under the permission of Elsevier Science)

lending credence to the simple approach of assuming flat plate boundary layer growth.

Figure 27.7 provides the classic result from Hoyt and Taylor showing the growth of instability waves near the orifice exit. More recent work from Portillo and Blaisdell [24] is shown in Fig. 27.6b that provides insight into the development of 3-D structures on the surface of the jet. The wave patches are attributed to instabilities in the boundary layer as it exits the orifice.

Recently, Yoon and Heister [25] compared most unstable wavelengths produced by column-based and boundary layer instability approaches. Results from this comparison are highlighted in Fig. 27.8. For orifice L/D in the 3–5 range, the boundary layer instability results give much smaller wavelengths at low jet speeds

Table 27.1 Comparison of wavelengths from experiments [20] with theory from (27.3) to (27.5)

L/D	Re_x	δ_2/d	Re_{δ_2}	f [Hz]	λ	λ_{exp}
1	4,748	1/103.8	46	22,758	d/2.89	d/2.8
5	23,738	1/46.41	102	10,178	d/1.3	d/1.4
10	47,477	1/32.82	145	7,197	1.1 d	1.0 d

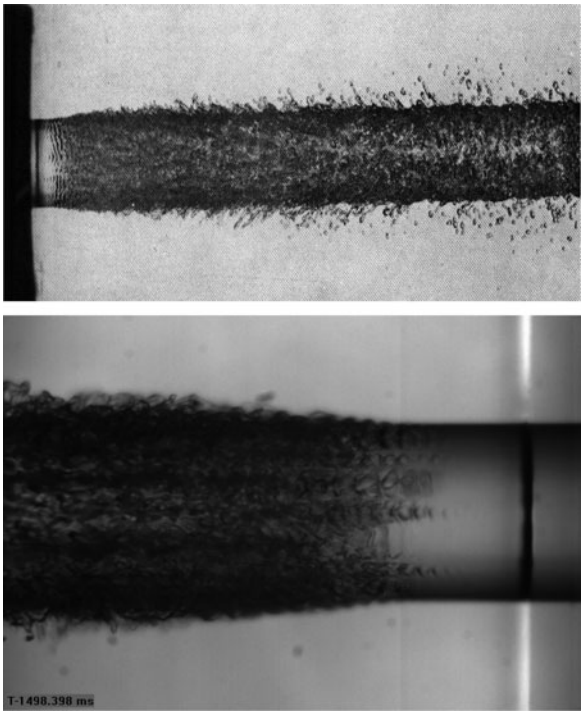


Fig. 27.7 Images of quasi-axisymmetric boundary layer instability due to Hoyt and Taylor [17] (**a**) and 3-D incipient instability imaged by Portillo and Blaisdell [24]

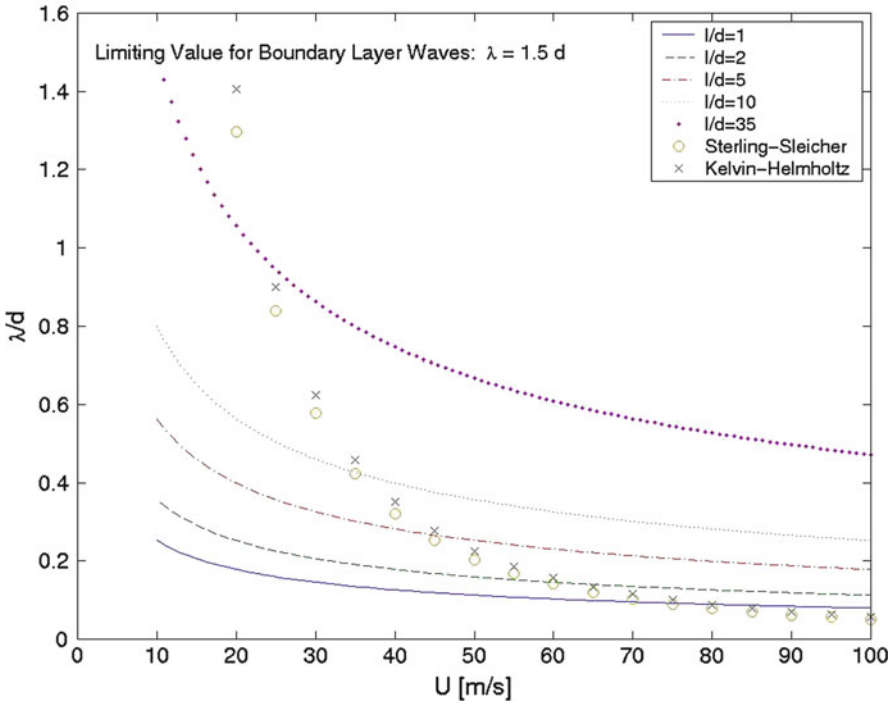


Fig. 27.8 Comparison of most unstable wavelengths for column-based and BLI-based theories [25]

and slightly larger wavelengths at higher jet speeds. It is also interesting to note that the Reitz/Bracco result give a very similar answer to a classic Kelvin-Helmholtz instability indicating that the aerodynamic forces on the jet periphery are dominant at modest and high jet velocities. More recently, a number of nonlinear computations have supplemented these efforts. For high-speed injection such as one might see in the atomization regime, it may be argued that the BLI mechanism is dominant as it leads to a nonlinear "swelling" of the free surface in the region immediately downstream of the injection plane [23, 26, 27]. This phenomenon is observed in low Reynolds number manufacturing processes and is known as "die swell" in these applications. As the amount of jet swelling is proportional to the boundary layer thickness at the orifice exit plane, it is much more readily observed in this latter application.

Both the BLI and the column-based theories tend to assume the initial liquid flow is steady, while the stability of high Reynolds number flows consistent with high-speed injection conditions makes this assumption tenuous at best. In fact, the transition Reynolds number for flow through an orifice is typically quoted in the 3,000–5,000 range, conditions below the operational range of many atomizers. Experimentalists [23, 28–30] have focused on unsteadiness within the orifice flow itself in the form of turbulence as a mechanism for primary atomization. Analyses

of the turbulence mechanism [14] have shown that aerodynamic forces are larger than turbulence-induced forces, but these conclusions were based only on relatively simple scaling arguments.

However, sharp-edged orifices used in many applications are subject to laminar instabilities that display turbulent-like qualities due to the hydrodynamic instability of the vena-contracta formed downstream of the orifice inlet plane. Recent studies [31, 32, 35] have shown a rich character of frequencies/wavelengths produced by these oscillations and they can in principle serve as a nonlinear forcing that would directly affect either a BLI or column-based analysis. Anyone who has observed the flow emanating from a high-speed orifice with a burr at the inlet recognizes the strong effect this imperfection can have on the orifice flow and spray production, so there is potential that axisymmetric laminar instabilities can greatly affect the jet behavior outside the orifice exit.

Vena-contracta pulsations, and their influence on orifice massflow production have recently been studied computationally [33, 35]. A series of high-resolution, laminar calculations were performed for a Reynolds number of 10,000 on simple orifice designs featuring a straight channel and an inlet lip with varying degrees of rounding. Figure 27.9 shows instantaneous streamlines over a single period, T, of the oscillation with time increasing from left to right and from top to bottom. Vortices are shed from the trailing portion of the vena-contracta and convect downstream to the orifice exit. The vena-contracta region then grows and the process repeats in a very periodic fashion for this modest Re condition. At higher Re, additional degrees of freedom are present and ever-more complex structures and massflow histories result.

A typical time history of the discharge coefficient is shown in Fig. 27.10 for the same conditions shown in Fig. 27.9. Fundamentally, the temporal variation in the discharge coefficient comes from a time varying displacement thickness resulting from the interactions of shed vortical structures with the boundary layer. As the Reynolds number is modest, a very simple massflow signal results. Processing of this signal via a Fast Fourier Transform (FFT) yields a single tone with some energy at a higher harmonic as noted in Fig. 27.11.

Longer nozzles tend to produce more degrees of freedom as indicated in results for an $L/D = 6$ case depicted in Fig. 27.12. Massflow pulsations are more complex and therefore yield a richer frequency spectrum. Increases in Reynolds number yield similar effects but it becomes challenging to compute these cases without incorporation of a turbulence model. The laminar-to-turbulent characteristics of this flowfield present substantial challenges for this flowfield as most two-equation turbulence models rely on turbulent inflow conditions to close the problem. Clearly this is an area ripe for future research.

A compilation of results summarizing the unsteady behavior for a variety of nozzle lengths and inlet rounding is provided in Figs. 27.13 and 27.14. In general, the magnitude of the massflow pulsations (Fig. 27.13) decreased with inlet rounding level. This is the expected result since as the inlet rounding is increased the vena-contracta size is decreased as is the amplitude due to the type of unsteadiness shown in Fig. 27.9. Indeed, for the $r_i/D = 0.05$ case when the $L/D = 8$ and 10 there were no

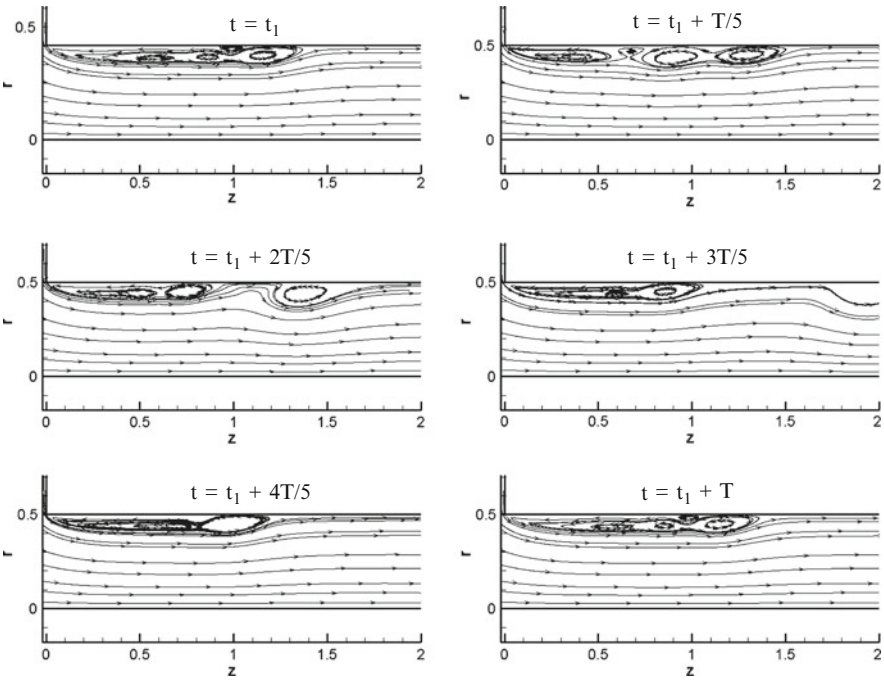


Fig. 27.9 Instantaneous streamlines for one period of oscillation in the Vena-Contracta [33] $Re = 10{,}000$, $r_i/D = 0.005$, $L/D = 3$

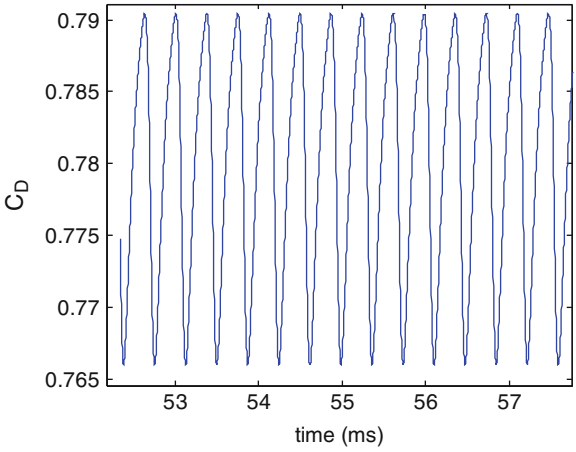


Fig. 27.10 Unsteady discharge coefficient for $r_i/D = 0.005$, $Re = 10{,}000$, $L/D = 3$ [33]

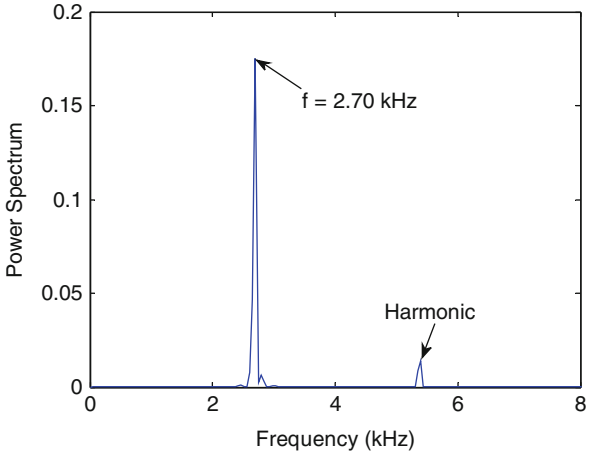


Fig. 27.11 Frequency content of the unsteady discharge coefficient in Fig. 27.9

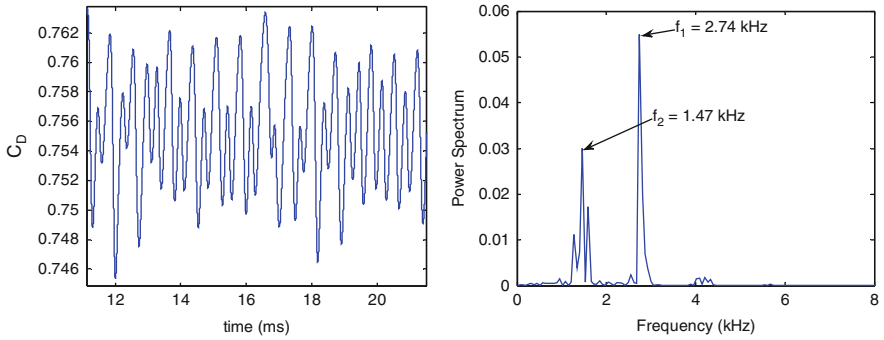


Fig. 27.12 Unsteady discharge coefficient and power spectrum for $r_i/D = 0.005$, $L/D = 6$ case [33]

pulsations in discharge coefficient. Moreover, when the inlet rounding was increased to r_i/D of 0.1, the flow was steady for $L/D > 2$. Nozzle length variations produced a more interesting result showing a local maximum in pulsations near $L/D = 4$ for several inlet roundness levels. For the sharp inlet $r_i/D = 0.005$ case, the global maximum of the magnitude of the unsteadiness occurs at an $L/D = 4$ with another local maxima at $L/D = 6$.

The amplitude of the fluctuations summarized in Fig. 27.13 are significant (relative to linear theory); the sharper inlets show pulsations greater than 1% for all conditions assessed. These large scale pulsations can be further amplified by either boundary layer instabilities or aerodynamic interactions outside the nozzle. This unsteadiness will lead to finite-amplitude waves on the free-surface immediately downstream of the orifice exit, i.e., as a small-amplitude Klystron effect. Depending on the capillary length scale, these waves could be amplified to the point

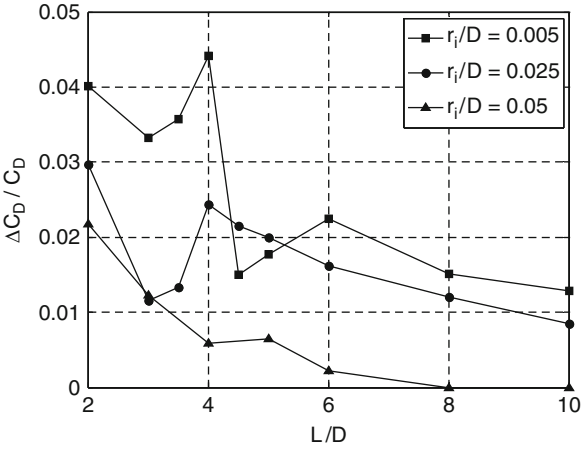


Fig. 27.13 Summary of massflow pulsation amplitudes for various nozzle designs [33]

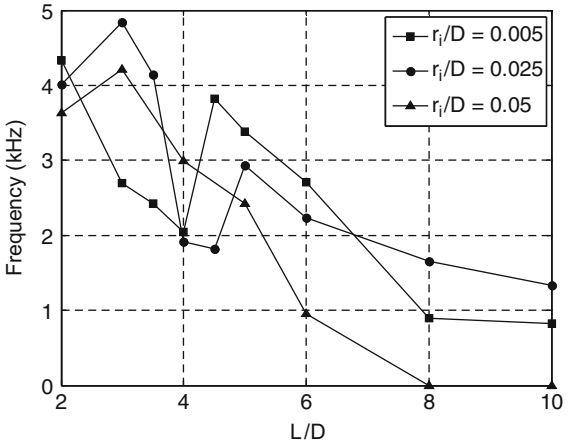


Fig. 27.14 Frequency of injector massflow oscillations for various nozzle designs [33]

of surface rupture and droplet sizes formed would then likely scale with these wavelengths.

The dominant frequency in each of the computationally determined spectra was determined and the results are shown in Fig. 27.14. Again, there are local maximum in the frequency as the L/D of the injector is varied. For the case of $r_i/D = 0.025$ and 0.05 the global maximum frequency occurs at an L/D of 3. While for the case of $r_i/D = 0.005$, the global maximum is at an L/D of 2 and a local maximum is present at an L/D of 5. These values provide a potential explanation for the general rule of thumb for orifice length (use L/D near 4) to maximize atomization efficiency.

Using the computed results for the cases where the inlet rounding were 0.005 and 0.025, the wavelengths associated of the pulsations were computed and are reported

in Fig. 27.15. Moreover, the theoretically predicated most unstable wavelength using boundary layer instability method by Brennen [22] is also included on the figures. The displacement thickness required from Brennen's analysis was determined by averaging the time varying displacement thickness from the computation. As the Brennen wavelength scales with this thickness, Fig. 27.15 shows that a local minima in displacement thickness exists at $L/D = 4$. The pulsations and unsteadiness lead to a slight reduction in average displacement thickness at this nozzle length.

In theory, the injector length at which the computed frequencies and Brennen's analysis overlap would produce the maximum atomization, as the massflow pulsations would provide harmonic amplification of the BLI mechanism. Clearly, nonlinear free surface simulations and careful experiments are needed to confirm this speculation. In any event, the similarities in the order of magnitude of the computations and Brennen's result suggest that the potential exists for amplification of the laminar instabilities by the boundary layer instability.

Nonlinear Spray Simulations

A complete nonlinear simulation of a high-speed jet is an incredibly daunting task, even in the current computational environment. The atomization of a high-speed jet shares many similarities to turbulence in that there are a large number of length scales involved. Typical Weber numbers may be of the order of 10^4 or even 10^5 in high-flow rocket injectors, while drops are formed when the local Weber numbers are of order unity. Accurate resolution of capillary forces is challenging because they depend on local surface curvature which depends on the second derivative of the surface shape. Schemes that place moving meshes on the surface require fewer nodes to resolve the local curvature but demand the additional overhead of moving grids. For three-dimensional problems such as the spray evolving from a high-speed

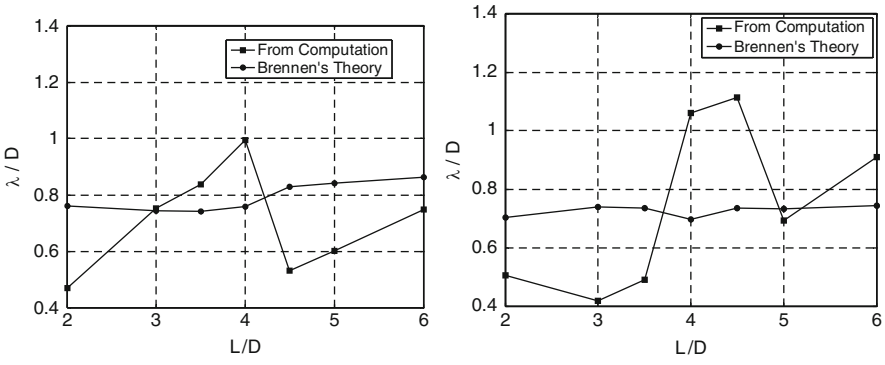


Fig. 27.15 Most unstable wavelengths for $r_i/D = 0.005$ (*left*) and $r_i/D = 0.025$ (*right*)

jet, these issues require grids far in excess of those affordable in the current or near-term computational environment.

One alternative that has been explored [27] is to conduct an axisymmetric computation (with its associated efficiency) and use a linear stability analysis to fractionate annular ring-shaped ligaments shed from the jet periphery in this case. A Boundary Element Method (BEM) was employed to compute the local surface dynamics. See Chap. 15 for details regarding the computational methodology. While Fig. 27.6 indicates that 3-D instabilities occur prior to pinching of axisymmetric structures, the wavelengths of the azimuthal modes appear to be comparable to those of the axisymmetric waves. Nevertheless, the axisymmetric assumption, while providing drastic simplification, still provides much room for improvement as more computational power becomes available.

Figure 27.16 highlights elements of the model. Because the BEM treatment employed is inviscid, the vorticity associated with the boundary layer at the exit plane is modeled assuming a bound ring vortex. The location and strength of the vortex is uniquely determined from the local character of the boundary layer. Using Brennan's result for the wavelength exiting the orifice, the strength of the ring vortex, Γ_v, can be written [27]:

$$\Gamma_v = U\lambda = U\left(\frac{2\pi}{0.175}\right)\delta_2 \tag{27.6}$$

Where U is the bulk velocity of injection and δ_2 is the momentum thickness at the exit plane as before. As indicated in Fig. 27.16, the ring vortex center is placed at the exit plane; the structure is placed radially such that the center of rotation is a distance δ_2 from the wall. The presence of the vortex leads to instabilities on the jet surface that grow as the fluid progresses from the orifice exit. Figure 27.17 depicts highly developed axisymmetric waveforms that develop during this process. The shed vorticity leads to development of ligaments that lean in the upstream direction in agreement with those observed in the experiments. We should point out that these structures are not attributed to aerodynamic drag as the model neglects any drag on the surface. As the waveforms are observed experimentally in the near-orifice

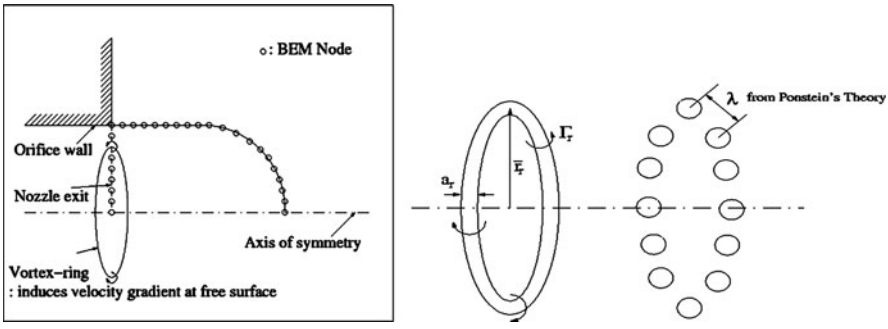


Fig. 27.16 Boundary element model (BEM) for nonlinear spray simulations



Fig. 27.17 Backward-leaning structures in Hoyt and Taylor experiment [xx] (**a**) (Printed under permission of J. Fluid Mech.) and in BEM computations [27] (**b**). Flow is from left to right

region it is likely that drag does not play a large role in the actual physical process as well. Figure 27.17 also indicates the limits of the model as computational restrictions on the mesh provide a very coarse resolution of the small structures forming on the surface of the jet.

At some point, ring-shaped structures are pinched from the jet periphery. To assess the resultant drop sizes that may be formed from these annular ligaments, the linear stability analysis due to Ponstein [34] is employed. Ponstein analyzed the stability of a rotating column, so the assumption employed here is that the radius of the ring-shaped ligament is much less than that of the jet itself ($a_r = a$). Ligaments are shed with a circulation Γ_r that can be determined from the instantaneous velocities of nodes on their surface at the time of pinching. Ponstein developed a dispersion equation for the growth rate ω of disturbances of wave number k:

$$w^2 = \left[\frac{\sigma}{\rho a_r^3}(1 - k^2 a_r^2) + \left(\frac{\Gamma_r}{2\pi a_r^2}\right)^2\right](ka_r)\frac{I_1(ka_r)}{I_o(ka_r)} \tag{27.7}$$

By finding the k value which maximizes ω determines the number and size of droplets formed from fractionation of the ring. As the velocity of the center of mass of the ligaments can be computed when they are shed from the parent surface, this approach permits further tracking of the droplet field as it evolves from the surface. Here, it is assumed that the ring fractionation takes place instantaneously and that the initial droplet velocity is that of the ring ligament. Droplets are distributed uniformly azimuthally to give a quasi-3-D construction of the spray. Figure 27.18 shows a spray development resulting from this process. Rings of various sizes are pinched from the jet periphery leading to a natural distribution of droplet sizes. Unfortunately, computer resources were insufficient to permit full development of the liquid core in this case, but near-term technology will permit such for modest injection speeds.

Table 27.2 provides a summary of droplet statistics from a few different simulations conducted with the model. The Sauter mean diameter (SMD) is the droplet

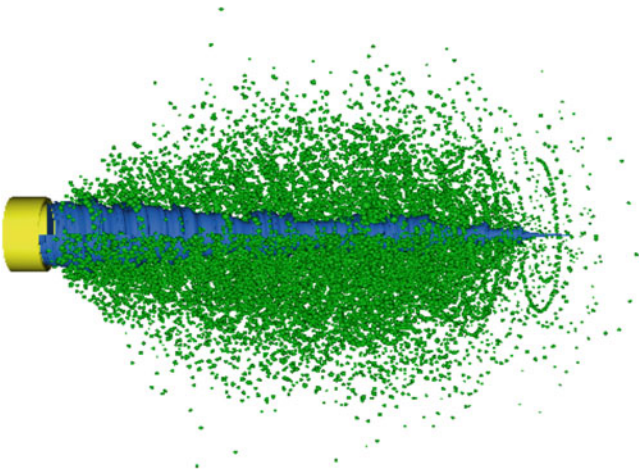


Fig. 27.18 Spray evolution using drop tracking algorithm [27]. Injection conditions are consistent with the Hoyt and Taylor jet shown in Fig. 27.16

Table 27.2 Results from simulations of various orifice lengths using BEM model [27]

L/D	δ_1/D	δ_2/D	Γ_v/Ua	r_v/a	SMD	N_D	$N_{D,avg}$
1	1/200	1/518	0.139	0.990	0.0655	3,884	11.48
2	1/141	1/367	0.197	0.986	0.0658	5,879	11.59
∞	1/6	1/24	0.667	0.667	0.0675	8,133	11.69

size that is of greatest interest in many applications; the Table shows slight variations in this parameter with orifice length (momentum thickness) variation. Simulations producing over 8,000 drops (N_D) were conducted – more recent work with swirl-type atomizers can now simultaneously develop and track over 80,000 drops. A comparison with droplet sizes measured in the Hoyt and Taylor jet reveals that the computed SMD is about 20% lower than the measured value. Viscous interactions in the pinching region may be responsible for this trend, but there is reason to be optimistic that the community will someday have a comprehensive capability to accurately predict spray distributions from first principles.

References

1. A. Lefebvre, *Atomization and Sprays*, Hemisphere Publishing, New York, 1989.
2. A. Lichtarowicz, R. K. Duggins, and E. Markland, Discharge coefficients for incompressible non-cavitating flow through long orifices, *Journal of mechanical Engineering Science*, 7(2), 210–219, 1965.
3. T. R. Ohrn, Senser, D. W., and Lefebvre, A. H., Geometrical effects on discharge coefficients for plain orifice atomizers, *Atomization and Sprays*, 1(2), 137–157, 1991.

4. V.I. Asihmin, Geller, Z. I., and Skobel'cyn, Yu. A., Discharge of a real fluid from cylindrical orifices (in Russian), *Oil Industry*, Vol. 9, Moscow, 1961.
5. W. S. Rayleigh, On the instability of jets, *Proc. Lond. Math. Soc.*, 10(4), 1878.
6. C. Weber, Zum Zerfall Eines Flussigkeitsstrahles, *Z. Angew. Math. Mech.*, 11, 138–245, 1931.
7. N. N. Mansour and T. T. Lundgren, Satellite formation in capillary jet breakup, *Phys. Fluids*, 2, 1141–1144, 1990.
8. J. H. Hilbing, S. D. Heister, and C. A. Spangler, A boundary element method for atomization of a finite liquid jet, *Atomization Sprays*, 5(6), 621–638, 1995.
9. C. A. Spangler, J. H. Hilbing, and S. D. Heister, Nonlinear modeling of jet atomization in the wind-induced regime, *Phys. Fluids*, 7, 964, 1995.
10. M. P. Moses, Collicott, S. H., and Heister, S. D., Visualization of liquid jet breakup and drop formation, *Atomization Sprays*, 9(4), 331–342, 1999.
11. J. H. Hilbing and Heister, S. D., Droplet size control in liquid jet breakup, *Phys. Fluids*, 8(6), 1574–1581, 1996.
12. V. G. Levich, *Physicochemical Hydrodynamics*, Prentice Hall, New Jersey, pp. 639–646, 1962.
13. A. M. Sterling and C. A. Sleicher, The instability of capillary jets, *J. Fluid Mech.*, 68(3), 477–495, 1975.
14. R. D. Reitz and F. V. Bracco, Mechanism of atomization of a liquid jet, *Phys. Fluids*, 25(10), 1730–1742, 1982.
15. S. P. Lin, Two types of linear theories for atomizing liquids, *Atomization Sprays*, 16, 147–158, 2006.
16. S. P. Lin and Z.W. Wang, Three types of linear theories for atomizing liquids, *Atomization Sprays*, 18, 273–286, 2007.
17. J. W. Hoyt and J. J. Taylor, Waves on water jets, *J. Fluid Mech.*, 83, 119–127, 1977.
18. J. W. Hoyt and J. J. Taylor, Turbulence structure in a water jet discharging in the air, *Phys. Fluids*, 20(10), s253–s257, 1977.
19. J. W. Hoyt and J. J. Taylor, Effect of nozzle boundary layer on water jets discharging in the air, *Jets Cavities-Int. Symp.*, pp. 93–100, 1985.
20. M. J. McCarthy and N. A. Molloy, Review of stability of liquid jets and the influence of nozzle design, *Chem. Eng. J.*, 7, 1–20, 1974.
21. V. Y. Shkadov, Wave formation on surface of viscous liquid due to tangential stress, *Fluid Dyn.*, 5, 473–476, 1970.
22. C. Brennen, Cavity surface wave patterns and general appearance, *J. Fluid Mech.*, 44(1), 33–49, 1970.
23. H. Park and S. D. Heister, A numerical study of primary instability on viscous high-speed jets, *Comput. Fluids*, 35, 1033–1045, 2006.
24. G. A. Blaisdell, Collicott, S. H., and Portillo J. E., Measurements of instability waves in a high-speed liquid jet, 61st Conference of the American Physical Society, Division of Fluid Dynamics, San Antonio TX, 2008.
25. S. S. Yoon and S. D. Heister, Categorizing linear theories for atomizing jets, *Atomization Sprays*, 13, 499–516, 2003.
26. J. H. Hilbing and S. D. Heister, Nonlinear simulation of a high-speed, viscous, liquid jet, *Atomization Sprays*, 8, 155–178, 1997.
27. S. S. Yoon, and S. D. Heister, A nonlinear atomization model based on a boundary layer instability mechanism, *Phys. Fluids*, 16(1), 47–61, 2004.
28. P. K. Wu and G. M. Faeth. Aerodynamic effects on primary breakup of turbulent liquids, *Atomization Sprays*, 3, 265–289, 1993.
29. P. K. Wu, L. K. Tseng, and G. M. Faeth. Primary breakup in gas/liquid mixing layers for turbulent liquids. *Atomization Sprays*, 2, 295–317, 1992.
30. Ph. Marmottant and E. Villermaux, On spray formation, *J. Fluid Mech.*, 498, 73–111, 2004.
31. C. Xu, R. A. Bunnell, and S. D. Heister, On the influence of internal flow structure on performance of plain-orifice atomizers, *Atomization Sprays*, 11, 335–350, 2001.

32. M. MacDonald, J. Canino, and S. Heister, Nonlinear response functions for drilled orifice injectors, *42nd AIAA/ASME/SAE/ASEE Joint Propulsion Conference & Exhibit*, 2006. AIAA-2006-4706.
33. J. Canino and Heister, S. D., Contributions of orifice hydrodynamic instabilities to primary atomization, *Atomization Sprays*, V19, 91–102, 2009.
34. J. Ponstein. Instability of rotating cylindrical jets, *Appl. Sci. Res.*, 8(6), 425–456, 1959.
35. J. Tsohas, J. Canino, and S. Heister, Computational modeling of rocket internal flows, *43nd AIAA/ASME/SAE/ASEE Joint Propulsion Conference & Exhibit*, 2007. AIAA-2007-5571.

Chapter 28
Pintle Injectors

S.D. Heister

Abstract Pintle injectors have been developed for applications in rocket propulsion, but could potentially have high flowrate in other applications due to their relative simplicity. The spray from a pintle injector is formed from the collision of radial jets of fluid issuing from the center of the pintle post with an annular sleeve of fluid travelling axially along the post. The resultant interactions produce a conical spray similar to a hollow cone swirl atomizer. This chapter reviews historical applications of pintle injectors and theoretical bases for their design.

Keywords Momentum ratio · Pintle nozzle · Rocket injector

General Description

The pintle injector was developed and is used nearly exclusively in liquid rocket engine applications. The device is generally fabricated as a post with numerous holes or slots machined at its tip. One fluid flows down the center of the post and out radially through the holes/slots, while the other fluid flows in a thin annular sheet along the surface of the post/pintle. The collision of the sheet with the radial jets emanating from the flow within the pintle creates a spray. Vigorous mixing and atomization of the propellants result from the collision of the radial jets with the thin liquid sheet. Figure 28.1 is a series of photographs of water flow tests on a single pintle injector, looking back toward the injector element. Figure 28.1a shows characteristic flow for the outer, annular injection; Fig. 28.1b shows a wider-angle view of the inner passage flow being injected as a radial sheet; and Fig. 28.1c shows the spray fan resulting from the combined flows.

S.D. Heister
School of Aeronautics and Astronautics, Purdue University, West Lafayette, Indiana, USA
e-mail: heister@purdue.edu

N. Ashgriz (ed.), *Handbook of Atomization and Sprays*,
DOI 10.1007/978-1-4419-7264-4_28, © Springer Science+Business Media, LLC 2011

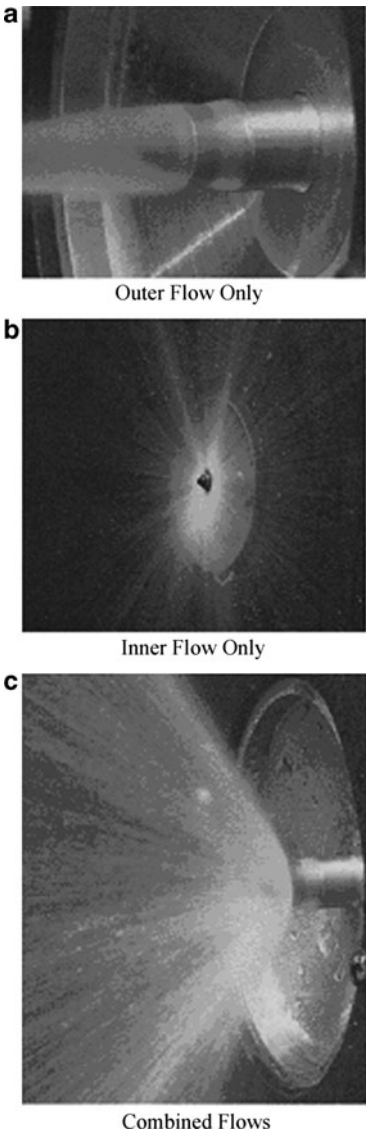


Fig. 28.1 Water flows showing annulus, pintle orifice, and resulting spray produced by pintle injector

The pintle injector is unique among the various injector options which have been successfully used in liquid rocket engines. Many early liquid engine injectors utilized impinging jets that create a spray due to the impact of the two streams, or coaxial injectors that mix propellants from shear or swirl induced in the inner fluid. These injector types are implemented in a "flat face" injector plate at the head-end of the combustion chamber. This resultant flowfield shown in Fig. 28.1c yields a curved spray/combustion zone which is substantially different than those formed by "flat face-type" injectors.

Pintle injectors enjoy several advantages over other types of liquid–liquid injectors. First, the design is inherently simpler in the sense that only a single injector element is required. This issue is somewhat misleading in that the "single element" can have many radial holes or slots, but in any case pintle engines have inherently a lower number of injection sites than face-type injectors. For this reason, pintle engines are inherently simpler to build; all machining operations involve placing holes normal to the local surface and the precise alignment issues associated with impinging element injectors are not present. At larger propellant flows, the relatively small number of injection sites in the pintle leads to larger-diameter streams and hence larger-diameter drops. It is challenging to maintain the efficiency of a flat face injector with many hundreds of injection sites with a pintle that may only have a few dozen holes/slots in its tip. In a sense, there is "no free lunch" for the simplicity of the pintle; for smaller engines performance can match other injector schemes at competitive cost, but the low cost afforded at high flows may come at the price of somewhat decreased performance.

The second advantage of the pintle concept is the inherent combustion stability afforded by this injector. There has never been an instance of combustion instability associated with pintle engines [1]; this factor reduces risk and eliminates the need for stability aids such as baffles and acoustic liners/cavities. The curved combustion zone developed as a result of this unique injection geometry leads to energy release, which, compared to uniformly distributed flat face injectors, is away from the pressure antinodes of the chamber. Also the radial flow component of the injected propellant ensures that there is always a significant mean velocity difference between the gas flow and the propellant drops. It is difficult to overestimate the importance of this advantage as many (if not most) large liquid rocket engine programs have suffered from combustion instability problems that led to lengthy and costly redesigns.

The third attractive feature of the pintle injector involves its throttle ability. By using a translating sleeve, the flow areas in both the annulus and the holes/slots can be adjusted to provide deep throttling and/or face shutoff of the propellant flows. Throttling ratios of 10–20:1 have been demonstrated with hypergolic propellants using this capability [1]. Pulsing applications demanding a face shutoff can also realize significant advantage using this injector design concept. The small dribble volume (volume within injector cavities downstream of shutoff valves) and face shutoff features associated with this injector type make for rapid pulsing capabilities; two ms pulses have been demonstrated using this methodology [2]. Undoubtedly, the most famous application of this injector was in the lunar module descent engine (LMDE) that was throttled to provide Apollo astronauts a safe and well-controlled landing on the surface of the moon.

Applications and Heritage of the Pintle Injector Concept

The pintle injector concept was pioneered by TRW Corporation in Redondo Beach, California, the facility now represented by Northrop Grumman Space Technology

(NGST) Division of Northrop Grumman Corporation. Reference 1 provides an excellent account of the serendipitous development of the concept in the early 1950s as the US rocket industry was attempting to develop hypergolic propellants.[1] Researchers were studying hypergolic reactions by mixing coaxial streams of the propellants and poor results were obtained. The notion of the pintle came out of the desire to impose direct contact of the two propellant streams. TRW continued to develop the technology into rocket injector designs and maintains the heritage of the pintle engine to this day.

Prior applications of pintle injector technology are summarized in [1–21]. The pintle injector design concept was initially developed as a standardized technique to test hypergolicity of storable propellant combinations under development in the late 1950s [1]. The first rocket engine applications were developed in the early 1960s [3]. Since that time, pintle engines have been successfully fired using 25 different propellant combinations in thrust levels from 5 to 650k lb_f [1]. Over 60 different engine designs have been developed over the past 40 years since the genesis of the concept.

The LMDE was one of the more notable achievements of the pintle injector technology. This engine used a translating sleeve to control both annular and slot flow areas to provide the 10:1 throttling ratio (from 10,000 to 1,000 lbf of thrust) demanded of this application [4, 5]. Figure 28.2 provides a photo of the engine and a

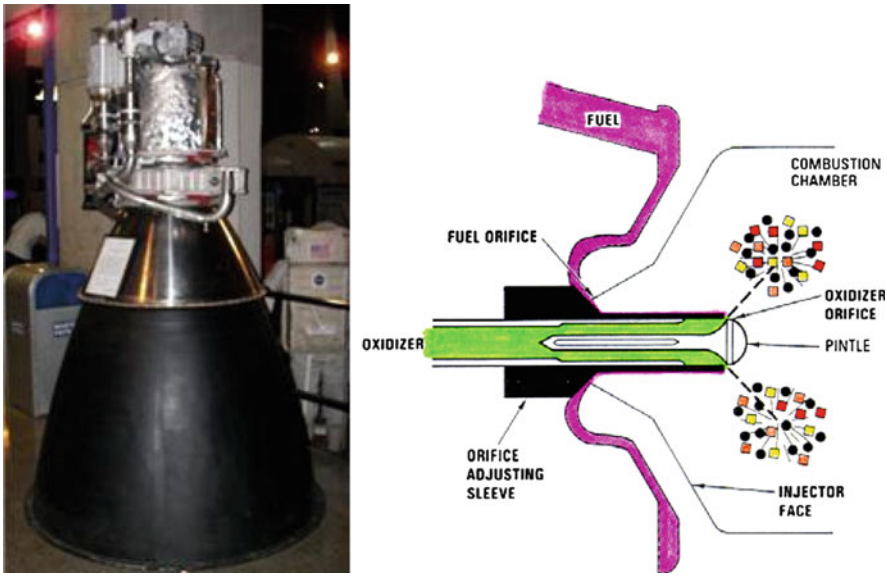


Fig. 28.2 Photo of LMDE and schematic of pintle design utilizing translating orifice adjusting sleeve [6] to control both fuel and oxidizer flow areas simultaneously

[1]Hypergolic propellants react/combust spontaneously upon contact thereby eliminating the need for a separate ignition system.

schematic [6] of the novel pintle design that enabled the required levels of throttling. Axial translation of the orifice adjusting sleeve simultaneously changed flow areas for both propellant streams, thereby keeping the desired mixture ratio over a large range of thrust levels.

At that time, the TR201 liquid apogee engine was developed as a fixed thrust version of the LMDE technology; this engine has flown nearly 80 times without failure as the second-stage engine of the Delta Launch Vehicle. Gas/liquid injection has recently been demonstrated in an 870 lbf engine using gaseous oxygen/ethanol propellants [7]. Austin et al. [8, 9] describe experiments with small engines (100–200 lb_f thrust) using nontoxic hypergolic propellants based on hydrogen peroxide and a methanol-based fuel. Most recently, SpacEx, a new launch vehicle developer, has implemented pintle engine technology in their Merlin engine [10] claiming performance on par or better than other flat face engines using a similar power cycle.

Pintle Injector Design Methodology

The high Reynolds numbers and turbulent impact conditions represented in most pintle engine designs makes for a very complex flowfield. In the rocket application, the main figures of merit on injector performance include combustion efficiency, combustion stability, and overall heat flux to the wall. While spray development and mixing play a critical role in all of these measures, it is generally not possible to separate spray efficiency from combustion efficiency, for example. Practical issues result from attempts to view flowfields inside high-pressure, high-temperature combustion chambers. Proprietary rights of firms undertaking the tedious steps in developing an injector of this type (or any type for that matter) also play a role in limiting general access and availability of detailed spray characterizations for these injector elements. For these reasons, our understanding of drop-size distributions from pintle injectors is poor at best.

Figure 28.3 highlights some of the major design features of a pintle injector. The most important design variable is the total momentum ratio (TMR), defined as the ratio of radial-to-axial stream momentum

$$TMR = \frac{(\dot{m}U)_r}{(\dot{m}U)_z} \tag{28.1}$$

The cone angle formed by the propellant spray increases with TMR; design experience shows that TMR values near unity provide optimal performance. The cone angle of the spray scales as $TMR^{0.5}$ is similar to the scaling of jet penetration in a crossflow with momentum ratio [11]. Typical injection velocities for both axial and radial streams range from 10 to 50 m/s in most cases.

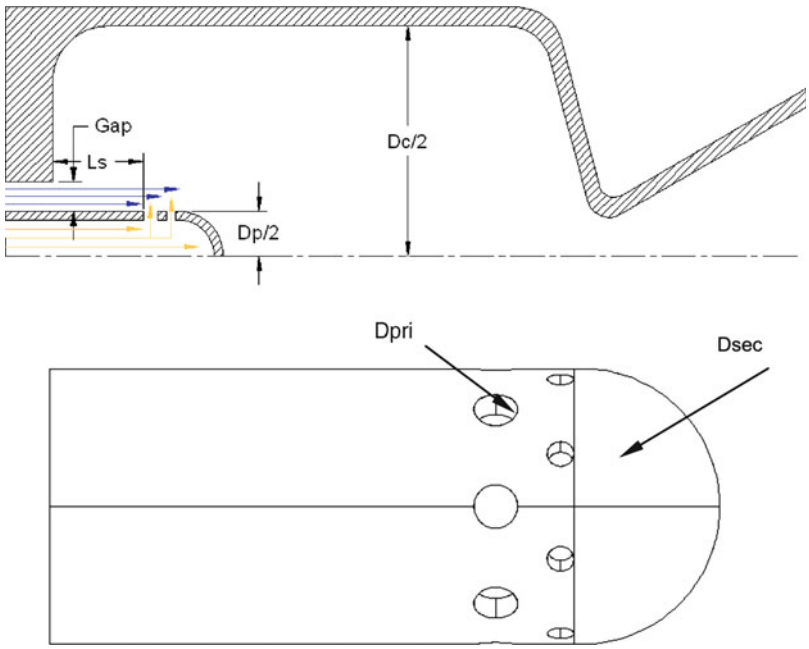


Fig. 28.3 Key design variables for a pintle injector

The blockage factor (BF), defined as the ratio of the total hole/slot circumferential length divided by the circumference of the pintle, is another important design variable

$$BF = \frac{N\, d_o}{\pi\, d_p} \tag{28.2}$$

where N is the number of holes/slots in the pintle tip (typically 20–36). In some designs, a set of "secondary" holes is placed just downstream of the primary holes in the pintle.

These holes are placed circumferentially to lie in the gaps formed by the primary holes; they generally are smaller in size than the primary holes.

Another important dimensionless variable is the ratio of chamber-to-pintle diameters, d_c/d_p. Typical values for this quantity range from 3 to 5 [2]. Finally, the "skip distance" is defined as the length that the annular flow must travel before impacting the radial holes divided by the pintle diameter, L_s/d_p. A typical value for this parameter is around 1; larger skip distances are subject to substantial deceleration of the liquid due to friction against the pintle post while very short skip distances may lead to spray impingement on the head-end of the combustion chamber.

Pintle flows are classified as "fuel-centered" or "oxidizer-centered," depending on which propellant flows inside the pintle tip. Typically, smaller engines utilize fuel-centered configurations and larger engines are oxidizer-centered [4]. When

using a fuel-centered design, it is possible to increase TMR such that fuel jets actually penetrate the axial oxidizer annulus and impact on the wall in order to provide film cooling. Oxidizer-centered designs would operate best at lower TMR values in order to ensure that the oxidizer does not impact chamber walls and cause damage or compatibility issues.

In general, the combustion chambers that use pintle injectors tend to have a higher contraction ratio than face-type injectors to accommodate the radial flows induced by this injection scheme. However, the combustor lengths may actually be shorter due to this same phenomenon; the overall chamber characteristic length values are not dramatically different between the two designs. Pintle thrusters have demonstrated high combustion efficiencies in the 96–99% range for most of the engines which have been developed for flight programs. Due to the limited number of holes in the pintle, the thrust per element (thrust per hole) can be very large for high-thrust engine designs and the combustion efficiency tends to be a bit lower on large engines for this reason. Of course, this difference in efficiency must be weighed against the inherent simplicity and cost of the injector.

The aforementioned design guidelines along with required propellant flowrates allow sizing of the dimensions shown in Fig. 28.3. Design changes are very easy to implement by simply machining another pintle tip. In general, it is difficult to manufacture very small thrust injectors (as in the case of all bipropellant engines) because both the orifice sizes and the annular gap become very small. Tight tolerances are required on the pintle outer surface to ensure a uniform propellant gap under these conditions.

Mechanistic Study

The physics associated with pintle injector flows and combustion has been much less studied than that of the flat face injector types. To date, the database for design has largely been developed empirically. Design analysis codes exist within the industry, but these are not generally available to the public. Limited academic studies have been reported [2, 12]. Even the very fundamental problem of multiple radial jets impinging on a flat liquid sheet has received little attention at this point in time. When hypergolic fluids are used, the “blowapart” phenomenon attributed to the gas evolution at the contact surface has not been addressed or quantified in this injector scheme. Even basic waterflow data on the drop sizes produced for various designs is not readily available in the open literature.

The issues which tend to complicate the development of these injectors include:

- Manufacturing issues associated with maintaining a small annular gap around the pintle for injection of the axial stream.
- Heat-affected regions at the tip of the pintle. The pintle tip lies in a recirculation zone and is subject to high heat flux. There is some limited evidence that use of a rounded tip tends to somewhat alleviate this effect.

- Heat-affected regions near axial/radial stream impact points. In engines using hypergolic fluids, small recirculation zones near the base of the radial jets can lead to pintle damage due to local combustion in this region. Careful design of the pintle surface can help alleviate this problem by creating shapes that minimize the size of recirculation zones.
- As with any bipropellant engine, wall heat flux problems can also be present, but these can normally be alleviated by variation of TMR.

Summary

Pintle injectors offer a unique alternative for high flowrate applications. While they have been solely used in the rocket community (to the author's knowledge) they would presumably be applicable to other applications demanding spray production at modest and high flows. In the rocket applications, the injector type offers simple high thrust-per-element designs. Very little fundamental work on pintle injectors is available in the open literature and the design process is highly empirical. More than the other injectors, the design of the pintle injector must be combined with the design of the combustion chamber to yield good results. Better understanding of the interactions between the pintle injector flow and the combustor could help reduce the combustor size.

References

1. Dressler, G.A. and Bauer, J.M., TRW Pintle Engine Heritage and Performance Characteristics, AIAA 2000-3871, 36th AIAA/ASME/SAE/ASEE Joint Propulsion Conference and Exhibit, Huntsville, July 2000.
2. Escher, D.W., Design and Preliminary Hot Fire and Cold Flow Testing of Pintle Injectors, MS thesis, Mechanical Engineering, The Pennsylvania State University, December 1996.
3. Siegel, B., Research of Low-Thrust Bipropellant Engines, Independent Research Program Annual Report, 1961, #9990-6020-RU-000, pp. VI-59 to VI-73, Space Technology Laboratories, Inc., Redondo Beach 1961.
4. Elverum, G., Staudhammer, P., Miller, J., Hoffman, A., and Rockow, R., The Descent Engine for the Lunar Module, AIAA 67-521, AIAA 3rd Propulsion Joint Propulsion Specialist Conference, July 1967.
5. Gilroy, R. and Sackheim, R., The Lunar Module Descent Engine – A Historical Perspective, AIAA 89-2385, 25th AIAA/SAE/ASME Joint Propulsion Conference, 1989.
6. Dressler, G.A., Summary of Deep Throttling Rocket Engines with Emphasis on Apollo LMDE, AIAA 2006-5220, 42nd AIAA Joint Propulsion Conference, Sacramento, 2006.
7. Calvignac, J., Design and Testing of a Non-Toxic 870-LBf Engine, AIAA 2000-3851, 36th AIAA/ASME/SAE/ASEE Joint Propulsion Conference and Exhibit, Huntsville, July 2000.
8. Austin, B., Matthews, J., and Heister, S.D., Engine/Injector Development for New Nontoxic, Storable, Hypergolic Bipropellants, 13th Propulsion Engineering Research Center Annual Symposium on Propulsion, Huntsville, 2001.

9. Austin, B., Heister, S.D., and Anderson, W.A., Development of Pintle and Splashplate Injectors for Nontoxic, Storable, Hypergolic Bipropellants, Journal of Propulsion and Power, 21(4), 627–635, 2005.
10. http://www.spacex.com/falcon1.php#merlin_engine
11. Heister, S.D., Nguyen, T.T., and Karagozian, A.R., Modeling of Liquid Jets Injected Transversely into a Supersonic Crossflow, AIAA Journal, 27(12), 1727–1734, 1989.
12. Austin, B.J., Development of a Pintle-Based Engine for Nontoxic Hypergolic Propellants, 38th AIAA/ASME/SAE/ASEE Joint Propulsion Conference, July 2002.
13. Fritz, D., Dressler, G., Mayer, N., and Johnson, L., Development and Flight Qualification of the Propulsion and Reaction Control System for ERIS, 28th AIAA 92-3663, AIAA/SAE/ASME/ASEE Joint Propulsion Conference, July 1992.
14. Fritz, D. and Gavitt, K., Gel Propulsion for the Fourth Generation Escape System, Paper presented at the 1993 SAFE Symposium, Las Vegas, November 1993.
15. Dressler, G., Stoddard, F., Gavitt, K., and Klem, M., Test Results from a Simple, Low-Cost Pressure-Fed Liquid Hydrogen/Liquid Oxygen Rocket Combustor, 1993 JANNAF Propulsion Meeting, November 1993, CPIA Pub. 602, Vol. II, pp. 51–67.
16. Hodge, K., Crofoot, T., and Nelson, S., Gelled Propellants for Tactical Missile Applications, AIAA 99-2976, 35th AIAA/ASME/SAE/ASEE Joint Propulsion Conference, June 1999.
17. Gavitt, K. and Mueller, T., TRW LCPE 650 Klbf LOX/LH2 Test Results, AIAA 2000-3853, 36th AIAA/ASME/SAE/ASEE Joint Propulsion Conference, July 2000.
18. Klem, M.D. and Stoddard, F.J., Results of 178 kN (40,00 lbf) Thrust LOX/LH2 Pintle Injector Engine Tests, JANNAF CS/PSH/EPTS/SPIRITS Joint Meeting, Huntsville, October 1995.
19. Klem, M.D., Jankovsky, A.L., and Stoddard, F.J., Results of LOX/RP-1 Pintle Injector Engine Tests, JANNAF CS/PSH/EPTS/SPIRITS Joint Meeting, Huntsville, October 1995.
20. Mueller, T. and Dressler, G., TRW 40 KLBf LOX/RP-1 Low Cost Pintle Engine Test Results, AIAA 2000-3863, 36th AIAA/ASME/SAE/ASEE Joint Propulsion Conference and Exhibit, Huntsville, July 2000.
21. Kim, P.Y., Majmaki, A., Papesh, C., Schneider, D., Thompson, M., and Weinstock, V.D., Design and Development Testing of TR108 – a 30Klbf Thrust-Class Hydrogen Peroxide/Hydrocarbon Pump-Fed Engine, AIAA 2005-3566, 41st AIAA Joint Propulsion Conference, Tuscon, 2005.

Chapter 29
Atomization of a Liquid Jet in a Crossflow

A. Mashayek and N. Ashgriz

Abstract This chapter provides a review on the penetration and atomization of liquid jets in subsonic crossflows (LJICF). More emphasis is put on the basic physics of the problem while a general overview of different types of research on the subject is presented. The categorization is based on the physics of the problem rather than the type of the studies (numerical, theoretical, or experimental) to help better understanding of the involving physics.

Keywords Jet in crossflow · Jet drag coefficient · Jet penetration · Jet trajectory · Shear stripping model

Introduction

Injection of liquid jets normal to a high-velocity and high-temperature cross streams at elevated pressures has various applications in fuel injection systems and advanced aircraft engines, such as gas turbines, afterburners, augmenters, and ramjet–scramjet combustors. This type of radial fuel injection into a crossflow improves fuel atomization and vaporization characteristics and is commonly used in turbojet augmenter sections and rich, burn-quick, quench-lean burn, lean premixed prevaporized, and ramjet and scramjet combustion systems. To date, several analytical, experimental, and numerical studies have investigated various characteristics of the liquid jet in crossflow (LJICF) atomization. Each of the experimental works has focused on a specific range of flow parameters. Several correlations have been developed based on the experimental data to predict various features of the LJICF atomization.

The very complex physics involved in the problem makes its three-dimensional (3D) numerical simulations quite expensive. Among the physical complexities involved are the strong vortical structures, small-scale wave formation, stripping of

A. Mashayek (✉)
Department of Physics, University of Toronto, Canada

N. Ashgriz (ed.), *Handbook of Atomization and Sprays*,
DOI 10.1007/978-1-4419-7264-4_29, © Springer Science+Business Media, LLC 2011

small droplets from the jet surface, and formation of ligaments and droplets with a wide range of sizes. Various types of studies have been applied to better understand the problem and to provide tools to enable predictions of various atomization characteristics for practical applications. Theoretical studies have been mainly used to obtain basic information on the deformation of the jet and the path it takes in the gas stream before it is disintegrated into smaller particles. Experimental studies have been used to obtain information on the jet path and also on the breakup processes involved in the problem. A large group of the experimental works has focused on bulk characteristics of the jet and its resulting spray plume such as the penetration and width of the jet. Some other experiments have focused on the various breakup processes involved. As the breakup processes often involve very small-scale motions and complicated interfacial physics that can be hard to visualize in experiments, 3D simulations have started to provide important information as they become stronger to tackle this problem. This chapter presents a general overview of the LJICF. We start by a general overview of the atomization processes followed by some introduction into the basic physics involved and the governing parameters.

A General Overview

In the simplest form of the liquid jet in crossflow injection, a single liquid jet is injected perpendicular to a uniform incoming gas flow as shown in Fig. 29.1a. Cross-stream aerodynamic forces deflect the jet in the cross-gas-streamwise direction (y-direction). The extent of the deflection is a function of the relative momentum of the air to that of the jet. Also due to the aerodynamic force acting on the jet, its cross-sectional shape deforms and changes from a round circular shape to an elongated sheet-like shape. The extent of the spreading of the jet into a sheet is governed by the relative strength of the gas flow to that of the jet. For a relatively weak gas flow, the jet's cross section exhibits oscillations as instabilities grow on the jet and lead to its breakup at some downstream location x_b as shown in the figure.

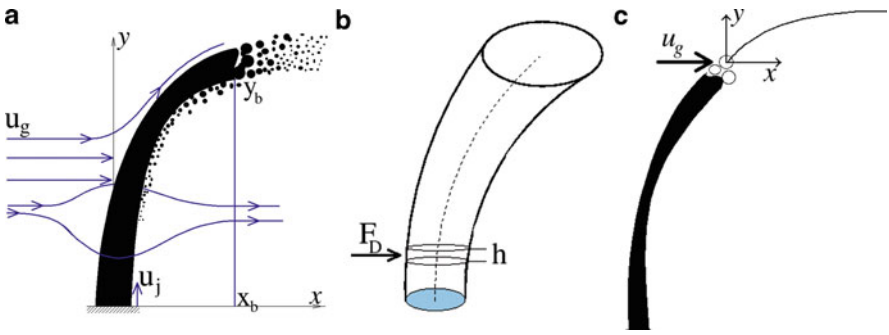


Fig. 29.1 (**a**) A schematic view of a liquid jet injected perpendicular to a uniform incoming gas stream; (**b**) a sample cross-sectional element; (**c**) schematic trajectory of the droplets formed at the CBL

This breakup mechanism is similar to that of a jet breakup in still gases. In the presence of a relatively strong crossflow, however, additional instabilities and waves form on the surface of the jet. These instabilities grow larger as the jet deflects and deforms and contribute to the final jet breakup at x_b. We refer to x_b as the "column breakup location" (CBL). At this location, the jet disintegrates into a number of relatively large droplets, which themselves undergo secondary breakup processes and become smaller as a part of the atomization process.

Along the path from the nozzle to the CLB, liquid droplets and ligaments can be pulled off the jet by the surrounding gas flow provided that the local velocity of the gas relative to the liquid phase is large enough. These liquid particles shed from the jet can themselves undergo secondary breakup. The sum of these particles and those formed at the CLB form a spray plume. In fact, the benefit of the LJICF atomization is that it provides a long jet normal to the gas flow. The gas flow deforms the jet into a sheet and breaks it down into small droplets very quickly. As mentioned at the outset, this scenario is the simplest possible. One can enhance the atomization by injecting air from the periphery of the jet in the same direction as the jet and make an air-blast jet in crossflow injection. The angle of the injection can also play a significant role in the atomization. In real applications such as gas turbines and aircraft augmenters, multiple jet configurations are also commonly used. Another possibility is to impinge jets onto each other to leverage the impact effect and produce smaller droplets faster. In this chapter, however, we remain focused on the configuration shown in Fig. 29.1 to learn about the basics and leave the complexities out.

As the above discussion suggests, one of the main characteristics of the LJICF is the extent to which the jet can penetrate into the gas flow. This penetration depth is an important parameter for design purposes as it imposes size restrictions for the injection chamber. A longer penetration depth also provides a longer jet for the gas flow to pull particles off and thus plays an important role in the droplet size distribution downstream of the nozzle. The nature of particle separation at the surface of the jet and the droplet breakup at the CLB are among the other important features of this problem which need to be characterized in detail. The flow structures formed in the lee-side of the jet play an important role in the advection and secondary breakup of the produced droplets and so knowledge of the details of the gas flow around the jet is another important feature of this problem. Once these features of the LJICF are characterized, one can focus on the secondary interactions and breakup of the droplets downstream of the nozzle to find a size distribution necessary for combustion purposes.

Basic Physics

Our main interest is to know how various LJICF characteristics such as jet trajectory and droplet size depend on basic fluid and geometric variables. As is the norm in many physical problems, it is useful to express the dependence in the form of nondimensional groups.

The first step in doing so is to determine the basic important variables. They can be divided into three categories. The first group contains the liquid-related parameters and includes the jet velocity, u_j, liquid density, ρ_j, liquid surface tension, σ, and liquid dynamic viscosity, μ_j. The second group contains the gas phase parameters and includes ρ_g, u_g, μ_g, which are the gas density, velocity, and viscosity, respectively. And finally, the third group contains the geometrical parameters; for a single jet injected perpendicular to the gas phase, the only parameter of this type is the nozzle diameter, d.

Although this list of variables is not inclusive by any means, it is adequate to help understanding the basic physics of the problem as we will show in the subsequent sections. For an angled injection, one could add another parameter to include the effect of the tilt of the nozzle. Using the Buckingham π theorem, we can form four nondimensional groups of parameters out of the mentioned seven parameters. So, a particular characteristic of the LJICF (such as the jet trajectory or droplet size distribution) can be written in the form

$$C = f\left(\frac{\rho_j}{\rho_g}, \frac{u_j}{u_g}, \frac{\rho_g u_g^2 d}{\sigma}, \frac{\rho_g u_g d}{\mu_j}\right). \tag{29.1}$$

Since we are allowed to multiply any two of the above nondimensional groups, we can reorder the above relation and write

$$C = f(q,\ We_g,\ Re_j) \tag{29.2}$$

where $q = \left(\rho_j u_j^2\right)/\left(\rho_g u_g^2\right)$ is the ratio of the liquid momentum to the gas phase momemtum, $We_g = \left(\rho_g u_g^2 d\right)/\sigma$ is the gas Weber number defined based on the nozzle diameter and liquid phase surface tension, and $Re_j = \rho_j u_j d/\mu_j$ is the jet Reynolds number. It is important to note that these choices are not unique. For example, multiplying the last term in (29.1) by μ_j/μ_g would lead to the gas phase Reynolds number (based on the nozzle diameter) instead of the jet Reynolds number. Nevertheless, the three parameters q, We_g and Re_j, have been used extensively in the LJICF literature for various parameterizations. The momentum flux ratio expresses the ratio of the momentum inflow of the jet to that of the gas. So, one expects the jet to bend less and penetrate more for a large value of q and to bend faster by the gas for smaller values of q. As we will see, this parameter is the key parameter in parameterization of the jet trajectory. The Weber number is a measure of the relative importance of the gas inertia compared to the liquid surface tension. So, it plays a primary role when it comes to studying sizes of the ligaments and droplets that form by different breakup mechanisms. The effect of the Weber number on the jet trajectory is, however, secondary and becomes more important when high-pressure flows or various injection fuels are considered. The Reynolds number also plays an important role in characterization of the droplet sizes and velocities as it determines the turbulence level in the jet and the scales of the secondary instabilities. A detailed study of the breakup processes should additionally take

the turbulence level of the system into account by introducing proper turbulent length scales and intensities. It should be noted that two turbulence regimes are present in the problem: one corresponding to the jet and one to the gas flow. As most LJICF studies up to date have been performed for nearly uniform gas flows with low turbulence intensities, the jet Reynolds number has been mostly used as a key parameter in atomization studies dealing with droplet sizes, their velocities, and breakup locations.

Jet Trajectory and Deformation

As mentioned earlier the trajectory of the liquid jet before and after the CBL is of importance for design purposes. As we will see, it is also a critical piece of information needed by some empirical-numerical models to simulate the atomization process. A considerable number of research studies have been merely focused on measurements and predictions of the jet trajectory and its variation with change in different parameters such as the pressure and the temperature. To develop a simple model for predicting the jet trajectory, we can think of the jet as a stack of thin cylindrical elements piled on top of each other to form a jet. One such element with infinitesimal thickness h is shown in Fig. 29.1b. Then, one can treat the motion of the element like that of a projectile moving up with initial y-direction velocity u_j and zero x-direction velocity. In the simplest approximation, the only force acting on the element is the aerodynamic drag force

$$F_D = \frac{1}{2}\rho_g u_g^2 A_F C_d, \tag{29.3}$$

where A_F is the frontal area of the element and is equal to $d \times h$ and C_d is the drag coefficient. Setting the drag force to the mass of the element times its acceleration we get

$$\frac{1}{2}\rho_g u_g^2 A_F C_d = \rho_j A_c h \frac{d^2x}{dt^2}, \tag{29.4}$$

where A_c is the cross-sectional area of the element equal to $\pi d^2/4$. Substituting for A_F and A_c and integrating (29.4) twice we get

$$\frac{x}{d} = \frac{1}{\pi} C_d \frac{\rho_g}{\rho_j} u_g^2 \frac{t^2}{d^2}, \tag{29.5}$$

where we have assumed that the element does not have any x-direction velocity as it exits the nozzle. Substituting for t from $y = u_j t$ we get

$$\frac{x}{d} = \frac{1}{\pi} C_d \frac{\rho_g}{\rho_j} \left(\frac{u_g}{u_j}\right)^2 \left(\frac{y}{d}\right)^2. \tag{29.6}$$

Rearranging (29.6) we get

$$\left(\frac{y}{d}\right) = \sqrt{\frac{\pi}{C_\mathrm{d}} q \left(\frac{x}{d}\right)}. \tag{29.7}$$

So, as expected from our dimensional analysis, the momentum ratio plays the key role in determining the trajectory of the jet. Several approximations have been used in obtaining (29.7). The first and most important one is neglecting the deformation of the element and assuming that it remains circular throughout its path from the nozzle to the CBL. Second, any mass stripping from the element during its path is neglected. Finally, viscous forces acting between the elements are also neglected. Any of these three assumptions (specially the first two) can play an important role in the jet trajectory. As we will shortly show, one can take these issues into consideration and develop a better model for predicting the jet trajectory. At this point, it is important to make a distinction between the two terms "jet trajectory" and "penetration." The former usually refers to the trajectory of the jet up to the CBL whereas the latter sometimes refers to the maximum penetration of the spray into the gas stream. In other words, the latter refers to the upper boundary of the spray plume when viewed from the side. Spray penetration is of more interest as it is the representative of the y-direction extent of the spray. Numerous experiments have been done and various correlations have been offered for the spray penetration for downstream distances of up to few hundreds of the nozzle diameter whereas empirical relations for the jet trajectory are only valid for downstream distances of up to few nozzle diameters (the CLB location). Nevertheless, for both groups, the correlations are mostly in the form of

$$\left(\frac{y}{d}\right) = C q^{\alpha} \left(\frac{x}{d}\right)^{\beta}, \tag{29.8}$$

where $C,\ \alpha,\ \beta$ are constants. Some studies have included the Weber number in their correlation to capture the effect of the change in the gas pressure (or air density) however, the dependence is not pronounced and the momentum ratio is the key parameter. It should also be noted that what is often meant by the jet trajectory is the upper boundary of the jet, whereas (29.7) was derived for the centerline (or core) of the jet. For parameter ranges corresponding to practical applications, the centerline and the upper boundary are very close as the jet deforms into a sheet-like shape.

Wu et al. [1] performed an experimental study on various characteristics of the LJICF and offered the following relation for the jet trajectory for ($4 < q < 148$):

$$\left(\frac{y}{d}\right) = 1.37 \sqrt{q \left(\frac{x}{d}\right)}. \tag{29.9}$$

Comparing (29.9) with (29.7), we find a value of $C_\mathrm{d} = 1.67$ for the average drag coefficient of a nonturbulent jet. As we will show, this value can also be justified by means of numerical simulations. However, some other studies have proposed larger

empirical values for the drag coefficient of nonturbulent jets. The drag coefficient can also vary for turbulent jets as the surface smoothness of the jet decreases with an increase in Re_j.

One can also find a functional form for the trajectory of the large droplets that are formed at the CBL. The path of these droplets represents the maximum spray penetration. Since they are not connected to the jet and are in direct contact with a strong gas flow, they do not necessarily follow a path of the form of (29.9) anymore. A schematic view of the trajectory of these drops is shown in Fig. 29.1c with a local coordinate system attached to the CBL for convenience. In general most applications of LJICF are concerned with high momentum ratios for which the jet deflection is not pronounced. For those cases, it is fair to assume that the droplets formed at the CBL have a zero initial velocity in the x-direction as they separate from the jet and have an initial upward velocity of u_j. As these droplets leave the jet, they lose their vertical velocity and speed up in the gas-streamwise direction and finally reach their terminal x-direction velocity. Of course, all these are true for one droplet without considering its interaction with other droplets and also with neglecting the effects of evaporation. With these assumptions, the equations governing the motion of the drop take the form

$$m\frac{\mathrm{d}^2x}{\mathrm{d}t^2} = A\rho_g\left(u_g - \frac{\mathrm{d}x}{\mathrm{d}t}\right)^2 C_{dx}, \tag{29.10}$$

$$m\frac{\mathrm{d}^2y}{\mathrm{d}t^2} = -A\rho_g\left(\frac{\mathrm{d}y}{\mathrm{d}t}\right)^2 C_{dy}, \tag{29.11}$$

where m is the mass of the droplet equal to $\rho_j(4/3)\pi r^3$, A is the frontal area of the drop equal to πr^2, and C_{dx} and C_{dy} are the corresponding drag coefficients in the x- and y-directions and are not necessarily the same. Solving (29.11) subject to the initial conditions of $y = 0$ at $t = 0$ and $(\mathrm{d}y/\mathrm{d}t) = u_j$ at $t = 0$ we get

$$y = \frac{1}{k_1}\ln\left(1 + k_1u_jt\right), \tag{29.12}$$

and solving (29.10) subject to initial conditions of $(\mathrm{d}x/\mathrm{d}t) = x = 0$ at $t = 0$ gives

$$x = k_2u_gt + \ln\left(1 - u_gk_2t\right), \tag{29.13}$$

where $k_1 = \left(A\rho_gC_{dy}\right)/m$ and $k_2 = \left(A\rho_gC_{dx}\right)/m$. As the gas velocity u_g is usually very large, the droplet moves from the CBL to its terminal state in a fraction of a second and so t can be considered to be much smaller than unity. Also, k_2 is a very small number as $\rho_g \sim 1$, $C_{dx} \sim 1$, and $A \sim r^3$ with r having typical values of less than 1 mm. So, the second term in the argument of the natural logarithm in (29.13) is much smaller than 1 and so the first term in (29.13) is dominant and we can say

$$x \sim k_2 u_g t. \tag{29.14}$$

Substituting (29.14) into (29.12) we get

$$y = \frac{1}{k_1} \ln\left(1 + \frac{k_1}{k_2}\frac{u_j}{u_g} x\right). \tag{29.15}$$

Noting that $k_1/k_2 = C_{dy}/C_{dx}$ and also noting that the droplet drag coefficients in the y- and x-directions are functions of the corresponding Reynolds numbers (defined based on y- and x-direction velocities, droplet diameter, and its kinematic viscosity), we can write

$$\frac{k_1}{k_2} \propto \frac{C_{dy}}{C_{dx}} \propto \frac{Re_x}{Re_y} \propto \frac{u_g}{u_j} \tag{29.16}$$

and so the $k_1 u_j / k_2 u_g$ coefficient in the second term in the argument of the natural logarithm in (29.15) is on the order of unity. It should also be noted that $1/k_1$ is proportional to $C_{dy}\rho_g/\rho_j$, where C_{dy} is in general a function of both u_j, which is the droplet's initial vertical velocity relative to the gas, and u_g, which is the initial x-direction velocity of the droplet relative to the incoming gas flow. So, $1/k_1$ can be expected to be a function of the momentum ratio, q. Thus, the general functional form of the droplet path upon its separation at the CBL (or spray penetration in other words) can be written in the form of

$$y = Cq^{\alpha} \ln(1 + \beta x), \tag{29.17}$$

where β is expected to be on the order of unity according to the above analysis. Although not all experimental studies have used a logarithmic functional form to fit their data for spray penetration, some have and we can compare their results to (29.17). Inamura et al. [2], Lakhamraju and Jeng [3], and Becker and Hassa [4] all presented expressions of the form of (29.17) for spray penetration with $\beta \sim 1$ even though their experiments were done for different flow parameters. The parameter α was reported to be around 0.3–0.5 in the three mentioned studies. Other studies have used other functional forms for the spray penetration.

Wu et al. [5] extended Wu et al. [1] by studying various characteristics of the spray plume and proposed the following relation for the maximum spray penetration:

$$\left(\frac{y}{d}\right) = 4.3 q^{0.33} \left(\frac{x}{d}\right)^{0.33}. \tag{29.18}$$

Although various correlations offered for the spray penetration have used different functional dependence on x/d, most agree on a power of around 0.3–0.5 for q. This smaller power (compared to that of q in (29.7) for jet trajectory) is reasonable because the droplets forming the upper boundary of the spray plume are mainly

those produced at the CBL due to the disintegration of the jet and so they lose their initial vertical velocity (which is close to u_j) quickly due to direct contact with the gas stream. Their motion is more a function of the interplay between their momentum and the gas momentum rather than the jet/air momentum ratio, q.

Mashayek et al. [6] presented a review of some of the correlations offered for jet trajectory and spray penetration and their applicable parameter ranges. The correlations are usually obtained by tracking the upper boundary of the spray plume. Various experimental methods can be used to do so, with the most common one being the time-averaged shadowgraph technique. Point particle measurement techniques have also been used to detect the highest point that the droplets can penetrate, and hence, a penetration curve can be obtained. Pulse laser imaging is another useful tool for this purpose. In this technique, one can capture consequent frames of a spray using pulse lasers (as is done for particle image velocimetry (PIV) measurements) and fit a curve to the upper boundary of the spray in each frame. An average of all the curves obtained for all the frames can be counted as a representative penetration curve for that case (Mashayek et al. [7]). Another high-quality imaging technique that has proved to be useful for both jet trajectory and spray penetration is time-gated ballistic imaging, which can also provide high–spatial resolution images of the atomization process as shown by Linne et al. [14]. All the mentioned techniques have different capabilities in detecting the droplets that penetrate the most into the gas stream. Thus, the difference between the measurement techniques is one of the main contributors to the large discrepancies observed between the correlations offered for the spray penetration (see Mashayek et al. [6] for a discussion on the discrepancies). The main reason for the discrepancies is, however, the differences between the test conditions and parameter range for each experimental study. In fact, one has to only use each available correlation within the range of the parameters for which the correlation is designed. Even for the areas of the q regime where two correlations coincide, their predictions for the spray penetration can be different. This is due to the fact that the mere consideration of q is not adequate and several other factors such as the nozzle properties and the turbulence level of the incoming jet and gas flows can play important roles in the results. In particular, the ability of the gas stream in breaking up the jet into pieces through various surface breakup processes has to be taken into account. This factor is important as it changes the surface roughness and jet deformation, and hence, the drag coefficient. To include this effect, some studies have included the Weber number in the correlations by varying the gas properties in the experiments through changes in the pressure or temperature or both. The dependence on the Weber is not pronounced though, mainly due to the limited range of the parameters in the experiments. Performing tests at practical parameter ranges often means dealing with high values of q and We and at high temperatures and pressures. Achieving these conditions is usually limited by experimental constraints. However, as we will show next, simple theoretical models can be developed to help explore the parameter ranges which are hard to work at in a laboratory setting.

Before we move on to a more advanced model for predicting the jet trajectory, we should point out that the appendix contains a chart which includes a number of

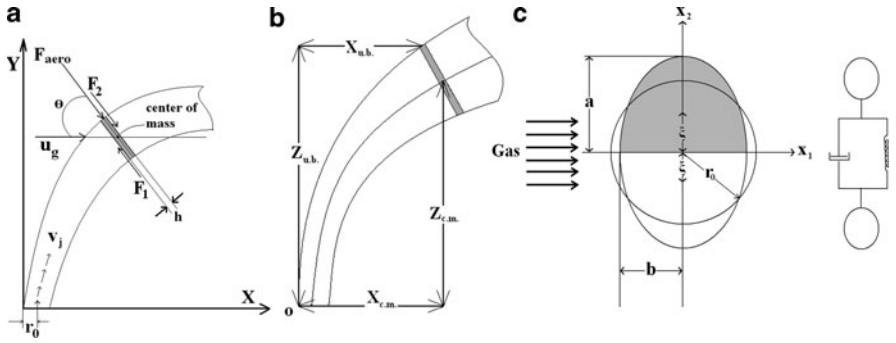


Fig. 29.2 (**a**) Schematic of the jet element movement along the trajectory with the direction of the forces and velocities involved; (**b**) coordinates of the upper boundary (shown by 'u.b.') and the center of the mass (shown by subscript 'c.m.') of the liquid element; (**c**) analogy between an oscillating 2D drop and a forced mass-spring system

empirical correlations from various experimental studies along with the experimental techniques used in obtaining the correlations.

One can take the simple theoretical force balance used to obtain (29.7) and with a few more steps obtain more insight into the effects of various parameters on the jet trajectory. To start, let us again assume a cylindrical element of infinitesimal thickness h from the liquid column as shown in Fig. 29.2a.

The cross-sectional area of the element is always normal to the trajectory of its center of mass. The initial radius of the cross-sectional area is denoted by r_0. As the element travels in the gas, it is deformed and spreads due to the aerodynamic force. The extent of its deformation is governed by the interplay between aerodynamic, surface tension, and viscous forces. For simplicity, let us assume that the jet cross section changes from a circle to an ellipse as shown in Fig. 29.2c. We will relax this assumption later to obtain a more realistic shape. The elliptic element's aspect ratio, e, defined as the ratio of the ellipse minor axis b to its major axis a, decreases with time until the element reaches the CBL.

Based on an analogy between the oscillations of a two-dimensional (2D) droplet and a mass spring system (similar to the Taylor analogy breakup (TAB) model), we assume that the deformation of our 2D liquid droplet is dependent on the viscous (F_v), surface tension (F_s), and inertial (F_a) forces. So, performing a force balance in the x_2-direction for the half element (shaded) in Fig. 29.2c, we can write

$$F_\mathrm{a} + F_\mathrm{v} + F_\mathrm{s} = m\frac{\mathrm{d}^2\xi}{\mathrm{d}t^2}, \tag{29.19}$$

where m is the mass of the half element and ξ is the distance between the center of the element and the center of the mass in either of the halves of the element as shown in Fig. 29.2c. So, ξ should not be mistaken with the semi-major axis of the elongated element, a. Providing proper expressions for the three forces and introducing θ, the tilt angle of the element at each instant as shown in the figure, (29.19) becomes (see Mashayek et al. [6] for details)

$$c_1\left(\frac{\mathrm{d}^2\xi}{\mathrm{d}t^2}\right)+c_1\left(\frac{\mathrm{d}\xi}{\mathrm{d}t}\right)+c_3=c_4, \tag{29.20}$$

where

$$c_1=\frac{1}{2}\rho_\mathrm{j}\pi ab,\quad c_2=\left(\frac{2\pi\mu_\mathrm{j}ab}{\xi^2}\right),\quad c_3=\frac{3\sigma\pi}{8}\left[4\left(1-r^2a^{-2}\right)+\frac{c}{d}\right],$$
$$c_4=\frac{1}{2}\rho_\mathrm{g}b\left[u_\mathrm{g}\cos(\theta)\right]^2.$$

Equation (29.20) can help us to approximate the jet cross-sectional deformation as long as we project the gas flow onto the plane of the element to account for the aerodynamic force F_a properly. Next, we perform a force balance on the element in the y–x plane as shown in Fig. 29.2a. In the x-direction the force balance gives

$$m\frac{\mathrm{d}^2x}{\mathrm{d}t^2}=F_\mathrm{aero}\cos(\theta)-F_\mathrm{shear}\cos(\theta), \tag{29.21}$$

where F_aero is the aerodynamic force on the element and is equal to

$$F_\mathrm{aero}=\frac{1}{2}C_\mathrm{d}\rho_\mathrm{g}u_\mathrm{rel}^2A=C_\mathrm{d}ah\rho_\mathrm{g}\left[u_\mathrm{g}\cos(\theta)\right]^2, \tag{29.22}$$

where $A=2ah$ has been used and u_rel is the velocity of the gas relative to the element and is very close to $u_\mathrm{g}\cos(\theta)$. F_shear is the resultant of the shear forces from the two neighboring elements shown in the figure and is equal to (F_1-F_2). Next we assume the jet velocity to be constant along its trajectory and equal to its initial velocity. Although this is not a particularly good assumption for small momentum ratios, it does not introduce a larger error for large enough values of q. So, for the center of mass of the element we can write

$$u_x=u_\mathrm{j}\sin(\theta),\quad u_y=u_\mathrm{j}\cos(\theta). \tag{29.23}$$

Combining (29.23) and (29.21) we can obtain an expression for the deflection angle of the jet in the form of

$$\frac{\mathrm{d}\theta}{\mathrm{d}t}=\frac{F_\mathrm{aero}-F_\mathrm{shear}}{\rho_\mathrm{j}\pi abhu_\mathrm{j}}, \tag{29.24}$$

and the shear force can be simply approximated by

$$F_\mathrm{shear}=\pi ab\mu_\mathrm{j}u_\mathrm{j}\kappa, \tag{29.25}$$

where κ is the local curvature of the jet. This simple approximation for the shear force does not play an important role, especially at larger momentum ratios where the jet deflection is not pronounced. Integrating (29.20), (29.23), and (29.24) simultaneously provides us with the trajectory of the center of mass of the element. Equation 29.20 provides the cross-sectional deformation, (29.24) provides the deflection angle and (29.23) provides the position of the center of mass. Before this integration is possible, however, two key pieces of information must be provided. First, the drag coefficient of the element cannot be considered a constant anymore as the droplet is deforming into an ellipse. Second, one has to somehow take the effect of mass stripping from the column into account. If we neglect the mass stripping and assume a nondeforming circular cross section with a constant drag coefficient, we will obtain results similar to (29.7) again.

Instead of choosing a constant value for the drag coefficient of the element, one can use results from numerical simulations of flows past a 2D circle or ellipse at various Reynolds numbers. Mashayek et al. [6] calculated the drag coefficient for flows passed ellipses with aspect ratios of 1 (circle), 0.5, and 0.25 (as shown in Fig. 29.3) using numerical simulations. The surfaces of the ellipses were assumed to be smooth in their study with the angle of attack being 90° for all cases.

They offered expressions for the drag coefficient versus the gas Reynolds number for each of the three aspect ratios (see chapter 5 for details). For $e < 0.25$, the ellipse becomes thin and close to a plate shape and one can assume a value of $C_d \sim 2$, which is a reasonable value for a flat plate over a wide range of Reynolds numbers. So, as the element is being deformed by the aerodynamic force in our model, its instantaneous Reynolds number (based on its semi-major axis) and the corresponding drag coefficient can be calculated by interpolating between the expressions offered for drag by Mashayek et al. [6]. As shown by their study,

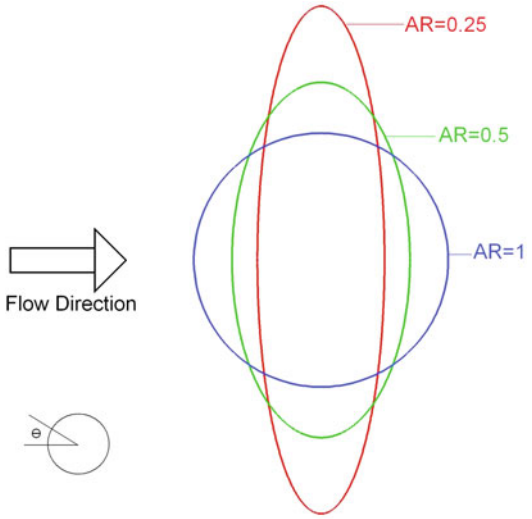


Fig. 29.3 Schematic diagram of the 2D ellipses with different aspect ratios

average values of $1.6<C_d<1.7$ were obtained which are very close to empirical values offered by Wu et al. [1].

With the drag coefficient specified, the only task left to do is to take the mass stripping into account. As we will see, this is important since for most cases the element loses a large portion of its initial mass by the time it reaches the CBL. We will discuss the rate at which mass leaves the liquid jet due to surface breakup mechanisms in the next section. For now, let us just assume that mass is lost from the liquid element at a rate of S. As we have already confined the deformation of the cross section to (unrealistic) elliptic shapes, the simplest approximation is to model the decrease in the mass of the element by scaling down its cross-sectional area, πab. To emphasize the importance of the stripping on the deflection of the jet, Fig. 29.4a shows the ratio of the mass lost from the element to the mass it initially possessed for two different cases. Clearly, up to 80% of the initial mass is lost on the way. If this loss is neglected in modeling, one can expect the jet deformation to be exaggerated. This leads to an unrealistically large value for the drag coefficient, and so, an overestimated jet deflection. To illustrate this, Fig. 29.4b shows isometric and side views of two jets with the same flow conditions as the top curve in panel (a), but for one jet with mass stripping and the other one without. The overpredicted cross-sectional deformation and the resulting fast deflection of the jet can be observed for the case with the mass stripping neglected.

Finally, with the drag coefficient defined and the mass stripping included, we can integrate (29.12), (29.15), and (29.16) simultaneously to obtain the trajectory of the center of mass of the element. We can apply the following transformations to transfer the coordinates from the center of mass of the element to the upper boundary of the liquid jet:

$$x_{ub} = r_0 + x_{cm} - b\cos(\theta), \quad y_{ub} = y_{cm} + b\sin(\theta), \tag{29.26}$$

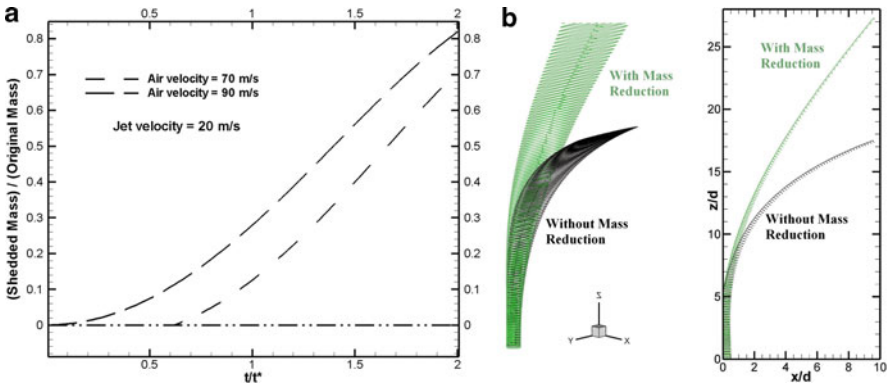


Fig. 29.4 (**a**) Ratio of the mass stripped from the elliptic element to its initial mass versus time; (**b**) deformation of the jet cross section with and without mass shedding for the case corresponding to the top curve of panel (**a**) (Pictures from Mashayek et al. [6]. Reprinted with permission of the American Institute of Aeronautics and Astronautics)

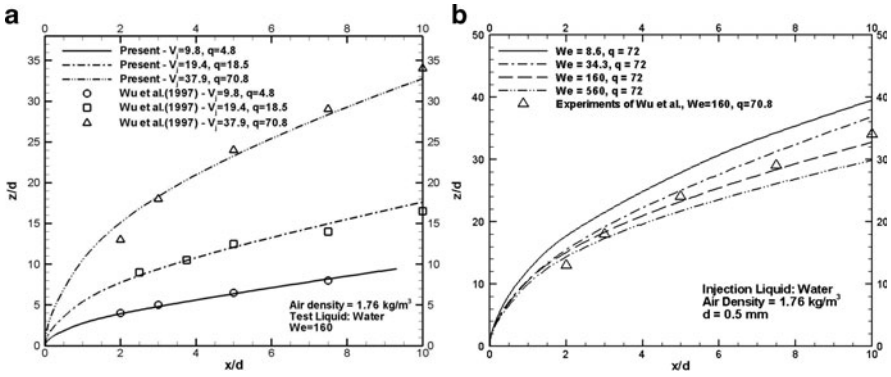


Fig. 29.5 (**a**) Calculated trajectories for various cases in comparison with the experiments of Wu et al. [1]; (**b**) effect of Weber number on the trajectory at a constant momentum ratio. The experimental data of Wu et al. [1] for $We = 160$ are plotted for comparison (Pictures from Mashayek et al. [6]. Reprinted with permission of the American Institute of Aeronautics and Astronautics)

where subscripts ub and cm correspond to "upper boundary" and "center of mass" respectively. Figure 29.5a plots the jet trajectories for three different cases and compares them with the experimental results of Wu et al. [1]. The good agreement between the results is owed greatly to the fact that the drag coefficient correlations used in the model give average drag coefficients close to the empirical value of Wu et al. [1]. As shown in the figure, the jet penetrates more into the gas as the ratio of the momentum of the jet to that of the gas increases. It should be noted that scales of the axes of the figure are not the same (for better illustration) and the actual jets have much smaller deflections than seen in the figure.

As discussed earlier, the momentum ratio is not the only important parameter in calculating the jet trajectory and the gas Weber number can also play a role. Figure 29.5b shows the variation in the jet trajectory as the Weber number increases at a constant liquid-to-gas momentum ratio. The Weber number is increased by increasing the gas velocity, and the jet velocity is also increased in such a way that the momentum ratio remains constant. This way of increasing the Weber number affects the jet trajectory in two ways. First, it changes the gas Reynolds number, and thus, the effective drag force on the jet. So, for a larger incoming gas velocity (larger We), the larger drag force leads to a larger jet deformation. The larger deformation means a larger drag force, and hence, a larger deflection. The second effect of increase in the gas velocity (while keeping q constant) is that it changes the rate of mass stripping from the liquid column. This is because the surface breakup mechanism owes its existence to the relative velocity of the gas to liquid (discussed in the next section). In general, a larger Weber number means more mass stripping from the liquid jet. This leads to less deformation of the cross-sectional area of the jet, and hence, less jet deflection. So, the two effects of increasing the Weber number at constant momentum ratio act in opposite ways. The first one tends to bend the jet more and the second one tends to bend it less. Figure 29.5b clearly

shows that the first effect is dominant and the jet penetrates less as the Weber number is increased. The Weber number changes from 8 to 560 in the figure. This wide range of Weber number at the relatively large momentum ratio of 72 is not easy to achieve in a lab experiment. In fact, most of the experiments are carried out for a much narrower range of the Weber number and the dependence of their resulting empirical correlations on the Weber number is not that pronounced. However, it should be noted that for Weber numbers of order of few hundred, the mass and ligament formation at the surface of the jet is so vigorous, and the jet deformation into a sheet is so intense and quick, that the basic assumptions of our model made in the formulations are violated. So, Fig. 29.5b should not be taken literally for very large Weber numbers.

The results of Fig. 29.5 are somewhat surprising in their agreement with the experiments considering the simplifications made in the model used to obtain them. One key simplification was to perform a force balance on a 2D element rather than considering the jet as one single body. Experimental results of Mazallon et al. [15] and Sallam et al. [8] showed that the deformation of nonturbulent liquid jets in uniform crossflows is almost independent of liquid jet velocities, implying a little interaction between the various cross-sectional planes of the liquid jet. This explains why various models such as those presented above have had some success with predicting some properties of the LJICF. Based on this fact, several studies have been devoted to investigating the deformation and breakup properties of the jet cross section using 2D numerical simulations such as Aalberg et al. [16]. Aalberg et al. performed a computational study by taking the liquid column behavior to be equivalent to the temporal behavior of an initially motionless circular 2D droplet subjected to a step increase in the ambient crossflow velocity. They also assumed that the liquid jet velocity remains constant at its initial value, u_j, up to the CBL. Similar types of calculations can be coupled with a model such as that presented above to provide a more realistic shape of the jet. Although the simple elliptic cross sections used in our model are capable of producing satisfactory results for the penetration, they are not useful when the focus is on the deformation and mass stripping from the column. The coupled theoretical-numerical models (with 2D simulations used for the cross-sectional deformation) can on the other hand provide useful information on jet deformation and the mass striping from the tips of the deformed jet's cross section.

Figure 29.6 shows an example of one of the 2D droplet deformation studies carried out specifically for the purpose of modeling the LJICF by Sarchami et al. [9]. The flow conditions for this case are more extreme than can be handled by the theoretical methods for droplet deformation. As the figure shows, not only can these types of results be used to obtain information about jet deformation and trajectory, but they also provide an estimate for the size of the droplets and ligaments that form due to shear breakup at the tips of the elongated cross section. They also show the pattern of the flow field around the droplet. Of particular interest are the double vortices that form behind the droplet and help stretching it out and into a thin shape. The formation of these vortices can play an important role in the secondary atomization processes of the droplets formed in the lee-side of the jet (2D drop).

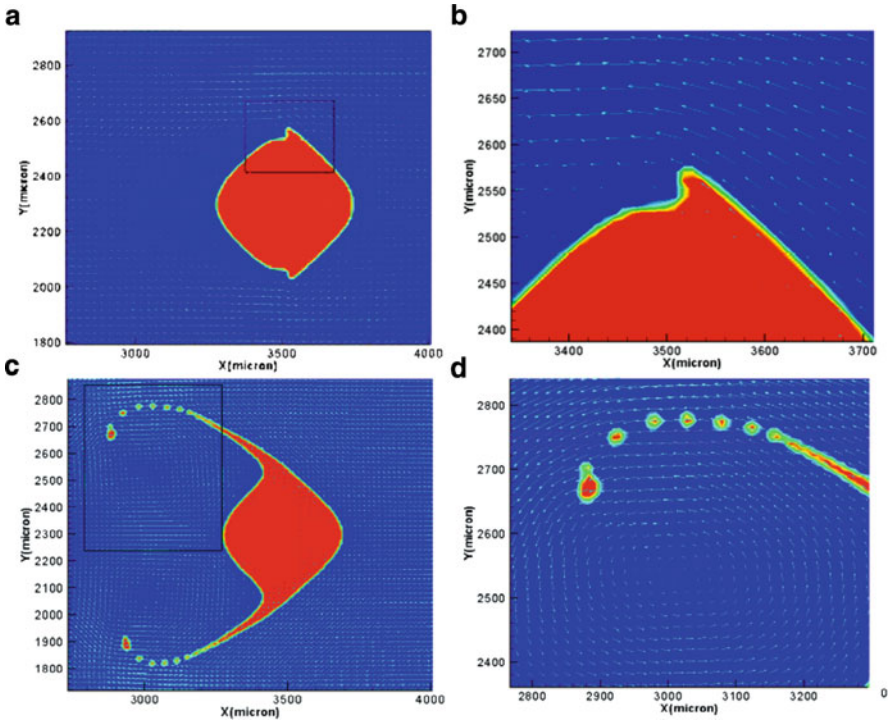


Fig. 29.6 (**a**, **b**) Initial period of the droplet deformation for $d = 0.46$ (mm), $u_g = 47$ (m/s), $\rho_g = 2.4$ (kg/m^3); (**c**, **d**) further deformation of the cross section and droplet breakup off the tip of the stretched drop. Note that the gas flow is from right to left. From Sarchami et al. [9]. Reprinted with permission

Although these 2D methods are useful, one has to note that they are still very crude approximations to the real 3D problem. For example, 2D simulations used to model the jet cross-sectional deformation can predict a size for the droplets being pinched off from the tips of the elongated and deformed cross section. Whether these separated 2D droplets correspond to drops or ligaments in the real world cannot be verified yet. However, as we will discuss, the full 3D simulations of LJICF in real conditions is still computationally very costly and theoretical or hybrid (theoretical-numerical) models can be useful. Even performing 2D numerical simulations for parameter regimes corresponding to most real applications (such as large density ratios and Reynolds numbers) is still relatively costly. Mashayek and Ashgriz [10] applied an analytical-numerical model to calculate the deformation and spreading of 2D liquid drops in a gas stream for large Reynolds numbers. Their model predicted the spreading of the cross section of liquid jets in crossflows without considering mass stripping from the jet. The penetration of the liquid jet in the gas flow was calculated using the methods already discussed in this chapter.

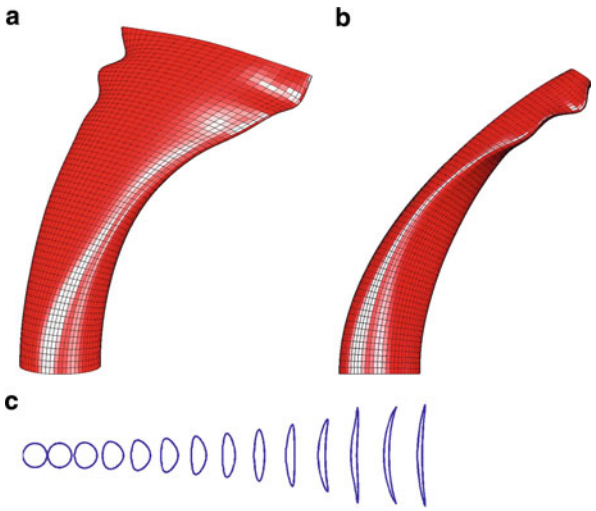


Fig. 29.7 Deformation of a water liquid jet in air stream at $We = 35$. (**a**) Side view; (**b**) 35° view; (**c**) evolution of the jet's cross section from the nozzle to the CBL (From Mashayek and Ashgriz [10]. Reprinted with permission of the American Institute of Aeronautics and Astronautics)

Figure 29.7 shows the deformation of a liquid jet from Mashayek and Ashgriz [10]. The deformation of the cross section is calculated using a 2D-drop model. The jet shape is then constructed from the 2D cross sections by mapping the cross sections onto an independently calculated jet trajectory. As we know, a 2D droplet undergoes small-amplitude oscillations at low Weber numbers. However, for large Weber numbers, the deformation is not reversible and the drop undergoes an irreversible spreading. Since the Weber number of the case shown in Fig. 29.7 is 35, there is no bounce back in the motion of the liquid column's cross section. To understand the reason behind the curly shape observed on the edge of the flattened jet, Fig. 29.7c shows the deformation of the jet cross section over time. The back-and-forth movement of the tip of the cross section leads to the wavelike shape formed on the jet surface. The surface pattern in panel (c) somehow mimics the wave patterns observed on the jet surface by experiments and 3D numerical simulations as will be seen in the next sections. It should be noted that the deformation shown in Fig. 29.7 was obtained without considering the amount of mass lost from the jet due to mass stripping. As was done in the elliptic cross-section model, it would be easy to reduce the mass from the jet cross section by scaling down the cross-sectional area. In Fig. 29.7, there was no bounce back to circular shape for the cross section. For smaller Weber numbers where the mass stripping is negligible or absent, one can expect the cross section to undergo oscillations. To show this, Fig. 29.8 compares the deformation and penetration of two liquid jets with momentum ratios of 9.54 and 1.94 with results of Madabhushi et al. [11]. The Weber numbers of the cases in the figure are small and no mass is shed from the liquid column. The side views show the oscillatory motion of the jet cross sections for the two cases. Although one cannot expect to capture all 3D characteristics of

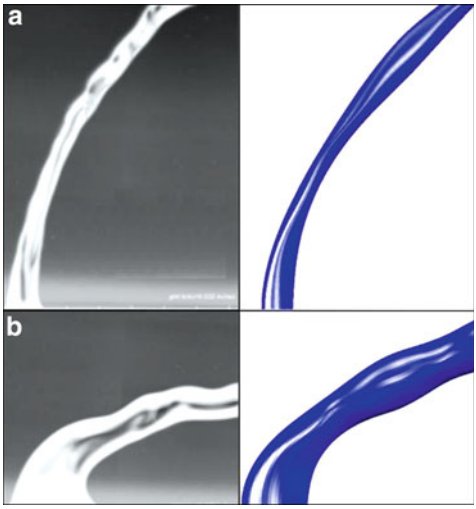


Fig. 29.8 Calculations from Mashayek and Ashgriz [10] (*right*) and the experiments of Madhabushi et al. [11]. Reprinted by permission. (**a**) $q = 9.54$, $Re_l = 1007$; (**b**) $q = 1.94$, $Re_l = 454$

the deformation of the liquid jet using the 2D mapping system of the present model, the resemblance of the calculated jet shapes to the experimental figures supports the similarities between the deformation and oscillation characteristics of liquid drops and jets in crossflows reported previously by various authors. However, it is important to note that these types of models are incapable of resolving the complicated physical aspects of the jet deformation such as the small-scale motions and droplet and ligament breakups. Results of 2D simulations such as those of Fig. 29.6 are of more value in those respects.

The more extreme the flow conditions, the less capable theoretical models of these types become in capturing the details of the flow structures, and one has to rely on numerical simulations. However, theoretical models can be applied beforehand for parametric studies and help deciding the range of parameters over which experimental or numerical studies are to be performed.

Breakup Mechanisms

The breakup processes involved in the LJICF problem can be divided into three main categories of primary breakup, column breakup, and secondary breakup. The primary breakup in general refers to the separation of ligaments and droplets from the surface of the liquid jet. The column breakup refers to the disintegration of the liquid column as a whole at the CBL. The secondary breakup refers to the secondary breakup processes that the separated particles undergo after they are detached from the main jet body. To understand the mechanisms responsible for the primary breakup of particles from the jet, one has to separate those related to the incoming

gas flow from those due to the jet's internal vorticity and turbulence. Sallam et al. [8] (hereafter referred to as SA04) studied the primary breakup (among other processes) at the surface of nonturbulent jets in subsonic crossflows. Their parameters were in a range where liquid viscosity did not play a great role in the jet characteristics (small Ohsenorge number). Special care was taken in their study to achieve a nonturbulent jet even at high Reynolds number. This way they ensured that the primary breakup processes they observed were merely due to the interaction of the gas flow and the liquid column. Figure 29.9a shows such a smooth jet without a crossflow for a jet Reynolds number of 3×10^4.

Figure 29.9b shows a case where the jet of panel (a) is exposed to a crossflow with a small Weber number of 8. As explained earlier, for small Weber numbers, the jet's cross section deforms into an ellipsoidal cross section, and gets deflected in the direction of the crossflow velocity due to the aerodynamic force. The interplay between the aerodynamic force and the liquid surface tension governs the deformation of the liquid jet. We observed that the deformation of the cross section is somewhat analogous to the behavior of individual drops when subjected to shock wave disturbances. So, the jet cross section can undergo oscillations for small Weber numbers and that is what happens as the liquid jet exits the nozzle in Fig. 29.9b. During each oscillation period the jet's cross section reaches a maximum deformed (flattened) shape, and so gets deflected more before it bounces back. As the jet reaches higher elevations, the flattening of the jet in each oscillation becomes larger. Once the liquid is flat enough for the stagnation pressure behind it to overcome its resistance (surface tension), baglike structures form as shown in the upper parts of the jet in panel (b). This phenomenon is quite similar to the baglike structures appearing at the center of the deformed drops in the bag breakup regime observed during the secondary breakup of drops subjected to shock wave disturbances. So, the breakup mechanism in Fig. 29.9b is often referred to as bag breakup mode. The sizes of the bags formed grow as the jet moves in the positive y-direction and droplets and ligaments get stripped off their edges. Once the bags are large

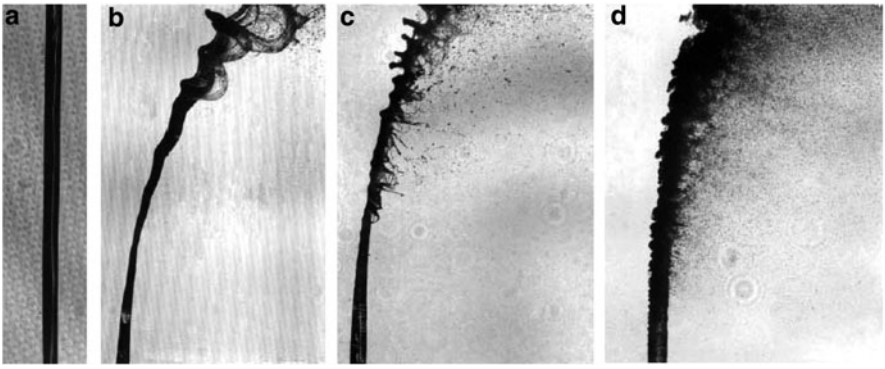


Fig. 29.9 Primary breakup processes of round nonturbulent liquid jets in gaseous crossflow: (**a**) $We = 0$, (**b**) $We = 8$, (**c**) $We = 30$, (**d**) $We = 220$. From Sallam et al. [8]. Reprinted with permission of the American Institute of Aeronautics and Astronautics

enough, they start to break down into ligaments and droplets through the same mechanisms as those in bag breakup of drops undergoing secondary breakup due to shockwave disturbances. The breaking up of the bags marks the disintegration of the liquid jet at the CBL. This sequence of events leads to a range of drop sizes along the liquid jet. The smallest drops are formed by breakup of the bag appearing first. Breakup of the liquid columns which connect the bags leads to larger drops and the largest drops are associated with the jet breakup as a whole at the CBL.

Skipping panel (c) of Fig. 29.9 for the moment and focusing on panel (d), the breakup regime is the so-called shear breakup regime. This regime is the dominant regime at high Weber numbers (roughly $We > 100$). In shear breakup, unlike the bag breakup, the main body of the jet is not distorted much and smaller-scale waves with wavelengths of $\lambda/d_j \sim 0.1$ are observed on the surface, which is much smaller than the wavelengths of the waves observed for the bag breakup mode ($\lambda/d_j \sim 1$). The surface disturbances grow into ligaments that form along the periphery of the liquid jet and separate from its downstream side. A close-up of a formation of such a ligament is shown in Fig. 29.10a from 3D numerical simulations of Herrmann [12]. Figure 29.10b also shows a schematic top view of the cross section of the deformed jet at a location where a ligament is forming. These ligaments themselves break into droplets through Rayleigh breakup mechanism and the resulting droplets have sizes approximately the same as the diameter of the parent ligaments. The wavelength of the surface disturbances grows larger as they move further up (away from the nozzle) on the jet surface and hence, the size of the resulting ligaments and droplets increase from the nozzle toward the CBL. In fact, it is very hard for droplets and ligaments to form very close to the nozzle due to the small amplitude of the disturbances. Thus, there is a particular y-location at which stripping starts along the jet trajectory for shear breakup regimes. The location of this point of onset of

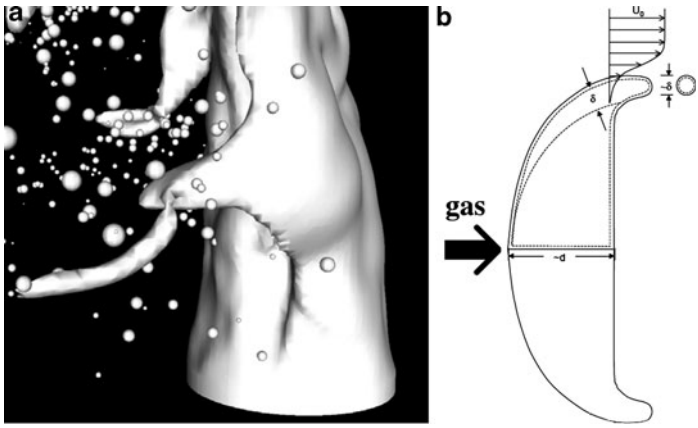


Fig. 29.10 (**a**) Formation of drops from ligaments formed on the downstream side of the jet in the shear breakup regime; (**b**) schematic top view of the cross section of a nonturbulent jet at which a droplet (or ligament) is being formed similar to panel (**a**) (**a**: From Herrmann [12]. Reprinted with permission, Copyright (2010) ASME)

primary breakup is itself a function of the Weber number and tends to zero as We becomes very large. SA04 assembled the results of their own experiments with previous works to conclude that the surface disturbance wavelength has a Weber dependence of

$$\lambda/d_{\mathrm{j}} \sim We^{-0.45}, \tag{29.27}$$

which corresponds to a value of ~1 for the bag breakup regime, ~0.1 for the shear breakup regime, and intermediate values for the multimode breakup regime. The multimode breakup happens when both shear and breakup processes are effective and is roughly effective for $30 < We < 110$ (SA04). Figure 29.9c shows an example of the multimode breakup. For practical applications of the LJICF, the flow conditions are generally in the shear breakup regime, and hence, most of the experimental and numerical studies have focused on this regime. Focusing on the shear breakup regime, SA04 proposed the following relation for the time of onset of ligament formation from the liquid jet:

$$\frac{t_{\mathrm{i}}}{t'} = 0.0004\left(\frac{\mu_{\mathrm{j}}}{\mu_{\mathrm{g}}We}\right), \tag{29.28}$$

where t' is a nondimensional time equal to $d_{\mathrm{j}}^2/u_{\mathrm{j}}$. They also proposed relations for the diameter of the formed ligaments with values increasing from the onset of breakup to the CBL. They indicated that Rayleigh breakup implies a constant ratio of the drop to ligament diameters of the form $d_{\mathrm{p}}/d_{\mathrm{l}} = 1.2$ where d_{p} and d_{l} correspond to droplet and ligament diameters, respectively.

As for the liquid column breakup, a closer look at Fig. 29.9 shows that the main mechanism responsible for jet final breakup at low Rayleigh numbers is column waves forming due to Rayleigh/Taylor type of instability. As the Weber number is increased and ligament formation begins, there are complicated interactions between the various surface disturbances of smaller sizes and larger column waves. In fact, as the Weber number grows large, the jet gets deformed into a sheet-like shape and 3D waves grow on its surface. In the meantime that the jet spreads into a sheet-like shape, a great amount of mass is lost due to mass stripping. SA04 provided empirical expressions for the rate of mass shedding which show that for Weber numbers in the shear breakup regime up to 90% of the mass rate of the jet can be lost to stripping. The interaction of the various instabilities along with the mass loss leads to the final breakdown of the jet at the CBL as can be seen in Fig. 29.11. From the figure, it seems that the sizes of the droplets formed at the CBL are large and on the same order of size as the wavelengths of the surface waves at the CBL prior to the disintegration. According to several studies such as Wu et al. [1] and SA04, the location of the column breakup is around $x_{\mathrm{b}} = 8d_{\mathrm{j}}$ for nonturbulent jets in subsonic crossflows. For turbulent jets, however, interaction of the various other types and scales of motion (due to turbulence and internal vorticity of the jet) with the instabilities explained so far leads to an earlier disintegration of the jet and the



Fig. 29.11 Shadowgraph of the CBL. From Sallam et al. [8]. Reprinted with permission of the American Institute of Aeronautics and Astronautics.

CBL is at $x_b = 5d_j$ (SA04). Lee et al. [13] extended the study of SA04 to turbulent jets in crossflows. Their study also incorporated results of several previous studies on primary breakup of jets in still gases and droplets in crossflows. Their expressions for droplet and ligament sizes and the rate of mass stripping all involve proper turbulence length scales.

Numerical Modeling

Like most problems in fluid dynamics, numerical modeling of the LJICF problem has made great progress in recent years. Although correlations for jet trajectory and spray penetration derived from experimental data have some discrepancies, they are in a better agreement compared to the discrepancies observed between the results of some numerical simulations. This is because under most operating conditions, the flow structures involved in the problem are so complex. The turbulent motion of the jet out of the nozzle and into the gas stream, the turbulent motion of the gas phase around the deformed jet, and the interaction of the two phases (for high density ratios ρ_j/ρ_g) are each a complex problem on their own and require a considerable amount of computational resources. Detailed numerical simulations of this problem are just beginning to be feasible although they are still quite expensive. Nevertheless, invaluable information is expected to be obtained from these simulations in the coming years as the computational resources grow stronger. In particular, simulations can help study the simultaneous presence of various breakup mechanisms at

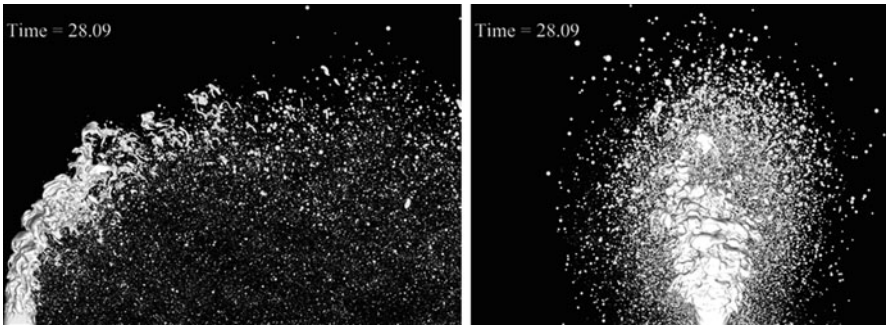


Fig. 29.12 Snapshots of a liquid jet atomization in a crossflow taken from simulations of Herrmann [12]. Reprinted with permission. *Left* and *right panels* correspond to side and front views respectively

different stages. Experimental techniques often have a hard time visualizing and quantifying the breakup mechanism at the gas–liquid interface, especially on the downstream side of the jet due to the presence of many particles. Numerical simulations, on the other hand, provide the luxury of taking a close look at the breakup processes. Figure 29.12 shows two sample snapshots of an LJICF atomization taken from the numerical simulation of Herrmann [12]. Some of the details shown in the picture are hard to obtain from experimental studies. As an example, the front view of the jet in the figure clearly shows that the term "column breakup" is not really a proper term as there is no specific location for it, and moreover, the jet ceases to have a columnar shape soon after it exits the nozzle. Among the pieces of information that can be obtained from numerical simulations are the sizes and velocities of the separated droplets and ligaments, processes that break the ligaments into smaller pieces, the size of the big liquid parcels formed at the CBL, and the rate of mass stripping from the jet at various locations.

In LJICF real applications, there is often more than one jet present and interaction between the jets needs to be taken into account. Various configurations of jets might be used (based on the application), such as a row of jets, opposing jets, or staggered positioning. Such complicated configurations are often hard to be replicated in a lab or to be simulated using full 3D numerical techniques. Even if possible, doing so might be too expensive if one's interest is to obtain basic information such as dimensions of the chamber needed to house the sprays or to investigate the effect of variation of various parameters on the atomization process. Hence, it is useful to develop models that can leverage the information obtained by experimental and numerical simulations and predict some characteristics of the LJICF such as the spray penetration and width along with downstream droplet sizes and velocities. We shall call these methods empirical-numerical models. We consider one such model by Mashayek et al. [17]. They calculate the jet trajectory using the methodology of Mashayek et al. [6] and using results of SA04 to provide the necessary information on the sizes and velocities of the droplets shed from the jet. The droplets stripped along the jet and those formed at the CBL are then tracked

downstream by means of conventional Lagrangian methods used extensively in spray modeling. A typical example of such a simulation is shown in Fig. 29.13. The left panel of the figure shows a three dimensional view of a sample jet, whereas the right panel shows a closeup of the same jet along with the air flow streamlines on a cross-air-streamwise plane. The streamline pattern clearly shows the formation of the double vortices in the wake of the jet. The vortices were captured by introducing a pre-calculated jet into the flow field. The mass stripping and particle production at the CBL were modeled by injecting droplets alongside the jet based on empirical correlations. Secondary breakup and motion of the particles were calculated using standard Lagrangian particle tracking methods and conventional breakup schemes. The structures associated with the presence of the jet (shown in the figure) can play a role in the droplet dynamics and their atomization downstream of the jet. Although the circular jet shape prescribed in the simulation of Fig. 29.13 has a rather simplified form, it still helps developing some of the structures of interest.

Numerical–empirical models such as the one discussed above are incapable of resolving the ligament formation and ligament breakup into droplets. Therefore, they can only be applied to high Weber number flows where the shear breakup is dominant and ligaments breakup into droplets shortly after they are formed. Fortunately, these conditions are satisfied in most practical applications. The validity of these models relies greatly on the empirical correlations which they are based on. Thus, these models become more credible as our basic understanding of the physics of the problem improves over time. Although empirical models still lack a lot of basic physics, their very low computational cost and their flexibility to be applied to various multi-spray configurations make them attractive for commercial and practical design purposes.

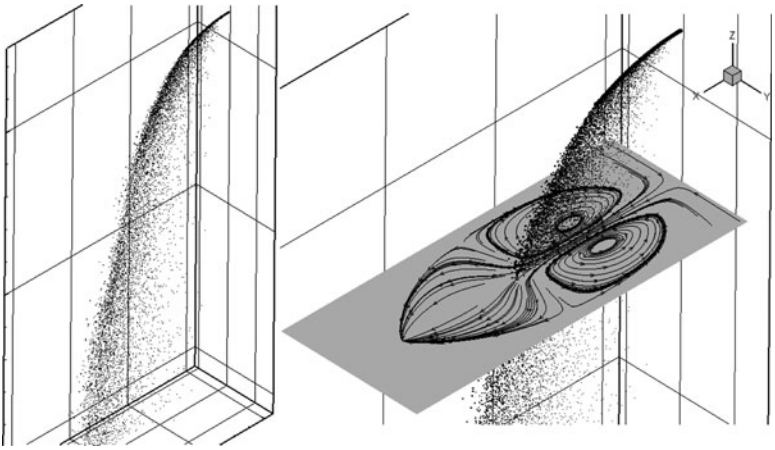


Fig. 29.13 A schematic view of an LJICF atomization obtained by empirical-numerical models. *Right* figure is a closer look at the *left* figure with gas flow streamlines depicted on a slice to show that the model mimics the effects of the jet body on the incoming gas flow (From Mashayek et al. [17])

To summarize, in this chapter a general review on the LJICF atomization was presented. More emphasis was put on the basic physics of the problem while a general overview of different types of research on the subject was presented. The categorization was based on the physics of the problem rather than the type of the studies (numerical, theoretical, or experimental). Although various interesting characteristics of the atomization process were introduced, other important parameters were left out as they did not fit within the scope of this chapter. Among those are the effect of the geometry of the nozzle, the turbulence characteristics of the jet, and the effects of various characteristics of the incoming gas flow (such as its pressure, temperature and turbulence level). The difference between the breakup processes for a turbulent and a non-turbulent jet is another important topic that deserves special attention (Lee et al. [13]). For further information on any of these issues, the reader is encouraged to refer to the relevant referenced materials.

Appendix

Authors	*Description of the study*	*Correlations for jet/spray penetration*
Schetz and Padhye [18]	Experimentally studied the penetration and breakup using optical measurement techniques	$\left(\frac{z_{\max}}{d}\right) = C\sqrt{q}C_{\text{dis}}\left(\frac{d_{\text{eq}}}{d}\right)$
Chen et al. [19]	Used laser-sheet imaging technique to study the jet penetration for $3<q<45$ and $1\ bar<p<2\ bars$	$\frac{z}{d} = 9.91(q)^{0.44}\left[1-\exp\left(\frac{-x/d}{13.1}\right)\right] \times\left[1+1.67\exp\left(\frac{-x/d}{4.77}\right)\right] \times\left[1+1.06\exp\left(\frac{-x/d}{0.86}\right)\right]$
Wu et al. [1]	A phenomenological model for the jet penetration, based on experiments using the shadowgraph technique	$\frac{z}{d} = 1.37\sqrt{q(x/d)}$
Wu et al [20]	Extended Wu et al. [1] for spray penetration and width	$\frac{z}{d} = 4.3q^{0.33}\left(\frac{x}{d}\right)^{0.33}$
Inamura et al. [21]	Experimental study focused on surface waves and spray characteristics	$\frac{z}{d} = (1.18+0.24d)q^{0.36}\ell_n \times\left(1+(1.56+0.48d)\frac{x}{d}\right)$
Becker and Hassa [22]	Shadowgraphs, Mie-scattering, and phase Doppler techniques used to study fuel flux and droplet size distributions. $1<q<40$ and $1.5\ bars<p<15\ bars$	$\frac{z}{d} = 1.48q^{0.42}\ell_n\left(1+3.56\frac{x}{d}\right)$
Lakhamraju and Jeng [23]	Pulsed shadowgraph technique. $1<q<50$, $0.2<Ma<0.9$, $363K<T<505K$	$\frac{z}{d} = 1.8444q^{0.546}\ell_n\left[1+1.324\left(\frac{x}{d}\right)\right] \times\left(\frac{T_\infty}{T_0}\right)^{-0.117}$

(*continued*)

Authors	*Description of the study*	*Correlations for jet/spray penetration*
Elshamy and Jeng [24]	Pulsed shadowgraph technique. *2<q<71, 1 bar<P<7 bars*	$\frac{z}{d} = 4.95\left(\frac{x}{d} + 0.5\right)^{0.279} q^{0.424} \times We^{-0.076}\left(\frac{p}{p_0}\right)^{-0.051}$
Heister et al. [25]	Theoretically calculated jet trajectory by assuming a cross-sectional deformation into elliptic shapes	——
Nguyen and Karagozian [26]	An analytical/numerical model for predicting the behavior of nonreacting and reacting liquid jets injected in subsonic crossflows	——

References

1. Wu, P. K., Kirkendall, K. A., Fuller, R. P., and Nejad, A. S., Breakup Processes of Liquid Jets in Subsonic Crossflow, Journal of Propulsion and Power, 13(1), 1997, 64–73.
2. Inamura, T., Nagai, N., Watanabe, T., and Yatsuyanagi, N., Disintegration of Liquid and Slurry Jets Traversing Subsonic Airstreams, Proceedings of the 3rd World Conference on Experimental Heat Transfer, Fluid Mechanics and Thermodynamics, Elsevier, Amsterdam, 1993, pp. 1522–1529.
3. Lakhamraju, R. R. and Jeng, S. M., Liquid Jet Breakup Studies in Subsonic Air Stream at Elevated Temperatures, 18th Annual Conference on Liquid and Atomization and Spray Systems, Inst. for Liquid Atomization and Spray Systems [CD-ROM], 2005.
4. Becker, J. and Hassa, C., Breakup and Atomization of a Kerosene Jet in Crossflow at Elevated Pressure, Atomization and Sprays, 12(1–3), 2002, 49–67.
5. Wu, P. K., Kirkendall, K. A., Fuller, R. P., and Nejad, A. S., Spray Structures of Liquid Jets Atomized in Subsonic Crossflows, Journal of Propulsion and Power, 14(2), 1998, 173–182.
6. Mashayek, A., Jafari, A., and Ashgriz, N., Improved Model for the Penetration of Liquid Jets in Subsonic Crossflows, AIAA Journal, 46(11), 2008, 2674–2686.
7. Mashayek, A., Behzad, M., and Ashgriz, N., A numerical-experimental study of the atomization of a liquid jet in a sub-sonic crossflows, Submitted to AAA Journal (2010).
8. Sallam, K. A., Aalburg, C., and Faeth, G. M., Breakup of Round Nonturbulent Liquid Jets in Gaseous Crossflow, AIAA Journal, 42(12), 2004, 2529–2540.
9. Sarchami, A., Jafari, A., and Ashgriz, N., Primary Breakup of a Liquid Jet in Gaseous Cross Flow: Droplet Size Distribution, 10th International Congress on Liquid Atomization and Spray Systems, ICLASS-2006, Kyoto, Japan, August 27–Sept 1, 2006.
10. Mashayek, A. and Ashgriz, N., Model or Deformation of Drops and Liquid Jets in Gaseous crossflows, AIAA Journal, 47(2), 2009.
11. Madabhushi, R. K., Leong, M. Y., Arienti, M., Brown, C. T., and McDonell, V. G., 19th Annual Conference on Liquid Atomization and Spray Systems, Toronto, Canada, May 2006.
12. Herrmann, M., Detailed Numerical Simulations of the Primary Atomization of a Turbulent Liquid Jet in Crossflow, ASME Journal of Engineering for Gas Turbines Power, 132(6), 2010, 061506.1–10.
13. Lee, K., Aalburg, C., Diez, F. J., Faeth, G. M., and Sallam, K. A., Primary Breakup of Turbulent Round Liquid Jets in Uniform Crossflows, AIAA Journal, 45(8), 2007, 1907–1916.

14. Linne, M. A., Paciaroni, M., Gord, J. R., and Meyer, T. R., Ballistic imaging of the liquid core for a steady jet in crossflow, Applied Optics IP, Vol. 44, Issue 31, pp. 6627–6634.
15. Mazallon, J., Dai, Z., and Faeth, G. M., Primary Breakup of Nonturbulent Round Liquid Jets in Gas Crossflows, Atomization and Sprays, Vol. 9, No. 3, 1999, pp. 291312.
16. Aalburg, C., van Leer, B., Faeth, G. M., and Sallam, K. A., Properties of crossflow are dominant in determining liquid column trajectories. of Nonturbulent Round Liquid Jets in Uniform Gaseous Crossflows, Atomization and Sprays, Vol. 15, No. 3, 2005, pp. 249–270.
17. A. Mashayek, M. Behzad, N. Ashgriz, A Numerical-Experimental study of the Atomization of a Liquid Jet in a Sub-Sonic Crossflow, Accepted by AIAA Journal (2010)
18. Schetz, J. A., and Padhye, A., Penetration and Breakup of Liquids in Subsonic Airstreams, AIAA Journal, Vol. 15, No. 10, 1977, pp. 1385–1390.
19. Chen, T. H., Smith, C. R., Schommer, D. G., and Nejad, A. S., Multi-Zone Behavior of Transverse Liquid Jet in High-Speed Flow, 31st Aerospace Sciences Meeting & Exhibit, Reno, NV, Jan 1993
20. Wu, P. K., Kirkendall, K. A., Fuller, R. P. and Nejad, A. S., Spray Structures of Liquid Jets Atomized in Subsonic Crossflows, Journal of Propulsion and Power, Vol. 14, No. 2, 1998, pp. 173–182.
21. Inamura, T., Nagai, N., Watanabe, T. and Yatsuyanagi, N., 1993, Disintegration of Liquid and Slurry Jets Traversing Subsonic Airstreams, Proceedings of the 3rd World Conference on Experimental Heat Transfer, Fluid Mechanics and Thermodynamics (Honolulu, HI), Elsevier, Amesterdam, 1993, pp. 1522–1529.
22. Becker, J. and Hassa, C., Breakup and Atomization of a Kerosene Jet in Crossflow at Elevated Pressure, Atomization and Sprays, 2002, Vol. 11, pp. 49–67.
23. Lakhamraju, R. R. and Jeng, S. M., Liquid Jet Breakup Studies in subsonic Air Stream at Elevated Temperatures, 18th Annual Conference on Liquid and Atomization and spray Systems, Irvine, CA, May 2005.
24. Elshamy, O. M. and Jeng, S. M., Study of Liquid Jet in Crossflow at Elevated Ambient Pressures, 18th Annual Conference on Liquid and Atomization and spray Systems, Irvine, CA, May 2005.
25. Heister, S. D., Nguyen, T. T. and Karagozian, A. R., Modeling of Liquid Jets Injected Transversely into a Supersonic Crossflow, AIAA Journal, Vol. 27, No. 12, 1989, pp. 1727–1734.
26. Nguyen, T. T. and Karagozian, A. R., Liquid Fuel Jet in Subsonic Crossflow, Journal of Propulsion and Power, Vol. 8, No. 1, 1992, pp. 21–29.

Chapter 30
Impinging Jet Atomization

N. Ashgriz

Abstract This chapter is an introduction to impinging jet atomizers, in which two or more jets are made to impinge on each other. High energy impingement of these jets results in the atomization of the liquid. The chapter provides the theory for the prediction of the sheet formed by the impingement of two jets, followed by estimates of droplet sizes based on the sheet thickness. This chapter also provides information on the mixing processes in impinging jet nozzles.

Keywords Area ratio · Hypergolic liquids · Impinging jet atomization · Mixing · Momentum ratio · Sheet thickness · Sheet breakup length

Introduction

Impinging jet atomizers are used in bipropellant liquid rocket engines, as well as in many chemical processes. Generally, impinging jet atomizers are used when rapid mixing between two fluids is needed. For instance, in bipropellant rocket engines, a liquid fuel is mixed with liquid oxidizer and combusted. In order to enhance the mixing between the two liquids, a jet of fuel is collided with a jet of oxidizer, resulting in rapid mixing and atomization at the same time. If the fuel and oxidizer react as soon as they touch, they are referred to as hypergolic liquids. Impinging jet injectors are commonly used for such fluids [1–2].

Two-impinging-jets are also used in reaction-injection-molding processing equipment to provide good micromixing for viscous fluids [3–6]. It is one of the techniques used to reduce the timescale of micro-mixing in precipitators [6].

There are numerous experimental as well as theoretical studies on the mechanisms of atomization of the impinging jets. These studies [7–36] show that when two jets collide they form a sheet in the direction perpendicular to the plane of the jets.

N. Ashgriz
Department of Mechanical and Industrial Engineering, University of Toronto, Toronto, Canada
e-mail: ashgriz@mie.utoronto.ca

N. Ashgriz (ed.), *Handbook of Atomization and Sprays*,
DOI 10.1007/978-1-4419-7264-4_30, © Springer Science+Business Media, LLC 2011

Waves form on the surface of the sheet and grow until the sheet breaks up into small droplets. The generated spray has an elliptical cross section with its major axis in the plane of the liquid sheet. The sizes of the droplets formed from the impinging jet atomizers are directly related to the thickness of the liquid sheet. Generally, the is inversely proportional to the radial distance from the impingement point and other parameters. This chapter provides a description of the characteristics of liquid sheets formed by impinging jets and provides methods to determine average droplet sizes produced by such nozzles.

Injector Design

There are different types of impinging jet injectors, which are selected based on the type of liquid (e.g., hypergolic, cryogenic, storable); condition of the liquid (e.g., liquid, gas, gel); and other conditions, such as engine conditions, chamber wall cooling, chamber length, mixture ratio, chamber pressure. The final droplet size distribution and flow mixing is dependent on the entire flow system distribution including individual injector element type, and arrangement and orientation of the elements.

The impinging jet nozzles are generally divided into unlike and like impinging jets depending on the type of the liquid used as shown in Fig. 30.1. In like impinging jets, same liquids or propellants are impinged on each other, whereas, in unlike impingement, two different liquids or propellants are collided. The main difference between the two is the process of mixing. They both have about the same atomization mechanism, but in unlike impingement, the mixing starts right from the impingement point. Most reactors have many impinging jets next to each other. Each pair generates a spray or fan. The spray of two pairs may have certain inclination with respect to each other, referred to as cant angle. The mass and mixture distribution depend on the orifice sizes, spacing between the two liquids (e.g., fuel and oxidizer), and cant angle.

Impinging Jet Characteristics

When two equal cylindrical jets collide they form an expanding sheet in the plane at a right angle to the plane containing the axes of the two jets. When the two jets are coaxial, a circular sheet is formed. Otherwise, the sheet takes a leaf-like shape.

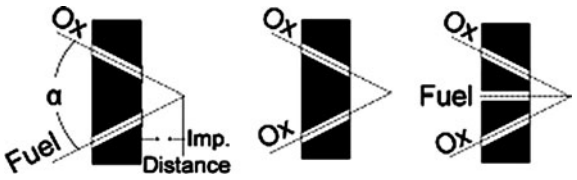


Fig. 30.1 Like and unlike injectors

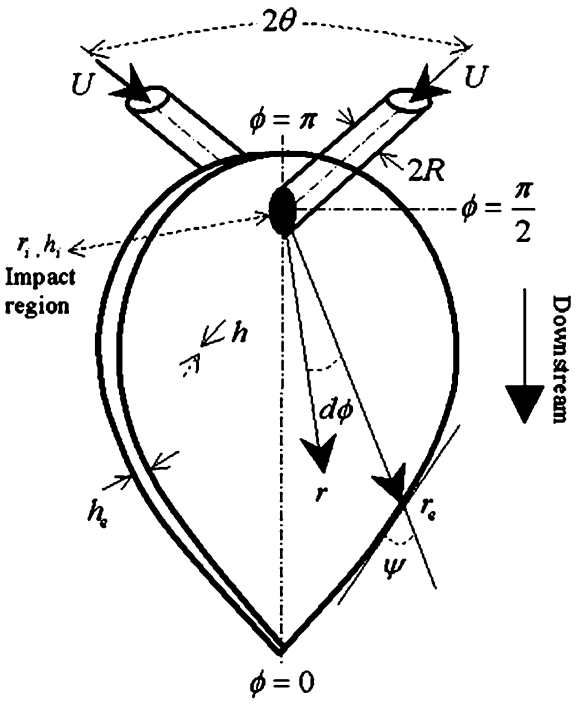


Fig. 30.2 Sketch of liquid sheets formed by two-jet impingement

This process is sketched in Fig. 30.2. To clearly describe the spray characteristics of the impinging jets, related parameters include impingement angle (2θ), jet velocity (U), and jet radius and diameter ($2R = D$), position angle (ϕ), and sheet thickness, h.

There are three major modes: closed-rim, open-rim, and the fully-developed mode. Typical sheet formations as a function of increasing jet velocities and of impingement angle of 60° is shown in Fig. 30.3 [23]. When two jets impinge at low velocities, they may merge forming a jet at their merging point. At the tip of the sheet, an irregular and distorted jet is formed, which breaks up into large droplets below the tip. The breakup of this final jet is governed by the capillary instability [24].

When two jets impinge at relatively low velocities or low Reynolds numbers, a relatively stable closed rim sheet is formed (picture 2, Fig. 30.3) [25]. At low velocities or high fluid viscosities, fluid is prevented from escaping or shedding from the sheet formed by impingement. After impingement, all of the liquid is confined in the rim enclosing the periphery of the sheet. Thereafter, liquid flows downward along the rim, and re-impinges on the lower tip of the sheet to form a jet or a secondary film.

Small disturbances may generate small beads on the edge. This is illustrated in Fig. 30.4b, when the sheet is slightly disturbed [25]. These beads continuously grow in size while moving along the edge, and finally are detached from the edge.

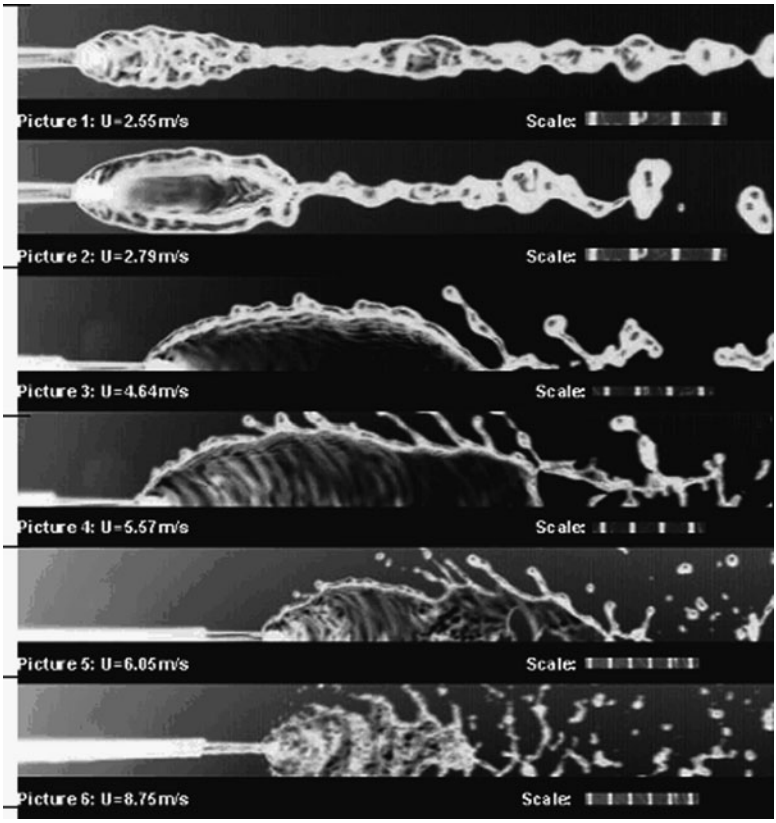


Fig. 30.3 Breakup of sheets formed by two jets impinging at $2\theta = 60°$. Picture 1: $U = 2.06$ m/ s; picture 2: $U = 2.67$ m/s; picture 3: $U = 3.98$ m/s; picture 4: $U = 5.13$ m/s; picture 5: $U = 5.5$ m/s; picture 6: $U = 7.64$ m/s [23] (Courtesy of American Institute of Physics)

This results in drops and ligaments. The formation of droplets is governed by Rayleigh or Capillary instability. The size of the sheet becomes larger when the jet velocities are increased.

Drops of almost the same diameter regularly shed from the periphery of the sheet. Shedding frequency is directly proportional to the jet velocity. However, if the viscosity is lowered, the regular shedding does not occur; drops of varying sizes randomly shed tangentially from the periphery of the sheet. For high viscosity fluids, liquid film extends widely and forms a closed-rim without drop shedding. Perforation may occur randomly if the liquid film expands to specific extent, because of increasing jet velocity. When the velocity of the sheet is increased further, air friction may result in the formation of waves on the sheet surface, making the sheet ruffled. These disturbances form antisymmetric waves propagating radially with growing amplitude. By increasing jet velocity further, the rim opens. Breakup initiates near the lower tip of the sheet. In this mode, sheet characteristics become

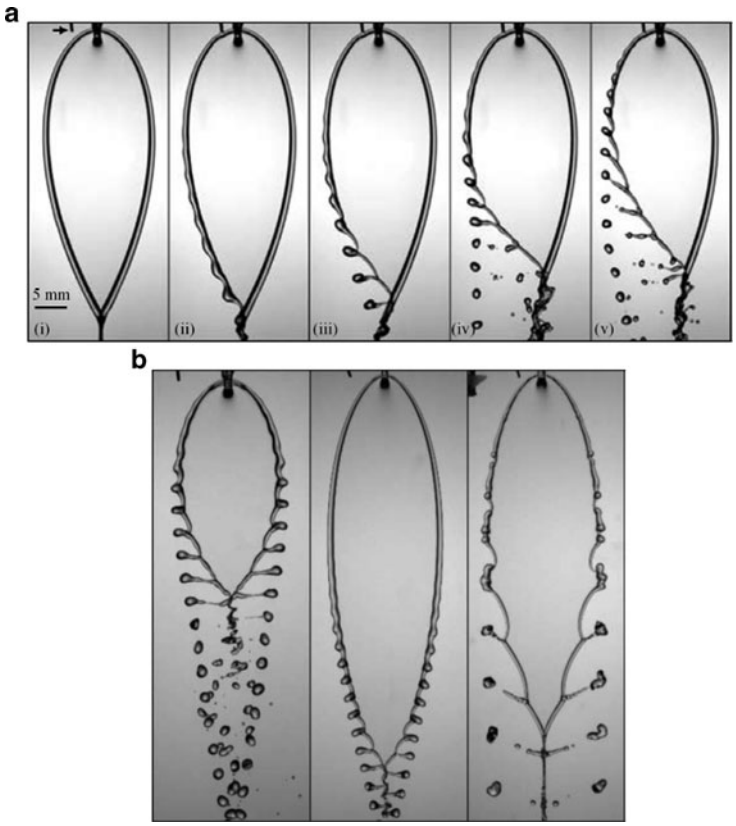


Fig. 30.4 (**a**) Perturbation with a small wire (indicated by an arrow) of an ethanol sheet rim with increasing levels of perturbation from left to right. (**b**) Periodic atomization. The injection conditions are identical for each picture, $2\alpha = 90°$, $d_j = 1.05$ mm, $U = 1.7$ ms^{-1} [25] (Courtesy of Cambridge University Press)

very sensitive to jet velocity and fluid properties. For higher viscosity fluids, open-rimmed, perforated, and even threads of shedding drops occur (see Figs 30.5 and 30.6 for the effect of various parameters on the sheet characteristics). When the jet velocity or the jet Reynolds number is further increases, the liquid sheet becomes distinctly unstable. The principal cause of instability is due to the interaction of the sheet with the surrounding atmosphere whereby rapidly growing waves are imposed on the sheet. Disintegration occurs when the wave amplitude reaches a critical value and sheet is torn off. The fragments breakup into ligaments, and subsequently ligaments disintegrate into drops.

Figure 30.3 (picture 4) shows waves on the sheet, which are also referred to as impact waves. These are high-frequency circumferential waves that dominate the sheet breakup at high impingement angles and velocities. The impact waves control the breakdown of the sheet over a wide range of ambient air densities, particularly below the atmospheric. Dombrowski and Hooper [11] found a critical value of

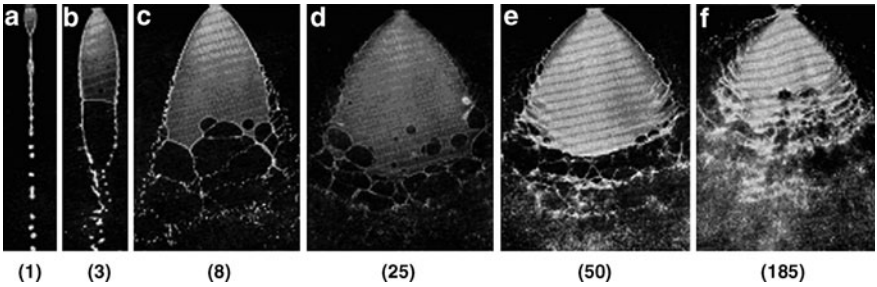


Fig. 30.5 Characteristics of a liquid sheet with increase of pressure (15% soluble oil/tap water), pressure in psi in brackets [34]

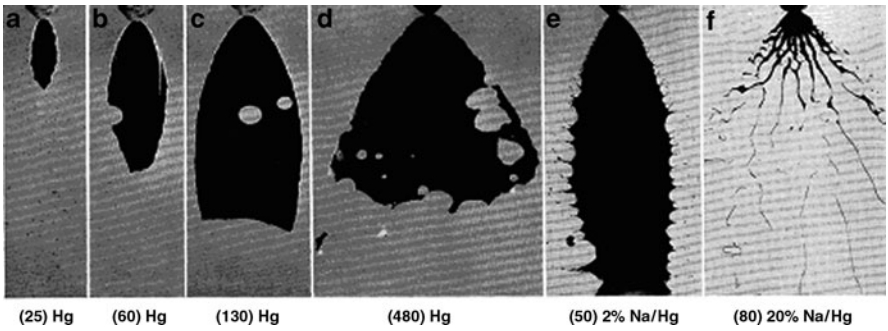


Fig. 30.6 The development of liquid sheets having high surface tension low viscosity and high density [34] (Courtesy of the Royal Society of London)

Weber number for these waves to appear when the two jets were turbulent, which lied between $66 < We < 165$, where the Weber number is defined as $We = \rho DU^2 \sin^2\theta/\sigma$. Heidman [8] did a similar work, and found a range of $84 < We < 126$.

Dimensional Characteristics of Spray Sheet

Dimensional characteristics of liquid sheets formed from impinging jets or flat fans have been extensively studied [26–36]. It is generally noted that the shape of a spreading sheet is proportional to the square of the jet velocity and jet diameter, provided that the velocity is not too high. The shape of a sheet can be determined by a force balance on the edges of the sheet. Figure 30.7 illustrates part of a liquid sheet and its cross section. The rate of change of fluid momentum (force per unit length), F_m, at the rim of the sheet (Fig. 30.7b) is expressed by

$$F_m = \dot{m}(V \sin(\psi)) \tag{30.1}$$

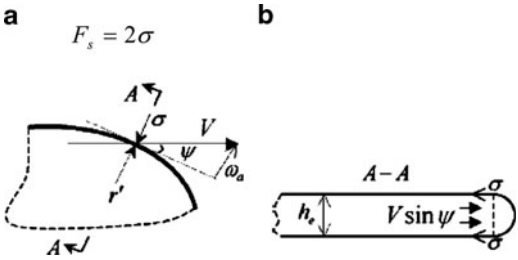


Fig. 30.7 Force balance on the edges of the sheet. (**a**) Part of the liquid sheet, where the curved line represents the edge of the sheet; (**b**) sheet cross section

where ψ is the angle between the velocity vector and the local tangent at the edges of the sheet, and V is the local fluid velocity. The mass flow rate, $\dot{m}$ can be written as:

$$\dot{m} = \rho(V \sin \psi)h_e$$

where ρ is the density of the fluid, and h_e is the edge thickness of the sheet. Combining the foregoing two expressions provides:

$$F_m = \rho(V \sin \psi)^2 h_e \tag{30.2}$$

The surface tension force counter acting the fluid inertia at the edges of the sheet is:

$$F_s = \sigma\left(\frac{2}{h_e} + \frac{1}{r'}\right)h_e \tag{30.3}$$

where σ represents the surface tension of the fluid, and r' denotes the local radius of curvature of the sheet rim as shown in Fig. 30.7. Generally, h_e is of the order of microns, whereas r' is in millimeters. Therefore, the surface tension forces caused by the curvature of the rim of the sheet is much smaller than that caused by the sheet edge thickness, and, therefore, it can be neglected. This simplifies (37.3) to:

$$F_s = 2\sigma \tag{30.4}$$

Equating (30.2) to (30.4) gives

$$\sin^2\psi = \frac{2\sigma}{\rho V^2 h_e} \tag{30.5}$$

Most models assume a uniform fluid velocity across the sheet, which is assumed to be equal to the mean jet velocity, U. Therefore, we can replace V with U, and rewrite (30.5) as

$$\frac{h_e}{R} = \frac{4}{We \sin^2 \psi} \tag{30.6}$$

where $We = 2\rho U^2 R/\sigma$ is the Weber number of the jet. For a radially thinning sheet with uniform fluid velocity, the product of local thickness and radial distance, hr, must be dependent only on the azimuthal angle, ϕ. In order to obtain hr, Hasson and Peck considered an elliptic impingement region, expressed as:

$$\frac{r_i}{R} = \frac{\sin\,\theta}{1 - \cos\,\phi\cos\theta} \tag{30.7}$$

The stagnation point where $r_i = 0$ is a focal point of the ellipse. By applying conservations of mass and momentum, they obtained hr as:

$$\frac{hr}{R^2} = \frac{\sin^2\theta}{(1 - \cos\phi\cos(\theta))^2} \tag{30.8}$$

The sheet thickness h_i can then be determined by dividing (30.8) with (30.7), which results in:

$$\frac{h_i}{R} = \frac{\sin^2\theta}{1 - \cos\phi\cos\theta} \tag{30.9}$$

An expression for the sheet shape can now be obtained by dividing (30.8) by (30.6) [18]:

$$\frac{r_e}{RWe} = \frac{\sin^2\theta\sin^2\psi}{4(1 - \cos\phi\cos(\theta))^2} \tag{30.10}$$

Ibrahim and Przekwas [18] considered the impingement region to be a circle of radius

$$\frac{r_i}{R} = \frac{1}{\sin\theta} \tag{30.11}$$

The thickness of this circle h_i which was originally proposed by Naber and Reitz [33] is expressed by

$$h_i(\phi) = h_\pi e^{\beta(1-\phi/\pi)}. \tag{30.12}$$

where h_π is the edge thickness of the circle at $\varphi = \pi$, and β is a decay factor which is determined by applying the conservations of mass and momentum to (30.11) and (30.12) [18]:

$$\frac{hr}{R^2} = \frac{\beta e^{\beta(1-\phi/\pi)}}{e^\beta} \tag{30.13}$$

where

$$\cos\theta = \left(\frac{e^{\beta}+1}{e^{\beta}-1}\right)\frac{1}{1+(\pi/\beta)^2} \tag{30.14}$$

The initial thickness of the impact region, h_i, can now be written by dividing (30.13) by (30.11) [18]:

$$\frac{h_i}{R} = \frac{\beta e^{\beta(1-\phi/\pi)}}{e^{\beta}-1}\sin\theta \tag{30.15}$$

The value of β is determined by the impinging angle and can be numerically calculated from (30.14). Another expression for the sheet shape is now provided by dividing (30.13) by (30.6):

$$\frac{r_e}{RWe} = \frac{\beta e^{\beta(1-\phi/\pi)}\sin^2\psi}{4(e^{\beta}-1)} \tag{30.16}$$

However, ψ is still unknown. Considering ψ as a function of θ and ϕ, Ibrahim and Przekwas [18] proposed the relation

$$\psi = \left(\pi/(2)e\ln(2\theta/(\pi)(1-\phi/\pi))\right) \tag{30.17}$$

Figure 30.8 compares the two models, (30.10) and (30.16), with experimental observation. Figure 30.8a is the picture of a liquid sheet formed by two jets impinging at $2\theta = 120^{\circ}$. Figure 30.8b presents normalized sheet shapes predicted by (30.10) and (30.16) with $2\theta = 120^{\circ}$ and 60°.

Sheet Breakup Length and Width

The breakup length of a liquid sheet is defined as the total length of the liquid sheet from the edge at $\phi = 180^{\circ}$ to that at $\phi = 0^{\circ}$, and the maximum width of the sheet is referred to as breakup width. Combining (30.16) and (30.17) gives an equation describing the shape of the sheet in polar coordinates (r, ϕ):

$$\frac{r_e}{RWe} = \frac{\beta e^{\beta(1-\phi/\pi)}\sin^2[(\pi/2)\exp(\ln(2\theta/\pi)(1-\varphi/\pi))]}{4(e^{\beta}-1)} \tag{30.18}$$

when $\phi = 0$,

$$\frac{r_e(\phi=0)}{RWe} = \frac{\beta e^{\beta}\sin^2\theta}{4(e^{\beta}-1)}$$

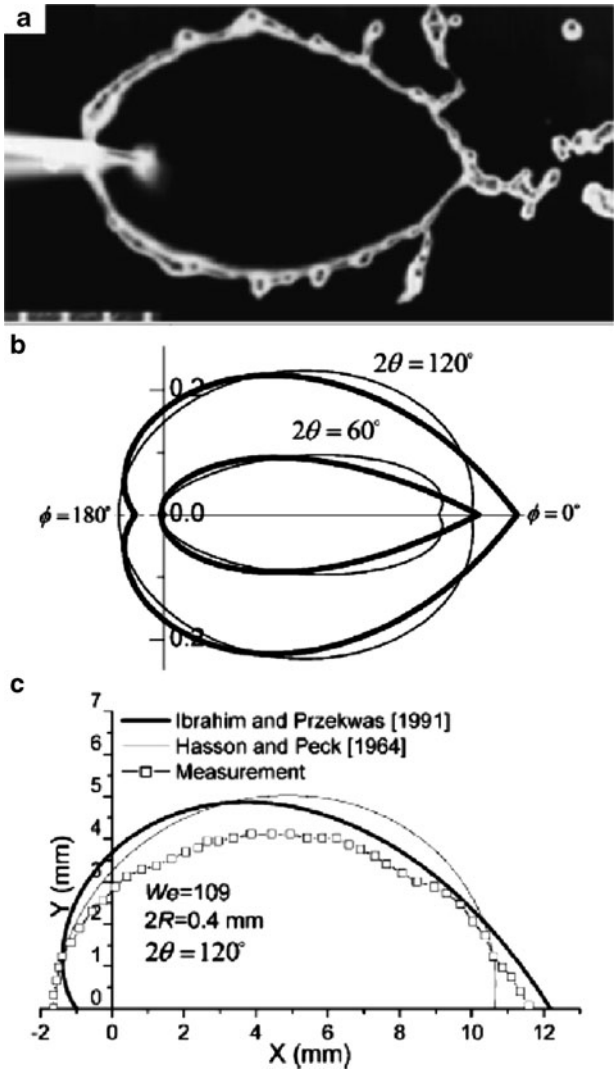


Fig. 30.8 This figure compares two analytical models (30.10) and (30.16) with experimental observations. (**a**) Photograph of a sheet formed with $2\theta = 120^\circ$ and $U = 5.18$ m/s; (b) plots of $r_e(RWe)^{-1}$; (**c**) plots of r_e/R in comparison to a measured sheet shape [23] (Courtesy of the American Institute of Physics)

which predicts radial distance between the downstream tip of the sheet and the impact point. When $\phi = \pi$,

$$\frac{r_e(\phi = \pi)}{RWe} = \frac{\beta}{4(e^{\beta} - 1)}$$

which predicts the radial distance of the upstream edge of the sheet. Summing up the foregoing two equations gives the maximum length of the sheet, denoted by L,

$$\frac{L}{RWe} = \frac{\beta\left(\mathrm{e}^{\beta}\sin^2(\theta+1)\right)}{4(e^{\beta}-1)} \tag{30.19}$$

To find an expression for the maximum width of the sheet, we need to solve

$$\frac{\partial(r_e\sin(\phi))}{\partial\phi} = 0$$

which results in

$$\frac{\beta}{\pi} = \cot[\phi - \cot[](\pi/2)e^{\ln(2\theta/(\pi)(1-\phi/\pi))}\Big]e^{\ln(2\theta(\pi)(1-\phi/\pi))}\ln(2\theta/\pi) \tag{30.20}$$

This equation gives the value of $\phi_{\max}$ where the spray sheet is the widest, which is only dependent on θ. Hence, the following expression predicts the breakup width, denoted by W,

$$\frac{W}{RWe} = 2\frac{r_e(\phi_{max})}{RWe}\sin(\phi_{max}) \tag{30.21}$$

Figure 30.9 presents the theoretical (30.19 and 30.21) and experimental results of sheet breakup length and width versus We [23]. The three vertical dotted lines are the demarcation lines between the closed-rim sheet and open-rim sheet. The open-rim sheet is measured only for the case of $\theta = 120^{\circ}$. A favorable agreement can be seen in Fig. 30.9 for liquid sheets with closed rims, which shows that the breakup width is linearly proportional to We. The slope of the linear relation is determined by the impinging angle. Figure 30.10 also shows that the breakup width increases

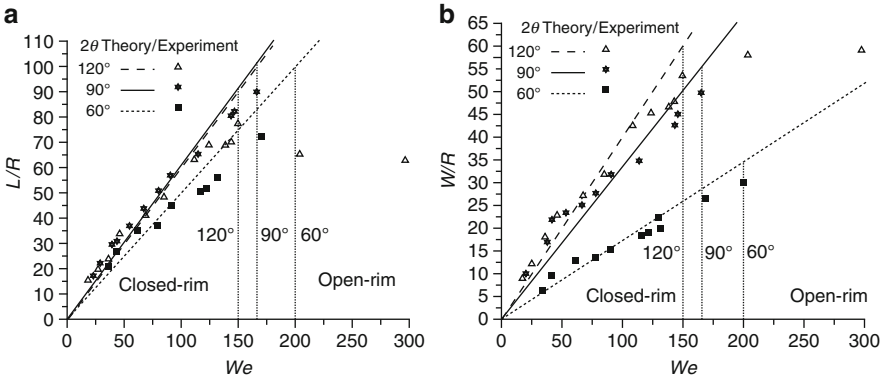


Fig. 30.9 Breakup (**a**) length and (**b**) width of sheet versus jet Weber number. The three vertical dotted lines are demarcation lines between closed-rim sheets and open-rim sheets [23] (Courtesy of the American Institute of Physics)

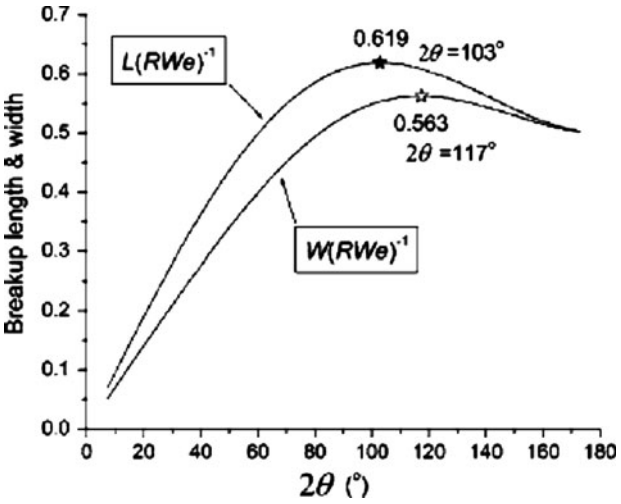


Fig. 30.10 Breakup length and width versus impinging angle [23] (Courtesy of the American Institute of Physics)

with increasing impinging angle. It is shown that both $L(RWe)^{-1}$ and $W(RWe)^{-1}$ first increase with 2θ and then decreases after passing different maxima at different impinging angles. For the case presented here, the maximum breakup length is 0.619 at $2\theta = 103°$, while the breakup width reaches its maximum of 0.563 at $2\theta = 117°$. To avoid the singularities of (30.12) at $\theta = 0°$ and 90°, Fig. 30.10 neglects the two singular points. However, it still shows a tendency that, with 2θ approaching 0° or 180°, $L(RWe)^{-1}$ and $W(RWe)^{-1}$ become identical.

The sheet thickness is plotted in Fig. 30.11 for $2\theta = 120°$. Using the same impinging angle, the edge thickness, $h_e We/R$, is also plotted in Fig. 30.11 by substituting (30.17) into (30.6). As shown in Fig. 30.11, both h_i and h_e decreases as θ increases and are the thickest at $\theta = 0°$. The sheet thickness between r_i and r_e is radially thinning, maintaining $hr = h_i r_i = h_e r_e$ for any azimuthal angle ϕ.

Droplet Size Distribution

Dombrowski and Hooper [11] conducted experiments on a pair of impinging jets and found the following correlation for the droplet size:

$$d_{32} = \frac{4}{U^{0.79}\sin^{1.16}\theta}$$

where d_{32} is the Sauter mean diameter, U is the jet velocity, and 2θ is the impinging angle. As they noted, the jet velocity and impingement angle are raised to different powers. They explained this effect due to the effect of the impingement angle both

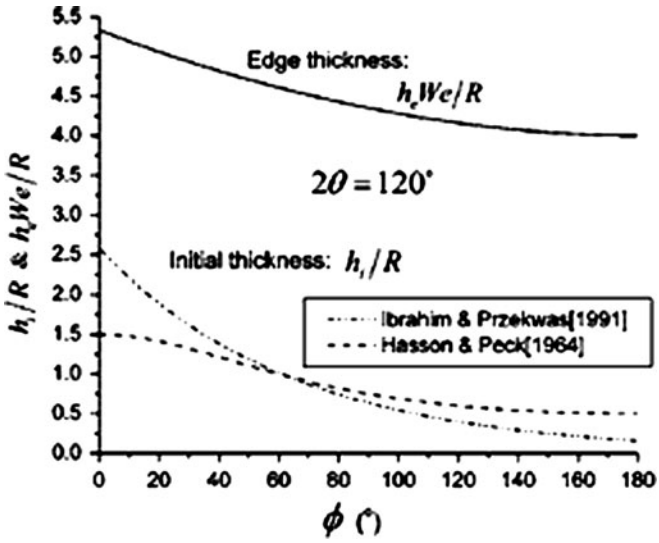


Fig. 30.11 Thickness distribution at the impact region and the sheet edge versus the azimuthal angle on the sheet [23] (Courtesy of the American Institute of Physics)

on the velocity component of the impinging jets and on the sheet thickness. Another correlation is provided by Dombrowski and Hooper [36] for 0.53 mm diameter jets impinging at 110°:

$$d_{32} = \frac{0.0231\sigma^{0.16}}{U^{0.32}\rho^{0.06}\rho_a^{0.1}}$$

which should be contrasted with the one provided by Tanasawa et al. [37] for head-on impingement of two jets with orifice diameters in the range of 0.4–1 mm:

$$d_{32} = \frac{1.73\sigma^{0.25}d^{0.75}}{U^{0.5}\rho^{0.25}\rho_a^{0.1}}$$

One reason for the observed differences between different correlations is the strong dependency of the spray on the nozzle characteristics, which changes the emerging jet characteristics [38]. Turbulence strength of each jet as well as the impact force of two jets, which is determined by the nozzle's internal characteristics, are important factors affecting the sheet breakup [38]. In addition, the droplet size distribution in two impinging jets can vary substantially across the spray. Figure 30.12 shows measurements of the droplet sizes and velocities across the whole spray cross section (x−y), where x is along the sheet and y is perpendicular to the sheet as provided by Vassalo and Ashgriz [20] for a two-jet impinging injector. The contour plots of the droplet diameter (Fig. 30.12) shows that the

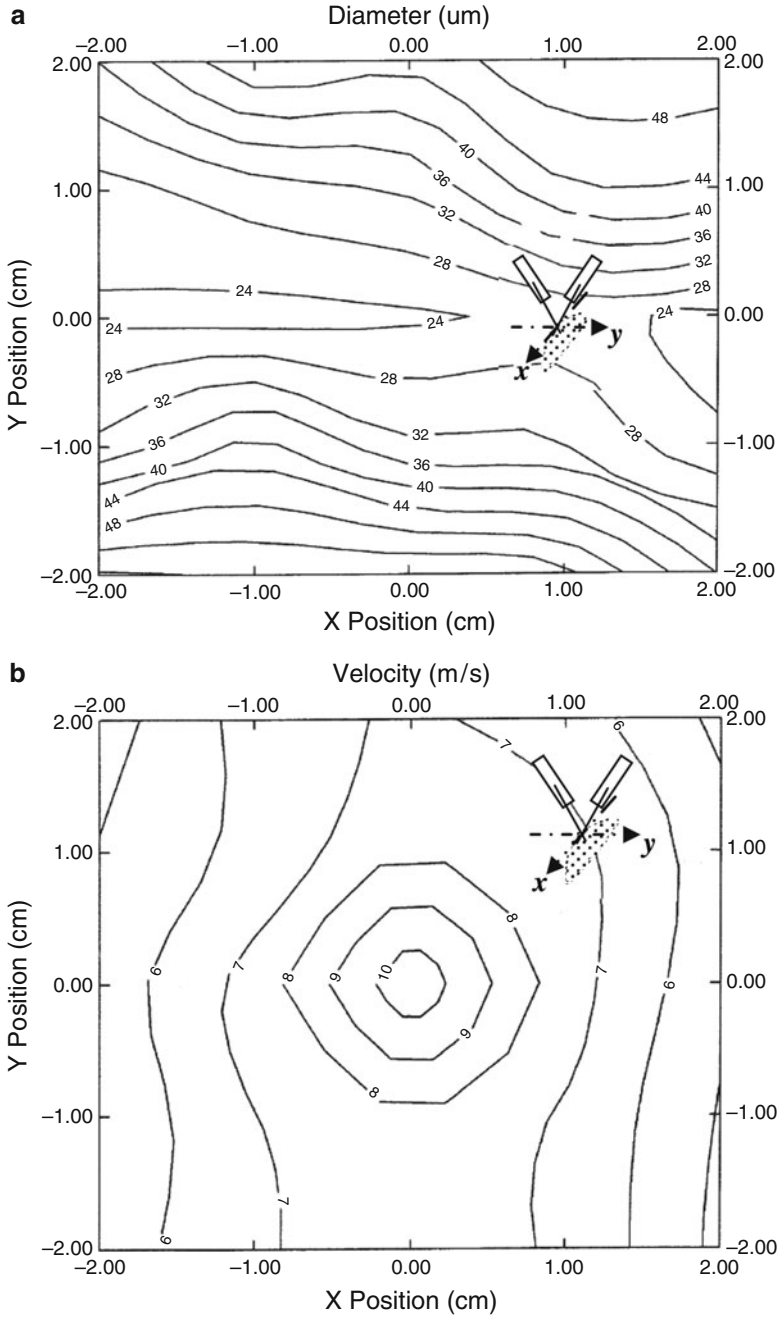


Fig. 30.12 (a) Diameter and (b) velocity contours for two impinging jets of a rocket injector, where x is in the plane of the sheet and y is in the plane of impinging jets. The orifice diameters are 0.3 mm located 6.5 mm apart, making a 90 degrees angle with each other, with jet flow rate of 3.18ml/s [20] (Courtesy of American Institute of Physics)

droplet sizes are relatively uniform along the spray sheet ($y = 0$). Also, droplet sizes are the smallest along the sheet and increase away from the center of the sheet. Therefore, small variations in impingement point of the two jets can disturb this distribution and, therefore, change the mean droplet diameter at the center of the spray. The counter plots of the droplet velocity for the same case are presented in Fig. 30.12b, which shows that the primary direction of contours of constant velocity is in the y-direction rather than the x-direction as it was for the diameters.

Dombrowski and John [36] provided a mean drop size d for an impinging jet based on sheet instability analysis (see Chapter 3):

$$d = \left(\frac{3\pi}{\sqrt{2}}\right)^{\frac{1}{3}} d_L \left[1 + \frac{3\nu_l \rho_l}{\sqrt{\rho_l \sigma d_L}}\right]^{\frac{1}{6}}$$

where d_L is the ligament thickness formed by the breakup of the sheet, obtained by setting volume of a half a wavelength to that of a ligament:

$$d_L = \sqrt{\frac{4h}{k}}$$

where k is the wavenumber of the fastest growing wave on the sheet and h is the sheet thickness at breakup. The initial sheet thickness h_i is related to angular position ϕ by (30.15). The drop size based on Dombrowski and John [36] can be written in the following form [22]:

$$\frac{d}{D} = 1.14 \left(\frac{\rho_g}{\rho_l}\right)^{-1/6} [Wef(\theta)]^{-1/3}$$

where

$$f(\theta) = \frac{(1 - \cos(\theta))^2}{\sin^3\theta}$$

There are numerous other empirical correlation for the droplet sizes generated by impinging jets. Ingebo [40] provided a correlation for the impingement of heptane jets collided at 90° with 9–30 m/s velocities and diameters in the range of 0.7–2.2 mm. His correlation for volume mean diameter is:

$$d_{30} = D\left[2.64\sqrt{DU} + 0.97D\Delta U\right]^{-1}$$

Where ΔU is the relative velocity between the jet and the air stream. Another correlation is by Kuykendal [42] for a wider range of jet velocities (11–60 m/s) and diameters (0.7–4 mm), and angles (20°–120°):

$$d_{30} = 9974 D^{0.25} U^{-0.44} \theta^{-0.2}$$

Hautman [43] provided the following experimental correlation for volume mean diameter (VMD) and mass median diameter (MMD) using water and Jet-A fuel in like-on-like doublets:

$$d_{30} = 1.3 \times 10^7 \left(\rho_j U^2\right)^{-0.7} \sigma^{0.6} \rho_g^{-0.09}$$

$$MMD = 5.34 \times 10^6 \left(\rho_j U^2\right)^{-0.62} \sigma^{0.42} \rho_g^{-0.16}$$

Correlation given by Lourme [44] is:

$$MMD = 240 U^{-1} D^{0.2} \sigma^{0.5} \rho_g^{-0.2}$$

Another correlation is by Zajac [45]:

$$MMD = 15.9 \times 10^4 U^{-1} D^{0.57} \left(\frac{P_c}{P_j}\right)^{-0.1}$$

where P_c/P_j is the centerline to the mean dynamic pressure ratio. Densities are in kg/m^3, velocities in m/s and surface tension in kg/s^2. Chapter 24 provides a compilation of drop size correlations for these nozzles.

Mixing in Impinging Jets

Ashgriz et al. [45] noted that "the mixing process in impinging jet atomizers is controlled by processes in the pre-atomization and post-atomization regions. The pre-atomization processes control the direction of the final flow of the droplets. At low jet velocities with steady and smooth surfaces, the jets basically bounce off of each other and a reflective type of atomization occurs. As the jet velocity increases, the jets atomize shortly after impingement and do not completely change direction. This results that the droplets formed from each stream cross to the other side of the impingement plane. This is transmitive atomization. In addition, if the jets are non-smooth, part of each jet does not interact with the other. The un-interacted part of the jets tends to stretch the liquid to the other side of the impingement plane, which enhances the transmitive atomization. The extent of jet crossing increases with the jet diameter, jet velocity, and impingement angle. An increase in the jet velocity, jet diameter and impingement angle reduces the time needed to redirect the momentum of each jet, in addition, it increases the amplitude of the surface disturbances and the momentum of the un-interacted region. In the post-atomization region the turbulent dispersion develops a mixing layer along the axis of the spray, which enhances the mixing. The overall results can be expressed in terms of

the extent of mixing which may decrease or increase with the jet momentum depending on the type of atomization. The mixing may improve or worsen along the axis of the spray depending on the competition between the turbulent dispersion, which improves the mixing, and the flow separation by the action of the initial reflective or transmitive atomization which make the mixing worse. Most practical impinging jets operate in the parameter range, which results in the transmitive atomization. Therefore, in these systems the extent of mixing decreases with increasing the jet velocity, jet diameter, and impingement angle."

Rupe [9] defined the following coefficient to describe the degree of mixing in the impinging injectors:

$$\phi = \sum_{0}^{N} \frac{w}{W}\left(\frac{F-f}{F}\right) + \sum_{o}^{\tilde{N}} \frac{w}{W}\left(\frac{F-\tilde{f}}{F-1}\right)$$

where ϕ is the mixing coefficient, $w = w_1 + w_2$ being the total local weight flow rate with w_i being the local weight flow rate due to stream i, $W = W_1 + W_2$ is the total nominal (input) weight flow rate of the spray with W_i being the nominal or input weight flow rate of stream i, $F = W_2/W$ is the nominal mixture ratio, $f = w_2/w$ is the local mixture ratio, $\hat{f}$ is the local mixture ratio for points where $f > F$, N is the number of samples with $f < F$ and $\hat{N}$ is the number of samples with $f > F$.

The percentage of this deviation represents the extent of mixing or mixing efficiency:

$$\Phi = 100(1 - \phi)$$

This coefficient is used to characterize, evaluate, and compare sprays of different configurations produced under various conditions. The quality of mixing has been evaluated by the determination of Φ over significant ranges of six distinct variables: (1) M_1/M_2; (2) impingement angle θ; (3) area ratio A_1/A_2, where A_i is the area of stream i; (4) area scale A_1/A'_2; (5) fluid physical properties; and (6) flow characteristics and impingement length l. The following is a general understanding from the effect of these parameters on the mixing process.

Effect of the Momentum Ratio

The maximum value of Φ occurs near $M_1/M_2 = 1$, and that the liquid-phase mixing is relatively insensitive to momentum ratio at or near a momentum ratio of 1.0 [9, 46].

The experimental results indicate that the distribution of each component of the liquid in the plane of stream center lines is not uniform. However, the local mixture

ratio along the major axis of the spray cross-section is nearly constant and equal to the nominal value (if the spray is produced by streams of equal momentum and area ratio). The mass distribution significantly changes with the momentum ratio. The maximum local mass flow shifts along the impinging plane in the direction of the high-momentum stream. As this shift takes place the spray cross-section assumes a kidney shape that is symmetrical about the impinging plane only [9].

Effect of the Impingement Angle

There is a linear correlation between the impingement angle and Φ [9, 47]. Better mixing is obtained at lower impingement angles [48]. The impingement angle influences the mixing in two different manners. Higher impingement angles result in a higher impact-induced turbulence and, therefore, higher turbulence mixing. On the other hand, higher impingement angles allow less contact time between the liquids of the two streams.

Effect of the Area Ratio

The area ratio indicates the extent of interaction between the two streams. Rupe [9] reported the following results: The maximum value of Φ (and hence point of best mixing) occurs for momentum ratios less than 1.0 as the area ratio becomes smaller than 1.0. It has also been observed that this shift in the maximum point for a given area ratio is accompanied by an increase in the value of Φ. Considering the maximum for all area ratios, an over-all maximum point apparently occurs in the region where $A_1/A_2 = 0.7$ and $M_1/M_2 = 0.81$. Based on the above conclusions, Rupe [9] correlated his data from a pair of impinging streams with the ratio of the velocity heads and stream diameters, i.e., $(\rho_1 V_1^2 D_1)/(\rho_2 V_2^2 D_2) = 1.0$. Elverum and Morey [46] later used this equation to show that the momentum ratio has to be equal to the jet diameter ratio in order to have optimum mixing, i.e.,

$$M_1 / M_2 = (\rho_1 V_1^2 D_1^2)/(\rho_2 V_2^2 D_2^2) = D_1 / D_2 .$$

Using the mixture ratio in this equation, they wrote the following correlation for optimum mixing:

$$\left(\frac{w_1}{w_2}\right)^2 \left(\frac{\rho_2}{\rho_1}\right) \left(\frac{D_2}{D_1}\right)^3 = 1$$

Effect of the Area Scale

Rupe [9] also considered the effect of the area scale. His mixing tests showed that a nearly linear trend existed between the mixing coefficient and the area scale. The mixing factor increased with increasing the area scale. However, the changes in mixing factor were small compared with area changes. He suggested that the available energy is utilized in a more efficient manner as the stream diameter increases or that the increase in kinetic energy available for mixing and/or increase in Reynolds number influences both scale and magnitude of stream turbulence so as to increase mixing.

Physical Properties

Changes in fluid properties influence mixing by changing the hydraulic characteristics of the orifices due to changes in Reynolds number, and by changing the stream dynamics. The physical properties of a liquid that could have an influence on the mixing include density, viscosity, surface tension, and miscibility. The influence of density on stream dynamics is basically incorporated in correlations with momentum or kinetic energy. The surface tension effect may have small influence on the mixing compared to large liquid inertia. The effect of viscosity, in addition to its effect on stream characteristics, may appear in the shear layer in the preatomization region. This effect has not been investigated [45].

Nozzle Characteristics

Hoehn and Rupe [48], and Nurick [49] have considered nozzles with different inlet conditions. They have found that for circular unlike-impinging-doublet elements the mixing uniformity decreases with using sharp edged orifices. They have attributed this reduction to the cavitation in the orifice. Orifices that are modified by length, entrance condition, and/or subjected to different operating conditions to prevent cavitation, have resulted in higher mixing factors. Noncavitating circular orifices produce maximum mixing factor of about 8% higher than those for the cavitating flow conditions.

McHale and Nurick [50, 51] have investigated the mixing efficiency in noncircular orifices. They have concluded that noncircular elements produce significantly better mixing efficiencies than a circular unlike-doublet at equivalent design conditions. However, Hoehn et al. [52] have shown that this mixing disparity cannot necessarily be related to shape alone, nor can it be extrapolated to all noncircular orifice geometry design conditions.

Pattern and Number of Streams

Elverum and Morey [46] have studied mixing in two-on-one, two-on-two, and four-on-one impinging jets with circular orifices, and have provided the mixing efficiency for various flow conditions. Falk and Burick [53], Dickerson et al. [54], and Nurick and Clapp [55] have studied the mixing in arrays of like-impinging injectors. They have investigated effects of fan spacing, fan inclination angle, and the fan cant angle. Ferrenberg and Jaqua [56] have studied mixing in triplet, pentad, and coaxial element injectors and have provided the mixing efficiency as a function of various mixing parameters. A review by Riebling [57] shows that the reported correlations can be expressed in the following form for the area ratio at the maximum mixing:

$$(A_2/A_1)_{\Phi_{max}} = k[(\rho_1 / \rho_2) F^2]^b$$

where constant k is a unique function of the ratio of the number of the streams of one fluid to the number of the streams of the other fluid (n_1/n_2) and b is a constant which is relatively insensitive to changes in (n_1/n_2). Riebling's results shows that, for a constant included impingement angle, the area ratio for maximum mixing efficiency is a function of the dimensionless grouping $(\rho_1/\rho_2)F^2$ which may thus play a key role in the mixing process.

Mixing in Hypergolic Liquids

Mixing studies with hypergolic liquids have not been very extensive because of the difficulty of the measurement of the mixture fraction in the highly reactive flows. These studies have mainly reported general qualitative information on the mixing. Lawver [58], Houseman [59], Johnson [60], and Zung and White [61] have conducted experiments on the mixing process in the impingement of a nitrogen tetroxide jet with a hydrazine jet. They have reported two distinctively different separated flows. At low chamber pressures and for nitrogen tetroxide temperatures above the boiling point, significant vaporization of the oxidizer resulted in a gas/liquid impingement. The resulting spray pattern showed that hydrazine droplets were mainly confined to the fuel side. Photographs of the flame also showed that combustion mainly occured on the fuel side indicating a separated flow, termed as "blow-apart." Separated flows are also observed with liquid/liquid impingement at high chamber pressures (above 230 psia). The resulting liquid sprays showed very poor intermixing of droplets and ligaments of two liquid propellants. Stream mixing was observed at lower chamber pressures (less than 230 psia) and with nitrogen tetroxide temperatures below the boiling point. The sprays resulting from such liquid/liquid impingement showed a very uniform brownish color, indicating good intermixing of droplets and ligaments of the two propellants.

References

1. Liquid Rocket Engine Injectors, NASA SP-8089, March 1976.
2. Rupe, J.H., The Liquid-Phase Mixing of a Pair of Impinging Streams, Progress Report No. 20-195, Jet Propulsion Laboratory, Pasadena, CA, Aug. 6, 1953.
3. Lee, L.J., Ottino, J.M., Ranz, W.E., and Macosko, C.W., Impingement Mixing in Reaction Injection Molding, Poly. Eng. Sci. Vol. 20, p. 868, 1980.
4. Tucker, C.L., and Suh, N.P., Mixing for Reaction Injection Molding. I. Impingement Mixing of Liquids, Poly. Eng. Sci. Vol. 20, p. 875, 1980.
5. Nguyen, L.T., and Suh., N.P., Processing of Polyurethane/Polyester Interpenetrating Polymer Networks by Reaction Injection Molding: Part II. Mixing at High Reynolds Numbers and Impingement Pressures, Poly. Eng. Sci., Vol. 26, p. 799, 1986.
6. Mahajan, A.J., and Kirwan, D.J., Micromixing Effects in Two-Impinging-Jets Precipitator, AICHE J. Vol. 42, No. 7, July 1996.
7. Heidmann, M.F., and Humphrey, J.C., Fluctuations in a Spray Formed by Two Impinging Jets, NACA Tech Note 2349, April 1951.
8. Heidmann, M.F., Priem, R.J., and Humphrey, J.C., A Study of Sprays Formed by Two Impinging Jets, NACA Tech Note 3835, March 1957.
9. Rupe, J.H., A Correlation Between the Dynamic Properties of a Pair of Impinging Streams and the Uniformity of Mixture-Ratio Distribution in the Resulting Spray, Progress Report No. 20-209, Jet Propulsion Laboratory, Pasadena, CA, Mar. 28, 1956.
10. Taylor, G.I., Formation of Thin Flat Sheets of Water, Proc. Roy. Soc. A, Vol. 259, pp. 1–17, 1960.
11. Dombrowski, N., and Hooper, P.C., A Study of the Sprays Formed by Impinging Jets in Laminar and Turbulent Flow, J. Fluid Mechanics, Vol. 18, Part 3, pp. 392–400, 1964.
12. Fukui, N., and Sato, The Study of a Liquid Atomization by the Impingement of Two Jets, Bull. JSME, Vol. 15, p. 609, 1972.
13. Becker, H.A., and Booth, B.D., Mixing in the Interaction Zone of Two Free Jets, AICHE J., Vol. 21, p. 949, 1975.
14. Kang, B.S., Shen, Y.B., and Poulikakos, D., Holography Experiments in the Breakup Region of a Liquid Sheet Formed by Two Impinging Jets, Atom. Sprays, Vol. 5, pp. 387–402, 1995.
15. Lai, W.H., Huang, W., and Jiang, T.L., Characteristic Study on the Like-Doubled Impinging Jets Atomization, Atom. Sprays, Vol. 9, pp. 277–289, 1999.
16. Arai, M. and Saito, M., Atomization Characteristics of Jet-to-Jet and Spray-to-Spray Impingement Systems, Atom. Sprays, Vol. 9, pp. 399–417, 1999.
17. Hasson, D., and Peck, R.E., Thickness Distribution in Sheet Formed by Impinging Jets, AICHE J., Vol. 10, p. 752, 1964.
18. Ibrahim, E.A., and Przekwas, A.J., Impinging Jets Atomization, Phys. Fluids A. Vol. 3, pp. 2981–2987, 1991.
19. Shen, Y. –B., and Poulikakos, D., Thickness Variation of a Liquid Sheet Formed by Two Impinging Jets Using Holographic Interferometry, Trans. ASME, Vol. 120, pp. 482–487, Sept. 1998.
20. Vassallo, P., Ashgriz, N., and Boorady, F.A., Effect of Flow Rate on the Spray Characteristics of Impinging Water Jets, AIAA J. Propul. Power, Vol. 8, No. 5, Sept.–Oct., 1992.
21. Anderson, W.E., Ryan, H.M., Pal, S., and Santoro, R.J., Fundamental Studies of Impinging Liquid Jets, AIAA Paper No. 92-0458, 1992.
22. Ryan, H.M., Anderson, W.E., Pal, S., and Santoro, R.J., Atomization Characteristics of Impinging Liquid Jets, AIAA J. Propul. Power, Vol. 11, No. 1, pp. 135–145, Jan.–Feb., 1995.
23. Li, R., and Ashgriz, N., Characteristics of Liquid Sheets Formed by Two Impinging Jets, Phys. Fluids, Vol. 18, No. 8, p. 087104, 2006.
24. Rayleigh, Lord "On the Instability of Jets", Proc. Lond. Math. Mech. Vol. 10, pp. 4–13, 1878.
25. Bremond, N., and Villermaux, E., Atomization by Jet Impact, J. Fluid Mech. Vol. 549, pp. 273–306, 2006.

26. Choo, Y, and Kang, B, A Study on the Velocity Characteristics of the Liquid Elements Produced by Two Impinging Jets, Exp. Fluids Vol. 34, pp. 655–661, 2003.
27. Huang, J.C.P., The Breakup of Axisymmetric Liquid Sheets, J. Fluid Mech. Vol. 43, p. 305, 1970.
28. Bush, J.W.M., and Hasha, A., On the collision of laminar jets: fluid chains and fishbones, J. *Fluid Mech*., Vol. 511, pp. 285–310, 2004.
29. Shen YB, Poulikakos D., Impinging jet atomization at elevated and supercritical ambient temperature and pressure conditions, *Experimental Heat Transfer*, JAN-MAR, Vol. 11, Issue: 1, pp. 23–40, 1998.
30. Ramamurthi, K., Nandakumar, K., and Patnaik, R.K., Characteristics of Sprays Formed by Impingement of a Pair of Liquid Jets, *J. of Prop & Power*, Vol. 20, No. 1, pp. 76–82, 2004.
31. Kang, B.S., and Poulikakos, D., Holography Experiments in a Dense High-Speed Impinging Jet Spray, J. of Prop. & Power, vol. 12, No. 2, pp. 341–348, 1996.
32. Taylor, G.I., Formation of Thin Flat Sheets of Water, Proc. Roy. Soc. A Vol. 259, p. 1, 1960.
33. Naber, J.D., and Reitz, R.D. SAE Paper No. 880107, 1988.
34. Dombrowski, N., and Fraser, R.P. A Photographic Investigation into the Disintegration of Liquid Sheets, Philos. Trans. Vol. 247, No. 924, pp. 101–130, 1954.
35. Dombrowski, N., Hasson, D., and Ward, D.E. Some Aspects of Liquid Flow Through Fan Spray Nozzles, Chem. Eng. Sci. Vol. 12, pp. 35–50, 1960.
36. Dombrowski, N., and Hooper, P.C., Fuel, 41, 323, 1962.
37. Tanasawa, Y., Sasaki, S., and Nagai, N., Tech. Rep. Tohoku University, 22, 73, 1957.
38. Jung, K., Khil, T., Yoon, Y., Effect of Orifice Internal Flow on Breakup Characterisitcs of Like-Doublet Injectors, J. Prop. & Power, Vol. 22, No. 3, pp. 653–660, 2006.
39. Dombrowski, N., and John, W.R., The Aerodynamic Instability and Disintegration of Viscous Liquid Sheets, Chem. Eng. Sci., Vol. 18, pp. 203–214, 1963.
40. Ingebo, R.D., Drop Size Distribution for Impinging-Jet Breakup in Airstream Simulating the Velocity Conditions in Rocket Combustors, NACA TN4222, March 1958.
41. Kuykendal, W., The Effect of Injector Design Variables on Average Drop Size for Impinging Jet, AFRPL-TR-70-53, May 1970.
42. Hautman, D.J., Spray Characterization of Like-on-Like Doublet Impinging Rocket Injectors, AIAA paper # 91-0686, presented at 29th Aerospace Sciences Meeting, Reno, NV, Jan. 7–10, 1991.
43. Lourme, D., Like-on-Like Injector Spray Characterization for the Ariane Viking Engine, AIAA/SAE/ASME 22nd Joint Propulsion Conference, Huntsville, AL, June 16–18, 1986.
44. Zajac, L., Correlation of Spray Dropsize Distribution and Injector Variables, Rocketdyne Report R-8455, Contract NAS7-726, February 1971.
45. Ashgriz, N., Talley, D., Brocklehurst, B., and Christensen, T., On the Mixing Mechanisms in a Pair of Impinging Jets, AIAA-1995-2421, ASME, SAE, and ASEE, Joint Propulsion Conference and Exhibit, 31st, San Diego, CA, July 10–12, 1995.
46. Elverum Jr., G.W., and Morey, T.F., Criteria for Optimum Mixture-Ratio Distribution Using Several Types of Impinging-Stream Injector Elements, Jet Propulsion Laboratory, Memorandum No. 30-5, 1959.
47. Elko, E.R., and Stary, M.L., Final Report and Design Handbook of Acid-Aniline Rocket Motor and Injector Design, Report No. 455, Azusa (CA): Aerojet Engineering Corporation, June 9, 1950.
48. Hoehn, F., and Rupe, J., Flow Cavitation Effects on the Mixing Characteristics of Bipropellant Doublets, 8th JANNAF Combustion Meeting, CPIA Pub. 220, Vol. 1, pp. 569–582, Nov. 1971.
49. Nurick, W.H., Orifice Cavitation and Its Effect on Spray Mixing, ASME J. Fluids Eng., pp. 681–687, Dec. 1976.
50. McHale, R.M., and Nurick, W.H., Noncircular Orifice Holes and Advanced Fabrication Techniques for Liquid Rocket Injectors Phase I Final Report, NASACR-108570, Rocketdyne Division of North American Rockwell Corp., Oct. 1970.

51. McHale, R.M., and Nurick, W.H., Noncircular Orifice Holes and Advanced Fabrication Techniques for Liquid Rocket Injectors, Comprehensive Program Summary (Phases I, II, II, and IV), NASA-CR-134315, Rocketdyne Division of North American Rockwell Corp., March 1974.
52. Hoehn, F.W., Rupe, J.H., and Sotter, J.G., Liquid-Phase Mixing of Bipropellant Doublets, Jet Propulsion Laboratory, Technical Report 32-1546, 1972.
53. Falk, A.Y., and Burick, R.J., Injector Design Guidelines for Gas/Liquid Propellant Systems, NASA CR-120968, 1968.
54. Dickerson, R., Tate, K., and Barsic, N., Correlation of Spray Injector Parameters with Rocket Engine Performance, Technical Report AFRPL-TR-68-147, Rocketdyne Division of North American Rockwell Corporation, Canoga Park, CA, June, 1968.
55. Nurick, W.H., and Clapp, S.D., An Experimental Technique for Measurement of Injector Spray Mixing, AIAA J. Spacecraft Vol. 6, No. 11, 1969.
56. Ferrenberg, A., and Jaqua, V., Atomization and Mixing Study, Rockwell International, Rocketdyne Division, Report No. RI/RD83-70, 1983.
57. Riebling, R.W., Criteria for Optimum Propellant Mixing in Impinging–Jet Injection Elements, AIAA J. Spacecraft Vol. 4, No. 6, pp. 817–819, 1967.
58. Lawver, B.R., An Experimental Study of the N_2O_4/N_2H_4 Jet Separation Phenomena, 5th ICRPG Combustion Conference, Oct. 1–3, 1968, CPIA Pub. No. 183, pp. 263–270, 1968.
59. Houseman, J., Combustion Effects in Sprays, 5th ICRPG Combustion Conference, Oct. 1–3, 1968, CPIA Pub. No. 183, pp. 255–261, 1968.
60. Johnson, B., An Experimental Investigation of the Effects of Combustion on the Mixing of Highly Reactive Liquid Propellants, Technical Report 32-689, Jet Propulsion Laboratory, Pasadena, CA, July 15, 1965.
61. Zung, L.B., and White, J.R., Combustion Process of Impinging Hypergolic Propellants, 7th JANNAF Combustion Meeting, CPIA Pub. 204, Vol. 1, pp. 455–474, Feb. 1971.

Chapter 31
Splash Plate Atomizers

A. Sarchami and N. Ashgriz

Abstract Prediction of droplet size and velocity distribution produced by splash plate requires information on the liquid sheet characteristics and its breakup process. This chapter focuses on the sheet produced by splash plate nozzles and their characteristics such as sheet breakup length and produced droplet size. It explains different flow regimes occurring in splash plate nozzles as well as various breakup lengths provided by different researchers. Sheet formation phenomenon is explained theoretically and at the end correlations for droplet size prediction are provided.

Keywords Breakup length · Droplet size distribution · Sheet thickness · Sheet perforation · Splash plate nozzle · Stability · Thickness

Introduction

A splash plate nozzle consists of a flat plate of round cross-section attached at an angle to the end of a pipe. Fluid enters the nozzle at a relatively low velocity. It accelerates in the tapered section and finally exits from the short straight section. The stream of fluid impinges on the flat plate fixed at an angle, typically between 35° and 55° depending on the manufacturer and the particular application. The jet spreads out on the plate into a broad flat sheet which continues to expand and finally breaks into ligaments and droplets [1]. This method has several advantages, such as low injection-pressure loss and high controllability of the general liquid films [2]. Schematic of the nozzle and formed fluid sheet is shown in Fig. 31.1.

Splash plate nozzles are used in many of the rocket engines (early versions of Lance booster engine and Gemini maneuvering engines), and variety of large engines and boilers (such as in Kraft recovery boilers) [8, 9]. Splash plate nozzles are categorized as liquid-film producing nozzles. These types of nozzles provides large contact area between the liquid and the surrounding air at the atomization

A. Sarchami (✉)
Department of Mechanical and Industrial Engineering, University of Toronto, Canada

N. Ashgriz (ed.), *Handbook of Atomization and Sprays*,
DOI 10.1007/978-1-4419-7264-4_31, © Springer Science+Business Media, LLC 2011

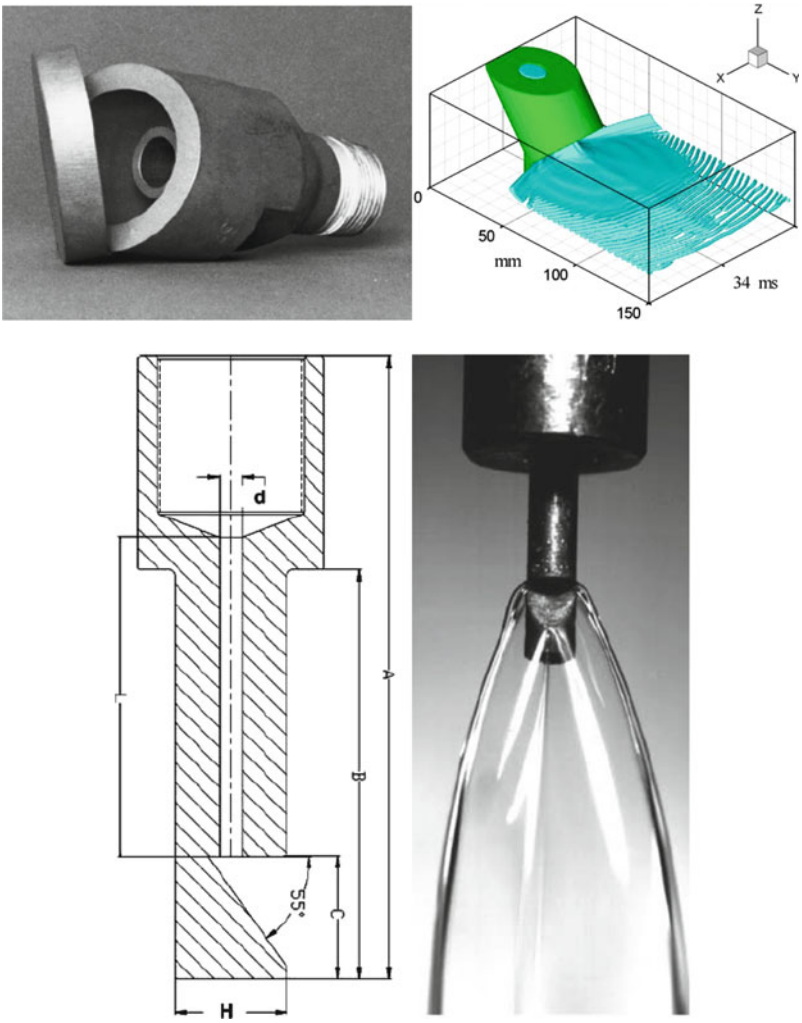


Fig. 31.1 Schematic of a splash plate nozzle [1, 25, 31] [Courtesy of TAPPI Press] [Courtesy of Springer] [Courtesy of MP. Fard et al.]

stage, and therefore, provide more efficient atomization [5–7]. The wall impingement nozzles are commonly used in devices where a large diameter orifice is necessary to either provide a large mean flow rate, such as in fire sprinklers, or where a highly viscous fluid is used, such as splash plate nozzles in recovery boilers [3]. Splash plate nozzles are also used in recovery boilers to inject black liquor (a by-product of pulping process) into the furnace. Recovery boilers are to burn black liquor, a by-product of chemical pulping [1]. Black liquor consists of many inorganic cooking chemicals along with lignin (the main non-carbohydrate constituent of wood that binds to cellulose fibers and hardens and strengthens the cell walls of plants) and other organic matter separated from the wood during the pulping process [1].

Sheet Characteristics

The sheet development in splash plate nozzles depends on the impinging jet velocity, fluid properties, and the splash plate design and it is similar to that in two-jet impingement, as illustrated in chapter 30. Figure 31.2 shows the sheet characteristics as a function of jet velocity and viscosity for a 1 mm diameter nozzle [25]. Fluid viscosity is changed by using mixture of water and corn syrup. At a low jet velocity of 15 m/s and a low viscosity of 1 mPa.s (water only), the liquid sheet formed is non-smooth but coherent. The sheet has an open rim and a bay leaf-like shape and it breaks into small droplets at its edges. At a higher viscosity of 14 mPa.s, the sheet becomes smooth and it is still open rim. Increasing the viscosity to 80 mPa.s, results in the contraction of the sheet angle and extension of the breakup point. The sheet becomes thicker and, consequently, it takes a longer time for it to breakup. Increasing viscosity to 170 mPa.s, results in a closed rim bay leaf without any atomization. Generally, increasing the viscosity dampens the surface waves and reduces the lateral spreading of the fluid. The second and the third columns in Fig. 31.2 show liquid sheets formed from the same nozzle but at higher jet velocities of 21 and 30 m/s, respectively. The high velocity increases the lateral spreading of the sheet. For low viscosity liquids, sheets become unstable more rapidly than for high viscosity cases. However, for high viscosity liquids, i.e., $\mu_l =$ 170 mPa.s, sheets become smoother, longer and narrower. Effects of velocity and viscosity on the sheet are somewhat different. An increase in jet velocity, forces the fluid to exit the splash plate through a wider angle, whereas an increase in viscosity limits spreading of the fluid. Therefore, fluid velocity sets the initial spreading angle, whereas the fluid viscosity limits the extension of fluid spreading. This may become evident by considering the first row in Fig. 31.2, which represents water sheets at three different velocities of 15, 21, and 30 m/s, from right to left, respectively. It is noted that the spreading angle substantially increases as the velocity increases. This is also evident for all other viscosities in Fig. 31.2. Considering the columns of Fig. 31.2 (constant velocity) shows that the initial spreading angle decreases and the width of the sheet reduces as the viscosity increases. After a certain viscosity, there is no rim breakup and droplets are formed only after the sheet is broken [25].

Various sheet breakup regimes are plotted in Fig. 31.3 in Ohnesorge-Reynolds plane, where Ohnesorge number is defined as $Oh = \mu/(\rho d\sigma)^{0.5}$. The *Oh–Re* plane is divided into three main regions. Below line I, sheet does not form and the breakup process is by capillary jet instability. Above line I, a clear liquid sheet is formed and the breakup process is mainly by the breakup of the sheet. The empirical relation for the transition from jet to sheet breakup is found to be:

$$Oh = \frac{75}{Re^{1.1}} \tag{31.1}$$

Line II represents the boundary between sheet breakup without (below the line) and with perforations. The transition from laminar to turbulent sheets is observed at $Re \sim 3{,}000$. The region between lines I and II can be divided into three zones.

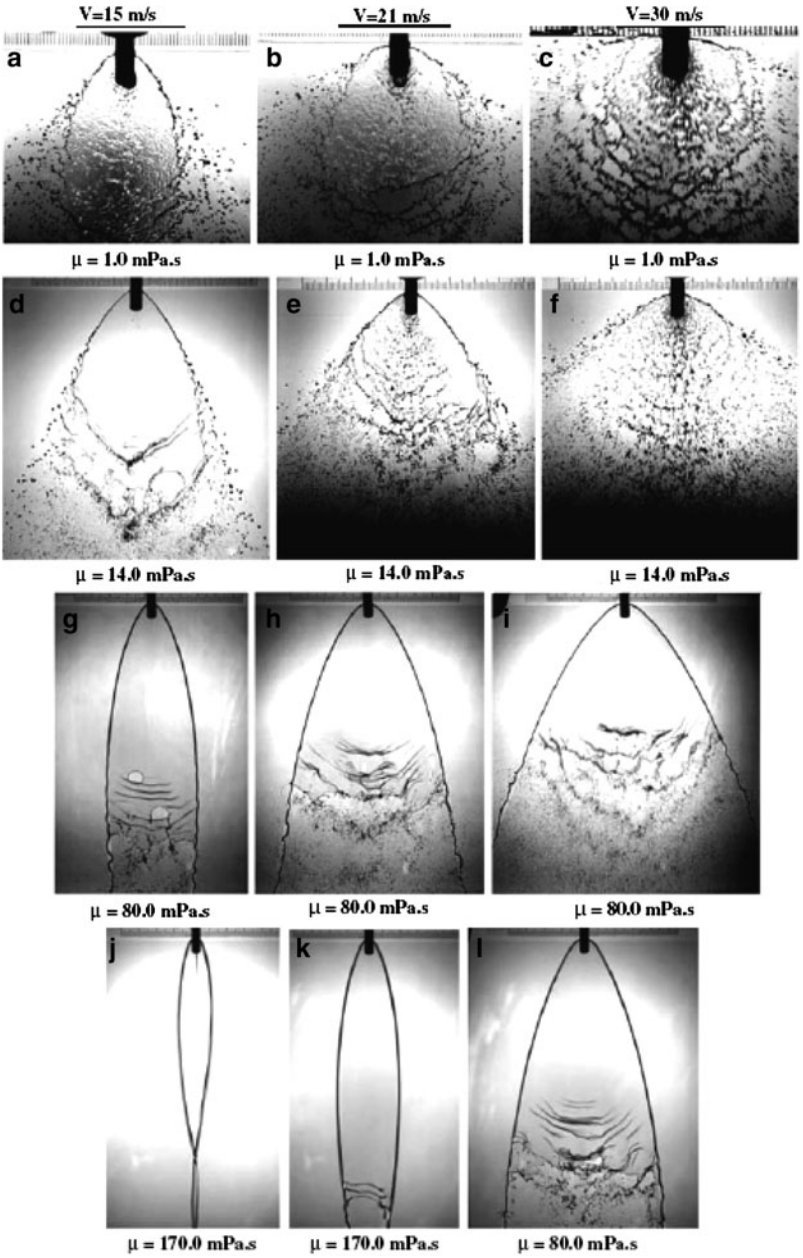


Fig. 31.2 Effect of the viscosity on break-up regime at different values of flow velocity using a splash-plate nozzle with 1.0 mm diameter [25]. [Courtesy of Springer]

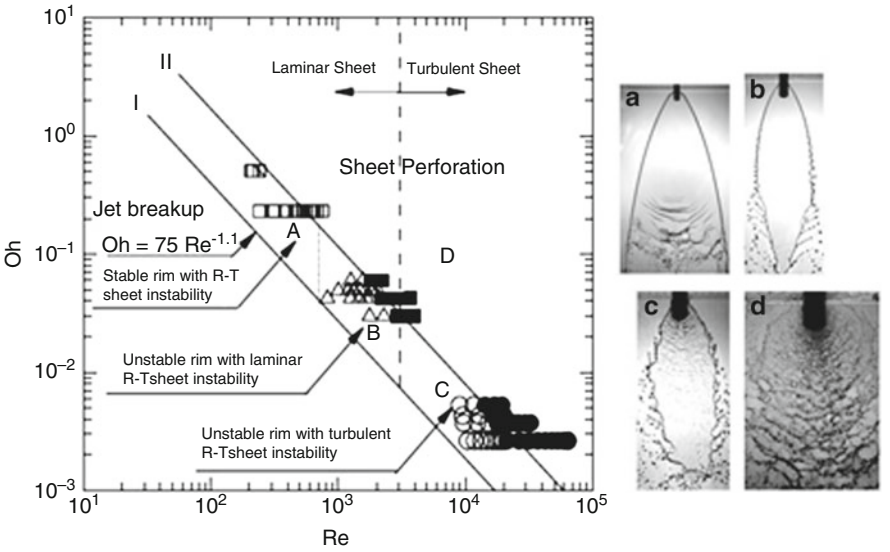


Fig. 31.3 Jet and sheet breakup regimes behavior with Reynolds number and Ohnserge number [26] [Reprint with permission of the American Institute of Aeronautics and Astronautics]

Sheets produced in zone ''A'' ($Re < 800$) have relatively stable rim. The Reynolds numbers are low, therefore, viscous effects are dominate. Open rim sheets are typically broken at their open edges. As the Reynolds number is increased, the rims become unstable rapidly. Therefore, in zone ''B'' ($800 < Re < 3{,}000$), the sheet breakup process includes both a laminar capillary instability at the rims and Taylor instability on open edges of the sheet. Similar breakup process is observed in zone ''C,'' except that the whole flow is turbulent. Therefore, the breakup process in this zone is identified as turbulent rim instability combined with turbulent sheet instability. The data points in this zone are within $7{,}000 < Re < 18{,}000$. For $Re >$ 18,000 the rim cannot be distinguished, and the breakup process is mainly turbulent sheet breakup [26].

Breakup Length

Based on a stationary antisymmetric wave theory, Dombrowski and Hooper [18] developed the following correlation for the break-up length of liquid sheets produced by fan nozzles:

$$L_b = 1.5\left[K\frac{\rho}{\rho_g} ln\left(\frac{\zeta_o}{\lambda}\right)\left(\frac{We_h^{0.5}(We_h - 1)}{(We_h - 1)^2}\right)\right]^{0.5} \tag{31.2}$$

where $We_L = \rho U^2 h/\sigma$ is the Weber number, U is the velocity of the liquid sheet, K is the thickness parameter for the fan spray nozzle, ρ and ρ_g are the densities of the

liquid and the gas, respectively, and ζ_o and λ are the initial disturbance and wave amplitudes, respectively. They concluded that the break-up length increases with increasing shear viscosity and decreases with increasing sheet velocity.

Arai and Hashimoto [19] reported the following correlation for the sheet break-up length of a viscous sheet:

$$\frac{L_b}{h} = \frac{416 Re_h^{0.6}}{h^{0.5} We_h^{0.5}} \tag{31.3}$$

The linear theories, however, do not properly predict the sheet break-up behavior. They under predict the break-up length by up to 50%, as reported by Ryan et al. [20]. Furthermore, the linear theories predict a decrease in sheet break-up length with increasing Weber number. However, experimental measurements indicate that the break-up length increases to a maximum, then decreases with increasing Weber number [10, 11]. In addition, the break-up length is linearly proportional to the Weber number, and it increases with decreasing impinging angle (more aligned with the impinging surface) and increasing jet velocity, as reported by Ryan et al. [20], Huang [21], Anderson et al. [22], and Li and Ashgriz [23].

Ahmad et al. [24] provided two correlations for the breakup length. One for increasing breakup length with flow rate, and the other one for decreasing breakup length with flow. For increasing breakup length they provided:

$$\frac{L_b}{d} = 126 \frac{We_d^{0.2}}{Re_d^{0.25}} \tag{31.4}$$

And when the break-up length decreases with increasing the flow velocity:

$$\frac{L_b}{d} = 1340 \frac{1}{We_d^{0.14} Re_d^{0.22}} \tag{31.5}$$

Fluid Sheet Formation – Sheet Thickness and Velocity

In order to predict the size of the droplets that form from splash plate nozzles, it is necessary to characterize the liquid sheet, namely its velocity and thickness distribution [4]. There are different theoretical, numerical and experimental studies on the liquid sheet formation. These studies include both jet impingement on a wall and jet on jet impingement.

Inamura et al. [2] have developed a model for oblique impingement of a jet on a solid wall. The model considers inclined impingement and it is based on boundary layer development on the wall.

Following assumptions are made for the analysis: (1) Flow is laminar and two dimensional with uniform jet velocity. (2) Upon impingement, laminar boundary layer develops. (3) A quadratic velocity profile is assumed for the flow inside the

boundary layer: $u_s = U(r)(2\eta - 2\eta^3 + \eta^4)$ where $\eta = z/h(r)$. (4) The liquid flowing in an angle $d\alpha$ in the liquid jet flows in an angle $d\phi$ in the liquid film. The following geometric relation exists between angles: $\tan(\phi) = \sin(\theta)\tan(\alpha)$ where the angles are shown in Fig. 31.4. (5) Due to the oblique impingement, center line of the jet is

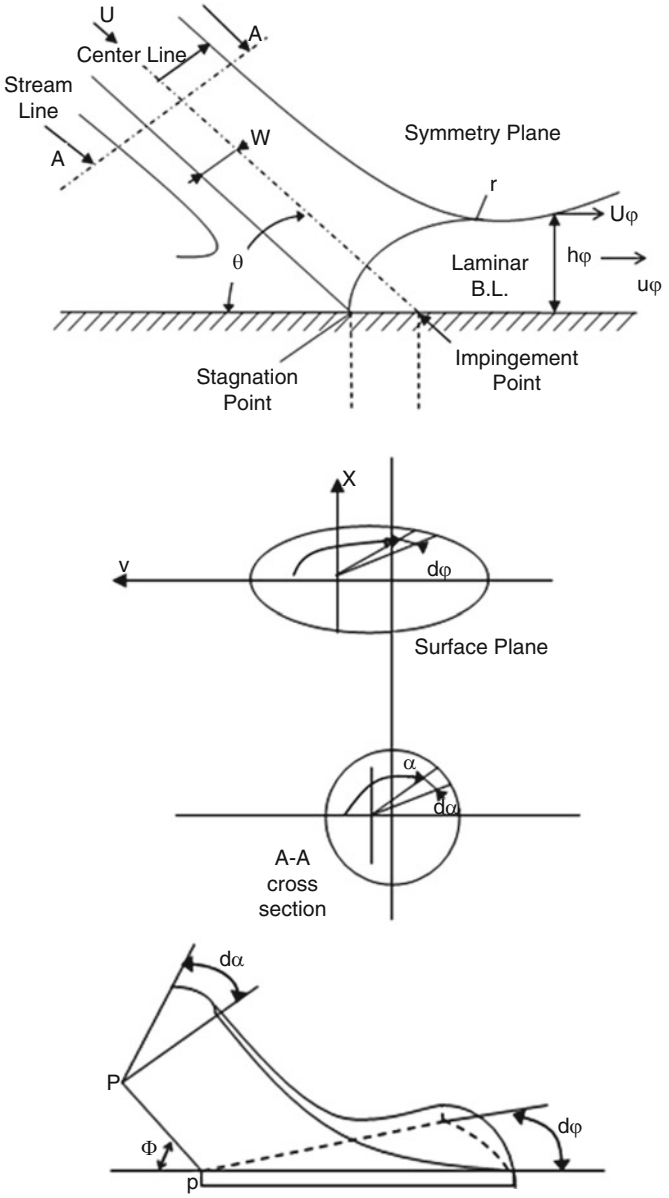


Fig. 31.4 Jet impingement orientation [2] [Reprint with permission of the American Institute of Aeronautics and Astronautics]

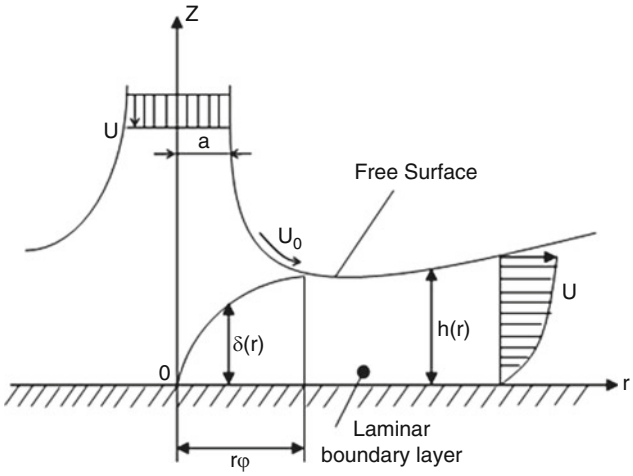


Fig. 31.5 Schematic of jet impingement on the wall [4] [Courtesy of A. Sarchami]

not the same with the streamline passing the stagnation point. The distance between these two lines are: $\omega = \mathrm{r}_0 \cos(\theta)$. (6) The effect of air flow and gravity is ignored.

Figure 31.5 demonstrates the schematic of the jet impingement. To simplify, the figure refers to the vertical impingement but the resulting equations are not limited to vertical impingement.

For the boundary layer the continuity and momentum equations are:

$$\frac{\partial(ru_s)}{\partial r} + \frac{\partial(rw_s)}{\partial z} = 0 \tag{31.6}$$

$$u_s \frac{\partial u_s}{\partial r} + w_s \frac{\partial u_s}{\partial z} = v \frac{\partial^2 u_s}{\partial z^2} \tag{31.7}$$

By changing the coordinate frame to cylindrical frame the momentum equation eventually becomes

$$\left(\frac{d}{dr} + \frac{1}{r}\right) \int_0^{\delta} (u_j u_s - u_s^2) dz = v \left(\frac{\partial u_s}{\partial z}\right)_{z=0} \tag{31.8}$$

Here the flow is categorized using, the point where the laminar boundary layer reaches the sheet surface, $r_\phi = r_{\phi db}$:

(1) In the case of $r_\phi \leq r_{\phi db}$ the velocity distribution across the boundary layer is expressed by: $u_s = u_0.(2\eta - 2\eta^3 + \eta^4)$. where $\eta = z/\delta_\phi(r)$

Considering that $r = 0$: $\delta = 0$ and substituting above velocity profile in the cylindrical form of momentum equation, following relations can be deduced

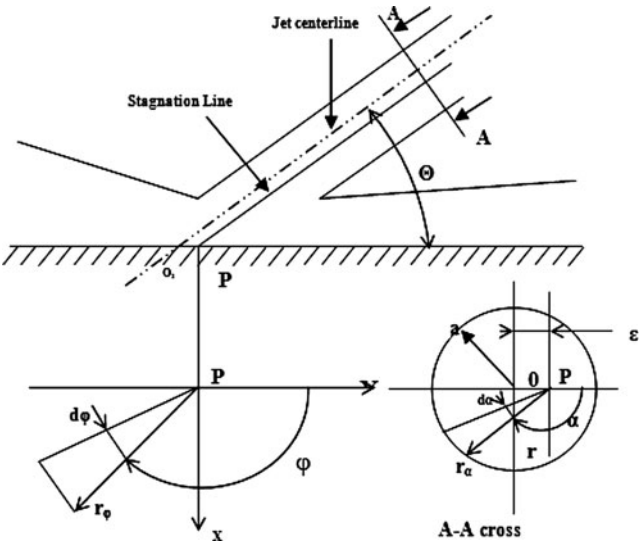


Fig. 31.6 Jet orientation for mass conservation relations [4] [Courtesy of A. Sarchami]

$$\delta_{\phi}^{*} = 5.97 r_{\phi}^{*\,1/2} \tag{31.9}$$

where $r_{\phi}^{*} = (r_{\phi}/r_j)Re^{-\frac{1}{3}}$, $\delta_{\phi}^{*} = (\delta_{\phi}/r_j)Re^{\frac{1}{3}}$, $Re = q/r_j\nu_{\ell}$, and $q = \pi r_j^2 u_0$.

In order to determine $r_{\phi db}$ and develop an independent relation for that, assume: $\varepsilon = \cos\theta$. According to Fig. 31.6, we have:

$$dq_{\alpha} = \int_0^{r_{an}} u_0 r_{\alpha} d\alpha dr_{\alpha} \tag{31.10}$$

where

$$r_{an} = -r_j\varepsilon\cos\alpha + \left\{\left(r_j\varepsilon\cos\alpha\right)^2 - \left(r_j\varepsilon\right)^2 + r_j^{\,2}\right\}^{\frac{1}{2}} \tag{31.11}$$

From the above equation using expression for dq_{α}:

$$dq_{\alpha} = \frac{u_0 d\alpha}{2}\left[-r_j\varepsilon\cos\alpha + \left\{\left(r_j\varepsilon\cos\alpha\right)^2 - \left(r_j\varepsilon\right)^2 + r_j^{\,2}\right\}^{\frac{1}{2}}\right]^2 \tag{31.12}$$

Now consider mass flux at the region of $r_{\phi} \geq r_{\phi db}$:

$$dq_{\phi} = d\phi.\, r_{\phi}.\int_0^{h_{\phi}} u_s dz \tag{31.13}$$

Also we have: $u_\phi = U_\phi(r)(2\eta - 2\eta^3 + \eta^4) = U_\phi(r)f(\eta)$ where $\eta = z/h_\phi(r)$ as a result,

$$dq_\phi = r_\phi d\phi \int_0^{h_\phi} u_\phi(r)f(\eta)dz - \frac{7}{10} r_\phi u_\phi h_\phi d\phi \tag{31.14}$$

Now considering that, at $r_\phi = r_{\phi db}$: $h_\phi = \delta_{\phi db}$, and $U_\phi = u_0$ and using (31.9), $r_\phi^* = (r_\phi/r_j)Re^{\frac{1}{3}}$, and $\delta_\phi^* = (\delta_\phi/r_j)Re^{\frac{1}{3}}$, the relation for $r_{\Phi 0}$ is

$$r_{\phi db} = 0.564\left\{\frac{(dq_\phi)^2}{vu_0(d\phi)^2}\right\}^{\frac{1}{3}} \tag{31.15}$$

On the other hand due to the assumption (6)

$$dQdq_\Phi = dq_\alpha$$

As a result, the dimensionless $r_{\phi db}^*$ will become

$$r_{\phi db}^* = \frac{0.564}{(4\pi)^{1/2}} A^{\frac{2}{3}} B^{\frac{4}{3}} \tag{31.16}$$

where $A = \frac{\sin\theta}{\sin\phi^2 + \cos\phi^2 \sin\theta^2}$, and $B = -\varepsilon\left(\pm\sqrt{\frac{\sin\theta^2}{\tan\phi^2 + \sin\theta^2}} + \sqrt{1 - \frac{\varepsilon^2 \tan\phi^2}{\tan\phi^2 + \sin\theta^2}}\right)$.

To find the sheet thickness distribution, use dq_Φ in the region of $r_\phi \le r_{\phi db}$ which is

$$r_\phi d\phi\left\{\int_0^{\delta_\phi} udz + u_0(h_\phi - \delta_\phi)\right\} = dq_\phi \tag{31.17}$$

Using the velocity distribution across the boundary layer, obtain

$$h_\phi = \frac{dq_\phi}{r_\phi d\phi u_0} + \frac{3}{10}\delta_\phi \tag{31.18}$$

Now, using $\delta_\phi^* = (\delta_\phi/r_j)Re^{\frac{1}{3}}$, (31.12), A, B, and (31.18) obtain

$$h_\phi = \frac{r_j^2}{2r_\phi} AB^2 + \frac{3}{10}\sqrt{\frac{420}{37}\frac{v}{u_0} r_\phi} \tag{31.19}$$

Also: $h_\phi^* = (h_\phi/r_j)Re^{\frac{1}{3}}$ as a result,

$$h_\phi^* = \frac{1}{2r_\phi^*} AB^2 + 1.79\sqrt{r_\phi^*} \tag{31.20}$$

(2) In the case that $r_\phi > r_{\phi db}$, the velocity distribution across the boundary layer is expressed by: $u_\phi = U_\phi(r)(2\eta - 2\eta^3 + \eta^4) = u_\phi(r)f(\eta)$ where $\eta = z/h_\phi(r)$

Momentum equation for this region has the form of

$$\frac{d}{dr_\phi}\int_0^{h_\phi} u_\phi^2 dz + \frac{1}{r_\phi}\int_0^{h_\phi} u_\phi^2 dz - U_0\frac{d}{dr_\phi}\int_0^{h_\phi} u_\phi dz - \frac{U_0}{r_\phi}\int_0^{h_\phi} u_\phi dz = -\nu\left(\frac{\partial U_\phi}{\partial z}\right)_{z=0} \tag{31.21}$$

Using (31.13), the velocity profile and above momentum equation, obtain

$$r_\phi^* = \frac{0.564}{(4\pi)^{\frac{1}{3}}} A^{\frac{2}{3}} B^{\frac{4}{3}} \tag{31.22}$$

$$h_\phi^* = \frac{1}{2r_{\phi db}^*} AB^2 + 1.79\sqrt{r_{\phi db}^*} \tag{31.23}$$

Thus

$$h_\phi^* = \frac{0.642AB^2}{r_\phi^*} + \frac{5.03r_\phi^{*2}}{AB^2} \tag{31.24}$$

And also using (31.12), (31.14) and (31.24) the velocity of the liquid film surface is expressed by:

$$U_\phi = \frac{5}{7}\frac{u_0 r_j^2}{r_\phi h_\phi} AB^2 \tag{31.25}$$

$$\frac{U_\phi}{u_0} = \frac{1}{0.9 + 7.042A^{-2}B^{-4}r_\phi^{-3}} \tag{31.26}$$

Final Droplet Size and Velocity Distribution

There have been several investigations on the droplet sizes generated by splash plate nozzles. For instance, Mahmoud et al. [26] conducted a detailed measurement of droplet sizes, considering effects of nozzle size, fluid velocity and fluid viscosity. They found that the droplet size depends on the type of sheet breakup, e.g., perforated or turbulent breakup. Figure 31.7 shows some of their results for the variation of droplet size with flow velocity at two-different nozzle diameters of 2 and 1 mm. Increasing the viscosity, results in an increase in the resistance of liquid to spreading and consequently, a reduction in the sheet spreading angle. This will lead to an increase in the sheet thickness and consequently, an increase in the droplet size.

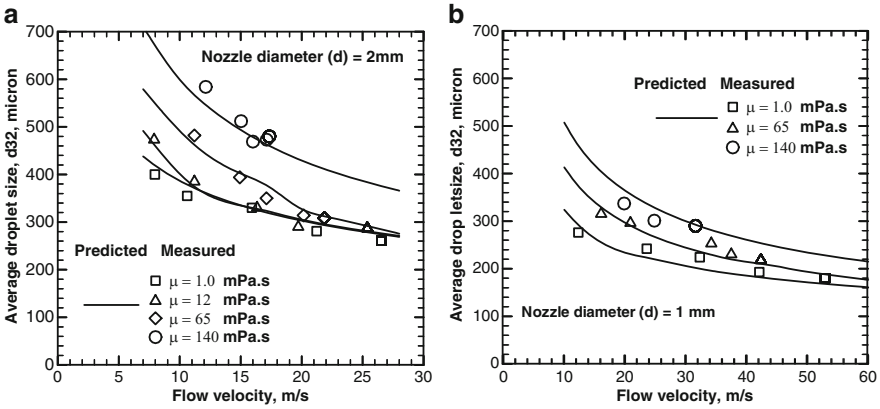


Fig. 31.7 Variation of average droplet size versus flow velocity at different values of viscosity and (**a**) nozzle diameter of 2.0 mm, and (**b**) nozzle diameter of 1.0 mm. [26] (Courtesy of AIAA)

A review of the past literature on the available correlations on the mean droplet size produced by splash plate nozzles shows that there are large discrepancies between the results. The prediction of the droplet sizes generated by splash plate nozzles is based on the Kelvin–Helmholtz (K–H) instability theory for a liquid sheet. Dombrowski and Johns [14], Dombrowski and Hooper [18] and Fraser et al. [13] developed such a theoretical model to predict droplet sizes from the breakup of a liquid sheet. They considered effects of liquid inertia, shear viscosity, surface tension and aerodynamic forces on the sheet breakup and ligament formation. Dombrowski and Johns [14] obtained the following equation for droplets produced by a viscous liquid sheet:

$$d_D = 1.882 d_L [1 + 3Oh]^{\frac{1}{6}} \tag{31.27}$$

where d_L is the ligament size and Oh is Ohnesorge number which are explained comprehensively in chapter 3. Later Adams [1] reduced Dombrowski's model to the following correlation for the droplet size:

$$d_{mm} = 1,880 \mu^{0.1} V^{-0.55} d_{or}^{0.65} \rho^{-0.21} \sigma^{0.24} \tag{31.28}$$

Bennington and Kerekes [17] developed the following empirical correlation for the Sauter mean droplet diameter generated by a splash plate atomizer used in large boilers.

$$d_{32} = 1,600 \mu^{0.18} V^{-0.54} d_{or}^{0.64} \rho^{0.36} \sigma^{0.18} \tag{31.29}$$

They used a mixture of glycerol and water to change the fluid viscosity in the range of μ = 1–15 mPa s and changed the orifice diameter in the range of 1.0.

Such large orifice diameters are typically used in boiler and furnaces. Note that the diameter is correlated with viscosity according to $d_{32} \propto \mu^{0.18}$.

Empie et al. [27] reported that the average droplet size was correlated to the viscosity according to

$$d_{mm} = 5.6\mu^{0.026}V^{-0.39} \tag{31.30}$$

This correlation was developed for splash plate nozzles used in Kraft recovery boilers. These boilers are used in the pulp and paper industry to burn black liquor, a by-product of paper making. Black liquor is a very viscous liquid and its viscosity is a strong function of temperature. Therefore, its viscosity is easily changed by changing the liquor temperature. They used splash plate nozzles with diameters of 8.5 and 9.5 mm, and the viscosity of black liquor was changed from 50 to 200 mPa s. Note that the drop diameter relates to viscosity as $d_{mm} \propto \mu^{0.026}$.

Helpio and Kankkunen [16] measured the droplet sizes for a splash plate nozzle with diameter 15–27 mm, and used black liquor as the fluid with viscosities up to 65 mPa s. They reported the following correlation:

$$d_{mm} = 1,350\mu^{0.26}V^{-0.26}d_{or}^{0.74}\rho^{-0.26} \tag{31.31}$$

They found that diameter correlated with viscosity according to $d_{mm} \propto \mu^{0.26}$.

Inamura and Tomoda [28], and Inamura et al. [2] investigated the behavior of liquid sheet generated by impingement of a liquid jet onto a solid wall. They [2] combined Dombrowski's model of sheet breakup with the sheet thickness model developed based laminar boundary-layer analysis to predict the droplet size. However, they did not provide any correlation for droplet size. Fard et al. [10] studied numerically the effect of liquid properties and nozzle geometry on the droplet size distribution produced by splash plate nozzle. Again, no correlation to relate the droplet size with the studied parameters was provided.

To conclude, there are large discrepancies among the reported correlations on the droplet size for splash plate nozzles. The theoretical predictions show that $d_{mm} \propto \mu^{0.1}$, yet the results obtained from actual industrial nozzles show a viscosity dependency of $d_{mm} \propto \mu^{0.026}$ to $d_{mm} \propto \mu^{0.26}$.

In most cases, the study has been resulted in a correlation of the droplet size as a function of the various parameters in the following general form:

$$D_m = \alpha D_n^a V_n^b \rho_l^c \mu^d \sigma^e \tag{31.32}$$

where α is a constant, D_n is the nozzle diameter, V_n is the injection velocity, ρ_l is the fluid density, μ is the fluid viscosity, σ is the surface tension, a to e are powers for each parameter, Table 31.1 shows different coefficients obtained by different researchers. Most of the studies are for specific ranges of nozzle operation [29]. Ahmed et al. [24–26] noted that case of discrepencies between various correlations is due to the sheet break-up regimes. Each regime of break-up or the type of

Table 31.1 Correlations for median droplet size in splash plate nozzles

	D_n	V_n	ρ_l	μ	σ
Theoretical [11–14]	0.65	−0.55	−0.21	0.10	0.24
Splash plate small scale [15]	0.74	−0.26	−0.26	0.26	–
Splash plate commercial scale [16]	0.75	−0.25	−0.25	0.25	–
Spalsh plate commercial scale [17]	0.64	−0.54	0.36	0.18	0.18
Splash plate general correlation [4]	0.83	−0.23	−0.11	0.12	0.46

atomization, they noted, should have its own correlation. They identified four break-up regimes; in the order of increasing Reynolds number, to be:

(i) aerodynamic sheet instability, (ii) laminar edge breakup, (iii) turbulent edge breakup, and (iv) perforation breakup. They showed that the droplet size is strongly affected by the liquid viscosity, $d_{32} \propto \mu^{0.27}$, at a low Re number and a high Oh number ($Re \leq 800$ and $Oh \geq 0.22$); it is moderately dependent on viscosity, $d_{32} \propto \mu^{0.07}$, at moderate Re and Oh numbers ($800 \leq Re \leq 3{,}000$ and $0.03 \leq Oh \leq 0.22$); whereas it is weakly dependent on viscosity, $d_{32} \propto \mu^{0.003}$, at high Re and low Oh numbers ($Re \geq 18{,}000$ and $Oh \leq 0.003$).

The exponents of the main variables (flow velocity (V), nozzle diameter (d_{or}), and liquid viscosity (μ) on correlations based on dimensionless variables were approximately the same as those developed based on dimensional variables. Nozzle diameter has a significant effect on the average droplet size. Increasing the nozzle diameter causes an increase in the average droplet size for all breakup regimes. Increasing the flow velocity results in a significant decrease in the average droplet size due to increasing the applied energy for the breakup process for all regimes.

Numerical Modeling

A model for the atomization and spray formation by splash plate nozzles is developed by Sarchami et al. [30]. This model is based on the liquid sheet formation theory due to an oblique impingement of a liquid jet on a solid surface. The continuous liquid sheet formed by the jet impingement is replaced with a set of dispersed droplets. The initial droplet sizes and velocities are determined based on theoretically predicted liquid sheet thickness and velocity. A Lagrangian spray code is used to model the spray dynamics and droplet size distribution further downstream of the nozzle.

The procedure begins with droplets injection right from the nozzle with the diameter equal to the splash plate nozzle diameter. The injected droplets hit the splash plate and break into several smaller droplets. Figure 31.8 shows side view of the splash plate atomizer at the time of injection. Each droplet at any specific trajectory has a specific velocity and size, equal to the sheet thickness and velocity at that trajectory (i.e., azimuthal angle). The model intends to substitute the smooth fluid sheet on the plate with discretized droplets having the same diameter (thickness) and velocity as the sheet. While droplets move further downstream, they interact with the surrounding gas and each other. Droplets will break, coalesce,

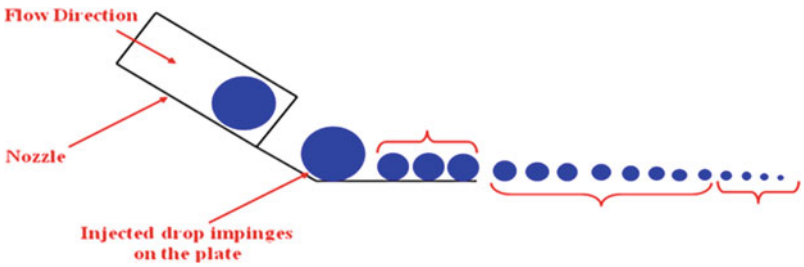


Fig. 31.8 Side view of splash plate atomizer [30] [Courtesy of American Institute of Chemical Engineers]

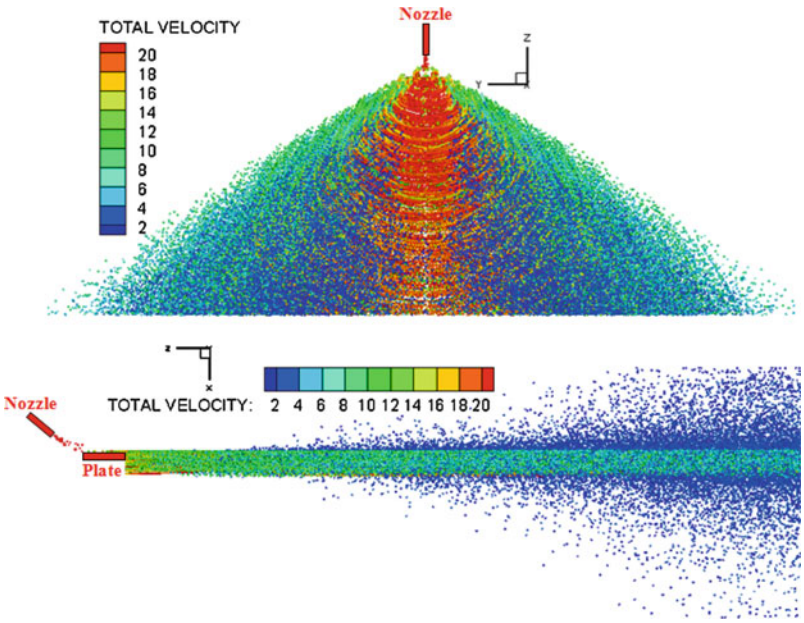


Fig. 31.9 Numerical simulation [30] [Courtesy of American Institute of Chemical Engineers]

disperse, and evaporate. Figure 31.9 demonstrates the outcome of the process while implemented in the numerical code [30].

Fard et al. [31, 32] have developed a 3D numerical model for the Impaction of a laminar liquid jet. Four different impinging velocities of 5, 8, 12, and 26.8 m/s are given in Figs. 31.10–31.13, respectively. For each figure, two images are shown: (a) a 3D view that displays the impinging jet as a whole, and (b) a close-up of the top view that shows the breakup process and droplet sizes. A comparison between the four cases shows that as the jet impinging velocity increases, the size of the droplets decreases. This is because the liquid disk formed as a result of the jet impact is thinner for a jet with a higher impact velocity. And droplets formed from the breakup of a thinner liquid sheet will have smaller sizes.

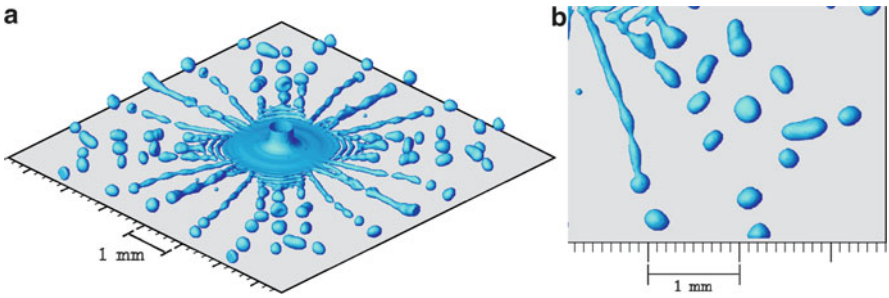


Fig. 31.10 Calculated images of the 5 m/s impact of a 0.45 mm dia. water jet on a 1.35 mm dia. splash-plate: (**a**) 3D view; (**b**) top view close-up [32] [Courtesy of J. of Atomization and Sprays]

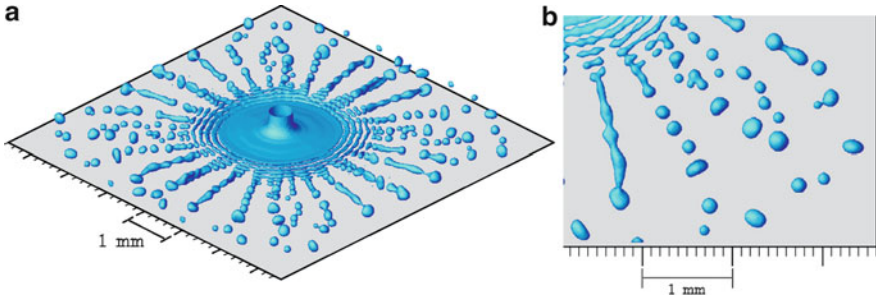


Fig. 31.11 Calculated images of the 8 m/s impact of a 0.45 mm dia. water jet on a 1.35 mm dia. splash-plate: (**a**) 3D view; (**b**) top view close-up [32] [Courtesy of Journal of Atomization and Sprays]

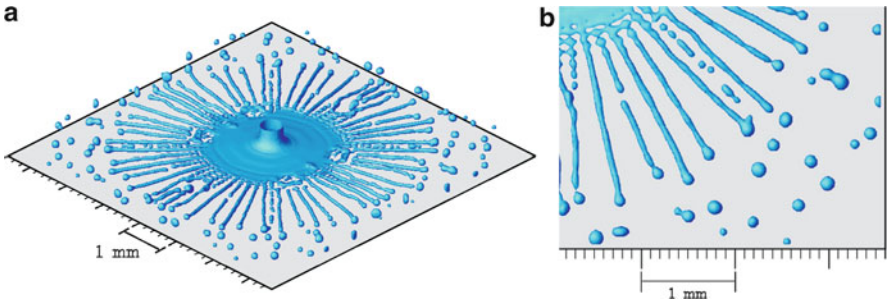


Fig. 31.12 Calculated images of the 12 m/s impact of a 0.45 mm dia. water jet on a 1.35 mm dia. splash-plate: (**a**) 3D view; (**b**) top view close-up [32] [Courtesy of Journal of Atomization and Sprays]

The breakup of liquid ligaments occurs at different locations around the periphery of the liquid sheet. The breakup locations are approximately constant with respect to time ($t > 0.5$ ms). As a result, droplets appear to form in straight lines directing outward from the liquid sheet. This configuration appears like

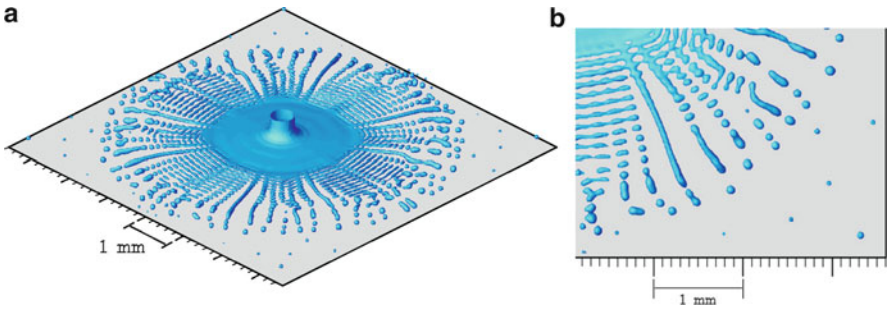


Fig. 31.13 Calculated images of the 26.8 m/s impact of a 0.45 mm dia. water jet on a 1.35 mm dia. splash-plate: (**a**) 3D view; (**b**) top view close-up [32] [Courtesy of Journal of Atomization and Sprays]

liquid fingers around the liquid disk. Figures 31.10–31.13 show the same feature in the shape of the jets at different impinging velocities with more fingers at higher velocities. Close inspection of the numerical results showed oscillations of the droplets due to surface tension effects. During these oscillations, some droplets coalesce and as a result bigger droplets are formed. The finger-like configuration of the liquid- sheet breakup and the coalescence of droplets need more investigation; these issues must be addressed based on a physical model of the breakup phenomenon.

References

1. T. N. Adams: Kraft Recovery Boilers, TAPPI Press, Atlanta (1997).
2. T. Inamura, H. Yanaoka, and T. Tomoda: Prediction of mean droplet size of sprays issued from wall impingement injector, AIAA Journal. 42 (3), 614–621 (1994).
3. N. Ashgriz, R. Washburn, and T. Barbat: Segregation of drop size and velocity in jet impinging splash plate atomizers. International Journal of Heat and Fluid Flow. 17 (5), 509–516 (1996).
4. A. Sarchami: Modeling of sprays produced by splash plate nozzles. MASc. Thesis, University of Toronto (2007).
5. G. I. Taylor: Formation of thin flat sheets of water. Proceedings of the Royal Society of London. 259, 1–17 (1960).
6. N. Dombrowski, D. Hasson, and D. E. Ward: Some aspects of liquid through fan spray nozzles. Chemical Engineering Science. 12, 35–50 (1960).
7. W. E. Ranz: Some experiments on the dynamics of liquid films. Journal of Applied Physics. 30, 1950–1955 (1950).
8. N. Bremond, and E. Villermaux: Atomization by jet impact. Journal of Fluid Mechanics 549, 273–306 (2006).
9. N. Obuskovic, and T. N. Adams: Fluid sheet thickness and velocity at the tip of a black liquor splash plate nozzle. Chemical Engineering Communications. 104, 1–20 (1990).
10. D. Levesque, M. P. Fard, S. Morrison and B. L. Spray: Understanding the effects of black liquor properties and splash-plate nozzle configuration on spray characteristics. Pulp & Paper-Canada. 106 (10), 34–39 (2005).

11. G. D. Crapper, N. Dombrowski, and W. P. Jepson: Wave growth on thin sheets of non-newtonian liquids. Proceedings of the Royal Society of London, A. 342, 225–236 (1975).
12. R. P. Fraser, P. Eisenklam, N. Dombrowski, and J. H. Routley: The atomization of a liquid sheet by an impinging air stream. Chemical Engineering Science, 18, 339–353 (1963).
13. R. P. Fraser, P. Eisenklam, N. Dombrowski, and D. Hasson: Drop formation from rapidly moving liquid sheets. AIChE Journal. 8 (5), 672–680 (1962).
14. N. Dombrowski, and W. R. Johns: The aerodynamic instability and disintegration of viscous liquid sheets. Chemical Engineering Science 18 (3), 203–214 (1963).
15. A. Kankkunen, T. Helpio, and P. Rantanen: Small scale measurements of black liquor spraying with splash plate nozzles. TAPPI Engineering Conference Proc., TAPPI Press, Atlanta, pp. 207–214 (1994).
16. T. Helpio, and A. Kankkunen: Measurements of the effect of black liquor firing temperature on atomization performance, Part 2: Drop size measurements. Helsinki Technical University, Laboratory of Energy Engineering and Environmental Protection, Research report (1994).
17. C. Bennington, and R. Kerekes: The effect of temperature on drop size of black liquor sprays. Journal of Pulp and Paper Science. 12 (6), J181–J186 (1986).
18. N. Dombrowski, and P. Hooper: A study of sprayed formed by impinging jets in laminar and turbulent flow. Journal of Fluid Mechanics. 18, 392–440 (1964).
19. T. Arai, and H. Hashimoto: Disintegration of a thin liquid sheet in a concurrent gas stream. International Journal of Turbo Jet Engines, 3, 301–306 (1986).
20. H. Ryan, W. Anderson, S. Pal, and R. Santoro: Atomization characteristics of impinging jets. Journal of Proportional Power, 11, 135–145 (1995).
21. J. Huang: The break-up of axisymmetric liquid sheets. Journal of Fluid Mechanics, 43, 305–319 (1970).
22. W. Anderson, H. Ryan, S. Pal, and R. Santoro: Fundamental studies of impinging liquid jets. 30th Aerospace Sciences Meeting and Exhibition, Paper No. AIAA 92-0458 (1992).
23. R. Li, and N. Ashgriz: Characteristics of liquid sheets formed by two impinging jets. Physics and Fluids, 18, 087104 (2006).
24. M. Ahmed, N. Ashgriz, H. N. Tran: Break-up length and spreading angle of liquid sheets formed by splash plate nozzles. Journal of Fluid Engineering, 131, 1–9.
25. M. Ahmed, A. Amighi, N. Ashgriz, and H. N. Tran: Characteristics of liquid sheets formed by splash plate nozzles. Experimental Fluids 44, 125–136 (2008).
26. M. Ahmed, N. Ashgriz, and H. N. Tran: Influence of breakup regimes on the droplet size produced by splash-plate nozzles. AIAA Journal, 47 (3), 516–522.
27. H. Empie, S. Lien, and W. Yang: Effect of black liquor type on droplet formation from commercial spray nozzles. Journal of Pulp and Paper Science, 21 (2), J63–J67 (1995).
28. T. Inamura, and T. Tomoda: Characteristic of spray through wall impinging nozzles. Atomization and Sprays, 14, 375–395 (2004).
29. A. Sarchami, N. Ashgriz, and H. N. Tran: Initial perturbation amplitude of liquid sheets produced by jet impingement nozzles. AIAA Journal, 47 (11), 2775–2778 (2009).
30. A. Sarchami, N. Ashgriz, and H. N. Tran: An atomization model for splash plate nozzles. AIChE Journal, 56 (4), 849–857 (2009).
31. M. P. Fard, N. Ashgriz, J. Mostaghimi, D. M. Levesque, and S. Morrison: Film thickness and velocity distribution in a splash-plate atomizer: Comparison between simulations and experiments. ICLASS 2003.
32. M. P. Fard, D. Levesque, S. Morrison, N. Ashgriz, J. Mostaghimi: Characterization of splash plate atomizers using numerical simulations. Atomization and Sprays, 17 (4), 347–380 (2007).

Chapter 32
Electrosprays

F. Sultan, N. Ashgriz, D.R. Guildenbecher, and P.E. Sojka

Abstract This chapter provides an introduction to electrosprays (ES). Electrosprays, also known as Electrohydrodynamic (EHD) sprays, are sprays created from the atomization of a bulk liquid due to electrostatic charging. The fundamental physics involved in such sprays is first introduced followed by results of experimental and theoretical characterization. Practical applications are briefly discussed with special attention paid to the use of electrospray in mass spectrometry where it is used as an ion source.

Keywords Aerodynamic effects · Charged droplets · Cone jet · Droplet evaporation · Droplet deformation · Electrohydrodynamic spray · Electrospray · Ion source · Mass spectrometry · Mass spectroscopy · Rayleigh charge limit · Spray modes · Taylor cone

Electrophoresis

When an ionic solution is exposed to an electric field, the positive and negative ions experience Coulombic forces, causing them to move in the solution [1]. This is known as electrophoresis [2]. The strength of these forces depends on the applied electric field strength and also the charge in the individual ions. Figure 32.1 shows a hypothetical fluid droplet, containing ions, in an electric field created by two oppositely charged plates:

The positive and negative ions, of charge q, will experience a Coulombic electrostatic force F_E given by:

$$F_E = q\vec{E} \tag{32.1}$$

N. Ashgriz (✉)
Department of Mechanical and Industrial Engineering, University of Toronto, Toronto, ON, Canada
e-mail: ashgriz@mie.utoronto.ca

N. Ashgriz (ed.), *Handbook of Atomization and Sprays*,
DOI 10.1007/978-1-4419-7264-4_32, © Springer Science+Business Media, LLC 2011

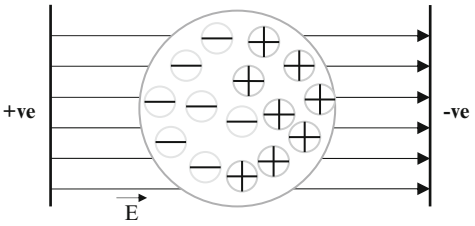


Fig. 32.1 Electrophoresis of a droplet in an electric field. The ions in the droplet are attracted towards the positive or negative plate depending on their charge

In Fig. 32.1, the positive ions experience a force in the direction of the electric field $\vec{E}$ towards the negatively charged plate. The negative ions experience a force in the opposite direction. If the ions were free to travel without any restrictions, as in a vacuum, these ions would move to the charged plates to reduce their electrostatic potential energy to zero. In this case however, the droplet is considered to be in air that is at room temperature and pressure and there are many forces impeding the ion movements within and outside the droplet. Within the droplet, the ions experience forces due to friction, partial pressure forces between the molecules and electrostatic forces between the other ions in the fluid [1]. Even if an ion overcomes these impeding forces and makes it to the liquid/air interface at the drop surface, one other major force has to be overcome; the liquid surface tension. Further information on the various electrostatic and non-electrostatic forces affecting droplets can be found in [3].

Spray Formation

When the ions are at the fluid/air interface they form an electric double layer [3]. Here they apply an electrostatic force on the interface, which opposes the surface tension forces and deforms the drop. If a large enough electric field is applied, these ions can actually overcome the surface tension forces and break through the liquid/air interface barrier [4]. This is essentially what happens in an electrospray (ES), also called electrohydrodynamic spray (EHD). This phenomenon is illustrated in Fig. 32.2.

In Fig. 32.2 the capillary on the top contains an ionic liquid whose ions are under the influence of an electric field created by the high voltage power supply. This field is created between the capillary and the plate surface at the bottom. The positively charged ions at the capillary migrate to the liquid/air interface and deform the fluid surface into a conical shape [5]. At the capillary and plate surfaces, the ions complete reduction and oxidation reactions and, therefore, resemble an electrolytic cell. The nature of these reactions is described in detail in [6].

Taylor [7] extensively studied and characterized the conical shape that an electrified fluid interface can deform into. This conical shape is referred to as the Taylor cone. Taylor stated, and proved experimentally, that the cone shape

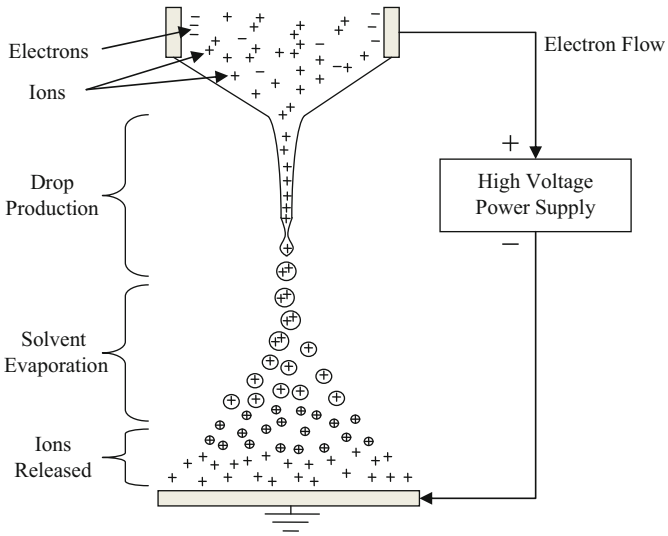


Fig. 32.2 Electrospray mechanism

is the equilibrium shape the meniscus fluid/air interface assumes when a strong enough electric field is applied to it. Taylor also determined the theoretical half cone angle for equilibrium as 49.3°. When a Taylor cone begins to form, the electric field strength is such that the electrostatic force at the fluid/air interface, due to the ions, is exactly balanced by the surface tension force [8]. This electric field strength is the field strength for the onset of electrospray and it is dependent on the surface tension of the ionic solution used as well as the capillary radius. The electric field strength E_{on} can be approximated using the following relation:

$$E_{on} = \left[\frac{2\sigma \cos\ \theta}{\varepsilon_0 r_c}\right]^{\frac{1}{2}} \tag{32.2}$$

The voltage V_{on} required for the onset of an electrospray can be approximated as follows:

$$V_{on} = \left[\frac{r_c \sigma \cos\ \theta}{2\varepsilon_0}\right]^{\frac{1}{2}} \ln\left(\frac{4d}{r_c}\right) \tag{32.3}$$

After the formation of the Taylor cone, a slight increase in the electric field can cause the ions to break through the liquid/air barrier and move freely under the influence of the electric field in the air.

Notice in Fig. 32.2 that the initial ejections from the Taylor cone show drops containing multiple ions of the same charge rather than single ions. This is due to the high amount of free energy required to bring an ion from the liquid phase into

the gas phase [2]. It takes far less energy to free clusters of solvated ions, which are referred to as charged drops.

Spray Current, Droplet Radius and Droplet Charge

For an electrospray to be formed, a minimum concentration of electrolytes, or ions, must be present in the fluid. This is intuitive as the electrospray process involves ions in the fluid and in particular, the movement of these ions by an applied electric field.

The minimum ion concentration for an electrospray has been experimentally determined as 10^{-5} mol L^{-1} [9]. When this minimum concentration is met, on the basis of theoretical reasoning and experimental measurements [10], the following relationships for spray current I, drop radius R and droplet charge q have been proposed:

$$I \approx f\left(\frac{\varepsilon}{\varepsilon_0}\right)\left[\gamma\sigma Q\left(\frac{\varepsilon}{\varepsilon_0}\right)\right]^{\frac{1}{2}} \tag{32.4}$$

$$R \approx \left(\frac{Q\varepsilon}{\gamma}\right)^{\frac{1}{3}} \tag{32.5}$$

$$q \approx 0.7\left[8\pi\left(\varepsilon_0\sigma R^3\right)^{\frac{1}{2}}\right] \tag{32.6}$$

These relationships are based on theoretical reasoning and experiments. In 32.4 $f\left(\varepsilon/\varepsilon_0\right)$ is a numerical function that has been tabulated and for liquids whose dielectric constant is $\varepsilon/\varepsilon_0 \geq 40$, $f\left(\varepsilon/\varepsilon_0\right) \approx 80$ [10]. These relations are valid when the electrospray is operated in the "cone-jet mode" [10] which is a particular mode of electrospray operation which will be discussed in a following section. Figure 32.3 shows experimental results that correlate well with the above relations for electrospray mean droplet size.

Forces at the Electrospray Capillary Tip

At the electrospray capillary tip, the fluid meniscus is exposed to a variety of different forces. First, if there is no electric field applied at the capillary tip, there exists the effect of hydrostatic pressure and surface tension. The hydrostatic pressure causes the meniscus to grow as more fluid flows into the emerging drop. The surface tension keeps the drop connected to the main fluid body in the capillary until a certain critical limit. At this critical limit, the gravitational force of the drop overcomes the surface tension and the top of the drop necks and separates from the capillary tip [12]. Second, if an electric field is applied to the capillary tip, an

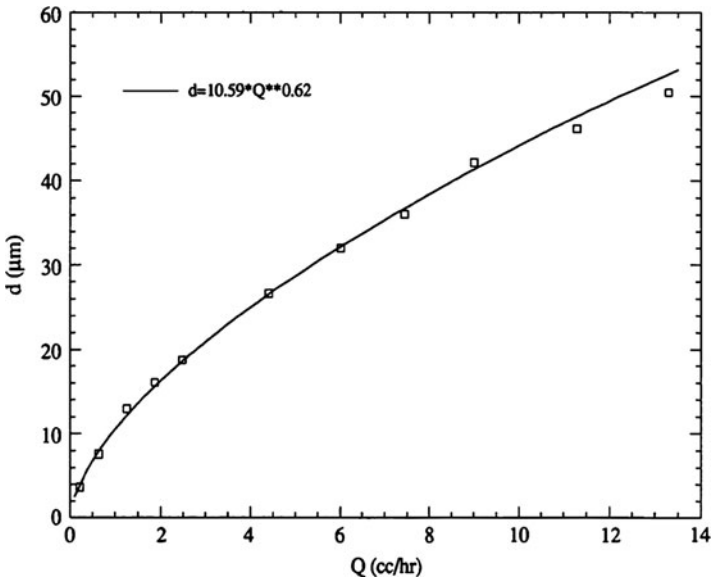


Fig. 32.3 Relation between droplet size and flow rate for an electrospray system using heptane (Reprinted with permission [11])

electrostatic force is added. The electrostatic force, as described previously, acts against the surface tension forces to deform the meniscus liquid/air interface. The deformation of the meniscus, under a constant electric field, depends on various liquid properties such as the viscosity, conductivity, dielectric permeability and surface tension.

In Fig. 32.4, the normal component of the electrostatic force is countered by the surface tension and the tangential component causes charge migration and subsequent stresses on the surface [13].

Electric Field at the Electrospray Capillary Tip

The electric field at the capillary tip depends on the geometry of the capillary, the distance of the ground electrode from the capillary tip, the geometry of the ground electrode and the applied voltage. To calculate the electric field at the capillary tip, mathematical models and analytical solutions have been developed [14, 15]. In the case of certain geometrical setups, it is possible to approximate the electric field at the capillary tip. One such instance is when the ground electrode is very large and planar in relation to the capillary tip. In this case, the electric field can be approximated using the following relationship [16]:

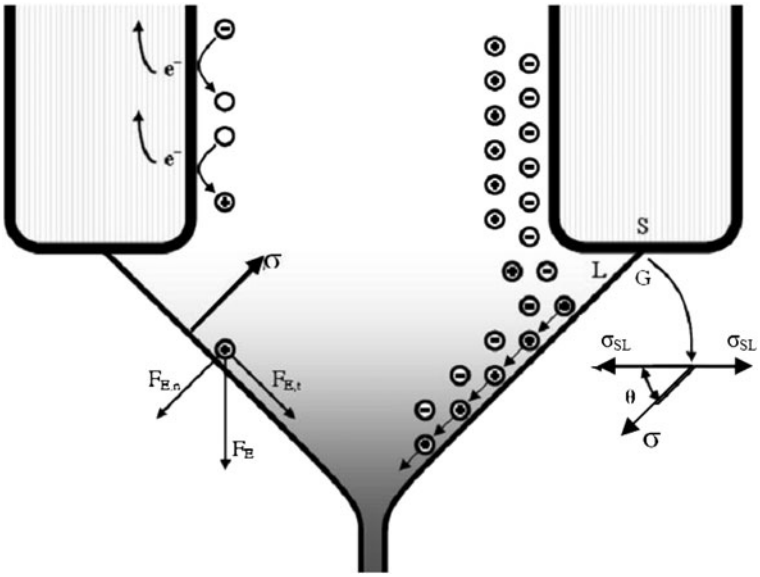


Fig. 32.4 Forces acting on the meniscus at the capillary tip under the influence of an applied electrical field. The capillary tip, in this case, is pointed downwards towards a ground electrode at a certain distance below the capillary tip (Reprinted with permission [13])

$$E_c = \frac{2V_c}{r_c \ln\left(\frac{4d}{r_c}\right)} \tag{32.7}$$

Generally, the electric field equipotential lines are densely packed near the emitter tip and diverge rapidly away from it.

Spraying Modes

Depending on fluid properties and other experimental conditions, many different droplet spraying modes are observed [17, 18]. A quick overview of the various spraying modes is presented here. For more details on the specific types of spraying modes one is directed to the referred work. Various spraying modes are a function of the following: fluid properties (electric conductivity, surface tension, viscosity, dielectric constant), other parameters (electric field – field strength applied at the capillary tip and field properties in the area of the electrospray, capillary geometry – orifice diameter, fluid flow rate).

By varying all of the above parameters, one can obtain a dynamic range of spraying modes. If the electric field strength at the capillary tip is varied, at fixed

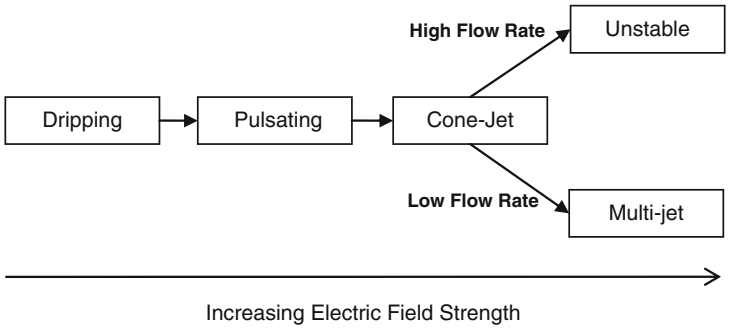


Fig. 32.5 Various electrospray modes obtained by varying the electric field strength applied at the capillary orifice

fluid properties and other parameters, the modes of electrospray operation can be summarized as shown in Fig. 32.5:

The following is a brief description of the major spraying modes identified in the literature in order of increasing the electric field applied to the capillary tip.

Dripping Mode

A relatively low strength electric field applied at the capillary tip will cause no significant difference to the droplet production as compared with a capillary with no charge. The pendant drops that form simply pinch off due to gravitational forces.

The effect of applied charge, and hence an electric field, is to pinch off the droplets at a faster rate than without an electric field and also to reduce the diameter of the droplets produced. This is due to the added electrostatic force of the ions in the drop as previously explained. This added force counters the surface tension force and assists the gravitational force in detaching droplets.

By increasing the electric field strength, the drop frequency increases and the radius decreases. Figures 32.6 and 32.7 illustrate the electric field effect on a capillary containing an ionic solution. In this case, the solution is distilled water. As can be seen in Fig. 32.6, the droplet radius decreases as the electric field strength is increased.

Pulsating Mode

While in the dripping mode if the electric field strength is increased the pulsating mode of electrospray operation begins. In this mode the shape of the

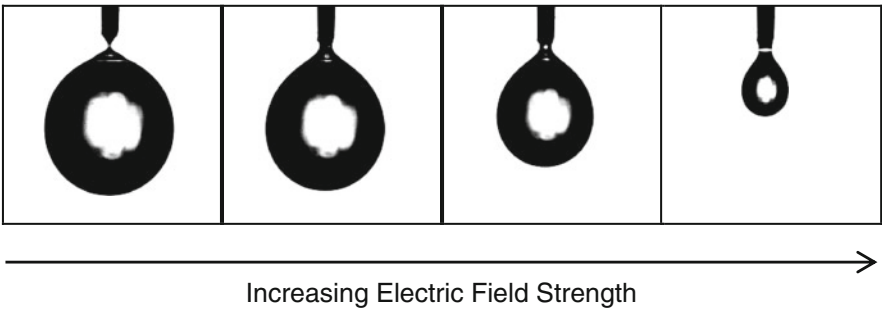


Fig. 32.6 Critical droplet size in the dripping mode. Electric field applied to a capillary containing distilled water. Experiment conditions: Voltage applied at capillary tip was varied from 0 to 10,000 V; flow rate set at 0.07 mL min^{-1}, ground electrode is set at 10 mm below the emitter tip

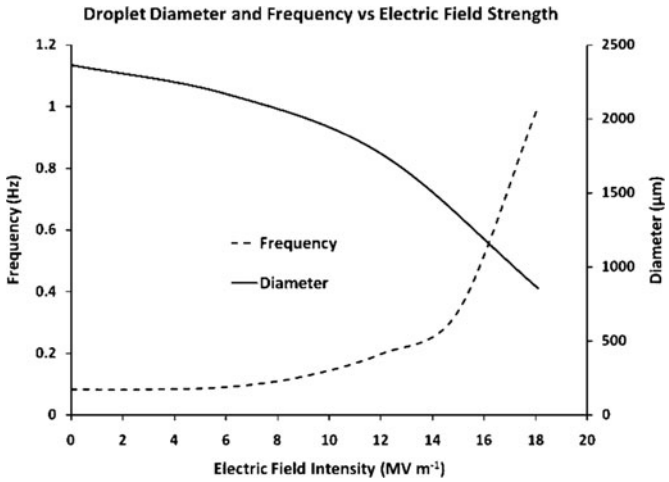


Fig. 32.7 Frequency and diameter of pendant water drop in dripping mode. Experiment conditions the same as for Fig. 29.6

meniscus is constantly pulsating between a hemispherical shape and a Taylor cone shape. This pulsation is due to the imbalance in forces between the surface tension and electric charge of the ions. Once the cone shape is achieved by the electrostatic force of the ions, a jet is emitted, in which most of the ions close to the surface are ejected. Therefore the electrostatic force decreases and the surface tension force pulls the meniscus inwards back to a hemispherical shape. After this, the ions once again migrate to the meniscus, deforming its shape back to a cone shape and the process repeats itself. The pulsating mode is shown in Fig. 32.8. The pulsating mode is also known as the spindle mode.

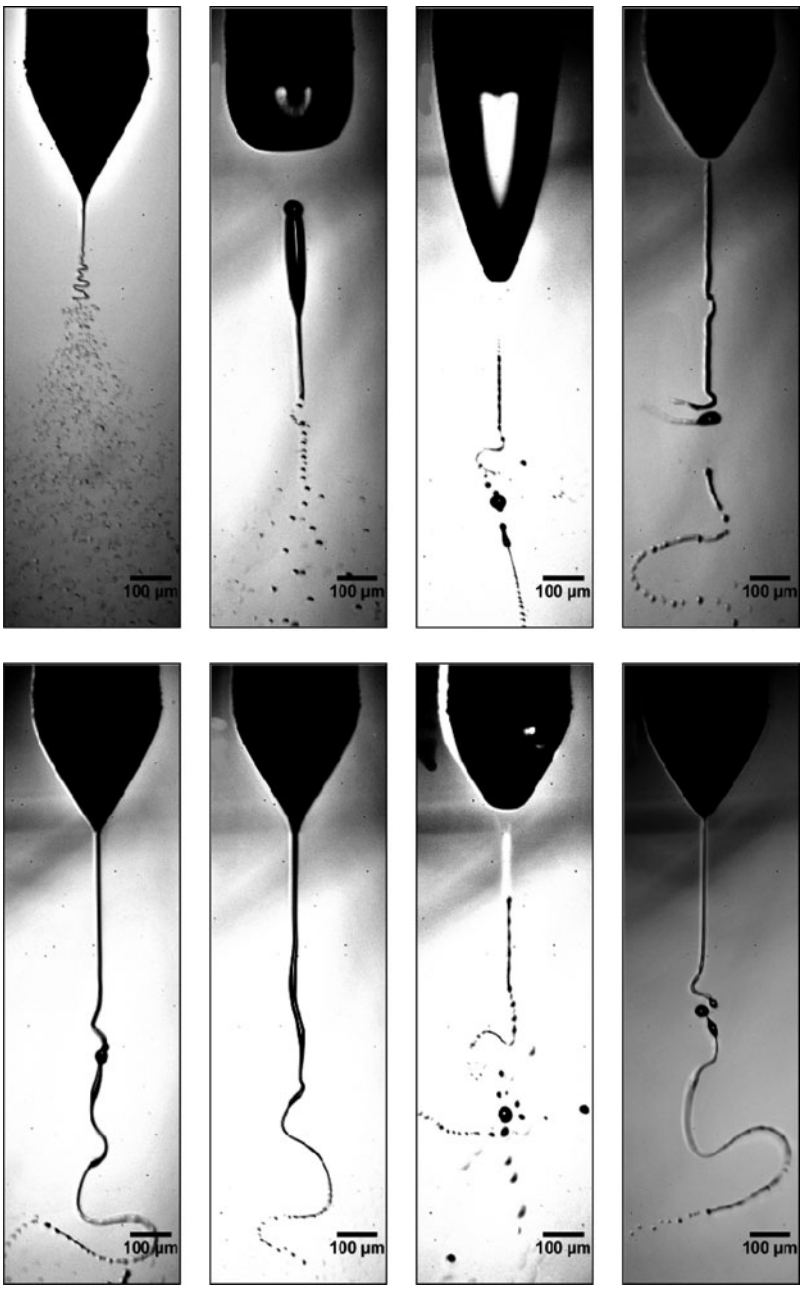


Fig. 32.8 Pictures showing the pulsating cone jet mode of electrospray operation. Experiment conditions: 2,500 V applied at emitter orifice, 2.4–4 µL/min flow rate of 75% methanol aqueous solution, 10 mm ground distance from emitter

Cone-Jet Mode

This mode of electrospray operation is one of the most interesting and studied cases. Cone-jet mode is when the meniscus at the liquid/air interface permanently takes the form of a Taylor cone and emits a steady jet of liquid from its apex. This jet of liquid travels a certain distance below the cone apex before breaking up into droplets. Depending on the fluid properties, the shape of the Taylor cone varies quite dynamically, as shown in Fig. 32.9.

Breakup of Jets Into Droplets

If the charge of the jet is low enough, the breakup of the initial drops takes place by the same Rayleigh jet instability mechanism as for a neutral jet as shown in Fig. 32.10 [17]. The droplet diameter can be related to the jet diameter in this case by the following relation [17]:

$$\frac{D}{D_j} = \left(\frac{3k}{2}\right)^{\frac{1}{3}} \tag{32.8}$$

where the droplet diameter is D, the jet diameter D_j and k is an experimentally determined parameter. For low viscosity inviscid liquids, the value of k is estimate to be 4.5 [17] (also see chapter 1), which leads to the following ratio:

$$\frac{D}{D_j} = 1.89 \tag{32.9}$$

This relation has been shown to correlate very closely with experimentally measured values [17].

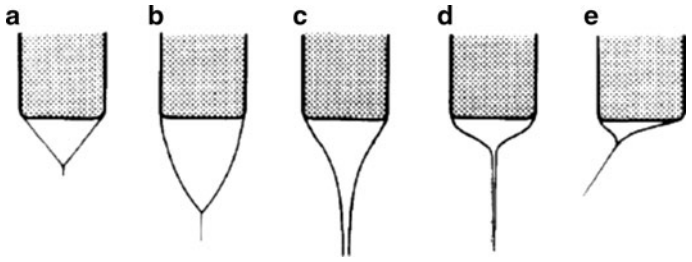


Fig. 32.9 Different forms of the meniscus in the cone-jet mode (Reprinted with permission [17])

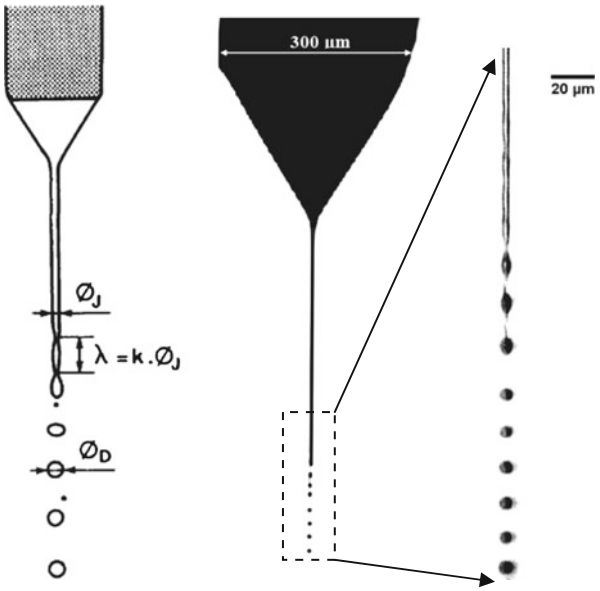


Fig. 32.10 The picture on the left shows varicose instabilities of an electrified jet (Reprinted with permission [17]). The picture in the center and on the right show the cone-jet mode of electrospray operation in an electrospray system in our lab. Experiment conditions: 3,200 V applied at emitter orifice, 11.5 µL/min flow rate of 90% aqueous methanol, 10 mm ground distance from emitter

By assuming that all the droplets are the same size and applying the minimization of energy principle, the following relationship between the charge-to-volume ratio of a drop has been established [19]:

$$\frac{q}{v} = 6\left(2\varepsilon_A \sigma D^{-3}\right)^{\frac{1}{2}} \tag{32.10}$$

The above relation is not fully justified as the droplet charging is greatly dependent on production conditions and can vary from one drop to the next of the same size as shown by past experiments [20, 21].

The above relation, however, can be used in another way as follows. The current measured at the ground electrode is equal to the current carried by the charges in the drops; therefore the ratio of current-to-flow rate is equal to charge-to-volume. If these ratios are switched in the relation shown in (32.10) then we end up with the following:

$$D = \left[6(2\varepsilon\sigma)^{\frac{1}{2}} \frac{Q}{I}\right]^{\frac{2}{3}} \tag{32.11}$$

The above relation gives the average emitted droplet size to the correct order of magnitude.

If a corona discharge occurs at the outlet of the capillary, the electric field is reduced significantly. The surrounding medium is ionized and the following two phenomenon can occur [17]:

(a) If the corona discharge occurs before the cone-jet mode is established, then the cone-jet mode may be prevented from being established at all.
(b) If the corona discharge occurs after the cone-jet mode is established, then there may be fluctuations in the discharge current. In this case, the cone-jet mode can be stabilized by increasing the electric field strength.

Variants of the Cone-Jet Mode

Once the cone-jet electrospray mode has been established, and the electric field is further increased in strength, several more jets may begin to be emitted from the capillary tip simultaneously. In this case the Taylor cone shrinks and splits up between the various emitted jets. This is referred to as a multi jet or multi-cone jet mode.

Droplet Size and Distribution Characteristics in Cone-Jet Mode

One of the reasons the electrospray is such a useful tool is that it produces relatively small and evenly distributed droplets. Using a Phase Doppler Anemometer (PDA) system, Keqi Tang has been able to characterize the droplets of an electrospray produced from Heptane and Methanol [11]. The results of these experiments show that the spray droplets are highly mono-dispersed as they travel from the emitter tip to the ground electrode as shown in Fig. 32.11.

In Fig. 32.11 the y axis shows the number densities and the x axis is the distance radially from the center of the emitter orifice. The various curves of different z values show the results of various analyses performed at distances z from the emitter orifice along the spray axis. It is interesting to note the double hump that forms very close to the emitter orifice. This can be related to the formation of satellite and offspring droplets which are smaller in size than the parent droplets and hence are pushed away from the center due to mutual Coulombic repulsion. The spreading out of the droplets over a large radial distance from the spray axis can be attributed to the strongly divergent electric field near the capillary tip.

Stability of the Cone-Jet Mode

The operation of the electrospray in the cone-jet mode is achieved only when the operational and fluid parameters are within certain ranges as already shown in

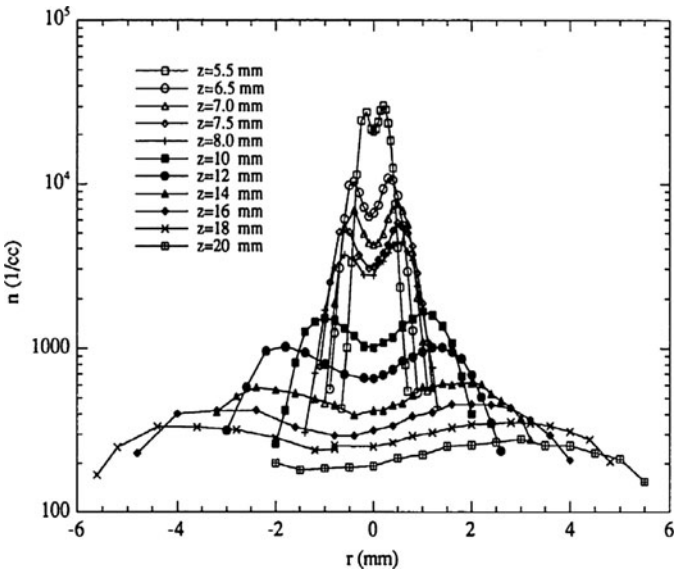


Fig. 32.11 Graph showing the results of a PDA analysis of an electrospray produced by Heptane (Reprinted with permission [11])

Fig. 32.5. For fixed geometric and fluid properties and also a fixed flow rate, varying the electric field strength applied at the emitter tip determines which mode of operation the electrospray is in. A stable cone-jet mode of operation is achieved at a particular field strength range. Below this range the electrospray will fall into the pulsating and dripping modes of operation and above this range it will go into the unstable modes of operation. If the flow rate of the electrospray system is changed while other parameters are kept constant, the stable electric field strength range will change. By varying the flow rates and electric field strength applied over the entire available values, one can determine the field ranges at all possible flow rates for which a stable electrospray can be achieved. This stable electric field strength range for all available flow rates where the cone-jet mode is observed is known as the electrospray stability island.

The main factors affecting the stability island of an electrospray system is the fluid properties themselves; in particular the surface tension and conductivity. The fluid surface tension directly affects the ability of a fluid to atomize an electrospray because it opposes the force applied by the ions at the fluid/air interface. Therefore, increasing the surface tension will increase the required field strength to establish a cone-jet mode. The conductivity of the fluid used has the effect of shifting the electrospray stability island to a narrower range and also to lower flow rates. This is shown in Fig. 32.12.

In Fig. 32.12 there are three sets of top and bottom curves. The top curves show the maximum voltage (field strength) at which a stable cone-jet mode can

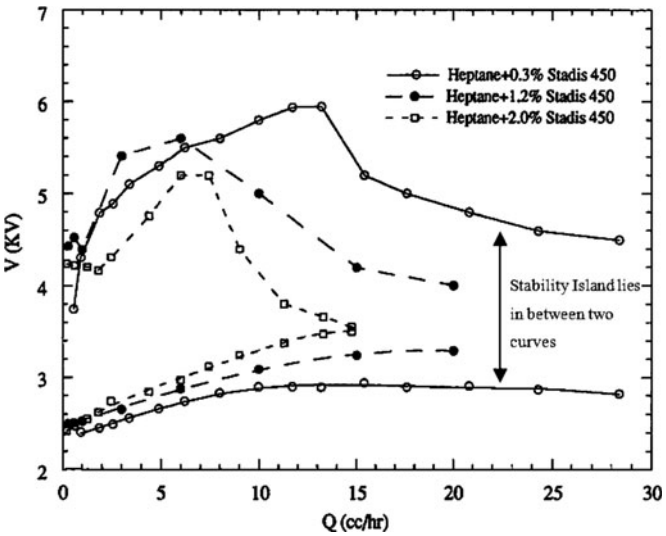


Fig. 32.12 Electrospray stability island, effect of varying conductivity (Reprinted with permission [11])

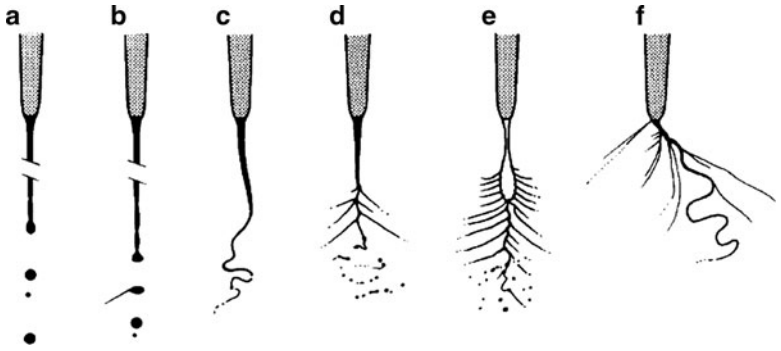


Fig. 32.13 Simple jet and ramified jet (Reprinted with permission [17])

be operated and the bottom curves the lowest field strength. The three curve sets are three different batches of Heptane, each with a different conductivity. The conductivity of the Heptane is increased by adding a certain percentage of Stadis 450. From Fig. 32.12 it is clear that increasing the conductivity decreases the highest flow rate at which a stable cone-jet mode will exist and narrows the range of electric field strength at which a stable cone-jet mode is achieved. Increasing the flow rate of the fluid used increases the diameter of the jet emitted from the cone-jet and therefore also the droplets produced by the electrospray [11].

Effect of Viscosity

Increasing the viscosity of the fluid used in an electrospray dramatically increases the droplet sizes produced and therefore increases the ligament breakup. A dimensionless number has been proposed [22] to determine the importance of viscosity on the electrospray ligament breakup:

$$\pi_{\mu} = \frac{\left(\frac{\sigma^2 \rho \varepsilon \varepsilon_0}{\gamma}\right)^{\frac{1}{3}}}{\mu} \tag{32.12}$$

In (32.12), π_{μ} is a dimensionless parameter comparing the viscosity of the fluid used in an electrospray to other fluid parameters such as fluid surface tension, fluid density, dielectric permittivity of the fluid and also the dielectric permittivity of free space. When π_{μ} is much greater than 1 then viscous effects are negligible.

Effect of Conductivity

The effect of increasing the conductivity of the electrospray fluid decreases the flow rate and also narrows the electric field strength range at which a stable cone-jet mode can be established. Another effect of increasing conductivity is that the filament jet radius emitted from the cone tip decreases and this in turn decreases the droplet size produced [11].

Effect of Surface Tension

The effect of increasing the electrospray fluid surface tension tends to increase the electric field strength required to create a stable cone-jet mode. If a fluid, such as distilled water ($\approx$0.074 N m^{-1} at 20°C), has a sufficiently large surface tension, the ionization potential of the air around the electrospray is reached before any kind of electrospray is created. Therefore a stable cone-jet mode is difficult and almost impossible to create without the use of some sheathing gas around the electrospray system.

Micro Dripping Mode

A mode of electrospray has been observed [23] that produces aerosol not from the breakup of a liquid jet, but from the emission of tiny droplets directly from the Taylor cone. The droplets are emitted at a very high frequency from roughly 4,000–6,000 Hz [17].

Simple Jet and Ramified Jet

When no electric field is applied at the capillary, the liquid may be emitted in the form of a jet if a high enough fluid flow rate is achieved. This is the critical flow rate at which the kinetic energy of the fluid is greater than the surface energy, creating the jet surface [24]. When this jet is formed, an electric field applied to it will charge and accelerate it. The behavior of this electrified simple jet is similar to the cone-jet mode. However, as you increase the voltage, ramifications begin to occur as shown in Fig. 32.13.

In Fig. 32.13a and b, the jet emits large droplets which in turn can emit a spray of finer droplets. As the electrical field strength is increased, the jet may whip around before disintegrating into fine drops as shown in Fig. 32.13c. Further increases in electrical field strength lead to the creation of fine jets being emitted from the main jet as shown in Fig. 32.13d and e. Eventually, jets are emitted directly from the capillary tip simultaneously with the main jet still being emitted as well, as shown in Fig. 32.13f.

Kink Instabilities

This type of mechanism is present when the electrostatic pressure in the jet approaches the capillary pressure. Here, once the largest droplets have separated from the jet, their charge is such that they exceed the Rayleigh limit [25]. They then emit a jet themselves, which resembles a miniature Taylor cone, and break up into even finer drops. If the electrical field strength is slightly higher, lateral kink-type

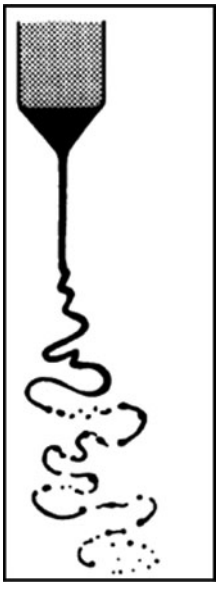


Fig. 32.14 Picture showing lateral kink-type instabilities (Reprinted with permission [17])

instabilities appear. These instabilities constitute a whipping jet that winds and thins out eventually disintegrating onto finer droplets as shown in Fig. 32.14.

Spindle Mode

Spindle mode is a combination of the cone-jet and dripping mode. This mode is illustrated in Fig. 32.15. In Fig. 32.15 from pictures 1–10, a complete cycle of operation of the spindle mode is shown. From 1–5 a Taylor cone is being formed, which then emits a fine jet and then disintegrates into fine droplets. In 6, the apex of the cone retracts, emitting a large elongated drop that continues emitting the fine jet as shown in 7. In 8, the elongated drop now forms a more spherical drop. This happens because charged droplets that it emitted reduces its own internal electrostatic force pressure and the surface tension of the drop pulls the elongated drop back into the low energy spherical shape. The previously emitted jet from 7 now starts to break up into small droplets in pictures 9 and 10. This entire cycle continuously repeats itself as long as conditions do not change.

From Charged Droplets to Gas-Phase Ions in an Electrospray

Solvent Evaporation from Charged Droplets

The charged droplets produced by an electrospray shrink due to solvent evaporation as long as the droplet charge remains constant. The energy required for the solvent evaporation is provided by the thermal energy of the ambient air. The charge on the droplets is assumed to remain constant because the emissions of ions from solution to gas phase are highly endothermic [26].

From kinetic theory for droplet evaporation, the time required for an initial droplet with radius R_0, to reach size R_1 can be estimated using the following equations [27]:

$$\frac{dR}{dt} = \frac{-\alpha U_v P_0 M}{4\rho R_g T} \tag{32.13}$$

$$R_1 = R_0 - \frac{\gamma U_v P_0 M}{4\rho R_g T} \tag{32.14}$$

The rate of droplet evaporation has been shown to depend greatly on the initial droplet diameter [11]:

$$\frac{dD}{dt} = -\frac{K}{D} \tag{32.15}$$

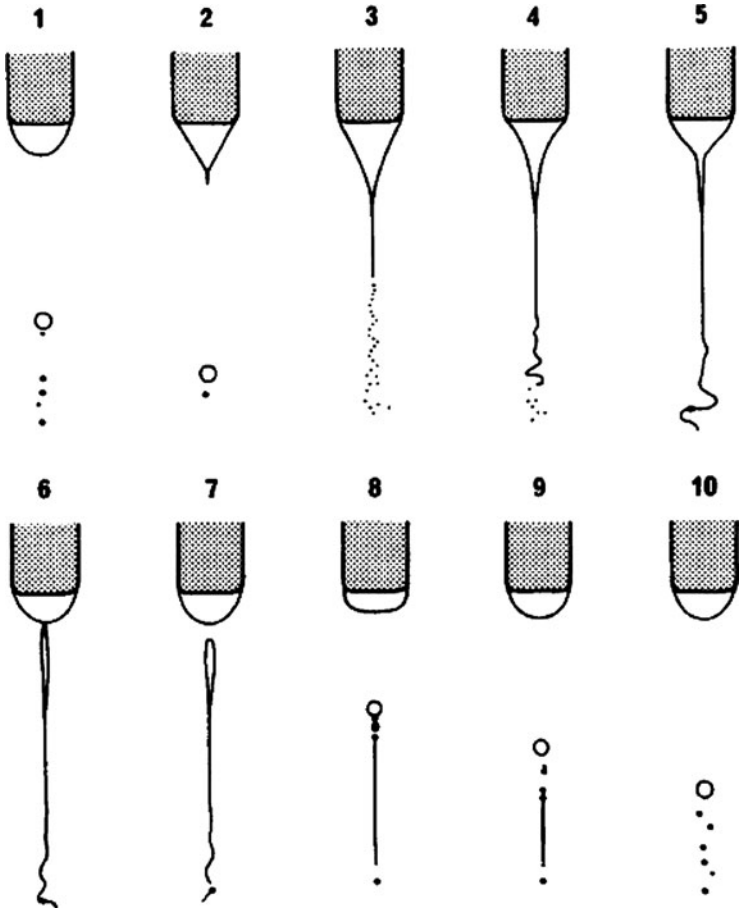


Fig. 32.15 Spindle mode of the electrospray (Reprinted with permission [17])

As can be seen in (32.15), the rate of droplet evaporation is inversely proportional to the droplet diameter and this relation has been verified as show in Figs. 32.16 and 32.17.

The droplet evaporation rate is higher for a small methanol droplet in Fig. 32.17 than a larger heptane droplet in Fig. 32.16.

Droplet Instability and the Rayleigh Limit

The decrease of the droplet radius R at constant charge q leads to an increase in the electrostatic repulsion of the charges at the droplet surface until the droplet reaches the Rayleigh stability limit [28] given by:

$$q_r = 8\pi\left(\varepsilon_0 \sigma R^3\right)^{\frac{1}{2}} \tag{32.16}$$

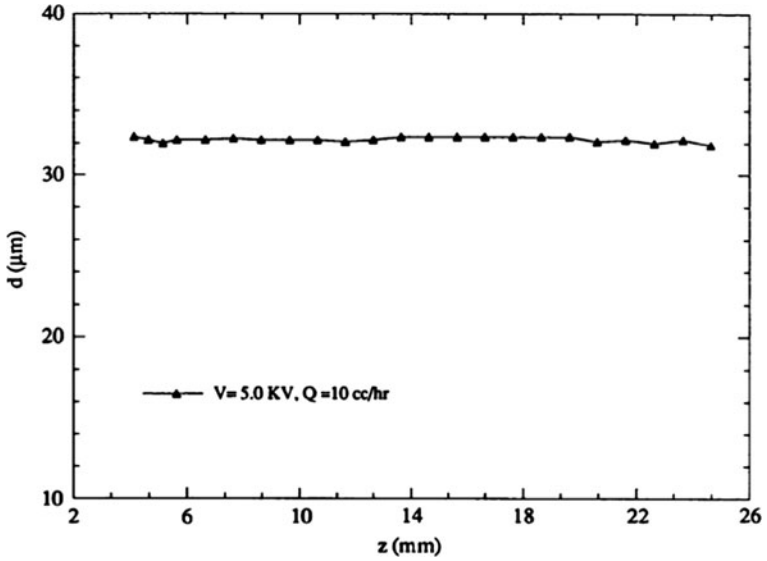


Fig. 32.16 Graph showing the average diameter (d) of a heptane droplet as it travels away from the emitter orifice (Reprinted with permission [11])

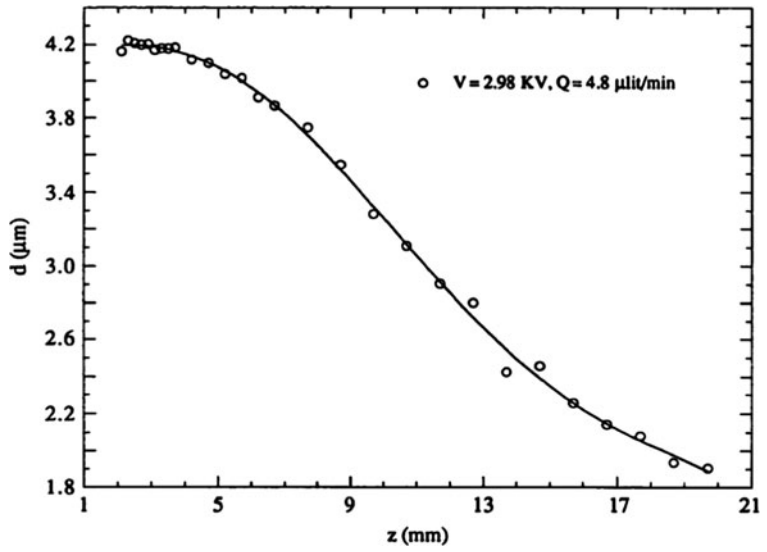


Fig. 32.17 Graph showing the average diameter (d) of a methanol droplet as it travels away from the emitter orifice (Reprinted with permission [11])

At this critical radius, the charged droplet becomes unstable. It has been experimentally observed that the droplets undergo an uneven fission [29] when they are close to the Rayleigh limit.

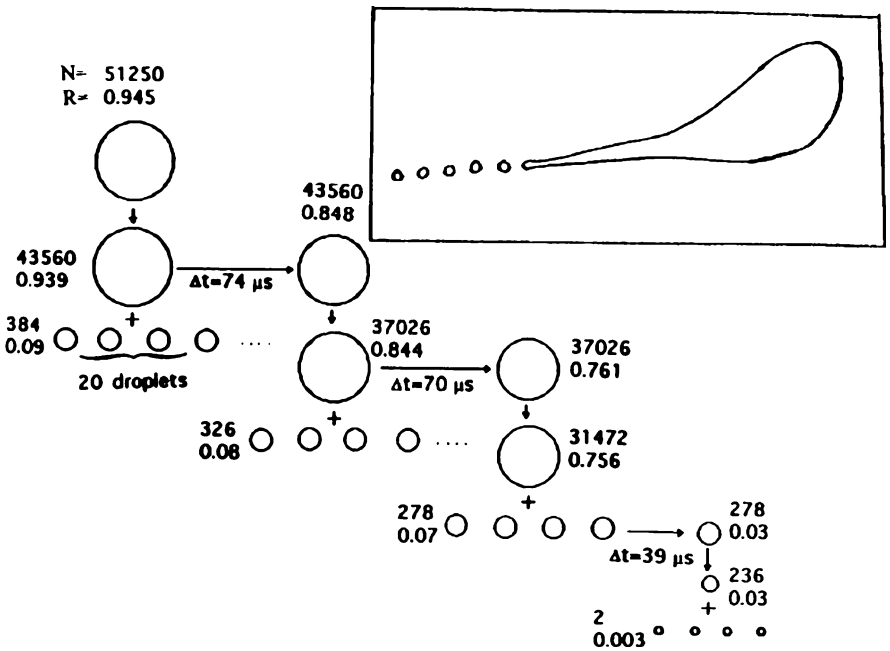


Fig. 32.18 Droplet evolution due to solvent evaporation and droplet jet fission (Reprinted with permission [2])

Figure 32.18 shows the evolution of a droplet undergoing uneven fission or droplet fission [2]. In Fig. 32.18, N is the number of elementary charges and R is the radius in μm. Also shown is the time Δt (μs) to reach the next fission as approximated by (32.13), (32.14) and (32.16). In Fig. 32.18 the first droplet shown is at the Rayleigh limit. The parent droplet produces 20 offspring droplets that carry off only 2% mass and 15% of the charge. The radius of the offspring droplets are approximately $\frac{1}{10}$ of the parent drop. The first generations of offspring droplets are predicted to have a 0.08 μm diameter, however, droplets smaller than 1 μm have been difficult to observe and therefore the occurrence of jet fission for such droplets has not been verified experimentally [29].

Aerodynamic Effect on Droplets

The aerodynamic deformation effect on a moving droplet can be defined by the Weber number (see Chapter 6):

$$W_e = \frac{\rho_g D U_r^2}{\sigma} \tag{32.17}$$

where ρ_g is the gas density, D is the droplet diameter, U_r is the relative velocity between the droplet and the surrounding gas and σ is the surface tension of the liquid. When the Weber number is greater than a critical value, which is of order 10 [30], the aerodynamic force will overcome the surface tension force and deform the droplet. To evaluate the aerodynamic effect on a charged droplet, we need to introduce an effective surface tension, which incorporates the electrostatic force on the drop surface due to charge [11]. The electric pressure acting on the droplet surface due to the surface charge is:

$$P_e = \frac{1}{2}\varepsilon_0 E^2 = \frac{1}{2}\varepsilon_0 \left(\frac{q}{\pi\varepsilon_0 D^2}\right)^2 \tag{32.18}$$

The electric pressure force acts in the opposite direction of the surface tension force and therefore reduces the surface tension. By taking this into account, an effective surface σ_e tension can be introduced as follows:

$$\sigma_e = \sigma_0 - \frac{q^2}{8\pi^2\varepsilon_0 D^3} \tag{32.19}$$

The effective surface tension is affected by two main properties of the drop, charge and diameter. As the diameter of the drop decreases, the droplet reaches the Rayleigh limit and then undergoes a Coulombic explosion. This Coulombic explosion indicates that the surface tension of the droplet has been overcome by the surface charge pressure and therefore the effective surface tension is zero at the Rayleigh limit. If we substitute the Rayleigh limit (32.16) in (32.19) we get:

$$\sigma_e = \sigma_0 \left(1 - \frac{q^2}{q_r^2}\right) \tag{32.20}$$

The relation obtained in (32.20) shows that the effective surface tension for a droplet is dependent on how close the droplet charge is to the Rayleigh limit charge. If the Weber number (32.17) is rearranged and the critical Weber number, at which aerodynamic forces become important, is treated as a constant we get the following:

$$\sigma_{cr} = \frac{\rho_g D U_r^2}{W_{e_{cr}}} \tag{32.21}$$

To estimate the aerodynamic effect on a charged droplet, the effective surface tension can be calculated using (32.20) and compared with the critical surface tension given by (32.21). If the effective surface tension is much lower than the critical surface tension, $\sigma_e \leq \sigma_{cr}$, then the aerodynamic effects on the drop are important. Conversely if $\sigma_e \geq \sigma_{cr}$ then the aerodynamic forces are negligible.

Mechanisms for the Formation of Gas Phase Ions

Once the droplets have undergone a few jet fissions, they are so small that they have not been directly observed through experiments as mentioned before. This has led to the creation of two main theories to explain what happens to these small, highly charged droplets.

The first theory is the charged residue model (CRM) first proposed by Dole [31], who was one of the first people to study the gas phase ion production in an electrospray. In Dole's model, the droplets undergo jet fission until very small droplets, on the order of a few nanometers, are created that contain only single ions. Continuing solvent evaporation from these drops yields a single gas phase ion.

The second theory is based on the ion evaporation model (IEM) proposed by Iribarne and Thompson [32]. In IEM, after the radii of the charged droplets have reduced to the order of tens of nanometers, due to solvent evaporation and jet fission, direct ion emission to the gas phase from the droplets becomes possible. The theory states that IEM becomes dominant over jet fission for droplets of radii $R \leq 10$ nm [29]. Figure 32.19 illustrates the two different theories of gas phase ion evolution in an electrospray.

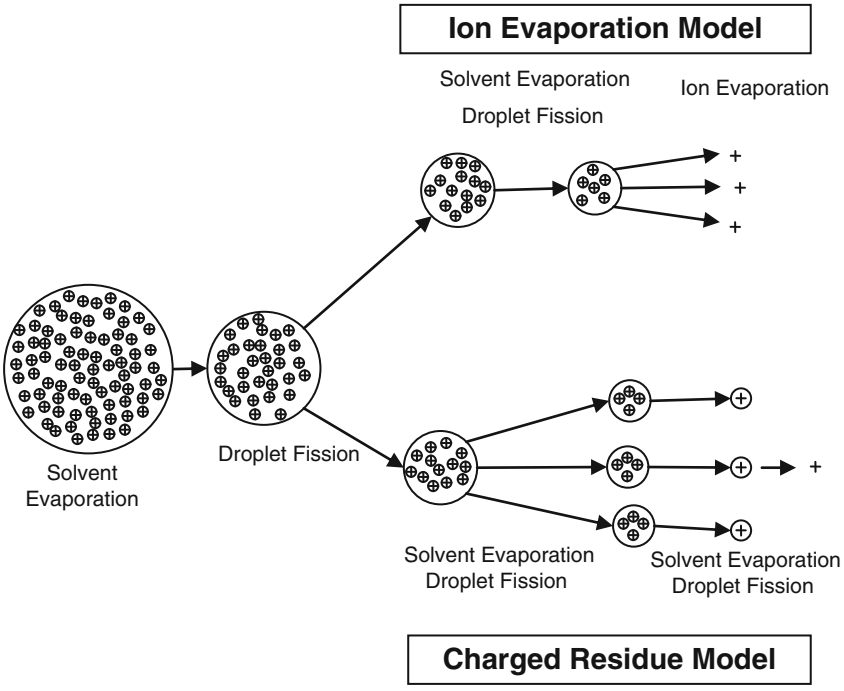


Fig. 32.19 The charged residue model (CRM) and ion evaporation model (IEM) of gas phase ion generation from charged electrospray droplets

In the IEM ion production method, Iribarne and Thompson [32] derived detailed equations for predicted ion emission rates k_I from charged droplets based on transition state theory:

$$k_I = \frac{k_B T}{h} exp\left(-\frac{\Delta G^{\neq}}{R_g T}\right) \tag{32.22}$$

Equation 32.22 predicts the rate of ion emission from a charged droplet based on transition state theory. The barrier in the transition state is a "late" transition state analyzed after the ion has left the droplet. This choice of transition state simplifies the energy calculations involved and creates a closed equation based on classical electrostatics and thermodynamics [29]. In reality, the transition state could occur earlier, as the ion disrupts the droplet surface. The energy of such an early transition state would be much harder to evaluate.

The barrier in the Iribarne and Thompson transition state is due to opposing electrostatic forces. These forces exist between the escaping ion and the remaining charges in the droplet. At short distances, the attractive force due to the polarizability of the droplet is large. However as the distance between the ion and droplet increases, this force falls faster than the repulsion force due to the ions present in the droplet.

An expression of the activation energy $\Delta G^{\neq}$ obtained by Iribarne and Thompson [32] is shown below:

$$\Delta G^{\neq} = \left(\frac{Ne^2}{4\pi\varepsilon_0(R + x_a)} - \frac{e^2}{16\pi\varepsilon_0 x_a}\right) - \left(\Delta G^{\circ}_{sol} - \frac{Ne^2}{4\pi\varepsilon_0(R - x_b)}\right) \tag{32.23}$$

In (32.23) the first term on the right hand side is the required solvation energy of the ion at a distance x_m from the droplet surface and the second term is the equilibrium solvation energy of the ion at a distance d below the drop's surface. The difference between these two terms gives the solvation energy barrier.

The overall predictions for obtaining gas phase ions from charged droplets due to the CRM theory and the IEM theory are only distinctly different for certain conditions. For charged droplets of radii $\geq$ 10 nm, the CRM model is favorable and for radii $\leq$ 10 nm, the IEM theory is favorable. For radii $\leq$ 1 nm, there are so few ions compared with solvent molecules that neither the IEM theory nor CRM theory strictly apply, however the process is closer to the IEM theory [29].

Application of an Electrospray to Mass Spectrometry

A wide variety of practical applications for electrosprays exists including spray painting and coating, agricultural [3], combustion [33, 34], space propulsion [35]

and medical [29, 36]. This section focuses on one of the newer and highly promising applications of the electrospray which is as an ion source for mass spectrometry.

In order to improve the mass spectrum analysis results, the mass spectrometer requires as many detectable gas phase ions as possible. As shown in previous sections, the electrospray produces gas phase ions from its charged droplets when the droplets reach a certain size and either the CRM of IEM model of gas phase ion formation occurs. To produce gas phase ions efficiently, an electrospray must operate in a mode where the droplets produced are relatively small, close to the Rayleigh limit, and also where the droplets are charged sufficiently. Once the droplets reach the Rayleigh stability limit at a fast pace, they can continue on to the CRM an IEM models of gas phase ion formation.

In a mass spectrometer, the operating conditions for the electrospray are affected by a wide range of variables such as the fluid properties, flow rate, electric field and also the ambient temperature and pressure. They have a large effect on the droplet evaporation and hence the ion formation from the droplets. A variety of electrospray setups have been developed and utilized in modern mass spectrometers to maximize the gas phase ion production and hence the quality of the mass spectrum analysis. Some of these methods will now be described.

In order to aid droplet evaporation and maximize the gas phase ion production from the charged droplets, most mass spectrometers utilize some mechanism for supplying dry gas, usually nitrogen, to the spray area. With the use of a drying gas, the charged electrospray droplets evaporate faster and therefore reach a smaller size quicker, where they can produce gas phase ions. Increasing the ambient temperature around the electrospray emitter in a mass spectrometer will also improve the production of gas phase ions by increasing the available energy for evaporation.

Sheath gas flow around the emitter orifice can be utilized when a stable electrospray in the cone-jet mode is difficult to achieve. One reason why a stable cone-jet mode electrospray can be difficult to obtain in a mass spectrometer application is an increased flow rate. An increase in flow rate causes the electrospray to operate outside the island of stability mentioned previously (Fig. 32.12). The effect that the sheath gas has on the electrospray is increased breakup of the spray droplets through the transfer of kinetic energy.

Another design is orthogonal injection. This design uses the momentum of the smaller gas phase ions to separate them from the main flow of electrospray droplets. Traditionally, when an electrospray is aimed directly at the inlet to the mass spectrometer, there can be unwanted solute droplets, and also ion containing solute droplets that never release their ions, sampled into the system, clouding the results and creating problems for cleaning the equipment. To avoid these issues, most designs now use orthogonal injection where the main electrospray flow is injected orthogonally to the mass spectrometer inlet. Only the lighter gas phase ions produced are sucked in via the pressure difference between the high pressure outside of the mass spectrometer inlet and the lower pressure inside.

Nomenclature

D	diameter of drop (m)
D_j	diameter of jet (m)
d	distance from the ground electrode to capillary tip (m)
E	electrical field intensity (V m^{-1})
E_{0n}	electric field intensity for the onset of electrospray (V m^{-1})
E_c	electrical field intensity at the capillary tip (V m^{-1})
EHD	electrohydrodynamic spray (different designation for an electrospray)
ES	electrospray
F_E	electrostatic force (N)
F_{En}	normal component of electrostatic force (N)
F_{Et}	tangential component of electrostatic force (N)
I	current in the electrospray circuit (C s^{-1})
K	experimentally determined parameter for droplet evaporation
k	experimentally determined parameter for Rayleigh jet breakup
k_I	ion emission rate
N	number of elementary charges
P_e	electric pressure (N m^{-12})
q	charge of a drop (C)
Q	flow rate (L min^{-1})
q_r	Rayleigh charge (C)
q_v	Vonnegut charge (C)
R	drop radius (m)
r_c	capillary tip radius (m)
R_g	gas constant (J K^{-1} mol^{-1})
U_r	relative velocity (m s^{-1})
U_v	thermal velocity of solvent vapor
v	volume of a drop (m^3)
V_c	voltage applied at the capillary tip (V)
V_{on}	voltage for the onset of electrospray (V)
W_e	Weber's number
W_{ecr}	Critical Weber's number

Greek Symbols

μ	dynamic viscosity (kg m^{-1} s^{-1})
γ	electrical conductivity (S m^{-1})
ε	dielectric permittivity (C^2 m^{-2} N^{-1})
ε_0	dielectric permittivity of free space (C^2 m^{-2} N^{-1})
ε_A	dielectric permittivity of air (C^2 m^{-2} N^{-2})
λ	distance between forming drops (m)
ρ	density (kg m^{-3})
ρ_g	gas density (kg m^{-3})
σ	surface tension (N m^{-1})
σ_{cr}	critical surface tension (N m^{-1})
σ_e	effective surface tension (N m^{-1})
σ_0	original surface tension (N m^{-1})

References

1. Castellanos, A. (1998). *Electrohydrodynamics*. New York: Springer Wien.
2. Tang, Kaberle, P., & Liang. (1993). From ions in solution to ions in the gas phase – the mechanism of electrospray mass spectrometry. *Analytical Chemistry*, Vol. 65 (22), 972A–986A.
3. Bailey, A. G. (1988). *Electrostatic Spraying of Liquids*. New York: John Wiley & Sons Limited.
4. Zeleny, J. (1914). Electrical discharge from liquid points. *The Physical Review*, Vol. 3 (2), 69–91.
5. Tatiana, C., & Rohner, N. L. (2004). Electrochemical and theoretical aspects of electrospray ionisation. *Physical Chemistry Chemical Physics*, Vol. 6, 3056–3068.
6. Kebarle, P. (2000). A brief overview of the present status of the mechanisms involved in electrospray mass spectrometry. *Journal of Mass Spectrometry*, Vol. 35, 804–817.
7. Taylor, S. G. (1964). Disintegration of water drops in an electric field. *Proceedings of the Royal Society of London. Series A, Mathematical and Physical* (Vol. 280 (1382), July 28, 1964, pp. 383–397). London: The Royal Society.
8. Smith, D. P. (1986). The electrohydrodynamic atomization of liquids. *IEEE Transactions on Industry Applications*, Vol. IA-22 (3), 527.
9. Ikonomou, G. M., Blades, A. T., & Kebarle, P. (1991). Electrospray-ion spray: a comparison of mechanisms and performance. *Analytical Chemistry*, Vol. 63 (18), 1989–1998.
10. Mora, J. F., & Loscertales, I. G. (1994). The current emitted by highly conducing Taylor cones. *Journal of Fluid Mechanics*, Vol. 260, 155–184.
11. Tang, K. (1994, November). The electrospray: fundamentals and feasibility of its application to targeted drug delivery by inhalation. A dissertation presented to the faculty of the graduate school of Yale university in candidacy for the degree of Doctor of Philosophy.
12. Zhang, X. (1999). Dynamics of growth and breakup of viscous pendant drops into air. *Journal of Colloid and Interface Science*, Vol. 212, 107–122.
13. Marginean, I. (2006, August). From chaotic cone pulsation to ion evaporation in electrosprays. Dissertation submitted to the George Washington University.
14. Tang, Gomez, A., & Keqi. (1994). Charge and fission of droplets in electrosprays. *Physics of Fluids*, Vol. 6, 404.
15. Chiarot, P. R. (2008). Characterization of an electrified fluid interface and the electrospray mechanism: development of microscale analytical techniques. PhD thesis submitted to the University of Toronto, Toronto, Ontario, Canada.
16. Loeb, L., Kip, A., Hudson, G. G., & Bennet, W. H. (1941). Pulses in negative point-to-plane corona. *Physical Review*, Vol. 60, 714.
17. Prunet-Foch, Cloupeau, M., & Bernard. (1994). Electrohydrodynamic spraying functioning modes. *Journal of Aerosol Science*, Vol. 25 (6), 1021–1036. Figures reprinted with permission from Elsevier.
18. Marijnissen, J. M. (1994). A review of liquid atomization by electrical means. *Journal of Aerosol Science*, Vo. 25 (6), 1005–1019.
19. Vonnegut, B., & Neubauer, R. L. (1952). Production of monodisperse liquid particles by electrical atomization. *Journal of Colloid Science*, Vol. 7, 616–622.
20. Cloupeau, M., & Prunet-Foch, B. (1989). Electrostatic spraying of liquids in cone-jet mode. *Journal of Electrostatics*, Vol. 22, 135–159.
21. Krohn, V. E. (1973). Evidence that the minimum-energy state is not accessible to a system of droplets produced by electrohydrodynamic spraying. *Applied Physics Letters*, Vol. 23 (5), 220.
22. Rossel-Llompart, J. F. (1994). Generation of monodisperse droplets 0.3 to 4mm in diameter from electrified cone-jets of highly conducting and viscous liquids. *Journal of Aerosol Science*, Vol. 25 (6), 1093–1119.

23. Kozhenkov, V. I., & Fuks, N. A. (1976). Electrohydrodynamic atomization of liquids. *Russian Chemical Reviews*, 45 (12), 1179.
24. Schneider, N. R. (1965). Production of uniform-sized liquid drops. *Journal of Scientific Instruments*, Vol. 42, 635.
25. Rayleigh, J. W. (1879). On the conditions of instability of electrified drops, with applications to the electric discharge from liquid points. *Proceedings of the Royal Society*, Vol. 29, 71–83.
26. Desnoyers, J. E., & Joliceur, C. (1969). In J. C. Bockris, *Modern Aspects of Electrochemistry* (Vol. 5, p. 20). New York: Plenum Press.
27. Shaw, D. T. (1978). *Fundamentals of Aerosol Science*. New York: John Wiley & Sons.
28. Rayleigh, L. (1882). On the equilibrium of liquid conducting masses charged with electricity. *Philosophical Magazine*, Vol. 14, 184.
29. Cole, R. B. (1997). *Electrospray Ionization Mass Spectrometry – Fundamentals, Instrumentation and Applications*. New York: John Wiley & Sons.
30. Lefebvre, A. H. (1989). *Atomization and Sprays*. New York: Hemisphere Publishing Corp.
31. Dole, M., Mack, L. L., & Hines, R. L. (1968). Molecular beams of macroions. *Journal of Chemical Physics*, Vol. 49 (5), 2240.
32. Iribarne, B. A., & V., T. a. (1979). Field induced ion evaporation from liquid surfaces at atmospheric pressure. *Journal of Chemical Physics*, Vol. 71 (11), 4451.
33. Kelly AJ (1984). The electrostatic atomization of hydrocarbons. *Journal of the Institute of Energy* Vol. 57, 312–320.
34. Shrimpton, J. S., & Yule, A. J. (2001). Atomization, combustion, and control of charged hydrocarbon sprays. *Atomization and Sprays*, Vol. 11, 365–396.
35. Gassend, B. L. P. (2007). A fully micro fabricated two-dimensional electrospray array with applications to space propulsion, PhD submitted to Massachusetts Institute of Technology.
36. Fenn, J. B., Mann, M., Meng, C. K., Wong, S. F., & Whitehouse, C. M. (1989). Electrospray ionization for mass spectrometry of large biomolecules. *Science*, Vol. 246 (4926), 64–71.

Chapter 33
Swirl, T-Jet and Vibrating-Mesh Atomizers

M. Eslamian and N. Ashgriz

Abstract This chapter discusses several other types of atomizers that were not considered in the previous chapters. This includes "swirl nozzles, T-jet nozzles, and vibrating mesh nebulizers." The droplet size correlations for different types of nozzles is provided in Chap. 24.

Keywords Swirl nozzles · T-jet nozzle · Vibration mesh nebulizers

Swirl Atomizers

Introduction

Swirl nozzles are one of the most commonly used nozzles. They can produce relatively small droplet sizes at low inlet pressures. They are used in gas turbines and gasoline direct injection engines, among a wide range of other applications. A simplex swirl nozzle is depicted in Fig. 33.1, which comprises a small swirl chamber with one or more tangential fluid inlets and an axial fluid outlet. The tangentially introduced fluid forms a rotating flow inside the chamber. As this rotating flow exits the axial orifice, a conical swirling sheet is formed. The conical sheet spreads out, thinning the liquid, which finally breaks into small droplets.

Swirl flows can also be generated by using vanes positioned inside the nozzle to introduce rotating flows, as shown in Fig. 33.2, or by using an external swirling gas. Some two-fluid swirl atomizers use a swirling gas that is formed by tangentially introducing gas into a swirl chamber, which also has an axially introduced liquid inlet. The liquid and the gas are mixed inside the swirl chamber and both exit

M. Eslamian (✉) and N. Ashgriz (✉)
Department of Mechanical and Industrial Engineering, University of Toronto, Toronto, Ontario, Canada
e-mail: m.eslamian@utoronto.ca; ashgriz@mie.utoronto.ca

N. Ashgriz (ed.), *Handbook of Atomization and Sprays*,
DOI 10.1007/978-1-4419-7264-4_33, © Springer Science+Business Media, LLC 2011

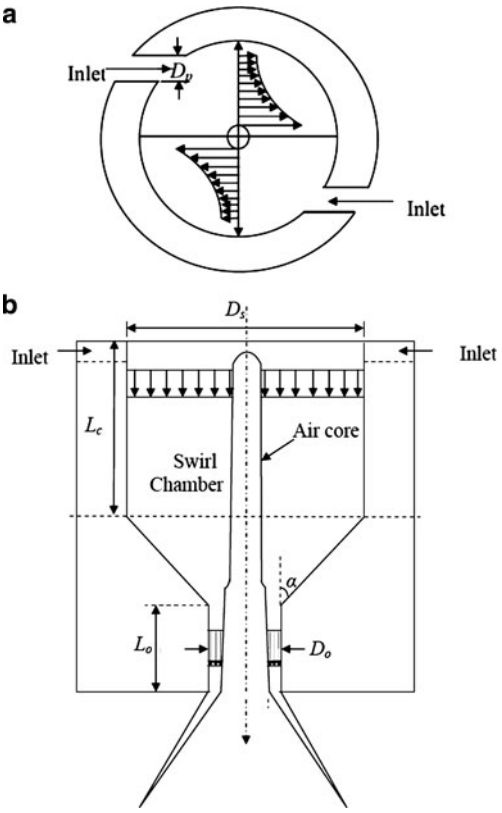


Fig. 33.1 Schematic of a simplex swirl nozzle: (**a**) top view, (**b**) side view

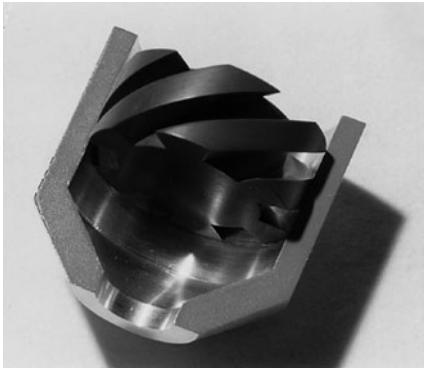


Fig. 33.2 A swirl nozzle with swirl-generating vanes [36]

together from an axial nozzle. Such nozzles can produce small drop sizes with good mixing capabilities. For a detailed description of different types of swirl nozzles see Lefebvre [1] and Bayvel and Orzechowski [2].

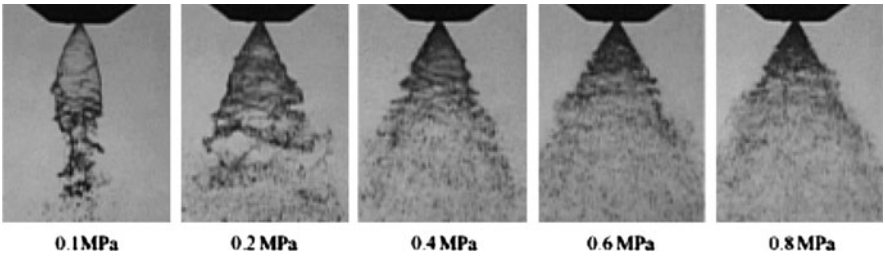


Fig. 33.3 Stages of spray development for neat oil at different pressures [3]

Figure 33.3 shows the development stages of a conical sheet at different pressures [3]. As the inlet pressure or flow rate is increased the initially rotating jet spreads radially, first forming a closed rim sheet, and then at higher flow rates forming an open conical sheet. When the sheet is fully developed, an air core develops inside the nozzle resulting in a thin film of liquid exiting the nozzle.

Because of their wide range of applications, swirl nozzles have been investigated extensively [4–70]. A review of the internal flow of swirl nozzles is given by Chinn [47, 48]. Chapter 24 provided correlation for the droplet sizes produced by swirl nozzles. This chapter provides only a brief discussion of some of the important parameters that affect the sprays formed by these nozzles.

Nozzle Characteristics

The nozzle geometry plays a significant role in the swirling sheet and spray characteristics. Figure 33.1 shows the main nozzle geometric parameters. These are the swirl chamber diameter, D_s, orifice diameter, D_o, entry port diameter, D_p, length of the orifice, L_o, length of the swirl chamber, and half cone angle of the swirl chamber α. A geometrical parameter that is found to correlate with some performance parameters is the nozzle constant, defined as

$$K = \frac{A_p}{D_s D_o} \tag{33.1}$$

where A_p is the total area of tangential entry ports [4].

Xue et al. [35] numerically studied the effect of various geometrical parameters on the formation of the sheet. Figure 33.4 shows the effect of the swirl chamber cone angle on the internal flow. In their condition, increasing the cone half angle from 45° to 90° resulted in 16% increase in dimensionless sheet thickness, 34% increase in the discharge coefficient, and 9% decrease in the spray half angle.

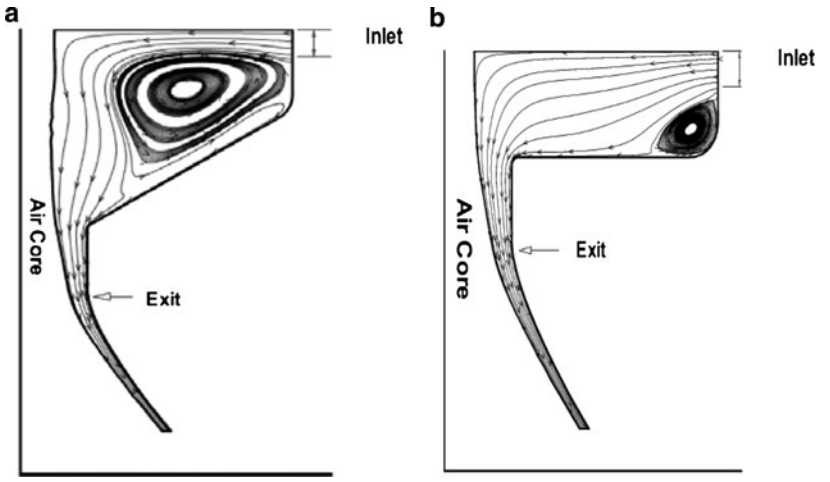


Fig. 33.4 Streamlines for flow inside a swirl atomizer (Reproduced from [35]. With permission)

Nozzle Discharge Coefficient

Another important parameter in swirl nozzles is the discharge coefficient, defined as

$$C_d = \frac{Q}{A_o(\Delta p/\rho)^{0.5}} \tag{33.2}$$

where Q is the liquid flow rate, A_o is the cross-sectional area of the discharge orifice, $\Delta p = p_{inj} - p_b$ is the difference between the injection pressure, p_{inj}, and the back pressure, p_b is the ambient pressure, and ρ is the liquid density. Since Δp depends on the nozzle geometry, so does the discharge coefficient [24]. The discharge coefficient (C_d) is weakly dependent on the inlet flow Reynolds number, defined as $\mathrm{Re} = \rho Q D_p/\mu A_p$ [27].

Radcliffe [52] studied a family of simplex/pressure swirl atomizers and demonstrated that at low Reynolds numbers C_D decreases with an increase of Reynolds number, and for larger Reynolds numbers, C_D is independent of the Reynolds number. It is also weakly dependent on the injection pressure within the normal operating range [42, 43]. Discharge coefficients for swirl nozzles are provided in [1, 51, 52], among others.

Air Core Characteristics

At low swirling flows, the liquid exiting the nozzle remains as a full jet. As the swirl increases, by increasing the inlet pressure or flow rate, the sheet opens. The swirling flow eventually forms an air core inside the nozzle as depicted in Fig. 33.1. For a given

nozzle, the formation of the air core depends on the inlet flow Reynolds number. Only above a critical Reynolds number, the air core is developed. Below the critical Reynolds number a full jet exits the nozzle producing a solid cone spray. The size of the air core increases with increasing the inlet Reynolds number. At a second critical inlet Reynolds number, the air core becomes fully developed and takes a cylindrical shape inside the nozzle [24]. The central air core is relatively uniform throughout the converging part of the nozzle but bulges at the entrance to the orifice of the nozzle and then remains almost cylindrical within the orifice up to the discharge plane [23].

The air core diameter and its turbulence characteristics determine the spray characteristics, such as drop size distribution. The larger the diameter of the air core, the thinner is the liquid film (sheet thickness), and, therefore, the smaller the droplet sizes. The air core reduces the effective flow area at the discharge orifice and causes a reduction in the volumetric flow rate through the nozzle for a given pressure drop. Therefore, the larger the air core diameter, the smaller is the discharge coefficient.

Cone Angle

The spray cone angle is inversely proportional to the nozzle constant [4]. The effective spray cone angle increases with increase in the injection pressure or liquid mass flow rate for all fluid viscosities and different nozzle geometries [20]. At the same time, the breakup point of the sheet approaches the nozzle, as shown in Fig. 33.5 [44]. An increase in the length/diameter ratio of the final discharge orifice reduces the spray cone angle. Liquid viscosity reduces the spray cone angle [20].

Chamber Back Pressure

High chamber back pressures occur in many systems, such as in liquid rocket engines, which can alter the spray characteristics. Kenny et al. [25] have shown

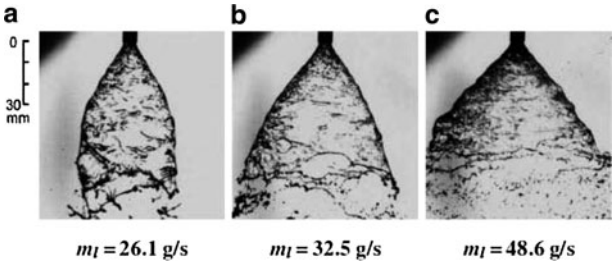


Fig. 33.5 Sheet cone angle increasing with flow rate (Reproduced from [44]. With permission)

that increasing the chamber back pressure causes an increase in the average film thickness, and, therefore, a reduction in the liquid velocity at a fixed mass flow rate. This was attributed to increased liquid momentum losses due to gas/liquid interfacial shear driven by the increasing gas density. The increase in the film thickness at the nozzle exit reduces the size of the air core. Therefore, an increase in chamber back pressure increases the flow discharge coefficient. They also noted that at high back pressures, necks or indentations form on the sheet. The necks vary in size and location based on the chamber backpressure value.

Effect of Fluid Properties

Fluid properties affect the liquid sheet appearance and the spray cone angle. They also affect the discharge coefficient. The discharge coefficient decreases with decreasing viscosity. Chung and Carry [56] noted that the change in discharge coefficient is reduced for $\mathrm{Re} > 2{,}000$. Liquid viscosity is the primary factor that influences breakup at $\mathrm{Re} < 2{,}000$. When $\mathrm{Re} > 2{,}000$, both the Reynolds number and Ohnesorge number affect the breakup length such that enhanced liquid inertia (via Reynolds number) reduces further the breakup length, and increased surface tension (via Ohnesorge number) enlarges breakup length.

Fluid surface tension is shown to cause a buildup of liquid around the circumference of the holes. This is presumed to thicken the sheet locally, producing a more stable structure and increasing the time to breakup [62].

Sheet Breakup

The breakup of the sheet into droplets is a complex process. The majority of the breakup models use aerodynamics sheet instability concepts for the breakup of the sheet. These models assume that small disturbances on the sheet grow, resulting in the breakup of the sheet. However, experiments show the formation of significant perforations on the sheet. The sheet and the spray have large-scale periodic features. Generally, three different mechanisms interact, resulting in a complex breakup mechanism. These are aerodynamic instability, perforated sheet, and periodic fluctuations of the air core. The latter affects the swirling liquid surface inside the nozzle. For instance, studies using glass nozzles have revealed the existence of helical waves on the surface of the liquid core inside the nozzle. This results in variations in the local film thickness profiles along the sheet [29].

The sheet perforation process is not well understood. Several different causes are suggested for the onset of perforation, including impingement of small droplets on the surface of the sheet, turbulent fluctuations inside the sheet, and small bubbles in some cases, and disturbances in the air core of the nozzle [65–67]. The main mechanism that is currently used to model swirling sheet atomization is based on the aerodynamics instability.

The instability theories for the breakup of a liquid sheet are discussed in Chap. 3. In those models, the growth rate of the fastest growing disturbance wave is used to

determine the breakup length of the sheet. However, information on the sheet thickness and velocity are needed for this calculation. This is obtained based on the information on the air core diameter and the spray cone angle. The swirling liquid exiting a nozzle forms a liquid film, the thickness of which can be obtained based on liquid mass flow rate: $\dot{m} = \rho u A$, where A is the cross section of the sheet at a certain distance from the nozzle and u is the mean velocity of the sheet at the same distance. The sheet thickness h is determined from conservation of mass: $urh = u_0 r_0 h_0$, where r is the radius from the injector centerline to the middle of the sheet, and the subscript 0 refers to the initial condition at the exit of the injector. The sheet thickness, right at the exit of the nozzle can be determined from $\dot{m}_l = \pi \rho_l u h (D_0 - h)$. The initial velocity u_0 can be obtained based on mean flow velocity, which depends on the injection pressure [41]:

$$U = K_v \sqrt{\frac{2\Delta p}{\rho_1}}. \tag{33.3}$$

Here K_v is an injector-specific dimensionless velocity coefficient represented by

$$K_v = \frac{C_D}{(1 - X)\cos\theta}. \tag{33.4}$$

C_D in Eqn. (33.4) is the fuel injector's coefficient of discharge and X is the ratio of the air core area at the nozzle exit to the nozzle area. If X is known then the sheet thickness is given by

$$h = \frac{D_0}{2}\left(1 - X^{\frac{1}{2}}\right) \quad \text{or} \quad X = \left(1 - \frac{2h}{D_o}\right)^2. \tag{33.5}$$

Several relations for the sheet thickness in terms of flow parameters are provided in Table 33.1. Schmith et al. [45] argued that K_v is about 0.7 based on the comparison with the discharge coefficient of a sharp-edge nozzle for a single fluid with $L/D = 4$, which is 0.78. If the cone angle is θ, then the axial velocity u_0 at the nozzle exit is

$$u_0 = U\cos\theta. \tag{33.6}$$

The instability of a liquid sheet was discussed in Chap. 3. It was shown that a viscous liquid sheet of thickness $2a$ moving with a relative velocity of U in another inviscid fluid (e.g., air) becomes unstable subject to a certain wave number. It was discussed earlier that above a critical Weber of 27/16, the fastest-growing waves are short waves. Therefore, it is reasonable to assume that $\lambda/a < \pi$ or tanh (ka) ≈ 1. This means that the wavelength can be on the same order as the sheet half-thickness and

Table 33.1 Analytical and empirical equations for the sheet thickness [69]

Authors	Equations
Rizk and Lefebvre [15]	$h = \left[\frac{1560\mu_l \dot{m}_l}{D_0 \Delta P} \frac{1+X}{(1-X)^2}\right]^{0.5}$
Suyari and Lefebvre [17]	$h = 3.66\left(\frac{D_0 \dot{m}_l \mu_l}{\rho_l \Delta P}\right)^{0.25}$
Kim et al. [61]	$h = 1.44 D_0 \left(\frac{\dot{m}_l \mu_l}{\rho_l \Delta P D_0^3}\right)^{0.25} \left(\frac{l_0}{D_0}\right)^{0.6}$
Lefebvre [1]	$\left(\frac{A_p}{2Rd_0}\right)^2 = \frac{\pi^2}{32} \frac{(1-X)^3}{X^2}$
Badami et al. [68]	$h = \left(\frac{D_0}{2}\right)(1-k) \quad \text{where} \quad \theta = 2\arctan\sqrt{\frac{k^2}{1-k^2}}$
Moon et al. [69]	$h = 0.97 A_p^{0.08} \left(\frac{\mu_l D_0}{\rho_l}\right)^{0.25} \left(\frac{l_0}{D_0}\right)^{0.76} (\tan\alpha)^{-0.12}$ when $\Delta P \geq 2\text{MPa}$

Note: k is the cavity factor. All other parameters are described in the chapter.

still be considered short. Senecal et al. [46] used the following maximum growth rate:

$$\omega_{\max} = MAX\left[-2\nu_l k^2 + \sqrt{4\nu_l{}^2 k^4 + \rho_r U_r{}^2 k^2 - \frac{\sigma k^3}{\rho_l}}\right] \tag{33.7}$$

where the maximum value of the term in the bracket is used. The sheet is assumed to be broken into ligaments when the wave amplitude reaches the sheet thickness:

$$L = \frac{U}{\omega_{\max}} \ln\left(\frac{\eta_b}{\eta_0}\right) = 12\frac{U}{\omega_{\max}} \tag{33.8}$$

where η_0 and η_b are the initial disturbance amplitude and the amplitude at the breakup point. Since the initial disturbance amplitude is not known, a value of 12 is used for $\ln(\eta_b/\eta_0)$.

Several other relations for the sheet breakup lengths are obtained. One is by Ren and Nally [39] based on Dombrowski and Hooper's [40] earlier model:

$$L = C_1 \left[\frac{\rho_l \sigma h \cos\theta}{\rho_g{}^2 U^2}\right]^{\frac{1}{2}}. \tag{33.9}$$

Another is by Han et al. [41]:

$$L = C_2 \left[\frac{\rho_l \sigma h D_0}{\rho_g{}^2 U^2 \tan\theta}\right]^{\frac{1}{3}} \tag{33.10}$$

where ρ_l and ρ_g are, respectively, the liquid and gas densities, σ is the liquid surface tension, and C_1 and C_2 are constants that are determined experimentally to be $C_1 = 1.7$ [39] and $C_2 = 3$ [41]. Table 33.1 summarizes different breakup lengths for comparison.

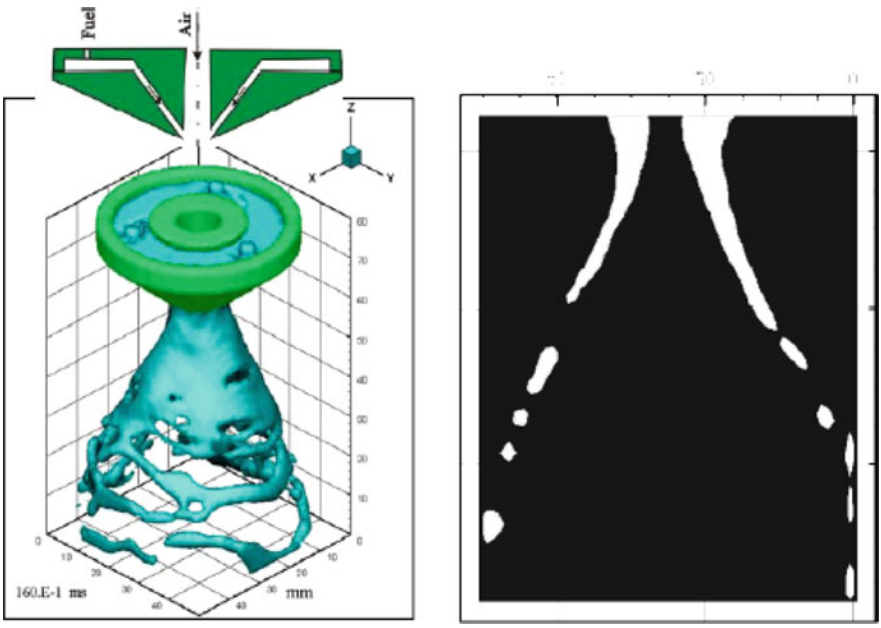


Fig. 33.6 Three-dimensional VOF modeling of a swirl atomizer. (*left*) Nozzle geometry having three 45° incline angle fuel inlets, and flow exiting the nozzle, and (*right*) sheet thickness at a certain time. Fuel properties used are: 700 kg/m^3 density, 5.0×10^{-7} m^2/s kinematic viscosity, and 0.02 N/m surface tension [38]

There has been some development in the numerical modeling of the sheet formation from swirl nozzles. A fully nonlinear model using an axisymmetric boundary element formulation has been developed for simulating the free surface shape and spray formed by simplex/pressure swirl atomizers [30, 32]. A linear instability analysis by Ponstein has been used to predict the number of droplets formed from each ring-shaped ligament shed from the parent surface.

The two-fluid modeling method using volume of fluid (VOF) is also used to simulate a swirl nozzle [38]. The schematic of the fuel injector used and typical results are shown in Fig. 33.6. In this design, fuel enters the injector in three inlets that are inclined 45° with respect to the top surface. The airflow through the center passage of the injector increases the liquid film breakup and atomization.

T-Jet and Y-Jet Nozzles

T-jet and Y-jet nozzles are special types of twin-fluid nozzles in which the liquid and the atomizing gas meet at a large angle, i.e., 90° for the T-jet and slightly less for the Y-jet nozzles. The operating principle of these nozzles is described in

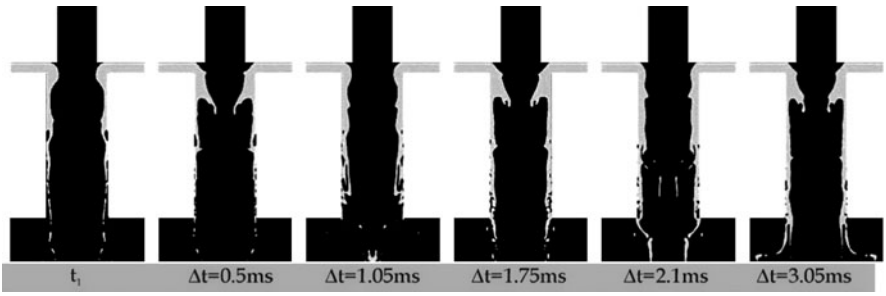


Fig. 33.7 Snapshots of a simulation with steam velocity = 100 m/s (case 1; $\Delta t = t - t_1$).

Fig. 33.7. In this figure the atomizing gas enters from the top while the liquid enters from a circumferential slot. As both fluids reach the core opening, the liquid is pushed toward the nozzle exit by the gas pressure. At an arbitrary time (t_1), the liquid flow is redirected by the gas pressure and a thin film is formed at the nozzle wall. The liquid partially blocks the gas flow, building a pressure. As the pressure builds to a critical value, a liquid chunk is removed. This process causes an oscillatory spray formation. The frequency of this oscillation depends on the liquid and gas flow rates. The frequency increases with increasing the velocity of the liquid or the gas. Two separate variables are important for the pulsation: (a) shear stresses at the liquid/gas interface, and (b) fluid momentum.

By increasing the gas velocity, the shear stress at the interface is augmented; consequently breakup is accelerated and the frequency is increased. By increasing the liquid velocity, the liquid momentum is increased which accelerates the rush of the liquid toward the axis of the nozzle, hence increasing the gas–liquid interaction and accelerating the liquid breakup and increasing the frequency. This self-induced pulsation is one of the major sources of noise in twin-fluid nozzles.

Also, changing the entrance angle increases pulsation. However, the amplitude of the pulsation is substantially decreased. The reason for this behavior lies in the gas–liquid interaction. As the entrance angle is reduced, liquid surface exposed to steam and consequently shear stresses at the interface are increased. Therefore, an increase in pulsation is observed. However, as the liquid direction is more aligned with the gas flow, the effect of liquid momentum opposing gas flow is reduced and as a result the amplitude of the pulsation is noticeably reduced. When the entrance dent is removed this effect becomes so pronounced that pulsation virtually disappears.

Vibrating Mesh Nebulizers

Nebulizers, the atomizers that produce a fine mist, are classified into three main commercialized types: air-jet (pneumatic), ultrasonic, and vibrating-mesh. Air-jet nebulizers atomize liquid into droplets using a high-velocity gas passing through

a narrow venturi nozzle. In ultrasonic nebulizers, a high-frequency vibrating piezoelectric crystal is employed to atomize the liquid. In this section, two types of the vibrating-mesh nebulizers, which are two new members of the nebulizer family, are considered [71].

Vibrating-mesh nebulizers are categorized as passively and actively vibrating-mesh devices. The passively vibrating-mesh nebulizer is the commercial inhaler, Omron model NE-U22. Figure 33.8a shows a schematic of this vibrating-mesh nebulizer and Fig. 33.8b shows the resulting spray image using the laser sheet illumination technique [72]. In Figure 33.8c a picture of an Omron NE-U22 is shown. In NE-U22, a liquid solution bottle is connected to a vibrating piezoelectric crystal attached to a transducer horn. The high-frequency (∼1.8 kHz) vibration of the piezoelectric crystal is transmitted to the transducer horn. The vibration of the horn pushes the liquid through the apertures in the mesh plate placed above it. The mesh plate contains thousands of tapered holes of about 3 μm in diameter [73].

Actively vibrating-mesh devices such as the Aeroneb® Professional Nebulizer may employ a micro-pump system which comprises an aerosol generator and a

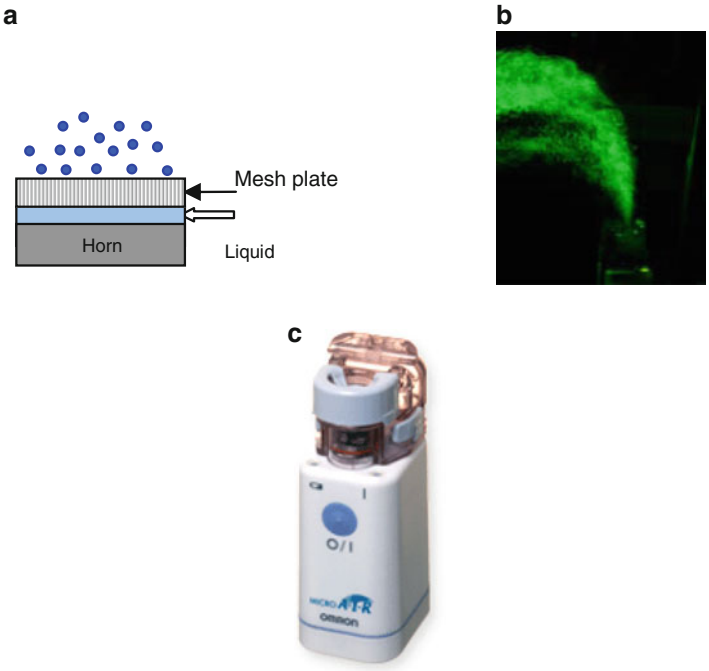


Fig. 33.8 (**a**) Schematic of the Omron NE-U22 vibrating-mesh nebulizer; (**b**) a spray image using laser sheet lighting in open atmosphere (Reproduced from [72]. With permission. Copyright 2007 the American Society of Mechanical Engineers (ASME)). (**c**) Photograph of an Omron NE-U22 vibrating-mesh nebulizer

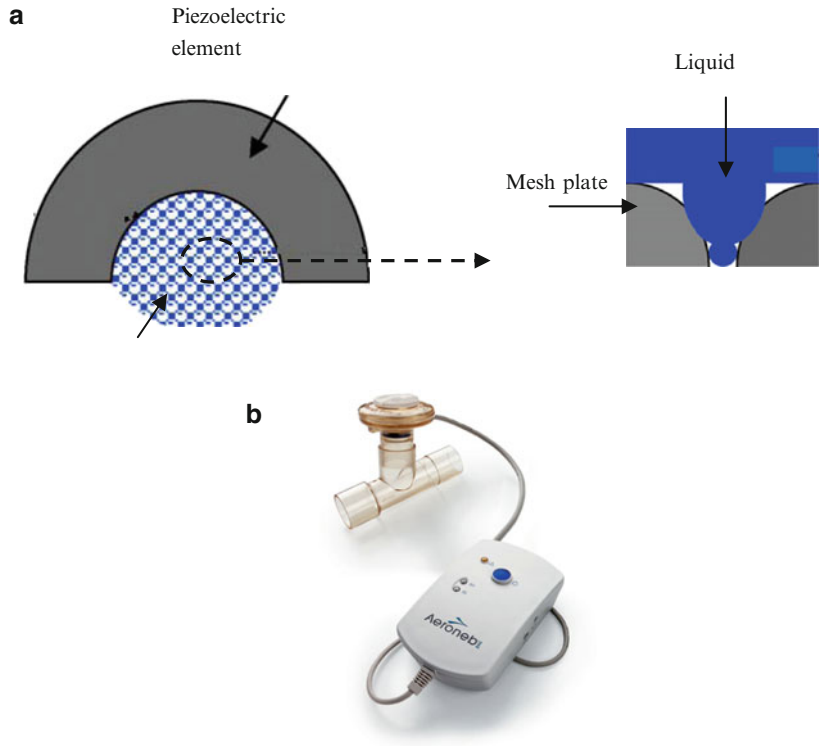


Fig. 33.9 (**a**) Schematic showing the principle of operation of an active vibrating mesh nebulizer (Reproduced from [71]. With permission. Copyright 2007 Elsevier). (**b**) Photograph of an Aeroneb® Professional Nebulizer System

vibrating element, where the former consists of a plate with up to 1,000 dome-shaped apertures. When an electric current is applied, this element contracts and expands, resulting in upward and downward movement of the mesh by a few microns and therefore extruding the fluid and generating droplets (Fig. 33.9a). Figure 33.9b shows a photograph of the Aeroneb® Professional Nebulizer.

From the inhaling perspective, vibrating-mesh nebulizers have several advantages over jet nebulizers. They are portable, silent, fast, do not require compressed air, and can operate with batteries or alternating-current power. There is no recirculation of drug from baffles, so there is little evaporative loss or cooling of the drug. The mesh can atomize fluids with normal viscosity, so there is the potential to significantly reduce residual dose and drug waste. However, the efficiency of delivery depends on the device housing that holds the mesh, which can be adapted to specific needs. The size of the droplet and aerosol produced is dependent on the size of the holes in the mesh and the physicochemical properties of the drug formulation. The output droplet size is usually about 5 μm.

One of the drawbacks to the vibrating-mesh devices is the potential to clog the tiny holes of the mesh. Suspension-type drugs may get caught in the mesh holes, and some solutions may be too viscous to pass through a mesh system. With repeated use, the nebulization time can gradually increase, and cleaning methods are necessary to maintain the efficient function of the mesh [71].

Very few research works are available on the spray characteristics of vibrating-mesh nebulizers. Eslamian and Ashgriz [72] studied the performance of a passively vibrating-mesh nebulizer, when water and several aqueous solutions with different concentrations were used. For instance, Figs. 33.10a and b respectively show the water droplet size and velocity distributions measured by a phase Doppler anemometer at 2 cm away from the nebulizer mesh plate. All histograms have Gaussian distribution curves. The droplet average size (d_{10}) and velocity are also shown in

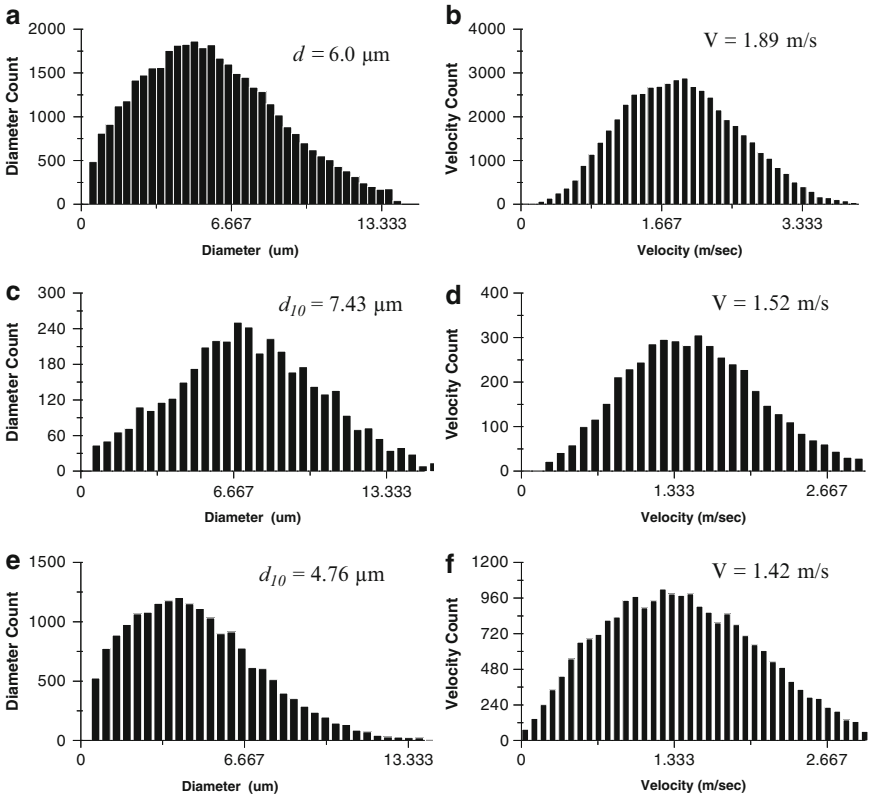


Fig. 33.10 (**a**) Water droplet diameter histogram of droplets produced by a vibrating-mesh nebulizer NE-U22 model; (**b**) droplet velocity histogram; (**c**) and (**d**) similar histograms to (**a**) and (**b**), but the liquid is 1 M solution of $MgSO_4$; (**e**) and (**f**) the liquid is 1 M solution of zirconium hydroxychloride. The measurements were taken at 2 cm away from the mesh plate using phase Doppler anemometry (Reproduced from [72]. With permission. Copyright 2007 the American Society of Mechanical Engineers (ASME).)

the figures. These figures show that the water droplet average velocity is 1.89 m/s and the droplet average size is about 6 μm, with a size range between 1 to 15 μm. In the results shown in Figs. 33.10c and d, water was replaced by a 1 M aqueous solution of magnesium sulfite ($MgSO_4$) and Figs. 33.10e and f show similar results when a 1 M solution of zirconium hydroxychloride (ZHC) is used. The droplet velocity decreases when a solution is used compared to the case where pure water is used. Although the mechanism of droplet generation by vibrating-mesh technique seems to be similar to that of the well-known ultrasonic atomization, there is no available theoretical work on this mechanism. Nonetheless, we can state that the droplet size and velocity are a function of liquid solution properties, such as surface tension and density. This is supported by experimental results.

Figure 33.11 shows the variation of the droplet velocity with distance from the mesh plate for water, and 1 M aqueous solution of $MgSO_4$, sodium chloride (NaCl), and ZHC. It is seen that regardless of the solution type, the droplet velocity deceases as the distance from the mesh plate increases. This is because droplets move upward against the gravity and therefore slow down quickly. It is also seen that the velocity of water droplets is higher than the velocity of the solution droplets, probably due to a higher viscosity associated with the aqueous solutions compared with pure water.

In another study by Ghazanfari et al. [71], a range of fluids with different properties were nebulized using an Omron NE-U22 (passively vibrating) and the Aeroneb Pro (actively vibrating) mesh nebulizers [71]. They found that the atomizer performance was dependent on both the fluid characteristics and the particular vibrating-mesh technology.

For all fluids, Ghazanfari et al. [71] found that the Omron nebulizer generated aerosols with slightly larger droplet size and similar or smaller fine particle fraction (FPF) than those of the Aeroneb Pro device. The total aerosol output was generally independent of fluid properties. However, increased fluid viscosity resulted in a decrease in droplet size and a consequent increase in the FPF, but the nebulization time was prolonged and output rate decreased (Fig. 33.12).

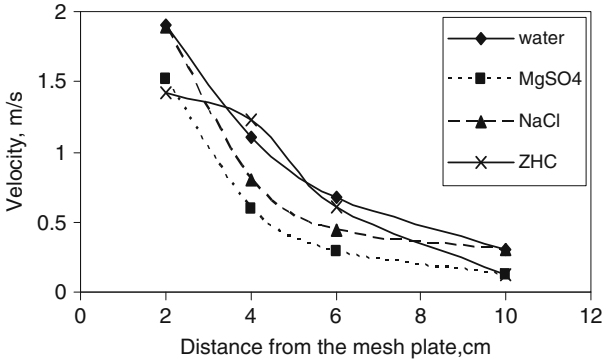


Fig. 33.11 Droplet velocity variations with distance from the tip of the nebulizer for water and three 1 M solutions of $MgSO_4$, NaCl, and ZHC

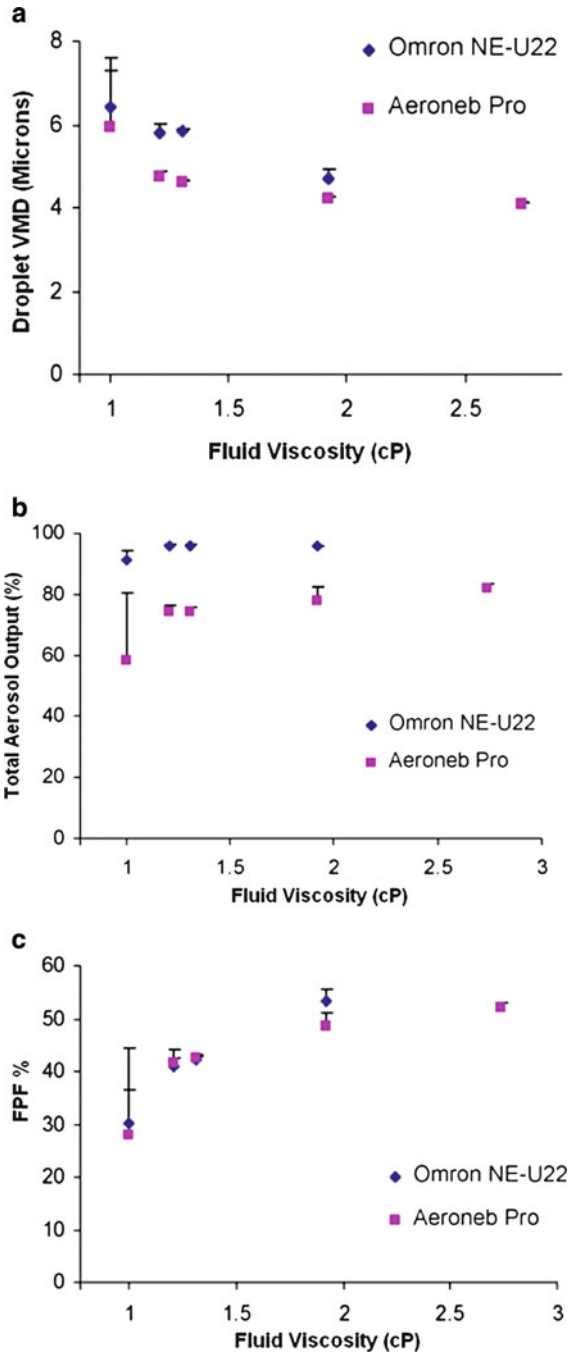


Fig. 33.12 Effect of fluid viscosity on (**a**) droplet VMD diameter, (**b**) total aerosol output, and (**c**) FPF (Reproduced from [71]. With permission. Copyright 2007 Elsevier)

A further increase in viscosity resulted in cessation of nebulization from the Omron nebulizer and intermittent aerosol generation from the Aeroneb Pro device, indicating that vibrating-mesh technology may be inappropriate for nebulizing highly viscous fluids.

The presence of low ion concentrations in the nebulizer fluid was desirable as it enhanced the aerosol generation and reduced the variability of droplet size and aerosol output. Increased ion concentration also resulted in a decrease in droplet size and a subsequent increase in the FPF, particularly for the Omron nebulizer.

No clear relationship was observed between fluid surface tension and aerosol properties. However, when viscosity was low, low surface tension seemed desirable as this dramatically shortened the nebulization time and increased the aerosol output rate, particularly for the Omron nebulizer, though for the Omron nebulizer this also increased the droplet size and slightly decreased the FPF. They found that the Omron nebulizer was superior to the Aeroneb Pro device in generating very high total aerosol outputs from the fluids investigated. On the other hand, the Aeroneb Pro nebulizer was superior in terms of completing nebulization in shorter times and producing higher aerosol output rates, especially when the viscosity was increased.

Kesser and Geller [74] reviewed some other aspects and also the challenges in treatment of the lung-related diseases and the delivery of drugs to the lungs using various inhalers, such as dry powder inhalers and also vibrating-mesh nebulizers.

References

1. A. H. Lefebvre, Atomization and sprays, Taylor & Francis, New York, 1989.
2. L. Bayvel, Z. Orzechowski, Liquid atomization, Taylor & Francis, Philadelphia, 1993.
3. J.-H. Rhim, S.-Y. No, Breakup length of conical emulsion sheet discharged by pressure-swirl atomizer, Int. J. Automot. Technol. 2(3), 103–107 (2001).
4. G. I. Taylor, The mechanics of a swirl atomizers, in: Proceedings of the Seventh International Congress for Applied Mechanics 2(1), 280 (1948).
5. G. I. Taylor, The boundary layer in the converging nozzle of swirl atomizer, Quart. J. Mech. Appl. Math. 3, 129 (1950).
6. A. M. Binnie, D. P. Harris, The application of boundary layer theory to swirling flow through a nozzle, Quart. J. Mech. Appl. Math. 3, 89 (1950).
7 E. Giffen, B. S. Massey, Some observations on flow in spray nozzles, Motor Industry Res. Assoc. Report No. 1948/4, (1950).
8. R. W. Tate, W. R. Marshall, Atomization by centrifugal nozzles, J. Chem. Eng. Prog. 49, 169 (1953).
9. A. M. Binnie, Viscosity effects in the nozzle of a swirl atomizer, Quart. J. Mech. Appl. Math. 8, 394 (1955).
10. A. M. Binnie, J. D. Teare, Experiments in the flow of a swirling water through a pressure nozzle and an open trumpet, Proc. R. Soc. London A 235, 78 (1956).
11. A. M. Binnie, G. A. Hakings, M. Y. M. Kamel, The flow of swirling water through a convergent–divergent nozzle, J. Fluid Mech. 3, 261 (1957).
12. S. P. Kutty, M. Narasimhan, K. Narayanaswamy, Design and prediction of discharge rate, cone angle and air core diameter of swirl chamber atomizers, in: Proceedings of the First International Conference on Liquid Atomization and Spray Systems, Tokyo, p. 93 (1978).

13. S. K. Som, S. G. Mukherjee, Theoretical and experimental investigations on the formation of air core in a swirl spray atomizing nozzle, Appl. Sci. Res. 36, 173 (1980).
14. A. R. Jones, Design optimization of a large pressure jet atomizer for power plant, in: Proceedings of the Second International Conference on Liquid Atomization and Spray Systems, p. 181 (1982).
15. N. K. Rizk, A. H. Lefebvre, Internal flow characteristics of simplex swirl atomizers, AIAA J. Propuls. Power 1(3), 193–199 (1985a).
16. N. K. Rizk, A. H. Lefebvre, Prediction of velocity coefficient and spray cone angle for simplex swirl atomizers, in: Proceedings of the Third International Conference on Liquid Atomization and Spray Systems, London, p. 111c/2/1 (1985b).
17. M. Suyari, A. H. Lefebvre, Film thickness measurements in simplex swirl atomizer, AIAA J. Propuls. Power 2(6), 528–533 (1986).
18. X. F. Wang, A. H. Lefebvre, Influence of ambient pressure on pressure swirl atomization, Atomization Spray Tech. 3, 209 (1987).
19. S. K. Chen, A. H. Lefebvre, J. Rollbuhler, Factors influencing the effective spray cone angle of pressure swirl atomizers, ASME J. Eng. Gas Turbine Power 114, 97 (1992).
20. S. M. Jeng, M. A. Jog, M. A. Benjamin, Computational and experimental study of liquid sheet emanating from simplex fuel nozzle, AIAA J. 36 (2), 201 (1998).
21. Y. Liao, A. T. Sakman, S. M. Jeng, M. A. Jog, M. A. Benjamin, A comprehensive model to predict simplex atomizer performance, ASME J. Eng. Gas Turbine Power 121, 285 (1999).
22. A.T. Sakman, M. A. Jog, S. M. Jeng, M. A. Benjamin, Parametric study of simplex fuel nozzle internal flow and performance, AIAA J. 38(7), 1214 (2000).
23. A. Datta, S. K. Som, Numerical prediction of air core diameter, coefficient of discharge and spray cone angle of a swirl spray pressure nozzle, Int. J. Heat Fluid Flow 21, 412 (2000).
24. M. R. Halder, S. K. Dash, S. K. Som, Initiation of air core in a simplex nozzle and the effects of operating and geometrical parameters on its shape and size, Exp. Thermal Fluid Sci. 26, 871–878 (2002).
25. R. J. Kenny, J. R. Hulka, M. D. Moser, O. N. Rhys, Effect of Chamber Backpressure on Swirl Injector Fluid Mechanics, J. Propuls. Power 25(4), (2009).
26. V. Bazarov, V. Yang, P. Puri, Design and dynamics of jet and swirl injectors, Liquid Rocket Thrust Chambers: Aspects of Modeling, Analysis, and Design, edited by V. Yang, M. Habiballah, J. Hulka, and M. Poppe, Vol. 200, Progress in Astronautics and Aeronautics, AIAA, Reston, pp. 19–103 (2004).
27. M. Doumas, R. Laster, Liquid-film properties in centrifugal spray nozzles, Chem. Eng. Prog. 49(9), 518–526 (1953).
28. S. K. Dash, M. R. Halder, M. Peric, S. K. Som, Formation of air core in nozzles with tangential entry, J. Fluids Eng. 123(4), 829–835 (2001).
29. D. Donjat, J. Estivalezes, M. Michau, G. Lavergne, Phenomenological study of the pressure swirl atomizer internal flow, Proceedings of the 9th International Conference on Liquid Atomization and Spray Systems, Sorrento, Italy, pp. 12–19 (2003).
30. S. M. DeCorso, G. A. Kemeny, Effect of ambient and fuel pressure on nozzle spray angle, American Society of Mechanical Engineers Paper No. 1956-GTP-3, April 1956.
31. J. Ortman, A. H. Lefebvre, Internal fuel distributions from pressure-swirl atomizers, J. Propuls. Power, 1(1), 11–15 (1985).
32. K. S. Park, S. D. Heister, Nonlinear modeling of drop size distributions produced by pressure-swirl atomizers, Int. J. Multiphase Flow 36, 1–12 (2010).
33. H. Park, S. D. Heister, Nonlinear simulation of free surfaces and atomization in pressure swirl atomizers, Phys. Fluids 18, 52103 (2006).
34. A. Mandal, M. A. Jog, J. Xue, A. A. Ibrahim, Flow of power-law fluids in simplex atomizers, Int. J. Heat Fluid Flow 29, 1494–1503 (2008).
35. J. Xue, M. A. Jog, S. M. Jeng, E. Steinthorsson, M. A. Benjamin, Effect of geometric parameters on simplex atomizer performance AIAA J. 42(12), 2408–2415 (2004).

36. S. Nonnenmacher, M. Piesche, Design of hollow cone pressure swirl nozzles to atomize Newtonian fluids, Chem. Eng. Sci. 55, 4339–4348 (2000).
37. S. Moon, E. Abo-Serie, C. Bae, Liquid film thickness inside the high pressure swirl injectors: Real scale measurement and evaluation of analytical equations, Exp. Thermal Fluid Sci. 34, 113–121 (2010a).
38. M. P. Fard, N. Ashgriz, J. Mostaghimi, L. A. Prociw, T. C. J. Hu, Modeling liquid film formation and breakup in an industrial spray nozzle, ILASS America, 15th Annual Conference on Liquid Atomization and Spray Systems, May 14–17, 2002, Madison, Wisconsin.
39. W. M. Ren, J. F. Nally Jr., Computations of hollow-cone sprays from a pressure-swirl injector, SAE Technical Paper 982610, Society of Automotive Engineers, Warrendale, 1998.
40. N. Dombrowski, P. C. Hooper, The Effect of ambient density on drop formation in sprays, Chem. Eng. Sci. 17, 291–305 (1962).
41. Z. Han, L. Fan, and R. D. Reitz, Multidimensional modeling of spray atomization and air-fuel mixing in a direct-injection spark-ignition engine, SAE Technical Paper 970884, Society of Automotive Engineers, Warrendale, 1997.
42. Z. Han, Z. Xu, S. T. Wooldridge, J. Yi, and G. Lavoie, Modeling of DISI engine sprays with comparison to experimental in-cylinder spray images, SAE Technical Paper 2001-01-3667, Society of Automotive Engineers, Warrendale, 2001.
43. J. Cousin, H. Nuglisch, Modeling of internal flows in high pressure swirl injectors, SAE Technical Paper 2001-01-0963, Society of Automotive Engineers, Warrendale, 2001.
44. T. Inamura, H. Tamura, H. Sakamoto, Characteristics of liquid film and spray injected from swirl coaxial injector, J. Propuls. Power 19(4), 632–639 (2003).
45. D. P. Schmidt, I. Nouar, P. K. Senecal, C. J. Rutland, J. K. Martin, R. D. Reitz, J. A. Hoffman, Pressure-Swirl Atomization in the Near Field, SAE Technical Paper 1999-01-0496, Society of Automotive Engineers, Warrendale, 1999.
46. P. K. Senecal, D. P. Schmidt, I. Nouar, C. J. Rutland, R. D. Reitz, M. L. Corradini, Modeling high-speed viscous sheet atomization, Int. J. Multiphase Flow 25, 1073–1097 (1999).
47. J. J. Chinn, An appraisal of swirl atomizer inviscid flow analysis, Part 1: The principle of maximum flow for a swirl atomizer and its use in the exposition and comparison of early flow analyses, Atomization Sprays 19(3), 263–282, (2009a).
48. J. J. Chinn, An appraisal of swirl atomizer inviscid flow analysis, Part 2: Inviscid spray cone angle analyses and comparison of inviscid methods with experimental results for discharge coefficient, air core radius and spray cone angle, Atomization Sprays, 19(3), 283–308 (2009b).
49. K. Ranganadha Babu, M. V. Narasimhan, K. Narayanaswamy, Prediction of mean droplet size of fuel sprays from swirl spray atomizers. Proc. ICLASS-82, Madison, Wisconsin, 3–4, 99–106 (1982).
50. M. M. Elkotb, N. M. Rafat, M. A. Hanna, The influence of swirl atomizer geometry on the atomization performance. Proc. ICLASS-78, Tokyo, 5–1, 109–115 (1978).
51. N. Dombrowski, D. Hasson, The flow characteristics of swirl (centrifugal) spray pressure nozzles with low viscosity liquids, AlChE J. 15(4), 604–611 (2004).
52. A. Radcliffe, The performance of a type of swirl atomizer, Proc. Inst. Mech. Engrs 169, 93 (1955).
53. J. C. Cooke, On Pohlhausen's method with application to swirl problem of Taylor, J. Aeronaut. Sci., 19(7), 486–490 (1952).
54. I. Novikov, Atomization of liquids by centrifugal nozzles, Engineers' Digest (British Edition), 10(3), 72–74 (1949).
55. P. W. Loustalan, M. H. Davy, P. A. Williams: Experimental investigation into the liquid sheet break-up of high-pressure DISI swirl atomizers, SAE paper 2003-10-27
56. I-P. Chung, C. Presser, Fluid property effects on sheet disintegration of a simplex pressure-swirl atomizer, J. Propuls. Power 17(1), 212–216 (2001).
57. S. Boyaval, C. Dumouchel, Investigation on the drop size distribution of sprays produced by a high-pressure swirl injector: Measurements and application of the maximum entropy formalism Part. Part. Syst. Charact. 18, 33–49 (2001).

58. P. W. Loustalan, M. H. Davy, Preliminary analysis of the near nozzle break-up from a pressure-swirl atomizer using a void fraction technique, presented at 5th International Congress on Direkteinspritzung im Ottomotor (Gasoline Direct Injection Engines), Essen, Germany, 1–2 July, 2003.
59. P. W. Loustalan, M. H. Davy, P. A. Williams, Experimental investigation into the liquid sheet break-up of high-pressure DISI swirl atomizers, SAE 2003 Transactions, vol. 112, section 4, J. Fuels Lubricants ISBN 0-7680-1451-4, pp. 2124–2134 (2004).
60. J. Galpin, J. Cousin G. Corbinelli, S. Siveri, A one dimensional model for designing pressure swirl atomizers, SAE Technical Paper 2005-01-2101, Society of Automotive Engineers, Warrendale, 2005.
61. S. Kim, D. Kim, D. Y. Yoon: Liquid film thickness measurement for swirl injector, J. Korean Soc. Propuls. Eng. 10, 70–77 (in Korean) (2006).
62. A. Mansour, N. Chigier, Disintegration of liquid sheets, Phys. Fluids A, 2(5), 706–719 (1990).
63. D. Cooper and A. J. Yule, Waves on the air core/liquid interface of a pressure swirl atomizer, Proc. ILASS-Europe, Zurich, Switzerland (2001).
64. J.J. Chinn, The analogy between waves on the surface of an aircore of a swirl atomizer and long, shallow water gravity waves, Proc. ICLASS-Europe, Sorrento, Italy, 2003.
65. N. Dombrowski, R. P. Fraser, A photographic investigation into the disintegration of liquid sheets, Phil. Trans. Roy. Soc. London A, 247(924), 101–130 (1954).
66. R. P. Fraser, P. Eisenklam, N. Dombrowski, and D. Hasson, Drop Formation from Rapidly Moving Liquid Sheets, AIChE J. 8(5), 672–680 (1962).
67. G. Taylor, The dynamics of thin sheets of fluid. III. Disintegration of fluid sheets, Proc. Roy. Soc. London A 253(1274), 313–321 (1959).
68. M. Badami, V. Bevilacqua, F. Millo, M. Chiodi, M. Bargende, GDI swirl injector spray simulation: Combined phenomenological-CFD approach, SAE Paper 2004-01-3005 (2004).
69. S. Moon, E. Abo-Serie, C. Bae, Liquid film thickness inside the high pressure swirl injectors: Real scale measurement and evaluation of analytical equations, Exp. Thermal Fluid Sci. 34, 113–121 (2010b).
70. Y. Khavkin, The theory and practice of swirl atomizers, CRC Press, London (2003).
71. T. Ghazanfari, A. M. A. Elhissi, Z. Ding, K. M. G. Taylor, The influence of fluid physico-chemical properties on vibrating-mesh nebulization, Int. J. Pharm. 339, 103–111 (2007).
73. R. Dhand, Nebulizers that use a vibrating mesh or plate with multiple apertures to generate aerosol, Respir. Care 47, 406–416 (2002).
72. M. Eslamian, N. Ashgriz, Effect of atomization method on the morphology of spray generated particles, J. Eng. Mater. Technol. 129(1), 130–142 (2007).
74. K. C. Kesser, D. E. Geller, New aerosol delivery devices for cystic fibrosis, Respir. Care 54(6), 754–768 (2009).

Part IV
Spray Applications

Chapter 34
Spray Applications in Internal Combustion Engines

K. Lee and J. Abraham

Abstract Modern internal combustion engines running on liquid fuels employ injection of the liquid as the means of delivering fuel to the engine. In spark-ignition (SI) engines, there may be port fuel injection (PFI), throttle-body injection (TBI), or direct injection (DI). In compression ignition (CI) engines, injection may be into the port as in homogeneous-charge compression ignition (HCCI) engines or into the chamber as in conventional diesel engines. Injection pressures vary from 2 to 3 bar in PFI engines to 2,000 bar or higher in conventional DI diesel engines. Injection systems may be electronically controlled as in PFI and common-rail injectors (CRIs), or mechanically controlled. Injectors, sprays, and modes of fuel–air mixing in the engines are reviewed in this chapter. Engines selected for detailed discussion are PFI homogeneous-charge SI engines, gasoline direct injection (GDI) SI engines, diesel engines, and low-temperature combustion compression-ignition engines.

Keywords Direct injection · Gasoline direct injection · High-pressure injection · Homogeneous-charge compression ignition · Low-temperature combustion · Port-fuel injection

Sprays in Port-Injected Gasoline Engines

Port fuel injectors (PFIs) are employed in SI automotive engines for fuel delivery. The PFI system in gasoline engines, also called multipoint fuel injection (MPI) system, in which each cylinder receives fuel from its own fuel injector located close to the intake valve has taken the place of carburetors in modern engines [1].

K. Lee (✉)
Department of Mechanical Engineering, Hanyang University, Korea
e-mail: hylee@hanyang.ac.kr

N. Ashgriz (ed.), *Handbook of Atomization and Sprays*,
DOI 10.1007/978-1-4419-7264-4_34, © Springer Science+Business Media, LLC 2011

Advantages of PFI relative to carburetion include more accurate fuel-metering and faster response to changes in engine operating conditions because of the shorter distance between the point of fuel delivery and the intake valve. Increased power and torque result from improved volumetric efficiency and more uniform fuel distribution among cylinders. Another advantage of the MPI system is its capability to accommodate alternative fuels with relatively simple modification of control parameters. The amount of fuel injected per cycle to each cylinder is varied in response to inputs derived from various sensors. While PFI has been employed for many years, injector design and spray characteristics are still the subject of research because of the interest in optimizing them for a broad range of operating conditions, especially cold-start conditions [2–5].

Mixture Preparation Processes in Port Injection Systems

The fuel injector has gone through a series of very rapid but subtle changes in its design in the past decade. The duration of the pulse exciting the injector solenoid coil controls the mass of fuel per injection. The injection can result in impingement of the spray on the walls, e.g., port walls, and back of valves, forming a liquid film of varying thickness. Spray and liquid film characteristics coupled with intake flow characteristics influence the fuel–air mixing in addition to factors such as fuel properties, duration of the injection, timing of the injection pulse relative to the intake valve opening profile, intake port and valve thermal condition, targeting accuracy, and the manifold absolute pressure. In prior work, the droplet behavior, vapor concentration, and air motion have been characterized using laser-based diagnostics to understand the mixture formation process [6].

Gasoline Fuel Injectors

Fuel injectors are nozzles that inject a spray of fuel into the intake air. They are normally controlled electronically. A metered amount of fuel is trapped in the nozzle end of the injector, and a moderate injector pressure (2–3 bar) generated by a fuel pump is applied to it. At the proper time, the nozzle is opened and fuel is sprayed into the intake manifold. The amount of injected fuel is controlled by pressure and dwell time of injection. An electronic fuel injector consists of solenoid coil, valve needle, plug, fuel inlet, and pintle. When not activated, the coil spring holds the plunger against its seat, which blocks the inlet flow of fuel. When activated, the electric solenoid coil is excited and moves the plunger and pintle. This opens the needle valve

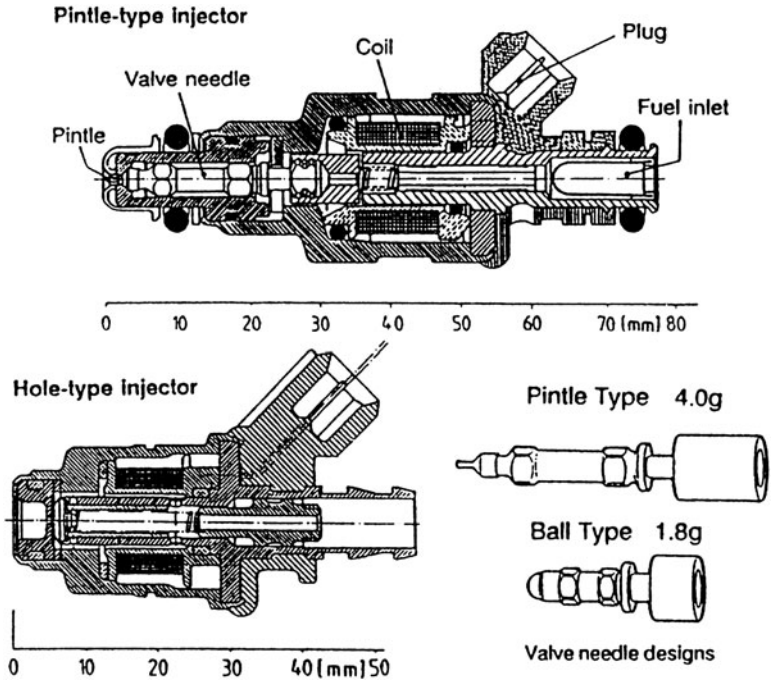


Fig. 34.1 Schematic of electronic gasoline injectors (*EGI*) (Reprinted from [7]. With permission. Copyright 1992 Springer)

and allows fuel from the fuel rail to be injected out of the valve orifice. Figure 34.1 shows the geometries of the low-pressure single-fluid injectors.

Spray Characteristics of Gasoline Port Injectors

Spray Structure of Pintle-Type Port Fuel Injectors

Figure 34.2 shows visualization images at three instances after start of injection (ASI) of the spray from a pintle-type injector. The spray developing process can be divided into three parts: the leading edge (Fig. 34.2a), the steady state (Fig. 34.2b), and the trailing edge (Fig. 34.2c). During the leading edge period, the spray has a hollow cone structure and the breakup of sheet is not apparent. The sheet converges downstream, and a liquid film is formed with a hollow spindle shape. Fuel droplets are formed from the point of convergence farther downstream. Figure 34.2b shows that aerodynamic forces in combination with the unstable waves cause instabilities of the fuel sheet and the sheet breaks into liquid ligaments regularly and droplets are

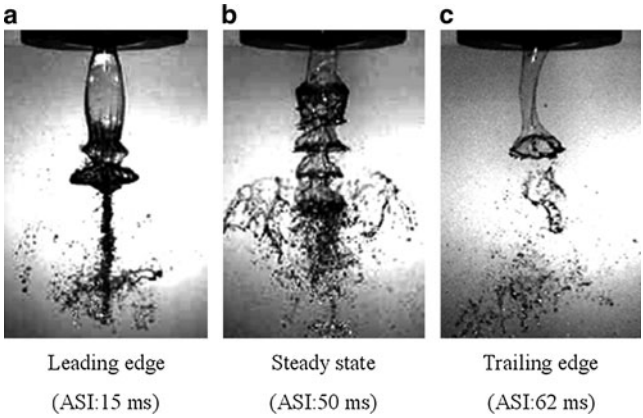


Fig. 34.2 Typical spray structure of pintle-type injector at several instances ASI. (**a**) Leading edge, (**b**) Steady state, (**c**) Trailing edge (Reprinted from [8]. With permission. Copyright 2007 of the Institute of Physics)

present in the outer and downstream regions of the spray. The breakup of the liquid sheet continues to generate a large number of droplets during the trailing edge period (Fig. 34.2c).

Spray Structure of Hole-Type Port Fuel Injectors

Figure 34.3 shows images illustrating the typical spray structure of a hole-type injector used in a four-valve gasoline engine. As the images show, liquid is injected through two holes. The spray develops into a ring shape downstream of the spray. Liquid ligaments are formed upstream which break into droplets downstream (see regions 1 and 3) as a result of interaction with air and growth of instabilities on the liquid surface (region 2). More fuel droplets are observed around the axis (region 1) of the injector between two sprays. Figure 34.4 shows the spray at several instances ASI. The angle between the two sprays is 19° and the sprays are symmetric in relation to the central axis. The penetration length increases linearly with time. Figure 34.5 presents the radial droplet number density distribution 100 mm downstream from the injector tip. The distribution is symmetric; this symmetry is important in a double overhead camshaft (DOHC) engine with two intake valves to accomplish homogeneous mixture formation and to reduce wall-wetting.

Nozzle Geometry Effects

Fujii et al. [9] studied how the needle-valve tip geometry affects the spray characteristics of a PFI. An increase in the angle of the needle-valve taper leads to a decrease in the droplet size. In addition, the standard deviation of the size

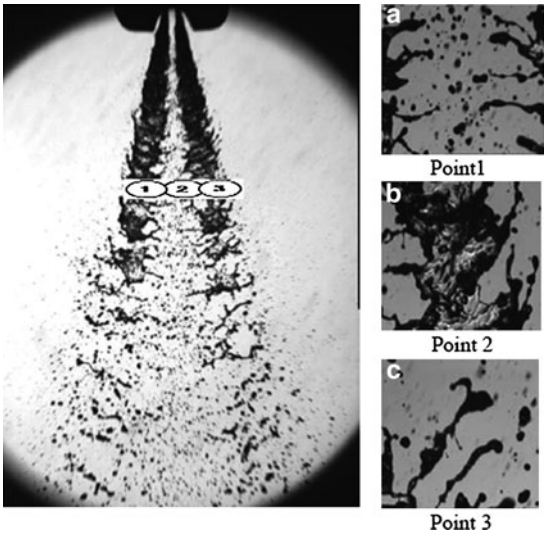


Fig. 34.3 Enlarged spray structure of two-hole-type injector (**a**) Point 1, (**b**) Point 2, (**c**) Point 3

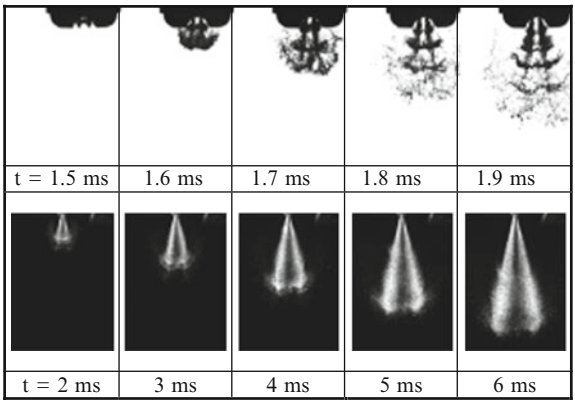


Fig. 34.4 Transient spray development. Time ASI is indicated

distribution becomes smaller and the spray angle increases. Fujieda et al. [10] developed an air-assisted gasoline injector to reduce the spray penetration. Figure 34.6 represents the geometries of the injectors. Type A has a spherical valve projection, which is located a few millimeters away from the seat. In type B a shroud with a diameter of 12 mm is installed at the tip of the injector, and consequently, the valve is recessed. In spite of these differences in geometry, the droplet size from the two injectors is identical in the core areas of the spray; the spray angles are, however, different. For type A, a spray is formed while air flows exist along the valve surface. As a result, the spray has a high velocity and small droplet size. For type B, the fuel is attached at the tip of the injector because

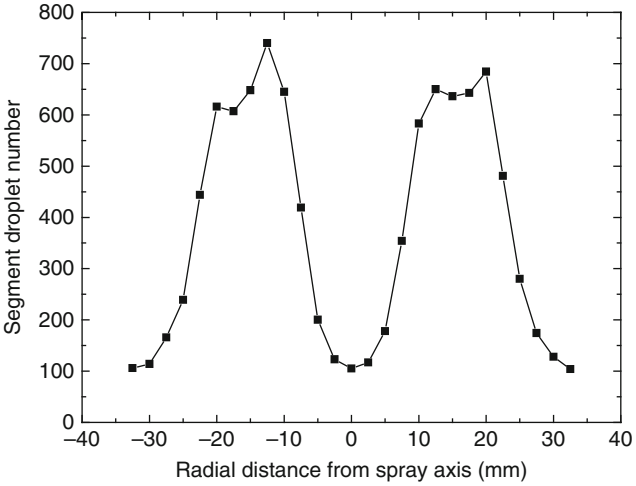


Fig. 34.5 The radial distribution of droplet number density

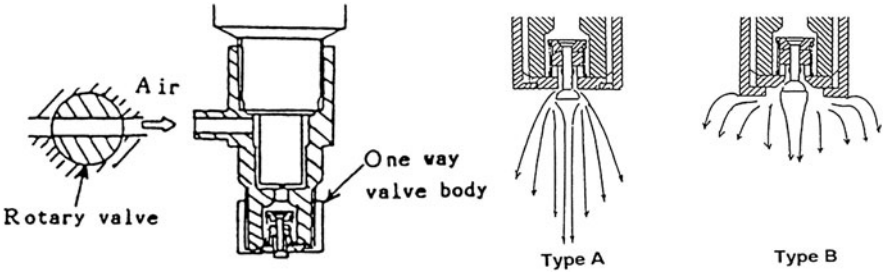


Fig. 34.6 Air-assisted injector and the associated spray structure with two different nozzle-tip geometries [10]

the spray expands along the nozzle surface. Therefore, the spray velocity is low and the droplet size is larger at the periphery.

Spray Atomization Technology

Atomization of the fuel increases the fuel surface area resulting in increased mass, momentum, and energy transfer between the liquid and gas phases. In addition, finer atomization reduces the fuel–air mixing time and minimizes wall-wetting, resulting in more uniform fuel–air mixture. High relative velocities between the liquid jet and the ambient gas cause high shear force, which is conducive to the breakup of the jet. Methods employed to atomize the liquid will now be discussed.

Air-Shrouded Injector

Air Supply Method

In air-shrouded injectors, fuel atomization is achieved efficiently without engine power loss by using the natural air flow generated by the pressure difference between the front and rear of the throttle valve. This type of injector is common in PFI engines [11].

The Shape of Atomizer

In these injectors, an adapter is attached to the injector tip as shown in Figure 34.7. The fuel supply from the injector is fed to the adapter, which has two holes generating two sprays. Air is introduced through the holes on the wall of the adapter. There are two types of air-shrouded atomizers classified according to the relative locations of the air and fuel streams. One is an external-air mixing type and the other is an internal-air mixing type. It is known that the latter has a better air utilization and atomization performance than the former. The angle (θ) and the diameter (ϕ) of the air entrainment hole are design factors which influence the atomization of the liquid.

Spray Characteristics of an Air-Shrouded Fuel Injection

In order to analyze the atomization mechanism of the air-shrouded injector, the atomization characteristics of the fabricated atomizer was investigated using a phase Doppler particle analyzer (PDPA). The Sauter mean diameter (SMD) and mean velocity distribution at 5 ms ASI are shown in Fig. 34.8. As the air pressure increases, the air velocity increases and the air dispersion area is enlarged proportionally. The maximum velocity achieved is 55 m/s when the air pressure is 50 kPa. The degree of atomization is greater at the center flow because the air velocity at the center flow is greater. Spray patterns for various air pressures are shown in Fig. 34.9. It can be seen that as the air pressure increases, the atomization process transitions from varicose wave to sinuous wave mode. Atomization at low air pressure and low fuel pressure can be seen to be affected by a twisted or sinuous mode. The spray angle

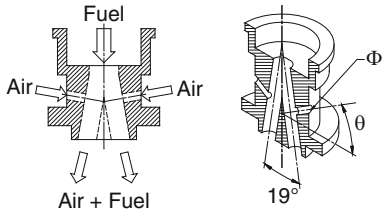


Fig. 34.7 Shape of an air-shrouded atomizer (Reprinted from [3]. With permission. Copyright 2002 Institute of Physics)

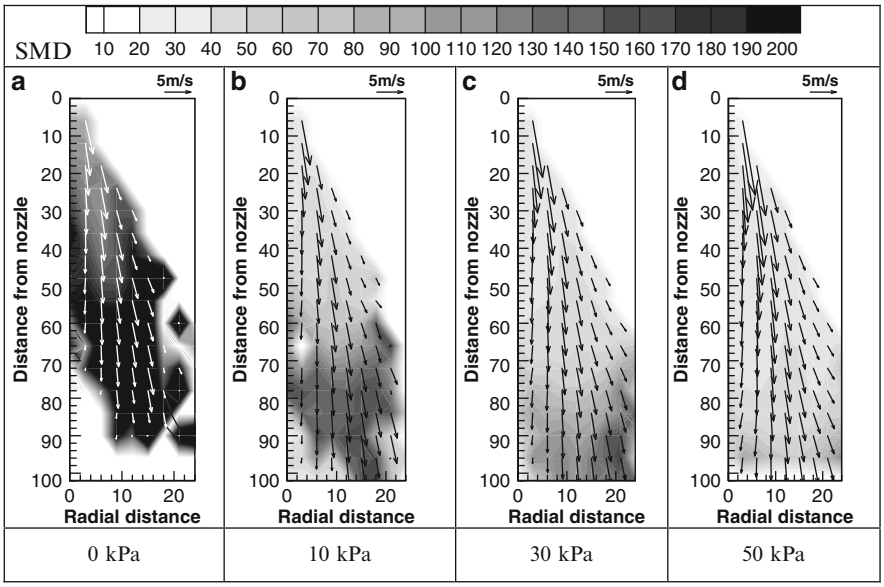


Fig. 34.8 The distribution of droplet velocity and SMD at 5 ms from the start of injection. (**a**) 0 kPa, (**b**) 10 kPa, (**c**) 30 kPa, (**d**) 50 kPa (Reprinted from [3]. With permission. Copyright 2002 Institute of Physics)

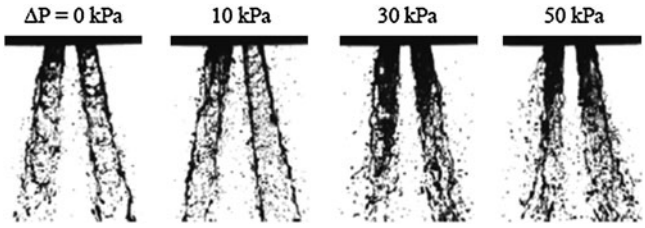


Fig. 34.9 The comparison of spray pattern with air pressure at 5 ms from the start of injection (Reprinted from [3]. With permission. Copyright 2002 Institute of Physics)

and the penetration of the spray are increased as air pressure is increased. It can be concluded that the air flow has a significant influence on the atomization and spray characteristics.

Swirl-Type Injector

In a swirl-type injector, angular momentum is generated in the exiting liquid stream to enhance atomization. High tangential velocities are generated by the angular momentum. These tangential velocities generate a conical sheet from the liquid

stream. The swirl flow also increases the turbulence level which is conducive to good atomization. Okamoto et al. [12] applied the swirl technique to a dual-stream injector to enhance the spray atomization characteristics of an injector. This dual-stream injector was fabricated by installing a special adapter on a swirl-type, single-stream injector. As the swirl number increases, the droplet size becomes smaller, and the separation of the two sprays is increased, thus increasing swirl, which enhances the desirable characteristics of the spray. From the standpoint of spray separation, the adapter is one of the basic requirements for the dual-stream injector.

Sprays in Gasoline Direct Injection Engines

Introduction

The gasoline direct injection (GDI) engine belongs to the broader class of engines which are referred to as direct-injection spark-ignition (DISI) engines. In GDI engines, the fuel is directly injected into the cylinder during the intake or compression stroke of the engine cycle. Typical injection pressures are lower than 200 bar. Injection may be through single or multiple holes. When the fuel is injected during the intake stroke, the engine operates like a homogeneous-charge stoichiometric SI engine. This mode of operation is employed at high loads. When the fuel is injected during the compression stroke, the mixture is overall lean and stratified – regulating the injected quantity of fuel can regulate the load as in conventional diesel engines. In principle, throttling would not be needed to regulate the load and pumping losses can be reduced relative to PFI homogeneous-charge engines. This mode of operation is employed at part-load. The vaporization of the fuel within the cylinder results in a decrease in mixture temperature. This reduces the tendency to knock – hence, GDI engines can have higher compression ratios than homogeneous-charge SI engines. Alkidas and El-Tahry [13] have reported that the GDI engine has about 15% lower fuel consumption than a corresponding PFI engine. They attribute this to the reduced pumping loss, lean-burn, lower heat losses, and higher compression ratio of GDI relative to PFI. Offsetting these factors is lower combustion efficiency. It has also been reported that heat losses can increase in GDI engines with contoured pistons since their surface area is increased by the contoured surface. It is important to point out that GDI engines have been under development for more than 50 years [14–16] though there has been an exponential increase in published literature during the last 15 years ([17–19] and many other references since then). The reference list at the end of this short summary is far from being exhaustive. Within the last couple of years, the number of publications has started to decrease. Comprehensive reviews of GDI engines have been published [20–23].

When the mixture is injected during the compression stroke, close to the top-dead center, it is important to inject the fuel so that the fuel is accessible at the spark plug during ignition. Various strategies are adopted to achieve this. Figure 34.10

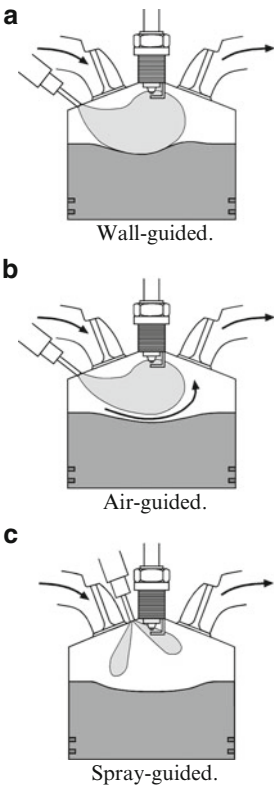


Fig. 34.10 GDI combustion chamber designs. (**a**) Wall-guided, (**b**) air-guided, (**c**) spray-guided

shows a schematic of three of the more common approaches: (a) wall-guided spray systems in which the spray is guided by the geometry of the wall toward the spark plug, (b) air-guided spray system in which the air motion, e.g., tumble, swirl, squish, within the chamber is exploited to convect the spray to the spark plug, and (c) spray-guided systems in which the spray orientation is such that the spray, or one spray in a multi-hole nozzle, is directed toward the vicinity of the spark plug [24–30].

Several types of injectors have been investigated for delivering the fuel. These include pressure-swirl atomizers, air-assisted atomizers, and single-hole and multi-hole injectors delivering solid-cone sprays. Injection pressures vary depending on the type of injector, but they are generally less than 20 MPa. In the case of solid-cone sprays, drop SMDs vary from about 50 μm at about 2 MPa to 15 μm at about 10 MPa. Air-assisted injectors typically deliver smaller diameters. Pressure-swirl atomizers can generate drops that are about 20 μm at about 5 MPa.

Emissions continue to be a problem with GDI engines. Wall-wetting in wall-guided systems can lead to higher unburned hydrocarbons and carbon monoxide because of cooler wall temperatures. Stratified-charge operation beyond a certain load can result in locally rich mixtures which can generate soot. Lean operation can

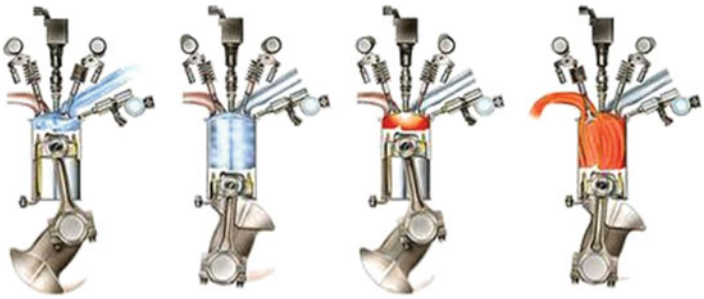


Fig. 34.11 Schematics illustrating the cycles of a GDI engine

lead to excessive carbon monoxide and unburned hydrocarbons. Wall-guided systems also have a challenge in that the coupling of the piston contour and spray impingement and redirect is mismatched when the injection timing is changed [31]. This factor along with the emissions issues discussed puts an upper limit on the load of stratified-charge engine operation. These difficulties are overcome by switching to standard homogeneous-charge operation beyond a certain load. Similar difficulties arise as speed is changed. Nevertheless, production GDI engines have been released by Mitsubishi [18, 32], Toyota [24, 33, 34], and Nissan [35, 36].

Figure 34.11 illustrates the cycles in a GDI engine. In the next sections, additional details about the injector, spray, and GDI technologies will be provided.

Characteristics of Spray Structure for a Swirl Injector

Fuel air mixing in the GDI engine is quite different from the port injection system (PIS) engine. While the PFI system allows enough time to evaporate the liquid fuel injected into the intake port, the DI method leaves less time for evaporation of the injected fuel. Thus, a finely atomized spray is desired to achieve rapid vaporization. Since a swirl injector has the advantages of good atomization and spatially dispersing the drops, high-pressure swirl injectors have been widely used in GDI engines. Therefore, an in-depth understanding of spray characteristics from a swirl injector will be useful.

Much research has, in fact, been carried out to achieve this understanding [37–39]. The spray structure has been investigated using visualization techniques such as laser sheet photography [40] and laser-induced fluorescence (LIF) [36], but detailed information of droplet characteristics cannot be obtained by planar measurements. Point measurements such as phase Doppler anemometer (PDA) can provide very high temporal resolution of droplet diameter and velocity, but lacks the ability to provide information about the spatial structure of the spray. Due to incomplete information about the spray, it is still difficult to optimize the pressure swirl injector. Computational studies of spray structure have revealed details of the

mechanism of the atomization and breakup process [41, 42], but the accuracy of these computational studies is dependent on the accuracy of initial and boundary conditions and of several sub-models, e.g., atomization sub-model. In many previous experimental studies, the SMD, measured by a PDA, is used to characterize the drop size; but the SMD by itself is not adequate to characterize the evaporation behavior. Data analysis [43, 44] which provides the size distribution is required. The aim of this investigation is to describe detailed spray characteristics such as drop size, velocities, penetration length, and spray cone angle.

Figure 34.12 shows a high-pressure swirl injector used for GDI engines [45]. The pressurized fuel is forced to flow through tangential passages on a small disk into the swirl chamber and then the fuel emerges from the orifice in the form of a thin conical sheet. To supply fuel to the injector at high pressure, the fuel supply system using high-pressure nitrogen gas was utilized instead of a high-pressure pump. This system can give low pulsations in fuel line, and maintain stable fuel pressure. In addition, the injection pressure and duration of 5 MPa and 7 ms, respectively, can be achieved. For this pressure and duration, the injected mass is 35.83 mg, representative of a high-load injection. Additional details about the spray structure from this specific injector will now be presented.

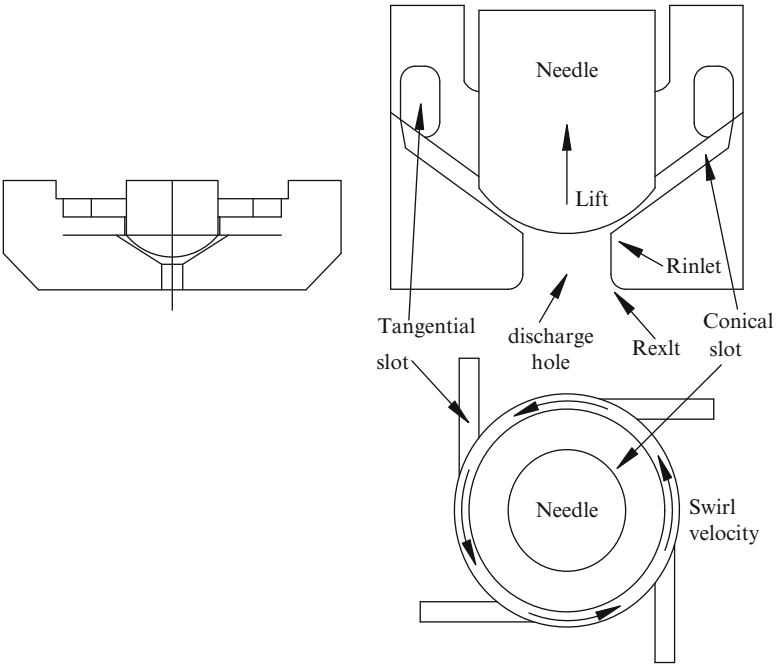


Fig. 34.12 Shape of test injector (Reprinted from [45]. With permission. Copyright 2003 Institute of Physics)

Evolution Processes of Global Spray

Figure 34.13 shows the development of a spray when fuel is injected at the pressure of 5 MPa with 7 ms of injection duration. As can be seen from the spray images, the spray shapes vary with time ASI. In the early stage of injection, the spray is not developed into a swirling conical spray. Instead, a bulk of the liquid consisting of large droplets and ligaments emerges from the nozzle hole. The conical hollow cone spray is observed at 3 ms ASI. At the same time, a vortex becomes evident at the outer edge of the spray. The 5 ms image shows droplets at the tip beginning to turn upward and toward the outside, as they are entrained in the vortex, and this recirculation zone suppresses the spray cone angle. The vortex flow also tends to carry the small drops, and as a result, the vortex cloud is seen at the spray tip in the final spray image. This result has important implications on the air–fuel mixing process in DISI engines.

Droplet Size Distribution

Figure 34.14 shows SMD distribution measured by PDA ASI. During the early stage of injection, large droplets are seen to be located in the central part of the spray. These probably originate from the early-injected liquid that is associated with the sac volume. At greater axial distances, droplet size increases probably because the larger droplets move to the leading edge of the spray faster due to their higher momentum. It is also expected that the recirculation zones carry the small drops upstream leaving the larger drops downstream. The drop size also increases with increasing radial distance. The reason is related to the centrifugal forces associated with the swirl velocity component of the film that emerges from the nozzle. The large droplets can be expected to have a tendency to move toward the periphery of the spray due to the centrifugal force. At longer time instances ASI, the drop sizes decrease and their distribution becomes more uniform, mainly due to the recirculation zones formed in the final stage of injection, which enhances air–fuel mixing. Secondary breakup in this recirculation area is promoted in the recirculation area because of higher relative velocities.

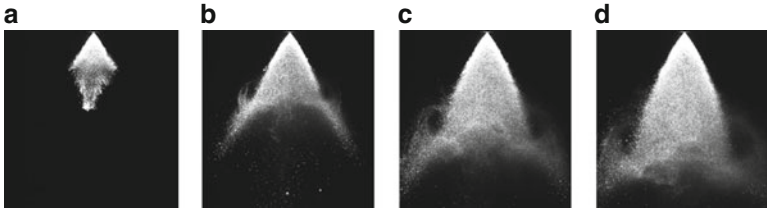


Fig. 34.13 Spray structure of a GDI injector (**a**) 1.5 ms, (**b**) 3 ms, (**c**) 5 ms, (**d**) 7 ms

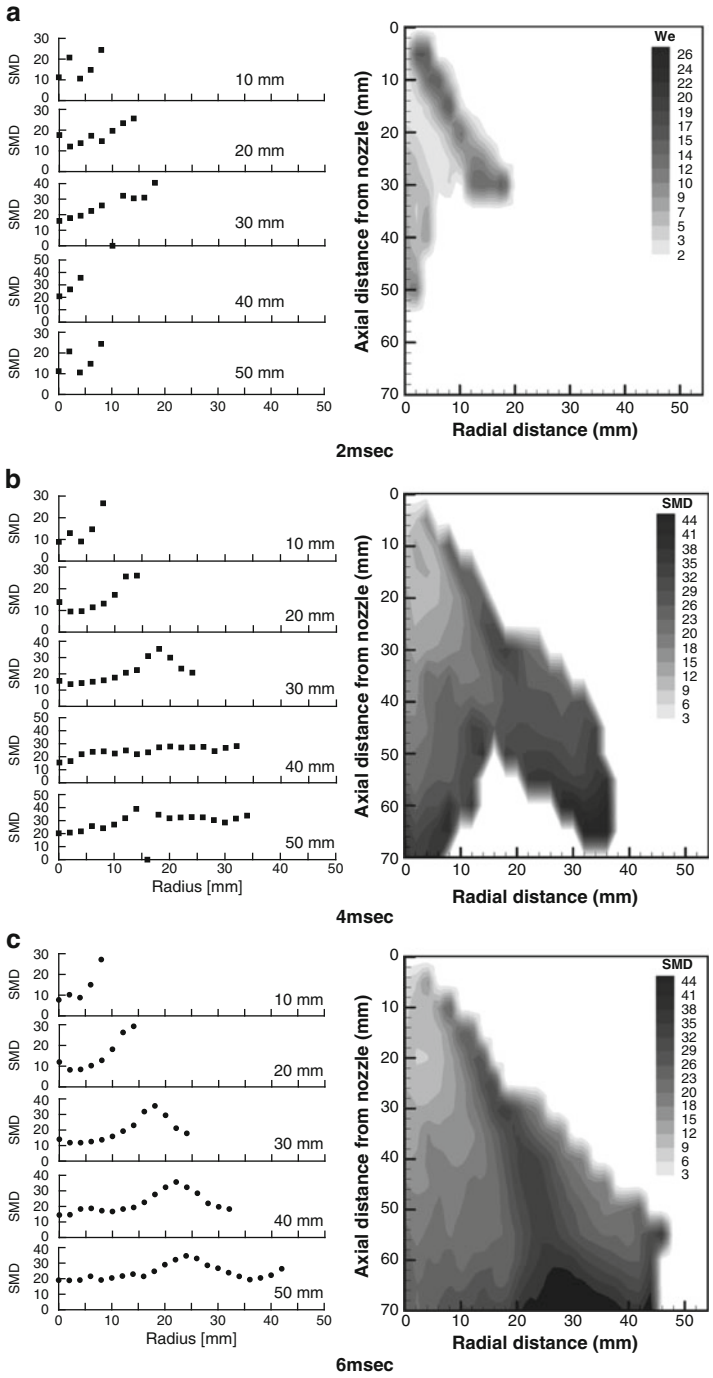


Fig. 34.14 SMD distribution contour (μm) (**a**) 2 ms, (**b**) 4 ms, (**c**) 6 ms

Spray Velocity Distribution

Figure 34.15 shows the mean velocity distribution at each measuring point for several instances. In the early stages, the velocities in the center of the spray are large because the larger droplets of liquid fuel that had remained in the sac volume of the injector are injected by high pressure. As time progresses, the velocity of the periphery area becomes faster than that of the center because of strong swirl flow, and a strong shear region is generated and grows continuously due to increased drag force between fuel droplets and ambient air. Moreover, since the outer air flows into the spray, the cone shape shrinks and the circulation region expands. This pattern is typical of a hollow cone spray. At 6 ms ASI, the vortex development occurs from 30 to 60 mm in the axial direction, and the velocity distribution near the spray tip becomes more uniform.

GDI Technologies

As discussed in the Introduction, there are two modes of operation of GDI engines. In the homogeneous mode, the fuel–air mixture is stoichiometric. The fuel is injected during the intake stroke (high load), and the mixed mode (part load) is when the fuel is injected during the compression stroke.

The GDI technologies can also be divided into two types based on injector position and injection strategy. One is the wall-guided type employing the side injection method. The other is the spray-guided type utilizing the center injection. Figure 34.16 shows three different types of GDI spray system. In side injection systems, the spray is guided by the wall head toward the spark plug. The side injection system has an advantage in that the cylinder shape used in PFI engines can be used. In fact, most automakers have adopted this system. In the center injection

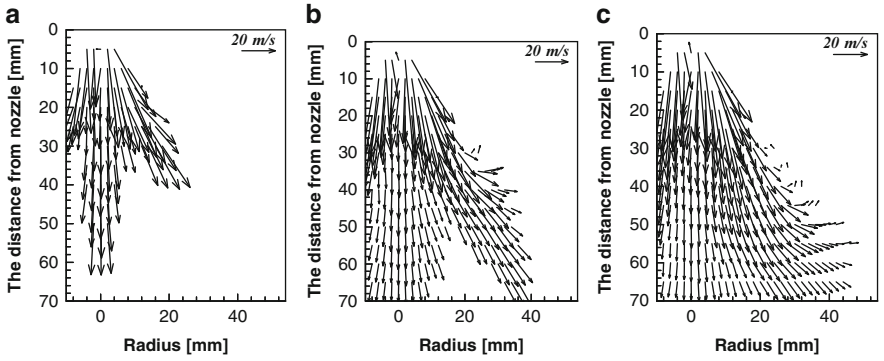


Fig. 34.15 Velocity distribution of the spray (**a**) 2 ms, (**b**) 4 ms, (**c**) 6 ms

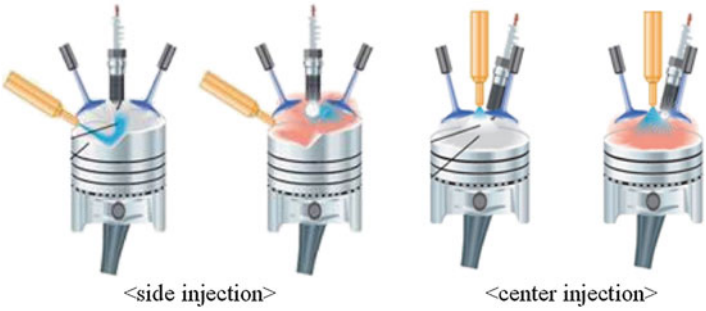


Fig. 34.16 Different types of GDI spray system



Fig. 34.17 Spray pattern of spray-guide-type injectors: (**a**) Solenoid injector, (**b**) Piezo injector

system, the injector is located at the center of combustion chamber and the fuel is directly injected toward the spark plug.

Spray Techniques in GDI System

The most significant factor to be considered for the GDI engines is the spray characteristics. In the first-generation GDI engines, the wall-guided spray, which strongly relied on the shape of the piston but not on the injector itself, was adopted. Side injection is used in this type of injection. More recently, the spray-guided system shown in Fig. 34.17 has become more common. This type uses the central

injection method such that a wider range of loads and speeds can be achieved. Piezo-type injectors having fast response time are generally adopted, and higher injection pressure is employed compared to solenoid-type injectors.

Recent Trend of GDI Technologies

The GDI engine has been under development for a quarter century, but it has faced challenges meeting emission regulations. Automakers in Japan have built successful engines which meet the regulations for the first time. The first successful development was in 1996 in Japan and it has had a significant influence on the European automotive market. Volkswagen and Renault have made significant strides in the development of GDI engines, and they began to produce cars in 2000. The wall-guided technique is more prevalent today, and Volkswagen as shown in Fig. 34.18 is the one that employs this concept widely. However, the improvement rate in terms of fuel consumption by this technology is less than 10%. The spray-guided concept is regarded as the next-generation technology and has been recently applied to BMW GDI engines as shown in Fig. 34.19, and other automakers are trying to develop the GDI engine with the spray-guided concept. Successful development of GDI technology is dependent on the development of an infrastructure which supplies low-sulfur gasoline with high octane value. To be competitive in the market with PFI engines, GDI engines must be cost-effective.

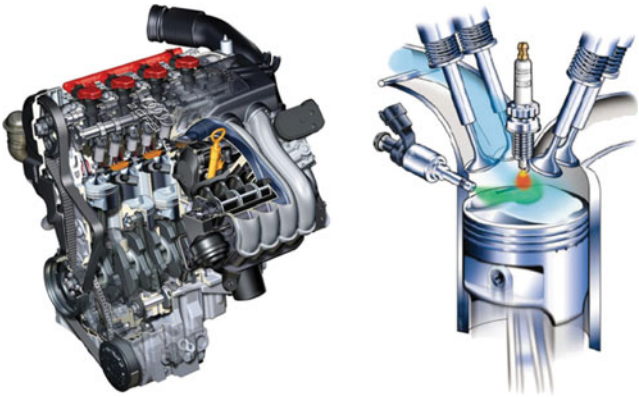


Fig. 34.18 Volkswagen FSI engine: side injection, wall-guided, solenoid injector

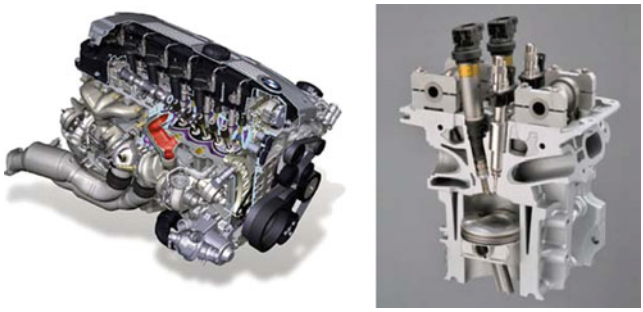


Fig. 34.19 BMW N57 engine: center injection, spray-guided, piezo injector

Sprays in Diesel Engines

Introduction

With their higher efficiency compared to gasoline engines, diesel engines are attractive alternatives to gasoline engines in light-duty applications. In the case of heavy-duty applications, the diesel engine has no substitute. Unlike in PFI engines, and even in DISI engines, diesel spray characteristics play a dominant role in determining the efficiency of combustion and in pollutant formation. The diesel spray has features closest to that of transient turbulent jets, which have been the subject of independent studies for many years. Injection in DI diesel engines is into a chamber where the temperature is in the range of 800–1,200 K and the pressure is 50–100 bar prior to combustion. The liquid is atomized to drops whose diameters lie in the range of 1–10 μm [46–50]. The earlier experimental works are typically at lower injection pressures whereas current diesel injectors can achieve pressures that are higher than 2,000 bar. Solid cone sprays are the norm in diesel engines. Note that measurements in the atomizing region of the spray are difficult and so drop sizes in this region have to be deduced from measurements at the periphery of the spray or from measurements in the dilute spray at several hundred diameters downstream of the orifice. This deduction often involves the use of multidimensional models in which drop sizes are estimated from models in the atomization region and then matched to those measured downstream. This is a difficult task prone to errors because of numerical inaccuracies in such models, and inadequate understanding of atomization and drop-interaction submodels [47, 51–59].

The drops generated through atomization transfer momentum to the chamber gas, entrain the gas, and undergo rapid vaporization. The jet penetrates as a vapor jet beyond the maximum length to which the drops penetrate, i.e., the liquid-phase length – this length can extend up to 2–3 cm [57, 60–62]. In addition to primary breakup of the liquid during atomization, the ligaments and drops which are formed undergo drop–drop interactions and secondary breakup in the near-field of the spray.

There has been discussion in the literature on the existence of an intake liquid core in the spray though no firm conclusions have been reached [47, 63–65]. The near-field of the spray where the liquid-phase length reaches its maximum length achieves a statistical steady state in a relatively short period of time (0.1–0.3 ms). While the physics of atomization and the structure of the spray in the atomizing region are not well understood, the quasi-steady structure downstream of the maximum liquid-phase length has been fairly well characterized through extensive experimental studies which will be reviewed below – in fact, it behaves like a gas jet [54, 55, 60, 66, 67]. Figure 34.20 shows a schematic of the structure of high-pressure diesel sprays. The spray angle in the near-field of the jet is generally smaller than in the far-field [47, 60, 68, 69]. In the far-field these angles tend to approach that of the turbulent gas jet. Identified in Fig. 34.20 are the intact liquid core (L_1), the liquid-phase penetration length (L_2), a quasi-steady region of the jet (L_3), and the transient head-vortex (L_4).

In the case of engine sprays, where the injection is intermittent, it is important to consider the transient nature of the spray in trying to understand mixing. In Fig. 34.20, this transient behavior is predominant in the head vortex. Note, however, that for a period of time after start of injection the part of the spray where transient mixing and development are important constitutes a significant fraction of the spray. The dynamics of the starting jet during the early stages of injection are still the subject of experimental and computational inquiry [67, 70–74]. Furthermore, the development of the head vortex and the mixing within it, both of which remain transient for the entire duration of spray penetration, are still not well understood. When injection ends, the behavior of the jets is again influenced strongly by transients. In fact, these transients can influence the mixing behavior in diesel engines and impact pollutant emissions [75].

With the increasing use of common-rail injectors (CRIs) to deliver the fuel, there is the opportunity of using multiple injections during one engine cycle, i.e., injection is pulsed. Pulse injection, or the special case where two pulses are employed – split injection, has been shown to result in decreased emissions of soot and nitrogen oxides. The reason for this decrease in engines is not clear. When the quantity of

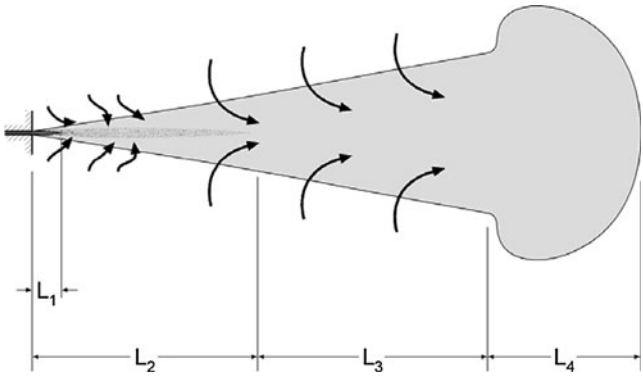


Fig. 34.20 Schematic of a full-cone diesel spray

fuel in the first pulse is fairly small, i.e., pilot injection or pre-injection, it is generally believed that the effect is to reduce the fuel burned, and heat release rates, during the premixed phase of combustion. In other situations, the timing and volume-phasing of injection certainly play a role, and separating these effects from those of pulsed-spray interactions is difficult. It is interesting to review more fundamental studies with gas jets which may provide some insight into the problem. Bremhorst and Hollis [76] showed increased entrainment in jets with pulses, and attributed the increase to larger Reynolds stresses in the unsteady jet. The pulsing frequency was fairly low compared to those employed in diesel sprays. Anders et al. [77] showed through their large-eddy simulation studies that the head vortex in the second pulse of a two-pulse jet is broken up faster than the head vortex of the first pulse by the residual turbulence. The pulsation frequency considered by Anders et al. is about two orders of magnitude larger than that of Bremhorst and Hollis, comparable to those in diesel engines. The faster breakup of the head vortex resulted in faster mixing, greater spreading, and slower penetration of the second pulse. The results were dependent on the dwell time between pulses, i.e., the frequency. At high frequencies, the mean flow induced by one pulse accelerated the subsequent pulse. Another way to think about this is that when the frequency is very high, the pulses behave like a quasi-steady jet.

The Diesel Injector

The performance of a diesel engine depends critically on the manufacturing quality and the operational conditions of the fuel injector. In diesel engines, the process of mixing of the fuel spray with air controls ignition, combustion characteristics, pollutant emissions – especially nitrogen oxides (NO_x), unburned hydrocarbons (HC), and soot – as well as noise emission. Mixing is dominated by the spray characteristics and therefore the properties of the fuel injector are of prime importance for the performance of diesel engines. Figure 34.21 shows the geometry of some high-pressure injector tips. Due to operational and manufacturing effects, optimum conditions may become impaired, which shows up immediately in the spray pattern. Therefore the spray pattern may be used as a sensitive indicator, allowing injector analysis outside the engine if engine conditions are simulated appropriately. Detailed studies revealed that most cases can be addressed at room temperature offering additionally an extended phase for investigations. Since the impulse of the fuel jet is much larger than the impulse of cross flows in the engine – swirl or squish flows – even quiescent pressurized chambers are suitable for analyzing injector properties with good accuracy.

Operating conditions and injector properties directly influence momentum and drop size of the developing fuel spray, and are thus immediately reflected in the four global spray parameters defined in Fig. 34.22: tip penetration S, cone angle θ, equivalence ratio ϕ, and Sauter mean diameter SMD.

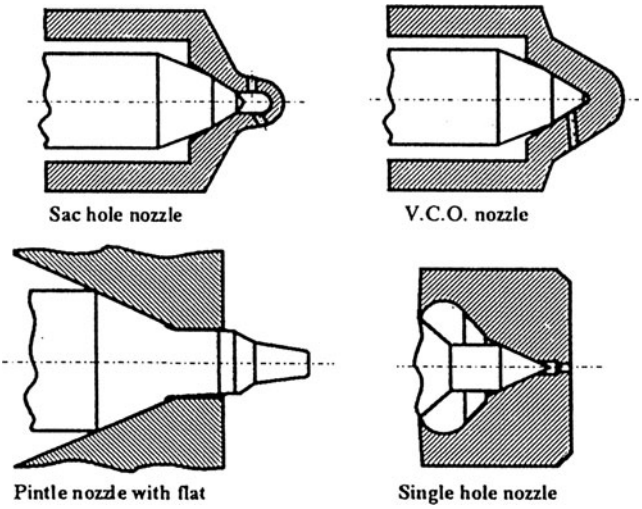


Fig. 34.21 Cross-sectional view of the most high-pressure automotive fuel injectors [78]

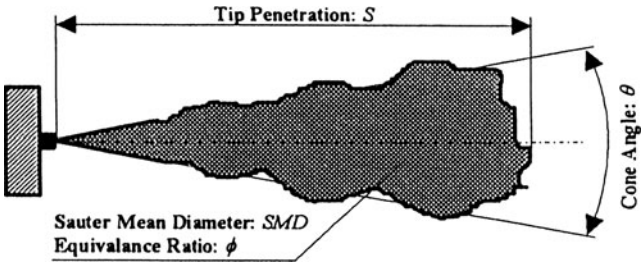


Fig. 34.22 Definition of the four global spray parameters: S, θ, ϕ, SMD [78]

These parameters may be easily measured with high temporal and spatial resolution by high-speed laser diagnostics (e.g., planar LIF of fuel and vapor) and diffraction–extinction techniques. These diagnostic tools have been used to study spray structures of automotive injectors and to investigate spray behavior by analyzing these structures [55, 59, 60].

Common-Rail System and High-Pressure Injector

DI diesel engines are much more efficient than indirect injection (IDI) engines. Emission regulations on UHC, NOx, carbon monoxide (CO), and particulate matter (PM) are getting stringent. In addition, increasing demands on fuel economy force diesel engine manufacturers to develop and use new injection technology. As pointed out earlier, fuel atomization is critical to increase engine efficiency and

reduce emissions. Increasing fuel injection pressure is found to be effective in promoting fuel–air mixing. Higher pressure improves fuel economy and reduces exhaust PM emissions significantly [79]. It is very important to control the fuel injection precisely and to understand the spray characteristics.

Figure 34.23 shows a CRI system. The injector in the system is designed to fulfill the requirement of high-speed DI diesel engines in terms of precise delivery control capability. It is also designed for mounting in a four-valve engine without any difficulty. Figure 34.24 (left) shows the hydraulically amplified injector. A new small control valve having hydraulic balancing is designed and implemented inside the injector holder body. The advantage of this concept is to be able to operate with low control current. Some important aspects have been considered to accomplish rapid control and reduce the stress in the nozzle seat. A piezo injector is shown in Fig. 34.24 (right). To control the injection valves, new CRIs use a rapid-action actuator made of piezo crystals to control the injection valve. The piezo crystals expand within an electrical field. The electronically controlled piezo actuator switches five times as fast as a solenoid. The movement of the piezo package is transmitted nonmechanically, and therefore, entirely without friction to the rapidly switching nozzle needle. This doubles the injector switching speed, allowing a more precise measurement of the amount of fuel injected and thus leading to a reduction in harmful combustion products.

The operating modes of the injectors are the following. When the electronic control unit (ECU) energizes the control valve solenoid, the control valve leaves its seat and the fuel pressure in the needle control chamber drops suddenly. As the fuel pressure at the nozzle seat is the same as the rail pressure, the needle opens and the injection starts. When the current in the solenoid valve is zero, the solenoid spring force returns the control valve to its seat [80].

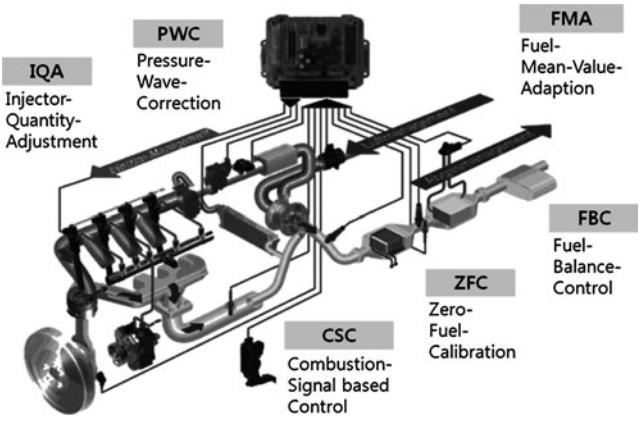


Fig. 34.23 Advanced control Robert Bosch® common-rail system

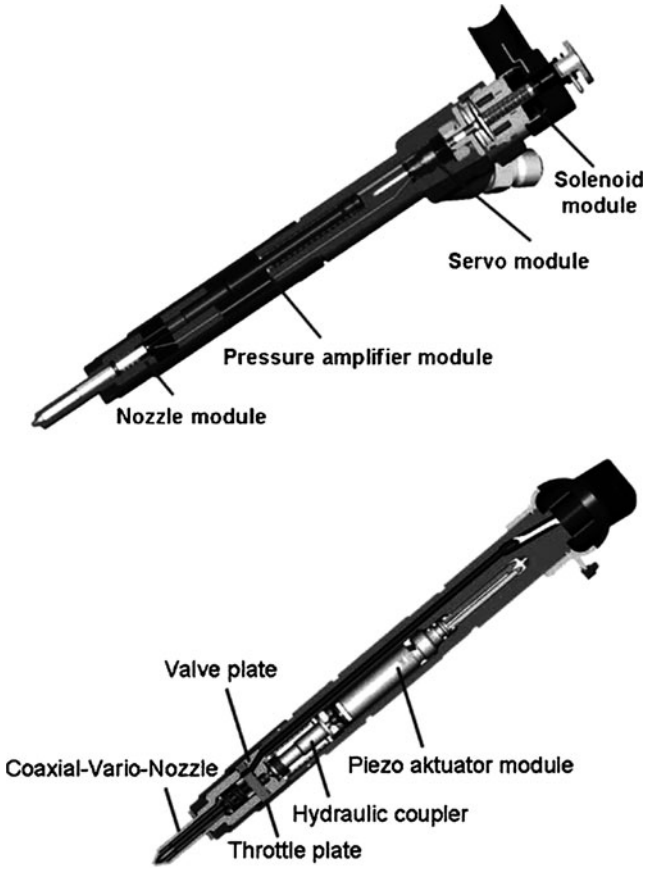


Fig. 34.24 Hydraulically amplified injector (*left*) and piezo injector (*right*)

Spray Characteristics

Effect of Nozzle Size

Cavitation and turbulence inside the nozzle hole influence the spray characteristics such as breakup length, drop sizes, and size distribution, and spray angle. Both cavitation and turbulence are strongly influenced by the nozzle geometry. Reducing the tendency for cavitation to occur and lowering turbulence levels result in longer break-up length and reduced variability in the spray angle as a result of reduced atomization close to the nozzle exit. Comparisons of cylindrical and conical nozzle show that spray hole geometry influences the internal flow characteristics such as pressure distribution, turbulence energy, velocity profile, cavitation, and therefore injection rate and spray atomization. An orifice with a convergent shape has a larger gas phase fuel penetration than an ordinary nonconical orifice. An orifice with

a divergent shape has much less gas phase fuel penetration than an orifice with a convergent shape. Conical orifices have proven to have a higher injection velocity and a smaller cone angle of the spray resulting in a positive impact on soot and NOx emissions. The conical shape also affects the discharge coefficient (Fig. 34.25).

Specification of injector nozzles

K	D_i(μm)	D_o(μm)
0	132	132
1.5	144	129
2	146	126

$$K = \frac{D_i - D_o}{10}$$

This high sensitivity to apparently small changes in geometry explains why high accuracy is required in manufacturing injectors. Two examples may serve to corroborate the need for fine control of injector details which might even arise unintentionally and cause serious problems in an engine. In Fig. 34.26, spray patterns are shown for a normal hole and a nozzle with a burr on the outer edge of the nozzle hole. This burr affects the outflow of the fuel. An abnormal design feature, in this case, causes a wider spray with reduced penetration. This minor flaw increases the Bosch smoke number by embarrassing 2–3 units. The second effect occurs most often in multi-hole nozzles with different positions and angles of the holes. Due to fluid dynamic processes inside the nozzle, the pressure forces are distributed unequally and thus the effect from minor manufacturing tolerances are amplified. An extreme example is shown in Fig. 34.27. These effects can be simulated by multidimensional models with good success [47].

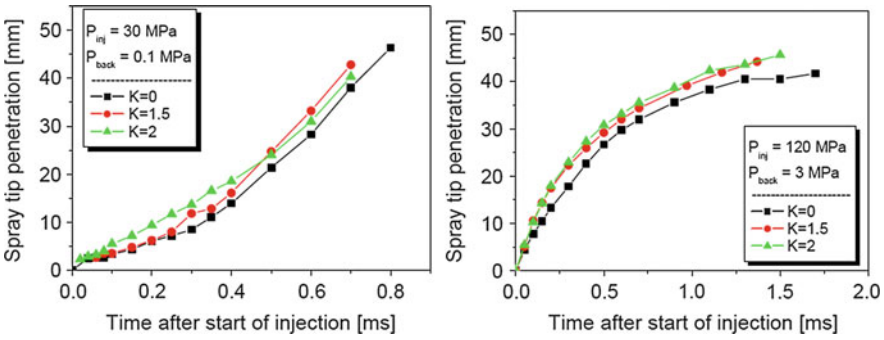


Fig. 34.25 Effect of tapered nozzle hole on spray tip penetration [81]

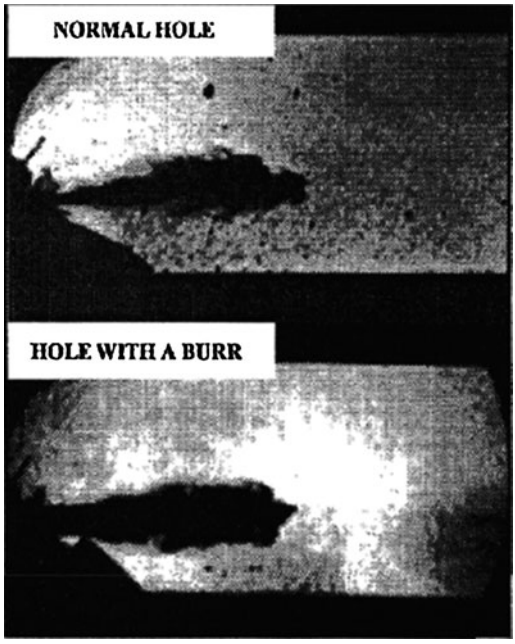


Fig. 34.26 Effect of a burr on the outer edge of a nozzle hole on the spray pattern. *Top*: normal injector; bottom: injector with needle offset. In the engine the smoke number is increased by 2–3 Bosch units [78]

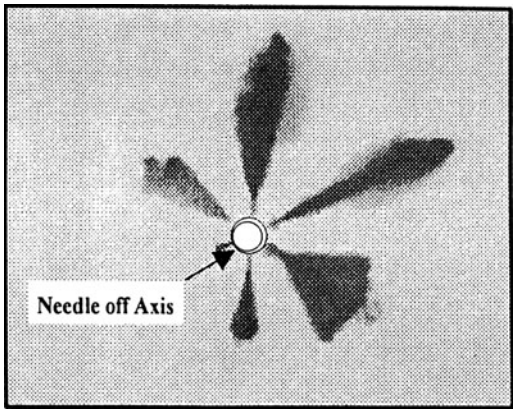


Fig. 34.27 Effect of an offset of the needle in a hole nozzle (V.C.O.) [78]

Effect of Injection Pressure

The effects of injection pressure on measured spray characteristics have been discussed in several references, for example [82]. At a given time ASI, a longer spray tip penetration length results from the higher injection pressure with diminishing effect as pressure is increased. The transient nature of the diesel spray and the gas entrainment during injection vary the cone angle throughout the spray event.

Large spray angles are usually observed at early times of the injection event. As the injection pressure increases, the SMD decreases. According to the breakup theory, higher injection pressure provides more energy and higher momentum due to the higher injection velocity, resulting in smaller droplet sizes. However, the SMD trend shows that the change of droplet sizes becomes smaller as the injection pressure increases.

Spray Penetration Distance

Adequate penetration is necessary for sufficient air utilization, but over-penetration can cause wall interactions associated with undesirable emissions. Recall that in a vaporizing diesel spray, the liquid penetration is not very long. In fact, the liquid penetration is likely to be important only at cold start. In this case, the liquid penetration length can be controlled by the orifice diameter of the injector summarized in Table 34.1. The liquid spray penetration distance decreases linearly with decreasing hole size. The injection pressure and the aspect ratio, i.e., the length to diameter of the orifice, have minimal influence on the liquid penetration length as discussed earlier. Vapor penetration is, however, influenced by the injection pressure. As the ambient gas density and temperature increase, the liquid penetration length decreases. In addition, as the fuel volatility decreases, the liquid penetration increases. Increasing the fuel temperature decreases the liquid penetration distance slightly, more significantly at low ambient densities and temperatures [83].

Table 34.1 Parameters affecting liquid penetration distance

System	Variable	Input	Effect on liquid sprays penetration distance (L)
Injector	Orifice diameter	↓	Strong decrease
			Linear decrease
			Strong decrease
	Injection pressure	↑	No significant effect, time to L_{max} reduced
			No significant
			Weak increase
	Nozzle aspect ratio	↑	No significant effect
Engine	Ambient density	↑	Strong decrease
			Strong decrease initially, reduced sensitivity as Density increases
			Strong decrease
	Ambient temperature	↑	Strong decrease
			Strong decrease initially, reduced sensitivity as temperature increases
			Strong decrease
Fuel	Fuel type		Distance increases as volatility decreases
			Can have significant effects
	Fuel temperature	↑	Linear decrease

Spray Evaporation

Generally the diesel spray contains both vapor and liquid phases simultaneously, which makes the quantitative measurement of vapor difficult. Rayleigh imaging [84] has been employed to make quantitative measurements of the vapor concentration at distances downstream of the maximum liquid penetration length. Another approach to measure the concentration distributions of vapor/liquid phases is the UV-Vis LAS technique [85]. The technique was employed in a high-pressure and high-temperature constant volume vessel providing the thermodynamic conditions similar to those of a diesel engine. The spray and mixture properties of the evaporating diesel spray were obtained in terms of spray tip penetration, liquid phase penetration, and concentration distributions of vapor and liquid phase.

Sprays in Low-Temperature Combustion Engines

As emission regulations become more stringent, advanced engine concepts are being explored to meet them. One approach that is under investigation and development is the homogeneous-charge compression ignition (HCCI) concept. In this engine, the fuel and air are premixed as in SI engines, but using compression ignition (CI). Figure 34.28 illustrates the HCCI combustion concept compared with conventional diesel engine combustion. Notice from the figure that multiple ignition spots result in rapid heat release rates. Controlling the timing of ignition and regulating the heat release rates and the resulting pressure rise rates are challenging issues which need to be addressed in such engines. Nevertheless, the approach has shown the potential to achieve near-zero NOx and PM emissions by maintaining lean combustion and low temperatures [86–90]. Variations of the

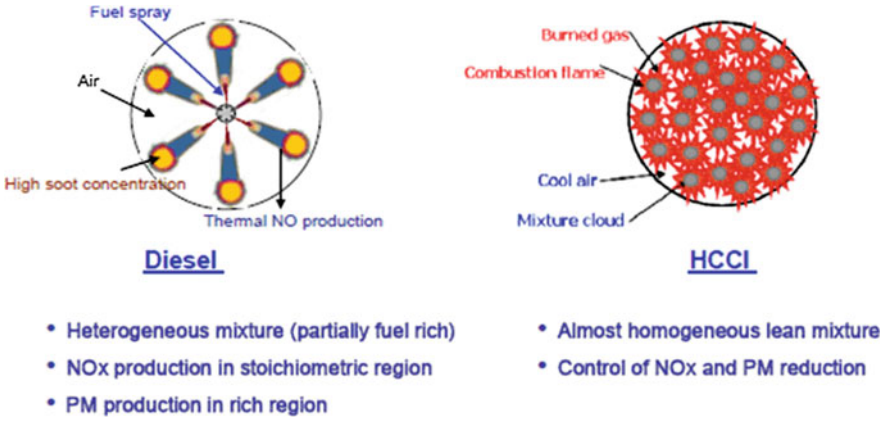


Fig. 34.28 Concept of homogeneous charge CI combustion

classical HCCI concept are being currently explored to control the onset of ignition and heat release rates. A promising approach is to inject the fuel directly into the cylinder early in the compression stroke, relative to a diesel engine, so that the mixture is partially premixed [91–93]. Of course, the extent to which the fuel and air premix can be controlled by the injection timing. Other factors, such as injector tip geometry, chamber geometry, and flow field characteristics, also play a role. Since the peak temperature in these engines is lower than in conventional diesel engines, these engines, including the HCCI engine, belong to the general class of "low-temperature combustion" (LTC) engines. As is well known the temperature has to be lower than about 1,800 K to minimize NOx emissions and the mixture has to be lean to minimize PM emissions. The LTC in lean mixtures can, however, result in significant CO and UHC emissions. Mixture stratification is considered to be a variable that can reduce these emissions [94]. Stratification can also control ignition and heat release rates [95]. Hence, it continues to be the subject of fundamental research employing optical diagnostics [94–99].

Mixture stratification (or, in other words, the extent of premixing) is determined to some extent by injection strategies. In the next section, some of these strategies will be discussed. Note that LTC engines are still under development and so fuel delivery strategies are evolving. Other approaches, not discussed below, have been reported in the literature.

Multiple Injection Strategies

In addition to the requirements for stratification, another consideration that arises in the selection of injection strategies in LTC engines is that there is a greater probability of wall impingement of liquid fuel than in a conventional diesel engine because the density of the gas in the chamber is relatively low when fuel is injected. To reduce fuel impingement and obtain a desired level of homogeneity, high-pressure pulsed injection has been tried using the CRI system. Pulsed injection can lead to better control over the mixture preparation process. The influence of multiple injections with different injection timings and fuel quantities was studied and comparisons were made with the normal CI mode of operation. The CRI system was capable of giving three injections at a maximum pressure of 1,200 bar. In the case of a CRI system, initially the engine was run in the HCCI mode with a single pulse with different injection timings. The injection timing was progressively advanced from a value of 0 before top dead centre (BTDC). With less injection advance, the combustion is normal diesel, as expected. With more advance, fuel injection leads progressively to the formation of a more homogeneous mixture because of longer residence time, leading to HCCI combustion. Examples of multiple injection strategies may be seen in references [100–102].

NADI™ (Narrow-Angle Direct Injection) Injector for LTC

Another approach to reduce wall wetting is the NADI™ (narrow-angle direct injection) concept [92, 103]. Figure 34.29 shows fuel consumption as a function of engine load. At high load, the exhaust gas recirculation (EGR) has been cooled to maintain the recycled gas temperature at about 90°C. The intake pressure has been progressively increased for indicated mean effective pressure (IMEP) higher than 0.5 MPa. Due to higher engine speed, it is possible to achieve good HCCI combustion mode at higher load. An IMEP value of 0.6 MPa is obtained with a compression ratio of 16:1, and 0.9 MPa of IMEP with a compression ratio of 14:1 [103].

Injector with Impinging-Spray Nozzle

To achieve a spray with not only low penetration and high dispersion, but also good atomization and a short injection period, it is necessary to maintain a high injection velocity. With a view to creating a spray with these characteristics, impinging-spray nozzles have been considered. Nozzles that have one set of impinged holes and high-pressure vessel were used for spray observation. As the impingement angle was increased, the spray angle increased, the penetration decreased, and the fuel concentration within the spray became more uniform. Increases in the impingement angle cause the spray angle to increase and the spray penetration to decrease [104].

In light of these findings, the impinging-spray nozzle was made and engine tests were performed with it. Owing to geometrical limitations, the impingement angle was 60°. A new seat hole was added in addition to the conventional sack hole, resulting in spray-to-spray impingement immediately after the liquid emerged from the nozzle holes. The added hole was located on the downstream side of the seat and

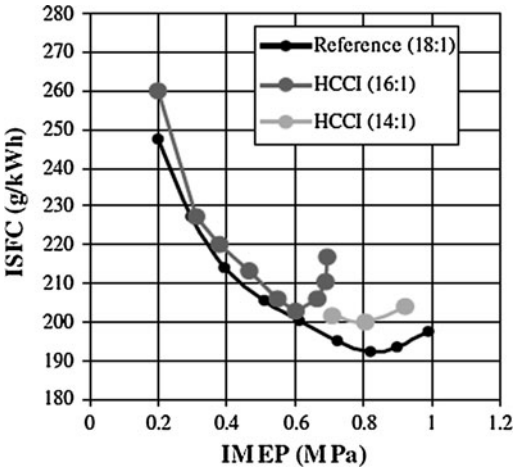


Fig. 34.29 Comparison of ISFC and IMEP between DI diesel and HCCI

designed such that the nozzle's seating was not impeded. The addition of a hole increased the total flow cross-sectional area, thereby facilitating a higher injection rate. The impinging-spray nozzle had a total of five sets of impingement holes. The spray was observed in a high-pressure vessel with the same atmospheric density as those in the engine tests, and the spray penetration was investigated. Vertical and horizontal penetrations were limited by the impinging-spray nozzle and impingement of fuel on the cylinder liner and combustion chamber wall was eliminated [104].

References

1. Heywood, J.B. (1988) *Internal Combustion Engine Fundamentals*, Mc-Graw Hill, New York.
2. Kim, H., Yoon, S., Xie, X.B., Lai, M.-C., Quelhas, S., Boyd, R., Kumar, N., and Moran, C. (2005) Effects of injection timings and intake port flow control on the in-cylinder wetted fuel footprints during PFI engine startup process. SAE Paper 2005-01-2082.
3. Lee, K.H., Kim, B., and Lee, C. (2002) Analysis of an atomization mechanism for an air-shrouded injector. Measurement Science and Technology, 13:65–77.
4. McGee, J., Curtis, E., Russ, S., and Lavoie, G. (2000) The effects of port fuel injection timing and targeting on fuel preparation relative to a pre-vaporized stream. SAE Paper 2000-01-2834.
5. Venugopalan, S., Lai, M.-C., Wu, F., and Washko, F.M. (2005) Experimental and simulation analysis of PFI-SI engine for fuel economy improvement. SAE Paper 2005-01-3691.
6. Zhao, F.Q., Lai, M.C., and Harrington, D.L. (1995) The spray characteristics of automotive port fuel injection- A critical review. SAE Technical Paper No. 950506.
7. Lenz, H.P. (1992) *Mixture Formation in Spark-Ignition Engines*, Springer-Verlag and SAE, Wien, New York, Warrendale.
8. Jeong, H., Lee, K.H., and Ikeda, Y. (2007) Investigation of the spray characteristics for a secondary fuel injection nozzle using a digital image processing method. Measurement Science and Technology, 18:1591–1602.
9. Fujii, H., Aoyama, S., and Katoh, M. (1987) Combustion stability of four-valve engine at low speeds. Transactions of JSAE, 35,67–73 (in Japanese).
10. Fujieda, M., Nogi, T., Ohsuga, M., and Ohyama, Y. (1990) Development of twin-fluid intermittent injector for gasoline engines. Proceedings of the Eighth Internal Combustion Engine Symposium, Kyoto, pp. 263–267 (in Japanese).
11. Iwata, M., Furuhashi, M., and Ujihashi, M. (1987) Two-hole injector improves transient performance and exhaust emissions of 4-valve engines. SAE Paper 870125.
12. Okamoto, Y., Arai, N., Nakagawa, K., Kosuge, T., and Atago, T. (1992) Atomization characteristics of two-stream injector for 4-valve engines. SAE Technical Paper No. 920705.
13. Alkidas, A.C. and El Tahry, S.H. (2003) Contributors to the fuel economy advantage of DISI engines over PFI engines. SAE Paper 2003-01-3101.
14. Bauler, E.M. (1951) Elimination of combustion knock – TEXACO combustion process. SAE Quarterly Transactions, 5:26.
15. Mitchell, E., Cobb, J.M., and Frost, R.A. (1968) Design and evaluation of a stratified-charge multi-fuel military engine. SAE Paper 680042.
16. Bishop, I.N. and Simko, A. (1968) A new concept of stratified-charge combustion. SAE Paper 680041.
17. Schapertons, H., Emmennthal, K.D., Grabe, H.J., and Oppermann, W. (1991) VW's gasoline direct injection (GDI) research engine. SAE Paper 910054.

18. Kume, T., Iwamoto, Y., Lida, K., Murakami, N., Akishino, K., and Ando, H. (1996) Combustion control technologies for direct injection SI engines. SAE Paper 960600.
19. Iwamoto, Y., Noma, K., Nakayama, O., Yamauchi, T., and Ando, H. (1997) Development of gasoline direct injection engine. SAE Paper 970541.
20. Zhao, F., Lai, M.-C., and Harrington, D.C. (1999) Automotive spark-ignited direct-injection gasoline engines. Progress in Energy and Combustion Science, 25:437–562.
21. Solomon, A.S., Anderson, R.W., Najt, P.M., and Zhao, F. (2000) Direct fuel injection for gasoline engines. SAE PT-80, Society of Automotive Engineers, Warrendale.
22. Drake, M.C., Fansler, T.D., and Lippert, A.M. (2005) Stratified-charge combustion modeling and imaging of a spray-guided direct-injection spark-ignition engine, Proceedings of the Combustion Institute, 30:2683–2691.
23. Drake, M.C. and Haworth, D.C. (2007) Advanced gasoline engine development using optical diagnostics and numerical modeling, Proceedings of the Combustion Institute, 31:99–124.
24. Harada, J., Tomita, T., Mizuno, H., Mashiki, Z., and Ito, Y. (1997) Development of a direct injection gasoline engine. SAE 970540.
25. Honda, T., Kawamoto, M., Katashiba, H., Sumida, M., Fukutomi, N., and Kawajiri, K. (2004) A study of mixture formation and combustion for spray guided DISI. SAE Paper 2004-01-0046.
26. Ortmann, R., Arndt, S., Raimann, J., Grzeszik, R., and Wurfel, G. (2001) Methods and analysis of fuel injection, mixture preparation and charge stratification in different direct injected SI engines. SAE Paper 2001-01-0970.
27. Katashiba, H., Honda, T., Kawamoto, M., Sumida, M., Fukutomi, N., and Kawajiri, K. (2006) Improvement of center injection spray guided DISI performance. SAE Paper 2006-01-1001.
28. van Romunde, Z., Aleieris, P.G., Cracknell, R.F., and Walmsley, H.L. (2007) Effect of fuel properties on spray development from a multi-hole DISI engine injector. SAE Paper 2007-01-4032.
29. Stach, T., Schlerfer, J., and Vorbach, M. (2007) New generation multi-hole fuel injector for direct-injection SI engines – optimization of spray characteristics by means of adapted injector layout and multiple injection. SAE Paper 2007-01-1404.
30. Dahlander, P. and Lindgren, R. (2008) Multi-hole injectors for DISI engines: Nozzle hole configuration influence on spray formation. SAE Paper 2008-01-0136.
31. Yang, J. and Kenney, T. (2002) Some concepts of DISI engine for high fuel efficiency and low emissions. SAE Paper 2002-01-2747.
32. Kuwahara, K., Ueda, K., and Ando, H. (1998) Mixing control strategy for engine performance improvement in a gasoline direct injection engine. SAE Paper 980158.
33. Tomoda, T., Sasaki, S., Sawada, D., Saito, A., and Sami, H. (1997) Development of direct injection gasoline engine study of stratified mixture formation. SAE Paper 970539.
34. Koike, M., Saito, A., Tomoda, T., and Yamamoto, Y. (2000) Research and development of a new direct injection gasoline engine. SAE Paper 2000-01-0530.
35. Takagi, Y., Itoh, T., Muranaka, S., Iiyama, A., Iwakiri, Y., Urushihara, T., and Naitoh, K. (1998) Simultaneous attainment of low fuel consumption, high power output and low exhaust emissions in direct injection S.I. engines. SAE Paper 980149.
36. Kakuhou, A., Urushihara, T., Itoh, T., and Takagi, Y. (1999) Characteristics of mixture formation in a direct- injection SI engine with optimized in-cylinder swirl air motion. SAE 1999-01-0505.
37. Yuny, G., Changwen, L., Yezhou, H., and Zhijun, P. (1998) An experimental study on droplet size characteristics and air entrainment of elliptic spray. SAE Paper 982546.
38. Preussner, C., Doring, C., Fehler, S., and Kampmann, S. (1998) GDI: interaction between mixture preparation, combustion system and injector performance. SAE Paper 980498.
39. Zhao, F., Lai, M.C., Harrington, D.C. (1997) A review of mixture preparation and combustion control strategies for spark-ignited direct-injection gasoline engine. SAE Paper 970627.

40. Parrish, S.E. and Farrell P.V. (1997) Transient spray characteristics of a direct injection spark-ignited fuel injector. SAE Paper 970629.
41. Han, Z., Parrish, S., Farrell, P.V., and Reitz, R.D. (1997) Modeling atomization processes of pressure-swirl hollow-cone fuel sprays. Atomization and Sprays, 7:663–684.
42. Arcoumanis, C., Gavaises, M., Arqueyrolles, B., and Galzin F. (1999) Modeling of pressure-swirl atomizers for GDI engines. SAE Paper 1999-01-0500.
43. Ikeda, Y., Nakajima, T., and Kurihara, N. (1997) Size-classified droplet dynamics and its slip velocity variation of air-assist injector spray. SAE Paper 970632.
44. Lee, K.H., Lee, C.H., and Lee, C.S. (2002) A study on the spray characteristics for a gasoline direct injector by using entropy analysis and PIV method. Proceedings of the Korean Society of Mechanical Engineers, pp. 1047–1054.
45. Lee, K.H., Lee, C.S. and Joo, Y.C. (2003) Application technique of particle image velocimetry and entropy analysis to investigate spray structure for gasoline direct injection injector. Measurement Science and Technology, 14:953–964
46. Hiroyasu, H. and Kadota, T. (1974) Fuel droplet size distribution in diesel combustion chamber. SAE Paper 74015.
47. Bracco, F.V. (1985) Modeling of engine sprays. SAE Paper 850394.
48. Wu, K.-J., Reitz, R.D., and Bracco, F.V. (1986) Measurements of drop sizes at the spray edge near the nozzle in atomizing liquid jets. Physics of Fluids, 29:941–951.
49. Labs, J. and Parker, T. (2003) Diesel fuel spray droplet sizes and volume fractions from the region 25 mm below the orifice. Atomization and Sprays, 13:45–62.
50. Labs, J. and Parker, T. (2006) Two-dimensional droplet size and volume fraction distributions from the near-injector region of high-pressure diesel sprays. Atomization and Sprays, 16:843–855.
51. O'Rourke, P.J. (1981) Collective drop effects on vaporizing liquid sprays. Ph.D. thesis, Princeton University, Princeton.
52. Reitz, R.D. (1987) Mechanisms of atomization processes in high-pressure vaporizing sprays. Atomization and Spray Technology, 3:309–337.
53. Tanner, F.X. and Weisser, G. (1998) Simulation of liquid jet atomization for fuel sprays by means of cascade drop breakup model. SAE Paper 980808.
54. Abraham, J. (1997) What is adequate resolution in the numerical computations of transient jets? SAE Paper 970051.
55. Iyer, V. and Abraham, J. (1997) Penetration and dispersion of transient gas jets and sprays. Combustion Science and Technology, 130:315–335.
56. Aneja, R. and Abraham, J. (1998) How far does the liquid penetrate in a diesel engine: computed results vs measurements? Combustion Science and Technology, 138:233–255.
57. Iyer, V., Post, S.L., and Abraham, J. (2000) Is the liquid penetration in diesel sprays mixing controlled? Proceedings of the Combustion Institute, 28:1111–1118.
58. Ricart, L.M., Reitz, R.D., and Dec, J.E. (2000) Comparisons of diesel spray liquid penetration and vapor fuel distribution with in-cylinder optical measurements. ASME Journal of Engineering for Gas Turbines and Power, 122(4):588–595.
59. Iyer, V. and Abraham, J. (2003) An evaluation of a two-fluid Eulerian-liquid Eulerian-gas model for diesel sprays. ASME Journal of Fluids Engineering, 125:660–669.
60. Naber, J.D. and Siebers, D.L. (1996) Effects of gas density and vaporization on penetration and dispersion of diesel sprays. SAE Paper 960034.
61. Siebers, D.L. (1998) Liquid-phase fuel penetration in diesel sprays. SAE Paper 980809.
62. Siebers, D.L. (1999) Scaling liquid-phase fuel penetration in diesel sprays based on mixing-limited vaporization. SAE Paper 1999-01-0528.
63. Chehroudi, B., Chen, S.-H., and Bracco, F.V. (1985) On the intact core of full-cone sprays. SAE Paper 850126.
64. Andrews, M.J. (1993) The large-scale fragmentation of the intact liquid core of a spray jet. Atomization and Sprays, 3:29–54.

65. Yue, Y., Powell, C.F., Poola, R., Wang, J., and Schaller, J. (2001) Quantitative measurements of diesel fuel spray characteristics in the near-nozzle region using X-ray absorption. Atomization Sprays, 11(4):471–490.
66. Abraham, J. (1996) Entrainment characteristics of transient gas jets. Numerical Heat Transfer, Part A, 30:347–364.
67. Huang, Y. (2000) Experimental studies of impulsively started liquid-into-gas and gas-into-gas turbulent jets, Ph.D. Thesis, Princeton University, Princeton.
68. Reitz, R.D. and Bracco, F.V. (1979) On the dependence of spray angle and other spray parameters on nozzle design and operating conditions. SAE Paper 790494.
69. Wu, K.-J., Su, C.-C., Steinberger, R.L., Santavicca, D.A., and Bracco, F.V. (1983) Measurements of the spray angle of atomizing jets. ASME Journal of Fluids Engineering, 105: 406–413.
70. Pawlak, G., Cruz, C.M., Bazan, C.M., and Hrdy, P.G. (2007) Experimental characterization of starting jet dynamics, Fluid Dynamics Research, 39:711–730.
71. Iglesias, I., Vera, M., Sanchez, A., and Linan, A. (2005) Simulations of starting jets at low Mach numbers. Physics of Fluids, 17(3), 38105.
72. Gharib, M., Rambod, E., and Shariff, K. (1998) A universal time scale for vortex ring formation. The Journal of Fluid Mechanics, 360:121–140.
73. Shariff, K. and Leonard, A. (1992) Vortex rings. Annual Review of Fluid Mechanics, 24: 235–279.
74. Takagi, T., Okamoto, T., Ohtani, A., and Komiyama, M. (1988) Measurements of velocity and concentration in transient jets by LDV and Rayleigh scattering. Japan Society of Mechanical Engineers International Journal, 31(1):119–126.
75. Musculus, M.P.B., Lachaux, T., Pickett, L.M., and Idicheria, C.A. (2007) End-of-injection over-mixing and unburned hydrocarbon emissions in low-temperature-combustion diesel engines. SAE Paper 2007-01-0907.
76. Bremhorst, K. and Hollis, P.G. (1990) Velocity field of an axisymmetric pulsed, subsonic air jet. AIAA Journal, 28:2043–2049.
77. Anders, J.W., Magi, V., and Abraham, J. (2008) A computational investigation of the interaction of pulses in two-pulse jets. Numerical Heat Transfer, Part A, 54:999–1021.
78. Renner, G. and Maly, R.R. (1994) Spray structures of automotive injectors. Paper Presented at the International Symposium on Advanced Spray Combustion, Hiroshima.
79. Hiroyasu, H. and Arai, M. (1990) Structure of fuel sprays in diesel engines. SAE Paper 900475.
80. Guerrassi, N. and Dupraz, P. (1998) A common rail injection system for high speed direct injection diesel engines. SAE Paper 980803.
81. Kong, J. and Bae, C. (2009) Effect of tapered nozzle hole on spray characteristics of high pressure diesel injection. Paper Presented at the International Annual Conference on Liquid Atomization and Spray Systems (ICLASS 2009), Vail.
82. El-Hannouny, E.M., Lee, T.W., Farrell, P.V. and Reitz, R.D. (2003) An experimental and numerical study of injector behavior for HSDI diesel engines. SAE Paper 2003-01-0705.
83. Smallwood, G.J. and Gulder, O.L. (2000) Views on the structure of transient diesel sprays. Atomization and Sprays, 10:355–386.
84. Idicheria, C.A. and Pickett, L.M. (2007) Quantitative mixing measurements in a vaporizing diesel spray by Rayeligh imaging. SAE Paper 2007-01-0647.
85. Gao, J., Nishida, K., Moon, S., and Matsumoto, Y. (2009) Characteristics of evaporating diesel spray: a comparison of laser measurements and empirical/theoretical predictions. SAE Paper 2009-01-0854.
86. Noguchi, M., Tanaka, Y., Tanaka, T., and Takeuchi, Y. (1979) A study on gasoline engine combustion by observation of intermediate reactive products during combustion. SAE Paper 790840.
87. Onishi, S., Jo, S.H., Shoda, K., Jo, P.D., and Katao, S. (1979) Active thermo-atmosphere combustion (ATAC) – a new combustion process for internal combustion engines. SAE Paper 790501.

88. Najt P.M. and Foster D.E. (1983) Compression-ignited homogeneous charge combustion. SAE Paper 830264.
89. Bression, G., Soleri, D., Savy, S., Dehoux, S., Azoulay, D., Hamouda, H., Doradoux, L., Guerrassi, N., and Lawrence, N. (2008) A study of methods to lower HC and CO emissions in diesel HCCI. SAE Paper 2008-01-0034 (2008).
90. Dec, J. (2009) Advanced compression-ignition engines – understanding the in-cylinder process, Proceedings of the Combustion Institute, 32(2):2727–2742.
91. Aoyama, T., Hattori, Y., Mizuta, J., and Sato, Y. (1996) An experimental study on premixed-charge compression-ignition gasoline engine. SAE Paper 960081.
92. Helmantel, A. and Denbratt, I. (2004) HCCI operation of a passenger car common-rail DI diesel engine with early injection of conventional diesel fuel. SAE Paper 2004-01-0935.
93. Cao, L., Bhave, A., Mosbach, S., Kraft, M., Dris, A., and McDavid, R.M. (2009) Influence of injection timing and piston bowl geometry on PCCI combustion and emissions. SAE Paper 2009-01-1102.
94. Hwang, W., Dec, J.E., and Sjoberg, M. (2007) Fuel stratification for low-load HCCI combustion: performance and fuel PLIF measurements. SAE Paper 2007-01-4130.
95. Sjoberg, M. and Dec, J.E. (2006) Smoothing HCCI heat-release rates using partial fuel stratification with two-stage ignition fuels. SAE Paper 2006-01-0629.
96. Richter, M., Engstrom, J., Frank, A., Alden, M., Hultqvist, A., and Johansson, B. (2000) The influence of charge inhomogeneity on the HCCI combustion process. SAE Paper 2000-01-2868.
97. Kumano, K. and Iida, N. (2004) Analysis of the effect of charge inhomogeneity on HCCI combustion by chemiluminescence measurement. SAE Paper 2004-01-1902.
98. Reuss, D. and Sick, V. (2005) Inhomogeneities in HCCI combustion: an imaging study. SAE Paper 2005-01-2122.
99. Herold, R.E., Krasselt, J.M., Foster, D.E., Ghandhi, J.B., Reuss, D.L., and Najt, P.M. (2009) Investigations into the effects of thermal and compositional stratification on HCCI combustion – Part II: optical engine results. SAE Paper 2009-01-1106.
100. Kokjohn, S.L., Swor, T.A., Andrie, M.J., and Reitz, R.D. (2009) Experiments and modeling of adaptive injection strategies (AIS) in low emissions diesel engines. SAE Paper 2009-01-0127.
101. Swami Nathan, S., Mallikarjuna, J.M., and Ramesh, A. (2007) An experimental study using single and multiple injection strategies in a diesel fueled HCCI engine with a common rail system. SAE Paper 2007-26-0028.
102. Yun, H., Wermuth, N., and Najt, P. (2009) Development of robust gasoline HCCI idle operation using multiple injection and multiple ignition (MIMI) strategy. SAE Paper 2009-01-0499.
103. Walter, B. and Gatellier B. (2002) Development of the high power NADI^{TM} concept using dual mode diesel combustion to achieve zero NOx and particulate emissions. SAE Paper 2002-01-1744.
104. Iwabuchi Y., Kawai K., Shoji T., and Takeda Y. (1999) Trial of new concept diesel combustion system premixed compression-ignited combustion. SAE Paper 1999-01-0185.

Chapter 35
Spray Modeling and Predictive Simulations in Realistic Gas-Turbine Engines

S.V. Apte and P. Moin

Abstract Large-eddy simulation (LES) is a promising technique for accurate prediction of reacting multiphase flows in practical gas-turbine engines. These combustors involve complex physical phenomena of primary atomization of liquid sheet/jet and secondary breakup, droplet evaporation, turbulent mixing of fuel vapor with oxidizer, and combustion dynamics. This chapter summarizes advances made in modeling spray fields with LES of turbulent reacting flows in realistic combustor configurations. Specifically, details of subgrid models for droplet dynamics including breakup, evaporation, deformation, droplet dispersion, and finite-size droplets are presented in the context of an Eulerian–Lagrangian simulation methodology on unstructured grids. Effectiveness of LES with advanced spray models in predicting spray behavior in a patternation study of realistic Pratt and Whitney injector is described.

Keywords Complex geometries · Gas turbines · LES · Sprays · Stochastic models

Introduction

Liquid spray dynamics plays a crucial role in analyzing two-phase, multispecies reacting flows in combustion chambers of many propulsion-related applications. The physics of such flows is extremely complex. In gas-turbine combustors, for example, the liquid fuel jet undergoes primary and secondary atomization, the resulting droplets evaporate and collide/coalesce, and fuel and oxidizer then mix yielding spray-flames. Owing to the complexities of the underlying processes as

S.V. Apte (✉)
School of Mechanical, Industrial and Manufacturing Engineering, Oregon State University, Corvallis, OR 97331, USA
e-mail: sva@engr.orst.edu

N. Ashgriz (ed.), *Handbook of Atomization and Sprays*,
DOI 10.1007/978-1-4419-7264-4_35, © Springer Science+Business Media, LLC 2011

well as combustor geometries, accurate quantitative observations of the flowfield are formidable and often subject to large measurement errors.

Figure 35.1a shows a cut section of a gas-turbine engine indicating three major components: (1) the compressor, (2) the combustor, and (3) the turbine. The combustor consists of a number of spray injectors placed symmetrically around the centerline. Figure 35.1b,c show the computational model of the combustor and an instantaneous snapshot of the flowfield in the symmetry plane of one of the injectors [2]. The level of geometrical complexity is evident. The combustor has numerous passages, holes of various sizes and shapes, swirlers, and obstacles in the flow path. The combustor chamber is fed by three coaxial swirlers and several dilution holes. The inlet air passes through the pre-diffuser and follows two paths: the main stream flows through the swirlers and enters the chamber, while the secondary stream is diverted to the outer diffusers and enters the combustor through the dilution holes. The Reynolds number based on radial height and mean velocity in the inlet section of the pre-diffuser is on the order of 600,000. The Reynolds number inside the core swirler channel is about 150,000. Fuel, in the form of a liquid sheet or a jet, is injected through multiple injectors and is atomized by strong shearing mechanism due to surrounding swirling, turbulent air. The combustion dynamics and eventual power generation are thus governed by the performance of the spray injectors. A complete computational model of a gas-turbine combustion

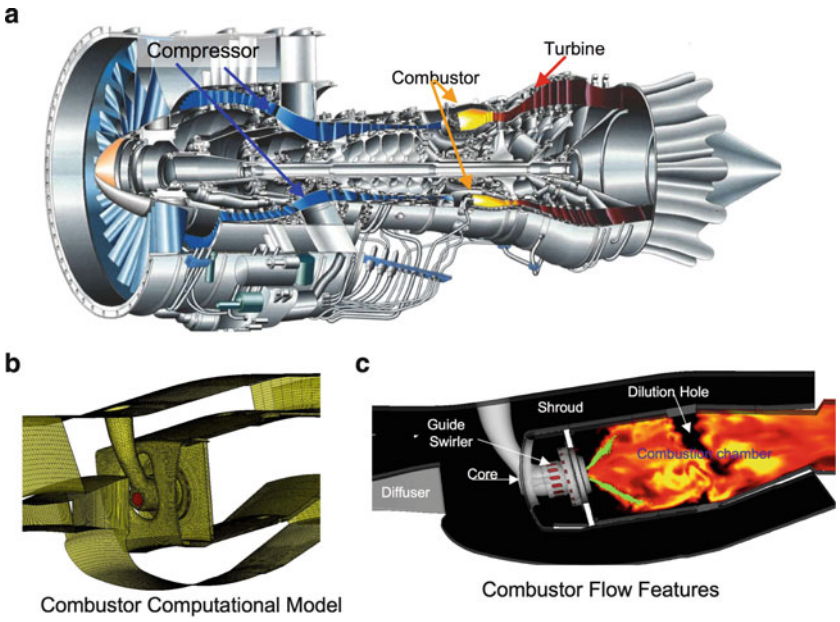


Fig. 35.1 Geometrical complexities of a real gas-turbine engine [1]: (**a**) the cut section showing compressor, combustor, and turbine, (**b**) computational model of one section of the combustor, and (**c**) instantaneous snapshot of temperature distribution in the symmetry plane of the combustor showing complex flow patterns through various sections of the combustor

chamber should account for the spray dynamics of atomization of the liquid sheet/jet, secondary breakup of the droplets, collision/coalescence and evaporation of droplets, turbulent mixing of the fuel vapor with the oxidizer, and turbulent flame dynamics and heat transfer in the presence of liquid and gas phase and multiple species.

High-fidelity simulations of these flows require the use of accurate numerical schemes with good conservative properties and advanced subgrid models to capture the physical phenomena associated with both phases, phase change, and chemical reactions in turbulent environments. To date the engineering prediction of such flows in *realistic configurations* has relied predominantly on the Reynolds-averaged Navier–Stokes (RANS) equations [1, 3, 4]. However, the predictive capability of standard RANS models applied to turbulent reacting flows is fairly limited. Large-eddy simulation (LES) technique has been convincingly shown to be superior to RANS in accurately predicting turbulent mixing and combustion dynamics [5] in simpler combustor geometries. Menon and coworkers [6, 7] have performed LESs of nonreacting and reacting flows in a swirling combustion chamber with liquid spray in complex configurations. They showed good predictive capability of LES in capturing spray evolution, droplet dispersion, and turbulence modulation by droplets in the presence of heat release. Their approach is based on compressible Navier–Stokes equations in generalized coordinates. In order to represent complex passages in combustors with relatively easy grid generation, use of unstructured grids is necessary. Unstructured grids handle complex configurations with relative ease as well as allow significant savings in the number of control volumes due to the flexibility of local grid refinement in regions of interest. The numerical algorithms used for LES should be energy-conserving and strictly nondissipative as numerical dissipation has been shown to be detrimental to accurate prediction of turbulent flows [8]. Recently Mahesh and coworkers [2, 9–11] have developed a new numerical method with the characteristics necessary for simultaneously accurate and robust LES on unstructured grids. These competing ends were achieved by developing a method around the principle of discrete kinetic energy conservation with no artificial dissipation.

The droplet formation and evaporation process in such flow configurations is also complex and can be characterized by different regimes as shown in Fig. 35.2. Three regimes of flow development are commonly observed inside these combustors: (1) "dense spray regime" where the liquid film/jet interacts with the gas phase and disintegrates into filaments due to primary breakup, (2) "intermediate regime" where the large drops formed undergo secondary breakup, and (3) "dilute regime" where the droplets evaporate and the fuel vapor mixes with the surrounding hot gases. The characterization of based on physical processes also indicates different methodologies/models necessary to capture the dynamics of different regimes. Very close to the injector, the liquid fuel is in the form of a sheet or jet (ℓ, the characteristic length scale associated with the liquid film, is much larger than the local grid resolution Δx, and the local liquid volume fraction Θ_p is on the order of 1) and a continuum formulation is necessary to capture the primary atomization processes. Slightly away from the injector, in the intermediate regime, the liquid

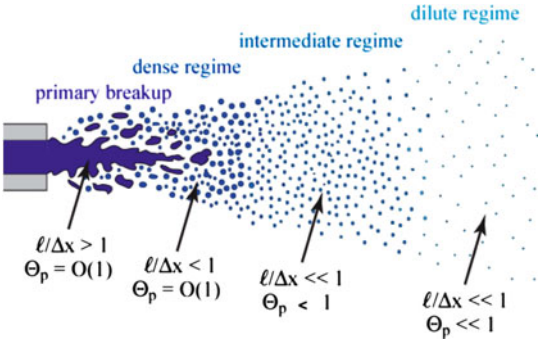


Fig. 35.2 Regimes of liquid spray evolution from injectors in gas-turbine engines

drops formed during primary atomization undergo further disintegration. Collision, coalescence, and droplet deformation effects are dominant in this region ($\ell << \Delta x Z$ and $\Theta_p < 1$). In the dilute regime, the droplets evaporate and the local liquid volume fraction is much smaller. In reality there is significant overlap of these regimes and the physical processes of primary/secondary atomization and droplet evaporation may not be distinguishable in a straightforward way.

Furthermore, the range of length (and time) scales associated with the liquid phase in different regimes could be enormous. The injector nozzle diameter is on the order of a few inches, whereas the smallest droplet size in the dilute regime is on the order of few tens of microns. Different numerical techniques are thus necessary to address different flow regimes. For example, near the injector, the liquid phase is in the form of a sheet or a jet and should be modeled by continuum approaches resolving (fully or partially) the evolution of the liquid–air interface and topological changes. However, such approaches require significant computational effort. Such numerical schemes capture the complex interactions and instabilities near the gas–liquid interface, formation of ligaments, and their disintegration into droplets. Considerable advances have been made in this area [12–15]. The predictive capability of such schemes may be strongly influenced by the grid resolutions used and capabilities for realistic injector geometries are still under development. In the traditional approach for spray computation, the Eulerian equations for the gaseous phase are solved along with a Lagrangian model for droplet transport with two-way coupling of mass, momentum, and energy exchange between the two phases [16]. In this approach, the details of the liquid–air interface evolution and primary atomization are not captured. Instead, the standard approach is to first perform spray patternation studies for the injector used in combustion chambers and measure the size distributions at various cross sections from the injector. These distributions are then used as an *input* to a numerical simulation which then computes the secondary atomization of the injected droplets. The secondary atomization is typically modeled by standard deterministic breakup models based on Taylor analogy breakup (TAB) [17] or wave [18] models. However, this requires performance of experimental tests for any new injector design which can be very costly.

Performing spray breakup computations using Lagrangian tracking of each individual droplet gives rise to a large number of droplets (≈20–50 million) in

localized regions very close to the injector. Simulating all droplet trajectories gives severe load imbalance due to the presence of droplets on only a few processors [11]. On the other hand, correct representation of the fuel vapor distribution obtained from droplet evaporation is necessary to capture the dynamics of spray flames. In their pioneering work, O'Rourke [19] and O'Rourke and Bracco [20] used a "discrete-parcel model" to represent the spray drops. A parcel or computational particle represents a group of droplets, N_{par}, with similar characteristics (diameter, velocity, temperature). Typically, the number of computational parcels tracked influences the spray statistics predicted by a simulation.

Droplet deformation and collision are also important features in the intermediate regime. In addition, in the intermediate region, the droplet loading could be severe. The variations in the local liquid-phase volume fraction also become important and should be considered in order to capture the droplet dynamics correctly. A robust algorithm capable of addressing all numerical issues related to spray modeling is necessary.

In this chapter, current advances in large-scale computations based on predictive simulation techniques such as LES with subgrid scale models for droplet dynamics and spray evolution are described. Emphasis is placed on subgrid models for spray computation. Accordingly, simplified models for droplet breakup, droplet drag and dispersion, evaporation, local variations in liquid-phase volume fractions are described, and a hybrid droplet–parcel approach for sprays is described. Finally, examples of spray computations in realistic gas-turbine engines, utilizing some of these modeling strategies together with LES, are presented.

Mathematical Formulation

The governing equations used for the gaseous and droplet phases are described briefly. In the Eulerian–Lagrangian formulation, the droplets are treated as point sources and influence the gas phase only through momentum-exchange terms [21]. The variable density, low-Mach number equations are solved for the gas phase and the reacting flow formulation is based on the flamelet, progress/variable approach developed by Pierce and Moin [5] for LES of non-premixed, turbulent combustion.

Gas-Phase Equations

The gas-phase continuity, scalar, and momentum equations are

$$\frac{\partial \overline{\rho}_{\mathrm{g}} \tilde{u}_j}{\partial x_j} = -\frac{\partial \overline{\rho}_{\mathrm{g}}}{\partial t} + \overline{\dot{S}}_{\mathrm{m}} \tag{35.1}$$

$$\frac{\partial \overline{\rho}_{\mathrm{g}} \tilde{Z}}{\partial t} + \frac{\partial \overline{\rho}_{\mathrm{g}} \tilde{Z} \tilde{u}_j}{\partial x_j} = \frac{\partial}{\partial x_j}\left(\overline{\rho}_{\mathrm{g}} \tilde{\alpha}_Z \frac{\partial \tilde{Z}}{\partial x_j}\right) - \frac{\partial q_{Zj}}{\partial x_j} + \overline{\dot{S}}_Z \tag{35.2}$$

$$\frac{\partial \overline{\rho}_{\mathrm{g}} \tilde{C}}{\partial t} + \frac{\partial \overline{\rho}_{\mathrm{g}} \tilde{C} \tilde{u}_j}{\partial x_j} = \frac{\partial}{\partial x_j}\left(\overline{\rho}_{\mathrm{g}} \tilde{\alpha}_C \frac{\partial \tilde{C}}{\partial x_j}\right) - \frac{\partial q_{Cj}}{\partial x_j} + \overline{\dot{\omega}}_C \tag{35.3}$$

$$\frac{\partial \overline{\rho}_{\mathrm{g}} \tilde{u}_i}{\partial t} + \frac{\partial \overline{\rho}_{\mathrm{g}} \tilde{u}_i \tilde{u}_j}{\partial x_j} = -\frac{\partial \bar{p}}{\partial x_i} + \frac{\partial \left(2\bar{\mu}\tilde{S}_{ij}\right)}{\partial x_j} - \frac{\partial q_{ij}}{\partial x_j} + \overline{\dot{S}}_i \tag{35.4}$$

$$\tilde{\rho}_{\mathrm{g}} = \tilde{\rho}_{\mathrm{g}}\left(\tilde{Z}, \tilde{C}, \tilde{Z}''\right) \tag{35.5}$$

$$\tilde{S}_{ij} = \frac{1}{2}\left(\frac{\partial \tilde{u}_i}{\partial u_j} + \frac{\partial \tilde{u}_j}{\partial u_i}\right) - \frac{1}{3}\delta_{ij}\frac{\partial \tilde{u}_k}{\partial x_k} \tag{35.6}$$

where the unclosed transport terms in the momentum and scalar equations are grouped into the residual stress q_{ij}, and residual scalar flux q_{Zj}, q_{Cj}. The dynamic Smagorinsky model by Moin et al. [22, 23] is used to close these subgrid terms as demonstrated by Pierce and Moin [5]. For a two-fluid (air + fuel) mixture, one conserved scalar (the mixture fraction, Z) and a nonconserved scalar (the progress variable, C) are solved. The gas-phase properties such as specific heat, molecular weight, density, viscosity, heat release, and source terms in the progress-variable equation, $\overline{\dot{\omega}}_C$, are obtained from lookup tables generated using flamelet theory for non-premixed combustion and are dependent on the local values of Z, C, and the subgrid mixture fraction fluctuations, Z''.

With the presence of the liquid-phase and interphase mass, momentum, and energy transport, additional source terms are added into the continuity, momentum, and scalar transport equations. As the droplets evaporate the heat of vaporization is taken from the gas phase and there is evaporative cooling of the surrounding gas. This gives rise to a sink term in the energy equation. By assuming adiabatic walls and unity Lewis number, the energy and scalar equations have the same boundary conditions and are linearly dependent [5].

Only one scalar equation (for mixture fraction, Z) is solved and other scalars including temperature are deduced using flamelet tables. The evaporative cooling effect (heat of vaporization) is accounted for in the equation of state during the generation of the flamelet tables. The heat content of the liquid fuel is taken into account by computing an effective gaseous fuel enthalpy and is used in solving the flamelet equations [2].

Subgrid Models for the Liquid Phase

Droplet dynamics are usually simulated using a Lagrangian point-particle model. It is assumed that (1) the density of the droplets is much greater than that of the carrier

fluid, (2) the droplets are dispersed, (3) the droplets are much smaller than the LES filter width, (4) the droplet deformation effects are small, and (5) the motion due to shear is negligible. It is assumed that the density of the droplet is much larger than that of the fluid $(\rho_p/\rho_g \sim 10^3)$, that droplet size is small compared to the turbulence integral length scale, and that the effect of shear on droplet motion is negligible. The high value of density ratio implies that the Basset force and the added mass terms are small and are therefore neglected. Under these assumptions, the Lagrangian equations governing the droplet motions become [24]

$$\frac{d\mathbf{x}_p}{dt} = \mathbf{u}_p; \quad \frac{d\mathbf{u}_p}{dt} = D_p(\mathbf{u} - \mathbf{u}_p) + \left(1 - \frac{\rho_g}{\rho_p}\right)\mathbf{g}, \tag{35.7}$$

where $\mathbf{u}_p$ are the droplet velocity components, $\mathbf{u}$ are the gas-phase velocities interpolated to the droplet location, ρ_p and ρ_g are the droplet- and gas-phase densities, respectively, $\mathbf{g}$ is the gravitational acceleration, and D_p is the inverse of the droplet relaxation timescale (τ_p).

Deformation and Drag Models

Helenbrook and Edwards [25] performed detailed resolved simulations of axisymmetric liquid drops in uniform gaseous stream using an *hp*-finite element method [25, 26] to quantify the effect of droplet deformation on drag. Based on their computations for a range of density and viscosity ratios, range of Weber (*We*), Ohnesorge (*Oh*), and Reynolds numbers (*Re*), a correlation was developed that provides the amount of deformation in the form of ellipticity, E, which is defined as the ratio of the height to width of the drop:

$$E = 1 - 0.11\,We^{0.82} + 0.013\sqrt{\frac{\rho_l}{\rho_g}\frac{\mu_g}{\mu_l}}\,Oh^{-0.55}We^{1.1}, \tag{35.8}$$

where μ_l and μ_g are the viscosities of the liquid and gas, and ρ_l and ρ_g are the densities, respectively. The nondimensional Weber and Ohnesorge numbers are defined as $We = \rho_g U^2 d_p/\sigma$ and $Oh = \mu_l/\sqrt{p_l \sigma d_p}$, where U is the relative velocity between the gas and liquid, d_p is the diameter of the droplet, and σ is the surface tension. Accordingly, $E < 1$ indicates that the drops have more width than height with deformation in a direction perpendicular to the relative velocity. These shapes are called oblate shapes. Similarly, $E > 1$ gives elongation in the direction of the relative velocity giving rise to prolate shapes. $E = 1$ implies spherical shapes.

The effect of droplet deformation is to change the drag force. This effect is modeled by using an effective equatorial droplet diameter, $d_p^* = d_p E^{-1/3}$. The droplet Reynolds number is also modified, $Re_p^* = Re_p E^{-1/3}$. This is used in

(35.10) and (35.11) to obtain the modified drag [25]. In addition, the effect of internal circulation is modeled by changing the drag on a solid sphere as

$$\frac{D_{\text{drop}}}{D_{\text{solid}}} = \left(\frac{2+3\mu_{\text{l}}/\mu_{\text{g}}}{3+3\mu_{\text{l}}/\mu_{\text{g}}}\right)\left(1-0.03\left(\frac{\mu_{\text{g}}}{\mu_{\text{l}}}\right)Re_{\text{p}}^{0.65}\right), \tag{35.9}$$

where the drag force on a solid particle is modeled using a drag coefficient, C_{d},

$$D_{\text{P solid}} = \frac{3}{4}C_{\text{d}}\frac{\rho_{\text{g}}}{\rho_{\text{p}}}\frac{\left|\mathbf{u}_{\text{g}}-\mathbf{u}_{\text{p}}\right|}{d_{\text{p}}}, \tag{35.10}$$

where C_{d} is obtained from the nonlinear correlation[24]

$$C_{\text{d}} = \frac{24}{Re}\left(1+aRe_{\text{p}}^{\text{b}}\right). \tag{35.11}$$

Here $Re_{\text{p}} = d_{\text{p}}\left|\mathbf{u}_{\text{g}}-\mathbf{u}_{\text{p}}\right|/\mu_{\text{g}}$ is the droplet Reynolds number. The above correlation is valid for $Re_{\text{p}} \leq 800$. The constants $a = 0.15$ and $b = 0.687$ yield the drag within 5% from the standard drag curve. Modifications to the solid particle drag are applied to compute the drag on a liquid drop and are given below.

Evaporation Model

Typical spray simulations do not resolve the temperature and species gradients around each droplet to compute the rate of evaporation. Instead, evaporation rates are estimated based on quasi-steady analysis of a single isolated drop in a quiescent environment [27, 28]. Multiplicative factors are then applied to consider the convective and internal circulation effects.

The simplest model for droplet evaporation is based on an equilibrium "uniform-state" model for an isolated droplet [28–30]. Miller et al. [31] investigated different models for evaporation accounting for nonequilibrium effects. Advanced models considering internal circulation, temperature variations inside the droplet, and effects of neighboring droplets [30] may alter the heating rate (Nusselt number) and the vaporization rates (Sherwood number). For the uniform-state model, the Lagrangian equations governing droplet temperature and mass become [28–30]

$$\frac{\mathrm{d}m_{\text{p}}}{\mathrm{d}t} = -\frac{m_{\text{p}}}{\tau_{\text{m}}}; \quad \frac{\mathrm{d}T_{\text{p}}}{\mathrm{d}t}\left(T_{\text{g,p}}-T_{\text{p}}^{\text{s}}\right) - \frac{1}{\tau_{\text{m}}}\frac{\Delta h_{\text{v}}}{C_{\text{p,l}}}, \tag{35.12}$$

where Δh_{v} is the latent heat of vaporization, m_{p} is the mass of the droplet, T_{p}^{s} is the temperature at the droplet surface, $T_{\text{g,p}}$ is the temperature of the gas phase at the

droplet location, and $C_{p,l}$ is the specific heat of liquid. The diameter of the droplet is obtained from its mass, $d_p = (6m_p/\pi\rho_p)^{1/3}$. Here, τ_m and τ_c are the droplet lifetime and the convective heating timescales respectively, and are given as

$$\frac{1}{\tau_m} = \frac{12}{d_p^2} D^s \ln(1+B_Y) Sh; \quad \frac{1}{\tau_c} = \frac{12}{\rho_p d_p^2} \frac{k^s}{C_{p,l}} \frac{\ln(1+B_T)}{B_T} Nu, \tag{35.13}$$

Here, D and k are the diffusivity and conductivity, respectively. The superscript s stands for droplet surface and Sh and Nu are the Sherwood and Nusselt numbers given as

$$Sh = 1 + \frac{0.27 Re_p^{1/2} [Sc^s]^{1/3}}{\sqrt{1 + 1.232/Re_p [Sc^s]^{1/3}}}; \quad Nu = 1 + \frac{0.278 Re_p^{1/2} [Pr^s]^{1/3}}{\sqrt{1 + 1.232/Re_p [Pr^s]^{1/3}}}. \tag{35.14}$$

B_Y and B_T are the mass diffusion and heat transfer coefficients, respectively. For $T_p^s < T_b$ (where T_b is the boiling point), $B_Y = (Y_F^s - Y_{Fg,p})/(1 - Y_F^s)$ and $B_T = C_p^s (T_{g,p} - T_p^s)/(\Delta h_v)$, where $Y_{Fg,p}$ is the fuel vapor mass fraction interpolated to the droplet location. For $T_p^s \geq T_b$, B_Y is set equal to B_T. The Clausius–Clapeyron equilibrium vapor–pressure relationship is used to compute the fuel mass fraction at the droplet surface. In addition, convective correction actors (based on Ranz and Marshall correlations) are applied to obtain spray evaporation rates at high Reynolds numbers. Liquid properties are evaluated using the one third rule for reference mass fractions [28]. Advanced models for droplet evaporation accounting for nonequilibrium effects can also be incorporated in the above framework by altering the timescales associated with the droplet lifetime and the convective heating.

Stochastic Modeling of Droplet Breakup

The physics of primary and secondary atomization are not well understood even in simple and canonical flow configurations. As described earlier, there exist regimes near an injector wherein different physical processes, such as shearing of liquid sheet/jet to form ligaments, stripping of ligaments and primary atomization, secondary breakup of stripped ligaments to form smaller sized droplets, among others occur. Modeling these phenomena in realistic configurations is difficult and involves empirical expressions. In order to address the uncertainties in spray breakup models, a heuristic approach based on stochastic modeling has been investigated. A stochastic breakup model capable of generating a broad range of droplet sizes at high Weber numbers has been developed [15, 32, 33]. For very large Weber numbers, there is experimental evidence indicating the fractal nature of the atomization process [34, 35] wherein large droplets can directly disintegrate into

tiny droplets. The breakup of parent drops into secondary droplets is viewed as the temporal and spatial evolution of this distribution function around the parent droplet size according to the Fokker–Planck (FP) differential equation

$$\frac{\partial T(x,t)}{\partial t} + \upsilon(\xi)\frac{\partial T(x,t)}{\partial x} = \frac{1}{2}\upsilon(\xi)\frac{\partial^2 T(x,t)}{\partial x^2}, \tag{35.15}$$

where the breakup frequency (υ) and time (t) are introduced. The moments $\langle\xi\rangle = \int_{-\infty}^{0} \xi S(\xi)\mathrm{d}\xi$ and $\langle\xi^2\rangle = \int_{-\infty}^{0} \xi^2 S(\xi)\mathrm{d}\xi$ are the two parameters of the model that need closure. Here, $T(x,t)$ is the distribution function for $x = \ln(r)$ and r is the droplet radius. Breakup occurs when $t > t_{\mathrm{bu}} = 1/\upsilon$ and $r > r_{\mathrm{cr}}$, the critical radius of the droplet. Following the arguments of scale similarity analogous to the turbulence cascade behavior at large Reynolds numbers, Gorokhovski and Saveliev [32] looked at the long-time behavior of the droplet breakup. They showed that the initial delta function for the logarithm of radius of the jth primary droplet evolves into a steady-state distribution that is a solution to the FP equation [32, 33, 36]

$$Tj(x,t+1) = \frac{1}{2}\left[1 + erf\left(\frac{x - xj - \langle\xi\rangle}{2\langle\xi^2\rangle}\right)\right]. \tag{35.16}$$

This long-time behavior of the distribution is characterized by the dominant mechanism of breakup. Improvements to the model, wherein presence of a liquid core near the injector is taken into account [37], have been proposed.

The value of the breakup frequency and the critical radius of breakup are obtained by the balance between the aerodynamic and surface tension forces. The critical (or maximum stable) radius for breakup is then given as $r_{\mathrm{cr}} = We_{\mathrm{cr}}\sigma/(\rho_{\mathrm{g}} u_{r,j}^2)$, where $|u_{r,j}|$ is the relative velocity between the gas and the droplet, σ is the surface tension coefficient, and We_{cr} is the critical Weber number, which is assumed to be on the order of 6 over a wide range of Ohnesorge numbers. For highly turbulent flows, however, the instantaneous value of Kolmogorov scale $(\eta)$is often less than the droplet size and the entire spectrum of turbulent kinetic energy can contribute to the stretching and disintegration of the droplet. In this case, the critical radius should be obtained as a balance between the capillary forces and turbulent kinetic energy supplied to the liquid droplet. Accordingly, the relative droplet-to-gas velocity is estimated from the mean viscous dissipation and Stokes timescale (τ_{st}) as $\left|u_{r,j}^2\right| \approx \varepsilon\tau_{\mathrm{st}}$.

Using this relative velocity, the critical radius of breakup becomes

$$r_{\mathrm{cr}} = \left(\frac{9}{2}\frac{We_{\mathrm{cr}}\sigma\upsilon_{\mathrm{lam}}}{\varepsilon\rho l}\right)^{1/3}, \tag{35.17}$$

where υ_{lam} is the kinematic viscosity, ρ_{l} is the liquid density, and ε is the viscous dissipation rate. In the present LES study, the viscous dissipation can be obtained

dynamically form the resolved scale energy flux. The breakup frequency is obtained following the analogy with expressions used for aerodynamic breakup and utilizing the relative velocity $\left(\left|u_{r,j}\right|\right)$ from above

$$t_{\mathrm{bu}} = B\sqrt{\frac{\rho_{\mathrm{l}}}{\rho_{\mathrm{g}}}}\frac{r_j}{\left|u_{r,j}\right|}, \tag{35.18}$$

where r_j is the radius of parent drop and $B = \sqrt{1/3}$ [17].

If the breakup criterion ($t > t_{\mathrm{bu}}$ and $r > r_{\mathrm{cr}}$) for a parent droplet is satisfied, secondary droplets are sampled from the analytical solution (35.16) corresponding to the breakup timescale. The parameters encountered in the FP equation ($\langle\xi\rangle$ and $\left\langle\xi^2\right\rangle$) are computed by relating them to the local Weber number for the parent drop, thereby accounting for the capillary forces and turbulent properties. Apte et al. [33, 36] assumed that in the intermediate range of scales between the parent drop element (large Weber number) and the maximum stable droplet (critical Weber number) there exists no preferred length scale, following the fractal nature of atomizing spray [35].

This closely resembles the inertial range of the energy cascade process in homogeneous turbulence at high Reynolds numbers. Analogously, assuming $u_{r,j}^3/r_j = u_{r,\mathrm{cr}}^3/r_{\mathrm{cr}}$, one obtains

$$\frac{r_{\mathrm{cr}}}{r_j} = \left(\frac{We_{\mathrm{cr}}}{We_j}\right)^{3/5} \Rightarrow \langle \ln\alpha\rangle \equiv \langle\xi\rangle = K\,\ln\left(\frac{We_{\mathrm{cr}}}{We_j}\right), \tag{35.19}$$

where $u_{r,\mathrm{cr}}$ is the relative velocity at which disruptive forces are balanced by capillary forces (similar to turbulent velocity scale of the smallest eddies) and the constant K is of order unity ($\sim$0.6). This gives expression for one of the parameters $\langle\xi\rangle$.

Furthermore, from Einstein's theory of Brownian motion, the diffusion coefficient in the FP equation is known to be the energy of Brownian particles multiplied by their mobility. The drift velocity is presented in the form of drag force times the mobility. The ratio of diffusion to drift velocity is given by the ratio of energy to drag force. In the breakup process, the energy in Einstein's theory is associated with the disruptive energy while the force is associated with the capillary force on the droplet. Normalized by the length scale of the parent drop, this ratio is characterized by the Weber number. Considering the FP equation (35.15), the diffusion to drift velocity ratio is scaled by $-\left\langle\xi^2\right\rangle/\langle\xi\rangle$. Then it is assumed that

$$-\frac{\langle\xi\rangle}{\left\langle\xi^2\right\rangle} \equiv -\frac{\langle\ln\alpha\rangle}{\left\langle\ln^2\alpha\right\rangle} = We_j^{-1}. \tag{35.20}$$

This relationship gives the maximum dispersion of newly produced droplet sizes. Thus, both the parameters in the FP equation are obtained dynamically by computing the local value of We_j, and knowing We_{cr}.

Once new droplets are created, the product droplet velocity is computed by adding a factor $\mathbf{w}_{\text{bu}}$ to the primary drop velocity. This additional velocity is randomly distributed in a plane normal to the relative velocity vector between the gas phase and parent drop, and the magnitude is determined by the radius of the parent drop and the breakup frequency, $|\mathbf{w}_{\text{bu}}| = r\upsilon$. This modification of newly formed droplets follows the physical picture of parent droplets being torn apart by aerodynamic forces giving momentum to the newly formed droplets in the direction normal to the relative velocity between the gas phase and parent drops [17]. As new droplets are formed, parent droplets are destroyed and Lagrangian tracking in the physical space is continued till further breakup events.

Subgrid Scale Modeling

In LES of droplet-laden flows, the droplets are presumed to be *subgrid*, and the droplet size is smaller than the filter width used. The gas-phase velocity field required in (35.7) is the total (unfiltered) velocity; however, only the filtered velocity field is computed in (35.4). The direct effect of unresolved velocity fluctuations on droplet trajectories depends on the droplet relaxation timescale and the subgrid kinetic energy. Considerable progress has been made in reconstructing the unfiltered velocity field by modeling the subgrid scale effects on droplet dispersion. Bellan [38] provides a good review on this topic in the context of spray modeling. Majority of the works related to subgrid scale effects on droplet motion have been performed for dilute loadings, wherein the droplets are either assumed smaller than the LES filter size or the Kolmogorov length scale. For dense spray systems, droplet dispersion and droplet interactions with subgrid scale turbulence are not well understood. In addition, in realistic configurations the droplet sizes very close to the injector can be on the order of the grid size used for LES computations.

In LES of practical combustor applications, the content of subgrid scale kinetic energy could be large in regions of poor grid resolution. These unresolved motions for the carrier phase are typically modeled using a dynamic Smagorinsky model. The equations of the dispersed-phase velocity field require an instantaneous *undisturbed* carrier-phase velocity at the droplet location. With two-way coupling between the two phases, the resolved velocity field of the carrier phase is modified due to the presence of the dispersed phase. In addition, the subgrid scale velocity field may influence the statistics of the dispersed phase and alter the spray evolution significantly.

Recently, Pozorski and Apte [39] performed a systematic study of the direct effect of subgrid scale velocity on particle motion for particle-laden forced isotropic turbulence using a stochastic model based on filtered particle tracking (FPT). The FPT approach statistically reconstructs the unresolved carrier-phase velocity along particle trajectories. A reasonable assumption for LES is to consider the residual turbulent motion as locally homogeneous and isotropic. Then, the fluid velocity

seen by particles is computed as $U_i^* = \tilde{U}_i(\mathbf{x}_\mathrm{p}, t) + u_i^*$, i.e., the sum of the filtered LES velocity $\tilde{U}_i$ interpolated at the particle location and the residual velocity *seen* by the particle. Crucial ingredients of an FPT model are the *sgs* turbulent kinetic energy of the fluid and an *sgs* timescale. By analogy to modeling turbulent diffusion of fluid elements, $\mathbf{u}^*$ is governed by the Langevin equation

$$\mathrm{d}u_i^* = -\frac{u_i^*}{\tau_\mathrm{L}^*}\mathrm{d}t + \sqrt{\frac{2\sigma_\mathrm{sg}^2}{\tau_\mathrm{L}^*}}\mathrm{d}W_i, \tag{35.21}$$

where σ_sg and τ_L^* stand for the respective velocity and timescales of residual motions *seen* by the particle; moreover, τ_sg denotes the timescale of residual motions. They are estimated from

$$\sigma_\mathrm{sg} = \sqrt{\frac{2}{3}k_\mathrm{sg}}, \quad \tau_\mathrm{L}^* = f\left(\frac{\tau_\mathrm{sg}, \tau_\mathrm{p}, \sigma_\mathrm{sg}}{g}\right), \quad \tau_\mathrm{sg} = C\frac{\Delta_\mathrm{f}}{\sqrt{(2/3)k_\mathrm{sg}}} \tag{35.22}$$

The model constant $C = \mathrm{O}(1)$ accounts for the uncertainty concerning the timescale of the residual velocity autocorrelation. The prediction $\tau_\mathrm{L}^* = \tau_\mathrm{sg}$ is expected to work well for small *St* (also in the limit case of fluid diffusion). A discrete version of the model (unconditionally stable, first-order accuracy in time) was devised by Pozorski and Apte [39]. It was shown that, in poorly resolved regions, where the subgrid kinetic energy is more than 30%, the effect on droplet motion is more pronounced. A stochastic model reconstructing the subgrid scale velocity in a statistical sense was developed [39]. However, in well-resolved regions, where the amount of energy in the subgrid scales is small, this direct effect was not strong.

In the computational examples presented below, the direct effect of subgrid scale velocity on the droplet motion is neglected. However, note that the droplets *do feel* the subgrid scales through the subgrid model that affects the resolved velocity field. For well-resolved LES of swirling, separated flows with the subgrid scale energy content much smaller than the resolved scales, the direct effect was shown to be small [21].

Dense Spray Model

In the intermediate and dense spray regime, the local volume fraction of the liquid phase could be high and variations in the volume fractions should be accounted for in the gas-phase equations. Accordingly, the unfiltered mass and momentum conservation equations become [40–42]

$$\frac{\partial}{\partial t}\left(\rho_\mathrm{g}\Theta_\mathrm{g}\right) + \nabla\cdot\left(\rho_\mathrm{g}\Theta_\mathrm{g}\mathbf{u}_\mathrm{g}\right) = 0, \tag{35.23}$$

$$\frac{\partial}{\partial t}\left(\rho_g \Theta_g \mathbf{u}_g\right) + \nabla \cdot \left(\rho_g \Theta_g \mathbf{u}_g\right) = -\Theta_g \nabla(p) + \nabla \cdot (\mu^* \mathbf{D}_C) + \mathbf{F}, \tag{35.24}$$

where ρ_g, Θ_g, and $\mathbf{u}_g$ are fluid density, volume fraction, and velocity, respectively. Also, p is the pressure in the gas phase and $\mathbf{D}_C = \nabla \mathbf{u}_g + \nabla \mathbf{u}_g^T$ is the average deformation rate of the fluid, $\mathbf{F}$ is the force per unit volume the droplets exert on gas, and Θ_p and Θ_g are the volume fractions of the liquid and gas phases, respectively: $\left(\Theta_p + \Theta_g = 1\right)$. This indicates that the average velocity field of the fluid phase does not satisfy the divergence-free condition even if we consider an incompressible fluid with droplets. For dense spray regimes, the fluid viscosity should be replaced by an effective viscosity μ^* by using [43] correlation

$$\mu^* = \mu_g \left(1 + 2.5\Theta_g + 10.05\Theta_g^2 + 0.00273 e^{16.6\Theta_g}\right). \tag{35.25}$$

The importance of the volumetric effects was demonstrated by Apte et al. [44] in nonreacting particle-laden flow simulations. The use of the volumetric displacement model requires addressing several issues of computing the liquid volume fractions, robustness of the numerical algorithm in the presence of large variations in volume fractions, and closure of correlations obtained after filtering the governing (35.1) and (35.24) [40, 41].

Numerical Method

The computational approach is based on a colocated, finite-volume, energy-conserving numerical scheme on unstructured grids [10] and solves the low-Mach number, variable density gas-phase flow equations. Numerical solution of the governing equations of continuum phase and droplet phase are staggered in time to maintain time-centered, second-order advection of the fluid equations. Denoting the time level by a superscript index, the velocities are located at time level t^n and t^{n+1}, and pressure, density, viscosity, and the scalar fields at time levels $t^{(n+3)/2}$ and $t^{(n+1)/2}$. Droplet position, velocity, and temperature fields are advanced explicitly from $t^{(n+1)/2}$ to $t^{(n+3)/2}$ using fluid quantities at the time-centered position of t^{n+1}. In this colocated scheme, the velocity and pressure fields are stored and solved at the centroids of the control volumes.

Lagrangian Droplet Equations

The droplet equations are advanced using a third-order Runge–Kutta scheme. Owing to the disparities in the flowfield timescale (τ_f), the droplet relaxation

time (τ_p or D_p^{-1}), the droplet evaporation timescale (τ_m), and the droplet heating timescale (τ_C), sub-cycling of the droplet equations becomes necessary. Accordingly, the time step for droplet equation advancement (Δt_p) is chosen as the minimum of these timescales and the time step for the flow solver (Δt). As the droplet size becomes very small, Δt_p reduces, and each droplet equation is solved multiple times per time step, giving good temporal resolution to capture droplet dispersion within a time step.

Care especially needs to be taken as the droplet diameter becomes very small due to evaporation. Under these conditions, the timescales associated with the droplet velocity, size, or the droplet heating may become much smaller than the flow solver time step. The fluid flow solution, then, is assumed locally frozen (or constant), and the ordinary differential equations are integrated analytically. The droplet mass, velocity, and temperature are then given by the following analytical expressions [45]:

$$m_\mathrm{p}(t) = m_\mathrm{p}(t^0)\left[1 - \frac{\Delta t_\mathrm{p}}{\tau_\ell}\right], \tag{35.26}$$

$$\mathbf{u}_\mathrm{p}(t) = \mathbf{u}_\mathrm{g,p}(t) - (\mathbf{u}_\mathrm{g,p} - \mathbf{u}_\mathrm{p})^0 \exp\left[-\frac{\Delta t_\mathrm{p}}{\tau_\mathrm{p}}\right], \tag{35.27}$$

$$\theta(t) - \frac{\tau_\mathrm{c}}{\tau_\ell}\frac{\Delta H_\upsilon}{C_{\mathrm{p},\ell}} = \left[\theta(t^0) - \frac{\tau_\mathrm{c}}{\tau_\ell}\frac{\Delta H_\upsilon}{C_{\mathrm{p},\ell}}\right]\exp\left(-\frac{\Delta t_\mathrm{p}}{\tau_\mathrm{c}}\right), \tag{35.28}$$

where m_p is mass of the droplet, $\theta = T_\mathrm{g,p} - T_\mathrm{p}$, and the superscript 0 stands for solution at an earlier time level. The linearized droplet equations are valid and used only when the timescales associated with a droplet become smaller than the flow solver timescale.

Locating the Droplet

After obtaining the new droplet positions, the droplets are relocated, droplets that cross interprocessor boundaries are duly transferred, boundary conditions on droplets crossing boundaries are applied, source terms in the gas-phase equation are computed, and the computation is further advanced. Solving these Lagrangian equations thus requires addressing the following key issues: (1) efficient search for locations of droplets on an unstructured grid, (2) interpolation of gas-phase properties to the droplet location for arbitrarily shaped control volumes, and (3) interprocessor droplet transfer.

Locating droplets in a generalized coordinate structured code is straightforward since the physical coordinates can be transformed into a uniform computational space. This is not the case for unstructured grids. The approach used in this work

projects the droplet location onto the faces of the control volume and compares these vectors with outward face-normals for all faces. If the droplet lies within the cell, the projected vectors point the same way as the outward face-normals. This technique is found to be very accurate even for highly skewed elements. A search algorithm is then required to efficiently select the control volume to which the criterion should be applied.

An efficient technique termed "the known vicinity algorithm" was used to identify the control volume number in which the droplet lies.

Given a good initial guess for a droplet location, the known vicinity algorithm identifies neighboring grid cells by traversing the direction the droplet has moved. In LES, the time steps used are typically small in order to resolve the temporal scales of the fluid motion. The droplet location at earlier time steps provides a very good initial guess. Knowing the initial and final location of the droplet, this algorithm searches in the direction of the droplet motion until it is relocated. The neighbor-to-neighbor search is extremely efficient if the droplet is located within 10–15 attempts, which is usually the case for 95% of the droplets in the present simulation. Once this cell is identified, the fluid parameters are interpolated to the droplet location using a conservative Gaussian kernel, which makes use of values at nearest neighboring cells. Similarly, the interaction terms from the droplets to the carrier fluid equations make use of the same interpolation function. This droplet-tracking algorithm is efficient and can locate droplets on complex unstructured grids allowing simulation of millions of droplet trajectories. In the present case, droplets are distributed over several processors used in the computation, and the load imbalance is not significant. Details of the algorithm are given in Apte et al. [21, 33].

Hybrid Droplet–Parcel Algorithm for Spray Computations

Performing spray breakup computations using Lagrangian tracking of each individual droplet gives rise to a large number of droplets (∼20–50 million) in localized regions very close to the injector. Simulating all droplet trajectories gives severe load imbalance due to the presence of droplets on only a few processors. On the other hand, correct representation of the fuel vapor distribution obtained from droplet evaporation is necessary to capture the dynamics of spray flames. In their pioneering work, O'Rourke and Bracco [20] used a "discrete-parcel model" to represent the spray drops. A parcel or computational particle represents a group of droplets, N_{par}, with similar characteristics (diameter, velocity, temperature). Typically, the number of computational parcels tracked influences the spray statistics predicted by a simulation.

In their original work, O'Rourke and coworkers [17, 20] injected parcels from the injector, resulting in a much fewer number of tracked computational particles. In this work, the parcel model is further extended to a hybrid particle–parcel scheme [33]. The basic idea behind the hybrid approach is as follows. At every

time step, droplets of the size of the spray nozzle are injected based on the fuel mass flow rate. New droplets added to the computational domain are pure drops ($N_{par} = 1$). These drops are tracked by Lagrangian particle tracking and undergo breakup according to the stochastic model creating new droplets of smaller size. As the local droplet number density exceeds a prescribed threshold, all droplets in that control volume are collected and grouped into bins corresponding to their size. The droplets in bins are then used to form a parcel by conserving mass. Other properties of the parcel are obtained by mass-weighted averaging from individual droplets in the bin. The number of parcels created would depend on the number of bins and the threshold value used to sample them. A parcel thus created then undergoes breakup according to the above stochastic subgrid model; however, it does not create new parcels. On the other hand, N_{par} is increased and the diameter is decreased by mass conservation. This strategy effectively reduces the total number of computational particles in the domain. Regions of low number densities are captured by individual droplet trajectories, giving a more accurate spray representation.

Simulations of Spray Dynamics in Gas-Turbine Combustors

In this section, some illustrative results from the simulations of spray patternation study for a Pratt and Whitney (PW) gas-turbine injector as well as turbulent reacting flow inside the combustor are presented [2, 36, 10].

Spray Patternation Study

Figure 35.3 shows a schematic of the computational domain used for the spray patternation of a PW injector corresponding to the experiments in nonreacting, low-temperature flows [1]. Figure 35.3a shows a cut through the symmetry plane of the computational domain along with the mesh and boundary conditions. For this case, 3.2 M grid points are used with high resolution near the injector. The grid elements

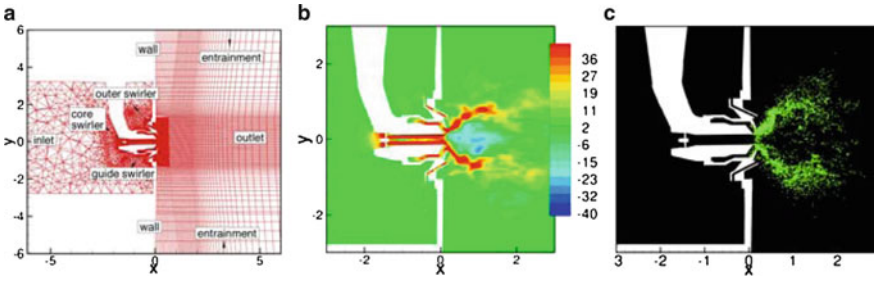


Fig. 35.3 Snapshots in the symmetry plane: (**a**) unstructured computational grid, (**b**) axial velocity contours, and (**c**) instantaneous snapshot of liquid droplets

are a combination of tetrahedra, prisms, wedges, and hexahedra to represent complex geometric passages inside the injector. Grid refinement study for LES of single-phase flow has been performed for different cases in complex configurations [9, 10]. The grid resolution for the present case was decided based on these validation studies.

The injector consists of a core, an outer, and a guide swirler creating highly unsteady, swirling, coaxial flow that enters a sudden expansion region. Air from the inlet plenum goes through the central core, guide, and outer swirlers to create highly unsteady multiple swirling jets. A substantial amount of air is entrained in the radial direction and the rate of air entrainment is specified based on the experimentally measured values. All the passages through the swirler are computed. The domain decomposition is based on the optimal performance of the Eulerian gas-phase solver on 96 processors. Brankovic et al. [1] provide details of the experimental measurement techniques and inflow conditions for a lower pressure drop across the fuel nozzle. The inflow conditions in the present study are appropriately scaled to a higher pressure drop providing the air mass flow rate of 0.02687 kg/s. The flow Reynolds number based on the inlet conditions is 14,960. A uniform mean inflow velocity was specified at the inlet without any turbulent fluctuations. In the present case, the downstream cylindrical plenum is open to atmosphere. The air jet coming out of the nozzle thus entrains air from the surrounding. Entrained flow along the surface of the downstream plenum was modeled as a radially inward velocity along the entire plenum surface. The experimental data profiles at different cross sections were integrated at each station to obtain the total flow rate at those locations. Knowing the net inflow rate, the entrained mass at each of the entrainment boundaries was estimated and assigned to the calculation. This modeling approach for entrained flow is subject to experimental verification; however, it was shown to have little impact on the predicted flowfield [1]. No-slip conditions are specified on the wall. Convective boundary conditions are applied at the exit section by conserving the global mass flow rate through the computational domain.

Liquid fuel is injected through the filmer surface which forms an annular ring near the outer swirler. A large number of droplets are created in the vicinity of the injector due to breakup. The location of droplet injection around the annular ring is chosen using uniform random distribution. This discrete representation of the film near the injector surface may not represent the physics of ligament formation and film breakup. However, the statistical nature of droplet formation further away from the injector is of interest in the present study and is well captured by the stochastic model together with LES of the air flow. With the hybrid approach, the total number of computational particles tracked at stationary state is around 3.5 M and includes around 150,000 parcels. Together these represent approximately 13 M droplets. The computations were performed on the IBM cluster at the San Diego Supercomputing Center.

Figure 35.3b, c show the instantaneous snapshots of the axial velocity contours and spray evolution (green dots) in the $Z/L_{\text{ref}} = 0$ symmetry plane. The swirling air jet from the core swirler enters the dump region and forms a recirculation zone. Jets from guide and outer swirlers interact with the core flow. The swirling air jets

entering the sudden expansion region create radially spreading conical jets with a large recirculation region just downstream of the injector. A complex vortex breakdown phenomenon is observed and its accurate prediction is necessary to correctly represent the injector flow. The swirl strength decays further away from the injector due to viscous dissipation. The scatter plot of the spray droplets show dense spray regimes close to the injector which become dilute further away. The parent droplets are injected at the edge of the annular ring. These droplets are carried by the swirling flow and form a conical spray. The concentration of the spray droplets is high on the edge of the recirculation region. The strong relative motion between the large inertial droplets near the injector and the fluid flow leads to breakup and generation of smaller droplets. The droplets spread radially outward and swirl around the injector axis as they move downstream.

Prediction of the gas-phase mean and rms velocity fields and the distribution of the liquid axial mass fluxes as predicted by the simulation are in good agreement with the experimental data. Details of these comparisons are provided by Apte et al. [36]. The breakup model does not include coalescence effects. In addition, the effect of injecting different size distributions near the injection must be investigated to address sensitivity of the model parameters to flow conditions. Specifically, size distributions further away from the injector (in the intermediate and dilute regimes) may be influenced by these inlet conditions.

Using the definition of ellipticity E (35.8), the variation of ellipticity for droplets in the near injector region at various cross sections was obtained by locally computing the Weber, Ohnesorge, and capillary numbers and relative velocities between the gas and the droplet. Accordingly, $E < 1$ implies that the drops have more width than height, implying deformation in a direction perpendicular to the relative velocity. These shapes are called oblate shapes. Similarly, $E > 1$ gives elongation in the direction of the relative velocity, giving rise to prolate shapes. $E = 1$ implies spherical shapes.

Figure 35.4 shows the variation of ellipticity with respect to the Weber, Reynolds, and capillary numbers at various axial locations. As observed from these figures, the droplets are big close to the injector and the Ohnesorge numbers are small. The Weber number is much larger than the critical Weber number ($\sim$6) and the drops undergo breakup. The deformation predicted by the above correlation

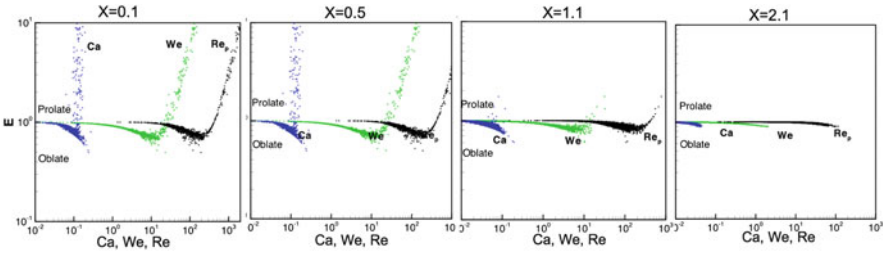


Fig. 35.4 Scatter plot showing ellipticity as a function of capillary, droplet Reynolds, and Weber numbers at different axial locations: $Ca = \mu_g U/\sigma$, $Re_p = \rho_g d_p/\mu_g$, $We = \rho g U^2 d_p/\sigma$

gives $E > 1$ close to the injector, indicating that the drops elongate in the direction of the relative velocity. Shear breakup is observed at these conditions. Further away from the injector, however, the drop size and the Weber and Reynolds number decrease. This gives $E < 1$, and bag breakup is observed. The degree of deformation characterized by the ellipticity is significant close to the injector and decreases away from the injector. In the combustor, the capillary number $C_a = \mu_g U/\sigma$ is very small, and dimpling of the droplets is absent.

In order to investigate the effect of deformation on the drag experienced by the droplet, time-series data for several droplets after their breakup was gathered. Looking at the frequency spectrum of the relative velocity, the dominant mode of droplet oscillation was determined. Based on the mean and rms data of the relative velocity, resolved simulation using the hp-finite element method [25, 26] of drops subjected to oscillating velocity field representing the realistic conditions was performed [46]. The temporal response of the droplet to underlying oscillatory flowfield is then investigated by evaluating results obtained from different drag models and the resolved direct simulations. Results for a single droplet are given below.

From the LES, data corresponding to a droplet with $\mu_l/\mu_g \sim 45$, $\rho_l/\rho_g \sim 700$, $Oh = 0.0624$ and mean droplet Reynolds number of 25 were gathered. Based on the frequency spectrum of the relative velocity, the most dominant mode of oscillation corresponds to a wave number of 2.5×10^5s. The mean and rms relative velocities were 50 and 5 m/s giving a Weber number of approximately unity with 20% variation. Accordingly, a normalized gas-phase inflow velocity for a droplet of unit diameter was chosen to give a mean Weber number of unity. This is given as $u_g = 1 + 0.1\ \sin(2\pi t/100)$. The frequency of $f = 100$ was chosen based on the observed dominant oscillation mode. Effect of droplet deformation and internal circulation was characterized by modifying the standard drag law (using (35.9)). Figure 35.5 shows the evolution of the droplet velocity field with time

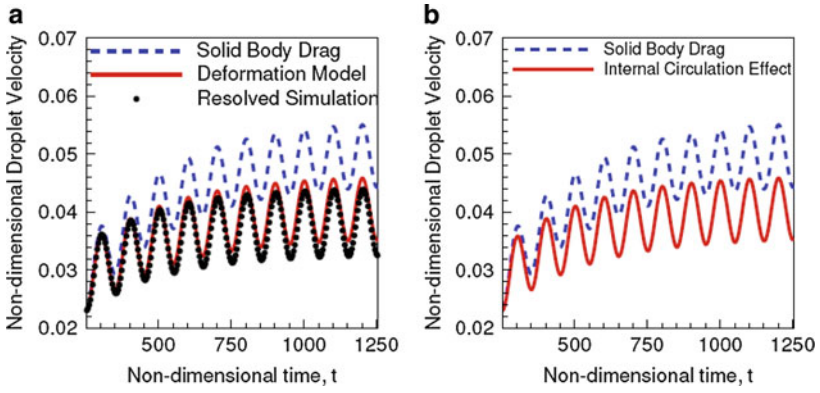


Fig. 35.5 Evolution of droplet velocity using different drag laws under imposed periodic oscillations in relative velocity: (**a**) comparison of solid body drag, and droplet deformation (including circulation effects) with resolved simulations [25], (**b**) effect of internal circulation (without droplet deformation) on droplet velocity

under the imposed periodic fluctuations, obtained by two different drag laws as well as from the resolved simulations [25]. It is found that the internal circulation has a pronounced effect on the droplet position and velocity. The droplet velocity is well predicted by the standard solid body drag modified by the internal circulation. For the droplet under investigation, the correction $D_{\text{drop}}/D_{\text{solid}}$ given by (35.9) oscillates by 1% around 0.98. Thus, a 2% reduction in the solid drag law corresponds to 20% change in the droplet velocity. This could perhaps be explained as follows. Because the drag force changes somewhat weakly with velocity, small changes in the drag model can lead to large changes in the velocity when the drop reaches its terminal velocity. It was found that the effect of droplet deformation for the present drop was not pronounced; however, internal circulation effects were found to be important. Further work is needed to study the effect of deformation on the drag at higher Weber numbers and for droplets undergoing breakup.

LES of Reacting Spray Flame in Real PW Combustor

A multiscale, multiphysics simulation of turbulent reacting flow in a PW combustor was performed to investigate the unsteady flame dynamics. This includes all the complex models for spray breakup, evaporation, and turbulent combustion mentioned earlier. Figure 35.1b shows the computational fluid dynamics (CFD) model for a single (1/18) sector of the full combustor. The computational grid consists of 1.9 M hybrid elements (hexes, pyramids, and tets) with fine resolution close to the injector. The grid inside the combustion chamber is hex-dominant to obtain good numerical accuracy. Figure 35.1c shows a section through the symmetry plane of the combustor geometry along with contours of temperature. Also shown are the instantaneous droplet locations in this plane forming a conical spray. The injector is the same as the one used in the liquid fuel patternation study described earlier.

The experimental data available for validation include mass splits through different components, temperature profile, and distribution of pollutants, NOx, at the measurement plane.

Liquid fuel (Jet-A) enters the combustion chamber through an annular ring at the injector exit. This liquid film is approximated by large drops of the size of the injector annulus. These drops are convected by the surrounding hot air, they break, evaporate, and the fuel vapor thus formed mixes with the surrounding air giving a non-premixed spray flame. The flamelet library for Jet-A fuel at gas-turbine engine operating conditions is generated by using a surrogate fuel (80% *n*-decane and 20% 1-2-4 tri-methyl-benzene) chemistry which closely follows the chemical kinetics and reaction rates of the Jet-A fuel. Around 1,000 elementary reactions among 100 chemical species are used to generate these tables. The chemical kinetics of surrogate fuel compared to the original fuel chemistry in terms of prediction of pollutants in laminar flames showed good agreement. The progress variable for this simulation represents the summation of mass fractions of CO_2 and H_2O. The comparison of the radial variation of the mean temperature is shown in Fig. 35.6

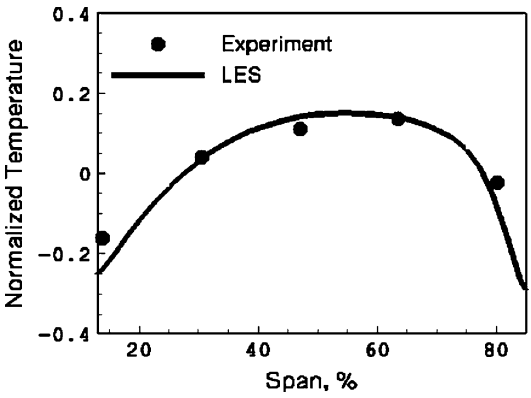


Fig. 35.6 Prediction of mean temperature at the measurement plane of a PW combustor. Span represents the normalized vertical distance in the measurement plane [2]

and was obtained by taking azimuthal average over the sector. The average temperature in the measurement plane is within 2% of the experimental data. Significant advances in numerical algorithms resulting in efficient speedup of the solver have been performed [11]. In addition, advanced models for prediction of pollutants and NOx are being developed and applied to compute their distributions within the combustion chamber. A variety of flow conditions including cruise, high power, and take-off are also being simulated for multiple sectors of the combustor [47].

Summary

A nondissipative, energy-conserving numerical solver for arbitrary-shaped unstructured grids is developed to simulate multiphase, multiscale turbulent reacting flows in realistic gas-turbine combustors. This numerical tool solves low-Mach number, variable density flow equations for the gas phase. Advanced models to capture atomization and droplet breakup, droplet evaporation, droplet deformation and drag, and turbulent combustion are used to simulate complex multiphase reacting flows. This numerical tool was applied to perform an LES atomizing spray in reacting and nonreacting flows in a PW combustor to show reasonable predictions of the two-phase flowfield.

Several advances in the modeling approaches addressing different spray regimes near the injector are still needed. Specifically, approaches capable of handling primary atomization and liquid sheet breakup, finite-size effect of the droplets in the dense spray regime, advanced combustion models for premixed/partially premixed turbulent flames, soot and pollutant formation, radiation modeling, and approaches modeling combustion instabilities are needed for predictive simulation-based design and modification of the combustors. Several advances in these areas have been made [15, 44, 48, 49]. Furthermore, new algorithmic developments

accelerating the time to solution are needed [11, 50, 51] such that multiphysics, multiphase computations of the full 18-injector combustor can become feasible using advanced parallel computing.

Acknowledgments Support for this work was provided by the US Department of Energy under the Advanced Scientific Computing (ASC) program. The computer resources at San Diego Supercomputing Center are greatly appreciated. We are indebted to Profs. Parviz Moin, Krishnan Mahesh, Gianluca Iaccarino, Brian Helenbrook, Heinz Pitsch, Drs. Frank Ham and Joeseph Oefelein, and the combustor group at Pratt & Whitney for their help and support at various stages of this work. We also thank Mr. Daniel Peterson for editing this document.

References

1. A. Brankovic, L. Porter, R. McKinney, H. Ouyang, J. Kennedy, R. Madabhushi, M. Colket, Comparison of measurements and predictions of flow in a gas turbine engine fuel nozzle, in: AIAA, Aerospace Sciences Meeting and Exhibit, 38th, Reno, 2000.
2. P. Moin, S. Apte, Large-Eddy simulation of realistic gas turbine-combustors, AIAA Journal 44 (4) (2006) 698–708.
3. M. Ruger, S. Hohmann, M. Sommerfeld, G. Kohnen, Euler/Lagrange calculations of turbulent sprays: the effect of droplet collisions and coalescence, Atomization and Sprays 10 (1) (2000) 47–82.
4. D. Schmidt, L. Chiappetta, G. Goldin, R. Madabhushi, Transient multidimensional modeling of air-blast atomizers, Atomization and Sprays 13 (4) (2003) 373–394.
5. C. Pierce, P. Moin, Progress-variable approach for large-eddy simulation of non-premixed turbulent combustion, Journal of Fluid Mechanics 504 (2004) 73–97.
6. N. Patel, M. KIrtas, V. Sankaran, S. Menon, Simulation of spray combustion in a lean-direct injection combustor, Proceedings of the Combustion Institute 31 (2) (2007) 2327–2334.
7. N. Patel, S. Menon, Simulation of spray–turbulence–flame interactions in a lean direct injection combustor, Combustion and Flame 153 (1–2) (2008) 228–257.
8. R. Mittal, P. Moin, Stability of upwind-biased finite difference schemes for large-eddy simulation of turbulent flows, AIAA Journal 35 (8) (1997) 1415–1417.
9. K. Mahesh, G. Constantinescu, P. Moin, A numerical method for large-eddy simulation in complex geometries, Journal of Computational Physics 197 (1) (2004) 215–240.
10. K. Mahesh, G. Constantinescu, S. Apte, G. Iaccarino, F. Ham, P. Moin, Large-Eddy simulation of reacting turbulent flows in complex geometries, Journal of Applied Mechanics 73 (2006) 374.
11. F. Ham, S. Apte, G. Iaccarino, X. Wu, M. Herrmann, G. Constantinescu, K. Mahesh, P. Moin, Unstructured LES of reacting multiphase flows in realistic gas-turbine combustors. Annual Research Briefs 2003, Center for Turbulence Research, Stanford, 2003.
12. Tanguy, S., Berlemont, A., Application of a level set method for simulation of droplet collisions, International Journal of Multiphase Flow 31 (2005) 1015–1035.
13. T. Menard, P. Beau, S. Tanguy, F. Demoulin, A. Berlemont, Primary break-up: DNS of liquid jet to improve atomization modelling, WIT Transactions on Engineering Sciences 50 (2005) 343.
14. T. Menard, S. Tanguy, A. Berlemont, Coupling level set/VOF/ghost fluid methods: validation and application to 3D simulation of the primary break-up of a liquid jet, International Journal of Multiphase Flow 33 (5) (2007) 510–524.
15. M. Gorokhovski, M. Herrmann, Modeling primary atomization, Annual Review of Fluid Mechanics 40 (2008) 343–366.

16. J. Dukowicz, A particle-fluid numerical model for liquid sprays, Journal of Computational Physics 35 (1980) 229.
17. P. ORourke, A. Amsden, The TAB method for numerical calculation of spray droplet breakup, SAE Technical Paper 872089, 1987, and in: International fuels and lubricants meeting and exposition, Vol. 2, 1987.
18. R. Reitz, Modeling atomization processes in high-pressure vaporizing sprays, Atomization and Spray 3 (1987) 307.
19. P. O'Rourke, The KIVA computer program for multidimensional chemically reactive fluid flows with fuel sprays, Lecture Notes in Physics 241 (1985) 74.
20. P. O'Rourke, F. Bracco, Modeling of droplet interactions in thick sprays and a comparison with experiments, in: Stratified charge automotive engines conference, mechanical engineering publications, London, 1980.
21. S. Apte, K. Mahesh, P. Moin, J. Oefelein, Large-eddy simulation of swirling particle-laden flows in a coaxial-jet combustor, International Journal of Multiphase Flow 29 (8) (2003) 1311–1331.
22. P. Moin, K. Squires, W. Cabot, S. Lee, A dynamic subgrid-scale model for compressible turbulence and scalar transport, Physics of Fluids A 3 (11) (1991) 2746–2757.
23. M. Germano, U. Piomelli, P. Moin, W. Cabot, A dynamic subgrid-scale eddy viscosity model, Physics of Fluids A: Fluid Dynamics 3 (1991) 1760.
24. C. Crowe, M. Sommerfeld, Y. Tsuji, Multiphase flows with droplets and particles, CRC Press, Boca Raton, 1998.
25. B. Helenbrook, C. Edwards, Quasi-steady deformation and drag of uncontaminated liquid drops, International Journal of Multiphase Flow 28 (10) (2002) 1631–1657.
26. B. Helenbrook, A two-fluid spectral-element method, Computer Methods in Applied Mechanics and Engineering 191 (3–5) (2001) 273–294.
27. G. Faeth, Current status of droplet and liquid combustion, in: Combustion Institute, Spring Technical Meeting, Cleveland, Paper, 1977, p. 29.
28. G. Faeth, Evaporation and combustion of sprays, Progress in Energy and Combustion Science 7 (1) (1983) 1–76.
29. C. Law, Recent advances in droplet vaporization and combustion, Progress in Energy and Combustion Science 8 (3) (1982) 171–201.
30. W. Sirignano, C. Law, Transient heating and liquid-phase mass diffusion in fuel droplet vaporization, in: Evaporation-Combustion of Fuels: A Symposium, American Chemical Society, Lisbon, 1978.
31. R. Miller, K. Harstad, J. Bellan, Evaluation of equilibrium and non-equilibrium evaporation models for many-droplet gas-liquid flow simulations, International Journal of Multiphase Flow 24 (6) (1998) 1025–1055.
32. M. Gorokhovski, V. Saveliev, Analyses of Kolmogorovs model of breakup and its application into Lagrangian computation of liquid sprays under air-blast atomization, Physics of Fluids 15 (2003)
33. S. Apte, M. Gorokhovski, P. Moin, LES of atomizing spray with stochastic modeling of secondary breakup, International Journal of Multiphase Flow 29 (9) (2003) 1503–1522.
34. U. Shavit, N. Chigier, Fractal dimensions of liquid jet interface under breakup, Atomization and Sprays 5 (6) (1995) 525–544.
35. W. Zhou, Z. Yu, Multifractality of drop breakup in the air-blast nozzle atomization process, Physical Review-Series E. 63 (1, Part A) (2001) 16302–16302.
36. S. Apte, K. Mahesh, M. Gorokhovski, P. Moin, Stochastic modeling of atomizing spray in a complex swirl injector using large eddy simulation, Proceedings of the Combustion Institute 32 (2) (2009) 2257–2266.
37. M. Gorokhovski, J. Jouanguy, A. Chtab, Simulation of air-blast atomization:floating guard-statistic particle method for conditioning of LES computation: stochastic models of break-up and coalescence, in: Proceedings of the international conference on liquid atomization and spray systems, 10th (ICLASS-2006), Madison, 2006.

38. J. Bellan, Perspectives on large Eddy simulations for sprays: issues and solutions, in: Eighth international conference on liquid atomization and spray systems, Pasadena, 2000.
39. J. Pozorski, S. Apte, Filtered particle tracking in isotropic turbulence and stochastic modeling of subgrid-scale dispersion, International Journal of Multiphase Flow 35 (2008) 118–128.
40. M. Van der Hoef, M. van Sint Annaland, N. Deen, J. Kuipers, Numerical simulation of dense gas-solid fluidized beds: a multiscale modeling strategy, Annual Review of Fluids Mechanics 40 (2008) 47–70.
41. A. Vreman, B. Geurts, N. Deen, J. Kuipers, Large-eddy simulation of a particle-laden turbulent channel flow, Direct and Large-Eddy Simulation V, Munich, 2003, pp. 271–278.
42. D. Snider, An incompressible three-dimensional multiphase particle-in-cell model for dense particle flows, Journal of Computational Physics 170 (2) (2001) 523–549.
43. D. Thomas, Transport characteristics of suspension: VIII. A note on the viscosity of Newtonian suspensions of uniform spherical particles, Journal of Colloid Science 20 (1965) 267–277.
44. S. Apte, K. Mahesh, T. Lundgren, Accounting for finite-size effects in simulations of disperse particle-laden flows, International Journal of Multiphase Flow 34 (3) (2008) 260–271.
45. S. Apte, K. Mahesh, P. Moin, Large-eddy simulation of evaporating spray in a coaxial combustor, Proceedings of the Combustion Institute 32 (2) (2009) 2247–2256.
46. S. V. Apte, B. Helenbrook, P. Moin, Modeling effects of droplet deformation and breakup in realistic combustors, in: Proceedings of the 16th conference of liquid atomization and spray systems, Monterey, 2003.
47. Center for Integrated Turbulence Simulations, (2003–2005), Annual Report, http://www.stanford.edu/group/cits/pubs/reports.html.
48. H. Pitsch, L. Duchamp de Lageneste, Large-eddy simulation of premixed turbulent combustion using a level-set approach, Proceedings of the Combustion Institute 29 (2) (2002) 2001–2008.
49. C. Wall, C. Pierce, P. Moin, A semi-implicit method for resolution of acoustic waves in low Mach number flows, Journal of Computational Physics 181 (2) (2002) 545–563.
50. F. Ham, An effcient scheme for large eddy simulation of low-Ma combustion in complex configurations, Annual research briefs, center for turbulence research, Stanford University, 2007.
51. G. Iaccarino, F. Ham, LES on Cartesian grids with anisotropic Refinement, Lecture Notes in Computational Science and Engineering 56 (2007) 219.

Chapter 36
Melt Atomization

B. Zheng and E.J. Lavernia

Abstract The science and technology underlying the process of melt atomization is introduced, paying particular attention to relevant thermal, solidification and other transport phenomena. Melt atomization has now been developed as one of major produce methods for various metal and alloy powder, and hence it is of both scientific and technological interest. The mechanisms of melt disintegration, the design of typical atomization devices, the influence of key process parameters, the thermal transport in the atomized droplets, and the characteristics of the size distribution are briefly described and discussed.

Keywords Atomization · Particles · Processing parameters · Transport phenomena

Introduction

Melt Atomization is the dominant method used commercially to produce metal and alloy powders from Al, Cu, Fe, Ti, Ni, and other alloys because high production rates favor economies of scale. Atomization, as the name implies, involves the energetic disintegration of a liquid into micrometer-sized droplets. In fact, any material that can form a liquid phase can be atomized. During melt atomization, a molten metal stream is forced through an orifice at moderate pressures, and is subsequently disintegrated into droplets by the impingement of high-energy jets of a particular fluid medium, which may be either gas or liquid, such as inert gas, water or oil. Gas atomization is often preferred over other atomization methods for the production of pre-alloyed powders since a careful degree of control can be exercised on powder chemistry, powder cleanliness, and powder size distribution and morphology. A schematic diagram of a typical gas atomization unit is shown in Fig. 36.1 [1]. The melt is delivered to an atomizer nozzle where it is fragmented into

B. Zheng (✉)
Department of Chemical Engineering and Materials Science, University of California, Davis, USA
e-mail: bzheng@ucdavis.edu

N. Ashgriz (ed.), *Handbook of Atomization and Sprays*,
DOI 10.1007/978-1-4419-7264-4_36, © Springer Science+Business Media, LLC 2011

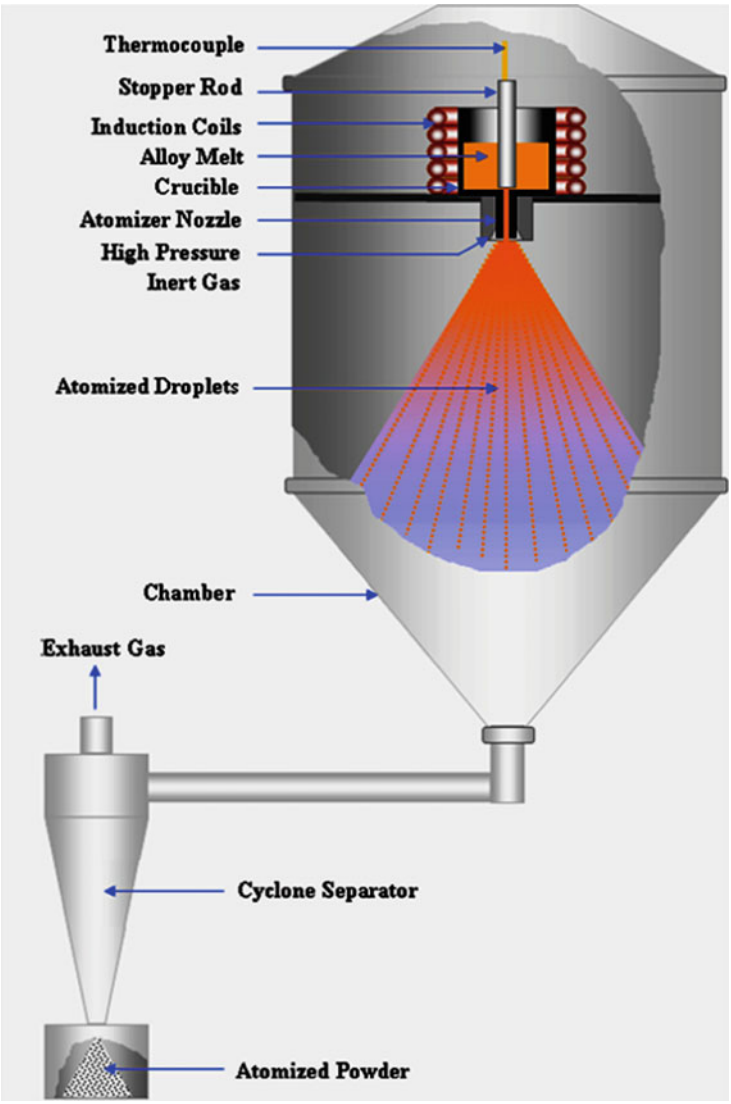


Fig. 36.1 Schematic diagram of gas atomization structure and processing [1]. (From B. Zheng et al. Metall. Mater. Trans. B 40, 2009)

micrometer-sized droplets by means of energetic jets. The ligaments and other irregular shapes that form first during disintegration, and subsequently during interactions with aerodynamic forces, are spheroidized, a process that is driven by the high surface energy that is typical of molten metals. The molten spheres subsequently experience solidification into powder particles during flight. Particles are collected normally in the lower region of the atomization chamber, frequently via a cyclone separator device. Another type of atomization process that is available

is centrifugal atomization, which uses the centrifugal forces of a spinning disk/cup or rotating electrode to disperse the liquid stream into droplets. However, melt atomization accounts for more than 95% of available atomization capacity worldwide [2]. Atomization is the most flexible technique, which allows for the production of a broad range of alloy compositions with extensive control over resulting powder characteristics and properties. Atomization is also the most critical step in spray deposition processing [3], in which melt atomization is used to produce the metallic droplets, which subsequently impinge and collect on a deposition surface to form a three-dimensional preform. Unlike conventional spray liquid processing, there is also thermal energy dissipation and phase transformation reactions during melt atomization of metal powders.

The principle of melt atomization is ancient and formed the basis for a British patent in 1872 to produce lead powders by drawing-off and spraying molten lead using a stream injector [4]. Since the first large-scale production of atomized iron powder during World War II, melt atomization technology has been steadily implemented and improved partly to the widespread application of prealloyed powders, for example in thermal spray coatings and net shaped components. The latter is generally achieved by compacting fine powders using various powder metallurgy technologies for aerospace, automotive, tools of petroleum, etc.

The melt atomization is generally referred to as two-phase atomization (or twin fluid atomization). The fluid being atomized is typically a molten metal, while a secondary fluid is used as the atomization media to break-up the molten metal into droplets. During atomization, jets of the secondary fluid are formed and accelerated using a stream injector. These jets are then focused onto a stream of molten metal to promote disintegration.

During atomization, the bulk liquid is disintegrated into fine droplets in the micro-sized range, which exhibit a much larger surface-to-volume ratio as compared to the starting materials. The driving force for atomization is generally provided by the kinetic energy of the atomization media. Hence, the atomization of molten metals inherently involves the transfer of energy from the atomization media to the molten metal and the creation of a large amount of surface area. From an energy conservation standpoint, the kinetic energy imparted by the atomization media on the molten metal is partially dissipated in two important processes: to overcome the viscous forces of the molten metal that resist deformation and to overcome the surface energy forces that resist free surface creation. The kinetic energy that retains in the atomization media is eventually dissipated in the environment. The energy that is transferred from the atomization media to the molten metal in the form of surface energy for unit mass of powders produced, ΔE_s, may be estimated from a simple formulation [3]:

$$\Delta E_s = s_1 \left(\sum S_d - \sum S_b \right) \tag{36.1}$$

where σ_1 is the surface energy of the molten metal; $\sum S_d$ and $\sum S_b$ are the total surface areas of the droplets and that of the bulk material for the unit mass of powder produced.

Classification of Melt Atomization

Melt atomization processes can be classified into various categories, according to the physical properties and flow characteristics of the atomization fluid: water atomization, oil atomization, and gas atomization. Gas atomization can be further classified into subsonic gas atomization, supersonic gas atomization, and ultrasonic gas atomization. The considerations in selecting a particular melt atomization method include economic factors, production scale, the physical and chemical properties of fluid to be atomized and powder to be produced, and the morphology of the powder desired [3, 5].

In the case of water and oil atomization, the atomization fluid is accelerated via a fluid injector and generally released as discrete jets. The basic mechanism in water atomization is based on momentum transfer, where the molten metal stream is broken up under the impact, rather than shear, from water droplets [6]. Separation and desiccation are normally necessary to collect the metallic powders from the slurry of atomization fluid and powders. Water atomized powders generally are quite irregular in morphology as compared to those generated using gas atomization since the cooling rate that is present during water atomization is approximately one to two orders of magnitude larger than that for gas atomization. Oil atomized powders have intermediate densities that fall between those corresponding to water and gas atomized powder as the quench rate is slower and oxidation not as pronounced. Water and oil atomization methods are generally used for high tonnage production of metallic powders when irregular particle shape and a certain degree of contamination can be tolerated.

Gas atomization is the process where the molten metal is disrupted by a high velocity gas. Subsonic, supersonic, and ultrasonic gas atomization utilize different gas velocity jets, as implied by the names used to describe the techniques. During gas atomization, a high pressure atomization gas, such as air, nitrogen, argon, or helium, is discharged from the pressuring reservoir of the atomizer into a chamber, which is typically maintained at a low environmental pressure. The compressible atomization gas is accelerated to a high velocity as it expands from the high reservoir pressure into the low pressure chamber. The energetic impingement of high velocity gas jet causes the molten metal stream to deform and disintegrate into fine droplets. The gas-to-metal ratio is an important factor that governs particle size for gas atomization, rather than being dominated by pressure of the medium like in the case of water atomization.

Atomizer and Processing Parameter

The gas atomizer can be classified into two basic types, open-type (free-fall design) and close-type (confined design) atomizers as shown in Fig. 36.2, according to the relative position between the atomization gas jets and molten metal stream [5, 8].

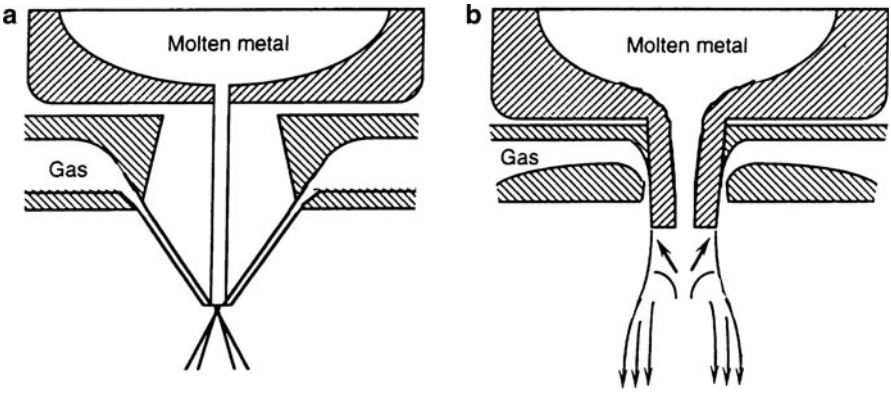


Fig. 36.2 Two-fluid atomizer designs: (**a**) free fall design (gas or water), and (**b**) confined design (gas only), according to the relative position between the atomization gas jets and molten metal stream [7]. (Courtesy of Syracuse University Press, Syracuse, New York, 1972)

In free-fall designs, the metal is allowed to fall under the action of gravitational forces for a certain distance (2–20 cm) prior to interacting with the atomization gas jets. Due to the rapid velocity decay as the gas moves away from the jet, it is very difficult to bring the mean diameter of powder below 60 μm on Fe-based alloys with free fall atomizers [2]. In confined designs, the metal travels a very short distance or is prefilmed before being impinged upon by the high energy gas jets. The fluid medium is introduced into the metal stream just before it leaves the nozzle, serving to create turbulence as the entrained fluid expands due to heating and exits into a large collection volume exterior to the orifice. Confined atomizers enhance the yield of fine powder particles by maximizing gas velocity and density on contact with metal. The advantages of confined atomizer designs include their higher atomization efficiency and more stable spray relative to that associated with free-fall atomizers. However, confined atomizers are extremely sensitive to metal freeze-up, a condition that occurs when the liquid metal at the end of the delivery tube solidifies as a result of the combined effects of prefilming and rapid heat extraction that occur at the orifice of the delivery tube [3]. The interaction of the gas stream with the nozzle tip can also generate either negative or positive pressure, causing increased metal flow rate or alternatively, completely blocking the flow of metal from the crucible. Thus, great care is needed in setting up confined nozzles. Supersonic atomizers are primarily close-type atomizers. As the gas jets exit the nozzle orifices, their velocity decays rapidly, resulting in the initially supersonic flow degrading into subsonic flow only a short distance from the orifices. Ultrasonic gas atomization has been widely used for fine powder ($\sim$10 μm) atomization [3]. Different from other gas atomization methods, the gas jets formed by an ultrasonic gas atomizer carry shock waves with frequencies beyond the audible range (i.e., 20–100 kHz) [9–11]. The shock waves are meant to increase the efficiency of the molten metal breakup process.

In confined annular atomizer designs, the rapid flow of atomization gas passing the nozzle edge creates a recirculating region and results in a negative pressure

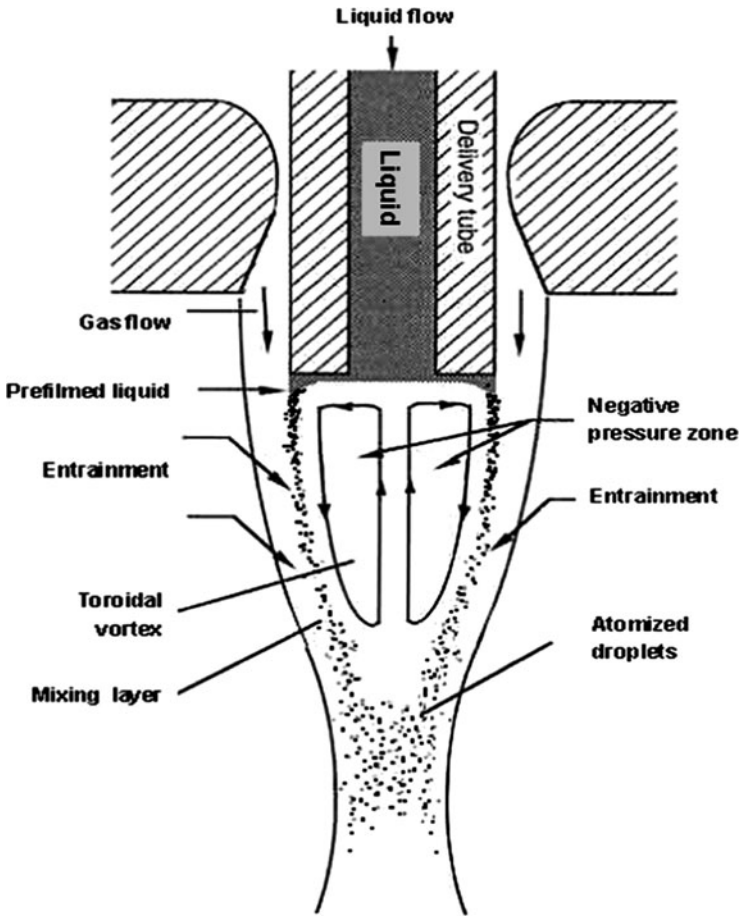


Fig. 36.3 Gas and melt flow patterns in a confined atomizer with the aspiration effect

region under the nozzle exit orifice (called aspiration effect) during gas atomization. The aspiration effect, as shown schematically in Fig. 36.3 [3], leads to shearing of the metal stream by the flowing gas, which then forms an envelope of liquid sheet right above the focal point of the gas jets. The liquid sheet is then disrupted into fragments and droplets.

The pressures used in conventional gas atomization are typically in the range of 100–600 psi (0.6–4 MPa) [8], and gas velocities in the nozzles range from Mach 1 to 3 [3]. The typical metal flow rates through single orifice nozzle range from about 1 to 90 kg/min, and typical gas flow rate ranges from 1 to 50 m^3/min. The effective gas velocities range from 20 m/s to supersonic velocities, depending on nozzle design. The superheat of the molten metal, the differential temperature between the metal melting point and the temperature for atomizing molten metal, is generally about 75–150°C [2].

Mechanism of Breakup and Powder Morphology

The atomization of a bulk liquid into droplets relies on the mechanical disturbances which an atomizer imposes on a liquid. As a result of the various atomizer designs and the large number of processing variables involved, the actual breakup process of liquid into droplets may differ from case to case, although the overarching driving force is provided by surface energy. The breakup of a liquid is intimately coupled to the interactions that occur between the liquid and the surrounding environment or atomization media. Review of various mechanisms that have been proposed to explain "atomization" shows that most of the mechanisms of droplet formation involve three basic stages during the gas atomization process for the disintegration of an instable liquid sheet into droplets as shown in Fig. 36.4 [12]. These are: formation and growth of disturbance waves; disruption of liquid sheet into fragments; and formation of droplets by further breakup of fragments. Atomization of molten metals may also be divided into three important fundamental processes: primary atomization, secondary atomization, and solidification. The solidification events that are associated with metals may affect the breakup processes and the resultant size distribution of the droplets. If the droplet size produced in the primary atomization is sufficiently small, droplets may already be solid or partially solid prior to secondary atomization. In this case, there may not be sufficient time for secondary atomization to occur.

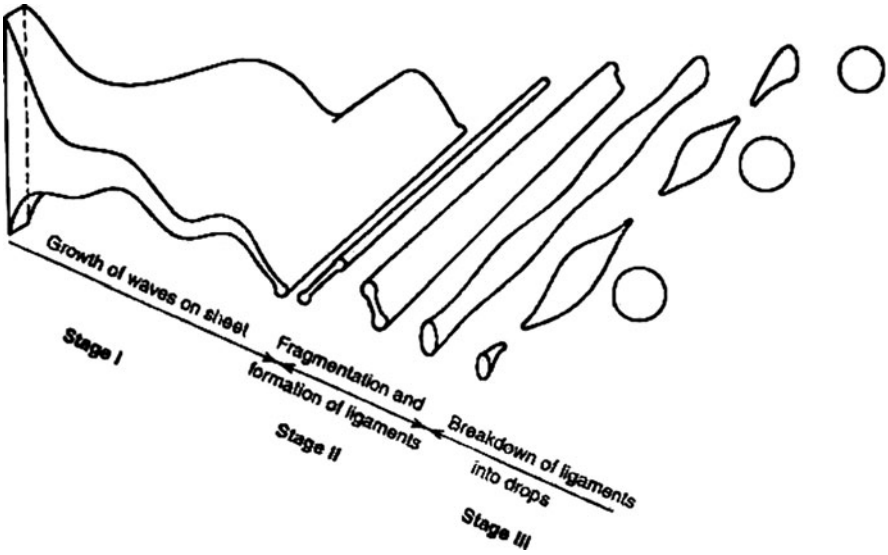


Fig. 36.4 Mechanism of disintegration of a liquid sheet into droplets with three basic stages during the gas atomization process [12]. (From N. Dombrowski, W. R. Johns: Chem. Eng. Sci. 18, 1963)

The particle morphology is determined largely by the rate of solidification and varies from spherical, if a low heat capacity gas is employed, to highly irregular if water is used. The irregular shape of water atomized powder is attributed to the relative higher solidification rate as compared to the spheroidizing rate of liquid droplets. If the spheroidization time (or residence time), t_{sph}, of liquid droplet is shorter than its solidification time, t_{sol}, particle shape tends to be spherical. Particles tend to be irregular if spheroidization time is longer. A more irregular morphology is sometimes observed when there are impurities present which lower surface tension and hence increase spheroidization time [2]. The morphology of gas atomized powder particles is generally spherical. "Satellite" powders are sometimes formed when finer powder is gas atomized, which is believed to be caused by the circulation of gas within the atomizing chamber. The fine particles are blown back into the spray plume, where they collide with larger and still partly molten particles. Spherical particles have ideal flow characteristic and are desirable for feeding thermal spray and laser powder cladding or net shaped deposition processes.

Particle Size Distribution

The relative velocity between the liquid and the gas is considered to be one of the most important factors that affect the liquid breakup process during gas atomization. For a given gas nozzle design, particle size is controlled by the atomizing media pressure and melt flow rate. The droplet size distribution for various gas-atomized alloys has been reported generally to follow a lognormal distribution [13–17]. Two numbers: d_{50}, median mass diameter, and σ_g, geometric standard deviation, are usually used to describe the entire size distribution. The mass probability density function, $p(d)$, of the droplet-size distribution can be expressed by [18–20]:

$$p(d) = \frac{1}{\sqrt{2\pi}\ln\ \sigma_g} \exp\left[-\frac{(\ln\ d - \ln\ d_{50})^2}{2(\ln\ \sigma_g)^2}\right] \tag{36.2}$$

where d is the droplet size. Generally, the powder size distribution is represented in terms of a cumulative frequency, $f(d_i)$, which is defined as the fraction of powders that fall in the size range that is smaller than d_i. The mass median diameter d_{50} is defined as the droplet size that corresponds to the 50% cumulative frequency. d_{50} can be well predicted for gas atomizing Al alloys powder by using a correlation developed by Lubanska [15]:

$$d_{50} = K_d D_n \left[\frac{\eta_m}{\eta_g W}\left(1 + \frac{\dot{M}}{\dot{G}}\right)\right]^{\frac{1}{2}} \tag{36.3}$$

where K_d is a constant, D_n is the melt stream diameter (i.e., the nozzle diameter), η_m (m^2/s) and η_g (m^2/s) are the kinematic viscosity of the melt and gas, respectively, $\dot{M}$ (kg/s) and $\dot{G}$ (kg/s) are the melt and gas flow rates, respectively, W is the Weber number, $W = v_i^2 \rho_m D_n / \gamma_m$, where ρ_m (kg/m^3) and γ_m (J/m^2) are the density and surface tension of the melt, respectively. σ_g is the geometric standard deviation characterizing the spread of the droplet size distribution centered around d_{50}, and can be estimated by the following empirical equation [16, 21]:

$$\sigma_g = q d_{50}^j \tag{36.4}$$

where q and j are constants, and the unit of d_{50} is micrometer herein.

Droplet Flow Dynamics

During gas atomization, the droplets are accelerated or decelerated due to the drag force resulting from the velocity difference with the local atomization gas. The motion of an individual droplet along the spray-axis is governed by the following equation [22, 23]:

$$\rho_d V_d \frac{dv_d}{dt} = V_d \left(\rho_d - \rho_g\right) g - \frac{1}{2} \rho_g A_s C_d \left|v_d - v_g\right| \left(v_d - v_g\right) \tag{36.5}$$

where v_d (m/s), ρ_d (kg/m^3), V_d (m^3), and A_s (m^2) are velocity, density, volume and cross-sectional area of a droplet, respectively; ρ_g (kg/m^3) and v_g (m/s) are the density and velocity of the GA gas, and g (m/s^2) is the gravitational acceleration. Since the gas-atomized droplets are treated as spherical in shape, $V_d = (\pi/6)d^3$ and $A_s = (\pi/4)d^2$, where d (m) is the effective droplet diameter. For a spherical droplet during GA, the drag coefficient, C_d, can be estimated by [24]:

$$C_d = 0.28 + \frac{6\sqrt{Re} + 21}{Re} \tag{36.6}$$

where Re is Reynolds number determined by:

$$Re = \frac{\rho_g d \left|v_g - v_d\right|}{\mu_g} \tag{36.7}$$

where μ_g (Ns/m^2) is the gas dynamic viscosity.

The gas velocity reaches a maximum at the exit of the atomizer nozzle, and subsequently decreases with an approximately exponential decay as the flight distance increases. Because of the velocity difference between the droplets and the impinging gas stream during gas atomization, the droplets are subjected to an

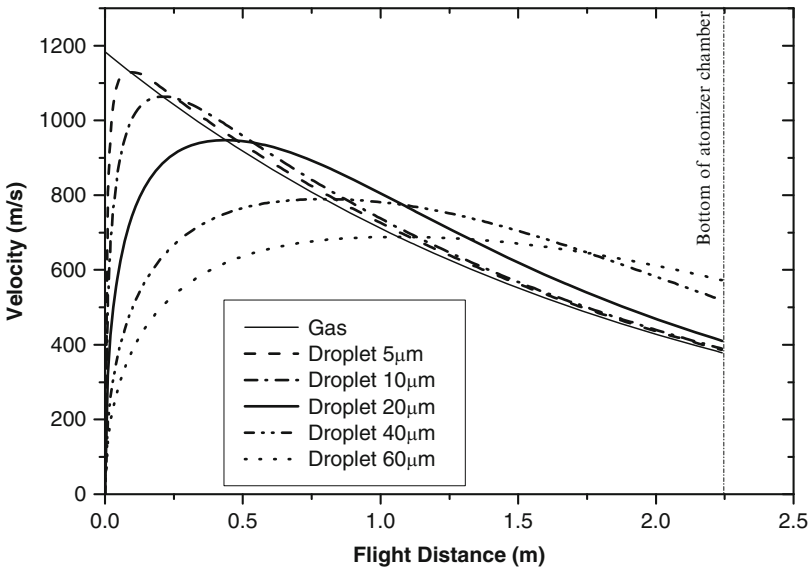


Fig. 36.5 Velocity variation of atomization gas and droplets with flight distance and droplet size during gas atomization of Al alloys for a gas pressure of 2.76 MPa [25]. (From B. Zheng et al. Metall. Mater. Trans. B 40, 2009)

accelerating drag force. The velocity of atomized droplets increases with increasing gas pressure. Figure 36.5 shows a typical Al alloy droplet velocity as a function of droplet size and flight distance for a gas pressure of 2.76 MPa [25]. In this case, the droplets are initially accelerated to a maximum value (the gas velocity at that point) due to the gas drag force. Once the gas velocity has been exceeded, the velocity decreases monotonically due to the retarding drag force from the gas. Small diameter droplets (e.g., 5–20 μm) are readily accelerated, whereas larger droplets have a larger inertia and hence resist the acceleration force.

Cooling Rates and Microstructure

The powder particles' size resulting from atomization allow cooling rates many orders of magnitude above those in casting processes, ranging from 10^2 to 10^7 K/s, which is known as rapid solidification, a non-equilibrium process. Gas atomization can produce high cooling rates also due to the initial high relative velocity to the droplets and the fast moving cold gas stream. The cooling rate of the droplets depends on several process parameters, such as gas composition, gas pressure, superheat, gas/melt mass flow ratio, and atomizer design, etc. The cooling rates depend on the heat exchange between the atomized particles and the surrounding

medium via two mechanisms: radiation towards the atomizer chamber, and convection into the cooling gas. The latter is the predominant mechanism, given the temperature gradient and flow conditions that are typical of melt atomization. As the cooling rate experienced by the atomized particles depend on their size, amorphous, supersaturated and well-developed microstructures can be found in a gas atomization batch with an appropriate composition [1].

In summary, melt atomization is a primary and widely used powder metallurgy process, in which an alloy melt jet is energetically disintegrated into micrometer-sized powders under a controlled environment and non-equilibrium thermal and solidification conditions. It is widely used to produce a variety of powders from almost any metal.

References

1. B. Zheng, Y. Lin, Y. Zhou, E. J. Lavernia: Gas atomization of amorphous aluminum: Part II. Experimental investigation, Metall. Mater. Trans. B 40B, 995–1004 (2009).
2. J. J. Dunkley: Atomization, ASM Handbook, Powder Metal Technologies and Applications, Vol. 7, ASM International, Materials Park, 35–52 (1998).
3. E.J. Lavernia, Y. Wu: Spray Atomization and Deposition, John Wiley & Sons, Inc., New York, (1996).
4. W. Marriott: British patent 3322 (1872).
5. A. Lawley: Rapid Solidification Technology Source Book, ASM, Materials Park, (1983).
6. R. J. Grandzol, J. A. Tallmadge: Effect of jet angle of water atomization, Int. J. Powder Metall. Powder Technol., 11, 103–116 (1975).
7. E. Klar, W. M. Shafer: Powder Metallurgy for High Performance Application, Syracuse University Press, Syracuse, New York, (1972).
8. A. Lawley: Atomization, the Production of Metal Powder, MPIF, Princeton, New Jersey, (1992).
9. G. Rai, E. J. Lavernia, N. J. Grant: Powder size and distribution in ultrasonic gas atomization, JOM 37, 22–26 (1985).
10. I. E. Anderson, R. S. Figliola, H. Morton: Flow mechanisms in high pressure gas atomization, Mater. Sci. Eng. A, 148, 101–114 (1991).
11. M. K. Veistinen, E. J. Lavernia, J. Baram, N. J. Grant: Jet behavior in ultrasonic gas atomization, Int. J. Powder Metall. 25, 89–92 (1989).
12. N. Dombrowski, W. R. Johns: The aerodynamic instability and disintegration of viscous liquid sheets, Chem. Eng. Sci. 18, 203–214 (1963).
13. X. Liang, E. J. Lavernia: Solidification and microstructure evolution during spray atomization and deposition of Ni_3Al, Mater. Sci. Eng. A 161, 221–235 (1993).
14. P. S. Grant, B. Cantor, L. Katgerman: Modelling of droplet dynamic and thermal histories during spray forming – I. Individual droplet behaviour, Acta Metall. Mater. 41, 3097–3108 (1993).
15. K. Lubanska: Correlation of spray ring data for gas atomization of liquid metal, JOM 22, 45–49 (1970).
16. E. J. Lavernia, T. S. Srivatsan, R. H. Rangel: Atomization of alloy powders, Atomization Sprays 2, 253–274 (1992).
17. A. Unal: Liquid break-up in gas atomization of fine aluminum powders, Metall. Trans. B 20B, 61–69 (1989).
18. E. L. Crow, K. Shimizu: Lognormal Distributions: Theory and Applications, Marcel Dekker, New York, (1988).

19. J. E. Smith, M. L. Jordan: Mathematical and graphical interpretation of the log-normal law for particle size distribution, J. Colloid Sci. 19, 549–559 (1964).
20. A. H. Lefebvre: Atomizations and Spray, Taylor & Francis, Bristol, 85 (1989).
21. A. Lawley: Atomization: the Production of Metal Powders, MPIF, Princeton, 74 (1992).
22. W. E. Ranz, W. R. Marshall: Evaporation from drops – Part I, Chem. Eng. Prog. 48, 141–146 (1952).
23. Q. Q. Lu, J. R. Fontaine, G. Aubertin: Numerical study of the solid particle motion in grid-generated turbulent flows. Int. J. Heat Mass Transf. 36 79–87 (1993).
24. R. Clift, J. R. Grace, M. E. Weber: Bubbles, drops and particles, Academic Press, New York, (1978).
25. B. Zheng, Y. Lin, Y. Zhou and E. J. Lavernia: Gas atomization of amorphous aluminum: Part I. Thermal behavior calculation, Metall. Trans. B 40B, 768–778 (2009).

Chapter 37
Spray Drying, Spray Pyrolysis and Spray Freeze Drying

M. Eslamian and N. Ashgriz

Introduction

In conventional spray pyrolysis (CSP or simply SP), a solution is sprayed into a carrier gas forming small droplets; owing to the high temperature of the surrounding gas, the solvent is vaporized and the solute is precipitated on and within the droplets. If the air temperature is high enough, solute is decomposed to form final solid particles. A schematic diagram of the spray pyrolysis process is shown in Fig. 37.1 [1]. Spray drying (SD) is similar to spray pyrolysis, except that there is no chemical decomposition in SD and usually the process temperature is lower. SP and SD techniques may produce fully-filled or hollow particles depending on the operating conditions. In general, for most materials, hollow particles are formed if at the onset of solute precipitation on the droplet surface, the solute concentration at the droplet center is lower than the equilibrium saturation (Jayanthi et al. [2]). However, Chau et al. [3] showed that Jayanthi's model is not applicable to the formation of NaCl particles.

Spray Freeze Drying (SFD) is a method of producing biopharmaceutical powders that are sensitive to high process temperatures, which may be experienced in spray drying (SD). The detail of the process is described by Costantino and Pikal [4]. This method involves the atomization of a precursor solution, such as protein plus a suitable substance that carries the droplets, into liquid nitrogen. The ice is removed from the frozen droplets by sublimation under vacuum. As this process involves no heat for drying, the denaturation associated with the spray drying process can be avoided. Still, aceptic powder handling is needed and the production yields are low.

A variation of this process is spray freezing into liquid, where the impingement of the feed solution onto the cryogenic liquid results in intense atomization into

M. Eslamian (✉) and N. Ashgriz (✉)
Department of Mechanical and Industrial Engineering, University of Toronto, Canada
e-mail: m.eslamian@utoronto.ca; ashgriz@mie.utoronto.ca

N. Ashgriz (ed.), *Handbook of Atomization and Sprays*,
DOI 10.1007/978-1-4419-7264-4_37, © Springer Science+Business Media, LLC 2011

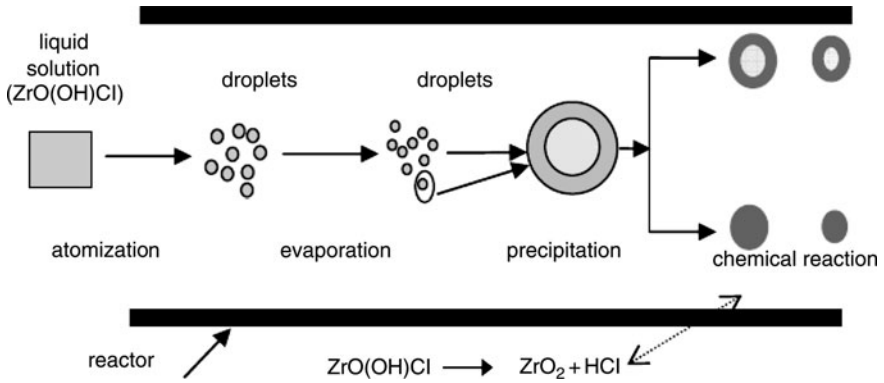


Fig. 37.1 Basic steps of spray pyrolysis method for zirconium hydroxychloride (ZrO(OH)Cl). Once the (ZrO(OH)Cl) powders are relatively dried, they decompose to ZrO_2 and HCl gas. ZrO_2 powders remain in the collector and HCl gas goes to the carrier gas. (Reproduced from [1] with permission. Copyright 2006 Institute of Physics)

micro-droplets, which freeze instantly. The microparticles can then be separated by sieving or evaporation of the cryogen and the sublimation of the solvent. Spray freezing into liquid allows particularly good size control and fast freeze, but it still involves aseptic powder handling.

Recently SFD has attracted the attention of formulation scientists. Spray-freeze drying of aqueous solutions of pure proteins or protein/sugar combinations (Maa et al. [5]) produced larger, more porous particles than those prepared by SD. When the modeling of SFD process is concerned, a mathematical model based on a steady-state heat-transfer condition has been derived by Maa and Prestrelski [6] that can be used to estimate the freezing time in liquid nitrogen, for instance.

Powder Characteristics

Operating conditions, such as the process temperature, ambient pressure and humidity, and also solution characteristics, such as its concentration and type, affect the shape, morphology and structure of the final particles. Effect of various parameters on powder characteristics has been studied both theoretically and experimentally. Several mathematical models for the conversion of solution droplets to particles have been developed, each of which focus on few specific aspects of the process [2, 7, 8]. Following a different approach, Farid [9] modeled drying of single solution droplets focusing on spatial temperature variations within a droplet which is the case for drying of large droplets ($\sim$1 mm), such as milk. Recently, Eslamian et al. [1, 10] modeled evaporation of micron-sized and nano-sized solution droplets and particle evolution and evaporation at various process pressures and temperatures. Their model is applicable to all droplet-to-particle processes, such as SP and SD.

The fundamental equations governing the process [10] are given in Chapter 40, Emulsion Combustion Method, where the basic phenomena involved in evaporation of solution droplets and evolution of particles are described mathematically. It should be noted that, especially for industrial SD process, commercial packages are available to simulate the process but only from a macroscopic point of view. These packages do not consider the detail of the molecular phenomena involved and just provide general information of the overall process.

The most important parameter affecting the morphology of powders is the process temperature. This is because the temperature has a great influence on the solvent evaporation rate. As discussed by Jayanthi et al. [2], for a particular precursor, at given operating conditions, the morphology of particles and whether they are solid and fully-filled, or hollow and disrupted, depends on the concentration distribution within the droplet. The concentration distribution is a strong function of the process temperature.

Figure 37.2 shows the effect of reactor temperature on the solute concentration profile at the onset of precipitation within a droplet with 5 μm initial diameter for a given initial droplet number density, N_0, carrier gas flow rate, Q, and initial relative humidity, RH_0, and initial solution concentration, C_0 [10]. The tubular reactor's inside diameter is 10 mm. The concentration profile inside the droplet depends on the operating conditions and reactor geometry. For reactor conditions of their study

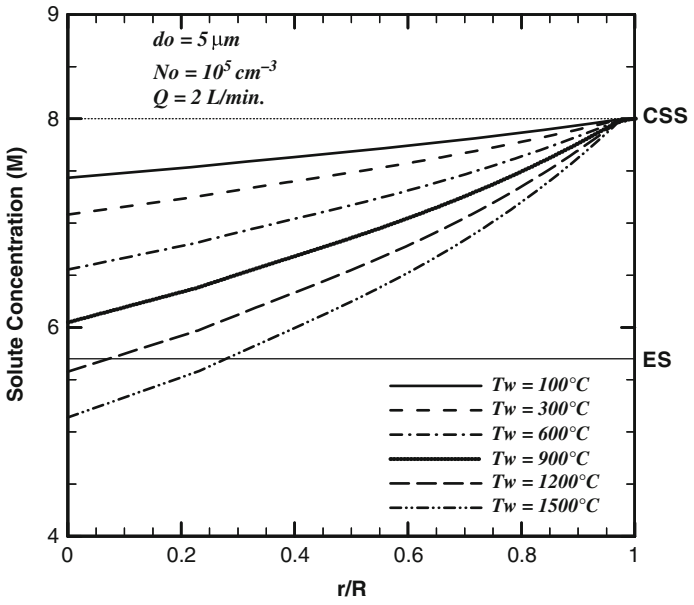


Fig. 37.2 Solute concentration profile within the droplet for various wall temperatures for given initial droplet size d_0, droplet number density N_0, carrier gas flow rate Q, initial relative humidity, $RH_0 = 10\%$, and initial solute concentration $C_0 = 2$ M. (Reprinted from [10] with permission. Copyright 2009 of Taylor & Francis)

as specified above, and for the wall temperatures up to about 1,000°C, the concentration profile entirely lies above the Equilibrium Saturation (ES) line, which is favorable for the production of fully-filled particles [2].

The gradient of the concentration within the droplet depends on the characteristic time of the droplet evaporation and solute diffusion from the droplet surface to the droplet center. As the reactor wall temperature and therefore the reactor bulk temperature increase, the solvent evaporation rate increases, and the characteristic time of evaporation compared to that of solute diffusion decreases. As a result, at high temperatures, at the onset of precipitation on the droplet surface, the concentration in the vicinity of the droplet center falls below the ES line. The occurrence of this type of concentration profile is an indication of having hollow particles as postulated by Jayanthi et al. [2].

Figure 37.3 shows the variations of non-dimensional droplet diameter squared in the shrinkage period as a function of distance from the reactor inlet for various reactor wall temperatures, T_w, for given d_0, N_0, Q, RH_0, and C_0. At reactor wall temperature of 200°C, in order for the shrinkage period (period during which no solute is precipitated yet) to terminate, the droplets need to travel 500 mm from the reactor inlet, whereas for the case of the reactor wall temperature of 1,000°C, this length is reduced to 50 mm. It is observed that the variation of droplet diameter squared with x (and therefore t) is not linear. In fact, it seems that the rate of droplet size reduction ($\sim$ evaporation rate) increases with distance from the reactor inlet.

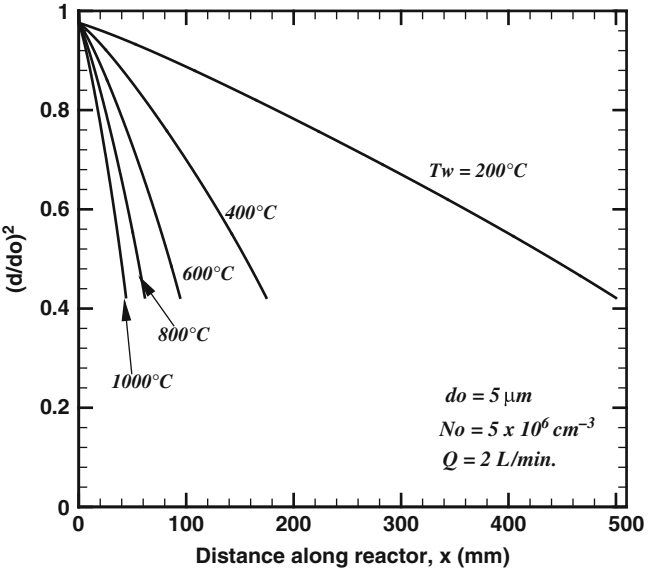


Fig. 37.3 Non-dimensional droplet diameter variations as a function of distance from the reactor inlet for various T_w, for given d_0, N_0, Q, RH_0, and C_0. Reactor inlet gas and droplet temperatures are 25°C $RH_0 = 10\%$, and initial solute concentration $C_0 = 2$ M. (Reprinted from [10] with permission. Copyright 2009 of Taylor & Francis)

One reason is that in spite of the reactor wall temperature, which is constant during the process, the reactor bulk temperature increases with the distance from the reactor inlet. Droplet evaporation rate is a function of the reactor bulk temperature. Also, note that regardless of the reactor wall temperature, the non-dimensional droplet diameter at the onset of precipitation for all cases is almost the same.

Eslamian and Ashgriz [11, 12] systematically investigated the effect of pressure on powder morphology and other powder characteristics. Particle shape and morphology depends on the precursor properties and precipitation mechanism, as well as on the droplet evaporation rate. Droplet evaporation rate is a function of the reactor pressure and temperature. Evaporation rate controls the solute distribution profile within the droplet, and determines whether the particles are solid or hollow. Eslamian and Ashgriz [11] have shown that, when the ambient pressure is reduced to 60 Torr, the decrease of the evaporation rate due to the non-continuum effects is about 60% of that of the continuum-based evaporation rate.

In SP, a low evaporation rate is favorable for the production of less hollow and more fully-filled particles. On the other hand, depending on the nature of the precursor, a relatively high reactor temperature, which causes a high evaporation rate, is essential for a chemical decomposition to occur within the precursor. Hence to increase the likelihood of forming solid particles, it is advantageous to conduct the SP process at reduced pressures.

Figures 37.4 and 37.5 show scanning electron microscope (SEM) images of zirconia powders produced by SP of a 1.0 mol/L solution of zirconium hydroxychloride (ZHC) at two reactor pressures, and at 100°C and 400°C, respectively. A vibrating mesh nebulizer was employed as spray generator. For each reactor ambient pressure, four SEM images at four different magnifications are displayed. At 100°C, particles are spherical and are mostly non-disrupted. The contrast variation in the SEM images shows that depending on the pressure, the particles are either shelly or have smooth surfaces. Figure 37.5 shows that at 400°C, regardless of the pressure, most of the particles are disrupted. The high magnification images show that the particle surface is uneven in this case. The average mean size of the

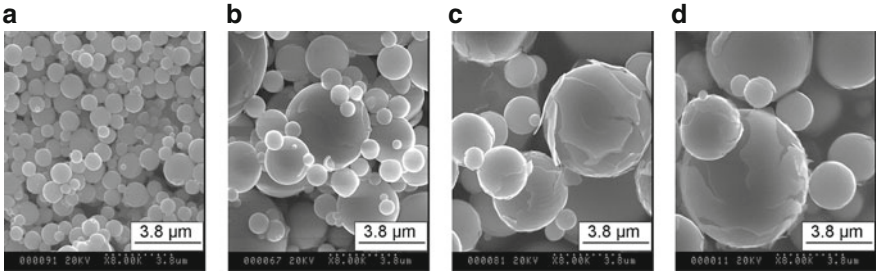


Fig. 37.4 SEM images of zirconia particles produced by spray pyrolysis of a 1.0 mol/L solution of ZHC at 100°C and at, (**a**) 760 Torr, (**b**) 400 Torr, (**c**) 250 Torr, and (**d**) 120 Torr

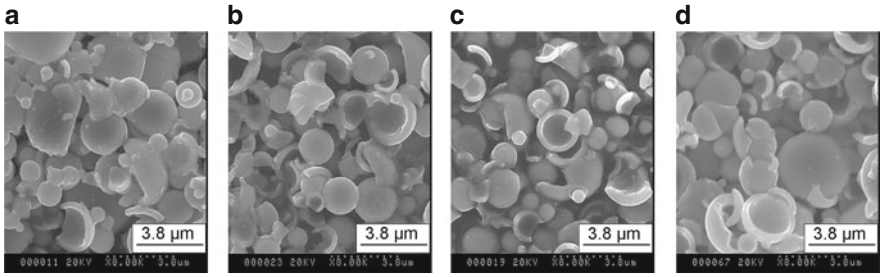


Fig. 37.5 SEM images of zirconia particles produced by spray pyrolysis of a 1.0 mol/L solution of ZHC at 400°C and at (**a**) 760 Torr, (**b**) 400 Torr, (**c**) 250 Torr, and (**d**) 120 Torr

powder at each reactor condition is provided in the figures. In general, as the reactor pressure decreases the size of the particles increases. On the other hand, at low pressures, as the reactor temperature increases, the increasing effect of the pressure on the particle size decreases. Although the pressure variation and, consequently, evaporation rate results in the variation of particle size, other effects, such as the variation of the initial droplet size may also be responsible for the substantial change in the particle size in low pressures. At low pressures, droplet number density and the dispersion behavior of the spray changes. If there is no air to interrupt the droplets, it is expected to see a narrow column consisting of thousands of droplets moving together. This close movement of droplets can result in droplet collision and coalescence. On the other hand, at 760 and 400 Torr the surrounding air disperses the droplets more effectively and the probability of droplet collision and coalescence decreases.

Figures 37.6 and 37.7 show SEM images of sodium chloride powders produced by spray drying of a 2.5 mol/L solution of NaCl at 760, 400, 250, and 120 Torr, and at reactor temperatures of 100°C and 400°C, respectively. In contrast to zirconia particles that were spherical, these powders are cubic. This is attributed to the crystal growth mechanism of sodium chloride, which is different from zirconia powder.

Effects of atomization method and solute concentration on the morphology of spray dried magnesium sulphate ($MgSO_4$) powders were investigated by Eslamian and Ashgriz [13]. They employed three different spray generators including a vibrating mesh nebulizer, a splash plate nozzle and an air mist atomizer. These spray generators produce droplets with a wide range of size and velocity. It was noted that increasing the initial solution concentration resulted in the formation of thicker-walled particles. It was also observed that increasing the initial solute concentration resulted in a reduction in the number of disrupted particles, which was attributed to an increase in the particle wall thickness and strength due to the increase of solute concentration.

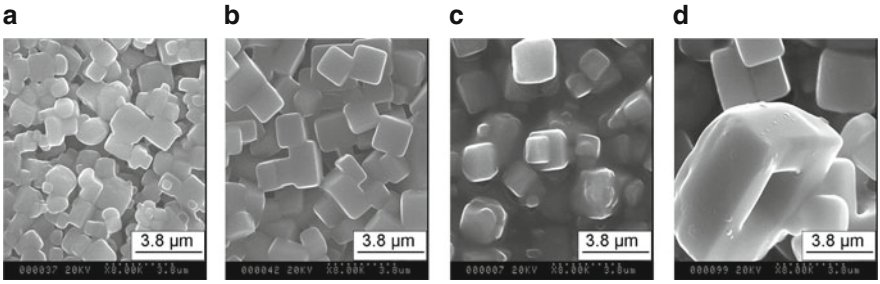


Fig. 37.6 SEM images of the particles produced by spray drying of a 2.5 mol/L solution of NaCl at 100°C and at (**a**) 760 Torr, (**b**) 400 Torr, (**c**) 250 Torr, and (**d**) 120 Torr

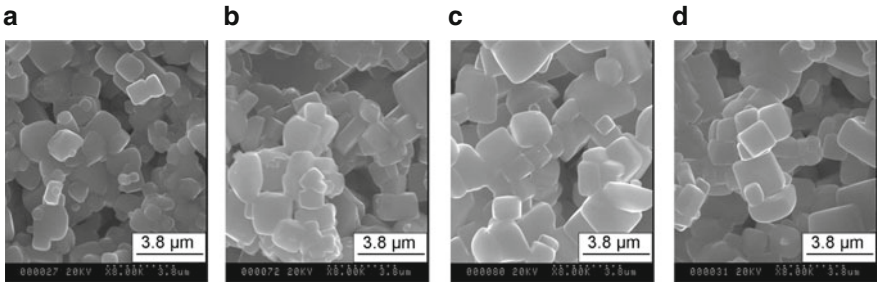


Fig. 37.7 SEM images of the particles produced by spray drying of a 2.5 mol/L solution of NaCl at 400°C and at, (**a**) 760 Torr, (**b**) 400 Torr, (**c**) 250 Torr, and (**d**) 120 Torr

Droplet number density, droplet velocity, presence of atomizing air, and droplet size have substantial effects on particle morphology. Low droplet number density, low droplet velocity and size, and accompanying atomizing air favor rapid droplet drying.

Figure 37.8 summarizes different possible final morphologies for hollow particles formed in SP and SD [13]. If a relative velocity between the air and the droplet exists, a boundary layer will form around the droplet, which results in a non-uniform solvent evaporation and, therefore, a non-uniform crust may form. Depending on the nature of the solute and the process conditions, the crust could be either permeable or impermeable. Pressure buildup in impermeable particles may cause several final particle morphologies. If the crust is uniform and contains no defects, the uniform stress applied on the internal wall of the shell may cause a uniform particle disruption and the particle will be cut into several pieces (type *a*). If the particle wall thickness is not uniform, it may break from the weakest part, and a particle with a small hole may form (type *b*). As another scenario, if the crust is strong enough to resist the internal pressure, the vapor trapped inside the particle

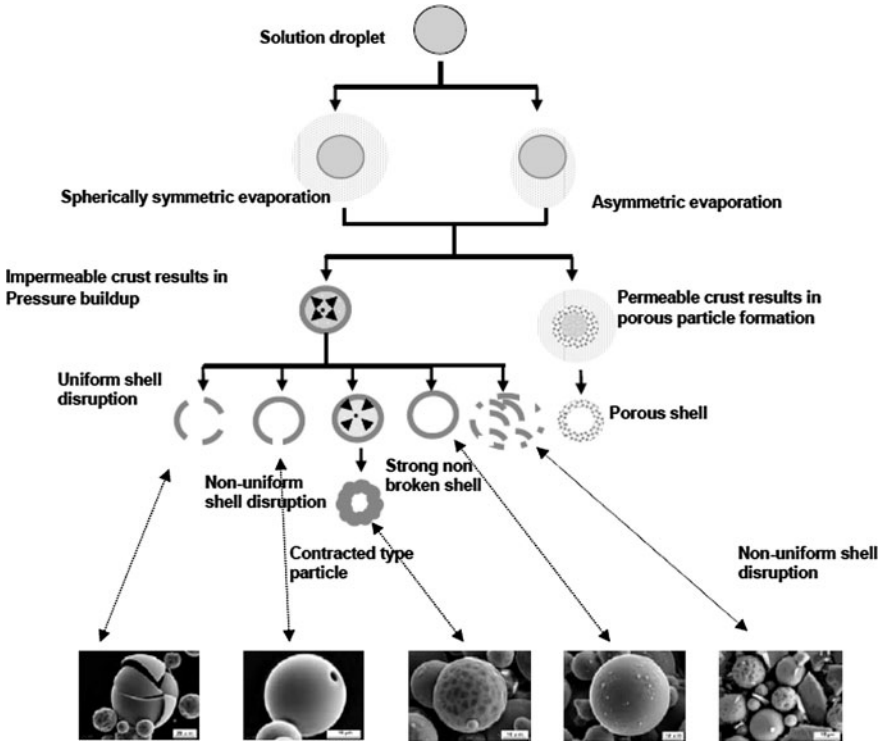


Fig. 37.8 Different possibilities for hollow particle formation during spray drying/pyrolysis. Type (**a**) uniform shell disruption, type (**b**) non-uniform shell disruption, type (**c**) contracted shell particle, type (**d**) non-disrupted smooth surface particle, type (**e**) non-uniform shell disruption, and type (**f**) porous particle. (Reprinted from [13] with permission. Copyright 2007, American Society of Mechanical Engineers)

may later condense and the shell may contract due to depression (type *c*). However, if the shell is fully dried, it is possible that the condensation can not cause any permanent deformation on the particle, and a hollow smooth-surface particle may form (type *d*). In addition, if the crust is thin and weak, or the pressure buildup is substantial, or the particles collide in the reactor, it is possible that the drying particle bursts to form particle flakes (type *e*). On the other hand, for the case of a permeable crust, the evaporated solvent leaves the particle, without increasing the internal pressure, and a non-disrupted porous particle forms (type *f*).

Production of Nanoparticles

As it was stated earlier, typically in SP and SD processes, one droplet in converted into one particle. As a result, the final particle size is dependent on the initial droplet size, unless the particle explodes and fragments into smaller pieces (nanoparticles)

or the solution concentration is very low. In other words, in order to produce nanoparticles via SP and SD processes, one should usually follow one or a combination of the following techniques: (a) use a dilute solution to allow the presence of slight amount of solute in one single droplet, so that finally a nanoparticle forms out of a large droplet; (b) generate nano-sized solution droplets by, for example, electrospraying technique; (c) use a technique to fragment the large mother particle into nanoparticles due to structural breakdown or abrupt solvent evaporation and microexplosion, (d) use a new method called the low-pressure spray pyrolysis. Low-pressure SP is considered in detail in Chapter 38 and the rest are considered below, briefly.

Using a Dilute Solution

This process is conceptually the same as the conventional SP, SD and SFD, except that to guarantee the production of nano-sized particles, the solution concentration has to be very low. A very dilute solution is atomized into small droplets, which may or may not be nano-sized. The solvent, which essentially occupies most of the volume of a solution droplet, evaporates and the remainder of the droplet, i.e., solute produces one nanoparticle. As an example, a salt of the desired semiconductor, such as ZnS, CdS, PbS, and GaN may be dissolved in a solvent to form a solution. Upon solvent evaporation, a stream of unsupported semiconductor nanoparticles are formed and collected on a solid substrate [14].

Electrospraying

In this method, a high voltage is applied to a liquid solution that is flowing through a capillary. Ideally, the liquid reaching the capillary tip forms a Taylor cone, which emits a liquid jet through its apex. When the liquid passes through the spray nozzle, the resulting nanodroplets become charged and produce a droplet stream or a mist due to the repulsive forces between charged particles. During this process, the solvent is vaporized forming charged nanoparticles. These particles then adhere to a substrate having the polarity apposite to that of the particles. By changing the voltage, employing a carrier gas, and placing a plate with a hole between the nozzle tip and the substrate, the migration and deposition of nanoparticles may be controlled to produce desired patterns and nanostructures [15]. This process is schematically shown in Fig. 37.9 [16].

Microexplosion

In the conventional spray techniques, one particle is formed from one droplet. It has been observed that in certain conditions, once a particle is formed, it may somehow

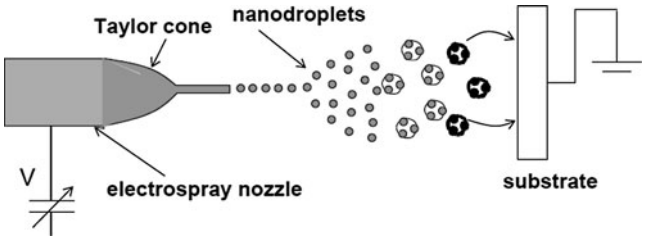


Fig. 37.9 Electrospraying technique for producing nanoparticles by spray methods. (Reprinted from [16] with permission. Copyright 2009 Bentham Science Publishers)

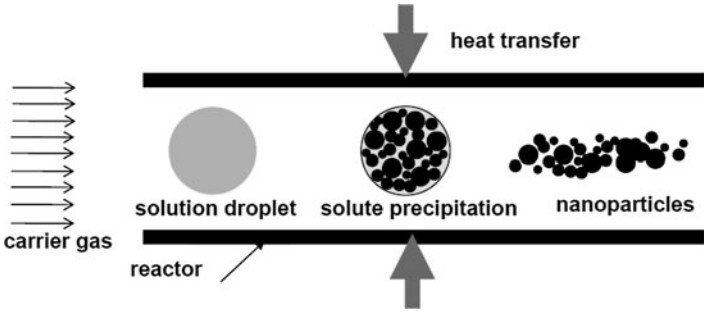


Fig. 37.10 Nanoparticle production method by structural destruction of larger particles. (Reprinted from [16] with permission. Copyright 2009 Bentham Science Publishers)

break down into several smaller pieces including nanoparticles (Fig. 37.10). For instance, in a process called salt-assisted spray pyrolysis, it was observed that provided the droplet/particle temperature exceeds the melting point of the salt added to the main precursor, the salt melts and acts as a high-temperature solvent [17]. The material or its components can then dissolve, undergo reactions, and upon exceeding the solubility limit, precipitate in the solvent. In salt-assisted spray pyrolysis, within a particle, the dissolution/precipitation cycle can lead to the dissolution of some nanocrystallites and the growth of other crystallites by precipitation. This may lead to the breakdown of the particle and disintegration of the individual nanocrystallites. In a process similar to the salt-assisted method, Jakic et al. [18] observed that addition of sodium chloride to the zinc nitrate precursor, even at moderate temperatures, resulted in the disruption of mother particles and the formation of nanoparticles.

Concluding Remarks

In this chapter, fundamentals of spray drying, spray pyrolysis and spray freeze drying processes were described. Using some experimental evidence and modeling results, the effects of operating conditions on characteristics of powders produced

by these methods were reviewed. One of the most important characteristics of a powder is particle morphology and, whether under certain process conditions, particles are hollow or solid and fully-filled. This depends on the condition of the concentration profile developed within the solution droplets, at the onset of solute precipitation on droplet surface. Parameters such as low process temperature, large droplet number density, small initial droplet size, and high initial solution concentration favor the formation of solid fully-filled particles.

In most research studies on SP and SD in the lab scale, ultrasonic atomization has been used to generate droplets/sprays. To increase the powder production rate, other atomization methods should be examined without affecting the particle size, size distribution and quality. For instance, a twin-fluid atomization technique was used to produce lead zirconate titanate (PZT) powder using a starting solution composed of lead acetate, zirconium acetate, and titanium propoxide (stabilized by acetylacetone) dissolved in water by Nimmo et al. [19]. Commercialization of SP technique is closely interrelated to its throughput and strong evidence that SP is a suitable method for the production of some particular advanced powders.

It has been shown that SP is capable of producing composite powders with applications in emerging technologies. In the future, SP will be used to produce a variety of other new composite materials. Fukui et al. [20] synthesized composite powders, such as NiOSDC and La(Sr)CoO_3 by spray pyrolysis, which may be used as anode and cathode of solid oxide fuel cells, respectively. As another example of the application of SP in power production, Bakenov et al. [21] reported the production of stable nano-structured lithium manganese oxide with spherical particles via ultrasonic spray pyrolysis technique. Rechargeable lithium-ion batteries have become the key components for a wide range of portable electronic devices and a promising energy source. The electrochemical performance of the nanostructured $LiMn_2O_4$ prepared was superior to the material prepared by conventional methods.

Another challenge is to address and elucidate the many complex physical and chemical phenomena involved in SP, SD and SFD. In these processes, similar to many other industrial processes, it is important to be able to predict the characteristics of the final product and also to design the components of the equipment and trouble-shoot the operation. Although several attempts have been made to model some aspects of the physical and chemical phenomena involved in these techniques, more work is needed in this area. Currently the commercial packages are adequate in modeling the flow patterns, but are weak when it comes to the intra-particle phenomena. Intra-particle phenomena are more important when the final morphology of particles plays an important role in particle characteristics. Fletcher et al. [22] have addressed the important issues regarding available CFD codes for the industrial spray dryers. They reviewed the fundamental flow behavior in dryers and their modeling using a commercial CFD code. They argued that the key point to emerge is the need to perform three-dimensional, transient calculations and to include hindered drying and wall interaction models. They also noted that coalescence and agglomeration models need to be validated and included in the simulations.

References

1. M. Eslamian, M. Ahmed, and N. Ashgriz: Modeling of nanoparticle formation during spray pyrolysis. *Nanotechnology*, 17, 1674–1685 (2006).
2. G. V. Jayanthi, S. C. Zhang, and G. L. Messing: Modeling of solid particle formation during solution aerosol thermolysis. *Aerosol Science and Technology*, 19, 478–490 (1993).
3. A. Chau, M. Eslamian, and N. Ashgriz: On production of non-disrupted particles by spray pyrolysis. *Particle and Particle Systems Characterization*, 25, 183–191 (2008).
4. H. R. Costantino and M. J. Pikal, Lyophilization of Biopharmaceuticals, Chapter 13: Spray Freeze Drying of Biopharmaceuticals: Applications and Stability Considerations. American Association of Pharmaceuticals Scientists; Springer, Arlington, (2004).
5. Y-F. Maa, P. Nguyen, T. Sweeney, S. Shire, and C. Hsu: Protein inhalation powders: spray drying vs. spray freeze drying. *Pharmaceutical Research*, 16, 249–255 (1999).
6. Y-F. Maa and S. Prestrelski: Biopharmaceutical powders: particle formation and formulation considerations. *Current Pharmaceutical Biotechnology*, 1, 283–302 (2000).
7. Y. Xiong and T. T. Kodas: Droplet evaporation and solute precipitation during spray pyrolysis. *Journal of Aerosol Science*, 24(7), 893–908 (1993).
8. I. W. Lenggoro, I. W. T. T. Hata, F. Iskandar, M. M. Lunden, and K. Okuyama: An experimental and modeling investigation of particle production by spray pyrolysis using a laminar flow aerosol reactor. *Journal of Material Research*, 15(3), 733–743 (2000).
9. M. Farid: A new approach to modeling of single droplet drying. *Chemical Engineering Science*, 58, 2985–2993 (2003).
10. M. Eslamian, M. Ahmed, and N. Ashgriz: Modeling of particle formation via droplet-to-particle spray methods. *Drying Technology*, 27, 1–11 (2009).
11. M. Eslamian and N. Ashgriz: The effect of pressure on the morphology of spray-dried magnesium sulfate powders. *Canadian Journal of Chemical Engineering*, 84(5), 581–589 (2006).
12. M. Eslamian and N. Ashgriz: The effect of pressure on the crystallinity and morphology of powders prepared by spray pyrolysis. *Powder Technology*, 167, 149–159 (2006).
13. M. Eslamian and N. Ashgriz: Effect of atomization method on the morphology of spray generated particles. *ASME Journal of Engineering Materials and Technology*, 129(1), 130–142 (2007).
14. L. Amirav and E. Lifshitz: WO06035425A2 (2006).
15. B. W. Han, J. S. Suh and M. S. Choi: US200693750A1 (2006).
16. M. Eslamian and M. Shekarriz: Recent advances in nanoparticle preparation by spray and microemulsion methods. *Recent Patents on Nanotechnology*, 3(2), 99–115 (2009).
17. B. Xia, I. W. Lenggoro and K. Okuyama: Synthesis of CeO2 nanoparticles by salt-assisted ultrasonic aerosol decomposition. *Journal of Material Chemistry*, 13, 2925–2927 (2001).
18. N. Jakic, J. Gregory, M. Eslamian and N. Ashgriz: Effect of impurities on the characteristics of metal oxides produced by spray pyrolysis. *Journal of Materials Science*, 44(8) 1977–1986 (2009).
19. W. Nimmo, N. J. Ali, R. M. Brydson, C. Calvert, E. Hampartsoumian, D. Hind and S. J. Milne: Formation of lead zirconate titanate powders by spray pyrolysis. Journal of American Ceramic Society, 86(9), 1474–1480 (2003).
20. T. Fukui, S. Ohara, K. Murata, H. Yoshida, K. Miura, T. Inagaki: Performance of intermediate temperature solid oxide fuel cells with La(Sr)Ga(Mg)O-3 electrolyte film. *Journal of Power Sources*, 106(1–2), 171–176 (2002).
21. Z. Bakenov, M. Wakihara and I. Taniguchi: Battery performance of nanostructured lithium manganese oxide synthesized by ultrasonic spray pyrolysis at elevated temperature. *Journal of Solid State Electrochemistry*, 12, 57–62 (2008).
22. D. F. Fletcher, B. Guo, D. J. E. Harvie, T. A. G. Langrish, J. J. Nijdam and J. Williams: What is important in the simulation of spray dryer performance and how do current CFD models perform? *Applied Mathematical Modelling*, 30(11), 1281–1292 (2006).

Chapter 38
Low-pressure Spray Pyrolysis

W.-N. Wang, A. Purwanto, and K. Okuyama

Abstract Low-pressure spray pyrolysis (LPSP) has been developed by generating micrometer-sized droplets under low-pressure environment. Unlike the conventional spray pyrolysis (CSP), a variety of nanoparticles, ranging from metals, metal oxides, to composite materials can be directly formed in the LPSP process, which was considered to follow a one-droplet-to-multiple-particles (ODMP) principle. The low-pressure is the direct driving force for the formation of nanoparticles. Inside the LPSP process, the micrometer-sized droplets are assumed to undergo rapid solvent evaporation upon entering the low-pressure environment that induces a fast nucleation rate to form primary nanocrystals. The aggregation of these nanocrystals is limited due to very short residence time under low-pressure conditions. In addition, the gas evolution due to thermal reactions and pressures inside the droplets/dried particles caused by high drying rates, are considered to be the main reasons for the fragmentation of primary nanocrystals into final nanoparticles.

Keywords Agglomeration · Brownian motion · Evaporative cooling · Fragmentation · Nucleation

As explained in Sect. 38.2, to produce particles using a conventional spray pyrolysis (CSP) process, the precursor is first atomized into a reactor where the aerosol droplets undergo evaporation and solute condensation; drying and thermolysis of the precipitate particles at higher temperature forms micro- or meso-porous particles, and, finally, sintering of these porous particles forms dense particles. However, sub-micrometer to micrometer-sized particles traditionally are formed using the CSP process based on the one-droplet-to-one-particle (ODOP) principle due to the difficulty of generating very fine droplets (below 1 μm) [1–3].

W.-N. Wang (✉)
Department of Chemical Engineering, Hiroshima University, Higashi Hiroshima, Japan
and
Department of Energy, Environmental and Chemical Engineering, Washington University in St. Louis, St. Louis, USA
e-mail: wnwang.yz@gmail.com

N. Ashgriz (ed.), *Handbook of Atomization and Sprays*,
DOI 10.1007/978-1-4419-7264-4_38, © Springer Science+Business Media, LLC 2011

A few attempts have been made to synthesize nanoparticles using a spray pyrolysis process. A typical method uses addition of fuels (alcohols, urea and sucrose, etc.) to precursor solutions. In these processes, the abrupt evolution of considerable heat and gasses aids in breaking, or fragmenting, the large particles into smaller pieces coupled with the evaporation-derived particle formation process [4]. Another strategy is to generate very fine droplets, which are necessary for the preparation of nanoparticles based on the ODOP principle. Electrospray pyrolysis (ESP) is such a process, and is capable of generating fine droplets (from nanometer to micrometer- size) as well as nanoparticles [1].

In this section, a low-pressure spray pyrolysis (LPSP) method is introduced, which is a promising method for one-step production of nanoparticles. The possibility for the synthesis of various nanoparticles using the LPSP method was explored, and the droplet-to-particles conversion mechanism used in the process is explained based on experimental and numerical results. Other researchers, such as the Ashgriz group, have conducted fundamental research on the low-pressure spray route [5–7]. The effect of reducing the reactor air pressure on the evaporation, evolution and morphology of spray pyrolyzed/dried powders was investigated. This section will focus mainly on the investigation of nanoparticle synthesis and its corresponding formation mechanism in the LPSP process.

A typical LPSP process using a filter expansion aerosol generator (FEAG) was first developed by Kang and Park [8]. The LPSP system is composed of an atomizer system, a reactor, a particle collector, and a pressure control system (Fig. 38.1) [9]. The atomizer used consists of a two-fluid nozzle and a glass filter with a pore size of several microns. Liquid is sprayed through the two-fluid nozzle by a carrier gas onto the glass filter surface where it forms a thin liquid film. This liquid film and carrier gas pass through the filter pores, aided by the pressure difference, and are expanded to the liquid jets then converted to droplets in a low-pressure chamber (10–100 Torr).

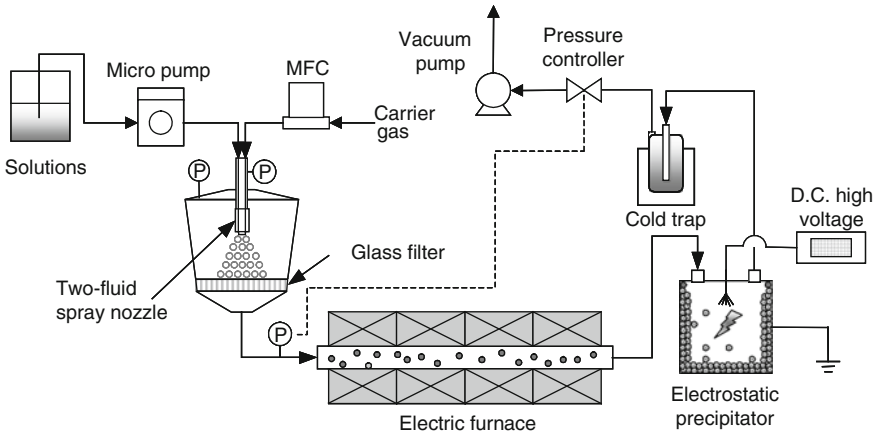


Fig. 38.1 Experimental setup of a typical low-pressure spray pyrolysis (LPSP) process with a glass filter as the atomizer [9] copyright of Elsevier Limited, 2004

The droplets are then delivered to the reactor and dried by heating in the furnace. Dry aerosol particles are collected in an electrostatic precipitator kept at approximately 150°C to avoid water condensation, while the gases are dried by passing them through a liquid nitrogen cold trap before being evacuated by a vacuum pump. The volume mean droplet size produced with this system was recently measured using a spray particle analyzer and found to be about 4–6 μm [10].

The morphology and size of particles prepared by the LPSP process are different from those produced by CSP using either an ultrasonic nebulizer or a two-fluid nozzle as atomizers under an atmospheric environment. For example, nickel oxide (NiO) nanoparticles can be formed via the LPSP route whereas, only submicron-sized NiO particles are produced by ultrasonic spray pyrolysis [9]. It is evident that the nanoparticle formation mechanism in the LPSP process is different from that in the CSP process. The calculated particle size based on the ODOP principle is much larger than 100 nm, indicating that the nanoparticles are formed based on one-droplet-to-multiple-particles (ODMP). The reason can be attributed to the difference in operating pressures and aerosol formation mechanisms between the two types of aerosol generators.

Using this method, various types of nanoparticles have been prepared, such as metals [9], metal oxides [8, 11–13], doped oxides [14–16], and multi-component nanoparticles [17–21]. Effects of operation temperature, pressure, carrier gas flow rate, precursor concentration, precursor type, and additives on nanoparticle formation have been investigated systematically.

Figure 38.2 shows the SEM images of NiO particles prepared by LPSP at different operating temperatures. It was found that the dispersion of the particles increases with increasing temperature. In the case of a low synthesis temperature (i.e., 400°C in Fig. 38.2a), only submicron spherical particles were produced, but at a temperature of 700°C (Fig. 38.2b), a mixture of submicron and nanoparticles was found. Dispersed nanoparticles with an average size of about 30 nm were observed in the case of a high synthesis temperature (900°C in this case). This indicates that the abrupt evolution of considerable heat and gases aids in the fragmentation of larger particles into small pieces, i.e., primary nanocrystals.

Pressure and carrier gas flow rate (i.e., residence time) were also found to be of great importance in determining the size of the nanoparticles that are produced.

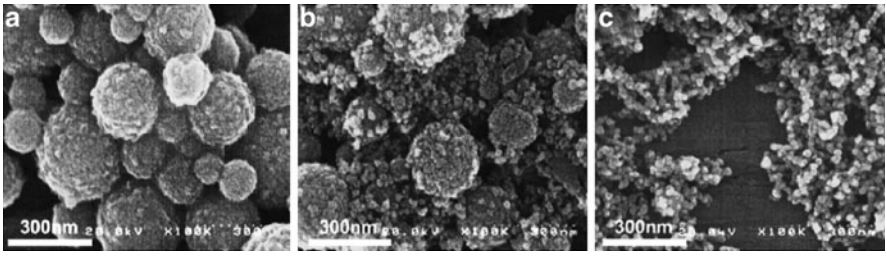


Fig. 38.2 NiO particles prepared from a nitrate precursor at different temperatures: 400°C (**a**), 700°C (**b**), and 900°C (**c**) [12] copyright of Elsevier Limited, 2003

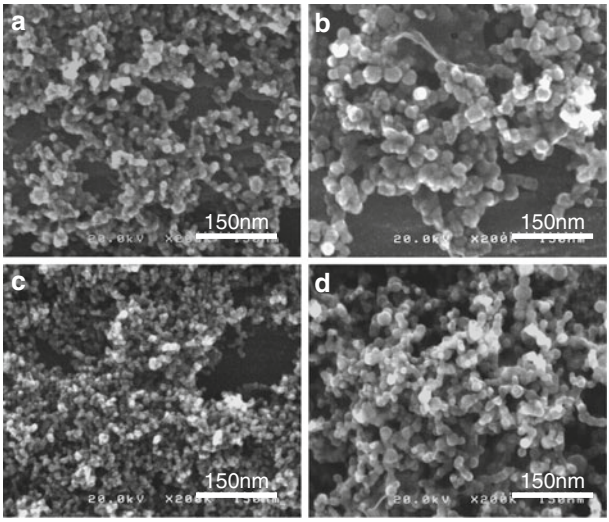


Fig. 38.3 Effects of operation pressure and carrier gas flow rate on Ni/NiO nanoparticle size (**a**) 40 Torr, $Q_c = 1$ L/min, (**b**) 80 Torr, $Q_c = 1$ L/min, (**c**) 40 Torr, $Q_c = 2$ L/min, (**d**) 80 Torr, $Q_c = 2$ L/min [9] copyright of Elsevier Limited, 2004

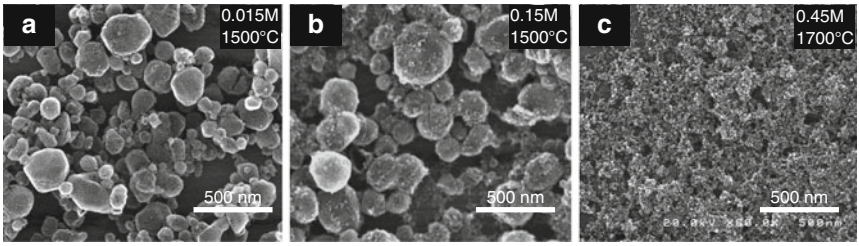


Fig. 38.4 FE-SEM images of Y_2O_3:Eu^{3+} samples prepared at different solution concentrations and temperatures: (**a**) 0.015 M, 1500°C, (**b**) 0.15 M, 1500°C, (**c**) 0.45 M, 1700°C. Other conditions: Eu-concentration 6 at%, carrier gas flow rate 2 L/min [16] copyright of Elsevier Limited, 2004

Figure 38.3 shows field emission scanning electron microscopy (FE-SEM) images of Ni/NiO nanoparticles prepared at different pressures and carrier gas flow rates. It was found that the particle size generally increased as the residence time increased. With an identical residence time, 40 Torr, there was a total carrier gas flow rate of 1 L/min, while at 80 Torr the total carrier gas flow rate was 2 L/min. However, particles formed in the latter case were bigger. Carrier gas flow rate also played a role in controlling particle size, as shown by the difference in particle size at the same pressure but with a different carrier gas flow rate. The effect of pressure played a more important role than the residence time (Fig. 38.3a, d).

The results also show that the physicochemical properties of precursors play an important role in nanoparticle synthesis. In the case of the Y_2O_3:Eu particle

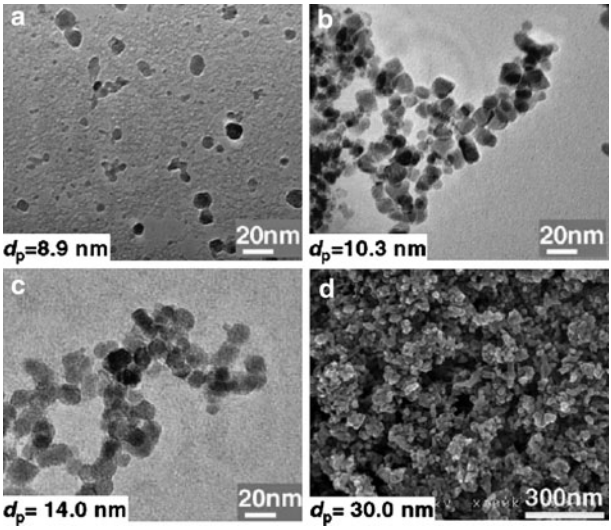


Fig. 38.5 FE-SEM and TEM images of indium tin oxide (ITO) nanoparticles by LPSP (**a**)–(**c**) and commercial ones (**d**) [20] copyright of Springer Science+Business Media 2006

preparation by LPSP, the relationship between the precursor concentration and particle size is shown in Fig. 38.4 [16]. In general, a high precursor concentration was favorable for nanoparticle formation. The production of smaller particles derived from a higher concentration of starting solution is contrary to the general tendency in particle synthesis studies. Most synthesis techniques, including CSP, produce large particles when solutions with higher concentrations are used. This indicates that LPSP is an effective route for the direct production of nanoparticles with high productivity and yield, and has considerable potential for use in industrial applications. Other types of doped nanoparticles, i.e., indium tin oxide (ITO), were also successfully synthesized by LPSP (Fig. 38.5) [19, 20]. In addition, organic precursors are also applicable in this process for the preparation of nanocrystals such as TiO_2 [13]. For multi-component nanoparticle preparation, additives such as fuels like ethanol and urea can improve the dispersion of the primary crystals. Previous studies have revealed that the addition of a solid fuel (e.g., urea) greatly improved the crystal growth and particle break-up due to the extra heat supplied during the combustion reaction, coupled with the evolution of gasses [17].

In order to further understand the mechanism in this low-pressure environment, a sol precursor containing colloidal nanoparticles was also studied [22]. From the experimental results, dispersed nanoparticles could be obtained at a relatively low pressure (20 Torr). A possible mechanism for the sol-to-dry particle formation in the spray-drying process under low-pressure conditions was proposed based on the experimental results and available theories. Droplet breakup due to competition between osmotic and Laplace pressure, and particle fragmentation due to fast drying, were considered to be two major factors.

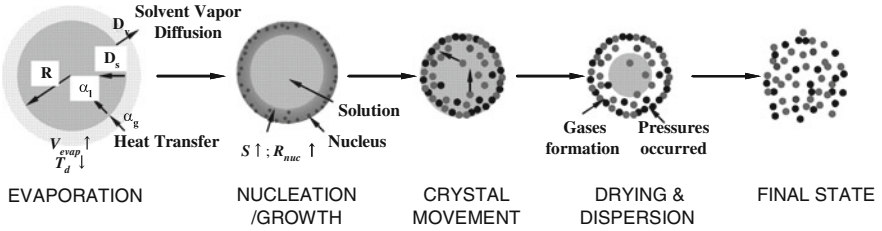


Fig. 38.6 Schematic diagram of a possible mechanism of nanoparticle formation in the LPSP process

In addition, a quantitative mathematical model was introduced to examine the evaporative cooling effect of micron-sized water droplets under low-pressure conditions [23]. From the experiment, the temperature of the gas-droplet mixture decreased significantly depending on the pressure applied. The cooling rate of the aerosol was found to be about 2×10^3 K/s at 20 Torr. The simulation results suggested that a constant low-pressure, the droplet size, and the flow rates of the carrier gas and solution were the major factors that affected droplet cooling.

Based on the above experimental and numerical results, a plausible mechanism for nanoparticle formation in the LPSP process was proposed and is schematically shown in Fig. 38.6. It is assumed that a micron-sized droplet first undergoes rapid solvent evaporation upon entering a low-pressure environment. The loss of latent heat from the droplets due to evaporation drastically decreases the droplet temperature (evaporative cooling effect) as well as the droplet size. Accordingly, supersaturation of the solution inside the droplets increases dramatically due to these effects, which then causes the nucleation rate and the crystal growth to increase. The primary crystals then undergo Brownian motion inside the droplets. The agglomeration of these primary crystals is limited due to their very short residence time under low-pressure conditions. In addition, gas evolution due to thermal reactions and the high drying rate from the furnace cause some pressure inside the droplets/dried particles, which could be the main reason for the dispersion of primary crystals into final nanoparticles. The droplets may break up depending on the precursor properties as well as process parameters (e.g., Reynolds number or Weber numbers). Furthermore, because of the rapid drying rate at high temperatures, the final particles could be fragmented into multiple nanoparticles that actually are single primary crystals. Low pressure is considered to be a driving force for the formation of nanoparticles. Submicron and even micron-sized particles may be formed, due to the slow drying rate and the physical properties of the precursor, which indicates that the mechanism of particle formation in the LPSP process is obviously complex including not only process parameters, but also the physicochemical properties of the precursor [10].

For industrial applications, however, this process still has limitations that need further modification and optimization: a low collecting efficiency of nanoparticles, difficulty in controlling the size of multicomponent nanoparticles, and the scale-up of the atomizer system [10]. Recent improvements have changed the atomizer from

FEAG to a two-fluid nozzle [24]. High crystalline nanoparticles could be achieved in a large production rate, which points out a strong possibility for industrial application of LPSP in the near future.

References

1. K. Okuyama, I. W. Lenggoro: Preparation of nanoparticles via spray route, *Chem. Eng. Sci. 58* (3–6), 537–547 (2003).
2. W.-N. Wang, W. Widiyastuti, I. W. Lenggoro, T. O. Kim, K. Okuyama: Photoluminescence optimization of luminescent nanocomposites fabricated by spray pyrolysis of a colloid-solution precursor, *J. Electrochem. Soc. 154* (4), J121–J128 (2007).
3. W.-N. Wang, I. W. Lenggoro, K. Okuyama: Nanoparticle Preparation by Spray Route. In *Encyclopedia of Nanoscience and Nanotechnology*, 2nd ed.; Nalwa, H. S., Ed. American Scientific Publishers: Stevenson Ranch (in press).
4. T. T. Kodas, M. Hampdent-Smith: *Aerosol Processing of Materials*. Wiley-VCH: New York (1999).
5. M. Eslamian, N. Ashgriz: Effect of precursor, ambient pressure, and temperature on the morphology, crystallinity, and decomposition of powders prepared by spray pyrolysis and drying, *Powder Technol. 167* (3), 149–159 (2006a).
6. M. Eslamian, N. Ashgriz: Effect of reactor ambient pressure on the morphology of spray dried magnesium sulphate powders, *Can. J. Chem. Eng. 84* (5), 581–589 (2006b).
7. M. Eslamian, N. Ashgriz: Evaporation and evolution of suspended solution droplets at atmospheric and reduced pressures, *Dry Technol. 25* (4–6), 999–1010 (2007).
8. Y. C. Kang, S. B. Park: A high-volume spray aerosol generator producing small droplets for low-pressure applications, *J. Aerosol Sci. 26* (7), 1131–1138 (1995).
9. W.-N. Wang, Y. Itoh, I. W. Lenggoro, K. Okuyama: Nickel and nickel oxide nanoparticles prepared from nickel nitrate hexahydrate by a low pressure spray pyrolysis, *Mat. Sci. Eng. B. 111* (1), 69–76 (2004).
10. W.-N. Wang: Synthesis of Nanoparticles via Spray Route under Low Pressure Conditions. Doctoral Dissertation, Hiroshima University, Higashi Hiroshima (2006).
11. Y. C. Kang, S. B. Park: Preparation of nanometre size oxide particles using filter expansion aerosol generator, *J. Mater. Sci. 31* (9), 2409–2416 (1996).
12. I. W. Lenggoro, Y. Itoh, N. Iida, K. Okuyama: Control of size and morphology in NiO particles prepared by a low-pressure spray pyrolysis, *Mater. Res. Bull. 38* (14), 1819–1827 (2003).
13. W.-N. Wang, I. W. Lenggoro, Y. Terashi, T. O. Kim, K. Okuyama: One-step synthesis of titanium oxide nanoparticles by spray pyrolysis of organic precursors, *Mat. Sci. Eng. B. 123* (3), 194–202 (2005a).
14. Y. C. Kang, Y. S. Chung, S. B. Park: Preparation of YAG:Europium red phosphors by spray pyrolysis using a filter-expansion aerosol generator, *J. Am. Ceram. Soc. 82* (8), 2056–2060 (1999).
15. Y. C. Kang, S. B. Park: Zn_2SiO_4:Mn phosphor particles prepared by spray pyrolysis using a filter expansion aerosol generator, *Mater. Res. Bull. 35* (7), 1143–1151 (2000).
16. I. W. Lenggoro, Y. Itoh, K. Okuyama, T. O. Kim: Nanoparticles of a doped oxide phosphor prepared by direct-spray pyrolysis, *J. Mater. Res. 19* (12), 3534–3539 (2004).
17. W.-N. Wang, I. W. Lenggoro, Y. Terashi, Y. C. Wang, K. Okuyama: Direct synthesis of barium titanate nanoparticles via a low pressure spray pyrolysis method, *J. Mater. Res. 20* (10), 2873–2882 (2005b).

18. W.-N. Wang, I. W. Lenggoro, K. Okuyama, Y. Terashi, Y. C. Wang: Effects of ethanol addition and Ba/Ti ratios on preparation of barium titanate nanocrystals via a spray pyrolysis method, *J. Am. Ceram. Soc. 89* (3), 888–893 (2006).
19. Y. Itoh, M. Abdullah, K. Okuyama: Direct preparation of nonagglomerated indium tin oxide nanoparticles using various spray pyrolysis methods, *J. Mater. Res. 19* (4), 1077–1086 (2004).
20. T. Ogi, F. Iskandar, Y. Itoh, K. Okuyama: Characterization of dip-coated ITO films derived from nanoparticles synthesized by low-pressure spray pyrolysis, *J. Nanopart. Res. 8* (3–4), 343–350 (2006).
21. D. Hidayat, T. Ogi, F. Iskandar, K. Okuyama: Single crystal ZnO:Al nanoparticles directly synthesized using low-pressure spray pyrolysis, *Mater. Sci. Eng. B. 151* (3), 231–237 (2008).
22. W.-N. Wang, I. W. Lenggoro, K. Okuyama: Dispersion and aggregation of nanoparticles derived from colloidal droplets under low-pressure conditions, *J. Colloid Interface Sci. 288* (2), 423–431 (2005c).
23. S. P. Fisenko, W.-N. Wang, I. W. Lenggoro, K. Okyuama: Evaporative cooling of micron-sized droplets in a low-pressure aerosol reactor, *Chem. Eng. Sci. 61* (18), 6029–6034 (2006).
24. T. Ogi, D. Hidayat, F. Iskandar, A. Purwanto, K. Okuyama: Direct synthesis of highly crystalline transparent conducting oxide nanoparticles by low pressure spray pyrolysis. *Adv. Powder Technol. 20* (2), 203–209 (2009).

Chapter 39
Flame Spray Pyrolysis

A. Purwanto, W.-N. Wang, and K. Okuyama

Abstract Flame spray pyrolysis (FSP) has been applied for the production of powders industrially. FSP allows production of powders with controlled characteristics at a high rate. In addition to the process parameters, several other factors are crucial for nanoparticle production. Precursor type, as an example, is an important factor determining the particle size. Using metalorganic precursors, particles in nano-sized order could be produced. While for aqueous salt precursors, atomizer type is critical. Two-fluid nozzle atomizers could be used to produce nanoparticles. Only submicron particles could be achieved by using ultrasonic nebulizers. The particle formation mechanism follows one-droplet-to-one-particle (ODOP) principle. If an organic additive, such as urea was added to the precursor, nanoparticles could be obtained. The thermal decomposition of organic additives facilitated the disintegration of primary particles producing nanoparticles. This mechanism refers to one-droplet-to-multiple-particles (ODMP) route.

Keywords Additive · Atomizer · Flame · Nanoparticles · Pyrolysis

Particle production from a flame process, especially soot and carbon black fabrication, has a history that can be traced to prehistoric times [1]. For several years, Titania and silica powder have been produced industrially via a flame process [2]. As a continuous process, the flame method allows production at a high rate with controlled-particle characteristics that result in an inexpensive process for powder fabrication [3]. In addition, the ability to control the fuel flow rate in flame is useful because it provides some control over the temperature at which a reaction can be carried out [3–5]. Generally, the characteristics of flame-made particles are highly crystalline, dense and free of impurities due to the high-temperature flame heat.

A. Purwanto (✉)
Department of Chemical Engineering, Hiroshima University, Higashi Hiroshima, Japan
and
Department of Chemical Engineering, Sebelas Maret University, Surakarta, Indonesia
e-mail: aguspur@uns.ac.id

N. Ashgriz (ed.), *Handbook of Atomization and Sprays*,
DOI 10.1007/978-1-4419-7264-4_39, © Springer Science+Business Media, LLC 2011

It is reported that many types of materials have been successfully produced via the flame spray pyrolysis (FSP) method – simple oxide materials include SiO_2, [3] TiO_2, [3] γ-Fe_2O_3, [6] α-Al_2O_3, [7] and ZnO [8]. FSP is also used to produce more complex materials, such as multicomponents, composites, and non-oxides. Multicomponent materials are frequently used in the application of phosphors: $Y_3Al_5O_{12}:Ce^{3+}$; [5, 9] $SrTiO_3:Pr^{3+}$, Al^{3+}; [10] and, $BaMgAl_{10}O_{17}:Eu^{2+}$ [11]. For catalyst applications, materials are fabricated as a composite of the host and their active material. A few examples of composite materials include Pt/TiO_2, [12] Rh/Al_2O_3, [13] and Cu/ZnO/Al_2O_3 [14]. Moreover, non-oxide materials have been successfully produced via the FSP method: pure metal (Ag and Pd); [15] phosphate ($FePO_4$); [16] carbonates ($BaCO_3$ and $CaCO_3$); [17, 18] and, halides (NaCl, CaF_2, SrF_2 and BaF_2) [19].

In a broad sense, FSP consists of spray pyrolysis of an aqueous/liquid precursor under heat treatment from a flame [20]. FSP is generally comprised of three main experimental parts: an atomizer, a burner and a collecting system [4]. The general setup of the experimental apparatus is shown in Fig. 39.1. The precursor can be atomized into droplets using an atomizer that is made up of an ultrasonic nebulizer, a two-fluid nozzle and an electrosprayer. Moreover, depending on the method used to mix the fuel and the oxidant, the burner can be divided into two types: the diffusion burner and the premixed burner. A diffusion burner is one in which the fuel and oxidant are not mixed before entering the flame zone. Generally, a burner is built from concentric cylinder pipes arranged in a series that depends on the number of flows needed. The innermost cylinder is used to deliver the precursor from the atomizer to the flame zone. Droplets generated from the atomizer are transported to the flame zone by the aid of a carrier gas. In contrast, a premixed burner mixes the fuel and oxidant before being inputted to the flame zone [3]. Many types of particle collectors can be used for collecting the prepared powder; two examples are an electrostatic precipitator and a bag filter.

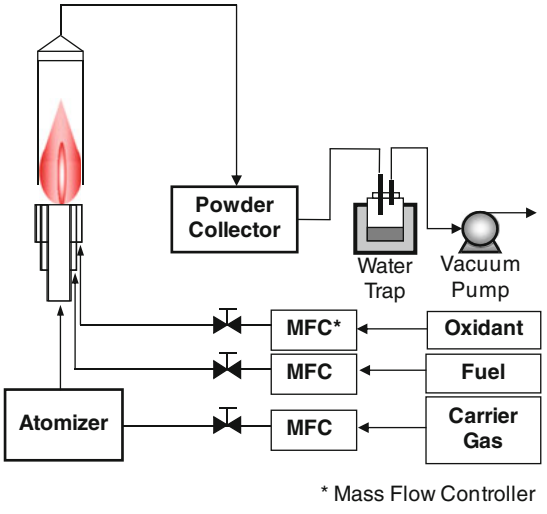


Fig. 39.1 Schematic diagram of the experimental setup of flame spray pyrolysis (FSP). The system is comprised of an atomizer, a burner and a particle collecting system

Powder fabrication using a two-fluid nozzle atomizer in FSP is well documented in the literature [1, 3, 6, 7, 21]. When using metalorganic compounds as a precursor, the prepared powder is generally of a nanosized order. The formation of nanoparticles proceeds via the following routes of reaction: nucleation, surface growth, aggregation, and agglomeration [22]. From this mechanism, there are three main processes that dominate during particle formation: chemical reaction, coagulation and coalescence. The chemical reaction of a precursor involves the formation of product monomers (clusters) by nucleation or direct inception and growth of particles that react on the surface of formed particles. Coagulation occurs when there is high particle concentration in the presence of aerosol. Particles in the fluid move randomly in a Brownian motion and collide with one another. Because of either strong adhesive forces or chemical bonding, these collisions result in coagulation. The coalescence or fusion process leads to the production of single-particle formation from many nanoparticles. Coalescence is produced from intense aggregation in a high temperature area due to the sintering process [22]. To prevent the agglomerated morphology of as-prepared particles, reducing the residence time in the reactor by flowing the precursor at a high flow rate is a possibility. However, this technique decreases the crystallinity of the as-prepared particles. The use of a nozzle to capture particles in-flight through the flame showed promise as a method for the dispersion of nanoparticles [3].

Despite the use of a metalorganic precursor, an aqueous solution of metal salt can also be used for the synthesis of nanoparticles using a two-fluid atomizer. Figure 39.2a shows the field emission-scanning electron microscopy (FE-SEM) images of Y_2O_3:Eu^{3+} nanoparticles prepared using a methane flow rate of 2.5 L/min with a dispersant gas (N_2) flow rate of 5 L/min. Nanoparticle formation may be due to a high velocity of fluid with a high drying rate of droplets. Generally, surface precipitation occurs in a high drying rate and produces a weak network of primary particles. The primary particles then disintegrate and produce nanoparticles when an external force is applied from a high-velocity fluid surrounding the dried droplets [4].

On the other hand, when the ultrasonic nebulizer was used, only submicron-sized particles of Y_2O_3:Eu^{3+} were produced (Fig. 39.2b) [4, 23]. This tendency also is found in the preparation of YAG:Ce^{3+}, $BaTiO_3$, $BaMgAl_{10}O_{17}$:Eu^{2+} and $SrTiO_3$:Eu^{3+} [5, 10, 11, 24]. It is obvious that the particle formation of the aforementioned materials follows a one-droplet-to-one-particle (ODOP) route. In the ODOP route, a particle is produced from a single droplet that undergoes evaporation, intra-particle reaction, sintering, and the densification process [5]. The particle size can be directly predicted using a mass balance equation, in which micron-sized droplets generally produce submicron-sized particles. The correlation of the average particle size with the physical properties of the precursor can be written as follows:

$$d_p = \left[\frac{C_D \cdot d_D^3 \cdot MW}{n \cdot \rho}\right]^{1/3} \tag{39.1}$$

In the preceding equation, C_D is the droplet concentration, d_D is the droplet diameter, MW is the molecular weight of the particles, n is the stoichiometric ratio

and ρ is the particle density. This equation shows that the particle size is strongly dependent on the precursor concentration. The dependency of particle's size on precursor concentration is shown in the FE-SEM images of YAG:Ce^{3+} (a yellow phosphor) in Fig. 39.3.

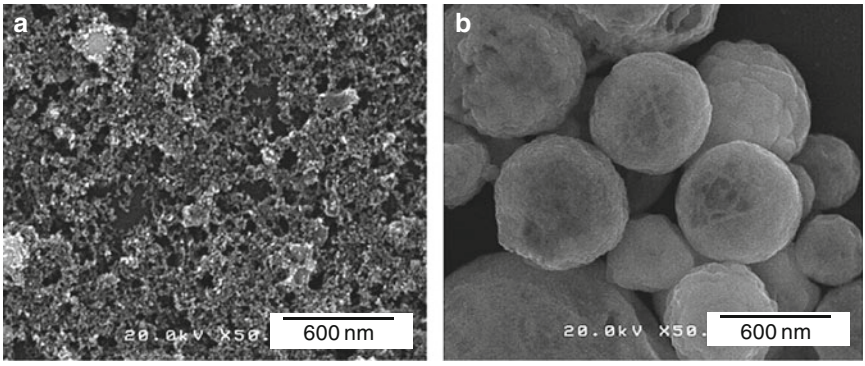


Fig. 39.2 FE-SEM images of Y_2O_3:Eu^{3+} powder prepared using two different atomizers, (**a**) two-fluid nozzle, (**b**) ultrasonic nebulizer. The powder was fabricated at under gaseous flow rates of CH_4: 2.5 L/min and O_2: 6.3 L/min. In the case of the two-fluid nozzle atomizer, the dispersant gas (N_2) flow rate was 5 L/min (**a**). When an ultrasonic nebulizer was used, the nitrogen (carrier gas) flow rate was 7 L/min (**b**). ([4] Reproduced by permission of The Society of Chemical Engineer-Japan)

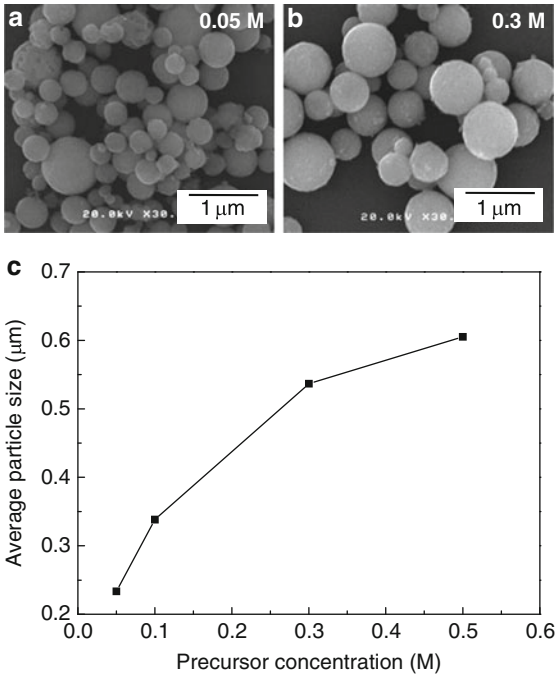


Fig. 39.3 FE-SEM images of $Y_3Al_5O_{12}$:Ce^{3+} (YAG:Ce^{3+}) powder prepared from different precursor concentrations of 0.05 M (**a**) and 0.3 M (**b**). (**c**) Average particle size as a function of precursor concentration. The powder was fabricated under gaseous flow rates of CH_4: 5.5 L/min, O_2: 13.8 L/min, N_2 (carrier gas): 2 L/min. The as-prepared powder was then annealed at 1100°C for 2 h to convert from a hexagonal structure to a garnet structure. ([5] Reproduced by permission of The Electrochemical Society)

Using the ODOP route, the addition of a chemical additive to the precursor can be used to produce nanoparticles. If an organic additive is added to the precursor, dried particles containing organic material will be produced after the evaporation of the solvent is completed. Further heating of the dried particles leads to decomposed gasses from the organic additive. The decomposition process implies the disintegration of the primary particles producing nanoparticles. This mechanism has been observed in the formation of YAG:Ce^{3+} nanoparticles using urea as an additive [9]. Hereafter, the formation of nanoparticles from droplets will be referred to as the One-Droplet-to-Many-Particles (ODMP) route.

Figure 39.4 shows the effect of urea addition on the morphology and nanoparticle formation of YAH (hexagonal $YAlO_3$, an intermediate phase of YAG). The urea-nitrate ratio, in which the nitrate represents the precursor solution, was varied from 0 to 30. Figure 39.4a shows that most of the particles prepared from a precursor without a urea addition were in the submicron size (400–700 μm) with a small amount of nano-sized particles. When 1 M of urea (urea-nitrate ration is 10) was added, the quantity of nanoparticles increased while the size of larger particles was reduced. Well-dispersed nanoparticles, with an average size of 20 nm, were produced from the addition of 2 M urea in the nitrate precursor, as shown in Fig. 39.4c. The addition of more than 2 M of urea produced nanoparticles with an agglomerated morphology, as shown in Fig. 39.4d (urea addition of 3 M). These results show that the addition of 2 M urea into 0.1 M nitrate precursor is an effective way to produce

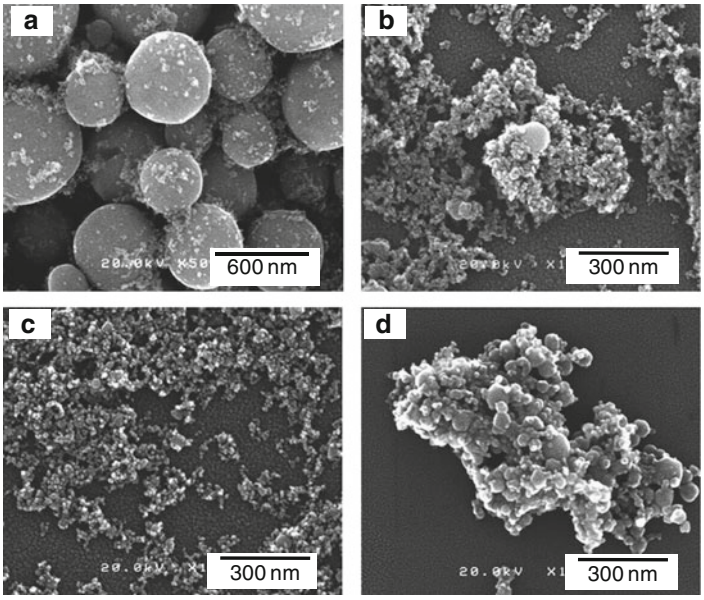


Fig. 39.4 FE-SEM images of hexagonal $YAlO_3$ (YAH, intermediate phase of YAG) indicating nanoparticle dispersion evolution as a function of urea-nitrate ratios of (**a**) 0, (**b**) 10, (**c**) 20, and (**d**) 30. ([9] Reproduced by permission of Elsevier)

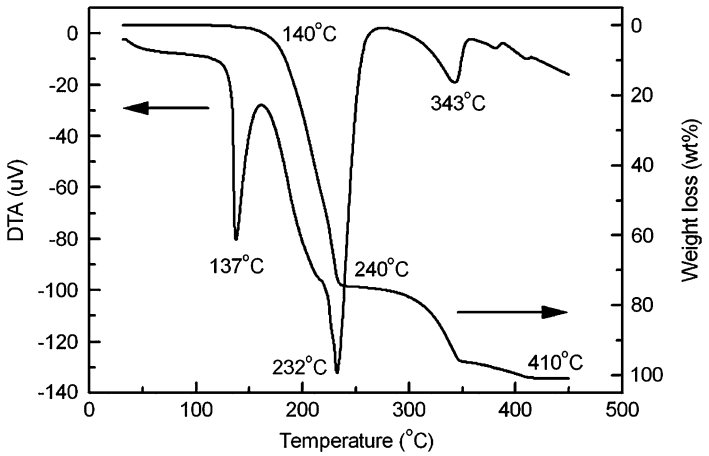


Fig. 39.5 Thermal gravimetric-differential thermal analysis (TG-DTA) spectra of urea recorded for temperatures ranging from 30°C to 1000°C with a heating rate of 10°C/min under air at a flow rate of 200 mL/min. ([9] Reproduced by permission of Elsevier)

non-agglomerated nanoparticles. To further convert the YAH phase into the YAG phase, annealing at an elevated temperature is required [9].

From the aforementioned results, it is obvious that the addition of urea into the precursor plays an important role in the formation of YAG:Ce^{3+} nanoparticles. To further investigate the decomposition characteristics of urea under elevated temperature, TG/DTA analysis was carried out with the spectra, as shown in Fig. 39.5. In the literature, it is shown that urea will decompose into biuret, and in higher temperature ranges, biuret will decompose into cyanuric acid, ammelide and melamine [25]. The full decomposition of urea occurs at 410°C. The overall reaction of urea under heat treatment in the presence of water can be written as follows:

$$NH_2CONH_2 + H_2O \rightarrow 2NH_3 + CO_2 \tag{39.2}$$

The reaction equation shows that 1 mol of urea should produce 3 mol of decomposed gasses. The large volume of decomposed gasses may produce internal pressure inside the particles that will break the interconnected structure inside the primary particles. Finally, the dispersed nanoparticles were obtained as indicated in Fig. 39.4.

It is well known that FSP provides a high temperature environment from the combustion of fuel with an oxidant. The temperature of the flame is easily controlled by varying the fuel flow rate. If the flame energy is high enough, the evaporation process of oxide particles may occur. The condensation of oxide vapor would lead to the production of nanoparticles, which is considered to be another ODMP route. $BaTiO_3$ is one example of material that can be produced in a nano-sized order using this mechanism [26, 27]. Figure 39.6 shows the FE-SEM images of $BaTiO_3$ nanoparticles produced from different concentrations of precursor. The variation of concentration offered good control of the average size of the

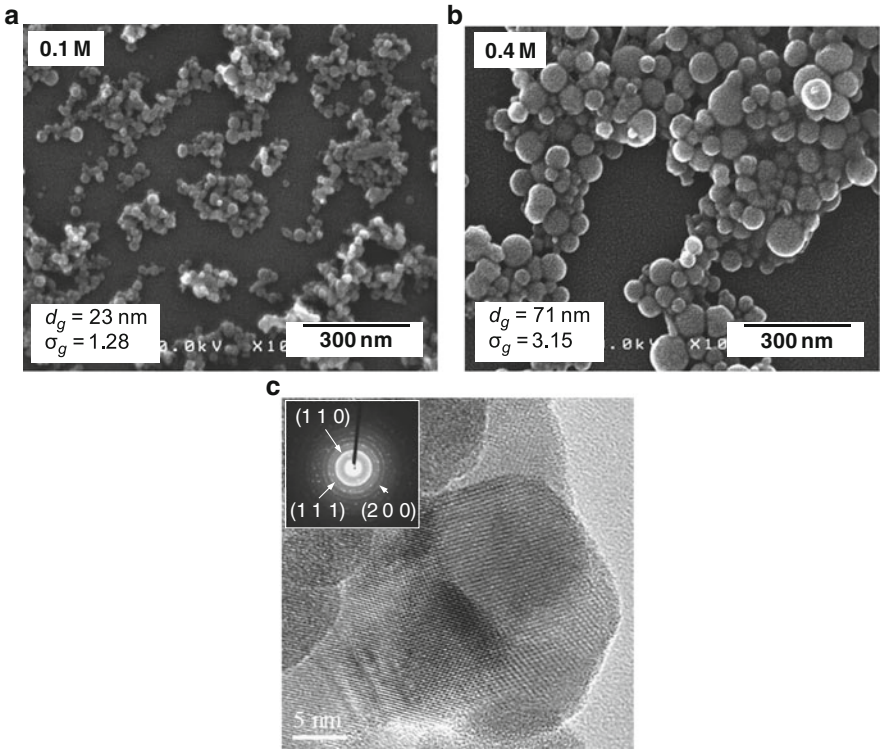


Fig. 39.6 Flame-made $BaTiO_3$ nanoparticles prepared from different concentrations, (**a**) 0.05 M, (**b**) 0.4 M, and (**c**) HRTEM image of $BaTiO_3$ powder prepared using a precursor concentration of 0.1 M and its electron diffraction pattern (*inset*). The powder was fabricated under gaseous flow rates of CH_4: 4 L/min, O_2: 8.4 L/min, O_2 (carrier gas): 4 L/min. ([26] Reproduced by permission of Elsevier)

prepared $BaTiO_3$ nanoparticles. The geometric mean diameters were 23 and 71 nm for nanoparticles prepared from precursor concentrations of 0.1 and 0.4 M, respectively. In this case, the flame was generated using a methane flow rate of 4 L/min with a carrier gas (oxygen) flow rate of 4 L/min. An increase in particle diameter with increasing precursor concentration also was found in a previous study of the production of nanomaterials using a flame process [3].

To further investigate nanoparticle production from solid evaporation via a flame method, silica was used as a model material. Monodispersed silica was fed to the flame and the effects were investigated both experimentally and numerically [28]. Figure 39.7 shows the FE-SEM images of silica after it was supplied to the flame reactor under different methane flow rates. It is evident that nanoparticles can be generated from monodispersed silica with the average size of 812 nm (submicron). To confirm this finding, the size distribution evolution was numerically calculated by considering nucleation, coagulation and surface growth of the generated silica vapors due to the solid silica evaporation. Figure 39.8 depicts particle size

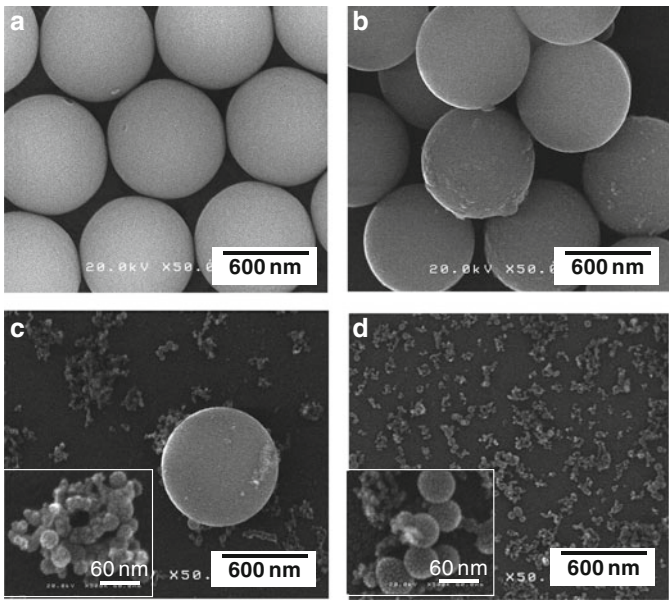


Fig. 39.7 FE-SEM images of silica particles under flame treatment at different methane flow rates. (**a**) Monodispersed silica as a precursor, (**b**) flame-treated at CH_4: 1 L/min, (**c**) 2 L/min, and (**d**) 3 L/min. ([28] Reproduced by permission of John Wiley & Sons)

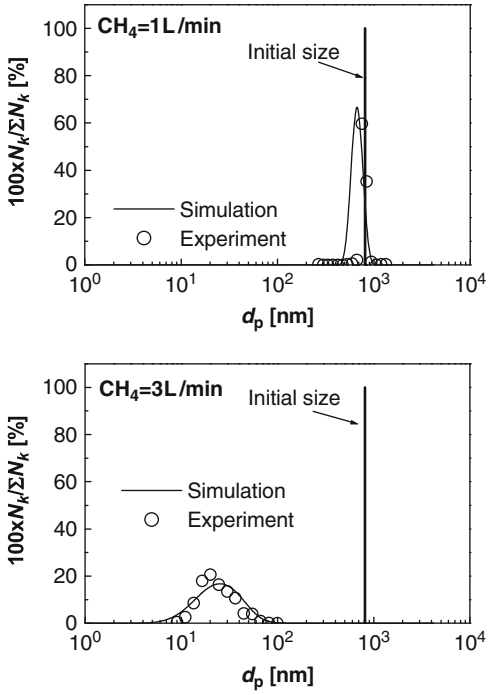


Fig. 39.8 Size distribution of silica particles after flame treatment at different methane flow rates, compared with simulation. ([28] Reproduced by permission of John Wiley & Sons)

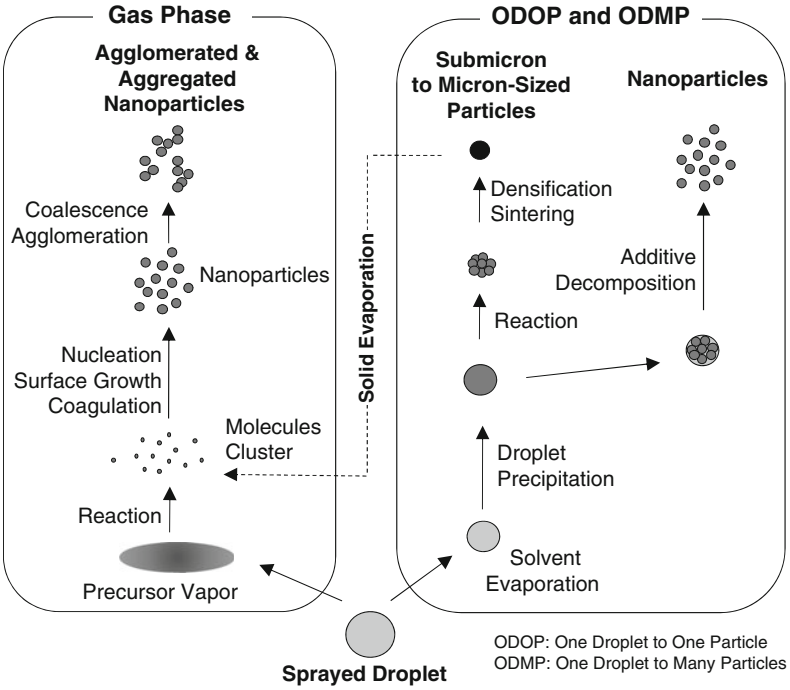


Fig. 39.9 Schematic diagram of the particle formation mechanism of FSP

distribution, comparing particles generated from the experimental process with those from simulation. The results show that the data are in good agreement for nanoparticle formation following the proposed experimental process. In addition, this shows that nanoparticle formation through solid precursor evaporation is possible using a flame reactor.

To clarify powder formation via the FSP method, a simple mechanism is drawn in Fig. 39.9. Three mechanisms are possible for powder production by FSP: the gas phase, ODOP, and ODMP. The gas phase mechanism occurs when metalorganic compounds are used as a precursor. The metalorganic precursor evaporates soon after it enters the flame zone, which leads to particle formation in the gas phase. When an aqueous precursor is used, droplet drying is followed by the reaction and annealing processes, which produces submicrometer particles. This route follows the ODOP mechanism in which one droplet produces one particle with the size strongly dependent upon the precursor concentration. When particle formation follows the ODMP route, one droplet produces many particles. The driving force for primary particle disintegration can stem from either physical or chemical interaction (adding of additives in the precursor). A recently identified driving force for nanoparticle formation in ODMP is called particle evaporation. The typical products from this route are nanoparticles that are similar to those produced from the gas-phase route.

Overall, we showed the potential of FSP to produce many types of materials and to control morphology and size. For industrial feasibility, a technology must comprise many aspects, such as scale-up ease, an inexpensive process, flexibility in the use of precursor chemicals, and easy control over product characteristics. FSP possesses all these features, which makes it a good candidate for use as a process in the powder (especially nanopowder) industry. The benefits of FSP could contribute to the future advancement of technology.

References

1. Strobel, R.; Pratsinis, S. E. Flame aerosol synthesis of smart nanostructured materials. *Journal of Materials Chemistry* 2007, 17, 4743–4756.
2. Wegner, K.; Pratsinis, S. E. Scale-up of nanoparticle synthesis in diffusion flame reactors. *Chemical Engineering Science* 2003, 58, 4581–4589.
3. Pratsinis, S. E. Flame aerosol synthesis of ceramic powders. *Progress in Energy and Combustion Science* 1998, 24, 197–219.
4. Purwanto, A.; Lenggoro, I. W.; Chang, H. W.; Okuyama, K. Preparation of submicron- and nanometer-sized particles of Y_2O_3: Eu^{3+} by flame spray pyrolysis using ultrasonic and two-fluid atomizers. *Journal of Chemical Engineering of Japan* 2006, 39, 68–76.
5. Purwanto, A.; Wang, W. N.; Lenggoro, I. W.; Okuyama, K. Formation and luminescence enhancement of agglomerate-free YAG: Ce^{3+} submicrometer particles by flame-assisted spray pyrolysis. *Journal of the Electrochemical Society* 2007, 154, J91–J96.
6. Grimm, S.; Schultz, M.; Barth, S.; Muller, R. Flame pyrolysis – A preparation route for ultrafine pure γ-Fe_2O_3 powders and the control of their particle size and properties. *Journal of Materials Science* 1997, 32, 1083–1092.
7. Laine, R. M.; Marchal, J. C.; Sun, H. P.; Pan, X. Q. Nano-α-Al_2O_3 by liquid-feed flame spray pyrolysis. *Nature Materials* 2006, 5, 710–712.
8. Tani, T.; Madler, L.; Pratsinis, S. E. Homogeneous ZnO nanoparticles by flame spray pyrolysis. *Journal of Nanoparticle Research* 2002, 4, 337–343.
9. Purwanto, A.; Wang, W. N.; Ogi, T.; Lenggoro, I. W.; Tanabe, E.; Okuyama, K. High luminance YAG: Ce nanoparticles fabricated from urea added aqueous precursor by flame process. *Journal of Alloys and Compounds* 2008, 463, 350–357.
10. Chang, H. W.; Lenggoro, I. W.; Okuyama, K.; Jang, H. D. Flame spray pyrolysis for preparing red-light-emitting, submicron-sized luminescent strontium titanate particles. *Japanese Journal of Applied Physics Part 1 – Regular Papers Brief Communications & Review Papers* 2006, 45, 967–973.
11. Chang, H. W.; Lenggoro, I. W.; Ogi, T.; Okuyama, K. Direct synthesis of barium magnesium aluminate blue phosphor particles via a flame route. *Materials Letters* 2005, 59, 1183–1187.
12. Johannessen, T.; Koutsopoulos, S. One-step flame synthesis of an active Pt/TiO_2 catalyst for SO_2 oxidation – A possible alternative to traditional methods for parallel screening. *Journal of Catalysis* 2002, 205, 404–408.
13. van Vegten, N.; Ferri, D.; Maciejewski, M.; Krumeich, F.; Baiker, A. Structural properties of flame-made Rh/Al_2O_3 and catalytic behavior in chemoselective hydrogenation. *Journal of Catalysis* 2007, 249, 269–277.
14. Jensen, J. R.; Johannessen, T.; Wedel, S.; Livbjerg, H. A study of $Cu/ZnO/Al_2O_3$ methanol catalysts prepared by flame combustion synthesis. *Journal of Catalysis* 2003, 218, 67–77.
15. Makela, J. M.; Keskinen, H.; Forsblom, T.; Keskinen, J. Generation of metal and metal oxide nanoparticles by liquid flame spray process. *Journal of Materials Science* 2004, 39, 2783–2788.

16. Rohner, F.; Ernst, F. O.; Arnold, M.; Hibe, M.; Biebinger, R.; Ehrensperger, F.; Pratsinis, S. E.; Langhans, W.; Hurrell, R. F.; Zimmermann, M. B. Synthesis, characterization, and bioavailability in rats of ferric phosphate nanoparticles. *Journal of Nutrition* 2007, 137, 614–619.
17. Strobel, R.; Maciejewski, M.; Pratsinis, S. E.; Baiker, A. Unprecedented formation of metastable monoclinic $BaCO_3$ nanoparticles. *Thermochimica Acta* 2006, 445, 23–26.
18. Huber, M.; Stark, W. J.; Loher, S.; Maciejewski, M.; Krumeich, F.; Baiker, A. Flame synthesis of calcium carbonate nanoparticles. *Chemical Communications* 2005, 41, 648–650.
19. Grass, R. N.; Stark, W. J. Flame synthesis of calcium-, strontium-, barium fluoride nanoparticles and sodium chloride. *Chemical Communications* 2005, 41, 1767–1769.
20. Kammler, H. K.; Madler, L.; Pratsinis, S. E. Flame synthesis of nanoparticles. *Chemical Engineering & Technology* 2001, 24, 583–596.
21. Gutsch, A.; Muhlenweg, H.; Kramer, M. Tailor-made nanoparticles via gas-phase synthesis. *Small* 2005, 1, 30–46.
22. Gutsch, A.; Averdung, J.; Muhlenweg, H. From technological development to the successful nanotechnological product. *Chemie Ingenieur Technik* 2005, 77, 1377–1392.
23. Chang, H.; Lenggoro, I. W.; Okuyama, K.; Kim, T. O. Continuous single-step fabrication of nonaggregated, size-controlled and cubic nanocrystalline Y_2O_3: Eu^{3+} phosphors using flame spray pyrolysis. *Japanese Journal of Applied Physics Part 1 – Regular Papers Short Notes & Review Papers* 2004, 43, 3535–3539.
24. Brewster, J. H.; Kodas, T. T. Generation of unagglomerated, dense, $BaTiO_3$ particles by flame-spray pyrolysis. *Aiche Journal* 1997, 43, 2665–2669.
25. Schaber, P. A.; Colson, J.; Higgins, S.; Thielen, D.; Anspach, B.; Brauer, J. Thermal decomposition (pyrolysis) of urea in an open reaction vessel. *Thermochimica Acta* 2004, 424, 131–142.
26. Purwanto, A.; Wang, W. N.; Lenggoro, I. W.; Okuyama, K. Formation of $BaTiO_3$ nanoparticles from an aqueous precursor by flame-assisted spray pyrolysis. *Journal of the European Ceramic Society* 2007, 27, 4489–4497.
27. Terashi, Y.; Purwanto, A.; Wang, W. N.; Iskandar, F.; Okuyama, K. Role of urea addition in the preparation of tetragonal $BaTiO_3$ nanoparticles using flame-assisted spray pyrolysis. *Journal of the European Ceramic Society* 2008, 28, 2573–2580.
28. Widiyastuti, W.; Purwanto, A.; Wang, W. N.; Iskandar, F.; Setyawan, H.; Okuyama, K. Nanoparticle formation through solid-fed flame synthesis: experiment and modeling. *AIChE Journal* 2009, 55, 885–895.

Chapter 40
Particle Production via Emulsion Combustion Spray Method

M. Eslamian, M. Ahmed, and N. Ashgriz

Abstract In many industrial applications powdered materials are used for the manufacturing and development of commodities, products, parts, tools, instruments, etc. Examples are in powder metallurgy, in the development of gas sensors, solar cells, thermal barrier coatings, catalysts, pigments, and pharmaceuticals. While in some applications, particle size and size distribution, and particle crystallinity and grain size may be immaterial or irrelevant, in some other applications particle characteristics may play an important role in the characteristics and quality of the final products. It is generally agreed upon that no matter the particles are crystalline or amorphous, as the particle size decreases, the particle reactivity increases. Nanocrystalline materials (grain size < 100 nm), either in bulk or powder form, compared to the polycrystalline materials have enhanced properties, such as hardness, yield strength, corrosion resistance, etc. Therefore, nanocrystalline nanoparticles (grain and particle size < 100 nm), such as quantum dots have superior properties.

The basic approach to classify powder production methods is based on whether a method is top-down or bottom-up. In a top-down method, micro- and nano-particles are produced due to the structure and size refinement through the breakdown of the larger particles; in a bottom-up method, the mechanism of particle formation is usually by means of nucleation, growth and aggregation of atoms and molecules. In a more practical approach, one may divide the powder synthesis methods as follows: (1) wet chemistry, such as the chemical precipitation, sol–gel, microemulsion, sonochemistry, and hydrothermal synthesis methods; (2) mechanical attrition, grinding and milling; (3) gas phase methods, such as the chemical and physical vapor deposition; (4) liquid phase spray methods, such as the molten metal spray atomization, spray pyrolysis, and spray drying, and (5) liquid/gas phase methods,

M. Eslamian (✉) and N. Ashgriz (✉)
Department of Mechanical and Industrial Engineering, University of Toronto, Toronto, ON, Canada
e-mail: m.eslamian@utoronto.ca; ashgriz@mie.utoronto.ca

N. Ashgriz (ed.), *Handbook of Atomization and Sprays*,
DOI 10.1007/978-1-4419-7264-4_40, © Springer Science+Business Media, LLC 2011

such as the flame spray pyrolysis and emulsion combustion method. Most of the above mentioned methods are bottom-up, while the mechanical attrition is a top-down method. The powder production methods may be divided based on other characteristics as well; for instance, liquid methods such as all wet chemistry versus the dispersion-phase or aerosol methods and powder production methods that somehow rely on spraying of a liquid precursor [1].

Spray techniques are simple, one step methods, suitable for the manufacturing of a broad range of powders with controlled properties for specialty applications. These methods include but are not limited to spray drying (SD) and spray freeze drying (SFD), mainly for producing pharmaceuticals and food powders, spray pyrolysis (SP) for fabricating non-agglomerated mono-dispersed fine and ultrafine ceramic powders, flame spray pyrolysis (FSP) for preparation of ceramic and complex nanoparticles, melt atomization (MA), mostly for the production of metal powders, and emulsion combustion method (ECM). This chapter will consider the emulsion combustion spray method, which is a one-step technique to produce simple and functional powders such as ceramics, using spray flames [2].

Takatori and his collaborators in Toyota Research Center were one of the first who developed and systematically studied the emulsion combustion method (ECM) [3]. This method is basically a combination of the microemulsion wet chemistry and the flame spray pyrolysis methods. In ECM, an aqueous solution of a metal salt is mixed with a fuel such as kerosene and a small amount of an emulsifier or surfactant to obtain a water-in-oil (W/O) type of emulsion. Using a spray nozzle, the solution is then atomized to produce a spray. The size of the mother emulsion droplets depends on the atomizer type and the atomization conditions, and is on the order of 10 μm for air-assist nozzles. The size of the dispersed micro-solution droplets depends on the string process and surfactant, and is about 1 μm [3]. Figure 40.1 shows a schematic diagram of the ECM.

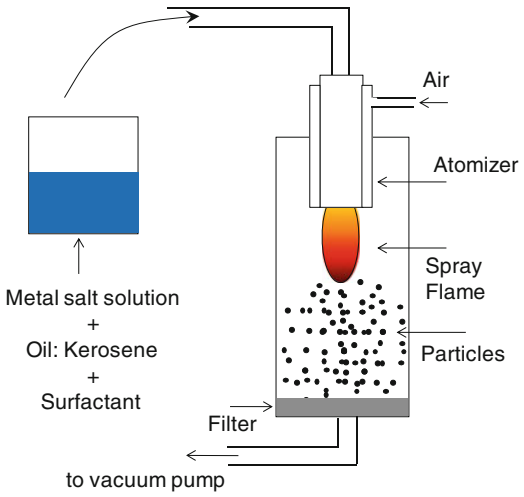


Fig. 40.1 Schematic diagram of the Emulsion Combustion Method. (Reprinted from [2] with permission. Copyright 2009 of Bentham Science Publishers)

In the ECM, burning of the fuel portion of the emulsion droplet is a heat source for drying of the dispersed micro-solution droplets. As a result, provided that the micro-solution droplets do not merge, they undergo rather similar drying and pyrolysis processes as those in the conventional spray pyrolysis (SP) method. The most significant difference between the ECM and SP is the size of the reaction field, and as a result, the reaction period. Although in the laboratory, one may spray a small amount of a precursor solution into very fine droplets whose sizes are the same as those of the dispersed droplets in the ECM, this cannot be done easily in a large-scale industrial process. An isolated small reaction field of about 1 μm is rather easily prepared using the emulsion process. The reaction period of the SP with the average droplet size of about 5 μm is longer than that of the ECM. On the other hand, if the process temperature is high enough to cause the complete evaporation of droplets including their solid content (solute), the vapor species nucleate and grow to produce nanoparticles in the gas phase. If this is the case, the ECM is similar to the FSP technique, discussed in other chapters.

Powder Production

The ECM is relatively a new powder production technique and as such very few physical or mathematical models are available to simulate this process. Different scenarios of particle formation are illustrated in Fig. 40.2 and will be elaborated later in this chapter.

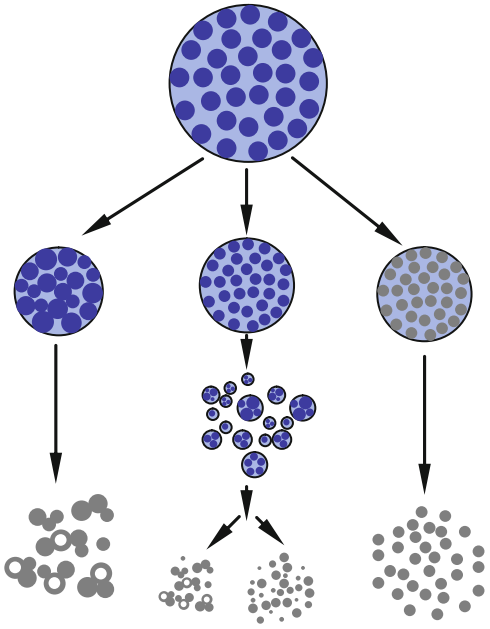


Fig. 40.2 Possible scenarios for particle formation via Emulsion Combustion Method. *Right branch*: each micro-solution droplet produces one particle. *Left branch*: shrinkage of the emulsion droplet is faster than that of micro-solution droplets, and therefore, some of the micro-solution droplets merge to form larger particles. *Middle branch*: microexplosion of the emulsion droplet and the formation of smaller emulsion droplets. (Reprinted from [2] with permission. Copyright 2009 of Bentham Science Publishers)

Depending on the process conditions, the relative size of the dispersed and emulsion droplets, and the properties of the fuel, the final particles may be either micro or nano-sized and either hollow or solid fully-filled.

In the lab scale, several powder materials have been produced by ECM, such as barium titanate [3] silica and zinc oxide [4] and alumina nanoparticles [5], etc. Figure 40.3 shows the Scanning Electron Microscope (SEM) images of the ECM-made SiO_2 particles, where two different precursors were used [4]. In the first case (Fig. 40.3a), the Si precursor is the previously prepared SiO_2 sols, whereas in the second case (Fig. 40.3b), the Si precursor is hexamethyldisiloxane solution. The powder in the former case consisted of submicron to micron-sized porous particles with openings on the surface, whereas in the latter case only nanoparticles of less than 50 nm in diameter were seen in the powder. Formation of nanoparticles in ECM method (Fig. 40.3b) implies that the entire solution droplets have first vaporized and then nanoparticles have formed from the vapor of the species. In the first case (Fig. 40.3a), probably each single droplet has produced one single particle.

Figure 40.4 shows the SEM images of barium titanate powders synthesized at 850°C. The effect of using various barium concentration and precursor sources for titanium was studied [3]: In Fig. 40.4a barium concentration is 0.3 mol/L and titanium source is TiO_2 sols, in Fig. 40.4b barium concentration is 0.03 mol/L and the titanium source is the same as above, i.e., TiO_2 sols; in Fig. 40.4c the barium concentration is 0.3 mol/L the same as Fig. 40.4a, but the titanium source is the $TiCl_4$ precursor. When a high concentration of barium was used (0.3 mol/L), the particles were spherical with diameters of 200–500 nm (Fig. 40.4a), whereas for a low concentration of 0.03 mol/L the particle diameter is from 100 to 200 nm (Fig. 40.4b). Therefore, the particle diameter of the barium titanate may be controlled by the metal ion concentration in the emulsion droplet. Particles in Fig. 40.4c exhibited a broader particle size distribution [3]. The diagram of Fig. 40.2 and the discussion provided later may help interpret the results observed in Figs. 40.3 and 40.4.

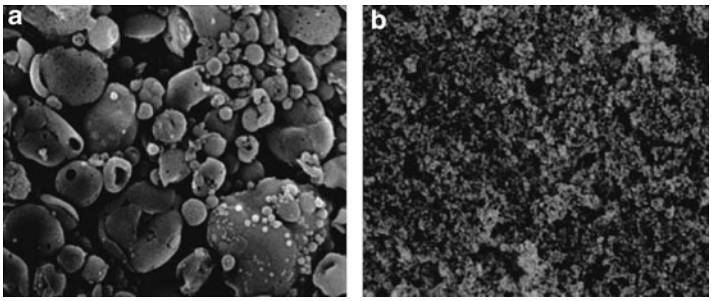


Fig. 40.3 Morphology of the ECM-made SiO_2 particles. (**a**) Si Precursor is SiO_2 sols; (**b**) Si precursor is hexamethyldisiloxane. The powder in (**a**) consisted of submicron to micron-sized porous particles with openings on the surface whereas in (**b**) only nanoparticles of less than 50 nm in diameter were observed. (Reprinted from [4] with permission. Copyright 2003 Springer)

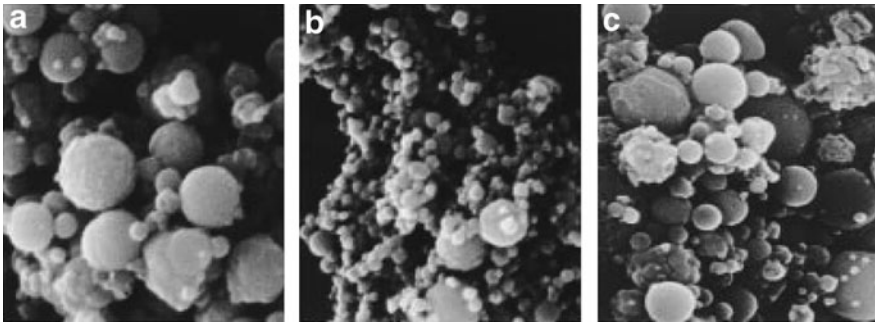


Fig. 40.4 SEM images of barium titanate powders synthesized at 850°C. (**a**) Barium concentration is 0.3 mol/L and titanium source is TiO_2 sols; (**b**) Barium concentration is 0.03 mol/L and titanium source is TiO_2 sols; (**c**) Barium concentration is 0.3 mol/L and titanium source is $TiCl_4$. (Reprinted from [3] with permission. Copyright 1999 Springer)

Tani et al. [6] patented an emulsion combustion process for the synthesis of hollow oxide particles with porous wall, with wall thickness of 20 nm or less. This may help to produce a powder with high surface area and low heat conductivity. According to one aspect of their patent, a water-in-oil emulsion is prepared by adding an organic solvent to an aqueous solution that dissolves and/or suspends at least one of the metal salts and metal compounds. The emulsion is sprayed and burned to form the hollow particles. A post-treatment process called water treatment is required to finely roughen the wall surface of the shells. In this step, the hollow particles are brought in contact with an aqueous solution. As an example, aqueous solution of aluminum nitrate was mixed with kerosene as the fuel. A commercial surfactant was added to the emulsion to stabilize it. The mixture of the three components was stirred by a homogenizer to obtain a water-in-oil emulsion; the size of the suspended microspheres was 1–2 μm. Using an emulsion burning apparatus, the emulsion was atomized and ignited to produce a flame with temperature of 700–1,000°C. The powder was collected by a bag filter. The prepared aluminum oxide shell-like particles had a wall thickness of 10 nm. Although in this example the size of the particles is not reported, since the flame temperature is low, it is deduced that each single droplet is converted into one shell-like particle.

Theory and Governing Equations

The process of particle formation from the micro-solution droplets dispersed in emulsion droplets has similarities to that of the spray pyrolysis, although under certain conditions (high temperatures) it could become totally different. In the ECM, burning of the fuel fraction of the emulsion droplet works as a heat source for drying of the dispersed micro-solution droplets. As a result, provided that the

micro-solution droplets do not merge, undergo rather similar drying and pyrolysis processes as those in SP method.

In drying/pyrolysis of most solution droplets (in ECM, micro-solution droplets), with evaporation of the solvent, solute concentration on droplet surface increases and it finally reaches a critical value, called the critical super saturation (CSS). If at the onset of precipitation, which will occur at the droplet (micro-solution droplet) surface for symmetric evaporation, the solute concentration everywhere within the droplet is equal to or is above the equilibrium saturation (ES) of that particular solute in the solution, the solute starts to precipitate everywhere within the droplet, known as volume precipitation explained by Jayanthi et al. [7]. Therefore, the whole droplet undergoes nucleation, crystallization and growth of the solute nuclei and the final particle is fully-filled, provided that the amount of solute available can fill the volume of the droplet, a condition that can be examined by the percolation theory [7]. For low initial solution concentrations or high reactor temperatures, it is likely that at the onset of precipitation on the droplet surface, solute concentration in a part of the droplet including the center is less than the ES. If this is the case, and provided the droplet temperature is uniform, which is the case for small droplets, solute precipitation occurs merely at locations where the local solute concentration is higher than ES. This leads to the formation of a thin layer of solute on the droplet surface. As the droplet evaporation and shrinkage continues, this layer thickens until the thickness reaches a critical value, thereafter the outer diameter of the droplet/particle remains constant. There is a time delay between the onset of solute precipitation on the droplet surface and the time at which a thin rigid shell is formed. However, the data on the induction period is still insufficient [8, 9]. It should be noted that fundamental experimental research on particle evolution have shown that the above-mentioned theory of particle formation [7] fails to predict the particle morphology at least at the following cases: for highly crystalline particles, such as NaCl [10], and also for solution droplets made of multi-component solutes, such as a mixture of NaCl and a precursor containing ZrO_2, such as zirconium oxychloride (ZHC) [11, 12]. Spray drying of ionic solutions such as NaCl results in the formation of cubic particles [10].

Vaporization and Burning of an Emulsion Droplet

Gas Phase Equations

Without affecting the physics of the problem, we may assume that an emulsion droplet burns in a spherically symmetric manner, with or without an enveloping diffusion flame. This is a valid assumption as long as the relative motion between the surrounding gas and the droplet is low so that no internal motion is induced within the droplet. This may happen if either the gas velocity or the droplet size is small. It has been shown that in a spray flame of ethanol and oxygen formed by a coaxial air-assist nozzle and used for the flame spray pyrolysis, the relative velocity between the gas and droplets close to the nozzle exit is on the order of 10 m/s and

vanishes fast within several centimeters downstream of the nozzle [13]. For a small droplet (~10 μm) burning at a high temperature spray flame (~1,000°C), *Re* number based on the droplet radius and droplet-gas relative velocity (10 m/s) is about 0.1.

The emulsion droplet consists of a fuel as the main component, and an aqueous solution in the form of micro-droplets, suspended within the emulsion droplet. Therefore, during the burning of the emulsion droplet, fuel (oil) and water vaporize, leading to an increase of the solute concentration within the suspended micro-solution droplets. Evaporated fuel reacts with oxygen at some distance from the droplet surface to form a flame. It is assumed that combustion occurs stoichiometrically in a thin flame according to the following reaction:

$$\mathrm{F} + (-\nu_{\mathrm{O}})\mathrm{O}_2 \rightarrow \nu_{\mathrm{C}}\mathrm{CO}_2 + \nu_{\mathrm{W}}\mathrm{H}_2\mathrm{O}$$

where F is the fuel and ν_i is the stoichiometric ratio of species ($\nu_i = 0$ for inert species and $\nu_F = -1$ for fuel) and the subscripts F, O, C, and W stand for fuel, oxygen, carbon dioxide, and water, respectively. Starting with the model of Leite and Lage [14], and accounting for the non-continuum effects as outlined in [8], the total burning rate of an emulsion droplet $\dot{m}$ is correlated with droplet and heat transfer parameters as follows:

$$\begin{aligned}\frac{\dot{m}}{4\pi}\left[1 + Kn\frac{\sqrt{\pi}Kn\xi + \zeta}{1 + Kn\xi}\right] &= \left(\frac{1}{R} - \frac{1}{r_{\mathrm{f}}}\right)^{-1}\frac{k_1}{\overline{C}_{\mathrm{P1}}}\ln(1 + B_{\mathrm{T}}) \\ &= r_{\mathrm{f}}\frac{k_2}{\overline{C}_{\mathrm{P2}}}\ln(1 + B_{\mathrm{T}}^{\mathrm{o}})\end{aligned} \tag{40.1}$$

where B_T and B_T^o are calculated as follows:

$$B_{\mathrm{T}} = \frac{\overline{C}_{\mathrm{P1}}(T_{\mathrm{f}} - T_{\mathrm{s}})}{H} \tag{40.2a}$$

$$B_{\mathrm{T}}^{\mathrm{o}} = \frac{\overline{C}_{\mathrm{P2}}(T_{\mathrm{f}} - T_{\infty})}{Q\varepsilon_{\mathrm{F}} - H - \overline{C}_{\mathrm{P1}}(T_{\mathrm{f}} - T_{\mathrm{s}})} \tag{40.2b}$$

In the above equations, $\overline{C}_{P1}$ and $\overline{C}_{P2}$ are the specific heats in regions 1 and 2 and are obtained using: $\overline{C}_{\mathrm{P1}} = \sum \varepsilon_{\mathrm{i}}\left(\overline{C}_{\mathrm{Pi}}^{0}\right)_1$ and $\overline{C}_{\mathrm{P2}} = \sum (\varepsilon_{\mathrm{i}} + \nu_{\mathrm{i}}\varepsilon_{\mathrm{F}})\left(\overline{C}_{\mathrm{Pi}}^{0}\right)_2$, where $\overline{C}_{\mathrm{Pi}}^{0}$ is the specific heat of pure substance i for each region. Due to the characteristics of combustion, burning of a fuel droplet is assumed to proceed in two regions: from the droplet surface to the flame front (region 1), and from the flame front to infinity (region 2). It is assumed that the in region 2, no fuel vapor is present. In (40.1), the term in the square brackets on the left-hand-side has a value of 1 for large droplets, and is greater than 1 for nanodroplets [8]. *H* and *L* in (40.2a and b), the effective and standard latent heats of vaporization are obtained from the following equations:

$$H = L + \frac{Q_L}{\dot{m}}, \quad L = \varepsilon_W L_1 + \varepsilon_F L_2 \tag{40.3}$$

Note that ε_W and $\varepsilon_F (= 1 - \varepsilon_W)$ are the fraction mass vaporization rates of water and fuel, respectively. ε_F is found from the following expression:

$$\varepsilon_F = \frac{Y_{O\infty}/\nu_O(1 - Y_{Ws} - \nu_W Y_{FS}) + Y_{Fs}(1 - Y_{W\infty})}{Y_{O\infty}/\nu_O(1 - \nu_W) + Y_{Ws} - Y_{W\infty} + Y_{Fs}} \tag{40.4}$$

Alternative to (40.1), the emulsion droplet burning rate and also the radius of the flame front may also be written as follows:

$$\dot{m} = 4\pi R \ln\left\{(1 + B_F)^{\rho_1 D_1}(1 + B_O^o)^{\rho_2 D_2}\right\}\left[1 + Kn\frac{\sqrt{\pi}Kn\xi + \zeta}{1 + Kn\xi}\right]^{-1} \tag{40.5}$$

$$\frac{r_f}{R} = \frac{\ln\left\{(1 + B_F)^{\rho_1 D_1}(1 + B_O^o)^{\rho_2 D_2}\right\}}{\ln\left\{(1 + B_O^o)^{\rho_2 D_2}\right\}} \tag{40.6}$$

where B_F and B_O^o are defined as follows:

$$B_F = \frac{Y_{Fs}}{\varepsilon_F - Y_{Fs}}, \quad B_O^o = \frac{-Y_{O\infty}}{\nu_O \varepsilon_F} \tag{40.7}$$

B_F and B_O^o are related to B_T and B_T^o through the Lewis numbers using the following equations:

$$B_T = (1 + B_F)^{\frac{1}{Le_1}} - 1, \quad B_T^o = \left(1 + B_O^o\right)^{\frac{1}{Le_2}} - 1 \tag{40.8}$$

where the gas phase Lewis numbers Le_1 and Le_2 are defined as $Le_i = k_i/\rho_i D_i \bar{C}_{Pi}$. In this equation, the gas phase properties for region 1 and 2 are obtained at the following average temperatures, respectively: $T_1 = T_s + 1/3(T_f - T_s)$, and $T_2 = T_f + 1/3\ (T_\infty - T_f)$. Diffusion coefficient in region 1, D_1, is the fuel vapor diffusivity in air, and in region 2 where the fuel vapor is not present any longer, D_2, is assumed to be the binary mass diffusivity of oxygen and nitrogen. Based on the kinetic theory of gases, at constant pressure the diffusion coefficient increases with temperature to the power of 1.5. In order to determine the gas density and thermal conductivity, it is assumed that the surrounding gas is air, although more sophisticated assumptions can be made, as well [14].

The droplet surface temperature (T_s) and surface mass fraction of water and fuel (Y_{Ws} and Y_{Fs}) are obtained from the liquid phase and interface equations, to be discussed later. The fractional mass vaporization rate of fuel (ε_F) is obtained from (40.4). The mass vaporization rate is then calculated using (40.5) and (40.7). Using (40.1) and (40.2a and b), H may be calculated. The transient heating rate of droplet, Q_L is obtained from (40.3).

Note that, the forgoing equations for the emulsion droplet combustion in the gas phase are also applicable to droplet burning in the flame spray pyrolysis.

Interface Model

The actual mole fraction of component i on the droplet surface (X_{is}) is related to the same variable but in the equilibrium state X_{is}^0, through the following model [14]:

$$X_{is} = \phi_{is} X_{is}^0, \tag{40.9a}$$

where

$$X_{\mathrm{is}}^0 = \frac{P_{\mathrm{i}}^{\mathrm{vap}}(T_{\mathrm{s}})}{P}, \quad \mathrm{i} = \mathrm{F}, \mathrm{W} \tag{40.9b}$$

ϕ_i is the liquid phase volume fraction, and ϕ_{is} is the volume fraction of component i (W for water and F for fuel) at the droplet surface, to be obtained from the liquid-phase equations. Equilibrium mole fraction of component i, X_{is}^0 is obtained from the Clasius-Clapeyron equation:

$$X_{is}^0 = \left(\frac{p_{\mathrm{b}}}{p_\infty}\right) \exp\left\{\left(\frac{L_i}{R_i}\right)\left(\frac{1}{T_{\mathrm{b}i}} - \frac{1}{T_{\mathrm{s}}}\right)\right\} \tag{40.10}$$

where $T_{\mathrm{b}i}$ is the boiling point of component i of the emulsion droplet at a reference pressure, p_{b} and R_i is the gas constant of component i. Also, note that the mole and mass fractions of component i on the droplet surface, are interrelated through the following equation:

$$X_{is} = \frac{Y_{is}}{M_i} \tag{40.11}$$

Liquid Phase Equations within an Emulsion Droplet

The liquid phase model proposed below considers the mass transfer inside the droplet and the changes in liquid phase properties due to the temperature and composition changes. In derivation of the following equations, it has been assumed that liquid circulation is absent, the droplet surface is at local thermodynamic equilibrium state, momentum, energy and mass transfer are spherically symmetric within the droplet, and the two liquids (fuel and water) are immiscible. With these assumptions, the conservation equations for the total mass, mass of water, and the energy equation are written as follows [14]:

$$\frac{\partial \rho}{\partial t} + \frac{1}{r^2}\frac{\partial}{\partial r}\left(r^2 \rho v\right) = 0 \tag{40.12}$$

$$\frac{\partial(\rho_{\mathrm{W}}\phi_{\mathrm{W}})}{\partial t}+\frac{1}{r^2}\frac{\partial}{\partial r}\left(r^2\rho_{\mathrm{W}}\phi_{\mathrm{W}}v_{\mathrm{W}}\right)=0 \tag{40.13}$$

$$\frac{\partial}{\partial t}(\rho C_{\mathrm{P}}T)+\frac{1}{r^2}\frac{\partial}{\partial r}\left\{r^2[\rho_{\mathrm{W}}\phi_{\mathrm{W}}\bar{C}_{\mathrm{PW}}v_{\mathrm{W}}+\rho_{\mathrm{F}}(1-\phi_{\mathrm{W}})\bar{C}_{\mathrm{PF}}v_{\mathrm{F}}]T\right\}=\frac{1}{r^2}\frac{\partial}{\partial r}\left(r^2k\frac{\partial T}{\partial r}\right) \tag{40.14}$$

where in above equations, the overall heat capacity, density and thermal conductivity of the emulsion droplet are assumed to be the weighted average of individual components, i.e., water and fuel:

$$C_{\mathrm{P}}=\frac{\left\{\rho_{\mathrm{W}}\phi_{\mathrm{W}}\overline{C}_{\mathrm{PW}}+\rho_{\mathrm{F}}(1-\phi_{\mathrm{W}})\overline{C}_{\mathrm{PF}}\right\}}{\rho} \tag{40.15}$$

$$\rho=\rho_{\mathrm{W}}\phi_{\mathrm{W}}+\rho_{\mathrm{F}}(1-\phi_{\mathrm{W}}) \tag{40.16}$$

$$k=k_{\mathrm{W}}\phi_{\mathrm{W}}+k_{\mathrm{F}}(1-\phi_{\mathrm{W}}) \tag{40.17}$$

where subscripts "W" and "F" denote the two immiscible liquid phases, i.e., water and fuel, respectively. $\overline{C}_{\mathrm{PW}}$ and $\overline{C}_{\mathrm{PF}}$ are the temperature independent heat capacities of pure water and fuel, and are evaluated at droplet initial temperature. The mean radial mass velocity of the two phases is related to the mass velocities of the individual components:

$$v=\frac{\left\{\rho_{\mathrm{W}}\phi_{\mathrm{W}}v_{\mathrm{W}}+\rho_{\mathrm{F}}(1-\phi_{\mathrm{W}})v_{\mathrm{F}}\right\}}{\rho} \tag{40.18}$$

To complete the model, the boundary and initial conditions of the liquid-phase equations are as follows [14]:

$$r=0,\quad v(0,t)=\frac{\partial\phi_{\mathrm{W}}}{\partial r}=\frac{\partial T}{\partial r}=0 \tag{40.19}$$

$$r=R(t),\quad \rho_{\mathrm{F}}\phi_{\mathrm{W}}(1-\phi_{\mathrm{W}})b\frac{\partial\phi_{\mathrm{W}}}{\partial r}=\frac{\dot{m}}{4\pi R^2}\left(\phi_{\mathrm{W}}-\frac{\rho}{\rho_1}\varepsilon_{\mathrm{W}}\right) \tag{40.20}$$

$$4\pi R^2k\frac{\partial T}{\partial r}=\dot{m}(H-L)=Q_{\mathrm{L}} \tag{40.21}$$

$$t=0,\quad v(r,t)=0,\quad \phi_{\mathrm{W}}=\phi_{\mathrm{l}0}(r),\quad T=T_0(r) \tag{40.22}$$

In above equations, b is a factor that accounts for the diffusivity of suspended micro-solution droplets inside an emulsion droplet. It is related to the liquid-phase

diffusion coefficient of the suspended micro-solution droplets, D, and the volumetric fraction of phase 1 (water) thorough the following equation:

$$b = \frac{D}{\phi_{\mathrm{W}}(1-\phi_{\mathrm{W}})} \tag{40.23}$$

where D for a non-slip boundary condition at the suspended micro-droplet surface is related to the Boltzmann's constant κ, micro-solution droplet diameter $d_{\mathrm{m}} = 2R_{\mathrm{m}}$, and surface temperature T_{s} and the continuous liquid viscosity μ, through the following equation [15]:

$$D = \frac{\kappa T_{\mathrm{s}}}{3\pi d_{\mathrm{m}}\mu} \tag{40.24}$$

To solve the liquid-phase equations, the continuity equation (40.12) is rearranged and the mean radial mass velocity is expressed as follows:

$$v(r,t) = \frac{-1}{r^2\rho}\int_0^r r^2\frac{\partial\rho}{\partial t}\mathrm{d}r \tag{40.25}$$

At the droplet surface, where $r = R(t)$, (40.25) may be shown as follows, using Leibnitz's integral rule, which relates the rate of change of the emulsion droplet radius with the mean radial mass velocity at droplet surface and droplet burning rate:

$$\frac{\mathrm{d}R}{\mathrm{d}t} = v_{\mathrm{s}} - \frac{\dot{m}}{4\pi\rho_{\mathrm{s}}R^2} \tag{40.26}$$

The liquid phase equations determine the droplet temperature $T(r, t)$ and also the volumetric fraction $\phi_{\mathrm{W}}(r, t)$ during the transient droplet heating. Then T_{s} and ϕ_{Ws} are used to solve the gas phase equations. Note that the boundary and initial conditions, (40.19)–(40.22) and also (40.26) show how the liquid-phase equations are coupled with the gas-phase equations, and therefore, an iterative method has to be employed to solve the equations.

Evaporation and Evolution of Micro-Solution Droplets

If the burning temperature is low, the solid content of an emulsion droplet does not evaporate and the micro-solution droplets undergo a process similar to spray pyrolysis, as discussed below.

In calculation of the total density of an emulsion droplet, the presence of solute may be neglected, if the concentration of micro-solution droplets is low. It is rational to assume that the temperature of the dispersed micro-solution droplets

equals the average or bulk temperature $T = T_s$ of the emulsion droplet. T, which is a function of time and radial location, is obtained from the liquid phase equations. On the other hand, due to the presence of the solute, which is a non-volatile phase, a concentration profile is developed within the micro-solution droplets. The concentration profile, which determines the characteristics of the final particle, is considered in this section.

While an emulsion droplet is burning, its fuel content and water content of the micro-solution droplets continuously evaporate. As a result of water evaporation, the concentration of the solute within the micro-solution droplets increases. Considering a uniform temperature within the micro-solution droplets, with no internal motion or circulation, the only transport equation that has to be considered within the micro-solution droplets is the spherically symmetric mass conservation of solvent, i.e., water, written as follows:

$$\frac{\partial Y_{\mathrm{m}}}{\partial t} - \frac{1}{\rho_{\mathrm{m}} r^2} \frac{\partial}{\partial r}\left(r^2 \rho_{\mathrm{m}} D_{\mathrm{m}} \frac{\partial Y_{\mathrm{m}}}{\partial r}\right) = 0 \tag{40.27}$$

The transformation proposed by Van Der Lijn [16] is used to simplify(40.27) for the time varying droplet radius [7]:

$$y = \frac{z}{z_0} = \frac{\int_0^r 4\pi r^2 \rho_{\mathrm{m}} Y_{\mathrm{ms}} \mathrm{d}r}{\int_0^{R_{\mathrm{m}}} 4\pi r^2 \rho_{\mathrm{m}} Y_{\mathrm{ms}} \mathrm{d}r} \tag{40.28}$$

In (40.28), z_0 represents the total mass of the solute within a micro-solution droplet and z denotes the mass of the solute between the micro-solution droplet center and radius r. Although the droplet radius decreases with time, the magnitude of y remains between 0 and 1. A new variable w, representing the ratio of the mass fraction of the solvent, (W_1) to that of the solute, $(W_s = 1 - W_1)$ is introduced:

$$w = \frac{W_1}{1 - W_1} \tag{40.29}$$

Using (40.27)–(40.29), the diffusion equation is transformed to the following form:

$$\frac{\partial w}{\partial t} = \frac{16\pi^2}{z_0^2} \frac{\partial}{\partial y}\left(D_1 \left(\frac{\rho_1^2}{(1+w)^2}\right) r^4 \frac{\partial w}{\partial y}\right) \tag{40.30}$$

The initial conditions are:

$$W_0 = \frac{W_{l0}}{1 - W_{l0}}, \quad m = m_0, \quad R_m = R_{m0}, \quad T_s = T_0 \tag{40.31}$$

And the boundary conditions are:

$$\frac{\partial w}{\partial y} = 0 \quad \text{at } y = 0 \tag{40.32}$$

$$\frac{4\pi R^2 \rho_1^2 D_1}{z_0 (1+w)^2} \frac{\partial w}{\partial y} = \frac{1}{4\pi R_m^2} \dot{m} \varepsilon_W \quad \text{at } y = 1 \tag{40.33}$$

Using the variables w and y, one can show that the droplet radius is expressed as follows:

$$R_m^3 = \frac{3z_0}{4\pi} \int_0^1 \frac{1+w}{\rho_1} \mathrm{d}y \tag{40.34}$$

In (40.33), $\dot{m}$ is the evaporation rate of the emulsion droplet, obtained from (40.5).

The solution of the gas and liquid phase equations supplies parameters such as the droplet temperature, concentration profile within the micro-solution droplet, etc. These data may be used to predict the morphology of particles produced by the ECM.

Particle Evolution

While water and fuel vaporize, emulsion droplet and micro-solution droplets shrink; also the overall solute concentration within the micro-solution droplets increases. This eventually leads to the precipitation of solute within the micro-solution droplets, and the formation of particles. There is some space between micro-solution droplets, which are dispersed within the emulsion droplet. This space may vary with time. Vaporization and burning of emulsion droplets may lead to the occurrence of three hypothetical phenomena, as elaborated below and shown in Fig. 40.2. If during droplet combustion, the temperature of the emulsion droplet remains below the superheat limit of water and fuel, one of the following situations may occur: If prior to the complete drying of micro-solution droplets, the diameter of the emulsion droplet decreases rapidly so that some or all of the evaporating micro-solution droplets merge and form larger dispersed micro-solution droplets, particles larger than those expected to form from the single micro-solution droplets will form. In order to find a criterion for this phenomenon to occur, note that using some geometrical calculations, the maximum volume fraction of the spherical micro-solution droplets of the same size packed in a larger spherical emulsion droplet is 0.74. Therefore, one can readily show that the criterion for each two

micro-solution droplets to come in contact and consequently merge is obtained as follows:

$$R_{\mathrm{m}}^{\mathrm{CCS}} > \left(\frac{0.74}{n_0}\right)^{1/3} R^{\mathrm{CCS}} \tag{40.35}$$

where n_0 is the number of micro-solution droplets in the emulsion droplet at initial state. $R_{\mathrm{m}}^{\mathrm{CCS}}$ and R^{CCS} are the radii of micro-solution and emulsion droplets at the onset of solute precipitation on the surface of micro-solution droplets, respectively. For low concentration micro-solution droplets it is justified to assume that the volume of the micro-solution droplets is merely filled by water. Thus, n_0 is related to the initial radii of the emulsion droplet (R_0) and micro-solution droplets (R_{m0}) and the initial volume fraction of micro-solution droplets (ϕ_{10}), as follows:

$$n_0 = \phi_{10}\left(\frac{R_0}{R_{\mathrm{m0}}}\right)^3 \tag{40.36}$$

As the second scenario, if each individual micro-solution droplet, without merging with other neighboring droplets, forms a particle, then the burning of each emulsion droplet, results in the formation of n_0 particles whose sizes are proportional to the sizes of the original micro-solution droplets. These two particle formation mechanisms are illustrated in Fig. 40.2 (left and right branches of the figure).

If during the vaporization of water and burning of fuel, the emulsion droplet bulk temperature exceeds the superheat limit of water or fuel, bubble nucleation may take place within the droplet; this may subsequently cause microexplosion. Based on the thermodynamic approach of finding the superheat limit, the non-dimensional superheat temperature of a liquid at pressures smaller than the critical pressure is a linear function of pressure and is approximated as follows [17]:

$$\hat{T}_{\mathrm{L}} = \left(\frac{27}{32}\right)^{1/(n+1)} + \frac{1}{(n+1)8}\hat{P} \tag{40.37}$$

In (40.37), $\hat{T}_{\mathrm{L}}$ and $\hat{P}$ are liquid superheat temperature and pressure divided by their corresponding values at the critical state. The exponent n is a parameter having a value between 0 and 1, while $n = 0$ and 1 respectively estimate the lower and upper bounds of the superheat temperature. The superheat limit of water ranges from 550 to 580 K, which is consistent with the prediction of (40.37), when n is chosen between 0 and 1.

If an emulsion droplet undergoes microexplosion, while the suspended micro-solution droplets are not formed yet, then several smaller emulsion droplets will form. These secondary emulsion droplets probably contain smaller micro-solution droplets than the original ones. As a result of microexplosion, compared to the case where microexplosion is absent, smaller particles will form (see Fig. 40.2, middle branch).

Nomenclature

b	a diffusivity factor defined in (40.23)
B	heat transfer number
C_0	initial solution concentration, (M)
C_p	specific heat of the emulsion droplet, (J/(mol K))
$\bar{C}^0_{\mathrm{Pi}}$	mean specific heat of pure substance i (water or fuel), (J/(mol K))
D_{i}	mass diffusivity of vapor species in the gas phase in regions 1 and 2, (m^2/s) (D_1: solvent/fuel vapor diffusivity in air, D_2: binary diffusivity of oxygen and nitrogen)
D	mass diffusivity of micro-droplets in the emulsion droplet, (m^2/s)
D_{m}	mass diffusivity of solute in the micro-solution droplet, (m^2/s)
k_{i}	thermal conductivity of component i in the gas phase, (W/m K)
L, L_{W}, L_{F}	latent heat of vaporization of emulsion droplet, water and fuel, (J/kg)
Le_i	Lewis number of component i in the gas phase
H	effective latent heat of vaporization, (J/kg)
$\dot{m}$	droplet burning rate, (kg/s)
M	molarity of solution, (mol/L)
M_{F}	molecular weight of the fuel
n	an exponent between 0 and 1 in (40.37)
n_0	initial number of micro-solution droplets in an emulsion droplet
p_{b}	reference pressure for droplet boiling point, (Pa)
P_∞	ambient pressure, (Pa)
$\hat{P}_{\mathrm{L}}$	liquid ambient pressure divided by its critical pressure
Q	lower heat of combustion per unit mass of fuel, (J/kg)
Q_{L}	droplet heating rate, (W)
R	rdial coordinate system, (m)
r_{f}	flame front radius, (m)
R	emulsion droplet radius, (m)
R_{m}	micro-solution-droplets average radius, (m)
R_i	gas constant of component i of an emulsion droplet, (J/kg K)
R_0	initial emulsion droplet radius ($=d_0/2$), (m)
R_{m0}	initial radius of the micro-solution-droplets, (m)
RH	Relative humidity, (%)
t	time, (s)
T	emulsion droplet temperature, assumed uniform within the droplet $T = T_{\mathrm{s}}$, (K)
T_{bi}	boiling point of component i at the reference pressure p_{b}, (K)
T_{f}	flame-front temperature, (K)
T_{s}	droplet surface temperature, (K)
T_∞	ambient temperature, (K)
$\hat{T}_{\mathrm{L}}$	superheat temperature of a liquid divided by its critical temperature
V	mean mass radial velocity in the emulsion droplet, (m/s)
v_i	mass velocity of component i, (m/s)
w	ratio of mass fraction of solvent to mass fraction of solute, (40.29)
X_{Fs}	mole fraction of fuel on the surface of an emulsion droplet
X^0_{is}, X_{is}	equilibrium and actual mole fraction of component i on the droplet surface
y	variable defined in (40.28)
Y_{Fs}, Y_{Ws}	mass fraction of fuel and water on the surface of an emulsion droplet
Y_{m}	mass fraction of solvent inside suspended micro-solution droplets
Y_{m0}	initial mass fraction of solvent inside suspended micro-solution droplets
$Y_{\mathrm{O}\infty}$	oxygen mass fraction far from the droplet (= 0.232)

$Y_{W\infty}$ water mass fraction far from the droplet (= 0, if RH = 0)
Y_{ms} mass fraction of solute within the micro-solution droplets
Y_s mass fraction of water on the surface of emulsion droplet
z mass of solute present from the suspended micro-solution droplet center to a radius r, (kg)
z_0 total mass of solute in a suspended micro-solution droplet, (kg)

Greek

ε_F, ε_W mass fraction of vaporized fuel and water
ϕ_F, ϕ_W liquid-phase volumetric fraction of fuel and water
ρ_m, ρ density of the micro-solution droplet and emulsion droplet, respectively, (kg/m^3)
ρ_F, ρ_W density of fuel and water in an emulsion droplet in liquid phase, (kg/m^3)
ρ_1, ρ_2 density of gas phase in region 1 (radius less than r_f) and 2 (radius greater than r_f), (kg/m^3)
v_o stoichiometric mass ratio of oxygen to Fuel

Superscripts

^{CSS} at the onset of precipitation on the droplet surface

Subscripts

^{s} value of a variable at the droplet surface
^{i} denotes each component in an emulsion droplet, $i = 1, 2$ for water and fuel, respectively

References

1. T. T. Kodas, M. J. Hampden-Smith: Aerosol Processing of Materials, Wiley-VCH, New York, (1999).
2. M. Eslamian, M. Shekarriz: Recent advances in nanoparticle synthesis by spray and micro-emulsion methods, Recent Patents in Nanotechnology, 3(2), 99–115 (2009).
3. K. Takatori, T. Tani, N. Watanabe, N. Kamiya: Preparation and characterization of nano-structured ceramic powders synthesized by emulsion combustion method, Journal of Nano-particle Research, 1(2), 197–204 (1999).
4. T. Tani, N. Watanabe, K. Takatori: Emulsion combustion and flame spray synthesis of zinc oxide/silica particles, Journal of Nanoparticle Research 5(1–2), 39–46 (2003).
5. T. Tani, K. Takatori, N. Watanabe, N. Kamiya: Metal oxide powder synthesis by emulsion combustion method, Material Research Society 13(5), 1099–1102 (1998).
6. T. Tani, K. Takatori, N. Kamiya, US6004525A, (1999).
7. G. V. Jayanthi, S. C. Zhang, G. L. Messing: Modeling of solid particle formation during solution aerosol thermolysis, Aerosol Science and Technology 19, 478–490 (1993).
8. M. Eslamian, M. Ahmed, N. Ashgriz: Modeling of nanoparticle formation during spray pyrolysis, Nanotechnology 17, 1674–1685 (2006).
9. M. Eslamian, M. Ahmed, N. Ashgriz: Modeling of solution droplet evaporation and particle evolution in droplet-to-particle spray methods, Drying Technology 27(3), 3–13, (2009).

10. M. Eslamian, N. Ashgriz: The effect of pressure on the crystallinity and morphology of powders prepared by spray pyrolysis, Powder Technology 167, 149–159 (2006).
11. N. Jakic, J. Gregory, M. Eslamian, N. Ashgriz: Effect of impurities on the characteristics of metal oxides produced by spray pyrolysis, Journal of Materials Science 44(8), 1977–1986 (2009).
12. A. Chau, M. Eslamian, N. Ashgriz: On production of non-disrupted particles by spray pyrolysis, Particle & Particle Systems Characterization 25, 183–191 (2008).
13. M. C. Heine, S. E. Pratsinis: Droplet and particle dynamics during flame spray synthesis of nanoparticles, Industrial Engineering Chemical Research 44, 6222–6232 (2005).
14. L.F.T. Leite, P.L.C. Lage: Modeling of emulsion droplet vaporization and combustion including microexplosion analysis, Combustion Science and Technology 157, 213–242 (2000).
15. R. B. Bird, W. E. Stewart, E. N. Lightfoot, Transport Phenomena, 2nd edition, John Wiley, New York (2002).
16. J. Van der Lijn, Agricultural Res. Report No. 845, (1976).
17. C. K. Law, A model for the combustion of oil/water emulsion droplets, Combustion Science and Technology 17(1), 29–38 (1997).

Chapter 41
Pharmaceutical Aerosol Sprays for Drug Delivery to the Lungs

W.H. Finlay

Abstract Respiratory illnesses are commonly treated with drugs delivered to the lungs as an inhaled aerosol. The inhaled aerosol route sometimes offers advantages over other routes such as injection or oral delivery. These advantages include rapid and predictable onset of action of drug, decreased adverse reactions, as well as safe and convenient delivery. However, the design of a device and formulation for reliable delivery of a pharmaceutical compound as an inhaled aerosol is more difficult than most other delivery routes. This is because of the need to transform the active ingredient into an aerosol having particle sizes of a few micrometers in diameter that is then supplied to the patient's mouth upon inhalation. Devices that can create sprays with particles in the micrometer size range, but which remain portable, inexpensive to manufacture, easy to use by patients, and are robust enough to withstand patient use, are relatively few in design. Indeed, at present only four basic spray production mechanisms are currently in use on the clinical market for drug delivery to the lungs: pressurized release of a volatile propellant, colliding liquid jets, air-blast atomization and high frequency vibration methods. While other methods have undergone development (e.g., Rayleigh breakup of an extruded liquid jet [1]; high voltage electrosprays [2]), they have not yet reached market release. In the following we consider the four clinically available methods.

Keywords Medical aerosols · Metered dose inhaler · Nebulizer · Pharmaceutical aerosols · Respiratory drug delivery

W.H. Finlay
Department of Mechanical Engineering, University of Alberta, Canada
e-mail: Warren.Finlay@ualberta.ca

N. Ashgriz (ed.), *Handbook of Atomization and Sprays*,
DOI 10.1007/978-1-4419-7264-4_41, © Springer Science+Business Media, LLC 2011

Pressurized Release of Volatile Propellant

Release of a volatile propellant is the spray production mechanism used in so-called pressurized meter dose inhalers, or pMDIs. These are the most common devices used to deliver aerosols in the treatment of respiratory diseases. Several hundred million pMDIs are sold to patients annually worldwide. Their basic operation has remained relatively unchanged since their first major commercial appearance in 1956. Current devices normally consist of a multidose, small volume canister that contains pressurized hydrofluoralkane (HFA) propellant, usually HFA 134, or less commonly, HFA 227, in a saturated liquid-vapor state. Older devices used CFC propellants, but these have been replaced with HFA propellants in most countries due to ozone depletion concerns. Within the liquid propellant in the canister, drug is either suspended colloidally as micrometer diameter particles, or less frequently, dissolved in the propellant. The drug–propellant mixture typically contains less than a few percent drug by volume. Upon actuation by the patient, a valve opens and releases a single metered dose (usually less than a few hundred microliters in volume) of drug–propellant mixture from a metering chamber. Since the vapor pressure of the propellant is several atmospheres at room temperature, the drug–propellant mixture rapidly exits the device through an expansion chamber and nozzle to the surrounding atmospheric pressure environment, as depicted schematically in Fig. 41.1.

The release of the propellant from the metering chamber results in a transient spray production process that has only recently been confirmed experimentally [4]. While the nature of the spray is transient and varies during the few hundred millisecond release period [5], the major part of the spray event is thought to be

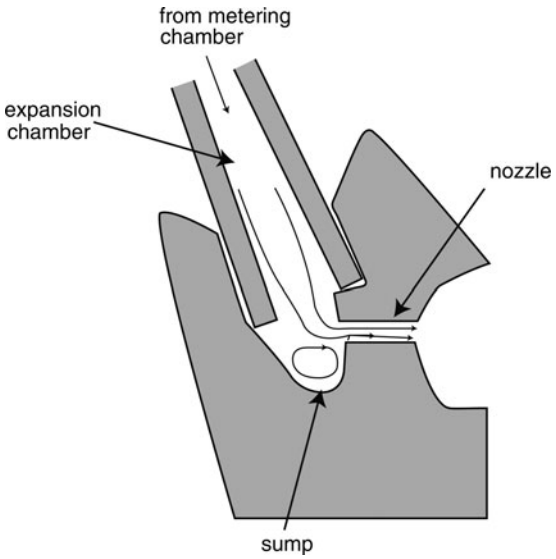


Fig. 41.1 Enlarged view of the expansion chamber and nozzle region in a typical pMDI. (From [3] with permission)

the result of flashing near the nozzle exit. This spray is inhaled into the patient's mouth, and has a very low droplet volume fraction and relatively high velocity [3, 5, 6]. The spray droplets subsequently undergo transient droplet size changes downstream of their release from the nozzle exit [6–8]. Since the wet bulb temperature of the droplets is well below typical ambient temperatures, this evaporation is largely controlled by the rate of heat transfer from the ambient environment [3]. However, the presence of water vapor, either via inhaled atmospheric air or mass transfer from the respiratory tract airways, complicates droplet size changes. In particular, droplet evaporation immediately downstream of the nozzle exit can be followed by transient particle growth due to condensation of water vapor onto the cold aerosol particles [9].

The main spray production process is characterized by high frequency pulsing [4, 6, 10] whereby the spray density oscillates between lean and dense states with a period of about a millisecond, possibly due to timescales associated with bubble growth in recirculation regions in a vena contract that leads to periodic flushing of the nozzle [11].

As the metering chamber empties and cools during its discharge, less vaporization of propellant occurs in the expansion chamber and nozzle, leading to larger droplet sizes [3, 11] in the later stages of the spray duration.

The sprays from pMDIs also have spatial droplet size variations in the crossflow directions, typified by larger droplets near the outer edges of the spray. Previous work [4] indicates that these larger droplets are formed from annular liquid propellant films accumulating on the nozzle surface.

While the sprays produced by pMDIs are highly transient and complex, they remain one of the most successful methods of delivering aerosols for respiratory drug delivery.

The basic design of a pMDI relies on the high vapor pressure of the propellants at room temperature to allow spray production. However, the propellants used with pMDIs are nonaqueous and therefore present challenges to the delivery of aqueous drug formulations. Since the vapor pressure of water at room temperature is too low to allow flash spray production under normal ambient conditions, other approaches must be used to create aqueous sprays, to which we now turn.

Colliding Liquid Jets

One approach to producing aqueous sprays, used in the Respimat inhaler, is to collide two narrow jets of liquid water at an angle to each other, as shown in Fig. 41.2. The streams exit a high pressure reservoir through nozzles and the resulting collisional stream breakup creates a water spray. The active therapeutic ingredient is dissolved in the water that is supplied to the nozzles, and is contained in solution in the spray droplets.

In order to achieve droplet sizes appropriate for lung delivery, the diameter of each colliding liquid jet must be exceedingly small. This is achieved by creating the

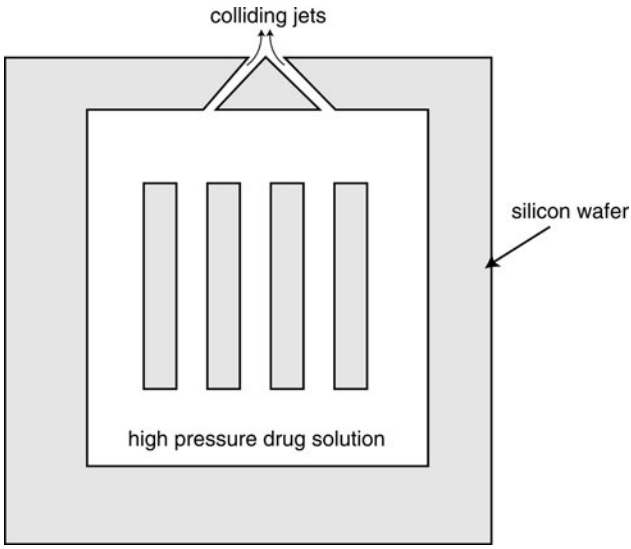


Fig. 41.2 Schematic of a single colliding jet nozzle, after [12], etched on a silicon wafer

jets using nozzles typically on the order of 10 μm in diameter [12], manufactured using silicon wafer electronic chip etching methods. Pressure gradients through such small diameter channels are very large at the required flow rates, so that reservoir pressures of hundreds of atmospheres are needed to generate the flow [13]. These high pressures are supplied by a spring-driven piston [14]. The collision of the jets occurs several diameters downstream of the nozzle exits [15]. Little published fundamental research exists on the spray breakup process, at least in part due to the active state of patents and marketing of this device.

Metered volumes of liquid are similar to those used with pMDIs, i.e., around a 100 μL. Volume flow rates through a single nozzle are not sufficient to deliver such liquid volumes during a single breath, and instead the metered volume flows in parallel through about 1,000 identical nozzles to generate the inhaled spray cloud.

This spray production process can of course be applied to nonvolatile liquid carriers other than water, and indeed has been used to deliver drugs dissolved in ethanol [12].

Both pMDIs and the Respimat require the drug to be sealed in high pressure canisters that require specialized filling equipment and manufacturing procedures. Other spray production devices must be used if it is desired that the patient or health-care worker instead load the drug into the device themselves.

Air-blast Atomization

The most common device in which the patient loads the drug immediately prior to use is the jet nebulizer, which operates by blasting air, supplied either from a portable compressor or a wall line (e.g., in hospital setting), through a liquid

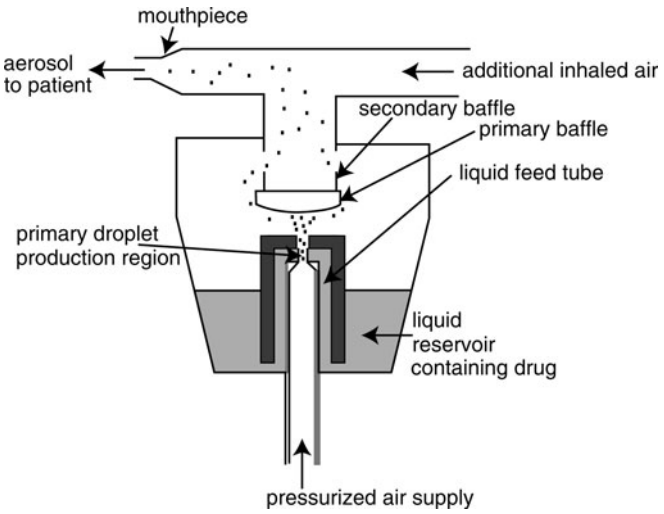


Fig. 41.3 Schematic of a jet nebulizer. (From [3] with permission)

reservoir in which the drug is dissolved or colloidally suspended, as shown in Fig. 41.3.

In a typical design, a converging nozzle accelerates the air to high speed. This air then flows across water in the primary droplet production region, which induces viscosity-induced instabilities at the air–water interface whose subsequent nonlinear growth leads to primary production of droplets [3]. These droplets are too large for inhalation into the lungs. Instead, they are entrained in the high speed airflow downstream of the nozzle and impact on a primary baffle, from which splashing occurs, resulting in the production of droplets with smaller sizes. Secondary baffles obstruct the flow on its way to the mouthpiece and cause further size reduction by inertial impaction of droplets which then return to the reservoir for subsequent reaerosolization.

The air entering the nebulizer is normally not humidified, and the large concentration of aerosol water droplets circulating in the device results in rapid two-way coupled mass transfer that causes droplet evaporation and humidification of the air. The latent heat associated with this evaporative mass transfer causes cooling of the liquid in the reservoir over time, and the humidification of the compressed air increases the concentration of the drug in the nebulizer reservoir over time [3, 16].

Delivery volumes with jet nebulizers are larger than with the other devices considered earlier, typically being several milliliters. Delivering such large volumes naturally requires more time. Unlike pMDIs or the Respimat, jet nebulizers are thus not single breath devices but require patients to breathe tidally for at least several minutes to complete a single treatment.

Because loading of the device with drug requires merely pouring an aqueous formulation into the reservoir, off-label use of jet nebulizers is common. Jet nebulizers are also the oldest modern aerosol delivery device for lung delivery [17].

For these reasons, they have delivered the widest variety of therapeutic compounds of any of the spray delivery devices and are commonly used in early research and development. It should be noted however, that liposomal formulations and large drug molecules may suffer degradation in a jet nebulizer, apparently due to mechanical forces in the droplet production process [18, 19]. In addition, delivery rate decreases with increases in viscosity, such that highly viscous liquids may not be amenable to jet nebulization [20]. Finally, many different variations in the design of the primary and secondary droplet production regions has resulted in a plethora of commercially available jet nebulizers that sometimes have considerable variations in lung delivery among them [21].

The need for a compressed air source with jet nebulizers makes them less transportable. An alternative approach to creating aqueous sprays, without resorting to high pressures as in the Respimat, is to use high frequency vibration, to which we now turn.

High Frequency Vibration

A number of different ways to create sprays of aqueous formulations for inhalation have been developed by relying on high frequency vibration of a solid surface. The oldest such approach, sometimes referred to as ultrasonic nebulization, relies on the vibration of a piezoelectric crystal immersed in a liquid to create pressure waves within a liquid reservoir. These pressure waves induce capillary waves at the air–liquid interface of the reservoir, possibly enhanced by vibrating cavitation bubbles, whose nonlinear growth leads to droplet formation [22]. It should be noted that heating of the liquid in the device can lead to denaturation of large molecules [23]. In addition, drugs formulated as suspensions are not well suited to delivery with this approach since the suspended particles may be preferentially retained in the device [24]. Also, device failure can occur with highly viscous liquids [20]. These disadvantages, as well as the relatively high cost of traditional ultrasonic nebulizers compared to jet nebulizers, have resulted in this method of spray production achieving relatively narrow market penetration.

More recently, several new devices have appeared on the market that rely instead on high frequency oscillatory flow though small openings in a plate or mesh containing a few hundred or thousand openings with dimensions of a few micrometers. This approach typically results in lower leftover (residual) volumes compared with jet or traditional ultrasonic nebulizers, allowing higher efficiency, as well as the possibility of delivering smaller drug volumes. In some of these devices, the mesh is stationary (i.e., passive), and a piezo-vibrator is used to push liquid through the mesh (e.g., the Respironics I-neb device). Each motion of the piezo-vibrator extrudes a set of droplets through the mesh. Droplet sizes with current realizations of this approach are somewhat larger than the other methods considered so far [25, 26].

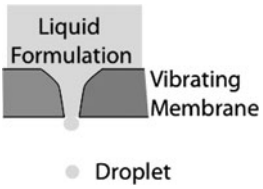


Fig. 41.4 Droplet production from one hole of many hundreds in a vibrating membrane nebulizer is shown schematically

By instead creating the droplets by vibrating an "active" membrane having liquid on one side, with the membrane covered in holes a few micrometers in diameter, devices producing smaller droplets have been realized [25, 27, 28]. Hole shape is important in the successful operation of this approach, with the holes normally being tapered, with larger diameter on the liquid supply side and narrowest diameter at the droplet release side (see Fig. 41.4).

The Pari eFlow nebulizer and AeroGen's nebulizers use this method of spray production. As with all nebulizers discussed so far, these devices can aerosolize several milliliters of formulation. However, spray densities are typically higher than with jet nebulizers, so that delivery times with vibrating plate nebulizers are typically lower than with jet nebulizers [29].

As with other types of nebulizers, some liposomal formulations may suffer degradation with vibrating mesh/plate nebulizers [30] but this is formulation dependent. Similarly, spray production may not be possible for highly viscous liquids [25], while clogging of the mesh/membrane openings after extended use may occur [31].

Because of the active state of patents arising from vibrating membrane nebulizers, fundamental studies examining their spray production process have not been well represented in the published archival literature.

Summary

While many different approaches exist to deliver aerosols to the lungs, the most commonly used device is the pMDI, which uses flash evaporation of a pressurized propellant to produce a spray containing the active pharmaceutical ingredient. For drugs requiring an aqueous formulation, other devices are preferable, with several different spray production methods being in use. None of these share the prevalence of the pMDI, but each has its attractions. The use of colliding liquid jets allows a compact, portable device to be achieved in the Respimat. Both pMDIs and the Respimat deliver relatively small doses and so are restricted to potent therapeutics. Use of air-blast atomization in jet nebulizers allows larger drug volumes that can be loaded by the patient, but requires a source of pressurized air, thereby reducing portability. The use instead of piezoelectric nebulizers, where high frequency vibration of mechanical surfaces induce droplet formation, allows delivery

of similar drug volumes as jet nebulizers, but with more portability. Recent use of piezo-driven vibrating membranes has allowed much smaller volumes to be delivered than with traditional ultrasonic nebulizers and has renewed this market segment. While each of these spray production methods has its advantages and disadvantages, all are used clinically to successfully treat diseases by aerosol administration to the lungs.

References

1. Ward, M. E., Woodhouse, A., Mather, L. E., Farr, S. J., Okikawa, J. K., Lloyd, P., Schuster, J. A., and Rubsamen, R. M. 1997. Morphine pharmacokinetics after pulmonary administration from a novel aerosol delivery system, Clin. Pharm. Ther. 62:596–609.
2. Meesters, G. M. H., Vercoulen, P. H. W., Marijnissen, J. C. M., and Scarlett, B. 1992. Generation of micron-sized droplets from the Taylor cone, J. Aerosol Sci. 23:37–49.
3. Finlay, W. H. 2001. *Mechanics of Inhaled Pharmaceutical Aerosols: An Introduction*. Academic. London
4. Versteeg, H. K., Hargrave, G. K., and Kirby, M. 2006. Internal flow and near-orifice spray visualisation of a model pharmaceutical pressurized metered dose inhaler, J. Phys. (Conf. Ser.) 45:207–213.
5. Crosland, B. M., Johnson, M. R. J., and Matida, E. A. 2009. Characterization of the spray velocities from a pressurized metered-dose inhaler, J. Aerosol Med. Pulm. Drug. Del. 22:85097.
6. Dunbar, C. A., Watkins, A. P., and Miller, J. F. 1997. An experimental investigation of the spray issued from a pMDI using laser diagnostic techniques, J. Aerosol Med. 10:351–268.
7. Clark, A. R. 1996. MDIs: physics of aerosol formation, J. Aerosol Med. 9S:19–26.
8. Kleinstreuer, C., Shi, H., and Zhang, Z. 2006. Computational analyses of a pressurized metered dose inhaler and a new drug-aerosol targeting methodology, J. Aerosol Med. 20:294–309.
9. Martin, A. R. and Finlay, W. H. The effect of humidity on particle sizing from metered-dose inhalers, Aerosol Sci. Technol. 39:283–289, 2005.
10. Domnick, J. and Durst, F. 1995. Measurement of bubble size, velocity and concentration in flashing flow behind a sudden constriction, Int. J. Multiphase Flow 21:1047–1062.
11. Dunbar, C. A., Watkins, A. P., and Miller, J. F. 1997. Theoretical investigation of the spray from a metered-dose inhaler. Atom. Sprays 7:417–436.
12. Zierenberg, B., Eicher, J., Dunne, S., and Freund, B. 1996. Boehringer Ingelheim nebulizer BINEB a new approach to inhalation therapy. In R. N. Dalby, P. R. Byron, and S. J. Farr, eds., Proceedings of Respiratory Drug Delivery V. Interpharm Press, Buffalo Grove, pp. 187–193.
13. Bartels, F., Bachtler, W., Dunne, S. T., Eicher, J., Freund, B., Hart, W. B., and Lessmoellmann, C. 1999. Atomizing nozzle and filter and spray generating device, US Patent 6007676.
14. Jaeger, J., Cirillo, P., Eicher, J., Geser, J., Freund, B., and Zierenberg, B. 2005. Device for producing high pressure in a fluid in miniature, US patent 69185467.
15. Zierenberg, B. 1999. Optimizing the in vitro performance of Respimat, J. Aerosol Med. 12: S19–S24.
16. Mercer, T. T., Tillery, M. I., and Chow, H. Y. 1968. Operating characteristics of some compressed-air nebulizers, Am. Ind. Hyg. J. 29:66–78.
17. Dessanges, J.-F. 2001. A history of nebulization, J. Aerosol Med. 14:65–71.
18. Niven, R. W., Speer, M., Schreier, H. 1991. Nebulization of liposomes II. The effects of size and modelling of solute release profiles, Pharm. Res. 8:217–221.

19. Lentz, Y. K., Worden, L. R., Anchordoquy, T. J., and Lengsfeld, C. S. 2005. Effect of jet nebulization on DNA: identifying the dominant degradation mechanism and mitigation methods, J. Aerosol Sci. 36:973–990.
20. Finlay, W. H., Lange, C. F., King, M., and Speert, D. 2000. Lung delivery of aerosolized dextran, Am. J. Resp. Crit. Care Med. 161:91–97.
21. Finlay, W. H., Stapleton, K. W., and Zuberbuhler, P. 1998. Variations in predicted regional lung deposition of salbutamol sulphate between 19 nebulizer models, J. Aerosol Med. 11: 65–80.
22. Topp, M. 1973. Ultrasonic atomization – a photographic study of the mechanism of disintegration, J. Aerosol Sci. 4:17–25.
23. Cipolla, D. C., Clark, A. R., Chan, H. K., Gonda, I., and Shire, S. J. 1994. Assessment of aerosol delivery systems for recombinant human deoxyribonuclease, STP Pharm. Sci. 4: 50–62.
24. Nikander, K., Turpeinen, M., and Wollmer, P. 1999. The conventional ultrasonic nebulizer proved inefficient in nebulizing a suspension, J. Aerosol Med. 12:47–53.
25. Ghazanfari, T., Elhissi, A. M. A., Ding, Z., and Taylor, K. M. G. 2007. The influence of fluid physicochemical properties on vibrating-mesh nebulization, Int. J. Pharm. 339:103–111.
26. Knoch, M. and Finlay, W. H. 2008. Nebulizer technologies. In Modified-Release Drug Delivery Technology, 2nd edn., ed. M. J. Rathbone, Marcel Dekker, pp. 613–622, Chap. 45.
27. Lass, J. S., Sant, A., and Knoch, M. 2006. New advances in aerosolised drug delivery: vibrating membrane nebuliser technology, Exp. Op. Drug Del. 3:693–702.
28. Zhang, G., Anand, D., and Wiedmann, T. S. 2007. Performance of the vibrating membrane aerosol generation device: aeroneb micropump nebulizer, J. Aerosol Med. 20:408–416.
29. Knoch, M. and Keller, M. 2005. The customised electronic nebuliser: a new category of liquid aerosol drug delivery systems, Exp. Op. Drug Del. 2:377–390.
30. Elhissi, A. M. A., Faizi, M., Naji, W. F., Gill, H. S., and Taylor, K. M. G. 2007. Physical stability and aerosol properties of liposomes delivered using an air-jet nebulizer and a novel micropump device with large mesh apertures, Int. J. Pharm. 334:62–70.
31. Rottier, B. L., van Erp, C. J. P., Sluyter, T. S., Heijerman, H. G. M., Frijlink, H. W. F., and de Boer, A. H. 2009. Changes in performance of the Pari eFlow® rapid and Pari LC Plus™ during 6 months use by CF patients, J. Aerosol Med. Pulm. Drug Del., ahead of print. doi:10.1089/jamp.2008.0712.

Chapter 42
Fire Suppression

C. Presser and J.C. Yang

Abstract Water sprinkler sprays (with relatively large droplet sizes) in residential and commercial structures are probably the most well-known application of sprays in fire suppression. In more recent years, water mists (characterized by reduced droplet sizes, which may contain additives) have been considered as a replacement for Halon 1301, the most common fire suppressant chemical aboard aircraft and ships, but banned as an ozone-depleting chemical by the Montreal Protocol in 1987. Much research has focused on characterizing the liquid discharge from agent storage bottles, spray transport in various obstructed environments, agent suppression of liquid-fueled, spray-type fires, and determination of the effectiveness of various liquid and powdered chemicals (with respect to gaseous agents) to extinguish a flame in well-controlled experimental facilities. Research during the past two decades to characterize liquid and powdered sprays may find sprays appealing alternatives to environmentally harmful gaseous agents in the near future, if properly engineered.

Keywords Fire suppression · Flame extinguishment · Flame suppression screens · Flash vaporized sprays · Spray transport · Sprinklers · Water mists

Introduction

A fire suppressant agent derives its effectiveness by extinguishing a burning surface through chemical, thermal, and physical mechanisms. Chemical mechanisms relate to an agent's ability to alter the radical pool that sustains combustion. Physical mechanisms remove fuel, oxygen, or heat by physical interactions (e.g., wetting a surface with agent to form a barrier between the surface and ambient, or by suppressant entrainment and dilution of the surrounding gases to strain the flame). Thermal

C. Presser (✉)
National Institute of Standards and Technology, 100 Bureau Dr., Stop 8320, Gaithersburg, MD 20899-8320, USA
e-mail: cpresser@nist.gov

N. Ashgriz (ed.), *Handbook of Atomization and Sprays*
DOI 10.1007/978-1-4419-7264-4_42, © Springer Science+Business Media, LLC 2011

mechanisms relate to heat extraction, which results in cooling of the flame until combustion can no longer be sustained or re-ignited.

Traditionally gaseous agents (in particular, bromotrifluoromethane, CF_3Br, Halon 1301) have served as suppressants on aircraft and ships due to their light weight and effectiveness to extinguish fires, while water sprays have been used for commercial and residential structures. As a result of the Montreal Protocol in 1987 (Chap. 1 [1]) and the banning of many ozone-depleting halogenated hydrocarbons (e.g., fluorocarbons, hydrofluorocarbons, and hydrochlorofluorocarbons), the use of liquid and powdered sprays have been considered as Halon replacements for extinguishment of different fire scenarios. Unlike gaseous agents, the suppression effectiveness (i.e., ratio of an agent mass fraction to the equivalent value of Halon 1301 at flame suppression) of liquid and powdered agents depends on the dynamics of the droplets/particles in a given flow arrangement [2]. Thus, physical processes such as spray release rate, dispersion, mixing, and vaporization become important parameters in assessing an agent's fire suppression effectiveness (Chapter 11 [3]).

Halon 1301 has been successfully applied to various system platforms, including aircraft nacelles (regions between the jet engine and engine shroud), aircraft dry bays (closed spaces adjacent to flammable fuel storage areas), shipboard machinery spaces, and computer facilities. Requirements for flame detection and suppression in engine nacelles and aircraft dry bays are on the order of seconds and tens of milliseconds, respectively (Section 1 [4]). For example, nacelle fires pose a significant challenge for suppression owing to the presence of electrical wiring, fuel and hydraulic lines, ribs, and other objects (e.g., mounting brackets), see Fig. 42.1, which can obstruct transport of a suppression agent to the fire (e.g., ignited spray from a broken fuel line, or flame from a puddle of fuel), and hot surfaces can re-ignite after suppression (Chapter 9 [3]). Also, aircraft pressurized fuel, lubricant, and hydraulic line leaks can provide fuel to stabilize a fire behind an obstacle in an engine nacelle, or an aerosol of volatile fuel from a punctured fuel tank in a dry bay area [5]. Thus, candidate Halon replacement agents have been identified and their applicability investigated through several research and development programs [1, 3, 4] to enable future operation of various

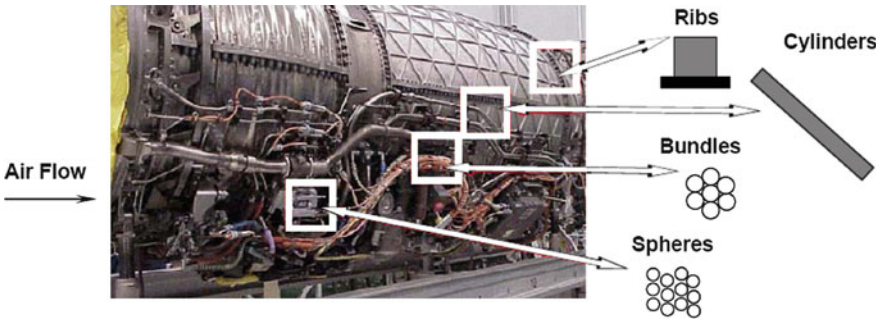


Fig. 42.1 Types of obstruction present in an engine nacelle [1]

platforms. The following article summarizes the association of droplets, particles, and sprays in fire suppression, in particular with regard to droplet formation and transport from pressurized storage bottles, suppression of spray flames by gaseous agents, and extinguishment of fires by liquid and powdered agents with fire suppression screens.

Flash Vaporized Sprays

A fire suppression storage bottle containing an agent requires nitrogen pressurization to typically 4.2 MPa at ambient temperature to ensure sufficient internal pressure to rapidly discharge the agent. Flash vaporization occurs when the superheated agent (stored at an ambient temperature above the agent normal boiling point) is released from the bottle and depressurized to the ambient pressure, resulting in the discharge of gas and liquid spray (see example in Fig. 42.2). If the bottle is exposed to ambient temperatures below the agent normal boiling point, the suppressant is no longer superheated, and de-gassing of dissolved nitrogen (as bubbles) from depressurization plays a role in the breakup of the liquid. Thus, liquid will vaporize completely over a short distance downstream from the discharge point if superheated, or remain as liquid for a longer period of time if the ambient temperature is below the agent normal boiling point. The higher the liquid is superheated, the more pronounced is the flashing to facilitate the breakup and dispersion of the discharged liquid. Transient high-momentum flashing sprays travelling at an average speed of more than 50 m/s during agent discharge have been observed using laser extinction techniques (Section 3 [4]). As an example of the spray penetration for different gaseous agents, Fig. 42.3 presents the decay in average streamwise velocity with downstream distance under standard discharge conditions. The discharge orientation, initial conditions (temperature, concentration, and nitrogen pressurization) of the bottle, suppression agent thermophysical properties, degree of nitrogen saturation in the liquid agent, discharge orifice size and release rate, and ambient conditions are important governing parameters that determine the highly transient flashing spray characteristics and the degree of dispersion, mixing, and evaporation.

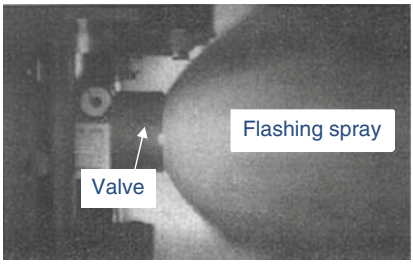


Fig. 42.2 Flash vaporizing spray of pentafluoroethane (HFC-125) [3]

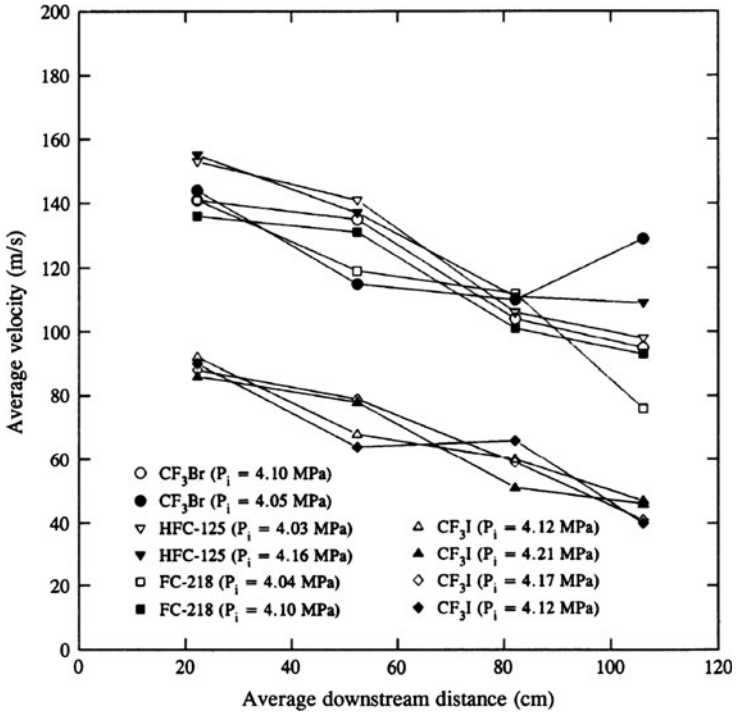


Fig. 42.3 Average streamwise velocity with streamwise position (Z) for different chemical agents during a standard discharge. P_i is the initial bottle pressure [3]

A twofold increase in discharge pressure has been found to decrease the emptying time by half (Chapter 8 [3], Section 3 [4]). A twofold increase in the orifice diameter increases the volumetric flow rate by four. Changing the orientation of the discharge bottle influences the discharge process significantly, depending on the agent's boiling point. If the bottle orientation is such that the gas is released before the liquid then the release time increases, and dispersion and evaporation are degraded. Ranking of agents has indicated that higher boiling point agents are not suitable for rapid flame suppression (i.e., when compared to Halon 1301). Lower boiling point agents have stronger flashing behavior and higher vaporization rates, which results in a different mixing behavior than that of Halon 1301. Agent dispersion and vaporization are effective due to the agent's lower boiling point and higher Jakob number (i.e., estimated fraction of a superheated liquid that can be vaporized adiabatically). Higher superheat temperatures result in more pronounced flashing with better agent acceleration, dispersion, and mixing. Average discharge velocities are reduced and the spray angle decreased when the agent temperature is below that of the ambient. Numerical simulation of flashing sprays discharged into confined spaces for varying initial droplet mean size has indicated that spray shape and penetration are influenced by a variety of parameters (Chapter 12 [3]). Penetration of the spray is decreased when the enclosure surrounding the injector is reduced in size. Dispersion is improved for

smaller droplet mean diameters at the injection inlet, and higher ambient temperatures. Droplet vaporization is enhanced for higher injection gas velocities. Discharged spray will also disperse over a longer period of time (forming a wider spray angle and having greater penetration) for agents with a lower Jakob number (i.e., less intense flash vaporization).

Flame Suppression Screens Involving Droplets, Particles, and Sprays

The use of screens provides a means to compare and rank the suppression effectiveness of potential agents under controlled and simplified conditions (Chapters 4 and 6 [1]). Screening apparatus are used generally to evaluate gaseous agents or pre-vaporized liquids. With increased interest in liquid and powdered chemicals, special screens are required that can assess the suppression effectiveness for both gaseous- and liquid-fueled flames. Examples of screens include opposed-flow (fuel and oxidizer flowing toward the flame zone from opposing sides) and coflow (fuel and oxidizer flowing in the same direction) diffusion flame configurations (Section 4 [4]). The important feature of laminar opposed-flow (or counterflow) diffusion flames is that flow residence time is accurately controlled to study finite-rate chemistry effects without the added complication of turbulence [6]. Fuels can be gaseous, liquid, or solid, and agents (entrained in the oxidizer stream) can be liquid droplets or powdered particles. As agent concentration increases, a flame strain rate is reached for which the flame can no longer be sustained. Depending on the burner configuration, flame strain rate is a parameter relating the oxidizer flow velocity and the separation distance between the fuel and oxidizer outlets, or a characteristic burner dimension [6]. The ranking of an agent's suppression effectiveness is based on the comparison of the agent concentration at the same extinction strain rate. In one recent study, Yang et al. [7] developed a counterflow screen arrangement for liquid agents, in which a propane-fueled cylindrical porous burner was operated within a wind tunnel [6]. A spray of liquid agent was introduced into the wind tunnel using a nebulizer located upstream of the burner to suppress the flame that was established at the cylinder forward stagnation point. Liquid agents tested included water with and without additives, skim milk, and other novel liquid fire suppressants, some of which could only be synthesized in small quantities. Powders could also be investigated with the design of an appropriate delivery system [8]. An example of coflow systems is the cup burner configuration for which a laminar flow of a gaseous agent, vaporizing droplets, or powdered particles entrained in a carrier gas, coflows around a small Pyrex cup burner using gaseous or liquid fuel (Section 4 [4]). As the agent concentration is increased, a critical value is reached for which the flame is extinguished. The advantage of this screen is that it is not too sensitive to small changes in the apparatus and compares well with full-scale test results [9].

More complex scenarios have been studied in the form of turbulent spray flames and pool fires, which are representative fires found in engine nacelles. Studies

carried out with halogenated hydrocarbons (e.g., fluorocarbons, hydrofluorocarbons, hydrochlorofluorocarbons, and inert gases) in a turbulent, baffle-stabilized spray flame (Section 4 [4]) have led to a ranking of agents according to suppression effectiveness. Discrete amounts of agent are injected and entrained into the air stream surrounding the fuel injector (the fuel being JP-8 or hydraulic fluid), as illustrated in Fig. 42.4. As the concentration of the gaseous agent increases with subsequent injections, a critical value is reached that extinguishes the flame. The agent average concentration is estimated by monitoring the gas temperature and pressure change in the storage vessel over the injection interval, and calculating the mass delivered. As an example, Fig. 42.5 presents the agent mass required to extinguish the flame after being injected over a controlled interval of time for different agents (i.e., extinction will occur above the indicated mass, and the flame will remain stable below this mass). As the time interval increases, more mass is required to suppress the flame (with the limit being the continuous flow situation) because of the decrease in agent delivery rate into the recirculation region downstream of the baffle. Extinction will depend on agent entrainment and an increased agent mole fraction in the recirculation region. For the baffle-stabilized spray flame, which was operated under a variety of conditions [5, 10, 11], results indicated that when compared to Halon 1301 twice the mass and volume of the gaseous agents tested were needed for flame extinguishment. Also, suppression was more difficult when the air was preheated. Figure 42.6 provides an example of the ranking of different agents (in order of increasing agent boiling point) for both

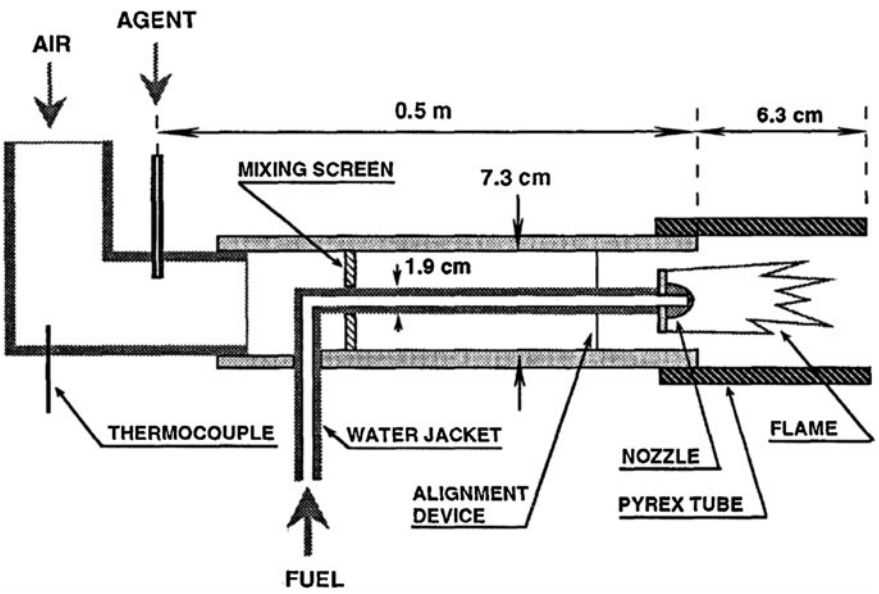


Fig. 42.4 Turbulent-jet spray burner used to examine flame suppression by different chemical agents [3]

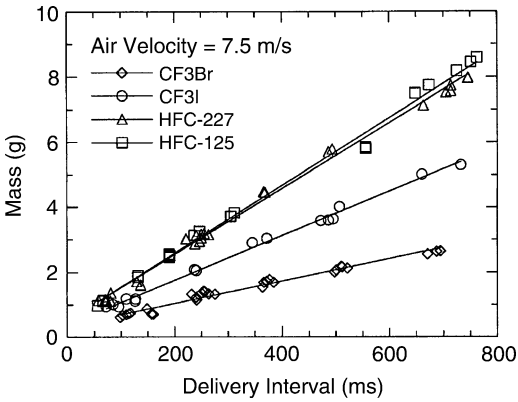


Fig. 42.5 Agent mass required for extinction of the spray flame with respect to delivery interval [3]

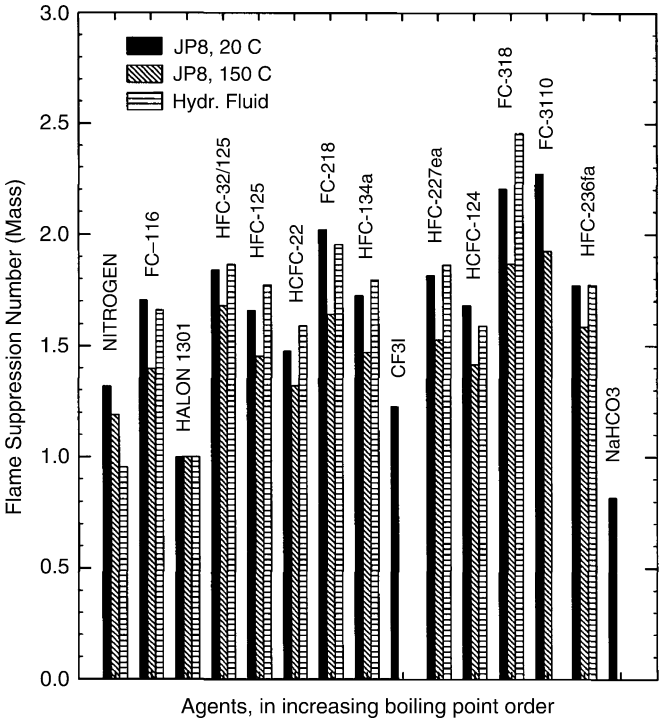


Fig. 42.6 Flame suppression number for different chemical agents [4]

JP-8 and hydraulic fluid sprays flames. The ranking is given in terms of a flame suppression number (on a mass basis), which is defined as the mass of agent relative to the mass of Halon 1301 needed to suppress an equivalent flame. Note that sodium bicarbonate powder ($NaHCO_3$) was as effective a suppressant as Halon 1301 (to be discussed further in the section 'Powders').

Suppression by gaseous agents of a baffle-stabilized (or backward-facing step) pool fire has been investigated for a variety of operating conditions including different air flows and baffle heights, which were placed upstream of the liquid or gaseous pool (Chapter 9 [3]). Unique to this facility is the application of solid propellant gas generators (derived from air-bag technologies) with discharge times of 60–600 ms (Chapter 6 [1], [12]). Re-ignition events were also investigated for heated protruding surfaces, which entrain fuel droplets within the downstream recirculation region. It was observed that baffle-stabilized pool fires were more difficult to suppress than baffle-stabilized spray flames. Agent entrainment into the recirculation zone was affected by combustion and the blockage ratio.

Halon-Replacement Liquid Fluids for Fire Suppression

Nongaseous Spray Transport

Liquids with a boiling point above 330 K (e.g., 1-methoxyheptafluoropropane, HFE7000; methoxy-nonafluorobutane, HFE7100; and perfluoro-*n*-hexane, FC-72) and powders have been considered as non-ozone-depleting halogen alternatives. Thermal absorption for liquids is higher per unit volume than gases, resulting in a greater reduction of flame and surface temperatures [13]. Spray transport and entrainment into the surrounding ambient flow is characterized by a high degree of turbulence, high blockage ratios, and significant liquid impingement onto surfaces [14, 15]. The complex dynamics have been characterized using phase Doppler interferometry (Chapter 8 [1]) for a droplet-laden, homogeneous turbulent flow past an unheated and heated cylinder (representing an obstruction). Yoon et al. [16] used these data to develop a simplified phenomenological droplet impact model for use in fire suppression applications (Fig. 42.7 compares the computed droplet transport process over the cylinder to that of the experimental arrangement). Also, particle image velocimetry was used to characterize the 3-D velocity field [17]. As an example, Fig. 42.8 presents the mean streamwise velocity field around the cylinder for seed (1 μm diameter particles generated with a fogging device) and water spray droplets, with an emphasis on the recirculation of droplets in the wake region downstream of the cylinder. Figures 42.9 and 42.10 present the droplet Sauter mean diameter and mean streamwise velocity around the cylinder, using phase Doppler interferometry. Figure 42.9 compares the transport of water droplets over the cylinder at ambient temperature to when preheated to 423 K. Figure 42.10 compares the water spray with two other fluids that have lower boiling points (307 K for HFE7000 and 334 K for HFE7100 [18]). One notes the accelerated flow around the cylinder, as well as the decrease in droplet mean diameter when the cylinder is preheated and the fluid boiling point is decreased. Also, the simulation results in Fig. 42.9 (accounting for droplet impingement on the cylinder surface) compare well with the measurements.

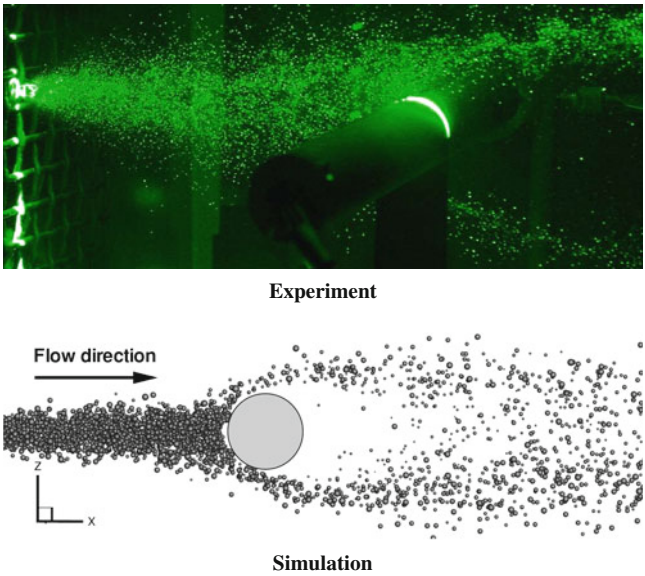


Fig. 42.7 View of the injected water spray over an unheated cylinder for the experiment and simulation [16] (Copyright/courtesy of or (used with permission) Elsevier Publishing Co 2010)

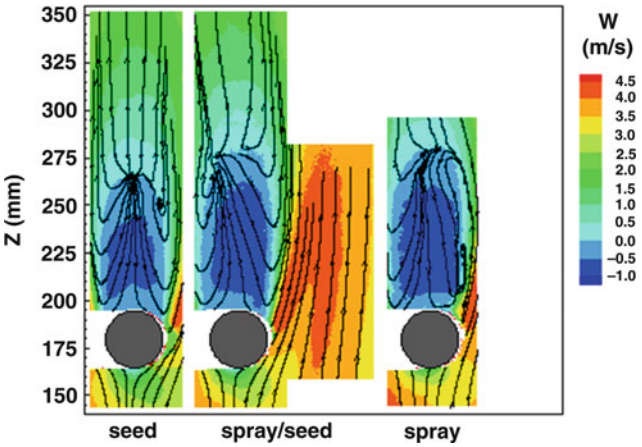


Fig. 42.8 Droplet mean streamwise velocity for varying streamwise position for flow over an unheated cylinder. Contours are stream traces of the in-plane vectors [1]

Figure 42.11 presents the streamlines for the droplet-laden flow past the cylinder, along with a solid and two dashed lines (for different cases when the cylinder is either unheated or heated), each indicating the demarcation between impacting droplets and those entrained in the air flow. Observations are used to determine whether impacting droplets either wet (leading to dripping) or rebound off the

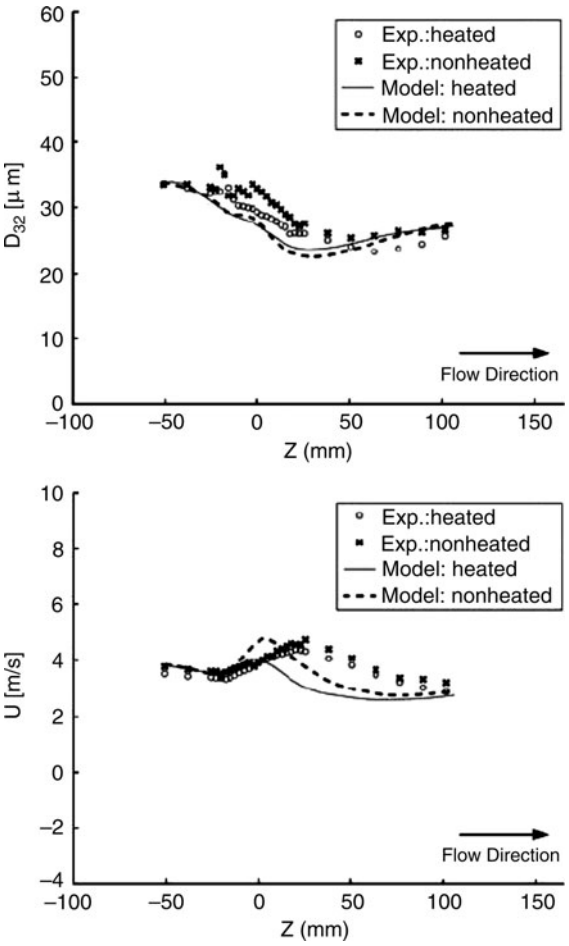


Fig. 42.9 Variation of Sauter mean diameter (D_{32}) and mean streamwise velocity (U) with streamwise position (Z) for an unheated (295 K) and heated (423 K) cylinder. Comparison of model simulations with experimental results [16] (Copyright/courtesy of or (used with permission) Elsevier Publishing Co 2010)

surface. Impingement on a heated surface of water droplets containing sodium acetate trihydrate additive has been shown to have similar physical properties to other known effective fire suppressant salts [19, 20]. Such investigations of droplet impingement dynamics is important since one can conceive of a liquid fire suppressant impacting and cooling a surface, as well as producing vapors that ultimately entrain into and extinguish a fire. Size classification is important since smaller droplets entrain into the air flow (having a higher probability of transport past obstacles), while larger droplets tend to impinge on obstacle surfaces, accumulate and drip off [18]. When individual droplets impact a surface, several post-impact states can occur [16]. The droplet may elastically rebound, it may stick to the surface, or it may shatter. The energetically preferred state depends on the relative surface and kinetic energies along with the viscous dissipation of energy during the impact process. At lower droplet kinetic energies, either sticking or

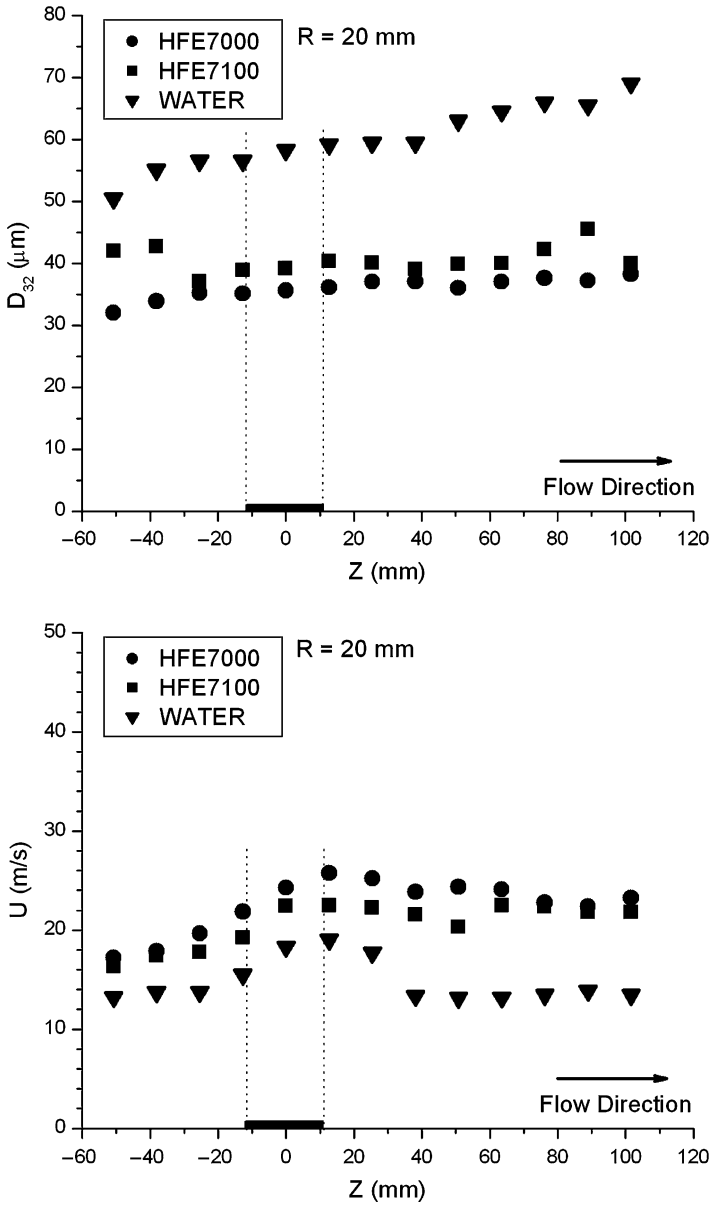


Fig. 42.10 Variation of Sauter mean diameter (D_{32}) and mean streamwise velocity (U) with streamwise position (Z) for different high-boiling-point chemical agents (the horizontal bar and vertical dashed lines represent the location of the cylinder) [1]

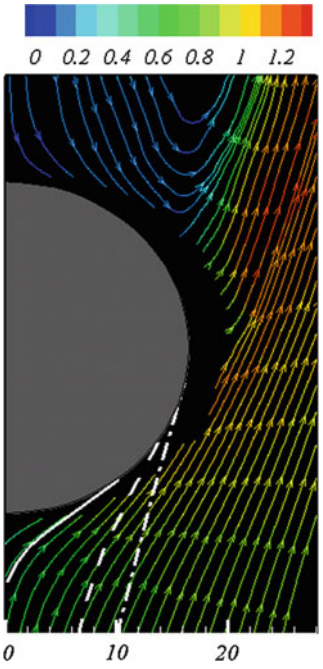


Fig. 42.11 Streamline of droplet-laden air flow over an unheated cylinder. White lines indicate the dividing streamlines separating the flow that impacts the cylinder to that transported around the cylinder surface: *solid* – droplet-laden air flow for unheated cylinder; *dash* – spray droplets for unheated cylinder; *dash*, *dot* – spray droplets for heated cylinder [17] (Copyright/courtesy of or (used with permission) Elsevier Publishing Co 2010)

elastic rebounding occurs, depending on the surface energy relative to the dissipated energy. At higher droplet kinetic energies, splashing (or shattering) occurs when the kinetic energy is distributed among smaller droplets with a higher overall surface energy (relative to the original droplet).

In certain instances, coating of a surface by liquid agent may be considered a positive attribute since the resulting surface cooling inhibits re-ignition. It takes a high obstacle blockage ratio (i.e., obstructed cross-sectional area for an equivalent area encompassing the face of an obstacle) to influence significantly the transport of agent past an obstacle and prevent agent from reaching the flame. Larger droplets tend to move ballistically and smaller droplets entrain into the surrounding aerodynamic flow field. Thus, control of the size distribution, physical properties (e.g., boiling point effects on droplet vaporization), and mixture state (multicomponent and multiphase agents) can result in optimizing droplet transport to locations far downstream of the atomizer and/or behind a close obstacle. Atomizer design must also be considered since it dictates the initial droplet dispersion characteristics.

Powders

Sodium bicarbonate powder ($NaHCO_3$) has been used widely as an effective fire suppressant (Chapter 4 [1], Section 4 [4]), in particular for dry powder fire

extinguishers (other effective powdered chemicals include ammonium phosphate and potassium bicarbonate), and thus has been considered as a replacement agent for Halon 1301. In addition, different aqueous salt solutions of varying concentration have been studied to improve the thermophysical properties of neat water. Examples include the ranking of discrete amounts of injected sodium bicarbonate powder along with other gaseous halogenated hydrocarbons in a turbulent spray flame [5]. Smaller particle sizes were found to be more effective in suppressing a fire and that increased injection pressure enhanced suppression effectiveness by improving powder entrainment within the flame. Injection of finite concentrations of $NaHCO_3$ powder into a liquid-pool, opposed-flow diffusion flame burner (Section 4 [4]) demonstrated that the effectiveness of $NaHCO_3$ on a mass basis was greater than that of Halon 1301, and that effectiveness increased with decreased powder size. Injection of $NaHCO_3$ into a modified cup burner and a turbulent baffle-stabilized spray flame again showed that the suppression effectiveness of $NaHCO_3$ on a mass basis was greater than all other tested agents. In cup burner experiments using laser extinction to monitor particle concentration, as illustrated in Fig. 42.12 [21], three size classes of sodium bicarbonate powder (between 2 and 15 μm) were aerosolized and delivered to both liquid and gaseous flames. The $NaHCO_3$ powder was found to be a highly effective suppressant for the smaller size ranges, whereas the largest size range was more difficult to disperse homogeneously and, as reported by Trees and Seshadri [22] for a counterflow configuration, particle vaporization in the flame was incomplete. The effect of $NaHCO_3$ particle size (for five particle size classes of up to 60 μm) on methane flame extinction was investigated in a non-premixed counterflow burner [23], with laser Doppler velocimetry used to monitor the velocity field. Larger particle size classes were less effective flame suppressants. As an example, results for extinction mass concentration with strain rate are presented in Fig. 42.13 and indicate that the mass required for flame extinction increases for larger particle sizes [24]. The figure for $KHCO_3$ also presents results for Halon 1301 and indicates that particle suppression effectiveness, as compared to CF_3Br, may be enhanced for small enough powder particle sizes. Numerical simulations suggested that particle sizes, which result in complete chemical decomposition before reaching the maximum flame temperature, are more effective in extinguishing flames.

Water Mists

According to the National Fire Protection Association [25], a water mist is defined as a spray having a droplet diameter with a flow-weighted cumulative volumetric fraction at 99 % of less than 1,000 μm at the minimum design operating nozzle pressure. One advantage of using water mists is the reduction in water demand, and as a result collateral damage by water is less severe. Another advantage of water mists is that several modes of fire suppression may be present when using smaller

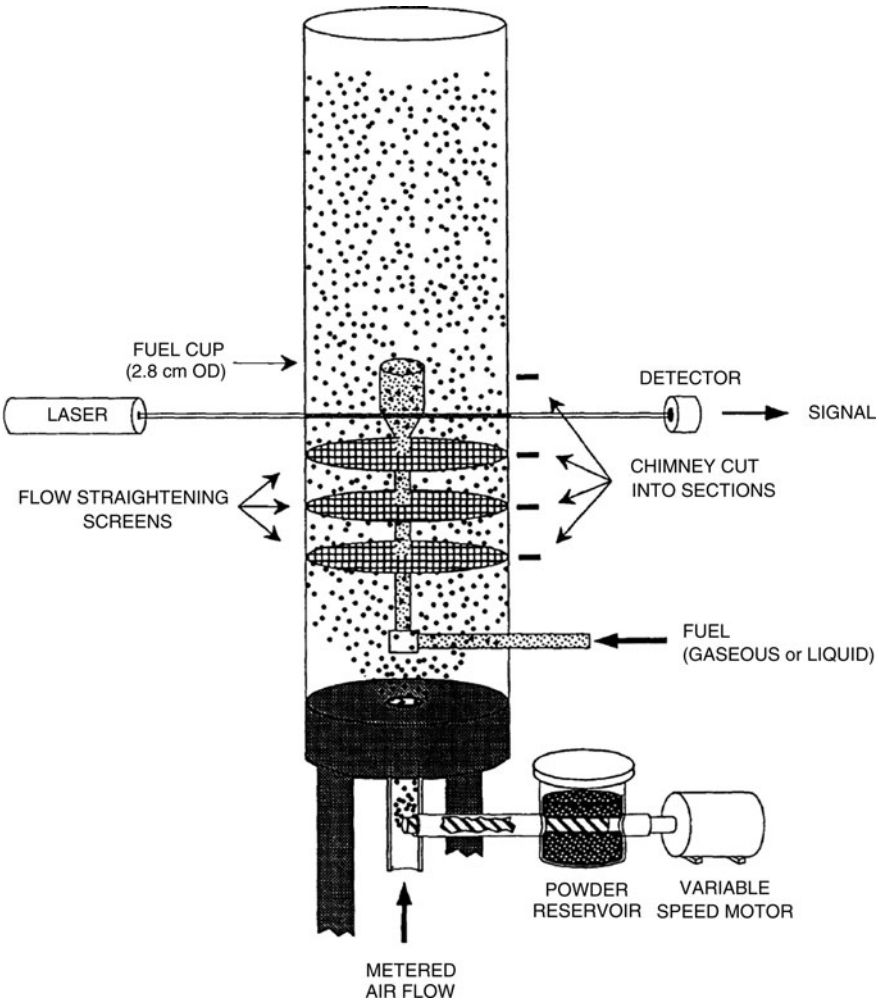


Fig. 42.12 Modified cup burner for delivery of solid powder [4]

water droplets and a concomitant delivery system. As opposed to conventional sprinklers, the predominant suppression mechanisms for water mist systems include, in addition to surface cooling, flame cooling (causing a reduction in flame radiation), dilution of reactants with water vapor (oxygen displacement), radiation blockage and attenuation by water droplets, and possibly flame stretch through momentum transport between the spray and fire plume [26]. Droplet size distribution, flux density, and spray momentum play an important role in determining the fire suppression effectiveness of a water mist system for a specific application.

A water mist can be generated using a high-pressure water jet impinging on a deflector, a high-pressure water jet emerging from a small orifice, or a gaseous media to atomize the water jet (twin-fluid atomization). Other innovative mist

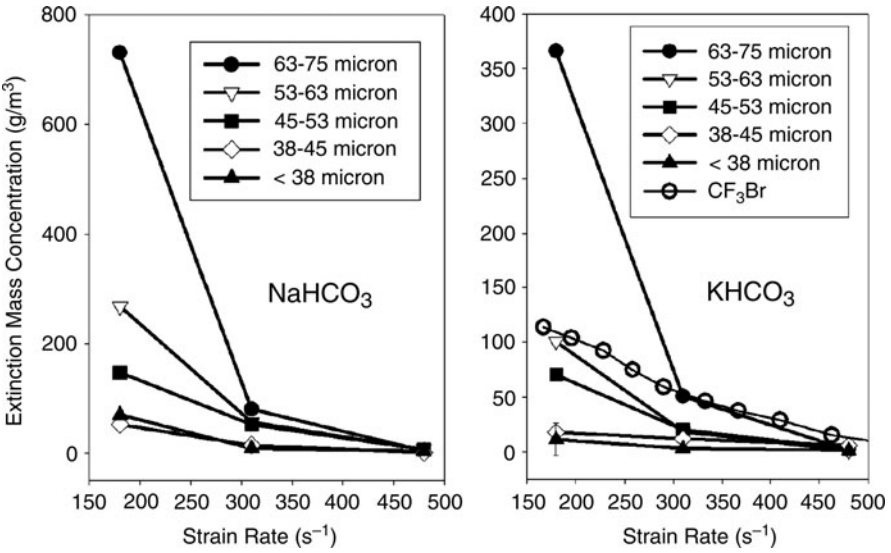


Fig. 42.13 Extinction mass concentration with respect to strain rate for different powder particle sizes in a propane/air, counterflow, non-premixed flame [1]

generation techniques involve the use of ultrasonic transducers and flashing of superheated water [26]. Solid propellant gas generators have also been used as an on-demand pressure source for self-contained portable water mist systems. Some novel techniques, including electrically charged water mist and the use of gas hydrates for self-atomization of water, have been attempted (Chapter 8 [1]). Water mist systems have found fire protection applications in maritime machinery spaces, gas turbine enclosures, marine accommodations, public spaces and service areas, hotels, heritage buildings, art galleries, electrical equipment rooms, computer rooms, wet benches used in semiconductor manufacturing, road tunnels, and aircraft passenger compartments [26]. Feasibility studies have also been conducted for tank crew compartment fire protection applications. The discharge of a Halon-replacement suppressant after a water mist application to a fire was found to have an added benefit of the water droplets acting as scrubbers to mitigate acid gases, and other harmful, corrosive by-products that are formed by reactions with the Halon-replacement agent [27].

Water-mist systems (with droplet sizes less than 100 μm) have been considered as replacements for Halon 1301. Phase Doppler interferometry has been used to characterize various surrogate fluids in misted liquid sprays that are generated by different screens [7, 28, 29]. The effect of mist droplet diameter (< 200 μm), density, and injection angle have shown that when the mist and flame are aligned spatially, flame suppression is enhanced with increased density, decreased velocity, and smaller size droplets [30]. Larger droplets and injection angles become important for asymmetric mist/flame alignment. Efforts to decouple the physical (suppression due to droplet size and dynamics), thermal (due to heat capacity and

latent heat of evaporation), and chemical (due to three-body recombination reactions and a shift in water-gas reactions) effects on suppression for a range of droplet sizes between 5 and 50 μm was carried out numerically in a nonpremixed counterflow methane-air diffusion flame [2, 31]. Mists with smaller droplets (optimally with diameters of 15 μm) and a corresponding larger surface area (with more rapid droplet evaporation), resulted in reduced gas temperatures and effective flame suppression. Water as a suppressant agent was found to suppress flames primarily through thermal effects (about 10 % chemically).

Fire Sprinkler Systems

Fire sprinkler systems are the most commonly used fire protection system. Fire protection with sprinkler droplets focuses on direct extinguishment of burning objects, cooling of the thermal environment, and wetting and cooling of the exposed unburned combustibles to prevent or delay ignition and subsequent fire spread. Cooling of the ambience prevents additional sprinklers from unnecessary activation, thus minimizing water damage to property. Spray dynamics are important in the design and operation of sprinkler systems for fire suppression [32]. Large droplets are transported ballistically to the flame front and wet surfaces, while aerosolized smaller droplets remain suspended in the air. The effectiveness of the sprinkler spray is dependent on the droplet size and velocity distributions, and mass flux.

Sprinkler research has focused on sprinkler droplet formation, water flux distribution, optimization of coverage area, droplet size and velocity distributions, droplet interaction with fire plumes and surfaces, and the delineation of various fire extinguishment and control mechanisms. Various measurement techniques have been employed to characterize sprinkler performance. These techniques include shadowgraphs, optical array probes, particle image velocimetry, particle-tracking velocimetry and imaging, and phase Doppler interferometry. For Phase Doppler interferometry, larger droplet size can be problematic by causing trajectory-dependent scattering errors and significant laser beam attenuation [33]. Another issue relates to the small probe area used in sprays with large coverage areas. Numerical simulations (e.g., zone models by Cooper [34], and field models by Nam [35] and McGrattan et al. [36]) have also been used to model sprinkler performance in the presence of a fire.

Concluding Remarks

Liquids and powdered sprays have been considered as possible replacement agents for Halon 1301 during the past several decades. Delivery of liquid and powdered sprays to a fire or flame, and the suppression effectiveness of these agents, have

been studied in a variety of systems. Model simulations have shown much promise as a tool to study droplet transport and surface impingement in highly obstructed flows. A variety of testing screens have been used successfully to rank the suppression effectiveness of different liquids and powders. Parametric investigations have touched upon the effects of agent physical and chemical properties, liquid breakup, droplet/particle size, velocity, composition, mixing mode, and transport past obstacles, spray pattern, injector design and location, and aerodynamic characteristics, which may ultimately lead to more effective spray delivery systems.

References

1. R. G. Gann, (ed.): Advanced technology for fire suppression in aircraft – final report of the next generation fire suppression program, NIST SP 1069, National Institute of Standards and Technology, Gaithersburg (2007).
2. A. M. Lentati, H. K. Chelliah: Physical, thermal, and chemical effects of fine-water droplets in extinguishing counterflow diffusion flames, 27th Symposium (International) on Combustion, pp. 2839–2846, Combustion Institute, Pittsburgh (1998).
3. R. G. Gann, (ed.): Fire suppression system performance of alternative agents in aircraft engine and dry bay laboratory simulations, NIST SP 890, National Institute of Standards and Technology, Gaithersburg (1995).
4. W. L. Grosshandler, R. G. Gann, W. M. Pitts (eds.): Evaluation of alternative in-flight fire suppressants for full-scale testing in simulated aircraft engine nacelles and dry bays, NIST SP 861, National Institute of Standards and Technology, Gaithersburg (1994).
5. W. L. Grosshandler, G. Gmurczyk, C. Presser: Effectiveness of Halon alternatives in suppressing dynamic combustion processes. In: Miziolek, A.W., and Tsang, W., (eds.) Halon Replacements: Technology and Science, ACS Symposium Series No. 611, Chapter 18, pp. 205–224, American Chemical Society, Washington. (1995).
6. H. Tsuji: Counterflow diffusion flames, Prog. Energy Combust. Sci. 8, 93–119 (1982).
7. J. C. Yang, M. K. Donnelly, N. C. Prive, W. L. Grosshandler: An apparatus for screening fire suppression efficiency of dispersed liquid agents, Fire Saf. J. 36, 55–72 (2001).
8. T. A. Milne, C. L. Green, D. K. Benson: The use of the counterflow diffusion flame in studies of inhibition effectiveness of gaseous and powdered agents, Combust. Flame 15(3), 255–264 (1970).
9. R. G. Gann, J. D. Barnes, S. Davis, J. S. Harris, R. H. Harris Jr., J. T. Herron, B. C. Levin, F. I. Mopsik, K. A. Notarianni, M. R. Nyden, M. Paabo, R. E. Ricker: Preliminary screening procedures and criteria for replacements for Halons 1211 and 1301, NIST TN 1278, National Institute of Standards and Technology, Gaithersburg (1990).
10. W. L. Grosshandler, C. Presser, D. Lowe, W. Rinkinen: Assessing Halon alternatives for aircraft engine nacelle fire suppression, J. Heat Transf. 117(2), 489–494 (1995).
11. A. Hamins, C. Presser, L. Melton: Suppression of a baffle stabilized spray flame by halogenated agents, Proceedings of the Combustion Institute, Vol. 26, pp. 1413–1420, Combustion Institute, Pittsburgh (1996).
12. W. Grosshandler, A. Hamins, K. McGrattan, S. R. Charagundla, C. Presser: Suppression of a non-premixed flame behind a step, Proceedings of the Combustion Institute, Vol. 28, pp. 2957–2964, Combustion Institute, Pittsburgh (2000).
13. P. Andersson, G. Holmstedt: Limitations of water mist as a total flooding agent, J. Fire Prot. Eng. 9, 31–50 (1999).
14. P. J. Disimile, J. R. Tucker, B. Croswell, J. M. Davis: The transport of water sprays past generic clutter elements found within engine nacelles, Fire Saf. J. 40, 65–78 (2005).

15. J. M. Davis, P. J. Disimile: Effect of engine nacelle clutter density on downstream water spray distributions, At. Sprays 18(6), 553–569 (2008).
16. S. S. Yoon, P. E. DesJardin, C. Presser, J. C. Hewson, C. T. Avedisian: Numerical modeling and experimental measurements of water spray impact and transport over a cylinder, Int. J. Multiphase Flow 32(1), 132–157 (2006).
17. C. Presser, G. Papadopoulos, J. F. Widmann: PIV measurements of water mist transport in a homogeneous turbulent flow past an obstacle, Fire Saf. J. 41(8), 580–604 (2006).
18. C. Presser, C. T. Avedisian: Transport of high boiling-point fire suppressants in a droplet-laden homogeneous turbulent flow past a heated cylinder, At. Sprays 16(6), 627–656 (2006).
19. S. L. Manzello, J. C. Yang: On the collision dynamics of a water droplet containing an additive on a heated solid surface, Proc. R. Soc. Lond., Ser. A 458, 2417–2444 (2002).
20. S. L. Manzello, J. C. Yang: An experimental study of high Weber number impact of methoxy-nonafluorobutane $C_4F_9OCH_3$ (HFE7100) and n-heptane droplets on a heated solid surface, Int. J. Heat Mass Transf. 45, 3961–3971 (2002).
21. A. Hamins: Flame extinction by sodium bicarbonate powder in a cup burner, 27th Symposium (International) on Combustion, pp. 2857–2864, Combustion Institute (1998).
22. D. Trees, K. Seshadri: Experimental studies of flame extinction by sodium bicarbonate ($NaHCO_3$) powder, Combust. Sci. Technol. 122:215–226 (1997).
23. H. K. Chelliah, P. C. Wanigarathne, A. M. Lentati, R. H. Krauss, G. S. Fallon: Effect of sodium bicarbonate particle size on the extinction condition of non-premixed counterflow flames, Combust. Flame 134(3), 261–272 (2003).
24. J. W. Fleming, M. D. Reed, E. J. P. Zegers, B. A. Williams, R. S. Sheinson: Extinction studies of propane/air counterflow diffusion flames: the effectiveness of aerosols, Proc. Halon Options Technical Working Conf., Albuquerque, pp. 403–414 (1998).
25. NFPA 750 Standard on water mist fire protection systems, 2006 edition, National Fire Protection Association, Quincy (2006).
26. J. R. Mawhinney: Water mist fire suppression systems. In Cote, A.E., (ed.-in-chief) Fire Protection Handbook (20th ed.), Volume II, Section 16, Chapter 8, NFPA, Quincy (2008).
27. R. S. Sheinson, B. Borman, A. Maranghides, R. Anleitner, P. Gunning: Use of water spray cooling systems in conjunction with HFP (HFC-227ea) to protect shipboard flammable liquid storage rooms, Proc. Halon Options Technical Working Conf., Albuquerque, pp. 447–456 (2001).
28. A. K. Lazzarini, R. H. Krauss, H. K. Chelliah, G. T. Linteris: Extinction conditions of nonpremixed flames with fine droplets of water and water-NaOH solutions, 28th Symposium (International) on Combustion, pp. 2939–2945, Combustion Institute, Pittsburgh (2000).
29. E. J. P. Zegers, B. A. Williams, R. S. Sheinson, J. W. Fleming: Dynamics and suppression effectiveness of monodisperse water droplets in non-premixed counterflow flames, Proceedings of the Combustion Institute, Vol. 28, pp. 2931–2937, Combustion Institute, Pittsburgh (2000).
30. K. Prasad, C. Li, K. Kailasanath: Optimizing water-mist injection characteristics for suppression of coflow diffusion flames, 27th Symposium (International) on Combustion, pp. 2847–2855, Combustion Institute, Pittsburgh (1998).
31. A. M. Lentati, H. K. Chelliah: Dynamics of water droplets in a counterflow field and their effect on flame extinction, Combust. Flame 115(1/2), 158–179 (1998).
32. Crowe, C., Sommerfeld, M., and Tsuji, Y.: Multiphase flows with droplets and particles, CRC Press, New York, pp. 15, 377–378 (1998).
33. J. F. Widmann: Characterization of a residential fire sprinkler using phase doppler interferometry, At. Sprays 12(1-3), 69–90 (2002).
34. L. Y. Cooper: Interaction of an isolated sprinkler spray and a two-layer compartment fire environment, Int. J. Heat Mass Transf. 38, 679–690 (1995).
35. S. Nam: Development of a computational model simulating the interaction between a fire plume and a sprinkler spray, Fire Saf. J. 26, 1–33 (1996).
36. K. McGrattan, H. Baum, R. Rehm, S. Hostikka, J. Floyd: Fire dynamics simulator (version 5) technical reference guide, NIST SP 1018–5, National Institute of Standards and Technology, Gaithersburg (2007).

Index

A
Accommodation coefficients, 317–320, 322–324
Area ratio, 216, 701, 702, 704
Aspiration effect, 841–842
Atomization, 75, 131, 145, 189, 215, 234, 258, 303, 339, 359, 384, 431, 443, 465, 484, 499, 615, 627, 641, 647, 657, 685, 709, 760, 782, 811, 837, 849, 881, 902, 922

B
BEM. *See* Boundary element method
Bending instability of liquid jets, 55–72
Binary drop collisions, 159–164, 171–177, 431–434, 473
Boiling evaporation, 450
Borghi diagram, 281, 282, 291, 303
Bouncing, 110–111, 161, 162, 165, 167–168, 171, 175–176, 190, 198–200, 437, 473, 586, 673, 675, 700
Boundary element method (BEM), 359–378, 630, 641–643
Boundary fitted coordinates, 340
Boundary integral (BI), 29, 340, 346
Breakup, 3, 55, 75, 101, 141, 146, 163, 187, 198, 217, 234, 258, 273, 336, 341, 360, 384, 434, 442, 470, 481, 507, 587, 604, 627, 658, 687, 711, 736, 759, 779, 813, 839, 865, 901, 911
  mode, 147, 148, 150–154, 201, 223, 372, 675–677
  time, 12, 20, 22, 23, 26–28, 31, 33, 37, 42, 89–91, 147, 148, 153, 155, 218, 221–223, 227, 228, 821
Bubble growth, 240–244, 246, 248, 249, 582–585, 901
Buckling of liquid jets, 55–72

C
CAB model. *See* Cascade atomization and drop breakup model
Capillary instability, 3–48, 59, 63–64, 68, 604, 606, 630, 687, 688, 713
Cascade atomization and drop breakup (CAB) model, 224–230
CB. *See* Cocoa butter
Characteristic drop diameter, 479–480
Charged droplets, 127, 131, 159, 374, 375, 613, 620, 730, 743–750
Chemical kinetics, 285–286, 411–412, 831
Chemical reactions, 280–282, 285–291, 295, 300, 318, 384, 388, 401–403, 410–416, 420, 813, 871
Coalescence, 161–169, 174–176, 190, 338, 341, 346, 401, 462–464, 466, 469, 470, 472, 473, 515, 516, 518, 585–586, 608–610, 617, 725, 812–814, 829, 854, 859, 871, 877
Cocoa butter (CB), 230, 332–338
Collision model, 174–177, 409–410, 427, 473
Collisions, 157–177, 203, 273, 354, 384, 401, 405, 409–410, 426–434, 444, 462, 465, 466, 469, 470, 472, 473, 518, 609, 610, 619–620, 647, 812–815, 854, 871, 901, 902
Combustion, 147, 229, 234, 257, 272, 279, 299, 384, 461, 502, 582, 648, 657, 704, 749, 777, 811, 851, 865, 874, 881, 909
Complex geometries, 349, 392, 419, 420, 827–828
Computational fluid dynamics (CFD), 255, 264, 287–289, 291–292, 335, 349, 359–360, 413, 418, 445–446, 470, 472, 473, 492, 493, 831, 859

N. Ashgriz (ed.), *Handbook of Atomization and Sprays*,
DOI 10.1007/978-1-4419-7264-4, © Springer Science+Business Media, LLC 2011

Condensation, 317–320, 322, 323, 406, 484, 856, 861, 863, 874, 901
Cone jet, 246, 376, 730, 733, 735–743, 750
Conservation equations, 134, 227, 264–267, 286, 288, 299, 340, 352, 383–384, 387–390, 393, 394, 397–399, 401–402, 405, 411–412, 415–416, 418–421, 469, 823–824, 889–890
Constitutive equations, 38–39, 44, 47, 390
Corona splashes, 187, 189, 190, 194, 202–205, 443
Correlations, 84, 98, 147, 189, 200, 223, 248, 257, 271, 323, 330, 348, 406, 450, 461, 483, 499, 618, 657, 696, 713, 757, 817, 844, 871
Critical point, 84, 102, 147, 255–259
Crossing separation, 168
Crystallization, 327, 328, 331–335, 886
Cumulative volume fraction, 482–483, 921

D

Damköhler number, 280, 291
Density, 5, 56, 77, 99, 126, 146, 160, 200, 218, 235, 255, 264, 286, 299, 316, 329, 339, 361, 384, 426, 445, 463, 480, 499, 582, 604, 629, 660, 690, 721, 741, 758, 780, 815, 841, 851, 872, 888, 901, 922
Deposition, 190, 200, 442, 444–445, 453, 839, 844, 857, 881
Diffusion flame, 282–285, 299, 303–304, 307–311, 469–472, 886, 913, 921, 924
Direct-injection (DI), 283, 284, 294, 296, 341, 785, 787, 794, 797, 798, 805
Direct numerical simulations (DNS), 16, 21, 259, 301, 355, 356, 392, 398, 490
Discrete polydisperse spray, 609, 615–621
Discrete probability function (DPF), 446, 481, 489–493
Disintegration, 84, 90, 184, 187–191, 193–195, 202, 223, 246, 401, 444, 449, 488, 541, 542, 544, 664–665, 674, 676–678, 689, 813–814, 820, 837–839, 843, 858, 873, 877
  limits, 188, 190, 191
Drag coefficient, 97–119, 148, 149, 217, 227, 406, 409, 661–665, 668–670, 818, 845
Drop
  breakup, 110, 153, 219, 224–230, 384, 401, 409, 482, 490, 491
  collisions, 157–177, 273, 384, 401, 405, 409–410, 431–434, 465, 466, 469, 470, 472, 473, 518, 609, 854
  deformation, 98, 107, 109–112, 115, 118, 119, 148, 154, 223, 225, 227, 384, 408–409
  impact, 361, 366, 431, 436, 442–444, 449, 453
Droplet, 4, 75, 97, 125, 145, 157, 183, 198, 217, 233, 255, 264, 299, 315, 327, 353, 360, 401, 441, 458, 490, 497, 581, 603, 627, 658, 686, 709, 727, 755, 778, 811, 837, 849, 861, 870, 882, 901, 910
  breakup, 193, 207–208, 220, 225, 273, 405, 490, 491, 659, 672, 815, 819–822, 832, 865, 925
  breakup modes, 147, 148, 150–154, 201, 219, 372, 675, 676
  evaporation, 272, 300, 303–305, 308, 309, 311, 315–324, 353, 604, 743, 744, 748, 750, 814, 815, 818, 819, 824–826, 832, 852, 853, 886, 901, 903, 924
  impact, 164, 183–195, 198, 200, 202–204, 206, 444–446, 603–604, 916
  interaction, 98, 116, 118, 119, 158, 159, 164, 176, 184–195, 220, 225, 299, 311, 401, 405, 416, 417, 441–444, 453, 470, 603–604, 620, 794, 822, 826, 924
  oscillation, 98, 109–110, 112, 125–142, 148, 226, 673, 725, 830
  size, 4, 75, 101, 134, 151, 158, 188, 200, 217, 233, 273, 303, 328, 360, 409, 444, 459, 479, 497, 590, 603, 627, 651, 658, 686, 714, 730, 755, 780, 814, 837, 850, 862, 871, 882, 901, 912
  size distribution, 151–152, 226–228, 446, 447, 453, 459, 473, 479–493, 499, 501, 518, 539, 540, 596, 651, 659, 660, 681, 686, 696–700, 721, 722, 759, 789–790, 799, 844, 845, 922
Droplet-on-demand (DOD) droplet generators, 582
Drop size distribution, 151–152, 226–228, 446, 447, 453, 479–493, 540, 651, 759

E

ECM. *See* Emulsion combustion method
Effervescent, 134, 489, 501, 514–519, 533, 534, 542, 565

EHD spray. *See* Electrohydrodynamic (EHD) spray
Electric droplet charging, 608, 609, 619–620, 630
Electrified jet, 43, 55, 60, 67, 69, 361, 366, 373–376, 737
Electrified liquid jets, 67–72
Electrohydrodynamics (EHD) droplet generators, 597
Electrohydrodynamic (EHD) spray, 728
Electrospinning, 60, 67–70
Electrospray (ES), 19, 60, 613, 727–750, 857, 858, 862, 870
Electrospray pyrolysis (ESP), 862
Electrostatic, 70, 361, 374–376, 499, 552–553, 579, 613, 619, 630, 727–729, 731, 733, 734, 742–744, 747, 749, 862–863, 870
Elongational rheology, 41
Empirical drop size distribution, 479–493
Emulsion combustion method (ECM). *See also* Particle production, ECM
  description, 882
  SiO_2 particles, 884
  and SP, 883
Emulsion droplet, vaporization and burning
  gas phase equations
    combustion reaction, 887
    flame front radius, 888
    fractional mass vaporization rate, 888
    internal motion, 886
    total burning rate, 887
  interface model, 889
  liquid phase equations
    boundary and initial conditions, 890
    diffusivity, 890–891
    mass transfer, 889
    mean radial mass velocity, 891
Entrainment, 116, 119, 461, 466, 473, 783, 796, 801, 823, 909, 914, 916, 921
ES. *See* Electrospray
ESP. *See* Electrospray pyrolysis
Evaporating droplets, 272, 273, 276, 300, 303–305, 308, 309, 311, 315–324, 353, 412, 468, 471, 604, 620, 722–723, 743–744, 750, 811, 813–816, 818, 819, 825, 826, 832, 851–853, 857, 886, 891, 903
Evaporation, 118–119, 264–275, 315–324, 743–744, 748, 803, 818–819, 891–893
Extension nozzle, 613, 614

F
Filter expansion aerosol generator (FEAG), 862, 866–867
Finite difference (FD), 339–340, 349, 384, 418
Finite element (FE), 339–340, 345, 349, 359, 360, 384, 418, 817, 830
Finite volume (FV), 339–340, 349, 384, 418, 824
Fire suppression, 471, 472, 909–925
Fixed mesh, 342, 345, 351
Flame extinguishment, 441, 910, 911, 914, 924
Flamelets, 282, 283, 291–292, 815, 816, 831
Flame propagation, 281, 300–305, 307–308, 311
Flame spray pyrolysis (FSP)
  $BaTiO_3$, 874–875
  burner divisions, 870
  dependency, particle size, 871–872
  dominating processes, 871
  experimental setup, 870
  hexagonal $YAlO_3$, 873
  mechanisms, powder production, 877, 878
  particle evaporation, 877
  parts, 870
  silica particles, 875, 876
  size distribution, silica particles, 876
  thermal gravimetric-differential thermal analysis (TG-DTA), 874
  titania and silica powder, 869
  urea addition, precursor, 873–874
  YAG:Ce^{3+} nanoparticles, 873
  Y_2O_3:Eu^{3+} powder, 871
Flame suppression screens, 911, 913–916, 923
Flash atomization, 134, 234, 242, 246–247, 250, 252
Flashing, 134, 198, 233–252, 328, 515, 900–901, 911–913, 922–923
Flash vaporized sprays, 911–913
Flow past a droplet, 99, 101–104, 109, 917
Formation of main and satellite drops, 21, 23, 28, 30–36, 89, 164, 167, 169, 175–177, 434, 486, 630, 738
Free liquid jets, 3–48, 55–72
Free-molecule regime, 317–319, 323
Free surface flows, 172–173, 347, 349, 354
Freezing, 198–200, 202, 206–207, 230, 327–338, 421, 841, 849–859, 882
FSP. *See* Flame spray pyrolysis
FV. *See* Finite volume

G
Gas atomization
  description, 840–841

Gas atomization (*cont.*)
structure and processing, 838
Gaseous environment, 15, 76, 164, 263, 353, 390, 401, 405
Gasoline direct-injection (GDI), 217, 219, 755, 785–794
Gas phase transport, 550–551, 620, 814
Gas turbines, 151, 257, 272, 283, 293, 515, 517, 657, 659, 755, 811–833, 923
GDI. *See* Gasoline direct-injection
Group combustion number, 310, 311

H
HCCI. *See* Homogeneous-charge compression-ignition
Heat transfer, 36, 37, 118, 202, 206, 241, 268–271, 275, 316, 322, 328–333, 335, 384, 408, 417, 442, 444, 449–453, 465, 583, 813, 819, 850, 866, 887, 901
regimes, 192–195, 450
High-pressure injection, 134, 217, 519, 528, 787, 788, 791, 796–799, 804
Homogeneous-charge compression-ignition (HCCI), 803–805
Hydraulic, 17, 499, 503, 520–530, 559, 569, 703, 798, 799, 910, 914, 915
Hydrodynamic instability, 234, 636

I
Ignition, 228, 280, 283, 284, 287–290, 401, 411–414, 462–466, 650, 785, 796, 803, 804, 916, 920, 924
Immersed boundary (IB), 341, 342, 351–352
Immiscible liquids, 158, 159, 167–169, 595, 597, 606, 889, 890
Impinging jet atomization, 685–704
Injection, 84, 217, 247, 255, 283, 336, 354, 369, 434, 441, 460, 517, 562, 629, 647, 657, 685, 709, 777, 828, 913
Ink-jet printing, 21, 553, 586–588, 604, 620, 625, 630
Interacting drops, 97, 116–118, 175, 444
Interactions, 26, 55, 76, 98, 137, 151, 157, 184, 220, 299, 311, 322, 342, 360, 384, 425, 441, 458, 516, 603, 654, 659, 689, 764, 780, 814, 838, 859, 877, 909
Interface tracking, 340–342, 345, 347, 353, 354
Interfacial flow modeling, 339–342
Interfacial instabilities, 426, 437
Ion source, 750

J
Jet breakup, 4–5, 12, 17, 20, 25, 33, 38, 40, 41, 61, 84, 169–170, 220, 228–229, 258, 434–436, 443, 507, 604, 609, 613, 615, 618, 659, 676, 713, 751
Jet drag coefficient, 661–663
Jet in cross flow, 526, 651, 657–682, 796
Jet instability, 5, 9, 20–28, 36, 77, 85, 630, 711, 736
Jet penetration, 258, 434, 464–465, 651–653, 658–660, 662, 665, 670–673, 681–682, 794

K
Karlovitz number, 280, 282, 283
Kelvin–Helmholtz Rayleigh–Taylor (KH-RT) model, 220–222
Knudsen regime, 319–324

L
Large eddy simulations (LES), 259, 354, 384, 393–395, 398–401, 403, 406, 410, 491, 796, 813, 815–817, 820–823, 826, 828, 830–432
Latent heat, 194, 234, 243, 268, 270, 275, 328–335, 407, 408, 450, 818, 866, 887–888, 903, 923–924
Lattice–Boltzmann method (LBM), 172, 353, 354, 425–437
Lattice–Boltzmann (LB)simulation, 171–173, 354
LBM. *See* Lattice–Boltzmann method
LBsimulation. *See* Lattice–Boltzmann simulation
LES. *See* Large eddy simulations
Level set (LS), 171, 341, 344, 349–351, 353, 354
Linearized instability sheet atomization (LISA), 217–218
Linear stability theory, 17, 19, 47, 60–61, 66–67
Liquid jet, 3, 55, 76, 215, 246, 258, 354, 360, 434, 464, 506, 595, 604, 627, 657, 715, 741, 782, 857, 862, 901
Liquid sheet instability, 75–93
LISA. *See* Linearized instability sheet atomization
Log-hyperbolic distribution, 483, 491, 493
Log-normal distribution, 249, 446, 449, 453, 482, 483, 490, 844
Low-pressure spray pyrolysis (LPSP)
agglomeration, primary crystals, 866
atomizer, 862, 863, 866–867

colloidal nanoparticles, 865
experimental setup, 862
indium tin oxide (ITO) nanoparticles, 865
industrial applications, 866–867
nanoparticle formation mechanism, 863, 866
nickel oxide (NiO) particles, 863, 864
one-droplet-to-one-particle (ODOP) principle, 861–863
operation pressure and carrier gas flow rate, 863–864
organic precursors, 865
quantitative mathematical model, 866
reactor air pressure reduction, 862
submicron particles, 863, 866
yttrium oxide (Y_2O_3):Eu particle, 864–865
Low-temperature combustion, 284, 293, 803–806, 863
LPSP. *See* Low-pressure spray pyrolysis
LS. *See* Level set

M
MA. *See* Melt atomization
Marker and cell (MAC), 341, 345–347, 349
Mass spectrometry, 373, 749–750
Maximum entropy formalism (MEF), 152, 481, 484–489, 491–493
Medical aerosols, 899–906
MEF. *See* Maximum entropy formalism
Melt atomization (MA)
atomizer and processing parameter
aspiration effect, 842
gas, classification, 840
gas velocities, 841, 842
supersonic, 841, 842
two-fluid atomizer designs, 840–841
breakup and powder morphology
liquid sheet, disintegration, 843
mechanical disturbances, 843
molten metals, 843
spheroidization time, 844
classification
considerations, selection, 840
water and oil atomization, 840
cooling rates and microstructure, 846–847
droplet flow dynamics
drag coefficient, 845
velocity variation, 846
gas atomization, 837–838, 840–843, 846, 847
kinetic energy, 839
particle size distribution
geometric standard deviation, 844–845
mass median diameter, 844
mass probability density function, 844
principle, 839
Metered dose inhaler, 900
Microfluidic droplet generators, 595–597
Micro-solution droplets, evaporation and evolution
density, 891
droplet radius, 892–893
mass, solute, 892
solute concentration, 886
Miscible liquids, 166–168
Mixing, 113, 255, 280, 305, 390, 461, 513, 582, 647, 685, 756, 778, 813, 910
Mixing-controlled combustion, 284–285, 289–290, 465
Modulated jet excitation, 615
Molten metal droplet impact, 621
Momentum ratio, 507, 651, 662–665, 667–668, 670–671, 673, 701–702
Monodisperse droplet stream, 605, 607, 609, 612
Monodisperse spray, 307, 471, 472, 608, 611, 612, 615–619, 738
Multihole orifice, 607–608, 612, 618
Multiple drop impacts, 443, 444, 449, 453

N
Nanoparticles, 110, 115, 515, 679, 856–858, 862–867, 871, 873–875, 877, 881–884
Navier–Stokes simulation, 171, 172, 813
Nebulizer, 764–770, 853, 854, 863, 870–872, 902–906, 913
Newtonian and rheologically complex liquids, 38–48, 63–65
Newtonian drops, 145–154
Newtonian fluids, 155, 384, 390
Nonlinear theory, 20, 21, 26, 28, 61–63, 66
Non-Newtonian drops, 152–155, 158, 170, 489
Nozzle hole shapes, 460, 466, 607, 617, 789
Nozzles, 3, 66, 75, 108, 134, 215, 233, 284, 354, 457, 491, 497, 553, 559, 582, 604, 625, 659, 686, 709, 755, 778, 814, 837, 870, 921
Nucleation, 234, 236–240, 242, 259, 327–328, 331–332, 450, 464, 582–586, 866, 871, 875, 877, 881, 883, 886, 894
Nukiyama–Tanasawa distribution, 483, 485–486, 488
Number distribution function, 304, 480, 486
Nusselt number, 270, 271, 275, 330, 335, 408, 818, 819

O
Ohnesorge number (Oh), 6, 7, 18, 22, 23, 25, 27, 29–31, 85, 129, 146–148, 152, 160, 164, 185, 221, 224, 430, 432–434, 437, 534, 568, 605–607, 618, 711, 713, 720, 722, 760, 817, 820, 829
One-droplet-to-many-particles (ODMP)
  description, 873
  particle evaporation, 877
One-droplet-to-one-particle (ODOP) principle, 861–863
Oscillation, liquid droplets
  decay time constant, 127
  frequency shift, 127
  internal circulations, 130–131
  inviscid drop, potential functions, 125, 126, 128
  second mode, 128–131
  small viscosity, frequency, 127, 128
  surface pressures and curvature, 126
  temporal variation, 130
  third mode, 129, 130
"Oscillation mode", 77, 126, 127, 129–131, 219, 830

P
Particle production, ECM
  divisions, 881–882
  micro-solution droplets, 882, 883, 885–886, 891–893
  powder
    barium titanate, 884, 885
    scenarios, 883
    SiO_2 particles, 884
    Si precursor, 884
    water treatment, 885
  spray techniques, 882
  theory and equations
    equilibrium saturation (ES), 886
    evaporation and evolution, micro-solution droplets, 891–893
    fuel fraction, emulsion droplet, 885
    particle evolution, 893–894
    vaporization and burning, emulsion droplet, 886–891
PDF. *See* Probability density function
Penetration distance, 311, 465, 662, 802, 803
PFI. *See* Port-fuel injection
Pharmaceutical aerosols, 899–906
Piezoelectric droplet generators, 166, 167, 586–593, 595, 610
Pintle, 506, 647–654, 778–780
Pneumatic droplet generators, 593–595
Pollution modeling, 293–296
Port-fuel injection (PFI), 777–780, 783, 785, 787, 791, 793, 794
Powder production, 328, 837, 839, 840, 849, 859, 870, 877, 881–885
Pressure atomizer, 459, 465, 488, 625, 628, 629
Primary and secondary atomization, 145, 146, 148–151, 190, 193, 195, 215–218, 223, 225, 370, 372–373, 445–450, 453, 490, 491, 493, 518, 519, 528, 565, 659, 671, 811, 814, 819, 839, 843
Probability density function (PDF), 151, 172, 228, 273, 292–293, 384, 405, 410, 420, 446, 448, 479–481, 484, 486, 489, 490, 492, 493, 844
  combustion models, 292–293

Q
Quasi-one-dimensional equations, 16–19, 21–22, 45, 47, 56–60, 63, 66, 70
  dynamics of liquid jets, 18, 21–22, 56–60, 66, 70

R
RANS. *See* Reynolds–averaged Navier–Stokes
Ranz–Marshall correlation, 272, 330, 407–408
Rapid prototyping, 621
Rayleigh charge limit, 736, 742, 744–747
Rayleigh-type jet break-up, 604, 605, 607, 613
Recalescence, 329, 331, 332
Reflexive separation, 162–168, 171, 174, 175, 177
Representative diameter, 481, 482, 486–489, 492, 493
Respiratory drug delivery, 901
Reynolds-averaged Navier–Stokes (RANS), 384, 393–396, 398–403, 410, 415, 416, 418, 813
Rheologically complex liquids (pseudoplastic, dilatant and viscoelastic polymeric liquids), 38–48, 63–65
Rocket injector, 640, 650, 698
Root-normal distribution, 151–153, 482
Rosin–Rammler distribution, 218, 446, 482, 483, 487, 491
Rotary, 459, 499, 514, 536, 538–549, 573–576

S
Satellite droplets, 4, 20–22, 28–35, 163, 164, 167, 169, 170, 175–177, 198–200, 202, 203, 206, 207, 366–368, 587, 588, 590, 630

Sauter mean diameter (SMD), 151, 195, 249, 250, 252, 370, 447, 448, 461–466, 468–469, 471, 472, 481, 498, 503, 505–506, 508–511, 513, 514, 516–519, 524, 525, 527, 528, 534–537, 540–547, 549, 551, 559, 565–566, 568, 621, 642–643, 696, 783, 784, 788–790, 796, 797, 802, 916, 918, 919
SD. *See* Spray drying
Secondary atomization, 145, 146, 148–151, 153, 189–195, 217, 223, 225, 370, 372–373, 442–443, 445–450, 453, 491, 493, 518, 519, 527–528, 565, 569, 671, 811, 814, 819, 843
SFD. *See* Spray freeze drying
Shear stripping model, 150, 223–224
Sheet, 75, 110, 126, 146, 198, 217, 246, 282, 351, 415, 443, 484, 502, 585, 604, 647, 658, 685, 709, 755, 779, 812, 842
  thickness, 75, 85, 91–93, 218, 484, 687, 692, 696, 697, 699, 714–719, 721, 722, 757, 759, 761–763
Small and finite perturbations, 4, 9, 10, 14, 19–21, 40, 44, 59–65, 69–70
Small perturbations, 3, 4, 9, 10, 20, 44, 70, 75
SMD. *See* Sauter mean diameter
Smoothed-particle hydrodynamics (SPH) simulation, 172–174
Solder ball production, 610–611
Solidification, 19, 70, 151, 206, 327–338, 401, 610–611, 621, 838, 843, 844, 846, 847
Source terms, 273, 286, 295, 299–300, 343, 348, 352, 397, 402–403, 405, 409–411, 415–416, 420, 421, 431, 484–486, 488, 492, 816, 825
SP. *See* Spray pyrolysis
SPH simulation. *See* Smoothed-particle hydrodynamics simulation
Splash plate nozzle, 246, 247, 709–725, 854
Spray drying (SD)
  hollow particle formation, 849, 852, 855–856
  industrial process, 859
  nanoparticles production
    dilute solution, usage, 857
    electrospraying, 857, 858
    initial droplet size, 856–857
    microexplosion, 857–858
    techniques, 857
  particle size, 856–857
  powder characteristics
    evaporation rate, 853
    generators, 854
    gradient, concentration, 852
    hollow particle formation, 855, 856
    mathematical models, 850
    non-dimensional droplet diameter variations, 852
    pressure buildup, 855–856
    process temperature, 851
    sodium chloride, 854–855
    solute concentration profile, 851
    zirconia, 853–854
  and spray pyrolysis, 849–859
  ultrasonic atomization, 859
Spray flow simulation, 174, 177
Spray freeze drying (SFD), 849–859, 882
Spray modes, 301–302, 310, 732–743
Spray PDF, 273, 405, 420
Spray pyrolysis (SP)
  evaporation rate, 853
  hollow particle formation, 856
  low-pressure (*See* Low-pressure spray pyrolysis)
  nanoparticles production, 856–858
  particle size, 856–857
  steps, zirconium hydroxychloride (ZrO(OH)Cl), 850
  ultrasonic atomization, 859
  zirconia powders, 853, 854
Sprays, 75, 98, 134, 148, 158, 219, 233, 263, 279, 300, 333, 383, 425, 442, 457, 479, 501, 563, 607, 628, 651, 690, 724, 731, 757, 777, 815, 859, 899, 910
Spray transport, 273, 405, 916–920
Spread, 110, 184, 186–189, 191, 193, 198, 200–207, 246, 257, 258, 302, 304, 331–332, 352, 361, 443, 487, 493, 502, 522, 531, 533, 539, 553, 658, 666, 672, 673, 677, 690, 709, 711, 719, 738, 755, 757, 796, 828–829, 839, 845, 924
Sprinklers, 520, 539, 710, 922, 924
Stability, 16, 18–19, 41, 43, 44, 47, 56, 60–61, 66, 67, 134, 138–142, 158, 163, 164, 174, 235, 236, 332–333, 367, 371, 421, 430, 431, 434, 436, 483, 489, 491–492, 515, 516, 518, 607, 613, 617, 627, 628, 632, 635, 641, 642, 649, 651, 738–740, 744, 750

Statistics, 114, 235, 238, 292, 304, 370, 393, 445–449, 453, 473–474, 481, 484, 499, 519, 642, 795, 815, 822, 823, 826, 828
Stochastic discrete particle method, 420
Stochastic models, 292, 481, 490–491, 819–823, 827, 828
Stretching separation, 162–168, 171, 172, 175–177
Supercooling, 236, 300–301, 328–329, 331, 332
Supercritical, 255–260
  injection, 256, 258–260
Surface
  capturing, 341
  tension, 3, 56, 76, 98, 125, 185, 198, 216, 240, 255, 360, 408, 445, 499, 559, 581, 604, 660, 690, 721, 728, 760, 817
  topography, 188, 190, 191, 195
  tracking, 171, 346, 347, 360, 363
Swirl, 38, 217, 258, 367, 370, 371, 391, 459, 462, 465, 488, 499, 503, 520, 523, 529–238, 542, 560, 570–572, 643, 648, 755–770, 784–789, 791, 796, 812, 813, 823, 828–829
  nozzles, 499, 503, 520, 523, 529–538, 542, 570–572, 755–758, 763

T
TAB model. *See* Taylor analogy breakup
Taylor analogy breakup (TAB) model, 154, 218–220, 225, 227, 409, 666, 814
Taylor cone, 72, 375, 613, 728–729, 733–734, 736, 738, 741–743, 857
Thermal induced atomization, 195
Thermal or bubble jet droplet generators, 582–586
Thermocapillarity, 36–37
Thermodynamics, 147, 185, 209, 235–236, 238, 255, 258, 259, 268, 353, 390, 430, 449, 450, 453, 484, 749, 803, 889, 894
Thickness, 76, 107, 154, 187, 189–191, 194, 201–204, 206, 208, 217, 218, 280–282, 291, 300, 303, 343, 350–352, 369, 437, 444, 450, 484, 502, 503, 505, 506, 513, 528, 534, 536–537, 549, 559, 560, 564, 569, 572, 578, 583, 584, 617, 629, 632–633, 636, 640, 641, 643, 661, 666, 692, 693, 759–760, 778, 854, 855, 885, 886
Three dimensional instability of liquid sheets, 91–93, 451
T-jet nozzle, 763–764
Transcritical injection, 255–260
Turbulence, 215, 216, 247, 280–282, 289–291, 301, 384, 390–404, 406, 415–417, 462, 470, 481, 525, 567, 629, 635–636, 640, 660–661, 665, 674–675, 677–678, 681, 697, 702, 703, 759, 785, 796, 799, 813, 817, 820–822, 841, 913, 916
Twin fluid, 464, 488, 497–521, 530, 533, 534, 539, 540, 546–550, 561, 576–577, 579, 763–764, 839, 859, 922
Twin fluid atomization. *See* Melt atomization
Two-phase atomization. *See* Melt atomization

U
Ultrasonic, 361, 488, 499, 539–540, 549–552, 578, 764–765, 768, 840, 841, 859, 863, 870–872, 904, 906, 922–923
Unified spray breakup (USB) model, 223–224, 409
Upper limit distribution, 482, 483
USB model. *See* Unified spray breakup model

V
Variable-density gas jets, 257–259
Vibration mesh nebulizers, 764–770, 853, 854
Viscoelastic polymeric liquids, 39, 44–45, 64, 155, 170, 515
Viscosity, 3, 56, 76, 99, 127–128, 146, 160, 185, 199, 219, 255, 274, 280, 330, 339, 360, 390, 427, 445, 489, 582, 604, 630, 660, 687, 711, 731, 759, 816, 845, 891, 903
Viscous sheets, 76, 80–81, 83, 714, 720, 761
VOF. *See* Volume of fluid
Volume distribution, 468, 480, 482–483, 487–488
Volume of fluid (VOF), 171, 255, 340–341, 344, 345, 347–349, 353, 354, 360, 377, 446, 763
Volume tracking, 344

W
Water mists, 471, 472, 921–924

Weber number (We), 6, 20, 30, 31, 35, 77, 79–82, 84, 86, 89, 90, 93, 109, 110, 146, 149, 160–177, 185, 189, 191, 194, 200, 206, 219, 223–226, 228, 242, 248, 249, 251, 252, 361, 367–368, 372, 377, 432–433, 437, 445, 447, 490, 491, 513, 515, 525, 534, 536, 540, 541, 544, 545, 563, 564, 567, 568, 607, 640, 660, 662, 665, 670–671, 673, 675–677, 680, 689–690, 695, 713–714, 746–747, 819–821, 829–831, 866
Wettability, 184, 185, 187, 188, 195, 200–201, 208, 373